Second Edition

Ductile Design of STEEL STRUCTURES

Michel Bruneau Chia-Ming Uang Rafael Sabelli

Ductile Design of Steel Structures

About the Authors

Michel Bruneau, Ph.D., P.Eng., is Professor in the Department of Civil, Structural, and Environmental Engineering at the State University of New York at Buffalo, and an ASCE Fellow. He is a member of various AISC and CSA committees developing seismic design specifications for bridges and buildings. Dr. Bruneau has conducted extensive research on the evaluation and retrofit of existing steel structures subjected to large destructive forces. He has authored more than 400 technical publications and has received many awards for his work.

Chia-Ming Uang, Ph.D., is Professor in the Department of Structural Engineering at the University of California, San Diego. A member of the AISC's Committee on Specification and Committee on Research, he received the AISC Special Achievement Award in 2007. Dr. Uang has authored numerous articles on seismic behavior and design of steel structures.

Rafael Sabelli, S.E., is a Principal and Director of Seismic Design at Walter P. Moore and Associates, Inc., and was President of the Structural Engineers Association of California from 2009 to 2010. He is a member of the AISC Task Committee on the Seismic Provisions for Structural Steel Buildings and the ASCE 7 Seismic Subcommittee. Mr. Sabelli is the coauthor of *AISC Design Guide 20: Steel Plate Shear Walls* as well as of numerous research papers on conventional and buckling-restrained braced frames.

Ductile Design of Steel Structures

Michel Bruneau, Ph.D., P.Eng.
Chia-Ming Uang, Ph.D.
Rafael Sabelli, S.E.

Second Edition

New York Chicago San Francisco
Lisbon London Madrid Mexico City
Milan New Delhi San Juan
Seoul Singapore Sydney Toronto

The McGraw-Hill Companies

ISBN 978-0-07-162523-4
MHID 0-07-162395-7

The material in this eBook also appears in the print version of this title: ISBN 978-0-07-162395-7, MHID 0-07-162395-7.

Contents

This page intentionally left blank

Preface

The first edition of *Ductile Design of Steel Structures*, published in 1998, arrived at a time when the structural design practice was undergoing important changes. Most significantly, the impact of the Northridge and Kobe earthquakes was still being felt in the engineering community, and substantial shifts in philosophy for the seismic design of steel structures were underway. This led to numerous and frequent changes to the relevant seismic design and detailing provisions for steel structures in many codes and design standards—all while the United States completed the process of unifying its three major regional model design codes into the International Building Code (first published in 2000, and eventually adopted by all states and most municipalities in the country), and while the American Institute of Steel Construction (AISC) unified its Load and Resistance Factor Design (LRFD) and Allowable Stress Design (ASD) requirements into a single specifications.

Although these whirlwind changes made the first edition a timely document in 1998, they also progressively left it in need of an update sooner than expected. Even though the fundamental principles and structural behaviors emphasized throughout the first edition of this book remained valid, design principles and examples were anchored in specifications that had changed in a number of subtle ways over time (more so than is typically the case from one code cycle to another). With publication of the AISC 2010 Seismic Provisions and of the 2009 CSA S16 Standard for the Design of Steel Structures, crystallizing the knowledge developed in the prior 15 years on this topic (and becoming more similar to each other in content and design philosophy), and with the evolution of code changes foreseen to return to a more regular pace—barring another major earthquake that would challenge design wisdom—publication of a revised second edition of *Ductile Design of Steel Structures* is again timely.

Two audiences were kept in mind when writing this book: practicing engineers and graduate students. With respect to the first audience, engineers are nowadays exposed to a wide range of professional development opportunities, and day courses on seismic design of steel structures are common. Similar information is also scattered over the World Wide Web (albeit covering the same topic with various degrees of technical rigor, depending on the source). This widely available and accessible information has been helpful to dispel the erroneous belief that the ductile nature of structural steel directly translates into inherently ductile structures, but a first introduction to the topic of ductile design usually leaves the engineer with many questions on the origin of many design requirements and strategies to achieve ductile structural behavior. With respect to the second group, although seismic design is not part of most undergraduate civil engineering curricula, substantial opportunities exist for graduate learning on this topic. Nowadays, most graduate structural engineering programs in North America offer a general seismic design course, often complemented by specialized courses on the design of ductile concrete and ductile steel structures, and textbooks that comprehensively cover design aspects related to this topic are needed.

In that perspective, the second edition of *Ductile Design of Steel Structures* is intended to serve both as a reference textbook on this topic and as a resource document providing breadth and depth in support of graduate and professional education opportunities. It aims to help senior undergraduate and graduate students, as well as professionals, design ductile steel structures in an informed manner. It summarizes the relevant existing information on this topic (often scattered in research reports, journal articles, and conference proceedings) into chapters on material, cross-section, component, and system response, providing useful guidance and design examples while presenting the concepts and key research results supporting the rationale underlying many of the current design principles. It is written starting from the assumption that the reader has background knowledge of conventional (nonseismic) steel design.

The emphasis of this book is on earthquake-resistant design because providing ductile structures is crucial to ensure seismic survival. However, there exist many other important applications of the principles and design approaches outlined in this textbook. For example, knowledge of how to design and detail steel structures to achieve ductile behavior is vital to ensure the satisfactory performance of structures exposed to other extreme events, such as blast forces, and to prevent their progressive collapse—two topics pushed to the forefront by the September 11, 2001 events. Other possible applications of ductile steel design include offshore structures subjected to extreme wave and ice loads, as well as bridges that can now be designed to carry normal traffic using an alternative bridge design procedure (the Autostress method) that relies heavily on ductile response and requires a good understanding of the shakedown theory. Likewise, for existing construction, plastic analysis can provide a much better estimate of a structure's actual strength than procedures based on elastic analysis, which in turn can be used advantageously to minimize the extent of needed rehabilitations—an important advantage given that the rehabilitation of existing buildings is a growing market in North America, as part of the revitalization activities taking place in many city centers of seismic and nonseismic regions (as a consequence of either commuters' frustrations, the aging North American infrastructure, the projected North American population growth patterns, the goals of historical or heritage building preservation, and/or other societal trends). Thus, although the focus of this text is earthquake engineering, the information presented herein is broadly applicable to the ductile design of steel structures.

For its second edition, this book has been substantially expanded as follows:

- Three entirely new chapters have been added, to respectively address the design of buckling-restrained braced frames (Chapter 11) and steel plate shear walls (Chapter 12), and to review some hysteretic energy dissipating systems and design strategies that have been the subject of growing interest and proposed to achieve the objective of ductile design (Chapter 13). The latter chapter addresses structural fuses, hysteretic energy dissipating devices, bimetallic friction, rocking, and self-centering systems; it replaces the former Chapter 11 that only provided a cursory overview of passive energy dissipation.
- The previous chapter on braced frames has been completely rewritten, to eliminate obsolete and/or ambiguous information and, more importantly, to reflect the substantial changes and new developments that have taken place and have been implemented in the AISC and CSA design requirements since the last edition of this book. Concentrically braced frames and eccentrically braced frames are now each covered in separate chapters. Each chapter provides thorough insights into the knowledge on those topics that has led to the current design provisions and corresponding capacity design procedures.
- The chapter on moment-resisting frames has been substantially expanded, to reflect the major changes and developments in design requirements that have taken place since 1997.
- Chapter 2 has been expanded to include additional information and new knowledge on steel's high-temperature properties, strain rate effects, k-area fractures, strain aging, and stress corrosion, as well as information on fatigue and ductility of corroded shapes, yielding mechanism, new steel grades, and low-cycle fatigue modeling. It also includes a new section on hysteretic models, which provides much needed information for the nonlinear

inelastic analyses more frequently required by specific engineering projects nowadays.

- Chapter 3 (on cross-section properties) has been revised to address biaxial bending, introduce layer models (required for some nonlinear analyses), and add information on plastic strength of concrete-filled steel tube cross-sections.
- Chapter 4 (on plastic analysis) has been expanded to introduce yield line analysis, which is important for calculation of connections' ultimate strength and resistance to out-of-plane loads (such as blast loads).
- Chapter 6 (on applications of plastic analysis) has been expanded to address global versus local ductility demand and some other important code-related issues.
- To better link with Chapters 8 to 13, focused on earthquake engineering applications, Chapter 7 (formerly Chapter 9) has been entirely rewritten, focusing on the basic principles to relate seismic design forces and corresponding ductile demands in structures.
- New design examples in Chapters 8 to 12 have been developed in compliance with the AISC Seismic Provisions (ANSI/AISC 341-10) and Load and Resistance Factor Design, and from a practicing engineering perspective. Note that the examples in the first edition of this book approached seismic design as a secondary design step called "ductile design" (coupled with "drift-control design" in the special case of moment-resisting frames), which consisted of a design iteration starting with the results from a first design step accomplished using conventional steel design principles in nonseismic applications (called "strength design"). That two-step approach is still valid and the examples contained in the first edition remain instructive in many ways. However, the publication by the American Institute of Design Construction of design aids for seismic design has made seismic design more expeditious, eliminating the benefits of the two-step approach. Therefore, this second edition contains only new design examples consistent with this new context.
- Self-study problems have been provided for most chapters; these could be assigned to students by instructors using this book as a textbook—note that all of the problems are former assignment or exam questions I gave to students at the University at Buffalo or the University of Ottawa. Partial solutions to the problems will eventually be accessible to instructors via a password-protected link posted on the website www.michelbruneau.com.

- Chapter 14 is the only chapter that remains unmodified since the first edition. While interesting research has been conducted since the mid-1990s on the topics covered in this chapter, it has not resulted in changes to the seismic design provisions at the time of this writing.

The authorship of this second edition reflects these numerous changes in scope, breath, and structure. I sincerely thank my coauthors for helping to bring this project to fruition, namely Chia-Ming Uang (Professor, University of California, San Diego) for writing most of Chapters 7, 10, 11, and 14, and Rafael Sabelli (Structural Engineer, Walter P. Moore, Oakland, CA) for developing the design examples at the end of Chapters 8 to 12 and contributing parts of Chapter 11. The challenges of bringing to life a second edition that is twice the length of the first can be overwhelming, and their commitment and contributions are gratefully acknowledged.

From a graduate curriculum perspective, the resulting expanded textbook provides enough material to support two graduate courses: a first course on plastic analysis and design, using the material in Chapters 2 to 6, and a second course on the seismic design of steel structures based on Chapters 7 to 13. However, another effective approach is to use some aspects of all chapters as part of a single graduate course, covering only the essential aspects of Chapters 2 to 6 needed to understand the capacity design in support of the material presented in Chapters 7 to 12 (or 7 to 10 for shorter academic terms), leaving the rest of the material for future self-study in answer to project needs or for professional development purposes. Other combinations also are anticipated, reflecting the preferences and teaching styles of various instructors.

Finally, suggestions and general feedback on this book are always welcome (including e-mails confirming that there are people in this world reading book prefaces). A list of errors brought to the authors' attention will be compiled into an errata list eventually posted on the website www.michelbruneau.com, until fixed by the publisher in subsequent printings.

Michel Bruneau, Ph.D., P.Eng.

CHAPTER 1
Introduction

In the context of structural engineering, a "ductile" material is one that is capable of undergoing large inelastic deformations without losing its strength. More formally, the *Metal Handbook of the American Society for Metals* (ASM 1964) defines "ductility" as "the ability of a material to deform plastically without fracture." "Brittleness," on the other hand, is the "quality of a material that leads to crack propagation without plastic deformations." In that perspective, structural steel is the most ductile of the widely used engineering materials. This advantageous property of steel is often implicitly used by design professionals. For example, many simple modern connections must plastify to perform as intended by the designer, and large ductile deformations are sometimes relied upon to provide early warnings of unexpected overloads. Many such beneficial incidental effects of plasticity are already integrated into steel design requirements and design practice.

However, there are many situations in which an explicit approach to the design of ductile steel structures is necessary because the inherent material ductility alone is not sufficient to provide the desired ultimate performance. For example, in nearly all buildings designed today, survival in large earthquakes depends directly on the ability of the framing system to dissipate energy hysteretically while undergoing large inelastic (i.e., plastic) deformations. To achieve this ductile response, one must recognize and avoid conditions that may lead to brittle failures and adopt appropriate design strategies to allow for stable and reliable hysteretic energy-dissipation mechanisms.

This sort of thinking is relatively new in structural engineering. Indeed, many practicing engineers have believed for years, albeit incorrectly, that steel structures were immune to earthquake-induced damage as a consequence of the material's inherent ductile properties. However, earthquake engineering research since the late 1970s has clearly demonstrated that special care must be taken to ensure ductile structural behavior. Moreover, numerous steel structures suffered damage during the Richter magnitude 6.8 Northridge (Los Angeles) earthquake of January 17, 1994 and the Richter magnitude 7.2 Kobe (Japan) earthquake that occurred, coincidentally, exactly one year later (January 17, 1995). Both earthquakes occurred in highly developed urban areas in nations known for their leadership in earthquake engineering, and both confirmed previous research findings that material ductility alone is not a guarantee of ductile structural behavior when steel components and connections can fail in a brittle manner (e.g., AIJ 1995; Bruneau et al. 1996; EERC 1995; EERI 1995, 1996; Tremblay et al. 1995, 1996). In particular, these earthquakes raised important concerns regarding the ductile behavior of some standard beam-to-column moment connections (as described in Chapter 8).

Fortunately, most of the body of knowledge on the design of ductile steel structures to resist earthquakes has been implemented in structural steel design codes and standards worldwide. Before 1988, there were no specific code regulations for detailing seismic-resistant steel structures in North America, but in the years since many new codes and standards detailing regulations have been introduced to ensure ductile response during earthquakes. And, as a side benefit, many other applications (e.g., offshore oil platforms) have benefited from the new knowledge on the ultimate cyclic behavior of steel structures generated by earthquake engineers, and from the recent emphasis on ductile design requirements for earthquake resistance.

The road to design and detailing of ductile structures has been a long one. A comprehensive historical description of this evolution is beyond the scope of this book. Nonetheless, an overview is worthwhile to help appreciate how the past has shaped today's structural engineering practice.

From a materials perspective (Timoshenko 1983), work on the plastic behavior of ductile metals can be traced back at least to the 1860s, with observations by Lüder that visible lines appear on the surface of specimens stretched beyond their elastic limit, as well as some mathematical papers by Tresca in 1868 and Saint-Venant in the 1870s. Bauschinger reported the first results from inelastic cyclic tests of mild steel coupons in 1886 and subsequently tested (with Tetmajer) short columns buckling in the inelastic range, which led to the development of an empirical column-strength equation that became widely used throughout Europe at that time.

In the first half of the 20th century, researchers investigated the plastic properties of steel and of steel cross-sections subjected to various stress conditions, with experimental work reported as early as 1914 by some sources (ASCE 1971). Much of that activity took place in Germany. In particular, the law of plastic behavior most commonly used in structural steel, the Huber-Hencky-Mises yield condition (also known as Von Mises yield criterion), results from work conducted by these researchers in 1904, 1913, and 1925, respectively (Popov 1968). The 1950s and 1960s witnessed a phenomenal growth of research activity in this area (ASCE 1971). Active research groups in England and the United States, complemented by valuable contributions by researchers in other countries, spearheaded the development and perfected the tools of plastic analysis and design in structural engineering, with the intent of providing a possible replacement for the allowable stress method (also known as working stress method), which was perceived as fraught with shortcomings and limitations. Extensive analytical and experimental research was conducted on the ultimate strength of members as well as on entire structural frameworks, henceforth establishing plastic design as a viable alternative design procedure. During those decades, a few buildings were designed using plastic design principles, and special provisions for plastic design were introduced in many structural steel design specifications (such as those of the American Institute of Steel Construction and Canadian Institute of Steel Construction, among many) and remain to this day.

However, until the end of the 1960s, research on plastic design did not address earthquake-induced loads. Consequently, when earthquake-resistant design became a major concern in some parts of the world, the field started to grow in two seemingly opposite directions as a result of diverging research interests. On one hand, for researchers not concerned with design for earthquakes, research focused on developing better models of member behavior, with a considerable effort being placed on understanding the requirements for member and structural stability. Plastic strength was perceived as the special case to which a member stability problem converges when proper bracing is provided. Out of that research endeavor evolved ultimate design methods (i.e., the Load and Resistance Factor Design and Limit States Design), in use at the time of this writing, that rely on elastic structural analysis but consider plasticity at the member level when determining ultimate member capacities. On the other hand, in the second research direction, emphasis was placed on developing design and detailing requirements that could ensure stable plastic behavior under the extreme cyclic inelastic deformation demands resulting from severe earthquake excitations. From that perspective the development of ductile details for steel construction was paramount, and stringent requirements were enforced to avoid (or make as ductile as possible) stability-related failures. From that research effort evolved ductile detailing requirements for earthquake engineering applications.

Interestingly, the two research paths seem destined to meet in the near future. For example, capacity design and push-over analyses (which are expressions of full-structure plastic design, as shown in Chapter 6) are being frequently conducted now as part of earthquake engineering projects, while engineers involved in nonseismic applications are advocating advanced analysis and design methods that recognize the ultimate capacity of structures, as well as of members. In some areas, the convergence of the two paths has already begun (Fukumoto and Lee 1992).

The design of steel structures for ductile response requires (1) material ductility, (2) cross-section and member ductility, and (3) structural ductility (it is generally preferable to protect connections against yielding, although in some instances such as with semirigid connections, connection ductility may be unavoidable and substitute for member ductility). Further, a hierarchy of yielding must be imposed on a structure to ensure a desirable failure mode. The material presented in this book follows this order.

Chapter 2 focuses on the structural steel material, with a particular emphasis on its desirable ductile properties as well as factors that can have a negative impact on that behavior, such as temperature, notch toughness, steel strength, strain rate, and material thickness and welding-related problems, such as hydrogen embrittlement, weld restraints, and lamellar tearing. The cyclic elastic-plastic behavior of common steels is described through various material models, and some of the advantages of plastic analysis over elastic analysis are illustrated by an example.

In Chapter 3, element ductility is reviewed through descriptions of the plastic strength of cross-sections subjected to axial force, flexure, shear, torsion, and combinations thereof. The influence of residual stresses, strain-hardening, and some other factors on cross-sectional strength is discussed.

Chapters 4 and 5 present plastic analysis at the structural level: the concepts of simple plastic analysis are enunciated and demonstrated in the former, and systematic methods of plastic analysis for more complex structures are formulated in the latter. The fundamental upper bound, lower bound, and uniqueness theorems of plastic analysis are presented in Chapter 4, together with the classical step-by-step method, equilibrium method, and kinematic method whose applications are illustrated by examples. Chapter 4 concludes with a presentation of the shake-down theorem. Methodical determination of the plastic collapse load of structures using direct combination of mechanisms and the method of inequalities are presented in Chapter 5.

A few nonseismic applications of plastic design are described in Chapter 6. These include the plastic moment redistribution method, the Autostress design method, the capacity design strategy, and the push-over (nonlinear static) analysis method.

Emphasis on earthquake engineering applications begins with Chapter 7, where basic principles to relate seismic design forces and corresponding ductile demands in structures are presented. These concepts are at the root of the seismic design procedures adopted in various design codes worldwide, and of the ductile design philosophy outlined in the subsequent chapters.

Chapters 8 to 12 address the five most commonly used earthquake-resistant ductile structural steel systems, namely, moment-resisting frames, concentrically braced frames, eccentrically braced frames, buckling-restrained braces, and steel-plate shear walls, respectively—the latter two having been implemented more recently in North American seismic design provisions. For each structural system, fundamental plastic cyclic behavior is thoroughly described to ensure a good understanding of the philosophy supporting the code requirements and the advantage of a well-defined hierarchy of yielding. Evolution of respective design requirements is also provided, as appropriate, to provide useful perspective in projects dealing with existing structures designed to earlier (now obsolete) ductile detailing design requirements. Each chapter concludes with a detailed design example.

Chapter 13 focuses on some special energy dissipation strategies of interest that have been proposed to achieve the objective of ductile design, and that have been the subject of a growing interest, namely, structural fuses, hysteretic energy dissipating devices, bimetallic friction, rocking, and self-centering systems. An overview of the fundamental behavior, advantages, limitations, and possible concerns for these various systems provides the reader with an introduction to a field that is the subject of much on-going research and that promises new applications for ductile steel structures.

Additional general detailing requirements that are needed to ensure satisfactory plastic behavior are presented in Chapter 14, along with research findings on this topic.

Chapters 2 to 13 also include some suggested problems for further self-study.

Although some other types of ductile steel structures are not covered in this book, it is believed that the information presented herein will provide the reader with sufficient background to successfully tackle analysis or design problems related to most types of ductile steel structures.

Note that various design provisions and standards from the American Institute of Steel Construction (AISC) and Canadian Standard Association (CSA) are referenced throughout this book. The general AISC "Specifications for Structural Steel Buildings" is often referenced by its acronym AISC 360-xx, where xx refers to the last two digits of the publication year of a specific edition. Likewise, the AISC "Seismic Provisions for Structural Steel Buildings" are AISC 341-xx. Because these documents are accredited by the American National Standards Institute (ANSI), they are also sometimes equivalently referenced as ANSI/AISC 360-xx and ANSI/AISC 341-xx. The CSA standard "Design of Steel Stuctures," which includes seismic design and detailing provisions, is referenced as either S16-xx or CSA/S16-xx. In conjunction to these steel design documents, seismic forces and loads are typically obtained from the American Society of Civil Engineers (ASCE)'s "Minimum Design Loads for Buildings and Other Structures" (SEI/ASCE 7-xx) or the National Building Code of Canada (NBCC-xx). In all cases, when the suffix "xx" is dropped, the citation typically refers to the document generically, or to its latest edition, depending on context.

With respect to terminology, note that "strength," "capacity," and "resistance" are at times used interchangeably here, the first term being used in U.S. practice (Load and Resistance Factor Design), the last one being used in Canadian practice (Limit States Design). Some international codes use both "capacity" and "resistance" as related by a capacity reduction factor. From an international perspective, due consideration of the context in which these terms are used in this book will eliminate the risk of confusion.

Finally, given the global economy, it is assumed here that practicing engineers are familiar with both S.I. units and U.S. units; while equivalencies have sometimes been provided in the text, this has not been done consistently, both for brevity and because conversion factors are widely available online. The design examples, being in compliance with the AISC Seismic Provisions, use U.S. units.

References

AIJ. 1995. *Preliminary Reconnaissance Report of the 1995 Hyogoken-Nanbu Earthquake* Architectural Institute of Japan: Tokyo. Nakashima, M., and Bruneau, M., editors of English Edition.

ASCE. 1971. *Plastic Design in Steel—Manual and Reports on Engineering Practice, No. 41.* American Society of Civil Engineers: New York.

ASM. 1964. *The Metal Handbook*, vol. 2, 8th ed. Materials Park, OH: American Society for Metals.

Bruneau, M., Wilson, J. C., and Tremblay, R. 1996. "Performance of Steel Bridges During the 1995 Hyogoken-Nanbu (Kobe, Japan) Earthquake." *Canadian Journal of Civil Engineering*, vol. 23, no. 3, 678–713.

EERC. 1995. *Seismological and Engineering Aspects of the 1995 Hyogoken-Nanbu (Kobe) Earthquake*. Earthquake Engineering Research Center, Report UCB/EERC-95/10. Berkeley, CA: University of California at Berkeley.

EERI. 1995. *The Hyogoken-Nanbu Earthquake, January 17, 1995: Preliminary Reconnaissance Report.* Oakland, CA: Earthquake Engineering Research Institute.

EERI. 1996. *Northridge Earthquake Reconnaissance Report*, vol. 2. Earthquake Spectra, Supplement C to Vol. 11. Oakland, CA: Earthquake Engineering Research Institute.

Fukumoto, Y., and Lee, G. 1992. *Stability and Ductility of Steel Structures under Cyclic Loading*. Boca Raton, FL: CRC Press.

Popov, E. P. 1968. *Introduction to Mechanics of Solids*. Englewood Cliffs, NJ: Prentice-Hall.

Timoshenko, S. P. 1983. *History of Strength of Materials*. New York: Dover Publications.

Tremblay, R., Bruneau, M., Nakashima, M., Prion, H. G. L., Filiatrault, A., and DeVall, R. 1996. "Seismic Design of Steel Buildings: Lessons from the 1995 Hyogoken Nanbu Earthquake." *Canadian Journal of Civil Engineering*, vol. 23, no. 3: 727–756.

Tremblay, R., Timler, P., Bruneau, M., and Filiatrault, A. 1995. "Performance of Steel Structures during the January 17, 1994, Northridge Earthquake." *Canadian Journal of Civil Engineering*, vol. 22, no. 2: 338–360.

CHAPTER 2
Structural Steel

2.1 Introduction

For the first half of the 20th century, there was essentially only one type of structural steel widely available in North America: Grade A-7 steel. (Although the names A-7 and A-9 were used for bridges and buildings before 1939, the two steels were virtually identical.) By the early 1960s, engineers needed to be familiar with five different types of structural steel, but they were likely to use only one or two for all practical purposes. However, with today's exponential growth of technology (and opening to the world's global market), the engineer is offered a "smorgasbord" of steel grades, and many engineers in some parts of North America already do not hesitate to commonly use two or more different steel grades for the main structural members in a given project.

Despite this growth in available products, the minimum requirements specified for structural steel grades remain relatively simple. They generally consist of a few limits on chemical composition, limits on some mechanical properties such as minimum yield and tensile strengths, and minimum percentage elongation prior to failure (definitely not very challenging for metallurgical engineers accustomed to dealing with the comprehensive lists of performance requirements specified for the steels needed in some specialty applications). As a result, in the last few decades, a wide variety of steel grades that meet the simple set of minimum requirements for structural steel has been produced. These steels will be adequate in many applications, but from the perspective of ductile response, the structural engineer is cautioned against hastily using unfamiliar steel grades without being fully aware of how these steels perform under a range of extreme conditions.

To increase this awareness, as well as to provide some fundamental material-related information for the design of ductile structures, this chapter reviews some of the lesser known properties of steel, along with information on the modeling of plastic material behavior.

2.2 Common Properties of Steel Materials

2.2.1 Engineering Stress-Strain Curve

Most engineers will remember testing a standard steel coupon in tension as part of their undergraduate studies and obtaining results similar to those presented in Figure 2.1, where the stress-strain curves for various structural steel grades tested at ambient temperature are plotted. For reference, engineering stress, σ, is calculated as the ratio of the applied force, P, to the cross-sectional area, A, and engineering strain, ε, is equal to $\Delta L/L$, where ΔL is the elongation measured over a specified gauge length, L. As shown in Figure 2.1, the operations necessary to achieve higher yield strengths [such as alloying or quenching and tempering (Van Vlack 1989)] generally reduce the maximum elongation at failure and the length of the plastic plateau. For the structural steels used in rolled shapes today, these side-effects are negligible as sizable plastic deformation capacity remains beyond yield. The stress-strain curve for a uniaxially loaded steel specimen can therefore be schematically described as shown in Figure 2.2, with

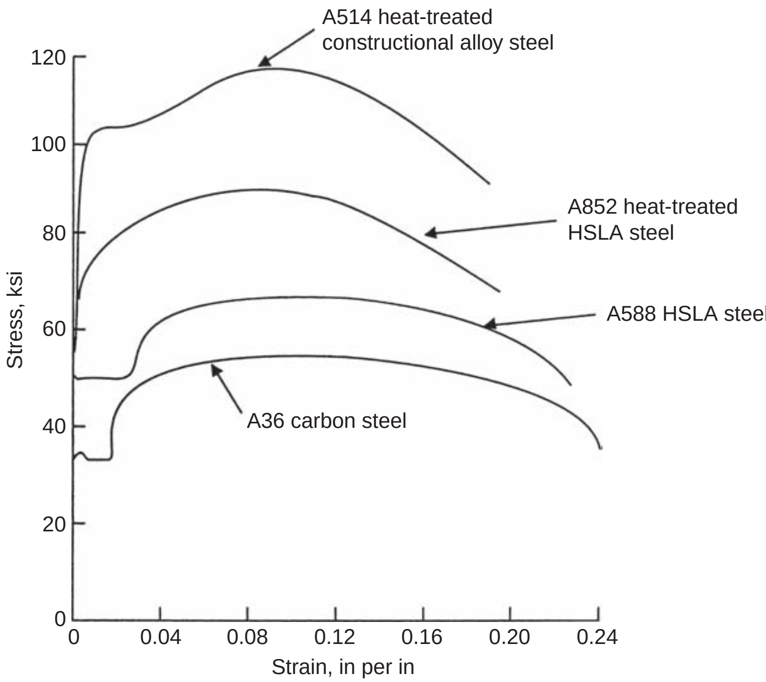

Figure 2.1 Stress-strain curves for some commercially available structural steel grades at ambient temperature. (*From R.L. Brockenbrough and F.S. Merritt*, Structural Steel Designer's Handbook, *2nd ed, 1994, with permission of the McGraw-Hill Companies*.)

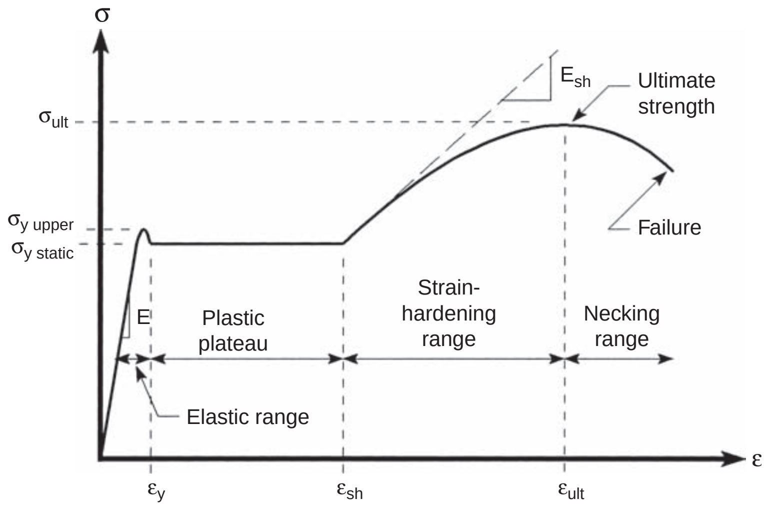

FIGURE 2.2 Schematic representation of stress-strain curve of structural steel.

an elastic range up to a strain of ε_y, followed by a plastic plateau between strains ε_y and ε_{sh}, and a strain-hardening range between ε_{sh} and ε_{ult}, where ε_y, ε_{sh}, and ε_{ult} are the strains at the onset of yielding, strain-hardening, and necking, respectively. Depending on the steel used, ε_{sh} generally varies between 5 to 15 ε_y, with an average value of 10 ε_y typically used in many applications. For all structural steels, the modulus of elasticity can be taken as 200,000 MPa (29,000 ksi), and the tangent modulus at the onset of strain-hardening, E_{sh}, is roughly 1/30th of that value, or approximately 6700 MPa (970 ksi); AISC (1971) reports E_{sh} values ranging from 4827 to 5655 MPa (700 to 820 ksi) for various steels (i.e., $E/40$ to $E/35$) , whereas Horne and Morris (1981) and Neal (1977), respectively cite values of $E/20$ and $E/25$. More recently, Byfield et al. (2005) computed an average value of 2700 MPa (i.e., E/75) from the stress-strain curves of 50 mill tests from UK steel producers, which is practically equal to the value of 2552 MPa (370 ksi) used by Lay and Smith (1965).

The Poisson's ratio, υ, which relates a material's transverse strain contraction under an applied axial strain elongation, is 0.3 for steel in the elastic range. When metals behave in a purely plastic manner, they preserve their volume (as first observed by Bridgman 1923, 1949a, 1949b), corresponding to a Poisson's ratio of 0.5 (i.e., incompressible materials). Following the stress strain curve for steel, Poisson's ratio in the plastic range, υ^p, is given by (Khan and Huang 1995):

$$\upsilon^p = \frac{1}{2} - \left(\frac{1}{2} - \upsilon\right)\frac{E'}{E} \tag{2.1}$$

where E' is the effective tangent modulus (see Section 2.4). Per this equation, in the elastic range, $E' = E$, and $\upsilon^p = \upsilon = 0.3$, and for $E' = E/30$ at the onset of strain-hardening, $\upsilon^p = 0.49$, approaching 0.5 as E' further decreases at larger strains.

Note that some applications (such as nonlinear finite elements analysis programs) require that the material properties be described in terms of true stress and strains (i.e., calculating stresses using the actual cross-section taking into account the Poisson effect, and strains using the actual length after elongation), rather than engineering stresses and strains (calculated using the initial cross-sectional area and length). These values can be obtained by the following relationships:

$$\sigma_{True} = (1 + \varepsilon_{Engineering})\,\sigma_{Engineering} \tag{2.2a}$$

$$\varepsilon_{True} = \ln(1 + \varepsilon_{Engineering}) \tag{2.2b}$$

by assuming that the volume of steel under consideration remains the same, such that the product of the initial length and area equals that of the instantaneous length and area. The resulting true stress versus true strain relationship is not symmetric, because the cross-section increases in compression and decreases in tension. Furthermore, these equations are only valid until the onset of necking, beyond which they would need to be corrected using actual measurements of cross-section measured during coupon tests. Hence, unless unavoidable due to the requirements of a specific application, and because reduction of cross-section is small until necking, engineering stresses and strains are generally used for most practical purposes.

2.2.2 Effect of Temperature on Stress-Strain Curve

The shape of the stress-strain curve varies considerably at very high and very low temperatures. The yield and ultimate strengths of steel, as well as its modulus of elasticity, drop (while maximum elongation at failure marginally increases) as temperature increases, as shown in Figures 2.3 and 2.4. This drop is relatively slow and not too significant up to 500°F (260°C), and is almost linear until these properties reach approximately 80% of their initial value, at a temperature of approximately 800°F (425°C). Beyond that point, weakening and softening of the steel accelerates significantly.

A number of equations that capture this behavior for different types of structural steel are presented in documents concerned with fire resistance (AISC 2005, ASCE 1992, ECCS 2001, NIST 2010). Finite element nonlinear analyses simultaneously accounting for fire spread within a structure and high-temperature degradation of the structural system require rigorous modeling of the steel properties. Such analyses can be simplified by assuming a constant coefficient of thermal expansion, α, of $7.8 \times 10^{-5}/°F = 1.4 \times 10^{-5}/°C$ (exact value varies

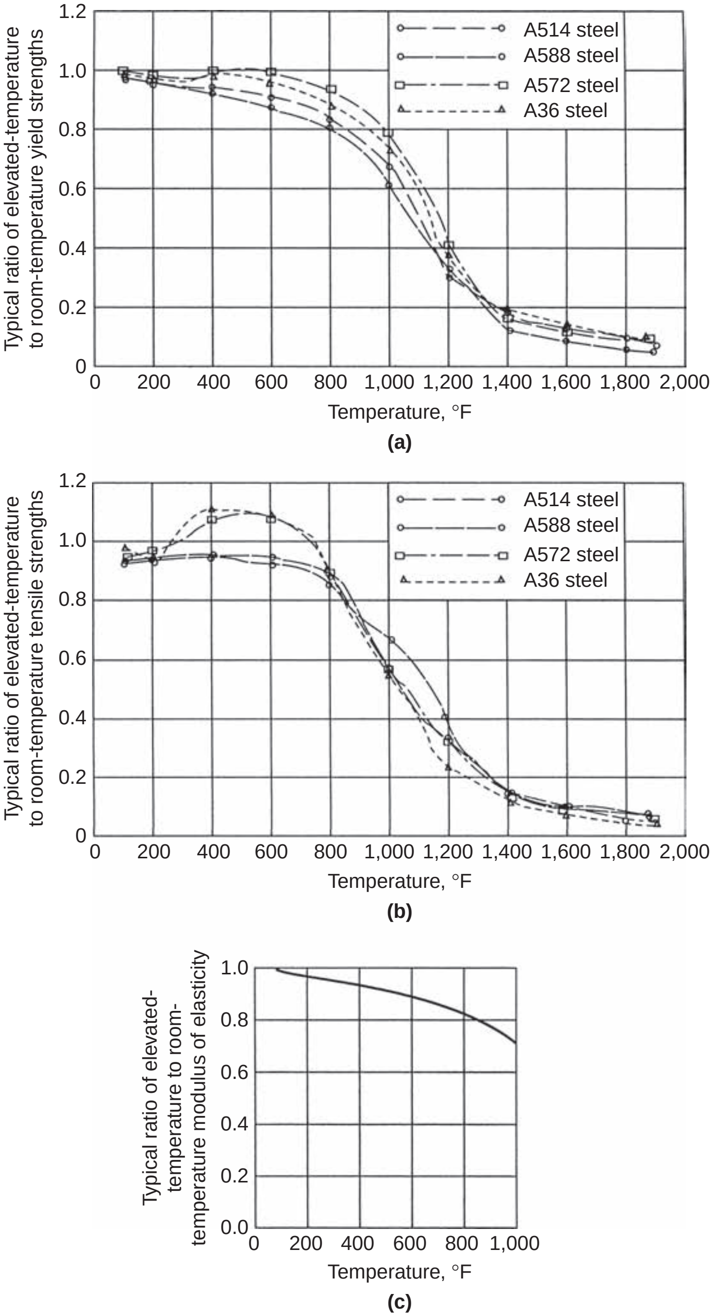

FIGURE 2.3 Effect of temperature on (a) yield strength, (b) tensile strength, and (c) modulus of elasticity of structural steels. (*From R.L. Brockenbrough and B.G. Johnston,* USS Steel Design Manual, *with permission of U.S. Steel.*)

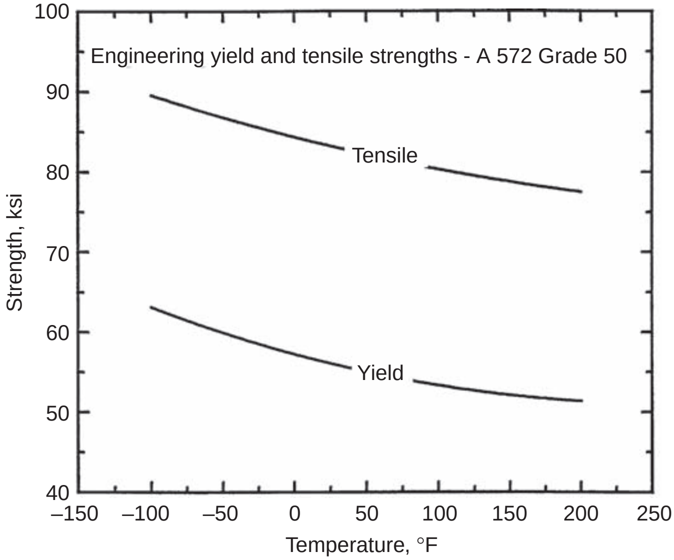

(a)

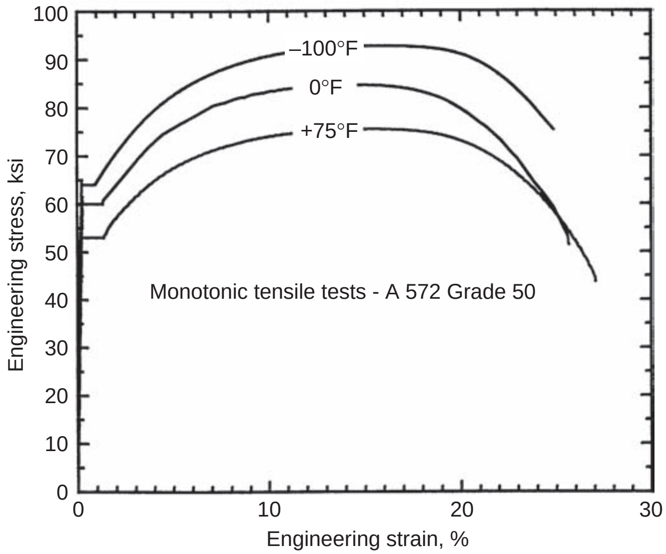

(b)

Figure 2.4 Examples of (a) yield and tensile strength and (b) stress-strain curves versus temperature. Composite curves constructed from data taken from several heats of ASTM A572 Grade 50 plate on the order of 1 in thick. (c) Elevated temperature stress-strain relationships of Eurocode 3. (d) Comparison of engineering stress-strain relationships proposed by NIST and by Eurocode 3 with data generated by NIST for the World Trade Center forensic investigation (NIST 2010). (*Figures a and b courtesy of H.S. Reemsnyder, Homer Research Laboratory, Bethlehem Steel Corporation, with permission. Note: The data in Figure 2.4 (a) and (b) should not be considered typical, maxima, or minima for all plates and rolled sections of this grade. Properties will vary with chemistry, thermomechanical processing, thickness, and product form.*)

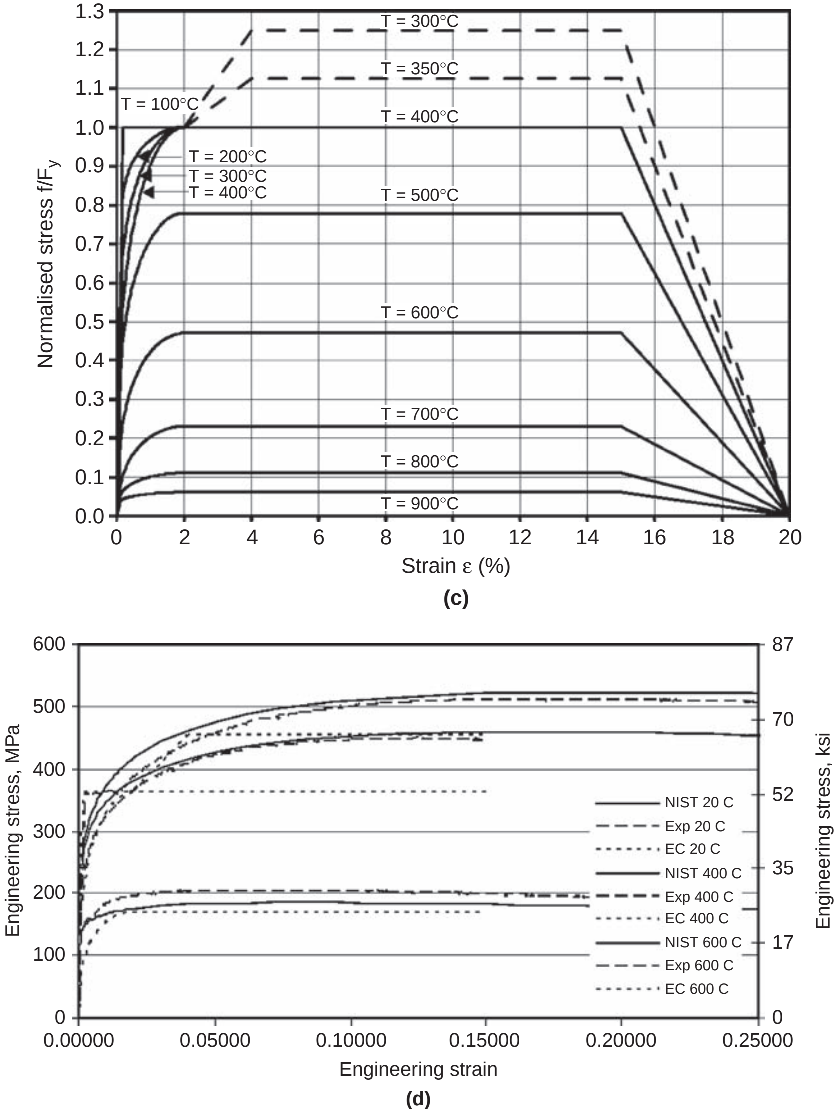

Figure 2.4 (*Continued*)

from 1.2 to 1.8 × 10^{-5}/°C from 20 to 700°C), and conservative values of 600 J/kg°C and 45 W/m°C for the specific heat and thermal conductivity properties of steel, respectively (NIST 2010). The complete stress-strain model adopted by the Eurocode 3 for this purpose (and replicated in tabular format in the AISC Specifications) is shown in Figure 2.4c. Eurocode permits consideration of strain-hardening at lower temperatures (shown by the dotted line in Figure 2.4c) only if advanced finite element models that reflect the state-of-the-art in fire analysis are used.

In its forensic study of the collapses of the World Trade Center towers, the National Institute of Standards and Technology (NIST) also developed the following equation by best fit to experimental data on steels having specified yield stresses ranging from 250 MPa (36 ksi) to 450 MPa (100 ksi), in which temperature is expressed in °C.

$$\sigma = K\varepsilon^{\eta} \tag{2.3}$$

where

$$K = (734 + 0.315F_Y)\exp\left[-\left(\frac{T}{575}\right)^{4.92}\right] \tag{2.4}$$

and

$$\eta = (0.329 - 4.23 \times 10^{-4} F_Y)\exp\left[-\left(\frac{T}{637}\right)^{4.51}\right] \tag{2.5}$$

The resulting stress-strain diagrams for the two models for a A572 Grade 50 steel are compared in Figure 2.4d. The testing procedure used to obtain these curves implicitly accounts for the creep of steel under sustained loading at elevated temperatures (NIST 2010). Although neither models included data from A992 steel, later tests revealed similar behavior (Hu et al. 2009).

Protecting steel from such extreme temperature is obviously the first line of defense against structural collapse during an uncontrolled fire. This is done by application of one of various types of coatings that will enhance fire resistance by delaying the rise of steel temperature, using either insulating, energy absorbing, or intumescent materials (e.g., Buchanan 2001, Gewain et al. 2003, Ruddy et al. 2003). A few specially alloyed steels have also been developed to experience no more than a 33% loss of their yield strength at 600°C—circumventing in some instances the need for such coatings when fire exposure can be controlled or ensured to not exceed this heat intensity—but their properties drop more rapidly beyond that point, back to matching that of other steels when temperatures reach 800°C (Mizutani et al. 2004, Sakumoto et al. 1992).

Beyond analyses of the fire resistance of structures having exposed or thermally insulated steel members (or having damaged insulation as the case in NIST 2005), information on properties at elevated temperatures may be necessary in other specialty applications. For example, given that special high-temperature heat treatments [up to 1000°F (540°C)] are often specified to reduce the residual stresses introduced by welding in industrial steel pressure vessels (particularly when a new steel plate is welded in place of an existing damaged or corroded one), a good knowledge of the high-temperature properties of structural steel is crucial to prevent collapse of these vessels under their own weight during the heat treatment.

2.2.3 Effect of Temperature on Ductility and Notch-Toughness

Temperatures below room temperature do not have an adverse impact on the yield strength of steel, as shown in Figure 2.4, but lower temperatures can have a substantial impact on ductility. Indeed, the ultimate behavior of steel will progressively transform from ductile to brittle when temperatures fall below a certain threshold and enter the appropriately labeled "ductile-to-brittle-transition-temperature" (DBTT) range. This undesirable property of structural steel led to a few notable failures in the late 1800s and early 1900s, but began to be fully appreciated only in the 1940s and 1950s when large cracks were discovered in more than 1000 all-welded U.S. steel ships built in that period. These included more than 200 cases of severe fractures and 16 ships lost at sea when their hulls unexpectedly "snapped" in two while they were cruising the Arctic sea.

The Charpy V-notch test (also known as a notch-toughness test) was developed to determine the DBTT range. In this test, a standard notched steel specimen is broken by a falling pendulum hammer fitted with a standard striking edge (Figures 2.5a and b). In principle, the energy absorbed by the specimen during its failure will translate into a loss of potential energy of the pendulum. Thus, a rough measure of this absorbed energy can be calculated from the difference between the initial height (h_1) of the pendulum when released and the maximum height (h_2) it reaches on the far side after breaking the specimen. A typical plot of the absorbed energy of a Charpy specimen as a function of temperature is shown in Figures 2.5c and d for a standard structural steel. Corresponding changes in fracture appearance and lateral expansion at failure are shown in Figures 2.5e and f.

Generally, structural engineering standards and codes will allow the use of only steels that exhibit a minimum energy absorption capability at a predetermined temperature—for example, 15 ft-lb at 40°F (20 Nm at 4.5°C). Although it may first appear to the reader, from the Charpy data of Figure 2.5, that a level of energy dissipation of 15 ft-lb corresponds to a nearly brittle material behavior and is insufficient to ensure ductile response, it must be recognized that the Charpy V-notch test produces failures at very high strain rates. As shown in Figure 2.5c for A572 Grade 50 steel, there exists a shift of 125°F between the DBTT range obtained from the Charpy V-notch tests and that range obtained from failure tests conducted at an intermediate

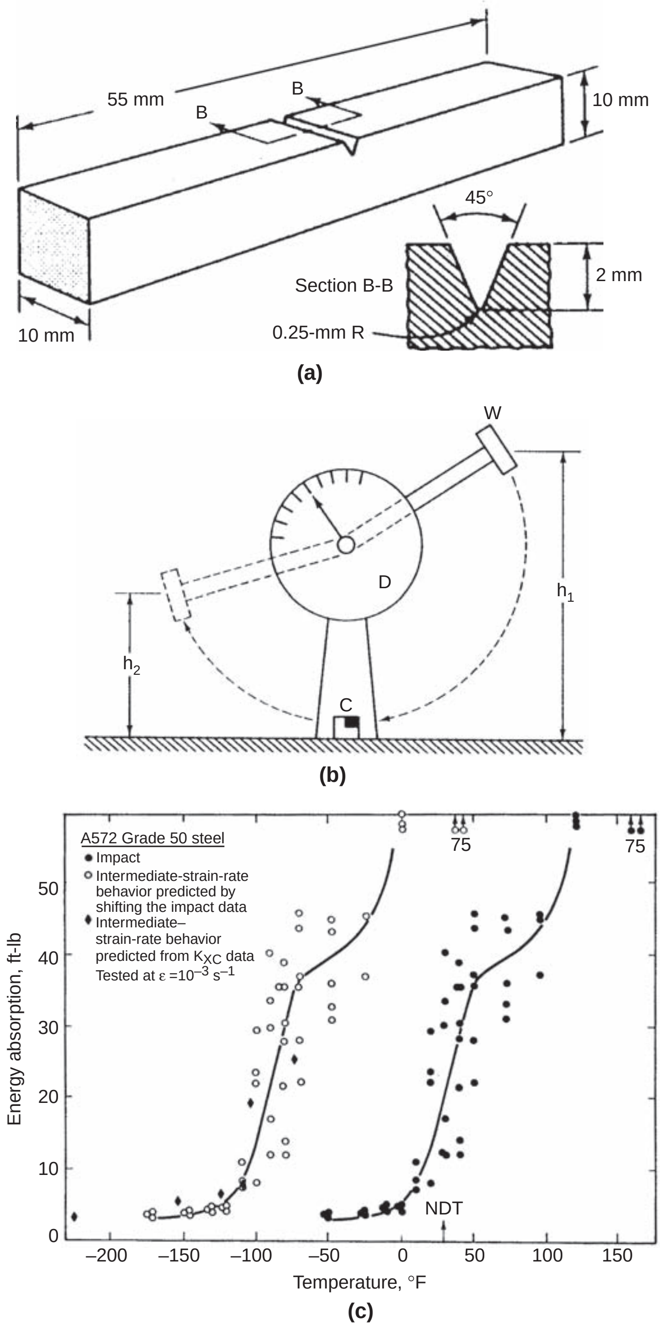

FIGURE 2.5 Charpy V-notch impact tests: (a) typical specimen, (b) schematic of testing procedure, (c) energy absorption behavior for impact loading and intermediate strain-rate loading for standard specimens for A572 Grade 50 steel.

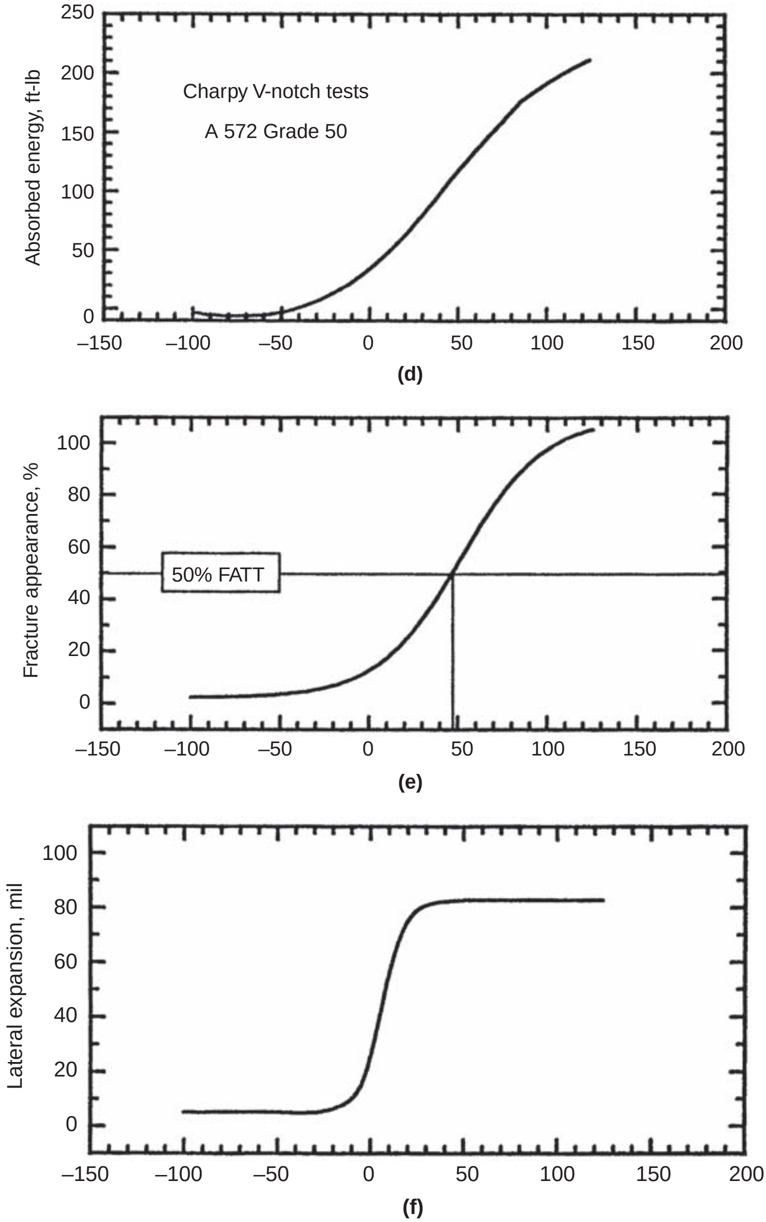

Figure 2.5 Composite plots of: (d) energy absorption, (e) fracture appearance, and (f) lateral expansion constructed from data taken from several heats of ASTM A572 Grade 50 plate on the order of 1 in thick. (*Figures a, b, and c from J.M. Barsom and S.T. Rolfe*, Fracture and Fatigue Control in Structures—Applications of Fracture Mechanics, *with permission from J.M. Barsom and S.T. Rolfe; Figures d, e, and f courtesy of H.S. Reemsnyder, Homer Research Laboratory, Bethlehem Steel Corporation, with permission. Note: The data in Figure 2.5 should not be considered typical, maxima, or minima for all plates and rolled sections of this grade. Properties will vary with chemistry, thermomechanical processing, thickness, and product form.*)

strain rate of 0.001/s, with more ductile behavior obtained at lower strain rates (see ASTM 1985a for details on tests at slower strain rates, and Rolfe and Barsom 1999 for techniques to compare different measures of fracture toughness obtained from different testing procedures). Hence, compliance with the specified Charpy V-notch 15 ft-lb energy absorption at 40°F should ensure ductile behavior over the practical range of service temperatures for structural elements subjected to such a strain rate. Tables 2.1 and 2.2, as well as Figure 2.6, summarize the Charpy V-notch test results for a number of commonly used steel grades and show that most comply with the above example specified Charpy limit. However, it should be noted from those tables that structural shapes having large flange and web thicknesses [such as those formerly known as AISC Groups 4 and 5 (AISC 1994)] generally have lower energy absorption capabilities. For specialty applications that require better performance than that which is commonly available, the structural engineer should request steel specially alloyed to provide the needed material properties at low temperatures, high strain rates, or both.

Beyond the energy absorption measure, a large number of descriptive indices exist in the literature to capture and quantify this ductile-to-brittle behavior. The nil-ductility-transition (NDT) temperature, defined as the highest temperature at which a specimen fails in a purely brittle manner (or alternatively as the temperature at which a small crack will propagate to failure in a specimen loaded exactly to the yield stress), can also be obtained from the ASTM E208 test (ASTM 1985b). The fracture appearance transition temperature (FATT) is the temperature at which 50% of the fracture surface corresponds to a cleavage failure (i.e., a flat crystalline surface characteristic of brittle failure), with the remaining 50% showing shear-lips of fibrous appearance typical of ductile failures. Figure 2.7 illustrates that this transition in texture of the failure surface is a function of both temperature and strain rate. Further, it shows that alignment of the surfaces exhibiting similar texture, but tested at different strain rates, provides a striking visual expression of the aforementioned temperature shift of the DBTT range.

Although notch toughness and ductility for a given steel are closely related, it is important to realize that notch toughness is not related to yield strength. In fact, in very thick steel sections, the notch toughness of some steels is known to vary quite significantly throughout the cross-section of members, even when a variation in yield strength is not observed. This is particularly true at the core of the web-flange intersection of very thick sections in which a larger steel grain structure exists as a consequence of a lesser amount of cold forming achieved there during the rolling process. For this reason, AISC (2010) specifies that samples for Charpy V-notch tests be taken from the core area, by reference to Supplement S30 of the ASTM A6 standard.

Steel Grade	Test Temp (°F)	ASTM Shape Group	Sample Size	Mode (ft-lb)	Minimum (ft-lb)	Mean (ft-lb)	Maximum (ft-lb)	First Quartile (ft-lb)	Median (ft-lb)	Third Quartile (ft-lb)
A36 QST	32	ALL	21	162	91	151	204	137	160	168
A36 HR	32	ALL	73	130	91	150	241	124	145	169
A36 HR	40	ALL	2011	66	16	112	286	65	98	147
		1	421	100	20	116	272	79	113	146
		2	1057	239	16	130	286	77	117	176
		3	315	36	19	86	240	63	77	98
		4	218	54	16	54	193	41	51	62
A36 HR	70	ALL	426	239	22	95	253	43	70	124
		1	262	43	25	59	177	36	50	75
		2	59	69	59	122	253	83	97	138
		3	24	239	25	200	240	235	239	239
		4	81	240	22	158	240	99	177	221
A572 Gr 50 QST	32	ALL	24	N/A	101	136	182	122	138	149
A572 Gr 50 HR	32	ALL	15	N/A	106	140	170	135	142	147

HR = Hot Rolled; QST = Quenched Self-Tempered
(*From American Institute of Steel Construction*, Statistical Analysis of Charpy V-Notch Toughness for Steel Wide Flange Structural Shapes, *with permission*)

Table 2.1 Compilation of Charpy V-Notch Test Results for Various Structural Steel Grades, from Data Provided by North American Producers

Steel Grade	Test Temp (°F)	ASTM Shape Group	Sample Size	Mode (ft-lb)	Minimum (ft-lb)	Mean (ft-lb)	Maximum (ft-lb)	First Quartile (ft-lb)	Median (ft-lb)	Third Quartile (ft-lb)
A572 Gr 50 HR	40	ALL	3930	79	16	91	288	64	80	97
		1	400	58	16	84	259	58	73	95
		2	2181	80	18	93	288	71	85	102
		3	813	86	16	83	280	65	82	96
		4	453	60	17	66	155	53	63	77
		5	83	49	29	62	155	47	59	71
A572 Gr 50 HR	70	ALL	598	47	15	61	241	31	51	74
		2	37	124	31	135	237	89	134	194
		3	90	74	31	76	202	56	68	91
		4	364	50	17	57	241	34	51	68
		5	104	26	15	33	116	23	27	32
A588 HR	40	ALL	223	21	16	140	290	71	129	204
		2	182	54	18	148	290	82	145	215
		3	41	N/A	16	103	249	58	75	155
A913 Gr65 QST	32	ALL	87	156	92	141	212	122	142	158
A913 Gr65 QST	70	ALL	34	48	33	61	108	45	57	79
Dual Certified	40	ALL	202	43	17	53	121	37	51	67
		1	142	38	17	51	121	35	48	63
		2	55	43	24	59	116	43	58	74
Dual Certified	70	ALL	368	65	15	59	131	41	55	74
		1	322	53	15	55	131	37	53	69
		2	46	65	60	86	123	67	91	99

Table 2.1 Compilation of Charpy V-Notch Test Results for Various Structural Steel Grades, from Data Provided by North American Producers (*Continued*)

Steel Grade	Test Temp (°F)	ASTM Shape Group	Observed Probability of Exceedance 15 ft-lb (%)	Observed Probability of Exceedance 20 ft-lb (%)
A36 QST	32	ALL	100	100
A36 HR	32	ALL	100	100
A36 HR	40	ALL	99	97
		1	100	97
		2	100	99
		3	100	99
		4	96	95
A36 HR	70	ALL	100	95
		1	100	95
		2	100	100
		3	100	94
		4	100	97
A572 Gr 50 QST	32	ALL	100	100
A572 Gr 50 HR	32	ALL	100	100
A572 Gr 50 HR	40	ALL	100	99
		1	99	99
		2	100	99
		3	98	98
		4	100	99
		5	100	99
A572 Gr 50 HR	70	ALL	95	87
		2	100	100
		3	100	100
		4	96	89
		5	85	60
A588 HR	40	ALL	98	97
		2	99	98
		3	97	95
A913 Gr65 QST	32	ALL	100	100

HR Rolled; QST = Quenched Self-Tempered
(*From American Institute of Steel Construction,* Statistical Analysis of Charpy V-Notch Toughness for Steel Wide Flange Structural Shapes, *with permission.*)

Table 2.2 Probability of Exceedance of Two Commonly Specified Charpy V-Notch Energy Absorption Material Requirements for Various Structural Steel Grades, from Data Provided by North American Producers

Steel Grade	Test Temp (°F)	ASTM Shape Group	Observed Probability of Exceedance 15 ft-lb (%)	Observed Probability of Exceedance 20 ft-lb (%)
A913 Gr65 QST	70	ALL	100	100
Dual Certified	40	ALL	99	94
		1	98	94
		2	100	99
Dual Certified	70	ALL	98	94
		1	98	93
		2	100	100

Table 2.2 Probability of Exceedance of Two Commonly Specified Charpy V-Notch Energy Absorption Material Requirements for Various Structural Steel Grades, from Data Provided by North American Producers (*Continued*)

2.2.4 Strain Rate Effect on Tensile and Yield Strengths

Strain rate is another factor that affects the shape of the stress-strain curve. Typically, the tensile and yield strengths will increase at higher strain rates, as shown in Figure 2.8, except at high temperatures for which the reverse is true. Consideration of this phenomenon is crucial for blast-resistant design in which very high strain rates are expected, but of little practical significance in earthquake-engineering applications. Past studies have repeatedly demonstrated that, for the steel grades commonly used, the expected increases of roughly 5 to 10% in yield strength at typical earthquake-induced strain rates is negligible compared with the much greater uncertainties associated with the earthquake input. The effect of strain rate on notch toughness, as described above, is also considerably more significant.

Blast-resistant design manuals and guides typically specify charts or tables of the factors by which the static yield and tensile stresses should be magnified to obtain the corresponding dynamic values to use in calculations, such as Figure 2.8e. Strain rates are a function of the blast pressures and structural system properties, and calculated values for common blast-resistant design scenarios vary between 0.02 to 0.3 in/in/s.

2.2.5 Probable Yield Strength

In seismic design, as will be demonstrated later, knowledge of the maximum probable yield strength is equally important as knowledge of the minimum reliable yield strength. Recent studies have reported that the margin between the actual average yield strength

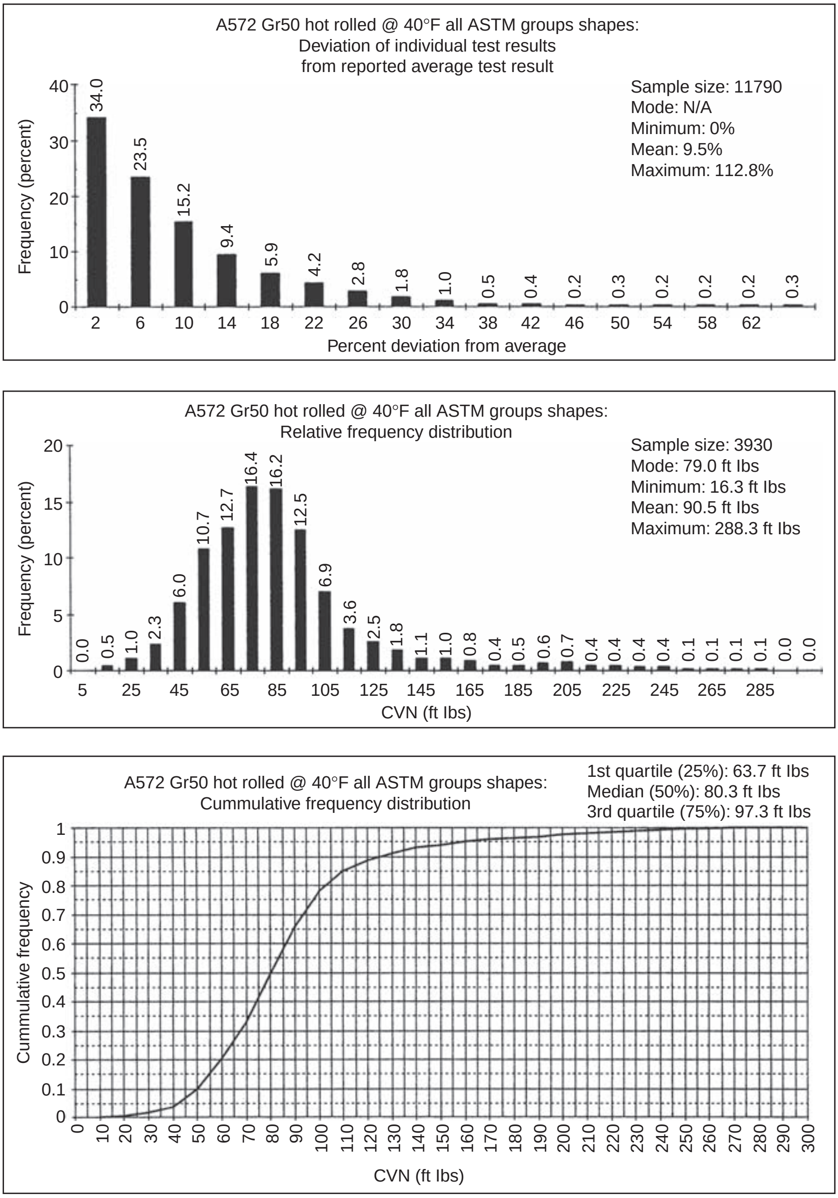

Figure 2.6 Compilation of Charpy V-notch test results for A572 Grade 50 structural steel, from data provided by North American producers. (*From American Institute of Steel Construction,* Statistical Analysis of Charpy V-Notch Toughness for Steel Wide Flange Structural Shapes, *with permission.*)

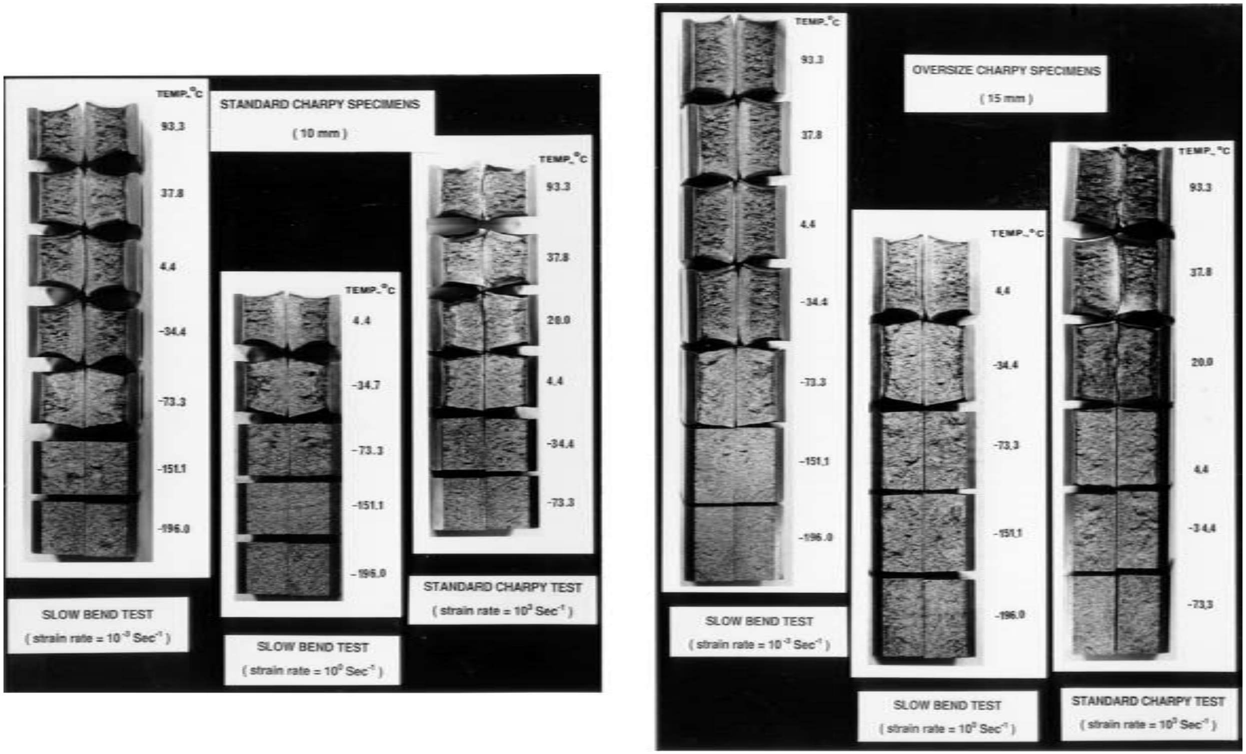

FIGURE 2.7 Failure surface texture of Charpy V-notch specimens at different test temperatures and strain rates. (*Courtesy of the Canadian Institute of Steel Construction, with permission.*)

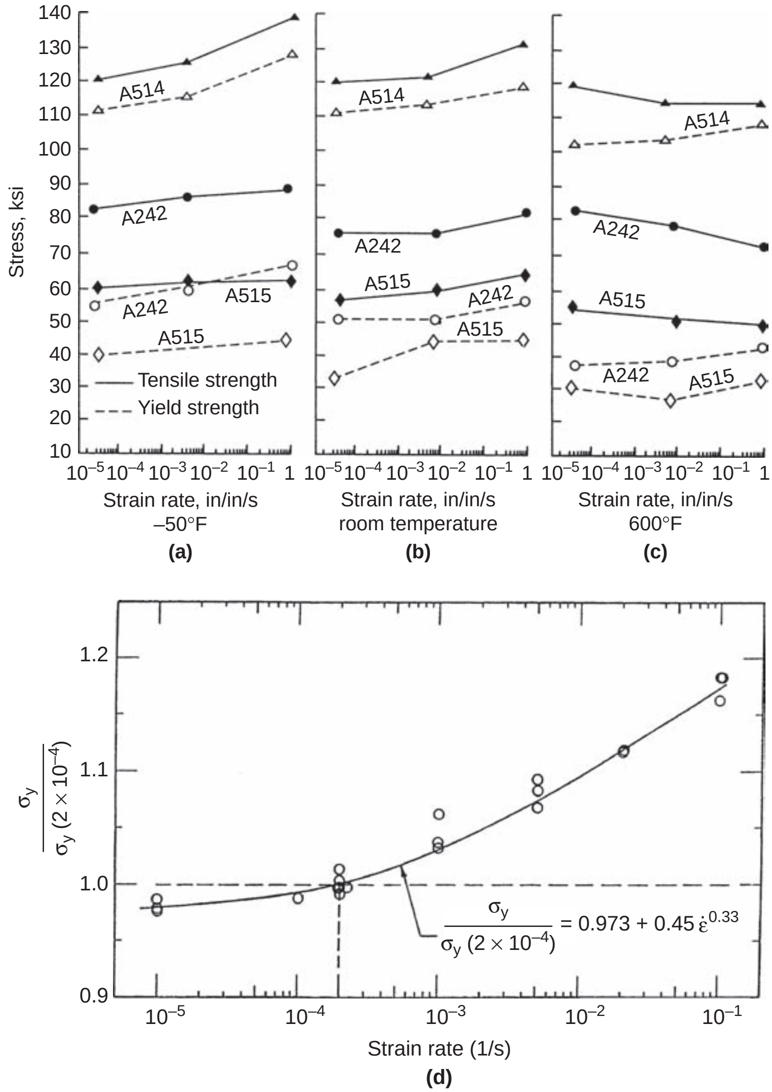

Figure 2.8 Yield stress as a function of strain rate and temperature for some structural steels. [*Figures a, b, and c from R.L. Brockenbrough and B.G. Johnston,* USS Steel Design Manual, *with permission from U.S. Steel; Figure d from Moncarz, P.D. and Krawinkler H.*, Theory and Application of Experimental Model Analysis in Earthquake Engineering, *Report No. 50, John A. Blume Earthquake Engineering Research Center, Department of Civil Engineering, Stanford University, with permission. Figure e from Unified Facilities Criteria* (*UFC 2008*).]

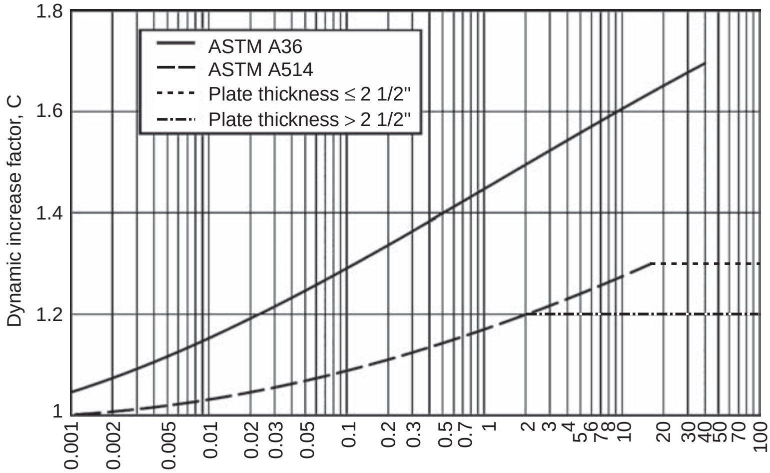

(e)

Figure 2.8 (*Continued*)

and specified yield strength has progressively increased over the years for some structural steels, even though the steel specification itself remained unchanged. For example, a few decades ago, yield strengths of 255 to 270 MPa (37 to 39 ksi) were typically reported for ASTM-A36 steel by researchers studying the behavior of structural members and connections (e.g., Galambos and Ravindra 1978, NBS 1980, Popov and Stephen 1971), whereas similar tests conducted 20 years later (e.g., Englehardt and Husain 1993) using the very same steel grade revealed a substantial increase of the yield strength, with values ranging from 325 to 360 MPa (47 to 52 ksi). Yield stress values in excess of 420 MPa (60 ksi) have also occasionally been reported for that steel grade (SAC 1995). In fact, some steel mills have apparently adopted a dual-certification procedure for steel conforming to both the ASTM-A36 and A572 specifications. Although this higher strength translates into safer structures for nonseismic design, an unexpectedly higher yield strength can be disadvantageous for seismic design. For example, a specific structural component can be designed to yield, absorb energy, and prevent adjacent elements from being loaded above a predetermined level during an earthquake, thus acting much like a "structural fuse." An yield strength much higher than expected could prevent that structural fuse from yielding and overload the adjacent structural components (such as the welded joints in moment-resisting frames), with drastic consequences on the ultimate behavior of the structure (see Chapter 8).

To address this concern, the ASTM A992 steel was introduced by North American structural shape producers in the late 1990s, and became the de-facto preferred grade for rolled wide-flange shapes. It is effectively an "enhanced" ASTM A572 Grade 50 steel with a maximum yield strength of 448 MPa (65 ksi) in addition to the traditionally specified minimum yield strength of 345 MPa (50 ksi). Furthermore, ASTM A992 has special requirements limiting its carbon equivalent (CE) to 0.47, to improve weldability (see Section 2.5.3), and limiting its yield-to-tensile ratio to a maximum of 0.85, to ensure ductile behavior (AISC 1997a, 1997b, Bartlett et al. 2003, Carter 1997, Cattan 1997, SAC 1995, Zoruba and Grubb 2003). Incidentally, the same maximum yield strength and yield-to-tensile ratio can also be delivered by ASTM A913 Grade 50 steel, but only if such optional supplementary requirements are explicitly specified as a special order.

Note, however, that greater-than-expected yield strength can also simply be the result of an inadvertent but well-intentioned substitution, by a supplier, from the originally requested steel grade to one of higher yield strength, to compensate, for example, for a temporary stock shortage. Therefore, in those circumstances that warrant it, the engineer should indicate on all construction documents the key members for which substitution to a higher strength material is not acceptable.

Special steels targeted for specific purposes have also been introduced in the construction market. For example, intended for use in applications that require greater ductility and energy dissipation more than strength, Japanese steel mills developed and started producing in the 1990s special ductile steels having more than 40% elongation at failure and well-controlled maximum yield values (Saeki et al. 1998, Yamaguchi et al. 1998). As shown in Figure 2.9, low yield point (LYP) steel rolled plates having a specified nominal yield strength as low as 100 MPa (17.5 ksi) have been produced, but the substantial strain-hardening (of 2 to 3 times the yield strength) of those lower strength steels must be considered in the design of their connections and surrounding frames. Low yield steel produced by Chinese mills have exhibited similar elongations, for yield strengths as low as 165 MPa (24 ksi) (Vian et al. 2009). Seismic design applications have already been found for that material (e.g., Dusicka et al. 2004, Matteis et al. 2003, Nakashima et al. 1994, Susanthaa et al. 2005, Vian et al. 2009).

Incidentally, also in the 1990s but with different goals in mind, high-performance steels (HPS) have been developed in North America (Wright 1996) for plates to meet the following specifications: (a) high strength, with yield strengths of 350 MPa (50ksi), 480 MPa (70 ksi), and 690 MPa (100 ksi); (b) excellent weldability due to improved resistance against heat-affected zone cracking, resulting in reduced requirements for preheating (see Section 2.5), provided cautious electrode selection and weld execution procedures are taken (AASHTO 2003, Miller 2000);

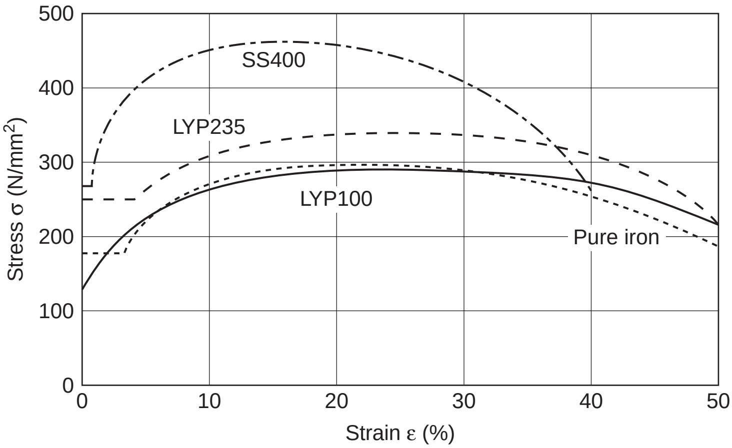

Figure 2.9 Stress-strain curves for low-yield steel grade plates (LYP) compared with regular Japanese JIS SS440 steel with 235 MPa specified yield strength. (*Yamaguchi et al. 1998, Courtesy of Nippon Steel.*)

(c) extremely high toughness, with Charpy V-notch values of roughly 200 ft-lb (270 N-m) at −10°F (−23°C), compared with the current bridge design requirements of 15 ft-lb (20 N-m) at −10°F (−23°C); and (d) corrosion resistance comparable to that of weathering steel. Designated as ASTM A709 Grades HPS 50W, 70W, and 100W steels ("W" following the yield strength indicating weathering steel), they have already been implemented as plate girders in hundreds of bridges across North America (Lwin 2002, Wilson 2006). Although these new steels have been developed for bridge applications, as beams intended to remain elastic, their outstanding properties might also make them appealing for general ductile design applications. For HPS 70W, Dusicka et al. (2007) reported stable hysteretic energy dissipation up to cyclic inelastic strains of 7% and low cycle fatigue life comparable to that of conventional constructional steels. However, research on this topic has been limited.

Finally, a number of special alloys have been the subject of research for potential structural engineering applications where ductile performance and good energy dissipation capacity are required, including superelastic nickel-titanium (NiTi) shape memory alloys (SMA) that are appealing for their ability to recover their original shape upon unloading after plastic deformations (e.g., Desroches et al. 2004, McCormick et al. 2007, Van de Lindt and Potts 2008, Wilson and Wesolowsky 2005, Youssef et al, 2008). However, actual implementations have been constrained by the high cost of such advanced materials and, in some instances, the maximum size of shapes/wires that can be produced.

2.3 Plasticity, Hysteresis, Bauschinger Effects

After steel has been stressed beyond its elastic limit and into the plastic range, a number of phenomena can be observed during repeated unloading, reloading, and stress reversal. First, unloading to $\sigma = 0$ and reloading to the previously attained maximum stress level will be elastic with a stiffness equal to the original stiffness, E, as shown in Figure 2.10. Then, as also shown, upon stress reversal (to $\sigma = -\sigma_y$), a sharp "corner" in the stress-strain curve is not found at the onset of yielding; instead, stiffness softening occurs gradually with yielding initiating earlier than otherwise predicted. This behavior, known as the Bauschinger effect, is a natural property of steel—its cause is explained in the next section. If the stress reversal is initiated prior to attainment of the strain-hardening range when the steel is loaded in one direction, a yield plateau will eventually be found in the reversed loading direction as shown in Figure 2.10a. However, once the strain-hardening range has been entered in one loading direction, the yield plateau effectively disappears in both loading directions (Figure 2.10b).

A most important property of steels subjected to large cyclic inelastic loading is their ability to dissipate hysteretic energy. The energy needed to plastically elongate or shorten a steel specimen can be calculated as the product of the plastic force times the plastic displacement (i.e., the work done in the plastic range) and is called the hysteretic energy. Unlike kinetic and strain energy, hysteretic energy is a nonrecoverable dissipated energy. As shown in Figure 2.11a, under a progressively increasing loading, followed by subsequent unloading, the hysteretic energy, E_H, can be expressed as:

$$E_H = P_Y(\delta_{MAX} - \delta_Y) \tag{2.6}$$

that is, the shaded area in this figure. For a full cycle of load reversal, the hysteretic energy will simply be the area enclosed by the

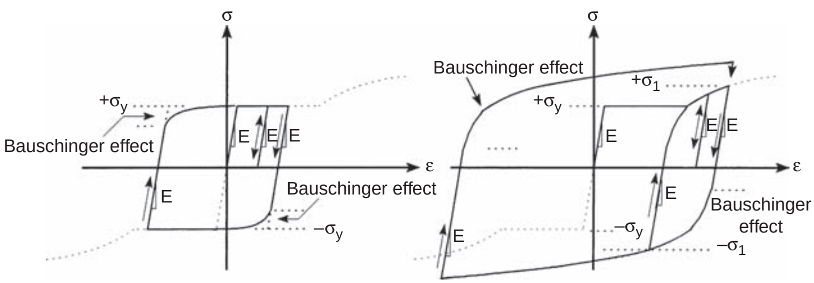

Figure 2.10 Cyclic stress-strain relationship of structural steel.

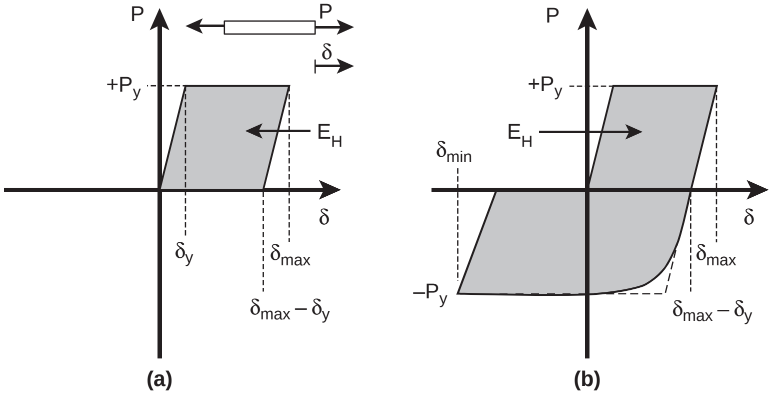

Figure 2.11 Hysteretic energy of structural steel: (a) half cycle and (b) full cycle.

loop of the force-displacement curve, as shown in Figure 2.11b, and approximately expressed as:

$$E_H \cong P_Y[(\delta_{MAX} - \delta_Y) + (\delta_{MAX} - \delta_{MIN} - 2\delta_Y)] \tag{2.7}$$

A more accurate calculation of hysteretic energy in this case would recognize the small loss of hysteretic energy at the rounded corners of the force-displacement curve due to the Bauschinger effect.

Under repeated cycles of loading, the energy dissipated in each cycle is simply summed to calculate the total energy dissipated. This cumulative energy dissipation capacity is a most important property that makes possible the survival of steel structures to rare but rather severe loading conditions, such as blast loading or earthquake loading.

Within the framework of this book, the above description of inelastic cyclic behavior is certainly adequate. However, it is noteworthy that a few additional minor phenomena also develop as steel undergoes numerous cycles of severe hysteretic behavior. For example, the threshold beyond which strain-hardening starts to develop, as well as the extent of the elastic range prior to onset of the Bauschinger effect, is a function of the prior plastic loading history. Mizuno et al. (1992), Dafalias (1992), and Lee et al. (1992) provide a good overview of these phenomena and progress on the development of constitutive relationships that can capture the complex behavior of structural steels subjected to arbitrary cyclic loading histories.

2.4 Metallurgical Process of Yielding, Slip Planes

As mentioned earlier, steel coupons tested axially exhibit a well-defined plastic plateau. In principle, the tangent modulus of elasticity of steel (i.e., the slope of the stress-strain curve) is effectively zero along this plateau, as shown in Figure 2.2. As a result, one may wonder how a steel member can ever reach the strain-hardening range in compression, knowing that the maximum stress that can be resisted by a steel plate prior to buckling is given by (Popov 1968):

$$\sigma_{cr} = \frac{k}{(b/t)^2}\left[\frac{\pi^2 E}{12(1-v^2)}\right] \tag{2.8}$$

Indeed, according to Eq. (2.8), buckling should occur as soon as the strain exceeds ε_y and the tangent modulus drops to zero (i.e., $E = 0$). To resolve this paradox, an understanding of the metallurgical process of yielding is needed.

Steel is a polycrystalline material that, when loaded beyond its elastic limit, develops slip planes at 45°. These visible yield lines, also known as Lüder lines, are a consequence of the development of slip planes within the material as yielding develops. A schematic representation of a slip plane is shown in Figure 2.12. By analogy, Figure 2.12d shows slip planes in a copper aluminum single crystal specimen (Elam 1935, van Vlack 1989).

At the precise location of the slip plane, the strains can be thought of as having "slipped" from ε_y to ε_{sh} in one single jump. Following this first slip, other planes will subsequently slip, one after the other in a random sequence as a function of the random distribution of various weaknesses and dislocations in the steel's crystalline structure, as their respective slip resistances are reached. Thus, under no perceptible variation in the applied stress, the number of sections that have jumped from ε_y to ε_{sh} will progressively increase until the entire length of member subjected to the yield stress has strain-hardened to a strain equal to ε_{sh}. Assuming for convenience that at any given time during this process, all slip planes can be grouped together over a length ϕL, where L is the length of the specimen subjected to the yield stress as shown in Figure 2.12b, and, knowing that all slipped segments have reached ε_{sh} while the others are still at ε_y, the average strain over the specimen length can be expressed as:

$$\begin{aligned}\varepsilon_{av} &= \frac{\Delta L}{L} = \frac{\varepsilon_y (L - \phi L) + \phi \varepsilon_{sh} L}{L} \\ &= (1-\phi)\varepsilon_y + \phi\varepsilon_{sh} \\ &= (1-\phi)\varepsilon_y + \phi s \varepsilon_y\end{aligned} \tag{2.9}$$

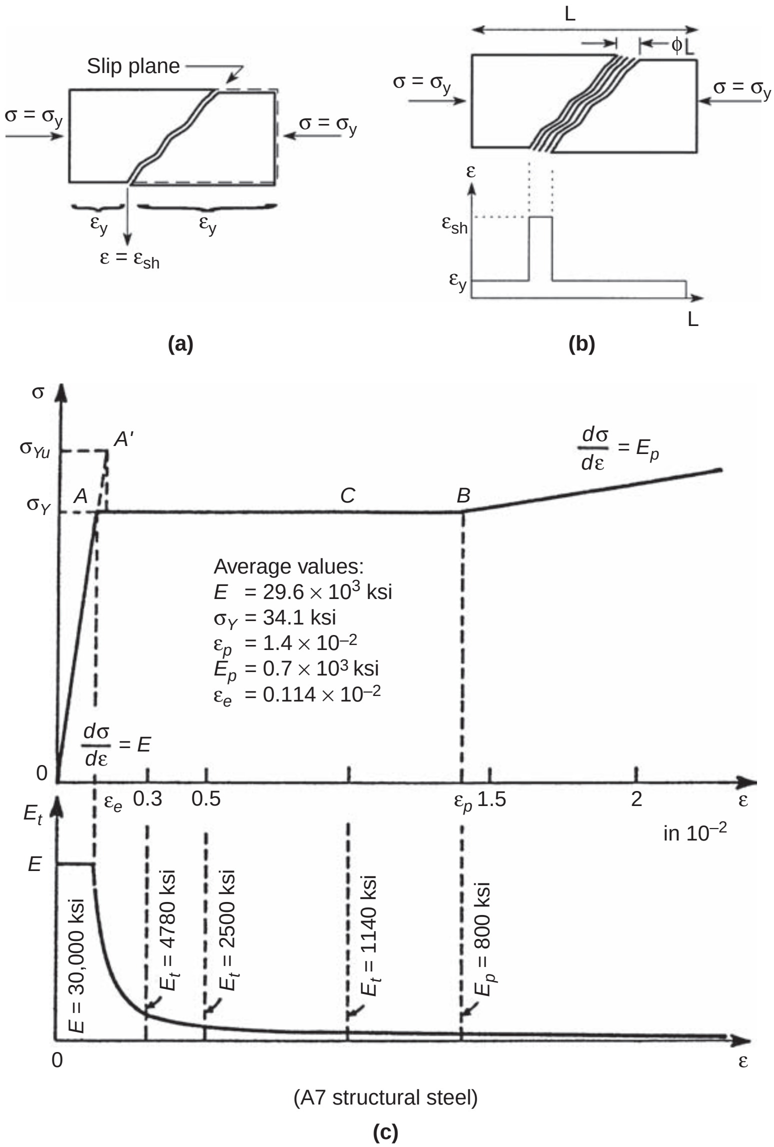

Figure 2.12 Slip planes during yielding: (a) schematic representation of single slip plane, (b) cumulative effect of multiple slip planes, (c) Effective modulus throughout development of slip planes in Grade A-7 steel, (d) Slip planes in single cooper-aluminium crystal, and (e) Movement of a dislocation along a slip plane in a metal crystal. [*Figure c from Massonnet, C. E. and Save, M. A.,* Plastic Analysis and Design, vol. 1: Beams and Frames; *Figure d from C.F. Elam 1935,* "Dislocation of Metal Crystals (Oxford Engineering Science Series)," *by permission of Oxford University Press—www.oup.com; Figure e from* Résistance des Matériaux, *A. Bazergui et al. 1987, with permission from Presses Internationales Polytechniques, Montreal*).]

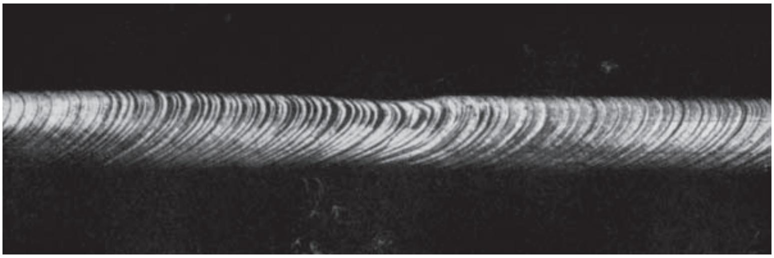

(d)

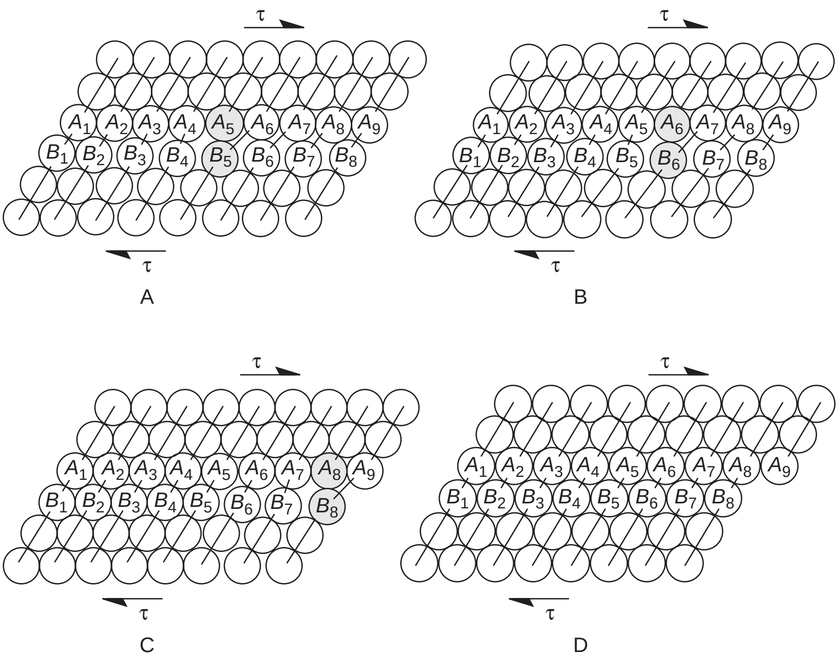

(e)

Figure 2.12 (*Continued*)

where s (>1.0) is the ratio of ε_{sh} to ε_y. This clearly illustrates how the average strain can increase progressively without any apparent increase in the applied stress, while the actual stiffness of the steel material during this yield process varies from E (when $\phi = 0.0$) to E_{sh} (when $\phi = 1.0$), but never zero. Defining the effective stiffness as $\sigma_y/\varepsilon_{av}$ in the yield plateau, Figure 2.12c shows the variation of this effective stiffness over the range $0.0 < \phi < 1.0$.

Therefore, the plastic plateau on the stress-strain curve is simply a consequence of standard testing methods for which yielding must spread over a specified gage length (e.g., 100 or 200 mm) before higher loads can be applied to a given specimen. This also explains why strain-hardening is usually reached before local buckling and other instabilities develop in a structural member (see Chapter 15).

An understanding of the slip plane phenomenon is also helpful in explaining the Bauschinger effect illustrated in Figure 2.10, recognizing that a piece of steel is actually an amalgam of randomly oriented steel crystals (Timoshenko 1983). Thus, a slip plane contains a large number of steel grains in which sliding has occurred along definite crystallographic planes of weakness (and hence contributed to the yield plateau) and others that have not. If a specimen is unloaded after yielding in tension but prior to attainment of ε_{sh}, the crystals that have slid are locked in their elongated position while others try to elastically return to their undeformed position. Because of continuity of the metal, this action generates internal residual stresses, with the slipped crystals compressed as they prevent the others from fully recovering their elastic deformations. If, after unloading, the specimen is subjected to a reversed loading (i.e., compression in this example), slipping of the most detrimentally oriented crystals triggers at a load much smaller than would have otherwise been necessary on a virgin specimen. This is logical because, prior to the application of the external compression load, these crystals are already in compression because of the residual stresses created upon unloading from the earlier tension yielding excursion. This could be illustrated following a step-by-step analysis analogous to the example in Section 2.8, in essence replacing the structure having multiple bars by a slip plane with multiple crystals, and substituting yielding in the bilinear material model in Section 2.8 for crystal slippage in the case at hand. As such, the softening shown in Figure 2.46h in Section 2.8 would represent earlier development of slip planes upon load reversal, instead of earlier yielding—hence, the Bauschinger effect.

From a more rigorous metallurgical engineering approach (e.g., Abbaschian and Reed-Hill 2008, van Vlack 1989), slip effectively occurs due to the movement of dislocations across the crystal lattice of the material, and plastic deformations are the result of sequential breakage and rearrangements of interatomic bonds from the slippage of these dislocations. This dislocation creep movement, one lattice point at the time along a crystal plane, occurs along a glide plane. Figure 2.12e illustrates how the atoms in a crystal along a glide plane successively shift under shear, resulting in movement of the dislocation (at atomic forces orders of magnitude less than what would be required otherwise in a perfect crystal).

The quantity and density of dislocations increases with the extent of plastic deformations, up to a saturation point where their number and entanglement start to interfere with the nucleation and movement of other dislocations. Consequently to this congestion, a greater force is required to overcome the resistance against further dislocation motions, resulting in the strain-hardening phenomena. "Bubble raft" models, created by clustering small soap bubbles on a flat control surface that can be distorted, can be effective to illustrate the formation and propagation of dislocations through the atomic structure of solids (DoITPoMS 2009, Wikipedia Contributors 2009a).

This also partly explains why, on an experimentally obtained stress-strain curve, the yield stress corresponding to the observed yield plateau (denoted $\sigma_{y\text{-}static}$ in Figure 2.2) is sometimes preceded by a slightly higher yield value (denoted $\sigma_{y\text{-}upper}$ in Figure 2.2) in specimens machined to a very high tolerance to have a uniform cross-section over the gauge length where yielding is expected and tested on high precision equipment (see Lay 1965 for more details). A simplistic analogy between the development of slip planes and the actual physical behavior of friction between solids makes clear that it takes more energy to initiate a slip plane (or to start sliding a body whose only resistance against motion is provided by friction) than to maintain it once it has initiated. In any case, $\sigma_{y\text{-}static}$ is the yield value of engineering significance.

2.5 Brittleness in Welded Sections

Brittleness can occur as a result of a variety of influences, as discussed in the following sections.

2.5.1 Metallurgical Transformations During Welding, Heat-Affected Zone, Preheating

The welding process can embrittle the steel material located in the vicinity of the weld. Simple solutions exist to circumvent most problems, although these become more difficult to implement when extremely thick heavy rolled sections are welded.

An important first step in avoiding brittle failures in welded members is to recognize that welding is a complex metallurgical process (and not a "gluing" operation that performs miracles). Not only is new material deposited during welding, but sound fusion with the base metal is necessary to provide the desired continuity between the welded components (AWS 1976).

The topology of a welded area consists of three important zones: the fusion zone, the heat-affected zone (HAZ), and the base metal (see Figure 2.13). The fusion zone consists of all the metal that is effectively melted during welding. Good penetration of the fusion zone into the base metal will generally provide a better-quality weld. This is one reason flux-cored arc welding (FCAW) provides better quality

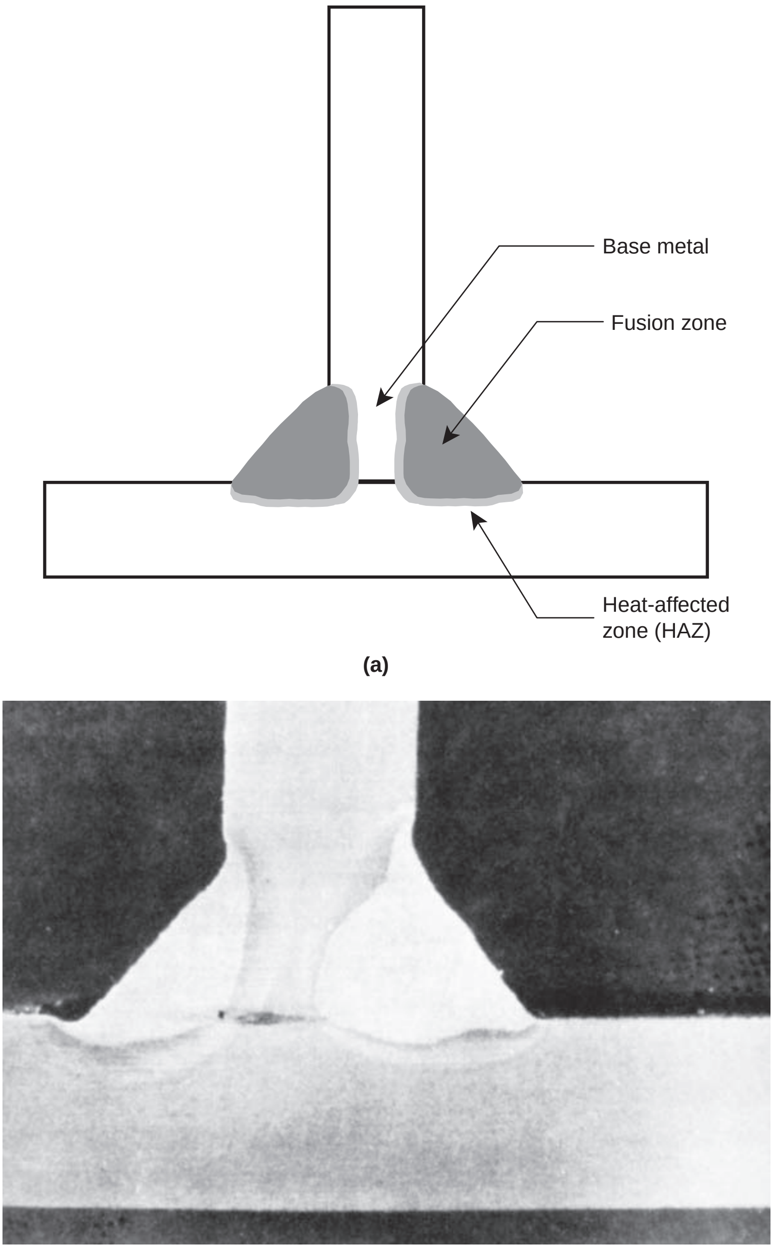

(b)

Figure 2.13 Topology of a welded area: (a) schematic illustration; (b) fillet welds by shielded metal arc welding (SMAW) on the left, and flux-cored arc welding (FCAW) on the right, in A36 steel (note the increased penetration of FCAW). (*Figure b from F.R. Preece and A.L. Collin*, Steel Tips: Structural Steel Construction in the '90s, *with permission from the Structural Steel Education Council.*)

welds than shielded metal arc welding (SMAW) for a given filler metal.

Immediately adjacent to the fusion zone lies the heat-affected zone, which, as the name implies, consists of steel whose grain structure has been modified by the high heat imparted during the welding process. The crystalline constitution of the HAZ will depend on the metallurgical content of the base metal and on the speed of cooling of the metal (Van Vlack 1989). Generally, if cooling is too rapid in high-strength steel, the metal in the HAZ will become a hard and brittle martensite layer that is highly susceptible to cracking in the presence of stress raisers or concentrations. Rapid cooling can be a significant problem in thicker steel sections because the heat introduced by welding will be more rapidly dissipated into larger volumes of colder steel, resulting in rapid cooling rates. To avoid introducing brittle martensite in the HAZ, it is generally recommended to preheat the base metal to a specified temperature prior to welding and to maintain that temperature (termed the interpass temperature) throughout the execution of the weld.

Table 2.3 provides information on heating requirements. Higher preheating and interpass temperatures are specified for thicker steels, in accordance with the above logic regarding heat dissipation. Additional and more extensive requirements are specified by the American Welding Society (AWS 2010, referenced by AISC 2010) and this document should be consulted for more details on this matter. A welding engineer can help determine the preheating, interpass, and postwelding heating needs for specialty applications and unusually congested details.

2.5.2 Hydrogen Embrittlement

An important distinction is made in Table 2.3 as to whether low hydrogen electrodes are used. Indeed, the introduction of hydrogen into the fusion or heat-affected zones increases the risk of embrittlement. Although the molten metal created during welding has a great propensity to absorb the surrounding hydrogen, much of this hydrogen is rejected during normal cooling. However, if cooling is too rapid, the hydrogen gas does not have sufficient time to escape and becomes entrapped at a high pressure within the steel, with the risk that micro-cracks will develop. Low-hydrogen electrodes have been developed to lessen this problem. Combined with preheating, they can generally eliminate hydrogen embrittlement. Nonetheless, it must be recognized that hydrogen may originate from other sources, the most common being water. For that reason, low-hydrogen electrodes must be stored in a dry environment. Preheating is also useful to evaporate moisture at the surface of the base metal before welding.

Steel Grade	Weld Process					AWS D1.1/D1.1M-2010 Minimum Temperature Requirement in °C (°F) for Various Maximum Thickness of Parts at Welding Location			
ASTM	SMAW w/o LHE	SMAW w/LHE	SAW	GMAW	FCAW	3 to 20 mm	20 to 38 mm	38 to 65 mm	65 mm or more
A36[a] A53[b] A500[c] A501 A709[d] A1011 SS[e]	X					0 (32)	65 (150)	110 (225)	150 (300)
A36 A53[b] A441 A500[c] A501 A529[f] A572[g] A588 A618[h] A709[i] A913[j] A992 A1011[k]		X	X	X	X	0 (32)	10 (50)	65 (150)	110 (225)

A572[l] A913 A709[mn] A852[n]		X	X	X	X	10 (50)	65 (150)	110 (225)	150 (300)

FCAW = Flux-Cored Arc Welding; GMAW = Gas Metal Arc Welding; LHE = Low Hydrogen Electrodes; SAW = Submerged Arc Welding; SMAW = Shielded Metal Arc Welding (commonly referred to as "stick" or manual welding).

[a]LHE only permitted for steel thicknesses less than 20 mm (3/4")

[b]Grades B

[c]Grades A, B, and C

[d]Grade 36

[e]Grades 30, 33, 36 Type 1, 40, 45, 50, and 55

[f]Grades 50 and 55

[g]Grades 42, 50, and 55

[h]Grades Ib, II, and III

[i]Grades 36, 50, 50S, and 50W

[j]Grade 50

[k]HSLAS Grades 45 (Class 1 and 2), 50 (Class 1 and 2), and 55 (Class 1 and 2), and HSLAS-F Grade 50

[l]Grades 60 and 65

[m]HPS70W (high performance steel)

[n]Maximum preheat and interpass temperature shall not exceed 200°C (400°F) for thicknesses up to 40 mm (1.5"), inclusive, and 230°C (450°F) for greater thicknesses.

Table 2.3 Minimum Preheat and Interpass Temperature Requirements

2.5.3 Carbon Equivalent

The "carbon equivalent" concept has been developed to convert into equivalent carbon content the effect of other alloys known to increase the hardness of steel. Although numerous compounds are added to increase the hardness of steel without causing much loss of ductility, increases in strength are always accompanied by a corresponding increase in hardness, some loss of ductility, and a reduced weldability. Most structural steels are generally alloyed to ensure their weldability, but some steels on the market still have rather high carbon equivalent content. The AWS (2010) mentions that for an equivalent carbon content above 0.40, there is a potential for cracking in the heat-affected zones near flame-cut edges and welds. Various formulas have been proposed to calculate the carbon equivalent content of certain steels. For structural steels, the American Welding Society (AWS 2010) recommends the following formula:

$$CE = C + \frac{(Mn + Si)}{6} + \frac{(Cr + Mo + V)}{5} + \frac{(Ni + Cu)}{15} \tag{2.10}$$

where CE is the carbon equivalent measure; and C, Mn, Si, Cr, Mo, V, Ni, and Cu are the percentage of carbon, manganese, silicon, chromium, molybdenum, vanadium, nickel, and copper, respectively, alloyed in the steel.

Interestingly, structural engineering standards do not specify carbon content equivalent limits for structural steels. Instead, control of their weldability is indirectly achieved through limiting the maximum percentage of certain alloys. This practice has endured largely because of the generally satisfactory performance of welded structures constructed with the weldable structural steels currently available on the market, even though some of those steels have a CE in excess of 50 and therefore a high cracking potential. However, as high-strength steels come into much greater use and reported instances of brittle failures continue to increase (e.g., Fisher and Pense 1987, Tuchman 1986), an awareness of the significance of the carbon content equivalent of steels is essential.

Finally, it is interesting that, although structural steel used to be produced directly from pig iron in the 1960s and 1970s, steel is now often produced from scrap metal. As a result of this change in practice, a large number of "foreign" metals such as aluminum are now found in trace amounts in these steels. There is no evidence that this metallurgical variance could have undesirable consequences on the physical properties of steel, but some structural engineers have expressed concerns regarding the unknown consequences of this practice (SAC 1995).

2.5.4 Flame Cutting

Some structural details can also introduce brittle conditions in steel structures. For example, weld-access holes are frequently flame-cut in the webs of beams near their flanges to facilitate welding. The weld-access hole may also relieve stresses by reducing the transverse restraint on the flange welds. However, flame-cutting generally creates an irregular surface along these holes and modifies the metallurgy of the steel into a brittle martensite up to a depth of 3 mm (0.12 in) along the edge of the hole. This martensite transformation along the roughened surface promotes crack formation. Therefore, when these holes must be flame-cut, it has been recommended that the martensite region be ground smooth prior to welding (Bjorhovde 1987, Fisher and Pense 1987).

2.5.5 Weld Restraints

Absorbed hydrogen, high carbon content, and flame cutting can all create an environment favorable for crack initiation and propagation, but an active external factor is usually needed to trigger fracture. The residual stresses induced by restrained weld shrinkage can sometimes provide this necessary additional factor (AISC 1973). The choice of welding sequence and weld configuration can severely restrain weld shrinkage.

To understand the nature and impact of these restraints, it is helpful to visualize welds as molten steel that solidifies when cooled. If unrestrained, the hot weld metal will shrink as it cools. It is well known that important distortions will occur as a result of this shrinkage in nonsymmetrical welds, as shown in Figure 2.14. Many examples of such distortions and information on their expected magnitude are available in the literature (e.g., Blodgett 1977a). However, if existing restraints prevent this distortion, internal stresses in self-equilibrium must develop. As shown in Figure 2.15 for single-pass welds, the weld metal will generally be in tension and the pieces being connected will generally be in compression where they are in contact. In multipass welds, some of the weld metal first deposited (usually at the root of the weld) will initially be in tension as it cools, but could eventually end up in compression after all the subsequently deposited weld material has cooled and compressed the previously deposited material. The weld material deposited last will generally be subjected to the largest residual tension stresses. Complex residual stress patterns will obviously exist in all but the simplest details. An example of how the residual stress condition in a detail can be qualitatively assessed is presented at the end of this section.

To minimize the tensile residual stresses in welds, at least for simple weld details such as those shown in Figure 2.15, it has been suggested (Blodgett 1977b) that a few soft wires could be inserted

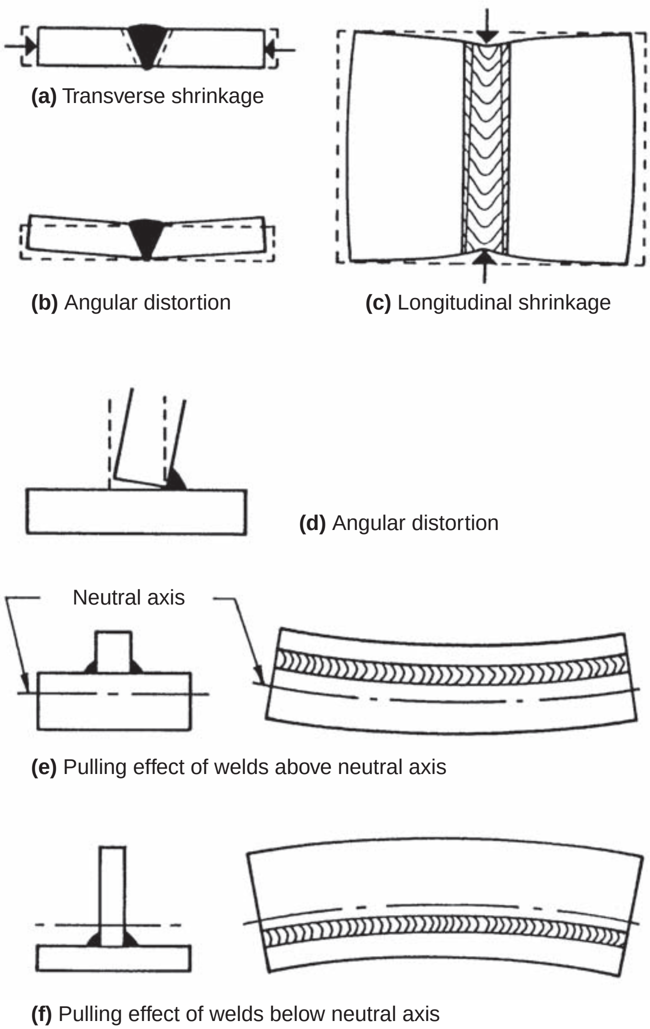

Figure 2.14 Examples of distortion and dimensional changes in assemblies due to unsymmetrical welds. (*From The Lincoln Electric Company*, The Procedure Handbook or Arc Welding, *12th Edition, with permission*.)

between the pieces to be welded. During welding, these wires will simply crush with little resistance, allowing the welds to shrink without restraints, thus preventing the development of residual stresses.

Assuming invariant material properties, it is generally preferable to choose a weld configuration that minimizes internal residual stresses. However, there are instances in which large residual stresses are bound to be present. For example, if a beam-to-column fully

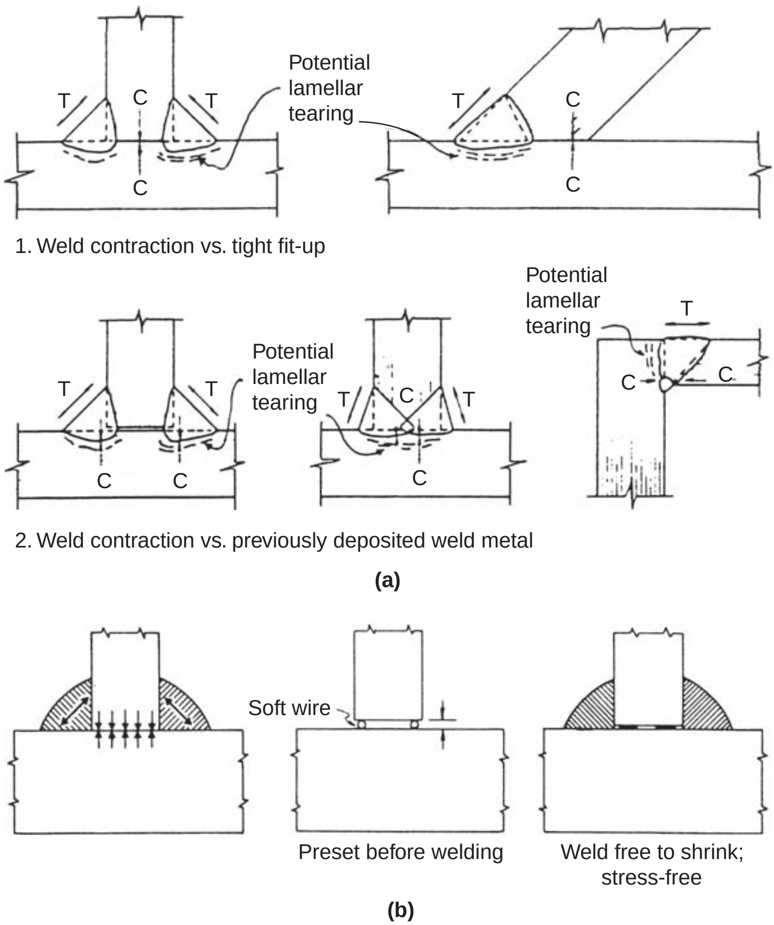

FIGURE 2.15 (a) Examples of internal stresses due to weld restraints. (b) Example of measure to reduce the magnitude of such stresses. (*Figure a from F.R. Preece and A.L. Collin*, Steel Tips: Structural Steel Construction in the '90s, *with permission from the Structural Steel Education Council*; *figure b from O.W. Blodgett, Special Publication G230 of The Lincoln Electric Company*: Why Do Welds Crack, How Can Weld Cracks Be Prevented, *with permission from The Lincoln Electric Company*.)

welded connection must be performed at both ends of a beam located between two braced frames, as shown in Figure 2.16, shrinkage of the welds is prevented by the rigid braced frames, and the likelihood of yielding (or cracking) these welds or the adjacent base metal is rather high. In such a case, preheating and postheating may be necessary, along with a stringent inspection program to check the integrity of the resulting welds. Alternatively, changes to the construction sequence should be contemplated.

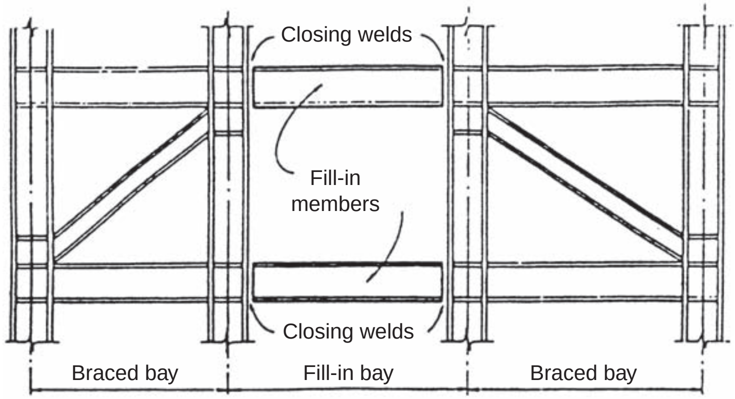

When final closure welds are made between rigid assemblies they are under high restraint. Weld metal and base metal contraction upon cooling must be accommodated either by yielding or cracking or elongation of the full member.

Figure 2.16 Closing welds for members between rigid assemblies as an example of poor construction sequence, leading to highly restrained welds. (*From F.R. Preece and A.L. Collin,* Steel Tips: Structural Steel Construction in the '90s, *with permission from the Structural Steel Education Council*.)

2.5.6 Lamellar Tearing

Steel is usually treated as an isotropic material. However, the available test data on steel plates generally demonstrates a significant anisotropy of strength and ductility (Figure 2.17a) because the properties of steel plates tested in the through-thickness direction vary significantly from those in any of the plane directions. The presence of small microscopic nonmetallic compounds (termed "inclusions") in the metal and flattened during the rolling process explains this difference. These flattened inclusions act as microcracks, of no consequence when a steel plate is stressed in its plane directions, but that can grow and link when stresses are applied in the through-thickness direction (z-direction), as shown in Figure 2.17b, producing a brittle failure mechanism known as lamellar tearing. However, this phenomenon has been observed only in thick steel plates with highly restrained weld details (thicker steel sections generally have more nonmetallic inclusions). An effective solution to the problem of lamellar tearing is to detail the welded connection with bevels that penetrate deep into the cross-sections to be welded, thereby engaging the full thickness of the plates in the resistance mechanism instead of relying on through-thickness strength to resist the tension force at the surface of the plate. Examples of alternative weld details are presented in Figure 2.17c. The engineer can visualize, in each of these

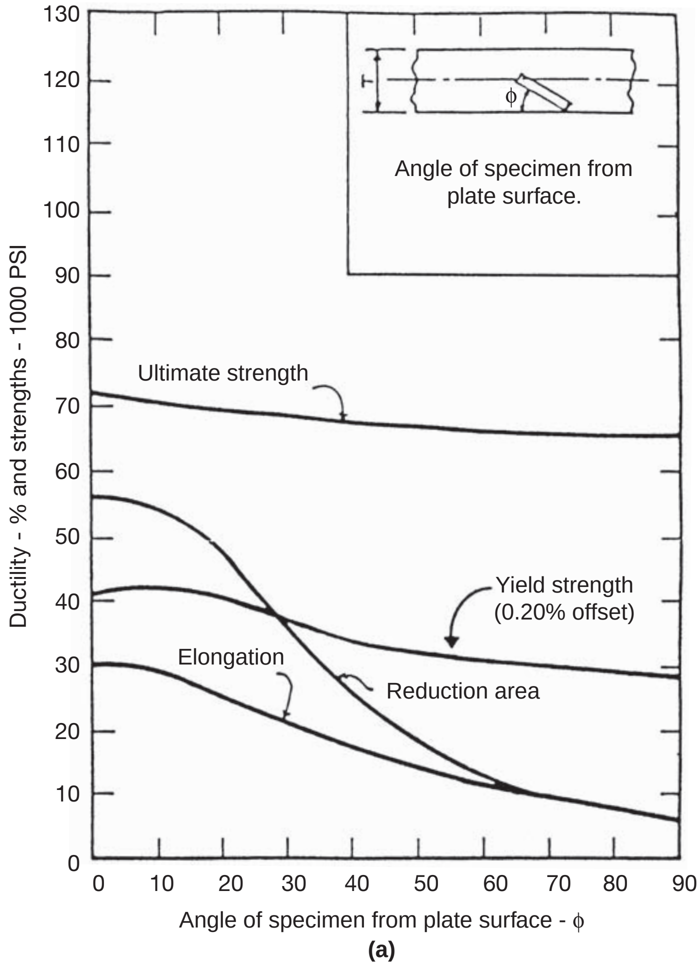

Figure 2.17 Lamellar tearing: (a) anisotropic properties of structural steel; (b) Photo of 0.07 to 0.10”planar inclusions (laminations); (c) schematic of mechanism of lamellar tearing, starting with microfissures initiation at flattened nonmetallic particle inclusions, growth of cracks due to cross-thickness tension forces, and rupture by interconnecting tears between cracks on different planes, resulting in a stepped rupture surface; (d) details prone to development of lamellar tearing and corresponding improved details. (*Figures a and c from F.R. Preece and A.L. Collin*, Steel Tips: Structural Steel Construction in the ‘90s, *with permission from the Structural Steel Education Council; Figure b from Barsom and Pellegrino 2000, copyright © American Institute of Steel Construction. Reprinted with permission. All rights reserved*)

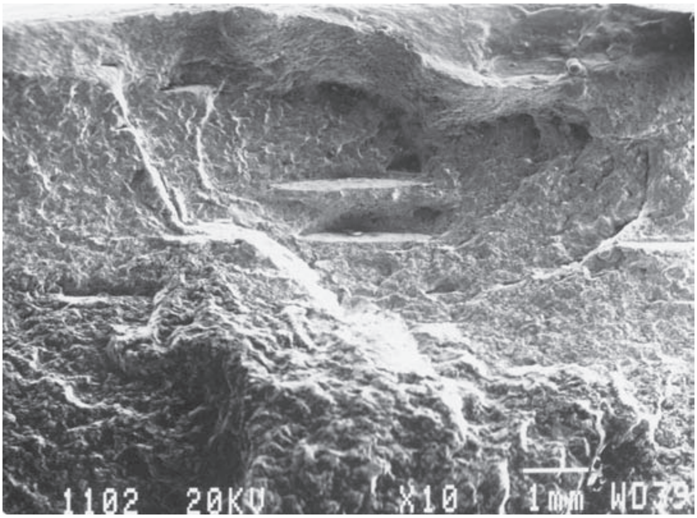

(b)

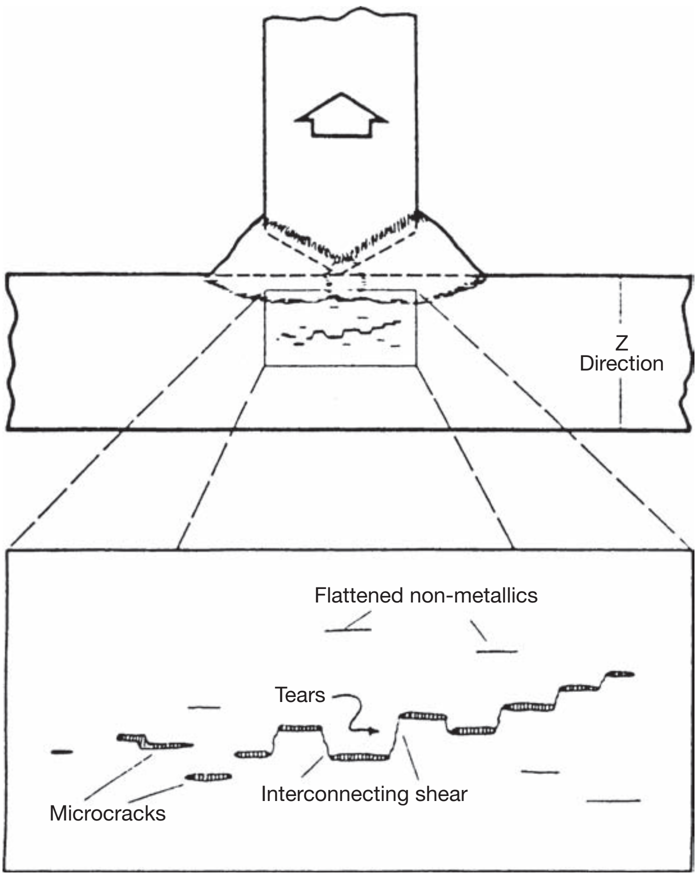

(c)

Figure 2.17 (*Continued*)

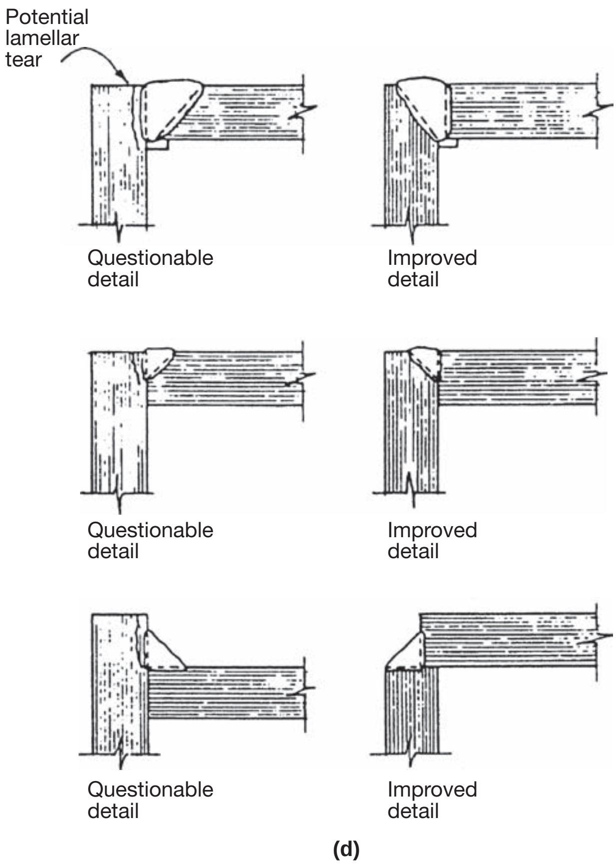

FIGURE 2.17 (*Continued*)

improved details, the weld pulling on all "layers" of the thick steel plate rather than on its surface.

2.5.7 Thick Steel Sections

Most of the aforementioned factors contributing to brittle failures will not lead to such failures in most cases. However, special care must be taken with very thick high-strength steel sections, roughly defined as 60 mm (2.4 in) and thicker, because these are known to be more prone to lamellar tearing and other fracture problems.

Likewise, the complex triaxial stresses induced by highly restrained weld details are of greater consequence for heavy thick steel sections. For example, brittle failures of fully welded heavy rolled wide-flange beam splices have been reported (Fisher and

Pense 1987, Fisher personal communication 1984) in which cracking initiated at the end of the flame-cut weld-access hole. Through use of existing qualitative information on weld shrinkage and distortion, orientation of the weld and the welding sequence can provide insight into the triaxial stress state at the end of a flame-cut hole. For the example shown in Figure 2.18a, the weld sequence is assumed to have been initiated with a root pass on each flange, followed by welding of the web, the outside of the flanges, and finally the inside of the flanges. Because of the presence of the root weld between the flanges, the web welds induce tension in the vertical plane (noted 1* on the triaxial stress diagram in Figure 2.18a), but the weld-access hole can effectively reduce these residual stresses. More critical is the welding

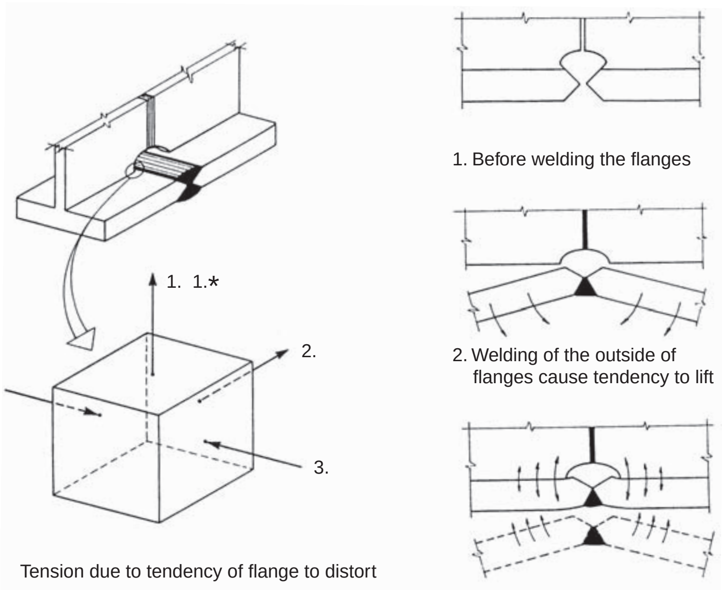

1. Tension due to tendency of flange to distort

1.* Tension due to high restraint against longitudinal shrinkage of web welds (may not be present if cope holes large enough)

2. Tension: Transverse welding restraint of flange

3. Compression due to longitudinal shrinkage of flange welds

3. By pulling action of the web, the flange stays in place but tension residual stresses are induced

(a) (b)

Figure 2.18 Qualitative illustration of: (a) triaxial state of stress at the point of cracking initiation, and (b) effect of weld shrinkage on internal stresses. (*Bruneau and Mahin 1987*.)

of the outside of the flanges prior to the inside of the flanges. As shown on Figure 2.18b, this creates a tendency of the flanges to rotate (bow) away from the web. Therefore, the web-flange region at the end of the hole is stressed in tension, and any initial crack or microcracks in this region could propagate further. Assuming that a crack has formed, crack propagation will reduce the flange curvature, which in turn should lower the tensile force at the end of the hole, and the crack will stop propagating once it reaches a finite length. The final path followed by the crack will depend on the magnitude of all the components of the triaxial stress state shown on Figure 2.18a. A crack may rest in a stable position until external loads applied to the structure raise the stresses to the threshold whereupon crack propagation will resume. Whether total fracture of flange will occur can be determined through use of fracture mechanics.

2.5.8 Fracture Mechanics

Fracture mechanics (i.e., the study of the behavior and strength of solids having crack discontinuities) is a field of engineering unto itself. A comprehensive presentation of this topic is beyond the scope of this book, and the interested reader is referred to the literature (e.g., Rolfe and Barsom 1999). However, although fracture mechanics has become part of the design process in some applications of engineering (e.g., in ships and airplane hull design and pressure vessels design), it is seldom used at this time for the design of mainstream civil engineering structures such as buildings and bridges (although fatigue, which is an extension of fracture mechanics, is obviously considered in many design situations). However, once brittle failures are encountered, investigators frequently resort to fracture mechanics to explain the observed behavior.

This state-of-practice is partly a consequence of the difficulty and limitations inherent in the currently available fracture mechanics analysis methods. For example, one simple and effective fracture mechanics approach requires comparison of a stress intensity factor, K_I, with the fracture toughness, K_{IC}, of the material (also termed critical stress intensity factor). Calculation of K_I for a given specimen and crack geometry requires resorting to empirically developed available solutions (Rooke and Cartwright 1976). K_{IC} must be determined by special fracture toughness tests (ASTM 1985a).

For cracks that propagate through base steel, fracture mechanics has proved to be an effective analytical tool. However, for fractures through welds, K_{IC} of the adjacent steel is irrelevant; K_{IC} of the weld itself is needed, a property sensitive to workmanship. This is a problem in postfailure investigations because the K_{IC} of a weld that has failed cannot be inferred from the other welds that have not fractured. Furthermore, K_{IC} values obtained on small standard welded specimens may be difficult to reliably extrapolate to large multipass welds; cracks tend to simply propagate through the weakest link between the passes in those welds. An example application of fracture mechanics principles to describe the brittle fracture of a high-strength heavy steel section splice with partial penetration welds is presented by Bruneau and Mahin (1987).

2.5.9 Partial Penetration Welds

Partial penetration welds should be avoided whenever ductile response is required (or implied) by design. When structural members connected by partial penetration welds are loaded to their ultimate strength in tension or flexure, only yielding of the weld is possible at best because the cross-sectional area of the weld is smaller than that of the adjacent base metal. As a result, because the weld's length is rather small, particularly at the root, large ductility of the weld metal translates into small or no ductility at the component level. Moreover, from a fracture mechanics perspective, the unwelded part of the connected metal can act as an initial crack; this cracklike effect at the toe of a typical partial penetration weld can be clearly seen in Figure 2.19 for a partial penetration weld executed on an 89-mm-thick (3.5-in) flange (cut, polished, and etched to allow visual observation of the weld).

The discontinuity of the base metal produced by the partial penetration weld also introduces a significant stress concentration at the toe of the weld. This is a problem particularly in heavy rolled steel sections because their metallurgy suffers from a reduced fracture toughness (K_{IC}), especially in the web-flange core area where the higher stresses occur as a result of this stress concentration. The web-flange core area of a heavy steel section does not get worked to the degree that thinner sections do during the rolling process. It has a "castlike" structure with large grains and inherently less fracture toughness. A higher fracture toughness is obtained away from this core area, closer to the outer surface of the flanges, the flange tips, and the bottom surface of flanges. This is in spite of adequate and constant yield stress properties throughout the flange.

2.5.10 K-Area Fractures

Even when a structural shape created by the hot rolling process has a fine grain structure, ductile properties, and excellent toughness, some amount of cold working after it has cooled down is often applied to ensure that it meets its specified geometric tolerances. This is achieved by a process called rotary straightening conducted at the mill itself. During rotary straightening, the shape is run through a series of rollers to give it its final geometry by removing the undesirable distortions that were created by residual stresses during the cooling process.

Figure 2.19 Polished and etched partial penetration weld on a 90-mm-thick (3.5-in) flange.

However, such cold working conducted to strengthen a wide-flange shape locally strain hardens the steel and increases its yield and ultimate strengths, its hardness, and its ratio of yield-to-ultimate strength, as well as decreases its ductility. These combined effects can have a detrimental affect on the Charpy-V notch toughness over an area where the web meets the flanges—commonly known as the “k-area” (Barsom and Pellegrino 2000, Kaufmann et al. 2001a, Iwankiv and Zoruba 2002, Tide 2000).

More specifically, the k-area in the web starts at the midpoint of the flange-to-web radius and extends approximately 1.5 in beyond the

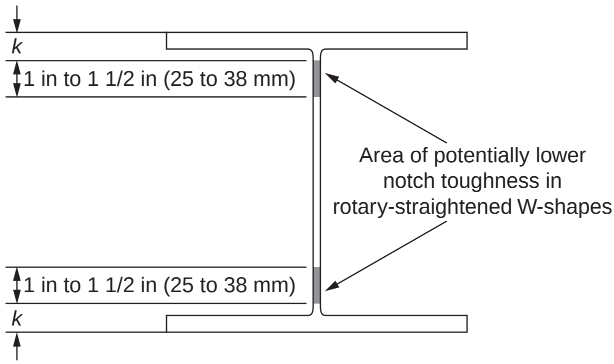

Figure 2.20 Typical k-area for a wide-flange shape. (*AISC 2010, copyright © American Institute of Steel Construction. Reprinted with permission. All rights reserved.*)

point of tangency between the curved fillet and the web (Figure 2.20); that region roughly corresponds to the part of the web that is cold worked to realign the flanges perpendicular to the web during rotary straightening. The term "k-area" is defined by reference to the distance, *k*, in wide-flange shapes, which is measured from the top of the flange to the point were the constant-thickness part of the web starts. This *k* distance is not uniform depending on mill practices. Typically, design manuals list both a minimum and a maximum value of *k* encompassing the products of the mills they represent—the lower value for calculating web compactness/stability and the high one for detailing purposes (AISC 2001).

Material studies on A572 and A913 Grade 50 steel shapes confirmed that pre-straining increased the yield and tensile strengths by 20 to 60% and 5 to 20%, respectively (Kaufmann et al. 2001a), as shown in Figure 2.21—a behavior consistent with the idealized behavior illustrated in Figure 2.10 when reloading occurs after an excursion in the strain-hardening range (cold forming), but in this case exceeding the monotonic curve envelope upon reloading. A lower toughness was measured and prestrains of 0.15 to 0.20 were found to initiate cracks within 5 to 10 cycles of hysteretic behavior. Okazaki and Engelhardt (2007) also observed fractures initiating in the k-area of many tested links of the types used in eccentrically braced frames after a few cycles of hysteretic behavior, along with higher tensile strength and reduced toughness and ductility in the k-area of the links. Yet, beam-to-column connections specimens tested by Chi and Uang (2004), with holes drilled in the k-area to act as crack initiator with intent of triggering early fractures, actually performed satisfactorily, with substantial hysteretic behavior.

In light of the above observed possible impact of rotary straightening and limited statistical data on expected levels of prestrains,

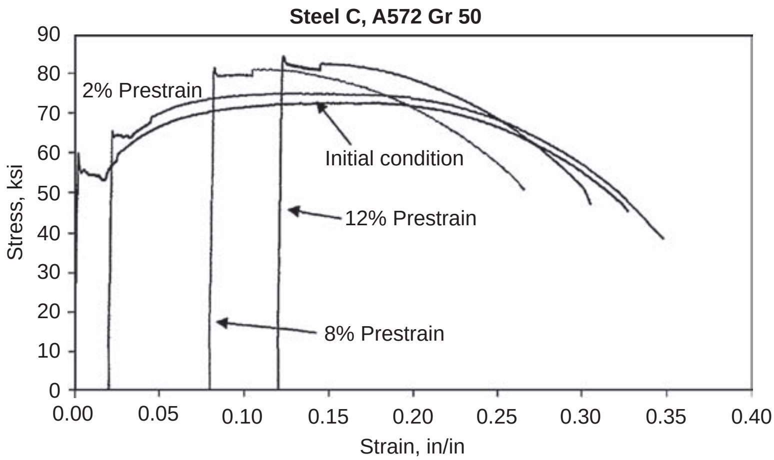

Figure 2.21 Stress-strain curves for A572 Grade 50 steel obtained after various amount of cold-forming. (*From Kauffman et al. 2001a, copyright © American Institute of Steel Construction. Reprinted with permission. All rights reserved.*)

some design specifications recommend to avoid welding in the k-area. Figure 2.22 shows a recommended compliant typical column stiffener details (AISC 2010) experimentally shown to provide satisfactory performance (Dexter et al. 2001, Lee et al. 2002). Iwankiv and Zoruba 2002 also suggested avoiding web doubler plates, reducing residual stresses in highly restrained joints by preheating and proper

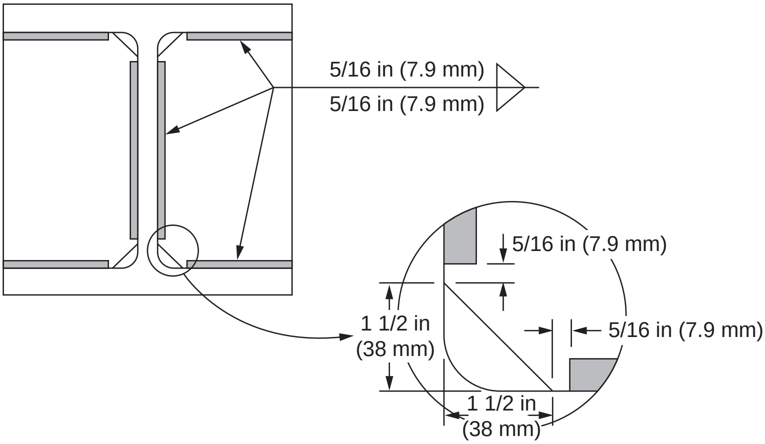

Figure 2.22 AISC recommendations to keep stiffeners' welds outside of k-area. (*AISC 2010, copyright © American Institute of Steel Construction. Reprinted with permission. All rights reserved.*)

sequencing of welding, and magnetic particle or dye penetrant inspection of the welds in the k-area.

Note that while embrittlement of the k-area was found likely to have a critical impact on steel structures that require highly ductile behavior at the component level (such as in seismic-resistant design applications), it was also occasionally reported to be problematic in some nonyielding applications where cracking in the k-area of galvanized beams was attributed to liquid metal embrittlement (BCSA 2005, Kinstler 2005), a phenomena whose definitive atomic mechanism is still being investigated.

2.5.11 Strain Aging

When unloaded after an excursion into the strain-hardening range, steels left unstressed for a period of time will experience a modification in their molecular structure that will translate, upon reloading, into an increase of their yield and tensile strengths as well as a decrease in ductility and fracture toughness (Barsom and Korvink 1998, Pense 2004), as illustrated in Figure 2.23. This phenomenon, known as static strain aging, is attributed to the filling of material dislocations by migrating nitrogen and carbon atoms. Dislocations are defects in the crystals structure of steel that facilitate the development of slip planes (i.e., yielding), and that are "locked" when filled by the migrating atoms (Baird 1963, 1971; Cottrell and Bilby 1949;

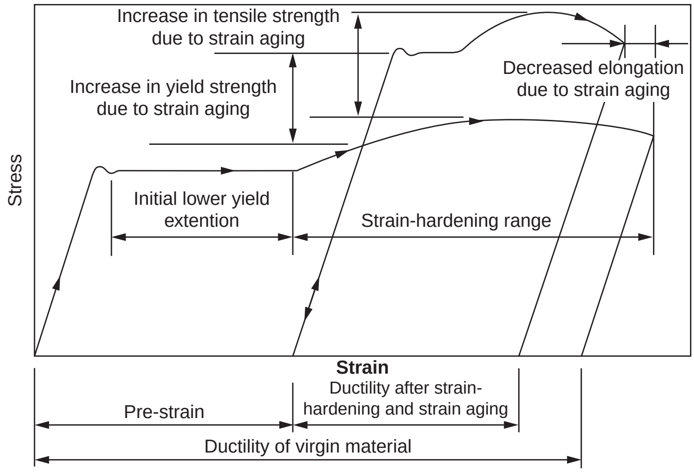

FIGURE 2.23 Effect of Strain Aging. (*Barsom and Korwink 1998—with permission from SAC Joint Venture, a Partnership of the Structural Engineers Association of California, Applied Technology Council, and Consortium of Universities for Research in Earthquake Engineering.*)

Pense 2004). Although some industries working with deformed sheet steel (such as the automotive industry) have had to contend with strain-aging issues, structural steels used in construction have more carbon and alloys and a more complex microstructure that has prevented strain aging at ambient temperature. However, at a temperature of 400°F (200°C), substantial strain aging can develop in those structural steel within a few hours. Caution is thus warranted when cold forming at relatively high temperatures. Incidentally, Barsom and Korvink (1998) indicated that if rotary straightening operations are conducted at less than 200°F (93°C), the degradation of properties in the k-area attributable to strain-hardening will be more significant than the secondary effects of strain aging.

2.5.12 Stress Corrosion

Many guides and documents address the topic of corrosion, providing engineering advice on how to protect steel against corrosive environments and detail structures such as to avoid trapping liquids or solids that could trigger or accelerate the corrosion process (e.g., Koch et al. 2002). Engineering procedures also exist to calculate the residual strength of structural members that have lost cross-sectional area due to severe corrosion, or to predict such losses as a function of time (e.g., Kayser and Novak 1989, Kulicki et al. 1990).

Stress corrosion is a less familiar phenomenon that is known to happen in various metals, such as certain steels and copper alloys, as well as numerous types of polymers. It can transform ductile steel into a brittle material without substantial visible evidence of this process taking place. Stress corrosion cracking can develop unexpectedly when materials under tensile stresses are exposed to specific chemicals (hydrogen embrittlement is sometimes considered a subset of stress corrosion). The process is accelerated at higher temperatures. Under these conditions, small surface cracks propagate inside the steel, even when exposed to low stress levels considered not critical per fracture mechanics models (e.g., stress corrosion cracks have been reported to propagate in conditions corresponding to less than 1% of the critical stress intensity factor, K_{IC}). Although this phenomenon is of obvious impact to chemical and petrochemical industries, it has also occasionally had adverse effects on conventional public infrastructures.

Certain types of stainless steel used structurally are known to be highly sensitive to stress corrosion if exposed to water or vapors containing traces of chlorides. Such a chloride attack led to the collapse of a concrete roof supported by stainless steel tension bars over a swimming pool at Uster near Zurich in 1985 (Faller and Richner 2003). Similar structures in Europe collapsed, or were found at immediate risk of failure and retrofitted with galvanized steel or stainless steel bars of a different grade having greater resistance to stress corrosion cracking. Although stainless steel has a history of satisfactory performance in multiple applications in which it is either unstressed or intermittently stressed, corrosion cracking can become a threatening failure mode under sustained tensile stresses of any magnitude.

Stress corrosion cracks in regions of large residuals stresses, together with other factors, led to the fracture of a critical eye-bar joint and the ensuing collapse of the Point Pleasant "Silver" Bridge in Ohio, in December 1967 (Fisher 1984, NTSB 1971). Sulphur, an element not belonging to the metal itself, was detected in the critical crack (and other subcritical cracks) during the forensic investigation, possibly diffused as a consequence of the sulphur dioxide emissions of a local power station using high-sulphur West Virginia coal and/or a foundry close to the east side of the bridge. Tests as part of the investigation indicated that exposure to hydrogen sulphide produced stress corrosion and reduced the fatigue resistance of the material used in the eyebars that fractured.

Figure 2.24 illustrates typical "branches" of stress corrosion cracks having penetrated inside the flange of a structural steel shape, virtually undetectable from the un-attacked steel surface (Ahluwalia 2003).

Stress corrosion due to the diffusion of atomic hydrogen at the tips of cracks in the wires used in cable-supported bridges has been

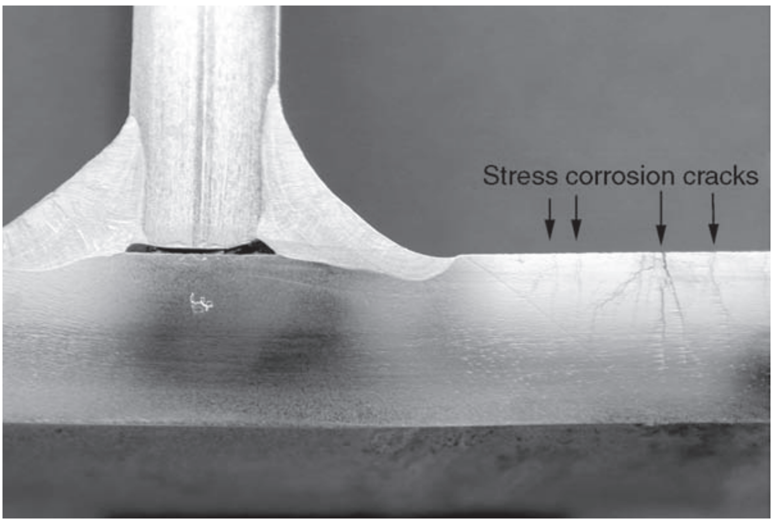

(a)

Figure 2.24 Chloride stress corrosion cracks developing in stainless steel Grade 304L, in region of residual tensile stresses due to welding. (*Courtesy of Dr. Hira Ahluwalia, Material Selection Resources Inc., www.doctormetals.com.*)

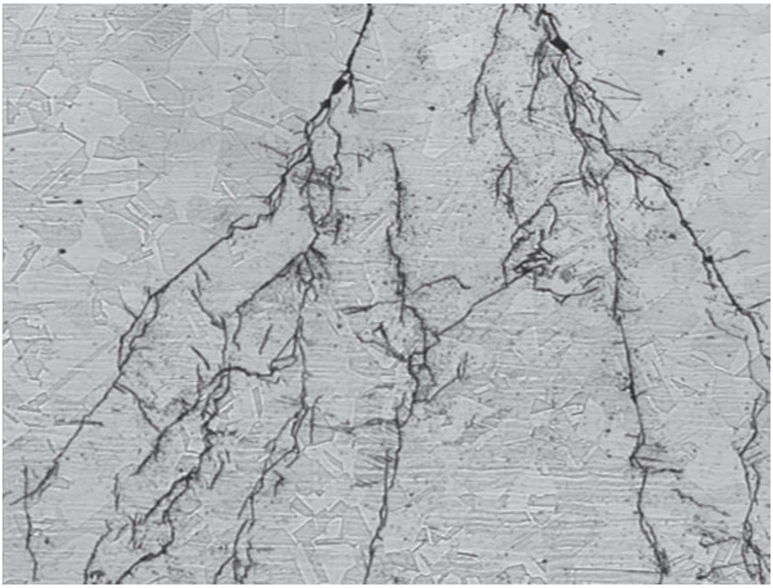

(b)

Figure 2.24 (*Continued*)

reported to explain the observed ductility losses in such wires (Mahmoud 2003a, 2003b). Figure 2.25 shows the relatively brittle fracture, without cross-sectional necking, of a wire affected by such hydrogenation, by contrast to a regular wire, underlining the need to consider this condition in structural safety evaluations.

Avoidance of stress-corrosion cracking can be best achieved by selection of materials not susceptible to such degradation when exposed to specific chemical or aqueous environments (e.g., using data compiled by NPL 1982), although this is not always possible. Other approaches include heat treatment to relieve residual stresses introduced by welding, avoiding details that induce stress raisers (e.g., using full penetration welds instead of fillet welds), avoiding cold work, or shot peening (Marsh 1993). That latter metal treatment consists of bombarding the surface of the steel at risk with spherical projectiles to plastically deform it into a layer of compression stresses, eliminating the tensile stresses at the surface (see MIC 2005 for details).

2.5.13 Corrosion Fatigue

Corrosion fatigue is another type of environmentally assisted cracking known to have led to structural failures—for example, it contributed to the collapse of Kinzua Viaduct in Pennsylvania during a wind storm in July 2003 (DCNR 2003). By contrast with stress corrosion cracking, it develops in uniformly corroded materials, with cracks that could be visible, if exposed, as for regular fatigue cracks. The detrimental consequence of corrosion fatigue is that it substantially reduces fatigue life of steel details, connections, and members under

Hydrogen embrittlement showing

Top: Tension specimen side view with minimal necking and low ductility

Right: Stress-strain curve

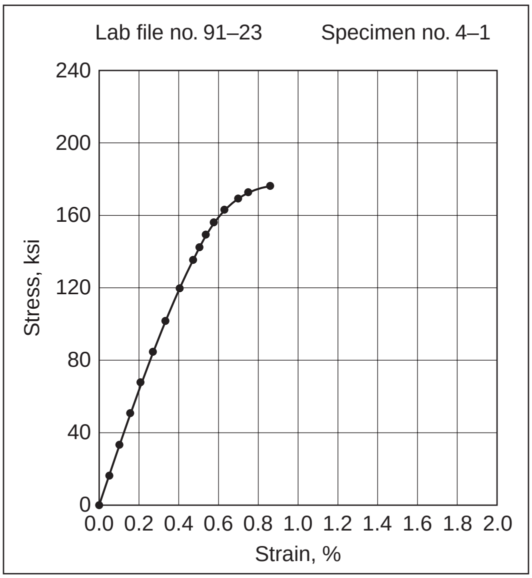

(a)

Figure 2.25 Fracture and force displacement response of wires taken from a suspension bridge cable, showing: (a) relatively brittle response and (b) ductile response. (*Courtesy of Khaled M. Mahmoud of Bridge Technology Consulting (BTC), New York.*)

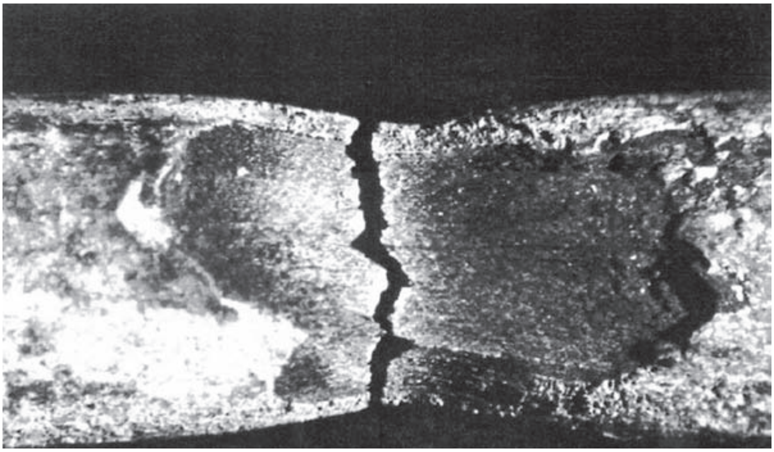

Stress corrosion cracking showing:

Top: Tension specimen side view with appreciable necking

Right: Stress-strain curve

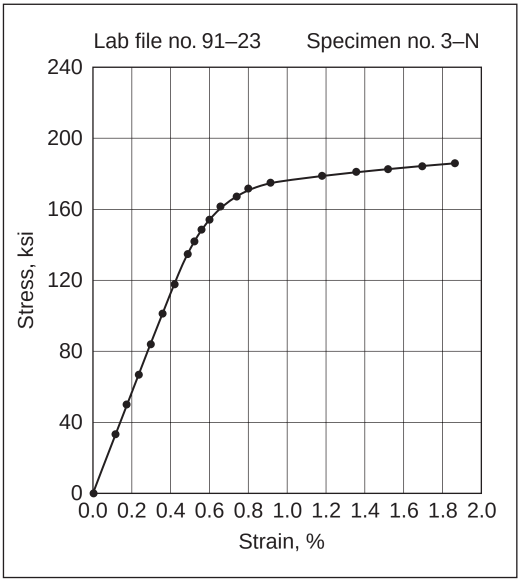

(b)

FIGURE 2.25 (*Continued*)

cyclic loading, and that it eliminates the fatigue limit (i.e., the stress below which high-cycle fatigue life is theoretically infinite for a specified detail). In stress corrosion the period of crack nucleation is substantially shorter, with crack propagation initiating sooner with sustained growth in stress regimes below the critical stress intensity factor (K_{IC}). However, given that high-cycle fatigue is beyond the scope of this book (as described in Section 2.6), so is a detailed exposé of the effects of corrosion fatigue. Corrosion fatigue can be prevented through the same mechanisms and procedures adopted to prevent regular fatigue and corrosion.

2.5.14 Ductility of Corroded Steel

It is recognized that the presence of severe corrosion can typically result in increased stress levels for a given load or in larger stress ranges under fatigue-type cyclic loading, as well as some notable shifts in the type of ultimate failure expected as some geometric properties and failure modes are related to the square or cube of member dimensions (Kayser and Nowak 1989). However, experimental studies on the behavior of corroded members, although few, indicate that the monotonic structural ductility of steel is not detrimentally affected by corrosion. For example, Fisher et al. (1990) conducted ultimate strength tests on two severely corroded bridge hangers having approximately 40% area loss and taken from an actual bridge. They found that the hangers could resist maximum axial loads corresponding to the tensile strength calculated using the effective net area of the most rusted region of the member, while exhibiting no considerable reduction in the monotonic structural ductility of the specimens. Similar behavior was observed by Bruneau and Zahrai (1997) for corroded A7 steel coupons taken from an existing bridge, although a 30% reduction in the elongation at failure was noted, as shown in Figure 2.26.

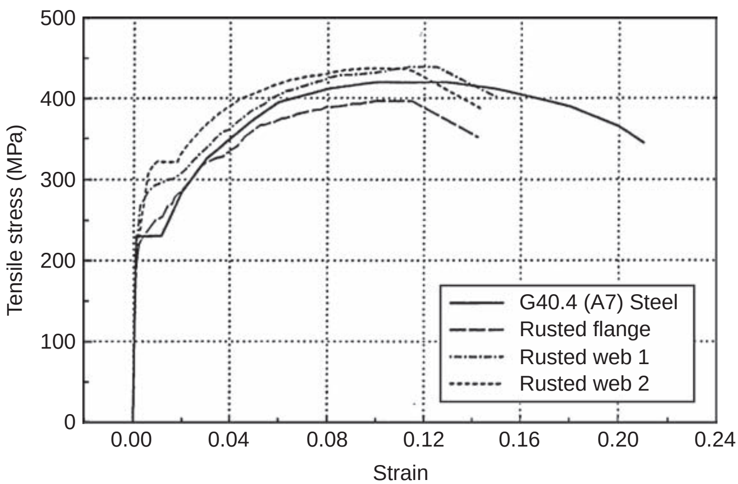

FIGURE 2.26 Experimentally obtained stress-strain relationship for rusted coupons (normalized by area computed using minimum thickness of rusted coupon), compared with typical stress-strain curve of unrusted A7 steel (*Zahrai and Bruneau 1998*).

Knowledge on the cyclic ductility of corroded steel is limited, but important given that the hysteretic behavior of steel members may be relied upon to dissipate earthquake energy. These members would need to perform as intended even if rusted by the time a major earthquake strikes (in a distant future). Cyclic inelastic flexural on structural members revealed that, although stable hysteretic behavior comparable with that of unrusted specimens is possible, fracture under alternating plasticity (i.e., low-cycle fatigue) will typically develop sooner than for comparable unrusted members. However, the considerable cumulative hysteretic energy dissipated in those tests prior to the development of fatal cracking was deemed sufficient to provide adequate seismic resistance in most applications, as shown in Figure 2.27. However, the impact of large corrosion notches or more severe levels and types of corrosion than considered by Bruneau and Zahrai (1997) deserve further experimental study.

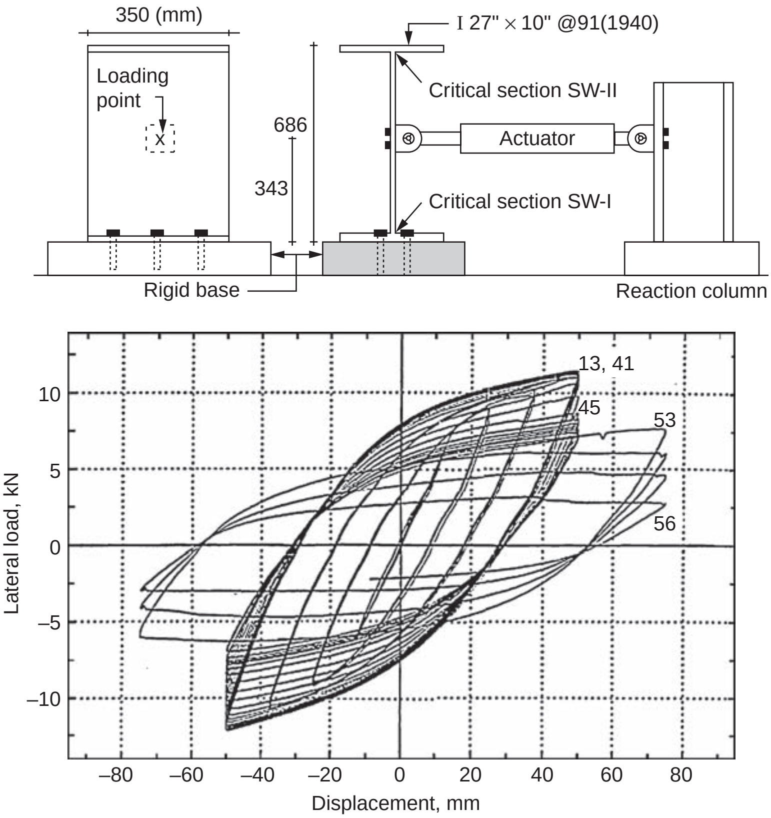

Figure 2.27 Cyclic ductility of corroded steel: (a) test set-up, (b) resulting hysteretic behavior (*Zahrai and Bruneau 1998*).

2.6 Low-Cycle versus High-Cycle Fatigue

2.6.1 High-Cycle Fatigue

Crystal imperfection, dislocations, and other micro cracks in steel can grow into significant cracks in structural components subjected to the action of repeated loads. For example, various components in bridges subjected to heavy traffic loading and offshore structures subjected to wave loading will be subjected to millions of cycles of load during their service life. These components must be detailed with proper care to provide adequate resistance against crack initiation and crack propagation. The ability of metals and specific welded details to resist many hundreds of thousand cycles of strain below the yield level is termed "high-cycle fatigue resistance." One accomplishes design to ensure this resistance by limiting the maximum stress range due to cyclic loading to values that are usually much below the yield stress and by selecting details that minimize stress concentrations (Rolfe and Barsom 1999, Stephens et al. 2001). The design of these members can be accomplished according to traditional steel design methods, with stress ranges presented in various standards, and is therefore beyond the scope of this book.

2.6.2 Low-Cycle Fatigue

Anybody who has ever destroyed paper clips knows that these can be bent back and forth only a limited number of times. Some may even have noticed that the maximum number of cycles these paper clips can resist is a function of the severity of their postyield plastic deformations. The ability of metals to resist a limited and quantifiable number of strain cycles above the yield level is termed "low-cycle fatigue resistance" or "resistance to alternating plasticity." Although both low-cycle fatigue and high-cycle fatigue failures result from similar crack initiation and crack growth mechanisms, only low-cycle fatigue resistance characterizes the cyclic response of components and connections deformed beyond the yield limit and is thus related to ductile design.

There is also a significant difference between the low-cycle fatigue resistance of the material obtained by tests on coupons of the base metal and that of actual structural members. This difference principally arises as a result of the rather large inelastic strains that develop upon local buckling. For example, although tests of coupons indicate that mild steel can resist more than 400 cycles at a strain of 0.025 (ASM 1986), Bertero and Popov (1965) showed that local buckling in a steel beam of compact cross-section in bending started after half a cycle at that strain and that fracture occurred after the 16th cycle. Indeed, in steel sections that can develop their plastic moment capacity (see Chapter 3), local buckling due to cyclic loading will occur at smaller strains than predicted for monotonic loads, because the inelastic curvatures introduced in the flanges of beams subjected to flexural moments above the yield moment will typically act as initial imperfections and help trigger local buckling upon reversal of loading. This explains why smaller maximum width-to-thickness ratios are required by codes for members subjected to cyclic loading (as will be shown later). Fortunately, low-cycle fatigue resistance increases rapidly with reductions in the maximum cyclic strain (Figure 2.28). Steel structures detailed for ductile response must be able to resist the expected cyclic inelastic deformation demands without prematurely failing by low-cycle fatigue—usually an implicit goal of design specifications.

The low-cycle fatigue life of a material is established by conducting axial tests on standard coupons subjected to fully reversed cycles of constant strain amplitudes. By repeating such tests for various values of strain amplitude, it is possible to correlate strain amplitude, ε_a, to the number of cycles, N_f, or the number of load reversals, $2N_f$, applied before fracture. Such a curve is schematically shown in Figure 2.29, and is asymptotic to two straight lines of slopes b and c: one for high-cycle fatigue in the elastic range, and one at large inelastic cyclic plastic strains, respectively. The total strain range, $\Delta\varepsilon$, being equal to twice the strain amplitude (i.e., ranging from $-\varepsilon_a$ to $+\varepsilon_a$), can be expressed in terms of elastic and plastic ranges, $\Delta\varepsilon_e$ and $\Delta\varepsilon_p$, respectively, such that:

$$\varepsilon_a = \frac{\Delta\varepsilon}{2} = \frac{\Delta\varepsilon_e}{2} + \frac{\Delta\varepsilon_p}{2} = \frac{\sigma'_f}{E}(2N_f)^b + \varepsilon'_f(2N_f)^c \tag{2.11}$$

where σ'_f/E and ε'_f are the intersects of the elastic and plastic asymptotic lines with the vertical axis of the graph in Figure 2.29, σ'_f and ε'_f are defined as the fatigue strength coefficient and fatigue ductility coefficient, and b and c are respectively known as the fatigue strength exponent and the fatigue ductility exponent.

The later half of that equation, concerned with low-cycle fatigue at large inelastic strains, is the original Coffin-Manson relationship (Coffin 1954, Manson 1953), namely:

$$\frac{\Delta\varepsilon_p}{2} = \varepsilon'_f(2N_f)^c \tag{2.12}$$

Regression analysis on experimental data is performed to obtain the values of σ'_f, ε'_f, b, and c. For example, these values derived for A572 Gr. 50 rolled shapes (Kaufmann et al. 2001b) and for four grades of steel plates (Dusicka et al. 2007) are summarized in Table 2.4 for the data shown in Figure 2.30.

In most applications, however, the cycles of inelastic strains applied to a structure are of variable amplitudes. To calculate low-cycle fatigue life, a procedure is required to convert the irregular cycles of variable strain amplitude into sets of equivalent regular

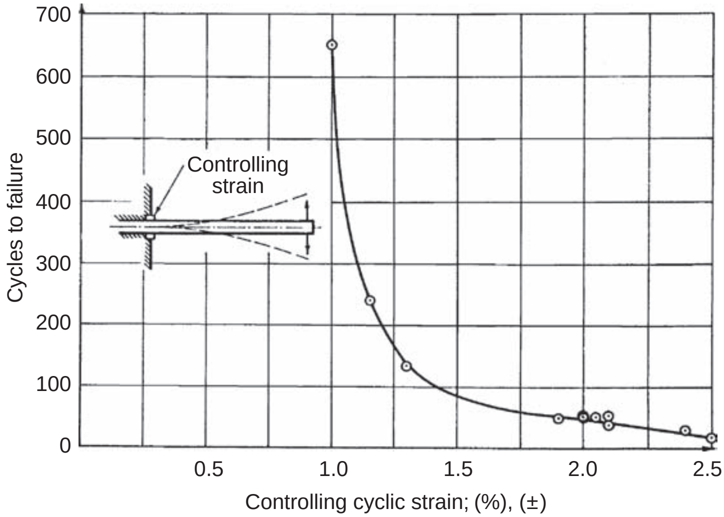

(a)

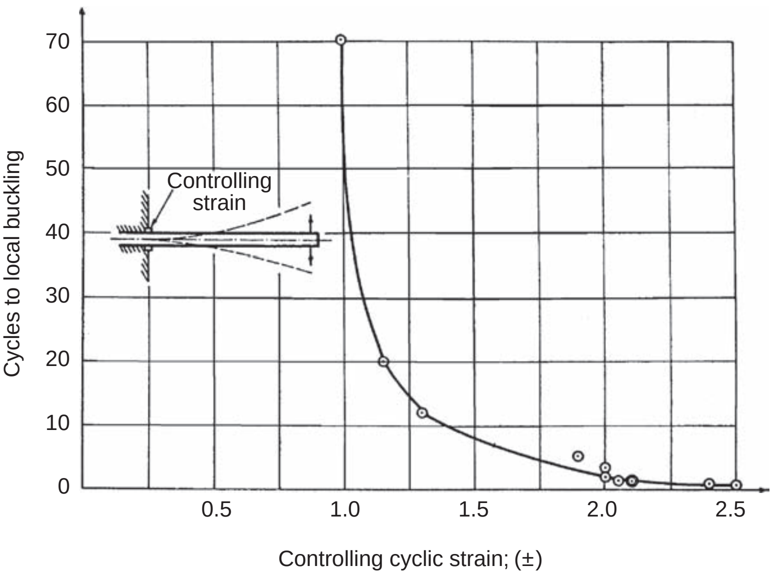

(b)

FIGURE 2.28 Low-cycle fatigue of structural shapes: (a) number of cycles required to attain fracture as a function of the controlling cyclic strain, (b) number of cycles required after which local buckling of flanges was detected as a function of the controlling cyclic strain, (c) typical initiation of fracture, (d) typical complete fracture. (*Figures a–d reprinted from "Effect of Large Alternating Strains of Steel Beams,"* Journal of Structural Engineering, *February 1965, V.V. Bertero and E.G. Popov, with permission of the American Society of Civil Engineers.*)

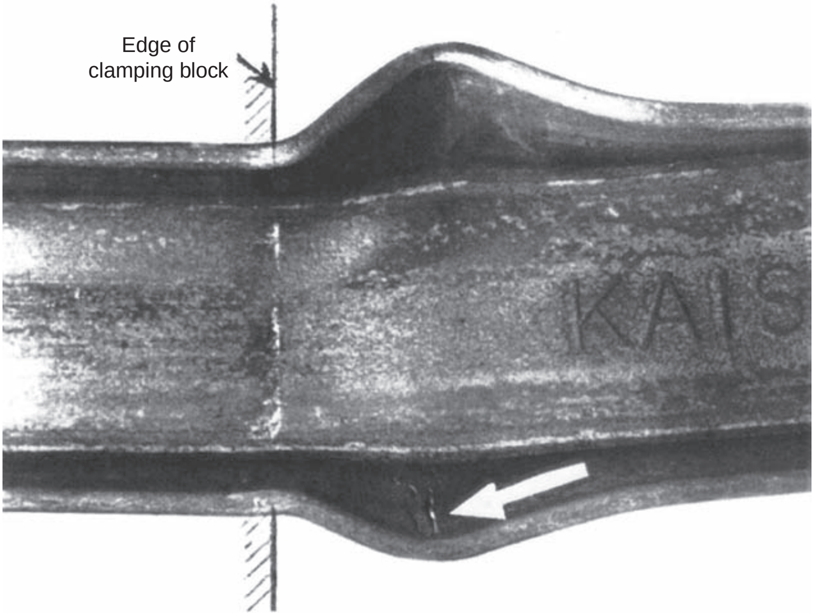

(c)

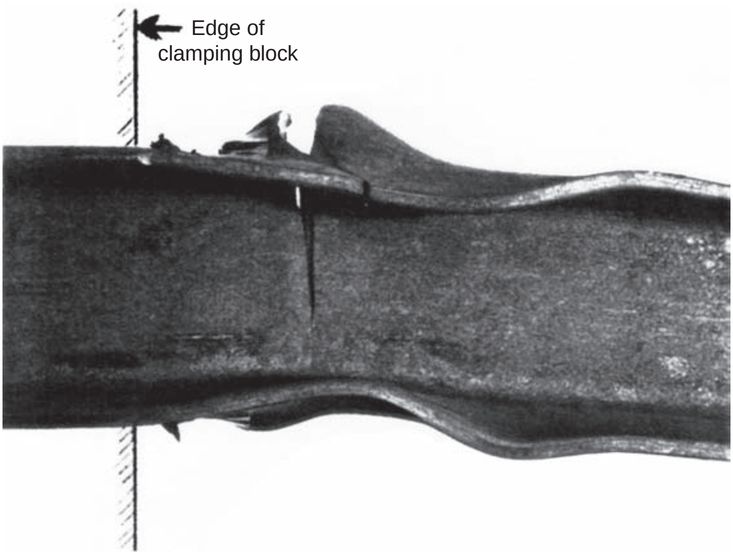

(d)

Figure 2.28 (*Continued*)

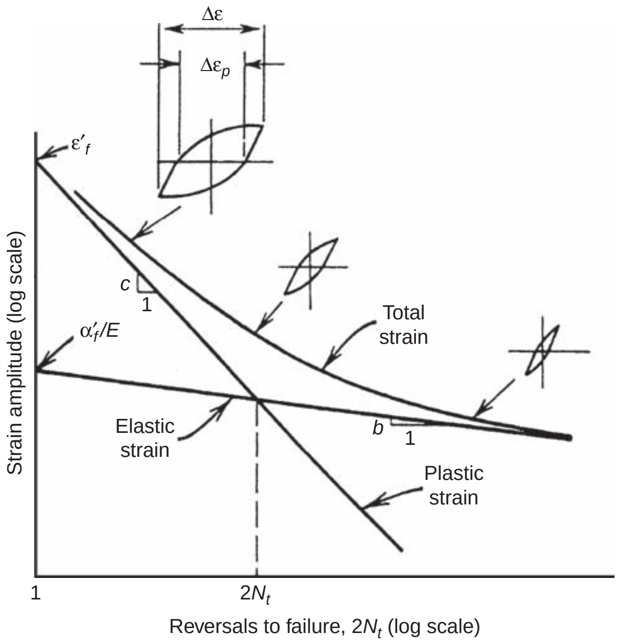

FIGURE 2.29 Strain amplitude versus number of load reversals to failure. (*Stephens et al. 2001, reprinted with permission of John Wiley & Sons, Inc.*)

	σ'_f **(MPa/ksi)**	***b***	ε'_f	***c***
A572 Grade 50[1]	–	–	0.03	–0.515
A709M Grade 345W[2]	894/130	–0.082	0.535	–0.590
A709M HPS 485[2]	886/129	–0.072	0.432	–0.575
BT-HT-440C[2]	1000/145	–0.101	0.422	–0.524
BT-LP100[2]	475/68.8	–0.081	0.275	–0.459
GT-LP225[2]	507/73.6	–0.063	0.446	–0.612

[[1]*From Kaufmann et al. (2001b);* [2]from Dusikca et al. (2007).]

TABLE 2.4 Estimated Coffin-Manson Parameters for Low-Cycle Fatigue of Various Steels

cycles of constant amplitude, and a combination rule must be used to establish how these sets of cycles at different constant amplitudes can be added. Such a procedure can also be used to assess "damage accumulation," that is, the percentage of the total fatigue life that has been used during a given strain history.

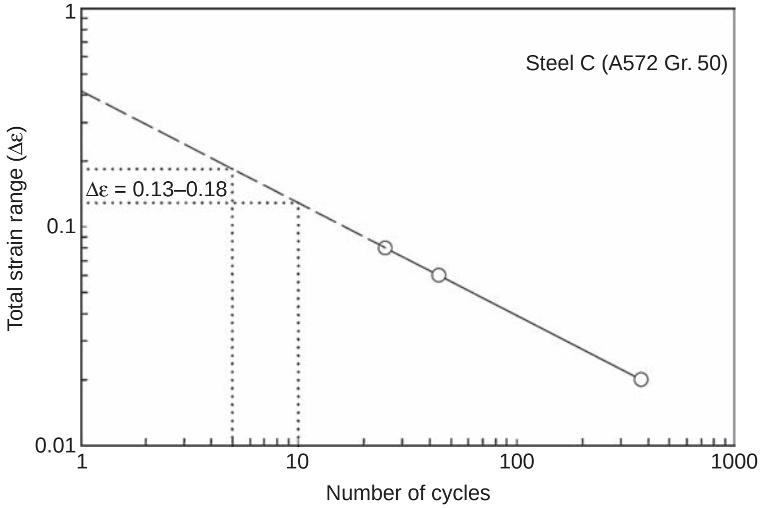

(a)

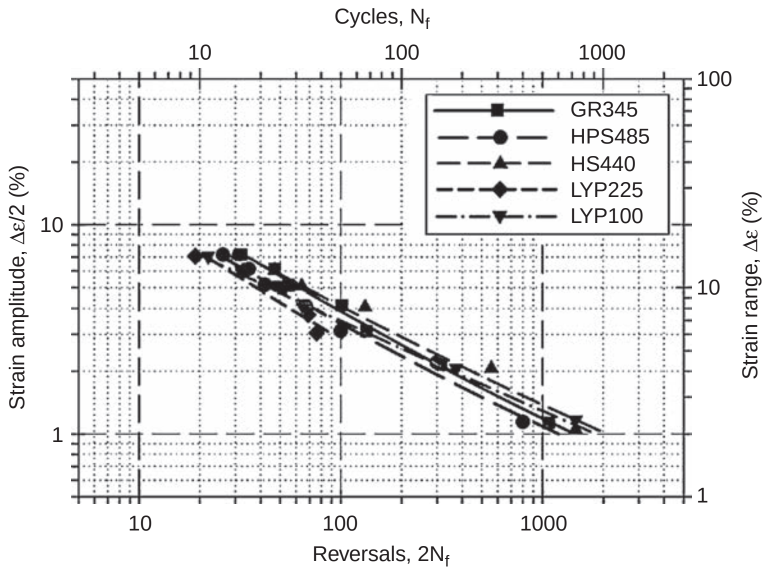

(b)

Figure 2.30 Low-cycle fatigue life of: (a) of A572 Gr. 50 rolled steel shapes (extrapolated for low fatigue cycle); (b) A709M Grade 345W (GR345), A709M HPS 485 (HPS485), BT-HT-440C (HT440), BT-LP100 (LYP100), and GT-LP225 (LYP225). (*Figure a from Kaufmann et al. 2001b, copyright © American Institute of Steel Construction. Reprinted with permission. All rights reserved.*; *figure b courtesy of Peter Dusicka, Department of Civil and Environmental Engineering, Portland State University.*)

The rainflow method (Matsuishi and Endo 1968) is the most frequently used technique to count the number of cycles of various amplitudes in an arbitrary strain history (although other equivalent approaches are also encountered in the literature, such as the range-pair, the racetrack counting, the level-crossing, and the peak counting methods). The rainflow-counting algorithm has been widely implemented in various software and freeware.

Figure 2.31 illustrates how the procedure is used to count cycles (which are strain cycles for the case of low-cycle fatigue calculations,

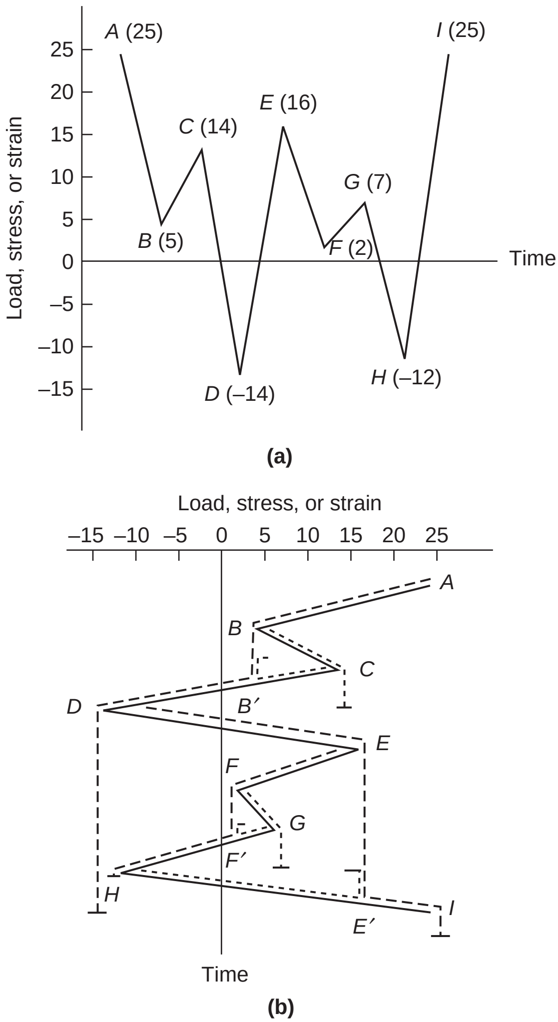

Figure 2.31 Rainflow counting procedure: (a) original stress or strain history, (b) rainflow analysis on rotated history, and (c) resulting cycles. (*Stephens et al. 2001, reprinted with permission of John Wiley & Sons, Inc.*)

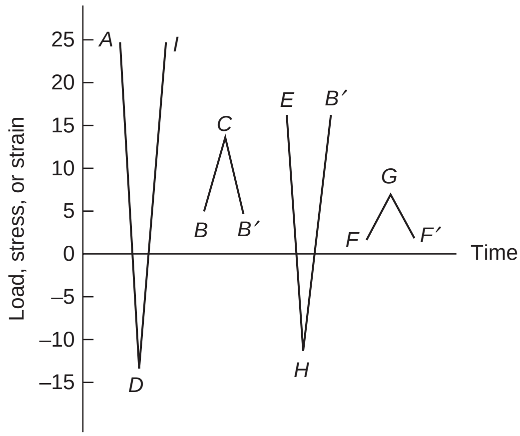

(c)

Figure 2.31 (*Continued*)

but could be stress cycles for other applications). First, the stain history is rearranged to start with the peak or valley of greatest absolute magnitude. Then, for the sake of the rainflow analogy, the plot of the strain history is rotated 90°, such that the time axis ends up pointing downward. The resulting strain history is akin to the roofline of a pagoda—albeit a highly irregular one. Completing the analogy, strain range cycles are counted by following rain drops deposited at the highest point of each roofline. The counting rules, illustrated in Figure 2.31, define a cycle by following rain from the upper edge of a roofline until it falls off the roof, continuing from that point on the inside of that edge until it falls off on the other side of the roof; however, the flow is considered terminated if it reaches rain falling from a higher roof. Calculation are repeated until rain starting at the top of each roofline has been considered (assuming somehow that rain could start at the apex of a narrower roof line even if protected by wider roof above it). This procedure will only count once each part of the strain history and results in pairs of half-cycles of equal magnitude. For the example shown in Figure 2.31 (Stephens et al. 2001), four equivalent cycles are obtained. The positive and negative peaks may not be of equal amplitude, but the resulting stress ranges are used in subsequent calculations.

Damage accumulation is typically computed using a linear combination rule; even though it is understood from a metallurgical perspective that strain cycles of greater amplitude generate more crack nucleation in the material, nonlinear damage accumulation models have not provided better agreement with experimental data. Miner (1945) proposed the following damage accumulation model, also known as the Palmgren-Miner linear damage rule:

$$D = \sum_{i=1}^{j} \frac{n_i}{N_i} = \frac{n_1}{N_1} + \frac{n_2}{N_2} + \cdots = 1 \tag{2.13}$$

where N_i is the number of cycles that can be resisted at a single given constant amplitude strain level S_i (this being essentially the data used to plot low-cycle fatigue life curves such as in Figure 2.30), n_i is the number of cycles in the strain history under consideration applied at this constant amplitude level (obtained from the rainflow method), and D is a damage index, assumed to be equal to 1.0 when median fatigue life is reached. Likewise, Miner's rule is commonly used to assess the expended percentage of fatigue life, that is, when the damage index calculated per the above equation is less than 1.0.

2.7 Material Models

Once an appropriately ductile steel material has been chosen for a specific application, suitable stress-strain or moment-curvature models must be adopted for the purpose of calculations. Because increases in model complexity often translate into additional computational difficulties, simple models may provide, in many cases, sufficiently accurate representations of behavior. Some of the simpler models commonly used are described below.

2.7.1 Rigid Plastic Model

As the name implies, the rigid plastic model neglects elastic deformations. The material is assumed to experience no strain until the yield stress is reached, and flexural components modeled with rigid plastic behavior undergo no curvature until the plastic moment is reached. This rudimentary model, illustrated in Figure 2.32a, can be useful, for example, when the plastic collapse load capacity of a structure is sought, as will be seen in Chapter 4. It has been used to model nonlinear friction hysteretic energy dissipation, in terms of forces versus displacement, in structures wherein this behavior could be relied upon to resist extreme dynamic lateral loads (e.g., Dicleli and Bruneau 1995). However, because this model implies infinite stiffness until plastification is reached and null stiffness thereafter, it is best suited for hand calculations and can be difficult to implement in structural analysis programs based on the stiffness-matrix method.

2.7.2 Elasto-Plastic Models

When response under progressive loading until collapse is desired, or when an accurate calculation of nonlinear deflections is needed,

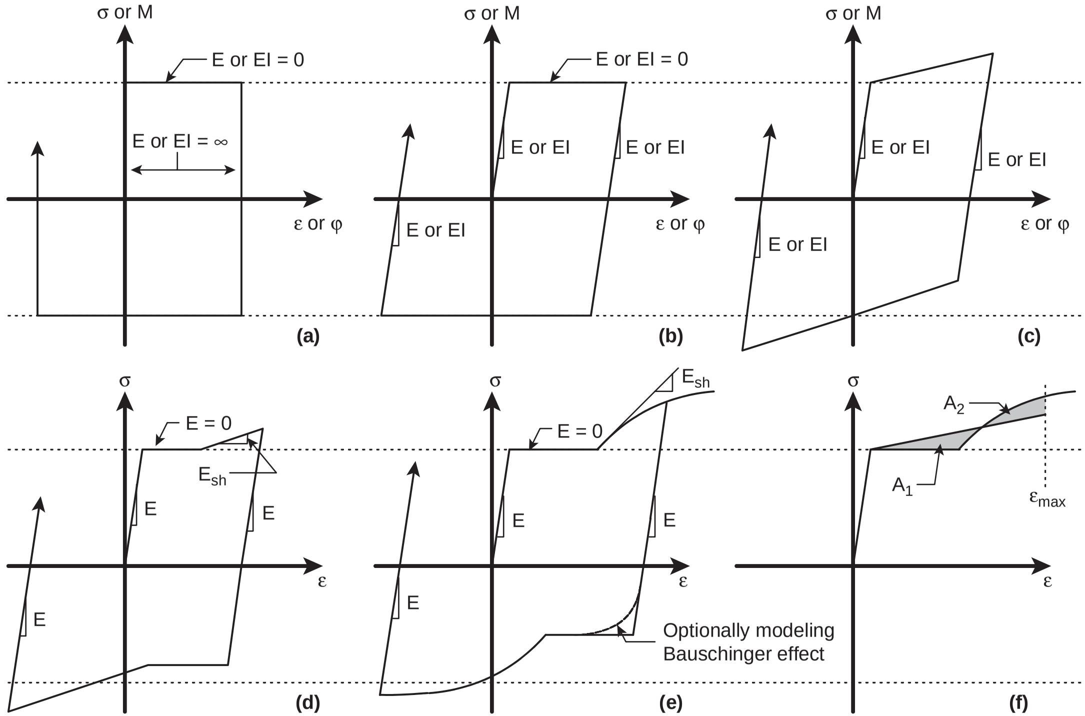

FIGURE 2.32 Some cyclic material models for structural steel: (a) bilinear rigid-perfectly plastic, (b) bilinear elasto-perfectly plastic, (c) bilinear elasto-plastic with strain-hardening, (d) trilinear elasto-plastic with strain-hardening, (e) cyclic model from monotonic-loading stress-strain curve, and (f) bilinear elasto-plastic with strain-hardening slope based on equal energy dissipation.

an elasto-perfectly plastic model is generally used. This hysteretic model considers two possible stiffness states: elastic or plastic, as shown in Figure 2.32b. The choice of zero postyield stiffness is suitable for many applications in which strain-hardening is not anticipated, and conservative for predicting the plastic collapse load and deformations whenever strain-hardening would be expected to develop.

A computer is generally needed to take advantage of the features of this bilinear model, so one can easily consider the effect of strain-hardening by assigning a nonzero postyielding stiffness; in fact, for numerical analysis reasons, nonzero positive stiffness is often desirable. Such an elasto-plastic model with nonzero postyield stiffness to account for strain-hardening is illustrated in Figure 2.32c. Various methods can be used to determine an appropriate postyield stiffness to model material or member behavior. One such reasonable approach, shown in Figure 2.32f, consists of finding the slope of the straight line that would bisect the true stress-strain diagram in the plastic range such that an equal amount of plastic energy is dissipated before failure. To equate the energy, however, iterative procedures are generally needed to determine the maximum strains, ε_{max}, of all the yielded members in the structure, which is by no means a simple task. Therefore, values ranging between 0.005 and 0.05 times elastic stiffness are commonly used for the strain-hardening (postyield) stiffness in bilinear models. Lower strain-hardening stiffness values will generally produce larger maximum plastic strains and curvatures, whereas higher values will translate into larger stresses and moments.

As reflected in the available literature, the bilinear elasto-plastic model has been widely used to model the cyclic hysteretic behavior of steel frame structures (although in some ways, this has often been constrained by the limitations of computer programs capable of cyclic hysteretic analysis). More complex piece wise linear stress-strain models (Figure 2.32d) or other models (Figure 2.32e) have sometimes been used for analysis. However, the presumed additional benefit gained from the use of such models must always be weighed against all of the uncertainties associated with the design process, particularly when earthquakes are responsible for these hysteretic cycles.

2.7.3 Power, Ramberg-Osgood, and Menegotto-Pinto Functions

Another class of material models, known as power functions, is particularly useful to analytically describe the experimentally obtained stress-strain relationships of various alloys. Although these functions complicate the characterization of the stress-strain relationship of low-grade steels having a well-defined yield plateau, they can effectively describe the inelastic moment-curvature relationships of members made with these steels, and even the inelastic shear force versus shear strain relationships in some other applications. Therefore, it is worthwhile to be familiar with these power function models.

Experimental Data		Power Function	Ramberg-Osgood	Menegotto-Pinto
σ (ksi)	ε	ε	ε	σ (ksi)
0	0	0.0	0.0	0.0
5	0.0005		0.0005	5.0
10	0.00102	0.0010	0.0010	10.2
15	0.00151		0.0015	15.1
20	0.00202	0.0020	0.0020	20.1
25	0.00251		0.0025	24.8
30	0.00301	0.0030	0.0030	29.2
31	0.00311		0.0031	30.0
32	0.00321		0.00321	30.7
33	0.00333		0.00333	31.6
34	0.00345		0.00348	32.4
35	0.0037		0.00371	34.0
36	0.0042	0.0041	0.00416	36.3
37	0.0052	0.0051	0.00516	38.8
38	0.008	0.0074	0.00748	40.1
39	0.015		0.01297	40.4
40	0.0265		0.0258	40.5
41	0.056	0.056	0.0555	41.0
42	0.122		0.123	42.0

1 ksi = 6.895 MPa

Table 2.5 Stress-Strain Data for Aluminum Alloy Tensile Test and Results from Various Models

To remove some of the mathematical abstraction associated with power function models, the discussion is presented within the context of a numerical example. The data tabulated in Table 2.5, obtained from a standard tensile test of an aluminum specimen, is used for this purpose. Although this example is expressed in terms of stresses and strains, note that power functions can also be developed to model other behaviors expressed by a pair of related parameters, such as moments and curvatures, with only minor modifications.

Before a demonstration of how power functions can be used to model the stress-strain behavior of this aluminum alloy, it is worthwhile to note that, in this particular example, an elasto-perfectly plastic model of this material would provide a reasonably accurate representation of the material behavior. Through a graphical method and the traditional 0.2% offset rule, the yield stress, σ_y, is calculated to be 37 ksi (255 MPa), and the corresponding yield strain, ε_y, is 0.0037. The resulting elasto-perfectly plastic material curve could be drawn by joining the following three stress-strain (σ, ε) points: (0, 0), (37, 0.0037), and (37, ∞). Likewise, an elasto-plastic strain-hardening model could be developed after some trial and error to define an appropriate strain-hardening stiffness.

2.7.3.1 Power Functions

The fundamental tenet of a power function is that the strain-stress relationship can be divided into an elastic part and a plastic part as shown:

$$\varepsilon_{total} = \varepsilon_{elastic} + \varepsilon_{plastic} = \frac{\sigma}{E} + a\left(\frac{\sigma}{E}\right)^n \tag{2.14}$$

Terms for this equation are defined in Figure 2.33a. The task therefore lies in determining the parameters a and n that will provide best fit to the data. From the above expression, it transpires that the plastic strain can be expressed as a function of the elastic strain if Eq. (2.14) is manipulated, to obtain:

$$\varepsilon_{plastic} = a\left(\frac{\sigma}{E}\right)^n = a\ \varepsilon^n_{elastic} \tag{2.15}$$

or, taking the logarithm of both sides of this equation,

$$\log \varepsilon_{plastic} = \log\left(a\ \varepsilon^n_{elastic}\right) = \log a + n \log(\varepsilon_{elastic}) \tag{2.16}$$

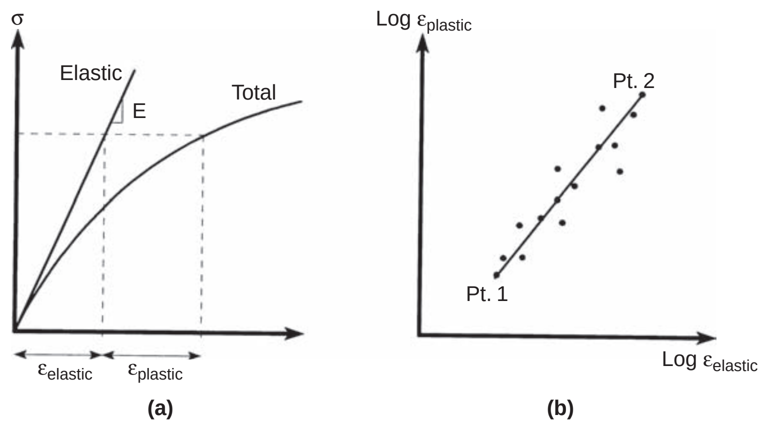

Figure 2.33 Power function material models for structural steel.

As illustrated in Figure 2.33b, Eq. (2.16) is the equation of a straight line of slope n in a logarithmic space—that is, a straight line when plotted on log-log paper. Because all experimentally obtained data points will not always fall on a straight line, a least-squares solution could be used to find the best approximation to the true stress-strain curve. However, in most practical cases, this level of refinement is not necessary. A reasonably accurate result can be obtained if one takes two strain data points as far apart as possible, but not on the linear branch of the stress-strain curve where $\varepsilon_{plastic}$ would be zero, and calculates the values of a and n using the following relationships:

$$n = \left(\frac{\log \varepsilon_{plastic-2} - \log \varepsilon_{plastic-1}}{\log \varepsilon_{elastic-2} - \log \varepsilon_{elastic-1}} \right) \tag{2.17}$$

and

$$\log a = \log \varepsilon_{plastic-1} - n \log \varepsilon_{elastic-1} \tag{2.18}$$

For the current example, assuming an elastic modulus of 10,000 ksi and arbitrarily taking for the two strain data points $\varepsilon = 0.0037$ (at $\sigma = 35$ ksi, for which $\varepsilon_{elastic} = 0.0035$ and $\varepsilon_{plastic} = 0.0002$) and $\varepsilon = 0.1220$ (at $\sigma = 42$ ksi, for which $\varepsilon_{elastic} = 0.0042$ and $\varepsilon_{plastic} = 0.1178$), Eq. (2.17) and (2.18) give $n = 35.0$ and $a = 1.66 \times 10^{82}$, respectively, which can be substituted in the general power function expression. This gives the following result:

$$\varepsilon = 0.0001\sigma + 1.66 \times 10^{82} \left(\frac{\sigma}{10000} \right)^{35.0} \tag{2.19}$$

The accuracy of this solution could be verified if it were plotted against the experimental data. However, because the resulting difference is rather small, results are instead compared through use of Table 2.5, and judged to be satisfactory.

Although the resulting expression may appear awkward to manipulate for hand calculations, the ability to express the entire stress-strain relationship by a single continuous function can be advantageous, particularly for computer programming purposes.

2.7.3.2 Ramberg-Osgood Functions

In earthquake engineering, Ramberg-Osgood functions are often used to model the behavior of structural steel materials and components. These functions are obtained when the above power function is normalized by an arbitrary strain, ε_0, for which the plastic component of strain, $\varepsilon_{plastic}$, is not zero. Generally, the yield strain, ε_y, provides a good choice for this normalizing strain, but other choices are also possible and equally effective. Therefore, the Ramberg-Osgood function is expressed as:

$$\frac{\varepsilon}{\varepsilon_0} = \frac{\sigma}{\sigma_0} + \frac{a}{\varepsilon_0}\left(\frac{\sigma}{E}\right)^n \tag{2.20}$$

where E is the initial elastic modulus, and σ_0 is equal to $E\varepsilon_0$. To define a Ramberg-Osgood model, one must evaluate a, n, and ε_0. Note that, when plotted in a parametric manner, normalized stresses as a function of the normalized strain give curves that meet at the point $(1 + a, 1)$, as shown in Figure 2.34a. In that figure, the physical significance of increasing n is also evident: curves with progressively larger values of n will gradually converge toward the elasto-perfectly-plastic curve.

Because the Ramberg-Osgood function is a power function, the calculation of n and a proceeds as described previously: two points must be selected to calculate the slope n of a straight line in the log-log space, from which the constant a can then be calculated. However, taking advantage of the normalized form of the Ramberg-Osgood function, it is possible to derive close-formed expressions for this purpose.

If point A is defined as the point on the real data curve where $\sigma = \sigma_0$ (Figure 2.34b), substituting known values in the above equation at point A and defining m_A as the slope of the secant joining point A with the origin, produces the following expression:

$$\frac{\varepsilon_A}{\varepsilon_0} = 1 + \frac{a}{\varepsilon_0}\left(\frac{\sigma_0}{E}\right)^n = \frac{1}{m_A} \Rightarrow a\frac{(1-m_A)/m_A}{\left(\frac{\sigma_0}{E}\right)^{n-1}} \tag{2.21}$$

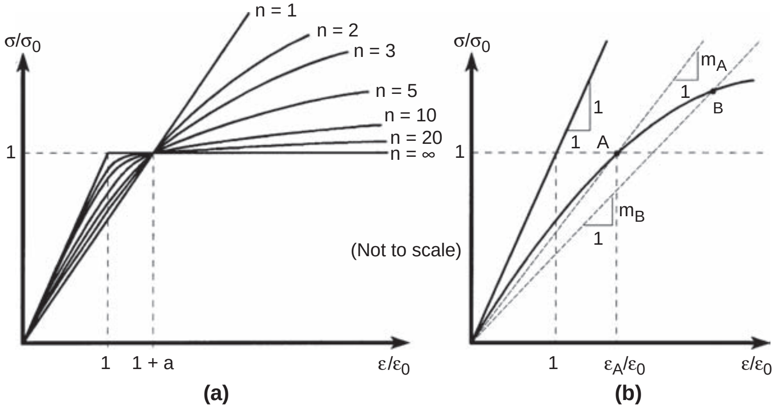

FIGURE 2.34 Ramberg-Osgood material model for structural steel.

Similarly, taking a point B sufficiently far removed from point A along the experimentally obtained stress-strain curve (and preferably the last data point of increasing stress), Eq. (2.21) becomes:

$$\frac{\left(\frac{\varepsilon_B}{\varepsilon_0}\right)}{\left(\frac{\sigma_B}{\sigma_0}\right)} = 1 + \frac{\left(\frac{a}{\varepsilon_0}\left(\frac{\sigma_B}{E}\right)^n\right)}{\left(\frac{\sigma_B}{\sigma_0}\right)} = \frac{1}{m_B} \tag{2.22}$$

Substituting a from Eq. (2.21) into Eq. (2.22) and solving for n, gives:

$$n = 1 + \frac{\log \frac{(1 - m_A)m_B}{(1 - m_B)m_A}}{\log\left(\frac{\sigma_0}{\sigma_B}\right)} \tag{2.23}$$

where σ_0 and σ_A have been constrained to be equal by this procedure. Once the slope n is known, the value a can be directly obtained from Eq. (2.21), and the Ramberg-Osgood function is completely defined.

To summarize, a systematic procedure to define a Ramberg-Osgood function can be outlined as follows:

1. Draw the stress-strain diagram (or moment-curvature diagram, or whatever other force-deformation diagrams of interest) for the data and determine the initial elastic modulus, E [or EI, or other parameter relating the selected force and deformation terms per an expression similar to Eq. (2.14)]. If good confidence exists in the accuracy and reliability of the first data points, this value can be determined analytically as the slope to the first data point from the origin. (For the example here, $E = 10{,}000$.)
2. The yield strain can be selected as ε_0. Therefore, use the 0.2% offset method to first determine σ_0, and then calculate $\varepsilon_0 = \sigma_0/E$. For the example here, the yield stress of 37 ksi and strains of 0.0037 as previously calculated are used.
3. Select point A as the point on the data curve for which $\sigma = \sigma_0$, and calculate the slope, m_A, of the secant joining point A with the origin. Note that for this secant modulus $m_A E$, m_A is always less than unity. Also, when σ_0 is graphically obtained through the 0.2% offset method, the intersect of the data curve and the 0.2% curve directly gives point A. For the example at hand, $\varepsilon_A = 0.0052$ and $m_A = 0.711$.
4. Select a second point (point B) along the experimentally obtained stress-strain curve as one of the last points for which

an increase in stress was measured and calculate the secant modulus $m_B E$.

5. Solve for n using Eq. (2.23).
6. Solve for a using Eq. (2.21).

For this example, $m_B = 0.0344$, $n = 34.7$, and $a = 3.53 \times 10^{81}$. The resulting Ramberg-Osgood equation becomes:

$$\frac{\varepsilon}{0.0037} = \frac{\sigma}{37} + \frac{3.53 \times 10^{81}}{0.0037}\left(\frac{\sigma}{10000}\right)^{34.7} \tag{2.24}$$

which can be simplified to:

$$\varepsilon = 0.0001\sigma + 3.53 \times 10^{81}\left(\frac{\sigma}{10000}\right)^{34.7} \tag{2.25}$$

The slight difference between this result and that obtained using power functions [Eq. (2.19)] can be attributed to the choice of different data points to derive the expressions. However, for all intents and purposes, the two equations give identical results, as shown in Table 2.5.

2.7.3.3 Menegotto-Pinto Functions

One can derive a class of normalized equations, known as Menegotto-Pinto functions, following an approach similar to that presented above, to express stresses as a function of strains, instead of strains as a function of stresses per the Ramberg-Osgood functions. The general form of the Menegotto-Pinto functions is as follows:

$$\frac{\sigma}{\sigma_0} = b\left(\frac{\varepsilon}{\varepsilon_0}\right) + d = b\left(\frac{\varepsilon}{\varepsilon_0}\right) + \frac{(1-b)\left(\frac{\varepsilon}{\varepsilon_0}\right)}{\left[1+\left(\frac{\varepsilon}{\varepsilon_0}\right)^n\right]^{1/n}} \tag{2.26}$$

where b is the ratio of the final to initial tangent stiffnesses, and d is a value that is graphically defined in Figure 2.35. In the normalized space of stress and strain, the initial stiffness has a slope of 1, the slope of the final tangent stiffness is b, and d varies from zero to $(1 - b)$ as $\varepsilon/\varepsilon_0$ progressively increases from zero to a maximum value at the last data point.

To use Eq. (2.26), one must evaluate the values of ε_0, σ_0, b, and n. A simple procedure to determine this needed information is outlined below:

1. Draw the initial and final tangent slopes to the data curves. The intersection of these two curves gives ε_0 and σ_0, which

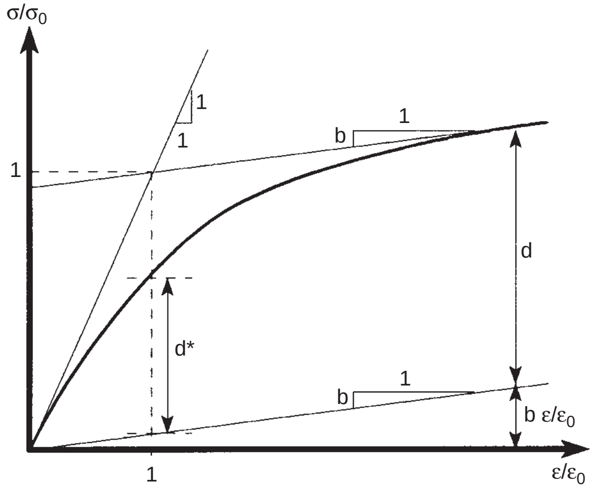

FIGURE 2.35 Menegotto-Pinto material model for structural steel.

should not be confused with the same variables used earlier for the Ramberg-Osgood case because these have a rather different meaning and cannot be chosen arbitrarily here. For this example, $\varepsilon_0 = 0.004$ and $\sigma_0 = 40.21$. In this case, it is possible for one to calculate these values using secants to the first and last pairs of data points, but normally, the engineer should make sure that these data points are reliable and representative.

2. Calculate the ratio of the tangent slopes. Here, this result is simply the slope of the last pair of data points, and therefore $b = 0.00152$.
3. At the point $\varepsilon/\varepsilon_0 = 1$, note that Eq. (2.26) simplifies to:

$$\frac{\sigma}{\sigma_0} = b(1) + d^* = b(1) + \frac{(1-b)(1)}{[1+(1)^n]^{1/n}} = b + \frac{1-b}{2^{1/n}} \tag{2.27}$$

The stress σ at strain ε_0 is obtained directly from the data (although some interpolation may be needed), and the value of d^* is calculated directly from Eq. (2.27). In this example, σ is found to be 35.6, and therefore d^* is equal to 0.884. With knowledge of the value of d^*, one can compute n from the above expression as:

$$n = \frac{\log 2}{\log (1-b) - \log d^*} \tag{2.28}$$

Here, this gives $n = 5.68$. The resulting Menegotto-Pinto expression becomes:

$$\sigma = 15.17\varepsilon + 9985\frac{\varepsilon}{[1+249\varepsilon^{5.68}]^{1/5.68}} \tag{2.29}$$

This model is slightly less accurate than the power models presented earlier, as evidenced by the results summarized in Table 2.5, but differences are not of practical significance.

2.7.4 Smooth Hysteretic Models

The multilinear and continuous models presented above to describe monotonic response can be extended to capture cyclic behavior. The concepts and equations are similar, with the difference that "memory" must be introduced in the models to keep track of the strength level and extent of yielding (or accumulated plastic deformation history) at each point of load reversal. Such models are typically formulated to also account for strain-hardening effects. Constitutive models relating stresses to strains are used in non linear inelastic finite element analyses (from a computational mechanics perspective), but similar relationships can be used at the element level to relate forces to deformations in nonlinear inelastic analyses of structural systems constructed of beams, columns, and other discrete elements, for example, in terms of moment-curvature or force-deformation relationships. In the latter case structural element models may need to capture complex physical behaviors, such as global or local buckling effects, in addition to material behavior, and numerous customized models of cyclic inelastic element behavior have been developed to account for such complex multiple phases of plastic behavior.

The following provides general information on some of the models commonly encountered in making modeling decisions. Extensive literature provides details on the mathematical formulations underlying these models, both from a computational mechanics perspective (e.g., Chakrabarty 2006, Lubliner 1990) or a structural analysis one (e.g., Carr 2004, Sivaselvan and Reinhorn 1999). Note that because these models require a definition of yielding in complex 2-D or 3-D stress conditions, and rules to model strain-hardening behavior in that space, the engineering mechanics principles underlying commonly used yield criteria are first reviewed. Readers already familiar with this information can proceed directly to Section 2.7.4.2 on cyclic hysteretic models.

2.7.4.1 Yield Criteria

Given that yielding is effectively a translational movement of dislocations along slip planes in crystals, as described in an earlier section, the criterion that define yielding in steel elements subjected to multi axial stress conditions are explicitly tied to the magnitude of shear stresses. Contrary to single crystals which have preferential planes along which slippage develops (analogous to cleavage planes in brittle materials), steel is an isotropic material consisting of randomly oriented crystals, and yielding develops where the maximum shear stresses are reached.

Recognizing that the maximum shear, τ_{max}, cannot exceed the value reached when a uniaxial coupon yields, Tresca used this calibrated shear stress value and basic stress transformations (that are conventionally illustrated using Mohr circles) to postulate the first classic yield criteria. Illustrating this for the simpler case of plane stresses, using the well-known fundamental equations from mechanics of materials (e.g., Popov 1968):

$$\sigma_{max} = \sigma_1 = \frac{\sigma_x + \sigma_y}{2} + \sqrt{\left(\frac{\sigma_x - \sigma_y}{2}\right)^2 + \tau_{xy}} \tag{2.30a}$$

$$\sigma_{min} = \sigma_2 = \frac{\sigma_x + \sigma_y}{2} - \sqrt{\left(\frac{\sigma_x - \sigma_y}{2}\right)^2 + \tau_{xy}} \tag{2.30b}$$

$$\tau_{max} = \sqrt{\left(\frac{\sigma_x - \sigma_y}{2}\right)^2 + \tau_{xy}} = \frac{\sigma_1 - \sigma_2}{2} \tag{2.30c}$$

where σ_1 and σ_2, respectively are the maximum and minimum normal principal stresses, and τ_{max} is the maximum shear stress acting on the principal planes for a general condition of stresses expressed in an arbitrary *x-y* space, one can obtain that when $\sigma_1 = \sigma_y$ and $\sigma_2 = 0$, then τ_{max} is $\sigma_y/2$.

For the more general three-dimensional case, the stress transformation equations become substantially more complex, but it remains that:

$$\sigma_{max} = MAX\ of\ [\sigma_1, \sigma_2, \sigma_3] \tag{2.31a}$$

$$\tau_{max} = \frac{\sigma_{max} - \sigma_{min}}{2} \tag{2.31b}$$

As a result, still in plane stresses, considering the additional principal stress $\sigma_3 = 0$, three possible scenarios are possible:

(a) $\sigma_1 > \sigma_2 > 0$ in which case $\tau_{max} = \sigma_y/2$ when $\sigma_1 = \sigma_y$
(b) $\sigma_1 > 0 > \sigma_2$ in which case $\tau_{max} = \sigma_y/2$ when $(\sigma_1 - \sigma_2) = \sigma_y$
(c) $0 > \sigma_1 > \sigma_2$ in which case $\tau_{max} = \sigma_y/2$ when $\sigma_2 = \sigma_y$

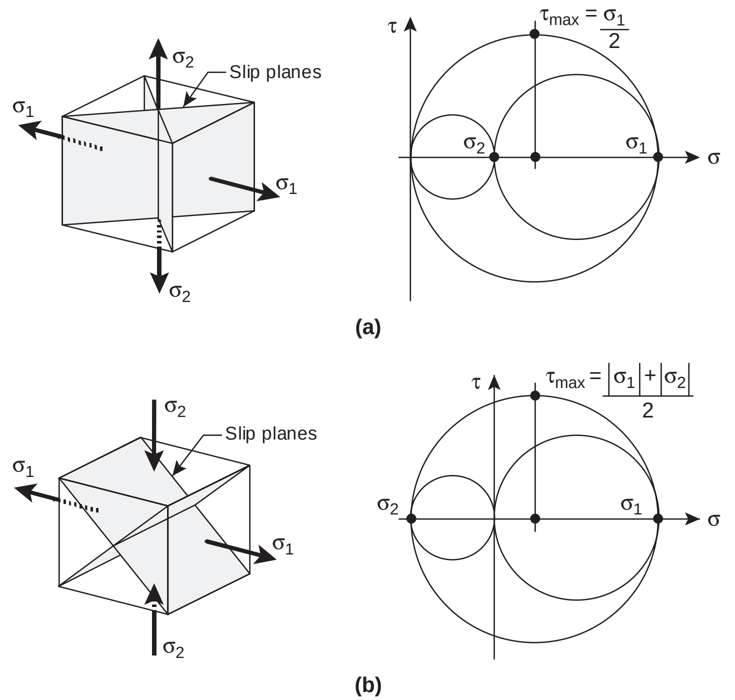

Figure 2.36 Stress conditions and slip planes for Tresca yield criterion, and corresponding Mohr circle, for: (a) $\sigma_1 > \sigma_2 > 0$ and (b) $\sigma_1 > 0 > \sigma_2$.

This is illustrated using Mohr circles in Figure 2.36. Three similar expressions can be derived when $\sigma_2 > \sigma_1$. The resulting Tresca yield surface is shown in Figure 2.37.

While the Tresca yield condition is simple, and Mohr circles provide a convenient vehicle to assess when yielding under three-dimensional stress states approach the yield criterion set by τ_{max}, it is slightly inaccurate in predicting yielding for steel and other metals. The Von Mises yield condition (also known as the Huber/Von Mises/Hencky criterion), based on energy concepts, provides better results.

The Von Mises criterion is best understood from a three-dimensional state of stresses. For a differential element of size dx, dy, and dz, and volume dV, shown in Figure 2.38, the normal and shear stresses acting on each face of that element can be expressed in the following matrix (known as the Cauchy stress tensor):

$$\sigma_{ij} = \begin{bmatrix} \sigma_x & \tau_{xy} & \tau_{xz} \\ \tau_{yx} & \sigma_y & \tau_{yz} \\ \tau_{zx} & \tau_{zy} & \sigma_z \end{bmatrix} \tag{2.32}$$

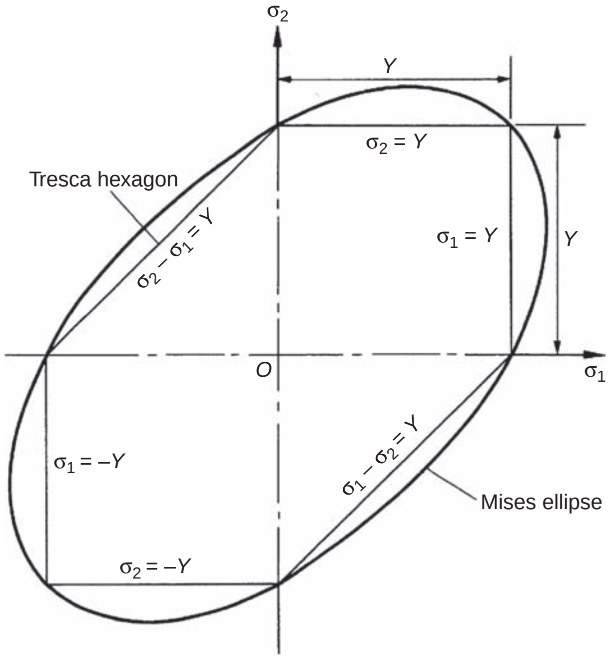

FIGURE 2.37 Tresca and Von Mises yield surfaces in the $\sigma_1 - \sigma_2$ space. (*From* Theory of Plasticity, *J. Chakrabarty 2006. Copyright Elsevier Limited. Reprinted with permission.*)

Knowing that for an elastic system, the strain energy, U, produced by a force, F, over a distance, Δ, is $U = ½ (F\Delta)$, the strain energy produced by each stress component can be calculated independently, and summed to get the total stain energy. For example, for the shear strain acting in the x-z plane, the force equal the shear stress times the area on which it is acting ($F = \tau_{xy}\, dxdz$) and the "distance" traveled by that force is $\Delta = ½\, \gamma_{xy}\, dy$. As a result:

$$dU = \frac{1}{2}\tau_{xy} dxdz\, \gamma_{xy} dy = \frac{1}{2}\tau_{xy}\, \gamma_{xy} dydxdz = \frac{1}{2}\tau_{xy}\, \gamma_{xy} dV \tag{2.33}$$

For the normal stress on that same x-z plane, $F = \sigma_y\, dx\, dz$ and $\Delta = ½\, \varepsilon_y dy$, and $dU = ½\, \sigma_y\, \varepsilon_y$. Summing for all stresses, the total energy for the element becomes:

$$\frac{dU}{dV} = U_o$$

$$= \frac{1}{2}\sigma_x \varepsilon_x + \frac{1}{2}\sigma_y \varepsilon_y + \frac{1}{2}\sigma_z \varepsilon_z + \frac{1}{2}\tau_{xy}\, \gamma_{xy} + \frac{1}{2}\tau_{yz}\, \gamma_{yz} + \frac{1}{2}\tau_{zx}\, \gamma_{zx} \tag{2.34}$$

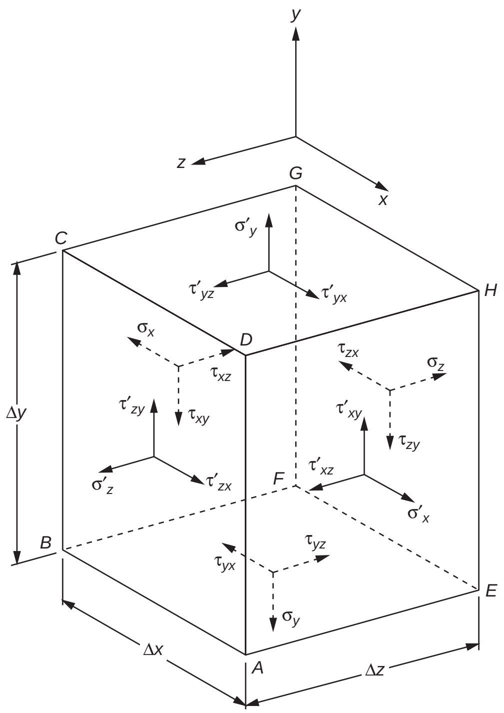

Figure 2.38 Three-dimensional state of stress on a differential element. (*From* Résistance des Matériaux, *A. Bazergui et al. 1987, with permission from Presses Internationales Polytechniques, Montreal.*)

Substituting in this equation the mechanics of materials relationships:

$$\varepsilon_x = \frac{1}{E}[\sigma_x - \upsilon(\sigma_y + \sigma_z)] \tag{2.35a}$$

$$\varepsilon_y = \frac{1}{E}[\sigma_y - \upsilon(\sigma_z + \sigma_x)] \tag{2.35b}$$

$$\varepsilon_z = \frac{1}{E}[\sigma_z - \upsilon(\sigma_z + \sigma x_z)] \tag{2.35c}$$

and

$$\gamma_{xy} = \frac{\tau_{xy}}{G} \tag{2.35d}$$

$$\gamma_{yz} = \frac{\tau_{yz}}{G} \tag{2.35e}$$

$$\gamma_{zx} = \frac{\tau_{zx}}{G} \tag{2.35f}$$

Then, the energy equation can be rewritten as:

$$U_o = \frac{1}{2E}\left(\sigma_x^2 + \sigma_y^2 + \sigma_z^2\right)$$
$$-\frac{\upsilon}{E}(\sigma_x\sigma_y + \sigma_y\sigma_z + \sigma_z\sigma_x) + \frac{1}{2G}\left(\tau_{xy}^2 + \tau_{yz}^2 + \tau_{zx}^2\right) \tag{2.36}$$

This can be simplified if expressed in terms of the principal stresses. For the three-dimensional case, from the theory of elasticity for solid bodies (e.g., Chakrabarty 2006, Fung and Tong 2001, Timoshenko and Goodier 1934, or even Wikipedia Contributors 2009b), the mathematical transformations required to calculate these values and their orientations can obtained by geometric relationships, or more directly by recognizing that these principal stresses are the eigenvalues of the Cauchy stress tensor. In both cases, the principal stresses are found as the root of a third degree equation. Taking the eigenvalue value approach is equivalent to finding the determinant of the following matrix:

$$\begin{vmatrix} (\sigma_x - \sigma) & \tau_{xy} & \tau_{xz} \\ \tau_{yx} & (\sigma_y - \sigma) & \tau_{yz} \\ \tau_{zx} & \tau_{zy} & (\sigma_z - \sigma) \end{vmatrix} = 0 \tag{2.37}$$

which is tantamount to solving:

$$\sigma^3 - I_1\sigma^2 - I_2\sigma - I_3 = 0 \tag{2.38}$$

where

$$I_1 = \sigma_x + \sigma_y + \sigma_z \tag{2.39a}$$

$$I_2 = -\left[\sigma_x\sigma_y + \sigma_y\sigma_z + \sigma_z\sigma_x - \tau_{xy}^2 - \tau_{yz}^2 - \tau_{zx}^2\right] \tag{2.39b}$$

$$I_3 = \left[\sigma_x\sigma_y\sigma_z + 2\tau_{xy}\tau_{yz}\tau_{zx} - \sigma_x\tau_{yz}^2 - \sigma_y\tau_{zx}^2 - \sigma_z\tau_{xy}^2\right] \tag{2.39c}$$

The roots of the equation are the principal stresses σ_1, σ_2, and σ_3. Given that the shear stresses are null in the principal directions, the energy equation becomes:

$$U_o = \frac{1}{2E}\left(\sigma_1^2 + \sigma_2^2 + \sigma_3^2\right) - \frac{\upsilon}{E}(\sigma_1\sigma_2 + \sigma_2\sigma_3 + \sigma_3\sigma_1) \tag{2.40}$$

Recognizing that yielding requires the development of shear planes, a state of pure compression (contraction) and tension (dilatation) would just compact or distend all of the atoms in the material, without the development of any shear planes. Therefore, all of the strain energy related to such a uniform stress condition doesn't contribute to yielding and must be subtracted from the above equation if one wishes to calculate the strain energy that produces yielding.

By analogy, a condition of equal principal stresses would exist if the differential element *dV* was submerged in water, and the average stress applied in this case, that would correspond to a volume change (but no shear distortions), is called the "hydrostatic" stress, expressed as:

$$\bar{\sigma} = \frac{\sigma_1 + \sigma_2 + \sigma_3}{3} \tag{2.41}$$

As shown below for the Cauchy stress tensor in the principal directions, each principal stress can be expressed as the sum of the hydrostatic stress and the remaining balance. In classic mechanics, the corresponding matrices are called the spherical (dilatational) stress tensor and the deviatoric (distortional) stress tensor, respectively contributing to volume change or pure distorsion without volume changes. Only the latter of the two can produce yielding:

$$\begin{bmatrix} \sigma_1 & 0 & 0 \\ 0 & \sigma_2 & 0 \\ 0 & 0 & \sigma_3 \end{bmatrix} = \begin{bmatrix} \bar{\sigma} & 0 & 0 \\ 0 & \bar{\sigma} & 0 \\ 0 & 0 & \bar{\sigma} \end{bmatrix} + \begin{bmatrix} \sigma_1 - \bar{\sigma} & 0 & 0 \\ 0 & \sigma_2 - \bar{\sigma} & 0 \\ 0 & 0 & \sigma_3 - \bar{\sigma} \end{bmatrix} \tag{2.42}$$

This decomposition of stresses is shown in Figure 2.39. The bottom half of this figure illustrates the case corresponding to uniaxial tension. Note in parts (f) and (g) of that figure, that equal compression and tension acting on perpendicular planes produced a pure shear stress along a plane at 45°—hence, slip planes.

As a result, the total energy, U_0, can be calculated as the sum of the dilatation and distortion energy. For the first term, setting $\sigma_1 = \sigma_2 = \sigma_3 = \bar{\sigma}$, and expanding back to express $\bar{\sigma}$ in terms of principal stresses, one obtains:

$$\begin{aligned} U_{Dilatation} &= \frac{1}{2E}(3\bar{\sigma}^2) - \frac{\upsilon}{E}(3\bar{\sigma}^2) = \frac{3(1-2\upsilon)}{2E}(\bar{\sigma}^2) \\ &= \frac{(1-2\upsilon)}{6E}(\sigma_1 + \sigma_2 + \sigma_3)^2 \end{aligned} \tag{2.43}$$

The distortion energy, obtained by subtracting the dilatation energy from the total energy, and substituting $E = 2G(1 + \nu)$, is:

$$U_{Distortion} = \frac{1}{12G}[(\sigma_1 - \sigma_2)^2 + (\sigma_2 - \sigma_3)^2 + (\sigma_3 - \sigma_1)^2] \tag{2.44}$$

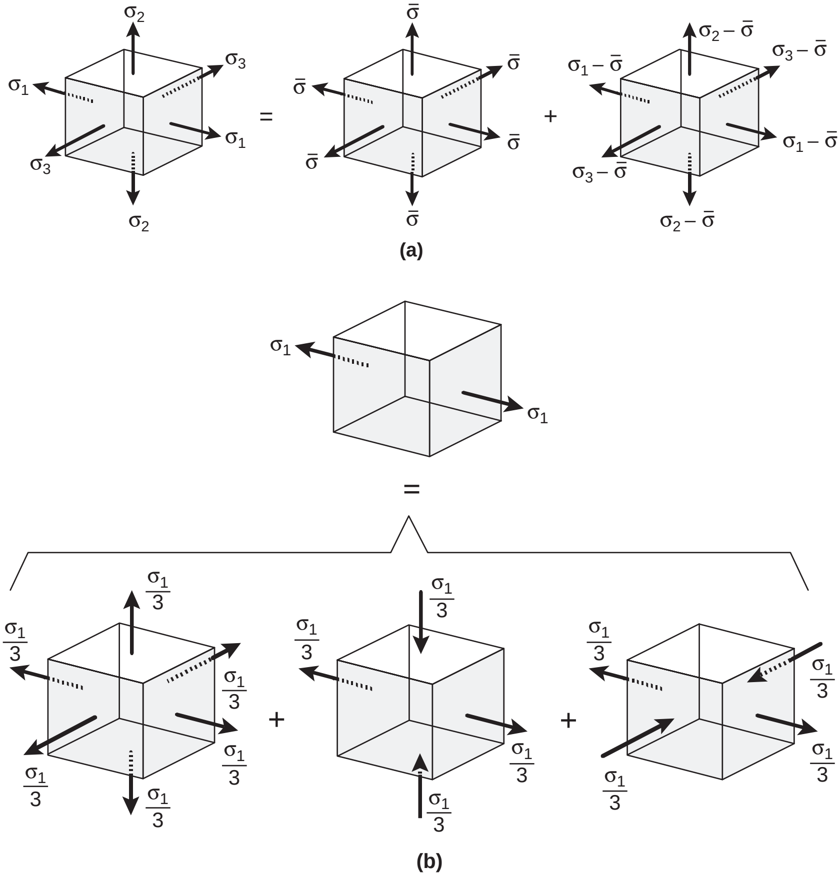

FIGURE 2.39 Decomposition of principal stresses into dilatational and distortional stresses: (a) general state of stress and (b) uniaxial state of stress.

As done earlier for the Tresca yield condition, the results from uniaxial testing are used for "calibration," to establish the critical yield condition. Hence, when $\sigma_2 = \sigma_3 = 0$ and $\sigma_1 = \sigma_{Yield} = \sigma_Y$ (not to be confused with σ_y above), the distortional energy at yield is:

$$U_{Distortion-Y} = \frac{1}{12G}[(\sigma_Y)^2 + (0)^2 + (-\sigma_Y)^2] = \frac{\sigma_Y^2}{6G} \tag{2.45}$$

Equating the general distortion energy equation to this maximum, on can obtain the following Von Mises Yield criterion:

$$\sigma_Y = \sqrt{\frac{1}{2}\left[(\sigma_1 - \sigma_2)^2 + (\sigma_2 - \sigma_3)^2 + (\sigma_3 - \sigma_1)^2\right]} \tag{2.46}$$

which, for the two-dimensional case in which $\sigma_3 = 0$, can be simplified into

$$\sigma_Y = \sqrt{\frac{1}{2}\left[(\sigma_1 - \sigma_2)^2 + (\sigma_2)^2 + (\sigma_1)^2\right]} = \sqrt{(\sigma_2)^2 + (\sigma_1)^2 - (\sigma_1\sigma_2)} \quad (2.47)$$

This is effectively draws an ellipse in the $\sigma_1 - \sigma_2$ plane, as shown in Figure 2.37, normalized by σ_Y. Note that for the pure shear case, $\sigma_1 = -\sigma_2$, and $\tau = \sigma_1$ (from Mohr circle), the equation gives $\sigma_Y = 3\tau^2$, and equivalently $\tau^2 = 0.58\ \sigma_Y \approx 0.6\ \sigma_Y$, which is typically used as the shear yield strength.

The corresponding Von Mises yield surface in three-dimensional, when $\sigma_3 \neq 0$, is shown in Figure 2.40. Note that an element only subjected to hydrostatic pressure (e.g., $\sigma_1 = \sigma_2 = \sigma_3$) would never yield, but rather crush or fracture without developing yielding, which is why the main axis of the three-dimensional yield surface is oriented in that direction. As such, the cylinder shown in Figure 2.40 shouldn't be misinterpreted—although shown to be of infinite length as an expression of the above yielding limit state, in reality it would be intersected by another critical surface for the brittle limit state (fracture or crushing) that would eventually develop under critical triaxial stress conditions. Incidentally, the same would also be true for the Tresca yield surface developed for an element under triaxial stress conditions (as could also be demonstrated using Mohr circles), which is circumscribed by the Von Mises yield surface as shown in Figure 2.40. Note that the two yield criteria intersect a number of times, and that the largest difference between the Tresca and Von Mises surfaces is approximately 16%. However, experiments on various metals have demonstrated a better agreement with the Von Mises criterion, as shown in Figure 2.41, and it is the one used in structural steel design.

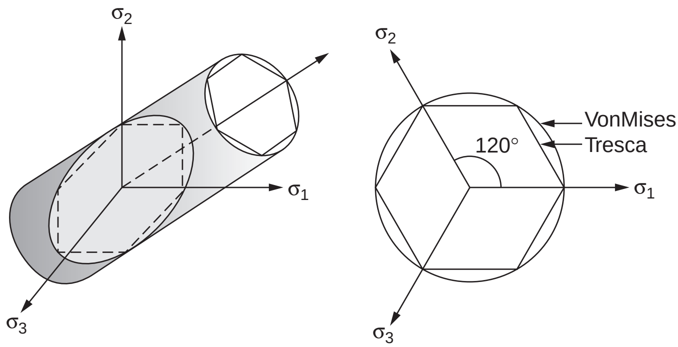

FIGURE 2.40 Von Mises and Tresca yield surfaces in three-dimensional principal stress space and corresponding intersect in $\sigma_1 - \sigma_2$ plane.

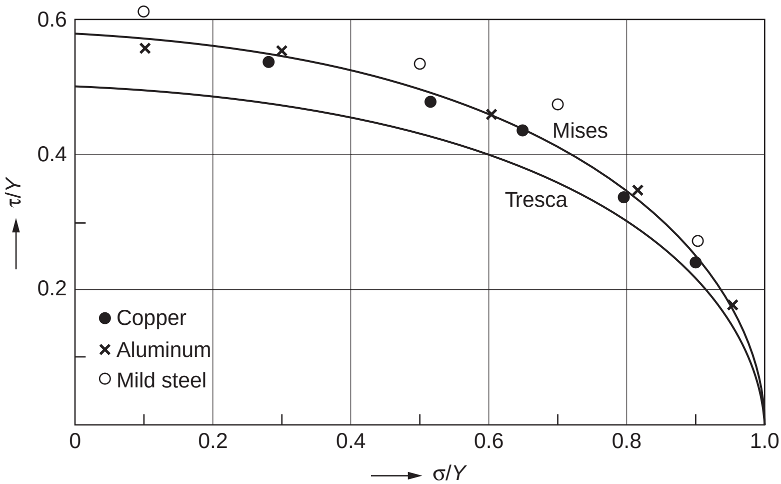

Figure 2.41 Comparison of experimental results with Tresca and Von Mises yield criteria, in terms of the uniaxial yield strength, *Y*. (*From* Theory of Plasticity, *J. Chakrabarty 2006, copyright Elsevier Limited. Reprinted with permission.*)

2.7.4.2 Isotropic Hardening, Kinematic Hardening, and Two-Surface Models

The yield criteria presented above define stress conditions at the onset of yielding. With the addition of plastic-flow rules, they can also be expanded to follow propagation of yielding. However, many applications require that both strain-hardening and cyclic inelastic loading be considered in sophisticated computational models. This is a broad topic with extensive literature investigating the relative advantages and accuracy of various proposed models and approaches—far exceeding the scope of this book. However, a brief overview of some general concepts is valuable in the current context. For simplicity, only the case of uniaxial yielding is considered in this section. Generalized mathematical formulations are available elsewhere (Lubliner 1990, Fung and Tong 2001, Chakrabarty 2006).

Figure 2.42a illustrate the simple isotropic and kinematic hardening models for a material assumed to exhibit linear strain-hardening. As shown on that figure, if a stress of σ_{YS} is reached beyond the initial yield σ_Y, the isotropic hardening model postulates that yielding would occur at σ_{YS} in the reversed loading direction. In a multidimensional space, this would be equivalent to proportionally expanding the Von Mises yield surface in each direction, such that it would not change shape (i.e., it would become a cylinder of greater radius in the $\sigma_1 - \sigma_2 - \sigma_3$ coordinate system). However, such a simple expansion of

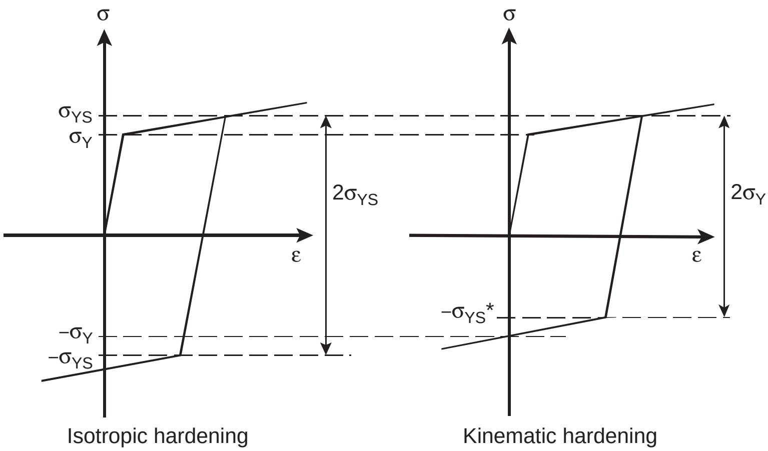

FIGURE 2.42 Uniaxial expression of: (a) isotropic hardening (expansion of yield surface) and (b) kinematic hardening (translation of yield surface).

the yield surface due to work hardening does not correctly represent the behavior of steel (and other metals), failing to account for the Bauschinger effects.

By contrast, the kinematic hardening model postulates that the yield surface translates in space without changing volume. For the uniaxial yielding case shown in Figure 2.42b, this implies that if a stress of σ_{YS} is reached beyond the initial yield σ_Y, yielding in the reversed loading direction would occur at $\sigma^*_{YS} = |\sigma_{YS} - 2\sigma_Y|$. In other words, the distance between yield points in opposite loading directions remains constant—which, in some measures, accounts for the Bauschinger effect and is more appropriate for materials that exhibit linear strain-hardening.

In spite of their respective shortcomings, both the isotropic and kinematic models are appealing for hand calculations when estimates of complex response are desirable. However, a better representation of stress-strain behavior for steel and other metals is achieved using a two-surface model that combines both the isotropic and kinematic effects. The Dafalias-Popov (1975) two-surface model, shown in Figure 2.43, is a set of rules that characterize how the yield surface varies as a function of past loading history, while remaining within two linear bounding surfaces (also known as memory surfaces). It is well suited for materials that exhibit a smooth transition into the strain-hardening range and that approach the straight line asymptotes that define the bounding surfaces. Although many researchers have expanded the model to enhance its ability to capture particular hysteretic steel behaviors or expand its range of applicability (e.g., Cofie and Krawinkler 1985, Mizuno et al.

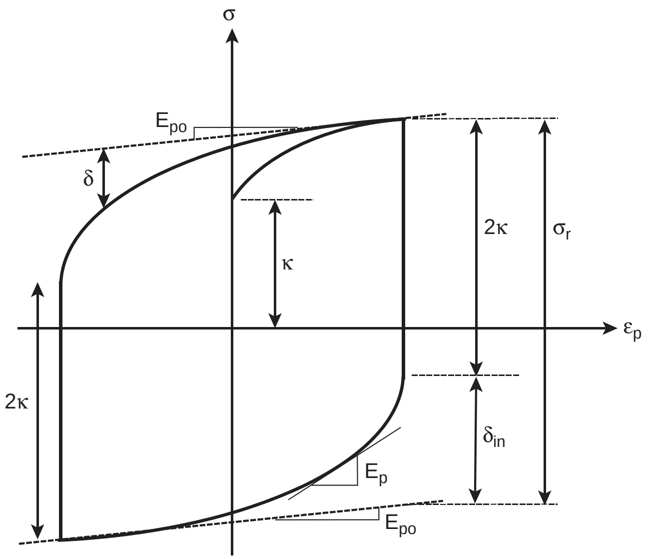

FIGURE 2.43 Uniaxial expression of plastic strains, ε_p, as a function of stress in two-surface model with bounding lines X-X′ and Y-Y′.

1992, Petersson and Popov 1977, Tseng and Lee 1983, to name a few), the main features of the original Dafalias and Popov two-surface model are summarized here.

Working from the assumption that, for any given increment of stress, $d\sigma$, on a stress-strain curve, the corresponding increment of strain, $d\varepsilon$, can be separated into its elastic and plastic components, $d\varepsilon_e$ and $d\varepsilon_p$, respectively, the following relationship can be derived between the total tangent modulus, E_t, and the elastic and plastic moduli, E_e and E_p, respectively:

$$\begin{gathered}\partial\varepsilon = \partial\varepsilon_e + \partial\varepsilon_p \\ \frac{\partial\sigma}{E_t} = \frac{\partial\sigma}{E} + \frac{\partial\sigma}{E_p} \\ \frac{1}{E_t} = \frac{1}{E} + \frac{1}{E_p}\end{gathered} \tag{2.48}$$

The Dafalias-Popov then postulates that:

$$E_p = E_p^o\left[1 + h\left(\frac{\delta}{\delta_{in} - \delta}\right)\right] \tag{2.49}$$

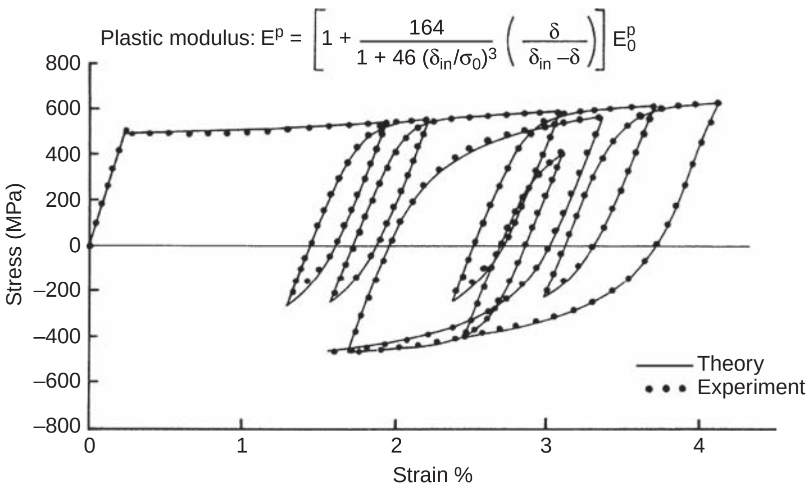

Figure 2.44 Comparison of stress-strain curve for a randomly loaded Grade 60 steel specimen and results obtained using a two-surface model. (*Courtesy of Professor Yannis Dafalias, University of California at Davis and National Technical University of Athens.*)

where E_p^o is the modulus of the asymptote, δ is the distance between the stress at the point of interest and the boundary curve, δ_{in} is the value of δ at the yield stress for a specific loading path, and h is a factor chosen to fit the experimental data. As the strain increases, δ decreases, and E_p varies from infinity at δ_{in} to the asymptote modulus. Knowing the tangent modulus, the complete hysteretic curve can be plotted for any value of strain (Dafalias 1992). Such an example is shown in Figure 2.44 against experimental data–more generalized elements also exist that can integrate the yield plateau with kinematic hardening rules into a single for constitutive model (Mahan et al. 2011).

Note that calibration to experimental results also reveal that the elastic range of the curve during any loading excursion is usually less than $2\sigma_Y$; Mizuno et. al (1992) reported a progressive reduction of that range as a function of accumulated plastic strain, down to 30% of that value after 1% of accumulated plastic strain, although others have reported good results using a constant reduced value (e.g., Cofie and Krawinkler 1985 considered it to be $1.2\sigma_Y$). Other refinements to the model, together with comparison to various versions of it, are presented by Mizuno et al. (1992).

2.7.4.3 Smooth Hysteretic Power Functions

Another general class of models, proposed by Wen (1976) expanding on the work of Bouc (1971), has been used in the literature—for example, to express the hysteretic behavior of buckling restrained braces (Andrews et al. 2008, Black et al. 2004), which are axially loaded members whose hysteretic behavior is directly proportional to its material stress-strain relationship, as described Chapter 11). A Bouc-Wen model for hysteretic stress-strain behavior states:

$$\sigma = \alpha\, E\, \varepsilon + (1-\alpha)E\varepsilon z \tag{2.50}$$

where all terms have been defined earlier, except α which is the ratio of postyielding to elastic stiffness, E_t/E, and z is a variable controlled by a differential equation expressed as:

$$\varepsilon_Y\, \dot{z} + \gamma\, |\dot{\varepsilon}|\, z\, |z|^{n-1} + \beta\, \dot{\varepsilon}\, |z|^n - \dot{\varepsilon} = 0 \tag{2.51}$$

where ε_Y is the yield strain, β, γ, and n are parameters that define the shape of the hysteretic curves. Given the additional constraint that $\beta + \gamma = 1$, the values of β and n are left to calibrate the model by curve fitting. Large values of n give results that approach bilinear behavior. For example, for buckling restrained brace, in which the above equation would be identical but instead expressed in terms of axial force, P, versus axial deformation, x, and in which E would be replaced by $K = EA/L$, a good match with experimental results was obtained for values of $\beta = 0.55$ and $n = 1$, and artificially increasing the calculated value of ε_Y by 25% (Black et al. 2004).

Note that many researchers have expanded the Bouc-Wen model to address various forms of more complex hysteretic behavior (e.g., as summarized in Song and Der Kiureghian 2006), often in attempts to address structural element behavior, rather than material behavior. However, the Bouc-Wen model is only one member of a broad family of *Smooth Hysteretic Models* (SHM) that have been developed and widely used, for example to model the plastic hinge moment-rotation behavior of structural elements made of various materials, while accounting for all potential physical phenomena that can degrade the strength, stiffness, and fullness of hysteretic curves, such as cracking, gap opening, debonding, slippage, local buckling, local fractures, and other effects. A general purpose SHM model able to integrate all these phenomena behaviors was developed and implemented by Sivaselvan and Reinhorn (1999). These more complex models are either phenomenological (i.e., fitted to experimental data) or physical (i.e., able to replicate experimental results from simple knowledge of geometry and fundamental material properties, on the basis of recognized physical principles).

Finally, other power models have also been used to capture the stabilized strain-hardened behavior of commonly used structural steel. For example, Kaufmann et al. (2001b) obtained reasonable accuracy in replicating the cyclic behavior of A572, A913, and A36 steels at 2%, 4%, 6%, and 8% strains, using the power equation $\sigma = K\varepsilon^n$, as

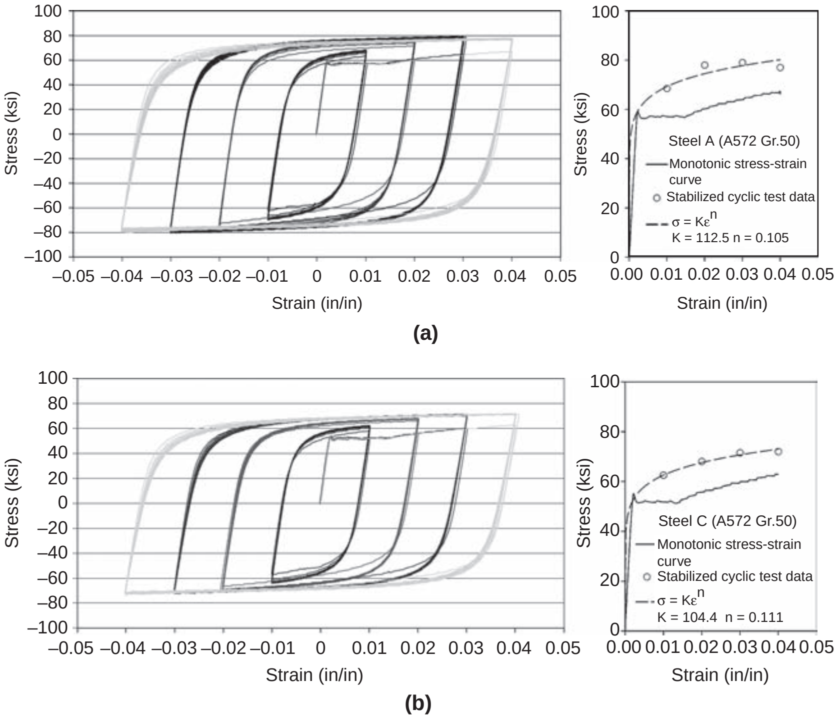

FIGURE 2.45 Smooth hysteretic behavior of A572 Grade steel at 2%, 4%, 6%, and 8% strain ranges and corresponding calibrated power model parameters: (a) sample "A" and (b) sample "C." (*Courtesy of Alan W, Pense, Department of Materials Science and Engineering, Lehigh University.*)

shown in Figure 2.45, where n is the work-hardening exponent. Values of K and n obtained by Kaufmann et al. for A572 steels are shown in Figure 2.45. Such an equation can be obtained from the Ramberg-Osgood relationship presented earlier if the inelastic deformations dominates and elastic response can be neglected, and by solving the resulting simplified Ramberg-Osgood for σ in terms of ε. However, if interested in the entire stress-strain range, including the elastic range, this approach is grossly incorrect because it gives an infinite initial stiffness and incorrect results in the elastic range. This can be corrected by breaking the stress-strain curve into a linear segment for which $\sigma = E\varepsilon$ up to the yield strength limiting, and the power equation beyond that point (Lubliner 1990).

2.8 Advantages of Plastic Material Behavior

To illustrate some of the advantages of plastic material behavior, the three-bar truss of Figure 2.46a is subjected to an increasing statically applied load, F, up to its ultimate capacity. Incidentally, two- or

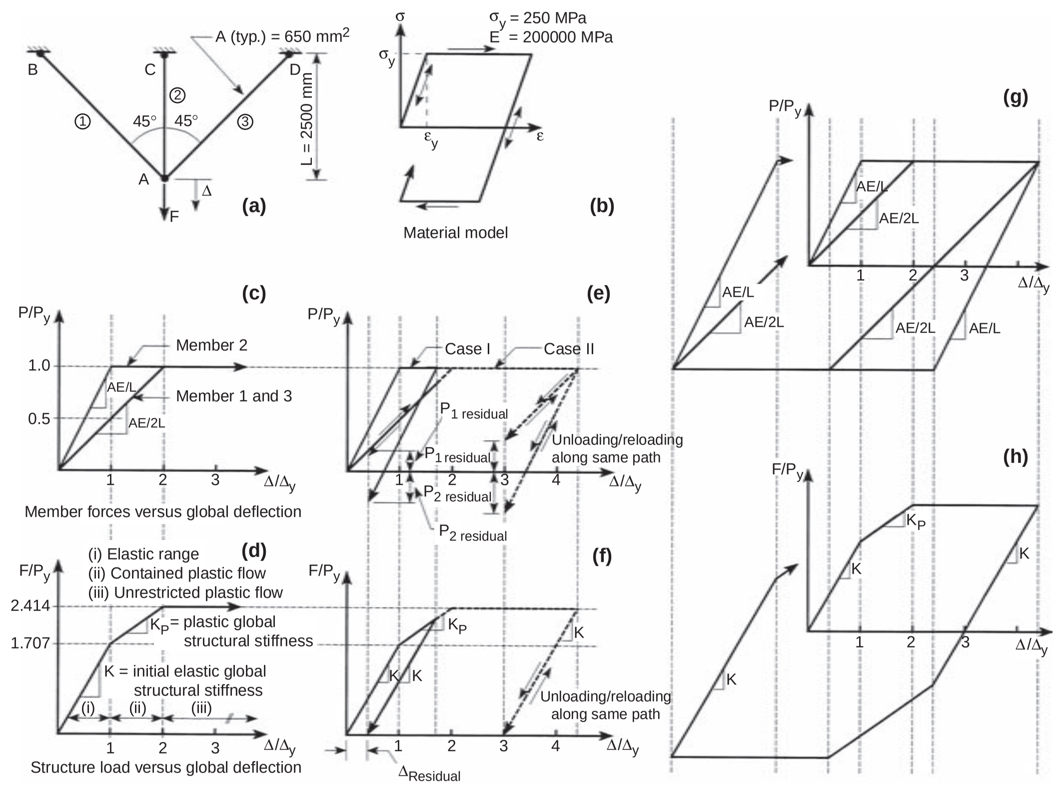

FIGURE 2.46 Simple example to illustrate cyclic plastic behavior of indeterminate structure.

three-bar trusses have been used by many authors to explain simple plasticity concepts. The simple truss of Figure 2.46 is one such classical example (e.g., Massonnet and Save 1967, Mrazik et al. 1987, Prager and Hodge 1951) that has been treated mostly from the perspective of noncyclic loading. However, here, behavior throughout at least one full plastic cycle is discussed, considering a simple elasto-perfectly plastic model. The section and material properties needed for this problem are indicated in Figure 2.46. All three bars are of same material (E and σ_y) and cross-sectional area (A). Moreover, the bars are assumed to be sufficiently stocky such that buckling will not occur prior to yielding in compression.

Although this structure is statically indeterminate, the force and elongation in member 3 will always be equal to that in member 1 as a result of structural and loading symmetry. Therefore, using small deformation theory, one can directly write the equation of static equilibrium for this problem as:

$$F = P_2 + 2P_1 \cos 45^\circ = P_2 + 1.414P_1 \tag{2.52}$$

Likewise, geometric compatibility here gives:

$$\Delta_1 = \Delta_3 = \Delta_2 \cos 45^\circ = \Delta \cos 45^\circ = 0.707\Delta \tag{2.53}$$

where F and Δ are defined in Figure 2.46. These two relationships must always remain true as long as deformations do not reach a magnitude that would violate the assumptions of small deformation theory. This will be reassessed at the end of this example. What will change as plastic behavior develops is the stress-strain or force-deformation relationship for each structural member. As long as structural members remain elastic, the following relationships are valid:

$$P_1 = \frac{AE}{L_1}\Delta_1 = \frac{AE}{L/\cos 45^\circ}\Delta \cos 45^\circ = \frac{AE}{2L}\Delta \tag{2.54}$$

and

$$P_2 = \frac{AE}{L_2}\Delta_2 = \frac{AE}{L}\Delta \tag{2.55}$$

Therefore, until first yielding of any member:

$$\begin{aligned} F = P_2 + P_1 \cos 45^\circ &= \frac{EA}{L}\Delta + 2\frac{EA}{2L}\Delta \cos 45^\circ \\ &= \frac{AE}{L}(1 + \cos 45^\circ)\Delta = K\Delta \end{aligned} \tag{2.56}$$

where K is the elastic stiffness for this structure. The equation above shows that member 2 reaches its yield strength (P_y) first, when members 1 and 3 are stressed to only half their capacity (i.e., 0.5 P_y). The yield displacement of the structure (Δ_y) could be defined in terms of the truss bar's properties and geometry:

$$\Delta_y = \frac{P_y L}{AE} \tag{2.57}$$

where all terms have been previously defined. The state of member forces and applied load as a function of the vertical deflection at point A are presented in a normalized format in Figures 2.46c and d. At $\Delta = \Delta_y$, the structure has been loaded to $F = 1.707\ P_y$. This case reflects the current standard structural engineering practice worldwide, in which linear elastic analyses are conducted to determine the maximum load that can be applied to a structure until the capacity of a single member is reached. Here, the capacity of member 2 is reached first, and members 1 and 3 are underutilized. Note that although one could conclude from elastic analysis that having bars of the same size is inefficient and likely propose a solution with bars of different cross-sections, this type of optimization based on minimum weight is often at odds with practical considerations, where architectural, manufacturing, or construction concerns may dictate equal size bars. Hence, in this problem, it is reasonable to constrain the bars to be of identical cross-section.

Even though truss bar 2 has yielded, the load applied to the structure can be increased beyond 1.707 P_y because members 1 and 3 have not reached their ultimate capacity. In the process, member 2 will undergo plastic elongation while sustaining its capacity. Therefore, for $\Delta > \Delta_y$:

$$P_1 = \frac{AE}{2L}\Delta \qquad \text{and} \qquad P_2 = P_y \tag{2.58}$$

and

$$F = P_2 + 2P_1 \cos 45^\circ = P_y + \frac{AE}{L}\Delta \cos 45^\circ \tag{2.59}$$

This condition of further loading beyond the elastic range, called contained plastic flow, is illustrated in Figures 2.46c and d. Note that the stiffness of the structure has decreased as a result of this partial yielding. Eventually, when the applied load reaches 2.414 P_y, all three truss bars yield, and a condition of unrestrained plastic flow develops. In this example, the ultimate capacity calculated by tolerating plastification of the structure is 41% larger than the elastic limit, providing some evidence that it is generally worthwhile to take advantage of the existing plastic strength available beyond the elastic range.

It is also important to realize that the maximum plastic capacity of a structure can be calculated directly through use of static equilibrium alone, without knowledge of prior elastic or plastic loading history. A logical conclusion from this observation is that lack-of-fit and other displacement-induced forces have no influence on the magnitude of the maximum load a structure can support, termed the plastic capacity. No supporting calculations are presented here, but the reader may wish to verify this remark by redoing the example assuming that member 2 was constructed 25 mm too short and forced to fit into the frame during construction before any loads were applied. Although doing so would reduce the value of the maximum load that can be applied if the structure is to remain elastic, it does not change the plastic capacity of the structure.

The behavior of this plastified truss-bar structure upon unloading is investigated next. As described in an earlier section of this chapter, steel unloads at a stiffness equal to the original elastic stiffness (as also shown in Figure 2.46b). However, in this example, two scenarios are evaluated, considering various states of plastification prior to unloading. In both cases, because the principle of superposition is not valid beyond the elastic range (as evidenced by Figure 2.46d), calculations must proceed following basic principles.

First, if unloading to $F = 0$ starts before all three truss bars have yielded (shown as Case I in Figures 2.46e and f), it can be shown that:

$$
\begin{aligned}
P_1 &= \frac{AE}{2L}\Delta_{MAX} - \frac{AE}{2L}\delta\Delta \\
P_2 &= P_y - \frac{AE}{L}\delta\Delta \\
\delta\Delta &= \Delta_{MAX} - \Delta
\end{aligned}
\tag{2.60}
$$

where $\delta\Delta$ is the incremental displacement imposed by the unloading, and Δ is the resulting displacement after unloading. The above approach also recognizes that only member 2 had plastified prior to unloading. Because the objective is to unload to $F = 0$, the equilibrium condition developed earlier can be used to solve for all other variables. As a result:

$$
\begin{aligned}
F = 0 = 2\left[\frac{AE}{2L}\Delta_{MAX} - \frac{AE}{2L}(\Delta_{MAX} - \Delta)\right]\cos 45^\circ \\
+\left[P_y - \frac{AE}{L}(\Delta_{MAX} - \Delta)\right]
\end{aligned}
\tag{2.61}
$$

and solving for Δ:

$$\Delta = \frac{\frac{AE}{L}\Delta_{MAX} - P_y}{\frac{AE}{L}(1+\cos 45°)} = \frac{\Delta_{MAX} - \Delta_y}{(1+\cos 45°)} = 0.586(\Delta_{MAX} - \Delta_y) \tag{2.62}$$

This residual displacement after unloading is shown in Figures 2.46e and f. Based on Figure 2.46g, it could be demonstrated that the residual displacement is also equal to:

$$\Delta = \Delta_{MAX} - \frac{F_{MAX}}{K} \tag{2.63}$$

where K is the global elastic structural stiffness defined earlier. Numerical examples would confirm the expediency of this alternative procedure.

Moreover, as shown in Figure 2.46e, residual member forces remain after unloading and exist simultaneously to that state of residual deformations. Because no external loads are applied to the structure, these member forces must be self-equilibrating. Numerical values can be obtained through simple substitution in the above equations.

In the second scenario considered here, unloading to $F = 0$ starts after all members have yielded (shown as Case II in Figures 2.46e and f). The approach remains the same, with slightly different results, as:

$$F = 0 = 2\left[P_y - \frac{AE}{2L}(\Delta_{MAX} - \Delta)\right]\cos 45° + \left[P_y - \frac{AE}{L}(\Delta_{MAX} - \Delta)\right] \tag{2.64}$$

and:

$$\Delta = \frac{\Delta_{MAX}(1+\cos 45°) - \Delta_y(2\cos 45° + 1)}{(1+\cos 45°)} = \Delta_{MAX} - 1.414\Delta_y \tag{2.65}$$

Again, this result could be obtained directly (and more easily) through use of the alternative method suggested above.

Note that substantial residual member forces develop in this second example (Figure 2.46e). Calculations would show that these reach approximately 30% and 40% of the yield force, P_y, in members 1 and 2, respectively.

As a result of the residual stresses left after unloading in cases I and II, the truss bars would follow their elastic path until the previously applied maximum load is reached anew if the structure is reloaded in the same direction (Figures 2.46e and f). This has a number of practical implications, as shown in the following chapters. However, this extended elastic range exists only as long as the state of residual stresses in the bars at $F = 0$ remains unchanged; cyclic loading is one factor that can alter these residual stresses.

When the loading cycle for this example structure is completed, the elastic range for the reversed loading is reduced because of the residual compression force in member 2, as shown in Figure 2.46h. The resulting hysteretic curve exhibits a shape similar, in principles, to a Bauschinger effect—and would be formally one if this example dealt with slip planes of crystals instead of yielding of bars. Formal analytical expressions to demonstrate this behavior, completing a full cycle of loading with yielding in both directions, can be derived from the same basic principles presented above, but it should be obvious that complex calculations and formulations are not necessary, given the clear graphical relationship already established in this example between the load-deformation relation of the structure and that of the members, as shown in Figure 2.46. Therefore, Figures 2.46g and h can be drawn directly as extensions of parts e and f, through use of simple trigonometric calculations to obtain numerical values. Note that the same structural plastic capacity is reached at $F = 2.414P_y$ in the reverse direction despite the earlier threshold of yielding, but this required greater contained plastic deformations.

More in-depth observations on the behavior of structural members subjected to inelastic cyclic loading are reserved for later chapters. Nonetheless, it is worthwhile to emphasize at this point that the plastic analysis presented above is possible only if connections of the structural members are stronger than the members themselves. Although this may sound obvious in the context of this simple example, this logical requirement sometimes become controversial when the severity of the expected ultimate loads is hidden in more simple static loading models or design philosophies (such as working stress design).

Finally, it is instructive to review the assumption of small deformations. For mild steels typically used in structural engineering applications, strains of up to 20% are possible. However, in this problem, calculations show that near this extreme level of deformations (corresponding to $100\varepsilon_y$), the angle of members 1 and 3 to the vertical is approximately 40°. Equilibrium in the deformed configuration gives a maximum value of F barely 5% greater. Such a gain in strength is hardly sufficient to warrant the consideration of large deformations theory, especially in the more practical range of 2% strains. A more important issue is the development of strain-hardening in the truss bars and its tangible impact on member strength. The effect of strain-hardening is addressed as necessary in this book.

2.9 Self-Study Problems

Problem 2.1 A simple structural system consists of the three pin-ended bars shown in Figure 2.46. All bars have a cross-section of 1 in^2 (645 mm^2). The material is a ductile structural steel which can be idealized as having elasto-perfectly plastic properties, with E of 29000 ksi and σ_y of 36 ksi (200,000 MPa and 250 MPa, respectively).

For that structure:

(a) What is the allowable load, P_{all}, which can be applied to that structure such that stresses in the bars do not exceed 0.66 Fy (i.e., allowable stress method)?

(b) What is the elastic limit load, P_u, which can be applied to that structure such that stresses do not exceed Fy anywhere (i.e., limit states design, with elastic analysis)? How would this change if the central member was constructed 1 in (25.4 mm) too short and forced to fit? Is a solution in the elastic range possible? Does it matter if member AC is elongated, or if members AB and AD are shortened, to achieve this fit (support answers by calculations)?

(c) What is the ultimate load capacity, P_{plast}, that the structure can carry accounting for plastic behavior (i.e., plastic design philosophy)?

(d) Draw the force-displacement (P-Δ) graph for the structure up to a maximum displacement of 1 in (25.4 mm) and followed by unloading to zero load. Express the vertical axis of this graph in a ratio of $P_{structure}$ over P_{ym}, where P_{ym} is the ultimate capacity of a single member, and the horizontal axis as a ratio of Δ/Δ_y, where Δ_y is defined at the occurrence of first yielding in the structure. Calculate and indicate on this plot all important numerical values.

(e) For the loading history described in (d), also plot the force displacement relation of all three members, superposed on a single graph, the vertical axis of this graph being the ratio of P_{member} over P_{ym}, the horizontal axis being the actual structural displacement in inches (mm). Calculate and indicate on this plot all important numerical values; in particular, indicate what are the forces in each bar following the above displacement history.

(f) If the central member was constructed 1 in (25.4 mm) too short and forced to fit during construction, plot the force displacement relation of all three members corresponding to the following two construction sequences: first, if the central member is elongated by 1 in (25.4 mm), connected to the other two members, and released; second, if the two inclined members are compressed to connect to the central member, and released. Does it matter if member AC is elongated, or if members AB and AD are shortened, to achieve this fit (support answers by calculations)?

(g) Comment on the differences between elastic and plastic behavior for analysis and design. In particular, comment on whether the principle of superposition is applicable for plastic design (i.e., whether usual computer programs could be used to assess plastic strength), whether lack-of-fit and other displacement-induced forces seem critical to the ultimate strength of the structure, and whether an extremely slender member could buckle under residual stresses upon unloading.

Problem 2.2 A simple structural system consists of three pin-ended bars, as shown in the figure below. All bars have the same cross-section A. The material is a ductile structural steel which can be idealized as having elasto-perfectly plastic properties, with E and σ_y.

For that structure, plot the force-displacement (F-Δ) for the structure on one graph, and the force-displacement relation of all three members on another graph (as done in the previous problem), for the displacement histories described below. Write parametric equations (in terms of E and σ_y, A, L, F, Δ, P, etc.) applicable at the various stages along the curve, clearly indicating the range of their applicability and key values along the graphs. For the cases of unloading (cases I and II below), also derive expressions for the structural residual displacements after unloading.

(a) Step 1: elastic behavior
(b) Step 2: post-elastic behavior up to full plastic capacity (also show unrestrained plastic flow)
(c) Step 3: unloading prior to reaching maximum plastic load (i.e., case I)
(d) Step 4: unloading after reaching of maximum plastic load and at $\Delta_{max} > 2\Delta_y$ (i.e., case II)
(e) Step 5: for both case I and II above, complete the plot until yielding in the reversed direction is achieved. The key values on the graphs can be derived graphically (i.e., closed-form solutions are not necessary)

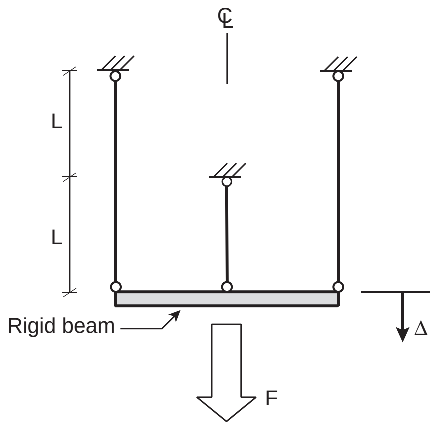

Problem 2.3 Using simple plastic analysis, what is be the maximum load, P (in kips), that can be applied to the structure shown here. This structure consists of seven steel bars, each having a cross-section of 1.5 in^2 (1450 mm^2).

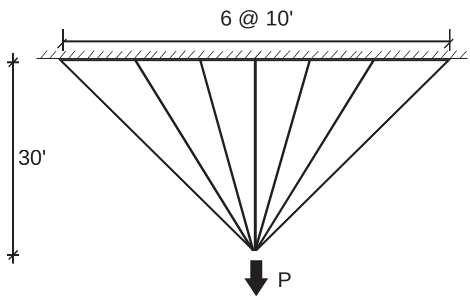

Problem 2.4 Experimental data has been obtained for the normalized moment-curvature relationship of a steel beam (see below). Use both the Menegotto-Pinto method and the Ramberg-Osgood method to define analytical expressions relating the normalized moments and curvatures for that steel beam.

M/M_y	φ/φ_y	M/M_y	φ/φ_y	M/M_y	φ/φ_y
0	0	1.204	1.3	1.42	2.5
0.5	0.5	1.245	1.4	1.434	2.75
0.75	0.75	1.278	1.5	1.444	3
1	1	1.337	1.75	1.469	4
1.087	1.1	1.375	2	1.48	5
1.153	1.2	1.401	2.25	1.486	6

Problem 2.5 Provide *clear and brief* answers (five lines of text or less) to the following questions:

(a) What property of steel does the Charpy-V test measure, and what non-metallurgical parameter affects this property?
(b) What is the Carbon Equivalent Formula, and what practical information does it provide?
(c) What is a slip plane?
(d) What is lamellar tearing? Draw a sketch to give an example of when such a problem could occur, and another one to show how to design to prevent that potential tearing.
(e) What is a typical value of the modulus of elasticity at the onset of strain-hardening?
(f) What does calculation of K_I for a given specimen requires?
(g) How can the percentage of manganese, silicon, chromium, molybdenum, vanadium, nickel, and copper in steel be quantified in a useful way with respect to their impact on brittleness?
(h) What is the difference between the steel grades ASTM A572 Gr. 50 and ASTM A993 Gr. 50?
(i) What is the heat-affected zone (HAZ)?
(j) What is a "contained plastic flow"?
(k) What are residual stresses (i.e., a definition of what they are, not why they exist)?
(l) Name three sources of residual stresses in structural members.

Problem 2.6 A very short specimen is tested in pure compression until failure. It is observed that, at failure, the whole specimen is undergoing considerable strain-hardening. Describe why there has been no buckling on the plastic plateau in spite of the fact that the tangent modulus of elasticity, E_t, is zero in theory on this plateau. How will this specimen eventually fail?

Problem 2.7 Some seismic design codes and standards specify that steels "shall have a minimum Charpy-V notch toughness of 20 ft-lb (27 J) at 0°F

(–18ºC).” Yet, looking at Charpy-V experimental results (Figure 2.5), 20 ft-lb seems to be in the brittle behavior range. Explain in a few sentences why a 20 ft-lb value is deemed acceptable in such applications, given that brittle steels are not acceptable in seismic applications.

Problem 2.8 A structural steel T-shape must be constructed from plates 4-inches-thick, as illustrated below:

(a) Indicate what might be a potential problem with this weld design.
(b) Propose an alternative weld design which will eliminate this problem.

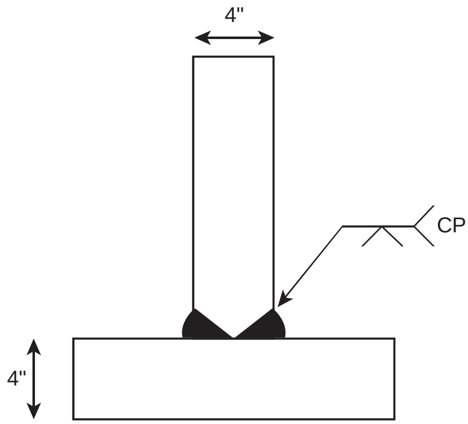

References

AASHTO. 2003. *Guide Specification for Highway Bridge Fabrication with HPS 70W (HPS 485W) Steel,* 2nd ed., Washington, D. C.: American Association of State Highway and Transportation Officials, p. 19.

Abbaschian, R., and Reed-Hill, R. E. 2008. *Physical Metallurgy Principles,* 4th ed. CL-Engineering.

Ahluwalia, H. 2003. “Combating Plate Corrosion—Improving Corrosion Resistance Through Welding, Fabrication Methods.” *The Fabricator*, October 2003, http://www.thefabricator.com/MetalsMaterials/MetalsMaterials_Article.cfm?ID=731

Andrews, B. M., Fahnestock, L. A., and Song, J. 2008. “Performance-Based Engineering Framework and Ductility Capacity Models for Buckling-Restrained Braces,” *NSEL Report Series, Report No. NSEL-012*. University of Illinois at Urbana-Champaign: Department of Civil and Environmental Engineering.

AISC. 1971. “Plastic Design I Steel—A Guide and Commentary,” *ASCE Manual and Reports on Engineering Practice No.41*. New York: American Society of Civil Engineers.

AISC. 1973. “Commentary on Highly Restrained Welded Connections.” *Engineering Journal,* vol. 10, no. 3, 61–73.

AISC. 1994. “Load and Resistance Factor Design Manual of Steel Construction, 2nd ed.” American Institute of Steel Construction, Chicago.

AISC. 1997a. “Steel Industry Announces Improved Structural Grade for Buildings.” *Modern Steel Construction*, vol. 37, no. 4, 18.

AISC. 1997b. *Technical Bulletin #3—New Shape Material*. Chicago: American Institute of Steel Construction.
AISC. 2001. "Changes to the T, k, and k1 Dimensions for W-Shapes," *AISC Advisory,* February 14, 2001. Chicago: American Institute of Steel Construction.
AISC. 2005. "Seismic Provisions for Structural Steel Buildings (ANSI/AISC 341-05)", American Institute of Steel Construction, Chicago, IL.
AISC. 2010. "Specification for Structural Steel Building—ANSI/AISC 360–05." Chicago: American Institute of Steel Construction.
ASCE. 1992. "Structural Fire Protection," *ASCE Manuals and Reports on Engineering Practice No. 78,* T. T. Lie, editor. New York: ASCE Committee on Fire Protection, American Society of Civil Engineers.
ASM. 1986. *Atlas of Fatigue Curves*, H. E. Boyer, editor. Materials Park, OH: American Society for Metals.
ASTM. 1985a. "Standard Method of Test for Plane-Strain Fracture Toughness of Metallic Materials—ASTM Designation E399-83," vol. 03.01, *ASTM Annual Standards.* West Conshohocken, PA: American Society for Testing and Materials.
ASTM. 1985b. "Standard Method for Conducting Drop Weight Test to Determine Nil-Ductile Transition Temperature of Ferric Steels—ASTM Designation E208," *ASTM Annual Standards.* West Conshohocken, PA: American Society for Testing and Materials.
AWS. 2010. "AWS D1.1/D1.1M-2010 Structural Welding Code—Steel". Miami: American Welding Society.
AWS. 1976, "Fundamentals of Welding," *Welding Handbook,* vol. 1, 7th ed. Miami: American Welding Society.
Baird, J. D. 1963. "Strain Aging of Steel; A Critical Review," *Iron Steel*, vol. 36, 186–192, 368–374.
Baird, J. D. 1971. "The Effects of Strain Aging due to Interstitial Solutes on Mechanical properties of Metals," *Met. Rev.,* vol. 5, 1–18.
Bartlett, M. F., Dexter, R. J., Graeser, M. D., Jelinek, J. J., Schmidt, B. J., and Galambos, T. V. 2003. "Updating Standard Shape Material Properties Database for Design and Reliability," *AISC Engineering Journal,* vol. 40, no. 1, 3–14.
Barsom, J., and Korvink, S. 1998. "Effect of Strain-hardening and Strain Aging on the k-Region of Structural Shapes," *Report No. SACIBD·98/02.* San Francisco, SAC Joint Venture, 47 pp.
Barsom, J. M., and Pellegrino, J. V. 2000. "Failure Analysis of a Column k-Area Fracture," *Modern Steel Construction.* Chicago: American Institute of Steel Construction.
Bazergui, A., Bui-Quoc, T., Biron, A., McIntyre, G., and Laberge, C. 1987. "Résistance des matériaux," *Editions de l'Ecole Polytechnique de Montreal,* Montreal, Canada, 477 pp.
BCSA. 2005. "Galvanizing Structural Steel Works—An Approach to the Management of Liquid Metal Assisted Cracking," *Publication No.40/06.* London: British Constructional Steel Association, 22 pp.
Bertero, V. V., and Popov, E. P. 1965. "Effect of Large Alternating Strains of Steel Beams." *Journal of the Structural Division, American Society of Civil Engineers,* vol. 91, no. ST1.
Bjorhovde, R. 1987. "Welded Splices in Heavy Wide-Flange Shapes," *National Engineering Conference and Conference of Operating Personnel.* New Orleans.
Black, C. J., Makris, N., and Aiken, I. D. 2004. "Component Testing, Seismic Evaluation, and Characterization of Buckling-Restrained Braces." *Journal of Structural Engineering, ASCE*, vol. 130, no. 6, 880–894.
Blodgett, O. W. 1977a. "Distortion … How to Minimize It with Sound Design Practices and Controlled Welding Procedures plus Proven Methods for Straightening Distorted Members," *Publication G261.* Cleveland: The Lincoln Electric Co.
Blodgett, O. W. 1977b. "Why Welds Crack—How Cracks Can Be Prevented," *Publication G230.* Cleveland: The Lincoln Electric Co.
Bouc, R. 1971. Modèl mathématique d'hysteresis. *Acustica,* vol. 24, 16–25.

Bridgman, P. W. 1923. "The compressibility of thirty metals as a function of pressure and temperature." *Proceedings of the American Academy of Arts and Sciences,* vol. 58, 165.

Bridgman, P. W. 1949a. *The physics of high pressure.* London: Bell and Sons.

Bridgman, P. W. 1949b. "Linear compressions to 30,000 kg/cm2, including relatively incompressible substances. *Proceedings of the American Academy of Arts and Sciences,* vol. 77, 189.

Bruneau, M., Mahin, S. A., and Popov, E. P. 1987. "Ultimate Behavior of Butt Welded Splices in Heavy Rolled Steel Sections," *EERC Report No. 87-10.* Earthquake Engineering Research Center. Berkeley, CA: University of California at Berkeley.

Bruneau, M., and Zahrai, S. M. 1997. "Some Observations on Effect of Severe Corrosion on the Cyclic Ductility of Steel." *ASCE Journal of Structural Engineering,* vol. 123, no.11, 1478–1486.

Buchanan, A. H. 2001. "Structural Design for Fire Safety." West Sussex, England: John Wiley & Sons, 415 pp.

Byfield, M. P., Davies, J. M., and Dhanalakshmi, M. 2005. "Calculation of the strain-hardening behaviour of steel structures based on mill tests." *Journal of Constructional Steelwork Research*, vol. 61, no. 2, 133–150.

Carr, A. C. 2004. *Ruaumoko Manual,* vols. 1 & 2. Department of Civil Engineering. Christchurch, New Zealand: University of Canterbury.

Carter, C. 1997. "Are you Properly Specifying Structural Steel," *Modern Steel Construction*, January 1997.

Cattan, J. 1997. "Steel Industry Embraces A992," *Modern Steel Construction*, April 1997.

Chakrabarty, J. 2006. *Theory of Plasticity.* Oxford, UK: Butterworth-Heinermann, 882 pp.

Chi, B., and Uang., C. M. 2004. "Effect of Straightening Method on the Cyclic Behavior of k-Area in Steel Rolled Shapes," *Engineering Journal,* American Institute of Steel Construction, first quarter, 2004, 15–22.

Cofie, N. G., and Krawinkler, H. 1985. "Uniaxial Cyclic Stress-Strain Behavior of Structural Steel," *Proceedings of ASCE,* vol. 111, no. EM9, 1105–1120.

Coffin, L. F. 1954. "A Study of the Effects of Cyclic Thermal Stresses on a Ductile Metal." *Transaction of the ASME,* vol. 76, 931–950.

Cottrell, A. H., and Bilby, B. A. 1949. "Dislocation Theory of Yielding and Strain Aging of Iron." *Proceedings of the Physical Society,* vol. 62, 49–62.

Dafalias, Y. F., and Popov, E.P. 1975. "A Model of Nonlinear Hardening Materials for Complex Loading." *Acta Mechanica,* vol. 21, 173–192.

Dafalias, Y. F. 1992. "Bounding Surface Plasticity Models for Steel under Cyclic Loading," *Stability and Ductility of Steel Structures Under Cyclic Loading*. Fukomoto, Y., and Lee, G., editors. Boca Raton, Florida: CRC Press.

DesRoches, R., McCormick, J., and Delemont, M. A. 2004. "Cyclic Properties of Superelastic Shape Memory Alloys." *ASCE Journal of Structural Engineering,* vol. 130, no. 1, 38–46

Dexter, R. J., Hajjar, J. F., Prochnow, S. D., Graeser, M. D., Galambos, T. V., and Cotton, S. C. 2001. "Evaluation of the Design Requirements for Column Stiffeners and Doublers and the Variation in Properties in Properties of A992 Shapes." *Proceedings, North American Steel Construction Conference.* Chicago: AISC, pp. 14-1–17-21.

Dicleli, M., and Bruneau, M. 1995. "An Energy Approach to Sliding of Single-Span Simply Supported Slab-on-Girder Steel Highway Bridges with Damaged Bearings," *Earthquake Engineering and Structural Dynamics*. vol. 24, 395–409.

DNCR. 2003. "Report on the July 21st Collapse of the Kinzua Viaduct," *Board of Inquiry investigation report.* Pennsylvania Department of Conservation and Natural Resources.

DoITPoMS. 2009. "Dislocation motions." *Dissemination of IT for the Promotion of Materials Science (DoITPoMS).* Cambridge, UK: Department of Materials Science and Metallurgy, University of Cambridge. http://www.doitpoms.ac.uk/tlplib/dislocations/dislocation_motion.php

Dusicka, P., Itani, A. M., and Buckle, I. G. 2004. "Shear Link Energy Dissipators Utilizing High Performance and Low Yield Point Steels," *4th National Seismic Conference and Workshop on Bridges.* Memphis, TN.

Dusicka, P., Itani, A. M., and Buckle, I. G. 2007. "Cyclic response of plate steels under large inelastic strains." *Journal of Constructional Steel Research,* vol. 63, no. 2 , 156–164

ECCS Technical Committee 3. 2001. Model Code on Fire Engineering, Brussels: European Convention for Constructional Steelwork.

Elam, C. F., 1935. *The Distortion of Metal Crystals* New York, Oxford.

Englehardt, M. D., and Husain, A. S. 1993. "Cyclic Loading Performance of Welded Flange Bolted Web Connections." *ASCE Structural Engineering Journal*, vol. 119, no. 12, 3537–3550.

Faller, M., and Richner, P. 2003. "Material selection of safety-relevant components in indoor swimming pools," *Materials and Corrosion,* vol. 54, S. 331–338. (in German).

Fisher, J. W. 1984. *Fatigue and Fracture in Steel Bridges—Case Studies.* New York:Wiley Interscience, 315 pp.

Fisher, J. W., and Pense, A. W. 1987. "Experience with Use of Heavy W Shapes in Tension," *AISC. Engineering Journal*, vol. 24, no. 2, 63–77.

Fisher, J. W., Yen. B. T., and Wang, D. 1990. "Fatigue strength of riveted bridge members." *Journal of Structure and Infrastructure Engineering ASCE,* vol. 116, no. 11, 2968–2981.

Fung, Y. C., and Tong, P. 2001. "Classical and Computational Solid Mechanics." Singapore: *World Scientific Publishing*, 930 pp.

Galambos, T. V., and Ravindra, M. K. 1978. "Properties for Steel Used in LRFD," *Journal of the Structural Division, ASCE*, vol. 104, no. 9, 1459–1468.

Gewain, R. G., Iwankiw, N. R., and Alfawakhiri, F. 2003. "Facts for Steel Buildings—Fire." Chicago: American Institute of Steel Construction.

Horne, M. R., and Morris, L. J. 1981. *Plastic design of low-rise frames.* Cambridge, MA: MIT Press.

Hu., G., Morivat, M. A., Lee, J., Schell, E., and Engelhardt, M. 2009. "Elevated Temperature Properties of ASTM A992 Steel," *ASCE Structures Congress.* Austin, TX.

Iwankiv, N., and Zoruba, S. 2002. "Steel moment frames: resolution of recent seismic detailing and material shape issues." *Journal of Constructional Steel Research,* vol. 58, 495–510.

Kaufmann, E. J., Metrovich, B., Pense, A. W., and Fisher, J. W. 2001a. "Effect of Manufacturing Process on k-Area Properties and Service Performance," *Proceedings of the North American Steel Construction Conference.* Fort Lauderdale, FL, May 9–12, 2001. Chicago, IL: American Institute of Steel Construction, Inc., pp. 17.1–17.24.

Kaufmann, E. J., Metrovich, B., and Pense, A. W. 2001b. "Characterization of Cyclic Inelastic Strain Behavior on Properties of A572 Gr. 50 and A913 Gr. 50 Rolled Sections," *ATLSS Report No. 01-13,* Lehigh University.

Kayser. J. R., and Nowak, A. S. 1989. "Capacity loss due to corrosion in steel-girder bridges." *J. Struct. Engrg., ASCE,* vol. 115, no. 6, 1525–1537.

Khan, A. S., and Huang, S. 1995. *Continuum Theory of Plasticity.* Wiley-Interscience, New York, 431p.

Koch, G. H., Brongers, P. H., Thompson, N. G., Virmani, Y. P., and Payer, J. H. 2002. "*Corrosion Costs and Prevention Strategies in the United States*," *Report No. FHWA-RD-01-156.* Washington, D. C.: Federal Highway Administration, March 2002.

Kinstler, T. J. 2005. *Current Knowledge of the Cracking of Steels During Galvanizing—A Synthesis of the Available Technical Literature and Collective Experience for the American Institute of Steel Construction.* Springville, AL, GalvaScience LLC, 79 pp.

Kulicki, J. M., Prucz. Z., Sorgenfrei, D. E., Mertz. D. R., and Young. W. T. 1990. "Guidelines for Evaluating Corrosion Effects in Existing Steel Bridges," *NCHRP Rep. No. 333.* Washington, D. C.: Transportation Research Board, National Research Council.

Lay, M. G. 1965. "Yielding of Uniformly Loaded Steel Members," *Journal of the Structural Division, Proceedings of the ASCE*, vol. 91, no. ST6, 49–66.

Lay, G., and Smith, P. D. 1965. Role of strain-hardening in plastic design. *Journal of Structural Divison, ASCE,* vol. 93, no. ST3, 25–43.

Lee, D., Cotton, S., Dexter, R. J., Hajjar, J. F., Ye, Y., and Ojard, S. D. 2002. "Column Stiffener Detailing and Panel Zone Behavior of Steel Moment Frame Connections," *Report No. ST-01-3.2,* Minneapolis, MN: Department of Civil Engineering, University of Minnesota.

Lee, G. C., Chang, K. C., and Sugiura, K. 1992. "The Experimental Basis of Material Constitutive Laws of Structural Steel under Cyclic and Nonproportional Loading," *Stability and Ductility of Steel Structures Under Cyclic Loading*. Fukomoto, Y., and Lee, G., editors. CRC Press: Boca Raton, FL.

Lubliner, J. 1990. *Plasticity Theory.* NY: Macmillan Publishing, 495 pp.

Lwin, M. 2002. *High Performance Steel Designers' Guide.* San Francisco: Federal Highway Administration, U.S. Department of Transportation, 28p.

Mahan, M., Dafalias, Y. F., Taiebat, M., Hoe, Y. A., and Kunnath, S. K. 2011. "SANISTEEL: Simple ANIsotropic STEEL Plasticity Model." *ASCE Journal of Structural Engineering,* vol. 137, no. 2, 185–194.

Mahmoud, K. M. 2003a. "Hydrogen Embrittlement of Suspension Bridge Cable Wires," *System-Based Vision for Strategic and Creative Design,* pp. 947–950.

Mahmoud, K. M. 2003b. "An Absorbing Process." *Bridge Design and Engineering,* no. 31, 2–4.

Manson, S. S. 1953. "Behavior of Materials under Conditions of Thermal Stress," *Heat Transfer Symposium,* University of Michigan Engineering Research Institute.

Marsh, K. J. 1993. *Shot Peening: Techniques and Applications.* London: Engineering Materials Advisory Services Ltd., Chamelion Press Ltd, 320 pp.

Massonnet, C., and Save, M. 1967. "Calcul Plastique des Constructions—Volume 1: Structures Dépendant d'un Paramètre," *Deuxième Édition.* Bruxelles: Centre Belgo-Luxembourgeois d'information de l'Acier, 547 pp.

Matsuishi, M., and Endo, T. 1968. *Fatigue of metals subjected to varying stress.* Fukuoka, Japan: Japan Soc. Mech. Engineering,

Matteis G. D., Landolfo, R., and Mazzolani, F. M. 2003. "Seismic response of MR steel frames with low-yield steel shear panels." *Engineering Structures,* vol. 25, 155–168.

McCormick, J., DesRoches, R., Fugazza, D., and Auricchio, F. 2007. "Seismic Assessment of Concentrically Braced Steel Frames with Shape Memory Alloy Braces," *ASCE J. Struct. Engrg,* vol. 133, no. 6, 862–870.

MIC. 2005. "Shot Peening Applications, Ninth Edition," Metal Improvement Company, Paramus, NJ.

Miller, D. K. 2000. "Welding HPS70W Steel," *Proceedng Conference on Steel Bridge Design and Construction for the New Millennium with Emphasis on High Performance Steel,* Lincoln, NE, pp. 107–114.

Miner, M. A. 1945. "Cumulative Damage in Fatigue." *Journal of Applied Mechanics, Transaction of ASME,* vol. 67, A159.

Mizuno, E., Tanaka, Y., Shen, C., and Usami, T. 1992. "A Uniaxial Stress-Strain Model for Structural Steels under Cyclic Loading," *Stability and Ductility of Steel Structures under Cyclic Loading*. Fukomoto, Y., and Lee, G., editors. Boca Raton, FL: CRC Press, pp. 37–48.

Mrazik, A., Skaloud, M., and Tochacek, M. 1987. *Plastic Design of Steel Structures.* New York: Halsted Press, John Wiley and Sons, p. 637.

Mizutani, Y., Ishibashi, K., Yoshii, K., Watanabe, Y., Chijiiwa, R., and Yoshida, Y. 2004. "590MPa Class Fire-Resistant Steel for Buildings Structural Use," *Nippon Steel Technical Report No. 90.* Tokyo, pp. 45–52.

Nakashima, M., Iwai, S., Iwata, M., Takeuchi, T., Konomi, S., Akazawa, T., and Saburi, K. 1994. "Energy Dissipation Behavior of Shear Panels Made of Low Yield Steel." *Earthquake Engineering and Structural Dynamics*, vol. 23, 1299–1313.

Neal, G. G. 1977. *The Plastic Methods of Structural Analysis,* 3rd ed. London: Science Paperbacks, Chapman and Hall.

NIST. 2010. "Best Practice Guidelines for Structural Fire Resistance Design of Concrete and Steel Buildings," *National Institute of Standards and Technology, Technical Note 1681.* Phan, L.T. McAllister, T. P. Gross, J. L., and Hurley, M. J., editors. 217 pp.

NIST. 2005. "Collapse of the World Trade Center Towers. Final Report. Federal Building and Fire Safety Investigation of the World Trade Center Disaster," *Report NIST NCSTAR1.* National Institute of Standards and Technology, National Construction Safety Team, 298p.

NBS. 1980. "Development of a Probability-Based Criterion for American National Standard A58 Building Code Requirements for Minimum Design Loads in Buildings and Other Structures," *NBS Special Publication 577.* National Bureau of Standards, U.S. Department of Commerce.

NPL. 1982. *Stress Corrosion Cracking—Guides to Good Practice in Corrosion Control.* Middlesex, UK: National Physical Laboratory.

NTSB. 1971. "Highway Accident Report—Collapse of U.S. 35 Highway Bridge, Point Pleasant, West Virginia, December 15, 1967," *NTSB/HAR-71/01.* US National Transportation Safety Board.

Okazaki, T., and Engelhardt, M. D. 2007. "Cyclic Loading Behavior of EBF Links Constructed of ASTM A992 Steel," *Journal of Constructional Steel Research,* vol. 63, 751–765.

Pense, A. 2004. "HPS Corrugated Web Girder Fabrication Innovations Final Report–Part 4: Literature And Experimental Study Of Strain Aging In Hps And Other Bridge Steels," Center for Advanced Technology for Large Structural Systems, Lehigh University.

Petersson, H., and Popov, E. P. 1977. "Constitutive Relation for Generalized Loadings." *Proceedings of ASCE,* vol.104, no. EM4, 611–627.

Popov, E. P. 1968. *Introduction to Mechanics of Solids.* Prentice Hall: Englewood Cliffs, NJ.

Popov, E. P., and Stephen, R. M. 1971. "Cyclic Loading of Full Size Steel Connections," *Bulletin No. 21.* Washington, D. C.: American Iron and Steel Institute.

Prager, W., and Hodge, P. G. 1951. *Theory of Perfectly Plastic Solids.* New York: John Wiley and Sons, 265.

Rolfe, S. T., and Barsom, J. M. 1999. *Fracture and Fatigue Control in Structures—Application of Fracture Mechanics,* 3rd ed. West Conshohocken, PA: ASTM International.

Rooke, D. P., and Cartwright, D. J. 1976. *Compendium of Stress Intensity Factors.* London: Procurement Executive, Ministry of Defense, Her Majesty's Stationery Office.

Ruddy, J. L., Mario, J. P., Ioannides, S. A., and Alfawakhiri, F. 2003. *Fire Resistance of Structural Steel Framing—AISC Steel Design Guide 19.* Chicago: American Institute of Steel Construction.

SAC. 1995. "Advisory No. 3—Steel Moment Frame Connections," *Report SAC-95-01.* Sacramento, CA: SAC Joint Venture.

Saeki, E., Sugisawa, M., Yamaguchi, T., and Wada, A. 1998. "Mechanical Properties of Low Yield Point Steels." *ASCE Journal of Materials in Civil Engineering,* vol. 10, no. 3, 143–152.

Sakumoto, Y., Yamaguchi, T., Ohashi, M., and Saito, H. 1992. "High-temperature properties of fire-resistant steel for buildings." *ASCE Journal of Structural Engineering,* vol. 118, no. 1, 392–407.

Sivaselvan, M. V., and Reinhorn, A. M. 1999. "Hysteretic Models for Cyclic Behavior of Deteriorating Inelastic Structures," *Technical Report MCEER-99-0018.* Multidisciplinary Center for Earthquake Engineering Research, University at Buffalo, NY, 99p.

Song, J., and Der Kiureghian, A. 2006. "Generalized Bouc-Wen model for highly asymmetric hysteresis." *Journal of Engineering Mechanics, ASCE,* vol. 132, no. 6, 610–618.

Stephens, R. I., and Fuchs, H. O. 2001. *Metal Fatigue in Engineering.* New York: John Wiley and Sons,, 472p.,

Susanthaa, K. A. S., Aokia, T., Kumanob, T., and Yamamotoa, K. 2005. "Applicability of low-yield-strength steel for ductility improvement of steel bridge piers." *Engineering Structures,* vol. 27, 1064–1073.

Tide, R. H. R. 2000. "Evaluation of Steel Properties and Cracking in "k"-area of W shapes." *Engineering Structures,* vol. 22, no. 2, 128–134.

Timoshenko, S. P., and Goodier, J. N. 1934. *Theory of Elasticity.* New York: McGraw-Hill, 567pp.

Timoshenko, S. P. 1983. *History of Strength of Materials.* New York: Dover Publications.

Tseng, N. T., and Lee, G. C. 1983. "Simple Plasticity Model of Two-Surface Type," *Proceedings of ASCE,* vol. 109, no. EM3, 795–810.

Tuchman, J. L. 1986. "Cracks, Fractures Spur Study." *Engineering News Record,* August 21.

UFC. 2008. "UFC 3-340-02 Structures to Resist the Effects of Accidental Explosions," *Unified Facilities Criteria.* Department of Defense, United States, 1867 pp.

Van de Lindt, J. W., and Potts. A. 2008. "Shake Table Testing of a Superelastic Shape Memory Alloy Response Modification Device in a Wood Shearwall,"*ASCE Journal of Structural Engineering,* vol. 134, no. 8, 1343–1352.

Van Vlack, L. H. 1989. "Elements of Materials Science and Engineering." Addison-Wesley: Reading, MA:

Vian D., Bruneau, M., Tsai, K. C., and Lin, Y. C. 2009. "Special Perforated Steel Plate Shear Walls with Reduced Beam Section Anchor Beams I: Experimental Investigation." *ASCE Journal of Structural Engineering,* vol. 135, no. 3, 211–220.

Wen, Y.-K. 1976. Method for random vibration of hysteretic systems. *Journal of Engineering Mechanics* vol. 102, no. EM2, 249–263.

Wilson, A. 2006. "Advances in High Performance Steels for Highway Bridges," *National Steel Bridge Alliance White Paper,* Omaha, Nebraska, 9 pp.

Wilson, J. C., and Wesolowsky, M. J. 2005. "Shape Memory Alloys for Seismic Response Modification: A State-of-the-Art Review," *EERI Earthquake Spectra,* vol. 21, no. 2, 569–601.

Wikipedia contributors. 2009b. "Stress (mechanics)," *Wikipedia, The Free Encyclopedia,* http://en.wikipedia.org/w/index.php?title=Stress_(mechanics)&oldid=291524785 (accessed May 26, 2009).

Wikipedia contributors. 2009a. "Bubble rafts," *Wikipedia, The Free Encyclopedia,* http://en.wikipedia.org/w/index.php?title=Bubble_rafts&oldid=286258585 (accessed April 26, 2009).

Wright, W. 1996. "High Performance Steels for Highway Bridges," *Proceedings 4th National Workshop on Bridge Research in Progress.* Buffalo, NY, pp. 191–194.

Yamaguchi, T., Nakata, Y., Takeuchi, T., Ikebe, T., Nagao, T., Minami, A., and Suzuki, T. 1998. "Seismic Control Devices Using Low-Yield-Point SteeL" *Nippon Steel Technical Report No. 77,* Tokyo, pp. 65–72.

Youssef, M. A., Alam., M. S., and Nehdi, M. 2008. "Experimental Investigation on the Seismic Behavior of Beam-Column Joints Reinforced with Superelastic Shape Memory Alloys," *Journal of Earthquake Engineering,* vol. 12, 1205–1222.

Zahrai, Z. M., and Bruneau, M. 1998. "Seismic Evaluation and Retrofit of Slab-on-Girder Steel Highway Bridges." *Ottawa Carleton Earthquake Engineering Research Centre report OCEERC 98-20,* Ottawa, March 1998.

Zoruba, S., and Grubb, K. A. 2003. "Do you 992?" *Modern Steel Construction*, January 2003.

CHAPTER 3

Plastic Behavior at the Cross-Section Level

Once material properties have been obtained and an appropriate stress-strain analytical model has been formulated, plastic capacities can be calculated at the cross-section level. This is a crucial phase of plastic analysis. The level of sophistication embraced in the calculation of these capacities will have the foremost impact on the resulting member and structural plastic strengths. Because plastic analysis is generally used to compute ultimate structural capacities, erroneous and potentially dangerous conclusions can be reached if an overly simplistic cross-sectional model is used, thus luring the engineer into a false sense of security. Hence, it is worthwhile to review how various expressions can be derived for these cross-sectional properties.

3.1 Pure Flexural Yielding

The basic case of pure flexural yielding should be familiar to engineers who have used Limit States Design or Ultimate Strength Design. Nonetheless, it is reviewed here because it provides some of the building blocks necessary to understand the more complex models presented later in the chapter.

A number of simplifying assumptions are made to calculate the plastic moment capacity as follows:

- Plane sections remain plane; even though plastic deformations are typically larger than elastic deformations, their overall magnitudes are still sufficiently small to satisfy this condition.
- Structural members must be prismatic and have at least one axis of symmetry parallel to the direction of loading.
- Members are subjected to uniaxial bending under monotonically increasing loading (neutral axis perpendicular to axis of

symmetry). Note that biaxial bending will be considered in Section 3.7.

- Shearing deformations are negligible.
- Member instability (flange local buckling, web local buckling, lateral-torsional buckling) is avoided.
- Structural members must not be subjected to axial, torsional, or shear forces. This assumption obviously will be relaxed in the later sections of this chapter.

The elasto-perfectly plastic model is generally used to calculate plastic moment capacities and leads to acceptable results for most practical problems in structural engineering (ASCE 1971). It is therefore used in the following derivations. However, nothing precludes the consideration of more complex models (or a smaller number of fundamental assumptions for that matter) because the corresponding cross-sectional strengths and other relevant plastic properties could be determined from the same basic concepts presented in this book.

3.1.1 Doubly Symmetric Sections

Doubly symmetric sections constitute the simplest cross-sections for which analytical expressions of plastic strength can be developed, because their neutral axis will always be located at their geometric centroid. With an elasto-perfectly plastic material model, for a given cross-section, the stress diagrams can be constructed directly from the strain diagrams, as shown in Figure 3.1, for various levels of increasing strains on an arbitrary doubly symmetric structural shape. At any point along a given loading history (such as that shown in Figure 3.1), the cross-section curvature, ϕ, can be calculated by simple geometry, as:

$$\phi = \frac{\varepsilon_{max}}{(h/2)} \tag{3.1}$$

where ε_{max} is the maximum strain acting over the doubly symmetric cross-section of depth h. If at a given curvature the yield strain, ε_y, is located at a distance y^* from the neutral axis, then, as shown in Figure 3.1, by similar triangles:

$$\phi = \frac{\varepsilon_{max}}{(h/2)} = \frac{\varepsilon_y}{y^*} \qquad y^* = \left(\frac{h}{2}\right)\frac{\varepsilon_y}{\varepsilon_{max}} \tag{3.2}$$

Once y^* is known for a given curvature, it becomes a simple matter to compute the corresponding moment using simple mechanics of materials principles:

$$M = \int_{-h/2}^{h/2} \sigma y \, dA = \int_{-h/2}^{h/2} \sigma y \, b(y) \, dy \tag{3.3}$$

where b is the cross-sectional width, expressed as a function of y.

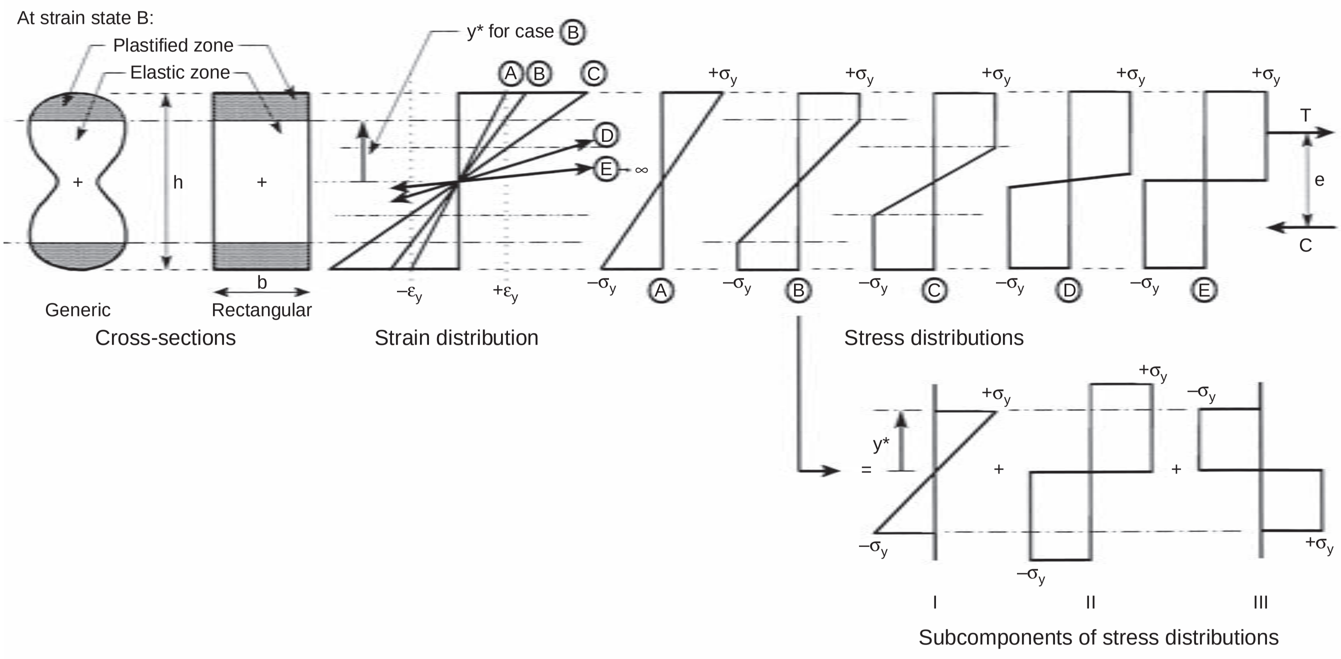

FIGURE 3.1 Strain and stress distributions in the plastic range for members of symmetric cross-section.

For any given curvature, the cross-section can be divided into elastic and plastic zones. Within $\pm y^*$ of the neutral axis, the section is elastic. Outside this zone, also termed the elastic core, strains exceed ε_y, and the material is plastified. As curvature increases, the elastic core progressively shrinks, and plastification progressively spreads over the entire cross-section.

The impact of this progressive growth of the plastified zone on the moment-curvature relationship is best understood from a case study. For simplicity, a rectangular cross-section is used. The calculations are directly related to the strain profiles identified in Figure 3.1, which use a rectangular section of height h and base b. For that example, in the elastic range, the flexural moment and curvature are given by:

$$M = S\sigma = \left(\frac{bh^2}{6}\right)\sigma \qquad \phi = \frac{M}{EI} = \left(\frac{12}{bh^3}\right)\frac{M}{E} \tag{3.4}$$

where S is the section modulus. For strain distribution A in Figure 3.1, the yield strain has just been reached at the top fiber of the cross-section. Replacing σ by σ_y in the above equation will give the yield moment, M_y, and the yield curvature, ϕ_y: the transition point between purely elastic and elasto-plastic behavior. From that point onward, any increase in curvature introduces partial plastification of the cross-section, a condition also sometimes called contained plastic flow. For example, for an arbitrary strain profile represented by B in Figure 3.1, the curvature is given by Eq. (3.1) above, and the corresponding moment can be expressed as a function of y^* as follows:

$$M = 2\int_0^{y^*} \sigma y b\,dy + 2\int_{y^*}^{h/2} \sigma_y y b\,dy \tag{3.5}$$

where the first term reflects the contribution of the elastic core to moment resistance, and the second term, that of the plastified zone. Using the relationship $\sigma/\sigma_y = \sigma_y y^*$ valid over the elastic core, Eq. (3.5) becomes:

$$M = \left[\frac{2b}{y^*}\int_0^{y^*} y^2 dy + 2b\int_{y^*}^{h/2} y\,dy\right]\sigma_y = \frac{2}{3}b(y^*)^2\sigma_y + \frac{bh^2}{4}\sigma_y - b(y^*)^2\sigma_y \tag{3.6}$$

Interestingly, the three terms on the right side of this equation correspond to the contributions to the moment that can be obtained by a piecewise decomposition of the stress diagram into the simpler subdiagrams I, II, and III, respectively, shown in Figure 3.1. Adding and subtracting stress diagrams in this manner is a statically correct procedure that can prove useful to simplify complicated problems or to graphically verify the adequacy of analytically derived results. For that matter, the integration approach [per Eqs. (3.5) and (3.6)] should be avoided whenever possible and only be used as a last resort, because integrating is more time consuming and error prone than working directly with stress diagrams to calculate the forces and lever arms acting on regularly shaped parts of cross-section. More importantly, the latter approach, based on physics rather than mathematics, is more conducive to sound engineering judgment.

To complete the above derivation, it is worthwhile to regroup the terms in $(y^*)^2$ and express the results in terms of curvature. Thus, when the following relationship is used (again, obtained through use of the properties of similar triangles):

$$\frac{y^*}{h/2} = \frac{\varepsilon_y}{\varepsilon_{max}} = \frac{\phi_y}{y}\frac{y}{\phi} = \frac{\phi_y}{\phi} \tag{3.7}$$

the expression for the flexural moment at a given magnitude of curvature (i.e., the moment-curvature relationship) becomes:

$$M = \left[\frac{bh^2}{4} - \frac{bh^2}{12}\left(\frac{\phi_y}{\phi}\right)^2\right]\sigma_y \tag{3.8}$$

Whenever possible, a solution expressed in a normalized manner, that is, in terms of both (M/M_y) and (ϕ/ϕ_y), should be sought. For example, when Eq. (3.4) is used to obtain an expression for the yield moment, the final result becomes:

$$\frac{M}{M_y} = \frac{3}{2}\left[1 - \frac{1}{3}\left(\frac{\phi_y}{\phi}\right)^2\right] = \frac{3}{2}\left[1 - \frac{1}{3}\left(\frac{\varepsilon_y}{\varepsilon_{max}}\right)^2\right] \tag{3.9}$$

The latter part of this equation, expressed in terms of the strain-ratio, is obtained if one takes advantage of the simple equivalence that exists between normalized curvatures and strains.

When Eqs. (3.4) and (3.9) are used over their respective range of validity, the entire moment-curvature relationship for this cross-section can be calculated and plotted. This has been done in Figure 3.2 for different sections. Figure 3.1 and Eq. (3.9) show that, theoretically, for any cross-section, full plastification and maximum flexural moment will be reached only at an infinite curvature (Case E in Figure 3.1). For the rectangular cross-section, this maximum moment is 1.5 times the yield moment, as can be easily deducted from Eq. (3.9). However, for practical purposes, as seen in Figure 3.2, this maximum moment is rapidly approached and nearly reached at only three or

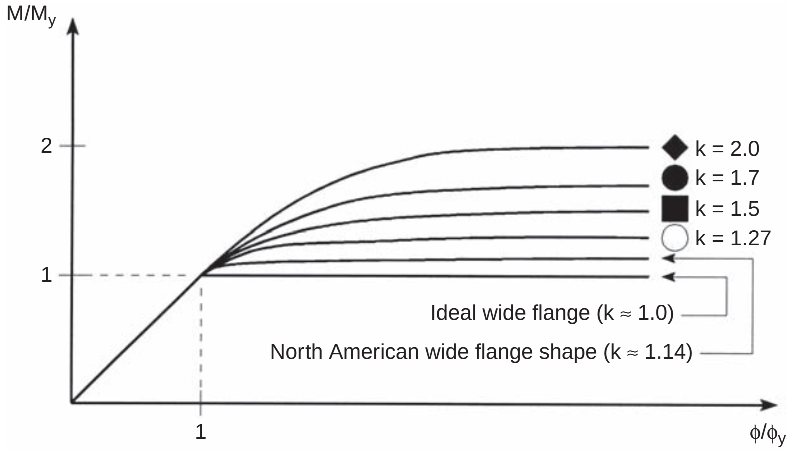

Figure 3.2 Normalized moment curvature relationship and flexural shape factor, *k*, for different cross-sections.

four times the yield curvature. In fact, when the maximum strain over the cross-section approaches the onset of strain hardening of the steel material, at approximately 10 times the yield strain value (as mentioned in the previous chapter), Eq. (3.9) indicates that 99.7% of the maximum moment has been reached. This demonstrates that a fully plastified cross-section can reliably be used to calculate the maximum moment, referred to hereafter as the "plastic moment."

For example, for the rectangular cross-section, one can calculate the plastic moment directly using the resulting forces and lever arms corresponding to the stress distribution E of Figure 3.1. This gives:

$$M_p = 2T\left(\frac{e}{2}\right) = 2\left[\sigma_y\left(\frac{h}{2}\right)b\right]\left(\frac{h}{4}\right) = \frac{bh^2}{4}\sigma_y = Z\sigma_y = 1.5M_y \tag{3.10}$$

where Z is the plastic section modulus, a geometrical property of any given cross-section. Incidentally, the above algebraic expression for Z of a rectangular section (i.e., $bh^2/4$) is used extensively when calculating the plastic moment for structural shapes built of rectangular parts, as will be seen later.

Another useful sectional property is given by the shape factor, k, which is the ratio between the plastic section modulus and the elastic section modulus. This factor, expressed by:

$$k = \frac{M_p}{M_y} = \frac{Z}{S} \tag{3.11}$$

provides information on the additional cross-sectional strength available beyond first yielding. The shape factors for various cross-sections are shown in Figure 3.2. For the wide-flange sections typically used in North American steel construction (AISC 2011, CISC 2010), the shape factors typically vary from 1.12 to 1.16, with an average of 1.14. Moreover, the following normalized moment curvature expressions could be derived:

1. When y^* is located in the flange:

$$\frac{M}{M_y} = \frac{\phi}{\phi_y}\left(1 - \frac{bd^2}{6S}\right) + \frac{bh^2}{4S}\left[1 - \frac{1}{3}\left(\frac{\phi}{\phi_y}\right)^2\right] \tag{3.12}$$

2. When y^* is located in the web:

$$\frac{M}{M_y} = \frac{M_p}{M_y} - \left(\frac{wd^2}{12S}\right)\left(\frac{\phi_y}{\phi}\right)^2 \tag{3.13}$$

where b is the flange width, d is the total depth of the structural section, h is the distance between flanges (or web length), w is the web thickness, and all other terms have been defined previously. In that case, M_p can be calculated from the individually calculated forces resulting from the constant yield stress acting on the flanges and web, and their respective lever arms, or by using Eq. (3.10) twice, to subtract the value of M_p for a rectangle of width $(b - w)$ and depth h from that for a rectangle of width b and depth d. In both hand calculation approaches, the area of the rounded corners where flanges connect to the web is usually neglected, but it is generally included in the sectional property values tabulated in design manuals.

Basic principles of mechanics of materials indicate that an ideal wide-flange section for flexural resistance would have all its material concentrated in flanges of infinitely small thicknesses (obviously an impractical theoretical case). The shape factor of such an ideal section would be unity, because the entire cross-section would reach the yield strain simultaneously, without any possible spread of plasticity given that no material would exist between these flanges. Hence, both the plastic and the elastic section moduli in that case would be equal to the area of one flange times the distance between the two flanges.

3.1.2 Sections Having a Single Axis of Symmetry

The procedure developed above is also applicable for sections having only a single axis of symmetry parallel to the applied load, with the essential difference that the location of the neutral axis must now be determined explicitly. Therefore, for any given curvature, the calculations must start by a determination of the neutral axis. There are two instances when this calculation is relatively simple. First, as long as the material is entirely linear-elastic, the location of the neutral axis remains located at the center of geometry of the cross-section. Second, when this same material is fully plastic, the neutral axis must be located such that it evenly divides the cross-sectional area. This latter case is simply a consequence of having the entire cross-section subjected to the yield stress, in either tension or compression. Summing the axial forces on the cross-section:

$$P = \int_{area} \sigma \, dA = A_{tension}\,\sigma_y + A_{compression}\,(-\sigma_y) = 0 \Rightarrow A_{tension} = A_{compression} \tag{3.14}$$

which defines the location of the neutral axis in the fully plastic condition. In the transition phase between the fully elastic and fully plastic conditions, where plastification progresses through the cross-section as the applied moment is increased, the neutral axis progressively migrates. This is schematically illustrated in Figure 3.3. For these intermediate cases, the development of analytical moment-curvature expressions, although possible, can be rather complex, except for the simplest cases.

Therefore, even though explicit moment-curvature relations can be derived, as done in Section 3.1.1, for many doubly or singly symmetric cross-sectional shapes, it is sometimes more convenient to simply calculate the moments corresponding to a large number of curvatures and fit the data using a Ramberg-Osgood or Menegotto-Pinto function. When using hand calculations, one can obtain each moment-curvature point by selecting a value for the strain at the top of the cross-section, arbitrarily choosing a location for the neutral axis, calculating the axial force resulting from that assumed strain diagram, and iterating by changing the position of that neutral axis until zero axial force is obtained. By repeating that process for various

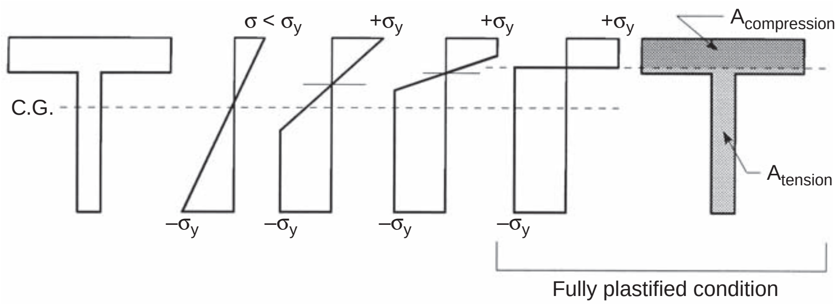

FIGURE 3.3 Migration of neutral axis in singly symmetric cross-section as applied moment increases during progressive plastification.

strain values, one can plot the moment-curvature relationship for a given cross-section. Following the same logic, moment-curvature points can be generated through the use of computer programs. The approximate moment-curvature relation obtained in that manner would still be sufficiently accurate to allow precise computation of member stiffnesses or deflections.

There exist numerous computer programs capable of developing moment-curvature relations for arbitrary cross-sections under uniaxial or biaxial bending, and these are often capable of considering axial and shear forces and other factors. Such programs can also easily be written because their structure is generally rather simple. For example, for an arbitrary section having a single axis of symmetry (parallel to the applied load) and subjected to uniaxial bending, it is sufficient to use a layered model of the cross-section. This consists simply of "slicing" the cross-section into a large number of layers, say 1000, and calculating and integrating the contributions of all layers to the flexural moment at a given curvature. To structure such a program, one could write subroutines to accomplish the following tasks:

- Perform an automatic layering of the cross-section (based on simple input of geometry characteristics).
- Initialize the stress values for all layers and establish other initial parameters.
- Set up controls for the iteration strategy.
- Increment the curvature for calculation of a given moment-curvature data point.
- Estimate the location of the neutral axis, adjusting this estimate in accordance with an iteration strategy (i.e., considering the results from previous iterations).
- For given curvature and neutral axis location, calculate strains for all layers.
- Calculate stresses for all layers per the assumed material model.
- Calculate the resulting moment by summing the contribution of all layers about the neutral axis.
- Calculate the resulting axial force on the cross-section by summing the contribution of all layers.
- Check for convergence using, for example, a user-specified tolerance on the axial force.
- Iterate until the axial force is equal to zero, within the specified tolerance. Convergence gives a single M and ϕ point and corresponding stresses at all layers of the cross-section (i.e., stress distribution). Repeat calculations at other curvatures to obtain the entire M-ϕ curve.

Note that any material model could be implemented in such a computer program, although the simple elasto-perfectly plastic model is frequently sufficient. Furthermore, the above algorithm can easily be modified to allow consideration of cyclic loading, biaxial bending, nonzero axial forces, residual stresses, and nonsymmetric cross-sectional shapes.

3.1.3 Impact of Some Factors on Inelastic Flexural Behavior

A large body of experimental research has confirmed that the plastic flexural moment can indeed be developed in beams. A summary of some of that earlier experimental work is presented in ASCE (1971). It is understood that, for this plastic moment to develop, the constraints set by the assumptions listed at the beginning of Section 3.1 must be respected. However, a few additional factors that may have an impact on this inelastic flexural behavior deserve the following brief review.

3.1.3.1 Variability in Material Properties

As the plastic moment directly depends on the yield stress of the steel, it is worthwhile to question what value can be reliably used for its calculation.

A potentially fatal mistake would consist of using the mill test certificate value. Steel mills typically perform a single coupon test per batch of steel produced (the size of a batch will vary depending on the mills, but typically consists of many tons of steel). This coupon is tested at strain rates that usually raise the yield strength by 30 MPa (4.4 ksi) or more and are intended only to provide confidence that the entire batch will meet the applicable specifications. Fluctuations in steel properties will exist within a given batch of steel produced from the same heat, and the mill test certificate can provide, at best, only one value for the entire tonnage of steel produced by that heat. Therefore, using the value reported on the mill test certificate is improper and fraught with danger; building failures have been documented wherein such a mistake has been identified as a major reason contributing to collapse (e.g., Closkey 1988).

For the design of new structures, the specified yield strength is the value that should be used. Engineers familiar with limit states design concepts [such as the Canadian Standards Association's Limit States Design (LSD), or the American Institute of Steel Construction's Load and Resistance Factor Design (LRFD), or others] appreciate the variability inherent in any engineering parameter, including material properties. These variabilities are generally included in the load and resistance factors.

However, when one is evaluating existing structures, it is important to appreciate the cross-sectional variability of yield strength. Extracting material from a steel member to obtain its yield stress using a standard coupon test (such as the standard ASTM E6 test) could give quite different results depending on whether the coupon is taken from the flanges or the web. Galambos and Ravindra (1976) reported that mean values of yield stress for coupons taken from flanges and webs were respectively 5% and 10% larger than the specified values, with coefficients of variation of 0.11 and 0.10, respectively. This is largely a consequence of the different treatment the web and flanges receive during the rolling process: thicker plates and members are less worked and cool more slowly, resulting in a slightly different grain structure of the metal and weaker strength properties. Likewise, variations exist depending on the thickness of the rolled shapes. In fact, special alloys are added to very thick steel section (such as W-shapes formerly known as “jumbo sections,” or AISC Group 4 and 5 shapes, before 2005) to provide the same yield strength as thinner sections for a given metallurgical composition. For some types of steels, when mills do not modify the chemical composition of the steel to compensate for this loss of strength, lower specified yield strengths are provided for use in design (e.g., CISC 2010).

3.1.3.2 Residual Stresses

Contrary to what is commonly assumed in design, a steel member is not stress-free prior to the application of external loads. In fact, large internal stresses exist there in a state of self-equilibrium. These are generally “locked in” during the rolling process and are also affected by welding or any other heat-imparting or cold-working operations. To understand the origin of these residual stresses, one must visualize the cooling process of a rolled steel section, keeping in mind that the modulus of elasticity of steel at high temperatures is very low, and increases rapidly as the steel progressively cools down below 1000°F, and that steel (like other materials) shrinks as it cools.

Thus, when a rolled section is cooled by the surrounding air, the tips of the flanges that are surrounded by air on three sides cool and gain stiffness first. Shrinkage is essentially unrestrained by the adjacent softer steel. However, as cooling progresses along the flanges, the tips of the flanges that have already partly cooled and acquired some stiffness provide partial restraint against shrinkage of the adjacent flange material. Hence, the tip of the flange is placed in compression, and the adjacent cooling material, in tension. As cooling progresses further along the flanges, the process repeats itself, and all previously partly cooled and stiffer material is compressed by the adjacent material that is beginning to cool. Consequently, the tips of the flanges that have cooled first will be the most compressed, and the flange-web core material, which is surrounded on all sides by steel and cools the slowest, will be subjected to the largest internal tensile stresses.

Members that can cool rapidly, such as thin steel plates, will be subjected to the largest magnitude of residual stresses, with values occasionally reaching up to the yield stress. However, in most rolled steel sections, the maximum residual stresses are approximately 33% of the yield stress.

The same logic also illustrates how welding introduces residual stresses. As welding is accomplished, the cooling and shrinking of both the weld metal and the steel in the heat-affected zone is restrained by the adjacent steel material. Therefore, following welding, the welds will be in tension. The existing residual stress pattern in the base metal is also locally affected by the welding operations.

A schematic representation of these self-equilibrating residual stresses is shown in Figure 3.4, using linear variations of stresses along the flanges and web. For comparison, an actual residual stress distribution in a steel section is illustrated in Figure 3.5. These internal stresses are in self-equilibrium because the integral of their effects produce no resulting axial force or moment on the cross-section.

Although residual stresses can be large, they have no impact on the plastic moment of a cross-section. For example, consider the section of Figure 3.4 for which residual stresses are assumed to be of a magnitude equal to half the yield stress. When that section is subjected to pure axial loading in compression, the tips of the flanges will reach their yield stress at only half the applied axial load that would produce full yielding of the cross-section if there were no residual stresses. From that point onward, plastification will start spreading over the cross-section. Essentially, because every individual point along the cross-section starts from a different initial stress,

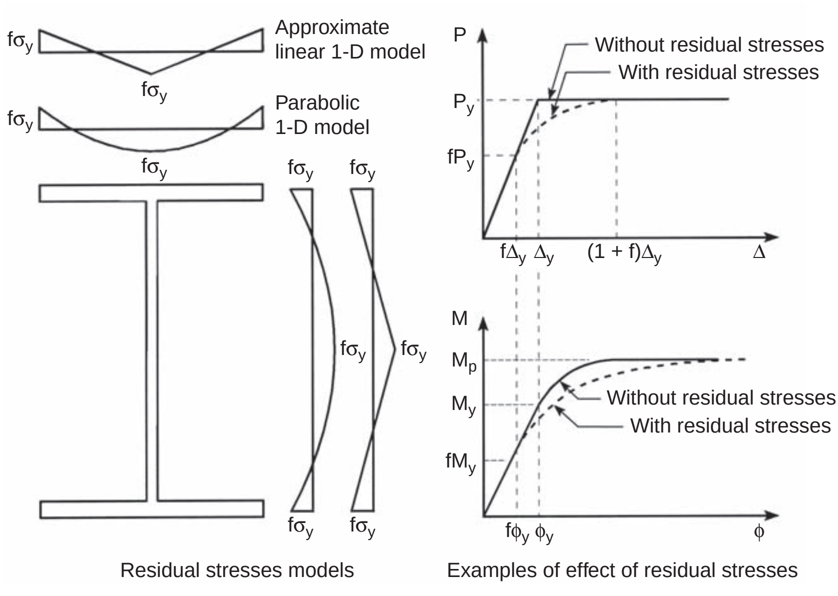

FIGURE 3.4 Schematic representation of self-equilibrating residual stresses in wide-flange structural shape.

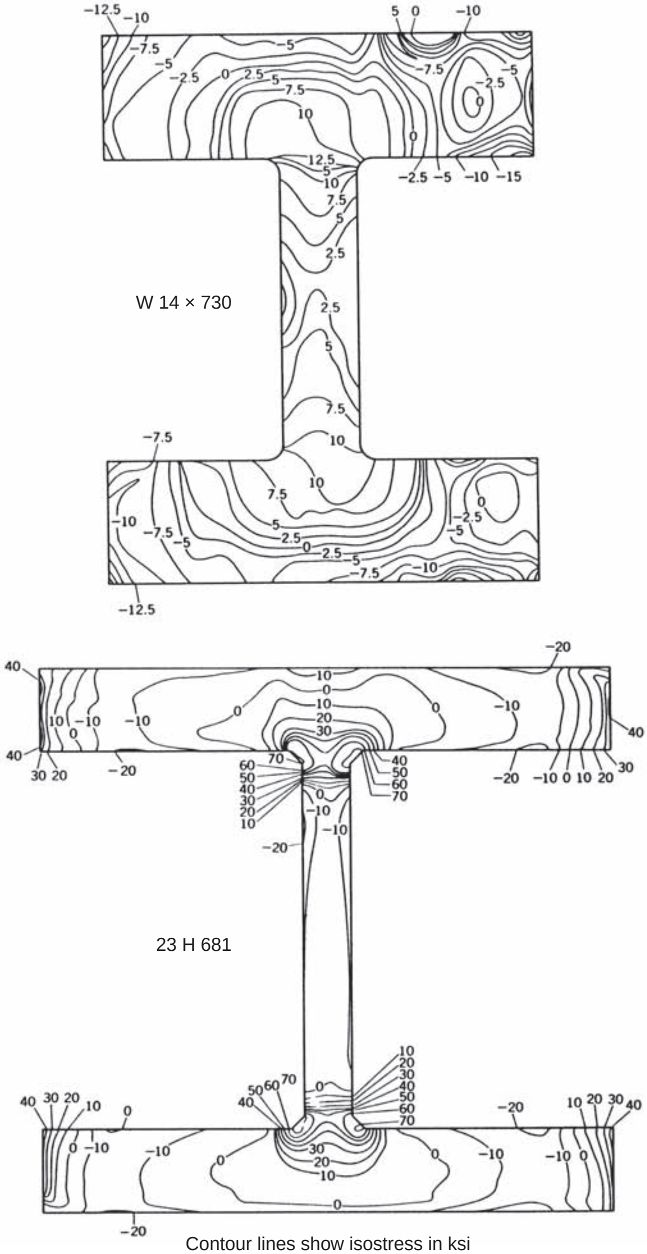

Figure 3.5 Two-dimensional distribution of residual stresses in rolled and welded wide-flange structural shapes. (*From L. Tall,* Structural Steel Design, *2nd ed., 1974.*)

it must be subjected to a different magnitude of strain prior to reaching the yield stress. Eventually, the flange-web core zones will be the last points to yield, when the applied strain will be 50% larger than would have otherwise been necessary to plastify a section free of residual stresses. Indeed, a force-elongation diagram similar to that shown in Figure 3.4 is usually obtained when one tests full cross-section stub-column specimens in axial compression (or tension) instead of standard material coupons.

If the same cross-section were subjected to flexure instead of axial force, it would start yielding at a moment equal to half of M_y, with plasticity spreading from the tips of the flanges inward for the flange in compression, and from the flange-core outward for the flange in tension, as the respective flanges would be subjected to larger compression and tension as the flexural moment increased. However, the plasticity moment would be unchanged and remain M_p. This is demonstrated in more detail in the example below.

Although residual stresses do not impact the strength of members, the accelerated softening of the axial force versus axial deformation or moment versus curvature curves, as well as the earlier initiation of the yielding process, will have an impact on members' deflections and buckling resistances. Incidentally, the analytical expressions included in steel-design codes and standards to calculate the stability and strength of structural members (such as for columns in compression) already take this into account.

3.1.3.3 Example: Ideal Wide-Flange Section with Residual Stresses

An "ideal" wide-flange section for flexural resistance has flanges of negligible thickness and area A_f, a height d, and negligible web area (Figure 3.6). The shape factor for this section is 1.0, and $M_p = dA_f\sigma_y$. It is assumed that the initial residual stresses introduced by the rolling process (thus prior to the application of any external loads) have a peak value of $0.75\sigma_y$ (in compression) at the tips of the flanges and $0.75\sigma_y$ (in tension) at the intersection with the web and that they vary linearly in between. The material is assumed to be elasto-perfectly plastic.

The M-ϕ curves for the initially stress-free case, and for the case having residual stresses, are to be drawn. For this purpose, although accurate analytical expressions could be derived, for simplicity here, the solution will proceed by calculating representative points to accurately plot these curves.

Using the principle of stress superposition, and the knowledge that, at any point, the newly applied stresses and strains are related as per the elasto-perfectly plastic model, one can construct Figure 3.6. In the resulting moment-curvature plot in this figure, the dashed line is obtained when one considers the cross-section free of residual stresses, using ϕ_y and ε_y corresponding, respectively, to the curvature and maximum strain at the onset of yielding M_y (which happens to be

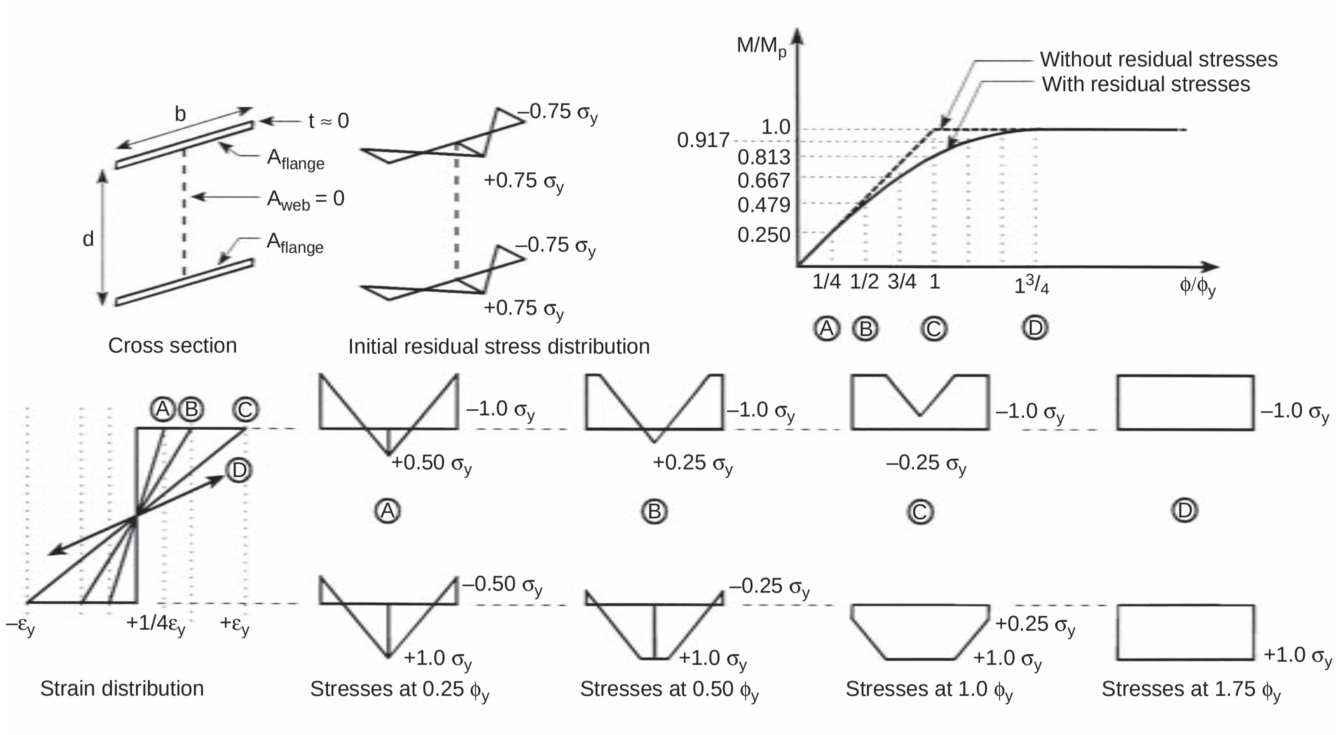

FIGURE 3.6 Plastic flexural behavior of ideal structural shape with residual stresses.

equal to M_p in this example). The resulting M-ϕ curve is bilinear for this ideal cross-section having a shape factor of unity.

More interesting, however, is the calculation of the M-ϕ curve for the case having residual stresses. Stage A identifies the end of the elastic range, because the application of strains equal to $\varepsilon_y/4$ will uniformly add a stress of $\sigma_y/4$ to the flanges and bring to yield the points for which the magnitude of residual stresses was $0.75\sigma_y$. Values of moments and curvature at multiples of this curvature are calculated. The resulting strains, stresses, and M-ϕ (solid line) are shown in Figure 3.6. As an example of an intermediate calculation, for stage C, when the curvature is ϕ, the corresponding moment calculated from the stress diagram is:

$$M_{stage-C} = 2\left[2\left(\frac{Af}{4}\sigma_y + \frac{1}{2}\left(\frac{\sigma_y}{4} + \sigma_y\right)\frac{Af}{4}\right)\frac{d}{2}\right] = 0.8125\ A_f d\sigma_y = 0.8125\ M_p \tag{3.15}$$

3.1.3.4 Local Instabilities

Plastic curvature cannot increase indefinitely, and eventually local buckling, or lateral torsional buckling, will occur. The problem of member instability receives a comprehensive treatment in Chapter 14. However, at this point, it is important to realize that local buckling must eventually occur in any structural member compressed far into the plastic range (such as the flange of wide-flange beams commonly used in structures) as the strain-hardening tangent section modulus progressively decreases when plastic strains increase (as demonstrated in Chapter 2). More stringent width-thickness limits imposed by plastic design procedures simply delay local buckling to ensure the development of large plastic deformations within the limits expected in normal applications.

3.1.3.5 Strain Hardening

Models that neglect strain hardening, such as the elasto-perfectly plastic model, are effectively much simpler to use and particularly useful for hand calculation. Although the consideration of strain hardening is always possible, at the cost of additional computational efforts, it has been proven to be generally conservative to neglect the effect of strain hardening in beams subjected to moment gradient, as long as strength is the primary concern. The influence of strain hardening on plastic rotation calculations can be more significant. For the special case of beams subjected to uniform moments (in which plastification occurs simultaneously over the entire uniform moment region), the consideration of strain hardening would bring few benefits as local buckling typically promptly occurs at the onset of strain hardening in such beams.

3.1.4 Behavior During Cyclic Loading

A major application of plastic analysis concepts is found in the design of earthquake-resistant structures. Consequently, it is important to examine the effect of cyclic loading on a partly or fully plastified cross-section. The key to understanding the plastic behavior of a cross-section is to consider it as a series of layers of material. All layers of a cross-section must abide by the same material model rules, but each layer is strained differently, so its stress history will also differ. For example, in Figure 3.7, the points A to F are assigned to

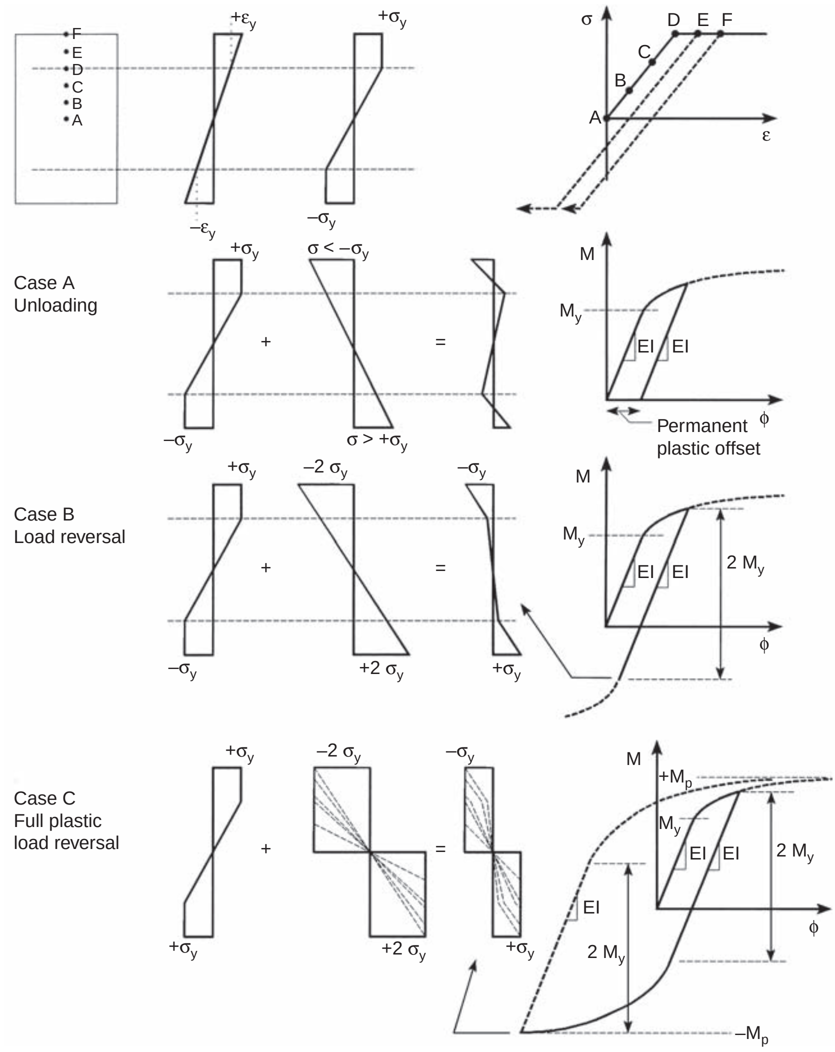

FIGURE 3.7 Example of cyclic cross-sectional plastic behavior.

various layers along the height of a rectangular cross-section that has been subjected to a moment larger than its yield moment, M_y, but less than its plastic moment, M_p. When the applied moment is removed, the cross-section is unloaded to its point of zero applied moment on the M-ϕ diagram, and all layers unload elastically according to the elasto-plastic element model. In fact, a layer will always unload elastically as long as its stress doesn't reach the opposite yield level of $-\sigma_y$. Therefore, one must first try to remove the applied moment elastically, as shown in Case A of Figure 3.7.

If none of the stresses in the resulting stress diagram exceed the yield stress, the solution is deemed acceptable. Note that although the externally applied load has been removed, an internal residual-stress diagram in self-equilibrium has been created. Moreover, as can be seen from the M-ϕ diagram, a residual curvature remains. One can obtain the magnitude of this curvature by first calculating the maximum curvature that was reached during the initial loading phase [for the rectangular section used, Eq. (3.9) derived previously can be used for this purpose] and subtracting from this value the curvature that would correspond to the removal of this moment, assuming elastic response [using Eq. (3.4), that is, $\phi = M/EI$]. Because the two values are quite different, a residual curvature must remain.

Following the above logic, one can observe, as in Case B of Figure 3.7, that for any cross-section that was first stressed above M_y, it is possible to remove elastically a moment as large as $2M_y$ without having any stresses exceed the yield value in the resulting stress diagram. In fact, the section can be subjected to reversed loading histories within this range of $2M_y$ without producing any new plastification. This is equivalent to having a new elastic range shifted upward by the difference between M and M_y. However, as soon as loading exceeds these bounds, new yielding occurs, and the stress-strain history of each layer must be followed to determine the actual stress distribution throughout the cross-section. To determine this stress profile, the procedure followed in the example on residual stresses in the previous section can be used, but one must account for the offset produced by the residual curvature at zero moment. A maximum moment of $-M_p$ will eventually be reached, as shown in Case C of Figure 3.7. The procedure can be repeated by reversing the loading and cycling repeatedly, thus producing M-ϕ hysteretic curves.

Generally, the ductile behavior of steel members will develop until a local instability occurs, because of either excessive straining under noncyclic loading or fracture under alternating plasticity (e.g., low-cycle fatigue under cyclic inelastic loading), as discussed in the previous chapter.

3.2 Combined Flexural and Axial Loading

In Section 3.1, it was assumed that no externally applied axial load acted on the cross-section. However, in many instances this will not be the case, and it is necessary to investigate how the plastic moment is affected by the presence of axial force. The same fundamental concepts and modeling previously presented still apply: strains linearly distributed across the member's cross-section are related to stresses using an elasto-plastic model, and the moments and axial forces are obtained by integrating the stresses acting on the cross-section (or, more simply, using the stress-resultant forces). Figure 3.8 illustrates how the stress diagram changes as the applied moment is progressively increased for a given axial force.

Calculation of the reduced plastic moment, M_{pr}, in the fully plastified state for a given axial load, P, is a straightforward operation. Directly, equilibrium of the horizontal forces acting on the cross-section gives:

$$P = C - T = A_{compression}\ \sigma_y - A_{tension}\ \sigma_y = (A_{compression} - A_{tension})\sigma_y \qquad (3.16)$$

Given that the sum of $A_{compression}$ and $A_{tension}$ must equal the total cross-sectional area, A, one can directly solve for the location of the neutral axis; the stress-resultant forces, C and T; and the corresponding reduced plastic moment, M_{pr}. By repeating the process for axial forces varying from zero to the axial plastic load ($= A\sigma_y$), one can plot an interaction diagram for a given cross-section. Alternatively, for the simplest cross-sections, closed-form solutions may be developed.

Some of these closed-form solutions are provided here, taking advantage of the fact that the fully plastified stress diagram for combined flexural-axial response can be divided into a pure moment contribution and a pure axial contribution, as shown in Figure 3.9. For convenience, that figure is developed using the same arbitrary neutral axis location for various cross-sections; the implication is that, for this generic state of full plasticity, different corresponding axial loads and moments would be obtained for each cross-section. The basic principle, nonetheless, remains the same: when a location for the neutral axis is assumed, expressions for the corresponding applied axial force and reduced plastic moment can be developed, which are valid over all or some depths of the cross-section. Through algebraic manipulations, it is possible to develop equations for interaction diagrams that express the applied axial force as a function of the reduced plastic moment, although this sometimes proves to be a tedious process.

These equations are developed hereunder for some simple doubly symmetric sections, for a neutral axis generically located at a distance y_o above the geometric center of these sections.

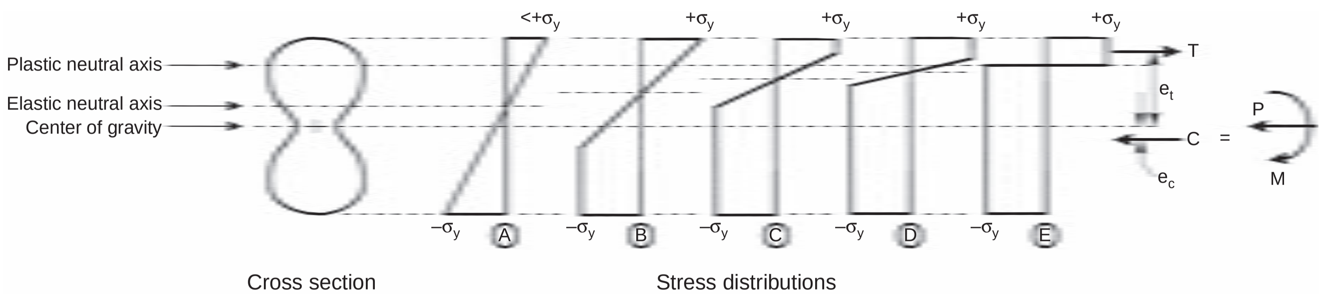

FIGURE 3.8 Stress diagrams as plasticity progresses in a cross-section subjected to combined flexural and axial loading.

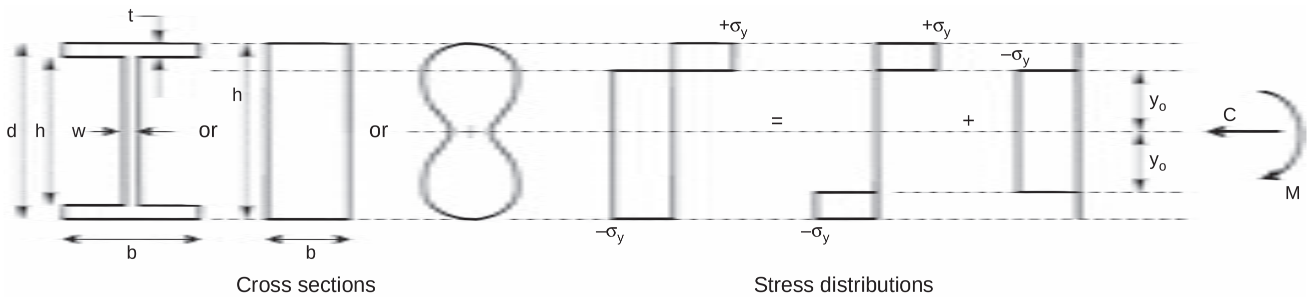

FIGURE 3.9 Fully plastified condition for an arbitrary location of neutral axis (corresponds to different set of *P* and *M* for the different cross-sections shown).

3.2.1 Rectangular Cross-Section

If one divides the stress diagram of Figure 3.9 into pure flexural and axial contributions, the resulting axial force is:

$$\left[\frac{P}{P_y}\right] = \left[\frac{(P = 2by_o\sigma_y)}{(P_y = hb\sigma_y)}\right] = \frac{2y_o}{h} \tag{3.17}$$

where P_y is the capacity of the cross-section fully plastified axially, and all geometric parameters are defined in Figure 3.9.

The expression for the reduced plastic moment can be developed if one subtracts the plastic moment of a section of depth $2y_o$ (i.e., that portion of the cross-section assumed to resist the axial load, P) from the plastic moment (i.e., the flexural strength in absence of axial load), making it possible to obtain:

$$M_{pr} = Z\sigma_y - Z_{y_o}\sigma_y = \left[\left(\frac{bh^2}{4}\right) - \left(\frac{b(2y_o)^2}{4}\right)\right]\sigma_y = \frac{b(h^2 - 4y_o^2)}{4}\sigma_y \tag{3.18}$$

In a normalized format, and substituting the result of Eq. (3.17):

$$\frac{M_{pr}}{M_p} = \frac{b\left(h^2 - 4y_o^2\right)\sigma_y}{4}\left(\frac{4}{bh^2\sigma_y}\right) = 1 - \frac{4y_o^2}{h^2} = 1 - \left(\frac{P}{P_y}\right)^2 \tag{3.19}$$

The resulting interaction diagram is plotted in Figure 3.10. Note that, for a rectangular cross-section, a significant difference exists between the elastic interaction curve for which no strain is allowed to exceed the yield strain, and the plastic interaction curve derived above.

3.2.2 Wide-Flange Sections: Strong-Axis Bending

For wide-flange sections (i.e., those having constant flange thickness), the closed-form solution will vary depending on whether the neutral axis falls in the web ($y_o \leq h/2$) or the flange ($h/2 < y_o \leq d/2$). For the former case:

$$\left[\frac{P}{P_y}\right] = \left[\frac{(P = 2y_o w\sigma_y)}{(P_y = A\sigma_y)}\right] = \frac{2wy_o}{A} \leq \frac{A_w}{A} \tag{3.20}$$

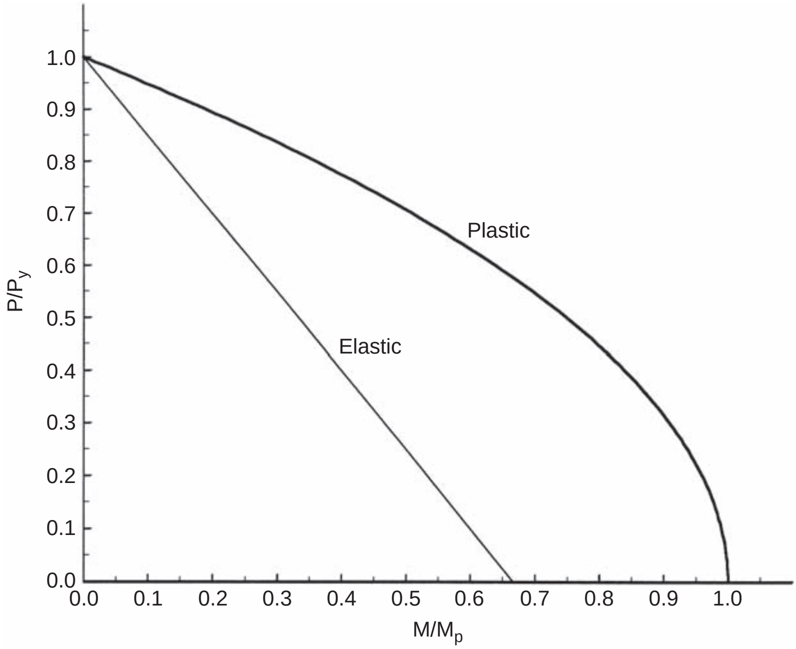

FIGURE 3.10 Elastic and plastic *M-P* normalized interaction diagram for a rectangular cross-section.

where A is the total cross-sectional area (= $2bt + wh$), A_w is the web area (= wh), and:

$$M_{pr} = Z\sigma_y - Z_{y_o}\sigma_y = \left[Z - \left(\frac{w(2y_o)^2}{4}\right)\right]\sigma_y = (Z - wy_o^2)\sigma_y \tag{3.21}$$

Then, to obtain a normalized *M-P* interaction curve, divide the above equation by M_p and substitute the result of Eq. (3.20):

$$\frac{M_{pr}}{M_p} = 1 - \left(\frac{Z_{y_o}}{Z}\right) = 1 - \left(\frac{wy_o^2}{Z}\right) = 1 - \left(\frac{P}{P_y}\right)^2 \frac{A^2}{4wZ} \text{ for } \frac{P}{P_y} \le \frac{A_w}{A} \tag{3.22}$$

When the neutral axis falls in the flange, the following expression is obtained using a similar procedure:

$$\frac{M_{pr}}{M_p} = A\left(1 - \frac{P}{P_y}\right)\left[d - \frac{A}{2b}\left(1 - \frac{P}{P_y}\right)\right]\left(\frac{1}{2Z}\right) \text{ for } \frac{P}{P_y} > \frac{A_w}{A} \tag{3.23}$$

Note that, until the axial force exceeds 30% of the axial plastic value, the reduction in moment capacity is typically less than 10% for these structural shapes. For most commonly available wide-flange sections, the normalized *M-P* interaction curve is a function of the ratio of the web area to total cross-sectional area (which can be alternatively expressed as the web area to sum of the flange areas, or many other variations). This could be demonstrated, as an example, by expansion of the non-normalized term of Eq. (3.22) as follows:

$$\begin{aligned}\frac{A^2}{4wZ_y} &= \frac{A^2}{4w\left(\dfrac{wh^2}{4}+\dfrac{A_f(d-t)}{2}\right)}\\ &= \frac{A^2}{A_w^2+2A_f(A_w+tw)}\\ &= \frac{1}{\left(\dfrac{A_w}{A}\right)^2+\left(\dfrac{2A_fA_w}{A^2}\right)+\left(\dfrac{2A_ftw}{A^2}\right)}\end{aligned} \tag{3.24}$$

where A_f is the total flange area (i.e., sum of the areas of both flanges). Simple observation, or trial calculation, reveals the very small significance of the third denominator term on the resulting normalized *M-P* interaction curve. This term is the only nonconstant value for a given ratio of web-to-flange area. As a result, normalized interaction curves can be conveniently expressed as a function of the flange-to-web area ratio, as shown in Figure 3.11a.

It can be observed from Figure 3.11a that the normalized *M-P* interaction curves of wide-flange sections that have the lowest ratio of flange-to-web areas are closest to the curve obtained previously for the rectangular cross-section, as is logically expected. Although this observation is useful to demonstrate the relative physical behavior of various cross-sections, it should be remembered that steel rectangular shapes inefficiently use material and are not desirable, in spite of their more extensive plastic range. Finally, note that wide-flange sections are usually rolled with a relatively constant ratio of flange-to-web area, normally between 2 and 3, approximately corresponding to the shaded area in Figure 3.11a. This has made possible the development of a convenient and reliable *M-P* design interaction curve for the plastic strength of wide-flange cross-sections in strong-axis bending, as shown in Figure 3.11b, and expressed by:

$$\frac{M}{M_p} = 1.18\left(1-\frac{P}{P_y}\right) \le 1.0 \tag{3.25}$$

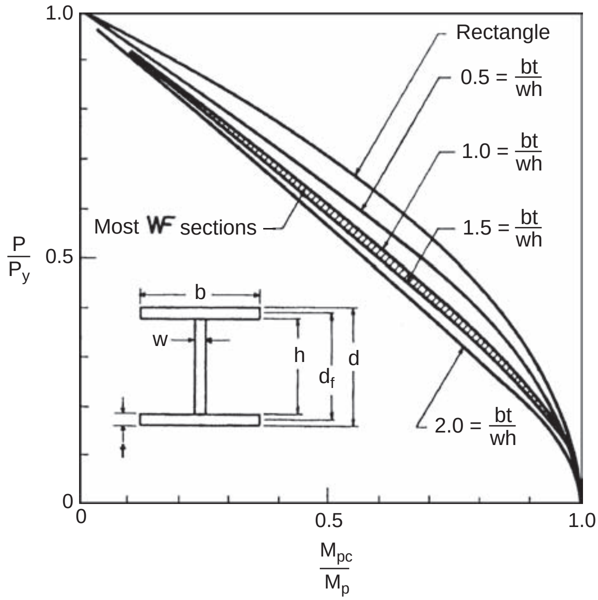

(a)

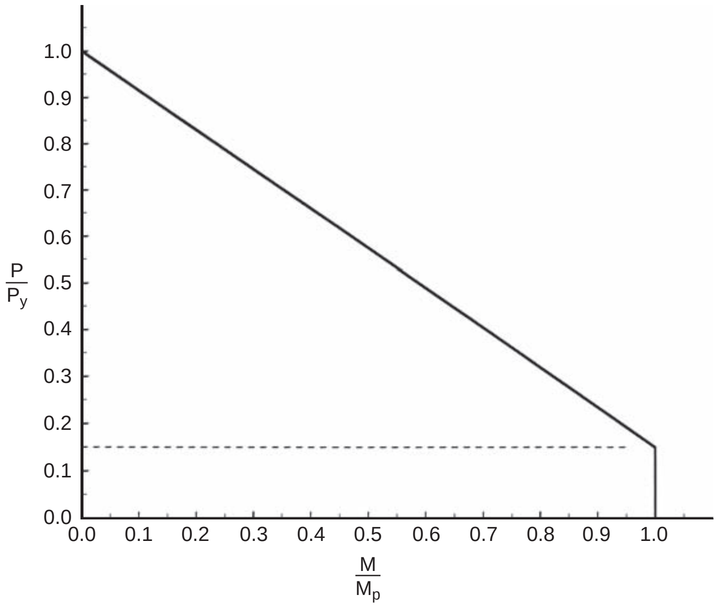

(b)

FIGURE 3.11 Plastic *M-P* normalized interaction diagrams: (a) for wide-flange structural shape, strong-axis bending; (b) simplified design interaction curve for wide-flange structural shape, strong-axis bending; (c) for wide-flange structural shape, weak-axis bending. (*Figures a and c reprinted from ASCE Manual #41:* Plastic Design in Steel: A Guide and Commentary, *2nd ed., with permission of American Society of Civil Engineers.*)

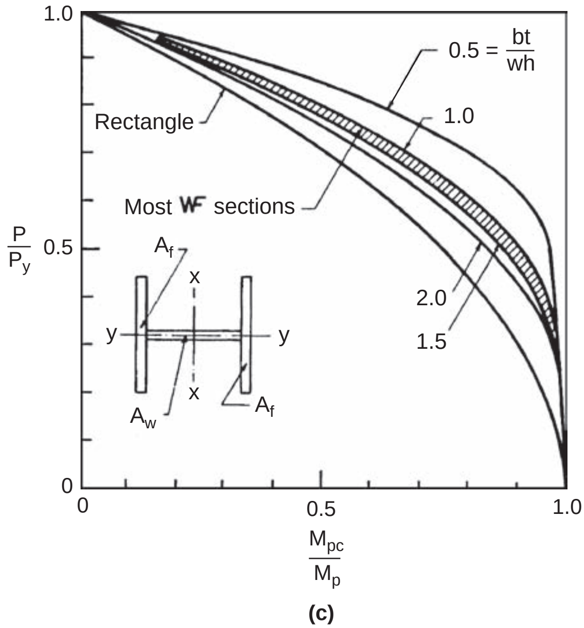

FIGURE 3.11 (*Continued*)

3.2.3 Wide-Flange Sections: Weak-Axis Bending

Normalized *M-P* interaction equations can be obtained for wide-flange sections in weak-axis bending following an approach similar to that presented above for strong-axis bending. Two cases must be considered, depending on whether the neutral axis falls in the web ($y_o \le w/2$) or outside the web ($w/2 < y_o \le b/2$). For the former:

$$\frac{M_{pr}}{M_p} = 1 - \left(\frac{P}{P_y}\right)^2 \frac{A^2}{4dZ_y} \quad \text{for} \quad \frac{P}{P_y} \le \frac{wd}{A} \tag{3.26}$$

whereas, for the latter case:

$$\frac{M_{pr}}{M_p} = \left[\frac{4bt}{A} - \left(1 - \frac{P}{P_y}\right)\right]\left(1 - \frac{P}{P_y}\right)\left(\frac{A^2}{8tZ_y}\right) \quad \text{for} \quad \frac{P}{P_y} > \frac{wd}{A} \tag{3.27}$$

Again, for most commonly available wide-flange sections, the normalized *M-P* interaction curve is a function of the ratio of the flange area to the web area. Normalized interaction curves expressed as a function of that ratio are shown in Figure 3.11c. This time, because a wide-flange shape in weak-axis bending is simply two rectangular cross-sections joined at their centroids by a thin member, the wide-flange sections that have the largest ratio of flange-to-web areas will have the interaction curves closest to those for a rectangular cross-section, as can be observed from Figure 3.11c. Again, the relatively narrow shaded area in that figure represents the range of flange-to-web area ratios corresponding to most wide-flange sections rolled today. Based on this observation, the following design interaction curve expression for the plastic strength of wide-flange cross-sections in weak-axis bending has been proposed:

$$\frac{M}{M_p} = 1.19\left[1 - \left(\frac{P}{P_y}\right)^2\right] \leq 1.0 \tag{3.28}$$

In some instances, however, simpler but more conservative equations have also been used in some design codes (e.g., CSA 2009).

3.2.4 Moment-Curvature Relationships

If the complete moment-curvature relationship for a given axial load and cross-section is desired, the use of numerical techniques is recommended, even though some closed-form solutions can be developed for the simplest cross-sections. In fact, to account for combined flexural and axial loading, only minor changes are necessary to the moment-curvature algorithm described in the previous section.

3.3 Combined Flexural and Shear Loading

The interaction between axial force and moment could easily be considered in the previous section because they both produce axial strains in a structural member. However, before one can consider the combined effect of flexural and shear loading on the plastic moment of a cross-section, the interaction between axial and shear stresses when yielding is reached must first be described. Based on experimental observations, two mechanics-of-materials rules have been formulated to describe this fundamental material behavior: the Tresca and the Von Mises yield conditions (Popov 1968). The latter has been most widely used to describe aspects of the behavior of steel structures. The Von Mises criterion can be expressed as follows:

$$\sigma^2 + 3\tau^2 = \sigma_y^2 \tag{3.29}$$

where σ is the axial stress, τ is the shear stress, and σ_y is the yield stress in uniaxial tension.

According to that criterion: (1) no shear stress, τ, can be applied when the axial stresses reach yield, and (2) in absence of axial stresses, the yielding shear stress, τ_y, is equal to $0.577\sigma_y$. Such a model neglects strain hardening, which is conservative and consistent with what has been done so far, although it is well known that a dependable and slightly higher shear stress can usually easily be reached because of strain hardening. With this criterion as a starting point, many models have been proposed to determine the plastic moment as reduced by the presence of shear forces. The solutions presented here are essentially those based on equilibrium considerations; such solutions are generally lower-bound solutions and conservative, as shown in Chapter 4.

For the rectangular cross-section used here to demonstrate flexure-shear interaction, a distribution of axial and shear stresses that respect the above Von Mises yield criterion is shown in Figure 3.12. The distribution of shear stresses is obtained considering only the remaining (nonyielded) elastic core and knowledge that shear stresses vary parabolically along a rectangular cross-section. Thus, with the knowledge that the maximum shear stress on a rectangular cross-section is 50% larger than the average shear stress, and through use of the Von Mises yield criterion, the depth of the elastic core, $2y_y$, required to resist the shear force, V, can be calculated as:

$$\tau_y = \frac{1.5\ V}{A_{effective}} = \frac{1.5\ V}{2y_y b} = \frac{\sigma_y}{\sqrt{3}} = 0.577\sigma_y \text{ thus } y_y = \frac{1.3\ V}{b\sigma_y} \tag{3.30}$$

The resulting axial stress diagram, elastic within $\pm y_y$ from the neutral axis and plastic beyond that value, is used to calculate the reduced plastic moment capacity. Using the principle of stress superposition demonstrated earlier, and the procedure demonstrated in Figure 3.12, one obtains the following formula for the plastic moment reduced by shear, M_{prs}:

$$\frac{M_{prs}}{M_p} = \frac{M_p - 2\left[\left(\frac{by_y}{2}\right)\left(\frac{y_y}{3}\right)\right]\sigma_y}{\left(\frac{bd^2}{4}\right)\sigma_y} = 1 - \frac{4}{3}\left(\frac{y_y}{d}\right)^2 = 1 - \frac{3}{4}\left(\frac{V}{V_p}\right)^2 \text{ for } \left(\frac{V}{V_p}\right) \le \frac{2}{3} \tag{3.31}$$

where the last equality in the above equation is obtained through substituting the value of y_y defined in the previous equation and by defining V_p as the shear corresponding to the fully plastified section under pure shear (a purely theoretical quantity because this would violate the important condition that shear stresses must become zero at the top and bottom of the cross-section). For the rectangular cross-section, V_p is equal to $bd\tau_y$. The limit of applicability of the above equation is simply a result of the parabolic shear stress

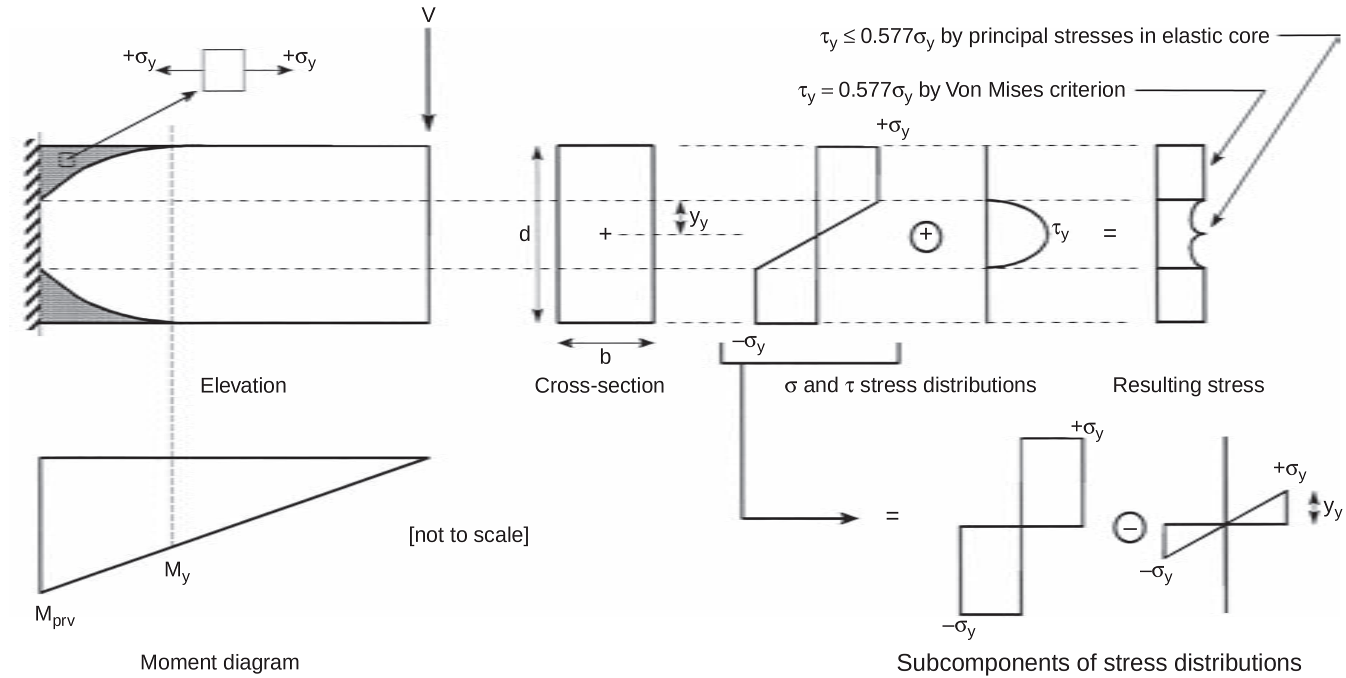

Figure 3.12 Axial and shear stress distribution on rectangular cross-section in plastic range.

distribution assumed; in other words, the maximum shear stress is limited to 1.5 times the maximum average stress that can act on the cross-section in the absence of axial yield stresses; that is, $\tau_y = 1.5\ \tau_{average} = 1.5\ V_{max}/bd$.

Given that axial stresses and shear stresses vary linearly and parabolically, respectively, over the $\pm\ y_y$ region, the following Mohr's circle expression can be used to calculate the principal shear stresses at any point in that region:

$$\tau_{max} = \sqrt{\left(\frac{\sigma_y}{2}\right)^2 + \tau^2} = \sqrt{\left(\frac{\sigma_y y}{2y_y}\right)^2 + \left[\frac{\sigma_y}{\sqrt{3}}\left(1-\left(\frac{y}{y_y}\right)^2\right)\right]^2}$$
$$= \sigma_y\sqrt{\frac{1}{3} - \frac{5}{12}\left(\frac{y}{y_y}\right)^2 + \frac{1}{3}\left(\frac{y}{y_y}\right)^4} \tag{3.32}$$

This equation demonstrates that a principal shear stress of τ_y is reached only at $y = 0$, and at $\pm\ y_y$, and is not exceeded anywhere in between because $(5/12)(y/y_y)^2$ is always greater than $(1/3)(y/y_y)^4$ in the region of interest (i.e., $y \le y_y$). Also, calculating the minimum shear stress in that region by making the first derivative of the above equation equal to zero gives a value of approximately 80% of τ_y; this illustrates how effectively the section is utilized. As for the part of the cross-section yielded under axial strains, σ_y, no shear forces can be applied per the Von Mises criterion, but for the sake of completing the principal stresses diagram, σ_y can be expressed as equivalent to $\sqrt{3\tau_y}$, or alternatively, $\tau_y = \sigma_y/\sqrt{3}$.

Although the same procedure could be followed to calculate the reduced moment capacity of wide-flange shapes commonly used in practice, a more expedient approach exists to provide a reliable estimate of this value. This alternative procedure is illustrated in Figure 3.13. First, a uniform shear stress is assumed to act on the web as a result of the applied shear force and is calculated as follows:

$$\tau_w = \frac{V}{hw} \tag{3.33}$$

Then, the Von Mises yield condition is used to calculate the maximum axial stress that can be applied on the web (i.e., remaining axial stress capacity available):

$$\sigma_w = \sqrt{\left(\sigma_y^2 - 3\tau_w^2\right)} = \sigma_y\sqrt{\left[1-\left(\frac{\tau_w}{\tau_y}\right)^2\right]} \tag{3.34}$$

The maximum axial stress that can be applied to the flange remains σ_y. Then, one can determine the reduced plastic moment

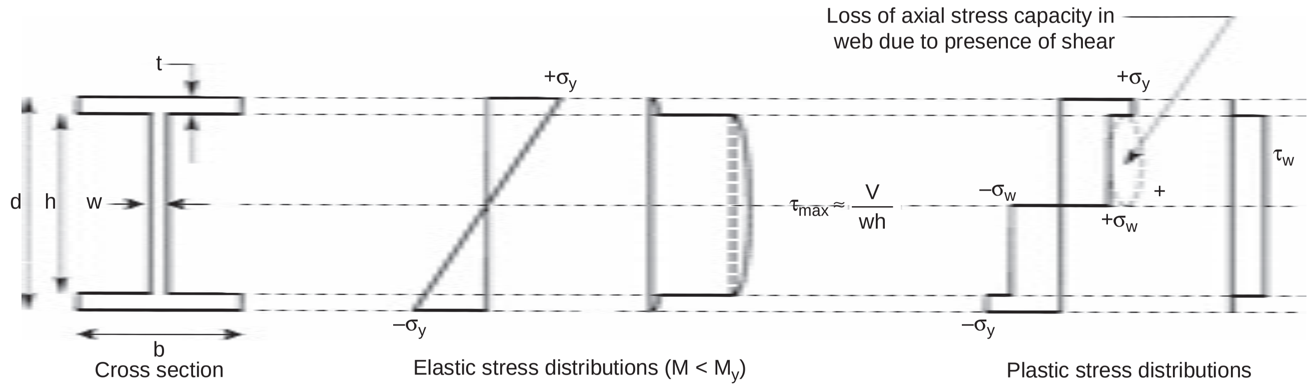

Figure 3.13 Elastic and plastic stress distributions in wide-flange structural shape subjected to shear and flexure.

directly from the resulting axial stress diagram, again using the principle of superposition of stress diagrams to simplify calculations. It is equal to:

$$M_{prv} = M_p - M_{loss} = Z_{prv}\,\sigma_y$$

where

$$M_{loss} = \frac{h^2 w}{4}(\sigma_y - \sigma_w) = \frac{h^2 w}{4}\left[1 - \sqrt{1 - \left(\frac{\tau_w}{\tau_y}\right)^2}\,\right]\sigma_y = Z_{loss}\sigma_y \qquad (3.35)$$

and where Z_{prv} is defined as the plastic section modulus reduced by the presence of shear. This procedure is valid only for shear forces smaller than or equal to what would produce shear yielding of the entire web. Furthermore, this procedure cannot be extended to other cross-sections, unless these also have webs similarly capable of resisting the bulk of the applied shear force in a condition of near uniform shear stresses. For example, for wide-flange shapes in weak-axis bending, the equations derived for the rectangular cross-section are actually more suitable.

Although many other expressions have been proposed in the available literature to describe flexure-shear plastic interaction, the above approaches are conservative and simple for hand calculations. Experiments have demonstrated that the reduction in plastic moment capacity is in fact less than predicted by the above equations (e.g., ASCE 1971, Kasai and Popov 1986). Furthermore, in most practical cases, the impact of shear forces on the plastic moment capacity is insignificant.

3.4 Combined Flexural, Axial, and Shear Loading

The combined interaction of flexural, axial, and shear loading can be considered through the above principles. Following the same procedure used in the previous section, by apportioning some of the cross-section to resist each load effect individually, one could develop close-form solutions, but in most cases, direct calculation of the needed result from the stress diagram is actually more expedient.

For example, the reduced plastic moment of a W920 × 238 shape (equivalent to a W36 × 160 in U.S. units) when a shear force, V, of 1334 kN (300 kips) and an axial force, P, of 2668 kN (600 kips) are simultaneously applied, can be calculated as follows, assuming that a mild steel that yields at 250 MPa (36 ksi) is used (some of the steps of this example are illustrated in Figure 3.14).

First, the average shear stress on the web of that wide flange resulting from the applied shear force is calculated:

$$\tau_w = \frac{V}{wh} = \frac{1{,}334{,}000 \text{ N}}{(16.5 \text{ mm})\,(863.2 \text{ mm})} = 93.7 \text{ N/mm}^2 = 93.7 \text{ MPa} \qquad (3.36)$$

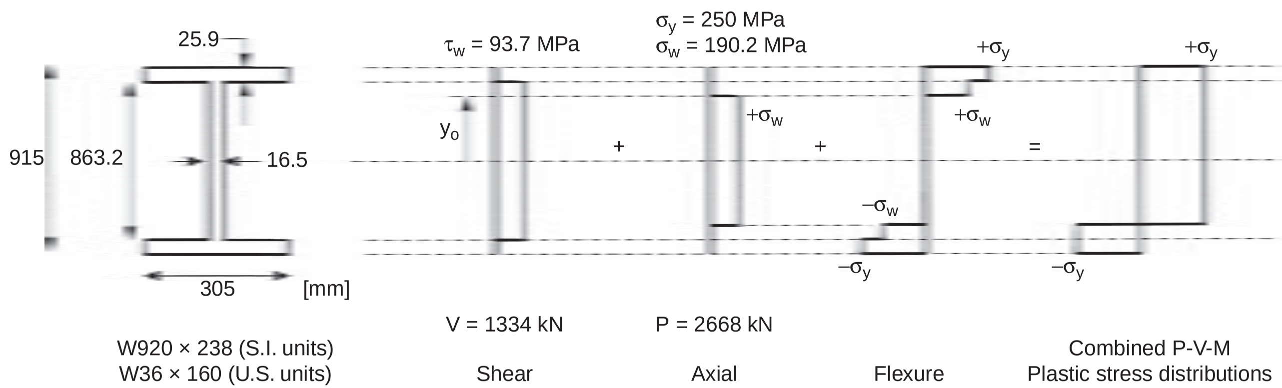

Figure 3.14 Example of plastic resistance of a wide-flange structural shape subjected to flexure, axial, and shear forces.

Incidentally, this is about 65% of the yield strength of the web, which is $0.577\sigma_y$, or 144.3 MPa (20.9 ksi). Then, the Von Mises yield criterion is used to calculate the axial stress capacity available in the web:

$$\sigma_w = \sqrt{\sigma_y^2 - 3\tau_w^2} = \sqrt{(250)^2 - 3(93.7)^2} = 190.2\ \text{MPa} = 0.761\sigma_y \tag{3.37}$$

With that remaining web axial stress capacity of 190.2 MPa (27.6 ksi) and a maximum axial flange stress capacity of 250 MPa, one can calculate the portion of the cross-section needed to resist the axial force using the procedure demonstrated earlier. In this case, it is found that the neutral axis is in the web:

$$\sigma_w = 190.2\ \text{MPa} = \frac{2{,}668{,}000\ \text{N}}{y_o(16.5)} \Rightarrow y_o = 425\ \text{mm} < \frac{h}{2} = 431.6\ \text{mm} \tag{3.38}$$

One can add the contributions of the web and flanges to the moment resistance as follows:

$$\begin{aligned} M_{pr-web}^{P,V} &= \frac{wh^2}{4}\sigma_w - \frac{w(2y_o)^2}{4}\sigma_w \\ &= \frac{(16.5)(863.2)^2}{4}(190.2) - \frac{(16.5)(850)^2}{4}(190.2) \\ &= 584.5 - 567\ \text{kN-m} = 17.5\ \text{kN-m} \end{aligned} \tag{3.39}$$

$$\begin{aligned} M_{pr-flange}^{P,V} &= 2\left[bt\left(\frac{d-t}{2}\right)\right]\sigma_y \\ &= (305)(25.9)\left(\frac{915-25.9}{2}\right)(250) \\ &= 1755.9\ \text{kN-m} \end{aligned} \tag{3.40}$$

$$M_{pr}^{P,V} = M_{pr-flange}^{P,V} + M_{pr-web}^{P,V} = (1755.9 + 17.5)\ \text{kN-m} = 1773.4\ \text{kN-m} \tag{3.41}$$

where the superscript (P,V) indicates that this plastic moment is reduced to take into account the applied axial and shear forces (Figure 3.14). This structural shape has a plastic modulus, Z, of 10,200,000 mm^3 (622.4 in^3) and therefore a corresponding plastic moment of 2550 kN-m (1882 kip-ft) in the absence of shear or axial forces. Therefore, the reduced plastic moment capacity in this example is 70% of the unreduced value.

When one takes advantage of the readily available value of the plastic section modulus (e.g., tabulated in AISC 2011 or CISC 2010), a subtractive approach to the above problem is actually more expedient. Indeed, deducting the stress diagrams associated with the axial and shear contributions to the moment resistance from the plastic moment, M_p, gives:

$$\begin{aligned} M_{pr}^{P,V} &= M_p - M_{pr}^{V} - M_{pr}^{P} \\ &= M_p - \frac{wh^2}{4}(\sigma_y - \sigma_w) - \frac{w(2y_o)^2}{4}\sigma_w \\ &= (2550 - 183.8 - 567) \text{ kN-m} \\ &= 1779.2 \text{ kN-m (1313.1 kip-ft)} \end{aligned} \tag{3.42}$$

The results obtained using the subtractive and additive approaches are slightly different because in the latter case, the value of the plastic section modulus from a design handbook/manual was used. Handbook/manual values usually consider the true rounded shape of the cross-section at the flange-web intersections, which are usually neglected when this section property is determined by hand calculation. Practically, this difference is insignificant.

3.5 Pure Plastic Torsion: Sand-Heap Analogy

The plastic torsional resistance of a given cross-section can be determined as a logical extension of the results obtained from the theory of elasticity. A complete derivation of the elastic torsion theory is beyond the scope of this book and is usually covered comprehensively in mechanics-of-material textbooks. However, some important results from that elastic theory needed to understand plastic torsion are summarized below.

3.5.1 Review of Important Elastic Analysis Results

For a structural member in pure-torsion, with its longitudinal axis parallel to the z-axis, the only nonzero stresses are the shear stresses acting in the cross-sectional plane, τ_{zx} and τ_{zy}, and their equal reciprocal components, τ_{xz} and τ_{yz}. The first and second indices, respectively, indicate the axis perpendicular to the plane on which these stresses are acting and the axis in the direction of their action. These values can be defined through the generalized Hooke's Law constitutive relationship (i.e., stress-strain relationship). To satisfy equilibrium, expressed in differential equations as defined in the theory of elasticity, the following relation must be satisfied:

$$\frac{\partial \tau_{zx}}{\partial x} + \frac{\partial \tau_{zx}}{\partial y} = 0 \tag{3.43}$$

An equation of compatibility for this problem is obtained by derivation of the shear stress expression obtained from the generalized Hooke's Law, with the following result:

$$\frac{\partial \tau_{zx}}{\partial y} + \frac{\partial \tau_{zy}}{\partial x} = \frac{\partial^2 \phi}{\partial y^2} + \frac{\partial^2 \phi}{\partial x^2} = -2G\,\theta \tag{3.44}$$

where θ is the angle of twist per unit longitudinal length, G is the shear modulus, and ϕ, called the Prandtl stress function, is a convenient mathematical substitution that will satisfy the above relationship if the following equalities are true:

$$\tau_{zx} = \frac{\partial \phi}{\partial y}; \quad \tau_{zy} \frac{\partial \phi}{\partial x} \tag{3.45}$$

Along the edge of the cross-section, the Prandtl stress function must be constant and is usually taken as zero for convenience. The search for an elastic solution to torsion problems therefore lies in finding a function of x and y, $\phi\,(x,y)$, that can satisfy the above conditions. Once that function is known, the corresponding torque applied to the member can be calculated because the two are related by the following relationship:

$$T = 2\iint \phi\, \partial x\, \partial y \tag{3.46}$$

The structure of the differential equation of the stress function [Eq. (3.44) above] is identical to the one describing the deflection of a membrane (or soap bubble) of the same shape as the cross-section of interest, tied at its edges and subjected to a uniform pressure (Prandtl's membrane analogy). A comparison of the two expressions shows that the stress function, ϕ, corresponds to the membrane deflection, and the shear stresses in the torsion problem are analogous to the slope of the membrane, as illustrated in Figure 3.15. Therefore, the torsional moment is equal to twice the volume of the bubble. The reader is referred to Popov 1968, Timoshenko and Goodier 1970, Ugural and Fenster 1995 (among many) for a complete derivation of Eqs. (3.43) to (3.46).

3.5.2 Sand-Heap Analogy

Under progressively increasing applied torque, the cross-section will begin to yield when the shear stress at any point within the cross-section reaches $0.577\sigma_y$ (per the Von Mises yield criterion). Visibly, as predicted by the membrane analogy, this should occur somewhere along the edge of the cross-section, at the edge point(s) closest to the

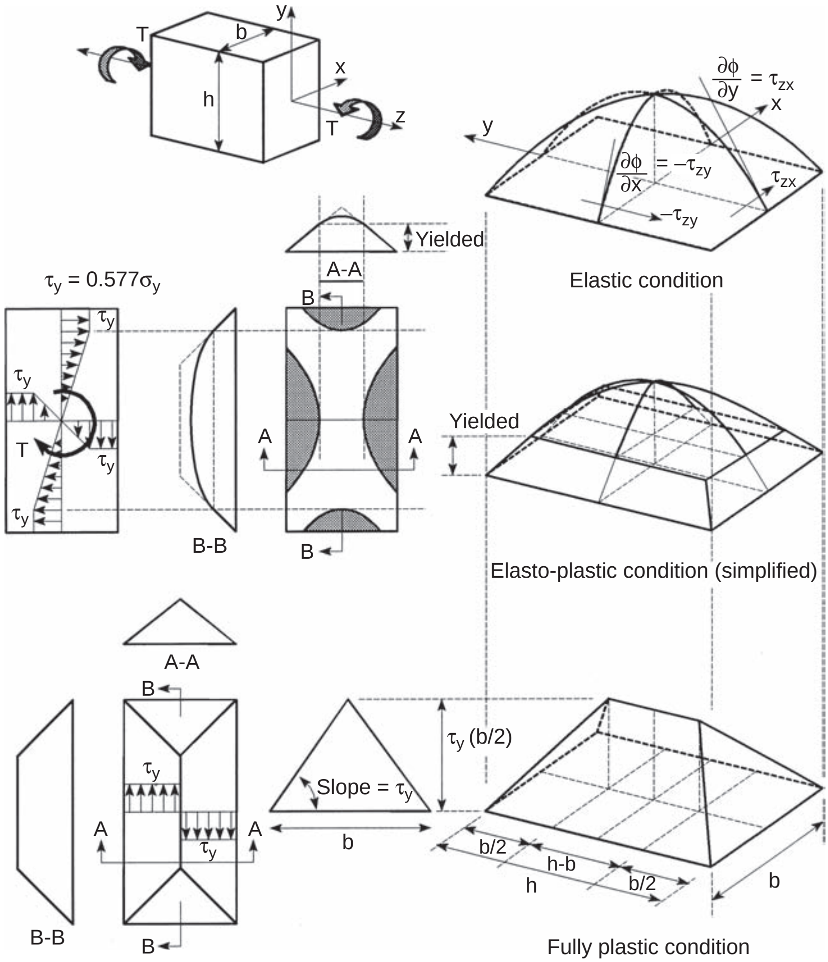

Figure 3.15 Rectangular cross-section subjected to progressively increasing torque up to plastic torque.

center of twist (i.e., where the slope of the soap bubble would be the largest). It can also be visualized that, upon application of larger torques, yielding will spread inward (Figure 3.15), and the plastic torque, T_p, will be reached upon yielding of the entire cross-section. In the fully yielded condition, because the resulting stress at any point cannot exceed the shear yield stress:

$$\tau = \sqrt{\tau_{zx}^2 + \tau_{zy}^2} = \sqrt{\left(\frac{\partial \phi}{\partial y}\right)^2 + \left(\frac{\partial \phi}{\partial x}\right)^2} = |\nabla \phi| = \tau_y = \frac{\sigma_y}{\sqrt{3}} \tag{3.47}$$

which demonstrates that the maximum slope at all points in the fully plastic condition must be equal to the shear yield stress value. From that knowledge, a plastic ϕ surface can be constructed rather easily, and it is still true that twice the area under this curve directly gives the magnitude of the corresponding plastic torque. The shape of that plastic surface can be compared with that of a sand heap. When one tries to pile up dry sand on a table having the same shape as the cross-section of interest, the resulting shape will resemble the plastic surface for that shape because dry sand is stable only up to a specific slope. This slope is also constant over the entire cross-section, making the sand-heap analogy obvious.

For example, for a rectangular cross-section, the plastic surface becomes a rectangular pyramid of slope τ_y, as shown in Figure 3.15; the corresponding plastic torque is:

$$
\begin{aligned}
T_p &= 2 \quad \text{(volume under stress function } \phi) \\
&= 2\left[\frac{b}{2}\left(\frac{b\tau_y}{2}\right)(h-b)\right] + \frac{1}{3}\left(\frac{b\tau_y}{2}\right)b^2 = 2\tau_y \frac{b^3}{6}\left[\frac{3}{2}\left(\frac{h}{b}-1\right)+1\right] \qquad (3.48) \\
&= \tau_y \frac{b^3}{3}\left[\frac{3}{2}\left(\frac{h}{b}-1\right)+1\right] \\
&= Z_T \tau_y
\end{aligned}
$$

where Z_T is defined as the torsional plastic section modulus. Results for a number of other cross-sections are shown in Table 3.1, along with the corresponding ratio of fully plastic torque to maximum elastic torque.

3.6 Combined Flexure and Torsion

The interaction of flexure and torsion also requires consideration of the plastic relationship between axial and shear stresses, as expressed by the Von Mises yield criterion. Expanding on the previously established principles, the flexure torsion interaction equations can be established as follows.

First, it is assumed that, because of the flexure/torsional interaction, only a reduced axial stress capacity, $\sigma_R < \sigma_y$, is available to resist the applied moment, and only a reduced shear stress capacity, $\tau_R < \tau_y$, is available to resist the applied torque, as shown in Figure 3.16.

Then, the Von Mises yield criterion is rewritten as:

$$
\sigma^2 + 3\tau^2 = \left(\frac{M_{pr}^T}{Z}\right)^2 + 3\left(\frac{T_{pr}^M}{Z_T}\right)^2 = \sigma_y^2 \qquad (3.49)
$$

Cross section	T_p	T_p/T_E
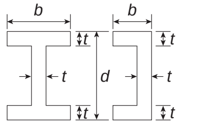	$\tau_y t^2\left[\frac{d}{2}+b-\frac{7t}{6}\right]$	$\approx \frac{3}{2}\left[\frac{2\rho_f+\rho_t^3\rho_w}{2(\rho_f-0.63)+\rho_t^4(\rho_w-0.63)}\right]$ *where* $\rho_f=\frac{b}{t}$; $\rho_t=\frac{w}{t}$ *and* $\rho_w=\frac{(d-2t)}{w}=\frac{h}{w}$ ≈ 1.80 for W shapes ≈ 1.67 for WWF shapes
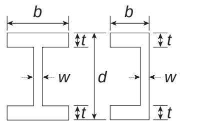	$\tau_y\left[t^2\left(b-\frac{t}{3}\right)+\frac{w^2}{2}\left(d-2t+\frac{w}{3}\right)-tw^2\right]$ $\approx\frac{1}{2}[2t^2b+w^2(d-2t)]\tau_y$	
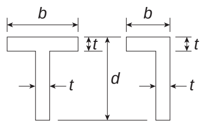	$\frac{\tau_y t^2}{2}\left[b+d-\frac{4t}{3}\right]$	—
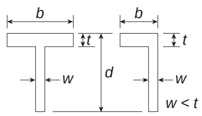	$\frac{\tau_y}{2}\left[bt^2+dw^2-\frac{t^3}{3}-w^2t\right]$	—
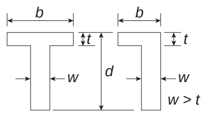	$\frac{\tau_y}{2}\left[bt^2+dw^2-\frac{w^3}{3}-t^2w\right]$	—
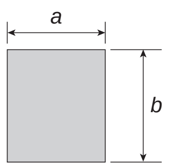	$\frac{1}{2}\tau_y a^3\left[\frac{b}{a}-\frac{1}{3}\right]\approx\frac{ba^2\tau_y}{2}$ *if* $b >> a$	1.605 if b/a = 1.0 1.690 if b/a = 2.0 1.590 if b/a = 4.0 1.500 if b/a = ∞
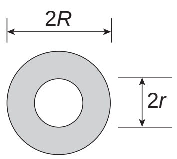	$\frac{2\pi}{3}\tau_y\ (R^3-r^3)$ $\approx 2\pi\tau_y\left(R-\frac{t}{2}\right)^2 t$ *if* $(R-r)=t=small$	1.33 1.0
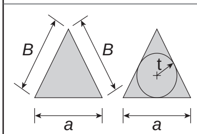	$\frac{a^3}{12}\tau_y=2\sqrt{3}r^3\ \tau_y$	1.67
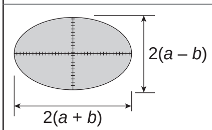	$\frac{2\pi}{3}a^3\left[1-4.5\left(\frac{b}{a}\right)^2+4\left(\frac{b}{a}\right)^3\right]\tau_y$	$1.33\left[\frac{1-4.5\beta^2+4\beta^3}{1-\beta-\beta^2+\beta^3}\right]$ where $\beta=b/a$

TABLE 3.1 Plastic Torques and Torsional Shape Factors for Some Structural Shapes

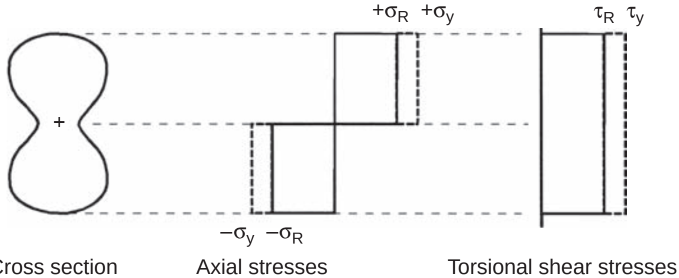

FIGURE 3.16 Reduced axial and shear stress conditions due to plastic flexure-torsion interaction.

where M_{pr}^{T} is the plastic moment reduced to account for the presence of torsion, and T_{pr}^{M} is the plastic torque reduced to account for the presence of flexure. Substituting into that equation the values of Z and Z_T, gives the following interaction equation:

$$\left(\frac{M_{pr}^{T}}{M_p}\right)^2+\left(\frac{T_{pr}^{M}}{T_p}\right)^2=1 \tag{3.50}$$

Thus, for any given magnitude of applied moment, M, the corresponding maximum plastic torque that can be developed is:

$$T_{pr}^{M}=T_p\sqrt{1-\left(\frac{M}{M_p}\right)^2} \tag{3.51}$$

Note that similar interaction equations could be developed following the same strategy to address the axial force and torque interaction, as well as flexure, axial force, and torque interaction. It is worthwhile to reemphasize that such interaction equations based on an assumed distribution of stresses satisfying equilibrium are usually conservative and safe, in accordance with the lower bound theorem presented in the next chapter.

3.7 Biaxial Flexure

3.7.1 General Principles

Biaxial bending only induces axial strains and stresses on the cross-section. Consequently, plastic strengths under biaxial bending, and corresponding interaction diagrams relating flexural strengths about

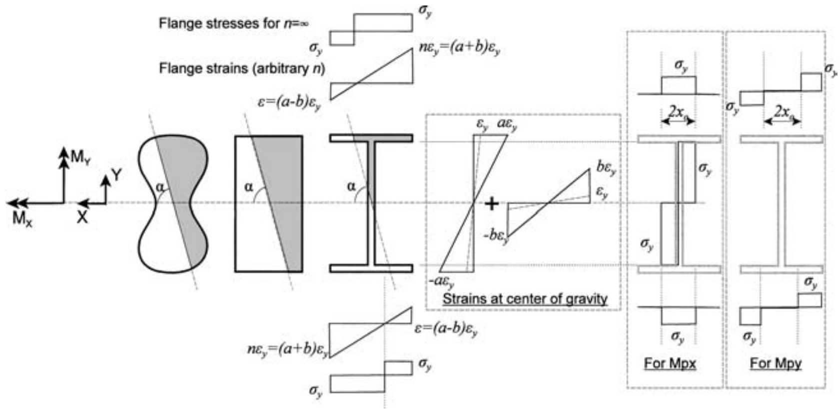

Figure 3.17 Plastic stress distribution for plastic moments in biaxial bending.

each of the two principal axes, can be obtained following principles similar to those outlined in Sections 3.1 and 3.2. For the case at hand, a few different approaches can be implemented.

First, a general-purpose cross-sectional analysis program can be developed to automate such calculations based on a fiber model, as will be described in Section 3.7.2. Second, for specific cross-sections, closed-form solutions may be possible. Finding the stress distribution for a given pair of applied moments may not be simple when the cross-section undergoes plastic behavior, but, reciprocally, calculating the moments for a given orientation of the neutral axis, α, together with a given magnitude of strains, is relatively straight forward (even though the algebraic complexity can be substantial in some instances). In particular, for the fully plastified cross-section, the plastic moments about principal orthogonal axes, respectively, reduced due to their simultaneous occurrence, can be computed. Results are generally expressed for orthogonal axes chosen parallel to key cross-section edges, as schematically illustrated in Figure 3.17 for a wide-flange structural shape, but other algebraically convenient orientations are possible. For example, the plastic strength of circular cross-sections is independent of α, in which case the biaxial flexure problem reduces to a uniaxial one about the axis of the resultant applied moment.

Closed-form solutions are presented below for the important case of a wide-flange shape. These equations can be also useful to verify results obtained during development of a computational analysis tool based on the fiber model.

3.7.1.1 Full Plastification of Wide-Flange Shape Under Biaxial Flexure

From Figure 3.17, in the fully plastified condition, note that for a wide-flange shape under biaxial flexure, the neutral axis must intersect the flange for a plastic moment to develop about the section's weak axis. Also note that the x and y axes are arbitrarily oriented such that both positive moments, in accordance with the "right-hand rule," induce compression in the upper right corner of the cross-section. To expedite calculations, it is important to recognize that stress diagrams can be decomposed into subcomponents of stress distributions (as first illustrated in Figure 3.1). In that perspective, the stress diagrams that need to be considered to compute the reduced plastic moment about both axes have been drawn separately in Figure 3.17, "trimmed" of the subcomponents that do not contribute to resist moments about the axis of interest.

For a neutral axis intersecting the flange at a distance x_o from the center of gravity of the cross-section, the plastic moment about the y axis is given by:

$$\begin{aligned} M^{Mx}_{pr-y} &= 2[M_{pyf} - M_{pyf,x_o}] = 2\left[\left(\frac{t\,b^2}{4}\right) - \left(\frac{t\,(2x_o)^2}{4}\right)\right]F_y \\ &= \left[\frac{t\,b^2}{2} - 2t\,x_o^2\right]F_y \end{aligned} \tag{3.52}$$

given that the web does not contribute to M_y, and where M_{pyf} is the plastic moment of a single flange about the y axis and M_{pyf,x_o} is the plastic moment for a length $2x_o$ of that flange. Note the notation used to express a plastic moment reduced to account for the exiting moment in the orthogonal direction, consistent with the syntax introduced earlier. Normalizing by the plastic moment for the entire section about that axis, again neglecting the small contribution of the web:

$$\frac{M^{Mx}_{pr-y}}{M_{py}} = \frac{2\left[\left(\frac{t\,b^2}{4}\right) - \left(\frac{t\,(2x_o)^2}{4}\right)\right]F_y}{2\left(\frac{t\,b^2}{4}\right)F_y} = \left[1 - \frac{4x_o^2}{b^2}\right] = (1 - \beta^2) \tag{3.53}$$

where $\beta = x_o/(b/2)$, which quantify the neutral axis location as a fraction of the distance to the edge of the flange, is introduced to simplify the equations here.

Subtracting from the total plastic moment about the x axis the parts of the flanges already used to resist the moment in the orthogonal direction (these parts having equal and opposite forces canceling each other on each respective flange), the reduced plastic moment corresponding to the contributing subcomponent of the stress diagram is:

$$M^{My}_{pr-x} = M_{px} - M_{px,loss} = M_{px} - [(b - 2x_o)\,t\,(d - t)]\,F_y \tag{3.54}$$

Normalizing by the plastic moment for the entire section about that axis:

$$\frac{M_{pr-x}^{My}}{M_{px}} = \frac{M_{px} - [(b-2x_o)\,t\,(d-t)]F_y}{M_{px}} = \left[1 - \frac{[(b-2x_o)\,t\,(d-t)]}{\left[A_f(d-t) + \dfrac{A_w h}{4}\right]}\right] \tag{3.55}$$

Using the approximate assumption that $(d - t) \approx h$, and rearranging the equation to express it in terms of the ratio of A_f/A_w, where $A_f = bt$ and $A_w = hw$:

$$\frac{M_{pr-x}^{My}}{M_{px}} = \left[1 - \frac{[(b-2x_o)t]}{\left[A_f + \dfrac{A_w}{4}\right]}\right] = \left[1 - \frac{\left[\dfrac{4A_f}{A_w} - \dfrac{8x_o t}{A_w}\right]}{\left[\dfrac{4A_f}{A_w} + 1\right]}\right] = \left[\frac{1 + \dfrac{4A_f\beta}{A_w}}{1 + \dfrac{4A_f}{A_w}}\right] \tag{3.56}$$

Using Eq. (3.56) to find an expression for β, and substituting it into Eq. (3.53), gives the following interaction equation relating the two reduced normalized flexural strengths:

$$\frac{M_{pr-y}^{Mx}}{M_{py}} + \frac{\left[\left(1 + \dfrac{4A_f}{A_w}\right)\dfrac{M_{pr-x}^{My}}{M_{px}} - 1\right]^2}{\left(\dfrac{4A_f}{A_w}\right)^2} = 1.0 \tag{3.57}$$

which is plotted in Figure 3.18. Note that as a consequence of the above assumptions and simplifications, the flexural capacity about the x axis cannot reduce to less than the plastic moment of the web alone, M_{px-web}. In other words, in the above model, only the flanges are relied upon to resist moments about the y axis, and the web is always fully available to resist flexure about the x axis. Figure 3.18 illustrates by dotted lines the range over which the plotted curves are invalid, namely below the point equal to M_{px-web}/M_{px}, which is obviously a function of A_f/A_w.

In its derivation of the same interaction curve, Mrazik et al. (1987) suggested a conservative approximate interaction equation, identified by the dash-dotted line in Figure 3.18, and obtained when $A_f/A_w = \infty$, in which case Eq. (3.57) becomes:

$$\frac{M_{pr-y}^{Mx}}{M_{py}} + \left[\frac{M_{pr-x}^{My}}{M_{px}}\right]^2 = 1.0 \tag{3.58}$$

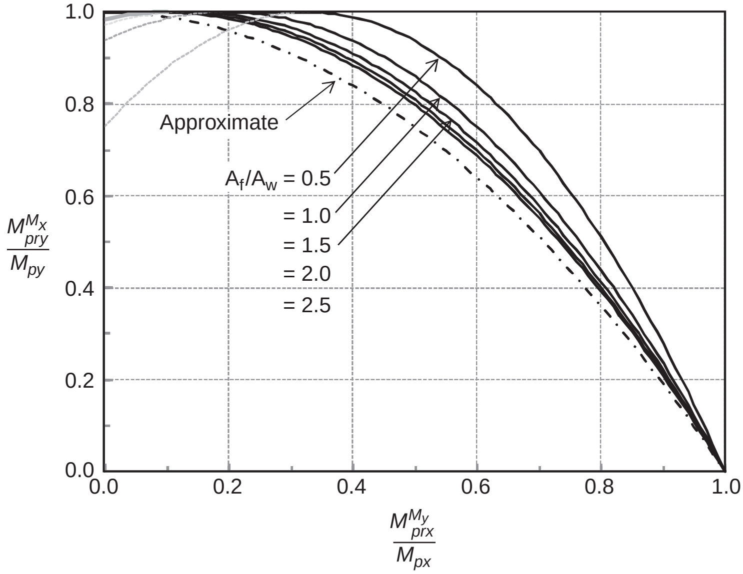

FIGURE 3.18 Plastic normalized biaxial bending interaction diagram for wide-flange structural shapes.

3.7.1.2 Partial Plastification of Wide-Flange Shape Under Biaxial Flexure

Biaxial bending interaction diagrams can similarly be derived for conditions of partially plastified cross-section (Mrazik et al. 1987). In this case, a suite of equations is necessary for this purpose to account for whether or not plasticity has spread into the web, and whether or not both tips of the flanges are plastified. These various conditions are illustrated in Figure 3.19 for various strain distributions sharing a common maximum value of $n\varepsilon_y$ at the wide-flange shape top-right edge, with x_o being the distance from the section's vertical axis of symmetry to the point where the neutral axis intersects the flange (i.e., point of zero strain) and x_i being the distance from that latter point to the point where the strain first reach ε_y. The geometric relationships that relate strains at various locations along the flange remain valid for all the strain distributions considered here. As such, from similar triangles:

$$x_i = \frac{b}{2n}\left(1 + \frac{2x_o}{b}\right) \quad \text{rearranged as} \quad \frac{x_i}{x_o} = \frac{1}{n}\left[\frac{\beta + 1}{\beta}\right] \tag{3.59}$$

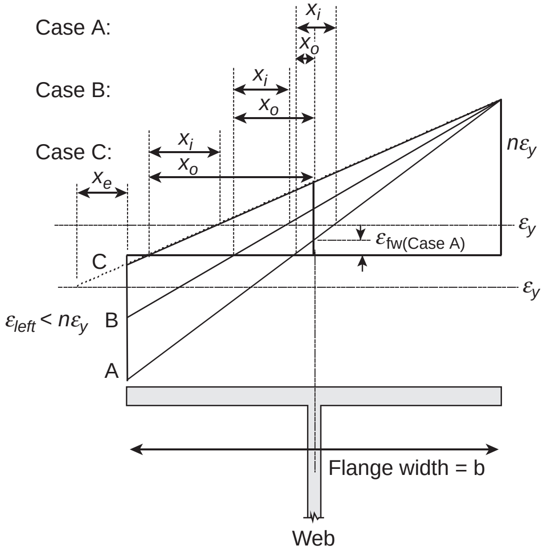

Figure 3.19 Strain distributions in flange for biaxial bending cases of partial plasticity considered.

and the strain at the web-to-flange intersection point, ε_{fw}, is:

$$\varepsilon_{fw} = \frac{x_o}{x_i}\varepsilon_y \tag{3.60}$$

When $x_o \geq x_i$, plasticity has spread into the web, and the distance along the web from the neutral axis to the location of the yield strain, y^*, is:

$$y^* = \frac{h}{2}\left(\frac{x_i}{x_o}\right) = \frac{h}{2n}\left[\frac{\beta+1}{\beta}\right] \tag{3.61}$$

It can also be shown that the web remains elastic ($x_o \leq x_i$) as long as $\beta \leq 1/(n-1)$, and that the flange tips remain plastified as long as $\beta \leq (n-1)/(n+1)$. Figure 3.20 shows the range of applicability of the following individual interaction equations (note that solutions are only presented for $n > 2$ here). Again, these results are developed taking advantage of the ability to decompose stress diagrams into subcomponents of stress distributions to expedite calculations. Some of the subcomponents used for this purpose are shown in Figure 3.21.

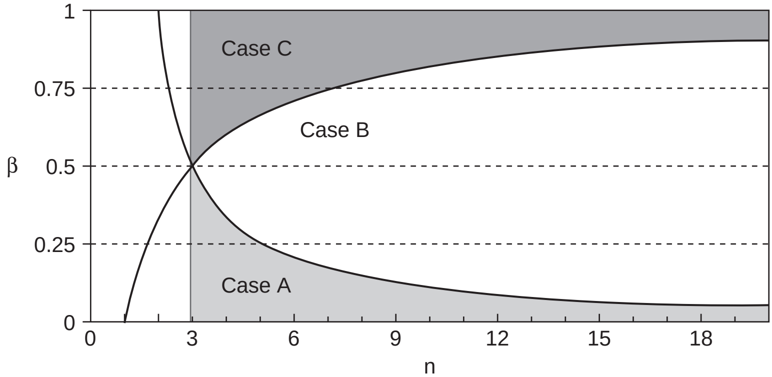

FIGURE 3.20 Range of applicability of biaxial equations.

For the case when $x_o \geq x_i$ and $x_o + x_i < (b/2)$, for which plasticity has spread into the web and both flange tips are plastified (Case B in Figure 3.19):

$$\frac{M_y}{M_{py}} = 1 - \beta^2 - \frac{1}{3n^2}(1+\beta)^2 \tag{3.62}$$

$$\frac{M_x}{M_{px}} = \left[\frac{1 + \dfrac{4A_f\beta}{A_w} - \dfrac{1}{3n^2}\left(\dfrac{\beta+1}{\beta}\right)^2}{1 + \dfrac{4A_f}{A_w}}\right] \tag{3.63}$$

For the case when $x_o < x_i$ and $x_o + x_i < (b/2)$, for which the web is elastic and both flange tips are plastified (Case A in Figure 3.19):

$$\frac{M_x}{M_{px}} = \left[\frac{\dfrac{4A_f\beta}{A_w} + \dfrac{2n}{3}\left(\dfrac{\beta}{\beta+1}\right)}{1 + \dfrac{4A_f}{A_w}}\right] \tag{3.64}$$

and the resulting equation for flexure about the weak axis is identical to Eq. (3.62), even though the stress diagram subcomponents and their lever-arm differ from the previous case.

For the case when $x_o \geq x_i$ and $x_o + x_i > (b/2)$, the web is partially plastified, but the left edge of the flange remains elastic (Case C in Figure 3.19). In this case, to add and subtract subcomponents of the stress diagram, it is mathematically convenient to work with a stress

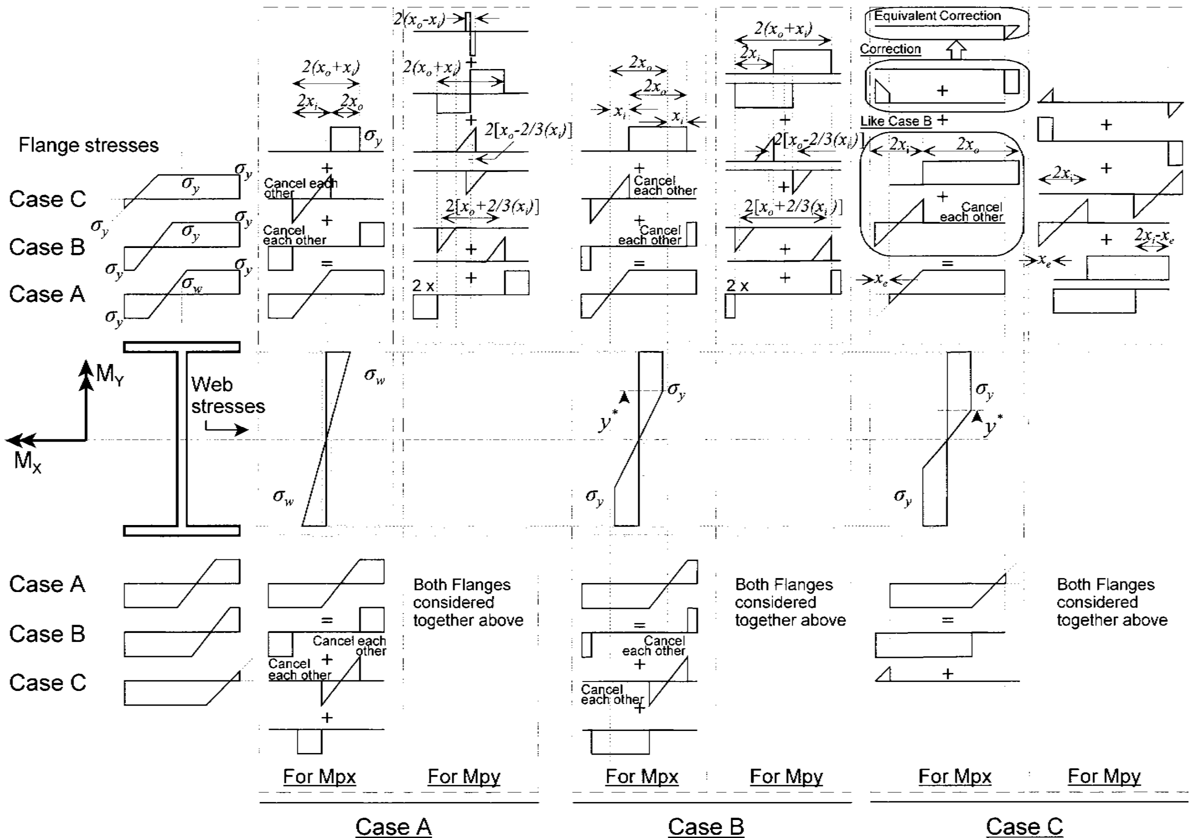

FIGURE 3.21 Subcomponents of stress diagrams to calculate biaxial bending interaction equations.

diagram extended beyond the left-flange edge up to the point where ε_y would be reached on the extrapolated strain diagram (located at $x_o + x_i$ from the section's vertical axis of symmetry, or equivalently at x_e from the edge of the flange, as shown in Figure 3.21). In this case, from geometry and algebraic relationships:

$$x_e = (x_o + x_i) - \frac{b}{2} \quad \text{and} \quad \frac{(x_o + x_i)}{b/2} = \beta + \frac{(\beta + 1)}{n} = \beta^* \tag{3.65}$$

The resulting normalized equations are:

$$\frac{M_y}{M_{py}} = \frac{1}{2}\left\{\left[1 - \beta^2 + \frac{2\beta}{n}(1+\beta) + \frac{1}{3n^2}(1+\beta^2)\right] + (1-\beta^{*2}) + n\left[\frac{\beta^{*2} + \beta^* - 2}{3}\right]\frac{(\beta^* - 1)}{(\beta + 1)}\right\} \tag{3.66}$$

$$\frac{M_x}{M_{px}} = \left[\frac{1 + \dfrac{4A_f\beta}{A_w} - \dfrac{1}{3n^2}\left(\dfrac{\beta+1}{\beta}\right)^2 - \dfrac{n\,A_f\beta^*}{A_w}\left(\dfrac{\beta^* - 1}{\beta + 1}\right)}{1 + \dfrac{4A_f}{A_w}}\right] \tag{3.67}$$

Using the above set of equations, calculating the normalized capacities about both principal axes for a range of β values, biaxial interaction diagrams can be plotted for various conditions of partially plastified cross-section. Examples shown in Figure 3.22 are for various ratio of flange-to-web areas, for given values of strain at the top right flange tip.

3.7.2 Fiber Models

Section 3.1.2 described how a simple computer program can be written to generate the moment-curvature relationship for an arbitrary structural shape subjected to uniaxial bending by dividing the cross-section into a large number of layers. Such a program would be designed to calculate each layer's individual area, center of gravity, stress, and force corresponding to a given curvature and neutral axis location. Forces from all layers would be summed together and the neutral axis would be iteratively moved until the sum would become equal to the applied axial force (or to zero if no axial force is applied). The corresponding moment at each curvature would then be calculated.

A similar strategy can be implemented for the case of biaxial bending, with or without the presence of an axial load, by layering the cross-section about both principal axes to create a grid of elements covering the cross-section, as shown in Figure 3.23. As such, the cross-section can be seen as a stack of parallel "fibers" subjected to various strains for the applied global strain distribution—such "fiber elements" have been implemented in various commercial

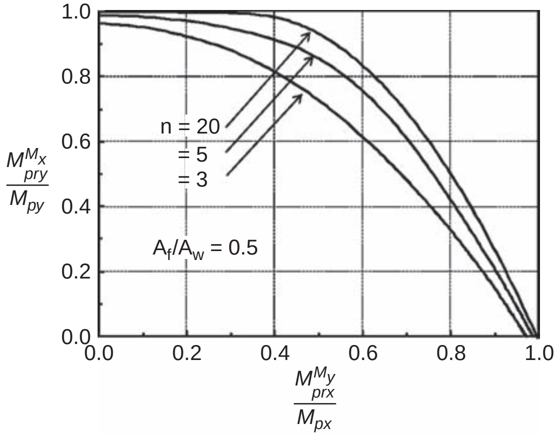

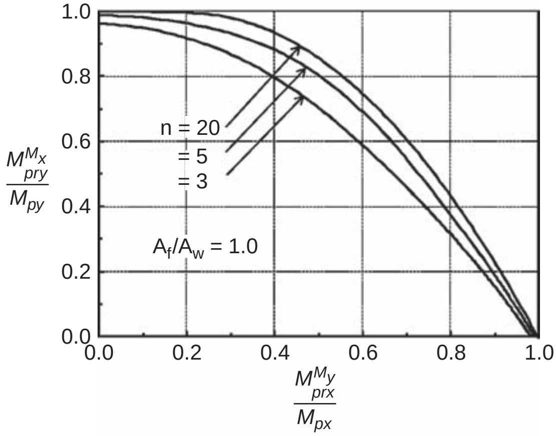

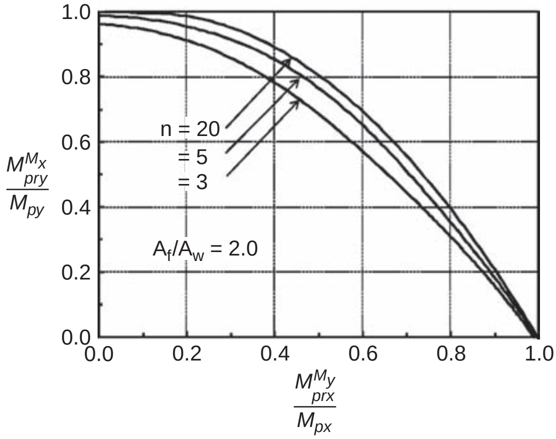

FIGURE 3.22 Biaxial bending interaction diagrams for partially plastified wide-flange sections.

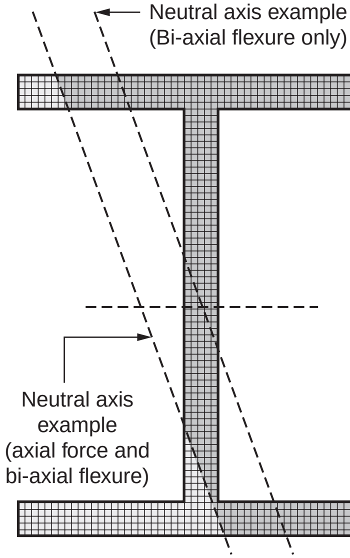

Figure 3.23 Example mesh of fibers for cross-sectional analysis under biaxial bending.

structural analysis programs. The core of the algorithm outlined in Section 3.1.2 remains the same, but would need to be expanded with additional iteration loops to consider curvature about both principal axes, with or without axial interaction. The engineering principles are identical to what has been considered so far, with biaxial bending only adding complexity to the "bookkeeping" of strains and stresses acting on all the fibers.

3.8 Composite Sections

The cross-sectional analysis principles presented in this chapter can be extended to structural members built-up using shapes of different steel grades or metals, as well as to composite members made of different materials altogether. Plastic moment of composite sections, and corresponding axial-flexure interaction diagrams, can be developed recognizing that the entire cross-section shares a common strain diagram and neutral axis (i.e., a condition of composite behavior), from which the stress distribution on each material can be established. For example, the following plastic moment equations for concrete-filled steel tubes, using a concrete model that develops f'_c up to high ductility (caused by the confinement of the steel tube) and a bilinear stress-strain model for the steel tube, have been validated by good correlation between predicted strength and experimental data (Bruneau and Marson 2004).

The flexural strength of a concrete-filled pipe is calculated using the equilibrium diagram shown in Figure 3.24.

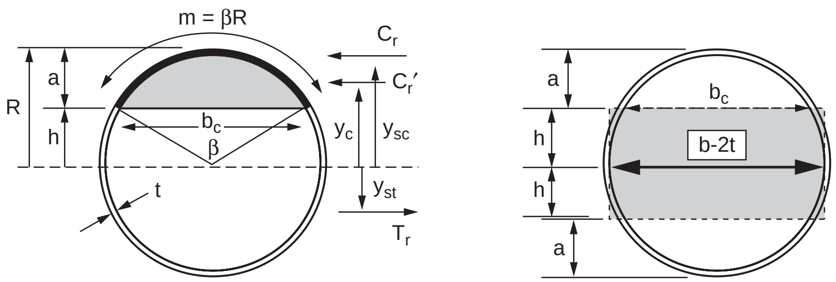

FIGURE 3.24 Free-body diagrams used to develop flexural strength equations for composite concrete-filled steel tube.

The following equations define the forces acting on the composite section:

$$
\begin{aligned}
T_r &= A_{st}F_y \\
T_r &= T_{max} - C_r \\
T_r &= C_r + C'_r \\
T_{max} &= A_s F_y
\end{aligned}
\tag{3.68}
$$

where T_r is the tensile force in the steel tube, A_{st} is the area of tensile steel, F_y is the yield strength of the steel tube, T_{max} is the total force if all steel is in tension, C_r is the axial compressive resistance of the steel tube, C'_r is the axial compressive resistance of the compressed concrete core, and A_s is the total area of steel. To solve for the neutral axis location, h, in Figure 3.24, the above four equations are combined to produce one equation:

$$2A_{st}F_y = A_sF_y + C'_r \tag{3.69}$$

The terms in the above equation are defined as follows:

$$
\begin{aligned}
&A_{st} = (2\pi R - m)t = (\pi D - m)t \\
&m = \beta R \\
&A_s = 2\pi R\, t = \pi D t \\
&C'_c = A_{conc} f'_c = \left[\frac{m\,D}{4} - \frac{c(R-a)}{2}\right] f'_c = \left[\frac{\beta\, D^2}{8} - \frac{b_c}{2}\left(\frac{D}{2} - a\right)\right] f'_c \\
&a = \frac{b_c}{2}\tan\left(\frac{\beta}{4}\right) \\
&c = D\sin\left(\frac{\beta}{2}\right)
\end{aligned}
\tag{3.70}
$$

where m is the arc length of the tube in compression, β is the angle in radians from the center of the tube and sustaining the arc m, R and D are the radius and diameter of the steel tube, respectively (Figure 3.24). Substituting these terms into Eq. (3.69), and expressing in terms of β, the equation becomes:

$$\beta = \frac{A_s F_y + 0.25D^2 f_c'[\sin(\beta/2) - \sin^2(\beta/2)\tan(\beta/4)]}{(0.125D^2 f_c' + DtF_y)} \tag{3.71}$$

There is no closed form solution for the above equation, so an iterative solution is required to obtain β. Once the value of β is found, C_r, C_r', and T_s can be calculated. The distances from the neutral axis for C_r, C_r', and T_s, are y_{sc}, y_c, and y_{st}, respectively, where:

$$\begin{aligned} y_{sc} &= \frac{Rb_c}{m} \\ y_c &= \frac{b_c^3}{6[Rm - b_c(R-a)]} \\ y_{st} &= \frac{Rb_c}{2\pi R - m} \end{aligned} \tag{3.72}$$

From simple statics, M_{rc} is defined as:

$$\begin{aligned} M_{rc} &= C_r'e + C_r'e' \\ e &= y_{st} + y_{sc} = b_c\left[\frac{1}{(2\pi - \beta)} + \frac{1}{\beta}\right] \\ e' &= y_{st} + y_c = b_c\left[\frac{1}{(2\pi - \beta)} + \frac{b_c^2}{1.5\beta D^2 - 6b_c(0.5D - a)}\right] \end{aligned} \tag{3.73}$$

Alternatively, using an approximate geometry method, in which the contribution of a rectangular central section of height $2h$ is subtracted from the plastic moment of the entire section (Figure 3.24), a closed-form solution is possible and a conservative value of M_{rc} is directly given by:

$$M_{rc} = \left(Z - 2th_n^2\right)F_y + \left[\frac{2}{5}(0.5D - T)^3 - (0.5D - t)h_n^2\right]f_c' \tag{3.74}$$

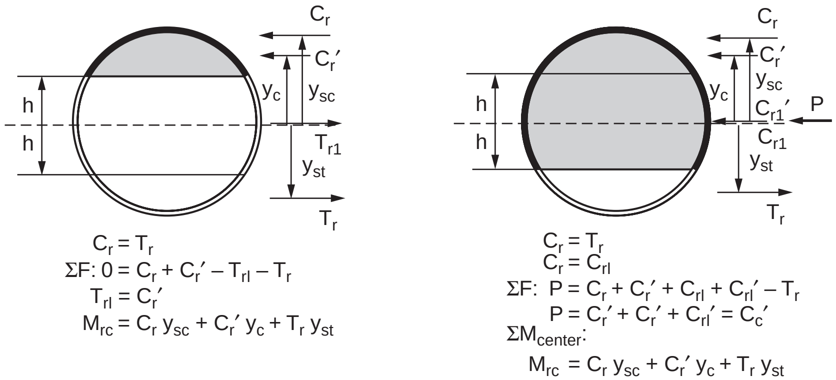

Figure 3.25 Free-body diagrams used as a step to develop axial and flexural interaction diagram.

where

$$h = \frac{A_c f_c'}{2Df_c' + 4t(2F_y - f_c')} \tag{3.75}$$

and Z is the plastic modulus of the steel section alone.

For capacity design purposes, in determining the force to consider for the design of capacity protected elements, it is recommended to increase the moment calculated by this approximate method by 10%.

Toward the development of an axial-flexure interaction curve, note that, as shown in Figure 3.25, the moment capacity with no axial force applied and a neutral axis location of h above the center of gravity is the same moment capacity as for an axial force equal to the compressive resistance of the concrete core and a neutral axis location of h below the center of gravity.

Proposed design axial-flexure interaction equations based on the above plastic moment equations (Bruneau and Marson 2004) were shown to predict well the behavior of concrete-filled steel pipe columns, and were implemented in the CSA-S16 "Limit State Design of Steel Structures" (CSA 2009) and in the "AASHTO Guide Specifications for LRFD Seismic Bridge Design" (AASHTO 2009).

3.9 Self-Study Problems

Problem 3.1 A 16-inch-deep (380-mm) and 8-inch-wide (203-mm) hollow steel member is constructed from 3/4-inch (19-mm) steel plates (outside to outside dimensions) of mild steel which may be idealized as elasto-perfectly plastic, E of 29,000 ksi (200,000 MPa), and F_y of 36 ksi (250 MPa).

(a) What is the shape factor of this section?

(b) Draw the moment-curvature relationship of this section. Rather than obtaining a continuous analytical function for this relationship, solve for moments corresponding the following events
- Strain at top fiber has reached 0.00062
- Yielding of top fiber, that is, ε_y
- Strain at top fiber has reached 0.002
- Point at which all of the flange has just fully yielded
- Strain at top fiber has reached 0.004
- Strain at top fiber has reached 0.010
- Strain at top fiber has reached 0.0128

Also present moment-curvature results in a tabular manner, in four columns for the resulting values of φ, φ/φ_y, M, and M/M_y.

Problem 3.2 A T-section is built from two steel plates; the flange plate is 6×0.75 in, and the web plate is 9×0.75 in. Find the shape factor for this section bending about an axis perpendicular to the web. Is this result a function of whether the section is under negative or positive bending?

Problem 3.3

(a) A unique steel cross-section has been created for a special application. For this cross-section (shown in the figure below), calculate the yield moment, the plastic moment, and the shape factor, k.

(b) Compare the answer to (a) with the known shape factor for a rectangular section, and explain why the answer obtained in (a) is logical on the basis of those observations (i.e., explanations must be based on fundamental engineering principles).

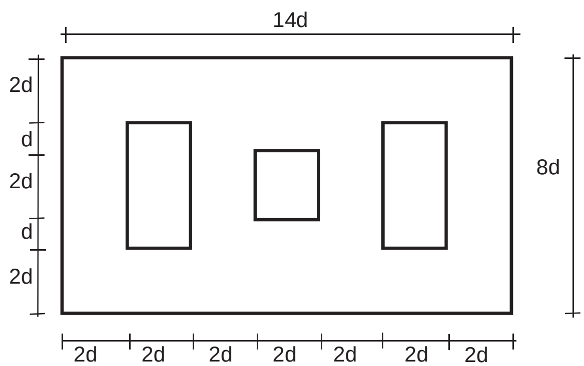

Problem 3.4

(a) For the cross-section shown in the figure below (square shaft with keyway), calculate and show the location of the elastic neutral axis, plastic neutral axis, and calculate the shape factor, k. Show distance of both neutral axis from the top of the cross-section.

(b) Compare the answer to part (a) with the known shape factor for a rectangular section, and explain why that answer is logical (i.e., explanations must be based on fundamental engineering principles).

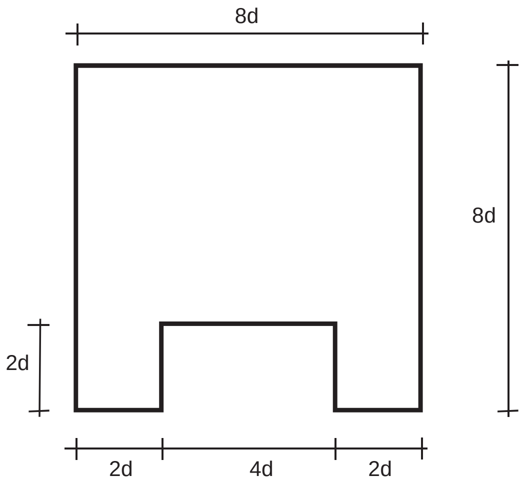

Problem 3.5 What is the plastic moment of the triangular section shown? Due to prior inelastic action, there is an initial stress distribution present, as shown. The material is elasto-perfectly plastic of strength F_y. The section is bent about an axis parallel to its base.

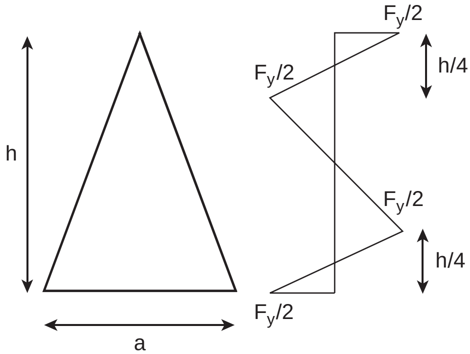

Problem 3.6 Derive an analytical function describing the relationship between M and P for a thin annular section of diameter, D, and thickness, t, for:

(a) First yield (i.e., onset of yielding)
(b) Fully plastic yielding

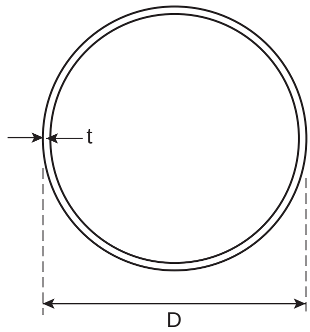

Problem 3.7 The unique steel cross-section shown below has been created by welding two WT10.5 × 100.5 of A992 Grade 50 steel to a 10′ × 0.75′ special Grade 70 plate having a yield strength, F_y, of 70 ksi.

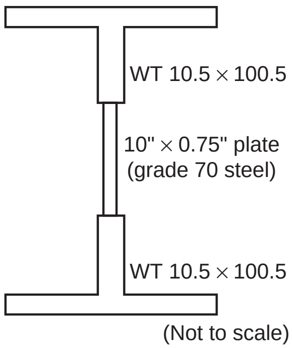

(a) For this cross-section, calculate the plastic moment.
(b) For the same cross-section, calculate the reduced plastic moment in the presence of an axial load of 525 kips.

Problem 3.8 The unique steel cross-section shown below has been created for a special application.

(a) For this cross-section, calculate the plastic moment, and the shape factor, k.
(b) For the same cross-section, calculate the reduced plastic moment in the presence of an axial load of 200 kips.

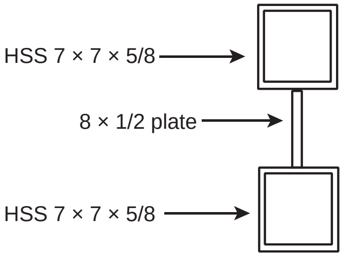

Problem 3.9 Calculate the *P-M* strength interaction curve for the steel cross-section shown in the following figure. Consider that *d* is much larger than *t* in this problem (i.e., d >>> t).

Also, using the above result, indicate how much of the pure bending plastic capacity of that section can be developed if axial loads equal to 25%, 50%, 75%, and 100% of the pure axial capacity are applied (i.e., four special cases to consider). Express all answers in terms of normalized moments and axial forces, and in terms of *d* and *t*.

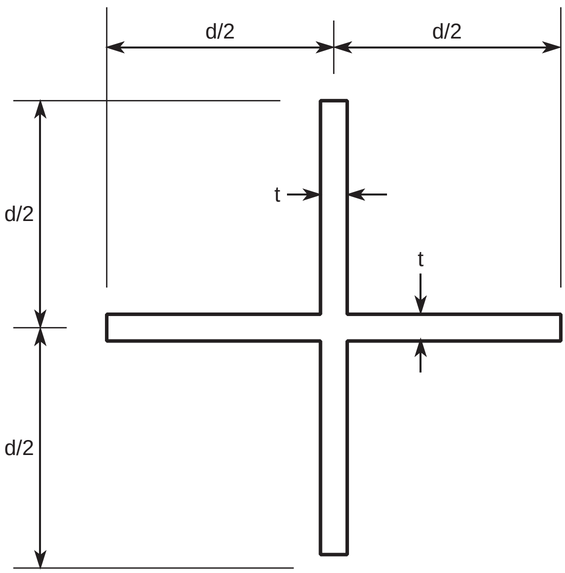

Problem 3.10 Calculate the *P-M* interaction curve (expressed parametrically) for the steel cross-section shown.

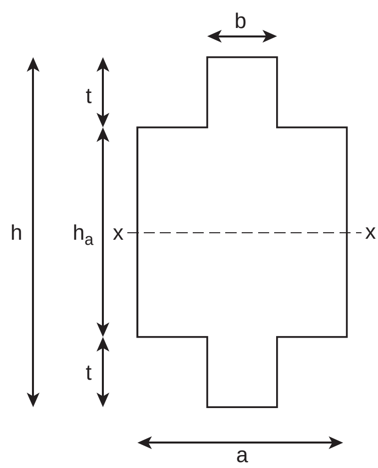

Problem 3.11

(a) Calculate the ratios P/P_p and M/M_p for the diamond shaped cross-section shown.

(b) Without making calculations, indicate how one would proceed to obtain an analytical expression for an interaction curve of P/P_p over M/M_p analytically. Then, indicate how the same interaction curve could be obtained numerically (i.e., without deriving a formal analytical expression).

(c) Calculate one point on this interaction curve for the case $P = P_p/2$ and $h = 100$ mm.

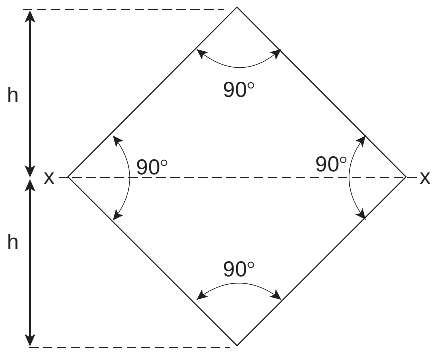

Problem 3.12 For the W-shape steel section shown here, assembled from steel plates having dissimilar yield stresses, calculate the reduced value of M_p that can be developed when a 112-kips shear force is applied.

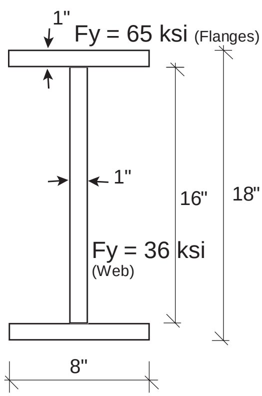

Problem 3.13 For the W18 × 71 structural shape:

(a) Verify (calculate) the values of Z about both the x-x and y-y axis that are tabulated in the AISC Manual of Steel Construction.

(b) Calculate the value of M_p that this section can resist about the x-x axis simultaneously with applied shear forces, V, of 100 kips, and axial forces, P, of 150 kips.

Problem 3.14 At one of the ends of a W920 × 238 (W36 × 160 in U. S. designation), the state of stress consists of a shear force (V), and axial force (P), and a bending moment (M). Determine the maximum reduced plastic moment that can be applied on this steel section if steel is 250 MPa (36 ksi), and:

(a) $P = 0$ and $V = 1334$ kN (300 kips)
(b) $P = 667$ kN (150 kips) and $V = 1334$ kN (300 kips)
(c) $P = 2668$ kN (600 kips) and $V = 1334$ kN (300 kips)

In all cases, express the calculated reduced plastic moment (M_{pr}) as a ratio (or percentage) of the plastic moment (M_p) which could be applied to this section in absence of shear and axial forces.

It is worthwhile to verify the calculations using both the additive and subtractive approaches to the calculation of M_{pr}. However, be aware that slight differences are possible if using values tabulated in design handbooks/manuals in the subtractive approach because tabulated values of Z and M_p consider the true rounded shape of the section at the flange-web intersections.

Problem 3.15

(a) A unique steel cross-section has been created for a special application. For this cross-section (in the figure shown), calculate the shape factor, k.
(b) Assuming that the cross-section must simultaneously resist an axial force (P) of 200 kips, a shear force (V) of 100 kips, and flexure, and assuming that this cross-section resists shear like a normal I-shape member, calculate the maximum moment that this cross-section can resist using plastic analysis principles. Clearly show the stress distributions correspond to shear, axial, and flexure.

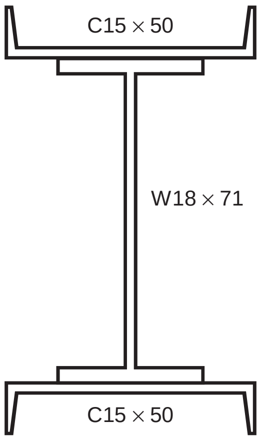

Problem 3.16 Derive equations for the expression of the full plastic torque (T_p) for the following cases:

(a) A rectangle of depth $2b$ and width $2a$
(b) A T-shaped section of flange width a, total depth b, and uniform thickness t

(c) An I-shaped section of flange width b, total depth a, and uniform thickness t

(d) A general I-shaped section of flange width b, total depth a, of flange thickness t_1, and web thickness t_2, where $t_1 > t_2$ (as normally the case for common I-shape sections)

Problem 3.17 A 16-feet-long (4.88-m) beam with fixed-supports at both ends is loaded by a point load (F) at its middle. This load is applied with an eccentricity of 75 mm (3 in). The selected beam is a W18 × 50 (W460 × 74 S.I. designation) of 36 ksi (250 MPa) steel. Calculate the load F that will fully plastify the cross-section when:

(a) The effects of shear and torsion are neglected

(b) The effect of shear is neglected, but the effect of torsion is included without considering the potential influence of warping restraints (consideration of warping restraint is beyond the scope of this book)

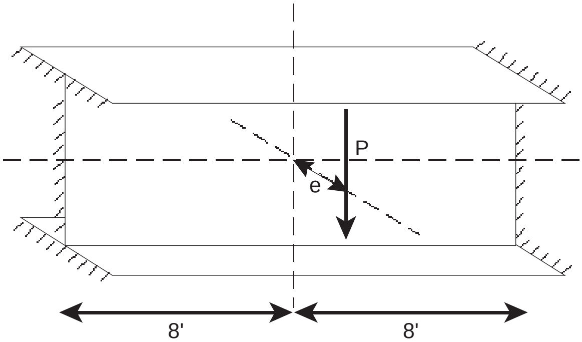

Problem 3.18 The steel section shown below is made from an elasto-perfectly-plastic material of strength F_y. It is an experimental structural shape of high strength steel rolled with extra edge-stiffeners to enhance local buckling strength. In this problem, only consider bending about the strong axis of the section.

(a) Calculate the yield moment (M_y), plastic moment (M_p), and shape factor for this section.

(b) Develop the P-M (axial force/bending moment) interaction curve for this steel section, expressed in terms of (M/M_p) and (P/P_p).

(c) Compare the resulting interaction curve with that for a corresponding W-shape beams (i.e., the same shape without the edge stiffeners), by plotting the resulting interaction diagram for both shapes.

(d) From the results in (c), could the interaction diagram for the case neglecting the stiffeners be used conservatively? Explain, based on fundamental principles, how this conclusion could have been predicted without any calculations.

(e) If that section had large residual stresses before any loads are applied to it, what would be their effect on the above findings?

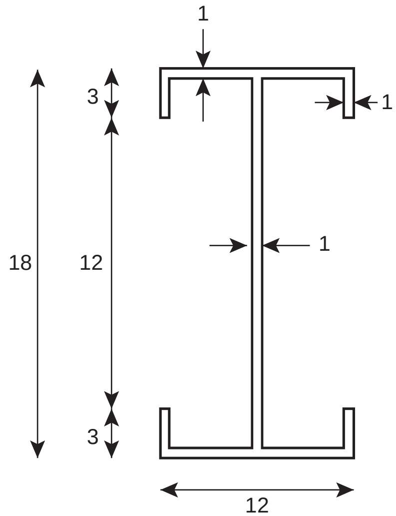

Problem 3.19 If the steel shape shown in Problem 3.18 was made of a peculiar elasto-perfectly-plastic material of strength σ_y which unfortunately could only reach a maximum strain of $5\varepsilon_y$, at which point brittle failure occurred, as illustrated below, still assuming strong axis bending:

(a) What would be the maximum moment that could be applied to this section?
(b) If this maximum moment was then removed, what would be the resulting residual stresses and the corresponding strain distribution?

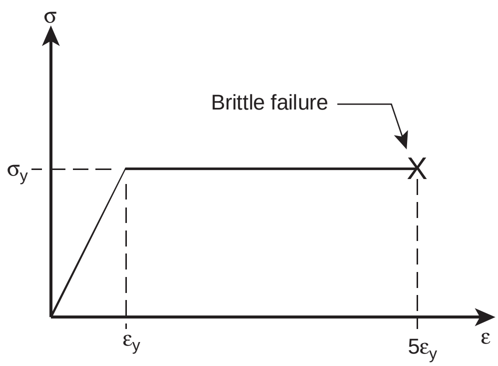

Problem 3.20 If the steel shape shown in Problem 3.18 was made of an elasto-perfectly-plastic material having infinite plastic straining capabilities (i.e., as assumed in simple plastic theory), calculate what is the maximum moment that can be applied to this section if it must simultaneously resist a shear force $V = 6.93\sigma_y$, and an axial force $P = 18.56\sigma_y$. The shear force can be assumed to be only resisted by the web.

Problem 3.21 Write a computer program to calculate the moment-curvature (M-ϕ) relationship for an arbitrary steel section having one axis of symmetry perpendicular to the axis of bending. The general cross-sections to consider are limited to those which can be built by the addition of rectangular sections having parallel baselines (i.e., the user of the program should only need to input data for three rectangles to define a W-shape).

This moment-curvature analysis is to be accomplished by subdividing the final section created into a high number of layers (the program should use a default of 100 layers, but also allow the user to specify this number, up to a maximum of 10,000 layers). Only flexure needs be considered (i.e., neglect the effect of axial, shear, or torsion forces). An elasto-perfectly plastic steel model is to be used.

Incremental loading up to 98% M_p is to be considered in generating the moment-curvature curve. The program should allow the print out of the stress values at all layers, if required.

It is highly recommended that each well identified task be assigned to a separate subroutine. Following are suggested subroutines which may be useful in the program architecture. Write and test each subroutine individually for efficient programming.

- Input and assembly of total cross-section. For example, a T-section would be defined by only two rectangles.
- Automate layering, subdividing into the number of specified layers.
- Initialize stress values for all layers, and set initial parameters.
- Create environment for iteration strategy.
- Increment curvature tentatively by a given step.
- Increment stresses for all layers per steel behavior model.
- Calculate the resulting moment by summing contributions from all layers.
- Calculate the resulting axial force by summing contributions from all layers.
- Guess location of neutral axis at a given step, and adjust the guess through iteration depending on the previous results.
- Determine if convergence is reached according to a selected tolerance on the axial force (maybe as a fraction of σ_y versus resulting P/A).
- Accept converged result and move on to additional curvature step. Print M and ϕ values for that step. Print stresses at all layers, if required.

Check the program using the cross-sections for some of the other above problems. In particular, present the resulting M-ϕ curve for a T-section built of two steel plates (flange is 6×0.75 in and web is 9×0.75 in) as well as stress-diagram at two intermediate points between M_y and M_p.

Comment on what changes would be necessary to:

1. Modify the program such that cyclic behavior can be considered.
2. Consider bi axial bending.
3. Include non-null axial force.
4. Include general nonsymmetric cross-sectional shapes.

Submit source code, compiled executable, input and output files of verification problems. Use comment-lines generously in the source code, identifying clearly purpose of subroutine and definition of all variables used. Any programming language can be used.

Problem 3.22 Expand the computer program developed for Problem 3.21 to be able to calculate and plot moment-curvature under cyclic loading:

(a) For the same elasto-perfectly model as in Problem 3.21
(b) For a Ramberg-Osgood material model
(c) Considering presence of an axial force, *P*

References

AASHTO. 2009. *AASHTO Guide Specifications for LRFD Seismic Bridge Design*. American Association of State Highway Transportation Officials: Washington, D.C.

AISC. 2011. *Steel Construction Manual*, 14th ed. Chicago: American Institute for Steel Construction.

ASCE. 1971. *Plastic Design in Steel—A Guide and Commentary*. ASCE manual and reports on engineering practice No. 41. New York: American Society of Civil Engineers.

Bruneau, M., and Marson, J. 2004. "Seismic Design of Concrete-Filled Circular Steel Bridge Piers." *ASCE Journal of Bridge Engineering*, vol. 9, no. 1, pp. 24–34.

CISC. 2010. *Handbook for Structural Steel Design*. Toronto: Canadian Institute for Steel Construction.

Closkey, D. J. 1988. "Report of the Commissioner's Inquiry—Station Square Development, Burnaby, BC," Inquiry Commissioner. Province of British Columbia.

CSA. 2009. *CSA S16-09, Design of Steel Structures*. Canadian Standard Association, Mississauga, ON, Canada, p. 198.

Galambos, T. V., and Ravindra, M. K. 1976. "Tentative Load and Resistance Factor Design Criteria for Steel Beam Columns," *Research Report No. 32.* Civil Engineering Department, Washington University, St. Louis.

Kasai, K., and Popov, E. P. 1986. "A Study of the Seismically Resistant Eccentrically Braced Steel Frame Systems," *Report UCB/EERC-86/01*. Earthquake Engineering Research Center. Berkeley, CA: University of California at Berkeley.

Mrazik, A., Skaloud, M., and Tochacek, M. 1987. *Plastic Design of Steel Structures*. Ellis Horwood Limited, West Sussex, UK, p. 637.

Popov, E. P. 1968. *Introduction to Mechanics of Solids*. Englewood Cliffs, NJ: Prentice-Hall.

Timoshenko, S. P., and Goodier, J. N. 1970. *Theory of Elasticity*, 3rd ed. New York: McGraw-Hill.

Ugural, A. C., and Fenster, S. K. 1995. *Advanced Strength and Applied Elasticity*, 3rd ed. Englewood Cliffs, NJ: Prentice-Hall.

This page intentionally left blank

CHAPTER 4

Concepts of Plastic Analysis

4.1 Introduction to Simple Plastic Analysis

Many of the cross-sectional plastic capacities developed in the previous chapter have already been integrated into ultimate or limit states design codes, alongside related equations that address member stability. Today, these equations are generally used in a design process in which all actions on the structural members (i.e., shear and axial forces, moments, and torques) have been obtained by elastic structural analyses. Although provisions exist in most steel design standards and specifications to allow plastic analysis as an alternative analysis procedure, the availability of matrix-based elastic analysis computer programs that effectively eliminate tedious calculations have made the elastic structural analysis the more popular procedure. As a result, most designs are now driven by member strength, not global structural strength. Although this is certainly expedient for standard designs, in many instances knowledge of the true ultimate resistance and strength is still necessary. This chapter presents simple plastic analysis methods suitable for hand calculations to determine such ultimate global structural capacities.

For simplicity's sake, throughout this chapter, unless stated otherwise, the moment capacities used for calculations will not be reduced to account for the effects of axial, shear, or torsion, as described in the previous chapter. These reductions can be considered when these effects are known (or suspected) to have a major impact on the results, but for many structures, this impact is negligible.

Various levels of modeling and analytical sophistication are possible in plastic analysis, with some approaches suitable only for computer nonlinear analyses. Some efforts have been invested to bring some of the more advanced analysis techniques within the reach of practicing engineers (SSRC 1993). This chapter, however, concentrates on simple but effective analysis methods that can be carried out by hand (i.e., simple plastic theory).

A number of assumptions are therefore necessary:

- Plasticity along a structural member can exist only at plastic hinges idealized as rigid-perfectly plastic hinges of zero length and of capacity M_P.
- Small deformation theory is applicable and geometric nonlinearity is not considered.
- The effect of strain-hardening is neglected.
- Structural members are properly braced to prevent instability due to either local buckling or lateral-torsional buckling.
- Plastic hinges can undergo an infinite amount of plastic deformation (or at least, deformations sufficiently large to allow the structure to align its ultimate strength).
- Loads of constant relative magnitude are monotonically applied—that is, progressively increased without load reversal.

Of those assumptions, only the concept of the zero-length plastic hinge which is fundamental to simple plastic theory, deserves some additional explanations. It is best described through an example, such as the cantilever beam loaded up to its plastic moment, shown in Figure 4.1. In such a member, some level of cross-sectional plastification exists at all points where the moment exceeds M_Y. The top fiber of the cross-section has just reached its yield stress at M_Y. Plastification spreads down the flanges and eventually into the web as the moment exceeds M_Y, and eventually, a fully plastified cross-section is reached at M_P.

Thus, plasticity is spread over some length of the member, called the real plastic hinge length, L_P. In this case, because the moment diagram is linear, one can calculate the value of L_P by similar triangles, knowing the ratio of M_P over M_Y. In steel structures where wide-flange members with shape factors of approximately 1.12 are typically used, this value is usually taken as approximately 10% of the distance from the point of maximum moment to the inflection point (and slightly more at the center of beams subjected to distributed loads).

Accurate calculation of the deflected shape of partly plastified members is possible, if one knows the mechanics-of-material relationship between deflection, y, slope, θ, and curvature, ϕ:

$$\frac{d^2y}{dx^2} = \frac{d\theta}{dx} = \phi \tag{4.1}$$

remains valid even in the inelastic range. To do this calculation, one must obtain the magnitude of this curvature at any point along the length of the beam directly from the actual nonlinear moment-curvature relationship for this structural shape, as shown in Figure 4.1

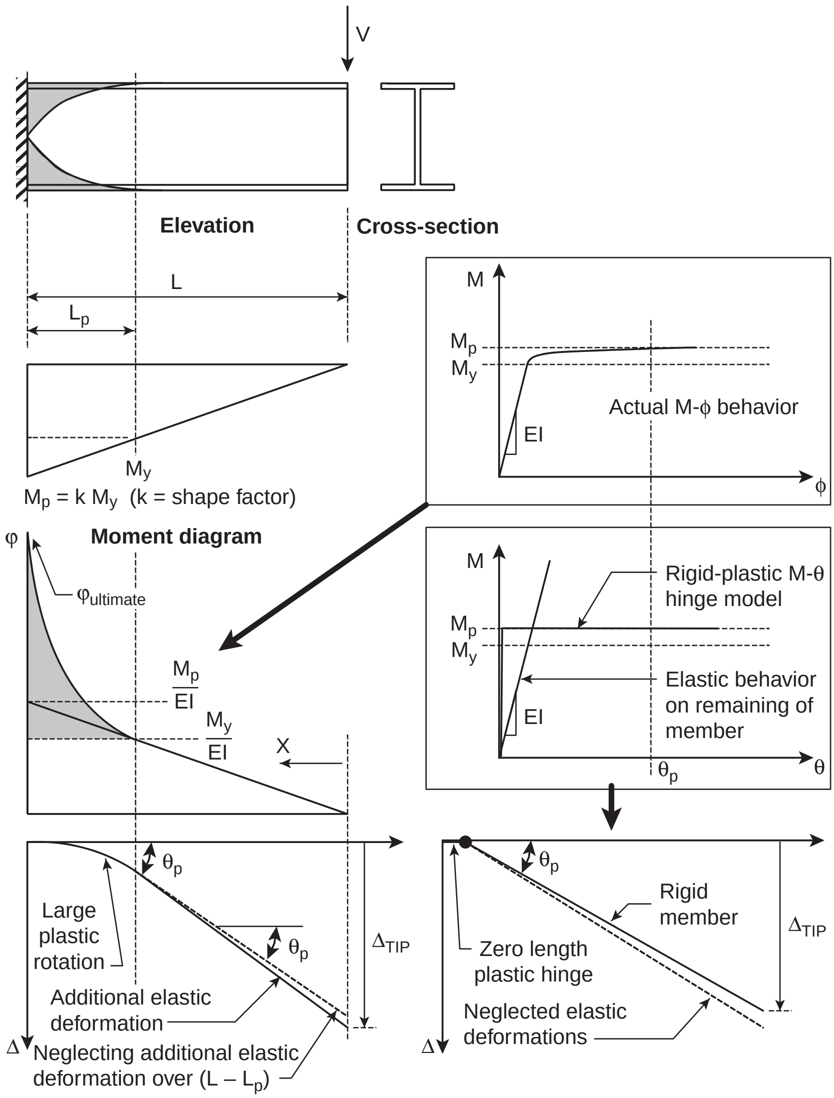

Figure 4.1 Real plastic hinge length and deflection model versus simplified zero-length plastic hinge model.

(methods to obtain moment-curvature relationships were presented in the previous chapter). Because maximum deformations are usually those of structural engineering interest, one can calculate the cantilever's tip deflection using the moment area method:

$$\Delta_{TIP} = \int \phi x\,dx = \int_{0}^{(L-L_p)} \frac{Mx}{EI}\,dx + \int_{(L-L_p)}^{L} x\phi\,dx \tag{4.2}$$

The large curvatures that exist over the real plastic hinge length can make a substantial contribution to the value of the cantilever's tip deflection. This is schematically illustrated in Figure 4.1.

Although such a procedure is theoretically exact, it is doubtful that such a level of accuracy is needed for engineering purposes. Therefore, a more expedient approach is to use a zero-length plastic hinge instead of the real plastic hinge length. Assuming a rigid-plastic hinge model, with a capacity M_p, the essence of the plastic structural behavior is captured, and the calculated deflections are sufficiently close to the more accurate values previously obtained. Hence, in this book, unless mentioned otherwise, the term *plastic hinge* will refer to a zero-length plastic hinge.

4.2 Simple Plastic Analysis Methods

There are three ways to calculate the ultimate capacity of a structure using plastic analysis:

- A systematic event-to-event calculation (also known as the step-by-step method), taking into account structural changes when they occur as the magnitude of the loading is progressively increased
- The equilibrium method (also known as the statical method), in which a statically admissible equilibrium state is directly proposed as a potential solution
- The kinematic method (also known as the virtual-work method), wherein a collapse mechanism is directly proposed as a potential solution.

These three methods are reviewed in the following sections.

4.2.1 Event-to-Event Calculation (Step-by-Step Method)

The step-by-step method, or event-to-event method, consists of simply following the structural behavior by a series of analyses, or steps, from the initial elastic behavior, through the formation of individual plastic hinges, and eventually to collapse. Although tedious, the method is straightforward, and best explained by an example.

As shown in Figure 4.2a, a W530 × 138 (W21 × 93 in U.S. units) wide-flange beam fully fixed at both ends and having a yield strength of 350 MPa (50 ksi) is loaded by a point load of progressively increasing magnitude until its plastic moment is reached. As a first step, elastic analysis of the structure is conducted, and the resulting moment diagram is computed (Figure 4.2b). This can be done with any standard method of structural analysis or, alternatively for such a simple structure, with a standard solution available in design handbooks (e.g., AISC 2011, CISC 2010). The latter approach is more

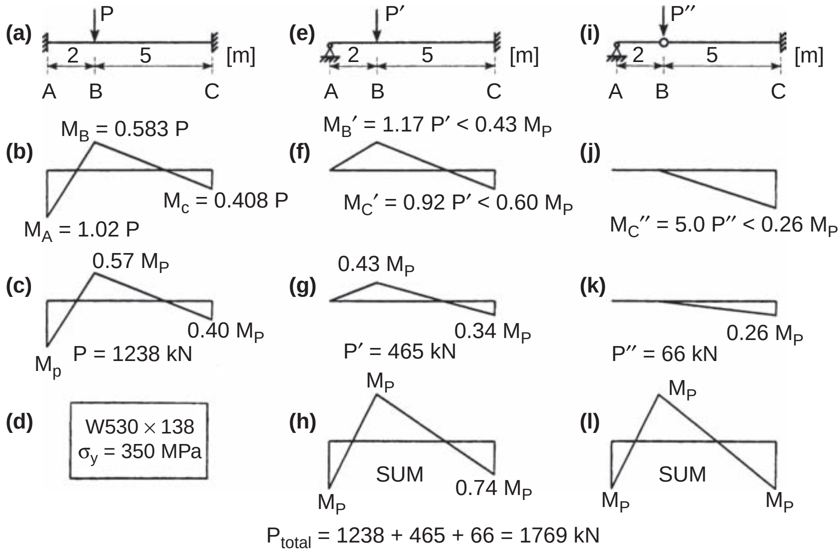

FIGURE 4.2 Example of step-by-step plastic analysis.

expedient and used here. Based on the results obtained, the plastic moment, M_p, will be reached first at point A under an applied load of 1238 kN (278 kips). The corresponding moment diagram normalized in terms of M_p is shown in Figure 4.2c. The incremental deflection under the applied load is calculated to be 7.0 mm (0.28 in).

According to simple plastic theory, M_p is the maximum moment that can be applied at point A. Therefore, the fixed-end condition that existed at point A cannot prevent the development of plastic rotations at that point (unless load reversal occurs, as described in Chapter 3). As a result, under increased applied loads, the support at point A now behaves as a simple support. This is consistent with the rigid-plastic moment-curvature hinge model described in Figure 4.1. Therefore, for the second step of analysis, a modified structure is analyzed, as shown in Figure 4.2e. In that modified structure, the fixity condition at point A has been changed to a simple support, with the implicit understanding that rotations that will develop there will actually be plastic rotations. The resulting moment diagram is shown in Figure 4.2f. These moments must be compared with the remaining capacities along the length of the structural member. In other words, the results at any given step are incremental results that must be added to those obtained during the previous analysis steps.

For the current example, the moments M_B' and M_C' are the incremental moments resulting from the load P' applied during step 2, and these need to reach only $0.43M_p$ and $0.6M_p$, respectively, before another plastic hinge develops, as shown in Figure 4.2f. The smallest value of P' that will produce such a plastic hinge is 465 kN (105 kips). The resulting normalized incremental moment diagram is shown in Figure 4.2g, and the corresponding moment diagram at the end of the second analysis step (i.e., for an applied load of 1238 + 465 = 1703 kN) is shown in Figure 4.2h. For a beam simply supported at one end and fixed at the other, the incremental deflection under the applied load of 465 kN is calculated to be 7.5 mm (0.30 in); the total deflection at the end of the second step is therefore 14.5 mm (0.57 in).

For the third step of analysis, following the same logic as above, the plastic hinges that now exist at points A and B are replaced by hinges in a new modified structure, as shown in Figure 4.2i. The incremental moment diagram resulting from this third analysis is shown in Figure 4.2j, and these moments must be compared with the capacities remaining at the end of step 2 along the structural member. In this case, the incremental moment M_C'' needs to reach only $0.26M_p$ before a plastic hinge develops there. This corresponds to a value of P'' of 66 kN (14.8 kips). The resulting normalized incremental moment diagram is shown in Figure 4.2k, and the corresponding moment diagram at the end of the third analysis step (i.e., for an applied load of 1238 + 465 + 66 = 1769 kN) is shown in Figure 4.2l. The incremental deflection under the applied load of 66 kN is calculated to be 16.0 mm (0.63 in) for a total deflection of 30.5 mm (1.2 in) at the end of the third analysis step.

At this point, because three plastic hinges have developed in a structure having only two degrees of indeterminacy, a mechanism is formed; that is, the structure is unstable, and it will deform as a system of rigid-link members between the plastic hinges. Unrestricted plastic deformations will develop when this load is reached, so this condition is called the plastic collapse mechanism (or simply "plastic mechanism" or "collapse mechanism"). For many applications, knowledge of this maximum capacity is sufficient, but for some others, it is also necessary to know that the structure can remain stable for some level of plastic deformation beyond formation of this plastic mechanism, as will be seen later.

It is also conceivable that, eventually, at very large deformations, catenary action may develop and that even larger loads could be resisted. Although this would be possible if members and their connections in structures could resist the large catenary-induced tension forces and allow such a large-displacement mechanism to develop in a stable manner (which is rarely the case), this type of behavior is beyond the scope of simple plastic theory defined by the assumption stated in the previous section.

Although the step-by-step method requires time-consuming calculations, it is the only suitable method if one wishes to know the load-deflection or moment-rotation relationships at some specific point along the structural member, over the entire loading history.

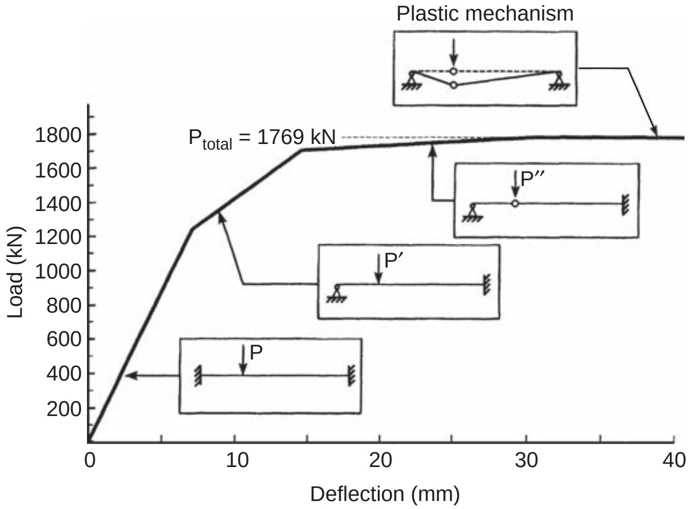

Figure 4.3 History of load versus deflection at load point for structure shown in Figure 4.2.

For instance, as a result of the above example, a complete load-deflection curve can be drawn, as shown in Figure 4.3. This illustrates well the changes in structural stiffness that occur at the formation of plastic hinges. It is notable that, in this example, the load that produces the plastic collapse mechanism is 43% larger than the maximum load permitted by elastic structural analysis methods (i.e., step 1 results), which typically do not account for the redistribution of load possible after formation of the first plastic hinge. The ratio of the load at the formation of the plastic collapse mechanism to the load at the formation of the first plastic hinge is frequently called the redistribution factor (equal to 1.43 in this example).

Finally, note that, for all but the simplest structures, the step-by-step method does not easily lend itself to parametric representation of results. The calculations for the above fixed-ended beam loaded by a single point load would have to be repeated if some numerical value were changed (such as span length or point load location). This is not necessarily the case for the other two methods described below.

4.2.2 Equilibrium Method (Statical Method)

The basic premise of the statical or equilibrium method is that any moment diagram in equilibrium with the externally applied loads, and for which the moment at any point along the structure does not exceed the specified member capacities, will provide an estimate of the plastic collapse load. The estimate will be the true collapse load if the moment diagram shows that a sufficient number of plastic hinges exist to form a plastic collapse mechanism; at worst, if not enough hinges are found, the calculated value of the collapse load is a conservative estimate.

A systematic description of the procedure applicable to any structure could be formulated as follows:

1. For any redundant structure, eliminate a number of internal redundancies (such as moment, shear, or axial points of resistance) to make the structure statically determinate.
2. Draw the moment diagram of the resulting statically determinate structure.
3. Draw the moment diagrams resulting from the application of each redundant action (i.e., those removed in step 1) onto the statically determinate structure.
4. Construct a composite moment diagram by combining the moment diagrams obtained in the two previous steps.
5. From the composite diagram, establish the equilibrium equations.
6. Establish at which points the moment diagram will reach the members' plastic capacities such that a sufficient number of plastic hinges will exist to form a plastic collapse mechanism and integrate this additional information into the equilibrium equations.
7. Solve for the plastic collapse load using the equilibrium equations.

As a good practice, it is worthwhile to check that the moments do not exceed M_p anywhere for the given resulting load, and that a collapse mechanism is indeed formed, although this is supposed to be ensured by step 6.

To demonstrate the effectiveness of this procedure, the same example problem presented in the previous section is reanalyzed using the statical method. Moreover, the solution is obtained in a parametric form before it is solved numerically.

The procedure is illustrated in Figure 4.4. In this example, as shown in Figures 4.4a to d, the two end moments are selected as the redundants, converting the fixed-ended beam into a statically determinate simply supported beam. This is an arbitrary choice because the moment and shear at midspan, for example, would have been an equally appropriate choice of redundants. The loading applied to this simply supported beam (Figure 4.4b) produces the moment diagram shown in Figure 4.4e; the redundant moments that load the same beam (Figures 4.4c and d) produce the moment diagrams shown in Figures 4.4f and g. The resulting composite moment diagram is shown in Figure 4.4h.

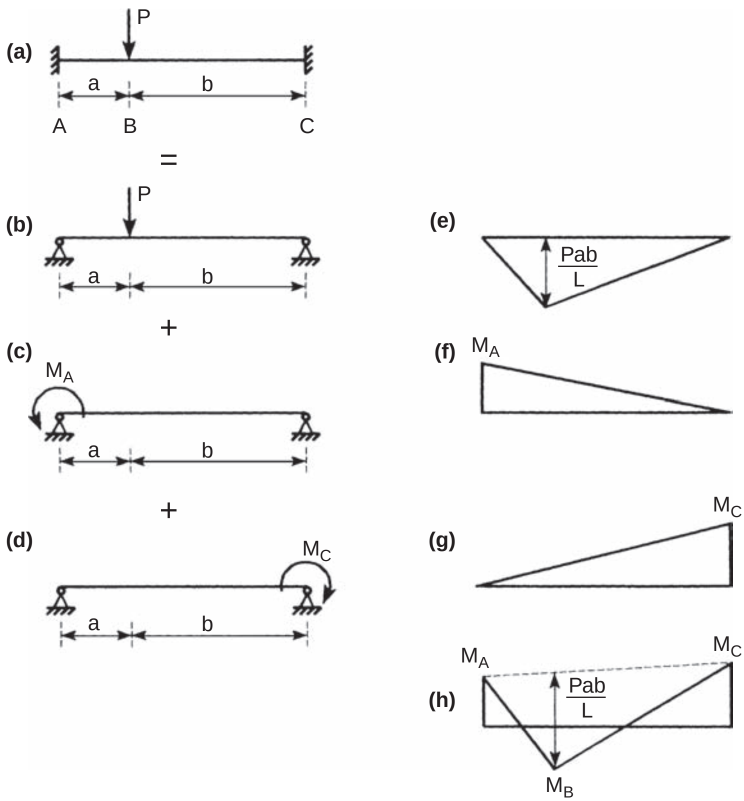

Figure 4.4 Example of plastic analysis by the equilibrium method: parametric representation.

In this case, a simple equilibrium equation can be written, based on the graphical information presented in Figure 4.4 and adopting the arbitrary sign convention that positive moments produce tension at the bottom of the beam:

$$M_B - \left(\frac{b}{L}\right)M_A - \left(\frac{a}{L}\right)M_C = \frac{Pab}{L} \tag{4.3}$$

with the constraints that:

$$|M_A| \le M_P \qquad |M_B| \le M_P \qquad |M_C| \le M_P \tag{4.4}$$

Three hinges are necessary in a beam having two degrees of indeterminacy to form a collapse mechanism. Therefore, observation of the moment diagram in Figure 4.4.h reveals that a plastic collapse mechanism would form if the values of M_A, M_B, and M_C all reach M_P. Hence, the equilibrium equation can be rewritten as:

$$M_P - \left(\frac{b}{L}\right)(-M_P) - \left(\frac{a}{L}\right)(-M_P) = M_P + \left(\frac{a+b}{L}\right)M_P = 2M_P = \frac{Pab}{L} \tag{4.5}$$

Solving for the applied load that would produce this collapse mechanism, and substituting numerical values from the previous example, gives:

$$P = \frac{2M_P L}{ab} = \frac{2(1263)(7)}{(2)(5)} = 1769 \text{ kN } (397.7 \text{ kips}) \tag{4.6}$$

which is the same result obtained previously, with the difference that a general solution has simultaneously been obtained for a beam having fixed ends and a point load applied anywhere along its length.

The difficulty of this method lies in step 6, which requires some judgment and experience, except for the simplest structures. The risk is to obtain a moment diagram that does not reach M_p at the number of locations necessary to produce a collapse mechanism. Such an oversight is unlikely to occur in simple structures; however, to illustrate its consequences without introducing an undue amount of calculations, the same simple example of Figure 4.4 is again used for this purpose. Although the incomplete plastic collapse mechanism is noticeable at first glance, it would not be so obvious in a more realistic and complex structure (such structures are presented in the next chapter).

Thus, assuming that all results of Figure 4.4 have again been obtained, but that, in step 6, the engineer erroneously assumes that plastic hinges will form only at points A and B, Eq. (4.3) can be rewritten as:

$$\begin{gathered} M_P - \left(\frac{b}{L}\right) - (-M_P) - \left(\frac{a}{L}\right)\left[-P\left(\frac{ba^2}{L^2}\right)\right] = \frac{Pab}{L} \\ M_P\left(1+\frac{b}{L}\right) = P\left[\frac{ab}{L} - \frac{a}{L}\left(\frac{ba^2}{L^2}\right)\right] \end{gathered} \tag{4.7}$$

where the elastic solution in a fixed-ended beam (CISC 2010, AISC 2011) has been substituted for M_C (i.e., $M_C = Pa^2b/L^2$), arbitrarily assuming that the results of elastic analysis would have been used at that location not identified as a plastic hinge. Solving this equation gives a maximum load, P, equal to 1651 kN (371 kips). This result gives a moment diagram that satisfies equilibrium, with moments equal to 1263 kN-m (932 k-ft) at points A and B, and 673 kN-m (497 k-ft) at point C, as shown in Figure 4.5a. This solution would therefore be an acceptable conservative estimate, per the equilibrium

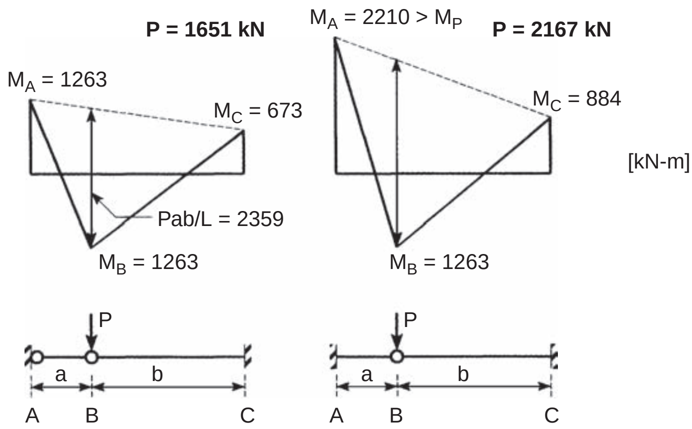

(a) Assuming plastic hinges at points A and B

(b) Assuming plastic hinge only at point B

Figure 4.5 Example of plastic analysis by the equilibrium method in which an insufficient number of plastic hinges is considered (incomplete plastic collapse mechanism).

method; however, note that a complete collapse mechanism does not form, which suggests that a better solution exists.

If it had been assumed that a plastic hinge would form only at point B, and if the elastic solutions were used for moments M_A and M_C (i.e., $M_A = Pb^2a/L^2$ and $M_C = Pa^2b/L^2$), a maximum load, P, of 2167 kN (487 kips) would have been obtained. However, that solution would not be acceptable according to the equilibrium method, because the resulting moment diagram would exceed M_p at point A, as shown in Figure 4.5b. This demonstrates the importance of step 6 in the above procedure.

The power of the statical method is that, for hand calculations, the above formal mathematical treatment can be greatly simplified through use of graphical solution methods. Two examples are provided in Figure 4.6, showing how a solution can rapidly be obtained when one graphically combines moment diagrams. In the first case, a uniformly distributed load is applied to a fixed-ended beam, whereas a two-span continuous beam is considered in the second case. In those cases, making all peaks of the composite moment diagram equal to M_p automatically ensures that equilibrium will be satisfied and that the moments will not exceed M_p anywhere along the span(s).

For the first example, working with absolute values, the graphical combination of moment diagrams gives:

$$\left(\frac{M_P}{2}\right)+\left(\frac{M_P}{2}\right)+M_p = 2M_P = \frac{\omega L^2}{8} \qquad \Rightarrow \qquad \omega = \frac{16M_P}{L^2} \tag{4.8}$$

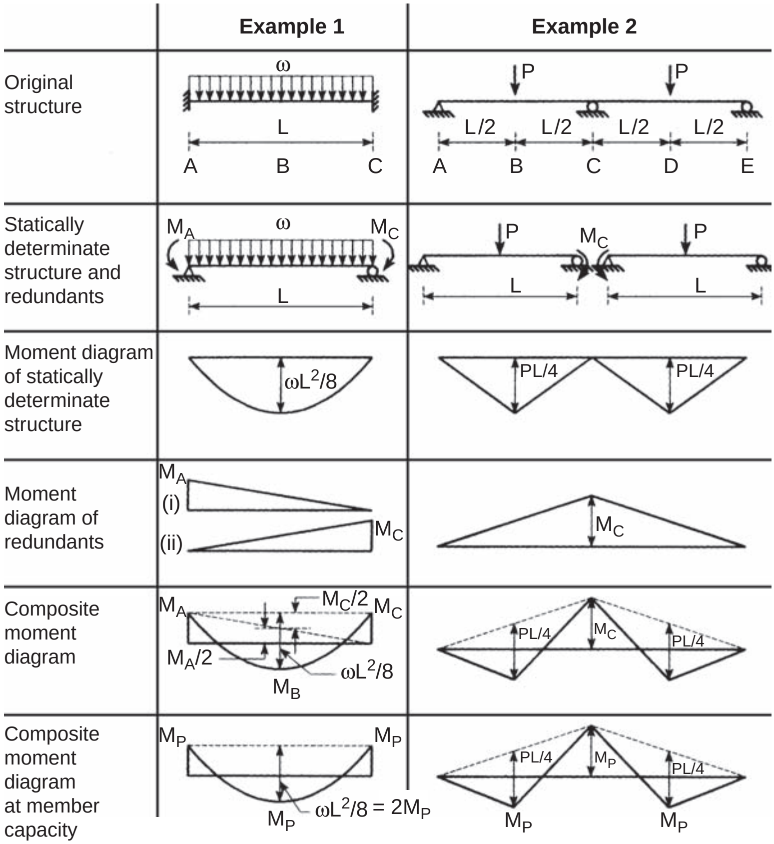

FIGURE 4.6 Example of graphical approach to solution of plastic analysis by equilibrium method.

Similarly, the composite moment diagram or the second example gives, for each span:

$$\left(\frac{M_P}{2}\right) + M_P = \frac{3}{2}M_P = \frac{PL}{4} \qquad \Rightarrow \qquad P = \frac{6M_P}{L} \tag{4.9}$$

These examples illustrate the effectiveness of the equilibrium method. However, for complex structures, a systematic approach suitable for computer implementation is needed. Such an approach is described in the next chapter.

4.2.3 Kinematic Method (Virtual-Work Method)

The basic premise of the kinematic, or virtual-work, method is that if the correct collapse mechanism is known (by either an educated guess or some of the techniques to be demonstrated later), the load that produces this plastic collapse mechanism is the exact value of the plastic collapse load. This collapse load is calculated by the virtual-work method considering only the plastic deformations from the rigid-link mechanism action. The drawback of this method is that incorrect estimates of the collapse mechanism will give unconservative results. Therefore, it is crucial to verify that the results obtained by the kinematic method produce moment diagrams that do not exceed at any point the plastic moment of the individual structural members.

In essence, once a plastic collapse mechanism has developed, the external work produced by the applied loads $W_{external}$ must be equal to the internal work produced at the plastic hinges $W_{internal}$. This can be generically expressed as follows:

$$\begin{aligned} W_{internal} &= W_{external} \\ \sum_{i=1}^{N} M_P \theta_i &= \sum_{j=1}^{N} P_j \delta_j + \int_{x=0}^{L} \omega(x)\, \delta(x)\, dx \end{aligned} \tag{4.10}$$

where θ_i is the plastic rotation at hinge i having a plastic moment M_{pi}, P_j and δ_j are applied loads, and deflection at point j, respectively, and $\omega(x)$ and $\delta(x)$ are expressions for the distributed applied load and deflections along the length of the structure, respectively.

The simplicity of this method is best illustrated by an example. The fixed-ended beam previously solved by the step-by-step and equilibrium methods is shown in Figure 4.7 along with an assumed collapse mechanism.

Using the same arbitrary sign convention as before (i.e., positive moments and positive rotations are those that produce tension on the bottom fiber of the beam) and the parameters defined in Figure 4.7, one can write the following work equations:

$$\begin{aligned} W_{internal} &= W_{external} \\ -M_P(-\theta) + M_P\left(\theta + \frac{a\theta}{b}\right) + (-M_P)\left(-\frac{a\theta}{b}\right) &= P(a\theta) \\ 2M_P\left(\frac{b+a}{b}\right)\theta &= P(a\theta) \\ \frac{2M_P L\theta}{b} &= P(a\theta) \\ \frac{2M_P L}{ab} &= P \end{aligned} \tag{4.11}$$

which is the same result obtained previously by the equilibrium method. Equilibrium is also checked parametrically in Figure 4.7.

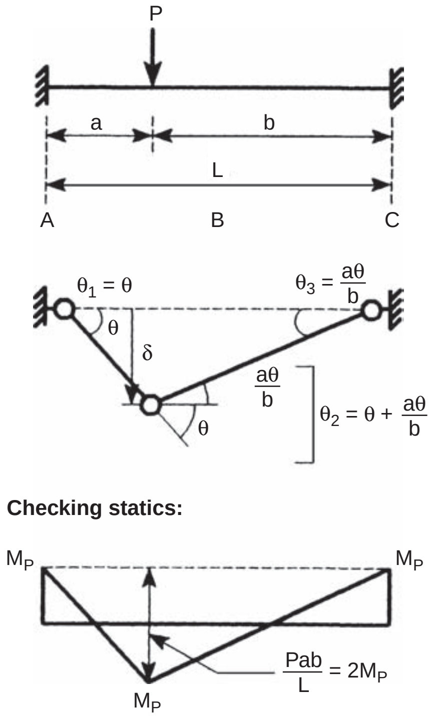

Figure 4.7 Example of plastic analysis by the kinematic method: parametric representation.

Note that moments are always of the same sign as their corresponding rotations; this observation is used advantageously to further simplify calculations in the remainder of this chapter.

Because three plastic hinges are needed to create a mechanism for this beam, it is relatively easy to guess the correct collapse mechanism. However, to illustrate how an incorrect solution can be identified, another (and obviously incorrect) collapse mechanism is considered for this same problem, as shown in Figure 4.8. Solving the work equation gives:

$$W_{internal} = W_{external}$$

$$M_P(1+2+1)\theta = P(a\theta)$$

$$4M_P\theta = P(a\theta) \tag{4.12}$$

$$\frac{4M_P}{a} = P$$

which is a larger collapse load than before because a is smaller than b. Two approaches are possible to verify whether equilibrium is satisfied.

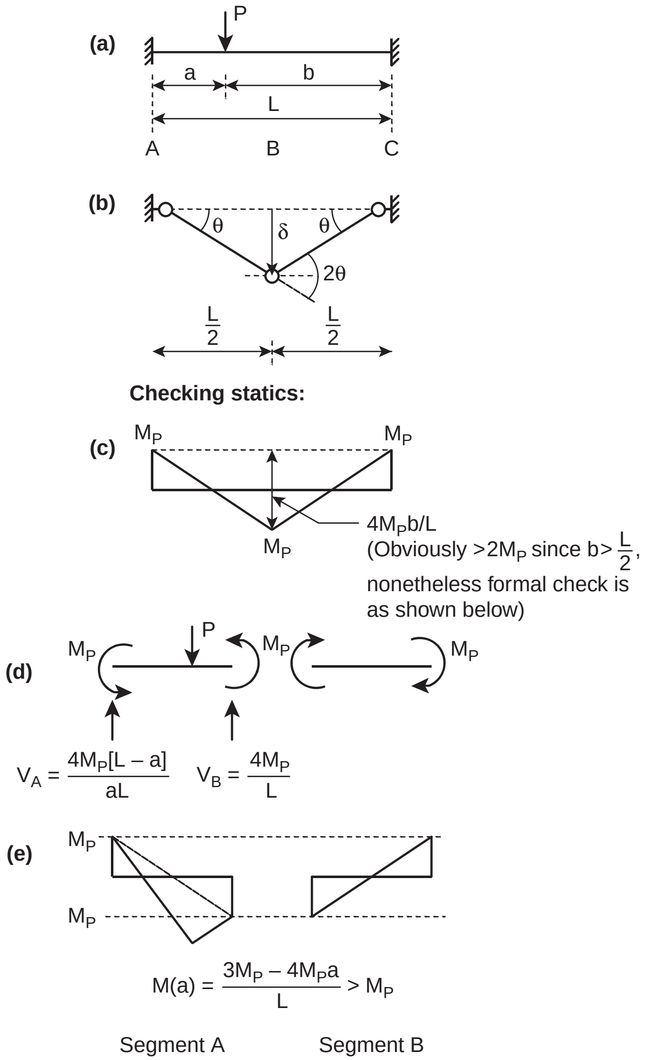

FIGURE 4.8 Example of plastic analysis by the kinematic method in which an incorrect plastic collapse mechanism is considered.

First, by graphical combination of individual bending moments, as shown in Figure 4.8c, it can be observed that the maximum positive moment exceeds M_p under the applied load of P equal to $4M_p/\alpha$. Second, for more complex structures for which the graphical method may be difficult to apply, equilibrium can be checked through use of free-body diagrams.

Indeed, the knowledge that a moment equal to M_p exists at each plastic hinge provides the necessary additional information to check equilibrium as if each segment of the structure's collapse mechanism were statically determinate. This is demonstrated in Figure 4.8d, in a parametric manner for this example, although in most cases this would be best done numerically. For this problem, two segments must be checked. The right segment satisfies equilibrium as the moment diagram varies linearly between $+M_p$ and $-M_p$ and therefore does not exceed M_p anywhere. For the left segment, the applied load [from the solution presented in Eq. (4.12)] and the two end moments ($=M_p$) are known. Shears at each end of that segment must first be calculated; results are shown in Figure 4.8d. From those results, the moment diagram in that segment is drawn, as shown in Figure 4.8e, and observed to exceed M_p locally. In fact, the maximum moment under the applied load is:

$$\begin{aligned} M_a &= -M_P + V_A a \\ &= -M_P + \left[\frac{4M_P(L-a)}{aL}\right]a \\ &= 3M_P - 4M_P\left(\frac{a}{L}\right) > M_P \text{ since } a \le \frac{L}{2} \end{aligned} \tag{4.13}$$

Therefore, this assumed plastic collapse mechanism is not acceptable, and other mechanisms must be tried until a satisfactory solution is found. Unless the solution obtained by the kinematic method also satisfies equilibrium, the results obtained shall not be used because they are unconservative. The degree of unconservatism is quite variable, depending mostly on how far the trial plastic mechanism is from the correct solution. However, although the method is a trial-and-error procedure, observation of the moment diagram obtained in a given attempt usually provides guidance to better locate the plastic hinges in the subsequent trial. For example, the resulting moment diagram in Figure 4.8 suggests that moving the plastic hinge from midspan to under the applied load (a point of maximum moment) would provide a better solution. In most cases, with experience, the correct collapse mechanism for a given structure can be found in only a few trials, sometimes even at the first or second attempt.

To provide some additional examples, the same two problems analyzed previously by the statical method (see Figure 4.6) are reanalyzed using the kinematic method. Results are shown in Figure 4.9. The same answers are obtained, thus showing the power of the kinematic method. A systematic description of the kinematic procedure, needed to handle more complex structures, is postponed to Section 4.4 because it relies on some additional concepts that must first be presented. Indeed, in the previous examples, a number of important observations have indirectly introduced some important theorems of plastic analysis that must now be presented more formally.

	Example 1	Example 2
Structure	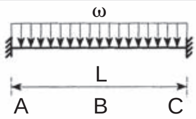	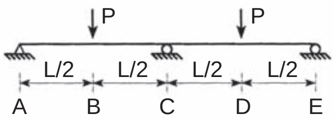
Collapse mechanisms	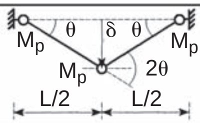	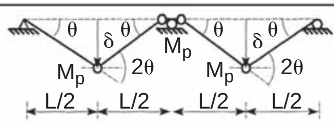
Internal work	$(1 + 2 + 1)M_p\theta = 4M_p\theta$	$(2 + 2 + 2)M_p\theta = 6M_p\theta$
External work	$\omega L\left[\left(\frac{L}{2}\right)\left(\frac{1}{2}\right)\theta\right] = \frac{\omega L^2}{4}\theta$	$2\left[P\left(\frac{L}{2}\right)\theta\right] = PL\theta$
Plastic collapse load	$\omega = \frac{16M_p}{L^2}$	$P = \frac{6M_p}{L}$
Static check	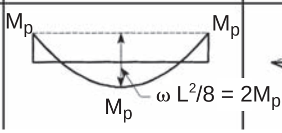	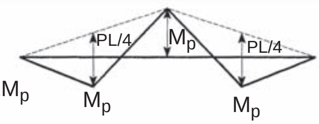

FIGURE 4.9 Example of solution of plastic analysis by the kinematic method.

4.3 Theorems of Simple Plastic Analysis

The previous examples have illustrated that, in any plastic analysis problem, three conditions must be satisfied:

- Equilibrium must exist between the externally applied loads and the internal actions that resist these loads.
- The calculated moment at any cross-section must never exceed the plastic moment at that cross-section.
- A valid plastic collapse mechanism must develop when the plastic collapse load is reached.

Except for the step-by-step analysis method, which painstakingly follows the progression of yielding under increasing load to ensure that no plastic or elastic condition is violated, the above examples demonstrate that an expedient plastic analysis procedure is possible when one operates on only one or two of the above three conditions, checking the other(s) only after a result is obtained. The implications from this approach are described in the following sections.

4.3.1 Upper Bound Theorem

When the kinematic method is used, a collapse mechanism is assumed and the collapse load is computed based on a plastic energy balance principle, as expressed by the virtual-work equation. In the computation of that collapse load, no attention is paid to whether the moment diagram exceeds the plastic moment resistance, M_p, at any cross-section (other than as a checking step after a solution is obtained), so the estimated collapse load is greater than, or at best equal to, the true solution. Therefore, in the search for the correct answer, any value calculated during a given trial is an upper bound to the true solution.

From this observation, the upper bound theorem can be formulated as follows:

> A collapse load computed on the basis of an assumed mechanism will always be greater than or equal to the true collapse load.

4.3.2 Lower Bound Theorem

When the statical method is used, a moment diagram is drawn to satisfy equilibrium. Because no attention is paid to whether a valid plastic collapse mechanism develops (again, other than by checking after a solution has been reached), the estimated collapse load is less than, or at best equal to, the true solution. Therefore, any value calculated during a given trial is a lower bound to the true solution, and a lower bound theorem can be stated as follows:

> A collapse load computed on the basis of an assumed moment diagram in which the moments are nowhere greater than M_p is less than or equal to the true collapse load.

4.3.3 Uniqueness Theorem

When all three plastic conditions are satisfied, both methods will give the correct and unique answer. Hence, the lower bound and upper bound meet at the exact solution, which allows the formulation of the following uniqueness theorem:

> The true collapse load is the one that has the same upper and lower bound solution.

Although the above three theorems may at first look trivial, they are most useful for plastic analysis, as well as for general structural engineering applications. In fact, many engineers have unknowingly used lower bound approaches in structural design by always giving preference to solutions that satisfy equilibrium rather than to solutions that satisfy compatibility of deformations.

4.4 Application of the Kinematic Method

The above examples demonstrate that although the kinematic method is a powerful tool to determine the plastic collapse mechanism, the risk of finding an unconservative solution exists, particularly for more complex structures in which the number of possible mechanisms can be quite large. Therefore, to eliminate this risk, the following procedure must be systematically followed for the kinematic method:

1. For any structure, clearly identify where plastic hinges can potentially develop to produce possible plastic collapse mechanisms. Hinges usually form at load points, supports, corners of frames, etc.
2. Define the basic independent mechanisms and possible combined collapse mechanisms.
3. Solve the work equations for all plastic collapse mechanisms. The best estimate of the true solution is provided by the mechanism that gives the lowest value for the collapse load.
4. Check whether the moment diagram for that best estimate exceeds the plastic moments of individual numbers at any point. If it does not, the true solution has been found; otherwise, return to step 2 because a potential plastic collapse mechanism has been overlooked.

A key step in the above procedure is the definition of basic independent and combined mechanisms; this deserves additional explanation, as provided in the following sections.

4.4.1 Basic Mechanism Types

For beam and column frame type structures, four basic independent mechanisms constitute the building blocks from which the most complex plastic collapse mechanisms can be constructed and understood. They are the beam, panel, joint, and gable mechanisms. Some tentative definitions are provided hereunder, with the understanding that these are purposely broad and intended solely to help the reader develop an appreciation of the concepts. In some of the more complex examples presented in this book, "gray areas" of interpretation exist because some structures, or parts of structures, can be broken down into basic independent mechanisms in more than one way.

4.4.1.1 Beam (Member) Mechanism

A beam mechanism (sometimes called member mechanism) can be defined as any mechanism produced by loads applied between the

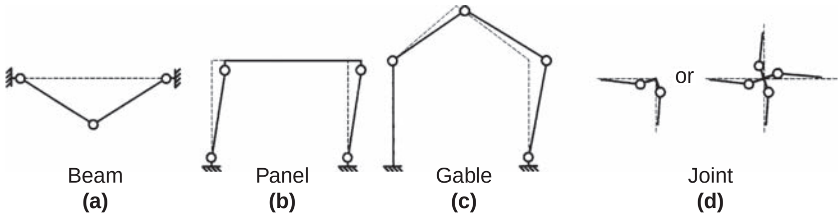

FIGURE 4.10 Examples of basic independent mechanisms.

ends of a member (point loads or distributed loads) that does not require displacement of the ends of that member (Figure 4.10a). Note that all examples presented in this chapter so far have involved only beam mechanisms.

4.4.1.2 Panel (Frame or Sidesway) Mechanism

A panel mechanism (also known as a frame mechanism or sidesway mechanism) is produced by the racking action of a square panel; members displace while remaining parallel, and plastic hinges form only at the ends of members (Figure 4.10b).

4.4.1.3 Gable Mechanism

Gables (sometimes called portal frames) are special frames having pitched roofs that have been widely used in industrial construction. As shown in Figure 4.10c, the gable mechanism is defined by the downward movement of the apex of the roof, accompanied by a sideways displacement of only one of the vertical supporting members. If one of the supporting members is conveniently kept vertical throughout the development of the plastic mechanism, the various angles of rotation involved in this mechanism can be more easily related to each other. However, in essence, the gable mechanism requires only that all members of the gable change angles with respect to each other.

4.4.1.4 Joint Mechanism

A joint mechanism can be defined by the rotation of a joint, with plastic hinges being developed in all members framing into that joint (Figure 4.10d). Thus, a joint mechanism involves rotation only locally at the joint and does not otherwise affect the geometry of the structure. Although this mechanism does not produce any external work, it is frequently a convenient mechanism to reduce internal work when one is trying to find the plastic collapse mechanism of a complex structure.

4.4.2 Combined Mechanism

The objective of the kinematic method is to find the lowest possible collapse load, so it could be advantageous for some structures to combine the basic mechanisms in ways that would reduce the amount of internal work, increase the amount of external work, or both. The examples in the following sections illustrate this concept.

4.4.2.1 Simple Frame Example

A frame is loaded by both a lateral load, H, and a gravity load, P, as shown in Figure 4.11a. For the purpose of this example, all frame members have the same plastic moment capacity, M_p. Two solution paths are possible, depending on whether one wishes to consider the joint mechanisms. When only two members frame into a joint, the basic joint mechanism does not serve a useful purpose and can usually be neglected (or implicitly considered, depending on the perspective). The simplest solution in this case is to neglect the joint mechanism. As a result, in this example, two basic independent mechanisms are possible: a beam and a panel, as shown in Figures 4.11b and c.

Although it happens at a floor level, the beam mechanism is essentially the same one considered in previous examples, and equating internal work to external work would give results identical to those already presented in Eq. (4.11). For the panel mechanism of Figure 4.11c, the virtual-work equation gives:

$$\begin{aligned} W_{internal} &= W_{external} \\ M_p(1+1+1+1)\beta &= H(h\beta) \\ 4M_p\beta &= H(h\beta) \\ \frac{4M_P}{h} &= H \end{aligned} \tag{4.14}$$

Although it is customary to use θ for all mechanisms, as is done throughout in this book, for the present discussion only, different parameters are used to identify the plastic rotations of the two different basic mechanisms.

In this simple example, there is only one possible way to combine basic independent mechanisms. The objective is to search for the lowest collapse load (by either increasing the external work or decreasing the internal work) and, in this example, combining the two basic mechanisms increases the amount of external work. Moreover, if β is made equal to θ, the plastic hinge rotations at the left corner of that frame cancel each other, but this is somewhat offset by a greater

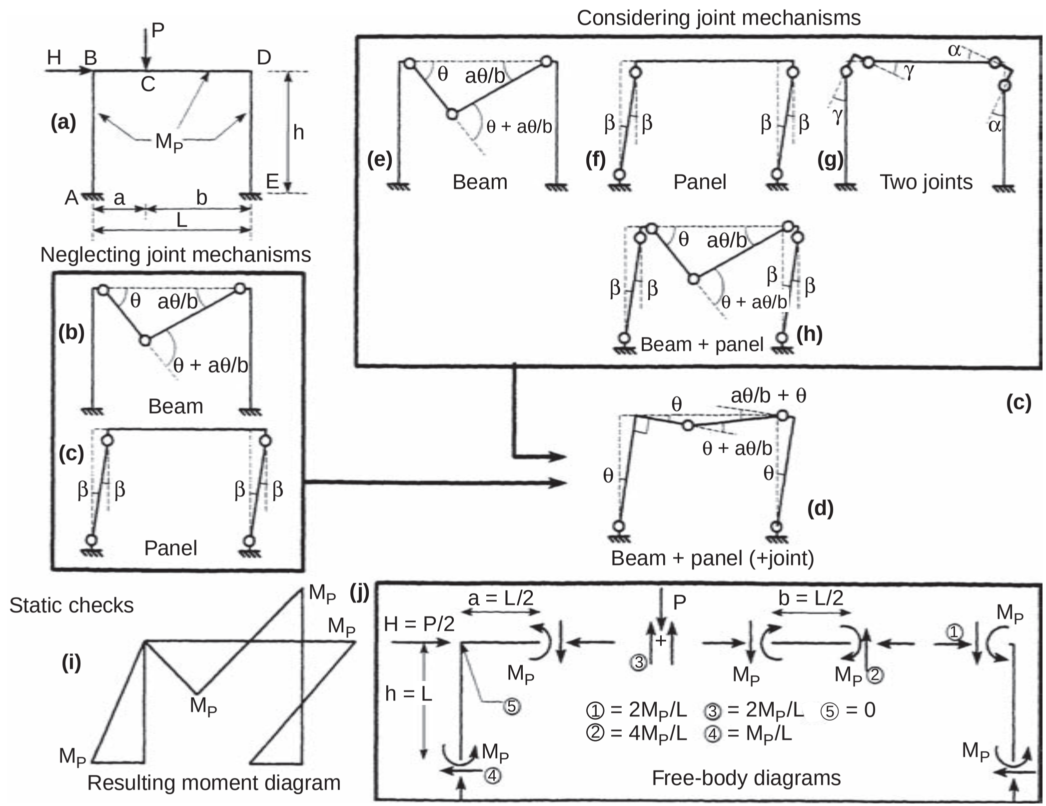

Figure 4.11 Search for plastic collapse mechanism in a simple frame.

plastic rotation at the right corner of that frame. The resulting combined mechanism is shown in Figure 4.11d. The virtual-work equation becomes:

$$
\begin{aligned}
W_{internal} &= W_{external} \\
M_P\left(1+1+\frac{a}{b}+1+\frac{a}{b}+1\right)\theta &= H(h\theta)+Pa\theta \\
\left(4+2\frac{a}{b}\right)M_P\theta &= (Hh+Pa)\theta \\
\left(4+2\frac{a}{b}\right)M_P &= (Hh+Pa)
\end{aligned}
\tag{4.15}
$$

No conclusions can be reached with results expressed in this parametric form. However, if a and b are equal, h is equal to L, and H is equal to half of P, the above expression can be simplified to:

$$
\begin{aligned}
6M_P &= \frac{PL}{2}+\frac{PL}{2} = PL \\
\frac{6M_P}{L} &= P
\end{aligned}
\tag{4.16}
$$

The corresponding results for the basic independent mechanisms are:

$$
\begin{aligned}
\frac{2M_PL}{ab} &= P \\
\frac{2M_PL}{\left(\frac{L}{2}\right)\left(\frac{L}{2}\right)} &= \frac{8M_P}{L} = P
\end{aligned}
\tag{4.17}
$$

for the beam mechanism, and

$$
\begin{aligned}
\frac{4M_P}{h} &= H \\
\frac{4M_P}{L} &= \frac{P}{2} \\
\frac{8M_P}{L} &= P
\end{aligned}
\tag{4.18}
$$

for the panel mechanism. These two values of P are both higher than the plastic collapse load for the combined mechanism. By virtue of the upper bound theorem, the combined mechanism is closer to the true solution. At this point, it is worthwhile to draw the moment diagram and check whether the plastic moments are exceeded anywhere. The results are shown in Figure 4.11i. Figure 4.11j shows how this result is obtained when the structure is broken into free-body diagrams between the plastic hinges. Numbers in circles indicate the sequence in which the calculated values were obtained to complete the moment diagram. As shown in Figure 4.11i, the plastic moment is not exceeded, and the plastic collapse load calculated for the combined mechanism is therefore the true solution.

As mentioned earlier, for joints connecting only two framing members, the joint basic mechanisms can be neglected. However, until some experience is gained with the kinematic method, there is a temptation to conduct plastic analysis as systematically as possible and therefore to include the joint basic mechanisms in the solution process even when this is not necessary. Therefore, Figures 4.11e to 4.11h illustrate, as an alternative solution, how joint mechanisms can be included as part of the solution process. In that solution, the beam and panel basic independent mechanisms remain the same as before, while two joint mechanisms are possible (as shown in Figure 4.11g). Again, different parameters are used to identify the plastic rotations of the two different basic mechanisms. A combined beam and panel mechanism is shown in Figure 4.11h. The virtual-work equation for that combined mechanism would give:

$$W_{internal} = W_{external}$$
$$\frac{2M_P L}{b}\theta + 4\ M_P\beta = Hh\beta + Pa\theta \tag{4.19}$$

which is unsolvable because β is unrelated to θ. Although both angles could be arbitrarily assumed to be equal, this decision could not be justified solely based on the shape of the combined mechanism. However, Figure 4.11h clearly illustrates that with the joint mechanism, one could eliminate three plastic hinges by rotating both joints by θ. At that point, it becomes justifiable to make β, θ, γ, and α equal because doing so reduces the amount of internal work by eliminating plastic hinges. The resulting combined mechanism, shown in Figure 4.11d, is obviously the same.

Finally, depending on the relative values of a, b, h, P, and H, the collapse mechanism giving the lowest plastic collapse load may change. For example, if b is equal to a, h is equal to $L/4$, and H to $P/4$, the beam collapse mechanism will give the lowest value, namely, $9.8M_p/L$ compared with $64M_p/L$ and $10.7M_p/L$ for the panel and combined mechanisms, respectively. Hence, engineers who frequently work with the same frames would benefit from conducting parametric studies to investigate which conditions provide the most cost-effective design. Incidentally, structural optimization using plastic design has received a considerable attention in the past, but is beyond the scope of this book.

4.4.2.2 Two-Span Continuous Beam Example

Frequently, more than one basic independent mechanism of a given type is possible in a structure or structural member. For example, for the two-span continuous beam of Figure 4.12, there are three possible beam

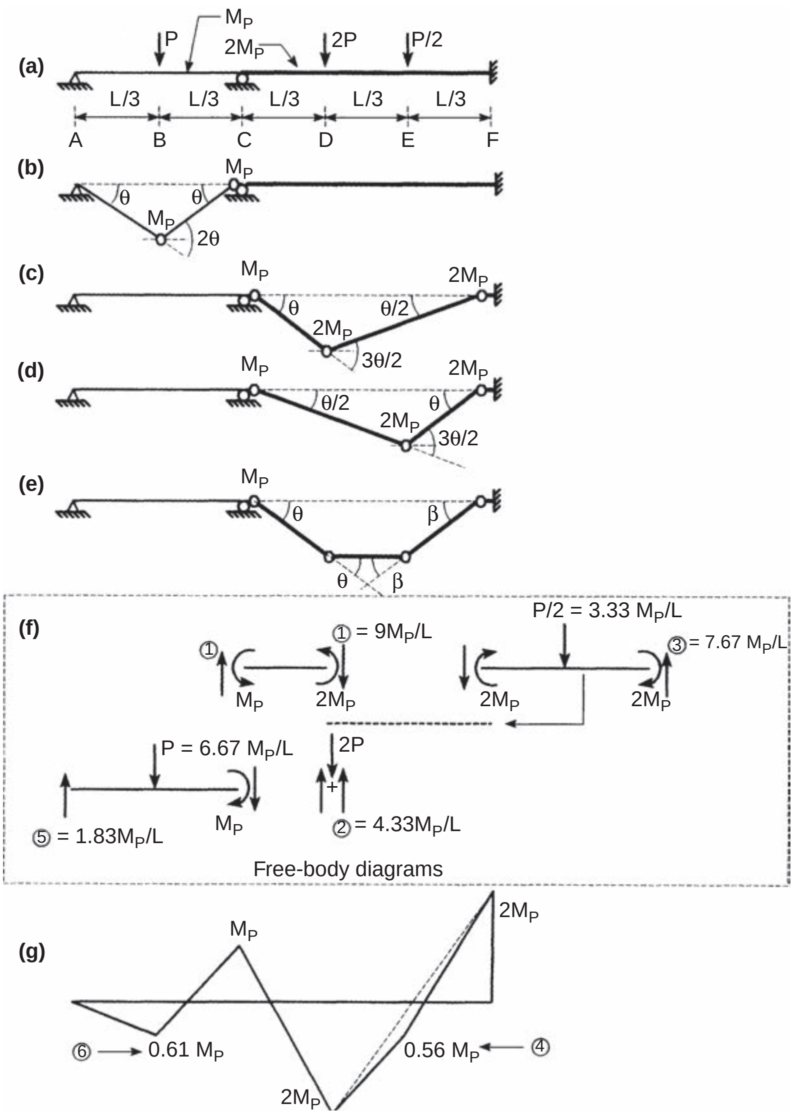

Figure 4.12 Search for plastic collapse mechanism in a two-span continuous beam.

mechanisms: one acting on the left span and two on the right span. For the left span, the plastic collapse load is given by Figure 4.12b:

$$
\begin{aligned}
W_{internal} &= W_{external} \\
M_p(0+2+1)\theta &= P\left(\frac{L}{3}\right)\theta \\
3M_p\theta &= \frac{PL\theta}{3} \\
\frac{9M_p}{L} &= P
\end{aligned}
\tag{4.20}
$$

Notice that the real hinge at the left end of that span rotates without producing plastic work. It would therefore be a mistake to include it in the internal work formulation.

The two-beam mechanisms possible on the right span are shown in Figures 4.12c and d. For the first of these two mechanisms, the work equation becomes:

$$
\begin{aligned}
W_{internal} &= W_{external} \\
M_p\theta + 2M_p(1.5+0.5)\theta &= 2P\left(\frac{L}{3}\right)\theta + \left(\frac{P}{2}\right)\left(\frac{L}{3}\right)\left(\frac{\theta}{2}\right) \\
5M_p\theta &= \frac{3PL\theta}{4} \\
\frac{20M_p}{3L} &= \frac{6.67M_p}{L} = P
\end{aligned}
\tag{4.21}
$$

Here, one must be careful to correctly locate the left hinge of that plastic mechanism immediately to the left of the middle support, that is, in the weaker member having a resistance of M_p instead of in the stronger member having a resistance of $2M_p$. Indeed, moment equilibrium at that interior support would reveal that it is impossible to develop $2M_p$ there. This indirectly accounts for the possible joint mechanism, as described earlier. Furthermore, as shown in the formulation of that equation, one must also include the external work contribution produced by all loads that displace in the collapse mechanism.

Following a similar approach (Figure 4.12d), a plastic collapse load of $11M_p/L$ can be obtained for the second beam mechanism of that right span. Based on the above results, the lowest plastic collapse load is the one that produces the collapse mechanism shown in Figure 4.12c.

It would not be appropriate to combine two-beam mechanisms acting on the same span as shown in Figure 4.12e, for demonstration purposes. This erroneous combination results in a collapse mechanism having too many hinges; only three hinges are needed to produce a beam mechanism. As a result, the virtual-work equation cannot be solved, unless some arbitrary decision is made to relate β to θ, a decision for which no rational basis can be found. The only instances in which more plastic hinges than necessary to produce collapse should be acceptable is when two independent plastic collapse mechanisms are found to have the same plastic collapse load. Such an example was presented in Figure 4.9 (Example 2), and although the plastic deformations of the left and right spans cannot be related in that example either, this was not needed because the simultaneous formation of a mechanism in both spans was merely coincidental and did not result from a deliberate attempt to combine mechanisms in ways they should not be combined. Incidentally, collapse mechanisms that develop more plastic hinges than otherwise necessary (as in Example 2 of Figure 4.9) are called "overly complete plastic mechanisms."

Finally, to verify that the above result is the true solution, the structure is broken into free-body diagrams between the plastic hinges (Figure 4.12f), and statics is used to find the unknown actions and draw the moment diagram (Figure 4.12g). It is verified that this moment diagram nowhere exceeds M_p, which confirms that the true solution has been found.

4.4.2.3 Example of an Overhanging Propped Cantilever Beam

For part of the structure shown in Figure 4.13 adjacent to the fixed support, reinforcing cover plates are welded to the wide-flange beam. These locally increase the capacity of this beam from M_p to M_{pr}. The objective of this problem is to determine the length of the cover plate reinforcement (i.e., minimum value of x) needed to develop this value of M_{pr} and to calculate the resulting collapse load, P, when Q is equal to $0.25P$.

Using the kinematic method, three possible beam collapse mechanisms should be considered, as shown in Figure 4.13. In two cases, the cantilever tip load produces negative external work, thus increasing the collapse load compared with the case for which there is no tip cantilever load. If the parametric expressions for the first two mechanisms are equated, the required length of the cover plate reinforcement is equal to $0.12L$. The resulting plastic collapse load is $8.54M_p/L$. It can be checked that the third mechanism gives a plastic collapse load of $13.33M_p/L$, and consequently does not govern (although if Q is progressively increased, it would eventually become the governing failure more).

This problem is actually easier to solve with the equilibrium method, when one realizes that the effect of the cantilever is to provide a moment equal to $0.3QL$ over the simple support and that the desired failure mode should develop a plastic capacity of M_{pr} at the fixed end. The desired resulting moment diagram can directly be drawn, and by similar triangles, the point nearest the fixed support where M_p is reached can be determined; cover plates would therefore need to extend at least up to that point.

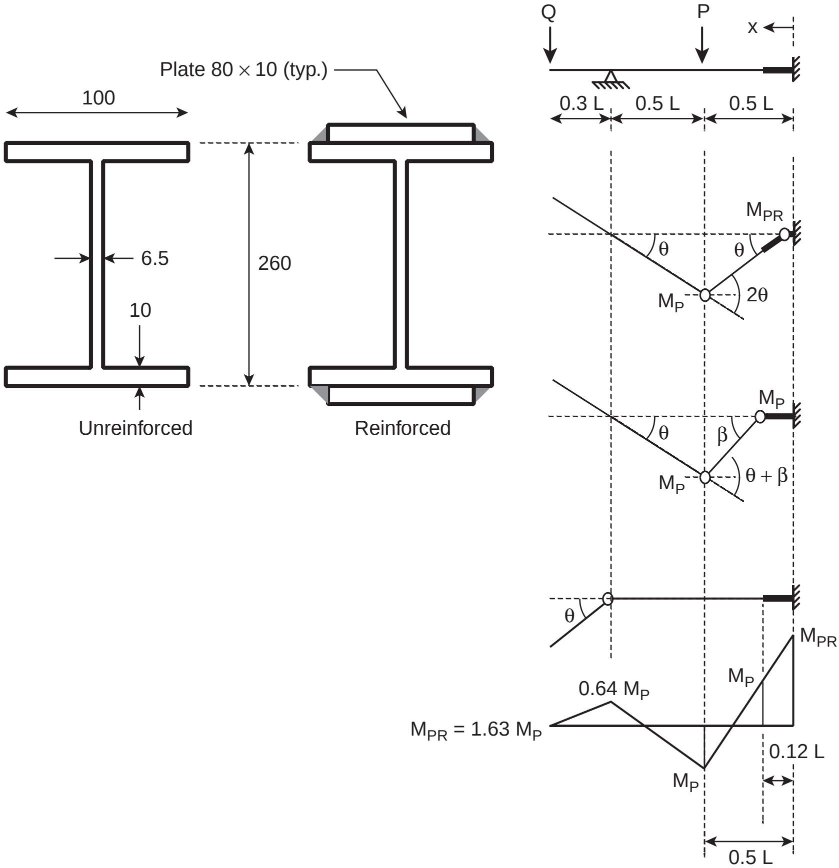

Figure 4.13 Search for plastic collapse mechanism in an overhanging propped cantilever beam.

4.4.3 Mechanism Analysis by Center of Rotation

For some types of mechanisms, it can be demonstrated that the articulated links of a resulting plastic collapse mechanism actually rotate around a point called the instantaneous center of rotation. This is generally the case for gable frames and other structures having inclined members that displace as part of the resulting plastic mechanisms. The center of rotation can be particularly useful to establish relationships between the angles of plastic rotation at the various hinges involved in the collapse mechanism. The following example gable frame demonstrates how this can be accomplished.

Here, loading and geometry of the gable frame are arbitrarily selected. Although the examples are treated parametrically, as would normally be done to allow further parametric sensitivity analyses or design optimization, it should be clear that other equations would need to be derived to study gable frames having different geometry or load conditions.

The key to a successful analysis using the center-of-rotation method lies in the ability to visually identify how the various rigid-link members involved in a given plastic mechanism rotate around various points. For example, for the gable frame and collapse mechanism shown in Figure 4.14, it is relatively easy to visualize that, during

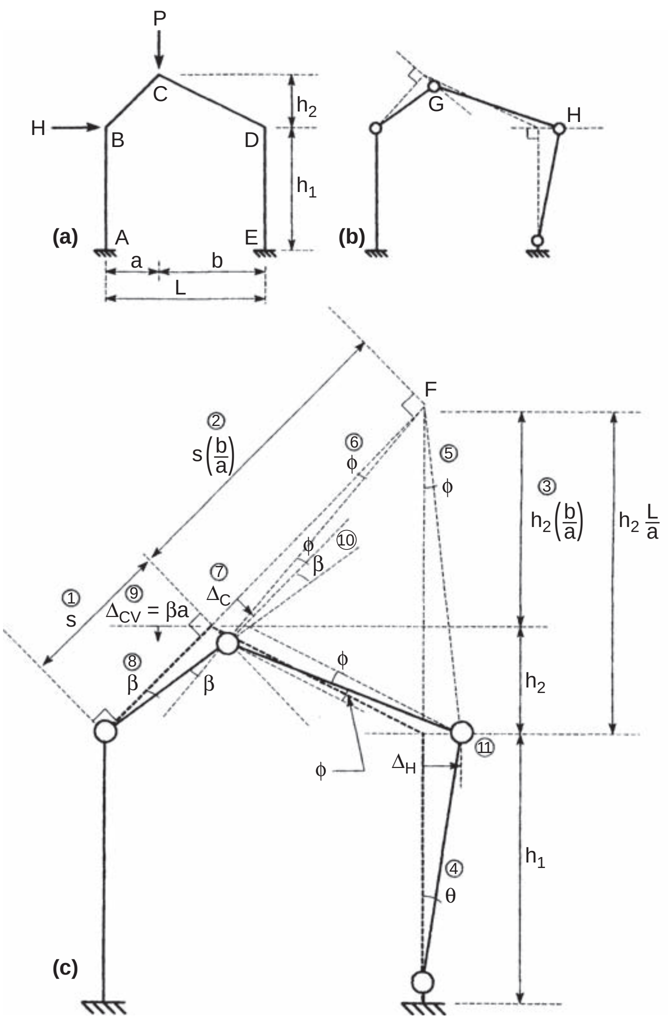

FIGURE 4.14 Basic plastic collapse mechanism in a gable using the center-of-rotation method.

development of the plastic mechanism, member BC rotates around point B and that member DE rotates around point E, and most will be able to draw Figure 4.14b without difficulty.

To determine the center of rotation of a member having two displacing ends (such as member CD) is a bit more challenging. First, the small displacement theory still holds, so each displacing joint must move perpendicularly to a line connecting the centers of rotation of the two members framing into that joint. Thus, joint C must move perpendicularly to lines BC and CF, which implies that point F is located somewhere on an extension of line BC. Likewise, extending this reasoning to joint D, point F must also be located on an extension of line DE. One can therefore schematically locate point F, in this case, at the intersection of the extension of lines BC and DE. To quantitatively find the location of that point, as well as the relative plastic rotation angles at each hinge, one must develop Figure 4.14c, starting from Figure 4.14b and take the following steps (numbered in Figure 4.14c):

1. Quantitatively locate point F. First, the known inclined distance from B to C is arbitrarily defined as s (step 1), and then the inclined (step 2) and vertical (step 3) distances from C to F are calculated from the properties of similar triangles.
2. Arbitrarily define one of the mechanism rotations as the reference angle θ (step 4), preferably where a joint does not displace (point E is chosen here), and calculate the angle at the other center of rotation that shares the same hinge. In this case, knowing that joint D displaces by Δ_H perpendicularly to member DE and line DF enables one to obtain the rotation angle ϕ at point F by the following (step 5):

$$\Delta_H = \theta h_1 = \phi\left(\frac{L}{a}\right)h_2 \qquad \Rightarrow \qquad \phi = \left(\frac{h_1}{h_2}\frac{a}{L}\right)\theta \tag{4.22}$$

3. Realizing that all points displacing around this center of rotation will undergo the same rotation ϕ (step 6) and knowing that the joint C displaces by Δ_C perpendicularly to member BC and line CF (step 7), calculate the rotation angle β at point B by the following (step 8):

$$\Delta_C = \beta s = \phi\left(\frac{b}{a}\right)s \qquad \Rightarrow \qquad \beta = \left(\frac{b}{a}\right)\phi = \left(\frac{h_1}{h_2}\frac{b}{L}\right)\theta \tag{4.23}$$

4. Calculate the displacements in the directions parallel to the applied loads to be able to calculate the external work. In this example, Δ_{CV} is needed and it is equal to βa (step 9).

5. Calculate all remaining unknown plastic rotation angles. By simple geometry, this angle at point G is the sum of β and ϕ (step 10), and at point H, the sum of ϕ and θ (step 11).
6. Calculate the plastic collapse mechanism by the usual work equation. For this problem, this gives:

$$W_{internal} = W_{external}$$

$$M_P[\beta + (\beta + \phi) + (\phi + \theta) + \theta] = Pa\beta$$

$$2M_P(\beta + \phi + \theta) = Pa\left(\frac{h_1}{h_2}\frac{b}{L}\right)\theta \qquad (4.24)$$

$$2M_P\left[\frac{h_1}{h_2} + 1\right]\theta = \frac{Pab}{L}\left(\frac{h_1}{h_2}\right)\theta$$

$$\frac{2M_P(h_1 + h_2)L}{abh_1} = P$$

Further simplifications of such a result are usually possible once all geometric dimensions are related to a common parameter. For example, if $L = 2h_1$, $a = b = h_1$, and $h_1 = 4h_2$, the plastic collapse load becomes $10M_p/L$.

Another example of calculation of the instantaneous center-of-rotation is provided in Figure 4.15, this time for a combined beam-panel-gable mechanism, which is frequently the governing failure mode of gable frames. The same procedure described above can be followed, with the difference that the centers of rotation are now A, G, and F for the respective rigid-links ABC, CDE, and EF.

The key step of the entire procedure lies in the schematic determination of point G, located at the intersection of lines AC and EF (a common mistake made in solving such a problem is to extend line BC instead of line AC, which is incorrect because B is not a center of rotation in this case). Again, solving this problem parametrically following the same procedure gives the following equations:

$$\Delta_J = \theta h_1 = \phi\left[\left(\frac{2L}{a} - 1\right)h_1 + \frac{h_2 L}{a}\right] = \phi h^* \quad \Rightarrow \quad \phi = \left(\frac{h_1}{h^*}\right)\theta \qquad (4.25)$$

$$\Delta_C = \beta s = \phi\left(\frac{2L}{a} - 1\right)s = \phi s^* \quad \Rightarrow \quad \beta = \left(\frac{s^*}{s}\right)\phi = \left(\frac{s^*}{s}\frac{h_1}{h^*}\right)\theta \qquad (4.26)$$

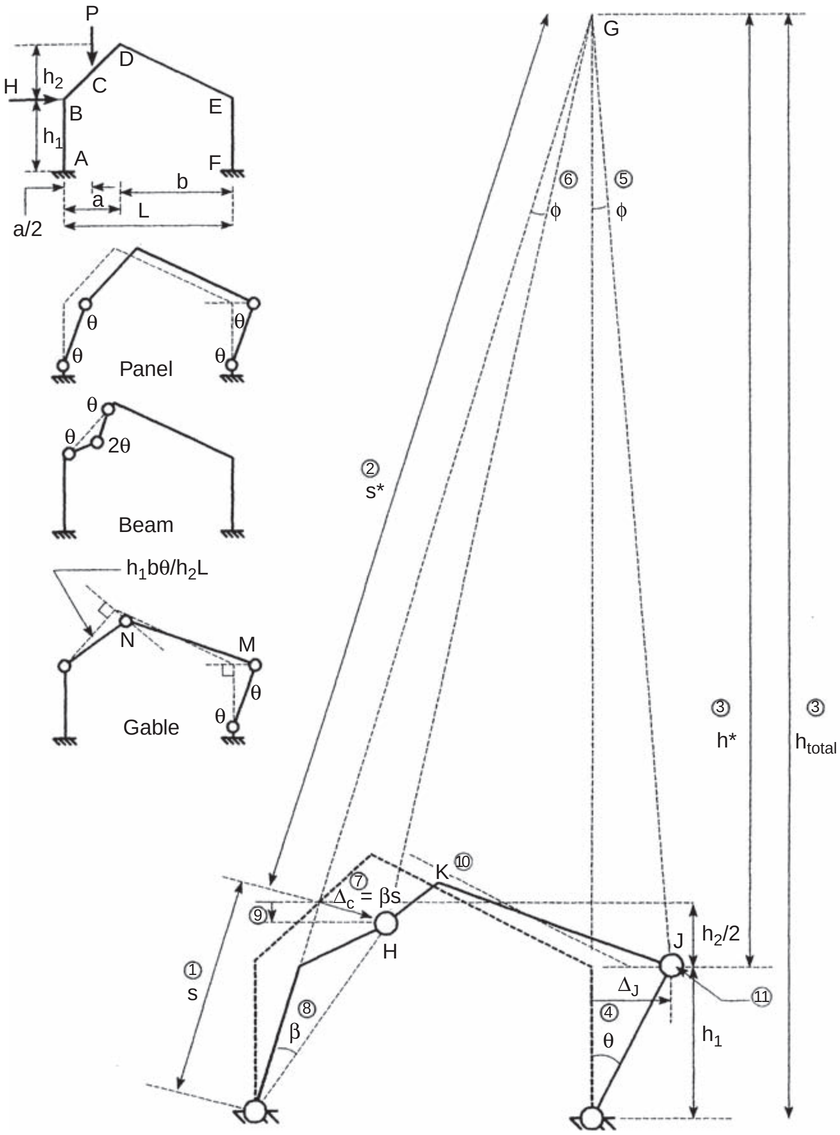

FIGURE 4.15 Combined beam-panel gable plastic collapse mechanism in a gable using the center-of-rotation method.

where all geometric parameters are defined graphically in Figure 4.15. Finally, from the work equation:

$$W_{internal} = W_{external}$$
$$M_P[\beta + (\beta + \phi) + (\phi + \theta) + \theta] = P\left(\frac{a}{2}\right)\beta + Hh_1\beta \tag{4.27}$$
$$2M_P\left[\left(\frac{s^*}{s}\frac{h_1}{h^*}\right) + \left(\frac{h_1}{h^*}\right) + 1\right]\theta = \left(\frac{Pa}{2} + Hh_1\right)\left(\frac{s^*}{s}\frac{h_1}{h^*}\right)\theta$$

Further simplifications are possible, if a relationship between P and H is established. For example, if $L = 3l$, $a = 2l$, $b = l$, $h_1 = 2l/3$, $h_2 = l$, and $H = P$, the plastic collapse load for this structure becomes $87M_p/20l$.

A comprehensive treatment of the plastic analysis and design of gable frames is beyond the scope of this book. However, the plastic analysis, design, and optimization of these frames, even including the effect of beam haunches at the eaves and apex, has been the subject of extensive study in the past, and the interested reader will easily find valuable information on that topic in the literature (e.g., Horne and Morris 1981).

Finally, note that the center-of-rotation method is not limited exclusively to gable frames or structures having inclined members. In fact, the combined plastic collapse mechanism of the regular frame shown in Figure 4.11 can also be analyzed by the center-of-rotation method. However, that method is obviously more tedious, so it is advisable to avoid it for regular frames that can be easily analyzed by other ways.

4.4.4 Distributed Loads

Distributed loads can be easily and directly considered when one is conducting plastic analysis by the equilibrium method, but a special treatment is sometimes necessary when one is using the kinematic method. The added difficulty arises from the fact that the kinematic method requires the assumption of a plastic mechanism and, therefore, identification of the possible plastic hinge locations. This is relatively easy in structures loaded by point loads, but sometimes far less obvious in members subjected to distributed loading. In accordance with the upper bound theorem, the true solution can be obtained only if the correct plastic mechanism is found, so some strategies must be adopted to expediently overcome this added complication.

Three approaches are commonly used to handle the effects of distributed loads:

- Exact analytical solution
- Iterative solution
- Equivalent load-set (or replacement loads) solution

4.4.4.1 Exact Analytical Solution

As the name implies, the exact analytical method requires direct calculation of the exact plastic hinge locations. Therefore, the virtual-work equation is first formulated parametrically, as a function of the unknown plastic hinge locations. Then, from the knowledge that the true solution is the one that gives the lowest plastic collapse load (i.e., upper bound theorem), one obtains the corresponding plastic hinge locations by setting the first derivative of this parametric equation to zero.

Some classic solutions are shown in Figure 4.16. For example, for the propped cantilever of Figure 4.16a, assuming that a plastic hinge will form at a distance x from the fixed support (as shown in Figure 4.16d), the work equation could be written as follows:

$$
\begin{aligned}
W_{internal} &= W_{external} \\
2M_p\theta\left(\frac{L}{L-x}\right)+2M_p\theta\left(\frac{x}{L-x}\right) &= \omega L\theta\left(\frac{x}{2}\right) \\
2M_p\theta\left(\frac{L+x}{L-x}\right) &= \omega L\theta\left(\frac{x}{2}\right) \\
\frac{4M_P}{L^2}\left[\frac{l}{k}\left(\frac{l+k}{l-k}\right)\right] &= \omega \qquad \text{if} \qquad x = kL
\end{aligned}
\tag{4.28}
$$

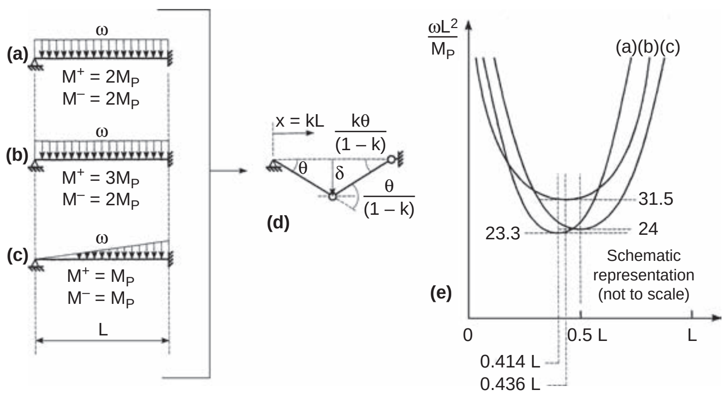

FIGURE 4.16 Plastic collapse mechanism of some beams subjected to distributed loads using exact analytical solution.

The first derivative of the work equation, with respect to x (or k according to the above substitution of variables), becomes:

$$\frac{\partial\omega}{\partial x} = \frac{\partial\omega}{\partial k} = 0 = \frac{(1+k)(-1)}{(1-k)(k)^2} + \frac{-(1+k)(-1)}{(1-k)^2(k)} + \frac{1}{(1-k)(k)}$$

$$0 = \frac{k^2+2k-1}{(1-k)^2(k)^2} \tag{4.29}$$

$$0 = k^2+2k-1 \qquad \text{if} \qquad (1-k)^2(k)^2 \neq 0$$

From the roots of the above equation, $k = 0.4142$, the plastic hinge location is determined to be located at $x = 0.4142L$. The corresponding plastic collapse load is $\omega = 23.31M_p/L^2$.

In Figure 4.16b, the same propped cantilever is considered, with the difference that the positive plastic moment is larger than the negative plastic moment, as would typically be the case in a composite floor beam. Following the same procedure as above:

$$W_{internal} = W_{external}$$

$$3M_p\theta\left(\frac{L}{L-x}\right) + 2M_p\theta\left(\frac{x}{L-x}\right) = \omega L\theta\left(\frac{x}{2}\right)$$

$$\left(\frac{6M_pL+4M_px}{L-x}\right)\frac{1}{Lx} = \omega$$

$$\left(\frac{10M_pL-4M_pL+4M_px}{L-x}\right)\frac{1}{Lx} = \omega \tag{4.30}$$

$$\left(\frac{10M_pL}{Lx(L-x)} - \frac{4M_p}{Lx}\right) = \omega$$

$$\frac{2M_p}{L^2}\left(\frac{5}{k(1-k)} - \frac{2}{k}\right) = \omega \qquad \text{if} \qquad x = kL$$

Then, taking the first derivative of this parametric solution gives:

$$\frac{\partial\omega}{\partial x} = \frac{\partial\omega}{\partial k} = 0 = \frac{5(-1)}{(1-k)(k)^2} + \frac{5(-1)(-1)}{(1-k)^2(k)} - \frac{2(-1)}{(k)^2}$$

$$0 = \frac{2k^2+6k-3}{(1-k)^2(k)^2} \tag{4.31}$$

$$0 = 2k^2+6k-3 \qquad \text{if} \qquad (1-k)^2(k)^2 \neq 0$$

From the roots of the above equation, $k = 0.4365$, the plastic hinge location is determined to be exactly located at $x = 0.4365L$. The corresponding plastic collapse load is $\omega = 31.49M_p/L^2$.

Clearly, the parametric derivative can rapidly become complex to solve, even for the simple cases shown above, and it is sometimes more expedient to numerically search for the minimum solution. As a result, curves like those shown in Figure 4.16e can be generated, in which the collapse load mechanism values are plotted as a function of the plastic hinge position. Nonetheless, even when the minima search is performed numerically and graphically, obtaining a parametric work equation of the collapse mechanism sometimes remains the most tedious aspect of the exact solution method.

Fortunately, as can be observed from the curves plotted in Figure 4.16e, the curves are rather flat near the true solution. In fact, the error in plastic collapse load introduced by assuming the plastic hinge to be at midspan is small, on the order of approximately 2%. This provides an additional incentive for a more expedient method.

4.4.4.2 Iterative Solution

The iterative procedure requires that plastic hinge locations be first assumed and relocated through subsequent iterations until the incremental accuracy gained in the plastic collapse load is deemed to be sufficiently small. This effectively eliminates the need to account parametrically for the possible plastic hinge locations and greatly simplifies calculations. However, to provide a more effective iteration strategy, it is sometimes worthwhile (but not necessary) to develop a standard expression for the plastic hinge location as a function of member loading and end moments. For example, for a beam subjected to a uniformly distributed load, a general expression for the moment by superposition of the bending moment diagrams can be derived from the moment diagrams shown in Figure 4.17. Because plastic hinges frequently occur at (or near) the center span, the origin of the x-axis variable is arbitrarily located at the middle of the span. The resulting expression for the bending moment diagram is:

$$M = -M_L\left[\frac{1}{2}-\frac{x}{L}\right] - M_R\left[\frac{1}{2}+\frac{x}{L}\right] + \frac{\omega}{2}\left[\frac{L^2}{4}-x^2\right] \tag{4.32}$$

One can obtain the third term of that equation using a free-body diagram of half the simply supported beam under a uniformly distributed loading, noting that the shear force is equal to zero at midspan in that case. The point of maximum moment can be again obtained by taking the first derivative:

$$\begin{gathered}\frac{\partial M}{\partial x} = \frac{M_L}{L} - \frac{M_R}{L} - \omega x = 0 \\ \frac{M_L - M_R}{\omega L} = x\end{gathered} \tag{4.33}$$

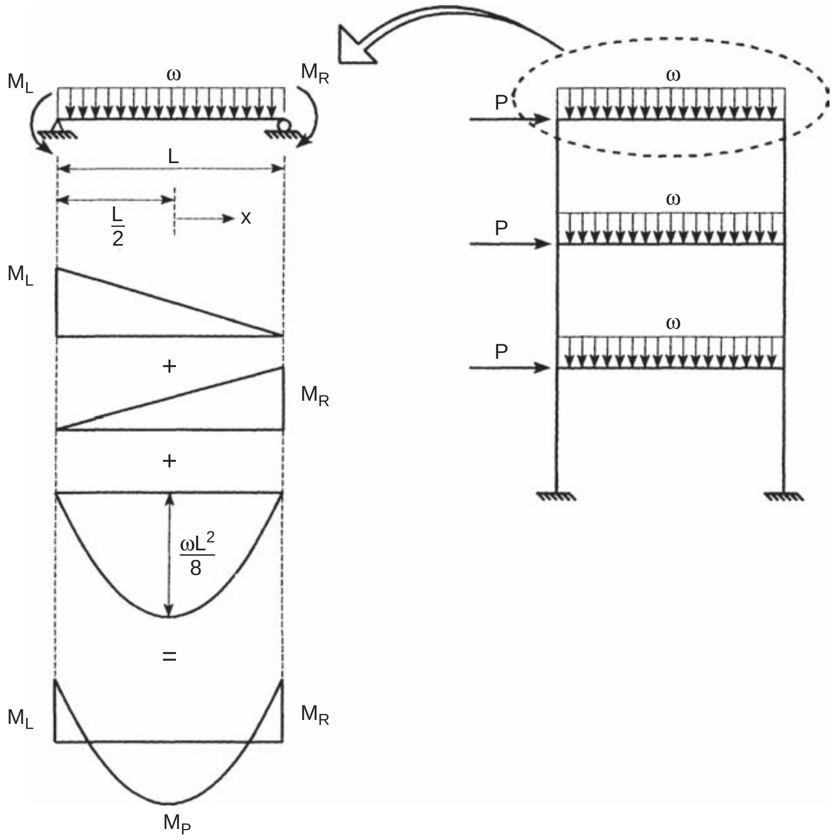

FIGURE 4.17 Moment-diagram constructions needed for determination of plastic collapse mechanism of beams subjected to uniformly distributed loads with arbitrary end-moments using iterative solution method.

The above equation is valid only for beams subjected to uniformly distributed loads, but equivalent relationships can easily be derived for other load patterns.

Conceptually, for the multistory frame example shown in Figure 4.17, solution by the iterative method requires that a first set of plastic hinge locations be assumed and that the corresponding plastic collapse load be calculated. From the resulting moment diagram one can find the new plastic hinge locations in each beam, either by using the above equation or by moving the plastic hinges to points where the moments are found to exceed M_p. The plastic collapse load corresponding to these new hinge locations would then be computed, and the process would be repeated until a satisfactory solution is found.

This method is numerically illustrated when one uses the propped cantilever of Figure 4.16a. In the first step of this procedure, plastic hinges are assumed to be located at midspan (this is usually a simple and effective starting assumption) and at the final support. The resulting work equation gives:

$$W_{internal} = W_{external}$$

$$2M_P\theta(0+2+1) = \omega L\left[\theta\left(\frac{L}{2}\right)\right]\frac{L}{2} \tag{4.34}$$

$$\frac{24M_P}{L^2} = \omega$$

Iterating to find the new plastic hinge location, knowing that a plastic hinge must also exist at the right support, gives the following for Eq. (4.33):

$$\frac{\partial M}{\partial x} = \frac{M_L}{L} - \frac{M_R}{L} - \omega x = 0$$

$$\frac{M_L - M_R}{\omega L} = x \tag{4.35}$$

$$\frac{0-2M_P}{\left(\frac{24M_P}{L^2}\right)L} = \frac{-L}{12} = -0.0833L = x$$

Based on previous observations, the engineer may wish to stop here, knowing that the above estimate of plastic collapse load will be sufficiently accurate and that the newly obtained plastic hinge position will not change substantially in subsequent iterations. However, if it is deemed necessary, one can continue the iteration process by calculating the updated plastic collapse load corresponding to the new plastic hinge locations:

$$W_{internal} = W_{external}$$

$$2M_P\theta\left(\frac{L}{0.583L}\right) + 2M_P\theta\left(\frac{0.417L}{0.583L}\right) = \omega L\theta\left(\frac{0.4167L}{2}\right) \tag{4.36}$$

$$\frac{23.36Mp}{L^2} = \omega$$

This equation would give a new plastic hinge location of $-0.0856L$, clearly indicating that a satisfactory solution has been reached. Checking that the moment diagram does not exceed the specified capacities (within some tolerance) would validate this conclusion.

4.4.4.3 Equivalent Load-Set Solution

The two solution methods presented above are manageable only for the simplest structures or to verify results obtained by other means. Direct solutions can be difficult to formulate, and the iteration process can be slow and tedious for large structures. The equivalent load-set (or replacement loads) method is proposed as a more direct procedure, also more suitable for large structures.

The equivalent load-set solution consists of replacing the distributed load applied on a member by the smallest possible number of equivalent point loads that would produce the same effect on both the member and the structure under consideration. Ideally, in order of priority, the replacement loads must exert the same gravity loading on the structure and produce the same maximum moments, at the same locations, on the member, as the original distributed load. Practically, however, it is not always possible to satisfy all of these conditions.

Some examples of equivalent load-sets are shown in Figure 4.18. These examples show that some trial and error (and at times some ingenuity) is initially needed to establish an acceptable set of replacement loads. For a uniformly distributed load, as shown in the first example of Figure 4.18, a resultant placed at midspan, although producing the same gravity load reactions and location of maximum moments, does not give an adequate plastic collapse load value. Some improvement occurs when the total load is split into two equidistant point loads (Case b).

There is no compelling reason to try only equally spaced point loads, and an even better solution results from locating the two point loads at the quarter points of the span from the ends (Case c). However, if the beam subjected to this equivalent load-set is part of a frame also subjected to lateral loads, the resulting combined gravity and sway mechanism would develop an in-span plastic hinge under one of the point loads and thus quite a distance from where it would occur under the uniformly distributed load (i.e., closer to the middle of the span).

Thus, under some loading conditions, this choice of equivalent load may not provide appropriate results. Dividing the total load into three equivalent loads makes it possible to keep a load at the middle of the span. By trial and error, a good solution for equal magnitude point loads can be found (Case d), but there is again no particular reason to require that the loads be equal, and the best solution is found when the loads are divided into a $\frac{1}{4}:\frac{1}{2}:\frac{1}{4}$ ratio (Case e). In all cases, as long as the equivalent loads are acting in the same direction and produce a collapse mechanism similar to what would have occurred under the distributed loads, the plastic collapse load of the equivalent load-set will never exceed that for the true loading.

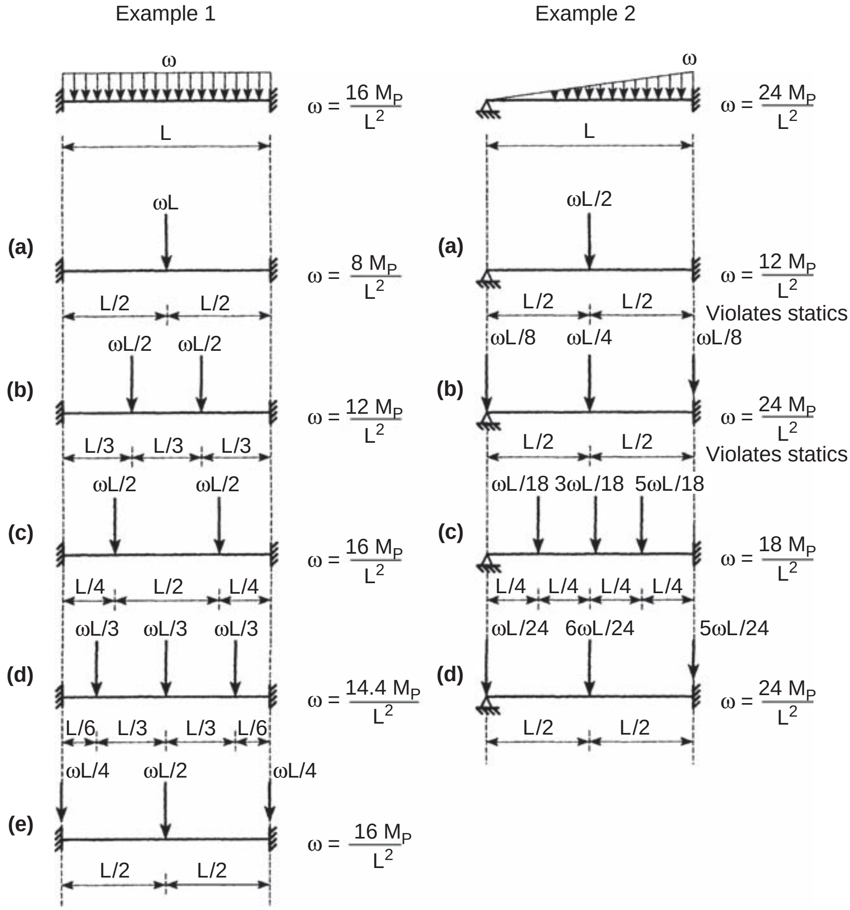

Figure 4.18 Examples of equivalent load-sets for beams subjected to distributed loads.

A triangular loading for a propped cantilever is considered in the second example of Figure 4.18. Again, following closely the approach adopted for the previous example, one first tries a single equivalent load (Case a), but this choice gives poor results. To force the development of a plastic hinge at midspan, the best solution obtained for the uniformly distributed load (Example 1) is then tried, and the correct plastic collapse load is obtained (Case b). However, both this and the previous solutions violate the static condition because the resulting support reactions do not equal those of the original loading. Given that it is more important to match the support reactions (static compatibility) than the maximum moments (mechanism condition), a better solution must be sought. Further, to some other trials (Cases c and d), a satisfactory solution is obtained (Case e).

Although sets of equivalent loads can be used directly in the analysis of complex frame structures, it must be remembered that the existence of a statically admissible moment diagram must always be checked once a tentative solution has been reached under the kinematic method. In that final check, it is worthwhile to consider the true loading conditions and assess the significance of the error introduced by the equivalent load-set.

4.4.4.4 Additional Comments

Knowledge of the exact plastic hinge location was shown to have a limited impact on the calculated plastic collapse load, but other reasons may require this location to be accurately known. For example, as will be shown later, lateral bracing must be provided at plastic hinges to prevent instability and ensure effective development of the plastic rotations needed to reach the calculated collapse load.

Fortunately, in many instances, point loads and distributed loads will be present simultaneously and the point loads will dominate the response. This would be the case, for example, when girders support beams or joists in addition to their own tributary distributed load (and self-weight). In those cases, the distributed loads could be lumped with the point loads, when one uses basic tributary area principles, without the introduction of a significant error.

4.5 Shakedown Theorem (Deflection Stability)

Up to now in this chapter, only monotonically proportional loading has been considered (i.e., loads that progressively increase while remaining proportional to each other). In most practical situations, loading is nonproportional, and one could conclude that the above plastic theory is not applicable to structures subjected to nonproportional cyclic loading. Fortunately, this is not the case. To demonstrate this, the shakedown phenomenon (also known as deflection stability) must be explained.

Unfortunately, the shakedown theorem was christened much before the advent of earthquake engineering, and in the contemporary engineering context, the term *shakedown* may erroneously conjure images of falling debris and of steel structures "shaken downward," thus collapsing. Nothing could be further from the truth. Instead, in the context of alternating cyclic loading, the shakedown theorem can be formulated as follows:

> If there exists an extreme state, beyond the threshold of first yielding, at which point the structure can behave in a purely elastic manner in spite of a previous plastic deformation history, the structure will be said to have shaken down to that complete elastic behavior if the applied cyclic loads do not exceed those that produced this extreme state.

The following classic example should help clarify this abstract statement of the shakedown concept.

First consider the case of monotonically applied loading. The two-span continuous beam shown in Figure 4.9 is used for this example (Figure 4.19a). One conducts step-by-step analysis using a

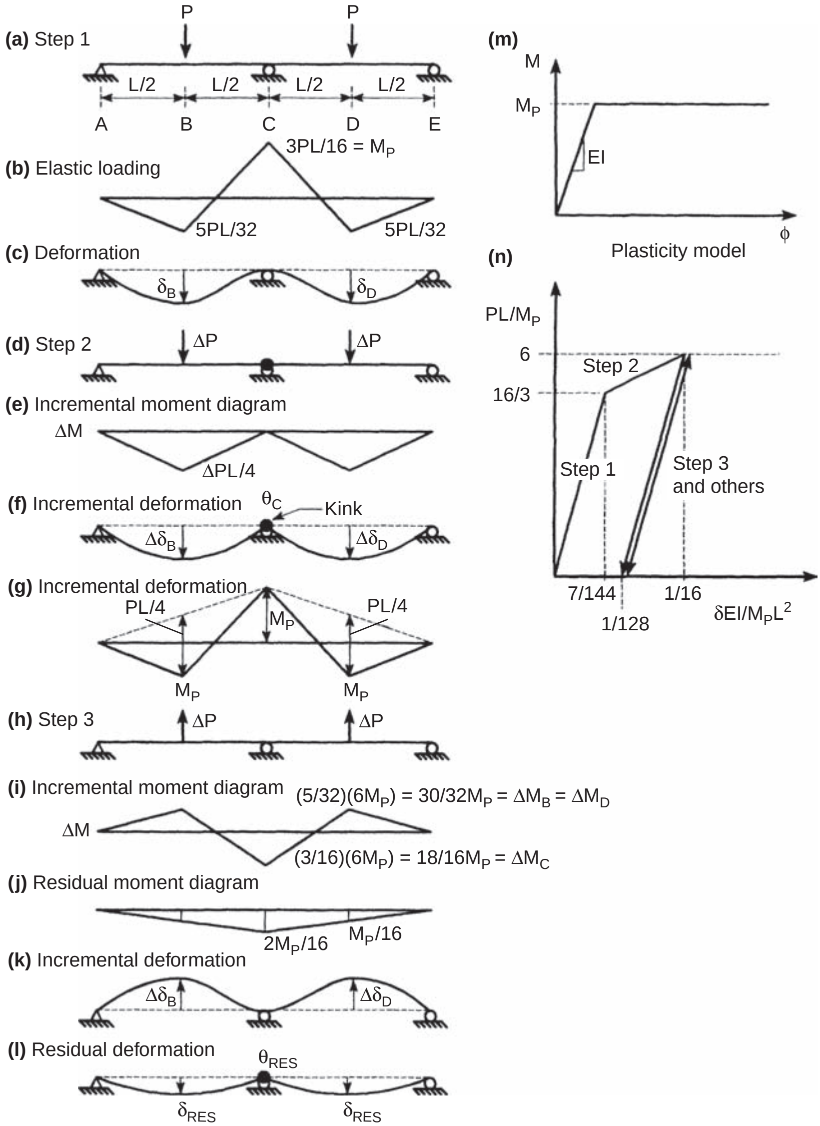

Figure 4.19 Two-span continuous example of shakedown for proportionally applied loads.

bilinear elasto-perfectly plastic moment-curvature model (Figure 4.19m). The first plastic hinge is found to occur at point C under an applied load of $16M_p/3L$ (Figure 4.19b). The corresponding elastic deflection at both points B and D is $(7/144)M_pL^2/EI$ (Figure 4.19c).

At the second step of the calculation, an incremental load of $2M_p/3L$ can be added on the resulting simply supported beams before plastic hinges develop simultaneously at points B and D (Figures 4.19d and e), with a corresponding additional deflection of $(2/144)MpL^2/EI$ (Figure 4.19f), for a total deflection of $M_pL^2/16EI$ at those locations. A plastic hinge rotation of $M_pL/12EI$ also develops at point C (being twice the elastic support rotation of a simply supported beam of span L under the incremental loading of $2M_p/3L$). The resulting moment diagram corresponding to the plastic collapse load of $6M_p/L$ (= $16M_p/3L$ + $2M_p/3L$) is shown in Figure 4.19g.

In the third step of analysis, both loads are removed simultaneously (Figure 4.19h). Interestingly, the entire load can be removed in an elastic manner (Figure 4.19i), leaving a residual moment diagram (Figure 4.19j). Moreover, a residual rotation remains at point C because the plastic rotations there are not recovered, and residual deflections of $M_pL^2/128EI$ remain at points B and D (Figure 4.19k) because the removed loads generate an elastic deflection recovery of smaller magnitude than the deflections reached at attainment of the plastic collapse load. Thus, in its new unloaded condition, the two-span continuous beam is no longer straight, and it has a kink at point C (Figure 4.19l). The resulting load-deflection diagram for this loading history is shown in Figure 4.19n. It shows that the structure can now be loaded and unloaded elastically up to its shakedown load of $6M_p/L$. In other words, the structure has shaken down to a complete elastic behavior for positive cyclic proportional loading.

Hence, if there is a residual bending moment diagram from which the structure will behave elastically under a given extreme state of loading, the structure will find its way to that moment diagram after only a finite amount of plastic flow. However, that residual bending moment diagram is not unique and depends on the structure's particular loading history.

Now, to illustrate how nonproportional positive cyclic loading can affect the value of the shakedown load, the same two-span continuous beam considered is reanalyzed. The difference is that the maximum possible load at point B (i.e., P_B) is first applied and sustained while the maximum possible load that can be applied at point D (i.e., P_D) is successively applied and removed.

Using a step-by-step analysis and the same bilinear elasto-perfectly plastic moment-curvature model of Figure 4.19m shows the first plastic hinge to occur at point B under an applied load of $P_B = 64M_p/13L$ (Figure 4.20b). The corresponding elastic deflection at point B is $(23/312)M_pL^2/EI$ (Figure 4.20c). A second step of calculation reveals that an incremental load of $14M_p/13L$ can be added at

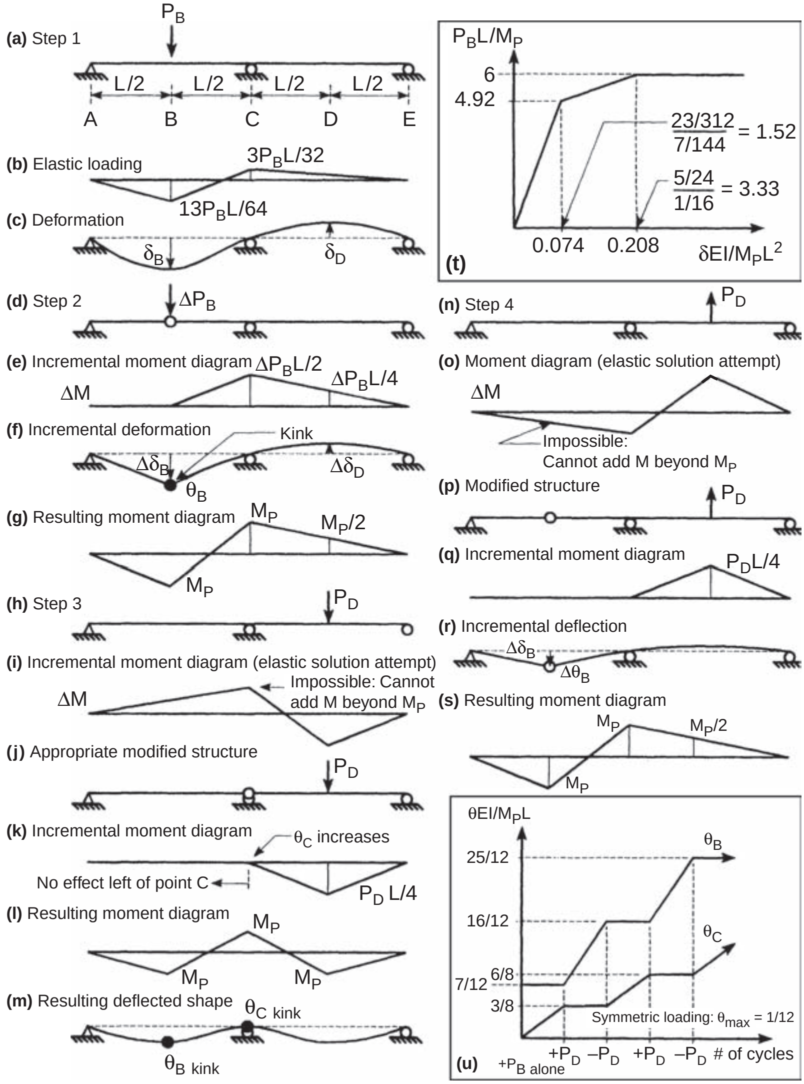

Figure 4.20 Two-span continuous example of shakedown for nonproportionally-applied loads.

point B before a plastic hinge develops at point C (Figures 4.20d and e), with a corresponding additional deflection at point B of $(7/52)M_pL^2/EI$ (Figure 4.20f), for a total deflection of $(5/24)M_pL^2/EI$ there. At the end of that step, a plastic hinge rotation of $7M_pL/12EI$ has developed at point B. Interestingly, the maximum load P_B that can be applied remains $6M_p/L$, as obtained in the previous example, but the moment diagram corresponding to this plastic collapse load is different, as shown in Figure 4.20g. As shown in Figure 4.20t, the calculated deflections at point B at the development of the first plastic hinge and at the plastic collapse mechanism are respectively 1.52 and 3.33 times larger than for the case in which both loads are applied simultaneously (Figure 4.19n).

The second point load, P_D, is then applied (Figure 4.20h). Note that this load cannot be applied in an elastic manner to the beam model of Figure 4.20a because the negative plastic moment at point C was already reached during application of P_B (Figure 4.20i). Therefore, a modified beam having a hinge at point C is analyzed (Figure 4.20j), and the resulting incremental moment diagram shown in Figure 4.20k is obtained when P_D equals $6M_p/L$. The resulting moment diagram (obtained by superposition of the moment diagrams) and deflected shape are shown in Figures 4.20l and m, respectively. As expected, because the plastic collapse load does not depend on the loading history, the ultimate plastic capacity of this continuous beam is reached when P_B and P_D both equal $6M_p/L$, as in the previous example. However, the final state of deformation is quite different, with plastic kinks at points B and C. As a rule, plastic deformations are loading-history dependent and greater in magnitude when nonproportional loading is applied.

Next, the entire load P_D ($= 6M_p/L$) is removed (Figure 4.20n). As shown in Figure 4.20o, this load cannot be removed in an elastic manner considering the beam model of Figure 4.20a because doing so would require increasing positive moment at point B, which is already stressed to its positive plastic moment capacity. However, elastic removal of P_D is possible considering a modified structure having a hinge at point B (Figure 4.20p). The resulting incremental moment diagram and deflection diagrams are shown in Figures 4.20q and r, respectively. Clearly, in the process of removing P_D, additional plastic deflections and rotations are introduced at point B.

The moment diagram after P_D is removed (Figure 4.20s) is identical to that obtained when P_B was first applied. Therefore, each subsequent cycle of application and removal of P_D will increase plastic rotations at point C (application of P_D) and plastic rotations and deflections at point B (removal of P_D). The plastic deformations will continue to grow without bounds until progressive collapse, as shown in Figure 4.20u. This implies that the above applied loads of $6M_p/L$ are in excess of the shakedown load for nonproportional loading on this structure; the shakedown load is the maximum load for which no unbounded plastic incremental deformations would occur.

The above calculations suggest that the value of the shakedown load for this beam is between the elastic and plastic load limits of $4.92M_p/L$ and $6M_p/L$. To systematically determine the shakedown load, one must formulate equations of equilibrium at each point of possible plastic hinge in terms of the incremental loads at that point (for complex structures, this undertaking can be formidable).

In this example, the equilibrium equation is established from the moment diagram obtained after a plastic hinge has formed at point B (Figures 4.21a and b). The moment at point C can be calculated as:

$$M_C = \frac{3}{32} P_{BY} L + \Delta P_B \frac{L}{2} \tag{4.37}$$

where P_{BY} is the load applied in step 1 (Figure 4.20a) necessary to form a plastic hinge at point B, and ΔP_B is the incremental load applied in step 2 at point B (Figure 4.20d). The two terms in Eq. (4.37) contributing to the moment at point C result from the sequential application of these loads. Given that the solution sought must permit application of loads P_B and P_D in any sequence, and assuming that both loads are constrained to have the same maximum value, then, $P_{D\text{-}MAX}$ must

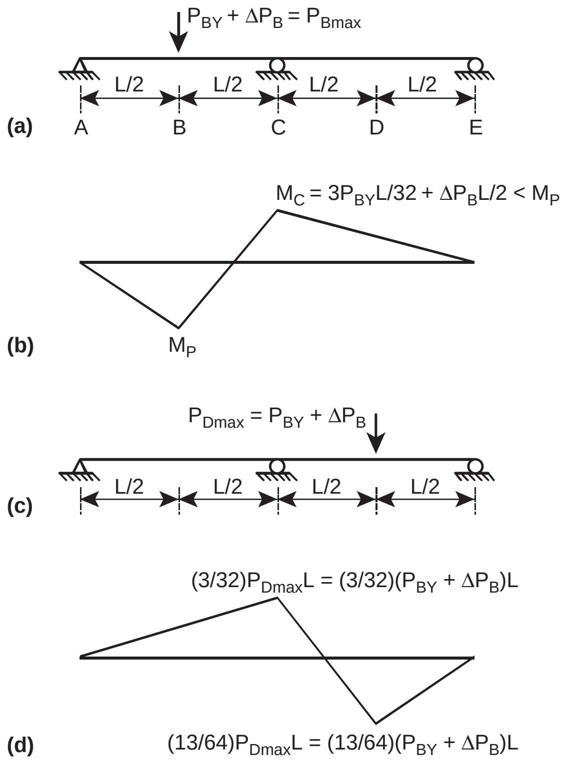

FIGURE 4.21 Systematic determination of shakedown load for nonproportionally applied loads using equation of equilibrium at points of possible hinge formation in terms of incremental loads.

also be equal to ($P_{BY} + \Delta P_{BY}$). The incremental moment diagram that results from a load applied at point D (Figure 4.21c) until a plastic hinge forms at point C is shown in Figure 4.21d. The resulting expression for that incremental moment at point C is:

$$M'_C = \frac{3}{32} P_{D-MAX} L = \frac{3}{32}(P_{BY} + \Delta P_B)L \qquad (4.38)$$

As long as no collapse mechanism is allowed to form, no incremental plastic deformations can be introduced into the structure by nonproportional loading. Therefore, to prevent formation of a plastic hinge at point C, the following equation must be satisfied:

$$M_C + M'_C = \left[\frac{3}{32} P_{BY} L + \Delta P_B \frac{L}{2}\right] + \frac{3}{32}(P_{BY} + \Delta P_B)L < M_P \qquad (4.39)$$

Because M_p and P_{BY} are known, this equation can be solved, and a value of ΔP_B equal to $32M_p/247L$ is found. The corresponding shakedown load limit is therefore the sum of P_{BY} and ΔP_B, which is $96M_p/19L$ in this case, or $5.05M_p/L$. This load is only 2.6% more than the elastic limit of $4.92M_p/L$. Given this limited gain and the fact that nearly all live loads are generally nonproportional in nature, the reader may wonder at this point whether plastic design is still worth considering. The answer is yes.

The above example is an extreme case because all the loads are applied and removed. This is not the case in real structures because the dead load is permanent. In this particular example, if the loads P_B and P_D included a dead load equal to $4.66M_p/L$, the likelihood of shakedown would be zero because the first plastic hinge would always form at point C, regardless of the nonproportional sequence of application and removal of the live load component of P_B and P_D. Many researchers have investigated whether the shakedown load limit could invalidate plastic theory, and all have concluded that normal wind and gravity loads are highly unlikely to cause such deflection instability problems in plastically designed structures because a rather large ratio of live load to dead load is necessary to trigger this process (typically the live loads would need to exceed two thirds to three fourths of the total load, depending on the type of structure). However, engineers using plastic design concepts should be familiar with the shakedown phenomenon and its consequences, to properly identify those instances when it may need to be considered.

Finally, although rare and unusually intense earthquakes can induce rather large loads in structures, the shakedown problem is typically not addressed during analysis for seismic response. Rather, dynamic nonlinear inelastic step-by-step analysis using earthquake ground motion records is preferred. Cumulative plastic deformations and rotations obtained from such analyses are useful to develop or validate simpler design rules more suitable for hand calculation.

4.6 Yield Lines

While the principles of plastic analysis that have been presented so far have been applied to structural members and systems, the same concepts are also applicable to small components and details. This can be useful in a number of applications, such as to assess the strength of connections, investigate fatigue life due to local buckling, or to study the behavior of plates subjected to out of plane loads. Some of these applications are reviewed below after the presentation of general principles of yield line analysis.

4.6.1 General Framework

Yield line analysis has been used extensively in the past to compute the ultimate strength of reinforced concrete slabs (Park and Gamble 1999). In those studies, given that different reinforcements can be designed to resist positive or negative flexure, a distinction is made between the positive and negative plastic strengths of slabs and a more general formulation has been derived. The expressions presented in the following text are applicable to steel plates that have the same plastic strength in either positive or negative bending. The more general formulation should be used instead when that is not the case (for instance, in composite panels having nonsymmetric steel plate thicknesses or reinforcement).

Using the example of a steel plate subjected to a pressure loading acting on its surface, Figure 4.22 shows the specific symbolic that is used here to schematically illustrate the boundary conditions and direction of bending of such plates. In plan views looking at flat surfaces, double hatched lines represent fixed edges, single hatched lines represent simply supported edges, and free edges are shown by straight lines. Parts of steel plates yielding in positive or negative bending are respectively shown as wiggled or dashed lines (i.e., yield lines), where positive bending is arbitrarily defined when a pressure pushing on the visible surface of the plate creates tension on the back of the plate (i.e., on its nonvisible side). Note that yield lines at supports are generally shown with a slight offset to make them visible in sketches, but located at the supports in all calculations.

The simple case of a plate fully fixed at both ends shown in Figure 4.22 is comparable to the beam case studied earlier (see Figure 4.9). Here, the beam has a rectangular cross-section of width, l, and depth, t. Equation (3.10) can be used directly to obtain the plastic strength of the plate. Alternatively, the plastic hinges can be recognized to be yield lines of strength:

$$m_P = \left(\frac{bh^2}{4}\right)F_y = \left(\frac{(1)(t)^2}{4}\right)F_y = \frac{t^2}{4}F_y \qquad (4.40)$$

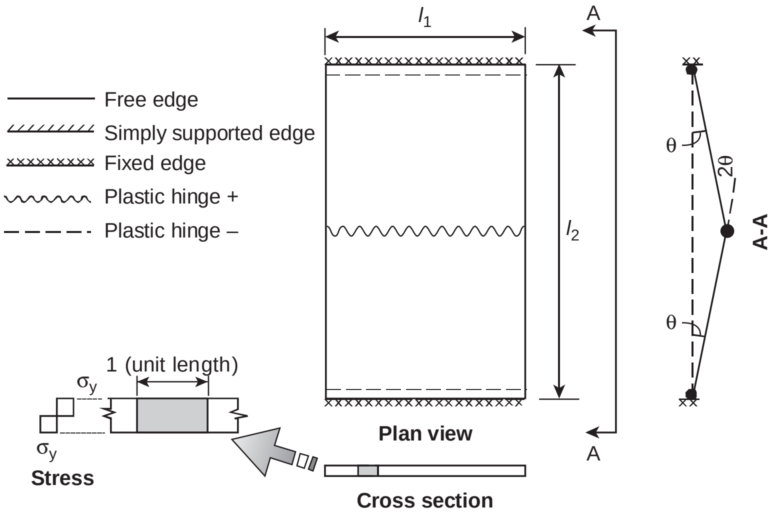

FIGURE 4.22 Yield lines on plate fixed at two opposite ends.

where m_p is the plastic moment per unit length along a yield line. As indicated earlier, for a steel plate, $m_p^- = m_p^+ = m_p$.

For this plate subjected to a uniformly distributed load on its surface, using the kinematic method, the external work and internal work can be respectively calculated as:

$$W_I = m_p l_1(2\theta) + m_p l_1(\theta) + m_p l_1(\theta) = m_p l_1(2+1+1)\theta = 4m_p l_1(\theta) \tag{4.41a}$$

$$W_E = (\omega l_1 l_2)\frac{1}{2}\left(\theta\frac{l_2}{2}\right) = \frac{\left(\omega l_1 l_2^2\right)}{4}\theta \tag{4.41b}$$

where ω is typically in pressure units (e.g., kPa, psi, or psf). Note that, in the internal work equation, the plastic moment per unit length of each yield line is multiplied by its respective length and plastic rotation. The value of the uniformly distributed load that creates the plastic collapse mechanism, obtained by setting the internal work equal to the external work, is:

$$W_I = W_E \qquad \therefore \qquad \omega = \frac{16m_p}{l_2^2} \tag{4.42}$$

Although a yield line analysis would not have been necessary to resolve the problem shown in Figure 4.22, the terminology and conventions outlined for that purpose are needed to address other plate geometries and boundary conditions that result in more complex yield line configurations.

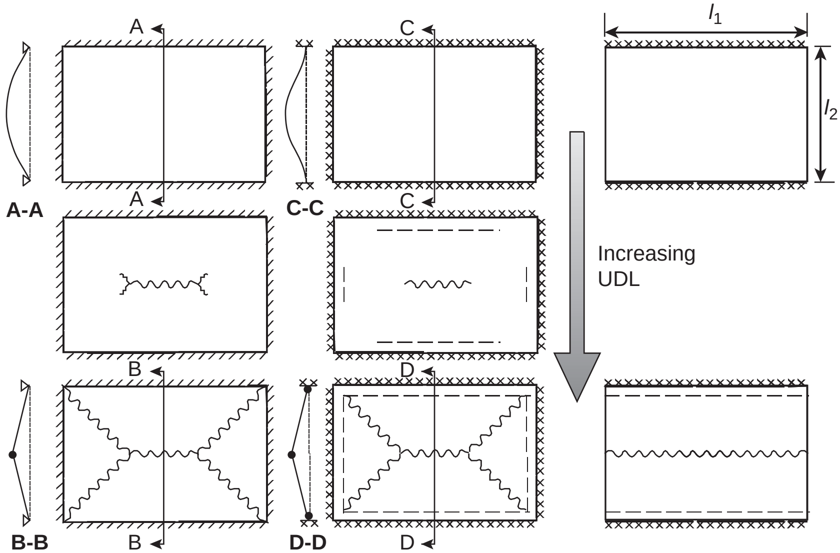

FIGURE 4.23 Progression of yield lines on plates having different boundary conditions.

Figure 4.23 shows yield line patterns for three identical plates similarly subjected to a progressively increasing uniformly distributed load, but having different boundary conditions (including the example from Figure 4.22). For the plate simply supported along its edges, yielding starts at midspan of the narrowest dimension (since larger moments develop along the stiffer of the two directions for a given span deflection). As the uniformly distributed load increases, plastic hinging spreads toward the other edges, eventually bifurcating into yield lines directed toward the plate's corners. Finally, the ultimate strength of the steel plate is reached when the plastic collapse mechanism shown in the figure develops. Folding a sheet of paper with creases along these yield lines can help the reader visualize that this deformation pattern indeed corresponds to a mechanism.

A similar collapse mechanism and progression in the development of yield lines is also schematically shown for the plate having fixed edges, the only difference in that case being that plastic rotations develop in regions of negative moment at the fixed supports and generate internal work.

The relationships derived below, using information shown in Figure 4.24, establish convenient equivalent approaches to calculate internal work, and thus the plastic strength of such plates.

For an arbitrary segment of yield line, of length l_o, acting in an arbitrary direction, α, undergoing a plastic rotation angle, θ_n, the

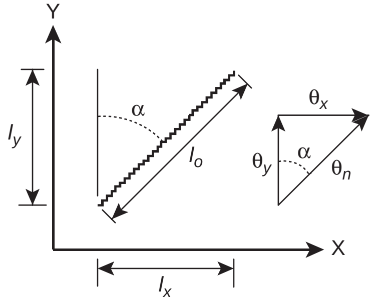

FIGURE 4.24 Arbitrarily oriented yield line.

respective components in the two orthogonal horizontal directions are:

$$l_x = l_o \sin\alpha \tag{4.43a}$$

$$\theta_x = \theta_n \sin\alpha \tag{4.43b}$$

$$l_y = l_o \cos\alpha \tag{4.43c}$$

$$\theta_y = \theta_n \cos\alpha \tag{4.43d}$$

and the corresponding products are:

$$l_x \theta_x = l_o \theta_n \sin^2\alpha \tag{4.43e}$$

$$l_y \theta_y = l_o \theta_n \cos^2\alpha \tag{4.43f}$$

Using these relationships, together with the trigonometric relationship $\sin^2\alpha + \cos^2\alpha = 1$, the internal work produced along the yield line acting in an arbitrary direction can be broken into its orthogonal components such that:

$$\begin{aligned} W_I &= m_P l_o \theta_n \\ &= m_P (\sin^2\alpha + \cos^2\alpha)\, l_o \theta_n \\ &= m_P l_o \theta_n \sin^2\alpha + m_P l_o \theta_n \cos^2\alpha \\ &= m_P l_x \theta_x + m_P l_y \theta_y \\ &= m_P (l_x \theta_x + l_y \theta_y) \end{aligned} \tag{4.44}$$

This shows that the internal work generated along a yield line oriented at an angle from the orthogonal directions can be calculated either using the plastic rotations about that yield line and the length of that line, or the orthogonal components of these values to obtain the same result. In some cases, the latter approach can greatly simplify calculations.

This is illustrated in Figure 4.25 where two approaches are used to calculate the plastic collapse load for the same rectangular plate

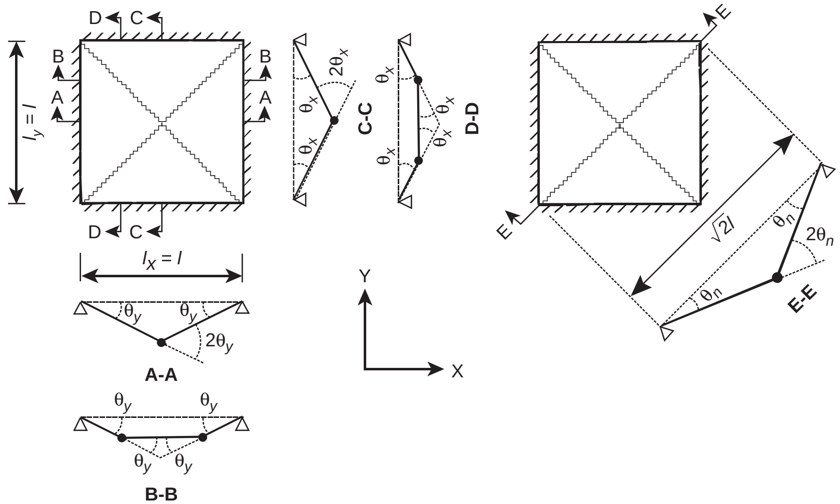

Figure 4.25 Plastic strength of a simply supported square plate.

with fixed edges. In the first approach, the exact plastic rotations along yield lines are calculated to obtain the internal work. A view of the collapse mechanism at 45° from the orthogonal directions illustrates how these values are obtained. The corresponding internal and external works, for the two diagonal yield lines, are respectively:

$$W_I = 2[m_P(\sqrt{2}\,l)2\theta_n] = 4\sqrt{2}\,m_P\theta_n l = 8m_P\delta \tag{4.45}$$

$$W_E = 4\left[\omega\left(\frac{1}{2}\frac{l}{2}l\right)\frac{\delta}{3}\right] = (\omega l^2)\,\frac{\delta}{3} \tag{4.46}$$

where

$$\theta_n = \frac{\delta\sqrt{2}}{l} \tag{4.47}$$

and the corresponding uniformly distributed load when the plastic strength of the plate is reached is:

$$\omega = \frac{24m_P}{l^2} \tag{4.48}$$

Alternatively, working directly with the orthogonal components and the corresponding side views of the collapse mechanism, given that $\sigma = \theta_x l_x/2 = \theta_y l_y/2 = \theta\, l/2$ and $m_{Px} = m_{Py} = m_P$, the internal work is:

$$W_I = 4\left[m_{Px}\left(\frac{l}{2}\right)\theta_x + m_{Py}\left(\frac{l}{2}\right)\theta_y\right] = 4m_P\theta l = 8m_P\delta \tag{4.49}$$

which is the same as before. Since external work also remains the same (being calculated on the same deformed geometry in both cases), the obtained ultimate load is again $24m_p/l^2$.

Note that if fixed boundary conditions were used instead of simply supported ones, for the same collapse mechanism to develop, yield lines would also develop along the fixed supports; in that case, solving using the corresponding internal work, the resulting plastic strength would be twice that calculated above (i.e., $48m_p/l^2$).

The challenge in using yield line analysis is that it is an upper bound method. As a consequence, the true plastic strength is only obtained if the assumed collapse mechanism is correctly guessed. For all other (incorrectly) assumed mechanism geometries, the calculated plastic strengths will be unconservative (as described in Section 4.2.3). In some cases, such as in Figure 4.25, the plastic mechanism can be assumed with reasonable confidence (even though an alternate mechanism exists that gives a slightly lower plastic strength for square plates, as will be shown later). However, in most instances, it is best to formulate the plastic mechanism in a parametric equation allowing for optimization. This is illustrated in Figure 4.26 for a rectangular plate simply supported at its edges, for which the internal and external works and plastic strength can be calculated as:

$$\begin{aligned} W_I &= m_{Px}(b-2x)(2\theta_x) + 4m_{Px}\theta_x x + 2m_{Py}a\theta_y \\ &= m_P[(2(b-2x)+4x)\theta_x + 2a\theta_y] \end{aligned} \tag{4.50}$$

$$\begin{aligned} W_E &= 2\omega\left(\frac{ax}{2}\right)\frac{\delta}{3} + 4\omega\left[x\left(\frac{1}{2}\right)\left(\frac{a}{2}\right)\right]\frac{\delta}{3} \\ &\quad + 2\omega(b-2x)\left(\frac{a}{2}\right)\frac{\delta}{2} = \frac{\omega a(3b-2x)\delta}{6} \end{aligned} \tag{4.51}$$

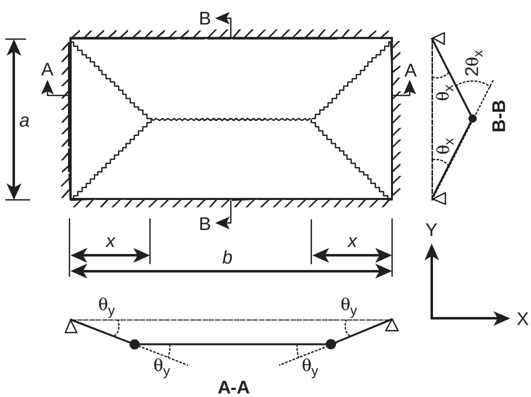

Figure 4.26 Plastic strength of a simply supported rectangular plate.

where

$$\delta = \theta_x\left(\frac{a}{2}\right) = \theta_y x \qquad \therefore \qquad \theta_y = \left(\frac{\delta}{x}\right) \qquad and \qquad \theta_x = \left(\frac{2\delta}{a}\right) \tag{4.52}$$

and

$$\omega = \frac{12m_p(2bx + a^2)}{a^2 x(3b - 2x)} \tag{4.53}$$

The smallest uniformly distributed load that will produce a plastic mechanism can be found by setting the first derivative of this expression to zero and solving the resulting equation. For this example, the resulting value of the unknown parameter is:

$$x = \frac{a}{2b}(-a \pm \sqrt{a^2 + 3b^2}) \tag{4.54}$$

Numerically, for values of a = 8 in and b = 16 in, the solution is x = 5.21 in.

Note that in some instances, instead of searching for a closed form solution, it may be more expedient to plot the value of the plastic strength as a function of the unknown variable, x, and to graphically identify the point of minimum strength along the curve.

Recognizing that the upper bound approach requires identification of the proper plastic mechanism, one could come back to Figure 4.25 and question whether the assumed mechanism is the correct one. Indeed, it can be envisioned that the corners of a rectangular plate would be subjected to uplift forces for the proposed deflected shape, and that the corresponding downward reactions at those corners would bend the plate in negative flexure, which could result in a yield line a short distance from the corners, as shown in Figure 4.27a. For that arbitrarily chosen pattern, optimizing the geometry of the yield lines, by trial and error or by rigorous optimization, would give a resulting plastic collapse load of $\omega = 22m_p/l^2$, which is 9% less than

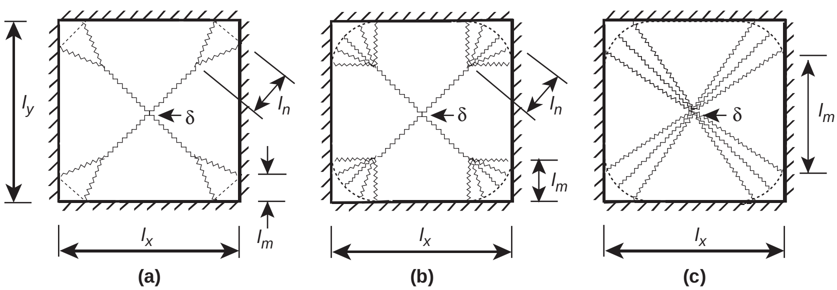

Figure 4.27 Example alternative yield line patterns for a simply supported square plate.

the simpler pattern considered in Figure 4.25. More complex yield line patterns (e.g., Figures 4.27b and c), can also be considered at the cost of substantially greater computational effort. For example, a plastic strength of $21.7m_p/l^2$ was obtained for a semicircular "fan-like" distribution of yield lines (Figure 4.27c) when neglecting the negative flexure corner folds (i.e., if supports cannot prevent uplift at the corners); however, the case with straight yield lines governed when negative flexure was considered (Park and Gamble 1999).

Considering the more complex configuration of yield lines, some engineering judgment and experience is necessary to determine if the benefit of increased accuracy warrants the extra work, or will be of marginal significance. The latter is often the case. Note that in many instances (as in the next section), experimental evidence provides visual clues as to the pattern of yield lines that develops upon reaching a known ultimate strength. In such cases, the available data allows assessing whether simplified patterns can provide reasonably accurate results.

4.6.2 Strength of Connections

Yield line analysis in steel structures has been commonly used to assess the strength of connections. This is illustrated in Figure 4.28 for a bolted T-stub connector (typically a WT shape) whose stem is pulled in tension, as would be the case when used to connect beam flanges to columns in some types of moment resisting connections. For the assumed location of yield lines and plastic mechanism shown in that figure, the corresponding plastic strength can be calculated as follows:

$$W_I = 2[m_p\theta(B-2\phi)] + 2[m_p\theta B] = 4m_p(B-\phi)\theta \tag{4.55a}$$

$$W_E = P\delta = Px\theta \tag{4.55b}$$

$$W_I = W_E \qquad \therefore \qquad P = \frac{4m_p(B-\phi)}{x} = \frac{t^2F_y(B-\phi)}{x} \tag{4.55c}$$

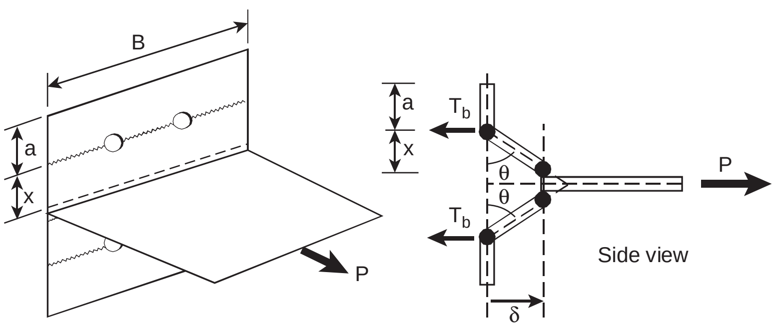

Figure 4.28 Yield line analysis of T-stub connector.

In a design perspective, rearranging Eq. (4.55c), the T-stub flange thickness required to resist the applied load is given by:

$$t \geq \sqrt{\frac{Px}{(B-\phi)F_y}} \tag{4.56}$$

Note that, for this detail and selected T-stub flange thickness, the plastic mechanism provides an upper bound to the force, T_b, defined in Figure 4.28, that can develop in the bolts due to prying action.

The above result assumes yield lines parallel to the longitudinal axis of the T-stub. This would not necessarily be the case if the T-stub was substantially longer than the width of the beam flange and the bolts connecting the stub to the column were widely apart, as often found in archaic constructions that used laced built-up columns. In such a case, plastic deformations concentrate near the bolts, like localized "folds." A similar yield line pattern was experimentally observed (Figure 4.29a) in wide-angle flange connectors of semi-rigid beam-to-column moment connections (Sarraf and Bruneau 1996). Good agreement with experimental results was obtained using the simplified yield line pattern geometry shown in Figure 4.29b, which gives the following internal and external works equations:

$$W_I = 2[2m_p h\theta_x + 2m_p x\theta_y] = 4m_p h\left(\frac{\delta}{x-b}\right) + 4m_p x\left(\frac{\delta}{h-a}\right) \tag{4.57a}$$

$$W_E = P\delta \tag{4.57b}$$

$$W_I = W_E \qquad \therefore \qquad P = 4m_p\left[\left(\frac{h}{x-b}\right)+\left(\frac{x}{h-a}\right)\right] \tag{4.57c}$$

The value of x that gives the least plastic strength for this assumed yield line pattern is:

$$x = b + \sqrt{h^2 - ha} \text{ which must be } \leq 0.5L \tag{4.58}$$

Per the upper bound approach, the lower plastic strength found from all yield line patterns considered must be used.

Other yield line patterns can be found in the literature for various other types of connections. For example, Figure 4.30a shows a yield line pattern originally proposed for unstiffened extended end-plate connections (Mann 1968, Surtees and Mann 1970, Mann and Morris 1979), assuming bolts strength adequate to allow development of this plastic mechanism. Drawing parts of the mechanism in a perspective view such as done in Figure 4.30b for the part of the end-plate between the beam flanges on one side of the beam web, although time

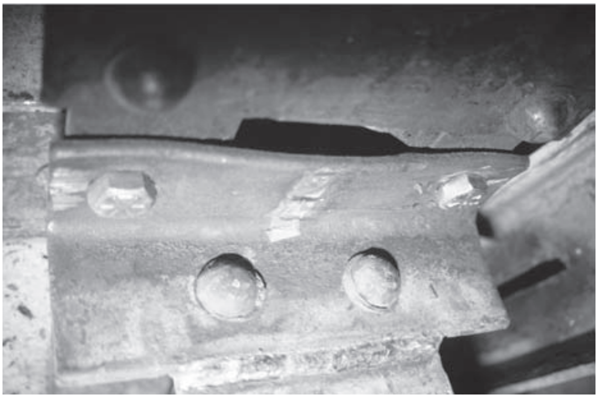

(a)

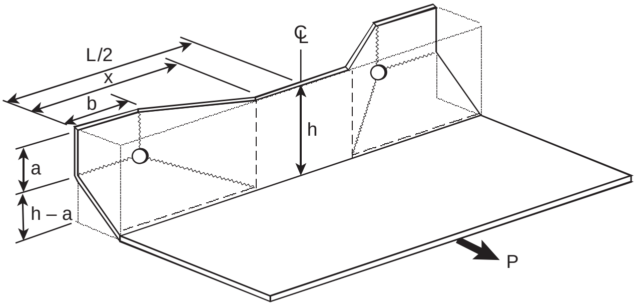

(b)

Figure 4.29 Yield lines on wide bolted angle. (*From Sarraf and Bruneau 1994.*)

consuming, can help visualize the deflected shape and calculate the relevant angles in complex connections. For this case:

$$W_I = 4m_P B\beta + 4m_P\left(S + \frac{C}{2}\right)\gamma$$

$$= 4m_P B\left(\frac{\Delta_1}{C/2}\right) + 4m_P\left(S + \frac{C}{2}\right)\left(\frac{S}{(S+C2)}\frac{\Delta_1}{A/2}\right)$$

$$= t^2 F_y\left[\frac{2B}{C} + \frac{2S}{A}\right]\Delta_1 \tag{4.59a}$$

$$W_E = P\Delta_1 = \left(\frac{M}{d}\right)\Delta_1 \tag{4.59b}$$

$$W_I = W_E \qquad \therefore \qquad P = \left[\left(\frac{2B}{C}\right) + \left(\frac{2S}{A}\right)\right]t^2 F_y \tag{4.59c}$$

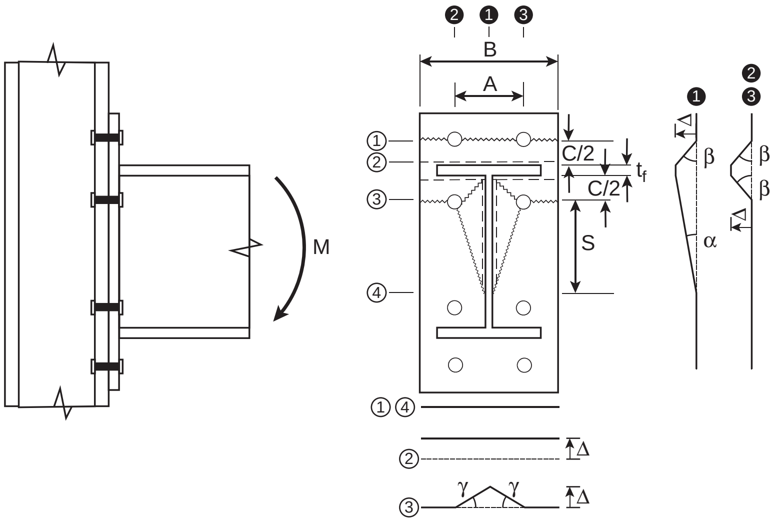

(a)

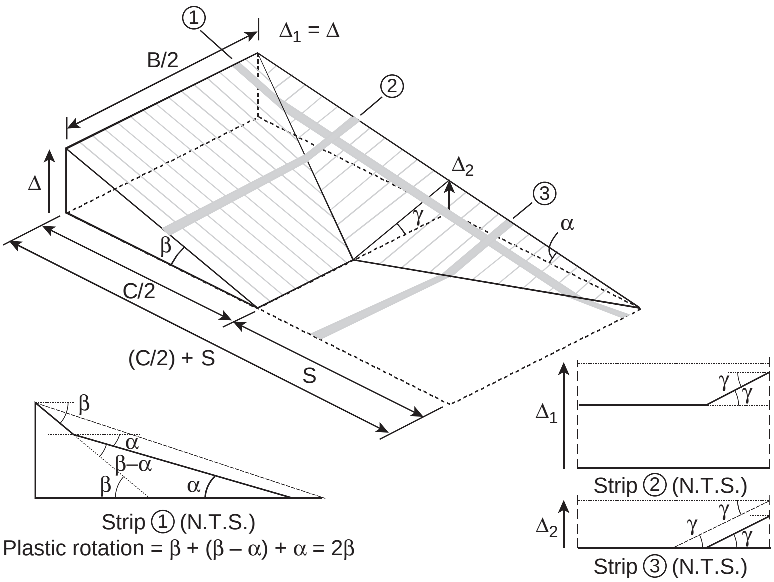

(b)

Figure 4.30 Bolted unstiffened extended end-plate connection: (a) Surtee and Mann's assumed yield lines; (b) perspective view of part of the plastic mechanism.

where d is the depth of the beam, M is the moment applied to the connection, $P = M/d$ is the load applied by the flange to the extended end-plate, and all other dimensions, displacements, and rotation angles are defined in Figure 4.30. For a given moment, Eq. (4.59c) can be rearranged to calculate the necessary end-plate thickness, such that:

$$t \geq \sqrt{\frac{M}{\left[\left(\frac{2B}{C}\right)+\left(\frac{2S}{A}\right)\right]dF_y}} \tag{4.60}$$

Based on experimental observations, Mann (1968) originally proposed that $S + (C/2) = d/2$.

With the benefit of subsequent research on the topic, AISC's design equations for the same unstiffened extended end-plate connections are based on the yield mechanism shown in Figure 4.31. For the entire end-plate:

$$\begin{aligned}
W_I &= m_P b_f\left[(\alpha)+(\alpha+\omega)+(\omega+\beta)+(\beta+\theta)\right]+2m_P(s+p_{fi})(\gamma+\gamma) \\
&= 2m_P b_f\left[\left(\frac{\delta_a}{s}\right)+\left(\frac{\delta_a}{p_{fi}}\right)+\left(\frac{\delta_b}{p_{fo}}\right)-\frac{\theta}{2}\right]+2m_P(s+p_{fi})\left(\frac{4\delta_a}{g}\right) \\
&= 2m_P\left\{b_f\left[h_1\left(\frac{1}{s}+\frac{1}{p_{fi}}\right)\theta+h_0\left(\frac{1}{p_{fo}}\right)\theta-\frac{\theta}{2}\right]+(s+p_{fi})\left(\frac{4h_1\theta}{g}\right)\right\} \\
&= t_{PL}^2F_y\left\{\frac{b_f}{2}\left[h_1\left(\frac{1}{s}+\frac{1}{p_{fi}}\right)+h_0\left(\frac{1}{p_{fo}}\right)-\frac{1}{2}\right]+\left[2(s+p_{fi})\left(\frac{h_1}{g}\right)\right]\right\}\theta \\
&= t_{PL}^2F_yY_P\theta
\end{aligned} \tag{4.61a}$$

$$W_E = P(\theta h) = \left(\frac{M}{h}\right)(\theta h) = M\theta \tag{4.61b}$$

$$W_I = W_E \qquad \therefore \qquad M = t_{PL}^2F_yY_P \tag{4.61c}$$

where, again, M is the moment applied to the connection, P is the load applied by the flange to the extended end-plate, Y_P is an end-plate yield line mechanism parameter defined for mathematical convenience, and all other dimensions, displacements, and rotation angles are defined in Figure 4.31, using a notation consistent with AISC (2010, 2011). Note that, to limit complexity of the equations, the plate material removed by the bolt holes is not considered, the width of the beam web is taken as zero, and yield lines around bolts near the compression region are neglected.

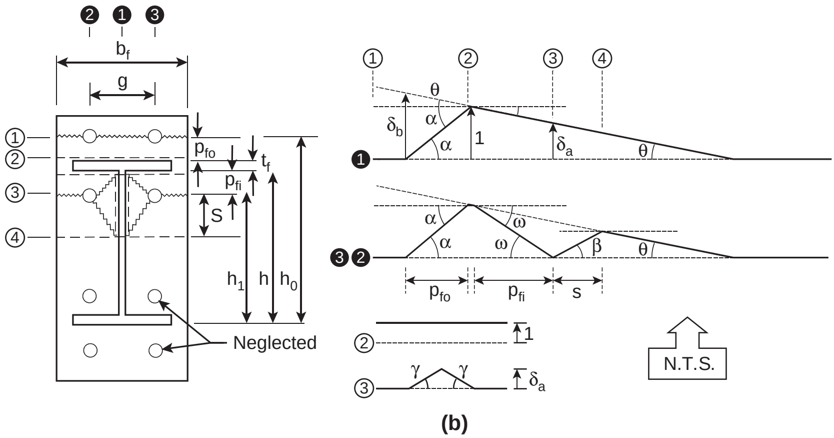

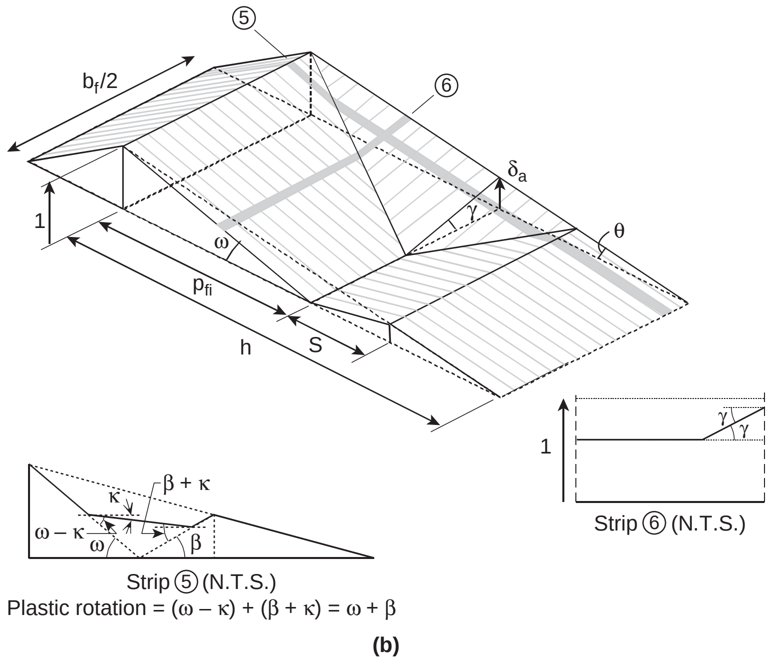

Figure 4.31 Bolted unstiffened extended end-plate connection: (a) AISC's assumed yield lines; (b) perspective view of part of the plastic mechanism.

Solving for the value of s that gives the lowest plastic strength for the connection (Murray and Sumner 2003, Srouji et al. 1983):

$$\frac{\partial W}{\partial s} = 0$$

$$\frac{\partial\left[b_f h_1\left(\frac{1}{s}\right) + (s)\left(\frac{4h_1}{g}\right)\right]}{\partial s} = 0 \tag{4.62}$$

$$-\frac{b_f h}{s^2} + \frac{4h_1}{g} = 0$$

$$s = \frac{1}{2}\sqrt{b_f g}$$

The required end-plate thickness is then:

$$t \geq \sqrt{\frac{M}{F_y Y_P}} \tag{4.63}$$

More general expressions for stiffened and unstiffened extended end-plate moment connections, having 4 or 8 bolts per flange connection, are presented in Murray and Sumner (2003).

Note that for some connection types, consistently with observations made in the previous section, simpler yield line patterns that do not perfectly match those observed experimentally are retained by virtue of providing either conservative results or reasonable approximations of connection strengths without unwieldy algebra.

4.6.3 Plastic Mechanisms of Local Buckling

Yield line analysis has also been used extensively in studies of local bucking in light-gage cold-formed steel members and thin-walled structural shapes. However, in those cases, the presence of compression forces makes the analyses substantially more complex and a number of challenges remain to be resolved. In particular, the analyses must differentiate between "true mechanisms" having only flexural yield lines, and "quasi-mechanisms" having a mix of axial yielding (a.k.a. plastic zones) and flexural yield lines. Some analyses may also need to account for incompletely formed yield lines. Results for plates in compression are also known to be more sensitive to the assumed plastic mechanism (with respect to both the location and the shape of the yield lines) than for plates in pure flexure, although some of that sensitivity is more acute for light-gage steel shapes than for the thicker hot-rolled plates used for ductile design. Hiriyur and Schafer (2005) and Gioncu and Mazzolani (2002) present a thorough overview of some of these issues.

Nonetheless, in spite of these challenges, the plastic mechanism approach provides an appealing way to investigate the postbuckling strength and behavior of ductile steel shapes without having to resort to complex nonlinear finite element analysis. For illustration purposes, Figure 4.32 shows a plastic mechanism model that expands on

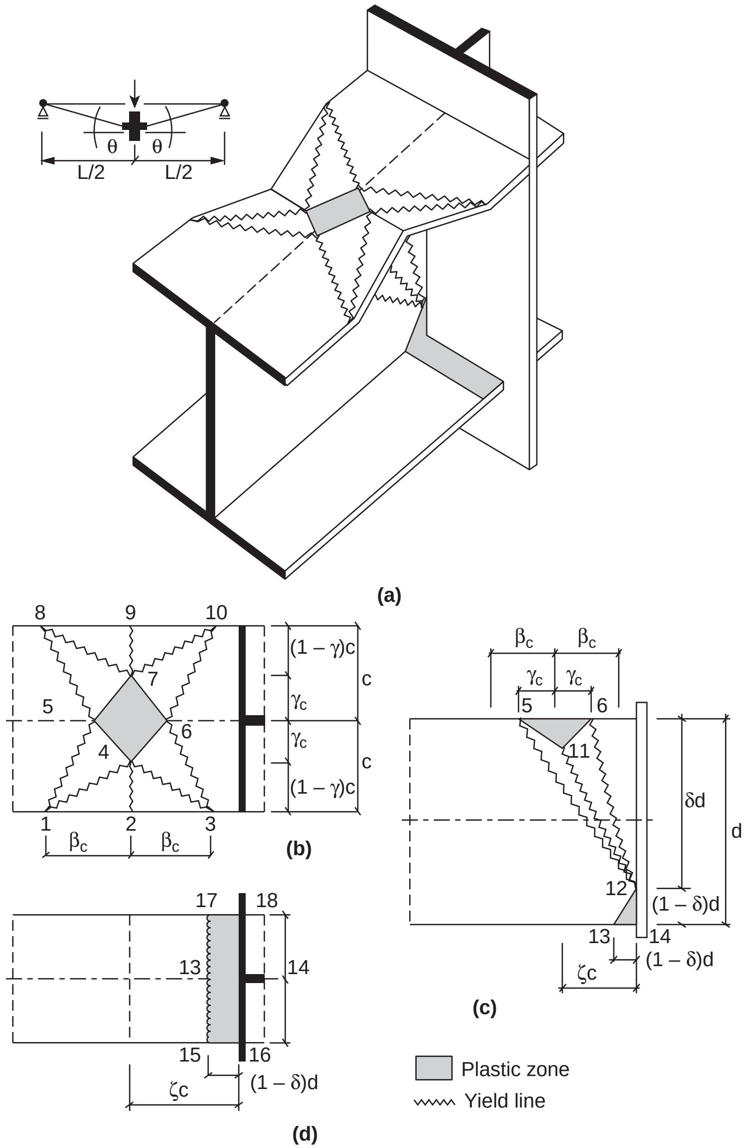

FIGURE 4.32 Plastic mechanism model for beam plastic local buckling. (*Courtesy of Professor Victor Gioncu, University Timisoara, Romania.*)

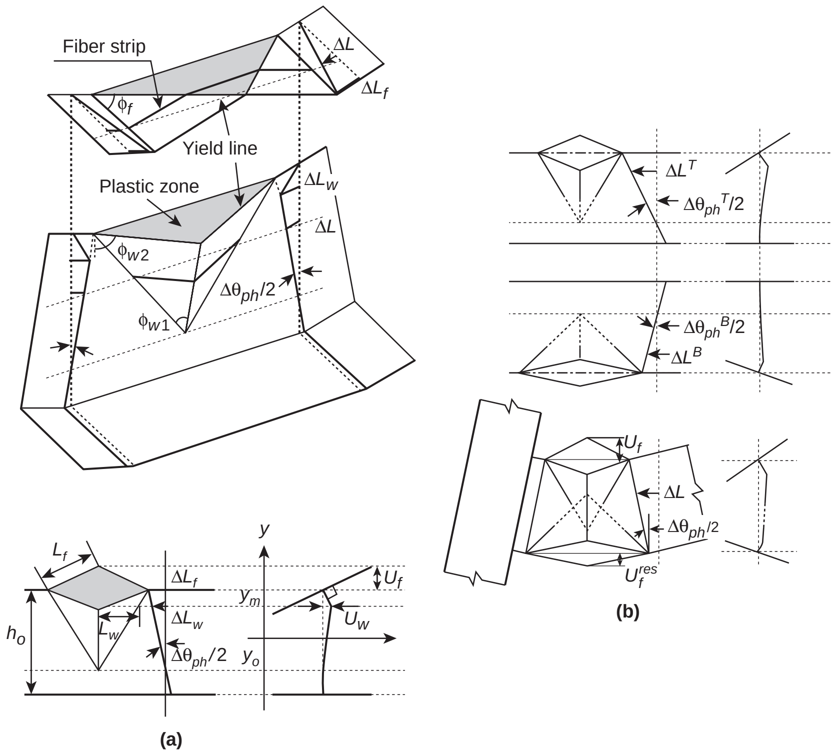

Figure 4.33 Plastic mechanism model for cyclic beam postbuckling behavior: (a) Monotonic plastic mechanism; (b) cyclic plastic mechanism (simultaneously shown for both flanges). (*Courtesy of Bozidar Stojadinovic, Department of Civil Engineering, University of California, Berkeley, and Kyungkoo Lee, Dankook University, Korea.*)

prior models and best captures postbuckling behavior while remaining relatively simple. Details of its formulation are presented in Petcu and Gioncu (2003).

In particular, yield line analysis has also been used to investigate local buckling behavior and estimate low cycle fatigue life of beams subjected to cyclic inelastic loading (Gioncu and Mazzolani 2002; Lee 2004; Lee and Stojadinovic 2005). Two sets of yield lines (Figure 4.33) must be considered in such analyses to account for: (1) the development of compression yielding and local buckling on alternating flanges during cyclic loading, and (2) the fact that when a previously buckled flange is pulled in tension, the residual out-of-plane deformations that remain act as large initial imperfections in subsequent compression cycles (this is because the flange can never be pulled back to perfectly flat before it yields in tension, similar to what will be discussed for braces in a later chapter). Computer programs are typically necessary to track the effect of all of these factors on the postbuckling behavior, negating some of the original appeal of the yield line approach in this particular application, but the ability to construct free-body diagrams anchored to a physical mechanism remains attractive for helping better understand the fundamental behavior of postbuckling behavior.

4.7 Self-Study Problems

Problem 4.1 A beam with constant strength, M_p, is fixed at one end and simply supported at the other. What is the maximum concentrated load that may be carried at the third point closest to the fixed end? Use both upper and lower bound methods. In the upper bound method, why doesn't the internal strain energy associated with elastic energy appear as part of the internal virtual work?

Problem 4.2 A fix–fix beam, loaded at midspan by a point load, P, originally had a uniform strength M_p over its entire length. However, as shown in the figure here, it is to be reinforced to have a strength of $2M_p$ in its midspan region as well as near its supports.

For that beam, use a lower bound approach (i.e., the statical method) to find the minimum lengths "x" and "y" over which the beam must be reinforced such that the load, P, that will produce the plastic collapse mechanism will be twice the corresponding value for the beam having a uniform strength of M_p.

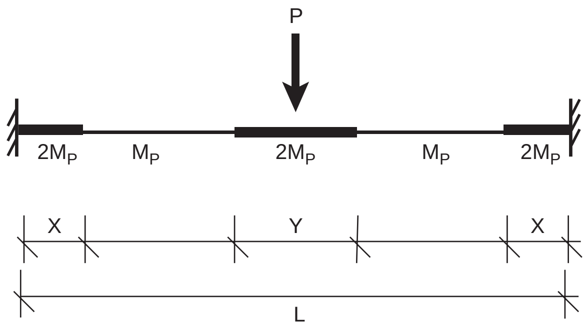

Problem 4.3 For the beam shown, determine the location of the plastic hinges and the collapse load using: (a) an "exact" method, (b) the method of adjustment of plastic hinges, and (c) replacement of distributed loads by equivalent concentrated loads. Compare and comment on these results.

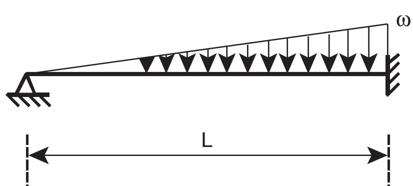

Problem 4.4 For the plastic mechanism that includes plastic hinges at both ends A and B, calculate where else along the span AB forms another plastic

hinge under the applied uniformly distributed load, ω. Also determine the value of ω when this plastic mechanism forms, and the corresponding reactions at A, B, and C.

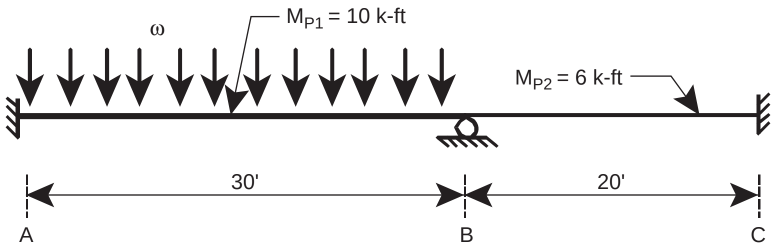

Problem 4.5 Use simple plastic theory and an upper bound approach to find the collapse mechanism and collapse load for the frame shown. Express the answer in terms of P, M_p, and L. Check that the solution obtained corresponds to a statically admissible field.

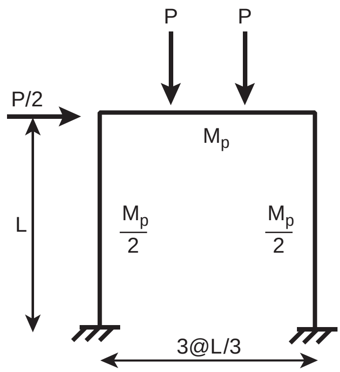

Problem 4.6 Use simple plastic theory and an upper bound approach to find the collapse mechanism and collapse load for the frame shown. Express the answer in terms of P, M_p, and L. Check that the solution obtained corresponds to a statically admissible field.

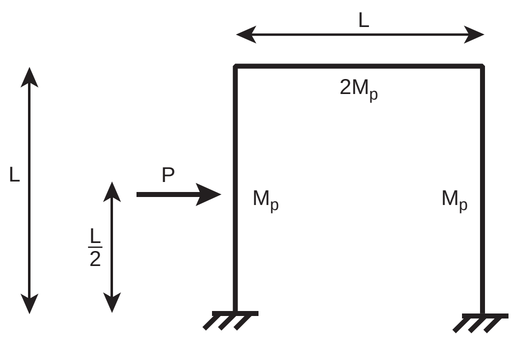

Problem 4.7 Due to errors in fabrication, there is a 1-in (25-mm) gap between the base of member AB and support A. Assuming the frame is forced into the correct position and then loaded as shown in the figure, find the collapse load using a step-by-step method. Verify this using the upper bound theorem. Discuss how the results would change if:

(1) No errors were made in initial fabrication.
(2) The height of AB was increased to approach infinity (but not equal to infinity).
(3) The height of AB was reduced to approach zero (but not equal to zero).

The members are all W21 × 57 (equivalent to W530 × 85 S.I. designation) beams with $Fy = 36$ ksi (250 MPa).

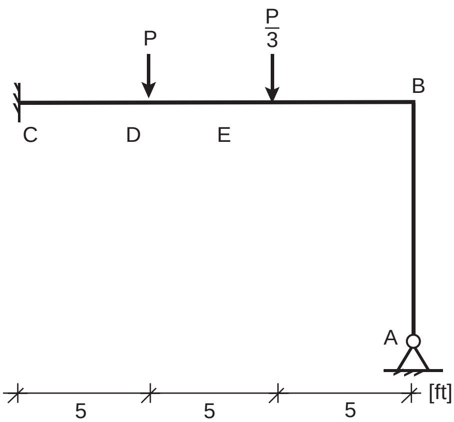

Problem 4.8 For the structure shown here, use the upper bound theorem to find the maximum load, P, that can be applied to this structure. Clearly sketch each plastic collapse mechanism considered. Also, show that the solution is statically admissible and draw the corresponding moment diagram.

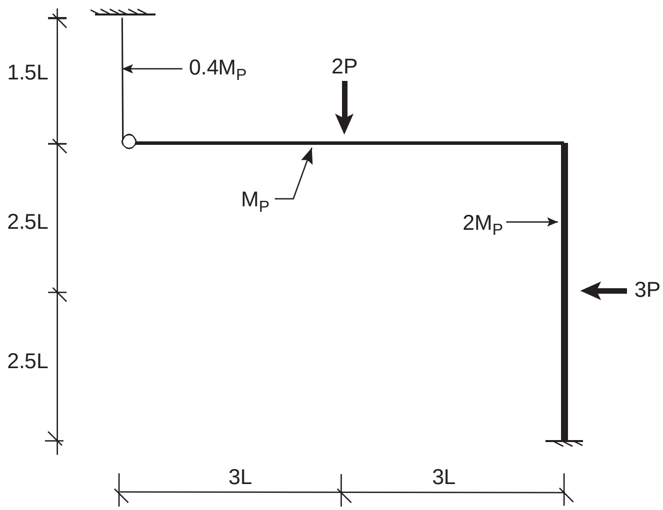

Problem 4.9 For the structure shown and the collapse mechanism proposed, determine the appropriate limit load:

(a) For the case $a = b$, $h_2 = 1.5h_1$, and $H = P$
(b) For the case $a = L/3$, $b = 2L/3$, $h_2 = 1.5h_1$, and $H = P$
(c) For the case $a = 2L/3$, $b = L/3$, $h_2 = 1.5h_1$, and $H = P$

What can be observed by comparing the results for these three cases? Explain why these results are logical in terms of fundamental engineering principles.

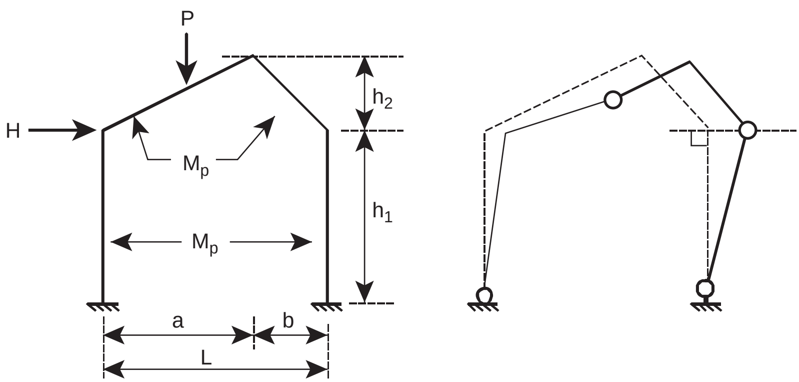

(a) (b)

Problem 4.10 Calculate the collapse load for the specific plastic mechanism shown as follows:

(a) For the case $a = b$, $h_2 = h_1/2$, and $H = P/2$
(b) For the case $a = L/3$, $b = 2L/3$, $h_2 = h_1/2$, and $H = P/2$
(c) For the case $a = 2L/3$, $b = L/3$, $h_2 = h_1/2$, and $H = P/2$

What can be observed by comparing the results for these three cases? Explain why these results are logical in terms of fundamental engineering principles.

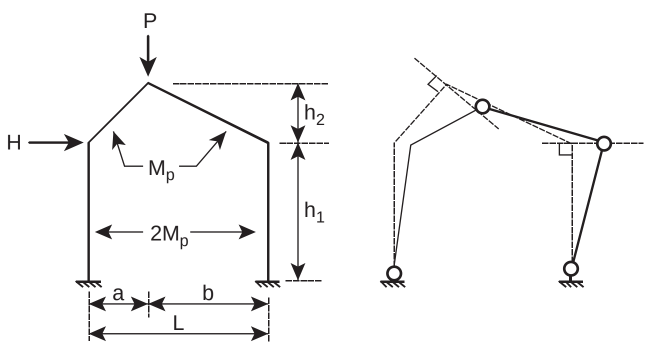

(a) (b)

Problem 4.11 Find the maximum value of P that can be applied to the structure shown. Use an upper bound approach and the concept of instantaneous center of rotation. Show that the collapse mechanism has a statically admissible moment distribution. Express the answer in terms of M_p and L.

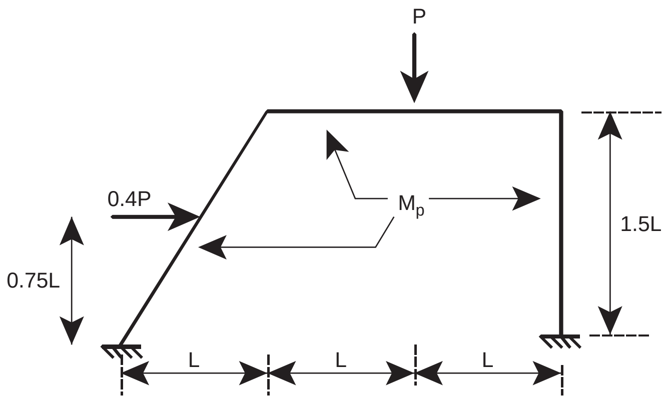

Problem 4.12

(a) Use simple plastic theory and an upper bound approach to find the collapse mechanism and collapse load for the frame shown. Note that the ends of the beams have been reinforced to $3M_p$, over a distance $L/20$, as shown in the figure. Express the answer in terms of M_p and L.

(b) Show that the solution leads to a statically admissible moment distribution.

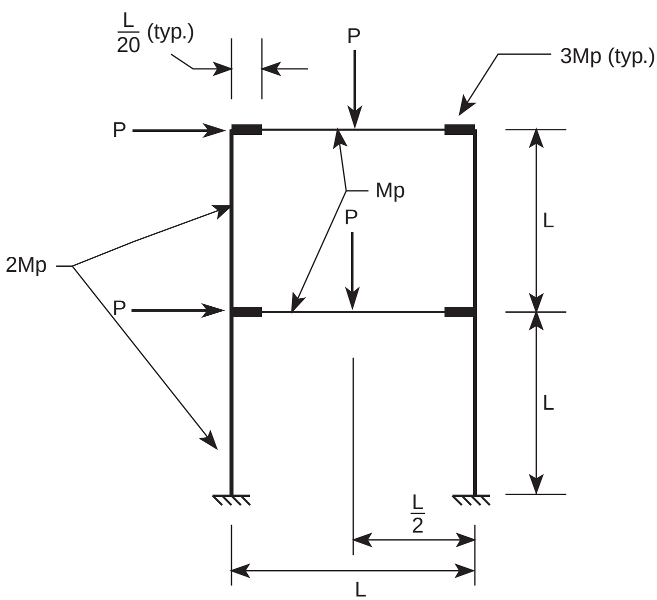

Problem 4.13 For the structure shown here, use the upper bound theorem to find the maximum load, P, that can be applied to this structure.

- For this particular problem, no need to show that the solution is statically admissible.
- Assume all plastic hinges to be flexural hinges.
- Assume the strength of all plastic hinges to be M_p, and neglect the reduction of M_p due to the possible presence of axial forces or shear.
- Express all results in fractions, not in decimals.
- Assume that the braces are infinitely rigid.

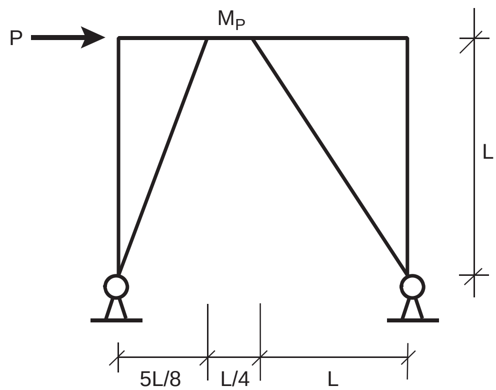

Problem 4.14 Use simple plastic theory and an upper bound approach to find the collapse mechanism and collapse load for the frame shown below. Express the answer in terms of P, N_y, M_p, and L (as appropriate).

(a) Assume that the knee braces are fully rigid (i.e., infinite areas) but that the beams have the flexural strengths shown in the figure.
(b) Assume that the beam and columns have infinite strength (i.e., infinite inertias), but that the knee braces have an axial plastic strength of N_y.

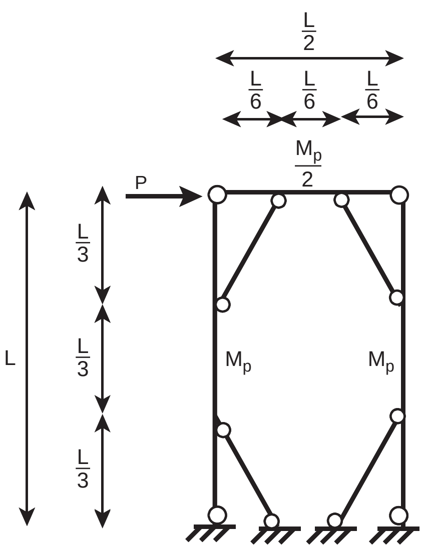

Problem 4.15 Using an upper bound approach, find the load P (expressed in terms of m_p, t, and L) for the yield line plastic mechanism shown in the figure. Note that P is a concentrated load applied at the center of the plate and perpendicular to it. The plate is isotropic and fixed on all edges; its thickness is t and its plastic moment per unit length is m_p.

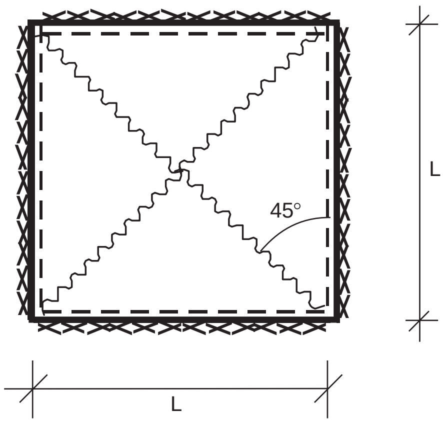

Problem 4.16 Using an upper bound approach, find the load P (expressed in terms of m_p, t, and L) for the yield line plastic mechanism shown in the figure. Note that P is a concentrated load applied at the center of the plate and perpendicular to it. The plate is isotropic and fixed on all edges; its thickness is t and its plastic moment per unit length is m_p.

(a) Derive an expression for the general case of an n-sided plate.
(b) Compare the solution in (a) with the result for Problem 4.15.
(c) Derive an expression for the case $n = \infty$.

Recall that for small angles, $\tan x \approx x + x^3/3 + 2x^5/15$.

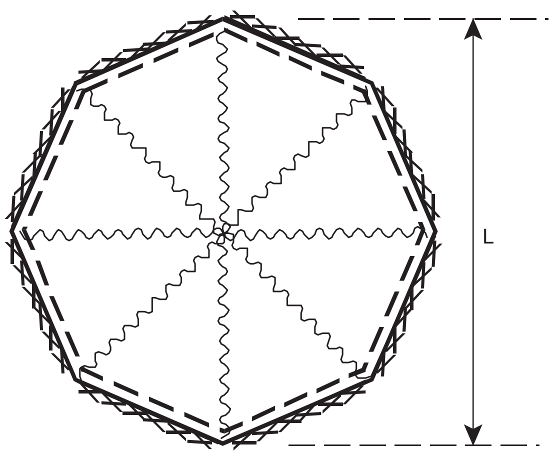

Problem 4.17 Determine the uniformly distributed load, ω (in kips/in^2), that can be applied on that 0.5 in thick steel plate for the assumed yield line pattern shown here. Make sure to use compatible units. (Beware that plate size is shown in feet on the sketch.)

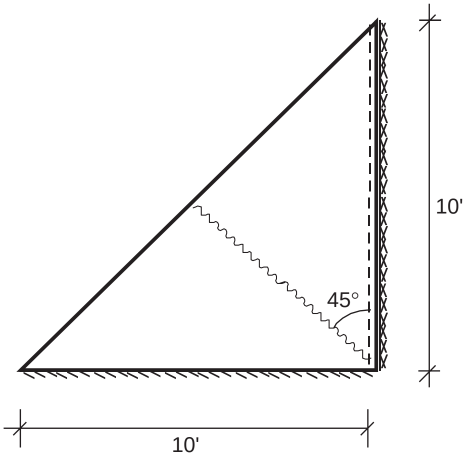

Problem 4.18 A steel cruiser ship has been entirely constructed of steel plates. One 9-ft × 7-ft room has a 2-in-thick steel floor. This steel plate is fully fixed on three sides, and completely free on the other side.

Determine what is the largest partition load, p_a (in kips/in), that could be applied on that plate, if that partition load is located as shown in the figure, and if no other loads are applied on that plate. This determination is to be based on a yield line analysis using the upper bound method. Note that a partition-load is essentially a line load.

(a) Calculate this maximum partition load, for the yield line pattern shown.
(b) Indicate if the value calculated in (a) is "conservative" or "unconservative." Explain why in a few sentences.

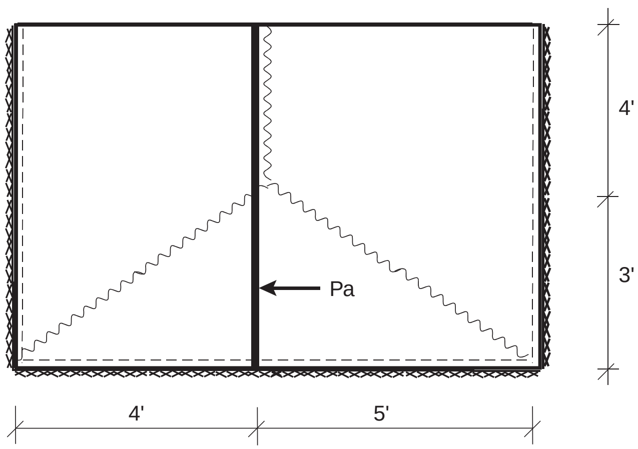

Problem 4.19 A series of triangular plates, fixed at their base and pinned at their top (as shown below) are subjected to a lateral load. What is the plastic strength of the system, P, as a function of the other parameters shown on that figure.

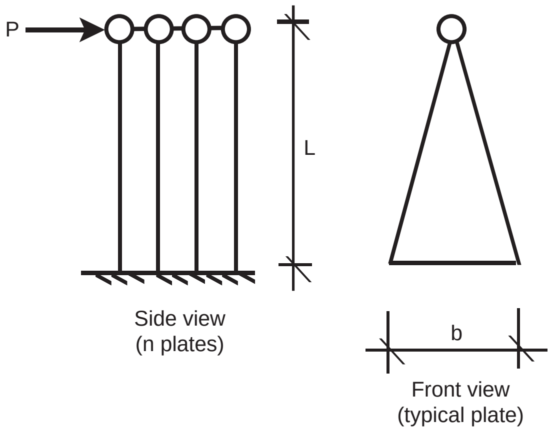

Problem 4.20 Determine the required angle thickness, t, to resist the moment, M, applied to the bolted-angle connection shown below using plastic analysis/ yield line theory.

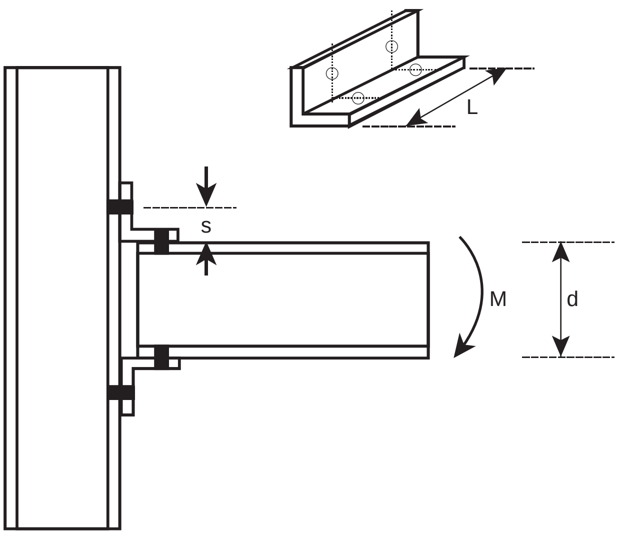

Problem 4.21

(a) What is the uniqueness theorem?
(b) What is a structure with an overly complete collapse mechanism?

References

AISC. 2010. *ANSI/AISC* 358-10, *Prequalified Connections for Special and Intermediate Steel Moment Frames for Seismic Applications*. Chicago: American Institute of Steel Construction.

AISC. 2011. *Manual of Steel Construction,* 14th ed. Chicago: American Institute for Steel Construction.

CISC. 2010. *Handbook for Structural Steel Design*. Toronto: Canadian Institute for Steel Construction.

Gioncu, V., and Mazzolani, F. M. 2002. *Ductility of Seismic Resistant Steel Structures*. London: Spon Press, p. 694.

Hiriyur, B. K. J., and Schafer, B. W. 2005. "Yield-line Analysis of Cold-Formed Steel Members." *International Journal of Steel Structures*, vol. 5, no. 1, 43–54.

Horne, M. R., and Morris, L. J. 1981. *Plastic Design of Low-Rise Frames*. Cambridge, MA: MIT Press.

Lee, K. 2004. "Response of Steel Moment Connections after Buckling," Ph.D. thesis, University of California, Berkeley, CA, p. 147.

Lee, K., and Stojadinovic, B. 2007. ''Rotation Capacity of Pre-Qualified Moment Connections: A Yield Line Approach,'' *Proceedings 2007 ASCE Structures Congress*, Long Beach, CA, CD, pp. 1–16.

Mann, A. P. 1968. "Plastically Designed End-Plate Connections." Ph.D. Thesis, University of Leeds, England.

Mann, A. P., and Morris, L. J. 1979. "Limit Design of Extended End-Plate Connections." *Journal of the Structural Division, ASCE*, vol. 105, no. 3, 511–526.

Murray, M., and Sumner, E. A. 2003. *Design Guide* 4*: Extended End-Plate Moment Connections Seismic and Wind Applications*, 2nd ed. Chicago: American Institute of Steel Construction.

Park, R., and Gamble, W. L. 1999. *Reinforced Concrete Slabs*. New York: Wiley, p. 736.

Petcu, D., and Gioncu, V. 2003. "Computer Program for Available Ductility Analysis of Steel Structures." *Computer and Structures*, vol. 81, 2149–2164.

Sarraf, M., and Bruneau, M. 1994. "Experimental Study on Cyclic Behavior of Riveted Stiffened-Seat Angle Connections," *Ottawa Carleton Earthquake Engineering Research Centre Report OCEERC 94-01*, Ottawa, December 1994, 172 pp.

Sarraf, M. H. K., and Bruneau, M. 1996. "Cyclic Testing of Existing and Retrofitted Riveted Stiffened-Seat Angle Connections." *ASCE Journal of Structural Engineering*, vol. 122, no. 7, 762–775.

Srouji, R., Kukreti, A. R., and Murray, T. M. 1983. "Yield-Line Analysis of End-Plate Connections with Bolt Force Predictions," *Research Report No. FSEL/MBMA 83-05*. Fears Structural Engineering Laboratory, School of Civil Engineering and Environmental Science, University of Oklahoma, Norman, OK.

SSRC. 1993. *Plastic Hinge Based Methods for Advanced Analysis and Design of Steel Frames—An Assessment of the State-of-the-Art*, White, D. W., and Chen, W. F., editors. Bethlehem, PA: Structural Stability Research Council.

Surtees, J.O., and Mann, A.P. 1970. "End-Plate Connections in Plastically Designed Structures," Conference on Joints in Structures, University of Sheffield, England, Vol. 1, Paper 5.

CHAPTER 5

Systematic Methods of Plastic Analysis

The examples of combined plastic mechanisms presented in Chapter 4 show that the challenge in analyzing complex structures lies in finding the collapse mechanism that will give the true (unique) plastic collapse load. Systematic methods of plastic analysis are therefore needed to efficiently identify this correct mechanism. A number of such methods have been developed in the past, and two are reviewed in this chapter: direct combination of mechanisms, which is more suitable for hand calculation, and the method of inequalities, more suitable for linear programming. However, in both these methods, knowledge of the number of basic mechanisms present in a given structure is imperative for a successful solution search, and this topic is therefore presented first.

5.1 Number of Basic Mechanisms

Four basic mechanism types were identified in the previous chapter:

- Beam
- Panel
- Gable
- Joint

In any given structure, the first task in systematic plastic analysis is to locate and identify those basic mechanisms. To provide some assistance in that endeavor, it is worthwhile to formalize the relationship between the degree of indeterminacy of a structure, X, the number of potential plastic hinge locations, N, and the number of possible basic mechanisms, n. This is accomplished by the following equation:

$$n = N - X \tag{5.1}$$

Figure 5.1 illustrates how this equation can be used. Note that the same single-bay moment-resisting frame is used throughout the

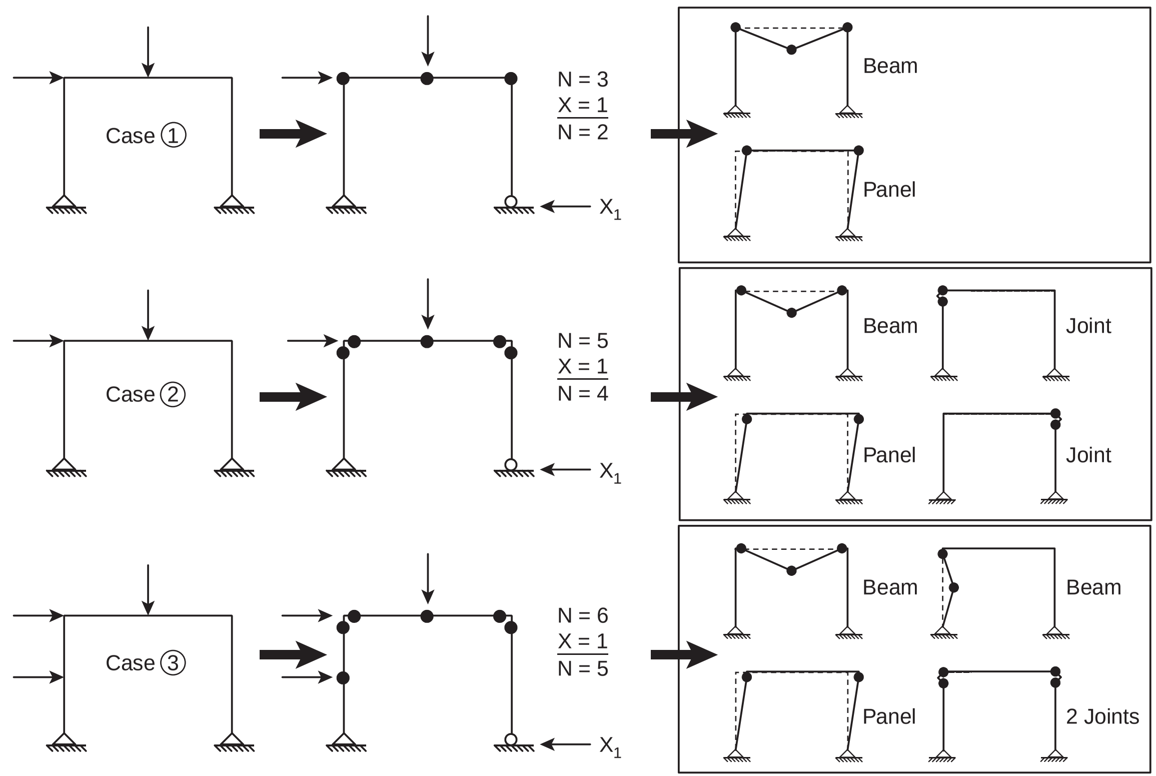

Figure 5.1 Examples of identification of basic mechanisms for a simple frame indeterminate to the first degree.

example shown in that figure. Simple observation reveals this frame to be indeterminant to the first degree, $X = 1$. Using the knowledge developed in Chapter 4, one can identify the number of potential plastic hinge locations, N. Cases 1 and 2 in Figure 5.1 illustrate that it doesn't matter whether one considers only one plastic hinge at each corner of that frame or two (i.e., one at the end of each member framing into the joint). Case 1 is a simplified version of Case 2 in which the joint mechanisms have been implicitly considered. In Case 1, the engineer must determine whether the flexural capacity at the corner joint is equal to the plastic moment of the column or the beam, whereas the more explicit approach used in Case 2 systematically manages this information.

For hand calculations, the approach of Case 1 is recommended when only two members frame into a joint, and the approach of Case 2 must be used at all joints in which more than two members meet (as shown in Figures 5.2 and 5.3). Real hinges (such as at the base of the frames in Figure 5.1) are never included in the value of N because they cannot do plastic work. Note that the number of potential plastic hinge locations is also a function of loading, as shown by a comparison of Cases 2 and 3 in Figure 5.1.

Once the number of basic mechanisms is known, judgment is often necessary to identify these possible mechanisms. Although it is straightforward to find the 16 basic mechanisms in Figure 5.2, more complex structures, such as the one shown in Figure 5.3, can be more challenging. Note that for the panel mechanisms in those two figures,

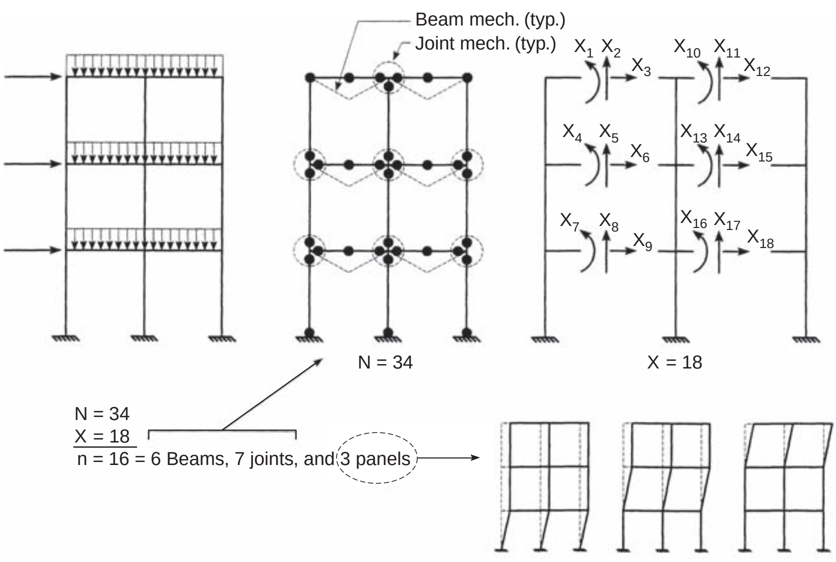

Figure 5.2 Examples of identification of basic mechanisms for a three-story frame loaded as shown.

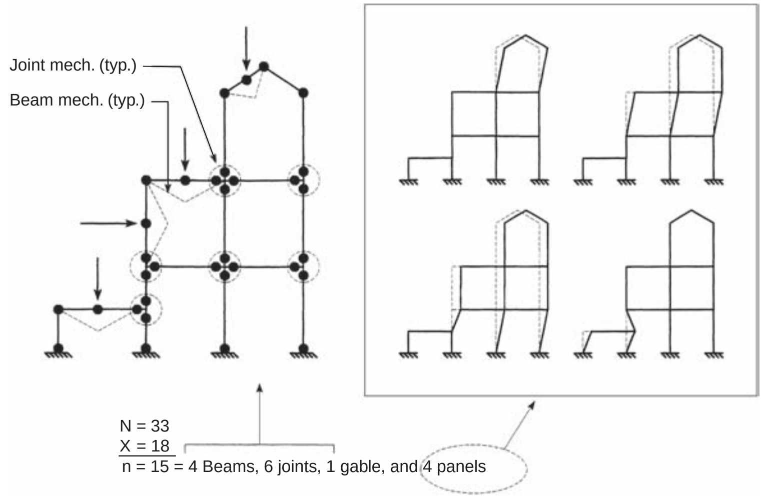

FIGURE 5.3 Examples of identification of basic mechanisms for a three-story frame loaded as shown.

the floors above the story displacing laterally move rigidly with the displacing floor; the characteristic of this approach is that a single "panel level" is distorted as a parallelogram for each mechanism. An alternative approach consists of preventing all parallel members from moving except the one being displaced for the panel mechanism considered (as done for the rightmost case in Figure 5.4); the characteristic

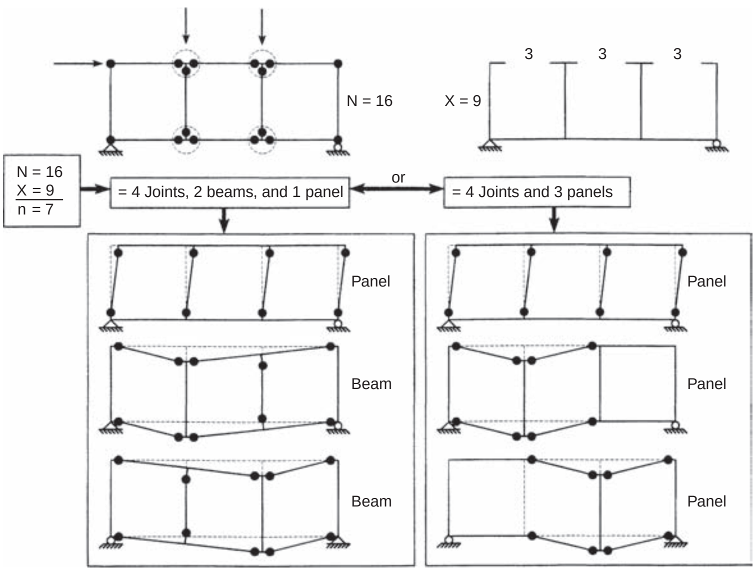

FIGURE 5.4 Examples of basic mechanisms identification for a Veerendel truss.

of this approach is that only one line of structural members sways for each mechanism. Both approaches are fine, but mixing together cases from both approaches is not recommended, being often a source of confusion (i.e., double-counting some panel mechanisms and missing others).

In some cases, the mechanism identification procedure can be subjective because two (or more) different sets of basic mechanisms can be obtained for the same structure. This is illustrated for the Veerendel truss in Figure 5.4. The basic mechanisms constitute only the building blocks for systematic plastic analysis, so any appropriate set of basic mechanisms will eventually lead to a correct solution (although the length of the "path" toward that goal may vary).

5.2 Direct Combination of Mechanisms

The direct-combination-of-mechanisms method is a systematic extension of the upper bound method presented in the previous chapter. In the upper bound method, various basic and combined mechanisms are added or subtracted by trial and error until the mechanism having the lowest plastic collapse load is found. By virtue of the uniqueness theorem, this calculated collapse load is the true solution if it also produces a statically admissible moment diagram.

Therefore, in this method, the search for the plastic collapse load proceeds through systematic combinations of mechanisms to either increase the external work or decrease the internal work. A tabular procedure is adopted to keep a manageable record of basic mechanisms and previously attempted combinations as well as to facilitate the identification of those combinations that can be best combined. This systematic tabular approach is best described through the use of examples.

5.2.1 Example: One-Bay, One-Story Frame

The one-bay, one-story frame previously analyzed in Chapter 4 with a trial-and-error approach (see Figure 4.11) is considered here for the case $a = L/2$. Obviously, a systematic method of plastic analysis is not necessary for such a simple example, but the objective at this point is to illustrate how to use the tabular procedure; additional complexities at this early stage would only detract from this goal.

First, in this systematic method, an arbitrary sign convention must be adopted. It is expedient to draw a dotted line along the frame members to visually define the adopted sign convention, as shown in Figure 5.5; moments and rotations are positive when they produce tension on the side of structural members adjacent to the dotted lines. Other sign conventions are possible (such as tracking clockwise and counterclockwise plastic hinge rotations) but not used here. Then, one establishes the number of basic mechanisms for the structure using the procedure described in Section 5.1.

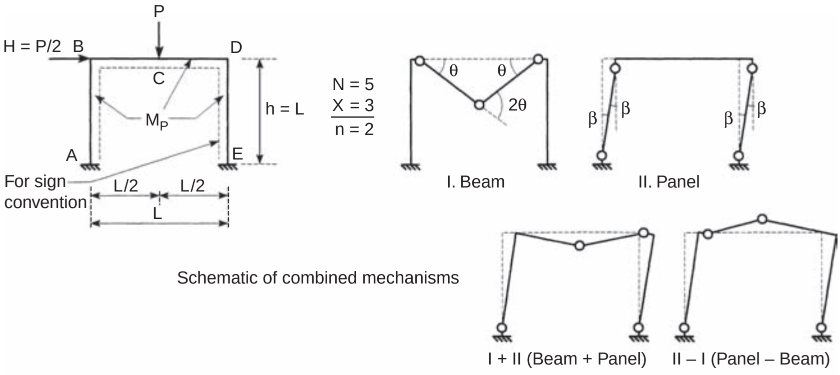

FIGURE 5.5 One-bay, one-story frame example.

With this information, the general layout of the table needed for the structure under consideration can be drawn, as shown in Table 5.1. In this example, there are five potential plastic hinge locations and the structure is indeterminant to the third degree, producing two basic mechanisms: one beam and one panel, as shown in Figure 5.5. Note that the sign of the plastic rotations is retained with the plastic hinge data in Table 5.1. Also, for the sake of clarity, basic and combined mechanisms are separated in this table.

The characteristics of the previously sketched basic mechanisms are first entered in this table. Normalized coefficients are used as much as possible for clarity and to expedite the mechanisms combination process. For each mechanism, the internal work that develops at each plastic hinge location is inventoried under Plastic Hinge Data. Thus, one can directly obtain the total internal work corresponding to any given mechanism by adding the absolute values of the plastic hinge data across a row of the table. For structures composed of more than one section shape, each member would have a different plastic moment. The plastic hinge data therefore simultaneously accounts for the magnitude of the plastic rotation ($\beta\,\theta$) and plastic moment ($\alpha\, M_p$), as shown in the header of Table 5.1.

One should always draw rough sketches of all mechanisms (using the tabulated plastic hinge data) to keep track of the physical meaning of each combination. The total external work should always be computed directly from these sketches. For small structures, the rough sketches can be inserted directly into the table.

Once the basic mechanisms have been logged, one must search for combinations that minimize the internal work, maximize the external work, or do both. The tabular format presented here facilitates the identification of combinations that will result in the cancellation of plastic hinges (i.e., reduction of internal work). In this simple example, the number of possibilities is limited. The two basic

Mechanism		Plastic Hinge Data $(\alpha M_p)(\beta\theta)/(M_p\theta)$					Internal Work	External Work		
Identifier	**Title**	**A**	**B**	**C**	**D**	**E**	$W_i/M_p\theta$	$W_e/PL\theta$	P	$P/(M_p/L)$
Basic Mechanisms										
I	Beam	0	− 1	+ 2	− 1	0	4	0.5	$8M_p/L$	8
II	Panel	− 1	+ 1	0	− 1	+ 1	4	0.5	$8M_p/L$	8
Combined Mechanisms										
I + II	Beam + panel	− 1	0	+ 2	− 2	+ 1	6	1.0	$6M_p/L$	6 ✔
II − I	Panel − beam	− 1	+ 2	− 2	0	+ 1	6	0	∞	∞

TABLE 5.1 Systematic Direct Combination of Mechanisms for One-Bay, One-Story Example (Figure 5.5)

mechanisms are first directly combined by simple addition, column by column, of the normalized plastic rotations listed in the respective rows of Table 5.1 corresponding to these two basic mechanisms. Then, these are subtracted to demonstrate that some combinations do not progress the solution. Inspection of the sketches of the mechanism reveals that subtracting the beam mechanism from the panel mechanism reduces the amount of external energy.

For each combination, the corresponding plastic collapse load must be calculated from the ratio of the internal work to the external work because these results from separate rows in Table 5.1 are not additive. Whenever one believes that the lowest plastic collapse load has been found, the resulting moment diagram should be drawn. A statically admissible moment diagram will reveal that the true solution has been found, whereas, in the alternative, the resulting diagram will indicate where plastic hinges should develop and thus provide guidance for the most promising subsequent combination.

5.2.2 Example: Two-Story Frame with Overhanging Bay

The two-story frame with an overhanging bay, shown in Figure 5.6, is analyzed to illustrate how to combine mechanisms in a more general

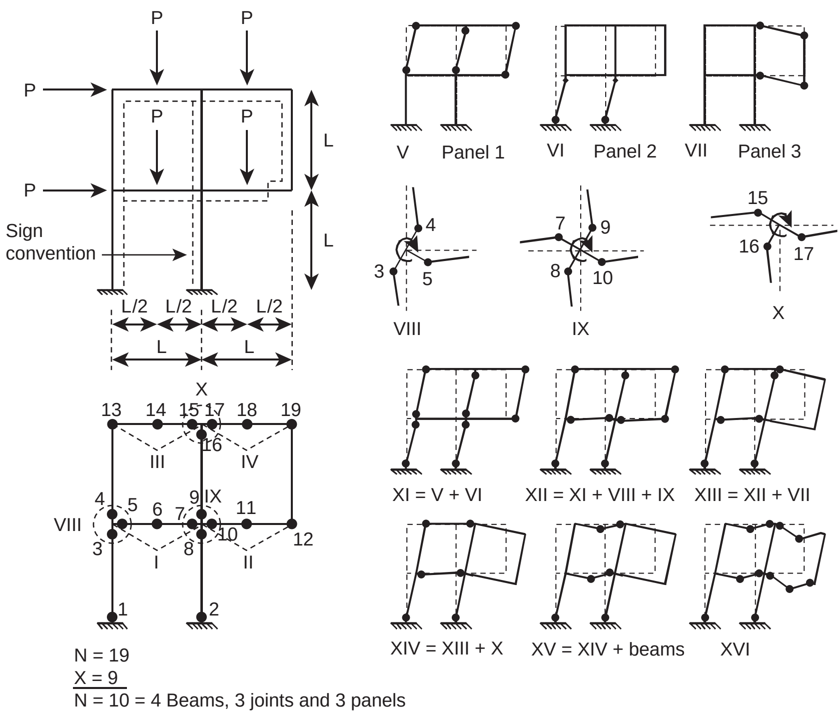

Figure 5.6 Two-story frame with an overhang example for application of direct combination of mechanism method.

situation. Per the systematic methodology presented in the previous example, a sign convention is selected, the potential plastic hinge locations are determined, and the basic plastic mechanisms are identified. The layout of Table 5.2 is then established, and the plastic collapse loads for each basic mechanism are calculated. Note that joint mechanisms are used only to eliminate internal work: therefore, no external work or plastic collapse load is calculated for those mechanisms. Also, when single hinges are used in joints connecting only two members (such as for hinges 12, 13, and 19 in this example), the dotted line indicating the sign convention must extend continuously across such joints to avoid possible confusion (as would have been otherwise the case for hinge 12 here)

There is no single strategy to find the combined mechanism that will produce the lowest plastic collapse load because the particulars of a given problem will suggest different approaches. (In fact, even for a given structure, different engineers may adopt different search sequences.) Here, results for the basic mechanisms indicate that the panel mechanisms produce the largest amount of external work, the lowest plastic collapse load being that of mechanism VI. Therefore, as an arbitrary starting point, one could first try to combine some panel mechanisms to increase the amount of external work. However, as shown by the combination of mechanisms V and VI (noted XI in the table), this also results in significantly more internal work because the plastic hinges of the two mechanisms are additive. This, as well as the sketch of this first combination, suggests that joint mechanisms must be introduced to reduce internal work. A combination of mechanisms V, VI, VIII, and IX is attempted (mechanism XII), but only one plastic hinge is eliminated in the process.

Examination of the results so far reveals that adding panel 3 would reduce the amount of internal work (trading hinges 10, 17, and 12 for 19) and increase the amount of external work. This is tried with mechanism XIII, which gives the lowest value of the plastic collapse load at this point. As examination of that mechanism in Figure 5.6 suggests, adding mechanism X removes one further plastic hinge (mechanism XIV) and gives a lower value for the collapse load. Mechanism XV investigates if the additional external work produced by the beam mechanisms exceeds the extra internal work thus introduced; the resulting plastic collapse load is found to be higher than for mechanism XIV. Although one could attempt some additional trial combinations if deemed necessary (such as mechanism XVI in Figure 5.6), it appears that no other combination of mechanisms would provide a lower value for the plastic collapse load. The moment diagram for mechanism XIV (not shown here) is found to be statically admissible confirming that the true solution has been found.

As demonstrated by the above examples, without engineering judgment, the direct combination method, even using a systematic procedure, can rapidly become excruciatingly laborious as structural

Mechanism		Plastic Hinge Data $(\alpha M_p)(\beta\theta)/(M_p\theta)$																			Internal Work	External Work		
Identifier	Name/ sketch	1	2	3	4	5	6	7	8	9	10	11	12	13	14	15	16	17	18	19	$W_i/M_p\theta$	$W_e/PL\theta$	P	$P/(M_p/L)$
Basic Mechanisms																								
I	Beam 1					− 1	+ 2	− 1													4	0.5	8 M_p/L	8
II	Beam 2										− 1	+ 2	− 1								4	0.5	8 M_p/L	8
III	Beam 3													− 1	+ 2	− 1					4	0.5	8 M_p/L	8
IV	Beam 4																	− 1	+ 2	− 1	4	0.5	8 M_p/L	8
V	Panel 1				− 1					+ 1			+ 1	+ 1			− 1			− 1	6	1.0	6 M_p/L	6
VI	Panel 2	− 1	+ 1	+ 1					− 1												4	2.0	2 M_p/L	2
VII	Panel 3										− 1		− 1					− 1		+ 1	4	1.0	4 M_p/L	4
VIII	Joint 1			− 1	+ 1	+ 1															3	–	–	–
IX	Joint 2							− 1	+ 1	− 1	+ 1										4	–	–	–
X	Joint 3															− 1	+1	+ 1			3	–	–	–
Combined Mechanisms																								
XI	V + VI	− 1	+ 1	+ 1	− 1				− 1	+ 1			+ 1	+ 1			− 1			− 1	10	3	3.33 M_p/L	3.33
XII	XI + VIII + IX	− 1	+ 1			+ 1		− 1			+ 1		+ 1	+ 1			− 1			− 1	9	3	3 M_p/L	3.0
XIII	XII + VII	− 1	+ 1			+ 1		− 1						+ 1			− 1	− 1			7	4	1.75 M_p/L	1.75
XIV	XIII + X	− 1	+ 1			+ 1		− 1						+ 1		− 1					6	4	1.5 M_p/L	1.5 ✔
XV	XIV + I + III	− 1	+ 1				+ 2	− 2							+ 2	− 2					10	5	2.0 M_p/L	2.0

Table 5.2 Systematic Direct Combination of Mechanisms for Two-Story Frame with an Overhanging Bay (Figure 5.6)

complexity grows. Partly for that reason, the method presented in the following section, although nearly suitable only for implementation in computer programs, is preferable when one is dealing with extremely large problems (or for small problems whenever one is ready to trade control against expediency, reserving engineering judgment for the task of checking the validity of the generated computer results).

5.3 Method of Inequalities

Although the systematic method of plastic analysis formulated in the previous section can also be computerized, the most computationally efficient solution procedure for plastic analysis is the method of inequalities, based on a matrix formulation of the lower bound method. However, because formal presentation of this mathematical procedure would be abstract, an example is presented instead to illustrate how a systematic lower bound method can proceed from the method of inequalities.

Considering the small size of this example problem, the corresponding amount of computations necessary for the solution presented hereafter may appear excessive, particularly when one can find the correct answer within minutes and with a minimum of calculations by using the graphical approach presented earlier. Nonetheless, the principal objective here is to illustrate how a systematic computerized procedure can be designed to automatically converge to the correct solution. In the process, for further clarity, expanded equations instead of matrix notation have been used (the matrix methods implemented in computer programs being too numerically intensive for hand calculations).

The frame considered in this example is shown in Figure 5.7, along with the four potential plastic hinge locations corresponding to the loading condition. Given that this frame is indeterminate to the second degree ($x = 2$), it is possible to express the moments at each of the potential plastic hinge locations as a function of any two arbitrarily selected redundant forces. The chosen sign convention, indicated by the dotted line, is drawn along the frame members in Figure 5.7. In this problem, the two reactions at the right support are selected as the redundant forces, and a set of equations can be written for the moment at the potential plastic hinge locations as a function of these forces.

$$M_4 = -2RL \tag{5.2a}$$

$$M_3 = -2RL + VL \tag{5.2b}$$

$$M_2 = -2RL + 2VL - 2FL \tag{5.2c}$$

$$M_1 = 2VL - 2FL - 6FL \tag{5.2d}$$

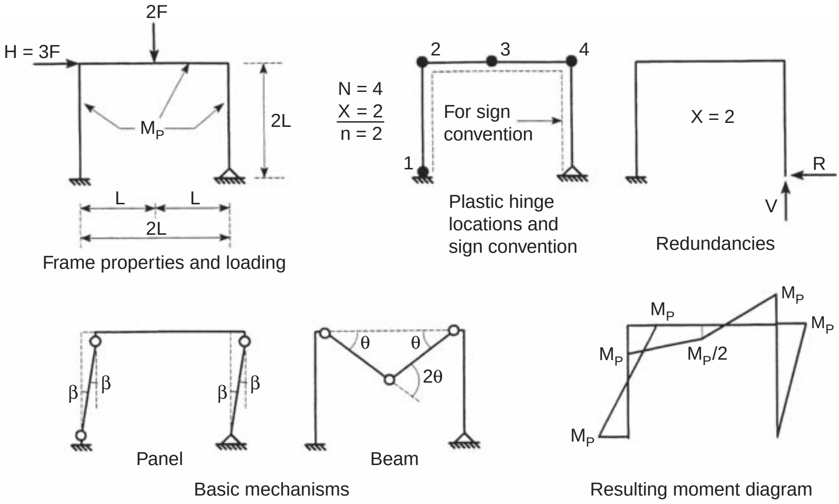

FIGURE 5.7 Frame example of the method of inequalities.

This set of four equations cannot be solved because it contains six unknowns (four moments and two redundant forces). However, one can eliminate the two redundant forces using algebraic manipulations and substitutions. As a result, the above system of equations is reduced to the following two equations and four unknowns:

$$-M_2 + 2M_3 - M_4 = 2FL \tag{5.3a}$$

$$-M_1 + M_2 - M_4 = 6FL \tag{5.3b}$$

Note that these two equations represent two equilibrium equations for this structure. Incidentally, one can obtain the same two equations, with much less difficulty, by writing the virtual-work equations for the two basic mechanisms of this structure. Hence, for the basic beam and the panel mechanisms shown in Figure 5.7, equating internal and external work (Chapter 4) gives:

$$-M_2\theta + 2M_3\theta - M_4\theta = 2FL\theta \tag{5.4a}$$

$$M_2\theta - M_1\theta - M_4\theta = 6FL\theta \tag{5.4b}$$

from which the θs can be eliminated. This should not be surprising because, in essence, work equations are also equilibrium equations.

However, for these basic mechanisms, the hinge moments, M_i, are expressed not in terms of M_p, but rather as unknowns whose values remain to be determined. For large structural systems, this approach to obtain a set of equilibrium equations is preferred because it is considerably easier to write virtual-work equations for a number of basic mechanisms than equilibrium equations in terms of redundants.

Nonetheless, at this point, the above remains a system with more unknowns (four) than equations (two). However, within the context of plastic design, a solution is possible because additional constraints exist that limit the magnitude of moment at each potential plastic hinge as follows:

$$-M_p \le M_1 \le M_P \tag{5.5a}$$

$$-M_p \le M_2 \le M_P \tag{5.5b}$$

$$-M_p \le M_3 \le M_P \tag{5.5c}$$

$$-M_p \le M_4 \le M_P \tag{5.5d}$$

In practical situations, the plastic moments would likely differ at the different plastic hinge locations; different positive and negative values of plastic moment are even possible at a given location for composite structures. However, for this example, a single value of plastic moment is assumed throughout the entire frame for the sake of simplicity.

The above equilibrium equations and inequality relationships, coupled with the knowledge that a lower bound approach is a search for the largest possible applied loads (while respecting all above equalities and inequalities), make possible a solution to this problem. The algorithm to achieve such a solution typically uses the equilibrium equations and the inequality conditions to systematically eliminate the unknowns, one by one, performing all possible cross-comparisons of inequality equations in the process, until all remaining equations are expressed in terms of known quantities. One can then find the largest possible value for the applied loads (often expressed as a function of a common load, F) simply by scanning all resulting inequalities. The largest value of F that satisfies all resulting constraints gives the collapse load.

For the example at hand, the equilibrium equations are first used to express two of the remaining unknowns in terms of the others:

$$M_3 = FL + \frac{1}{2}(M_2 + M_4) \tag{5.6a}$$

$$M_1 = -6FL + M_2 - M_4 \tag{5.6b}$$

These results from the equilibrium equations are then substituted in the appropriate inequalities:

$$-M_p \le -6FL + M_2 - M_4 \le M_p \tag{5.7a}$$

$$-M_p \le M_2 \le M_p \tag{5.7b}$$

$$-M_p \le FL + \frac{1}{2}(M_2 + M_4) \le M_p \tag{5.7c}$$

$$-M_p \le M_4 \le M_p \tag{5.7d}$$

From this point on, further elimination of unknowns through the inequality relationships proceeds by construction of all possible inferences from the inequality set. For example, to eliminate M_2 from the inequality set, all inequality equations that contain M_2 must be rearranged to isolate that term within the inequalities. This gives:

$$-M_p \le M_2 \le M_p \tag{5.8a}$$

$$-2M_p - 2FL - M_4 \le M_2 \le 2M_p - 2FL - M_4 \tag{5.8b}$$

$$-M_p + 6FL + M_4 \le M_2 \le M_p + 6FL + M_4 \tag{5.8c}$$

Then the left side of the inequalities given in Eq. (5.8) is systematically compared with the right side of the same inequalities. More explicitly, the left-side inequality of Eq. (5.8a) is compared with the right side inequalities of Eqs. (5.8a), (5.8b), and (5.8c); the left-side inequality of Eq. (5.8b) is compared with the same three right-side inequalities; and finally, the left side of Eq. (5.8c) is similarly compared. This gives:

$$-M_p \le M_p \tag{5.9a}$$

$$-M_p \le 2M_p - 2FL - M_4 \tag{5.9b}$$

$$-M_p \le M_p + 6FL + M_4 \tag{5.9c}$$

$$-2M_p - 2FL - M_4 \le M_p \tag{5.9d}$$

$$-2M_p - 2FL - M_4 \le 2M_p - 2FL - M_4 \tag{5.9e}$$

$$-2M_p - 2FL - M_4 \le M_p + 6FL + M_4 \tag{5.9f}$$

$$-M_p + 6FL + M_4 \le M_p \tag{5.9g}$$

$$-M_p + 6FL + M_4 \le 2M_p - 2FL - M_4 \tag{5.9h}$$

$$-M_p + 6FL + M_4 \le M_p + 6FL + M_4 \tag{5.9i}$$

Equations (5.9a), (5.9e), and (5.9i) are automatically satisfied. Then, by finding matching pairs, one can write Eq. (5.10a) [from Eqs. (5.9c) and (5.9g)], Eq. (5.10b) [from Eqs. (5.9b) and (5.9d)], and Eq. (5.10c) [from Eqs. (5.9f) and (5.9h)] as follows:

$$-2M_p - 6FL \le M_4 \le 2M_p - 6FL \tag{5.10a}$$

$$-3M_p - 2FL \le M_4 \le 3M_p - 2FL \tag{5.10b}$$

$$-\frac{3}{2}M_p - 4FL \le M_4 \le \frac{3}{2}M_p - 4FL \tag{5.10c}$$

$$-M_p \le M_4 \le M_p \tag{5.10d}$$

By repeating the above process to eliminate M_4, that is, by systematically comparing each left side of the inequalities given in Eq. (5.10) with the corresponding four right sides of the same set of inequality equations, one obtains the following set of 16 inequalities:

$$-2M_p - 6FL \le 2M_p - 6FL \tag{5.11a}$$

$$-2M_p - 6FL \le 3M_p - 2FL \tag{5.11b}$$

$$-2M_p - 6FL \le \frac{3}{2}M_p - 4FL \tag{5.11c}$$

$$-2M_p - 6FL \le M_p \tag{5.11d}$$

$$-3M_p - 2FL \le 2M_p - 6FL \tag{5.11e}$$

$$-3M_p - 2FL \le 3M_p - 2FL \tag{5.11f}$$

$$-3M_p - 2FL \le \frac{3M_p}{2} - 4FL \tag{5.11g}$$

$$-3M_p - 2FL \le M_p \tag{5.11h}$$

$$-\frac{3M_p}{2} - 4FL \le 2M_p - 6FL \tag{5.11i}$$

$$-\frac{3M_p}{2} - 4FL \le 3M_p - 2FL \tag{5.11j}$$

$$-\frac{3M_p}{2} - 4FL \le \frac{3M_p}{2} - 4FL \tag{5.11k}$$

$$-\frac{3M_p}{2} - 4FL \le M_p \tag{5.11l}$$

$$-M_p \le 2M_p - 6FL \tag{5.11m}$$

$$-M_p \le 3M_p - 2FL \tag{5.11n}$$

$$-M_p \le \frac{3M_p}{2} - 4FL \tag{5.11o}$$

$$-M_p \le M_p \tag{5.11p}$$

By eliminating Eqs. (5.11a), (5.11f), (5.11k), and (5.11p), which provide no useful information, one obtains the following 12 inequalities for F, respectively:

$$-\frac{5M_p}{4L} \le F \tag{5.12a}$$

$$-\frac{7M_p}{4L} \le F \tag{5.12b}$$

$$-\frac{M_p}{2L} \le F \tag{5.12c}$$

$$F \le \frac{5M_p}{4L} \tag{5.12d}$$

$$F \le \frac{9M_p}{4L} \tag{5.12e}$$

$$-\frac{2M_p}{L} \le F \tag{5.12f}$$

$$F \le \frac{7M_p}{4L} \tag{5.12g}$$

$$-\frac{9M_p}{4L} \le F \tag{5.12h}$$

$$-\frac{5M_p}{8L} \le F \tag{5.12i}$$

$$F \le \frac{M_p}{2L} \tag{5.12j}$$

$$F \le \frac{2M_p}{L} \tag{5.12k}$$

$$F \le \frac{5M_p}{8L} \tag{5.12l}$$

The range of values of F that can satisfy all the above inequalities is $-M_p/2 \le F \le M_p/2$, or in absolute value, $F = M_p/2$. From this result, one can calculate the actual value of each previously eliminated unknown by going in reverse through the elimination order. Hence, one calculates M_4 first by substituting the value for F into Eq. (5.10). This gives, for the positive value of F (negative value would simply give a reversed moment diagram):

$$(-2M_p - 3M_p = -5M_p) \le M_4 \le (-M_p = 2M_p - 3M_p) \tag{5.13a}$$

$$(-3M_p - M_p = -4M_p) \le M_4 \le (2M_p = 3M_p - M_p) \tag{5.13b}$$

$$(-1.5M_p - 2M_p = -3.5M_p) \le M_4 \le (-0.5M_p = 1.5M_p - 2M_p) \tag{5.13c}$$

$$-M_p \le M_4 \le M_p \tag{5.13d}$$

These inequalities, in particular Eqs. (5.13a) and (5.13d), constrain M_4 to be equal to $-M_p$, which indicates presence of a plastic hinge at that location. Then, substituting this result together with the value of F into Eq. (5.8) gives:

$$-M_p \le M_2 \le M_p \tag{5.14a}$$

$$\left(-2M_p - 2\left(\frac{1}{2}\right)M_p - (-M_p) = -2M_p\right) \le M_2 \le \left(2M_p = 2M_p - 2\left(\frac{1}{2}\right)M_p - (-M_p)\right) \tag{5.14b}$$

$$\left(-M_p + 6\left(\frac{1}{2}\right)M_p + (-M_p) = M_p\right) \le M_2 \le \left(3M_p = M_p + 6\left(\frac{1}{2}\right)M_p + (-M_p)\right) \tag{5.14c}$$

From those inequalities it follows that M_2 must be equal to M_p. Finally, when one substitutes all previously obtained results into the equilibrium equations, Eq. (5.6), the remaining two unknowns can be calculated:

$$M_3 = \frac{1}{2}M_p + \frac{1}{2}(M_p - M_p) = \frac{1}{2}M_p \tag{5.15a}$$

$$M_1 = -6\left(\frac{1}{2}\right)M_p + M_p - (-M_p) = -M_p \tag{5.15b}$$

These results indicate, according to the previously defined sign convention, that the plastic collapse mechanism for this structure for the given loading condition is the basic panel mechanism. The resulting statically admissible moment diagram is shown in Figure 5.7.

Formally, for any given structure, a computerized solution is possible provided that the following two mathematical constructions can be formulated:

- A set of $n = N - X$ equilibrium equations, obtained directly from the basic independent mechanisms expressed in the following matrix format:

$$\begin{bmatrix} c_{11} & c_{12} & c_{13} & c_{14} & \cdots & c_{1N} \\ c_{21} & c_{22} & c_{23} & c_{24} & \cdots & c_{2N} \\ c_{31} & c_{32} & c_{33} & c_{34} & \cdots & c_{3N} \\ \cdots & & & & & \\ c_{n1} & c_{n2} & c_{n3} & c_{n4} & \cdots & c_{nN} \end{bmatrix} \begin{bmatrix} M_1 \\ M_2 \\ M_3 \\ M_4 \\ \cdots \\ M_N \end{bmatrix} = \begin{bmatrix} k_1 \\ k_2 \\ k_3 \\ k_4 \\ \cdots \\ k_N \end{bmatrix} P \tag{5.16}$$

- A series of N inequalities expressing the plastic moment constraints at each potential plastic hinge location, such that:

$$
\begin{aligned}
-M_{p1} &\leq M_1 \leq M_{p1} \\
-M_{p2} &\leq M_2 \leq M_{p2} \\
&\cdots \\
-M_{pN} &\leq M_N \leq M_{pN}
\end{aligned}
\tag{5.17}
$$

The matrix solution of this problem per the philosophy expressed in the above example can be accomplished through use of the standard simplex method algorithm developed for multidimensional optimization in linear programming (Cambridge 1992, Dantzig 1963, Livesley 1975).

5.4 Self-Study Problems

Problem 5.1 Redo Problem 4.12 using the systematic approach of Section 5.2.

Problem 5.2 For all the structures shown here (Cases A to G), use an upper bound approach to find the maximum load, P, that can be applied. Make sure to:

(a) Determine the number of basic plastic collapse mechanisms and sketch each one of them.
(b) Also clearly sketch all the combined plastic collapse mechanisms considered in solving this problem.
(c) Except for Case G, verify that the solution is statically admissible and draw the corresponding moment diagram. Also show the value and direction for all the reactions obtained in the process.

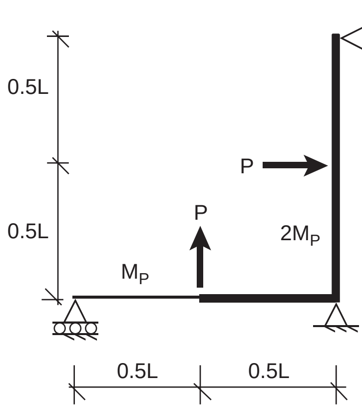

Case A

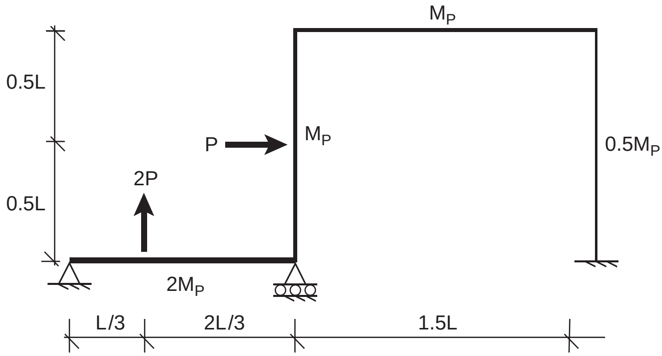

Case B

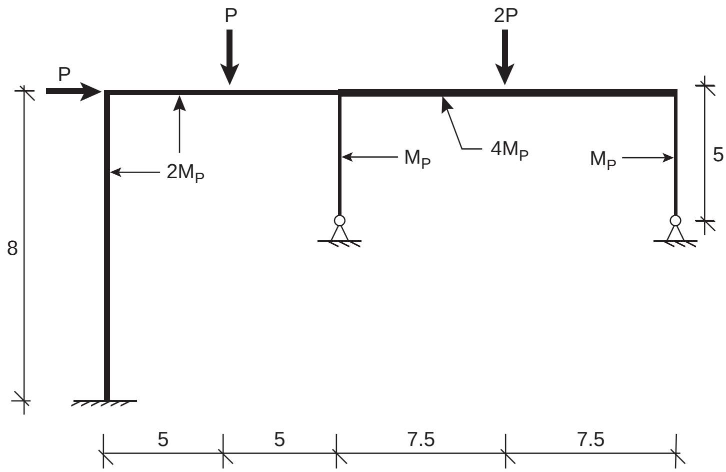

Case C

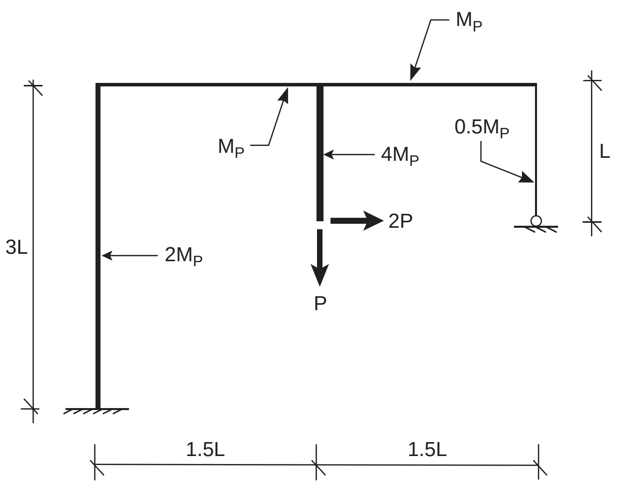

Case D

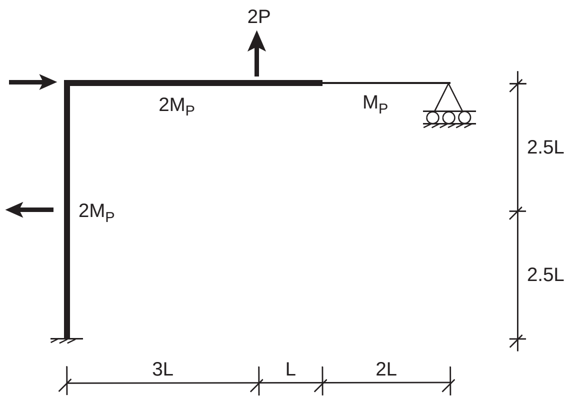

Case E

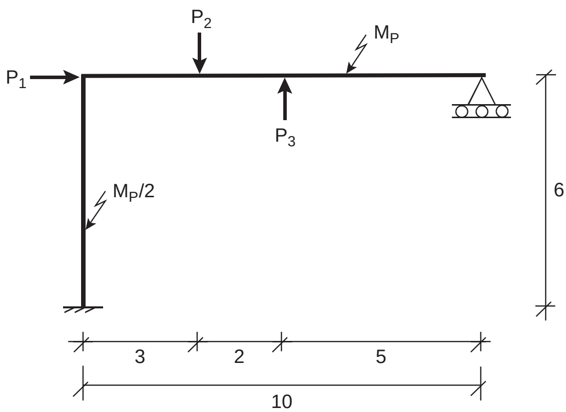

Case F

Note: For Case F, $P_1 = P$, $P_2 = 2P$ and $P_3 = 1.5P$:

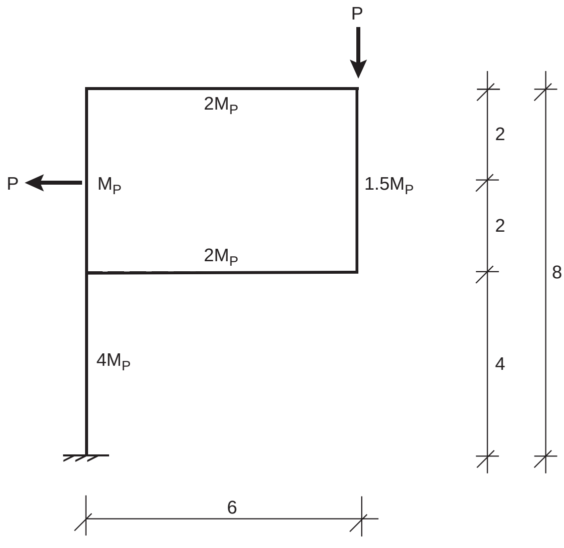

Case G

Problem 5.3 For all the structures shown below (Cases A to C), assuming that loads could be applied at any ends of any member and acting in any direction, but not within the span of any member, find the number of basic plastic mechanisms, and sketch them. Here, it is not required to calculate the plastic collapse load, but only to show the correct number of basic plastic mechanism and sketch how these mechanisms would deform.

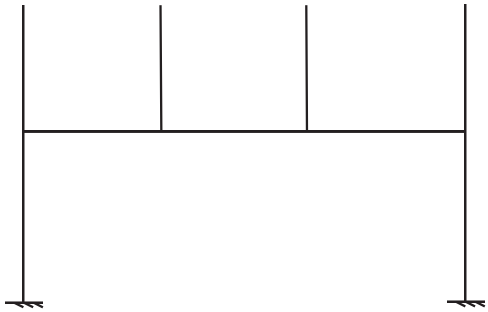

Case A

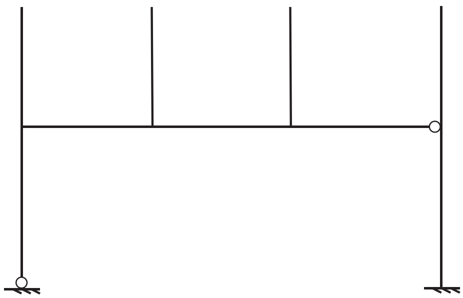

Case B

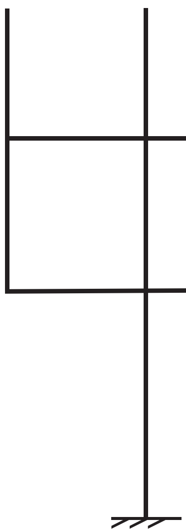

Case C

Problem 5.4 For all the structures shown (Cases A to C), determine the number of basic plastic collapse mechanisms, and sketch each one of them. Here, it is not required to calculate the plastic collapse load, but only to show the correct number of basic plastic mechanism and sketch how these mechanisms would deform.

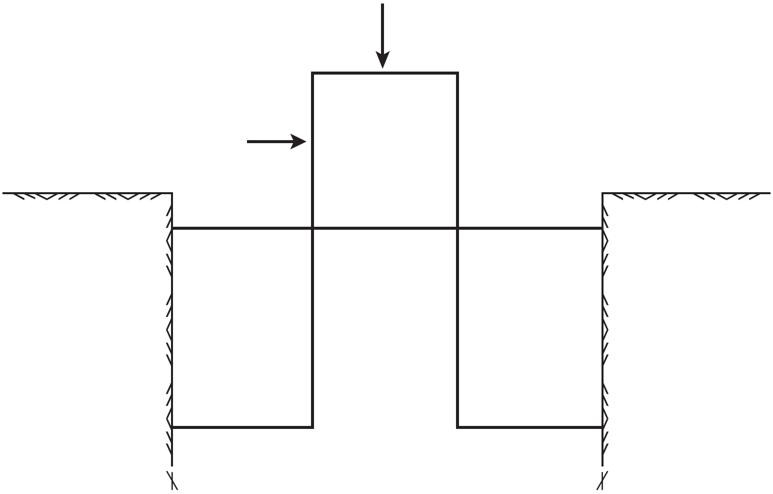

Case A

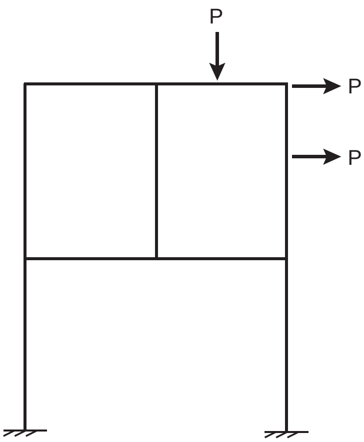

Case B

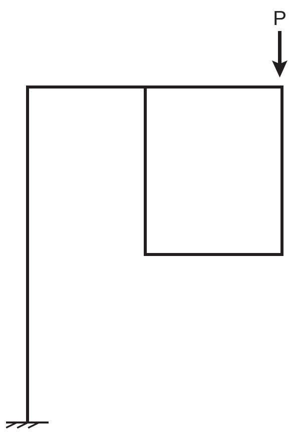

Case C

Problem 5.5 For the structure shown below, use the upper bound theorem to find the maximum load V that can be applied to this structure. First, draw a sketch showing the plastic mechanism for each of the plastic mechanism that would need to be considered for generic values of V and P. Then, solve for the case $P = 0$. Note that all beams have a strength of M_p, and all columns have a strength of $3M_p$.

For this problem, it is not required to check whether the solution is statically admissible.

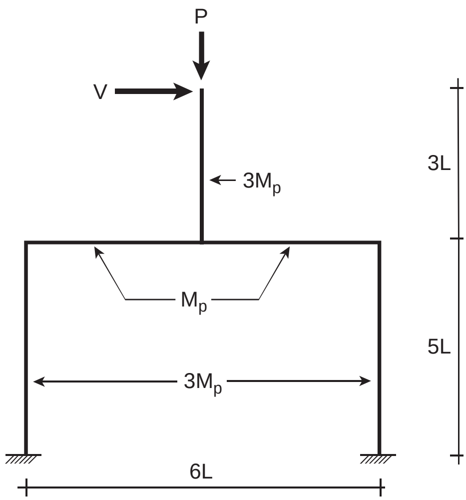

Problem 5.6 For the structures shown below, all structural members have a strength of M_p, except the rightmost column which has a strength of $0.5M_p$.

(a) Calculate the number of basic plastic mechanisms for the structure shown in part (a) of the figure below. Draw a sketch showing the plastic mechanism for each of the basic plastic mechanism identified.

(b) Calculate the number of basic plastic mechanisms for the structure shown in part (b) of the figure below. Draw a sketch showing the plastic mechanism for each of the basic plastic mechanism identified. Note that the only difference between the structures in parts A and B of the figure below is that the two middle columns for the structure in part B have hinges at their top and bottom.

(c) For the structure shown in part (b) of the following figure, use the upper bound theorem to find the maximum load V that can be applied to this structure. For this problem, check that the solution is a statically admissible solution.

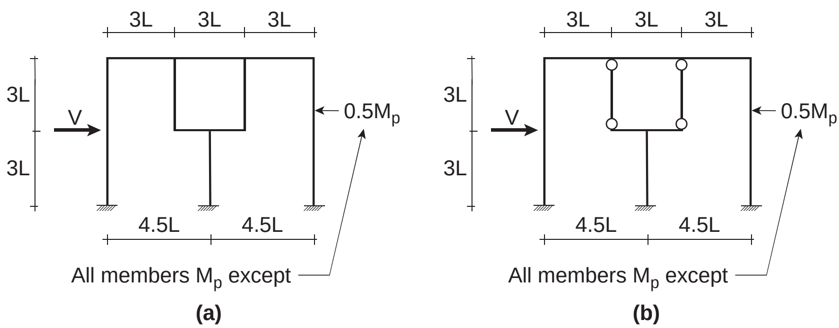

Problem 5.7 For the structures shown (Cases A and B), only:

(a) Determine the degree of indeterminacy of the structure shown.
(b) Determine the number of basic mechanisms, and illustrate them by sketches.

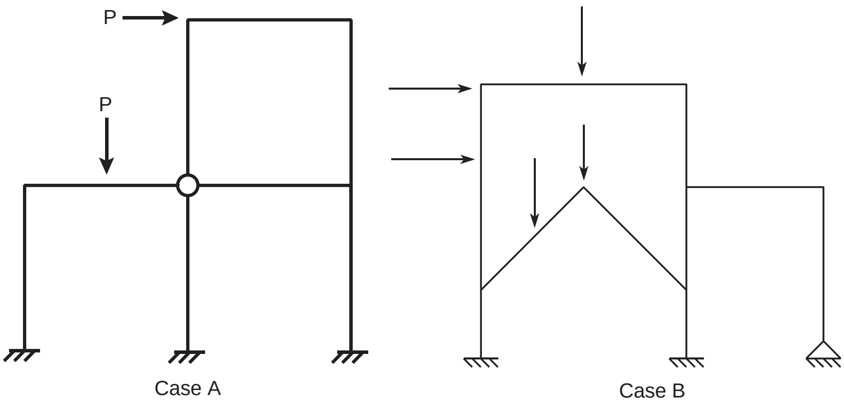

Problem 5.8 Determine the plastic strength of the Vierendeel truss shown below. All connections are moment resisting.

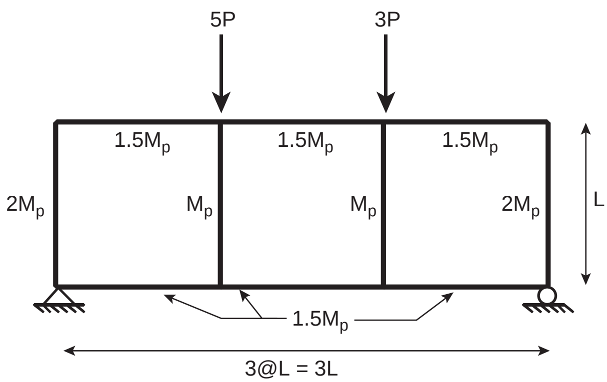

References

Cambridge University Press. 1992. *Numerical Recipes in Fortran*. Cambridge, MA.
Dantzig, G. B. 1963. *Linear Programming and Extensions*. Princeton, NJ: Princeton University Press.
Livesley, R. K. 1975. *Matrix Methods of Structural Analysis*, 2nd ed. Oxford, UK: Pergamon Press.

CHAPTER 6

Applications of Plastic Analysis

Previous chapters have demonstrated how the plastic collapse mechanism for a given structure and set of loads can be determined. Although the techniques described in those chapters are conceptually simple, computations can rapidly become tedious when one is analyzing complex structures. Fortunately, from a design perspective, engineers familiar with plastic-analysis concepts can effectively couple this knowledge with the creative freedom of the design process to eliminate many of these analysis complications. As a result, many plastic-design tools can be, and have been, created. These vary greatly from one application to the other because different tools are needed for different tasks. In some, numerous plastic-based design solutions can be rapidly developed and assessed. In other cases, the engineer can decide a priori which specific plastic collapse mechanisms are desirable and design the structure such that no other failure mechanism can develop.

The number of applications using the plastic-design concepts has grown considerably in recent years; only a sample of these can be presented in this chapter wherein the concepts are stressed over the details. More comprehensive examples are provided in the following chapters in which emphasis is on the earthquake-resistant design of ductile steel structures, which implicitly considers many of the concepts presented in this chapter.

Incidentally, for design, specified applied loads are multiplied by load factors, and various load combinations must be considered. Currently, slight variations exist in the magnitude of those factors and the required load combinations among the various international codes and standards based on Limit States Design (LSD) or Load and Resistance Factor Design (LRFD). Although load factors have not been used so far in this book to provide a broader presentation of concepts untied to any particular code, it must be understood that they should always be considered. Likewise, in a design process, the plastic moments provided should always be slightly larger than the required values calculated by analysis. In compliance with the LRFD (and LSD) philosophy, the required plastic moments should be reduced by the appropriate resistance factor (typically expressed as ϕ). This will be illustrated in the design examples provided in later chapters.

6.1 Moment Redistribution Design Methods

6.1.1 Statical Method of Design

Using the statical method to design continuous beams constitutes one of the simplest possible applications of plastic analysis principles. In the example shown in Figure 6.1, a four-span continuous beam must be designed to resist a set of factored point loads identified to constitute the critical load combination. As for most design processes, many satisfactory solutions can be found.

If the beam is constrained to be one continuous member of constant cross-section over its entire length, the statical method [i.e., superposition of the moment diagrams for span loading (Figure 6.1b) and redundants (Figure 6.1c) is schematically shown in Figure 6.1d] indicates that the left span will reach its beam plastic collapse mechanism first. This solution is shown in Figure 6.1e. Systematically, one could find this by expressing mathematically the statical moment combination for each span, although spans visibly not critical need not be checked. For example, for span AC, for the beam plastic collapse mechanism to form, considering all moments in absolute value, the following expression can be written:

$$\frac{M_A + M_C}{2} + M_B = \frac{0 + M_p}{2} + M_p = 250 \text{ kN-m}(184 \text{ kip-ft}) \tag{6.1}$$

which gives M_p = 166 kN-m (123 kip-ft), or the minimum strength that must be provided to resist the specified loads. Following the same logic, M_p = 160 kN-m (118 kip-ft) would be obtained for span CE. Spans EG and GI would not need to be checked because it can be deducted visually from Figure 6.1e that they would not govern. Therefore, a beam having a plastic moment of 166 kN-m would be required as a minimum satisfactory design. This approach makes for an expedient design process.

However, as a result of the above design, all spans except span AC would be overdesigned, and it may be of interest to investigate whether a minimum weight solution would provide much savings in material. Although systematic optimum design techniques have been developed for plastic analysis, these are beyond the scope of this book. Nonetheless, using simple reasoning, one can find a more economical solution. Observation of the result previously obtained

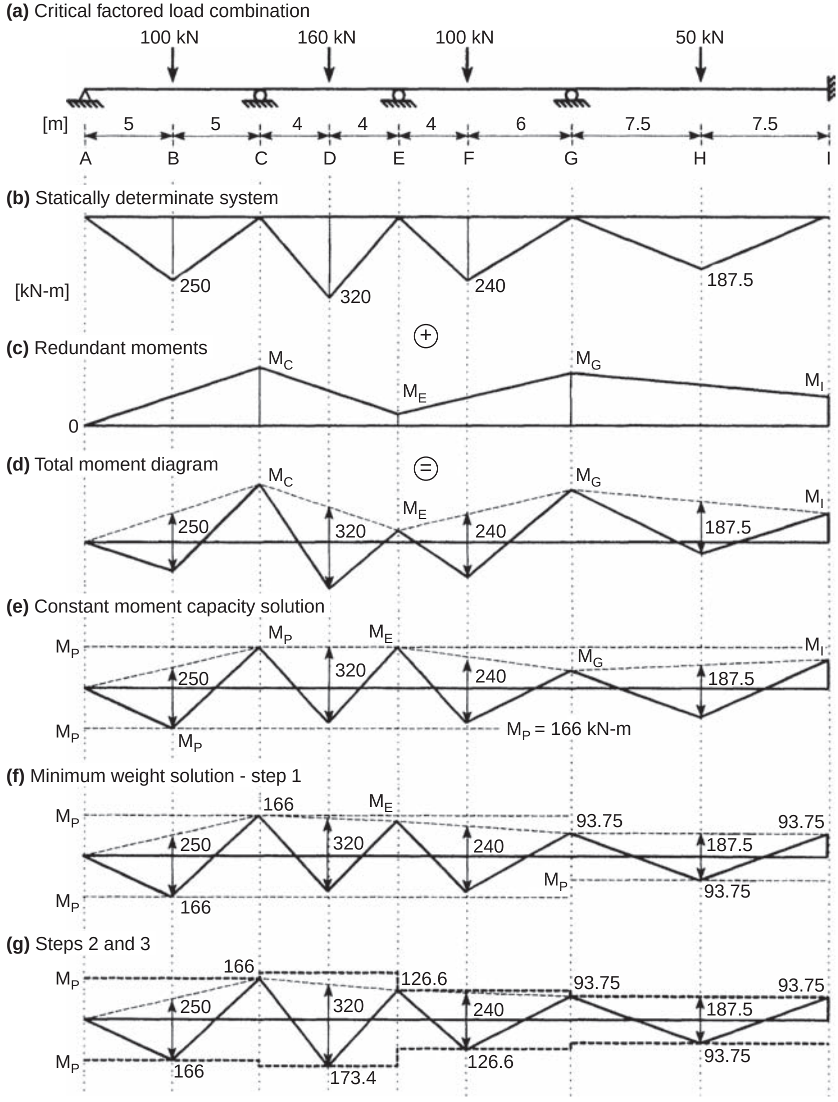

Figure 6.1 Example of statical method of design using four-span continuous bridge.

reveals that span GI would be the most severely overdesigned because its statical moment is only 187.5 kN-m (138 kip-ft). Therefore, one could focus initially on that span. Writing an expression similar to Eq. (6.1), one finds a required plastic moment over span GI, M_{P-GI}, of 93.75 kN-m (69.1 kip-ft) (Figure 6.1f). Note that because of the change in cross-section over span GI, the maximum value of M_G can now be only 93.75 kN-m. As a result, the required plastic moment capacity of span EG is given by:

$$\left(\frac{6}{10}M_E + \frac{4}{10}M_G\right) + M_F = 0.6M_{P-EG} + 0.4(93.75) + M_{P-EG}$$
$$= 240\,\text{kN-m}\,(177\,\text{kips-ft}) \tag{6.2}$$

which translates into a required plastic moment over span EG, M_{P-EG}, of 126.6 kN-m (93.1 kip-ft). Repeating the process for span CE would give:

$$\left(\frac{M_C + M_E}{2}\right) + M_D = \frac{166 + 126.6}{2} + M_{P-CE} = 320\,\text{kN-m}\ (236\,\text{kips-ft}) \tag{6.3}$$

and a required moment over span CE, M_{P-CE}, of 173.4 kN-m (127.6 kip-ft). Although this required plastic moment exceeds the previous value of 166 kN-m, an overall saving is achieved when the new weight of the entire structure is compared with the previous solution (6.1g). This optimization is somewhat academic, because many other factors would need to be addressed in a practical design. First, no beam would be spliced immediately over the support, and it may be more economical to extend the heavier beams a short distance beyond the supports, allowing for more efficient use of material at minimal extra cost. Moreover, consideration would be given to fabrication costs, maximum member length (for transportation logistic), and erection costs. For those reasons, the optimization process illustrated is not pursued further. However, the above concepts can be easily adapted to address whatever practical considerations are encountered.

Note that for moment redistribution to occur, significant plastic rotations need to develop at the plastic hinges. Therefore, it is important that only properly laterally supported compact sections be used in all plastic design applications (which also requires braces at all potential plastic hinge locations).

6.1.2 Autostress Design Method

The Autostress design method (ADM), which is an integral part of the Load and Resistance Factor Design (LRFD) edition of the AASHTO Bridge Design Code, is a relatively new design procedure that recognizes the ability of continuous steel members to redistribute moments plastically. It takes advantage of the fact that a steel structure will shakedown under a truck overload and thereafter behave elastically over an extended range (the shakedown range, as described in Chapter 4). In a less abstract way, the fundamental concept underlying the Autostress design method is usually explained by the following analogy (e.g., Haaijer et al. 1983).

If a two-span continuous steel bridge girder could be lifted in one piece and placed over three nonlevel supports, as shown in Figure 6.2a, with the middle support higher than the two exterior supports, the girder would bend under its own weight until it came in contact with the three supports (Figure 6.2b). In the process, given a sufficient difference in the height of the supports, the plastic moment of the girder would be reached at the middle support. The resulting moment diagram is shown in Figure 6.2c.

This process is equivalent to introducing into the girder a residual moment diagram varying linearly from 0 at the exterior supports to (M_p − $\omega L^2/12$), if the dead load could be removed, as shown in Figure 6.2d (see Section 4.5). Upon first crossing of the maximum overload across that bridge, additional plastic rotation will develop over support C, but unloading and reloading will be elastic over an extended range without further plastic rotations (Figure 6.2f). At that point, the girder has shaken down according to the definition presented in Chapter 4.

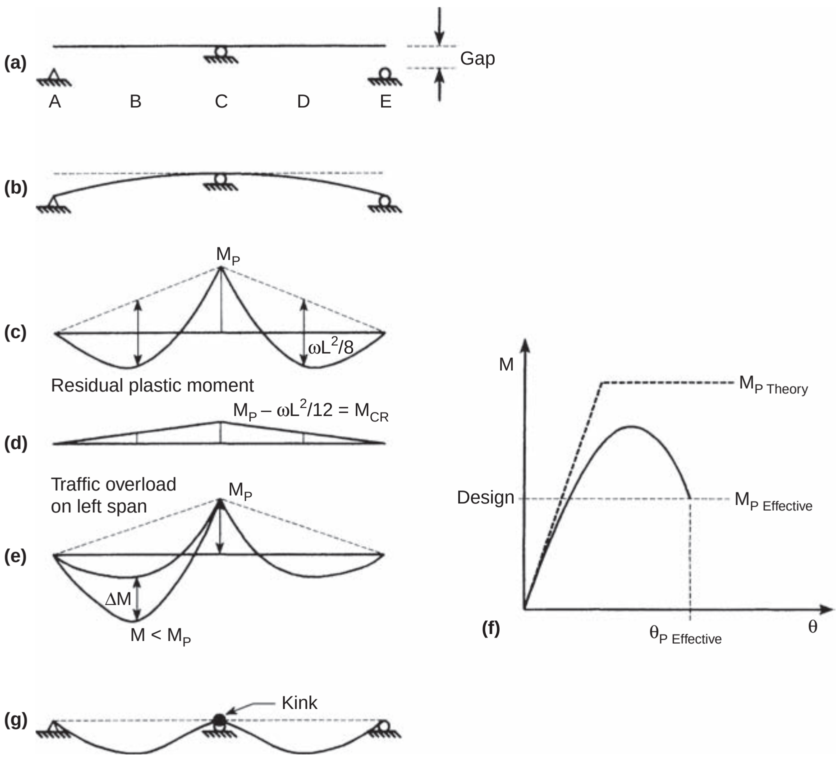

Figure 6.2 Illustration of the Autostress design method.

However, it is necessary neither to place the girders on unequal supports nor to jack up the middle support after construction (as some astute engineers might propose) to reach the above shakedown condition. In fact, no physical intervention is needed other than a large traffic overload. Indeed, the plastic hinge at support C and an equivalent residual moment diagram will automatically develop once a live load sufficiently large to produce yielding at that location occurs. The structure will then behave elastically until a larger load occurs. That larger load will introduce some additional plastic rotations at point C and extend further the elastic range. Then all subsequent loads of equal or lesser magnitude will be resisted elastically. The maximum load resistance will obviously be dictated by the plastic collapse mechanism that could be calculated by the methods shown in Chapter 4. The term Autostress emphasizes that this plastic moment redistribution occurs automatically.

Special design requirements must be satisfied to ensure that the steel girders designed under the Autostress Design Method will have sufficient plastic rotation capacity. Because most steel bridge girders are generally noncompact shapes that do not meet the width-to-thickness limits generally prescribed for plastic design, effective slenderness ratio and effective plastic moment concepts have been derived and verified experimentally. A detailed review of these concepts is not presented in this book, but the underlying general ideas are as follows:

- Noncompact steel beams will typically reach a maximum strength smaller than their theoretical M_p because of local buckling.
- The effective stresses at which local buckling of the flanges and web initiates can be obtained by algebraic manipulations of the design equations limiting width-to-thickness ratios.
- The ratio of the effective stress to the yield stress can be calculated.
- This ratio multiplied by the theoretical plastic moment of the cross-section defines an effective plastic moment used for design.

These concepts have been proven to provide a satisfactory design basis. Indeed, when a noncompact section is subjected to progressively increasing rotations, after reaching its maximum moment (which is larger than the calculated effective plastic moment because of strain-hardening and other factors), it slowly loses some flexural capacity. An effective plastic rotation capacity for a given section can therefore be defined as the point at which the descending branch of its moment-curvature relationship crosses the effective plastic moment defined by the above procedure (see Figure 6.2f); values obtained are typically greater than those required to achieve the shakedown condition described earlier.

Finally, as shown in Figure 6.2g, a kink in the girders will obviously be introduced as a result of the overload and plastic hinge formation at point C. However, calculations and experimental results confirm that this kink is small and unlikely to be visually perceptible or felt by vehicles driving over the bridge.

6.2 Capacity Design

6.2.1 Concepts

The concept of capacity design is very important in earthquake engineering practice, and although a pure capacity design approach has not been adopted in North America at this time, aspects of this philosophy are implicitly embedded in many code-detailing requirements (for both reinforced concrete and steel structures).

Capacity design was developed in the late 1960s in New Zealand as an approach to resist the effects of severe earthquakes. In capacity design, acknowledging that inelastic action is unavoidable during severe earthquakes, the designer dictates where inelastic response should occur. Such zones of possible inelastic action are selected to be regions where large plastic deformations can develop without significant loss of strength; these regions are detailed to suppress premature undesirable failure modes, such as local buckling or member instability in the case of steel structures. Then, one eliminates the likelihood of inelastic action or failure elsewhere in the structure by making the capacities of the surrounding structural members greater than that needed to reach the maximum capacity of the so-called plastic zone.

The classical example to explain this concept is the capacity-designed chain (Figure 6.3). In this chain, one link is designed to absorb a large amount of plastic energy in a stable manner prior to failure (e.g., link 4). Therefore, the other links (e.g., 1, 2, 3, 5, 6, and 7) can be designed without concern for plastic deformations, provided their capacities exceed the maximum capacity of the plastic link, thus avoiding the need for special detailing in all but one link.

Many other examples can be created based on the same philosophy. One such illustration of capacity design is shown in Figure 6.4. There, a cantilever beam of total length L consists of a brittle segment (such as a fiber composite material) of length a at the fixed end and a ductile steel segment of length b. A traditional design approach would require the use of large safety factors to provide protection against failure of the brittle material. Alternatively, a capacity design approach would aim at making the brittle material stronger than needed to ensure that plastic hinging occurs first in the steel segment

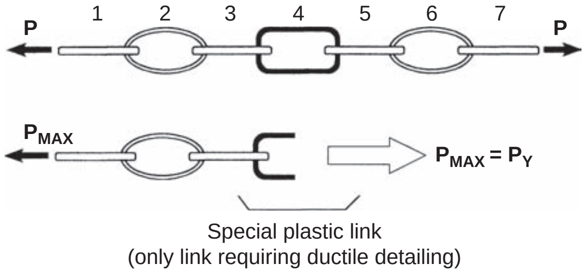

FIGURE 6.3 Illustration of capacity design principle.

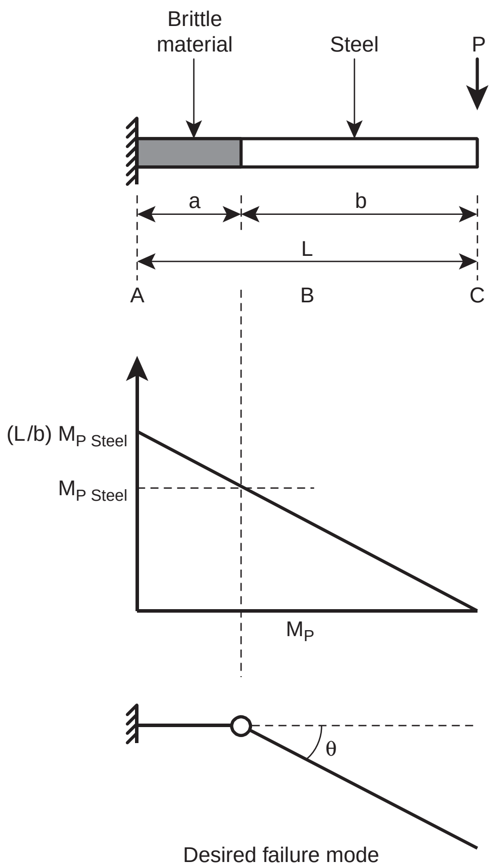

FIGURE 6.4 Illustration of an application of capacity design.

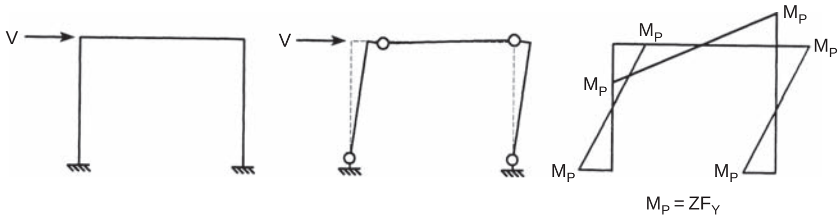

Figure 6.5 Illustration of a capacity design application.

of the cantilever. Therefore, the moment resistance of the brittle segment would only need to exceed:

$$M_{BRITTLE} \geq \alpha\left(\frac{L}{b}\right)M_{P\text{-}STEEL} \tag{6.4}$$

where all parameters are defined in Figure 6.4, and α is a number greater than 1.0 to account for the possible reserve strength of the steel cantilever beyond its nominal yield strength.

Clearly, capacity design is deeply rooted in plastic analysis and design. In theory, once a fully plastic state (also known as a plastic collapse mechanism) has been reached, no additional force can be imparted to the structure, and as a result, regions outside the critical plastic locations are protected against the effects of additional loading. For the small one-bay moment frame shown in Figure 6.5, if the plastic moment capacity of the beam is less than that of the columns, yielding will occur only at the base of the columns and at the ends of the beam. The rest of the structure is therefore certain to remain elastic (Figure 6.5) and requires no special ductile detailing. Practically, this remains true, although some allowance (such as the α factor in the previous example) must be made for the statistical variability of material properties (particularly the yield stress), the possible development of strain-hardening in the critical plastic locations, dynamic-loading effects (i.e., strain-rate effects), and a few other case-dependent factors.

6.2.2 Shear Failure Protection

Capacity design can be used to check the potential adverse impact of nonstructural elements on key structural members. For example, in a frame subjected to lateral loads, the shear force in columns can be considerably larger than expected because of the presence of rigid nonstructural elements not considered during the design process. This is clearly illustrated in Figure 6.6, in which a rigid partial-infill masonry wall restrains the elastic deformations of the steel columns. As a result, the plastic hinges required in the columns to produce a

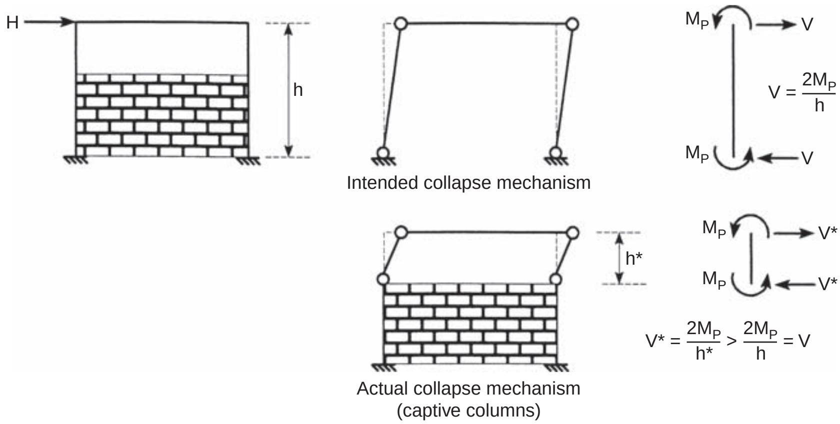

FIGURE 6.6 Impact of rigid nonstructural elements on shear force in columns.

plastic collapse mechanism must relocate from the base of the columns to just above the infill where frame-action is unrestrained. A higher lateral force, H, is required to develop the collapse mechanism, and higher shear strength is required of the structural members and the connections to ensure development of this ductile mechanism. Mathematically, using simple free-body diagrams, the column shear strength required to form plastic hinges in this frame with masonry infill is:

$$V = \frac{2M_P}{h^*} \tag{6.5}$$

where h is the unrestrained column height, as shown in Figure 6.6. This shear strength is h/h^* more than the shear strength that would have been sufficient to permit plastic hinges to form in the bare frame without any infills, where h is the full column height.

Fortunately, contrary to reinforced concrete columns for which this phenomenon has created a number of disastrous failures in past earthquakes (referred to as "short-column" or "captive column" failures in the literature), steel columns usually have a constant shear strength that is in excess of that required to form plastic hinges, and to date, steel columns have not suffered the same fate as some reinforced concrete columns. However, designers should be aware of this phenomenon and recognize instances in which it could lead to problems. For example, column splices located in such captive columns could be damaged if they are designed without consideration of the nonstructural walls.

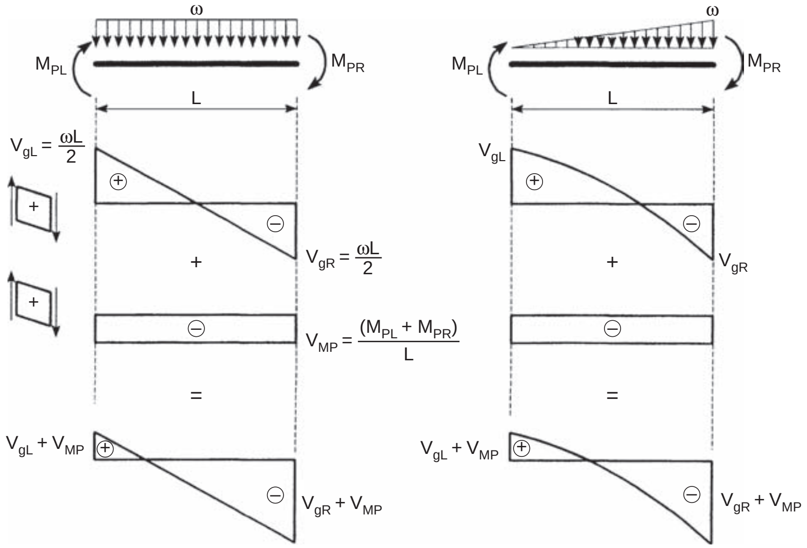

FIGURE 6.7 Examples of maximum shear force calculation in beams using capacity design principles.

A similar strategy can be used to protect against shear failures in gravity-resisting members. In this case, the effect of gravity loads must be considered, as must the fact that positive and negative moment capacities may differ (e.g., in composite constructions). This is illustrated in Figure 6.7. For example, for a segment of beam between two plastic hinges and subjected to a uniformly distributed load, the gravity shear force diagram must be added to the shear force diagram corresponding to the plastic moments, with the following result:

$$
\begin{aligned}
V_{left} &= V_{gL} + V_{MP} = \frac{\omega L}{2} - \left[\frac{M_{PR} + M_{PL}}{L}\right] \\
V_{right} &= V_{gR} + V_{MP} = \frac{\omega L}{2} + \left[\frac{M_{PR} + M_{PL}}{L}\right]
\end{aligned}
\tag{6.6}
$$

where all terms are defined in Figure 6.7.

Similar relationships could be derived for other loading distributions between the plastic hinges as shown in Figure 6.7.

Likewise, using these principles and the free-body diagrams presented in Figure 6.8, the maximum axial load that can be applied to

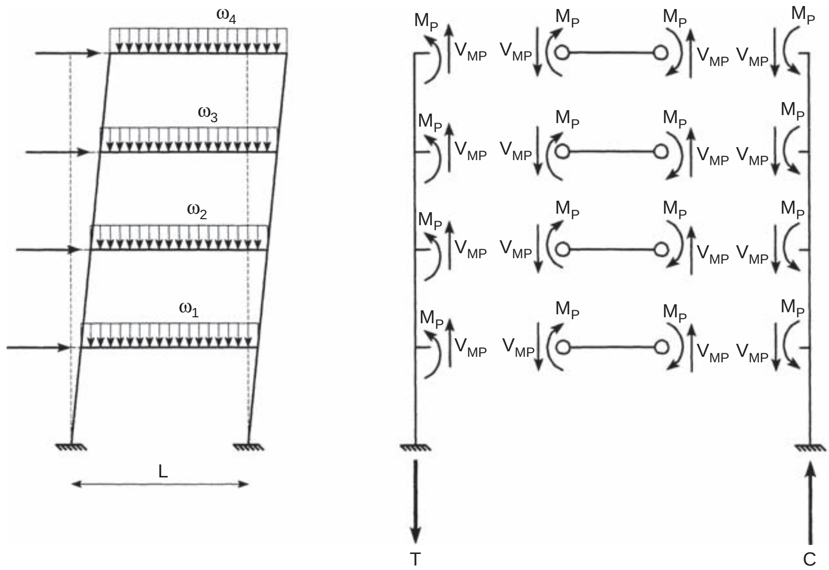

FIGURE 6.8 Calculation of maximum axial force in columns using capacity design.

columns at story i of a multistory frame as a result of a sway-type plastic collapse mechanism can be calculated as:

$$C_{max\text{-}i} = \sum_{i}^{n}[V_{gR\text{-}max\text{-}i} + V_{MP\text{-}i}] = \sum_{i}^{n}\left[\frac{\omega_{max\text{-}i}L}{2} + \left(\frac{M_{PR-i} + M_{PL-i}}{L}\right)\right]$$
$$T_{max\text{-}i} = \sum_{i}^{n}[V_{gL\text{-}min\text{-}i} - V_{MP\text{-}i}] = \sum_{i}^{n}\left[\frac{\omega_{min\text{-}i}L}{2} - \left(\frac{M_{PR-i} + M_{PL-i}}{L}\right)\right] \tag{6.7}$$

Compression is arbitrarily taken to be positive in that equation. An understanding of the concept used to derive this equation matters more than the equation itself. For example, the same approach could be used to assess the impact of extreme load conditions, such as loss of a column due to an explosion or other causes, as shown in Figure 6.9.

6.2.3 Protection Against Column Hinging

For many reasons, beam yielding is generally preferable to column yielding, particularly in multistory frames (see Chapter 8). Beam yielding greatly enhances the energy absorption capability of a structure because more plastic hinges are involved in the development of the plastic collapse mechanism. This is illustrated in Figure 6.10. In that example, for the same total roof displacement, the column plastic rotation demand for the column-sway mechanism is approximately

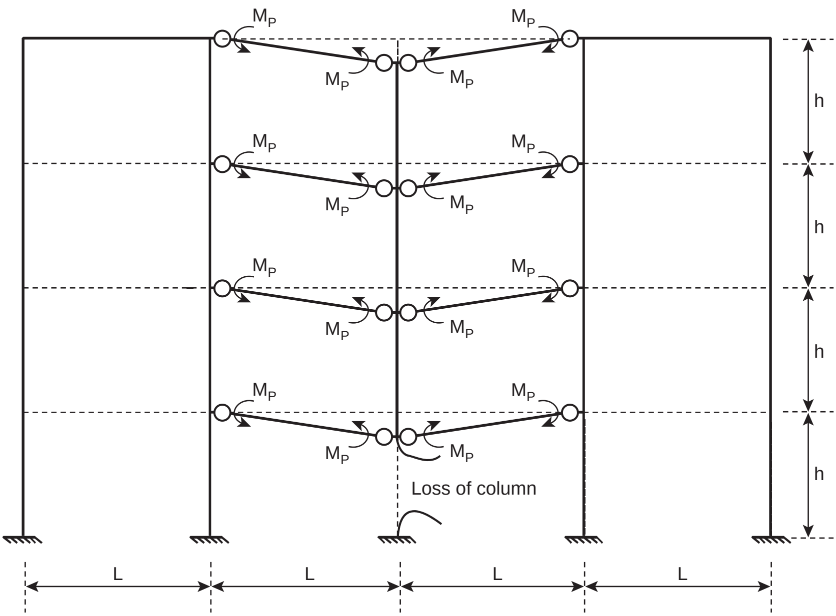

Figure 6.9 Plastic collapse mechanism due to loss of a column in a structural frame.

eight times larger than the beam plastic rotation demand for the beam-sway mechanism, resulting in a greater risk of collapse because of limits in the plastic rotation capacity of structural members (see Chapters 8 and 15).

Although this philosophy, also known as "strong-column/weak-beam" design, has been widely accepted as desirable in reinforced concrete structures, its implementation in structural steel design code has met considerable resistance. In low-rise steel buildings, beams are generally considerably deeper than columns, and the adoption of such a philosophy may affect the economical balance between competing proposals in steel and other materials. However, many other capacity design principles have found their way into steel design codes and standards, as will be seen in subsequent chapters.

6.3 Push-Over Analysis

A push-over analysis is basically a step-by-step plastic analysis for which the lateral loads of constant relative magnitude are applied to a given structure and progressively increased until a target displacement is reached, while gravity loads are kept constant. Thus, as the name implies, the structure is truly pushed sideways (or pushed over) to determine its ultimate lateral-load resistance as well as the

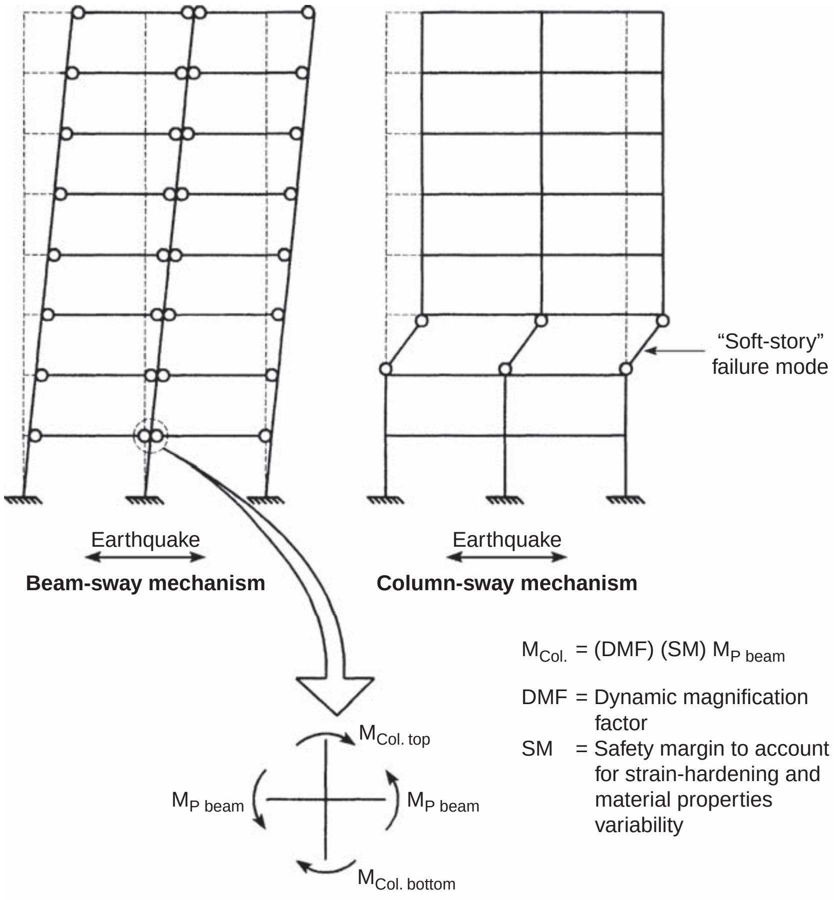

Figure 6.10 Comparison of plastic collapse mechanism in presence (beam sway) and in absence (column sway) of "strong-column/weak-girder" design philosophy.

sequence of yielding events needed to reach that goal, or the magnitude of plastic deformations at the target displacement. Originally, engineers accomplished this by repeatedly running linear elastic structural analysis computer programs, modifying the model of a structure as necessary to account for the progressive appearance of plastification at finite locations throughout the structure; nowadays, many computer programs for nonlinear inelastic analysis explicitly offer push-over analysis capabilities. As a result, the push-over analysis method is relatively accessible and has been used in addition to conventional analyses to determine the ultimate capacity of important existing structures, to validate proposed retrofit or design solutions, to compare the ultimate capacity, and, to some extent, the ductility of various design alternatives.

Although, in principle, nothing precludes the extension of this concept to conduct cyclic push-over analysis for a limited number of cycles, this rapidly becomes excessively arduous even with the help of computer programs for nonlinear inelastic analysis. Consequently, nearly all practical applications of the push-over analysis so far have considered monotonically increasing lateral loads. However, only a limited amount of information can be extracted from noncyclic push-over analyses, and extrapolating the findings from those analyses may lead to erroneous conclusions. The examples presented in the subsections below have been constructed to illustrate some of these limitations and risks of misinterpretation.

Finally, it must be recognized that the information acquired from a push-over analysis is highly dependent on the lateral load distribution adopted (Lawson et al. 1994). Therefore, whenever the chosen lateral load distribution is intended to capture the possible effects of dynamic excitation, it may be wise to consider multiple lateral-load distribution patterns.

6.3.1 Monotonic Push-Over Analysis

The three-story braced frame shown in Figure 6.11a was designed in four different ways to resist a set of statically applied lateral loads. First, a tension-only design was considered (Case I). In a tension-only design approach, the braces in compression are ignored and the tension braces are designed to resist all the applied loads. Such braced frame designs have been popular and are still used in nonseismic regions to provide wind resistance.

In Case I, the brace slenderness ratio, *KL/r*, was limited to 200 and 300, as suggested by some buildings codes, for members in compression and tension, respectively. Therefore, double angles back-to-back were chosen for the brace members.

In Case II, both the compression and tension members were designed to resist loads. Design was governed by the compression capacity of the brace members. As a result, bigger double-angle braces were necessary to provide a satisfactory design.

In Case III, to reflect that some earthquake-resistant design requirements restrict the maximum brace slenderness ratio to less than for nonseismic applications, the frame was redesigned as done for Case II but considering a maximum brace slenderness ratio of 110, which is the limit permitted for seismic design by some codes for steels having a specified yield strength of 300 MPa (43.5 ksi). As a result, W-shapes were chosen for the braces of that frame.

Finally, in Case IV, a tension-only design without any brace slenderness restrictions was undertaken, leading to braces made of steel plate. Information on the four resulting designs is presented in Table 6.1. In all cases here, the floor beams are joined to the columns using only shear connections (i.e., simply supported beams)

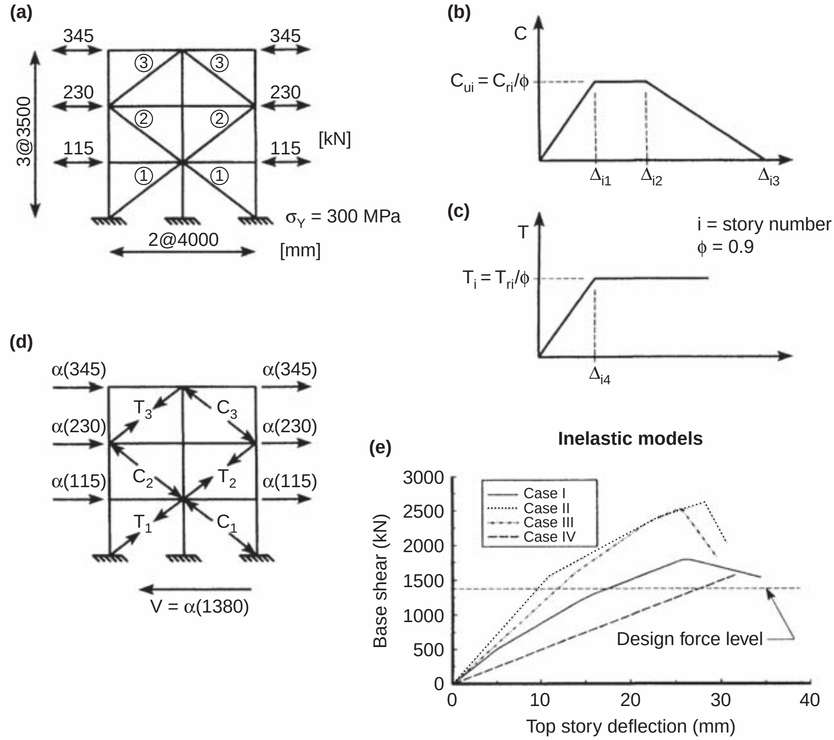

FIGURE 6.11 Monotonic push-over analysis examples on three-story braced frames with braces having various slenderness ratios.

because nothing prevents this practice in some parts of North America.

To simplify calculations, the inelastic models shown in Figures 6.11b and c were adopted for the compression (C) and tension (T) braces, respectively. Numerical values for the parameters of these models are listed in Table 6.1. The trilinear compression brace model represents the following states of behavior:

- Buckling occurs at a load of C_{ui}, which corresponds to a maximum elastic axial compression shortening of Δ_{i1}.
- When axial shortening reaches a value of Δ_{i2}, a flexural plastic hinge forms at the midlength of the brace as a result of the compression load acting eccentrically on the member that has buckled sideways.
- The axial strength progressively reduces to zero as a result of large plastic deformations that develop at the brace's midlength, reaching zero when the corresponding axial shortening reaches Δ_{i3}.

Story	Analysis Results (Factored Loads) (kN)		Designed Members	Factored Resistance (kN)		Ultimate Capacities (kN)		KL/r	Inelastic Model Additional Parameters (mm)			
	C_f	T_f		C_r	T_r	C_u	T_u		Δ_{i1}	Δ_{i2}	Δ_{i3}	Δ_{i4}
Case I: Tension-Only Design with (KL/r) Limits of 200 and 300 for Compression and Tension Members, Respectively												
3	0	917	2L90 × 90 × 10	150	918	167	1020	193	1.3	8.6	17.2	8
2	0	1528	2L150 × 150 × 10	607	1566	674	1740	112	3.1	6.4	12.8	8
1	0	1833	2L150 × 150 × 13	774	2014	860	2238	114	3.1	6.4	12.8	8
Case II: Elastic Design Considering Tension and Compression Member Capacities												
3	458	458	2L125 × 125 × 13	485	1663	539	1848	138	2.3	6.4	12.8	8
2	764	764	2L150 × 150 × 13	774	2014	860	2238	114	3	6.4	12.8	8
1	916	916	2L150 × 150 × 16	932	2454	1036	2727	115	3	6.4	12.8	8
Case III: Elastic Design Considering Tension and Compression Member Capacities and (KL/r) Limit of 110												
3	458	458	W200 × 46	693	1583	770	1759	104	3.5	7.2	14.4	8
2	764	764	W200 × 52	800	1798	889	1998	102	3.5	7.2	14.4	8
1	916	916	W310 × 67	958	2298	1064	2553	107	3.5	7.2	14.4	8
Case IV: Tension-Only Design Without (KL/r) Limits												
3	0	917	Pl. 175 × 20	0	945	0	1050	921	—	—	—	8
2	0	1528	Pl. 300 × 20	0	1620	0	1800	921	—	—	—	8
1	0	1833	Pl. 350 × 20	0	1890	0	2100	921	—	—	—	8

1 kN = 0.2248 kips and 1 mm = 0.0394 in

Table 6.1 Characteristics of Braced Frames Design for Push-Over Analysis Example

Values for Δ_{i2} were calculated by consideration of a simplified brace model, and the values of Δ_{i3} were arbitrarily set equal to twice Δ_{i2}. Likewise, only the contribution of brace elongation/shortening to the story drift is considered.

Push-over analysis was conducted to determine the base shear strength, V, of each proposed design and to obtain some knowledge of its ductile behaviors. Throughout this example, a factor α is used to express the ratio of the calculated capacity over the specified design loads. As shown in Figure 6.11d, all applied loads are scaled by this same value of α. Note that although factored member strengths (ϕ = 0.9) have been used for design purposes, the ultimate resistances (ϕ = 1.0) are used for all subsequent calculations in this section. Therefore, $\alpha = 1.11$ (i.e., 1/0.9) would correspond to a maximum base shear force equal to that required by design. Numerical results for the push-over analyses are presented in Table 6.2.

For Case I, the application of monotonically increasing lateral loads reveals that buckling of braces at the third, second, and first stories occurs sequentially and at loads much below those specified (i.e., at values of α equal to 0.364, 0.883, and 0.939, respectively, all less than 1.11). This is expected because the behavior of compression members was disregarded during the tension-only design. Tension yielding of a brace first occurs at the third story when α reaches 1.294. At that point, the axial displacement in the compression and tension braces (assuming the floor beams are axially rigid) is Δ_{i4}, and the axial force in the buckled compression member equals C_{ui} per Figure 6.11b because Δ_{i2} is larger than Δ_{i4}. However, as soon as Δ_{i2} is exceeded, both the force in the compression member and the shear strength of the third story drop. A stable story mechanism develops when α = 1.11—that is, exactly at the design level.

For Case II, buckling of braces simultaneously starts at the first and second stories (α = 1.124) and rapidly spreads to the third story (α = 1.176). These events occur at loads slightly above the design level. However, a significant strength capacity is available beyond that point as a result of the design philosophy that considers the resistance of both the tension and compression members. Loss of brace compression strength starts to develop (α = 1.733) at the first and second stories when the axial displacement of these compression braces exceeds Δ_{i2}. Because the tension brace in each story is elastic at that displacement, with an axial stiffness greater than the negative stiffness of the corresponding compression brace = $C_{ui}/(\Delta_{i3} - \Delta_{i2})$, it can carry the loss in brace compression strength for a given incremental lateral displacement. As a result, the lateral loads can be increased until the second-story tension brace yields (α = 1.89). For displacements beyond this point, lateral load resistance drops, and a plastic collapse mechanism develops at the second story.

Ratio of Applied Load over Design Load	Member Forces (kN)						Member Deformation (mm)			Top Story Lateral Deformation (mm)	
α	C_3	C_2	C_1	T_3	T_2	T_1	Δ_3	Δ_2	Δ_1	Δ_{TOT}	Description of Event
Case I: Tension-Only Design With (KL/R) Limits of 200 And 300 for Compression and Tension Members, Respectively											
0.364	167*	278	333	167	278	333	1.3	1.3	1.2	5.0	Buckling at C_3
0.883	167	674*	809	642	674	809	5.0	3.1	2.9	14.6	Buckling at C_2
0.939	167	674	860*	693	759	860	5.4	3.5	3.1	15.9	Buckling at C_1
1.294	167	674	860	1020*	1302	1512	8.0	6.0	5.4	25.8 to 26.6	Yield at T_3 Onset of C_3's loss of compression strength
1.11	0*	674	860	1020	1022	1177	17.2	4.7	4.2	34.5	Top-story mechanism
Case II: Elastic Design Considering Tension and Compression Member Capacities											
1.124	516	860*	1036*	515	859	1036	2.3	3.0	3.0	10.98	Buckling at C_2 and C_1
1.176	539*	860	1036	539	938	1120	2.3	3.3	3.4	11.9	Buckling at C_3
1.733	539	860	1036	1051	1790	2144	4.6	6.4*	6.4*	23.1	Onset of C_1 and C_2's loss of compression strength
1.89	539	646	777	1190	2238*	2683	5.2	8.0	8.0	28.2	Yield at T_2
1.47	539	0*	429	814	2238	2289	3.5	12.8	6.7	30.6	Mid-story mechanism

*Critical event at that step.

TABLE 6.2 Push-Over Analysis Results for the Four Frames Considered

Ratio of Applied Load over Design Load	Member Forces (kN)						Member Deformation (mm)			Top Story Lateral Deformation (mm)	
α	C_3	C_2	C_1	T_3	T_2	T_1	Δ_3	Δ_2	Δ_1	Δ_{TOT}	**Description of Event**
Case III: Elastic Design Considering Tension and Compression Member Capacities and (KL/R) Limit Of 110											
1.16	532	889*	1064*	532	887	1064	4.2	3.1	3.1	13.8	Buckling at C_2 and C_1
1.68	770*	889	1064	770	1676	2013	3.5	6.7	6.3	21.9	Buckling at C_3
1.76	770	889	1064	843	1798	2162	3.8	7.2*	6.8	23.6	Onset of C_2 loss of compression strength
1.83	770	790	1064	902	1998*	2281	4.1	8.0	7.1	25.6	Yielding at T_2
1.31	770	0*	1064	809	1998	1338	3.7	14.4	4.2	29.6	Mid-story mechanism
Case IV: Tension-Only Design Without (KL/r) Limits											
1.14	0	0	0	1050*	1755	2100*	8.0	7.8	8.0	31.6	Top- and bottom-story mechanisms (simultaneous)

*Critical event at that step.

TABLE 6.2 Push-Over Analysis Results for the Four Frames Considered (*Continued*)

Structural behavior in Case III closely parallels that of Case II, with the only notable difference being that buckling in the third story is delayed with respect to that at the other levels. In Case IV, as a result of the extreme brace slenderness ratios, buckling is immediate, and tension yielding and plastic collapse mechanisms occur in the first and third stories simultaneously ($\alpha = 1.14$).

The base shear versus lateral displacement diagrams for each of the four frames is shown in Figure 6.11e. These push-over analyses reveal that, for Cases II and III respectively, lateral forces 70% and 65% greater than those considered during design are necessary to trigger their collapse failure mechanisms, whereas Cases I and IV have little (16.5%) or no reserve strength. Figure 6.11e also provides some evidence that Cases II and III have a relatively more ductile behavior, with more plastic energy dissipated for a given frame displacement.

The push-over analyses also exposed the lack of force redistribution in these frames; story plastic collapse mechanisms always developed following tension yielding of the brace at a given story, with Case IV being the only exception. In fact, analysis of braced frames modeled using idealized pin-connections, as done in simplified truss models (and in this example), inevitably predicts the development of a soft-story mechanism, as no greater lateral force can be applied to the structure once brace yielding develops at a given story (braces yielding over multiple stories being only possible if they start to yield at the exact same time, as in Case IV, which is practically never the case). Yet, as described in Chapter 9, distribution of brace yielding along the height of concentrically braced frames is observed during earthquakes; this satisfactory behavior develops because of the additional shear transfer mechanism provided by the continuity of columns in structural frames (MacRae et al. 2004, MacRae 2010).

Attempts to extrapolate the results from this example beyond the context of monotonic loading may lead one to erroneously conclude that the more stringent member slenderness limits imposed for seismic design provide no tangible benefit because Case III exhibits less ductile behavior than does Case II. One could also argue that Case IV is superior by virtue of it being the only case for which a plastic collapse mechanism develops in two stories, with energy dissipation better distributed along the height. Such conclusions are faulty because they address behavioral aspects that are beyond the scope of the push-over analysis. Evaluation of the hysteretic energy dissipation merits of various designs can be reliably supported only by results from cyclic inelastic analyses, not by monotonic push-over analyses. Cyclic push-over analysis, as a minimum, is needed to reveal the impact of brace slenderness on hysteretic energy dissipation, as demonstrated in the next section.

6.3.2 Cyclic Push-Over Analysis

Cyclic push-over analysis can be useful to investigate the cyclic inelastic behavior of structures or subassemblies, particularly when the intent is to investigate the impact of unidirectional energy dissipation mechanisms on structural response. For hand calculations, simple element models and small structures are preferable.

Here, a few cycles of push-over analysis are used to illustrate the detrimental impact of brace slenderness on seismic response. In this example, a one-bay frame having X-braces with a large slenderness ratio, KL/r, is analyzed (Figure 6.12a). Such braced frames are typical of tension-only designs, as described in the previous example.

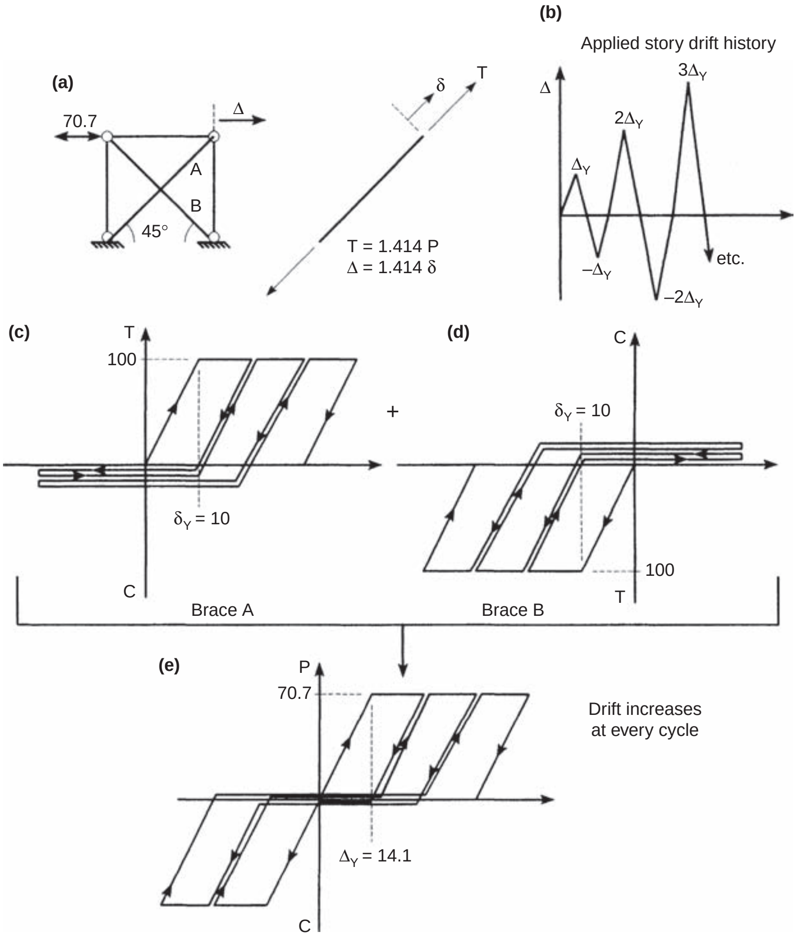

FIGURE 6.12 Cyclic push-over analyses examples on a single-story braced frame having slender braces.

A reasonably accurate force-elongation model of very slender braces can be constructed by assuming that:

- Elastic buckling of a brace occurs as soon as compression forces are introduced in the brace.
- All buckling deformations are elastically recovered upon unloading.
- Each brace behaves as an elasto-perfectly plastic material in tension.

This example uses generic members that yield at forces and axial deformations of 100 and 10, respectively (units are not needed). The history of the cyclic displacement applied at the top of the braced frame is shown in Figure 6.12b, along with the resulting forces and deformations in braces A and B, respectively (Figures 6.12c and d). One obtains the resulting force-displacement diagram of that braced frame by combining the force-elongation contributions of each brace as shown in Figure 6.12e. For the sake of clarity in parts c, d, and e of Figure 6.12, many lines that should actually be superimposed have been separated.

Walking step by step through the applied cyclic displacement history, one observes that after the first yielding excursion and first unloading, the brace member that yielded is now longer in its stress-free condition and must buckle when the frame returns to its initial zero-deflection position. The second brace undergoes a similar process upon its first yielding and unloading. Hence, both braces become buckled when the frame returns to its initial position. As very slender compression braces provide little or no lateral resistance, the frame must drift until one member recovers all of its elastic buckling deformation before the structure can resist loads anew, and it must reach its previous maximum drift before any new plastic energy dissipation can take place. Therefore, when subjected to severe cyclic loading or dynamic excitations such as those produced by large earthquakes, this frame will progressively drift to very large deformations if a given amount of plastic energy must be dissipated during each cycle. This partly explains why brace slenderness ratios have sometimes been limited to relatively low values in seismic applications.

6.4 Seismic Design Using Plastic Analysis

Current design procedures recognize that structures cannot economically be designed to elastically resist the effects of earthquakes. Therefore, inelastic response (i.e., plastification of structural members) will develop if an earthquake as large as anticipated by the design procedures occurs. The role of the designer is to ensure that this plastification can develop in a stable manner without the risk of structural collapse. Engineers may elect to forgo this requirement, but as a trade-off, they will have to absorb a code-specified penalty of much larger required design forces. However, if a rare and unusually intense earthquake occurs, one that is greater than expected by the design code, structures that have been designed for ductile response could have a significant advantage over those that have not, despite the higher design forces considered in the latter case.

A more comprehensive assessment of the philosophy of earthquake-resistant design is presented in Chapter 7. However, with an appreciation that ductile structural systems are by far preferable to nonductile systems in seismic regions, the following two chapters address the behavior, design, and detailing of ductile braced frames and ductile moment-resisting frames. It should transpire from the following that, to a large extent, satisfactory seismic performance can be achieved through use of capacity, design principles, and good ductile detailing practice.

6.5 Global versus Local Ductility Demands

The maximum inelastic demand on a cross-section, structural member, or complete system, is often expressed as a "ductility ratio," μ, obtained by normalizing the maximum demand by the corresponding one at the onset of yielding. For example, displacements ductility is given by:

$$\mu = \frac{\Delta_{max}}{\Delta_y} \tag{6.8}$$

where Δ_{max} is the maximum displacement reached and Δ_y is the yield displacement. Values of μ greater than 1 imply plastic deformations.

The details of how this ductility ratio (a.k.a. ductility factor) is used in seismic design will presented in the subsequent chapter. Structural systems can be designed such that specially detailed structural elements are located in ductile frames that span the entire height of a structure, or in a smaller number of strategically located structural elements. In either case, it is important to recognize that different types of ductility quantification exist and that they are not linearly related to each other. The following sections illustrate two such examples.

6.5.1 Displacement Ductility versus Curvature Ductility

As described in Section 4.1, the deformation of a partially plastified structural member can be obtained by double integration of the curvature along that member, which can be done rigorously (but not necessarily easily) using either exact moment-curvature relationships, such as those derived in Section 3.1.1 when available, or simplified approximations of the plastic curvature distribution. However, because deformations in the plastic range are mostly due to the plastic hinges rotations, curvature ductility increases faster than displacement ductility and the relationship between the two ratios is nonlinear.

Various curvature distributions are considered here to illustrate the relationship between displacement and curvature ductility for the cantilever column shown in Figure 6.13. In all cases, displacement ductility for a lateral load applied at the tip of the cantilever is given by Eq. (6.8), using the yield displacement of:

$$\Delta_y = \frac{P_y L^3}{3EI} = \frac{M_y L^2}{3EI} = \frac{\phi_y L^2}{3} \tag{6.9}$$

where the yield curvature, ϕ_y, is given by Eq. (3.4), valid only in the elastic range. In some cases, to simplify calculations, the moment-curvature relationship is assumed linear up to M_p and a displacement ductility of 1.0 is reached when $\Delta_{max} = \Delta_p$; when such a model is used, M_p, ϕ_p, and Δ_p are often relabeled M_y, ϕ_y, and Δ_y respectively, but "yield" in that case identifies the end of the elastic range on the idealized moment-curvature relationship rather than the curvature at which the yield strain is first reached on the cross-section. To avoid confusion, this is not done here.

The first case in Figure 6.13 illustrates the exact curvature distribution obtained using an elasto-plastic stress-strain model, and shown previously in Figure 4.1. While convenient for simplified plastic analysis, this approach can be problematic as curvature asymptotically approaches infinity as the moment approaches M_p. It is possible to derive closed-form solutions that give the lateral deflection at the tip of the cantilever by limiting the maximum curvature to arbitrarily selected large values (such as $10\phi_y$, which corresponds to M_p for practical purposes), but the more direct approaches presented below are satisfactory for the current purpose.

One approach is to add to the elastic results the contribution from a concentrated inelastic curvature, of magnitude $(\phi_{max} - \phi_p)$, acting over a plastic hinge length, L_p, as shown for the second case in Figure 6.13. When this approach is used for reinforced concrete members, the plastic hinge length is typically taken as half of the cross-sectional depth. The corresponding deflection at the tip of the cantilever is:

$$\Delta_{max} = \Delta_p + (\phi_{max} - \phi_p) L_p \left(L - \frac{L_p}{2} \right) \tag{6.10}$$

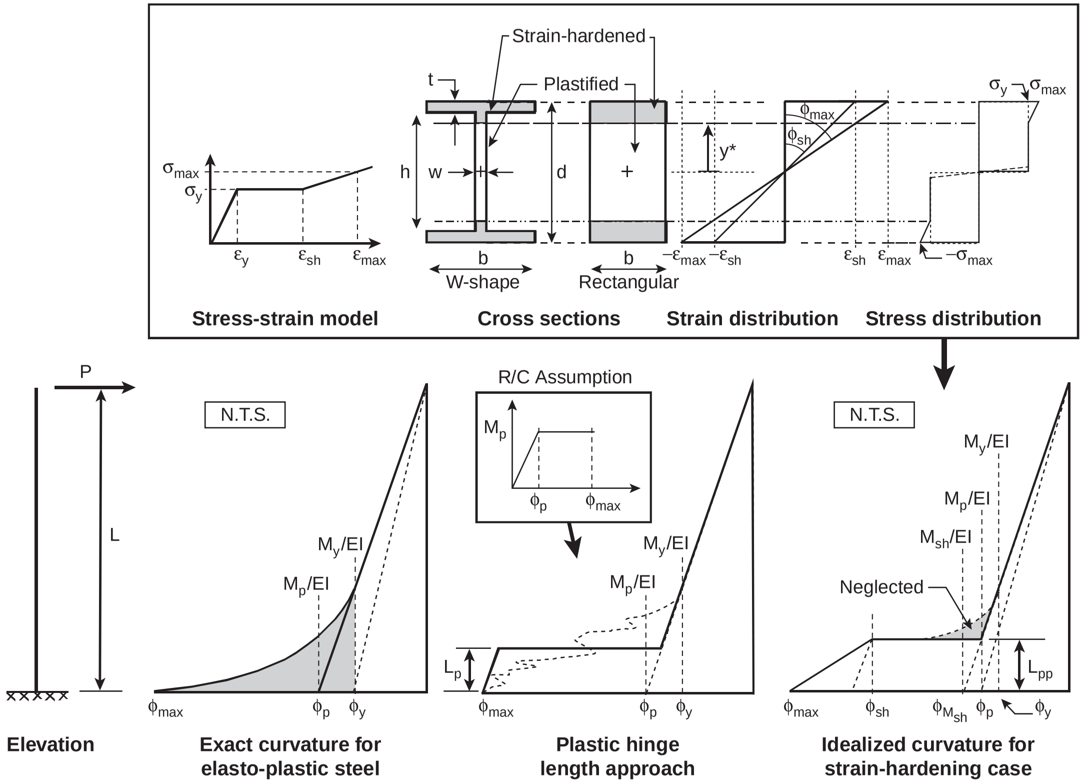

FIGURE 6.13 Curvatures for calculation of curvature and displacement ductilities.

where Δ_p is given by Eq. (6.9), substituting M_p and ϕ_p for M_y and ϕ_y, respectively. The corresponding displacement ductility is:

$$\mu = \frac{\Delta_{max}}{\Delta_p} = 1 + \frac{(\phi_{max} - \phi_p)L_p\left(L - \frac{L_p}{2}\right)}{\frac{\phi_p L^2}{3}} \tag{6.11}$$

and the corresponding curvature ductility, μ_ϕ, expressed as a function of the displacement ductility, is:

$$\mu_\varphi = \frac{\phi_{max}}{\phi_p} = 1 + \frac{(\mu - 1)}{3\left(1 - \frac{L_p}{2L}\right)\frac{L_p}{L}} \tag{6.12}$$

For a displacement ductility of 4, for plastic lengths equal to 5%, 10%, and 20%, the respective curvature ductility is 21.5, 11.5, and 6.6, respectively with corresponding increases in strains [which are linearly related to curvatures per Eq. (3.1)]. This approach is typically used in analyses for reinforced concrete and composite members (substituting ϕ_p by ϕ_y for the reasons outlined earlier).

Deflections for steel members can be calculated using an idealized moment-curvature relationship accounting for strain-hardening. For this third case, shown in Figure 6.13, curvature is assumed linear up to M_p and ϕ_p, at which point it increases in a step up to a strain-hardening curvature value of ϕ_{sh}, after which it is assumed to increase proportionally to the moment, up to a maximum moment of M_{sh}. The plastic hinge length, L_{pp}, in this case corresponds to the strain-hardening range. The plastic zone that would correspond to the region of $M_y < M < M_p$ is conservatively neglected. For such a curvature diagram, the deflection at the tip of the cantilever is:

$$\Delta_{max} = \Delta_{Msh} + (\phi_{sh} - \phi_p)L_{pp}\left(L - \frac{L_{pp}}{2}\right) + \left(\frac{(\phi_{max} - \phi_{sh})L_{pp}}{2}\right)\left(L - \frac{L_{pp}}{3}\right) \tag{6.13}$$

where Δ_{Msh} is given by Eq. (6.9) for the strain-hardened moment, M_{sh}. That moment can be obtained by cross-sectional analysis using the idealized tri-linear stress-strain diagram shown in that figure, with a stress-hardening modulus, $E_{sh} = E/75$ (Byfield et al. 2005). For illustration purpose, for a maximum curvature of $\phi_{max} = 1.5\phi_{sh}$, and a strain-hardening curvature of $\phi_{sh} = 10\phi_y$, the maximum stress reached is $1.067\sigma_y$. From the resulting stress distribution (Figure 6.13), the strain-hardened moment can be calculated. For a rectangular cross-section, it is:

$$M_{sh} = M_P + 0.067\sigma_y \left[b\left(\frac{d}{2}\right)\left(\frac{1}{3}\right)\right]\left[2\left(\frac{d}{2} - \frac{1}{3}\left(\frac{d}{6}\right)\right)\right]$$

$$= M_P + 0.04\left(\frac{bd^2}{4}\right)\sigma_y = 1.04M_P \tag{6.14}$$

By similar triangles, the plastic length, L_{pp}, is equal to $0.04L$. The corresponding lateral deflection at the tip of the cantilever is:

$$\Delta_{max} = 1.04\Delta_p + 8.5\phi_y(0.04L)\left(L - \frac{0.04L}{2}\right)$$

$$+\left(\frac{5\phi_y(0.04L)}{2}\right)\left(L - \frac{0.04L}{3}\right) = 1.05\phi_y L^2 \tag{6.15}$$

Dividing by the yield displacement (Eq. 6.9) gives a displacement ductility of 3.18, reached for a curvature ductility of 15.

For a W-shape, following the same steps but assuming for expediency an idealized shape such that a strain-hardened moment of $1.067M_p$ is reached, the corresponding plastic hinge length is $0.067L$ and the lateral deflection is $1.244\phi_y L^2$, resulting in a displacement ductility of 3.73 (for the same curvature ductility of 15).

Although the above approaches can be helpful to calculate strain histories for low-cycle fatigue life calculations, recall that strains are further magnified when local buckling develops at large plastic curvatures. For that reason, as described in subsequent chapters, plastic rotation capacity has been frequently used to quantify the ductile performance of steel members, rather than curvature.

6.5.2 Ductility of Yielding Link for Structural Element in Series

A simple relationship between local and global ductility demands can be formulated for a single-mass two-spring system (Figure 6.14), where a "weak link" spring of initial stiffness, K_w, and a "protected" spring of stiffness, K_p, are connected in series. In a capacity design perspective, it is assumed that the "weak link" spring exhibits elastic-perfectly plastic (EPP) behavior and has a finite yield strength, $V_{w,y}$, smaller than that of the "protected" spring. It is apparent, that the yield strength, V_y, of the system is equal to $V_{w,y}$. The yield displacement, Δ_y, of the mass consists of the local yield displacement, $\Delta_{w,y} = V_y/K_w$, of the "weak link" spring and the displacement contribution, $\Delta_p = V_y/K_p$, of the "protected" spring:

$$\Delta_y = \Delta_{w,y} + \Delta_p = \frac{V_y}{K_w} + \frac{V_y}{K_p} \tag{6.16}$$

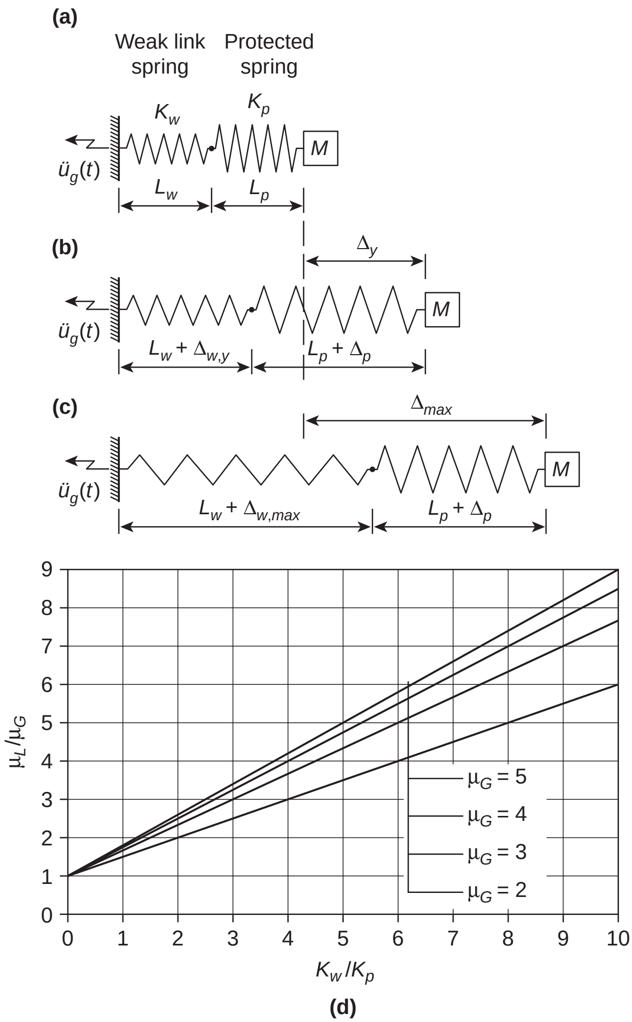

Figure 6.14 Single-mass two-spring system: (a) initial position; (b) at yield; (c) at maximum displacement; and (d) normalized local ductility demands.

It follows from the above definitions that $V_y = K_w \Delta_{w,y} = K_p \Delta_p$. If the system undergoes inelastic deformations, the peak displacement, Δ_{max}, of the mass, consists of the peak displacement contributions, $\Delta_{w,max}$ and $\Delta_{p,max}$, provided by the "weak link" spring and the "protected" spring, respectively. Since the strength of the system is limited by V_y, the maximum displacement of the "protected" spring is V_y/K_p, and therefore:

$$\Delta_{max} = \Delta_{w,max} + \Delta_{p,max} = \Delta_{w,max} + \frac{V_y}{K_p} \tag{6.17}$$

The local ductility demand, μ_L, for the "weak link" spring and the global ductility demand, μ_G, for the system are defined by:

$$\mu_L = \frac{\Delta_{y,max}}{\Delta_{w,y}} \quad \text{and} \quad \mu_G = \frac{\Delta_{max}}{\Delta_y} \tag{6.18}$$

Using these equations, for the case $\mu_G \geq 1$, the following relationship between local and global ductility can be derived (Alfawakhiri and Bruneau 2001):

$$\mu_L = \mu_G + (\mu_G + 1)\frac{\Delta_p}{\Delta_{w,y}} = \mu_G + (\mu_G + 1)\frac{K_w}{K_p} \tag{6.19}$$

Figure 6.14 shows plots of the normalized local ductility demands, μ_L/μ_G, for several values of μ_G. It illustrates that the local ductility demand is larger than the global ductility demand for any nonzero positive finite value of K_p. If the "protected" spring is infinitely rigid ($K_p = \infty$), then $\mu_L = \mu_G$. Similar equations to accommodate any number of "protected" springs in series, with or without strain-hardening of the yielding spring have been also presented by Alfawakhiri and Bruneau (2001).

The above relationship between local and global ductility is integral to the design requirements for ductile end-diaphragms in slab-on-girder bridges (AASHTO 2009), in which yielding diaphragms inserted in the steel superstructure of a slab-on-girder bridge are designed to exhibit ductile behavior and dissipate energy during earthquakes while protecting a stiff but nonductile substructure (Zahrai and Bruneau 1999a, 1999b). A similar concept relying on ductile cross-frames along the two load-paths traveled by seismic forces in deck-trusses bridges (Sarraf and Bruneau 1998a, 1998b) has been implemented as part of the seismic retrofit of the third-longest cantilever truss span in the world, located in Osaka in Japan (Kanaji et al. 2005).

Similar relationships between local and global ductility in slab-on-girder bridges also have been derived for the case when considerable superstructure flexibility in the horizontal transverse direction is encountered, such as in relatively narrow (slender in plan view) spans of highway or railroad bridges for which the assumption of infinitely rigid superstructure cannot be justified (Alfawakhiri and Bruneau 2001).

6.6 Displacement Compatibility of Nonductile Systems

When ductile and nonductile structural systems are configured to act like springs in parallel (rather than springs in series as was the case in Figures 6.3 and 6.14), the nonductile structural elements will undergo

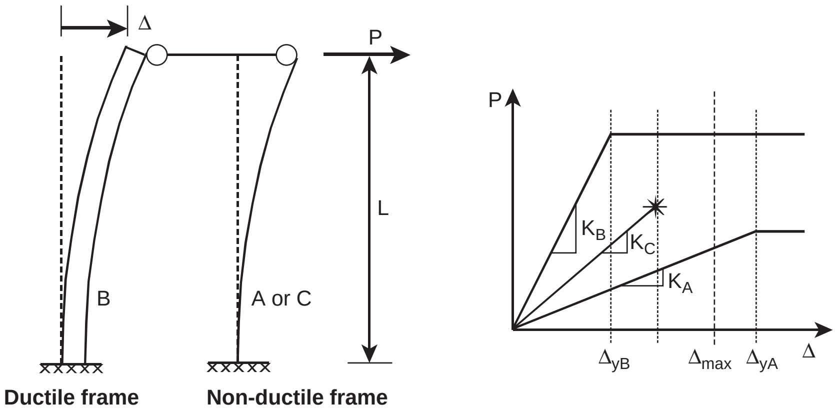

Figure 6.15 Structural systems in parallel.

the same displacements as the ductile ones, as shown in Figure 6.15. However, when the nonductile elements are not designed and detailed to tolerate large displacements without loss of strength, care must be taken to either limit the displacement demands, prevent nonductile failures, or ensure that such failures are of no consequences. For the schematic structure in Figure 6.15, Frame A performs satisfactorily, not yielding when the lateral load resisting system (Frame B) reaches it maximum displacement demand, Δ_{max}, contrary to Frame C which fails in a brittle manner.

In that perspective, columns of a building frame that are only designed to carry gravity loads, as well as their splices and connections, must retain their integrity when displacing laterally together with the ductile lateral load resisting system; even if not intended to resist lateral loads, as a result of compatibility of deformations at the floor levels, all columns and frames displace laterally and resist lateral loads proportionally to their stiffness. Avoiding stiff elements in a gravity frame is one approach to safeguard against undesirable failures, together with ensuring its elastic response up to the large displacements reached when the lateral load resisting system reaches it maximum ductility demand. For the same reason, stiff cladding or nonstructural walls should be designed to allow unrestrained sway of the entire framing system, such that deformations of the ductile frames do not impose distortions and forces on the cladding and walls.

6.7 Self-Study Problems

Problem 6.1 A two-story concentric braced frame is to be studied using a displacement response history analysis method (i.e., push-over analysis using plastic analysis). The intent here is to compare the behavior of two structures under the following assumptions. Two brace tension-compression models are as shown below, where δ is the brace axial displacement (not the story displacement). The braces of the first structure are entirely made of model A, whereas the braces of the second structure are of model A at the top story, and model B at the bottom story. All columns can be assumed to remain elastic.

In both cases, a load is applied at the top of the second story. The displacement at the point of load application is increased until the compression brace at the second story has no more strength (the end of the compression range on the brace tension-compression model shown as follows).

For each structure, plot the base shear (V) as a function of the frame's top displacement, Δ. Compare the hysteretic behavior of the two frames. Comment on:

- Which frame has the best energy dissipation capacity? Note that energy is expressed by the area under the force-displacement curve (force times displacement equals work, which itself is a measure of energy), less the elastically recoverable part of the energy (i.e., work done in the initial elastic range).
- Which frame has members undergoing the largest inelastic excursions for a given frame displacement, and which frame undergoes the largest inelastic excursion for a given member deformation?
- Which frame has the best capacity for a given frame displacement?
- Which frame sees the largest member deterioration for a given frame displacement?

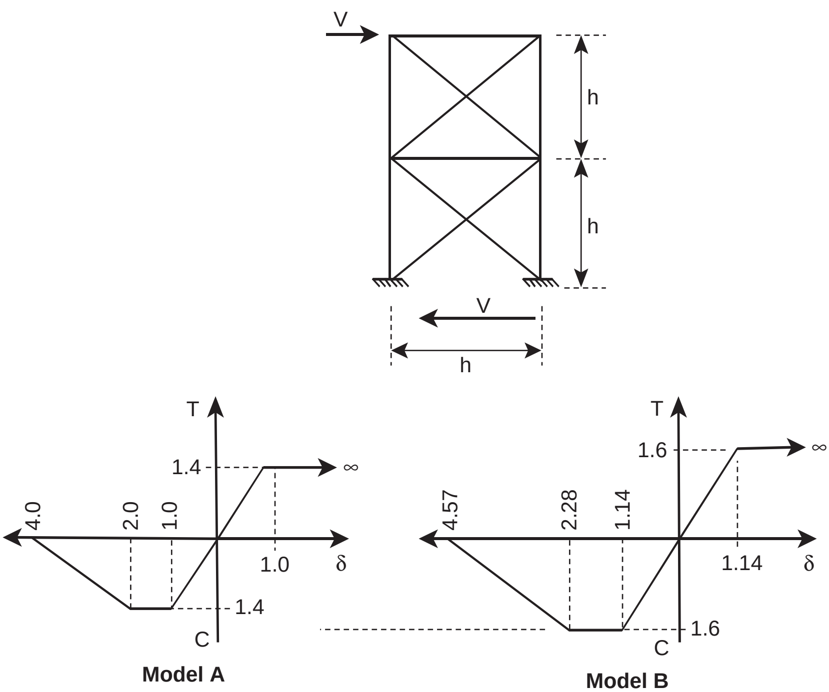

Problem 6.2 To dig a foundation, an excavation is being placed next to an adjacent building. Even though tiltmeters and other instruments will be installed to monitor possible incipient failure of the shoring, the insurance company has requested that the consequences of possible shoring failures be investigated. As a first step to estimate these consequences, determine:

1. If the building will remain stable if failure occurs only under one footing of one exterior column (i.e., take advantage of moment framing in both directions in this evaluation)—consider both the cases of corner columns and noncorner columns.
2. If the building will remain stable if the shoring fails adjacent to all of the exterior footings of that building located next to the excavation (i.e., the exterior row of columns' foundation support is completely gone).
3. The maximum compressive load the building can put on the soil adjacent to the shoring in the even of a major earthquake or wind storm.

For all beams, Z = 144 in^3 and F_y = 36 ksi. The columns can be assumed to be stronger than the beams. The frames are spaced at 20 ft center-to-center from each other. The actual floor live load acting on the frame is 20 per square ft (psf), the design floor live load is 50 psf, and the dead load is 120 psf. Neglect overturning of the building and catenary action (i.e., small displacement theory still applies).

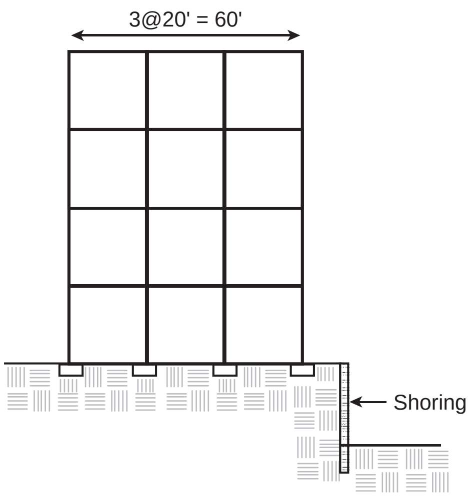

Problem 6.3 Use the upper bound theorem to find the maximum load, V, that can be applied to this structure for the two cases shown below. Draw a sketch showing the plastic mechanism for each of the plastic mechanisms considered.

Case 1: the link is a flexural link (i.e., designed to yield in flexure prior to yielding in shear) of strength = $6M_p$.

Case 2: the link is a shear link (i.e., designed to yield in shear prior to yielding in flexure) of strength $V_p = 12M_p/e$.

In both cases, show that the solution is statically admissible.

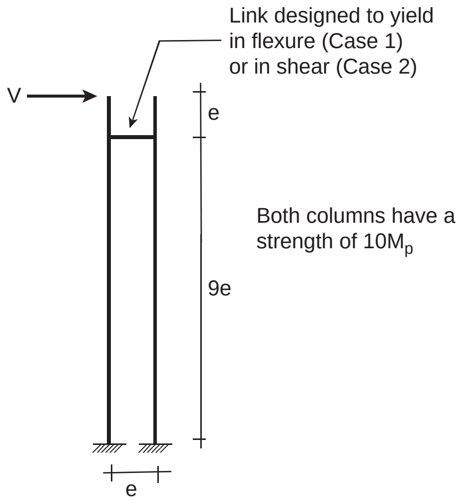

Problem 6.4 An architect has designed a sculpture that consists of two massive precast concrete triangles, linked together by two steel beams. The sculpture is linked to an adjacent building, such that a lateral load, P, could be applied to the top of one of the concrete triangles under some lateral loading conditions. The precast concrete triangles are to remain elastic under extreme loading conditions.

(a) Use the upper bound theorem to find the maximum load, P, that can be applied to this structure. Draw a sketch showing the plastic mechanism. In this problem, it is not required to show that the solution is statically admissible.

(b) Calculate the maximum uplift force that can act on the foundation for this system.

(c) If the top beam can be of a different size than the bottom beam, and assuming (for simplicity) that the weight of a steel beam is directly proportional to its value of M_p, select M_{P-TOP} and $M_{P-BOTTOM}$ such that the least total weight of steel is used.

(d) Using fundamental engineering principles, explain why the answer to (c) is logical.

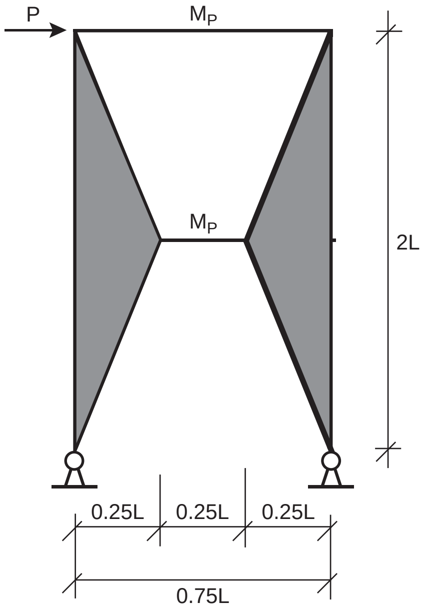

Problem 6.5 A push-over analysis indicates that the ultimate lateral capacity of a five-story frame is reached when a sway mechanism of the type shown in Figure 6.8 develops (i.e., with plastic hinges at the ends of all beams, and at the base of the columns). A lateral load, P, is applied at each story (floors and roof), and a gravity uniformly distributed load of 8kN/m is applied on each beam. Stories are 5 m tall, and the frame is 10 m wide. Plastic strength of the beams: $M_{p-beam} = 180$ kN-m. The columns are W-shapes built up by welding 166-mm × 11.8-mm flanges to a 181.4-mm × 7.2-mm web; these steel plates have a specified minimum yield strength of 300 MPa.

Calculate the magnitude of the load P that would produce this plastic sway mechanism of the frame for the following conditions:

(a) Neglecting the effect of shear and axial force on the plastic moment capacity, M_p, of the column base
(b) Neglecting the effect of axial force on the plastic moment capacity, M_p, of the column base, but still neglecting the effect of shear

Comment on whether the difference in results obtained for (a) and (b) is significant or not, and why that is the case (based on fundamental principles).

References

Alfawakhiri, F., and Bruneau, M. 2001. "Local versus Global Ductility Demands in Simple Bridges." *Journal of Structural Engineering, ASCE*, vol. 127, no. 5, 554–560.

AASHTO. 2009. *Guide Specifications for LRFD Seismic Bridge Design*. Washington, D. C.: American Association of State Highway and Transportation Officials.

Byfield, M. P., Davies, J. M., and Dhanalakshmi, M. 2005. "Calculation of the strain hardening behaviour of steel structures based on mill tests." *Journal of Constructional Steel Research*, vol. 61, 133–150.

Haaijer, G., Carskaddan, P. S., and Grubb, M. A. 1983. "Autostress Design of Steel Bridges." *ASCE Structural Journal*, vol. 109, no. 1, 188–199.

Kanaji, H., Kitazawa, M., and Suzuki, N. 2005. "Seismic Retrofit Strategy using Damage Control Design Concept and the Response Reduction Effect for a Long-span Truss Bridge," US-Japan Bridge Workshop, Tsukuba, Japan, 2005.

Lawson, R. S., Vance, V., and Krawinkler, H. 1994. "Nonlinear Static Push-Over Analysis: Why, When, and How?" *Proceedings of 5th US National Conference on Earthquake Engineering*, July 10–14, 1994 Chicago. Edited by *Earthquake Engineering Research Institute*, vol. 1, 283–292.

MacRae G. A., Kimura Y., and Roeder C. W. 2004. "Effect of Column Stiffness on Braced Frame Seismic Behavior." *Journal of Structural Engineering, ASCE*, vol. 130, no. 3, 381–391.

MacRae, G. 2010. "The Development and Use of the Continuous Column Concept," *Joint 7th International Conference on Urban Earthquake Engineering (7CUEE) & 5th International Conference on Earthquake Engineering (5ICEE)*, March 3–5, 2010, Tokyo Institute of Technology, Tokyo.

Sarraf, M., and Bruneau, M. 1998a. "Ductile Seismic Retrofit of Steel Deck-Truss Bridges. I: Strategy and Modeling." *Journal of Structural Engineering, ASCE*, vol. 124, no. 11, 1253–1262.

Sarraf, M., and Bruneau, M. 1998b. "Ductile Seismic Retrofit of Steel Deck-Truss Bridges. II: Design Applications." *Journal of Structural Engineering, ASCE*, vol. 124, no. 11, 1263–1271.

Zahrai, S. M., and Bruneau, M. 1999a. "Cyclic Testing of Ductile End-Diaphragms for Slab-on-Girder Steel Bridges." *Journal of Structural Engineering, ASCE*, vol. 125, no. 9, 987–996.

Zahrai, S. M., and Bruneau, M. 1999b. "Ductile End-Diaphragms for the Seismic Retrofit of Slab-on-Girder Steel Bridges." *Journal of Structural Engineering, ASCE*, vol. 125, no. 1, 71–80.

CHAPTER 7

Building Code Seismic Design Philosophy

7.1 Introduction

Plastic analysis and design methods presented in the previous chapters were mainly developed in the 1960s and 1970s. With the advent of computers, however, elastic design was soon favored over plastic design due to the emergence of computer structural analysis software able to perform linear elastic analysis of large structures. It was also about the same time that active research in earthquake engineering and seismic design started in North America. Although plastic design has not been widely accepted for routine design, the seismic design community soon realized that allowing structures to respond in the inelastic range was beneficial and most often unavoidable. When properly designed, plastic mechanisms would form and dissipate energy imparted by the earthquake ground motion to the structure.

Modern seismic design codes are based on decades of research and field observation after earthquakes. Although such codes to date do not explicitly use the plastic design method, a key fundamental concept of these codes is the need for ductility and ductile plastic mechanism. The seismic design community goes one step further by incorporating the capacity design concept in parallel with ductility design (as shown in the subsequent chapters). Those two underlying concepts form the basis for seismic design of structures.

7.2 Need for Ductility in Seismic Design

Structural design codes usually specify a set of load combinations that need to be considered in design. For example, ASCE 7 (ASCE 2010) requires the following for building design:

$$1.4(D + F)$$

$$1.2(D + F + T) + 1.6(L + H) + 0.5(L_r \text{ or } S \text{ or } R)$$

$1.2D + 1.6(L_r \text{ or } S \text{ or } R) + (L \text{ or } 0.8W)$
$1.2D + 1.6W + L + 0.5(L_r \text{ or } S \text{ or } R)$
$1.2D + 1.0E + L + 0.2S$
$0.9D + 1.6W + 1.6H$
$0.9D + 1.0E + 1.6H$

where D = dead load, L = live load, L_r = roof live load, S = snow load, W = wind load, and E = earthquake load. Of all the design loads, the earthquake load, E, is often the subject of much misunderstanding, as it is actually an inertia effect due to base excitation produced by an earthquake instead of a real load.

7.2.1 Elastic Response and Response Spectrum

To study the seismic effect on a structure, it is first assumed that a one-story frame can be idealized as a single-degree-of-freedom (SDOF) system, as shown in Figure 7.1a, where K is the lateral stiffness, and M is the lumped mass tributary to the roof level. The angular natural frequency, ω, and the natural period, T, of the structure are:

$$\omega = \sqrt{M/K} \tag{7.1a}$$

$$T = \frac{2\pi}{\omega} = 2\pi\sqrt{K/M} \tag{7.1b}$$

It is also assumed that this system has a 5% equivalent various damping ratio. With a sample earthquake ground motion like the one shown in Figure 7.1b as the input at the base of the frame, the elastic structural response in terms of lateral displacement relative to the base can be computed from structural dynamic theory (Chopra 2007). See Figure 7.1c for one sample response when the period of the structure is 1.0 s. Of particular interest from a design point of view is the maximum relative displacement of the mass relative to the base. This maximum displacement is defined as the spectral displacement, $S_d(T)$ at period T. By varying either M or K, the natural period of the system is also changed. If the above process is repeated for other period values, a displacement response spectrum like that shown in Figure 7.2a can be constructed. Once a response spectrum is constructed, time-consuming time-history analysis is no longer needed as the maximum relative displacement for a given period value can be simply read off from the spectrum.

To design the structure, it is necessary to know the maximum force in the member. From Hooke's law, the maximum structural force or base shear, V_e, in the elastic system is:

$$V_e(T) = K\Delta_{max} = KS_d(T) \tag{7.2}$$

Together with Eq. (7.1a), the above equation can be rewritten as:

$$V_e(T) = M\omega^2 S_d(T) \tag{7.3}$$

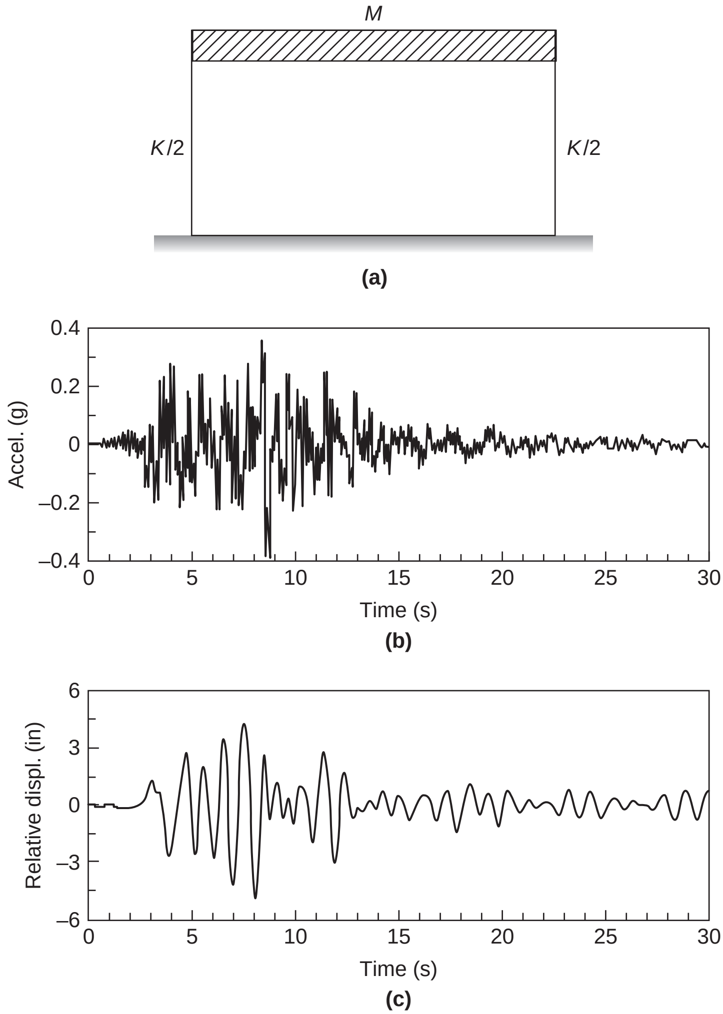

FIGURE 7.1 Elastic response of an SDOF system: (a) idealized one-story frame; (b) earthquake ground motion (Canoga Park, 1994 Northridge, California Earthquake); (c) relative displacement response.

Defining the pseudo-acceleration, $S_a(T)$, as the following:

$$S_a(T) = \omega^2 S_d(T) \tag{7.4}$$

then the displacement response spectrum in Figure 7.2a can be converted to a pseudo-acceleration response spectrum in Figure 7.2b, and Eq. (7.3) becomes:

$$V_e(T) = MS_a(T) = W\left(\frac{S_a(T)}{g}\right) \tag{7.5}$$

where W is the reactive weight of the system.

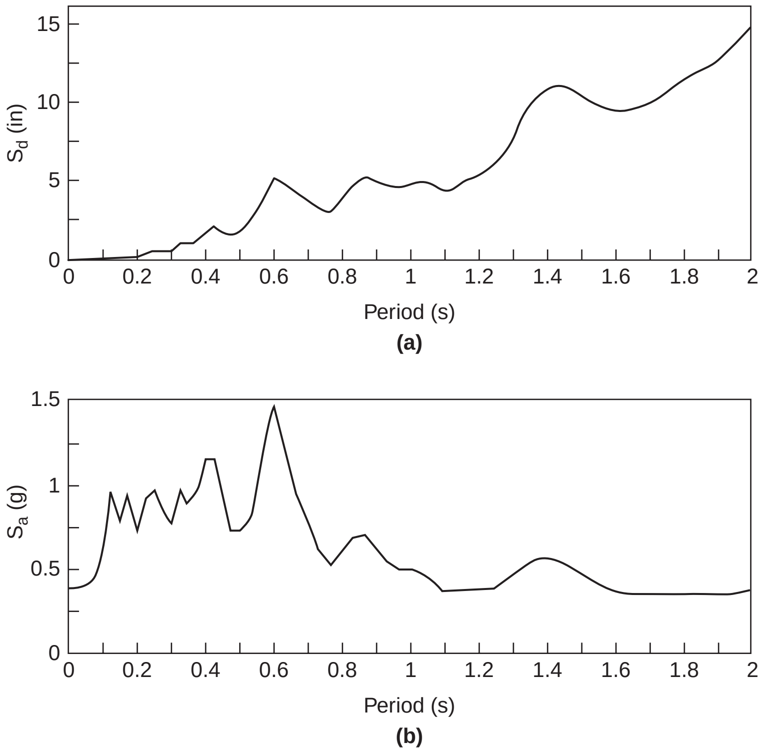

FIGURE 7.2 Elastic response spectra: (a) relative displacement response spectrum; (b) pseudo-acceleration response spectrum (5% damping).

7.2.2 Inelastic Response and Ductility Reduction

For the example frame to remain elastic, Figure 7.2b indicates that the structure needs to be designed for a base shear of 0.5*g*:

$$V_e(T) = M(0.5g) = 0.5W \tag{7.6}$$

That is, for this structure to remain elastic, it needs to be designed for a lateral load that is equal to half of the reactive weight, which is large. Normalizing the base shear, V, by the reactive weight, W, is defined as the base shear ratio, C. Then C_e represents the elastic base shear ratio. This required force level corresponds to point A in Figure 7.3, where the elastic response is shown in dashed line O-A.

Generally, it is not economical to design a structure to remain elastic during a strong earthquake. If an effort is made to ensure that the structure possesses ductility, the required base shear force can be significantly reduced. In such a case the expected elasto-plastic

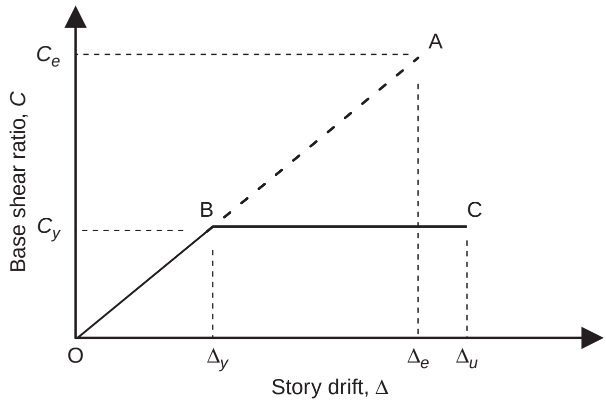

Figure 7.3 Definition of ductility factor and ductility reduction factor for an SDOF system.

structural response is shown as O-B-C in Figure 7.3; C_y is the yield shear ratio of the frame. This defines the ductility factor, μ, as follows:

$$\mu = \frac{\Delta_u}{\Delta_y} \tag{7.7}$$

where Δ_u and Δ_y are the maximum and yield displacements, respectively. Referring to the one-story frame in Figure 7.1a again, assume the frame has a ductility capacity of 3. As a 1-s period structure, it can be shown that the required yield base shear ratio only needs to be 35% of the elastic base shear ratio. Figures 7.4a and b show the inelastic response. The reduced yield base shear can be expressed as:

$$C_y = \frac{C_e}{R_\mu} \tag{7.8}$$

where R_μ is defined as the ductility reduction factor. In this example, the value of R_μ is 2.8 for a target μ value of 3.0.

By varying the period of the structure, the constant-ductility R_μ spectrum can be constructed. Newmark and Hall (1982) proposed a very simple ductility reduction rule for SDOF systems. In the moderate and long period range (i.e., in the velocity and displacement amplification regions of the response spectrum), it was observed that the maximum displacement of the elastic and inelastic systems are about the same. This observation leads to the following:

$$R_\mu = \mu \tag{7.9a}$$

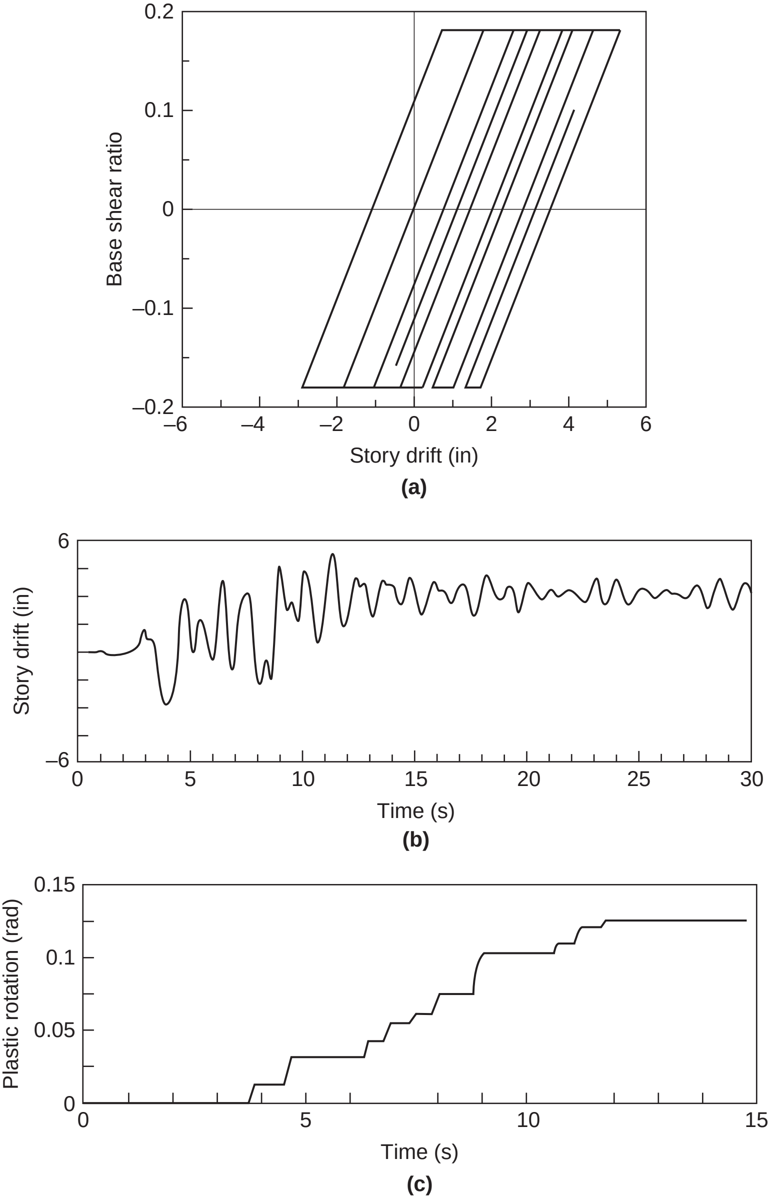

Figure 7.4 Inelastic response of an SDOF system: (a) hysteresis response; (b) relative displacement response; (c) cumulative plastic rotation.

This corresponds to the so-called equal displacement rule. The above relationship can be easily derived from Figure 7.3 by assuming the inelastic displacement, Δ_u, is equal to elastic displacement, Δ_e.

In the short period range (i.e., in the acceleration amplification region of the response spectrum), the relationship is closer to:

$$R_\mu = \sqrt{2\mu - 1} \tag{7.9b}$$

This corresponds to the so-called equal energy rule. The above equation can be derived from Figure 7.3 by equating the areas (i.e., energies) under both the O-A and O-B-C response curves. For a structure with a very short period, Newmark and Hall also observed that $R_\mu = 1$, that is, ductility is ineffective in reducing the required elastic seismic force. However, this would only be the case for structure very short in height and/or extremely stiff; the majority of building structures do not fall in this period range.

More refined ductility reduction rules have also been proposed. See, for example, Miranda and Bertero (1994) for a comparison of several force reduction rules. It should be noted that these rules were derived for SDOF systems, which cannot be applied directly to multistory building structures. See Section 7.5 for more discussion on this issue.

7.3 Collapse Mechanism versus Yield Mechanism

In plastic analysis and design, the term "collapse mechanism" is used to describe a state beyond which the structure has reached its capacity to carry monotonically increasing, static or dynamic load and becomes unstable. The term "collapse" is appropriate when the load is monotonically applied in one direction. However, this definition is not applicable for earthquake "loading" because seismic response is cyclic and transient in nature. This can be demonstrated for the inelastic response of the one-story frame presented earlier. Because the structure is designed and, thus, allowed to yield, a mechanism starts to form once plastic hinges from both ends of the columns. As shown in Figure 7.4c, plastic rotation will develop and accumulate in these hinges before the structural response is reversed in direction. Upon load reversal, the columns will respond elastically again before plastic moment is reached in the reverse direction and plastic rotation starts to accumulate again. It is through this "on" and "off" process that the earthquake energy is dissipated by plastic deformation in the structure. One major goal of seismic design is to maximize energy dissipation while controlling damage. Therefore, the term "yield" or "plastic" mechanism, rather than "collapse" mechanism, is more appropriate to describe the seismic response of structures.

7.4 Design Earthquake

The discussion so far suggests that, at least conceptually, inelastic dynamic analysis is needed for reliable seismic response prediction and design. However, this is not practical for routine design for two main reasons.

On the loading side, it is not possible to deterministically define an earthquake ground motion time history. A recorded motion like that shown in Figure 7.1b is unique by itself; it is affected by many factors like earthquake rupture mechanism, earthquake magnitude, distance from epicenter, local site (or soil) condition, duration of shaking, etc. The intensity of shaking is also dependent on the recurrence interval between large earthquakes at the site of the structure.

On the analysis side, time-history analysis is time consuming and not practical for routine design. Because in design only the maximum structural response is of concern, elastic response spectra like those shown in Figure 7.2 can be more effective. However, because the zigzag-shaped response spectra in this figure are also unique for each recorded ground motion, for design purposes, seismic codes usually provide uniform hazard, smoothed elastic pseudo-acceleration response spectra, not ground motion time histories, to represent design ground motions. A design response spectrum represents statistically an average response spectrum based on many recorded ground motions for a given recurrence interval, expressed in the form of a probability of exceedance in a number of years.

In the United States, Section 1613 of the International Building Code (ICC 2009) references to ASCE 7, *Minimum Design Loads for Buildings and Other Structures* (ASCE 2005), for the construction of elastic design spectra. ASCE 7 first specifies the spectral acceleration values for a maximum considered earthquake (MCE) with a 2475-year recurrence interval (2% probability of being exceeded in 50 years). Two thirds of these values are then used to construct the design basis earthquake (DBE) with a 475-year recurrence interval (10% probability of being exceeded in 50 years). The DBE design spectral shape is shown in Figure 7.5. A brief summary of the procedure to construct the spectrum with a direct reference to relevant sections in ASCE 7 is provided as follows.

(1) Determine site ground motion.
Use ASCE 7 Section 11.4.1 to determine mapped acceleration parameters (S_s and S_1), which are based on (a) maximum considered earthquake (MCE), a 2475-year seismic event; (b) Site class B; and (c) 5% damping. S_s is the spectral acceleration at short period (= 0.2 s), and S_1 is the spectral acceleration at $T = 1$ s.

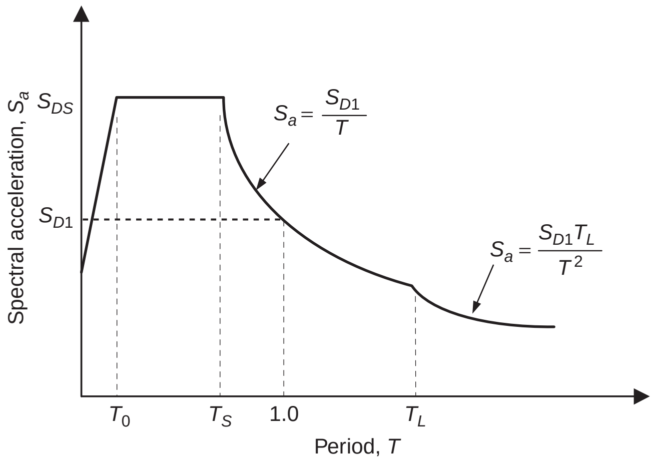

FIGURE 7.5 ASCE 7 design basis earthquake (DBE) elastic design spectrum.

(2) Determine site (or soil) classification.
Use Table 20.3-1 in Chapter 20 to classify the site. The default site class is D.

(3) Adjust mapped MCE spectral accelerations for the site effect (Section 11.4.3):

$$S_{MS} = F_a S_S \tag{7.10a}$$

$$S_{M1} = F_v S_1 \tag{7.10b}$$

where F_a and F_v are the site coefficients obtained from Tables 11.4-1 and 11.4-2.

(4) Determine design spectral accelerations (Section 11.4.4).
DBE spectral accelerations are two-thirds those from MCE:

$$S_{DS} = \frac{2}{3} S_{MS} \tag{7.11a}$$

$$S_{D1} = \frac{2}{3} S_{M1} \tag{7.11b}$$

The DBE elastic design spectrum in Figure 7.5 is then uniquely defined. For design purposes, ASCE 7 also requires each structure to be assigned a Seismic Design Category (SDC), which ranges from A, B, C, to D. This important category is a function of the S_{DS} value and the Occupancy Category, which depends on the level of hazard to human life in the event of structural failure. Most buildings care classified as Occupancy Category II, but essential buildings like hospitals and fire stations are classified as Occupancy Category IV; these buildings need to be designed more conservatively.

7.5 Equivalent Lateral Force Procedure

In concept, inelastic time-history analysis is needed for seismic response prediction and design. To facilitate routine design, however, it is highly desirable to use an equivalent lateral force procedure that treats the dynamic inertia effect by equivalent loads, such that a static analysis can be used instead of a dynamic one. The Equivalent Lateral Force (ELF) procedure, which has been in use in North America for more than half a century, was developed with this intent in mind. For its simplistic nature, however, ASCE 7 limits the use of ELF procedure for certain situations. For example, more sophisticated dynamic analysis, either linear or nonlinear, will be required if the structure is highly irregular in plan or height.

Analogous to Eq. (7.8b), ASCE 7 takes into consideration of the energy dissipation capacity of the structure by introducing a Response Modification Factor, R, to reduce the required elastic design base shear:

$$C_s(T) = \frac{C_e(T)}{R} \tag{7.12}$$

where C_e, which is a function of T, is obtained from the DBE elastic design response spectrum.

$$C_e(T) = \begin{cases} \dfrac{S_{D1}}{T} \le S_{DS} & \text{for} \quad T \le T_L \\ \dfrac{S_{D1}}{T^2} \le S_{DS} & \text{for} \quad T > T_L \end{cases} \tag{7.13}$$

T_L is the long-period transition period beyond which the spectrum acceleration is inversely proportional to T^2. The relationship between C_e and C_s spectra is shown in Figure 7.6. Note that in determining the design base shear for the ELF procedure, ASCE 7 conservatively extends the horizontal plateau of the design response spectrum from T_0 to 0 second.

ASCE 7 also introduces an Importance Factor, I, to account for the importance of occupancy. The default value is 1.0. But a value of 1.5 is assigned to I for essential facilities like hospitals and fire stations. To achieve a better protection against earthquake damage for more important structures, ASCE 7 reduces the elastic base shear by R/I, which can be interpreted as the effective Response Modification Factor. For a structure whose period is not too long ($T < T_L$), ASCE 7 expresses Eq. (7.12) as follows:

$$C_s(T) = \frac{S_{D1}}{T(R/I)} \le \frac{S_{DS}}{(R/I)} \tag{7.14}$$

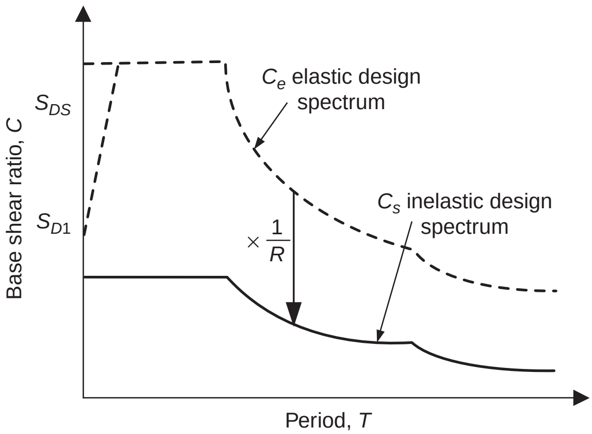

FIGURE 7.6 Relationship between ASCE 7 DBE elastic and inelastic design spectra.

The value of R ranges from 1.25 (least ductile structures) to 8.0 (most ductile structures). See Table 7.1 for the values of R for some steel seismic force-resisting systems.

The design base shear C_sW is used to define the statically applied equivalent lateral force. At this seismic design force level, a linear static structural analysis is performed and the corresponding story drift is designated as Δ_s. Because the structure is expected to respond in the inelastic range, ASCE 7 then requires Δ_s be multiplied by a Deflection Amplifications Factor, C_d, to estimate the maximum story drift. For steel structures this story drift cannot exceed the allowable value, which, based on the Occupancy Category, varies from 0.01 to 0.025 of the story height.

In addition to the two seismic performance factors, R and C_d, the third factor specified in ASCE 7 for capacity design is called the Structural Overstrength Factor, Ω_o. This factor will be discussed in the next section.

Steel Seismic Force-Resisting System	R	C_d	Ω_o
Special moment frames	8	5½	3
Ordinary moment frames	3½	3	3
Special concentrically braced frames	6	5	2
Ordinary concentrically braced frames	3¼	3¼	2
Eccentrically braced frames	8	4	2
Buckling-restrained braced frames	8	5	2½
Special steel plate shear walls	7	6	2

TABLE 7.1 ASCE 7 Sample Seismic Performance Factors

7.6 Physical Meaning of Seismic Performance Factors

Central to the ASCE 7 ELF seismic design procedure is the Response Modification Factor, R. Together with C_d and Ω_o, these three seismic performance factors greatly simplify the design process. The physical meaning of the ductility reduction factor, R_μ, for an SDOF system was discussed in Section 7.2.2. Although both R and R_μ factors are used to reduce the elastic seismic forces, the physical meaning of these two factors is somewhat different. As shown in Figure 7.3, R_μ is defined for an SDOF system where the inelastic behavior can be approximated by an elasto-perfectly plastic response. For application to seismic design of more redundant structures including multistory frames, however, the redundancy of the structure would cause the structure to yield progressively before the ultimate strength of the structure is reached. Therefore, the Newmark-Hall type of ductility reduction rule cannot be applied directly. The physical meaning of the seismic performance factors used in ASCE 7 is described in the following.

Figure 7.7 shows a typical response envelope of a structure, which can be used to explain the R-factor seismic design procedure. Based on the fundamental period of the structure, a designer first calculates the elastic design base shear, C_e (see point E in the figure). In ASCE 7, C_e is then reduced by a factor R to a design seismic force level C_s at point S [see Eq. (7.12)]. Point S is called the first significant yield point, beyond which the structure will respond inelastically. In other words, under lateral loads, a structure designed based on this reduced seismic force level first responds elastically, followed by inelastic response

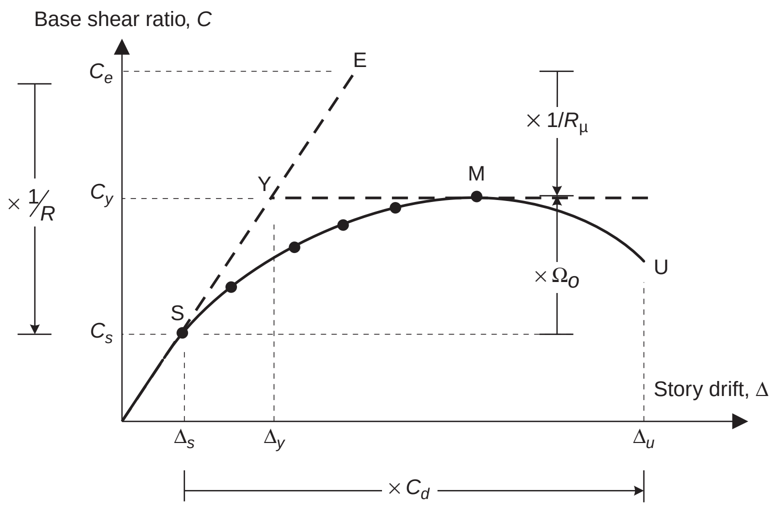

FIGURE 7.7 Seismic performance factors used in ASCE 7.

as the lateral forces are increased beyond that level. The redundancy that is built into the system together with ductility allows a series of plastic hinges to form in the structure, leading to a yielding mechanism at the strength level C_y.

If the actual structural response curve can be idealized by an elasto-perfectly plastic curve, the system ductility factor, μ_s, can be defined as:

$$\mu_s = \frac{\Delta_u}{\Delta_y} \tag{7.15}$$

Then the system ductility reduction factor, R_μ, can be defined like Eq. (7.8) for an SDOF system:

$$R_\mu = \frac{C_e}{C_y} \tag{7.16}$$

The reserve strength that exists between the yield level (C_y) and the first significant yield level (C_s) is defined as the system overstrength factor, Ω_o:

$$\Omega_o = \frac{C_y}{C_s} \tag{7.17}$$

System overstrength results from a number of factors including internal force redistribution, code requirements for multiple loading combinations, code minimum requirements regarding proportioning and detailing, material strength higher than that specified in the design, strain hardening, deflection constraints on system performance, member oversize, effect of nonstructural elements, and strain-rate effects.

Based on the definition of the above terms, the Response Modification Factor, R, for use with strength design can be derived as follows (Uang 1991a):

$$R = \frac{C_e}{C_s} = \frac{C_e}{C_y}\left(\frac{C_y}{C_s}\right) = R_\mu \Omega_o \tag{7.18}$$

The deflection amplification factor, C_d, is the ratio of Δ_u and Δ_s (see Figure 7.7):

$$C_d = \frac{\Delta_u}{\Delta_s} = \frac{\Delta_u}{\Delta_y}\left(\frac{\Delta_y}{\Delta_s}\right) \tag{7.19}$$

where Δ_u/Δ_y is the structural ductility factor [see Eq. (7.15)], and Δ_y/Δ_s from Figure 7.7 is equal to:

$$\frac{\Delta_y}{\Delta_s} = \frac{C_y}{C_s} = \Omega_o \tag{7.20}$$

Therefore, Eq. (7.19) can be rewritten as:

$$C_d = \mu_s \Omega_o \tag{7.21}$$

Both R and C_d factors are functions of the structural overstrength factor, structural ductility factor, and damping ratio; the effect of damping is generally included in the ductility reduction factor, R_μ. Furthermore, Eq. (7.18) shows that it is not appropriate to refer to R as a ductility reduction factor because system overstrength and ductility may contribute equally to R. Similarly, C_d is generally not equal to the system ductility factor.

7.7 Capacity Design

Ductility design and capacity design are two key concepts in seismic design. To demonstrate this concept, refer to a few commonly used lateral-load resisting systems in Figure 7.8. A thorough coverage of the design of these systems is provided in the following chapters. For the Special Moment Frame (SMF) in Figure 7.8a, energy dissipation is provided through plastic hinge formation in the beams. Therefore, only beams need to be designed to provide ductility. These members are also called the deformation-controlled element (DCE) as it is the deformation (or ductility) capacity that distinguishes these elements from the rest of the structure (ASCE 2006). To ensure that yielding will be confined to DCEs, it is essential that the remaining part of the structure, including columns and connections, have sufficient strength to remain essentially elastic. These latter elements are called force-controlled elements (FCE). Ductility is not the main concern for FCEs. Figures 7.8b and c show that diagonal braces and links are DCEs in special concentrically braced frames (Chapter 9) and eccentrically braced frames (Chapter 10), respectively.

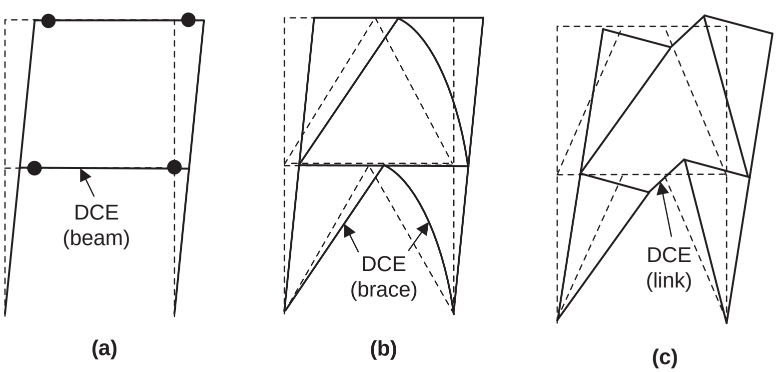

Figure 7.8 Deformation-controlled elements: (a) special moment frame; (b) special concentrically braced frame; (c) eccentrically braced frame.

Refer to Figure 7.7 again for the general response of a redundant, multistory frame. By reducing the elastic seismic force, by the R factor, DCEs are designed for a code-specified seismic force at the C_S base shear level. In ASCE 7, the basic load combinations for the design of DCEs are:

$$(1.2+0.2S_{DS})D+\rho Q_E+L+0.2S \tag{7.22a}$$

$$(0.9-0.2S_{DS})D+\rho Q_E+1.6H \tag{7.22b}$$

The value of the redundancy factor, ρ, is equal to 1.0 if certain requirements are satisfied; otherwise, the value is 1.3. The intent of the code is to encourage the use of more redundant structures.

The multiple DCEs within a structure usually will not yield at the same time. Once the most critical DCE is yielded, the ductility of this element allows more lateral load to be applied to the structure such that other DCEs will yield progressively until a full yield mechanism is formed (as shown in Chapters 2 to 6 in various examples). Therefore, the FCEs will experience and need to be designed for the higher force reached at that point. In the United States, the concept of using an amplified seismic force to design FCE was first implemented in the 1988 Uniform Building Code.

Although the concept is clear, difficulties arise when implementing it in design. Figure 7.7 shows that a structure responds elastically up to point S, beyond which nonlinear analysis is required to quantify the ultimate strength of the structure. Because in a typical design it is not practical to perform nonlinear analysis including plastic analysis, building codes provide alternate methods to overcome this obstacle. These methods can be classified as the global-level and local-level approaches.

7.7.1 Global-Level Approach

In this greatly simplified approach, ASCE 7 provides a system overstrength factor, Ω_o, to amplify the prescribed seismic design forces for the ultimate strength at point M in Figure 7.7:

$$C_yW=\Omega_o(C_sW) \tag{7.23}$$

See Table 7.1 for the values of Ω_o for a few popular structural systems. Note that these empirical values were developed mainly using engineering judgment. Although the actual system overstrength varies from one structure to the other, the code intends to provide a conservative, upper bound value for Ω_o. Because capacity design is needed for FCE, the load combinations specified in ASCE 7 are:

$$(1.2+0.2S_{DS})D+\Omega_oQ_E+L+0.2S \tag{7.24a}$$

$$(0.9-0.2S_{DS})D+\Omega_oQ_E+1.6H \tag{7.24b}$$

In AISC Seismic Provisions (AISC 2010), $\Omega_o Q_E$ is called the "amplified seismic loads." Taking the frame in Figure 7.8a for example, the axial load and the moment in the FCE column can be determined from an elastic analysis as shown in Figure 7.9a.

In summary, the basic seismic load combinations [Eq. (7.22)] are used to design the DCEs, whereas the basic seismic load combinations with overstrength factor [Eq. (7.24)] are used for the design of FCEs.

7.7.2 Local-Level Approach

The global approach is approximate in nature as it uses an empirical factor to amplify the prescribed seismic design forces. For many FCEs it is possible to calculate the maximum forces developed in the DCEs and are transferred to the neighboring FCEs in a rational way. This approach provides the upper bound value to the global-level approach. To demonstrate this concept, refer to the same simple moment frame shown in Figure 7.9b. The beam serves as the DCE. Plastic hinges are expected to form near the beam ends. The seismic moment diagram when the yield mechanism is reached is also shown. It is assumed that each plastic hinge is located at a distance *c* away from the column centerline. From Eq. (3.10), the nominal plastic moment of the beam is:

$$M_{pn} = ZF_y \tag{7.25}$$

Note that F_y is the specified minimum yield stress. Although this yield stress is used to size the member, in reality the actual yield stress is higher. The actual or the expected yield stress is:

$$F_{ye} = R_y F_y \tag{7.26}$$

where R_y is the yield stress adjustment factor. Based on a statistical evaluation of the steel material strength, AISC 341 provides values of R_y for different grades of steel (see Table 7.2[1] for some sample values). The actual beam plastic moment is then equal to the following:

$$M_{pe} = ZF_{ye} = R_y ZF_y = R_y M_{pn} \tag{7.27}$$

---

[1]R_t in Table 7.2 is used to adjust the tensile strength of the steel:

$$F_{ue} = R_t F_u$$

where F_u and F_{ue} are the specified minimum and expected tensile strengths, respectively.

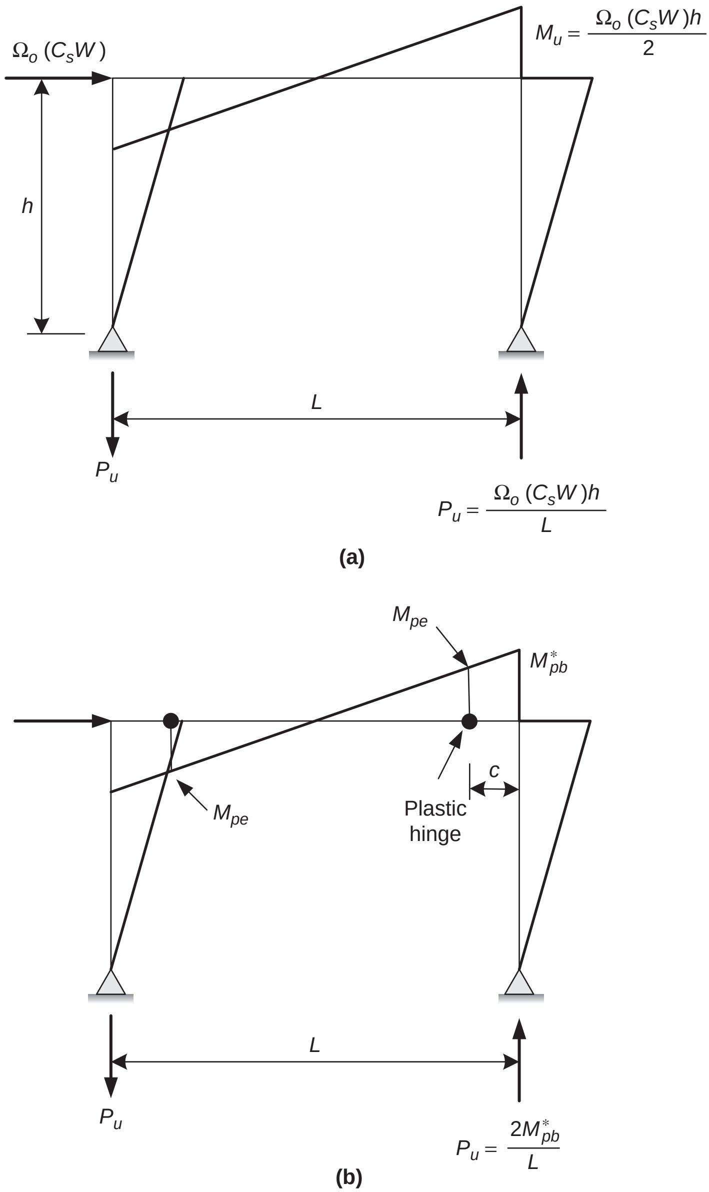

Figure 7.9 Force determination of FCE (column): (a) global-level approach; (b) local-level approach.

Application	R_y	R_t
Hot-rolled structural shapes		
• ASTM A36	1.5	1.2
• ASTM A572 Gr. 50, A992	1.1	1.1
Hollow structural sections (HSS)		
• ASTM A500 Gr. B or C	1.4	1.3
Pipes		
• ASTM A53	1.6	1.2
Plates		
• ASTM A36	1.3	1.2
• ASTM A572 Gr. 50	1.1	1.2

Table 7.2 ASCE 341 Sample R_y and R_t Values

Steel not only yields but also strain hardens under cyclic loading, making the beam moment at the plastic hinge even larger. So the probable maximum moment at the plastic hinge is:

$$M_{pr} = C_{pr} M_{pe} = C_{pr} R_y M_{pn} \tag{7.28}$$

where C_{pr} is the factor to account for the cyclic strain-hardening effect. This factor is assumed to be 1.1 in AISC 341. But a slightly higher value is used in AISC 358:

$$C_{pr} = \frac{F_y + F_u}{2F_y} \leq 1.2 \tag{7.29}$$

It appears at first glance that a higher flexural strength developed in the beam plastic hinge is beneficial, but this is not true from the viewpoint of capacity design for the column and beam-to-column moment connections. Because the moment diagram of the beam produced by the lateral load varies linearly along the beam span, the moment at the plastic hinges extrapolated to the column is M^*_{pb}. The axial force in the column is then equal to $2M^*_{pb}/L$.

Another example to demonstrate the local-level approach is shown in Figure 9.29 for the design of beam in a Special concentrically Braced Frame (SCBF). It will be shown in Chapter 9 that an SCBF is designed to dissipate energy through brace buckling and yield. Therefore, braces are the DCEs, whereas beam and columns are the FCEs. The beam is subjected to axial force and bending moment when braces buckle and yield. When the yield mechanism is developed, the compressive brace will buckle, and its strength will drop significantly (to be discussed in Chapter 9). To design the beam, which is a FCE, AISC 341 assumes the expected postbuckling brace strength, C, to be 30% of the expected brace compressive strength. The other brace is assumed to be yielded with an expected tensile strength, T, of $R_y F_y A_g$. Because the expected tensile strength is generally much higher than the postbuckling strength of the brace, the vertical component of these two forces will not balance, and will produce a net pull-down force at the midspan of the beam. A large moment produced by this unbalanced form, which cannot be obtained from an elastic analysis, then needs to be considered for beam design. See Chapter 9 for a more detailed discussion.

7.8 Performance-Based Seismic Design Framework

7.8.1 Seismic Performance Objective

In addition to the above summary of the US seismic design provisions based on ASCE 7, it is worthwhile to briefly summarize the performance objectives states in various similar design requirements.

The basic seismic design philosophy that appeared in the *Recommended Lateral Force Requirements and Commentary* [also known as the Blue Book and first published by the Structural Engineers Association of California (SEAOC) in 1959], stated that the intent of the recommended design provisions was to produce a structure that should be able to resist:

- A minor level of earthquake ground motion without damage
- A moderate level of ground motion without structural damage but possibly experience some nonstructural damage
- A major level of ground motion having an intensity equal to the strongest, either experienced or forecast for the building site, without collapse, but possibly with some structural as well as nonstructural damage

Although the SEOAC's seismic design philosophy intended to control building performance for both structural and nonstructural components at different levels of earthquake intensities, both the expected building performance and the ground shaking intensity were described in a qualitative manner. It wasn't until 1995 that SEAOC published Vision 2000 (SEAOC 1995) to outline a performance-based framework to address a broad range of building performance and seismic hazard levels.

In the 1990s, efforts to develop seismic design provisions for rehabilitating existing building structures eventually led to the first performance-based design code: ASCE 41–Seismic Rehabilitation of Existing Building (ASCE 2006). ASCE 41 states the rehabilitation objective in a more quantitative manner. For design of new structures,

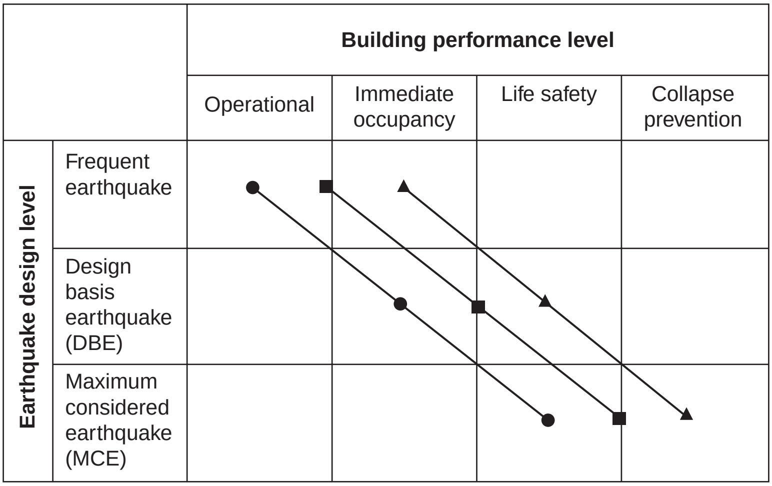

▲ : Basic safety objective for ordinary structures; ■: Enhanced objective for high occupancy buildings; ●: Safety critical objective for essential buildings

Figure 7.10 ASCE 7 Building seismic performance objectives.

the seismic design objective of ASCE 7 is also stated in a similar manner, expressed in a matrix format in Figure 7.10 (BSSC 2009). The three hazard levels of design ground motions are expressed in a probability format.

Four building performance levels (Operational, Immediate Occupancy, Life Safety, and Collapse Prevention) are used. For example, at the Collapse Prevention level, the seismic force-resisting system is deemed to have lost most of its original stiffness and strength, and little margin against collapse remains. Similarly, at the Life Safety level, significant structural and nonstructural damage are expected, but the damage is not life threatening and a significant margin against collapse still remains. This framework is used to evaluate the seismic design approach adopted in the United States, Canada, and Japan as follows.

7.8.2 USA: ASCE 7

The seismic design provisions in ASCE 7 intend to achieve the Basic Performance Objective for ordinary buildings (Occupancy Category II). As is shown in Section 7.4, only the DBE, which is defined as two thirds of the MCE, is used for design, and the target performance level is Life Safety. Although ASCE 7 explicitly requires design for only one level of ground motions, it is implicitly assumed that structures thus designed will also achieve the other two goals shown in Figure 7.10: collapse prevention at MCE and immediate occupancy at frequent earthquake with a recurrence interval of 72 years.

7.8.3 Canada: NBCC

7.8.3.1 1995 NBCC

National Building Code of Canada (NBCC) also adopts a one-level seismic design procedure. In its 1995 edition, the 475-year DBE elastic design spectrum is expressed as:

$$C_e = \nu SIF \tag{7.30}$$

where ν is the specified horizontal ground velocity, S is a period-dependent seismic response factor, I is a seismic importance factor, and F is a foundation factor. The elastic seismic force is then reduced by two factors to compute the prescribed design base shear ratio:

$$C_s = U\left(\frac{C_e}{R}\right) \tag{7.31}$$

where R is the force modification factor to account for the ductility capacity of the structure, and U (= 0.6) is a calibration factor "representing level of protection based on experience…" (NBC 1995). Although both NBCC and ASCE 7 use the same symbol R for seismic force reduction, their physical meaning is very different. The R values used in NBCC range from 1.0 for nonductile structural systems to 4.0 for the most ductile systems (see Table 7.3 for some typical values), which are significantly smaller than those ($1.0 \le R \le 8.0$) used in ASCE 7 (see Table 7.1).

Equation 7.31 can be rewritten as follows:

$$C_s = U\left(\frac{C_e}{R}\right) = \frac{C_e}{R(1/U)} \tag{7.32}$$

Steel Seismic Force-Resisting System	2005 Edition		1995 Edition	
	R_d	R_o	R	$1/U$
Moment-resisting frames				
• Ductile	5.0	1.5	4.0	1.67
• Moderately ductile	3.5	1.5		↓
• Limited ductility	2.0	1.3		↓
Concentrically braced frames				↓
• Moderately ductile	3.0	1.5	3.0	↓
• Limited ductility	2.0	1.3		↓
Eccentrically braced frames	4.0	1.5	3.5	↓
Ductile steel plate shear walls	5.0	1.6	4.0	↓

Table 7.3 NBCC Sample Seismic Force Reduction Values

Comparing the previous equation to Eq. (7.18), it is observed that:

$$R_u = R \tag{7.33}$$

$$\Omega_o = \frac{1}{U} \tag{7.34}$$

That is, the R factor in NBCC is the system ductility reduction factor, and a constant system overstrength factor, $1/U$ (= 1.67), is assumed for all the lateral force-resisting systems. Note that the R factor in ASCE 7 includes the contribution from both system ductility reduction and system overstrength; the ductility reduction component of the R factor is not given.

The story drift produced by the prescribed seismic design force is then amplified by R, which corresponds to the C_d factor in ASCE 7. The drift limits are $0.01h$ for post-disaster building and $0.02h$ for all other buildings, where h is the story height.

7.8.3.2 2005 NBCC

Major revisions are made in the 2005 edition of NBCC. The design earthquake used to compute the design seismic forces is similar but not the same as that used in ASCE 7. The procedure to reduce elastic seismic force is maintained but with some adjustments.

NBCC first specifies an elastic base shear ratio based on MCE:

$$C_e = S(T)M_v I_E \tag{7.35}$$

where $S(T)$ is the 5% damped spectral acceleration, expressed as a ratio of gravitational acceleration at period T. M_v, with a value ranging from 0.4 to 2.5, is a factor to account for the higher mode effect, and I_E (1.0, 1.3, or 1.5) is the importance factor. This elastic base shear ratio is then reduced by two factors to compute the prescribed seismic design base shear ratio:

$$C_s = \frac{C_e}{R_d R_o} \tag{7.36}$$

where R_d and R_o are ductility-related and overstrength-related force modification factors. A comparison of the denominator of the above equation with that in Eq. (7.32) shows that R_d is equivalent to R and R_o is equivalent to $(1/U)$ in the 1995 NBCC. The values of R_d range from 1.0 to 5.0; Table 7.3 shows the R_d values for some steel systems. These values are similar to and some are slightly higher than the R values in the 1995 NBCC. Other than using as a constant system overstrength factor (= 1.67), the 2005 NBCC uses R_o,which varies from 1.0 to 1.7. See Mitchell et al. (2003) for the background information on calibrating the R_o values.

The procedure to compute the story drift is also changed. In the 1995 NBCC, only the ductility-related force modification factor, R, is used to amplify the story drift produced by the prescribed seismic design force, and the drift limit is set to $0.02h$ for ordinary buildings. The 2005 NBCC requires the use of the total force modification factor, R_dR_o, to amplify story drift. Although the limit is relaxed to $0.025h$ based on the recommendation of SEAOC Vision 2000 (Devall 2003), the resulting structure is likely to be much stiffer than that designed based on the 1995 NBCC (and ASCE 7) for two reasons. First, the seismic design force is based on MCE, not DBE, yet the values of the total force modification factor are similar to those ($= R/U$) used in the 1995 NBCC (or R in ASCE 7). Therefore, the prescribed seismic design base shear ratio and the corresponding story drift is about 50% higher. Second, this higher story drift is amplified by the total force modification factor, not the ductility-related component of the total force modification factor as was done in the 1995 NBCC. Because the slightly relaxed story drift limit in the 2005 NBCC is not likely to compensate for this much larger design story drift, the 2005 NBCC could, in some instances, result in more conservative designs.

7.8.4 Japan: BSL

Based on the discussions presented so far, both the US and Canadian seismic design provisions attempt to achieve similar seismic performance objectives. For ordinary structures (Occupancy Category II in ASCE 7), the Basic Performance Objective is the target for design. As is shown in Figure 7.10, in concept three levels of design earthquake intensities (i.e., seismic hazards) need to be considered. For ease of design in actual implementation, however, both the US and Canadian codes adopt the same approach by explicitly considering only one seismic hazard level and the associated building performance level, while implicitly assuming that the other two building performance levels at the associated hazard levels will be met automatically. Although both ASCE 7 and NBCC use this "one-level" seismic design procedure, they differ because the ASCE 7 design procedure is anchored at the DBE for Life Safety, whereas the 2005 NBCC is anchored at the MCE for Collapse Prevention.

Unlike the North American seismic codes, the Building Standard Law (BSL) of Japan adopted a "two-level" seismic design procedure since 1981 (IAEE 2004). Although the BSL provides exceptions, allowing the designer to consider only a one-level design when certain height limitation and regularity requirements are met, the central concept in the BSL is to anchor the seismic design on two points along a performance objective line similar to that shown in Figure 7.10, and explicitly consider two seismic hazard levels in design.

As such, the BSL constitutes a two-level design procedure. Designers must consider service limit state requirements for the moderate earthquake associated with the Level 1 design and ultimate limit state requirements for the severe earthquake associated with the Level 2 design.

7.8.4.1 Level 1 Design

In Japan, moderate earthquake shaking corresponds to a peak ground acceleration of between 0.07 g and 0.10 g (Kato 1986), and with a recurrence interval between 30 and 50 years (Kuramoto 2006). The BSL service limit state requires that a regular building remains in the elastic range when subjected to lateral seismic forces associated with a base shear ratio, C_w:

$$C_w = 0.2ZR_t \tag{7.37}$$

where ZR_t ($\equiv C_e$) represents the linear elastic design response spectrum for *severe* earthquake shaking. The intensity of the moderate earthquake is one-fifth that of the severe earthquake. To control nonstructural damage, the maximum story drift is limited to 0.5% of the story height, which is very similar to that used in the Uniform Building Code before 1997 (Uang and Bertero 1991). To avoid structural damage, the maximum allowable stress for steel design is limited to approximately 90% of the yield stress. One establishes this stress level by increasing the basic allowable stress for gravity-load design, which is about 60% of the yield stress, by 50%. Because the structure is expected to respond in the elastic range, ductility is not considered for the service limit state check.

7.8.4.2 Level 2 Design

A severe earthquake is assumed to have a peak ground acceleration ranging from 0.34 g to 0.4 g (Kato 1986), and the recurrence interval is similar to that of the DBE in ASCE 7. Using the terminology in Figure 7.7, the base shear ratio, C_y, is computed as:

$$C_y = D_s ZR_t \tag{7.38}$$

where D_s is a structural characteristics factor that accounts for the energy dissipation capacity (ductility) of the structure (Kato and Akiyama 1982). For steel building structures, the value of D_s ranges from 0.25 for a ductile system to 0.50 for a nonductile system (see Table 7.4). Note that the BSL requires the designer to check the ultimate strength of the structure, not the first significant yield as is done in the North America, which means the designer has to perform nonlinear analysis in order to ensure that the structure has a sufficient ultimate strength. Based on Eq. (7.16), the BSL effectively provides the following system ductility reduction factor:

$$R_\mu = \frac{1}{D_s} \tag{7.39}$$

Types of Moment-Resisting Portion of Braced Frames*	Types of Braces	
	Moment Frames or Braced Frames with $\beta_u^{\dagger} \le 0.3$	Braced Frames with $\beta_u^{\ddagger} > 0.7$
FA	0.25	0.35
FB	0.30	0.35
FC	0.35	0.40
FD	0.40	0.50

*Classification of moment-resisting frames is based on the compactness ratio of beams and columns. See IAEE (2004) for details.

†β_u = ratio of ultimate shear carried by braces to total ultimate shear.

‡For braces with effective slenderness ratio between $50/\sqrt{F_y}$ and $90/\sqrt{F_y}$ only, where yield stress F_y has a unit value of t/cm^2. See IAEE (2004) for other ranges of effective slenderness ratio.

Table 7.4 Typical BSL D_s Values For Steel Structures

Therefore, it is appropriate to compare $1/D_s$ with either the R factor in the 1995 NBCC or the R_d factor in the 2005 NBCC, but not the R factor in ASCE 7. See Uang (1991b) for a comparison of the seismic force reduction factors used in the US and Japanese codes.

In summary, the C_w force level is used for the service limit state design, and the C_y force level is used to check the ultimate limit state design. For buildings that satisfy certain height limitations and regularity requirements, a simplified, yet conservative, one-level design procedure can be used. Also see Uang (1993) for a comparison of one-level and two-level seismic design procedures.

7.8.5 Seismic Design of Tall Buildings

The performance-based methodology also finds its way into the seismic design of tall buildings in high seismic regions in the United States. Building code provisions (e.g., ASCE 7) are intended for a wide range of building types. As a result of this broad intended applicability, code provisions produce tall building design that may not be optimal, both from cost and safety perspectives. One limitation of the current prescriptive building codes is the building height. For buildings in the high seismic design categories, ASCE 7 sets a height limit to many popular lateral force-resisting systems. For example, steel braced frames and reinforced concrete shear walls are limited for buildings up to either 160 ft (49 m) or 100 ft (30 m), depending on the SDC. However, building codes always allow the use of alternative analysis and design methods that can be justified by well-established principles of mechanics and supported by tests. Therefore, several efforts have been made in the United States to develop performance-based design procedures such that the intended performance objectives in the model codes are met.

The Los Angeles Tall Buildings Structural Design Council (LATBSDC) published in 2005 a document entitled, *An Alternative Procedure for Seismic Analysis and Design of Tall Buildings Located in the Los Angeles Region*. This document led to the development of a similar document *AB-083–Recommended Administrative Bulletin on the Seismic Design and Review of Tall Buildings Using Non-prescriptive Procedures* for the City of San Francisco Department of Building Inspection (SFDBI) in 2007 (SEAONC 2007). In this document, tall buildings are defined as those with an overall height exceeding 160 ft (49 m). Unlike the model building codes, this performance-based design procedure requires two levels of earthquakes to be considered. The conventional code-level, 475-year DBE, is used to define the minimum lateral strength and stiffness requirements for Life Safety. In addition, the 2475-year MCE is evaluated to check for collapse prevention building performance. This latter evaluation requires nonlinear dynamic analysis by using a minimum of seven sets of properly scaled earthquake ground motion records. As part of the acceptance criteria, the average story drift should not be larger than 3% of the story height. For those deformation-controlled members that are designed to yield, the deformation demand cannot exceed the deformation capacity obtained from either test results or applicable documents. For force-controlled members and elements that are not designed to yield and are protected by capacity design principles, the design strength can be based on the expected, not nominal, material strength. However, this document does not require checking nonstructural elements at the MCE level.

The serviceability evaluation for a lower seismic hazard level is generally not required. It is required only when there is a reason to believe that the serviceability performance of the design would be worse than that anticipated for a code-prescriptive design. When needed, the serviceability ground motion shall be that having a recurrence interval of 43 years (i.e., a 50% probability of exceedance in 30 years).

The LATBSDC issued an updated edition on the Alternative Procedure in 2008. Like its 2005 edition, this document intends to meet the Basic Performance Objective. Several significant changes were made over the 2005 edition. First of all, this document explicitly adopts the capacity design approach, followed by performance-based evaluations. Unlike the 2005 edition, the prescriptive code-level Life Safety evaluation is eliminated. Instead, both the serviceability evaluation for a Frequent Earthquake (a 43-year recurrence interval) and Collapse Prevention evaluation for a 2475-year MCE are needed. For serviceability evaluation, the building response is not intended to be limited to be fully elastic. Instead, limited yielding is allowed in deformation-controlled members. But the story drift cannot exceed 0.5% of the story height, which is similar to the drift requirement of the Japanese BSL Level 1 design. For Collapse Prevention evaluation through the nonlinear dynamic analysis, this document refers to ASCE 41 for the deformation capacities.

The latest guidelines for performance-based seismic design of tall buildings are publisher by the Pacific Earthquake Engineering Research Center. See PEER, 2010 for details.

7.8.6 Next-Generation Performance-Based Seismic Design

All the performance-based design procedures presented above introduced the concept of performance in terms of discretely defined performance levels with names intended to connote the expected level of damage: Collapse Prevention, Life Safety, Immediate Occupancy, and Operational Performance. They also introduced the concept of performance related to damage of both structural and nonstructural components. Performance Objectives were developed by linking one of these performance levels to a specific level of earthquake hazard. These procedures also introduced a set of analytical procedures of varying levels of complexity that could be used to simulate the seismic response of buildings. Also, all these procedures require a MCE response evaluation in order to demonstrate adequate safety against collapse in an implicit manner. This response evaluation does not provide a quantifiable margin against (or a probability of) collapse, but is intended to demonstrate that collapse under the selected ground motions does not occur, that is, the structure maintains stability, and forces and deformations are within acceptable limits.

In order to fulfill the promise of performance-based engineering and help ensure that performance-based seismic design delivers on its full potential for reducing future losses from earthquakes, next-generation performance-based design procedures are being developed under an ATC-58 project funded by FEMA (ATC 2009). This long-range effort includes the following tasks:

- Revise the discrete performance levels defined in first-generation procedures to create new performance measures (e.g., repair costs, casualties, and time of occupancy interruption) that better relate to the decision-making needs of stakeholders, and that communicate these losses in a way that is more meaningful to stakeholders (Krawinkler and Miranda 2004).
- Create procedures for estimating probable repair costs, casualties, and time of occupancy interruption, for both new and existing buildings.
- Expand current nonstructural procedures to explicitly assess the damageability and post-earthquake functionality of nonstructural components and systems, which can constitute a significant percentage of the economic loss associated with damaging earthquakes.
- Develop a framework for performance assessment that properly accounts for, and adequately communicates to

stakeholders, limitations in our ability to accurately predict response, and uncertainty in the level of earthquake hazard.

In a significant way, this also ties with broader efforts to quantify seismic resilience (Bruneau et al. 2003; Bruneau and Reinhorn 2007; MCEER 2008; Cimellaro et al. 2010a, 2010b).

7.9 Historical Perspective of Seismic Codes

Although the design practice is likely to move toward the performance-based seismic design in the next decade, it is proper and instructive, in closing this chapter to provide a historical basis for the seismic force reduction factor, R. The numerical values assigned to those factors by codes for various types of structural systems were not obtained by rigorous analysis and experimentation, but rather by consensus of expert engineers.

The first North American design requirements intended to prevent building collapse during earthquakes originated in California. Interestingly, after a major earthquake struck San Francisco in 1906, reconstruction of the devastated city proceeded with an updated building code that required the consideration of a wind force of 30 pounds per square ft (1.44 kPa) for the design of new buildings (Bronson 1986). No specific earthquake-resistant design clauses were introduced. Given that many building codes of that time did not even have requirements for wind resistance (such as the Los Angeles building code in which wind pressure was not considered in design until 1924), it was hoped that the new "stringent" wind pressure requirement would simultaneously address both wind and earthquake effects.

The 1927 Uniform Building Code (UBC) introduced the first seismic design requirements in North America, partly in response to the Santa Barbara earthquake of 1925. This model code proposed clauses for consideration for possible inclusion in the building codes of various cities, at their discretion, and was not binding. The 1927 UBC proposed that a single horizontal point load, F, equal to 7.5 or 10% (depending on the soil condition) of the sum of the building's total dead and live load, W, be considered to account for the effect of earthquakes.

Hard soil/rock

$$F = CW = 0.075W \tag{7.40a}$$

Soft soil

$$F = CW = 0.10W \tag{7.40b}$$

where C is a seismic coefficient. No justification can be found for these values of C, but they likely reflected the consensus of the engineering community. Interestingly, Prof. Toshikata Sano in Japan who visited San Francisco after the 1906 earthquake got the idea of using seismic inertia force as the design earthquake action (Towhata 2008). Sano stated that the seismic force is given by the ground acceleration multiplied by the mass of a structure and then recommended the acceleration to be 10 to 30% of that of gravity. This proposal of using a seismic coefficient of 0.1 was adopted in Japanese building design regulations in 1924. Dr. Kyoji Suyehiro of Japan visited California and reported in a series of lectures that buildings designed using a value of C equal to 0.10 in Japan survived the tragic Kanto (Tokyo) earthquake of Richter Magnitude 8.2 in which 140,000 died (Suyehiro 1932).

Enforceable earthquake-resistant design code provisions in North America were implemented following the 1933 Long Beach earthquake of Richter Magnitude 6.3. This earthquake produced damage in Long Beach and surrounding communities in excess of $42 million in 1933 dollars (more than $400 million in 1995 dollars), and the death toll exceeded 120 (Alesch and Petak 1986, Iacopi 1981). It was significant that a large number of the buildings that suffered damage were schools and that the total number of casualties and injuries would have undoubtedly been considerably larger had this earthquake not occurred at 5:54 P.M., when the schools were fortunately empty. Nonetheless, this economic and physical loss provided the necessary political incentive to implement the first mandatory earthquake-resistant design regulations. The California State Legislature passed the Riley Act and the Field Act, the former requiring that all buildings in California be designed to resist a lateral force equal to 2% of their total vertical weight, the latter mandating that all public schools be designed to resist a similar force equal to between 2 and 10% of the dead load plus a fraction of the live load; the magnitude of the design lateral force depended on the building type and the soil condition. At the same time, a Los Angeles building ordinance was issued, calling for 8% of the sum of the dead load plus half of the live load to be used as a design lateral force.

Once researchers brought forth the difference between the dynamic and static response of structures, showing that the seismically induced forces in a flexible (high-rise) building are typically smaller than those in stiff (low-rise) ones, simplified empirical equations to attempt to capture this observed dynamic behavior, and suitable for hand calculations, were developed. The 1943 Los Angeles Building Code was the first to introduce a seismic coefficient and a lateral force distribution that indirectly reflected building flexibility. The lateral forces were calculated as $V = CW$, where V and W were the story shear and total weight of the building above the story under consideration, respectively. The seismic coefficient was calculated as:

$$C = \frac{0.60}{N + 4.5} \tag{7.41}$$

where N is the number of stories above the story under consideration. This formula was slightly modified (SEAOC 1980) when the building height restriction of 13 stories, in effect in Los Angeles in 1943, was removed in 1959.

The 1950s saw the introduction into the lateral force equation of a numerical coefficient, K, intended to reflect the relative seismic performance of various types of structural systems and a more refined consideration of building flexibility through calculation of the fundamental period of vibration, T, of the building in the direction under consideration (Anderson et al. 1952, Green 1981). The generic expression for the base shear became:

$$V = KCW \tag{7.42}$$

where

$$C = \frac{0.05}{T^{1/3}} \tag{7.43a}$$

and

$$T = \frac{0.05H}{\sqrt{D}} \tag{7.43b}$$

where V is the base shear, W is the total dead load, and H and D are, respectively the height of the building and its dimension (in ft) in the direction parallel to the applied forces. The distribution of the base shear along the building height was specified to be inverted-triangular. Types of construction that had been observed to perform better in past earthquakes were assigned low values of K, whereas those that had not performed as well were assigned high values of K. Buildings relying on ductile moment-resisting space frames to resist seismic forces were designed with $K = 0.67$. Buildings with dual structural systems were assigned a value of K equal to 0.8; K for bearing wall systems was set equal to 1.33, and buildings with types of framing systems other than those specified above were assigned a value of K equal to 1.00 (SEAOC 1959). Over time, the equation evolved slightly to include an importance factor, I (equal to 1.0 for normal buildings), a seismic zone factor, Z (equal to 1.0 in the more severe seismic zones), and a soil condition factor varying between 1.0 and 1.5, depending on site conditions. The magnitude of the specified base shear was also increased in 1974, following the San Fernando earthquake of 1971, because many felt that it was too low. This was accomplished by changing the seismic coefficient to the following:

$$C = \frac{1}{15\sqrt{T}} \tag{7.44}$$

Detailed descriptions of the significance of each of the above factors and the way to calculate them, as well as descriptions of the various changes that occurred in seismic codes in the 1960s, 1970s, and some of the 1980s, are available elsewhere (SEAOC 1980, Green 1981, ATC 1995b). However, it is of utmost importance to appreciate that numerical values for K that were introduced into the SEAOC Recommended Lateral Force Requirements in 1959 (and that eventually made their way into other codes worldwide) were based largely on judgment, reflecting the consensus of the SEAOC code committee membership (consisting of expert design professionals and academicians).

A fundamental change in the format of the base shear equation was proposed in 1978 with publication of the ATC-3-06 (ATC 1978) report "Tentative Provisions for the Development of Seismic Regulations for Buildings." That document, prepared by multidisciplinary task groups of experts, proposed new comprehensive seismic provisions that introduced many innovative concepts, among which were the elastic design spectrum and the seismic performance factors, R and C_d. The elastic design spectrum is expressed as follows:

$$C_e(T) = \frac{1.2C_v}{T^{2/3}} \leq 2.5C_a \tag{7.45}$$

where C_v and C_a are seismic coefficients based on the soil profile and the effective peak velocity or the effective peak acceleration, respectively. This elastic seismic force demand is then reduced by the R factor for strength design:

$$C_s(T) = \frac{C_e(T)}{R} = \frac{1.2C_v}{RT^{2/3}} \leq \frac{2.5C_a}{R} \tag{7.46}$$

The authors of the ATC-3-06 elected not to substantially change the required force levels but rather to concentrate on providing ductile detailing (ATC 1995a). This was a paradigm shift that essentially promoted ductile detailing as a top consideration for design.

Numerical values for R were determined largely by calibration to past practice (ATC 1995a). For example, for ductile steel moment-resisting space frames, equating the proposed ATC equation for base shear at the strength level V_{ATC}, to that in effect at the time, V_{SEAOC} (SEAOC 1974):

$$V_{SEAOC}\left(\frac{1.67}{1.33}\right) = \frac{V_{ATC}}{0.9} \tag{7.47}$$

where 1.67 was the typical margin of safety between allowable-stress and ultimate-strength design values, 1.33 accounted for the 33% increase in allowable stresses that was permitted by these codes for load combinations involving earthquakes or wind, and 0.9 was the capacity reduction factor for flexure in the context of ultimate strength design. Substituting the respective base shear equations in this expression:

$$(ZIKCSW)_{SEAOC} W\left(\frac{1.67}{1.33}\right) = \frac{V_{ATC}}{0.9} \tag{7.48}$$

Assuming a site in California, a fundamental period of 1.0 s, identical soil conditions for which $S_{SEAOC} = 1.5$ and $S_{ATC} = 1.2$, and using $Z = 1.0$, $A = 0.4$, $I = 1.0$, $T = 1.0$:

$$(1.0)(1.0)K\left(\frac{1}{15\sqrt{(1.0)}}\right)(1.5)W\left(\frac{1.67}{1.33}\right) = \frac{1.2(0.4)(1.2)}{0.9R(1.0)^{2/3}}W \tag{7.49}$$

and

$$R = \frac{5.1}{K} \tag{7.50}$$

For a ductile steel moment-resisting frame, K per SEAOC (1959) was 0.67 giving a value of R equal to approximately 8.0 (rounded up from the calculated value of 7.61). Values of R for other types of structural systems (see Table 7.1) were also calculated using Eq. (7.47) and adjusted to reflect the consensus of the ATC-3-06 committee members. The ATC-3-06 equations have also been implemented in the 1988 Uniform Building Code, with some minor modifications, including calibration to accommodate the working stress design (a.k.a. allowable stress design) format of the UBC at the time. The 1988 UBC specifies the DBE elastic design spectrum in the following form:

$$C_e(T) = \frac{1.25ZIS}{T^{2/3}} \leq 2.75ZI \tag{7.51}$$

where Z is a seismic zone factor, I is the importance factor, and S is a site soil coefficient. For working stress design, the elastic seismic force demand is reduced by a seismic force reduction factor R_w, not R, for design:

$$C_w(T) = \frac{C_e(T)}{R_w} = \frac{1.25ZIS}{R_w T^{2/3}} \leq \frac{2.75ZI}{R_w} \tag{7.52}$$

Through use of a procedure similar to that described above (ATC 1995a), the following relationship was used to obtain R_w factors for use in working stress design:

$$R_w = \frac{7.86}{K} = \frac{7.86R}{5.1} = 1.54R \approx \frac{8}{K} \tag{7.53}$$

Before it was replaced by the International Building Code in the United States, the 1997 UBC specified the design base shear ratio for strength design and replaced R_w by R as the seismic force reduction factor:

$$C_s(T) = \frac{C_v I}{RT} \leq \frac{2.5 C_a I}{R} \tag{7.54}$$

This expression was modeled after ATC-3-06. Instead of using C_d as a deflection amplification factor, UBC used $0.7R$ for the same purpose.

Since then, with the objective of providing a more rigorous and systematic framework on how the values of the seismic performance factor described in this chapter (i.e., R, C_d, and Ω_o) are established for various structural systems, particularly for new systems proposed for adoption in future editions of the seismic design provisions, a detailed procedure has been developed and is outlined in the FEMA P-695 report (FEMA 2009). This methodology provides a thorough framework to assess the appropriateness of such factors, complete with consideration of collapse probabilities and other uncertainties inherent to seismic analysis and design. The proposed methodology is being considered by various code-writing bodies for possible use, as a desirable approach to determine the substantiating data required for adoption of any new structural system into codes and specifications. A complete description of this complex procedure is however beyond the scope of this book.

References

AISC. 2010. *Prequalified Connections for Special and Intermediate Steel Moment Frames for Seismic Applications, ANSI/AISC 358*. Chicago: AISC.

AISC. 2010. *Seismic Provisions for Structural Steel Buildings, ANSI/AISC 341*. Chicago: AISC.

AISC. 2010. *Specification for Structural Steel Buildings, ANSI/AISC 360*, 2005 and 2010. Chicago: AISC.

Alesch, D. J., and Petak, W. J. 1986. *The Politics and Economics of Earthquake Hazard Mitigation.* Boulder: Institute of Behavioral Science, University of Colorado.

Anderson, A. W., Blume, J. A., Degenkolb, H. J., Knapik, E. M., Marchand, H. L., Powers, H. C., Rinne, J. E., Sedgwick, G. A., and Sjoberg, H. O. 1952. "Lateral Forces of Earthquake and Wind." *Transaction of ASCE*, vol. 117.

ASCE. 2006. *Seismic Rehabilitation of Existing Buildings, ASCE/SEI 41*: Reston, VA: ASCE.

ASCE. 2010. *Minimum Design Loads for Buildings and Other Structures, ASCE/SEI 7*, 2005 and 2010. Reston, VA: ASCE.

ATC. 1978. *Tentative Provisions for the Development of Seismic Regulations for Buildings*. Redwood City, CA: Applied Technology Council.

ATC. 1995a. *Structural Response Modification Factors, Report No. ATC-19*. Redwood City, CA: Applied Technology Council.

ATC. 1995b. *A Critical Review of Current Approaches to Earthquake Resistant Design, Report No. ATC-34*. Redwood City, CA: Applied Technology Council.

ATC. 2009. *Guidelines for Seismic Performance Assessment of Buildings, Report No. ATC-58*, (50% Draft). Redwood City, CA: Applied Technology Council.

Bronson, W. 1986. *The Earth Shook, the Sky Burned—A Moving Record of America's Great Earthquake and Fire*. San Francisco: Chronicle Book.

Bruneau, M., Chang, S., Eguchi, R., Lee, G., O'Rourke, T., Reinhorn, A., Shinozuka, M., Tierney, K., Wallace, W., and von Winterfelt, D. 2003. "A Framework to Quantitatively Assess and Enhance the Seismic Resilience of Communities." *EERI Spectra Journal*, vol. 19, no. 4, 733–752.

Bruneau, M., and Reinhorn, A. 2007. "Exploring the Concept of Seismic Resilience for Acute Care Facilities." *Earthquake Spectra*, vol. 23, no.1, 41–62, EERI.

BSSC. 2009. *NEHRP Recommended Seismic Provisions for New Buildings and Other Structures, FEMA P-750*. Washington, D. C. :Federal Emergency Management Agency.

Cimellaro, G., Reinhorn, A., and Bruneau, M. 2010a. "Framework for Analytical Quantification of Disaster Resilience." *Engineering Structures Journal*, vol. 32, no. 11, 3639–3649.

Cimellaro, G., Reinhorn, A., and Bruneau, M. 2010b. "Performance-Based Metamodel for Health Care Facilities." *Journal of Earthquake Engineering and Structural Dynamics*, DOI: 10.1002/eqe.1084.

Chopra, A. K. 2007. *Dynamics of Structures*. Upper Saddle River, NJ: Pearson Prentice Hall.

Devall, R. H. 2003. "Background Information for Some of the Proposed Earthquake Design Provisions for the 2005 Edition of the National Building Code of Canada." *Canadian Journal of Civil Engineering*, vol. 30, no. 2, 279–286.

FEMA. 2009. *Qualification of Building Seismic Performance Factors, FEMA P695*. Washington, D. C.: Federal Emergency Management Agency.

Green, N. B. 1981. *Earthquake Resistant Building Design and Construction*. New York: Van Nostrand Reinhold.

Iacopi, R. 1981. *Earthquake Country—How, Why, and Where Earthquakes Strike in California*. Menlo Park, CA: Sunset Books, Lane Publishing.

IAEE. 2004. *Earthquake Resistant Regulations, a World List–2004* . Tokyo: IAEE.

ICBO. 1997. *Uniform Building Code*. Whittier, CA: International Building Code Council.

ICC. 2009. *International Building Code*. Falls Church, VA: International Code Council.

Kato, B. 1986. "Seismic Design Criteria for Steel Building." *Proceedings of Pacific Structural Steel Conference*, vol. 1, 133–147, Auckland, NZ.

Kato, B., and Akiyama, H. 1982. "Seismic Design of Steel Buildings." *Journal of Structural Engineering, ASCE*, vol. 108, no. ST8, 1709–1721.

Krawinkler, H., and Miranda, E. 2004. "Performance-Based Earthquake Engineering." *Earthquake Engineering: from Engineering Seismology to Performance-Based Engineering*, Chapter 9, editors Bozorgnia and Bertero, V.V., CRC Press, Boca Raton, FL.

Kuramoto, H. 2006. "Seismic Design Codes for Buildings in Japan." *Journal of Disaster Research*, vol. 3, no. 3, 341–356. Fuji Technology Press.

LATBSDC. 2008. *An Alternative Procedure for Seismic Analysis and Design of Tall Buildings Located in the Los Angeles Region*. Los Angeles: Los Angeles Tall Buildings Structural Design Council.

Miranda, E., and Bertero, V. V. 1994. "Evaluation of Strength Reduction Factor for Earthquake-Resistant Design." *Earthquake Spectra*, vol. 10, 357–379.

Mitchell, D., Tremblay, R., Karacabeyli, E., Paultre, P., Saarcioglu, M., and Anderson, D. L. 2003. "Seismic Force Modification Factors for The Proposed 2005 Edition of the National Building Code of Canada." *Canadian Journal of Civil Engineering*, vol. 30, no. 2, 308–327.

MCEER. 2008. "Engineering Resilience Solutions: From Earthquake Engineering to Extreme Events: 1997–2007—A Decade of Earthquake Engineering and Disaster Resilience." *MCEER-08-SP09*. Multidisciplinary Center for Earthquake Engineering Research, University at Buffalo, State University of New York.

NBC. 2005. *National Building Code of Canada (NBCC)*, 1995 and 2005. Ontario: National Research Council.

Newmark, N. M., and Hall, W. J. 1982. *Earthquake Spectra and Design*. Berkeley, CA: EERI.

PEER. 2010. "Guidelines for Performance-Based Seismic Design of Tall Buildings." PEER Report No. 2010/05. Pacific Earthquake Engineering Research Center, University of California, Berkeley.

SEAOC. 1995. *Vision 2000–Performance Based Seismic Engineering of Buildings*. Sacramento, CA: Structural Engineers Association of California.

SEAOC. 1980. *Recommended Lateral Force Requirements and Commentary*. 1959, 1974, and 1980,Structural Engineers Association of California, Sacramento, CA.

SEAONC. 2007. *Recommended Administrative Bulletin on the Seismic Design and Review of Tall Buildings Using Non-prescriptive Procedures*. San Francisco: Structural Engineers Association of Northern California.

Suyehiro, K. 1932. "Engineering Seismology Notes on American Lectures." *Proceedings of ASCE*, vol. 58, no. 4. 9–110.

Towhata, I. 2008. "History of Geotechnical Earthquake Engineering in Japan." *Proceedings of 14th World Conference on Earthquake Engineering*, Oct. 12–17, Beijing, China, IAEE.

Uang, C. M. 1991a. "Establishing R (or R_w) and C_d Factors for Building Seismic Codes." *Journal of Structural Engineering, ASCE*, vol. 117, no. 1, 19–28.

Uang, C. M. 1991b. "Comparison of Seismic Force Reduction Factors Used in U.S.A. and Japan." *Earthquake Engineering and Structural Dynamics*, vol. 20, 389–397.

Uang, C. M. 1993. "An Evaluation of Two-Level Seismic Design Procedure." *Earthquake Spectra*, *EERI*, vol. 9, no. 1, 121–135.

Uang, C. M., and Bertero, V. V. 1991. "UBC Seismic Serviceability Regulations: Critical Review." *Journal of Structural Engineering, ASCE*, vol. 117, no. 7, 2055–2068.

This page intentionally left blank

CHAPTER 8

Design of Ductile Moment-Resisting Frames

8.1 Introduction

This chapter provides an overview of the behavior and design of ductile steel moment frames. Section 8.2 discusses some basic concepts of overall frame behavior. Sections 8.3 and 8.4 cover basic concepts of column and panel zone behavior and design, which both influence the behavior of steel moment frames. Section 8.5 discusses beam-to-column connections. Typical North American practice for beam-to-column moment connections prior to the 1994 Northridge earthquake is presented, along with observations of connection damage from this earthquake and a review of the reasons for this damage. Some of the moment-connection strategies developed after the Northridge earthquake are presented, together with detailed information on connections prequalified for use in special moment-resisting frames. The corresponding moment frame design procedures specified by AISC 358 (AISC 2010a) are addressed in Section 8.6. Issues related to the consideration of P-Δ effects follow in Section 8.7. Finally, Section 8.8 presents a design example for a special moment-resisting frame designed in compliance with the AISC requirements.

Throughout this chapter, the AISC Seismic Provisions (2010b), a.k.a. AISC 341, are used when necessary to illustrate how principles of ductile design have been implemented in codes. Numerous code documents have introduced and updated specific detailing requirements for earthquake-resistant steel structures since the first comprehensive provisions formulated in code language appeared in 1988 (SEAOC 1988). Although differences remain across international codes and standards (e.g., CSA 2009), the fundamental principles are similar to a broad extent. Emphasis on the AISC requirements here is solely intended to help focus the discussion. Finally, note that although steel frames damaged by the Northridge earthquake were generally designed per the Uniform Building Code—a forerunner to the International Building Code—the ductility detailing requirements of the 1992 Edition of AISC Seismic Provisions in effect at the time were similar to those of the Uniform Building Code.

8.1.1 Historical Developments

The history of steel moment frames is tied to the emergence of high-rise construction in Chicago and New York City in the late 1880s, the 12-story Home Insurance Building in Chicago being often credited as the first building that used a "skeleton construction" steel frame (Bennett 1995). In those early concepts, steel frames were designed to carry gravity loads, including those from the non–load-bearing unreinforced masonry walls. Although engineers often intuitively relied on the stiff cladding to resist lateral loads, beams were connected to columns in a manner that allowed for the development of some frame action. Requirements for wind and earthquake design only became mandated decades later. For example, in San Francisco's building code, wind forces were first specified following the 1906 San Francisco earthquake, whereas, paradoxically, earthquake design was not required until 1948 (EERI 1994, 1997).

Although seismic design didn't formally exist at the time, empirical evidence from that 1906 San Francisco earthquake convinced many engineers of the unparalleled effectiveness of steel moment frames to resist earthquakes, as photos taken after the earthquake but before the ensuing conflagration showed that many such tall buildings survived, either intact or without part of their facade (Bronson 1959, Freeman 1932). However, steel frame construction evolved and changed substantially over the subsequent decades, with striking differences between the framing connections used at the beginning and end of that century (Hamburger et al. 2009). As a result, these perceptions regarding the expected ductile performance of steel moment frames in earthquakes were significantly challenged by the 1994 Northridge (Los Angeles) earthquake in the United States, and by the 1995 Hyogo-ken Nanbu (Kobe) earthquake in Japan. In both earthquakes, steel moment frames did not perform as well as expected. Brittle failures were observed at beam-to-column connections in modern steel moment frame structures, challenging the assumption of high ductility and demonstrating that knowledge on the behavior of steel moment-resisting frames was incomplete.

To best understand the factors that contribute to either desirable or undesirable seismic performance of moment-resisting frames, and because many engineers are involved in retrofitting older buildings, parts of this chapter are structured as a chronology to differentiate the state of knowledge before and after the Northridge earthquake.

8.1.2 General Behavior and Plastic Mechanism

Moment-resisting frames (also called moment frames) are, in their simplest form, rectilinear assemblages of beams and columns, with the beams rigidly connected to the columns. Resistance to lateral forces is provided primarily by rigid frame action—that is, by the development of bending moments and shear forces in the frame members and joints. By virtue of the rigid beam-to-column connections, a moment frame cannot displace laterally without bending the beams and columns. The bending rigidity and strength of the frame members is therefore the primary source of lateral stiffness and strength for the entire frame. Sway frame action under loads is generally well understood, because it is a fundamental behavior studied as part of the undergraduate structural engineering curriculum (Leet et al. 2011).

Steel moment-resisting frames have been popular in many regions of high seismicity for several reasons. First, as described above, and based on evidence from experimental research (presented in the later sections), moment frames have been viewed as highly ductile systems. Building code formulae for design earthquake forces typically assign the largest force reduction factors (and therefore the lowest lateral design forces) to moment-resisting frames, reflecting the opinion of code writers that moment-resisting frames are among the most ductile of all structural systems. Second, moment frames are popular because of their architectural versatility. There are no bracing elements present to block wall openings, providing maximum flexibility for space utilization. A penalty for this architectural freedom results from the inherent lateral flexibility of moment-resisting frames. Compared with braced frames, moment frames subjected to lateral loads generally require larger member sizes than those required for strength alone to keep the lateral deflections within the code-mandated drift limits. The inherent flexibility of moment frames may also result in greater drift-induced nonstructural damage under earthquake loading than with other stiffer systems.

As described in Chapter 6, the most ductile system behavior is achieved when the desirable sway plastic mechanism can develop, with plastic hinging at the ends of all beams over the frame height. Plastic hinging of columns, which would lead to a plastic mechanism confined to a single story, is undesirable.

8.1.3 Design Philosophy

The design of moment-resisting frames is a direct extension of the plastic analysis and capacity design principles presented in Chapters 3 to 6, with a few major differences. First, to ensure achievement of the desirable yielding hierarchy, the simple plastic properties assumed in these earlier chapters must be modified to account for a number of practical considerations, such as expected yield strength, strain-hardening effects, panel zones, and others that are in part the subject of this chapter. Second, for reasons described later in this chapter, in some cases, the development of plastic hinges a small distance away from the face of columns is preferable to hinging immediately at the face of the column. All other aspects of the design of moment-resisting frames are predicated by these concepts and other details intended to allow development of the desired plastic mechanism.

8.2 Basic Response of Ductile Moment-Resisting Frames to Lateral Loads

8.2.1 Internal Forces During Seismic Response

A steel moment-resisting frame is composed of three basic components: beams, columns, and beam-column panel zones. These are illustrated in Figure 8.1 for a simple two-story, single-bay moment frame. Beams span the clear distance from face-of-column to face-of-column, L_b, and columns are divided into a clear span portion, h_{ci}, and a panel zone region of height, h_{pzi}. The panel zone is the portion of the column contained within the joint region at the intersection of a beam and a column. This definition is useful when one is considering sources of elastic and inelastic deformations, as well as possible plastic hinge locations.

In traditional structural analysis, moment frames are often modeled as line representations of horizontal and vertical members, with the lines intersecting at dimensionless nodes. Such models do not explicitly consider the panel zone region, and they provide an incomplete picture of moment frame behavior. Design of ductile moment frames requires explicit consideration of the panel zone region (inelastic behavior and design of the panel zone are addressed in Section 8.5).

Figure 8.1 also shows qualitatively the distribution of the bending moment, shear force, and axial force in a moment frame under lateral load. These internal forces are shown for the beam, clear span portion of the column, and the column panel zone and they do not include gravity load effects. The beams exhibit high bending moments, typically under reverse curvature bending, with maximum moments occurring at the member ends. The shear and axial force in the beam are generally much smaller and less significant to the response of the beam as compared with bending moment, although they must be considered in design. Similarly, the clear span portions of the columns are typically subjected to high moments, with relatively low shear forces. Axial forces in columns, both tension and compression, can be significant because of overturning moments on the frame. Finally, the column panel zone is subjected to high moments, high shear forces due to a severe moment gradient, and possibly high axial forces.

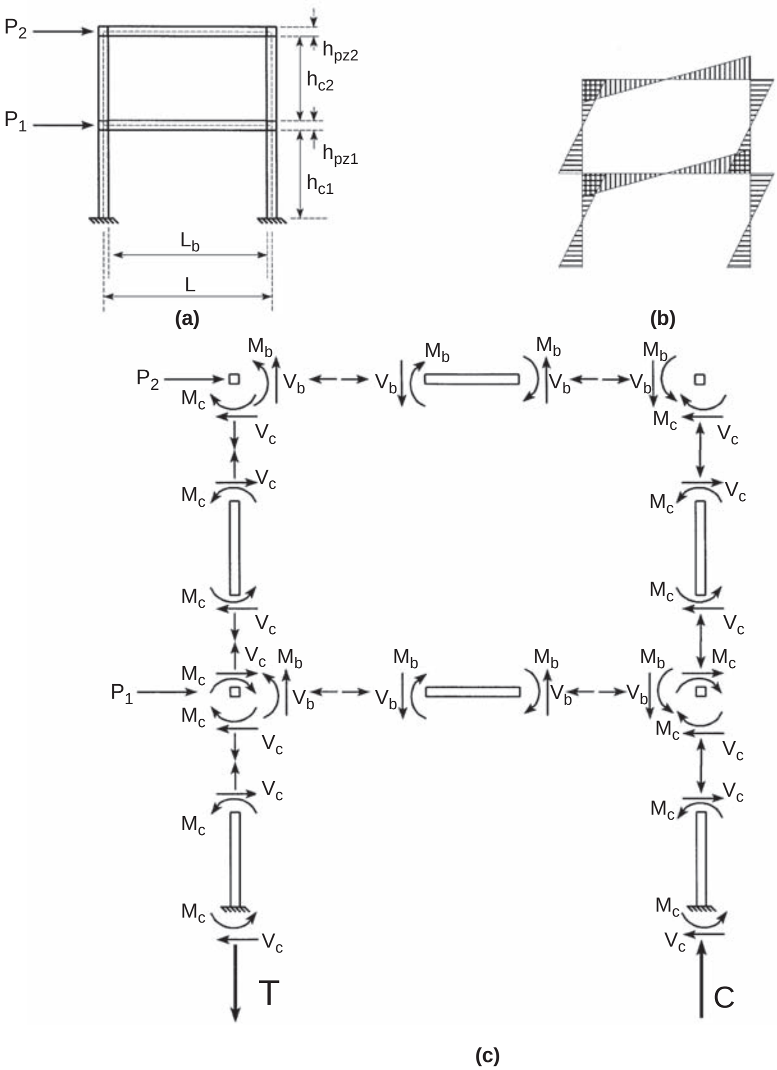

Figure 8.1 Ductile moment-resisting frame: (a) geometry considering finite dimensions of members, (b) typical moment diagram under lateral loading, and (c) corresponding member forces on beams, columns, and panel zones.

The qualitative distribution of internal forces illustrated in Figure 8.1 is fundamentally the same for both elastic and inelastic ranges of behavior. The specific values of the internal forces will change as elements of the frame yield and internal forces are redistributed. The basic patterns illustrated in Figure 8.1, however, remain the same. Inelastic step-by-step response-history analysis is needed to obtain exact values for the internal forces in moment frames, but this analytical complexity can be avoided if capacity design principles are integrated into the design process along with the conventional elastic analyses.

Plastic analysis of moment frames was described in Chapters 4 through 6. It was shown that, depending on the relative strength of beams and columns framing into a joint, different plastic collapse mechanisms can develop and that, as described in Chapter 6, the development of plastic hinges in the beams is the superior mechanism (see Figure 6.10). In actual frames, however, as opposed to frames studied using simple plastic analysis, strain-hardening makes possible yielding of more than one component at any given joint. In an example sequence of events, the panel zone may yield first, but still exhibit significant postyielding stiffness because of strain-hardening and other effects described in Section 8.4. As a result, greater forces can be applied at the joint, and other framing members, such as a beam, may reach their plastic capacities. Thus, the beam, column, and even panel zone could contribute to the total plastic deformation at the joint, depending on their relative yield strengths and yield thresholds. A structural component considerably weaker than the others framing into the joint will have to provide alone the needed plastic energy dissipation, whereas components of comparable strength would share this burden.

Once identified, those structural components expected to dissipate hysteretic energy during an earthquake must be detailed to allow development of large plastic rotations, without significant loss of strength. Only those components and connection details capable of providing cyclic plastic rotation capacities in excess of the demands should be used to ensure satisfactory seismic performance.

8.2.2 Plastic Rotation Demands

Estimates of the plastic rotation demands for a given moment frame are typically obtained by inelastic response-history analyses. Results from such analyses are sensitive to modeling assumptions and vary when different ground motion records are considered. The amount of the plastic energy dissipated by beams, panel zones, and columns will also be a function of the design philosophy adopted.

For those reasons, general expectations of plastic rotation demand for generic moment frames are based on the synthesis of observations from past analytical studies. Prior to the Northridge earthquake, the largest plastic rotations expected in beams alone (in the absence of panel zone plastic deformations) were expected to be 0.02 radian (Popov and Tsai 1989, Tsai and Popov 1988), although some studies reported values as high as 0.025 radian (Roeder et al. 1989). Smaller plastic rotation demands are obviously expected in flexible frames whose design is governed by compliance to code-specified drift limits.

An approximate way to estimate the plastic rotation demands in a frame is to examine its plastic collapse mechanism at the point of maximum drift. For example, if the beam sway mechanism shown in Figure 6.10 develops in a frame designed in compliance with the code-specified interstory drift limit, the maximum plastic hinge rotations in a beam can be estimated as Δ_e/h, where h is the story height and Δ_e is the inelastic interstory drift. Inelastic interstory drifts are approximately related to those one calculates using design-level forces, Δ_c, by simple relationships such as $\Delta_e = R\,\Delta_c$ (NRCC 2010) or $\Delta_e = C_d\,\Delta_c$ (ASCE 2010), where $R = R_d R_o$ is a seismic force reduction factor per the National Building Code of Canada and C_d is a deflection amplification factor serving the same purpose in U.S. practice (see Chapter 7 for more details). Typically, for code-specified drift limits, the use of these relationships produces plastic rotation demands of approximately 0.02 radian. This procedure is conservative because a large percentage of the total frame drift occurs elastically before plastic hinges form, provided that the method to calculate Δ_e and the seismic hazard characterization are accurate.

After the Northridge earthquake, the required connection plastic rotation capacity was increased to 0.03 radian for new construction and 0.025 radian for postearthquake modification of existing buildings (SAC 1995b). This target rotation was a consensus value developed following the earthquake based on analysis of code-compliant moment frames using ground motion histories recorded during the earthquake (e.g., Bertero et al. 1994). Although this rotation capacity may exceed real earthquake demands on most structural connections, it will likely remain as the target value until substantial research demonstrates that lower values are acceptable.

8.2.3 Lateral Bracing and Local Buckling

Selected structural members must be able to reach and maintain their plastic moment through large plastic rotations that permit hysteretic dissipation of earthquake-induced energy. The engineer must therefore delay local flange and web buckling, and lateral-torsional buckling, to prevent premature failures due to member instability.

For that reason, only seismically compact structural shapes should be used for structural members expected to develop plastic hinges. For example, AISC 341 (AISC 2010b) limits the flange width-to-thickness ratios, $b_f/2t_f$, of W shapes to $0.3\sqrt{E/F_y}$, for F_y in ksi (which roughly corresponds to the $145/\sqrt{F_y}$ limit in CSA 2009, for F_y in MPa). Moreover, lateral bracing to both flanges of these members should be provided at each plastic hinge location and spaced at no more than $0.086 r_y E\sqrt{F_y}$, with F_y in ksi and where r_y is the member's radius of gyration about its weak axis; ASCE 358 (AISC 2010) may also prescribe alternate limits for specific types of prequalified connections, as will be discussed later. This requirement recognizes that top and bottom flanges will alternatingly be in compression during an earthquake and accounts for some uncertainty in the location of plastic hinges under various load conditions. Local buckling of flanges and webs and lateral-torsional buckling will unavoidably develop at very large plastic rotations (at least in commonly used structural shapes), but compliance with the above requirements will slow the progressive loss in strength and help ensure good inelastic energy dissipation. This topic is further discussed in Chapter 14.

8.3 Ductile Moment-Frame Column Design

8.3.1 Axial Forces in Columns

Column buckling is not a ductile phenomenon and must be prevented. Columns should therefore be designed to remain stable under the maximum forces they can be subjected to during an earthquake. These forces will generally exceed those predicted by elastic analysis using code-specified earthquake loads, but may be difficult to estimate. As an upper bound, with some allowance for strain-hardening effects, one can obtain maximum axial forces using capacity design principles (as described in Figure 6.8). However, during an earthquake, plastic hinges do not form simultaneously at all stories, but rather develop in only a few stories at a time, often in a succession of waves traveling along the height of the building. As a result, the capacity design approach may be conservative, particularly in multistory buildings.

There is no agreement on what constitutes a proper alternative method to capture the maximum axial force acting on a column during earthquake shaking. Some codes typically resort to an additional load case, with higher specified earthquake loads to be considered only for the design of columns. For example, AISC 341 uses a special "amplified" seismic load combination in which the seismic forces are multiplied by an overstrength factor, Ω_o, only to be used for specific purposes, such as column design (note that some earlier editions now obsolete used a constant $2R/5$ overstrength factor). Application of the SRSS technique in conjunction with capacity design principles, presented in Chapter 9 for ductile concentric braced frames, is another method to estimate more realistic maximum column axial forces. All of these methods have flaws and limitations as discussed in that chapter.

8.3.2 Considerations for Column Splices

Typically, the bending moment diagram for the beams and columns will show a point of inflection somewhere along the length of the member. Frequently, for preliminary design, the points of inflection are assumed to be at midlength of the members. Although this is a convenient assumption, it is important to recognize that the location of the inflection points will vary significantly. This is particularly true as yielding occurs in the frame during an earthquake and bending moments are redistributed within the frame. Even though the basic pattern of bending moments remains the same, the location of inflection points can shift substantially from the locations indicated by an elastic frame analysis.

Assumptions regarding the location of inflection points can substantially impact the design of column splices. A designer may elect to locate a column splice near an inflection point based on elastic frame analysis (or slightly lower than midheight to provide convenient site-welding conditions) and design the splice for a relatively small bending moment, based on those same elastic frame analysis results. This would be an error because the possibility of significant bending moments at the splice location must be considered, regardless of the results of elastic analysis.

Tests have showed partial penetration welds in thick members to be brittle under tensile loads (Bruneau et al. 1987, Bruneau and Mahin 1991, Popov and Stephen 1977). For example, a standard partial penetration splice detail frequently used in seismic regions, shown in Figure 8.2a, was tested for the largest column sizes that could be accommodated in a 17,800 kN (4000 kips) capacity universal testing machine (Bruneau and Mahin 1991). This specimen, fabricated from A572 Grade 50 steel, was tested in flexure instead of tension to permit consideration of the largest specimen for which cross-section could be kept whole; cutting away part of the section that would have released some of the lock-in residual stresses. The test setup is illustrated in Figure 8.2b. As shown in Figure 8.2c, the moment-curvature relationship remained practically linear up to a value corresponding to approximately 60% of the nominal plastic moment of the smaller column section at the splice, at which the weld fractured in a brittle manner (Figure 8.2d).

For the above reasons, partial penetration welded joints in column splices are viewed apprehensively. Therefore, seismic codes typically require splices subjected to net tension forces to be designed for no less than half of the column axial cross-sectional plastic strength, or 150% of the required splice strength calculated by analysis.

8.3.3 Strong-Column/Weak-Beam Philosophy

Structural frames can dissipate a greater amount of hysteretic energy when plastic hinges develop in the beams rather than in the columns (see Figure 6.10). This beam-sway mechanism enhances overall seismic resistance and prevents development of a soft-story (column-sway) mechanism in a multistory frame. Frames in which measures are taken to promote plastic hinges in the beams rather than in the columns are said to be strong-column/weak-beam (SCWB) frames. The alternative is weak-column/strong-beam (WCSB) frames.

Most codes and design guidelines have moved toward the SCWB philosophy by requiring that, at a joint, the sum of the columns' plastic moment capacities exceed the sum of the beams' plastic moment capacities, based on simple moment equilibrium at the joint (as in Figure 8.1), in which case:

$$\sum M_{pc} = \sum Z_{cr} F_{yc} = \sum Z_c \left(F_{yc} - \frac{P_{uc}}{A_g} \right) \geq \sum M_{pb} \tag{8.1}$$

and, generally, at least

$$\sum M_{pc} = \sum Z_{cr} F_{yc} = \sum Z_c \left(F_{yc} - \frac{P_{uc}}{A_g} \right) \geq \sum Z_b F_{yb} \tag{8.2}$$

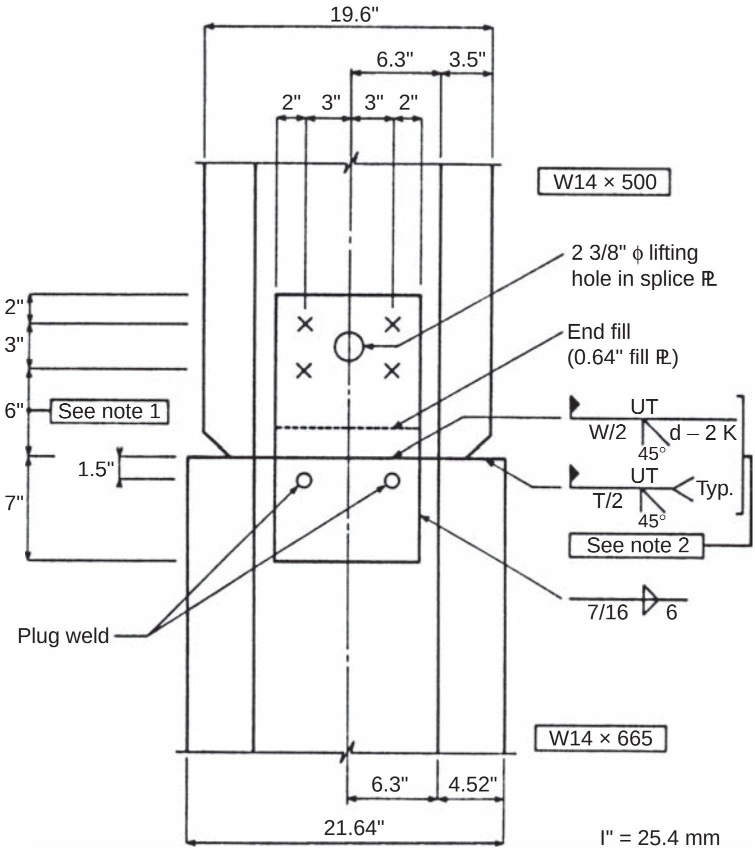

Notes:

1. Provide 6" *as specified* instead of 3" as on standard detail.
2. A certified inspector is to be present during construction and perform ultrasonic testing of the weld.

(a)

Figure 8.2 Test column splice with partial penetration welds in thick members: (a) splice detail; (b) test setup; (c) moment-curvature results; (d) splice after brittle fracture.

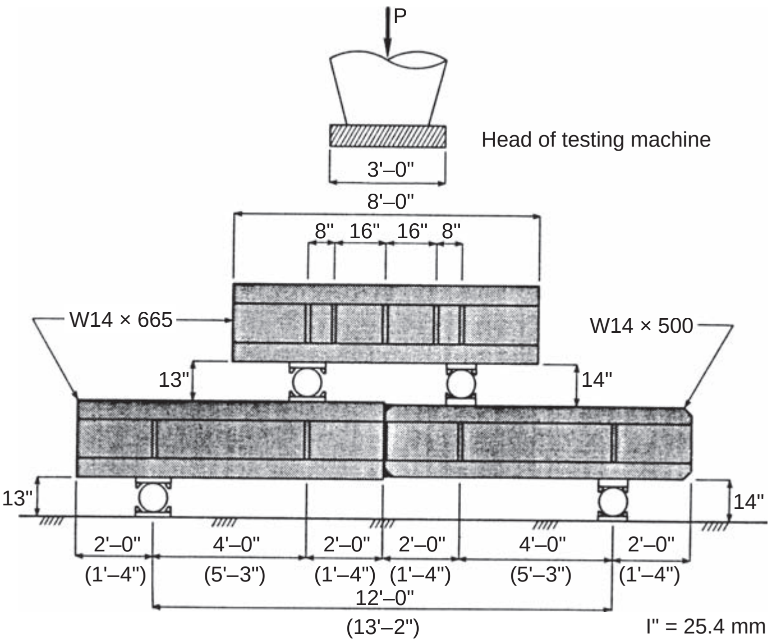

(b)

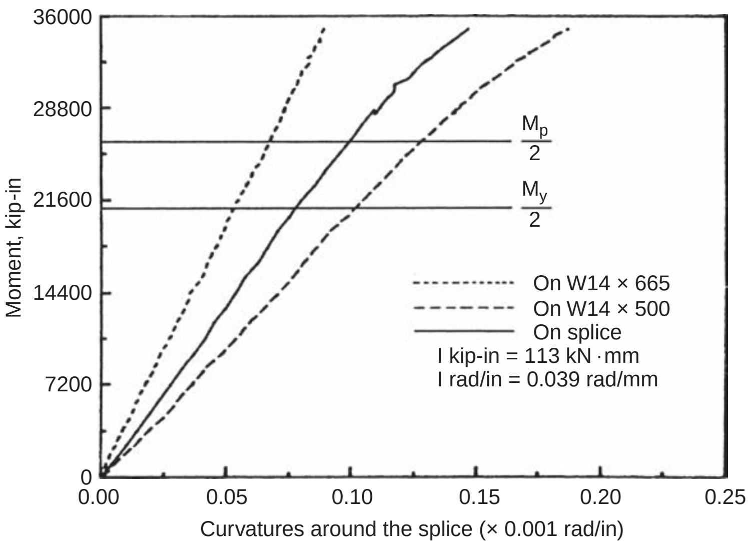

(c)

Figure 8.2 (*Continued*)

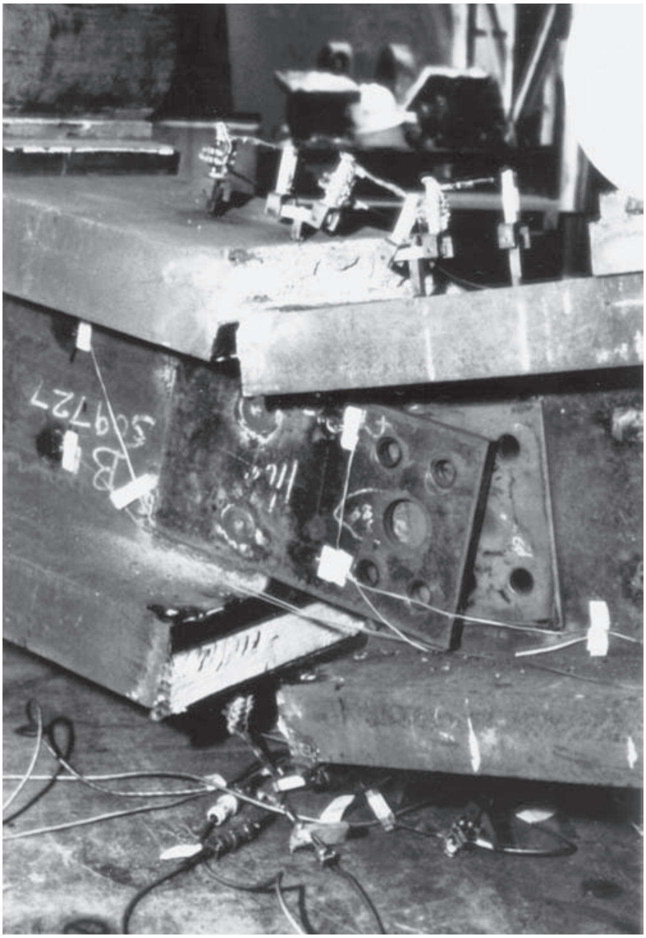

(d)

Figure 8.2 (*Continued*)

where ΣM_{pc} is the sum of the projections to the beam centerline of the *nominal* flexural strengths of the columns above and below the joint, A_g is the gross area of the column, F_{yc} is the column nominal yield strength, P_{uc} is the required axial strength in the column from the load-combination considered, Z_c is the column plastic section modulus, and Z_{cr} is the plastic modulus reduced to account to the presence of axial force (see Chapter 3), and ΣM_{pb} is the sum of the *expected* (i.e., *probable*) flexural strengths of the plastic hinges in the beams, projected from the hinge location to the column centerline. Here, *probable* capacities (as opposed to *nominal* capacities) are obtained by taking into account the impact of strain-hardening, larger-than-specified beam yield strength, and other factors contributing to reserve strength (many of these concepts will become clear after a reading of the material presented in Section 8.6).

Conceptually, however, the above requirements cannot fully prevent column plastic hinging at beam-to-column joints because the ratio of the column moments acting at the top and bottom faces of a joint varies greatly during an earthquake because of the movement of each column's inflection point. The column demands also increase significantly as a function of ground motion severity (FEMA 2000e, Nakashima and Sawaizumi 2000). It is believed that satisfying the above equation will limit column yielding to a level that is not detrimental, and, most importantly, result in columns strong enough to spread beam plastic hinging over multiple frame levels.

8.3.4 Effect of Axial Forces on Column Ductility

Exceptions to the SCWB philosophy are sometimes permitted in single-story buildings or at the top story of a multistory building, when the risk of soft-story plastic mechanisms is not significant. For example, according to AISC 341, the SCWB requirement can be waived for such columns provided that the maximum axial load acting on them is less than $0.30P_y$, where P_y equals $F_{yc}A_g$, F_{yc} is the column nominal yield strength, and A_g is the gross area of the column. Engineers taking that route must recognize that plastic hinges may form in columns of WCSB frames and recognize the possible deleterious impact of axial forces on the rotation capacity of columns. Other exemptions exist when the capacity design approach is difficult to implement and other precautions can be taken to prevent soft-story mechanisms.

There is a paucity of research results on the effect of axial loads on the ductility of steel columns. Adherence to the above strong-column/weak-beam philosophy may partially explain this situation. Popov et al. (1975) showed that the cyclic behavior of W-shaped columns is a function of the applied load to yield load ratio, P/P_y, and the magnitude of interstory drifts. In those tests, for specimens braced to prevent lateral buckling about their weak axis, sudden failure due to excessive local bucking and strength degradation were observed when P/P_y exceeded 0.5. The aforementioned limit of $0.30P_y$ ($0.40P_y$ in some other codes) is historically tied to this series of tests.

The adequacy of the existing code limits has been challenged by Schneider et al. (1992); test results showed that moment-resisting steel building frames designed according to the WCSB philosophy suffered rapid strength and stiffness deterioration when the columns were subjected to axial loads equal to approximately 0.25 P/P_y.

Beyond the above concerns, large axial loads on a ductile column can also lead to column shortening during plastic hinging, which can be problematic in many ways, particularly if developing unevenly in various columns. MacRae et al. (1990) tested columns subjected to constant axial compression, P, and reverse cyclic horizontal displacements, for P/P_y values of 0.0, 0.3, 0.4, 0.5, 0.6, 0.7, and 0.8. Although column shortening of more than 7% of their length was obtained for the larger ratios, this is a function of cumulative plastic rotations, and shortening due to actual earthquake excitations were less than 1% of column length (MacRae et al. 2009).

Columns subject to plastic deformations should be compact sections and be laterally braced in accordance with the requirements for plastic design. This requires lateral bracing at each plastic hinge location and a maximum brace spacing of $0.086 r_y E \sqrt{F_y}$ as discussed earlier for beams.

8.4 Panel Zone

The satisfactory seismic response of a ductile moment-resisting frame depends on the adequate performance of its beam-column joints. For multistory building frames, in which beams connected to columns are expected to develop their plastic moment, the designer must prevent undesirable beam-column joint failures. In steel structures, doing so requires measures to avoid column flange distortion, column web yielding and crippling, and panel zone failure. This section mostly focuses on the behavior and design of ductile panel zones, but matters relevant to the first and second failure modes are first addressed.

8.4.1 Flange Distortion and Column Web Yielding/Crippling Prevention

The addition of continuity plates (i.e., stiffeners joining the beam flanges across the column web) can effectively prevent flange distortion and column web yielding/crippling. Examples of continuity plates are shown in Figure 8.3. When beams reach their plastic moment at the column face (Figure 8.4a), the beam flanges apply large localized forces to the columns (Figure 8.4b). The beam flange in tension pulls on the column flange. In the absence of continuity plates, and if otherwise unrestrained, the column flange would bend under that pulling action, with greater deflections in column flanges of low stiffness and small thickness (Figure 8.4c). However, the column flange is not free to deflect because the beam flange framing into it is rigid in its plane (Figure 8.4d). Because deformations of the connected elements must be compatible, stresses concentrate in the beam flange where column flange is stiffest, that is, near the column web (Figures 8.4e and f).

In some tests of connections without continuity plates, localized cracking originated in the beam flange weld at the column centerline and rapidly propagated across the entire flange width and thickness. To prevent this type of failure, most seismic codes require the addition

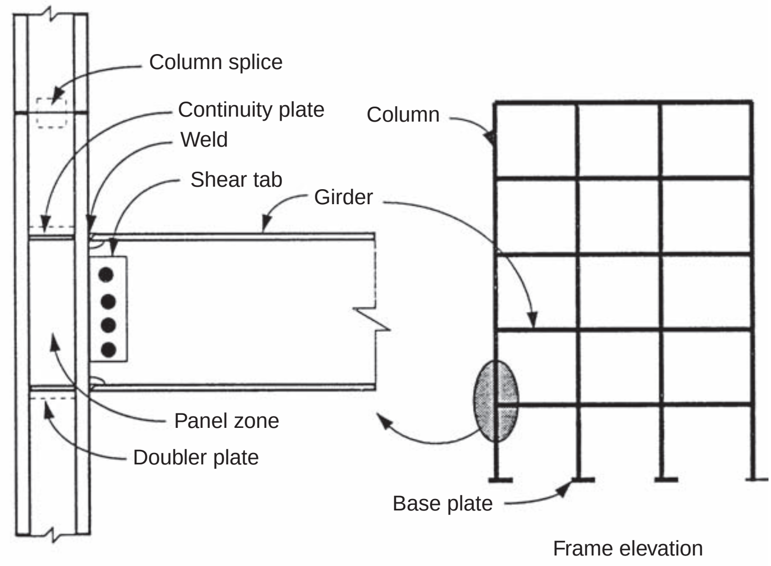

FIGURE 8.3 Fundamental elements of a ductile moment-resisting frame. (*From* Interim Guidelines: Evaluation, Repair, Modifications, and Design of Steel Moment Frame Structures, *SAC Joint Venture, 1995b, with permission.*)

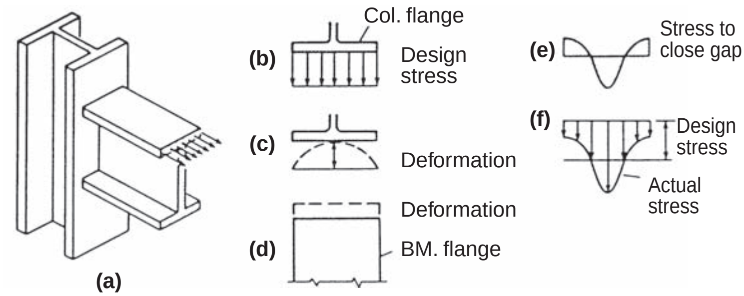

FIGURE 8.4 Stress distribution in welded beam flange at column face in absence of column continuity plates (stiffeners). (*From* Journal of Constructional Steel Research, *vol. 8, E.G. Popov*, Panel Zone Flexibility in Seismic Moment Joints, 1987, *with permission from Elsevier Science Ltd., Kidlington, U.K.*)

of continuity plates if the maximum expected beam flange force exceeds the factored flange strength of ϕR_n where:

$$R_n = 6.25 t_{cf}^2 F_{yf} \tag{8.3}$$

where t_{cf} is the column flange thickness, F_{yf} is the column flange nominal yield strength, and ϕ is equal to 0.9. This equation is based on yield line analyses by Graham et al. (1959). Note that AISC (1992) specified that maximum expected beam flange force to be taken as 1.8 $A_f F_y$, where A_f is the flange area of the connected beam and F_y is the nominal strength of the beam. This value assumes a strain-hardened beam moment 30% greater than the nominal plastic moment, and it assumes that the bolted beam web is ineffective in transferring moment. Thus, if only the beam flanges can effectively transfer the maximum beam moment at the connection, and assuming that the flanges-only plastic modulus, $Z_f(\approx A_f d$, where d is the beam depth), is approximately 70% of a beam's plastic modulus, Z, the maximum expected beam flange force becomes:

$$T_{max} = \frac{M_{max}}{d} = \frac{1.3M_p}{d} = \frac{1.3(ZF_y)}{d} = \frac{1.3\left(\dfrac{Zf}{0.7}\right)F_y}{d} \approx \frac{1.8A_f dF_y}{d} = 1.8A_f F_y \tag{8.4}$$

Other codes (e.g., CSA 2009) arrive at a similar result by specifying a reduced column flange resistance for seismic applications [e.g., 0.6 of (Eq. 8.3)], instead of using the 1.8 magnification factor for the beam flange forces in Eq. (8.4).

Opinions varied substantially over time on the effectiveness of the above equations. Prior to the Northridge earthquake, AISC (1992) suggested that designers use continuity plates even when the above requirement was satisfied because continuity plates had been used in nearly all cyclic tests (prior to 1994) that exhibited satisfactory ductile behavior. Interim design guidelines released following the Northridge earthquake (SAC 1995b) also recommended the use of continuity plates in all ductile moment frame connections, to avoid the stress concentration depicted in Figure 8.4 in the highly stressed welded region. Subsequent review of past test data (FEMA 2000f) showed that good seismic performance was still possible in the absence of continuity plates when the above equations were satisfied, even recognizing that those equations were at best approximations given the complex behaviors at play. Limited experiments by Ricles et al. (2000) led to similar conclusions, demonstrating that although connections having continuity plates exhibited better inelastic seismic performance, comparable ones without such plates still developed appropriate plastic rotations provided that the heavy column flanges met the above requirement, and provided that $t_{cf} \geq b_{cf}/6$, where b_{cf} is the column flange width. Hajjar et al. 2003 summarizes this evolution in thinking and the supporting research evidence.

Accordingly, AISC 341 specifies that continuity plates of thickness at least equal to the thicker of the two beam flanges connecting to a column in two-sided connections (or equal to half of the beam flange thickness in a one-sided connection) be provided, except when:

$$t_{cf} \geq 0.4\sqrt{1.8 b_{bf} t_{bf} \frac{F_{yb} R_{yb}}{F_{yc} R_{yc}}} \tag{8.5}$$

$$t_{cf} \geq \frac{b_{bf}}{6} \tag{8.6}$$

where R_{yb} and R_{yc} are respectively the ratios of the expected yield stress to the specified minimum yield stress of the beam and column framing at the joint under consideration, or except when superseded by results from qualification testing or alternate requirements for connections prequalifed by the AISC 358 specification (2010a) discussed in later sections. Note that Eq. (8.5) is obtained by equating and rearranging Eqs. (8.3) and (8.4) and substituting expected yield strengths instead of minimum specified strengths.

When the beam flange applies compression to the column flange, column web yielding must be prevented, as would normally be done in nonseismic applications, using the traditional equations for bearing resistance:

$$B_r = (5k + N)\ t_{cw} F_{yw} = (5k + t_{bf})\ t_{cw} F_{yw} \tag{8.7}$$

where k is the distance from the outer face of the column to the web toe of the fillet, N is the bearing length of the applied force, F_{yw} is the yield strength of the column web, and t_{bf} and t_{cw} are the beam flange and column web thicknesses, respectively. Resistance to web crippling must also be checked, using:

$$B_r = 0.8 t_w^2 \left[1 + 3\left(\frac{N}{d}\right)\left(\frac{t_w}{t_f}\right)^{1.5}\right]\sqrt{\frac{E F_{yw} t_f}{t_w}} \tag{8.8}$$

where B_r is the bearing resistance. Again, variations of these equations and additional requirements are prescribed for specific AISC 358 prequalified connections.

Note that seismic design codes generally do not require consideration of strain-hardening in the beam flange in compression because web-crippling is not a brittle failure mode. Also note that doubler plates are frequently used instead of continuity plates when increases in web crippling or web yielding resistance are necessary.

8.4.2 Forces on Panel Zones

The panel zone of a beam-column joint is the rectangular segment of the column web surrounded by the column flanges (left and right vertical boundaries) and the continuity plates (top and bottom horizontal boundaries). Typically, the panel zone is simultaneously subjected to axial forces, shears, and moments from the columns and beams, as shown in Figure 8.5.

Resolving equilibrium on the free-body diagram of Figure 8.5 and taking the forces shown acting on the face of the panel as positive, the horizontal shear acting in the panel zone can be calculated as:

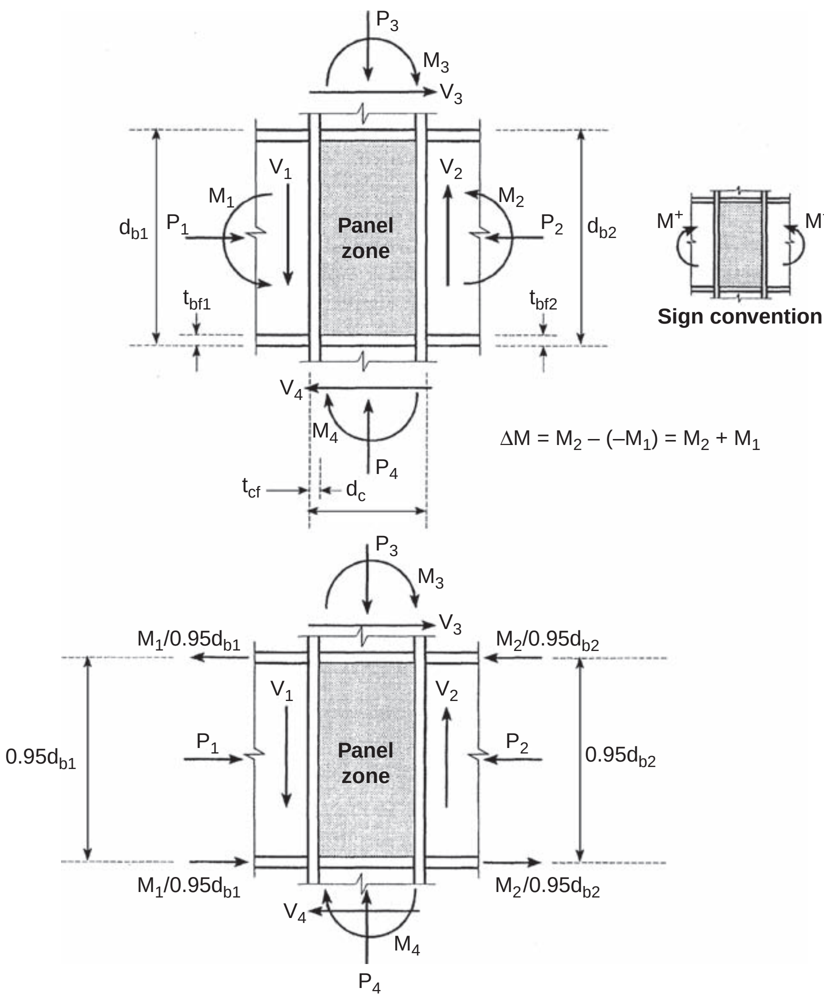

Figure 8.5 Moments, shear forces, and axial forces acting on the panel zone of a ductile moment-resisting frame subjected to lateral loading.

$$V_w = \frac{M_1}{0.95d_{b1}} + \frac{M_2}{0.95d_{b2}} - V_c \tag{8.9}$$

where d_{b1} and d_{b2} are the depths of beams 1 and 2, respectively, and 0.95 d_{b1} and 0.95 d_{b2} are approximations for the lever arm of the beam flange forces resulting from the applied moments, as shown in Figure 8.5. V_c is the subassembly equilibrating shear given by:

$$V_c = \frac{M_1\left(\dfrac{L_1}{L_{b1}}\right) + M_2\left(\dfrac{L_2}{L_{b2}}\right)}{h} \tag{8.10}$$

where h is the average of story heights above and below the joint, L_i is the total span length of beam i measured center-to-center of the columns to which it connects, and L_{bi} is the clear span length of beam i equal to the distance from face-to-face of the columns (i.e., deducting half of the column width at each end of the beam) as shown in Figure 8.1. When member forces are available from computer analysis, one can obtain an estimate of V_c by averaging the column shears at the edges of the panel zone:

$$V_c = \frac{V_3 + V_4}{2} \tag{8.11}$$

This approximation is usually conservative because it gives smaller values of V_c and thus higher values of V_w.

The above equations show that the critical loading condition for the panel zone occurs when it is subjected to large unbalanced moments from the beams framing into the columns. Large shear forces will develop in the panel zones of interior columns participating in a sway frame collapse mechanism (of the type shown in Figure 6.10a) when the beams on all sides of such a panel zone reach their plastic moment. In fact, the panel zone shear in that case is substantially greater than the shear in the adjacent columns and beams, and the possibility of panel zone yielding must be considered.

If Eq. (8.8) is substituted into Eq. (8.7), the panel zone shear, V_w, can be shown to depend only on beam moments M_1 and M_2. In other words, the magnitude of the unbalanced moment, $\Delta M = M_1 + M_2$, controls the force demand on the panel zone. Different philosophies regarding the magnitude of ΔM to be considered for design had been developed prior to the Northridge earthquake. Tsai and Popov (1990b) reported three such philosophies: strong panel zones, intermediate-strength panel zones, and minimum-strength panel zones. For strong panel zone design, $\Delta M = M_{p1} + M_{p2} = \Sigma M_p$, following capacity design principles (SEAOC 1980). For intermediate strength panel zone design, $\Delta M = \Sigma M_p - 2M_g$, where M_g is the moment due to gravity loads. Assuming this moment to be 20% of M_p, the design requirement becomes $\Delta M = \Sigma 0.8M_p$ (Popov 1987, Popov et al. 1989). For minimum-strength panel zone design, in an allowable stress design perspective, $\Delta M = \Sigma(M_g + 1.85M_e) < \Sigma 0.8M_p$, where M_e is the beam moment obtained when the specified earthquake loads are acting alone, and 1.85 is a factor chosen to further reduce the design force on the panel zone and promote a greater energy dissipation by panel zone yielding. Prior to the Northridge earthquake, only a few studies had investigated the consequences of these various design approaches in terms of the relative levels of plastic deformation in beam and panel zones (Popov et al. 1989, Tsai and Popov 1990b, Tsai et al. 1995). These indicated larger panel zone inelastic demands and interstory drifts in frames designed per the minimum-strength panel zone approach. However, arbitrarily reducing the demands to create weaker panel zones is an approach that lacks transparency by confounding actual demands and capacities.

The strong panel zone philosophy was used prior to 1988 in the United States, together with a panel zone shear strength of $0.55F_yA_w$, where A_w is the column web area (SEAOC 1980). The intermediate strength and minimum strength approaches are indirect means to obtain weaker panel zones that will yield sooner and respectively dissipate a greater percentage of the total hysteretic energy. Despite the lack of a sound theoretical basis, the latter two approaches were adopted by many codes and guidelines in the United States (e.g., SEAOC 1988, AISC 1992) after 1988 to be used in conjunction with the panel zone shear strength equation described in Section 8.4.5 below. However, in the post-Northridge context, further to multiple successive changes in code requirements (summarized in Lee et al. 2005b), AISC 341 and 358 requires that the shear in the panel zone be determined from the moments acting at the column face, determined by projection of the expected plastic moment developing in the beam, considering strain-hardening of the plastic hinge and consistently with the free-body diagrams presented in Section 8.6. In that instance, strength of panel zones is independently assessed as a function of intended ultimate behavior.

8.4.3 Behavior of Panel Zones

Studies of panel zone inelastic behavior started in the 1970s and included the work of Krawinkler et al. (1971, 1975, 1978), Fielding and Huang (1971), Fielding and Chen (1973), and Becker (1975). Tests of large-scale specimens clearly revealed the dominance of shear distortions on panel zone behavior. Krawinkler et al. (1971) visually captured this phenomenon using photogrammetric techniques, as shown in Figures 8.6c and d, at large shear strains for the specimens shown in Figures 8.6a and b. These tests also demonstrated that panel zones, when carefully detailed to avoid column web yielding and crippling, as well as column flange distortion, can exhibit

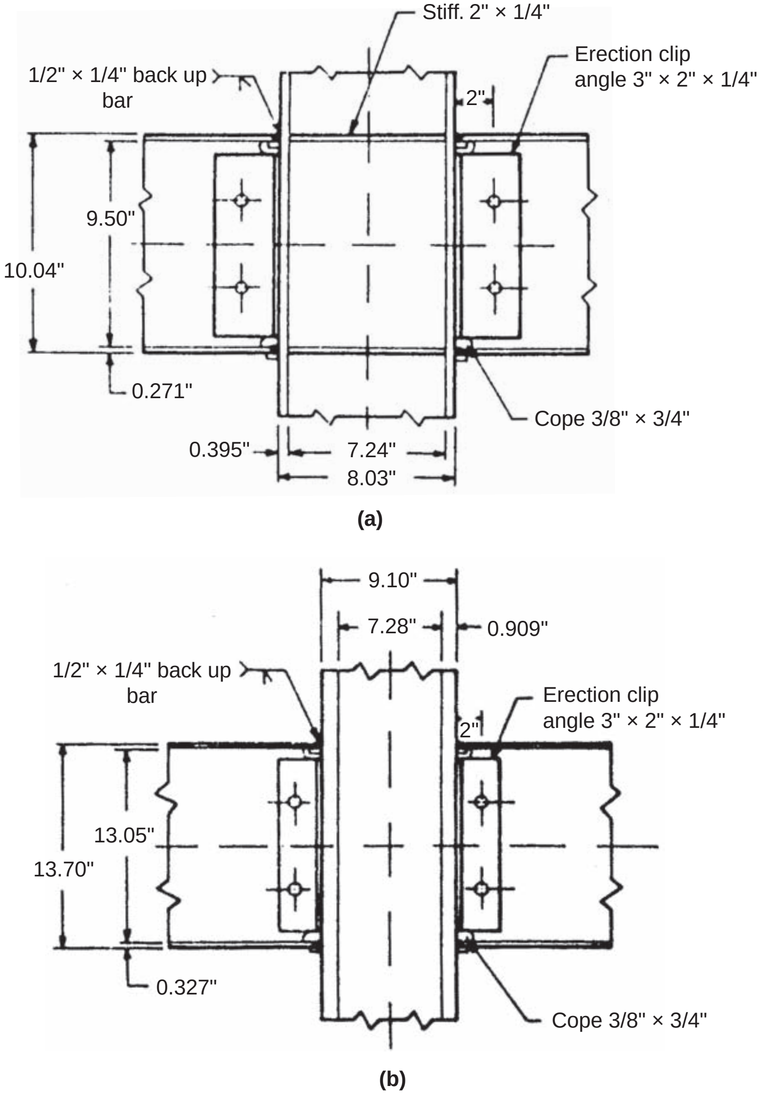

Figure 8.6 Panel zone deformation experimental results: (a) Connection details of specimen A; (b) specimen B. Column in specimen A is W200 × 36 section (W8 × 24 in U.S. units) with flanges milled to simulate W360 × 101 (W14 × 68 in U.S. units), and column in specimen B is W200 × 100 (W8 × 67 U.S. units) to simulate W360 × 339 (W14 × 228 U.S. units); (c) deformation pattern in panel zone of specimen A; (d) deformation pattern in panel zone of specimen B; (e) ΔM versus γ_p diagram for specimen A; (f) ΔM versus γ_p diagram for specimen B; (g) effects of excessive panel zone distortions. (*Parts a to g from* Earthquake Engineering Research Center Report UCB/EERC 71-7*, "Inelastic Behavior of Steel Beam-to-Column Subassemblages" by H. Krawinkler et al., 1971, with permission from the author.*)

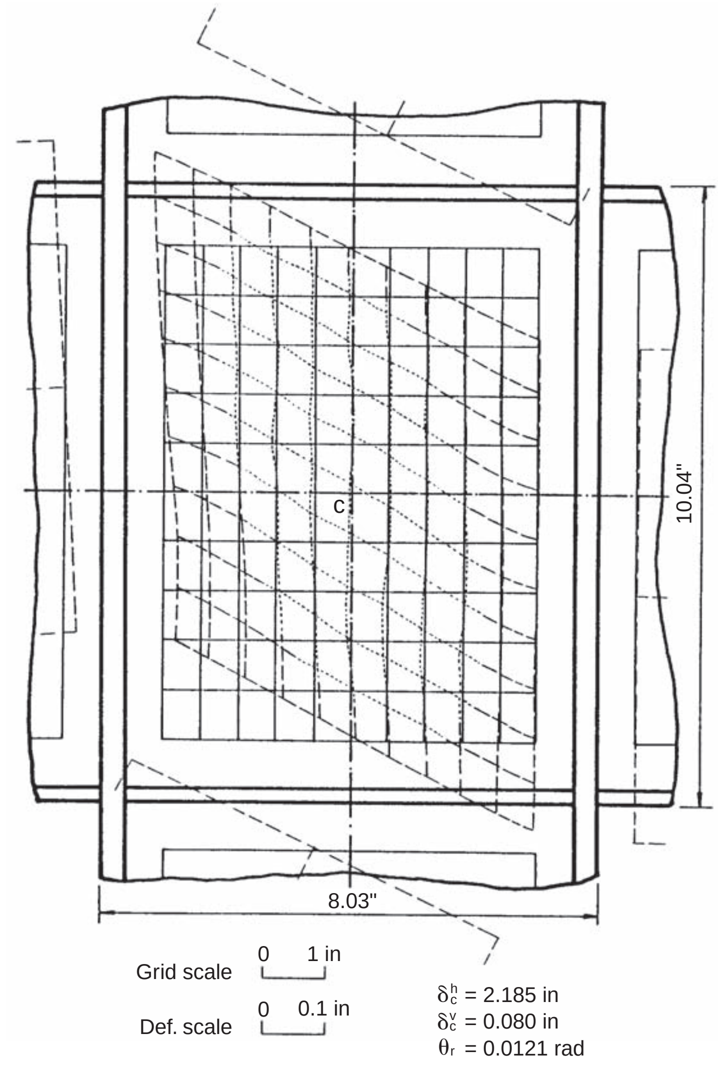

Specimen A-2 LP 9

(c)

FIGURE 8.6 (*Continued*)

excellent hysteretic energy dissipation characteristics in shear, up to large inelastic deformations. Typical results from cyclic inelastic testing are presented in Figures 8.6e and f, expressed in terms of the unbalanced beam moment ($\Delta M = M_1 + M_2$) versus average panel zone shear distortions (γ_p, also called shear strains or shear deformations in the literature).

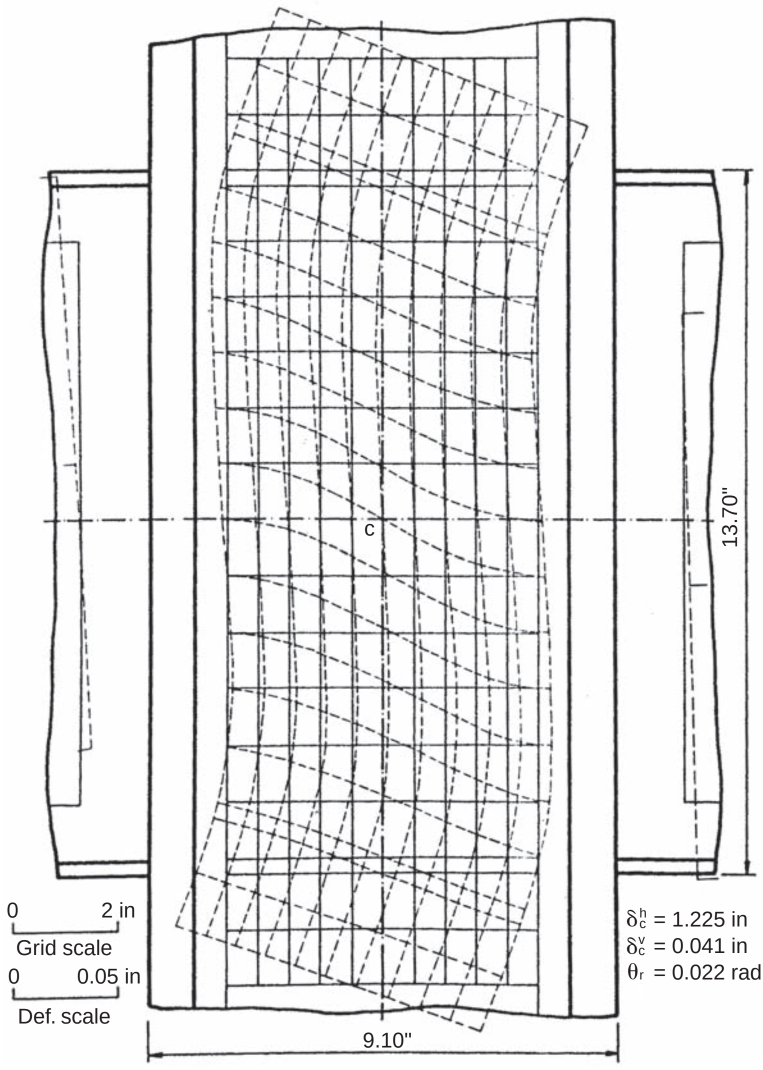

Figure 8.6 (*Continued*)

Examination of these hysteretic loops shows that panel zones exhibit considerable reserve strength beyond first yield, with a steep strain-hardening slope. This results from the complex state of stress that develops inside the panel zone as shear stresses are progressively increased. Typically, yielding starts in the middle of the panel, consistently with elastic theory, and progresses approximately in a radial

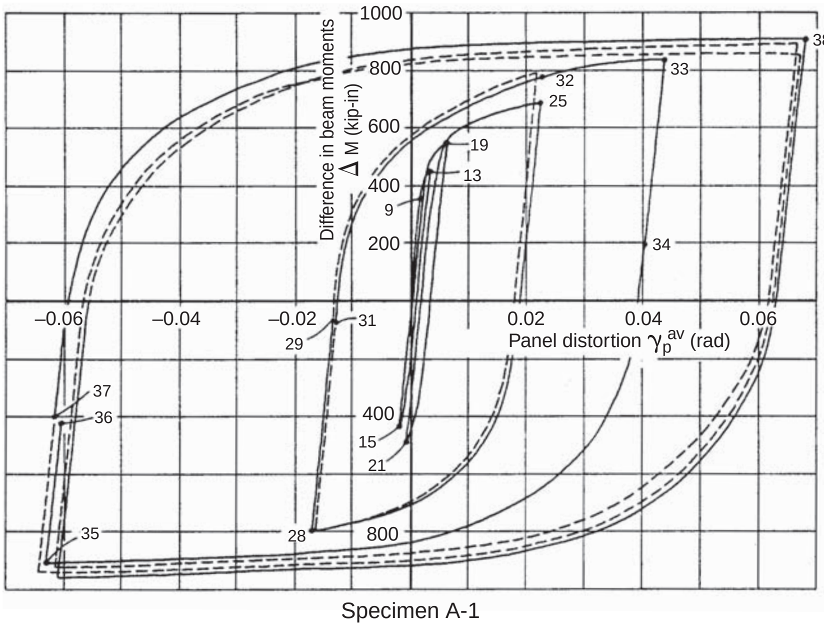

Specimen A-1

(e)

Figure 8.6 (*Continued*)

manner over the entire panel zone as the unbalanced moment further increases. As a result, shear distortion is largest at the center of the panel and smallest at the corners. Once the web is fully yielded, the panel zone stiffness depends in a complex manner on the panel aspect ratio, d_c/d_b per Figure 8.5, and the stiffness of its surrounding elements, such as the column flanges and the webs of the connecting beams. These factors, together with strain-hardening of the web in shear, produce the considerable post-yield stiffness observed during tests (see Figures 8.6e and f).

The column axial load also has an impact on the behavior of the panel zone. In the presence of axial stress, the onset of shear yielding in the panel zone is hastened, in accordance with the Von Mises yield criterion. Nonetheless, experiments have shown that the ultimate shear strength of the panel is not substantially affected by column axial loads; column flanges were observed to provide axial load resistance when the panel yielded in shear. This redistribution is possible when the column flanges remain elastic during panel zone yielding. Ultimately, at large shear strains, the column flanges will in turn develop their full plastic flexural capacity, in a state of combined flexure and axial force. When that occurs, large kinks in column

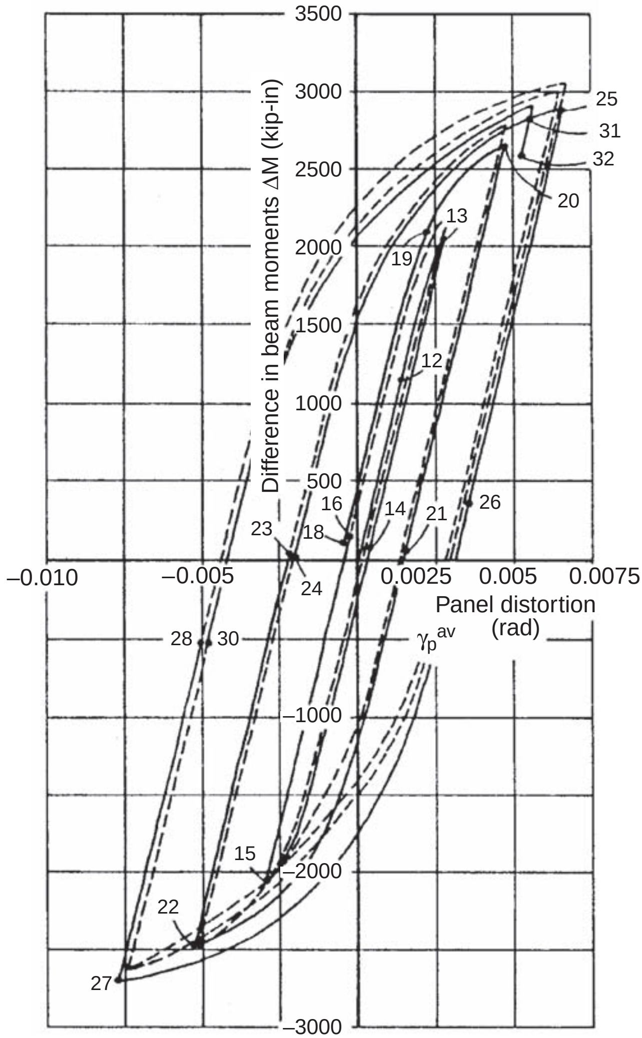

Specimen B-1
(f)

FIGURE 8.6 (*Continued*)

flanges may develop, producing large strains in or near the welds connecting the beam flanges to the column, and possibly joint fracture. For this reason, researchers have recommended that the maximum shear distortion in a panel zone, γ_{max}, be limited to four times the shear yield distortion, γ_y (Krawinkler et al. 1971).

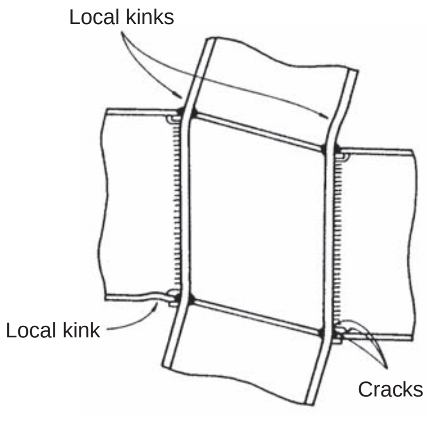

(g)

Figure 8.6 (*Continued*)

8.4.4 Modeling of Panel Zone Behavior

Formulation of a simple model that captures the complex behaviors described above remains elusive. Elastic stiffness and yield threshold are relatively simple matters, but modeling postyield stiffness, which was observed to vary considerably from specimen to specimen, is particularly difficult. Krawinkler et al. (1971) proposed a model "…simple enough to permit its inclusion into practical computer programs…" at the "…sacrifice [of] accuracy in modeling actual boundary conditions." The model proposed, presented in Figure 8.7a, consists of an elastic-perfectly plastic column web surrounded by four rigid sides connected by springs at the corners.

These springs mostly capture the effect of the column flanges on panel zone behavior and neglect other behaviors. In the elastic range, the stiffness of the panel zone is approximately:

$$K_e = \frac{V}{\gamma} = \frac{1}{\dfrac{1}{0.95 d_c t_{cw} G} + \dfrac{d_b^2}{24 E I_{cf}}} \tag{8.12}$$

where G is the shear modulus, E is the modulus of elasticity, I_{cf} is the moment of inertia of a single column flange, t_{cw} is the column web thickness, and all other terms have been defined previously. Recognizing that the flange typically contributes approximately only 10% of the total elastic stiffness, one can ignore the second term in the

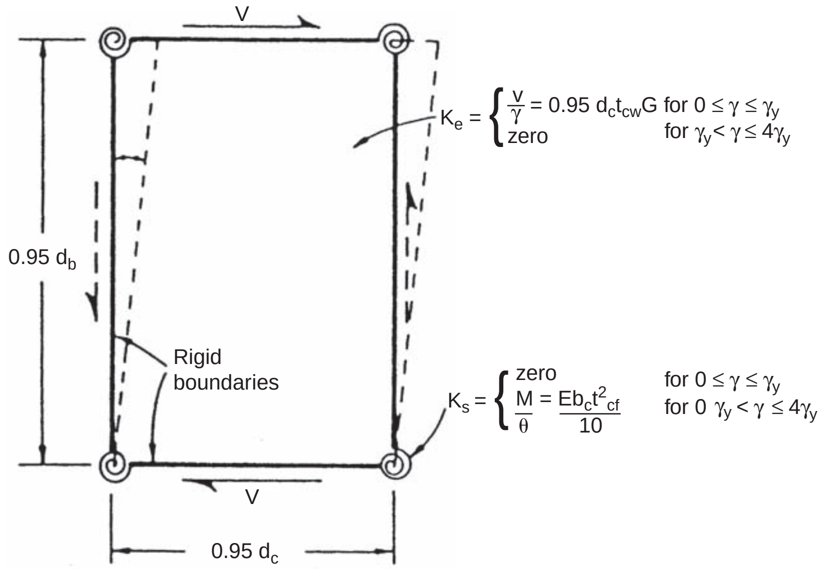

(a)

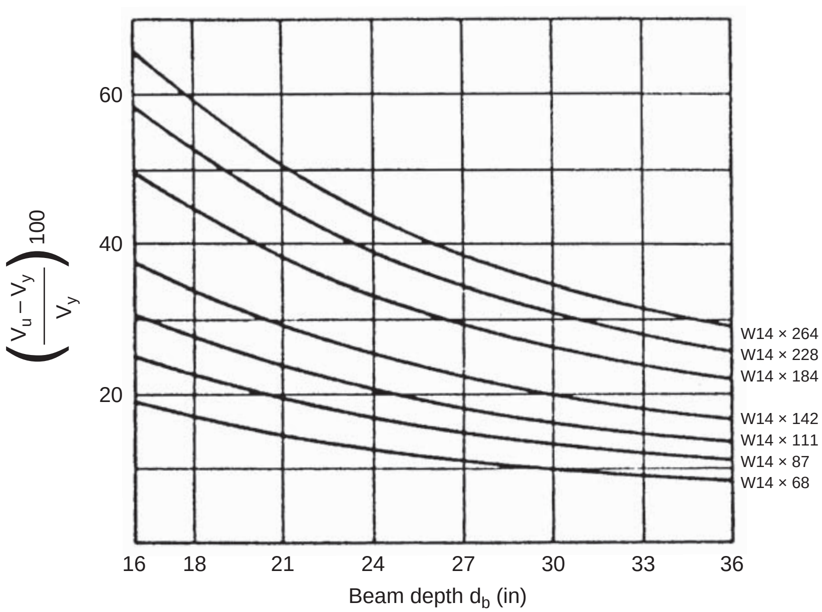

(b)

Figure 8.7 Panel zone behavior: (a) mathematical model; (b) Example of ultimate strength per Krawinkler model, V_u, compared with Von Mises yield strength, V_y; (c) experimental versus theoretical panel zone shear (expressed in terms of ΔM) for specimen A; (d) experimental versus theoretical panel zone shear (expressed in terms of ΔM). Specimen B (Krawinkler model is identified as Model 3 on that figure). (*Parts a to d from* Engineering Journal, *3rd Quarter 1978, "Shear in Beam-Column Joints in Seismic Design of Steel Frames" by H. Krawinkler, with permission from the American Institute of Steel Construction.*)

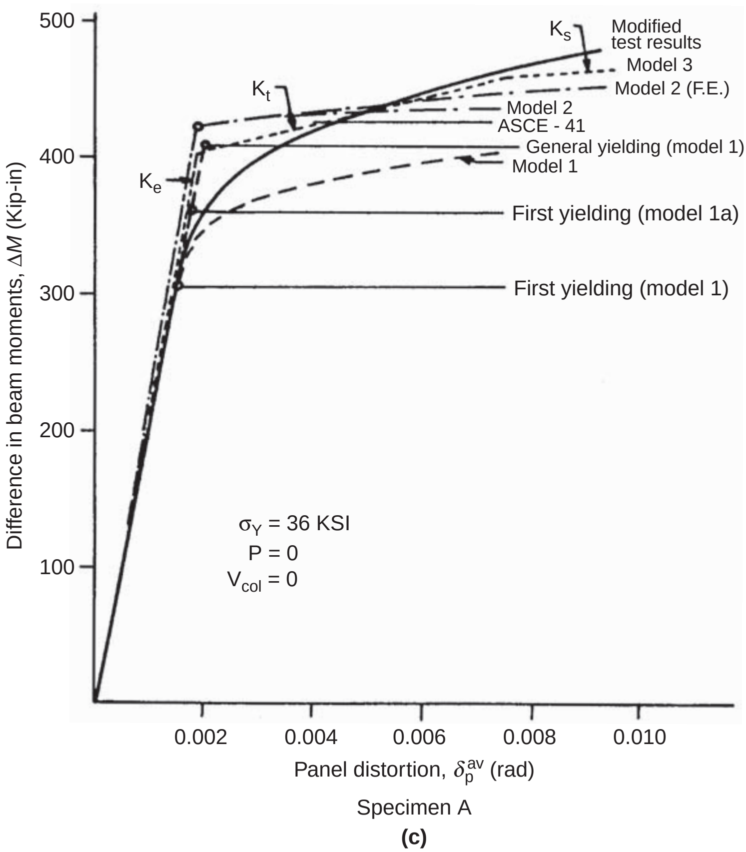

Figure 8.7 (*Continued*)

denominator, which results in the following simpler expression for the elastic stiffness:

$$K_e = \frac{V}{\gamma} = 0.95\, d_c t_{cw} G \tag{8.13}$$

In the postyield range, the panel zone shear stiffness is taken as zero, whereas the spring stiffness is taken as:

$$K_s = \frac{M}{\theta} = \frac{E b_c t_{cf}^2}{10} \tag{8.14}$$

where θ is the concentrated spring rotation, and b_c and t_{cf} are the width and thickness of the column flange, respectively. This definition of K_s cannot be proven through the use of simple models. Krawinkler et al. (1971) report that finite element analyses have been used to

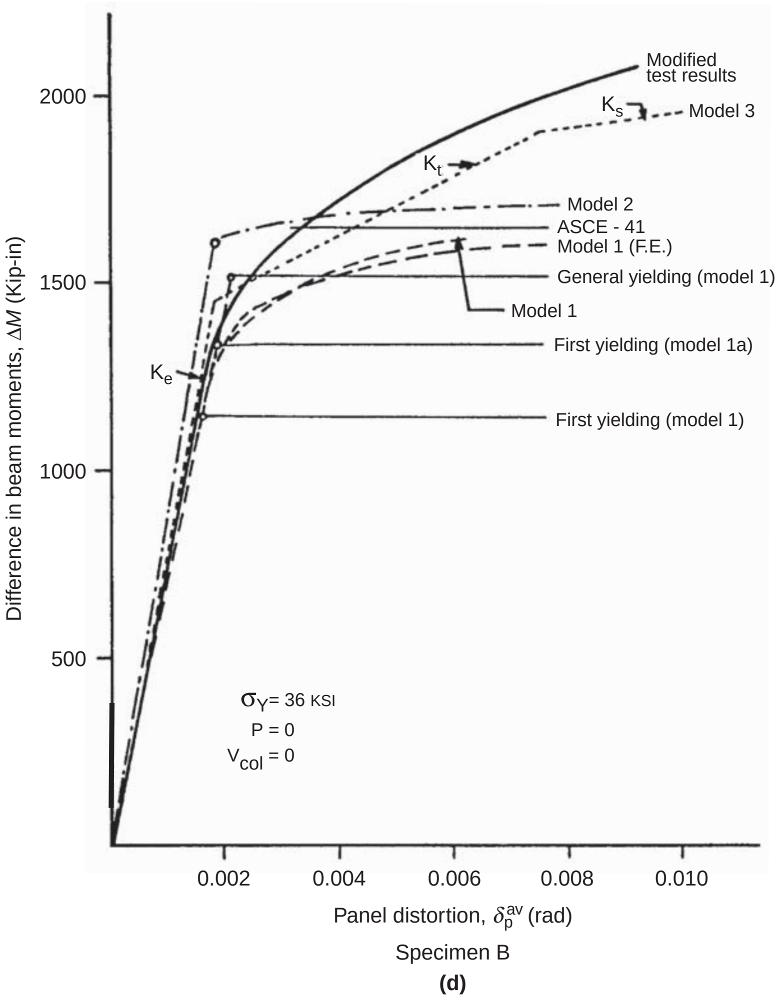

Figure 8.7 (*Continued*)

determine the concentrated column flange rotation at each corner corresponding to this model. The post yielding stiffness of the panel is thus given by:

$$K_t = \frac{V}{\gamma}\left[\frac{4M}{0.95d_b}\right]\frac{1}{\gamma} = \left[\frac{4}{0.95d_b}\right]\frac{M}{\theta} = \frac{1.095b_c t_{cf}^2 G}{d_b} \tag{8.15}$$

using static equilibrium on the panel and knowledge that γ is equal to θ for this model. This equation is reasonable over the range $\gamma_y < \gamma < 4\gamma_y$, where γ_y is the shear yield distortion. Hence, the panel zone shear strength, reached at an angle of distortion of $4\gamma_y$, is:

$$V_u = K_e\gamma_y + 3K_t\gamma_y = V_y\left(1+3\frac{K_t}{K_e}\right) = 0.55F_y d_c t_{cw}\left(1+\frac{3.45 b_c t_{cf}^2}{d_b d_c t_{cw}}\right) \quad (8.16)$$

The ratio of the second term over the first term inside the parenthesis represents the increase in panel zone shear resistance beyond that predicted by the Von Mises criterion. Heavy columns with large flanges will benefit more from the higher resistance provided by this second term, as illustrated in Figure 8.7b. However, tests to date have been conducted on specimens scaled to represent moderate size columns, such as those indicated in Figure 8.6.

Note that the above model fails to check whether the flange flexural plastic capacity is reached before the shear deformation reaches $4\gamma_y$. It also does not consider many other effects that influence panel zone inelastic behavior, such as shear strain-hardening and true boundary conditions (in particular, plastic hinges in column flanges can be closer than $0.95d_b$ for different boundary conditions). However, given that this model was found to capture the few available experimental results reasonably well (as shown in Figures 8.7c and d where this model is called Model 3), it has been adopted in many seismic codes.

8.4.5 Design of Panel Zone

Until the Northridge earthquake, inelastic panel zone action was generally considered to be desirable for energy dissipation. By comparing the behavior of frame subassemblies tested to identical interstory drift levels, Krawinkler et al. (1971) observed that specimens exhibited greater energy dissipation when panel zone shear yielding occurred in combination with beam flexural yielding. When the panel zones tested by Krawinkler did not yield, greater beam flexural plastic rotations were necessary to reach the same interstory drifts, and the beams suffered more of the inelastic local buckling and lateral-torsional buckling that typically develop at large hysteretic flexural deformations, and thus exhibited more strength degradation (a logical consequence consistently observed in other tests, such as by Lee et al. 2005a for example). It was therefore suggested that "controlled" inelastic panel zone deformations would improve the overall seismic behavior of steel frames, particularly because the cyclic shear hysteretic behavior of well-designed panel zones does not exhibit strength degradation. Designers were also advised to consider panel shear deformations when calculating drifts.

Post-Northridge, the prevailing view is that, even though past studies have shown properly proportioned panel zones to be ductile, large panel zone distortions are not desirable because they can have a detrimental impact on behavior of beam-to-column connections (El-Tawil et al. 1999, El-Tawil 2000, Englekirk, 1999). Statistical variations in beam and column yield strengths also make it difficult to achieve in practice an ideal target "balance" of shared panel zone and beams yielding. For those reasons, the panel zone strength per the above equation can only be used to resist the panel shear demands corresponding to the beam plastic hinges having developed their expected strain-hardened strengths (AISC 341 and 358), when panel zone flexibility is considered in analysis (AISC 360). However, sharing of inelastic deformations between the panel zones and beams is not encouraged when beam flanges are directly welded to column flanges, because of the risk of crack initiation and propagation at that location under large panel shear distortions (Hamburger et al. 2009).

Unless superseded by requirements for specific prequalified connections, the panel zone design equation typically implemented in AISC 360 and CSA S16 respectively is:

$$V_u = 0.60 F_y d_c t_w \left(1 + \frac{3 b_{cf} t_{cf}^2}{d_b d_c t_w}\right) \tag{8.17}$$

and

$$V_u = 0.55 F_y d_c t_w \left(1 + \frac{3 b_{cf} t_{cf}^2}{d_b d_c t_w}\right) \le 0.66 F_y d_c t_w \tag{8.18}$$

with ϕ factors of 1.0 and 0.9, respectively for seismic applications, where t_w is the thickness of the panel zone including doubler plates if any, and all other terms have been defined previously (Lee et al. 2005b summarizes the ϕ factors used in various design code editions). The upper bound in CSA S16 is to limit the extent of panel zone deformations. When beams of different sizes frame into the column, it is conservative to use the largest of the beam depths for d_b. In nonseismic applications, the AISC 360 decreases the strength given by Eq. (8.15) to as low as 70% of the calculated value when the axial load exceeds 75% of the column plastic axial strength (i.e., 0.75 P_y); some researchers have argued that further reductions are necessary to properly account for the effect of axial forces (Chen and Liew 1992). However, in seismic applications, such high axial loads are rarely found in the columns of ductile moment frames.

When the panel zone of a column has insufficient strength, doubler plates can be added locally to increase the column web thickness; this has proven to be an economical solution in North America. To be considered effective in seismic applications, doubler plates must be detailed in accordance to AISC 341 requirements. In one such detail, for which doubler plates are placed next to the column web, typically fillet welded along the plate width and welded to the column flanges to develop the design shear strength of the doubler plate, magnetic particle testing is required to ensure that flaws have not been induced in the k-area region (see Chapter 2). An alternative detail permitted by AISC 341 uses a pair of doubler plates symmetrically located away from the column web, one-third to two-thirds of the distance between the beam flange tip and column centerline (Lee et al. 2005b), but has been reported to be more expensive as thicker plates are required due to stability requirements (Hamburger et al. 2009).

In addition to traditional web slenderness limits, seismic design codes typically require that panel zone thickness be at least:

$$t_z \geq \frac{d_z + w_z}{90} \tag{8.19}$$

to prevent premature local buckling under large cyclic inelastic shear deformations. In this empirical equation, d_z is the panel zone depth between the continuity plates, w_z is the panel zone width between the column flanges, and t_z is the panel zone thickness. If doubler plates are used to increase the thickness of the panel zone, their individual thickness must also satisfy the above equation. Note that t_z can be taken as the sum of the panel zone and doubler plate thicknesses only if the doubler plates are connected to the panel zone with plug welds in a manner to preclude independent buckling of these individual elements. Hamburger et al. (2009) indicated that selecting bigger columns that would not need doubler plates can be more economical that installing doubler plates (for column weight increases of up to 100 lb/ft for standard frame geometries).

Finally, note that one should consider panel zone deformations when calculating frame deformations. However, designers have typically neglected panel zone flexibility when conducting analyses with line representations of frames. In such models, finite joint sizes are ignored, structural members are modeled by line elements at their centers of gravity, and the flexible lengths of beams and columns are taken as the center-to-center distances between their intersection points. In more exact models, finite joint sizes are considered, member flexibility is derived from the free lengths between the faces of columns and beams, and the flexibility of panel zones is included. For the types and geometries of frames typically used in buildings, the error obtained through use of the simpler model has been reported to be negligible, particularly in view of all other uncertainties involved in the process (Englekirk 1994, Wakabayashi 1986), and AISC 341 considers that use of that simpler model meets the AISC 360 requirement to account for the effect of panel zone deformations in the analysis. The engineer should nonetheless beware of instances when design conditions and/or frame geometry would make this error significant.

8.5 Beam-to-Column Connections

The seismic response of a ductile moment frame will be satisfactory only if the connections between the framing members have sufficient strength to permit attainment of the desired plastic collapse mechanism, sufficient stiffness to justify the assumption of fully rigid behavior typically assumed for analysis, and adequate detailing to permit development of the large cyclic inelastic deformations expected during an earthquake without any significant loss of connection strength. Beams, panel zones, and to some extent, columns can dissipate seismic energy through plastic cyclic rotations, but connection failure is not acceptable. From that perspective, bolts and welds are considered to be nonductile elements that must be designed with sufficient strength to resist the maximum forces that can develop in the connected elements. Even though bolts and, to some extent, welds are capable of plastic deformations, their small size and limited ductility generally make those deformations ineffective at the structural level.

Moment frames acquired their excellent reputation as seismic framing systems following the San Francisco 1906 earthquake. However, even though the few midrise steel buildings constructed at that time weathered the earthquake well, one must recognize that the heavily riveted moment connections of that era bear little resemblance to current seismic moment connections. Examples of connections used in the first half of the 1900s are shown in Figure 8.8 for comparison with the standard modern connections illustrated later in this chapter. The oft-stated "excellent performance of steel moment frames in past earthquakes" was biased, to some degree, by the track record of buildings with details that became obsolete in the 1960s when high-strength bolts and welding became the preferred fastening methods in seismic regions. It is the behavior of these modern moment connections that is addressed here.

8.5.1 Knowledge and Practice Prior to the 1994 Northridge Earthquake

The welded moment connection details widely used in many North American seismic regions (notably California) during the 25 years preceding the Northridge earthquake are shown at the top of Figure 8.9. Although the simple plastic theory formulated in the first chapters of this book would suggest that full-penetration groove welds are required in both flanges and the web of a beam to create a connection capable of resisting the beam's plastic moment, by the 1960s the building industry was already frequently using an alternative more economic (easier to construct) connection detail with fully welded flanges and a bolted web connection.

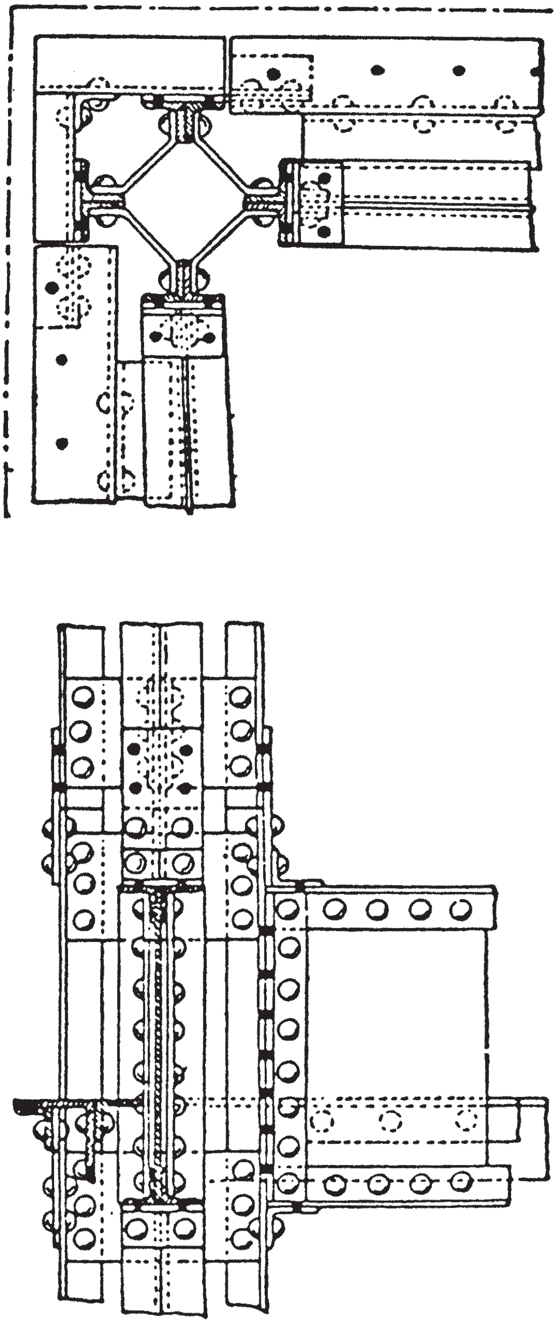

(a)

Figure 8.8 Examples of frame connections: (a) at turn-of-the-century; (b) in the 1930s. (*Part a from* Journal of Constructional Steel Research, *vol. 10, William McGuire, Introduction to Special Issue, 1988, with permission from Elsevier Science Ltd., U.K. Part b from* Steel Tips—Structural Steel Construction in the '90s *by F. R. Preece and A. L. Collin, with permission from the Structural Steel Education Council.*)

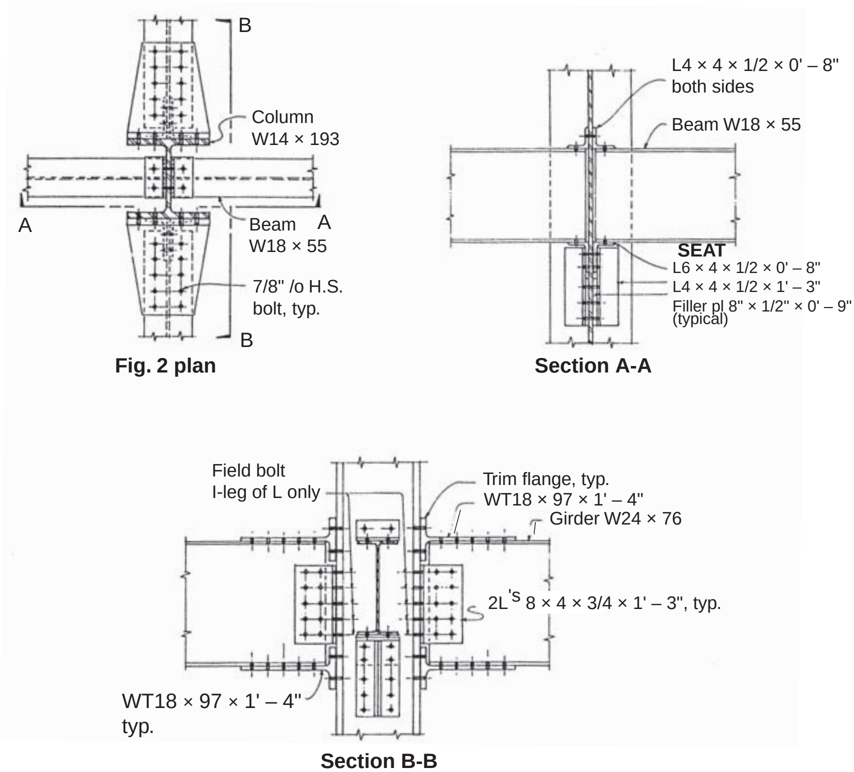

(b)

FIGURE 8.8 (*Continued*)

The first tests to investigate the cyclic plastic behavior of moment connections were conducted in the 1960s (Popov and Pinkney 1969). Various popular details were considered, as shown in Figure 8.9, and specimens with welded flanges and bolted web connections showed superior inelastic behavior compared with the cover-plated moment connection and the fully bolted moment connection alternatives. Typical hysteretic loops are presented in Figure 8.10. The fully bolted detail was considered less desirable because slippage of the bolts during cyclic loading produced a visible pinching of the hysteretic loops and because tensile rupture occurred along a net section between bolt holes.

Further tests in the 1970s (Popov and Stephen 1970) compared the relative performance of the commonly used welded flange-bolted web detail and fully welded connections. Sample results are shown in Figure 8.11. Both details were significantly stronger than predicted by the simple plastic theory (with F_y = 36 ksi), as clearly shown in Figure 8.11, and the fully welded connection exhibited more ductile behavior (Figure 8.11a versus 8.11b). The moment connections with

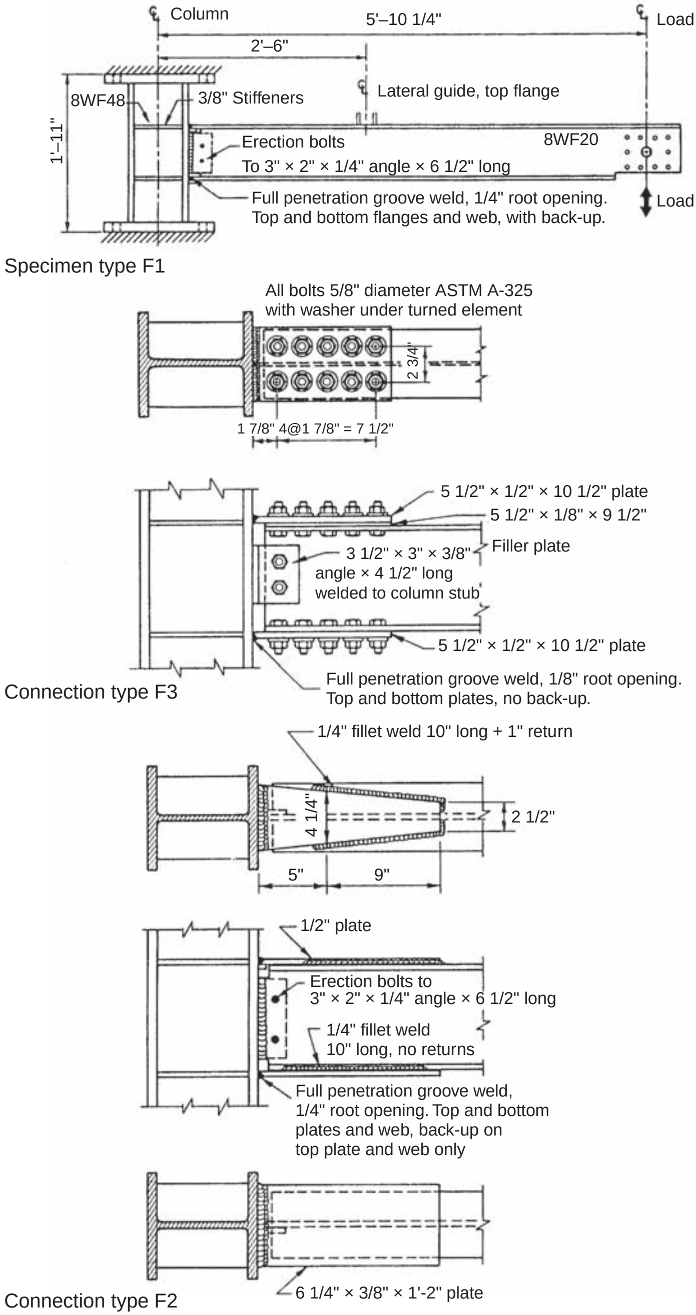

Figure 8.9 Typical connection details considered in early tests of moment connections by Popov and Pinkney. (*From ASCE* Journal of the Structural Division, *vol. 95*, *"Cyclic Yield Reversal in Steel Building Connections" by E. P. Popov and R. B. Pinkney, 1969, with permission from the American Society of Civil Engineers.*)

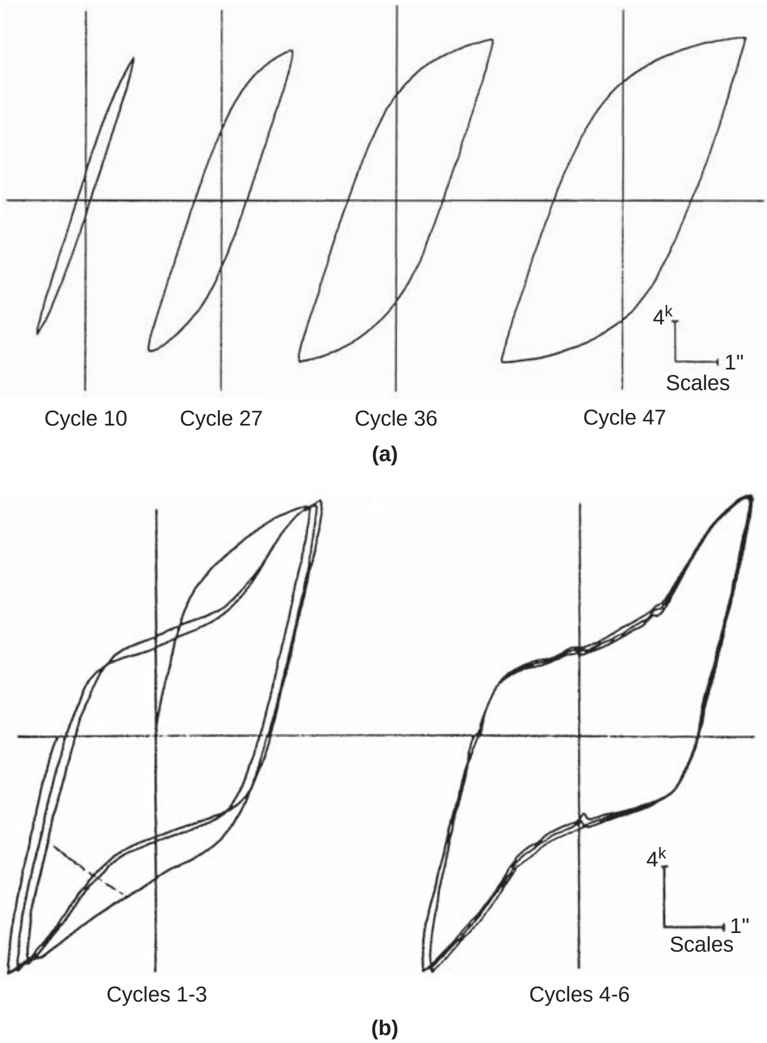

Figure 8.10 Examples of hysteretic behavior obtained in Popov and Pinkney's experiments for (a) specimen type F1, (b) specimen type F3—See Figure 8.9. (*From* ASCE Journal of the Structural Division, *vol. 95*, "*Cyclic Yield Reversal in Steel Building Connections" by E. P. Popov and R. B. Pinkney, 1969, with permission from the American Society of Civil Engineers.*)

bolted webs were also reported to fail abruptly, and their ductility was more erratic (Popov 1987, in a retrospective of past research). Nonetheless, connections with bolted web were judged to be sufficiently ductile and reported to be less costly to fabricate. It is interesting to note that Popov and Stephen (1972) also concluded that "the quality of workmanship and inspection is exceedingly important for the achievement of best results."

Further studies on frame subassemblies (Bertero et al. 1973, Krawinkler et al. 1971, Popov et al. 1975) investigated the effect of panel zone and column plastic hinging and helped make the welded flange-bolted web detail a prequalified moment connection provided that it was detailed according to predetermined rules. This standard

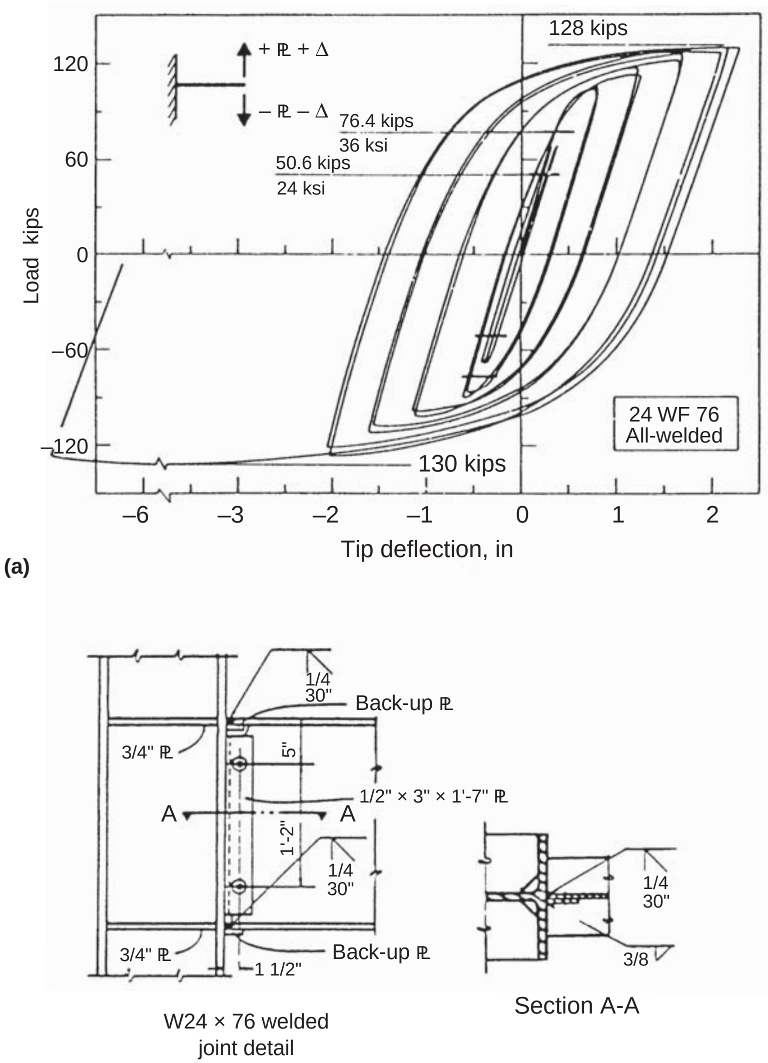

Figure 8.11 Hysteretic behavior of typical connection details having (a) fully welded webs. Results from tests conducted in early 1970s; (b) bolted webs. This connection is otherwise identical to the one shown in (a). Results from tests conducted in early 1970s. (*Parts a and b from* Journal of Constructional Steel Research, *vol. 8, E. G. Popov, "Panel Zone Flexibility in Seismic Moment Joints," 1987, with permission from Elsevier Science Ltd., U.K.*)

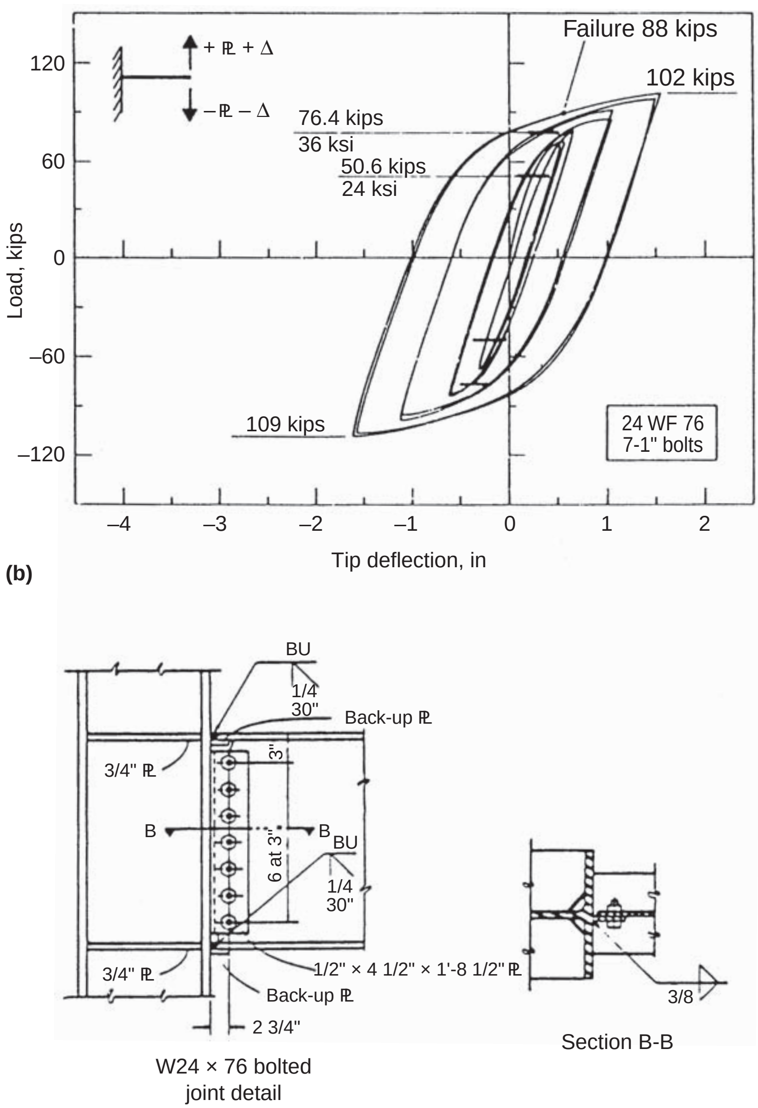

Figure 8.11 (*Continued*)

connection is illustrated in Figure 8.12, although some aspects shown on that detail (such as the supplemental fillet welds along part of the web tab) were actually implemented only in the late 1980s (ICBO 1988). This figure also summarizes some of the doubler plate details described in Section 8.4.5. Note that self-shielded flux-cored arc welding was commonly used, with E70T-4 or E70T-7 electrodes as the filler metal, as there was no specified notch toughness requirement for the filler metal.

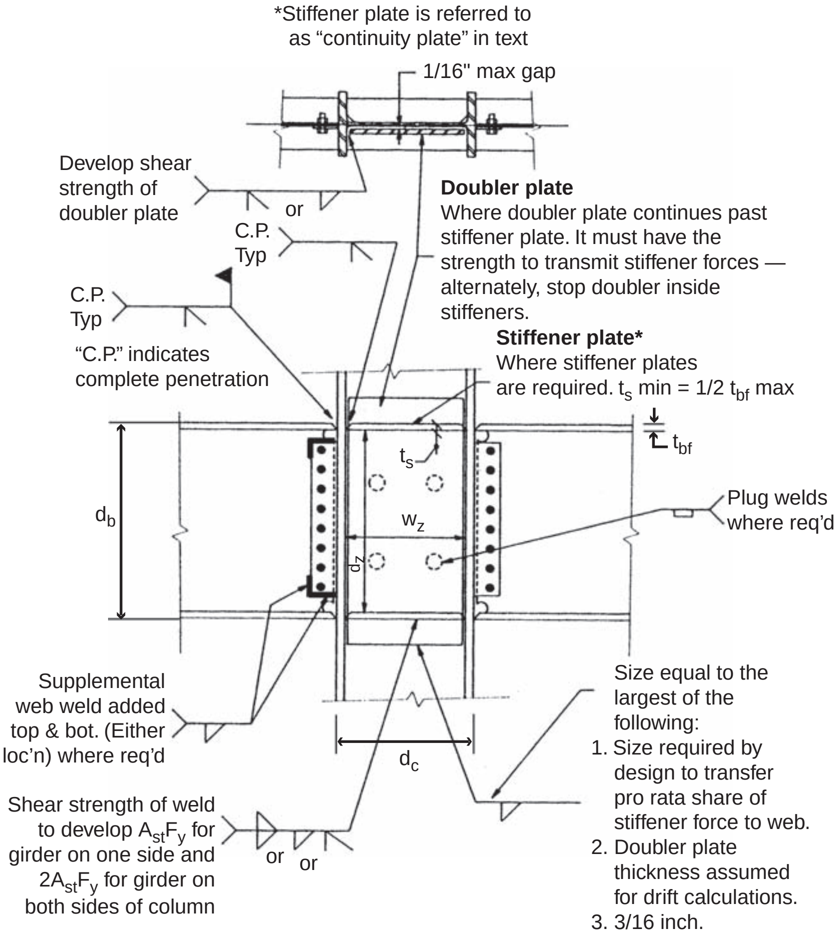

FIGURE 8.12 Prequalified moment-resisting frame detail in use prior to Northridge earthquake.

For a number of years, nearly all beam-to-column connections in structural systems designated as ductile moment-resisting frames were detailed to be able to transfer the nominal plastic moment of the beams to the columns (Roeder and Foutch 1995). As a result, relatively modest column and beam sizes were sufficient in those moment frames to provide the necessary seismic resistance. However, over the years, as a result of the cost premium commanded by full moment connections compared with shear connections, many engineers concluded that it was economically advantageous to limit the number of bays of framing designed as ductile moment-resisting frames. In the extreme, prior to the Northridge earthquake, some engineers routinely designed buildings having only four single-bay ductile moment frames (two in each principal direction, with each in a different plane to provide torsional resistance). This trend developed at the expense of a dramatic loss in structural redundancy, which can be argued to be a nonnegligible reduction in overall structural safety, particularly in the event of construction defects. Moreover, considerably deeper beams, columns with thicker flanges, and bigger foundations were needed in these single-bay ductile moment frames than in the multi-bay ones previously used to resist the same seismically induced forces.

In that regard, some pre-Northridge tests on beam-to-column subassemblies provided an opportunity to investigate potential size effects. In particular, tests by Tsai and Popov (1988, 1989) indicated that some prequalified moment connections in ductile moment frames with W460 and W530 beams, equivalent to W18 and W21 in U.S. units and thus similar in depth to those tested by Popov and Stephen (1970, 1972), were not as ductile as expected when the web accounted for a substantial portion of the beam's plastic moment capacity. As shown in Figure 8.13, specimens with the welded flange-bolted web connections (specimens 3 and 5) failed abruptly before developing adequate plastic rotations. These specimens were constructed by a commercial fabricator, and the welds had been inspected ultrasonically and found to be satisfactory. The use of bolts with twist-off ends for tension control in the beam web (specimens 17 and 18) or the use of supplemental web welds (specimens 13 and 14) improved hysteretic performance and delayed abrupt failure. It is noteworthy that two specimens with bolted webs failed prior to reaching M_p (even though they were supplied from a commercial fabricator), and two other specimens with fully welded flanges and webs exhibited significant ductility (specimens 9 and 11), as shown in Figure 8.13.

Further to these findings, the prequalified welded flange-bolted web connection detail was modified in the late 1980s for beams having a ratio Z_f/Z less than 0.7, where Z_f is the plastic modulus of the beam flanges alone, and Z is the plastic modulus of the entire beam section. For those beams, supplemental welds on the bolted web shear tabs were required (i.e., in addition to the usual complete penetration single-bevel groove welds on the beam flanges and the bolted shear tab for the web), as shown in Figure 8.12. The supplemental welds were also required to have a minimum strength of 20% of the nominal flexural strength of the beam web.

Given that those new requirements were supported by only limited test data, Engelhardt and Husain (1993) conducted additional tests to investigate the effect of Z_f/Z on rotation capacity using slightly deeper beams than those tested by Tsai and Popov (W460 to W610 shapes, equivalent to W18 to W24 in U.S. units). Interestingly, some of the specimens tested by Engelhardt and Husain showed a disturbing lack of ductility, even though all specimens had been constructed by competent steel fabricators using certified welders, and all welds had been ultrasonically tested by certified inspectors. Some specimens exhibited almost no ductile hysteretic behavior (e.g., Figures 8.14a and d), whereas others behaved in a ductile manner

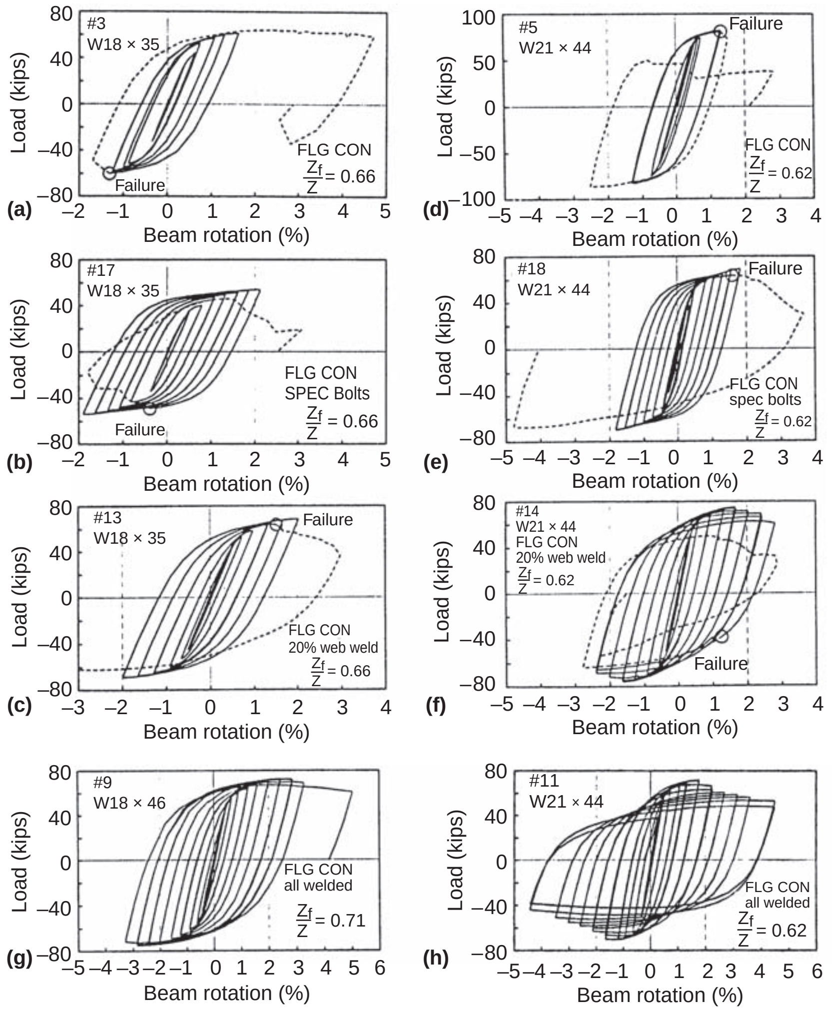

Figure 8.13 Hysteretic loops for moment-resisting frame connections with low Z_f/Z values and different beam web connection methods: (a) W460 × 52 (W18 × 35) beam with bolted web, (b) W460 × 52 beam with tension-control bolts (special bolt whose ends twist off upon reaching specified bolt tension), (c) W460 × 52 beam with bolted web and 20% supplementary weld, (d) W530 × 66 (W21 × 44) beam with bolted web, (e) W530 × 66 beam with tension-control bolts, (f) W530 × 66 beam with bolted web and 20% supplementary weld, (g) W460 × 68 (W18 × 46) beam with fully welded web, and (h) W530 × 66 beam with fully welded web. (*From* Engineering Journal, *2nd Quarter 1989, "Performance of Large Seismic Steel Moment Connections under Cyclic Loads" by E. P. Popov and K. C. Tsai, with permission from the American Institute of Steel Construction.*)

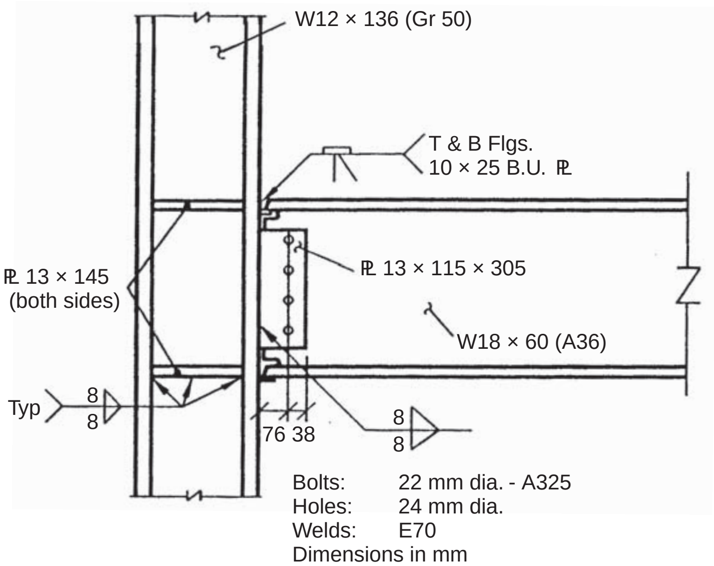

(a)

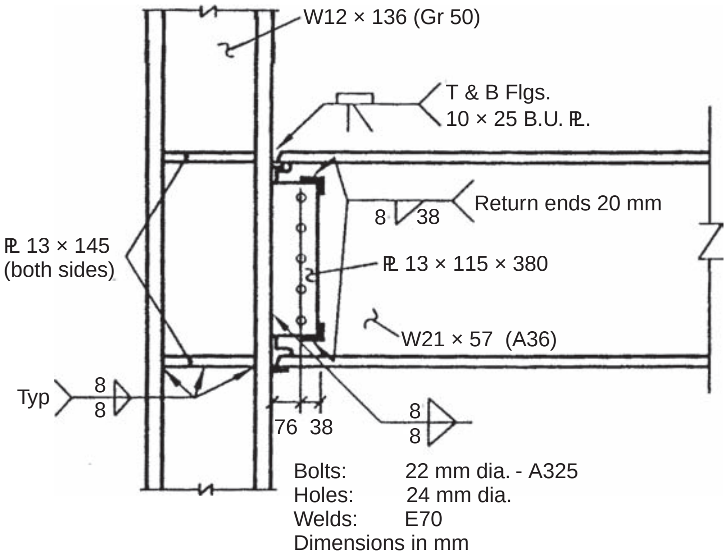

(b)

Figure 8.14 Engelhardt and Husain's tests: (a) specimen 4 details; (b) specimen 7 details. (c) typical weld and cope details; (d) resulting moment versus plastic rotation hysteretic curves for Specimen 4; (e) resulting moment versus plastic rotation hysteric curves for specimen 7. (*Parts a to e courtesy of M. D. Engelhardt, Dept. of Civil Engineering, University of Texas, Austin.*)

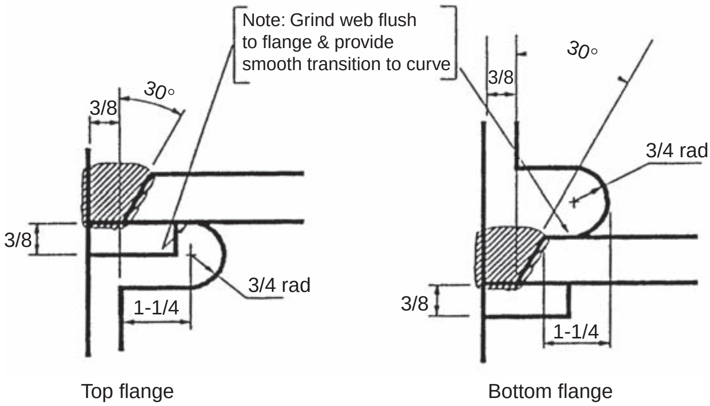

(c)

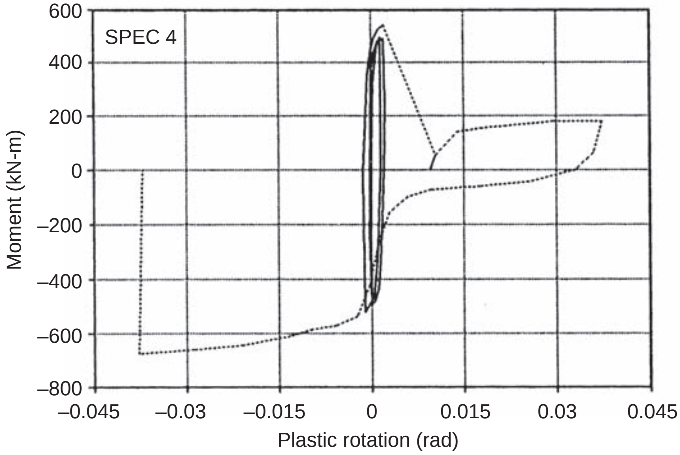

(d)

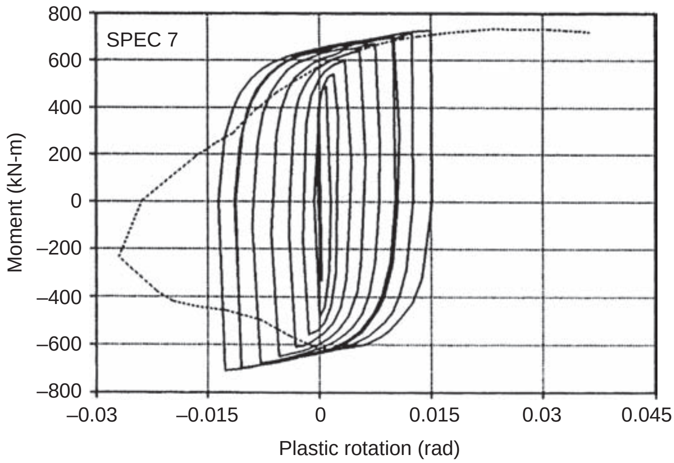

(e)

Figure 8.14 (*Continued*)

until a sudden rupture developed in the connection (e.g., Figures 8.14b and e). The amount of hysteretic behavior developed prior to failure bore no relationship to Z_f/Z. Three specimens suffered sudden fracture at the weld-to-column interface at the beam bottom flange (such as the specimen shown in Figure 8.14a); the remaining specimens suffered gradual fracture at the same location (three specimens), at the top flange (one specimen), or through the bottom beam flange outside the weld (one specimen).

Engelhardt and Husain also compared their results with past experimental data. Assuming that connections must have a beam plastic rotation capacity of 0.015 radian to survive severe earthquakes, they found that none of their seven specimens could provide this rotation capacity (Figure 8.15), nor could most connections in tests conducted by other researchers. As a result of these observations, Engelhardt and Husain expressed concerns about the welded flange-bolted web detail commonly used in ductile moment frames in severe seismic regions.

And then the Northridge earthquake happened.

8.5.2 Damage During the Northridge Earthquake

On January 17, 1994, an earthquake of moment magnitude 6.7 struck the Los Angeles area. The epicenter of the earthquake was at Northridge in the San Fernando valley, 32-km northwest of downtown Los Angeles. This earthquake caused over $20 billion in damage, becoming the most costly disaster ever to strike the United States at the time (EERI 1995). Structural and nonstructural damage to buildings and infrastructure was widespread and considerable, but there were no reports of significant damage to steel building structures immediately following the earthquake. This should not come as a surprise. Inspectors, as well as reconnaissance teams dispatched by various engineering societies and research centers following a major earthquake can report only readily visible damage not obstructed by nonstructural elements. Careful inspection of a building's steel frame requires the removal of architectural finishes (cladding, ceiling panels, etc.) and of the fireproofing material covering the steel members—an expensive and time-consuming process. Given that no steel building collapsed or exhibited noticeable signs of structural distress (EERI 1996; Tremblay et al. 1995), the discovery of critical but nonfatal damage was precluded without authority to expose part of the structure.

However, in the months following the earthquake, engineers discovered important damage to steel structures, including a large number of beam-to-column connection fractures. Initially, damage was often found accidentally, while engineers were trying to resolve nonstructural problems reported by owners following the earthquake. In one case, for example, beam-to-column connection fractures would

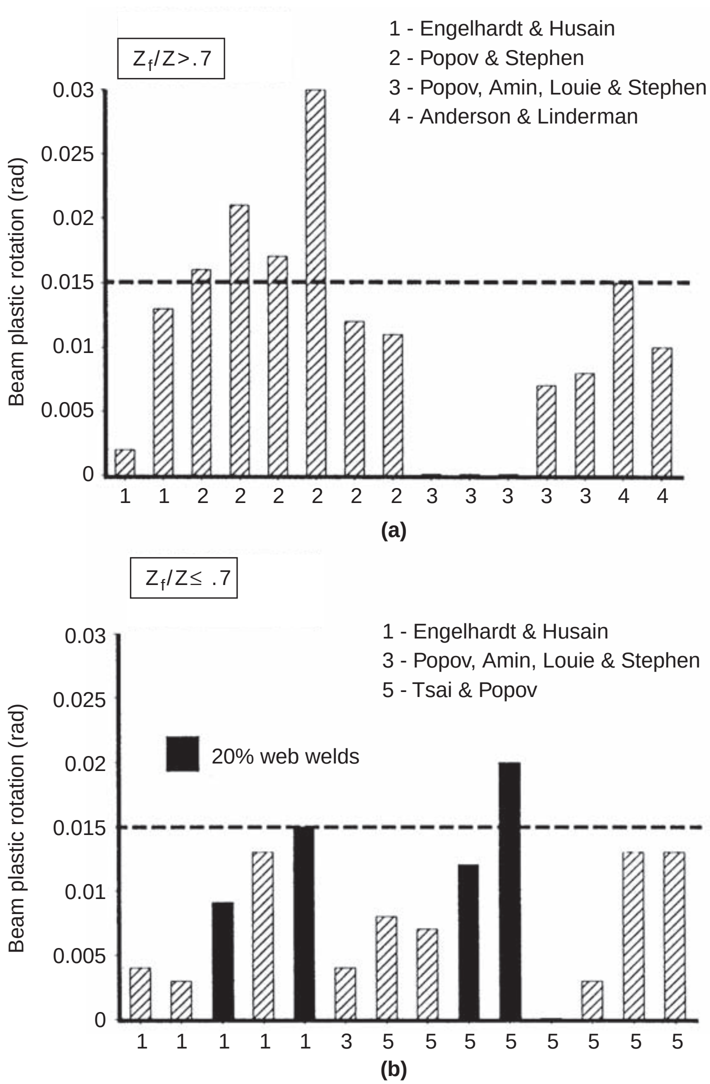

FIGURE 8.15 Engelhardt and Husain's comparison of beam plastic rotations obtained in past test for (a) specimens with $Z_f/Z > 0.70$ and (b) specimens with $Z_f/Z \leq 0.70$. (*Courtesy of M. D. Engelhardt, Dept. of Civil Engineering, University of Texas, Austin.*)

have remained hidden, if not for complaints by occupants about persisting elevator problems.

The structural engineer noticed that the building was leaning in one direction and requested that some connections be exposed. Informal discussion of such problems within the profession led other structural engineers to recognize the potential significance of the problem and to require random inspection of joints in various steel structures. This led to the discovery of more failures. Connection fractures were found in buildings of various vintages and heights (1 to 27 stories), including new buildings under construction at the time of the earthquake (Engelhardt and Sabol 1995, FEMA 2000g, SAC 1995a, Youssef et al. 1995). For example, in a steel building still under construction at the time of the Northridge earthquake, one that had apparently survived the earthquake intact, random inspection revealed severe fractures in nearly all beam-to-column connections in one moment-resisting frame. Typically, in the damaged connections of that building, the column flange fractured at the level of the full-penetration weld of the beam's bottom flange to the column, and the crack propagated horizontally a short distance into the column web and then vertically toward the other flange of the same beam (Figure 8.16).

Within two months, more than a dozen buildings with brittle failures of beam-to-column moment connections attributable to the Northridge earthquake had been reported. This became a rather delicate issue given that most buildings in which fractures were discovered were still occupied after the earthquake. A first special AISC task committee meeting allowed researchers and practicing engineers to meet and exchange information (AISC 1994). Tentative provisions for the repair of observed damage were formulated, and although many potential causes for the problem could be identified, failures could not be conclusively explained.

Three months following the earthquake, approximately 50 steel buildings were known to have suffered moment frame damage, based on records from the Los Angeles Department of Building and Safety. By the end of 1994, approximately 100 had been identified, but the actual number of buildings with damaged moment frames was suspected to be higher, given that some owners disallowed inspection of their buildings (SAC 1995a, SAC 1995b, FEMA 2000g). For perspective, approximately 500 buildings with steel moment frames were located where severe ground shaking occurred during that earthquake. Lessons from the Northridge earthquake also prompted engineers to suspect that damage to steel moment frames might have occurred in previous earthquakes, and remained hidden. In the San Francisco Bay Area, hit by the Loma Prieta earthquake in October 1989 (EERI 1990), this suspicion has been confirmed as buildings with damaged connections were discovered as inspection opportunities arose (Rosenbaum 1996). Similar damage was also reported in a limited number of buildings previously affected by the 1992 Landers and 1992 Big Bear earthquakes (FEMA 2000a).

Various types of damage were discovered during the surveys conducted following the Northridge earthquake. Cracks that developed at or near beam bottom flanges were most frequently reported.

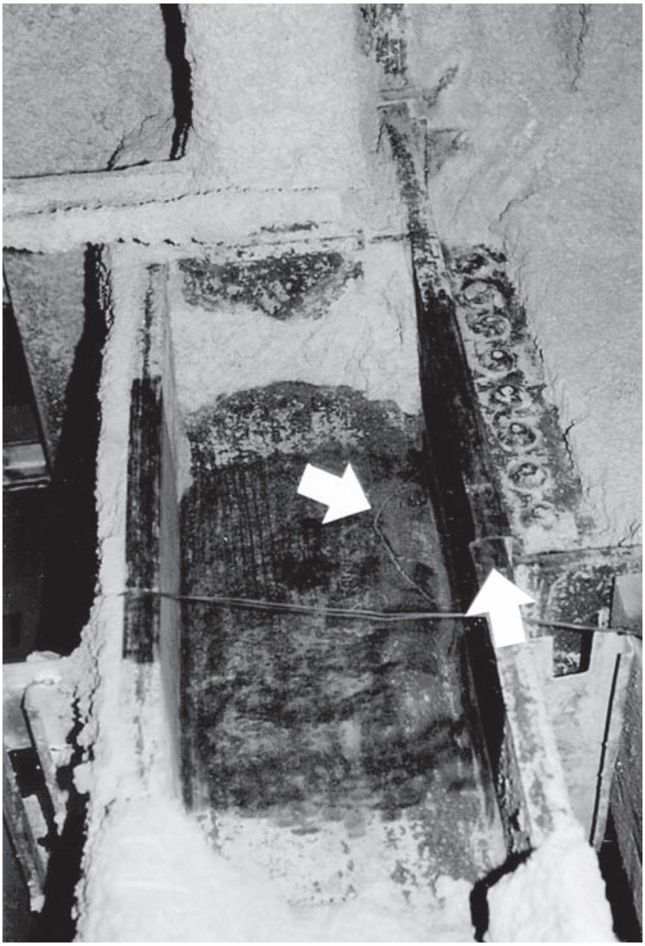

(a)

Figure 8.16 Examples of Northridge fractures propagating through column flanges: (a) column without stiffener, with fracture propagating into column web and vertically toward top flange; (b) close-up view of fracture shown in (a); (c) column with partial stiffener, with fracture through column flange; (d) close-up view of fracture shown in (c).

Figure 8.17 summarizes the various types of fractures observed in that case (types 1 to 8). Most frequently, cracking initiated near the steel backup bar in the root pass of the weld. Those cracks either remained within the weld material, propagating through part or all of the flange weld (type 1 and 2 respectively), or spread into the adjacent base metal (types 3 to 6). Cracks in the adjacent steel propagated into the column flange either vertically (types 3 or 4, depending on

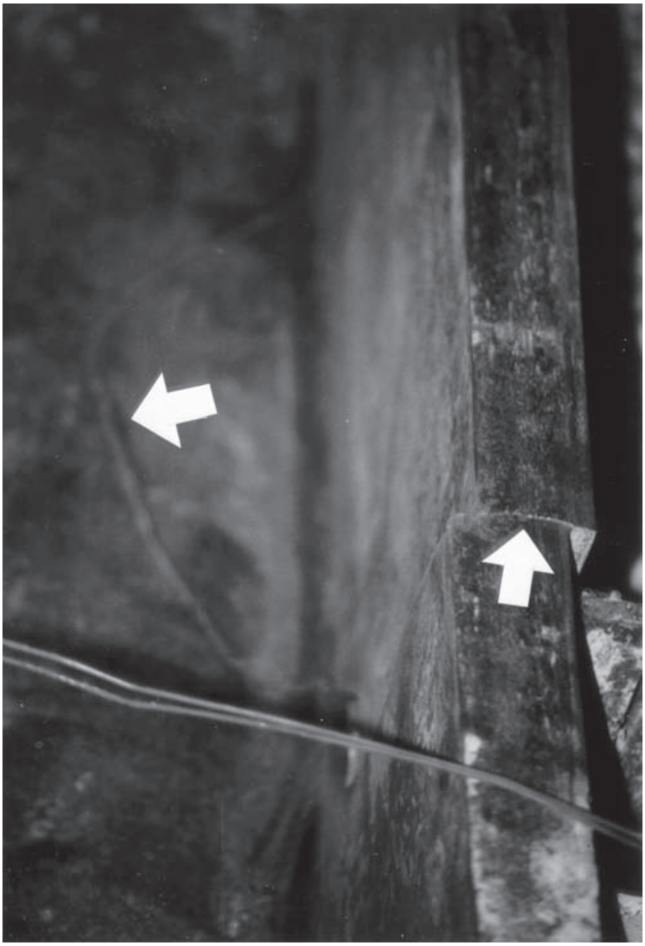

(b)

Figure 8.16 (*Continued*)

whether a piece of the column was completely pulled out in the process) or horizontally by fracturing the entire column flange (type 5) and sometimes a significant portion of the column web (type 6). In some cases, cracks that extended into the column web ruptured the entire column section horizontally or were found to bifurcate and propagate vertically toward the other flange of the beam in which it initiated. In a few instances, cracking initiated at the weld toe and propagated through the flange heat-affected zone (type 7), and at least one case of lamellar tearing of a column flange has been reported (type 8) (Bertero et al. 1994). Examples of such damage are shown in Figures 8.18, 8.19, and 8.20.

(c)

Figure 8.16 (*Continued*)

These cracks and fractures were frequently reported in the absence of similar damage to the top flange. In a few buildings, there were instances of weld damage at the beam top flanges without damage to the corresponding bottom flange welds, but generally, both flanges were found to have suffered damage when cracks were found in the top flange welds. Only a few instances of base metal fractures adjacent to beam top flanges were reported, but other such failures may have been left undetected in many cases because floor slabs frequently obstruct inspection at that location (Youssef et al. 1995).

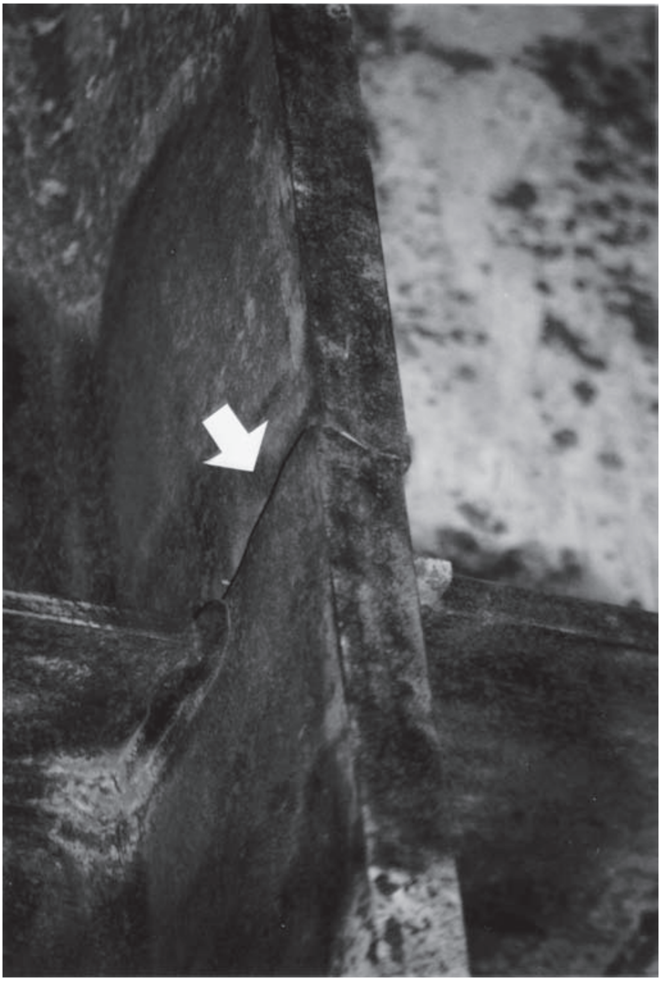

(d)

Figure 8.16 (*Continued*)

The damage reported above was sometimes accompanied by severe damage to the beam's shear tabs, with vertical net section fractures between the bolt holes over part of the height of the web connector (this occurred after the beam flange fractured completely). Note that gravity load resistance could be seriously jeopardized when complete rupture of such shear tabs follows flange fracture. Finally, in a few instances, panel zone yielding was also observed (Youssef et al. 1995).

Given that the above damage was reported in buildings having widely different characteristics, attempts were made to correlate

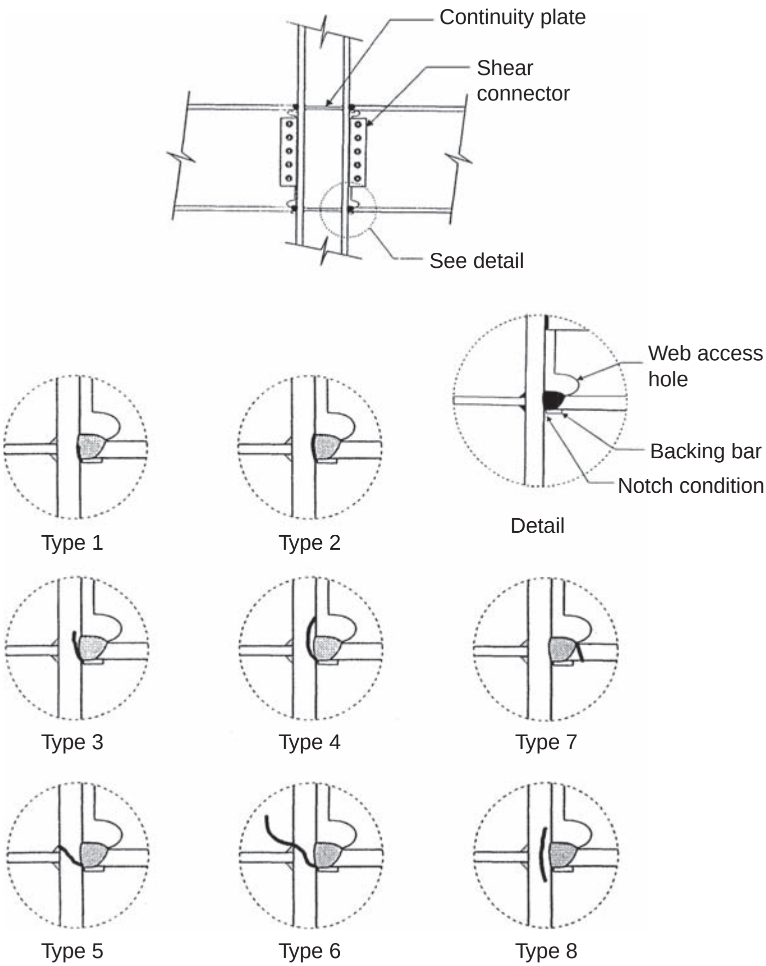

Figure 8.17 Typical welded flange and bolted web beam-to-column connection in moment-resisting frames, with close-up view of notch condition at backing bar, and eight types of reported Northridge fractures. (*Courtesy of R. Tremblay, Dept. of Civil Engineering, Ecole Polytechnique, Montreal, Canada.*)

damage statistics to beam depth, beam span, steel grade, design details, shear connection type, weld process, composite-beam behavior, material, and construction quality. These studies have proven inconclusive (Youssef et al. 1995).

Although no steel buildings collapsed during the Northridge earthquake, the discovery of these unexpected failures forced the structural engineering community to reexamine its design, detailing, and construction practice for steel moment frames. A sense of urgency was fueled by the recognition that the Northridge earthquake was

(a)

(b)

FIGURE 8.18 Four examples of bottom flange welds fractures. In case (a), for a fracture located near the face of a box column, a business card is dropped in to illustrate that the fracture passes completely through the weld. (*Parts a to c are courtesy of M. D. Engelhardt, Dept. of Civil Engineering, University of Texas, Austin*. *Part d is courtesy of David P. O'Sullivan, EQE International, San Francisco*.)

(c)

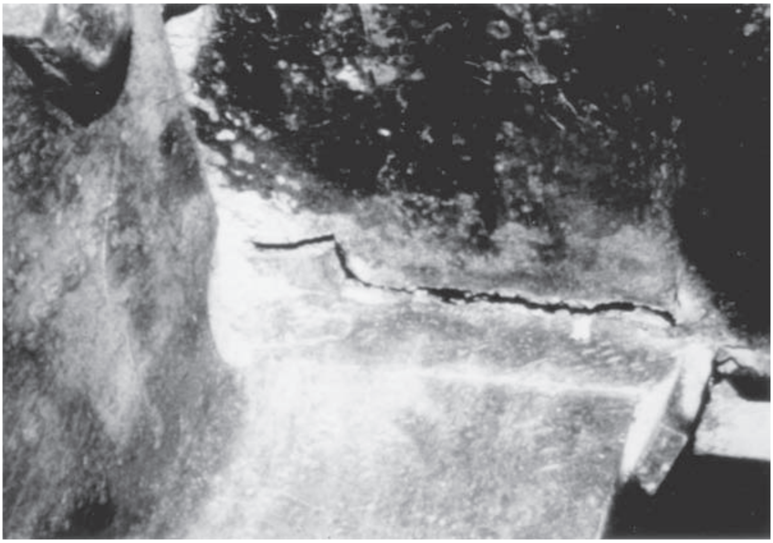

(d)

Figure 8.18 (*Continued*)

certainly not the largest earthquake expected to occur in North America and that steel frames could be subjected to larger inelastic deformation demands in future earthquakes. To develop short-term and long-term solutions, extensive research activities were initiated by federal agencies and private industries. More notable was a

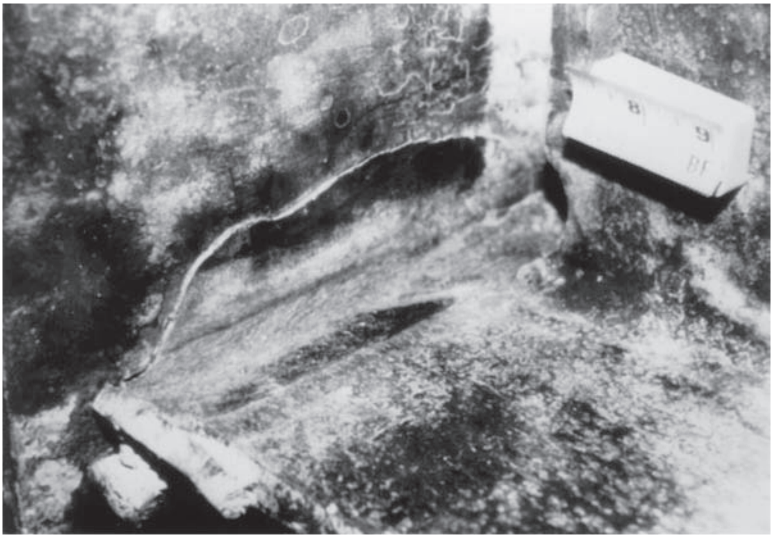

(a)

(b)

Figure 8.19 Two examples of divot fracture at beam bottom flange. (*Courtesy of David P. O'Sullivan, EQE International, San Francisco.*)

coordinated research effort initiated through a joint venture of the Structural Engineers Association of California (SEAOC), the Applied Technology Council (ATC), and the California Universities for Research in Earthquake Engineering (CUREe). The SAC Joint Venture combined the efforts of practicing engineers, code writers, industry

(a)

(b)

Figure 8.20 Examples of fractured columns, with fractures propagating from near the beam bottom flange weld (on the right side in both cases) to the column flange and into the column web. (*Part a courtesy of M. D. Engelhardt, Dept. of Civil Engineering, University of Texas, Austin. Part b courtesy of David P. O'Sullivan, EQE International, San Francisco.*)

representatives, and researchers who share either a professional or a financial interest in the resolution of the problems in beam-to-column connections that arose as a result of the Northridge earthquake. This venture published important documents reporting findings (e.g., SAC 1995a, 1995b, 1997, 1999), and design recommendations (FEMA 2000a, 2000b, 2000c, 2000d) later integrated in various consensus codes, specifications, and standards.

8.5.3 Causes for Failures

Numerous factors have been identified as potentially contributing to the poor seismic performance of the pre-Northridge steel moment connections, and failures may have been caused by different combinations of those factors. After much research, debate, and deliberation, the professional engineering community did not single out a unique or dominant reason for the observed failures, but rather concluded that all of those factors had a relative detrimental influence. Thus, design solutions and changes to practice enacted since then have aimed to redress deficiencies related to every plausible cause of connection damage. A review of some of these conjectured causes is therefore worthwhile and is presented below. The most important concerns are addressed here, and related issues have been grouped under arbitrarily defined broad categories. A more complete summary of all major and minor concerns expressed following the Northridge earthquake is available elsewhere (SAC 1995a).

8.5.3.1 Workmanship and Inspection Quality

A percentage of the damage observed following past earthquakes worldwide has been a consequence of substandard workmanship and improper inspection, particularly in countries with poor code enforcement and contractors who hide construction (detailing) mistakes. Hence, as Northridge failures started to appear, many asserted that deficient workmanship and inspection were to blame. Ignorance of standard welding requirements was found to be disconcertingly widespread among structural engineers (SAC 1995a), and some have reported evidence of poor quality welds with defects that escaped detection prior to the earthquake. Nonetheless, although lack of adherence to standard welding procedure generally made matters worse, improved workmanship and inspection quality alone would not have been sufficient to prevent the Northridge failures (specimens constructed under controlled conditions still exhibited erratic behavior in post-Northridge laboratory tests, as described later).

8.5.3.2 Weld Design

In the pre-Northridge connection described earlier, the beam web creates an obstacle when one is executing the bottom flange groove weld; deposition of weld metal is interrupted at the beam web at every pass. As a result, there is a high probability of defects in the bottom flange weld at that location. Those defects are particularly difficult to detect through ultrasonic inspection because they are frequently hidden in the portion of the testing signal that is interpreted as interference because of the presence of the beam web.

8.5.3.3 Fracture Mechanics

The backup bars used for downhand welding of beam flanges were typically left in place prior to 1994 after completion of the weld. From a strength perspective, these small bars were perceived as additional material that could be left in place without detrimental effects. However, from a fracture mechanics perspective, the small unwelded gap between the edge of the backup bar and the column flange can be considered a notch or crack that acts as a stress raiser, from where new cracks can originate and propagate into the weld or adjacent base metal (see Figure 8.21). This problem is further compounded if the weld metal has low notch-toughness.

Similarly, a large number of defects can exist in the weld runoff tabs installed to allow extension of the weld passes beyond the flange width (as required by the American Welding Society). Runoff tabs collect the defects commonly introduced by the starting and ending of each weld pass in a zone removed from the flange. If left in place, the weld runoff tabs provide an opportunity for these defects, even though located outside the flange, to propagate into the weld proper. This propensity to crack propagation was further accentuated by the very low Charpy-V notch toughness of the E70T-4 electrodes (Figure 8.22) that were commonly used as filler metals in pre-Northridge welds (Kaufman et al. 1996).

8.5.3.4 Base Metal Elevated Yield Stress

Many engineers had resorted to using A36 steel for beams and A572-Grade 50 for columns to facilitate compliance with the philosophy of strong-column/weak-beam design. The use of Grade 50 steel for columns also increased the panel zone strength, minimizing the need for doubler plates. However, a significant increase in the actual yield and ultimate strengths of the standard A36 steel produced in the United States has been observed over the years, in spite of the absence of changes to the steel grade specification itself. This increase is primarily due to changes in the steel-making process in the 1980s, when integrated mills were replaced by mini-mills that use highly efficient electric arc furnaces to produce steel shapes from scrap steels. SSPC (1994) and SAC (1995b) reports average yield and ultimate strengths of 338 MPa (49 ksi) and 475 MPa (69 ksi) for A36 steel, and maximum yield strengths as high as 496 MPa (72 ksi), as shown in Table 8.1. Some steel producers have also introduced dual-certified steel, which is steel simultaneously in compliance with all the minimum chemical and strength requirements of both A36 and A572-Grade 50 steels.

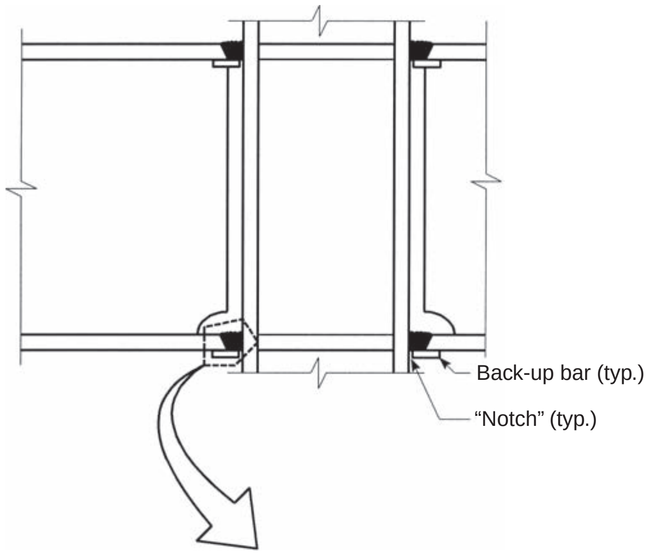

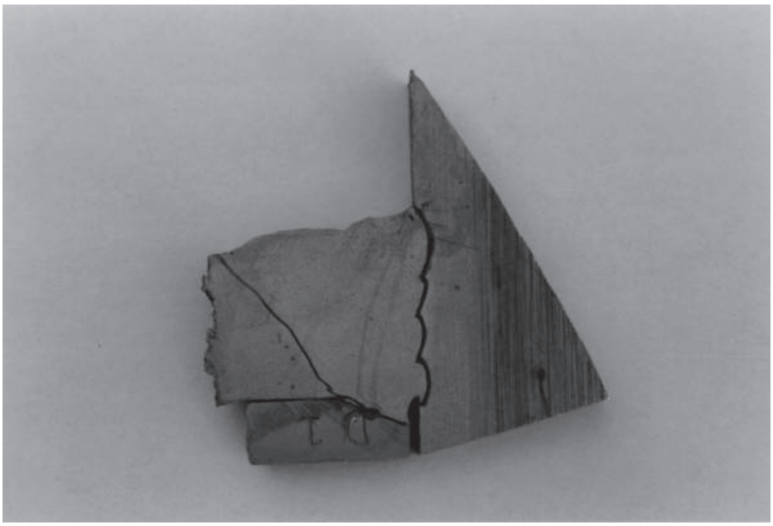

Figure 8.21 Example of fractured beam bottom flange in which a crack originated at the unwelded gap between the edge of the backup bar and the column flange. (*Courtesy of J. E. Patridge, Smith-Emery Co., Los Angeles.*)

Therefore, engineers who assume A36 steel properties for the design of beams may seriously underestimate the beam flange forces acting on the groove welds, and unintentionally select welds weaker than the base metal, if the contractors supply steel with yield strength in excess of 350 MPa (50 ksi). Furthermore, the intended strong-column/

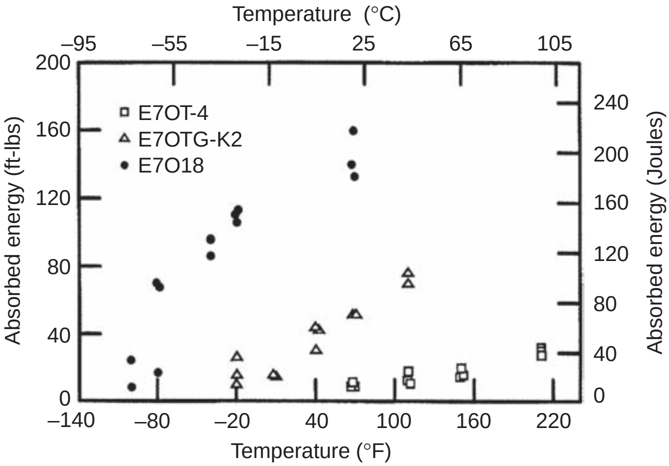

FIGURE 8.22 Charpy-V notch test results on three different types of weld filler metal. (*From* Modern Steel Construction, *vol. 36, no. 1, "Achieving Ductile Behavior of Moment Connections" by E. J. Kaufmann et al., 1996, with permission from the American Institute of Steel Construction.*)

weak-beam design may in practice be a weak-column/strong-beam system if the yield strength of the beam substantially exceeds the nominal value.

To ensure that representative yield and tensile strength values are used in design when this knowledge is critical, correction factors were developed to relate actual expected strength to minimum specified strengths, using the data from Table 8.1 and other complementary studies (Bartlett et al. 2003, Liu 2003). The corresponding expected yield strength, F_y^{exp}, and expected tensile strength, F_u^{exp}, (called "actual" strengths in some references) are defined as $F_y^{exp} = R_y F_y$ and $F_u^{exp} = R_t F_u$, where R_y is the ratio of the expected yield stress to the specified minimum yield stress, and R_t is the ratio of the expected tensile strength to the specified minimum tensile strength.

Table 8.2 shows sample results specified by AISC 341 for various structural shapes and steel grades, including the A992 and A913 grades having specified upper limits on yield strength (see Section 2.2.5). Values for other structural shapes and steel are provided in AISC 341.

8.5.3.5 Welds Stress Condition

The ultimate stress applied to the weld of the beam flange can be estimated if one assumes that the bolted web cannot transfer bending moments. Indeed, researchers have observed that web bolts

Statistics	A36 Steel	Dual Grade	A572 Grade 50
Yield Stress (ksi)*			
Specified	36.0	50	50
Mean	49.2	55.2	57.6
Minimum	36.0	50	50
Maximum	72.4	71.1	79.5
Standard deviation	4.9	3.7	5.1
Mean plus one standard deviation	54.1	58.9	62.7
Tensile Stress (ksi)*			
Specified	58–80†	65 (min)	65 (min)
Mean	68.5	73.2	75.6
Minimum	58.0	65.0	65.0
Maximum	88.5	80.0	104.0
Standard deviation	4.6	3.3	6.2
Mean plus one standard deviation	73.1	76.5	81.8
Yield/Tensile Ratio			
Specified	0.62 (max)	0.77 (max)	0.77 (max)
Mean	0.72	0.75	0.76
Minimum	0.51	0.65	0.62
Maximum	0.93	0.92	0.95
Standard deviation	0.06	0.04	0.05
Mean plus one standard deviation	0.78	0.79	0.81

*1 ksi = 6.895 MPa.
†No maximum for shapes heavier than 426 lb/ft.
(*SSPC 1994*)

Table 8.1 Statistical Yield and Tensile Properties for Structural Shapes Based on Data Reported by the Structural Shape Producers Council (SSPC)

typically slip during testing, leaving the stiffer welded flanges alone to resist the total applied moment at the connection (Popov et al. 1985, Tsai and Popov 1988). As a result of the incompatible stiffnesses of the bolted web and the welded flanges, the connection resistance is reached when the flanges reach their ultimate tensile stress, F_u (Figure 8.23).

Structural Shape and Steel Grades	R_y	R_t
Hot-rolled structural shapes and bars:		
• ASTM A36/A36M,	1.5	1.2
• ASTM A1043/1043M Gr. 36 (250)	1.3	1.1
• ASTM A572/572M Gr. 50 (345) or 55 (380), ASTM A913/A913M Gr. 50 (345), 60 (415), or 65 (450), ASTM A588/A588M, ASTM A992/A992M,	1.1	1.1
• ASTM A1043/A1043M Gr. 50 (345)	1.2	1.1
Hollow structural sections (HSS):		
• ASTM A500 (Gr. B or C), ASTM A501	1.4	1.3
Pipe:		
• ASTM A53/A53M	1.6	1.2
Plates, Strips and Sheets:		
• ASTM A36/A36M	1.3	1.2
• ASTM A1043/1043M Gr. 36 (250)	1.3	1.1
• A1011 HSLAS Gr. 55 (380)	1.1	1.1
• ASTM A572/A572M Gr. 42 (290)	1.3	1.0
• ASTM A572/A572M Gr. 50 (345), Gr. 55 (380), ASTM A588/A588M	1.1	1.2
• ASTM 1043/1043M Gr. 50 (345)	1.2	1.1

Table 8.2 R_y and R_t Values for Steel

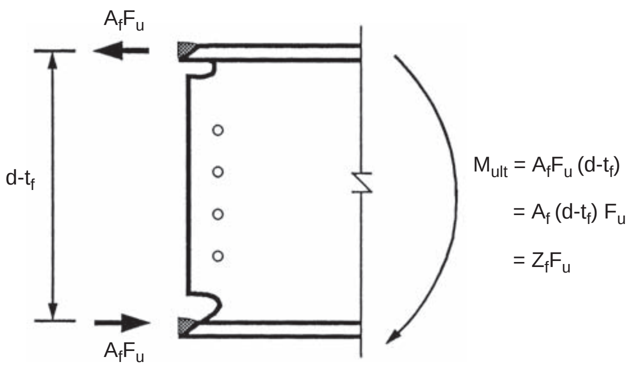

Figure 8.23 Free-body diagram for simplified model of connection strength. (*Courtesy of M. D. Engelhardt, Dept. of Civil Engineering, University of Texas, Austin.*)

As a result of strain-hardening, beams will reach bending moments of 1.2 to 1.3 times the expected plastic moment, M_p^{exp}, at the required plastic rotations, and flange fracture will develop unless:

$$A_f F_u(d - t_f) = Z_f F_u \geq 1.2M_p^{exp} = 1.2ZF_y^{exp} \tag{8.20}$$

where A_f and t_f are, respectively, the area and thickness of a beam flange, d is the beam depth, and F_y^{exp} is the expected yield stress of the beam. Assuming the plastic section modulus of the flanges alone, Z_f is approximately 70% of the beam plastic modulus, Z, the ratio of F_y^{exp} over F_u needed to develop significant plastic rotations is given by:

$$\frac{F_y^{exp}}{F_u} \leq \frac{0.83Z_f}{Z} \approx 0.60 \tag{8.21}$$

Given that the mean ratio of F_y^{exp} over F_u for currently available steels has been reported to vary between 0.72 and 0.76 (SAC 1995a, SAC 1995b), as shown in Table 8.1, it may not be possible to reliably develop the required plastic deformations in beams, even with perfect groove-welded connections.

8.5.3.6 Stress Concentrations

The absence of continuity plates opposite the beam flanges in a column produces stress concentrations in the flange near the column web (see Figure 8.4). Some engineers also alleged that this stress concentration could not be eliminated by the addition of thick continuity plates (Allen et al. 1995). Note that the use of overly thick continuity plates will generally require large welds that will introduce greater residual stresses in the connection: another condition conducive to crack initiation.

8.5.3.7 Effect of Triaxial Stress Conditions

Triaxial stress conditions can have an adverse effect on the ductility of steel. This is illustrated in Figure 8.24 in a comparison of the Mohr circles for steel elements with free or constrained lateral deformations when they are subjected to uniaxial yield stress (Blodgett 1995).

As described in Chapter 2, yielding requires the development of slip planes. For a steel element unrestrained laterally and subjected to uniaxial stress, ductile behavior develops when the shear stress equivalent to the uniaxial yield stress is exceeded. For a steel with $\sigma_y = \sigma_3 = 350$ MPa (50.8 ksi), the corresponding yield shear stress is 175 MPa (25.4 ksi) from Mohr's circle (Figure 8.24). The corresponding axial strains, obtained from the classical equations of elasticity (Popov 1968), using a value of Poisson's ratio, μ, of 0.3 are $\varepsilon_3 = \sigma_3/E = 0.00175$, and $\varepsilon_2 = \varepsilon_1 = -\mu\sigma_3/E = -0.00053$. However, if the same axial strain

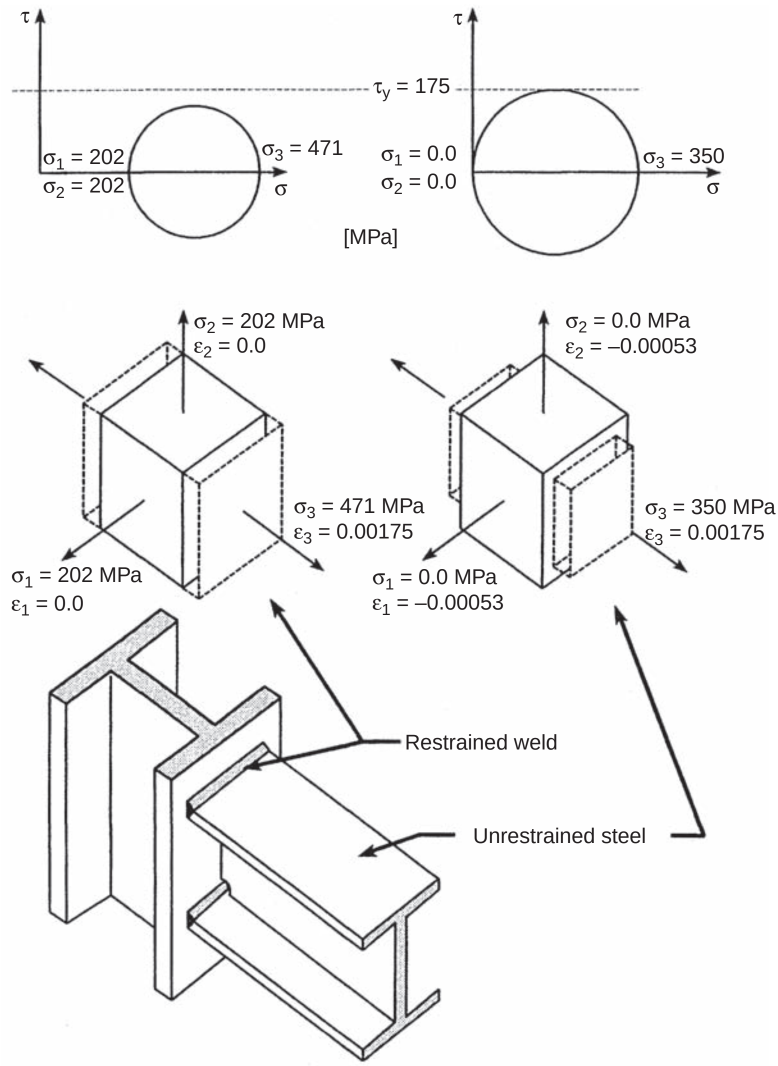

FIGURE 8.24 Comparison of triaxial stresses in unrestrained and restrained steel elements. (*Adapted from Blodgett 1995.*)

$\varepsilon_3 = 0.00175$ is applied when lateral deformations of the steel element are fully restrained (i.e., $\varepsilon_2 = \varepsilon_1 = 0$), the resulting stresses are:

$$\sigma_3 = \frac{E[1-\mu]\varepsilon_3 + \mu\varepsilon_2 + \mu\varepsilon_1}{(1+\mu)(1-2\mu)}$$

$$= \frac{200000[(1.0-0.3)(0.00175)]}{(1.3)(0.4)} \tag{8.22a}$$

$$= 471 \text{ MPa } (68.3 \text{ ksi})$$

$$\sigma_2 = \frac{E[\mu\varepsilon_3 + (1-\mu)\varepsilon_2 + \mu\varepsilon_1]}{(1+\mu)(1-2\mu)}$$

$$= \frac{(200000)[0.3\ (0.00175)]}{(1.3)(0.4)} \tag{8.22b}$$

$$= 202\ \text{MPa}\ (29.3\ \text{ksi})$$

$$\sigma_1 = \frac{E[\mu\varepsilon_3 + \mu\varepsilon_2 + (1-\mu)\varepsilon_1]}{(1+\mu)(1-2\mu)}$$

$$= \frac{(200000)[0.3\ (0.00175)]}{(1.3)(0.4)} \tag{8.22c}$$

$$= 202\ \text{MPa}\ (29.3\ \text{ksi})$$

As can be seen from the corresponding Mohr circle, even though the axial stress has exceeded the uniaxial yield stress of 350 MPa (50.8 ksi), the maximum shear stress is only 135 MPa (19.6 ksi). The shear stress needed to initiate slip planes would be reached only at an axial stress of 610 MPa (88.5 ksi), a value most likely in excess of the ultimate yield stress of the material (based on data in Table 8.1). Hence, ductile behavior will not develop, and brittle failure will occur instead. This simplified model also suggests that compression in the column ($\varepsilon_2 < 0$) would enhance the potential for ductile behavior at the weld, whereas tension ($\varepsilon_2 > 0$) would reduce it. Practically, the above condition of full restraint against lateral deformations is an extreme constraint not encountered in most welds of small to moderate sizes, but may be approached when large welds are executed on very thick steel members. Elasto-plastic studies of the behavior of constrained welds would help clarify the relationship between degrees of restraint and ductility.

8.5.3.8 Loading Rate

Given that all large-scale specimens in past experimental studies prior to the Northridge earthquake had been subjected to quasi-static loading, it was suggested that rate of loading may have had a detrimental effect on the behavior of beam-to-column moment connections. Dynamic testing of pre-Northridge full-size beam-to-column connections with W760 × 147 beams (W30 × 99 in U.S. units) revealed that beam flanges experienced strain rates on the order of 10^{-1} mm/mm/s for moment frames located in buildings having a fundamental period of vibration of approximately 1 s (Uang and Bondad 1996). At such a strain rate, yield stress can be increased by 10% (see Figure 2.8), thereby increasing the force demand on the groove-welded joint. It is also known that strain rate will decrease the notch toughness of the material. The combined effects resulted in a poorer cyclic behavior under dynamic loading conditions.

8.5.3.9 Presence of Composite Floor Slab

The development of composite action due to the presence of a concrete floor slab may have been responsible for the dominant number of beam bottom flange fractures (compared with top flange fractures). The different neutral axis positions in positive (composite) flexure versus negative (noncomposite) flexure translate into greater axial deformation demands on the beam bottom flange than on the top flange. However, other factors also likely contributed to the greater damage to the beam bottom flanges. For example, the top flange groove weld is easier to accomplish and inspect than the bottom flange weld. Furthermore, the strain demands at the level of the backup bar to the top flange weld are smaller than those on the backup bar to the bottom flange weld, which is farther from the center of the steel section.

Note that in California, engineers have commonly ignored composite action in design of moment-resisting frames, even though 19-mm (¾-inch) diameter shear studs spaced 300 mm (12 in) on center are popular to transfer seismic forces from the slab to the steel frame. Welded wire fabric is commonly used there as reinforcement in the concrete slab.

8.5.4 Reexamination of Pre-Northridge Practice

8.5.4.1 Reexamination of Past Literature

The extensive damage to steel moment frames in the Northridge earthquake prompted a reexamination of past experimental data. This review essentially revealed that the Northridge failures should have been expected (Bertero et al. 1994, Roeder and Foutch 1995, Stojadinovic et al. 2000). Although past experimental studies on standard moment connections generally reported satisfactory performance, sometimes with impressive ductile behavior, most studies reported instances of failures after only a limited amount of inelastic energy dissipation. For example, beyond the numerous sudden failures already reported in Section 8.5.1, Popov and Bertero (1973) reported a number of abrupt specimen failures, sometimes with fractures through welds or flanges, and Popov et al. (1985) noted that most of their specimens failed abruptly after exhibiting more or less satisfactory levels of plastic deformations. That latter test series was conducted to verify the adequacy of the design criteria for beam-to-column joints, using larger specimens than tested to that time and A36 beams framing into A572-Grade 50 columns. The beams' flanges were fully welded, webs were bolted only, and researchers reported hearing the slippage of the web bolts at each load reversal during testing. They also noted that specimens with continuity plates and doubler plates performed better than those without.

The abrupt failures reported in past North American beam-to-column tests were limited to fractures of the welded connections; cracks propagating into columns had not been observed prior to the Northridge earthquake. However, Bertero et al. (1994) reported that Japanese researchers had experienced such column fractures decades earlier (Kato 1973, Kato and Morita 1969). In those tests performed on large columns, cracks were observed to propagate from the beam welds through the entire column cross-section when the column was subjected to low axial forces; crack propagation stopped after rupture of the column flange when columns were subjected to high axial compression forces.

Thus, beam, column, and weld fractures similar to those documented following the Northridge earthquake had been observed in past studies. Unfortunately, although some of the specimens that exhibited inadequate ductility were brought forth (e.g., Engelhardt and Husain 1993), other instances of erratic behavior received cursory treatment and were attributed to faulty workmanship, even when the test specimens were provided by commercial fabricators.

8.5.4.2 Post-Northridge Tests of Pre-Northridge Details

Shortly after the Northridge earthquake, many tests of typical pre-Northridge connections were conducted in an attempt to replicate the observed failures under controlled conditions. A first series of tests involved heavy beam and column specimens (W360 × 677 A572-Grade 50 columns and W920 × 233 A36 beams, corresponding to W14 × 455 and W36 × 150, respectively, in U.S. units) representative of those that fractured during the earthquake (Engelhardt and Sabol 1994). Special care was taken to ensure superior welding quality and inspection. Backup bars and weld runoff tabs were also removed, and the weld root pass was gouged out and filled with new weld material to locally reinforce the weld. Two specimens had bolted webs (with supplemental welds on the web connector plate), and two specimens had webs fully welded to the column flanges; continuity plates were not used. The four specimens were tested by a standard quasi-static method, which is at strain rates much less than those that typically occur during earthquakes. All specimens failed at a low level of inelastic deformation (attaining plastic rotations of 0.0025 rad to 0.009 rad, depending on the specimen), with brittle fractures observed in both top and bottom flanges. Specimens with fully welded webs did not perform any better than those with bolted webs. These results showed the need for joint reinforcement and/or an alternative welding procedure to be validated through an extensive experimental program.

Tests on eight full-scale specimens of other pre-Northridge connections (W360 × 262 A572 Grade 50 columns with W760 × 147 A36 beams, corresponding to W14 × 176 and W30 × 99, respectively, in U.S. units) showed similar results (Whittaker et al. 1995, Uang and Bondad 1996). All eight specimens had the supplemental welds required on the web connector plate. First, three nominally identical specimens (Whittaker et al. 1995) were constructed under close supervision and rigorous inspection and thus were likely of greater than average quality. Tested at low strain rates, these pre-Northridge specimens suffered top flange weld fracture at beam plastic rotations of approximately 0.4%, 0.4%, and 1.0%, respectively (Whittaker et al. 1995). Panel zone yielding, observed in all three specimens, increased the total plastic deformation of the specimens by 0.7%, 0.7%, and 1.1%, respectively. Repairs that consisted of rewelding the failed flanges with toughness-rated filler metal failed in a similar manner at beam plastic rotations of 0.3%. Five different specimens tested by Uang and Bondad (1996) failed in a similar manner. Three specimens, tested quasi-statically, achieved maximum beam plastic rotations ranging between 0.2% and 1.6%, and total plastic rotations varied from 0.8% to 2.3% when panel zone plastic deformations were included. Two additional specimens tested at strain rates of 0.1 cm/cm/s failed without exhibiting any beam plastic rotation; maximum panel zone plastic rotations of 0.15% and 1.0% were measured respectively in the two tests. The fractures propagated into the column flanges and bolted beam web plates in the dynamically tested specimens, suggesting that loading rate may have contributed to that failure pattern observed in many Northridge-type failures. The propagation of damage in the dynamic tests has been documented on video (Uang 1995).

As soon as the first preliminary test results became available, the prequalified standard moment connection was deleted from most building codes and regulations for applications in moderate to high seismic regions, and it was replaced by general clauses requiring that welded or bolted moment connections be able to sustain inelastic rotations and develop the required strength, as demonstrated by approved cyclic tests or calculations supported by test data. Interpretation of these clauses, particularly regarding what constitutes acceptable levels of inelastic rotations and test procedures, had been left to the regulatory authorities and professional organizations (e.g., SEAOC 1995) while awaiting consensus agreement. As a result, for a few years, building officials in many jurisdictions required mandatory testing of any new connection detail not previously proven by cyclic inelastic tests, or any connection with beams and columns larger than tested previously. This expensive proposition pushed many engineers toward other lateral-load resisting systems. The findings from an extensive coordinated research program conducted to establish acceptable moment-resisting connections is described in the next section.

8.5.5 Post-Northridge Beam-to-Column Connections Design Strategies for New Buildings—Initial Concepts

Numerous proposed solutions to the moment frame connection problem were attempted in the years following the Northridge earthquake, as part of a coordinated research effort funded by the Federal Emergency Management Agency and the California Office of Emergency Services, as well as from other initiatives. A broad range of innovative ideas were proposed, often boldly departing from existing practice, sometimes with an entrepreneurship spirit. This section focuses on some successful and nonsuccessful initial concepts, to provide a useful perspective of the context that led to the solutions and constraints adopted in design provisions that are presented later.

Generally, two key concepts were originally pursued to circumvent the problems associated with the pre-Northridge moment frame connection, namely:

- Strengthening the connection, or
- Weakening the beam(s) that frame into the connection

In both cases, the objective is to move the plastic hinge away from the face of the column, to avoid the aforementioned problems related to the potential fragility of groove welds subjected to triaxial stress conditions. Figure 8.25 schematically illustrates the corresponding beam moment diagrams to achieve this. For the strengthening case (reinforced beam ends), developing the plastic moment of the beam, M_p, at a distance e from the face of a column induces greater moments at the column face. On the contrary, weakening solutions locally reduce the beam plastic moment at that same distance e, and ensure plastic hinging at that location by selecting a strength, m_p such that the maximum moment reached at the column face is less than M_p, which can be advantageous given that this moment dictates column and panel zone design.

Solutions that circumvented the need to develop the plastic moment of the beam were also proposed (such as friction-based energy dissipation concepts, or pre-tensioned connections, to name a few), but such

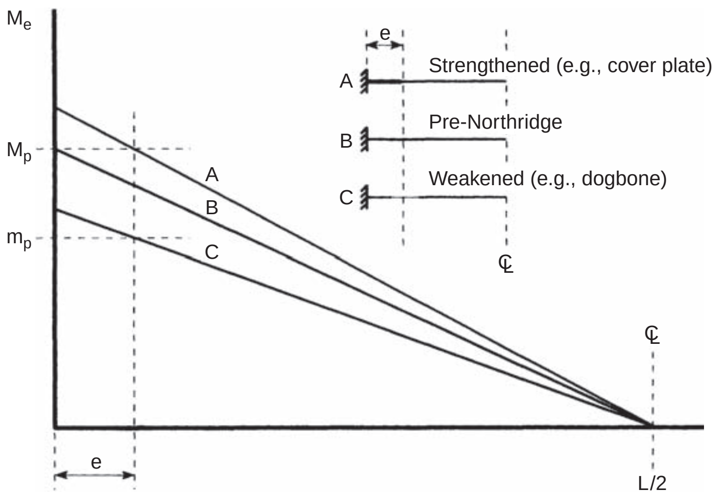

FIGURE 8.25 Consideration of moment gradient to promote development of plastic hinges at distance *e* from face of column.

outright departures from design approaches relying on hysteretic behavior are presented in Chapter 13, the focus here being on connections that can develop the plastic hinging of the connected beam.

On the strength of results from nonlinear inelastic analyses of example buildings conducted using contemporary knowledge on seismic demands (FEMA 2000e), it was shown that drifts of 4% could develop in special moment-resisting steel frames. Therefore, to ensure the satisfactory performance of such ductile moment-resisting connections, proposed connections were required to experimentally achieve plastic rotations of 0.03 radian without exhibiting strength degradation of more than 20% of their plastic moment (SAC 1995b, FEMA 2000a) when subjected to a specified protocol of cyclic inelastic deformations (e.g., similar to the one in Appendix S of the 2005 edition of AISC 341, or Appendix K of the 2010 edition). A minimum of three satisfactory tests was required to ensure reliable results.

Incidentally, all proposed post-Northridge connections were recommended to be implemented in conjunction with the use of high toughness weld filler metal, better welding practice, and high-quality inspection. Furthermore, even though removal of the backup bars and weld runoff tabs did not enhance performance noticeably in the tests of pre-Northridge connections, the arguments presented earlier regarding the notch effect created by the backup bar are compelling, and their removal is recommended. In some of the post-Northridge test though, a fillet weld applied between the backup bar and column flange was alternatively used to seal the cracklike gap described in Section 8.5.3.

8.5.5.1 Initially Investigated Strengthening Strategies: Cover Plates and Flange Ribs

Many ideas were initially proposed to make the connection stronger than the beam framing into the connection, some of which being illustrated in Figure 8.26. The use of beam strengthening schemes to reinforce beam-to-column connections has the advantage of relocating the plastic hinge(s) away from the column face(s), but the disadvantages of: (1) increasing the beam moment(s) at the face(s) of the column, thereby increasing the column size to maintain the strong-column/weak-beam system; (2) increasing the unbalanced moment on the panel zone; and (3) increasing the plastic hinge rotation demand (see Section 8.6)—all issues that must be considered by the designer.

Among the strengthening strategies, the use of cover plates or flange ribs appeared to be an obvious and promising solution to strengthen the beam at the column face (e.g., Engelhardt and Sabol 1996; Noel and Uang 1996; Kim et al. 2000; Whittaker et al. 1995, 2002). In nearly all cases (Noel and Uang, 1996 and Kim et al., 2000 providing typical exceptions), to make downhand welding possible for both flanges, the top cover plate was tapered and narrower than the beam top flange, whereas the bottom plate was rectangular and

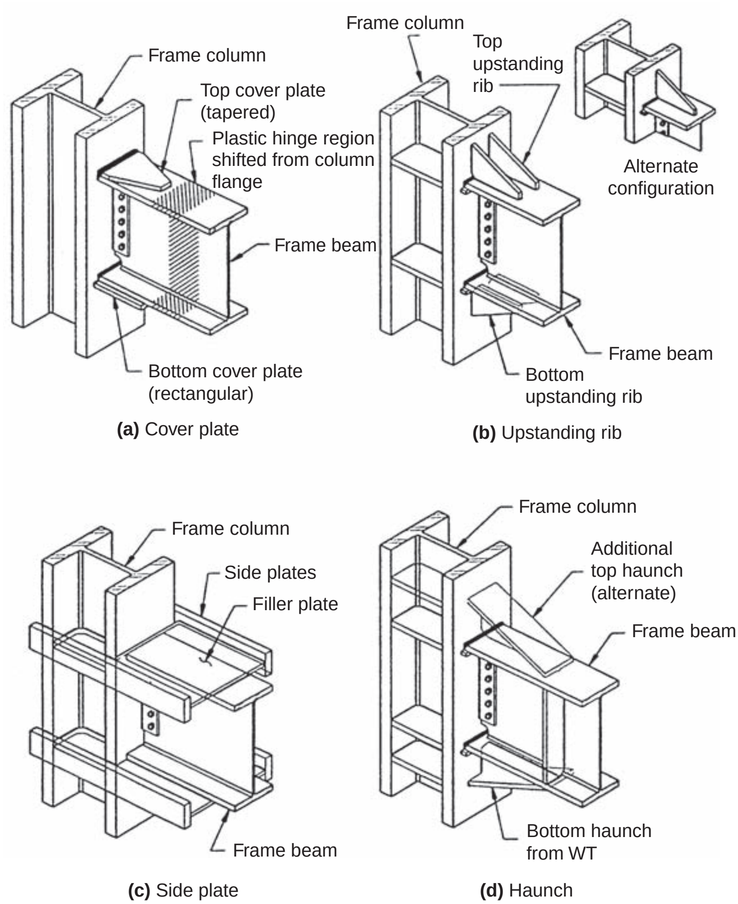

Figure 8.26 Examples of initially proposed moment connections per strengthening strategies. (*Courtesy of M.D. Engelhardt, Dept. of Civil Engineering, University of Texas, Austin.*)

wider than the bottom flange (Figure 8.26a). Plate tapering was also believed to result in a smoother stress transfer between each flange and its cover plate. However, this originally envisioned simple cover plate details ended-up not being prequalified for new construction, for the reasons described below.

Results from a series of cover plate tests by Engelhardt and Sabol (1996) are instructive. Details of 12 specimens considered are summarized in Table 8.3, along with brief description of their performance. Details with bolted web or welded web connections were evaluated, as shown in Figures 8.27a and b, respectively. Note that for new construction with that proposed cover plate detail, the

Specimen	Beam Size§	Beam Flange Strength		Beam Web Strength		Column Size§ W14×	Top Cover Plate (tapered) (thickness × width × length) (mm)	Bottom Cover Plate (rectangular) (thickness × width × length) (mm)	Web Connection	Electrode*	Maximum Plastic Rotation (rad)	Description of Failure
		Fy (MPa)	*Fu* (MPa)	*Fy* (MPa)	*Fu* (MPa)							
AISC-3A	W36 × I50	294	425	320	435	455	19 × 300 × 430	16 × 355 × 405	bolted	E70T-4	1.5%	Brittle fracture at top flange and cover plate groove weld
AISC-3B	W36 × I50	294	425	320	435	455	19 × 300 × 430	16 × 355 × 405	bolted	E70T-4	2.5%	Gradual strength deterioration due to local budding, followed by gradual tearing of bottom flange at end of cover plate
AISC-5A	W36 × I50	318	460	375	494	426	25 × 300 × 610	25 × 300 × 585†	bolted	E70TG-K2‡	2.5%	Same as AISC-3B
AISC-5B	W36 × 150	370	492	380	520	426	25 × 300 × 610	25 × 300 × 585†	bolted	E70TG-K2‡	0.5%	Brittle fracture at beam bottom flange connection. Fracture contained within column flange base metal
AISC-7A	W36 × I50	318	460	375	494	426	19 × 300 × 430	16 × 355 × 405	bolted	E70T-7	3.5%+	Gradual strength deterioration due to local buckling, and gradual tearing of fillet welds of cover plates to beam flanges

AISC-7B	W36 × 150	318	460	375	494	426	19 × 300 × 430	16 × 355 × 405	bolted	E70T-7	5.0%+	Same as AISC-7A
AISC-8A	W36 × 150	311	444	343	465	426	19 × 300 × 430	16 × 355 × 405	bolted	E70T-7	3.5%+	Same as AISC-7A
AISC-8B	W36 × 150	311	444	343	465	426	19 × 300 × 430	16 × 355 × 405	bolted	E70T-7	3.5%+	Same as AISC-7A
SAC-4	W36 × 150	292	421	329	437	257	25 × 300 × 405	25 × 355 × 405	bolted	E70T-8	3.7%+	Same as AISC-7A + significant panel zone yielding
NSF-5	W36 × 150	296	417	310	415	426	12 × 300 × 355	12 × 380 × 355	welded	E70T-8	3.3%+	Same as AISC-7A
NSF-6	W30 × 148	321	445	334	450	257	16 × 266 × 355	16 × 300 × 355	welded	E70T-8	3.8%+	Gradual tearing of fillet welds of cover plates to beam flanges; panel zone dominated inelastic response
NSF-7	W36 × 150	340	456	360	467	455	12 × 300 × 355	12 × 380 × 355	welded	E70T-8	3.8%+	Same as AISC-7A

*All bolted webs with fully tensioned high strength bolts and supplemental welds on web shear tab to develop 20% of nominal plastic moment of beam web; all welded webs by directly welding to column using complete joint penetration groove weld.
†Tapered bottom cover plate
‡Except E70T-7 used for bottom cover plate to column flange weld
§In S.I. units, W36 × 150 is W920 × 223, W30 × 148 is W760 × 221, W14 × 455 is W360 × 677, W14 × 426 is W360 × 634, W14 × 257 is 360 × 382.
(*From Engelhardt and Sabol 1996*)

Table 8.3 Summary of Results for Cover-Plated Connection Test Series

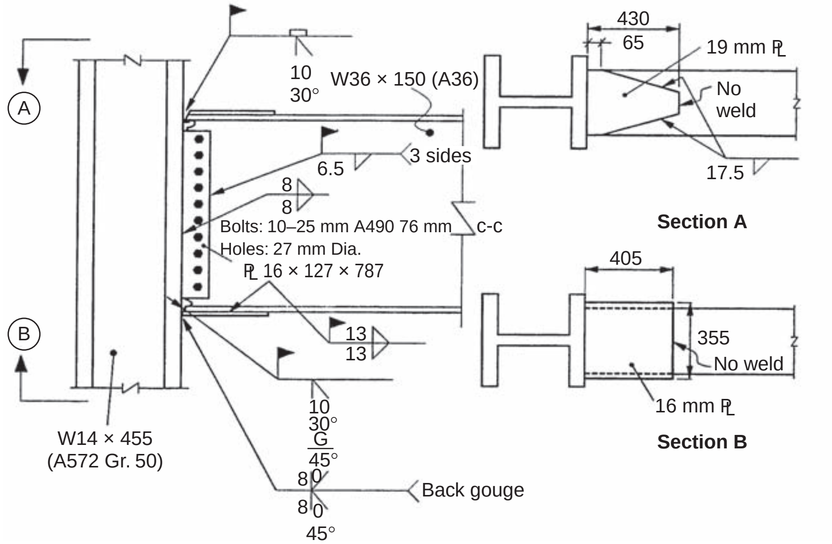

(a)

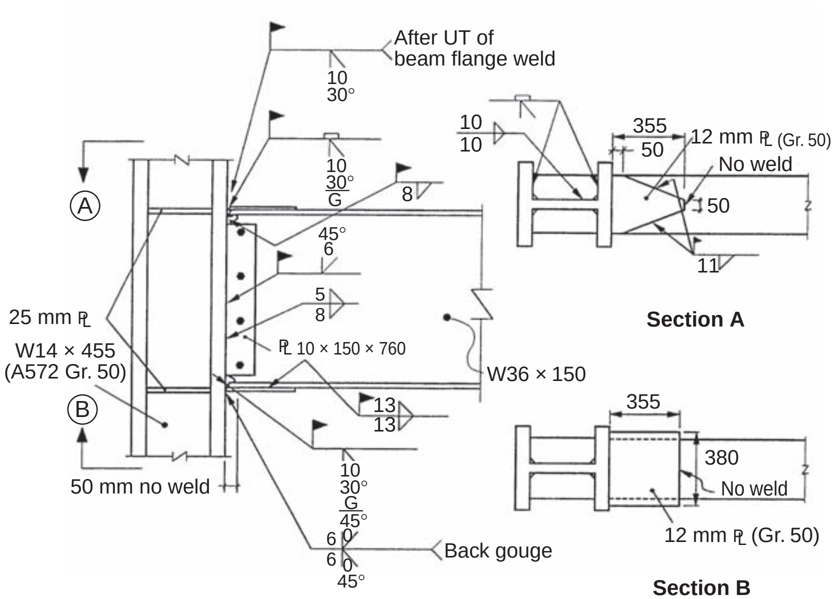

(b)

FIGURE 8.27 Moment connections with cover plates: (a) bolted web (specimen AISC-3A), (b) fully welded web (specimen NSF-7). (*Courtesy of M. D. Engelhardt, Dept. of Civil Engineering, University of Texas, Austin.*)

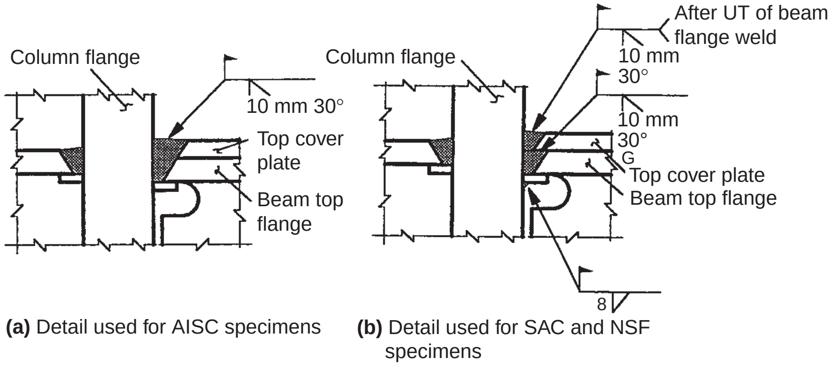

Figure 8.28 Typical groove weld details at top flange used for moment connection strengthened by cover plates. (*Courtesy of M. D. Engelhardt, Dept. of Civil Engineering, University of Texas, Austin.*)

bottom cover plate would have been shop-welded to the column flange and used in the field as an erection seat for the beam. This particular construction sequence also would have made it possible to perform ultrasonic testing at various stages of connection assembly and to fully weld the beam web, using the web tab as a backup plate. A welded web can transfer its share of the beam plastic moment, which makes possible the use of smaller cover plates. Smaller plates also minimize residual stresses due to weld shrinkage, and the likelihood of high triaxial tensile stresses at the column face. Separate welds for the flange and cover plate (Figure 8.28) also reduce this likelihood of developing detrimental triaxial stresses in the connection and enable individual ultrasonic inspection of the two welds.

As shown in Table 8.3, two-thirds of the cover-plated specimens developed total plastic rotations of 0.03 rad without brittle fracture. Note that in those specimens, the columns were designed with a strong panel zone that remained elastic throughout testing, with the exception of specimens SEC-4 and NSF-6 designed with lighter columns and for which panel zone yielding dominated the inelastic response. Results for a specimen with a fully welded web connector plate are shown in Figure 8.29. Yet, cover plates by themselves are not a panacea. As seen in Table 8.3, two of the specimens with bolted webs tested by Engelhardt and Sabol (AISC-3A and AISC-5B) failed in a brittle manner at plastic rotations of less than 0.02 rad, even though the groove welds had passed ultrasonic inspection. Each specimen that failed had a counterpart that exhibited satisfactory behavior.

Note that for the AISC-#B specimens, a Welding Procedure Specification was written and enforced, whereas for the AISC-#A specimens, the welder was permitted to weld on the basis of his experience.

Two different welders executed the AISC-3A and -3B specimens; both were uncomfortable with the setting recommendations from the

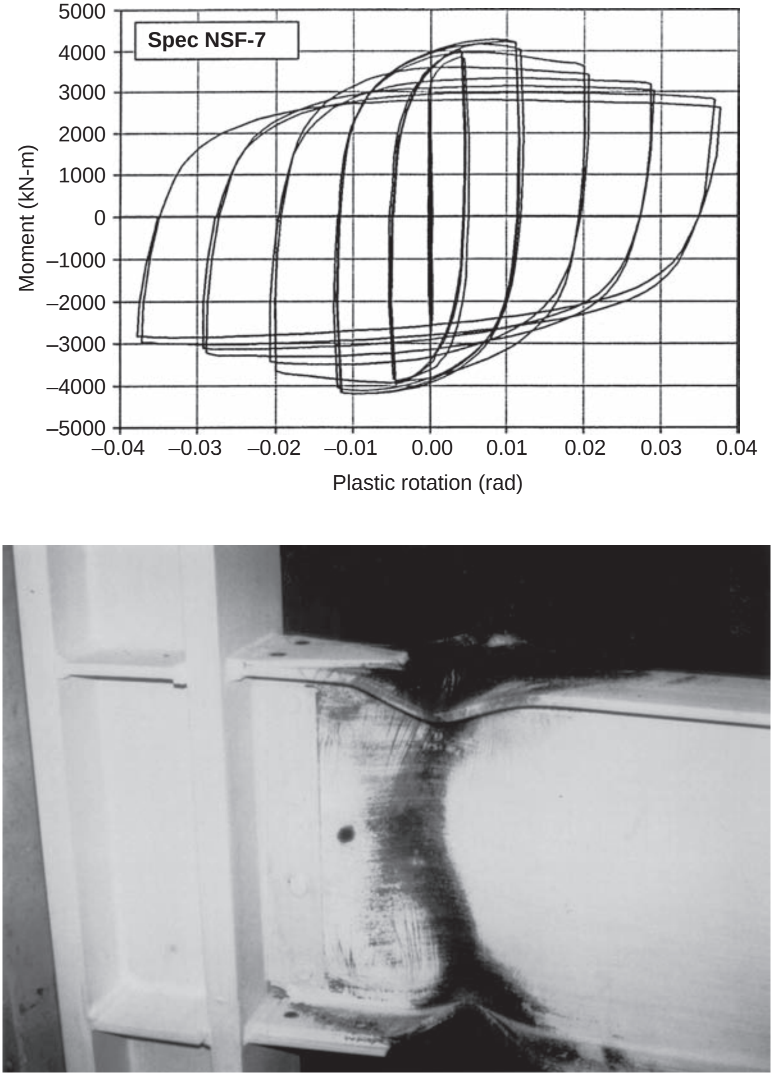

Figure 8.29 Moment connection with cover plates and fully welded web (specimen NSF-7): (a) hysteretic behavior. (b) specimen state at completion of test. (*Parts a and b courtesy of M. D. Engelhardt, Dept. of Civil Engineering, University of Texas, Austin.*)

electrode manufacturers. The Welding Procedure Specification was enforced for specimen AISC-3B, but the welder of specimen AISC-3A increased the voltage and current of the welding machine to enhance workability. Metallurgical study of the groove welds revealed the greater heat input to AISC-3A (that suffered brittle fracture) resulting in a fivefold lower weld toughness than in AISC-3B. As for the other specimen with poor performance, AISC-5B, fracture was attributed to the larger-than-anticipated beam yield strength and the fact that long cover plates were used. These long plates developed the beam plastic moment farther from the column, resulting in larger bending moments at the column face.

Reviewing all the evidence, concerns remained regarding the use of cover plates. First, the panel zones in the very large columns tested by Engelhardt and Sabol (1996) did not yield—poor performance was reported in other tests that developed large panel zone deformations (Obeid 1996, Whittaker and Gilani 1996). Second, it was cautioned that overlaid welds should be accomplished only through use of identical electrodes; loss of weld toughness due to the mixing of weld metals has been reported (Wolfe et al. 1996). Note that section J2.7 of AISC (2010c) also warns that low notch-toughness welds may result from the mixing of two incompatible weld metals of high notch-toughness. Third, Hamburger (1996) reported that an estimated failure rate of 20% has been experienced when laboratory qualification testing of these connections was performed for specific design projects, which suggests that the cover plate detail may not be sufficiently reliable; Kim et al. (2000) also listed past instances of brittle failures. Fourth, the SAC Interim Guidelines (1995b) indicated that, conceptually, this connection could be exposed to some of the same flaws that plagued the pre-Northridge connections, namely, dependence on weld quality and through-thickness behavior of the column flange, potentially exacerbated by the thicker groove welds made necessary by the addition of cover plates. Finally, SAC (1997) reported that when the bottom cover plate is shop-welded to the column flange to be used as an erection seat for the beam, premature fracture can develop across the column flange as the seam between the bottom flange and cover plate acts as a notch that can trigger crack propagation.

Fewer tests on the use of upstanding beam flange ribs (Figure 8.26b) have been conducted since the Northridge earthquake, although this detail was investigated prior to 1994 (Tsai and Popov 1988). Overall, this type of rib detail appeared effective, but it was judged that additional testing was needed to determine how various design and detailing parameters influence its inelastic performance.

8.5.5.2 Initially Investigated Strengthening Strategies: Haunches

Haunches provide another intuitive way to make a connection stronger that its beam. Different haunch details have been tested, and many have exhibited satisfactory performance. Given the availability of less expensive alternatives, haunches have typically not been prequalified for new constructions (FEMA 2000a); however, they have been pre-qualified for the upgrading of existing structures, as fewer solutions can be easily implemented in that case (FEMA 2000b). A sample of typical experimental results is provided here to illustrate their behavior.

Uang and Bondad (1996) tested pre-Northridge specimens repaired with bottom flange triangular T-shaped haunches only, as shown in Figure 8.30. Continuity plates were added to the column at the level of the haunch flange. Two specimens were tested in a quasi-static manner, and two were tested dynamically with a maximum strain rate of 0.1 mm/mm/s. The repaired specimens performed much better than the pre-Northridge specimens, with beam plastic hinges developing

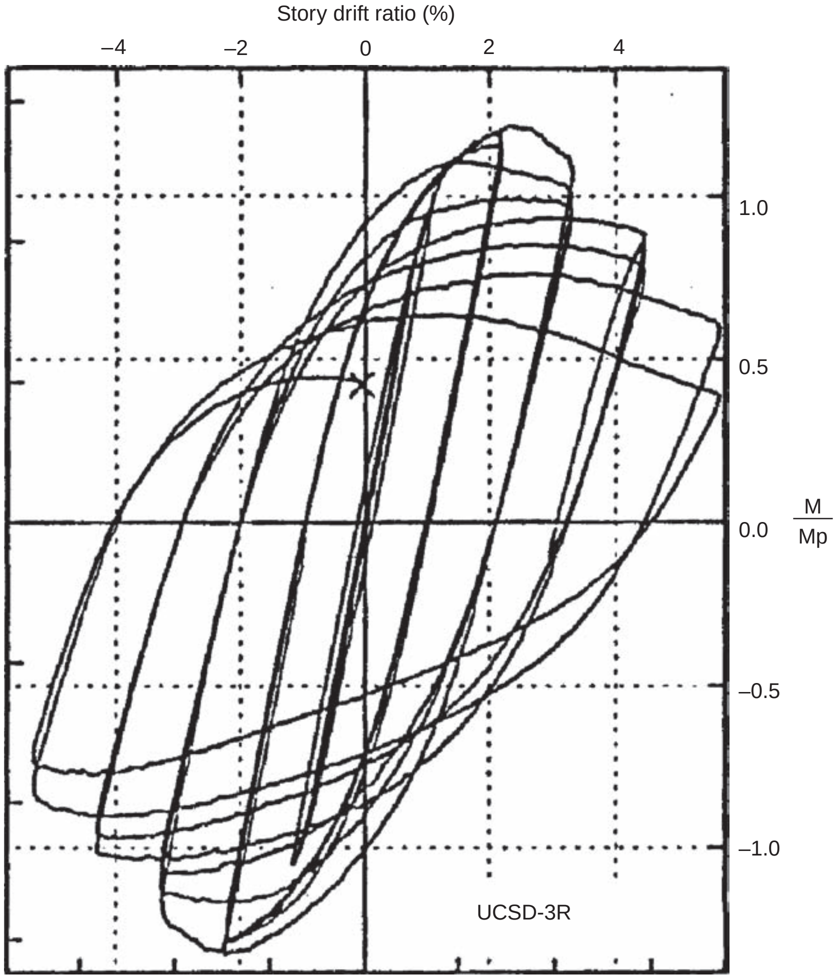

(a)

Figure 8.30 Moment connection of W760 × 147 beam (W30 × 99 in U.S. units) of A36 steel to W360 × 262 column (W14 × 176 in U.S. units) of A572 Grade 50 steel, with bottom flange haunch: (a) hysteretic behavior in terms of load versus cantilever beam tip deflection at 3.6 m from centerline of the column; (b) specimen state at first cycle of –7.0 in tip deflection.

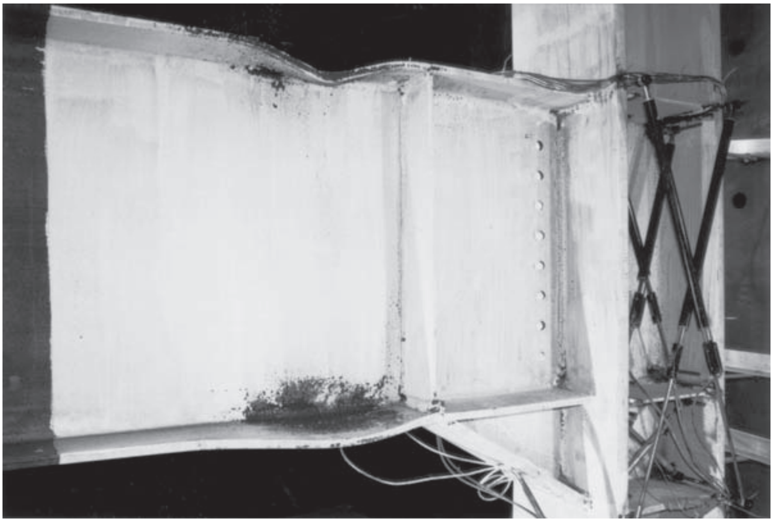

(b)

Figure 8.30 (*Continued*)

outside the haunch. Plastic deformation of the panel zones was also reduced, and nearly all of the inelastic action was concentrated in the beams. Note that the presence of a haunch increases the depth of the panel zone, thus reducing the extent of panel zone yielding.

Total beam plastic rotations in excess of 3% were obtained in the quasi-static tests. Failure was defined by excessive strength degradation due to local buckling of the beam flanges (Figure 8.30), although the specimens could sustain larger plastic rotations and dissipate further hysteretic energy while undergoing further strength degradation. In one of the dynamically tested specimens, in addition to repairing the fractured bottom flange with a haunch, the beam top flange with pre-Northridge type of groove-welded joint was strengthened by the addition of a pair of rib plates on the underside of the flange. This detail, developed for strengthening existing connections, avoids the need to remove the concrete slab around the column, but would still require removal of the building's facade (i.e., cladding panel or other architectural finishes) to provide access to one half of the beam flange for perimeter frames. Although the welded top flange joint fractured during retesting, the two vertical ribs served their intended purpose by maintaining the integrity of the connection.

Whittaker et al. (1995) reported adequate performance for pre-Northridge specimens repaired and strengthened by the addition of triangular T-shaped haunches to both top and bottom flanges. Panel zone yielding was substantially eliminated in the strengthened specimen and significant beam plastic rotations were obtained (Figure 8.31). However, with failure defined as the point at which the

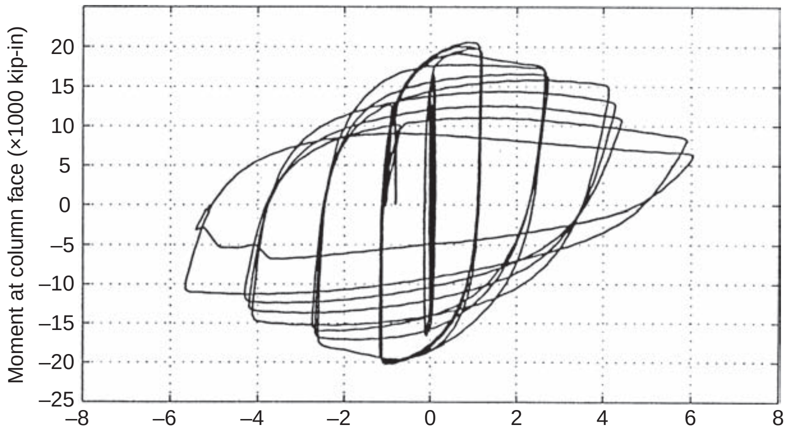

(a)

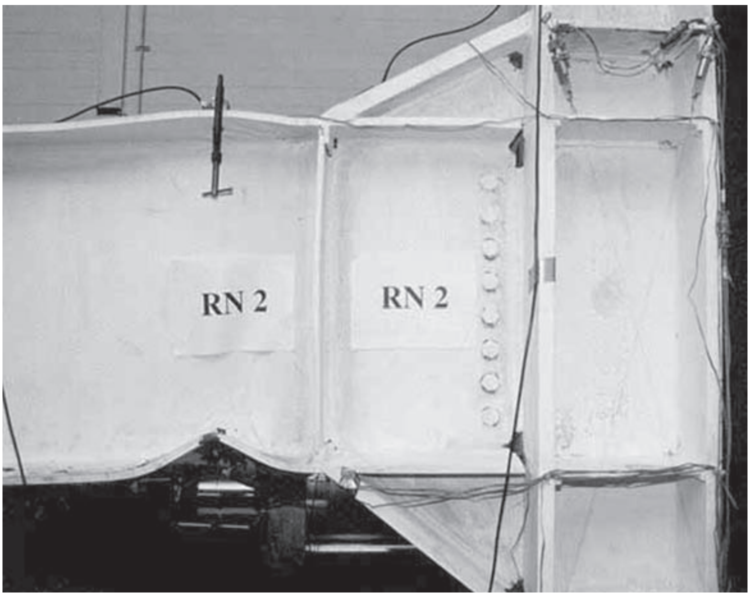

(b)

Figure 8.31 Hysteretic behavior of moment connection with top and bottom flange haunches, in terms of moment versus beam plastic rotation, and specimen state upon completion of test. (*Courtesy of the SAC Joint Venture, a Partnership of the Structural Engineers Association of California, Applied Technology Council, and Consortium of Universities for Research in Earthquake Engineering.*)

resistance degraded to 80% of the maximum value, beam plastic rotations of 2.7% was reached prior to failure.

Hybrid connections with cover plate reinforcement of the top flange and haunch reinforcement of the bottom flange have also been considered. Excellent performance was obtained for a particular configuration and detailing (Figure 8.32). For this particular design, the

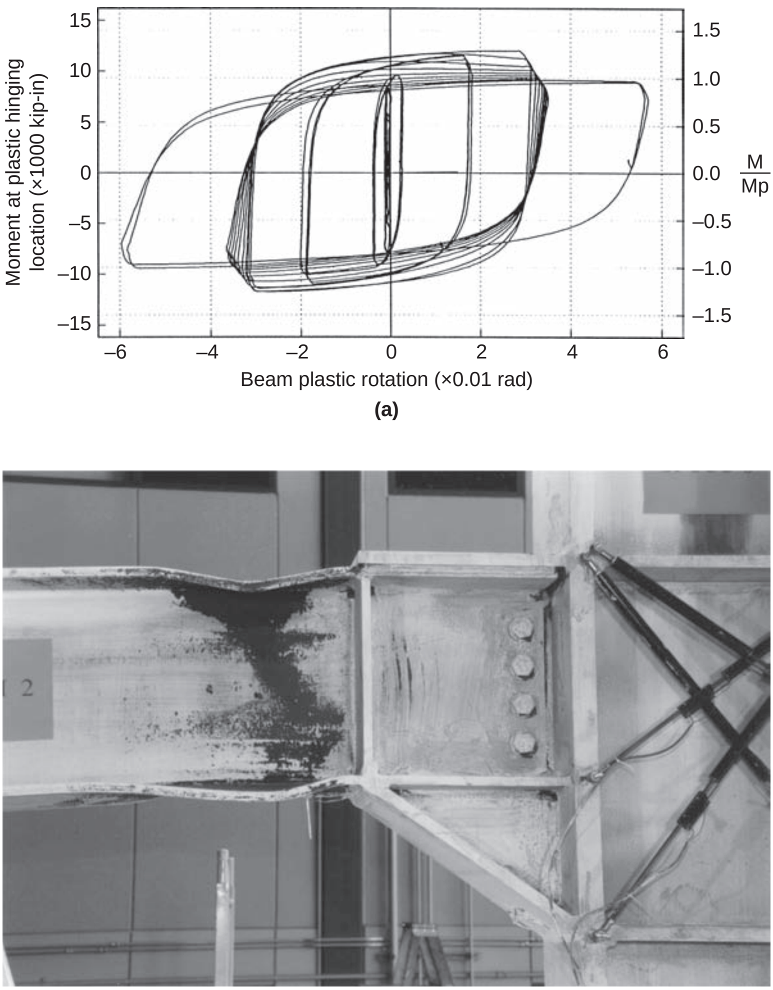

(a)

(b)

Figure 8.32 Hysteretic behavior of moment connection with top flange cover plate and bottom flange haunch, in terms of moment at hinge location versus beam plastic rotation at hinge location and specimen state at ninth cycle of +3.5 inches tip deflection. (*Courtesy of M. S. Jokerst, Forell/Elsesser Engineers Inc., San Francisco.*)

cover plate was shop-welded to the beam with a fillet weld, and only the cover plate (not the beam top flange) was groove welded to the column; the backup bar was left in position with a closure fillet weld (Noel and Uang 1996).

In summary, the available experimental data suggest that using triangular T-shaped haunches is an effective means by which to strengthen a connection. Their high redundancy also contributes to preserve good plastic behavior if one of the full penetration groove welds fails. However, haunches are expensive to construct, and the top haunch, when present, can be an obstruction above the floor level.

Straight haunches have been proposed as a more economical alternative solution (Uang and Bondad 1996). The direct strut action that develops in sloped haunch flanges is not possible in this alternative, and the beam flange force must be transferred to the haunch flange via shear in the haunch web. In the specimen tested, stress concentration at the free end of the haunch fractured the weld between the beam flange and haunch web at that free end (Figure 8.33). Additional stiffeners at the free end of the haunch to tie the beam and haunch together, or the use of a sloped free end to reduce the stress concentration, might be effective in preventing the observed fracture, but the adequacy of such enhancements must be validated by testing.

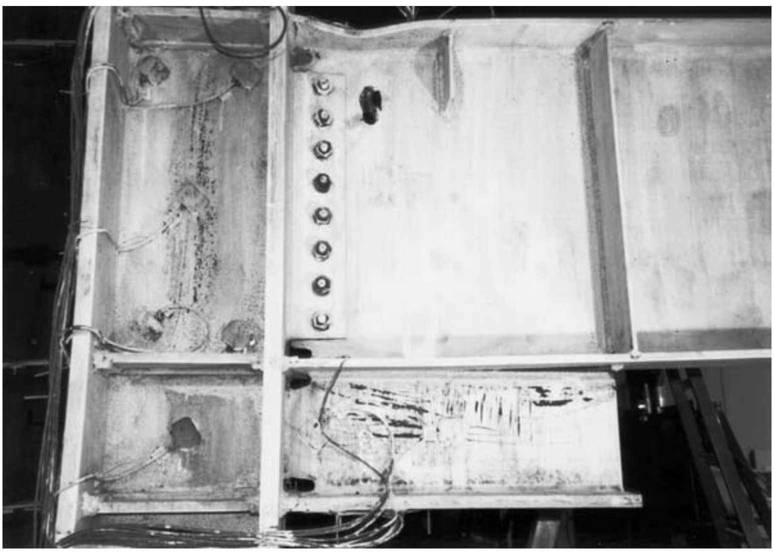

Figure 8.33 Fracture between straight haunches and beam bottom flange at the free end of the haunch and beam top flange local buckling.

8.5.5.3 Initially Investigated Weakening Strategies

Plastic hinges can be moved away from the face of a column if one reduces the area of the beams' flanges at a selected location. By strategically weakening the beam by a predetermined amount over a small length, at some distance from the welded connection, and by taking into account the shape of the moment diagram to ensure that yielding will occur only at this location of reduced plastic moment capacity, one can effectively protect the more vulnerable beam-to-column connection. One can do this in a number of ways, such as by drilling holes in the flanges or by trimming the flanges. The latter solution has found broad acceptance in a relatively short time.

The idea of shaving beam flanges to improve the seismic performance of steel connections was first proposed and tested by Plumier (1990). Chen and Yeh (1994) confirmed the effectiveness of this approach to enhance the ductility of beam-to-column connections. Although this concept was patented in the United States in 1992, the owner of the patent waived any commercial royalty rights for its public use after the Northridge earthquake.

Two flange shapes have received considerable attention following the Northridge earthquake (Figure 8.34). The first type

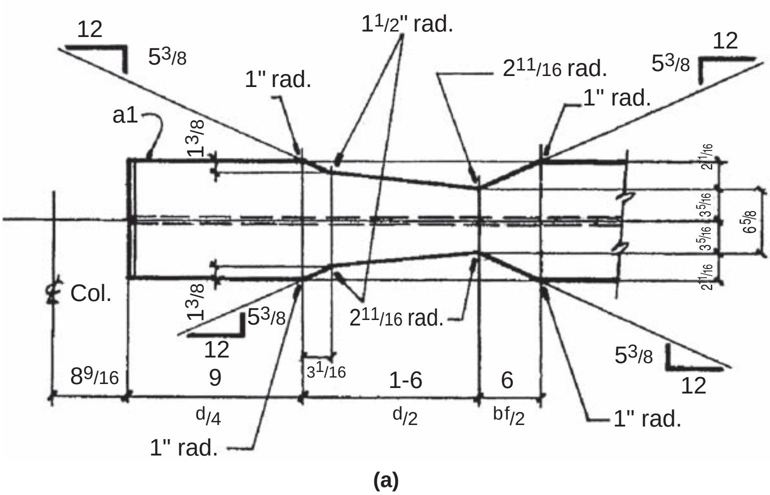

Figure 8.34 Reduced beam section designs: (a) Tapered flange profile. (b) elevation and plan view of radius-cut flange profile; (c) information on radius-cut typical flange profile. (*Part a from* Modern Steel Construction, *vol. 36, no. 4, "The Dogbone: A New Idea to Chew On" by N. R. Iwankiw and C. J. Carter, 1996, with permission from the American Institute of Steel Construction. Parts b and c Courtesy of M. D. Engelhardt, Dept. of Civil Engineering, University of Texas, Austin.*)

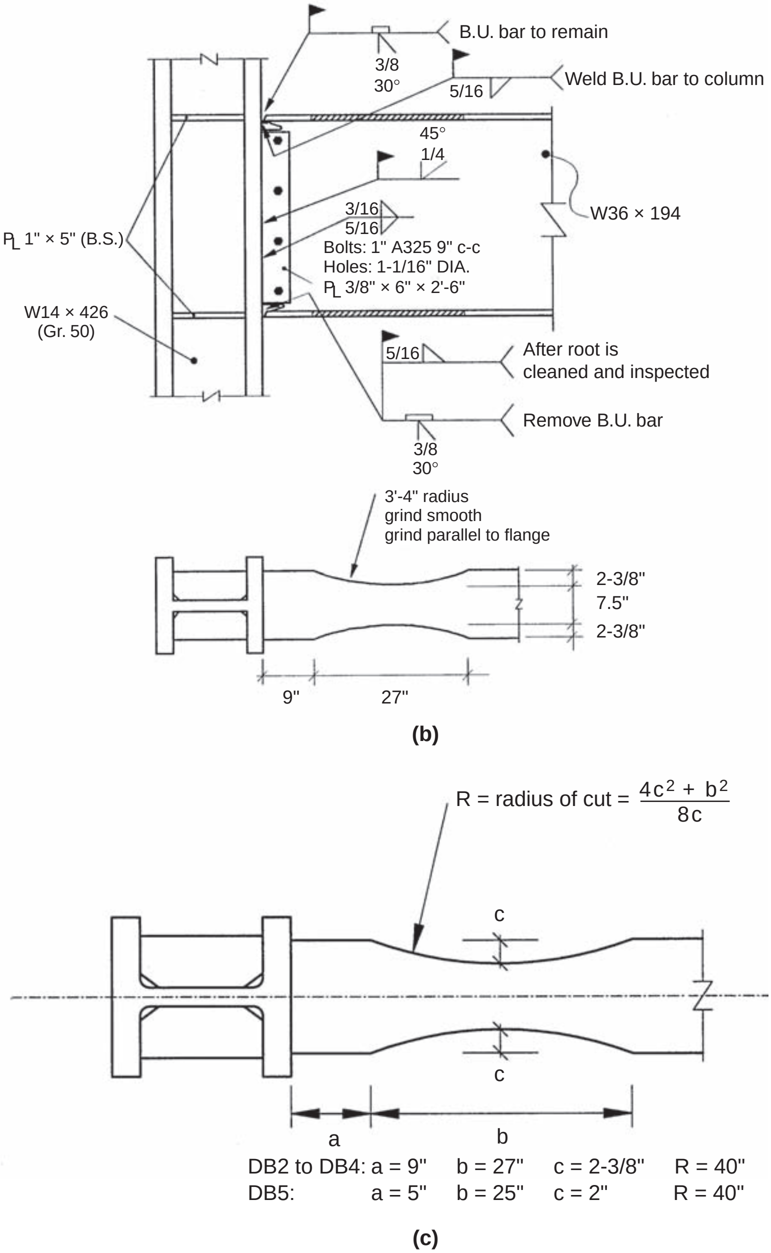

FIGURE 8.34 (*Continued*)

(Chen et al. 1996, Iwankiw and Carter 1996) has flanges tapered according to a linear profile intended to approximately follow the varying moment diagram (Figure 8.34a). The second profile (Engelhardt et al. 1996 and many others subsequently) is shaved along a circular profile as described in Figures 8.34b and c. Both reduced beam section (RBS) profiles (a.k.a. "dogbone" profiles) have achieved plastic rotations in excess of 3%, as shown in Figure 8.35. A variant of the linear taper, with additional rib plates welded to the beam flanges to further reduce stresses in the flange groove welds, has also been successfully tested (Uang and Noel 1995).

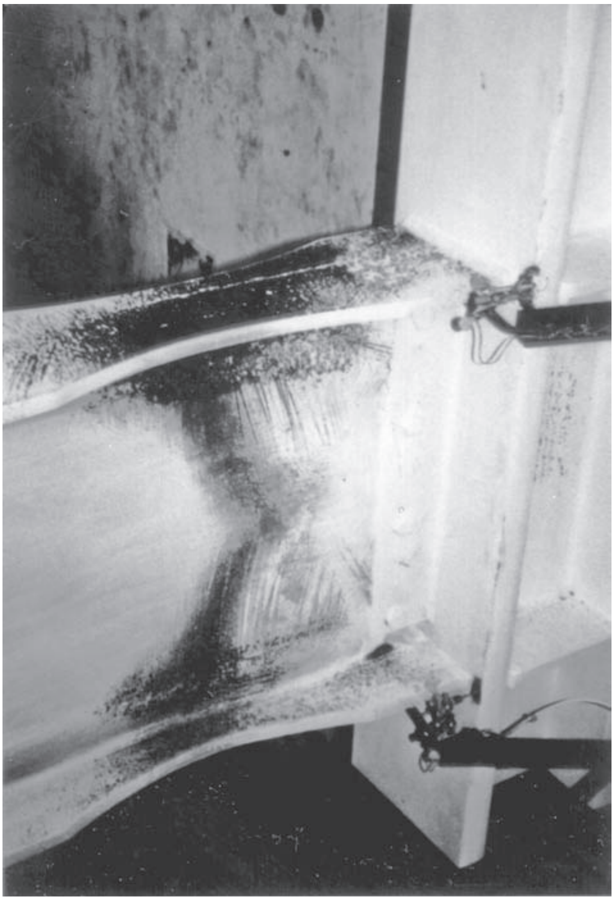

(a)

Figure 8.35 Radius-cut flange profile moment connection: (a) specimen state at completion of test, (b) specimen state at completion of test: side view and top view, (c) hysteretic behavior in terms of moment at column face versus beam plastic rotation. (*Parts a to c courtesy of M. D. Engelhardt, Dept. of Civil Engineering, University of Texas, Austin.*)

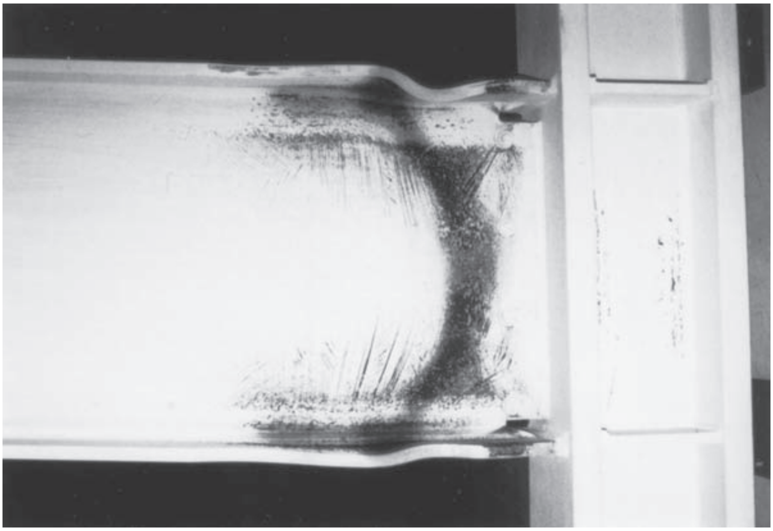

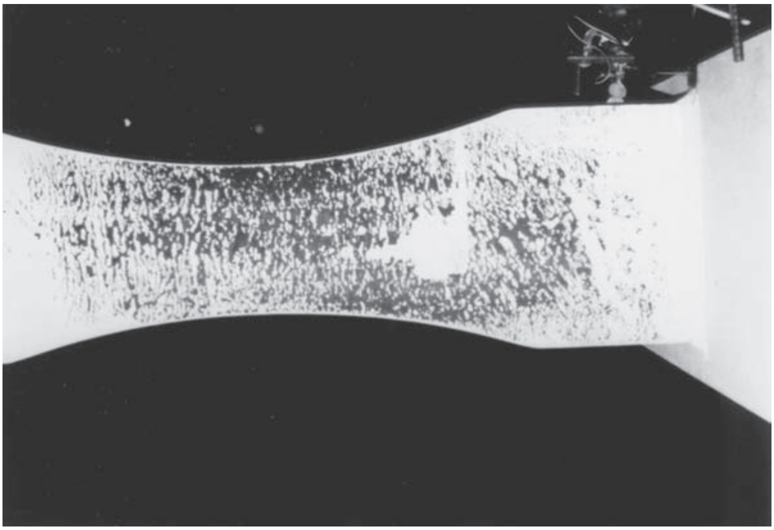

(b)

Figure 8.35 (*Continued*)

In all cases, trimming of the flanges delays local buckling, but increases the likelihood of web buckling and lateral-torsional buckling due to the reduction in flange stiffness. The RBS connection usually experiences web local buckling first, followed by flange local buckling and lateral-torsional buckling, resulting in significant strength degradation. The addition of lateral bracing at the reduced

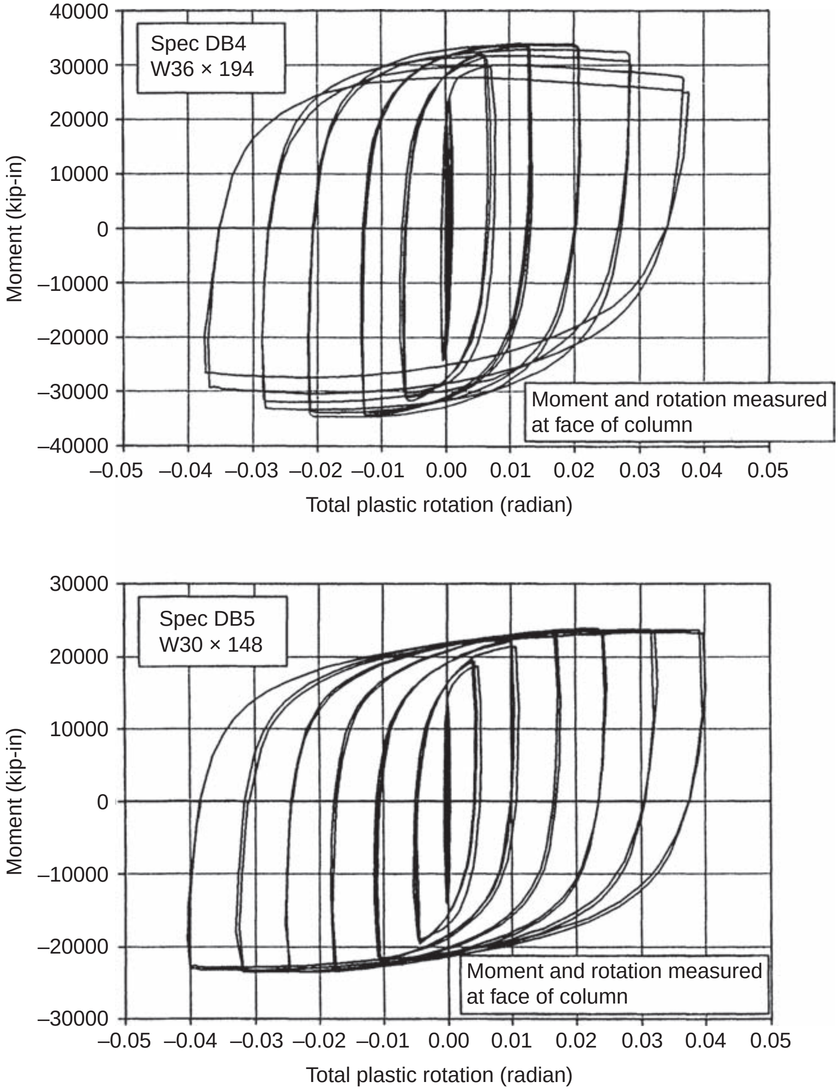

(c)

Figure 8.35 (*Continued*)

beam section delays this strength degradation. High plastic rotation capacities have been achieved when lateral bracing was provided at the end of the dogbone farthest away from the column. Tests indicate a required lateral bracing strength of approximately 4% of the actual force developed by the beam flange (Uang and Noel 1996); AISC 341 specifies that 6% of the expected beam flange capacity at the hinge location be used instead. The RBS concept was eventually prequalified, as described in a later section.

8.5.6 Post-Northridge Beam-to-Column Prequalified Connections

8.5.6.1 New Construction

The selected results presented above provide only a sample of the numerous beam-to-column connection tests conducted in the years following the Northridge earthquake. The online database of tests performed as part of the FEMA/SAC project alone contains results for 513 specimens (available at www.sacsteel.org/connections). Review of this extensive information led to a selected number of pre-qualified connections presented as part of the FEMA 350 "Recommended Design Criteria for Moment Resisting Steel Frames" (FEMA 2000a), to be used together with the design principles described later. This same information was later considered by an AISC Review Panel in developing the AISC 358 "Prequalified Connections for Special and Intermediate Moment Resisting Frames for Seismic Applications," a document referenced by standard specifications and thus more readily accepted by building officials. The FEMA-350 prequalified connections have not all been simultaneous approved into the AISC 358 document; the latter document being an American National Standards Institute (ANSI)-approved consensus-based standard, the critical reassessment of all experimental evidence for some specific types of connections was either incomplete at key publication times, or failed to convince the AISC Review Panel.

Focusing here on connections for SMRF applications, Table 8.4 lists the various prequalified connections recognized by each documents (at various times). Those prequalified by AISC 358-10 are schematically illustrated in Figure 8.36. FEMA 350 prequalifies four welded and three bolted connections, namely, the Welded Unreinforced Flanges-Welded Web (WUF-W), the Free Flange (FF), the Welded Flange Plate (WFP), the Reduced Beam Section (RBS), the Bolted Unstiffened End Plate (BUEP), the Bolted, Stiffened End Plate (BSEP), and the Bolted Flange Plates (BFP)—note that a Double Split Tee (DST) connection is also prequalified as a partially restrained connection. Of those, AISC 358-10 only prequalifies the WUF-W, RBS, BUEP, BSEP, and BFP connections, and adds the proprietary cast-steel Kaiser Bolted Bracket (BB) connection for which licensing fees have been waived (Hamburger et al. 2009).

The characteristics of the RBS detail have been thoroughly described in a previous section; the prequalified connection is a radius cut of prescribed geometry, allowing up to a 50% reduction of the flange width. The WUF-W connection essentially relies on complete joint penetration welded web and flanges using a shear tab of specified

	WUFW*	FF*	WFP*	RBS*	BUEP*	BSEP*	BFP*	BB*
Prequalified By:								
FEMA 350	X	X	X	X	X	X	X	
AISC 358 2005†				X	X	X		
AISC 358 2010	X			X	X	X	X	X
Critical Beam Parameters								
Max. Depth	W36	W30	W36	W36	W24 (55")	W36 (Table)	W30 (W36)	– (W33)
Max. Beam Weight (lb/ft)‡	– (150)	– –	– –	– (300)	– (None)	– (None)	– (150)	– (130)
Min. Span to Depth Ratio	7	7	7	7	7	7	8 (9)	– (9)
Max. $b/2t_f$ ‖	–	$52/\sqrt{F_y}$	–	$52/\sqrt{F_y}$ §	–	–	–	–
Max. Flange Thickness	1"	0.75"	1"	1.75"	0.75"	1" (Table)	0.75" (1")	– (1")

Note: Permissible material per FEMA 350: Beam can be A572 Grade 50, A992, A913 Grade 50/S75; columns can be A572 Grade 50, A913 Grade 50 and 65, A992. Note that A913 Grade 50/S75 has a specified maximum yield point to tensile strength ratio. AISC 358 permitted material are same as in AISC 341, except BB which is an ASTM A958 Grade SC8620 class 80/50 cast steel.

FEMA 350 only prequalifies W12 and W14 columns, except for BUEP case for which W8 and W10 are also permitted. AISC 358-10 permits a broad range of rolled and built-up columns (I-shaped, cruciform, box-shaped, and boxed wide-flange).

*WUF-W = Welded Unreinforced Flanges-Welded Web; FF = Free Flange; WFP = Welded Flange Plate; RBS = Reduced Beam Section; BUEP = Bolted, Unstiffened End Plate; BSEP = Bolted, Stiffened End Plate; BFP = Bolted Flange Plates; BB = Kaiser Bolted Bracket

†Prior to Supplement 1, published in 2009

‡Required only by AISC 358

§Measured at the ends of the center 2/3 of the reduced section of the beam

‖AISC 358 requires web and flange width-to-thickness ratios to conform to AISC 341 limits. Values in Table are listed when specified by FEMA 350.

Table 8.4 Partial List of Limits of Applicability of Prequalified SMRF Connections (Values in Parenthesis Are AISC 358-10 Values when Different from FEMA 350)

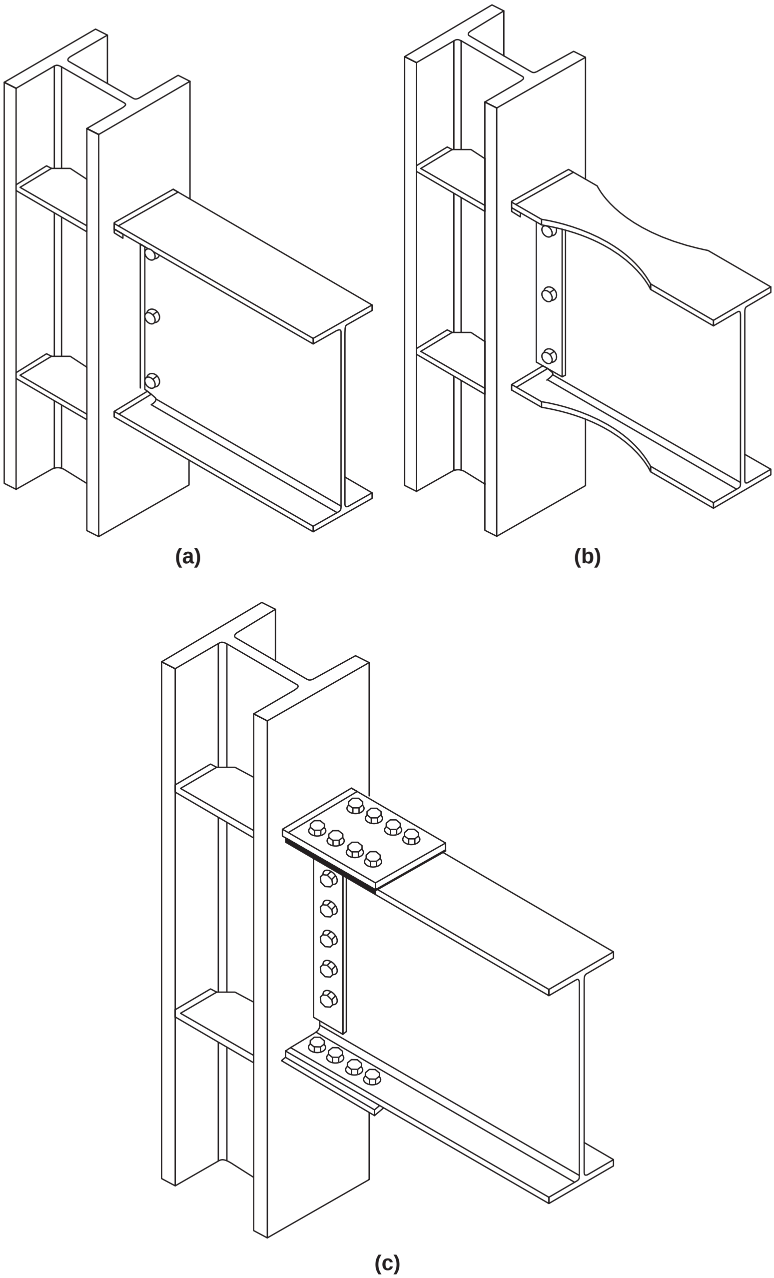

Figure 8.36 Sketch of AISC 358 2010 prequalified SMRF connections: (a) WUF-W; (b) RBS; (c) BFP; (d) BUEP and BSEP, and; (e) BB. Acronyms are defined in a footnote of Table 8.4. (*Courtesy of Ron Hamburger, Simpson Gumpertz & Heger, San Francisco, CA.*)

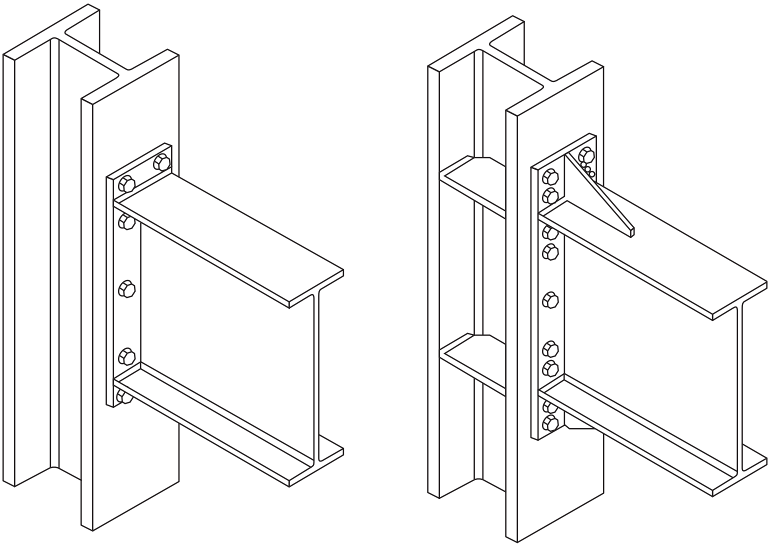

(d)

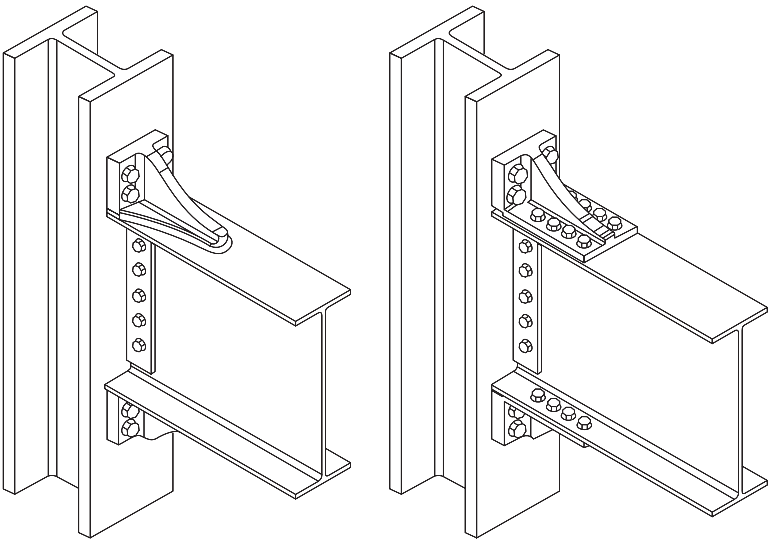

(e)

Figure 8.36 (*Continued*)

minimum geometry, prescribed detailing and welding procedures, and rigorous quality controls. The FF (Figure 8.37) detail was developed building on the observation from finite element analyses that, contrary to classic beam theory, the beam flanges in pre-Northridge moment connections contributed substantially in transferring the

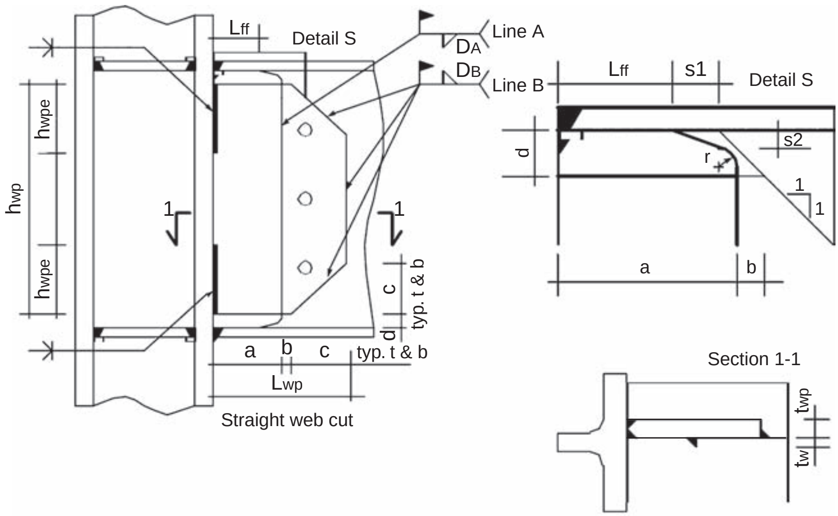

FIGURE 8.37 Free flange connection concept. (*Courtesy of B. Stojadinovic, Dept. of Civil and Environmental Engineering, University of California, Berkeley.*)

shear to the columns, resulting in "flange overload" (Goel et al. 1997). The particular geometry of FF connections is designed to prevent that shift of the shear from the web to the flanges, by substantially cutting back the beam web and using a large welded shear tab to transfer the beam's shear to the column (Choi et al. 2003). The WFP connection uses welded shear tabs and flange cover plates, without welding the ends of the beam flanges to the column.

The prequalified bolted connections require that substantially more limit states be checked, and are sometimes only workable for smaller beams. The BFP connection is analogous to the WFP one, but with cover plates and shear tabs bolted to the beam. The BUEP and BSEP connections are sized to remain elastic and allow development of beam plastic hinging. As such, bolts or end-plate yielding are undesirable failure modes. Bolted end-plate moment connections are popular where shop-welding and field-bolting is the preferred assembly method. Connections with added plate stiffeners, or with a thicker end plate and stronger bolts, detailed per the BUEP or BSEP requirements, have exhibited superior energy dissipation capacity compared with the limited cyclic plastic deformation capacity of others sized in compliance with the conventional design procedure in place prior to the Northridge earthquake (Ghobarah et al. 1990; Ghobarah et al. 1992; Osman et al. 1990; Tsai and Popov 1988, 1990a).

The BB connection consists of high-strength cast steel brackets, either welded or bolted to the beam flanges and bolted to the column, and available in a fixed number of sizes. These castings are subjected to prescribed quality control measures.

Table 8.4 summarizes some of the limits that restrict the applicability of each connection type. Beyond those listed in that table, AISC 358 specifies additional limits that restrict various column parameters, various geometry aspects for welded and bolted configurations, and various other connection-specific details. Guidance is also provided with respect to the lateral bracing requirements, protected zone region, and respective location of plastic hinging, that are to be considered for the design of each connection (as will be discussed later). A testing program conducted in compliance with the requirements outlined in the Appendix of AISC 341 is required to qualify connections that exceed any of the limits listed in that table, or for different types of connections altogether, which in either case can be an expensive endeavor.

In that perspective note that some proprietary connection systems have also been developed (Nelson 1995), and although these are not prequalified by either FEMA 350 or AISC 358, some jurisdictions and authorities have accepted their implementation in various projects on the basis of experimental evidence. The database of past tests conducted to investigate and demonstrate satisfactory seismic performance varies from one type of patented connection to the other, and peer review is sometimes required before project-specific implementation. Examples of proprietary systems used in a number of past projects include the Side Plate (SP) connection and the Slotted Web (SW) connection; information on their performance and implementations can be obtained from the respective licensors of these technologies.

There is no definite answer either as to which of the above connections is the most cost effective. Cost comparisons need to account for cost of connections, royalty fees for proprietary systems, and influence of the connection detail on the weight of the steel frame and the cost of the foundations.

The FEMA 350 and AISC-358 procedures to design beam-to-column connections of the type described above are sensibly similar; however, only the AISC procedures are considered from this point onward—and presented in Section 8.6. Nonetheless, the FEMA 350 report is a comprehensive resource that documents much of the fine points that are part of this methodology and refers to the relevant literature. As such, it is a valuable recommended reading.

8.5.6.2 Retrofits and Repair of Existing Construction

FEMA 350 and AISC-358 are focused on new construction. Different types of connections and levels of expected seismic performance may be adopted with respect to repair and rehabilitation works. Often, repairs are emergency measures that bring a damaged structure back to its pre-earthquake condition. If the exact same earthquake that initially damaged a structure would strike again after completion of repairs to the structure, one could reasonably expect the same damage to recur (assuming, obviously, that repairs were not accompanied by some measures of strengthening). Rehabilitations (also called retrofits or modifications in some documents) are measures intended to enhance the seismic performance of an existing structure.

Seismic rehabilitation is a complex subject whose breadth exceeds the scope of this book. In principle, the connection strategies developed for new construction should be equally effective in existing buildings. Unfortunately, many of those solutions cannot be economically implemented in existing buildings without major modifications. For example, new structural elements added to a connection, such as haunches, will have to work in parallel with the existing flange groove welds recognized as likely to perform poorly in future earthquakes, and additional measures may also be necessary to correct these weld deficiencies. Likewise, moment-resisting frames in existing buildings are frequently located at the edge of buildings (i.e., the optimal location to provide seismic torsional resistance in plan); as a result, access to the outside face of the connection is not possible without removal of the exterior cladding, by itself a practical impediment to the implementation of some seismic rehabilitation strategies. Although many of the concepts and details presented here for new construction can be applied to seismic rehabilitation, the FEMA 351 and FEMA 352 reports (FEMA 2000b, 2000c) provide specific information respectively targeted to address retrofits and repairs.

8.5.7 International Relevance

Moment frame connections identical to those that fractured during the Northridge earthquake have also been commonly used in other countries (e.g., Tremblay et al. 1995). Furthermore, irrespective of the types of moment connections used, the Northridge experience reinforces the need for substantial full-scale experimental verification of connection details, for quality workmanship and inspection, and for periodic experimental re-evaluation of accepted practices to assess the significance of accumulated changes in materials properties, welding procedures, and other issues as the steel industry further evolves. A brief review of the Japanese experience is instructive in this regard.

8.5.7.1 Kobe Earthquake Experience

Steel design practice in Japan has favored the use of "column trees" in the construction of moment-resisting frames. This concept typically involves the welding of stub-beams to a column prior to its shipment to the building site where the remaining beam segments are field-bolted to the stub-beams (Figure 8.38). In principle, all welds of columns, beams, and continuity plates (known as diaphragms in Japan) are accomplished in the shop, with automated welding processes and under tight quality control (Nakashima et al. 2004). For that reason, such connections were thought to be superior to the prequalified moment connection used in the United States prior to the Northridge earthquake. Unfortunately, the Kobe earthquake, striking exactly one year after the Northridge earthquake, revealed this belief to be partly unfounded (Tremblay et al. 1996).

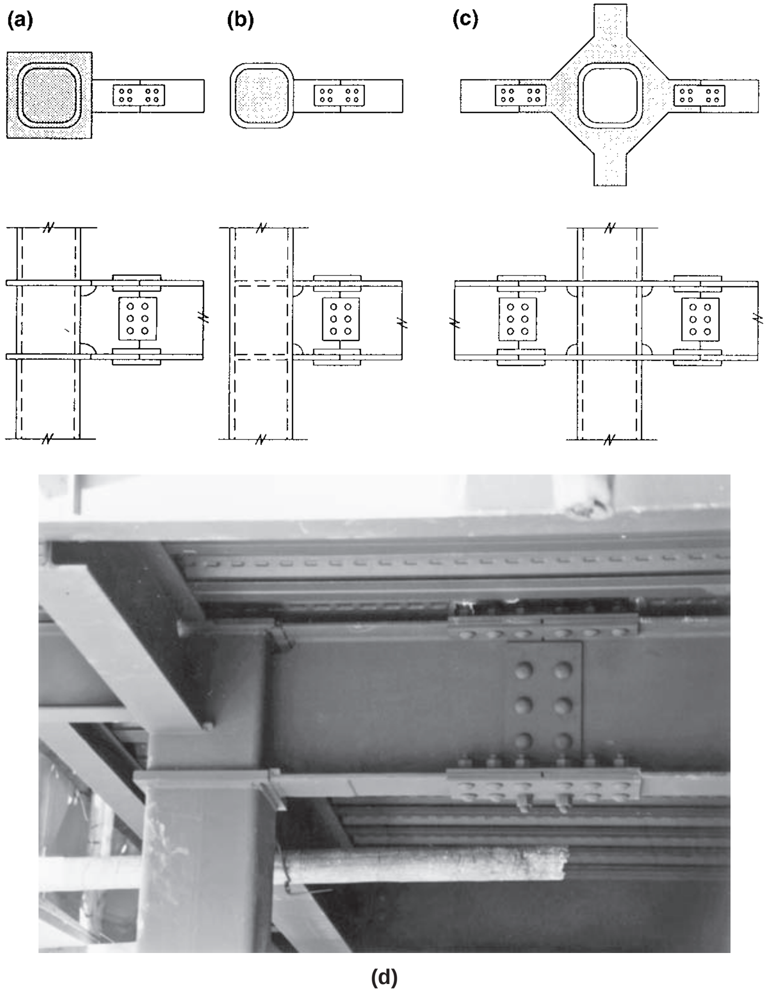

Figure 8.38 HSS columns in Japanese column-tree moment-resisting frames, with: (a) through-diaphragm; (b) interior diaphragm; (c) exterior diaphragm; (d) typical column-tree construction with through-diaphragm.

An investigation by the Steel Committee of the Architectural Institute of Japan covering 988 modern steel buildings following the 1995 Hyogo-ken Nanbu (Kobe) earthquake reported 332 cases of severely damaged buildings, 90 collapses, and 113 buildings for which damage to beam-to-column connections was observed (AIJ 1995, Nakashima 2001, Nakashima et al. 1998, Nakashima et al. 2000). Numerous cases of brittle fractures occurred, and 47 of the buildings that collapsed were moment frames constructed with the column tree system. The tallest steel frame buildings that collapsed had five stories. It is significant in this regard that in typical Japanese buildings, all frames throughout a building have rigid moment-resisting beam-to-column connections, contrary to North American practice, in which moment-resisting connections are limited to a few frames in each principal directions of a building.

The beam-to-column failures observed during the Kobe earthquake differed somewhat from the Northridge failures in that cracking and fractures were frequently (but not always) accompanied by plastic hinging in the beams. This evidence of plastification was observed mostly in the more modern moment frames having square-tube columns and full penetration welds of the stub-beams to the diaphragms. In the majority of these cases, no sign of plastification was observed in the columns. Most of the fractures occurred in the lower flange of the beams, and the beams exhibited clear signs of plastic hinging accompanied by local buckling of the flanges (Figure 8.39), although, in some cases, the level of plastification was modest. Typically, fracture initiated either from the corner of a weld access hole, near a run-off tab or a weld toe, or in the heat-affected zones in the beam flange or diaphragm. In many cases, the fracture progressed into the beam's web (e.g., Figure 8.39b), and, in some cases, propagated into the column flanges (e.g., Figure 8.39d).

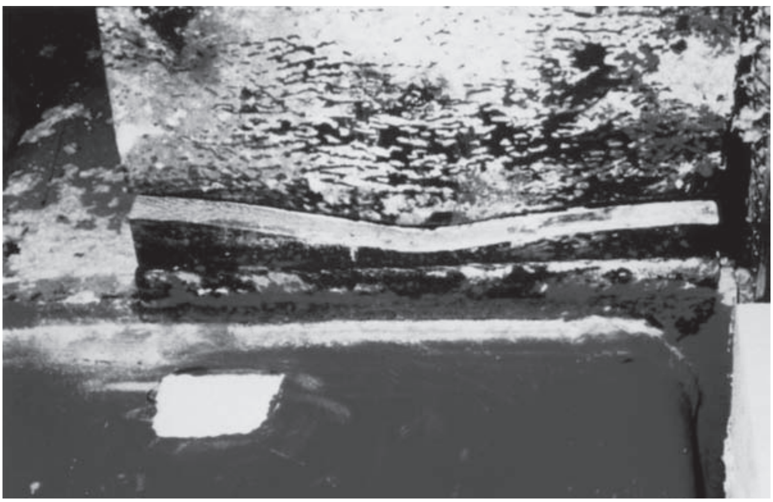

(a)

Figure 8.39 Damage to Japanese column-tree moment connections in modern moment-resisting frames with square-tube columns and full penetration welds at the beams, due to the Hyogo-ken Nanbu (Kobe, Japan) earthquake: (a) fracture at the lower beam flange; (b) propagation of fracture in the beam web; (c) fracture initiated in the heat-affected zone of the diaphragm, (d) propagation of fracture in the column. (*Parts a to d from* Performance of Steel Buildings during the 1995 Hyogo-ken Nanbu Earthquake *by Architectural Institute of Japan, courtesy of the Committee on Steel Structures of the Kinki Branch of the Architectural Institute of Japan.*)

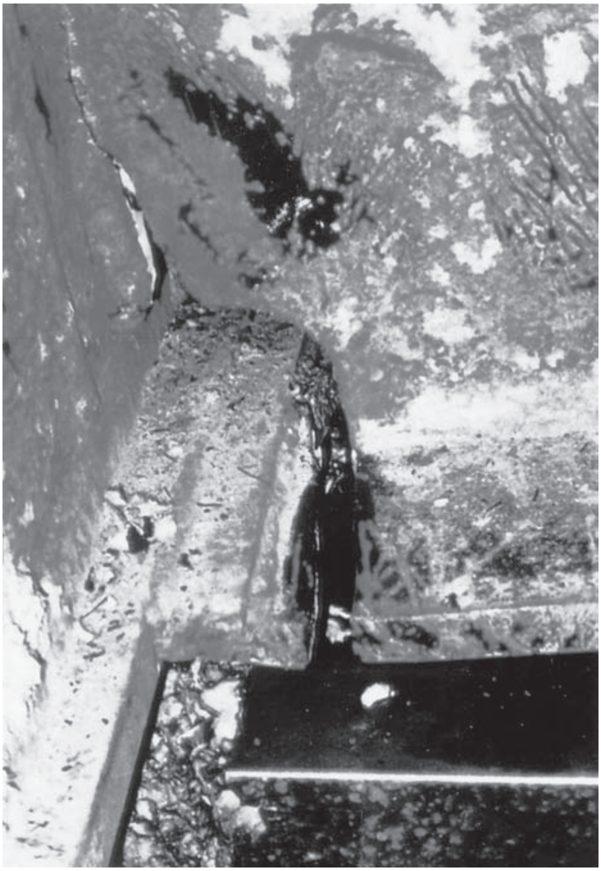

(b)

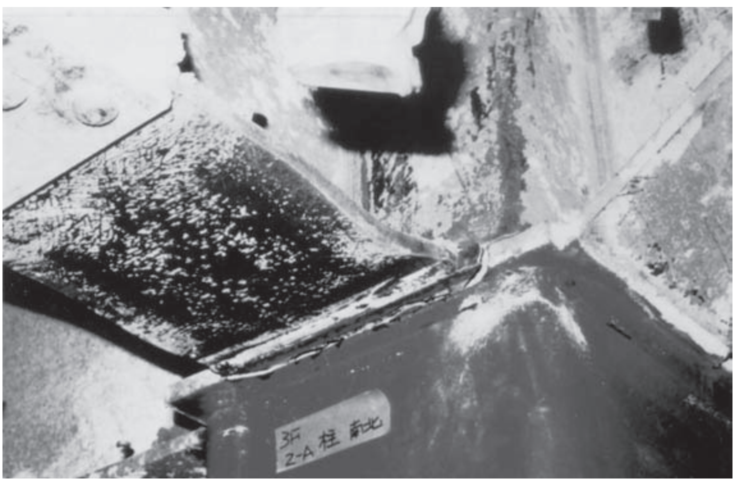

(c)

Figure 8.39 (*Continued*)

(d)

Figure 8.39 (*Continued*)

Many beam-to-column connections cracked and fractured without any signs of plastification when fillet welds were used in lieu of full penetration groove welds. These fillet welds were often too small to develop the capacity of the connected members (Figure 8.40a). Many other types of moment connections also suffered serious damage (Figure 8.40b). Notably, when tube columns were used, cracking and fracture frequently occurred in the columns above or below the top or bottom diaphragm (Figure 8.41a), sometimes leading to complete overturning and collapse of the structure (Figure 8.41b). Damage to the beam-to-column connections of at least 59 moment frames having square-tube columns was reported by the AIJ, with about 70% of those rated as either collapsed or severely damaged. Although most of those surveyed buildings that collapsed had fillet-welded moment connections, at least three buildings having full-penetration welded moment connections collapsed (AIJ 1995).

8.5.7.2 Post-Kobe Beam-to-Column Connections

Notable differences existed between North-American pre-Northridge and Japanese pre-Kobe practices (Nakashima et al. 2000), and logically still remains after these two earthquakes (Nakashima 2001, Nakashima et al. 2000). Moment frames designed and constructed in compliance with the best Japanese practices at the time of the Kobe earthquake arguably performed relatively well in spite of the reported failures. Consequently, the post-Kobe modifications to beam-to-column connection details were more evolutionary than revolutionary. Although

(a)

(b)

FIGURE 8.40 Examples of beam-to-column welded connections damaged by the Hyogo-ken Nanbu (Kobe, Japan) earthquake: (a) fracture along fillet welds of moment connection at the first story of a multistory residential building; (b) large residual interstory drift in a moment frame with damaged connections; (c) close-up view of fractured welds along box-column plate for frame shown in Figure 8.40b.

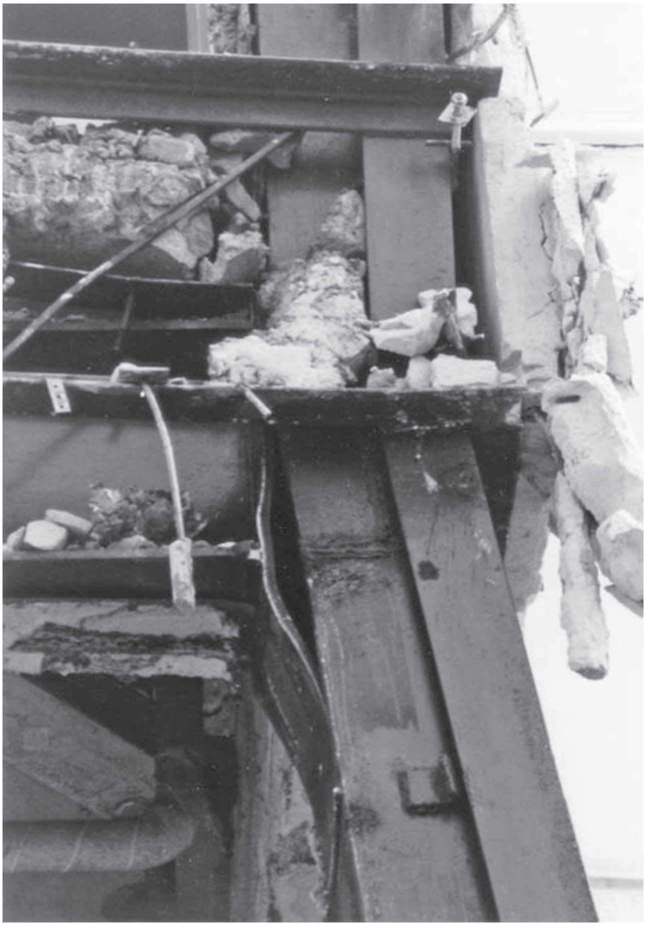

(c)

Figure 8.40 (*Continued*)

no single factor alone could explain the observed failures, a number of issues of paramount importance with respect to the Northridge failures had already been addressed in Japan prior to the Kobe earthquake. For one, existing Japanese steels having good notch toughness were already being used—for example, tests on the base metal of a fractured beam gave Charpy-V values of 50 J at 0°C (Nakashima et al. 1998). Likewise, steels having both upper and lower yield and tensile strengths, and an upper bound of 0.8 for the ratio of the yield to the tensile strength, were being introduced at the time of the earthquake, and became rapidly accepted (although not mandatory).

Given that 20.5% of the damaged moment connections fractured in the base metal, with cracks initiating from the toe of the weld access

(a)

(b)

Figure 8.41 Examples of beam-to-column damage due to the Hyogo-ken Nanbu (Kobe, Japan) earthquake: (a) fracture in column-to-diaphragm welded connections; (b) overturning of a building as a consequence of such fractures.

hole, many post-Kobe studies focused on modifying connection details to minimize the stress and strain concentrations at that access hole location. Interestingly, although 24.4% of the damaged moment connections fractured in the weld metal, 10.3% had cracks at craters, and 37.2% had fractures initiating from run-off tabs, these were

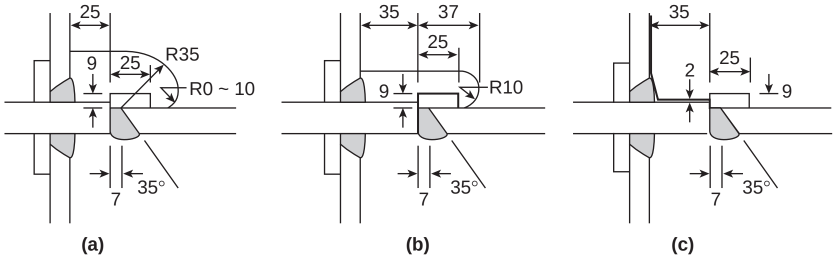

Figure 8.42 Weld access hole: (a) pre-Kobe standard detail; (b) post-Kobe modified detail with smaller hole; (c) post-Kobe no-hole detail. (*Courtesy of M. Nakashima, Disaster Prevention Research Institute, Kyoto University, Japan.*)

speculated to have been caused by welding voltages and deposition rates exceeding specified values, together with excessive weld "weaving" (i.e., welding along a zigzag path rather than directly along the weld axis), given that the use of gas-shielded arc welding (which typically contribute to greater weld toughness) was already a common practice (Nakashima 2001).

The revised JASS-6 steel fabrication specifications published following the Kobe earthquake (AIJ 1996) proposed revised shapes and sizes for weld access holes, but did not require removal of the backing bars and run-off tabs. Along that same line of thinking, subsequent research demonstrated that details without any access hole could ensure highly ductile seismic performance (Suita et al. 1999). Figure 8.42 shows the Japanese access hole details specified before and after the Kobe earthquake, together with the proposed no-hole detail. A test specimen with the no-hole detail is shown in Figure 8.43 together with a reference specimen having a RBS connection representative of North American best practice at the time. The moment-rotation hysteretic curves obtained for both of these connections are shown in Figure 8.44, together with that for a pre-Kobe detail. The no-hole and RBS connections exhibited stable hysteretic behavior up to plastic rotations of 0.03 to 0.04 radians. The pre-Kobe connection, although relatively ductile, did not perform as well.

8.5.8 Semi-Rigid (Partially Restrained) Bolted Connections

Although fully rigid moment connections are preferred in contemporary seismic design, all connections have an inherent flexural resistance; this strength may be marginal in the case of connections considered as "flexible" (or "pin" connections), or more substantial in the case of semi-rigid or partially restrained connections. In many instances, particularly in older frames, these connections were present at the ends of every beam throughout the entire building—

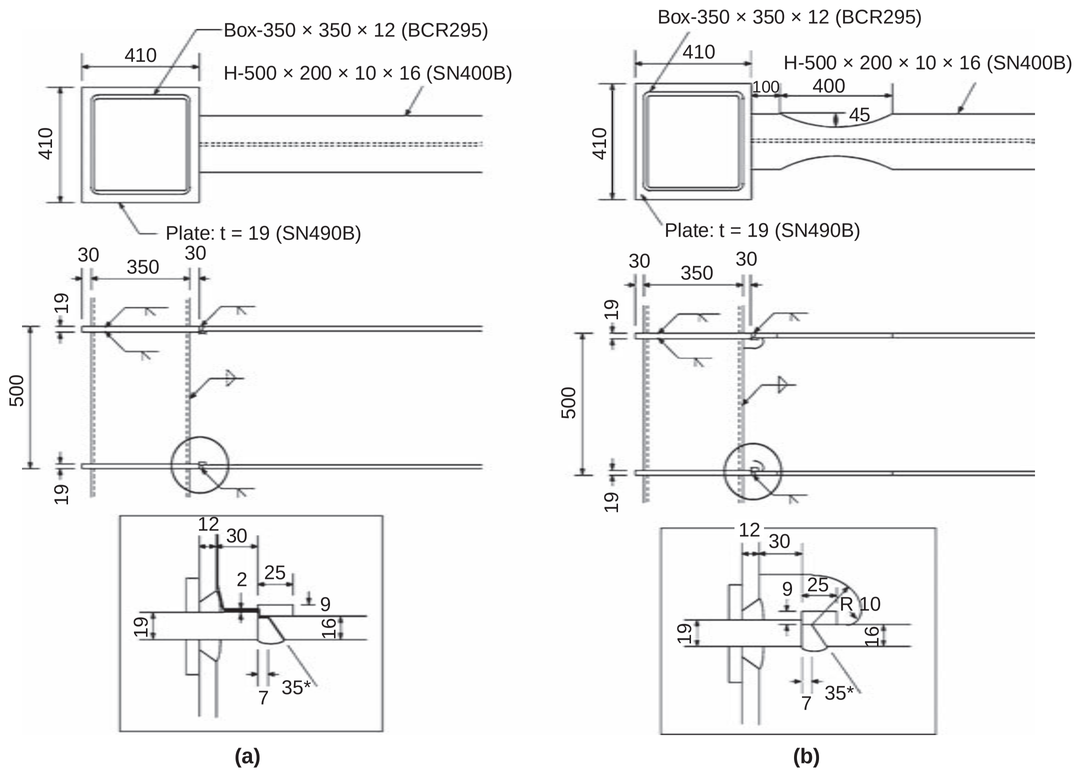

Figure 8.43 Moment connection specimens considered for Japanese practice: (a) no-hole detail; (b) RBS detail. (*Courtesy of M. Nakashima, Disaster Prevention Research Institute, Kyoto University, Japan.*)

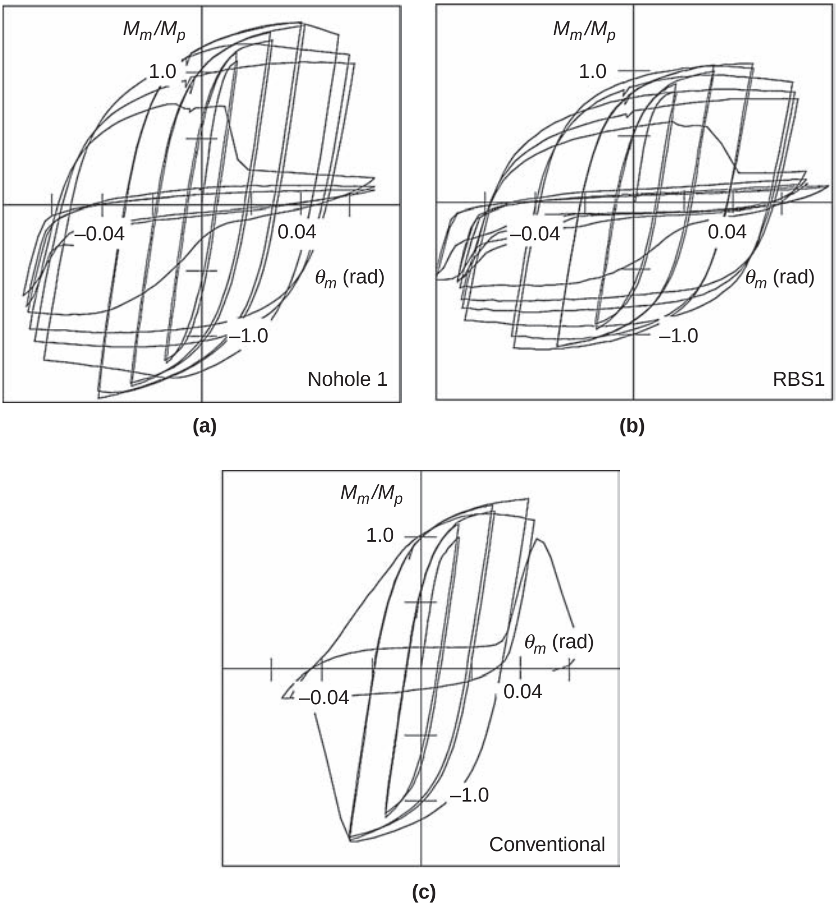

FIGURE 8.44 Hysteretic behavior of moment connections: (a) no-hole connection detail; (b) RBS connection detail; (c) pre-Kobe connection detail. (*Courtesy of M. Nakashima, Disaster Prevention Research Institute, Kyoto University, Japan.*)

a redundancy that compensated somewhat for the fact that each individual connection developed less than the beam's flexural capacity.

Much of the past research on seismic beam-to-column connections has focused on fully rigid welded connections. Semi-rigid connections may be viable alternatives in some cases, but they have not received as much attention as fully rigid ones from engineers practicing in regions of high seismic risk. Although the behavior of semi-rigid connections subjected to a limited level of reverse loading (to assess their rigidity under wind loads) was first investigated approximately a century ago (e.g., Moore and Wilson 1917), full-scale cyclic tests intended to be representative of seismic demands started in the mid-1980s (e.g., Astaneh et al. 1989, Elnashai and Elghazouli 1994, Leon et al. 1994, Liu and Astaneh 2000, Radziminski and Azizinamini 1986, Roeder et al. 1996, Sarraf and Bruneau 1996). Notably, FEMA 350 included design requirements for a Double Split Tee detail prequalified as a full-strength but partial stiffness connection (FEMA 2000a), and FEMA 355d (2000d) discusses the cyclic behavior of a number of semi-rigid partial-strength connection details.

Bolted partial-strength semi-rigid connections are easier to implement than fully rigid connections for deep beams framing into heavy columns, given that the strength, stiffness, and ductility of such typical semi-rigid connections are governed by that of the connecting elements (e.g., angles, plates). Semi-rigid connections are often capable of developing plastic rotations of 0.03 radian, as shown in Figure 8.45 for an existing riveted connection retrofitted to develop a

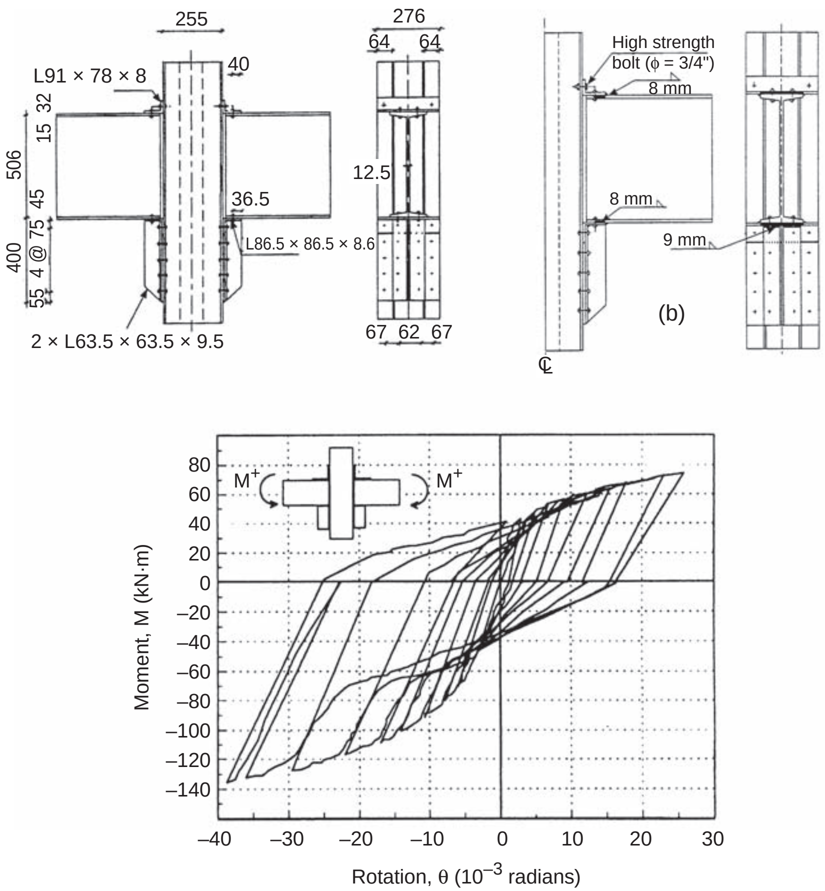

Figure 8.45 Hysteretic behavior of riveted stiffened seat-angle semi-rigid connection retrofitted using selective welding strategy, in terms of moment versus beam plastic rotation. (*From Sarraf and Bruneau 1994.*)

ductile semi-rigid behavior. Semi-rigid connections can also be easily repaired if necessary following an earthquake. However, the lower stiffness of semi-rigid connections with respect to fully rigid connections will require stiffer (and heavier) beams and columns to comply with code-specified drift limits and thus larger beam-to-column connections. In computer models, beams are typically connected to columns using spring, or modeled with equivalent flexural rigidities, and the additional flexibility of these frames often require rigorous consideration of P-Δ effects.

Seismic behavior of semi-rigid connections, an enormous topic by itself, is beyond the scope of this book. Some of that information is presented in Chen et al. (2010).

8.6 Design of a Ductile Moment Frame

8.6.1 General Connection Design Issues

AISC 358, with appropriate references to AISC 341, systematically outlines the issues that must be addressed for each type of prequalified connection. Specifically, the specific steps of that process include:

- A description of the prequalified connections and their intended energy dissipation mechanism (which would be, for example, yielding and hinge formation primarily within the reduced section of the beam in an RBS connection).
- A list of the beam and column limits that must be respected for the connection to be prequalified for various types of structural shapes; some of these limits for beams are summarized in Table 8.4. Note that although various types of column cross-sections are permitted, only W-shape beams are allowed (or equivalent built-up beams having their web joined to their flanges by full-penetration welds).
- Seismic compactness requirements (i.e., limits on width-to-thickness ratios) and lateral bracing requirements.
- A description of the location and size of the "protected zone," these being the parts of the structural members or connections over which alterations, perforations, and attachments are prohibited so as to not impair their ability to undergo large inelastic deformations.
- A description of the requirements that must be satisfied to ensure strong-column/weak-beam design, and thus prevent column hinging.
- Specified requirements for column panel zone and continuity plates design.

- Prescribed bolting and welding detailing requirements for the connection to be prequalified. For example, for a beam bottom flange having complete penetration welds to a column, the steel backing plate used at that location must be removed, the exposed root pass must be backgouged to sound weld metal and backwelded with a reinforcing fillet—the fillet leg adjacent to the column flange being at least 5/16 in (8 mm), and the fillet leg adjacent to the beam flange being long enough to ensure that the fillet toe is located on the beam flange base metal.
- Specific fabrication details applicable to individual connections (e.g., the thermal cutting process, maximum permissible surface roughness of the cut, geometry details, tolerances, procedure to repair gouges and notches, and inspection procedure, are specified for the RBS connection).
- A design procedure, outlining in sequence all the limit states that must be checked to obtain a satisfactory prequalified connection (see Section 8.6.2).
- A specified design value for the distance of the plastic hinge located away from the column face.
- Prescribed bolted and welded details required for the connection to be prequalified (as shown in Section 8.8 example).

This chapter has already provided insights into some of the above important aspects governing the behavior of moment frames (e.g., design of panel zones and their modeling in structural analysis described in Section 8.4.5; need to use seismically compact sections and to provide bracing against lateral torsional buckling described in Section 8.2.3). A few additional important considerations follow.

8.6.2 Welding and Quality Control Issues

As mentioned in Section 8.5.3, factors contributing to the connection failures during the Northridge earthquake included the low fracture toughness of the welding metal used (typically E70T-4 electrodes), weld defects (such as those frequently found at the midwidth of bottom flange, on runoff tabs, etc.), and detrimental weld details. For example, dynamic loading tests indicated that the use of weld metals with high notch toughness properties, such as those accomplished with E7018 filler metal, improved performance when used in conjunction with good detailing practice, including among many things removal of backup bars and weld runoff tabs (e.g., Kaufmann et al. 1996, Xue et al. 1996).

The FEMA-353 recommended welding requirements and quality assurance guidelines for seismic applications, developed following the Northridge earthquake (FEMA 2000d), have for the most part been adopted into consensus codes. Minor conflicting requirements between AISC 341 (2005) published before AWS D1.9 2005 (Stockmann and Schlafly 2008) have been resolved in subsequent editions of these specifications. Both AISC 341 and AISC 358 reference the AWS D1.9 (AWS 2009) for numerous issues related to "demand-critical welds," which are those welds in seismic applications connecting yielding elements and whose failure would produce significant strength and stiffness degradation of the energy dissipating elements. For example, demand-critical welds are specified for beam-to-column complete joint penetration welds or other yielding applications when cross-thickness loading or triaxial stress states exist.

Given the recognized benefits of using filler metal with relatively high notch toughness and better weld quality, demand critical welds are required to have a minimum Charpy-V notch toughness of 20 ft-lbs (27 J) at 0°F (−18°C). More stringent requirements are required if the steel frame is exposed to service temperatures lower than 50°F. AWS D1.8 also limits hydrogen content for all welding electrodes and electrode-flux combinations to prevent hydrogen-induced cracking, and specifies requirements for workmanship, inspection, welder qualification, welding procedure and material, and other issues to ensure quality welds (AWS 2009, Hamburger et al. 2007, Miller 2006).

For each prequalified connection, AISC 358 also refer to the appropriate documents for weld access hole configuration, surface smoothness, and inspection, to prevent notches and surface defects that can lead to cracking in this region of complex stress flow. A similar approach is taken to specify when backing bars need be removed, and when additional weld fillet and special detailing is required.

For example, for WUF-W connections, AISC 358 specifies that the weld access hole geometry shall conform to the requirements of AWS D1.8. Although AWS D1.8 indicates that the standard access hole geometry specified in its main structural welding code (AWS D1.1) is acceptable in most conditions, it also includes an "alternate geometry" access hole detail identical to the one recommended by FEMA 350 on the basis of finite element analyses and experiments that demonstrated improved performance for some connection types (Figure 8.46).

8.6.3 Generic Design Procedure

Selection of a specific type of prequalified connection is typically driven by cost comparisons, past experiences, engineering/fabricator preferences, or other reasons. For each prequalified connection, AISC 358 provides a different step-by-step design procedure—the complexity of the design requirements integral to each procedure being proportional to the number of its limit states, given the need to prevent all undesirable failure modes. However, some basic fundamental principles are applicable to most of the prequalified connections, as described below.

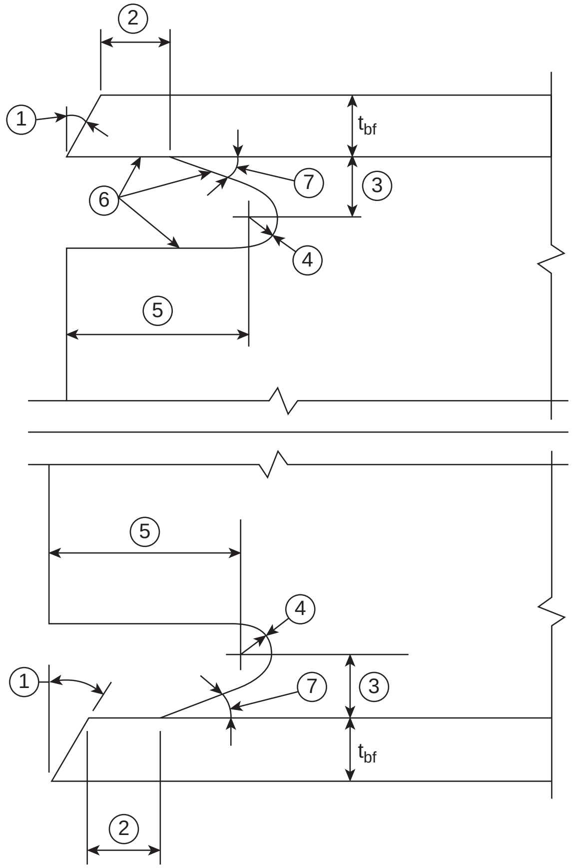

Notes:
1. Bevel as required for the WPS.
2. t_{bf} or 1/2 in [12 mm], whichever is larger (plus 1/2 t_{bf}, or minus 1/4 t_{bf}).
3. The minimum dimension shall be 3/4 t_{bf}, or 3/4 in [20 mm], whichever is greater. The maximum dimension shall be t_{bf} (+1/4 in [6 mm]).
4. 3/8 in [10 mm] minimum radius (–0, +unlimited).
5. 3 t_{bf} (±1/2 in [12 mm]).
6. See 6.10.2.1 for surface roughness requirements.
7. Tolerances shall not accumulate to the extent that the angle of the access hole cut to the flange surface exceeds 25°.

Figure 8.46 AWS D.18 Alternate Geometry for Beam-Flange Weld Access Hole Detail—surface roughness requirements of 500 μin (13 μmm) per clause 6.10.2.1. (AWS D1.8/D1.8M:2009, Figure 6.2; *Reproduced with permission of the American Welding Society* [*AWS*], *Miami, Florida*.)

8.6.3.1 Free-Body Diagram for Plastic Hinge Away from Column Face

Generically, the design procedures rely on capacity design concepts and strategies to relocate plastic hinges away from the column faces. This forces the development of a plastic mechanism like the one in

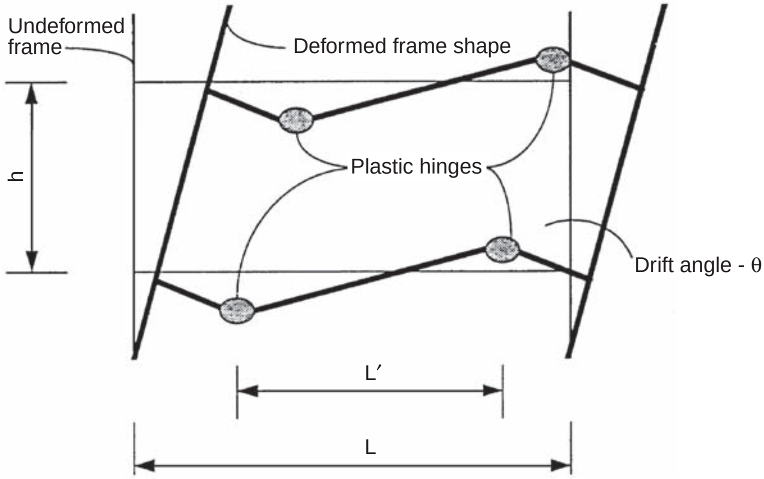

Figure 8.47 Desired plastic collapse mechanism in post-Northridge ductile moment-resisting frames. (*From* Interim Guidelines: Evaluation, Repair, Modifications, and Design of Steel Moment Frames, *SAC Joint Venture, 1995, with permission.*)

Figure 8.47 (shown for a single bay frame for expediency, recognizing that moment-frames of multiple bays are encouraged to promote redundancy).

Figure 8.48 shows the corresponding free-body diagrams that are used as part of the AISC 358 design procedure (showing haunches as beam reinforcement for schematic simplicity and convenience, recognizing that haunch connections are not prequalified per AISC 358). The distance to plastic hinge from the face of the column, S_h, specified by AISC 358 for each connection type based on experimental evidence, is used to determine the moments and shears at the plastic hinge locations, column faces, and center of columns, from which all other needed parameters can be calculated.

For example, for end-plate connections, S_h is specified as the lesser of $d/2$ or $3b_{bf}$ for the BUEP unstiffened connection, and as $L_{st} + t_p$ for the BSEP stiffened connection, where d and b_{bf} are the beam's depth and flange width respectively, L_{st} is the length of the end-plate stiffener, and t_p is the thickness of end plate. For the BFP connection, it is equal to $S_1 + s\ (0.5n - 1)$, where S_1 is the distance from face of column to nearest row of bolts, s is the spacing of bolt rows, and n is the number of bolts rounded to the next higher even number increment. For BB connections, the plastic hinge is located at a distance equal to the length of the bracket.

For an RBS connection, $S_h = a + b/2$, where a is the horizontal distance from the column face to the start of the RBS cut, and b is the

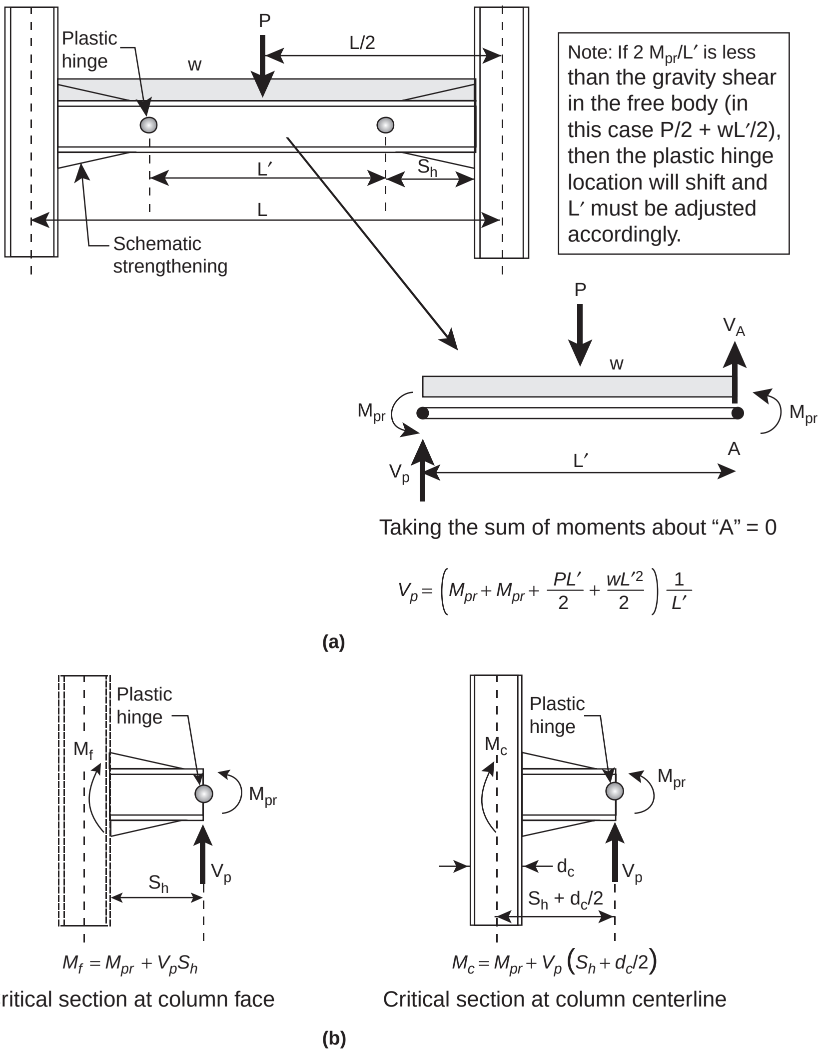

Figure 8.48 Design of post-Northridge ductile moment-resisting frames: (a) free-body-diagram to calculate shear at plastic hinges; (b) free-body diagrams to calculate moments at column face and column centerline. (*Adapted from* Interim Guidelines: Evaluation, Repair, Modifications, and Design of Steel Moment Frames, *SAC Joint Venture, 1995, with permission.*)

length of the RBS cut, as shown in Figure 8.33c. The AISC 358 design procedure also restricts the geometry of RBS connections to

$$0.5b_{bf} \le a \le 0.75b_{bf} \tag{8.23a}$$

$$0.65d \le b \le 0.85d \tag{8.23b}$$

$$0.1b_{bf} \le c \le 0.25b_{bf} \tag{8.23c}$$

where c is the depth of the cut at the center of the reduced beam section (Figure 8.33c), and all other terms have been defined earlier. Note that the RBS section itself, like all other beams and columns throughout the frame, must have adequate strength to resist the moments, shears, and axial forces computed for all the applicable code-specified forces and load combinations. Design story drift limits must also be met, either by specifically accounting for the actual reduction in stiffness at the RBS or, more expeditiously, by increasing by 10% the drifts calculated using beam gross cross-sections for the RBS case having 50% reduction in flange width (this drift magnification factor can be interpolated for lesser flange width reductions).

Note that, in a significant departure from FEMA 350, AISC 358 specifies $S_h = 0$ for WUF-W connections, even though yielding of beams having such connections has been observed to spread from the face of columns up to a distance of one beam depth beyond that point. This was done to simplify the design calculations, with other deviations from the standard design procedure introduced later on to compensate for this simplification.

Caution is also warranted in comparing FEMA 350 and AISC 358, because S_h is inconsistency defined in those documents, being measured from the column centerline in FEMA 350 rather than from the column face as done here and in AISC 358.

8.6.3.2 Probable Maximum Moment at Plastic Hinge Location

The probable maximum moment, M_{pr}, at the plastic hinge location specified for the prequalified connection, is given by:

$$M_{pr} = C_{pr} R_y F_y Z_e \tag{8.24}$$

where R_y is the ratio of the expected yield stress to the specified minimum yield stress F_y, Z_e is the effective plastic section modulus at that plastic hinge location, and C_{pr} is a magnification factor to account for the peak connection strength expected due to the effects of strain-hardening, local restraints, additional reinforcement, and other conditions.

For plastic hinges in beams, Z_e is the plastic section modulus about the x-axis of the full beam cross-section, Z_x, except in RBS connections where it is computed at the center of the reduced beam section and therefore equal to:

$$Z_e = Z_x - 2ct_{bf}(d - t_{bf}) \tag{8.25}$$

where t_{bf} is the thickness of the beam flange and all other terms have been defined previously.

In general, C_{pr} is given as:

$$C_{pr} = \frac{(F_y + F_u)}{2F_y} \leq 1.2 \tag{8.26}$$

except for WUF-W connections, for which C_{pr} shall be taken as equal to 1.4 because the specified plastic hinge distance is zero. In Eq. (8.26), F_u is the specified minimum tensile strength of the yielding steel.

8.6.3.3 Shear Forces at Plastic Hinge Location

Shear forces acting at the plastic hinge locations are obtained by equilibrium equations from a free-body diagram of the beam segment between plastic hinge locations, as shown in Figure 8.48. The largest of the shear forces at these two beams ends, considering the effects of gravity, is called V_p here (for different prequalified connections, AISC 358 uses the terms V_u, V_h, and V_{RBS}, practically for the same purpose), and given by:

$$V_p = \frac{2M_{pr}}{L'} + V_{Gravity} \tag{8.27}$$

For the example shown in Figure 8.48, with a uniformly distributed load and an additional point load at the beam's midspan:

$$V_{Gravity} = \frac{\omega L'}{2} + \frac{P}{2} \tag{8.28}$$

The shears for beams having other gravity loading patterns would be similarly obtained. Note that factored gravity loads per the applicable building code load combinations must be considered.

8.6.3.4 Forces at Column Face and Column Center Line

As shown by the other free-body diagrams in Figure 8.48, the moment acting at the face of the column, M_f, is given by:

$$M_f = M_{pr} + V_p S_h \tag{8.29}$$

while the moment at the column centerline is:

$$M_c = M_{pr} + V_p\,(S_h + 0.5\,dc) \tag{8.30}$$

where d_c is the column depth.

Note that, for simplicity, the above equations neglect the gravity load over the distance S_h. For consistency, AISC 358 also considers the shear acting at the column face to be V_p. Obviously, consideration of the gravity load over that small segment is permitted, as it would be more rigorous and statically correct.

The moment at the column centerline is required to verify if the strong-column/weak-beam design requirement is met. The shear and moments at the face of the column are needed to size various aspects of the prequalified connections at that location.

For RBS connections, it must also be ensured that the moment at the column face does not exceed the plastic strength of the beam (based on expected yield stress) when the minimum section of the RBS is fully yielded and strain hardened, therefore:

$$M_f \leq M_{pe} = R_y Z_x F_y \tag{8.31}$$

Adjusting the geometry of the RBS may be needed to meet this requirement.

8.6.3.5 Other Detailing Requirements

The details of each of the prequalified connection are then designed to resist the above appropriate moments and shears. AISC 358 spells out the various limit states to consider for each prequalified beam-to-column connections (such as tension and shear strength of bolts and filet welds, block shear strength, and effect of prying action, to name a few), providing design equations as appropriate. For bolted connections, it is also required that the tensile strength at the net section of flanges be greater than the yield strength at their gross section (i.e., $R_t A_n F_u > R_y A_g F_y$, where R_t is the ratio of the expected tensile strength to the specified minimum tensile strength for the flange under consideration, and all other parameters have been defined previously). Specific required welding procedures are also outlined as appropriate.

The AISC 341 requirements for strong-column/weak-beam design, continuity plates, and panel zone design are referenced as part of the design procedure. On that latter point, it is worthwhile to caution that even though the combined action of panel zone yielding and beam hinging can be helpful in reducing plastic rotation demands in beams, substantial panel zone yielding will develop (up to $4\gamma_y$ in principle) if Eq. (8.15) is used. For many reasons, it may be preferable to concentrate plastic hinging in the beams. Experimental observations indicate that uncertainties in true material strengths make the intended sharing of plastic rotation between the beam and panel zone impossible to control. For example, panel zones in columns with weaker than average yield values would have to provide all of the required hysteretic energy dissipation if coupled with beams having stronger than average strengths, and vice versa. Also, although panel zones can be reliable energy dissipators, the kinking of column flanges at large panel shear strain deformations generates complex triaxial stress conditions and possible fracture at the beam flange welds.

8.7 *P*-Δ Stability of Moment Resisting Frames

Consideration of P-Δ effects in moment frames has long been recognized as important to prevent collapses due to instability during earthquakes. Also, more recently, the topic has been the subject of a renewed research interests to more reliably define the conditions of incipient collapse during earthquakes and methods to model behavior through all stages of collapse, in parallel with intensified research efforts on progressive collapse. However, a broad consensus is still lacking on many aspects related to these issues.

For the current purpose, a brief overview of some fundamental concepts is presented, followed by a description of the ASCE design requirements. Other design codes and standards internationally have similar, but not identical, provisions. A survey of existing research on structural stability during earthquakes excitations is available in Ziemian (2010).

8.7.1 Fundamental Concept and Parameters

The concept of P-Δ effects under static loading is illustrated in Figure 8.49a using a single degree of freedom (SDOF) structure subjected to gravity and lateral loads: a single column represents the lateral load resisting system, P is the force due to gravity acting on the mass lumped at the top of the structure, L is the column height, V is the lateral force on the mass, and Δ is the horizontal displacement of the mass. As the structure sways by Δ under the effect of the lateral force, the product of P by Δ produces an additional moment at the base of the column, which can be obtained by considering static equilibrium in the deformed configuration. For any given structure, this effect results in an increased demand on the lateral load resisting elements, without any increase in the horizontal forces and base shear.

For the bilinear elastic-perfectly plastic model shown in Fig. 8.49b, the ultimate lateral force, ignoring the P-Δ effect, which can be applied to each identical column of that frame, is reached when the plastic moment of the column, M_p, develops at the top and bottom of the column, and is given by:

$$V_{yo} = \frac{2 \cdot M_p}{L} \tag{8.32}$$

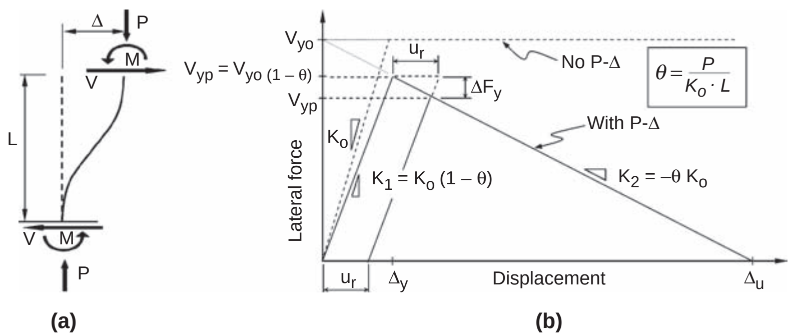

FIGURE 8.49 SDOF structure subjected to P-Δ effects: (a) free-body diagram; (b) bilinear lateral force versus displacement model. (*Vian and Bruneau 2001, Courtesy of MCEER, University at Buffalo.*)

The corresponding yield displacement is:

$$\Delta_y = \frac{V_{yo}}{K_o} \tag{8.33}$$

Now, as shown in Fig. 8.49b, considering P-Δ effects on the single column, moment equilibrium gives:

$$2 \cdot M = VL + P\Delta \tag{8.34}$$

where V is the lateral force at the top of the column.

Rearranging Eq. (8.34), the lateral force, V, can be expressed as:

$$V = \frac{(2 \cdot M - P\Delta)}{L} = \frac{2 \cdot M}{L} - \frac{P\Delta}{L} = V_o - \frac{P\Delta}{L} \tag{8.35}$$

where V_o is the lateral force that would be obtained ignoring the P-Δ effect.

Shown in Figure 8.49b, as a consequence of P-Δ effects seen in Eq. (8.35), V decreases relative to V_o, as the displacement, Δ, increases. This equation can also be expressed as:

$$V = V_o - \frac{P\Delta}{L} = V_o - \theta \cdot K_o\Delta \tag{8.36}$$

where Δ is the P-Δ stability coefficient given by:

$$\theta = \frac{P}{K_oL} = \frac{P\Delta}{V_oL} = \frac{P\Delta_y}{V_{yo}L} \tag{8.37}$$

From Eq. (8.36), the elastic stiffness considering P-Δ, K_1, is therefore:

$$K_1 = K_o(1 - \theta) \tag{8.38}$$

Similarly, the lateral force at which the column, including P-Δ effects, yields, V_{yp}, is:

$$V_{yp} = V_{yo}(1 - \theta) \tag{8.39}$$

When elastic-perfectly plastic material properties are assumed for the idealized frame, lateral force V_o in Eq. (8.36) remains constant in the post-elastic region of the force-displacement graph as the plastic moment, M_p, is developed. However, when P-Δ effects are considered, the corresponding lateral force versus displacement curve exhibits a negative slope past the yield point, with a stiffness of:

$$K_2 = -\theta \cdot K_o \tag{8.40}$$

as shown in Figure 8.49b.

Therefore, the monotonic bilinear force-displacement response of this SDOF structure, including P-Δ effects, can be summarized as follows:

$$V = \begin{cases} K_1 \cdot \Delta & \textit{if} \quad \Delta \le \Delta_y \\ V_{yo} + K_2 \cdot \Delta & \textit{if} \quad \Delta > \Delta_y \end{cases} \tag{8.41}$$

The ultimate displacement of the structure designated as Δ_u, as shown on Fig. 8.49b, is the point at which the post-elastic lateral strength curve or negative-slope, intersects the displacement axis. This theoretically implies that for any additional lateral displacement, lateral instability develops (i.e., lateral strength becomes negative for any additional positive displacement).

Some additional parameters are useful to further characterize inelastic behavior of columns up to collapse. The ratio of postelastic to elastic stiffness, K_2 and K_1, respectively, known as the stiffness ratio, r, is given by:

$$r = \frac{K_2}{K_1} = \frac{\alpha - \theta}{1 - \theta} \tag{8.42}$$

where $\alpha \cdot K_o$ is the stiffness (in absence of stability effects) of the strain-hardening segment of a bilinear elastic-plastic material model. Here, the value of $\alpha = 0.0$ is considered.

The displacement ductility—displacement as a ratio of yield displacement—at ultimate displacement, Δ_u, known as the static stability limit, μ_s, is derived from the geometry and relations given in Figure 8.49b, in terms of θ and r:

$$\mu_s = \frac{\Delta_u}{\Delta_y} = \frac{1}{\theta} = 1 - \frac{1}{r} \tag{8.43}$$

8.7.2 Impact on Hysteretic Behavior

Figure 8.49b also shows that, for the assumed bilinear force-displacement model, after a first yield excursion and unloading to a residual displacement, u_r, the structure has a new reduced yield strength, V_{yp}', upon reloading, given by:

$$V_{yp}' = V_{yp} - \Delta F_y = K_1 \cdot (\Delta_y - \theta \cdot u_r) \tag{8.44}$$

where ΔF_y is the structure's yield base shear reduction, and all other terms have been previously defined. As a consequence of the structure's lower yield strength in the direction it has previously yielded, continued yielding in that direction is relatively easier, and the hysteretic behavior obtained from seismic excitations exhibits a bias in one displacement direction compared with the balanced hysteretic loops typically obtained otherwise. The severity of this bias is a function of the stability factor.

Figure 8.50 illustrates this phenomenon for shake table tests of a small-scale single story frame having a θ value of 0.138 and subjected

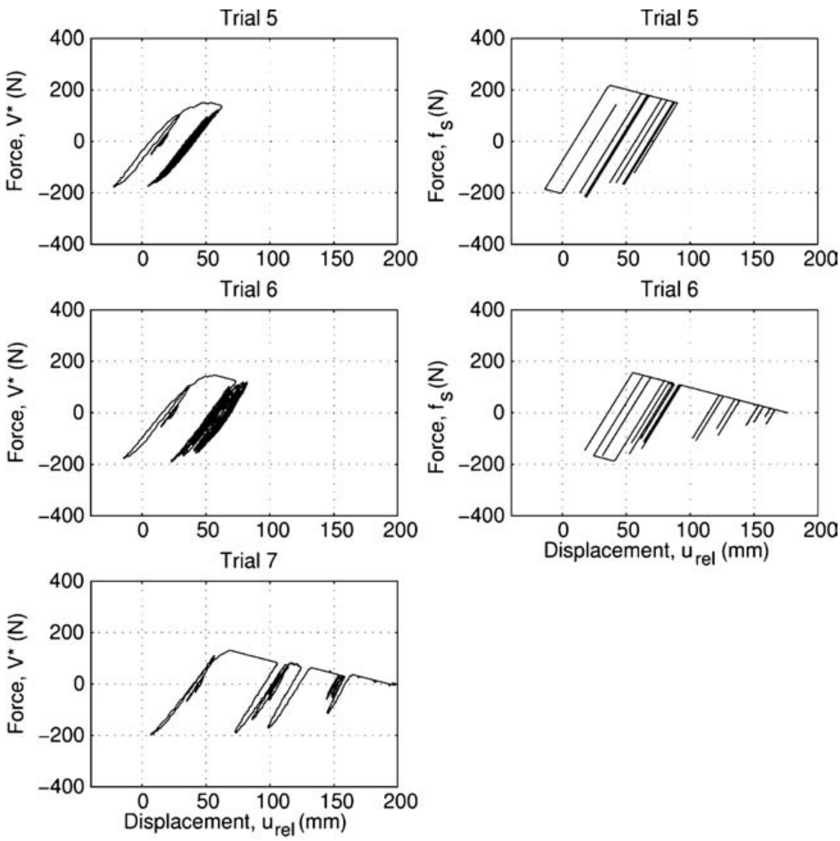

Figure 8.50 Hysteretic force-displacement measured for Specimen 11 upon successive earthquake excitations (left), and results from bi-linear analytical model (right). (*Vian and Bruneau 2001, Courtesy of MCEER, University at Buffalo.*)

to a series of progressively more severe earthquakes until the structure collapsed, together with the results from nonlinear dynamic analyses using a bilinear elastic-perfectly plastic model, a damping ratio of 1.8%, and adjusting the model to account for the reduced yield strength at the experimentally obtained residual displacements. Both the experimental and analytical hysteretic curves exhibit dynamically unstable behavior following a clear negative postyield stiffness, as a consequence of the systems' tendency to drift in a given direction once yielding has started. This results in large cumulative residual displacements and lower cyclic energy absorption capability prior to failure. These detrimental effects become progressively more significant for larger values of the stability coefficient (results for all 15 specimens tested are presented in Vian and Bruneau 2001, 2003).

Analytical results from the above simple analyses are for illustration purposes. More accurate and refined analytical models have been developed to capture behavior up to and through collapse (e.g., Lavan et al. 2009; Sivaselvan and Reinhorn 2002, 2006). Villaverde (2007) also summarizes findings from other shake table experimental results and methods to assess the seismic collapse capacity of building structures.

In addition to the above issues related to idealized frames having bilinear behavior, degradation of structural strength at large inelastic deformations (i.e., beyond the drifts up to which plastic strength can be sustained) can actually produce substantially more steep negative postyield stiffness, and thus more rapidly lead to instability and collapse (Ibarra et al. 2005, Lignos et al. 2008, Rodgers and Mahin 2006, Suita et al. 2008). Attempts to formulate equations quantifying how various response parameters are affected by structural instability during earthquake are further compounded by the fact that such response also varies as a function of many ground motion characteristics (e.g., Bernal et al. 2006, Williamson 2003). This complex variability is often probabilistically considered by subjecting sets of representative structures to incremental dynamic analyses (IDA), which requires using time history analyses for suites of ground motions, progressively increasing the severity of each ground motion until collapse is reached, and using appropriate hysteretic models that appropriately capture strength and stiffness degradation (e.g., FEMA 2009, Krawinkler 2006, Sivaselvan and Reinhorn 2000). Many of the above studies have also reported that collapse of an individual story in a multistory frame is significantly more likely than global instability of the entire building, in part due to the effect of higher vibration modes. Some have recommended special design requirements for continuous columns to better distribute drift demands over the entire frame height and prevent such localized story failures (e.g., Krawinkler 2006, MacRae 1994, MacRae et al. 2004).

8.7.3 Design Requirements

The design objective is to limit the magnitude of lateral drifts to prevent global instability of the entire structure, or of individual stories.

Various strategies have been proposed to that effect. Designing to achieve a post-yield stiffness such that $\alpha \geq \theta$ would eliminate the negative post-yielding stiffness and thus prevent such instability. A similar concept is also possible for more complex hysteretic behaviors (Kawashima et al. 1996, MacRae and Kawashima 1993, MacRae 1994, MacRae et al. 1993). This could be achieved using a structural fuse philosophy (Chapter 13) or a secondary system designed to provide the needed lateral stiffness beyond yielding of the primary lateral load-resisting system. Alternatively, expressions have been proposed to increase the design lateral strength to compensate for the increased displacements induced by P-Δ effects (Bernal 1987, Davidson and Fenwick 2004, Mazzolani and Piluso 1996, Miranda and Akkar 2003, Rutenberg and DeStefano 2000).

For simplicity, given that θ is generally less than 0.060 for actual structures (MacRae et al. 1993), many building codes and standards specify that P-Δ effects can be neglected in seismic design when the stability coefficient is less than a specific value, and prescribe a maximum permitted value for that coefficient. However, various codes differently define the stability coefficient (Ziemian 2010). In accordance to ASCE 7-10, simplifying some terms, the stability coefficient is defined and limited by:

$$\theta = \frac{P_x \Delta}{V_x h_{sx}} \leq \frac{0.5}{\beta C_d} \leq 0.25 \tag{8.45}$$

where P_x is the total vertical design load at and above level x, Δ is the design story drift at that level determined from elastic analysis and occurring simultaneously with V_x which is the seismic shear force acting between levels x and $x - 1$, h_{sx} is the story height below level x, C_d is a deflection amplification described in Chapter 7, and β is the ratio of story shear demand over capacity (accounting for possible overstrength of the lateral-load-resisting system between Levels x and $x - 1$). ASCE states that P-Δ effects can be ignored when $\theta \leq 0.10$, and considered by rational analysis otherwise. Alternatively to such a rational analysis, ASCE permits to multiply displacements and member forces by $1.0/(1 - \theta)$ to simulate the results of such an analysis.

Additional recommendations for design to prevent global instability are available elsewhere (FEMA 2009, Krawinkler 2006, Villaverde 2007, Zareian and Krawinkler 2007).

8.8 Design Example

The following section illustrates the design of a Special Moment Frame. The design applies the requirements of ASCE 7 (2010), AISC 341 (2010b), and AISC 358 (2010a). The example is not intended to be a

S_S	1.0 g
S_1	0.60 g
Site class	D
S_{DS}	0.733 g
S_{D1}	0.60 g
R	8
I	1.0
C_D	5.5
Ω_o	3

Table 8.5 Seismic Design Data

complete illustration of the application of all design requirements. Rather, it is intended to illustrate key proportioning and detailing techniques that are intended to ensure ductile response of the structure.

8.8.1 Building Description and Loading

The example building is a five-story structure located in an area of moderate to high seismicity. Tables 8.5 and 8.6 below give the seismic design data and building information. Figure 8.51 shows the plan and Figure 8.52 shows the typical frame elevation.

8.8.2 Global Requirements

In areas of high seismicity, the required base-shear strength prescribed by the building code does not typically govern the selection of members in SMF systems and it is typically advantageous to select members based on drift control and then check the member strengths later. (In areas of low seismicity the opposite may be true: strength requirements may govern the design.) The drift limit is dependent on system type and occupancy. For this building the drift limit is 0.020 times the story height. Conversely, in areas of low or moderate seismicity drift governs the design much less often and it may be advantageous to design for strength and check drift. Strength-controlled designs are somewhat easier to perform and optimize than are drift controlled ones, which typically require some iteration. However both cases

Typical floor weight	100 psf	2310 kips
Typical cladding weight	20 psf	160 kips
Roof weight	100 psf	2310 kips

Table 8.6 Building Information

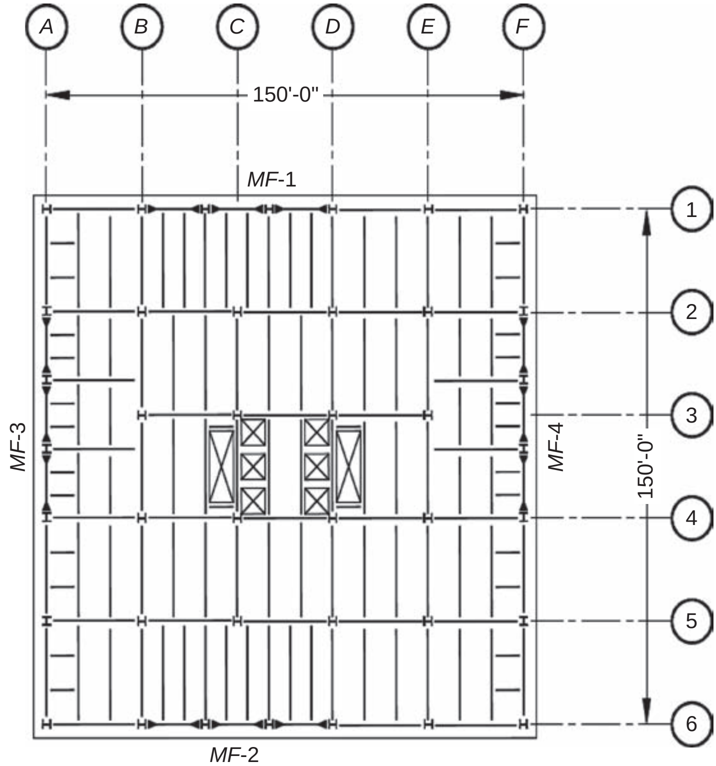

Figure 8.51 Typical floor plan.

involve preliminary design, analysis, and final confirmation of adequate strength and drift control.

This example is set in a zone with high seismicity and thus the former strategy (design for drift; check strength) is adopted.

8.8.3 Basis of Design

The design of SMF is based on the expectation of a global yield mechanism in which plastic hinges form at the ends of some (or all) beams and at the column bases. Although it is acknowledged that some column hinging at other locations may occur in actual building response, the design procedures are derived from the beam-hinging assumption.

The analysis procedure utilized is a linear Modal Response Spectrum (MRS) analysis. This is typically advantageous due to the reduction in design forces. ASCE 7 permits for this method and the reduction in overturning moment that typically results from this approach compared with the vertical force distribution used in the equivalent lateral force procedure of ASCE 7. Based on the seismic-design data

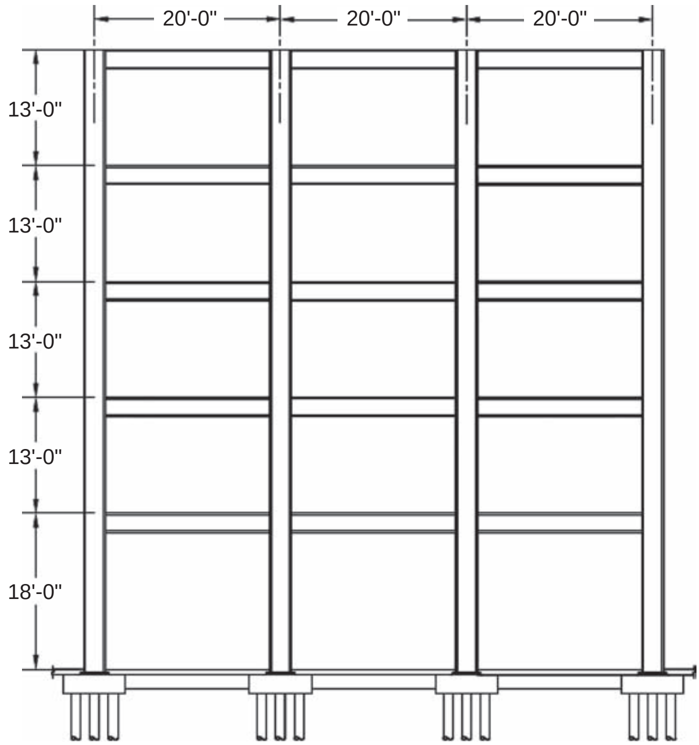

Figure 8.52 Typical frame elevation.

a generic seismic response spectrum is constructed in accordance with ASCE 7.

As required by AISC 341, the design utilizes a connection that can provide a rotation angle of 0.04 radians through a combination of elastic and inelastic deformation. The connection is a Welded Unreinforced Flange-Welded Web (WUF-W) prequalified per AISC 358. AISC 358 prequalifies several connections, many of which have limit states or calculations specific to that connection. However, the general design methodology is similar.

8.8.4 Iterative Analysis and Proportioning

The forces used to evaluate the design drift are dependent on the building period. Thus some iteration is required to select members that satisfy the drift requirements efficiently (i.e., to avoid inefficient overdesign). Initially the building period is assumed to equal the ASCE 7 upper limit for static analyses, C_uT_a. Member selection must also satisfy proportioning requirements intended to favor beam hinging over column hinging (the "strong-column/weak-beam" rule addressed in the connection-design section). Thus designers often apply proportioning rules in preliminary design to prevent failing this rule at a later stage in design. (This is checked in Section 8.6.2 below.) In order for the beam to be able to undergo flexural yielding, "highly ductile" members are selected based on Table D1.1; these members are sufficiently compact that local flange buckling does not limit the ability of the section to undergo large inelastic rotations while maintaining its strength.

In order to ensure adequate drift control, panel zone flexibility must be captured in the model. This is rarely done explicitly by use of a separate panel-zone element permitting relative rotation between beam and column. More often, this is done by centerline modeling (i.e., not employing rigid-end offsets in the model). This reasonably captures panel-zone flexibility for typical spans (Charney and Horvilleur 1995).

Some connection types have an effect on the stiffness of SMF frames. For example, the reduced-beam section connection, by virtue of removing material from the beam, causes additional flexibility that must be modeled, often resulting in larger required members. Other connections add material and thus reduce flexibility, sometimes to a degree that can permit lighter members to be used.

To commence the preliminary design the following steps are taken using the equivalent lateral force procedure:

- Determination of base shear
- Vertical distribution of forces
- Horizontal distribution of forces to frames
- Use of approximate equations relating story shear, beam and column moments of inertia, and deflection to determine preliminary member sizes

A commonly used equation for estimating drift is given below (Wong et al. 1981):

$$\Delta_i = \frac{V_i h_1^2}{12}\left[\sum \frac{h_i}{EI_{ci}} + \sum \frac{L}{EI_{bi}}\right] \tag{8.46}$$

where V_i is the frame shear at level I, h_i is the height of level i (average of adjacent stories), E is modulus of elasticity, I_{ci} is the moment of inertia of each column in the frame at level I, I_{bi} is the moment of inertia of each beam in the frame at level I, and L is the span of each beam in the frame.

In the equation above the design frame shear V_i (reduced by the Response Modification Coefficient R) is used, and thus drifts must be amplified by the factor C_d. The drift can be set equal to the drift limit at each floor level and members can be selected corresponding to that drift value. The drift limit is a function of the story height and the allowable drift angle, θ_{max}, which is typically 0.02:

$$\Delta_{max} = \theta_{max} h \tag{8.47}$$

For preliminary design the static base shear is used; member sizes can be refined subsequently considering the results of a modal response spectrum analysis. Accidental torsion may be considered in the determination of the frame shear using approximate methods. In this design it was not considered at this stage due to its likely limited effect compared with other approximations.

To simplify the preliminary member selection further, the column moment of inertia can be assumed to be twice the beam moment of inertia. Furthermore, the moment of inertia of the columns at the end of the frame (which connect to one moment frame beam at each floor) can be assumed to be one half that of the interior columns (which connect to two moment frame beams at each floor). This proportioning will make it likely that the strong-column/weak-beam requirements will be met, which can only be checked later in the design.

With the simplifications outlined above the minimum moment of inertia of the beams can be solved for:

$$I_{bi} = \frac{V_i h_i}{12\, EN} \frac{C_d}{\theta_{max}} \left[\frac{h_i}{2} + L \right] \tag{8.48}$$

where N = number of bays.

Preliminary beam sizes are presented in Table 8.7.

In the selection of beams the section compactness and the span-to-depth ratio must be considered. With the short 20-ft span used, limiting the depth to no more than 30 inches in the beam selection allows for the use of deep W27 columns, which are more efficient than W14 columns, while maintaining a clear span-to-depth ratio of 7 (the minimum permitted for SMF). The resulting span-to-depth ratio for a W30 beam (from face of column to face of column, based on nominal sizes) is 7, exactly the limit in AISC 358.

Level	Beam Size
Roof	W18 × 50
Fifth Floor	W27 × 94
Fourth Floor	W30 × 108
Third Floor	W30 × 116
Second Floor	W30 × 148

Table 8.7 Preliminary Beam Sizes

	Interior Column	Exterior Column
Upper Column	W27 × 217	W27 × 129
Lower Column	W27 × 307	W27 × 178

Table 8.8 Preliminary Column Sizes

Preliminary column sizes can be determined based on the beam sizes selected. Columns are typically spliced every two or four stories, and so the column size is determined from the strongest connecting beams. The column plastic section modulus Z should be checked in preliminary design so that it will meet the strong-column/weak-beam requirements of AISC 341 E3.4a; for preliminary design a minimum column to beam plastic section modulus ratio of at least 1.75 at interior (low axial load from overturning) moment frame columns and 2.5 at exterior (high axial load from overturning) moment frame columns is recommended to minimize the chance of failing the criterion in the later stages of design. Keep in mind these preliminary plastic section modulus ratios will ultimately be reduced by both connection overstrength in the beam and axial loads in the columns.

In this example columns are only spliced once: 4 ft above the third floor. Preliminary column sizes are shown in Table 8.8. Sizes are determined based on the moment of inertia assumptions, with the plastic section modulus checked as described above.

Using these preliminary sizes a three-dimensional computer model is constructed and a modal response spectrum analysis is performed. The interstory drift is found to be 2.15 in at the critical third story, resulting in an interstory drift ratio of 1.38%. Member sizes are revised so that the calculated drift is just below the allowable.

Because the proportioning assumptions used in the preliminary design are biased toward column strength, to allow for increased building drift the column size may be reduced. Similarly, to stiffen the building the beam sizes may be increased. Also, one might optimize the design by simultaneously increasing beam strength and decreasing column strength. However, in so doing one runs the risk of violating the strong-column/weak-beam proportioning.

Final member sizes based on drift control and stability requirements are presented in Table 8.9.

8.8.5 Member Checks

The column is checked for the combined effects of bending and axial forces. The effective length factor is determined using alignment

Level	Beam		Interior Column	Exterior Column
Roof	W18 × 50	Upper Column	W27 × 114	W27 × 94
Fifth Floor	W24 × 55			
Fourth Floor	W24 × 76			
Third Floor	W24 × 94	Lower Column	W27 × 161	W27 × 146
Second Floor	W24 × 94			

Table 8.9 Final Member Sizes

charts and including the destabilizing effects of leaning columns. Forces are determined using the basic load combinations:

$$R_u = 1.2D + 0.5L + E \tag{8.49}$$

$$R_u = 0.9D - E \tag{8.50}$$

Substituting the vertical component of seismic acceleration:

$$R_u = (1.2 + 0.2S_{DS})D + 0.5L + E \tag{8.51}$$

$$R_u = (0.9 - 0.2S_{DS})D - E \tag{8.52}$$

For the first-story interior-column the design forces are:

$$P_u = 284 \text{ kips}$$

$$M_u = 15{,}810 \text{ kip-in}$$

A separate check is performed on the columns for the axial forces determined using the amplified seismic load. For this check it is permitted to neglect moments. Implicit in this check is the expectation that some flexural yielding can be tolerated in the column.

$$R_u = 1.2D + 0.5L + \Omega_o E \tag{8.53}$$

$$R_u = 0.9D - \Omega_o E \tag{8.54}$$

Again, substituting the vertical component of seismic acceleration:

$$R_u = (1.2 + 0.2S_{DS})D + 0.5L + \Omega_o E \tag{8.55}$$

$$R_u = (0.9 - 0.2S_{DS})D - \Omega_o E \tag{8.56}$$

$$P_u = 291 \text{ kips}$$

The beam is likewise checked using the forces from the basic load combinations. Beam axial and flexural forces are considered in combination. Typically axial forces are small and can be neglected. For the second floor beam the maximum moment is:

$$R_u = (1.2 + 0.2S_{DS})D + 0.5L + E \tag{8.57}$$

$$M_u = 8770 \text{ kip-in}$$

Both column and beam members have been selected from seismically compact shapes. For the column web, the exact compactness limit is a function of the axial force.

8.8.6 WUF-W Connection Design

The connection considered is at an interior column at the second floor. The column is a W27 × 161 and the connecting beams are W24 × 94.

This connection is not actually designed in the strictest sense. The use of a prequalified connection dictates conformance to the details of the connection as defined in AISC 358. The designer checks that this detail is adequate given the members used, the bay proportions, gravity load, and other relevant particulars of the condition under consideration. Figure 8.53 shows the connection design.

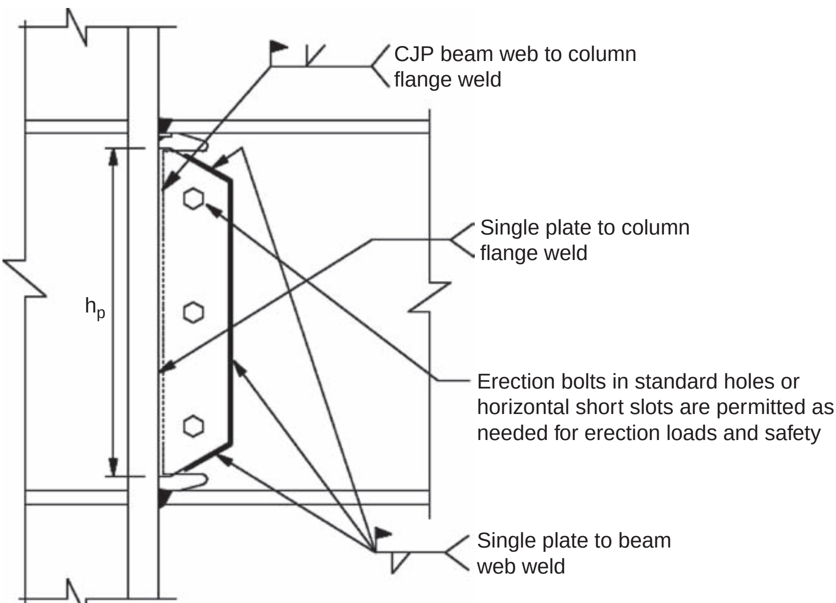

Figure 8.53 WUF-W beam-to-column connection (from AISC 358). (*Copyright © American Institute of Steel Construction. Reprinted with permission. All rights reserved.*)

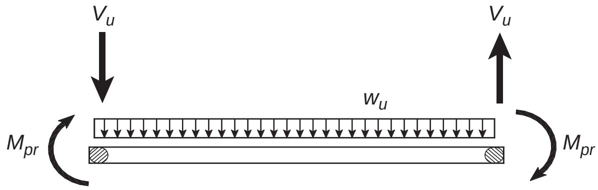

Figure 8.54 Free-body diagram of beam.

The determination of the forces used to check the connection begins with a free-body diagram of the beam (Figure 8.54). For consistency of reference, the frame will be considered to be deforming to the right such that the seismic moments imposed on each end of the beam are clockwise (and the seismic moments imposed on the column by each beam are counter-clockwise).

Following the AISC 358 method for a WUF-W connection the plastic hinge location is assumed to be at the column face. Plastic hinge moments are assumed to be the "probable moment" (M_{pr}), which includes both the expected material overstrength factor, R_y, and a factor for strain-hardening and other sources of connection overstrength, C_{pr}. For the WUF-W connection, $C_{pr} = 1.4$ per AISC 358.

$$\begin{aligned} M_{pr} &= C_{pr}R_yF_yZ \qquad (8.58) \\ &= (1.4)(1.1)(50)(254) \\ &= 19{,}600 \text{ kip-in} \end{aligned}$$

The seismic shear is thus:

$$V_E = \frac{2M_{pr}}{L_h} \qquad (8.59)$$

where L_h is the distance between plastic hinges. For this connection, L_h is taken to be the distance between column faces. L_h is $L - 2(½\, d_c) = 240 - 2(½\, 27.6) = 212.4$ in, V_E is $2(19{,}600)/(212.4) = 184$ kips.

The gravity shear is determined from the appropriate load combination:

$$V_g = \frac{w_u L_h}{2} \qquad (8.60)$$

$$w_u = 1.2D + 0.5L \qquad (8.61)$$

Thus the shear at left side of the beam (where the seismic shear is aligned with gravity) is:

$$V_u = V_E + V_g = 196 \text{ kips} \qquad (8.62)$$

and the shear at the right side of the beam is:

$$V_u = V_E - V_g = 172 \text{ kips} \qquad (8.63)$$

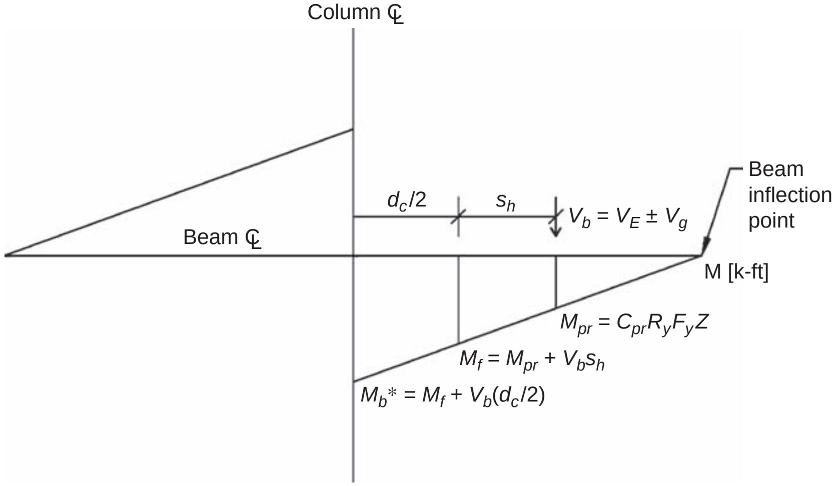

Figure 8.55 Projection of probable beam moment capacity to column centerline.

These shears are used to calculate the beam moments at the column face (for determining panel-zone shear) and at the column centerline (for checking the strong-column/weak-beam requirement). Figure 8.55 shows the projection of the probable moment to the column face and to the column centerline.

For reference, the beams are given the following designations (see Figure 8.56 below): Beam 1 is to the left of the column and Beam 2 is to the right.

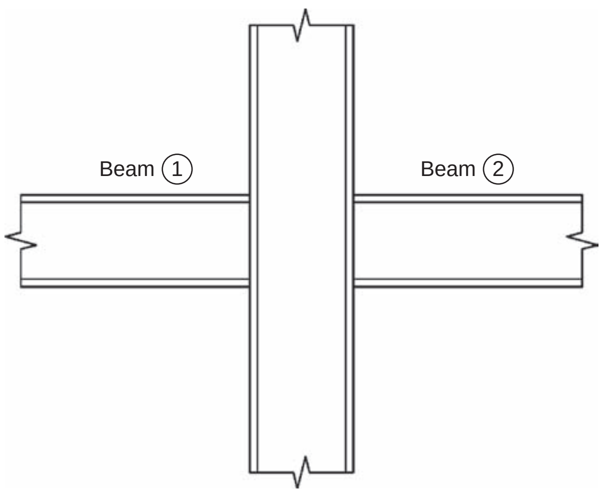

Figure 8.56 Beam identification convention.

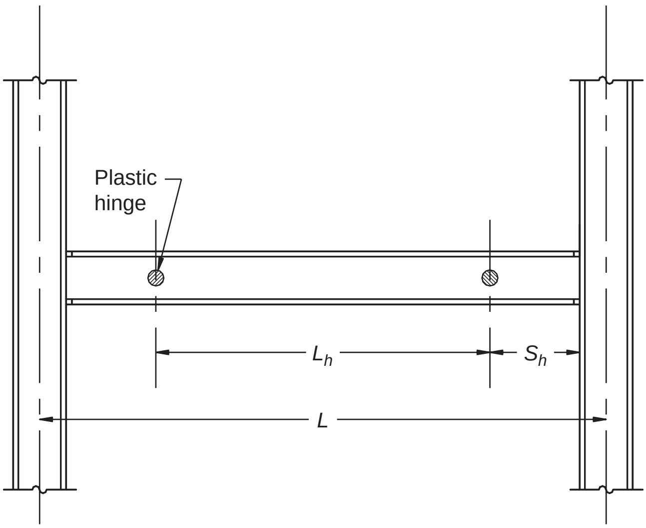

Figure 8.57 Location of plastic hinge.

At the left face of the column (at Beam 1) the moment is:

$$M_{f1} = M_{pr} + V_u s_h \tag{8.64}$$

$$M_{f1} = 19{,}600 \text{ kip-in}$$

where s_h is the distance from the face of the column to the center of the plastic hinge as shown in Figure 8.57. For this connection, s_h is taken to be 0.

At the right face of the column (at Beam 2) the moment is:

$$M_{f2} = M_{pr} + V_u s_h \tag{8.65}$$

$$M_{f2} = 19{,}600 \text{ kip-in}$$

At the centerline of the column the moment due to Beam 1 framing in from the left is:

$$M_{b1}{}^* = M_{pr} + V_u(s_h + ½\, d_c) \tag{8.66}$$

$$M_{b1}{}^* = 22{,}300 \text{ kip-in}$$

At the centerline of the column the moment due to Beam 2 framing in from the right is:

$$M_{b2}{}^* = M_{pr} + V_u(s_h + ½\, d_c) \tag{8.67}$$

$$M_{b2}{}^* = 21{,}900 \text{ kip-in}$$

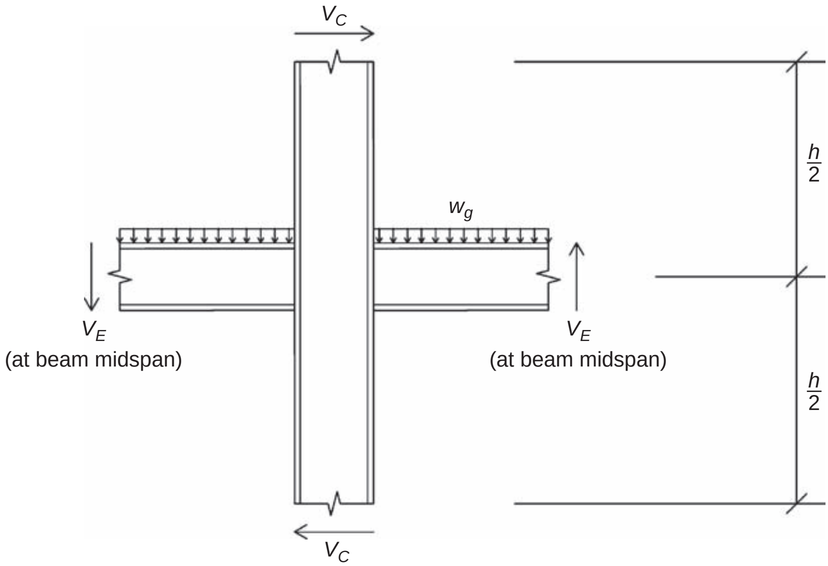

Figure 8.58 Free-body diagram of beam and column assembly.

The column shear corresponding to the probable beam strength can be estimated by assuming an inflection point at the column midheight above the connection and again at the column midheight below. Similarly, the beam inflection points are assumed to occur at midspan. Figure 8.58 shows the free-body diagram of a beam and column assembly from inflection point to inflection point.

To simplify the determination it is conservatively assumed that the column shear is the same above and below the connection. Thus:

$$V_c = \frac{\sum M_b^*}{\sum H/2} \tag{8.68}$$

$$V_c = \frac{(22{,}300 + 21{,}900)}{[(156 + 216)/2]}$$

$$V_c = 238 \text{ kips}$$

Now that these forces have been determined, the beam shear, strong-column/weak-beam, panel-zone, and continuity-plate requirements can be checked.

8.8.6.1 Beam Shear

The shear at the column face is compared with the beam shear strength:

$$\phi V_n = \phi\, 0.6 R_y F_y A_w \tag{8.69}$$

$$\phi V_n = 413 \text{ kips}$$

$$\phi V_n \geq V_u$$

8.8.6.2 Strong-Column/Weak-Beam

A virtual beam moment is calculated by projecting the moment at the column face to the column centerline. It is compared with a virtual column capacity which is determined by projecting the true capacity from the top flange level to the beam centerline.

A typical interior connection involves two beams (one to the left and one to the right of the columns), whereas an exterior one involves just one. At intermediate floors the continuous column is considered to be two columns (i.e., to represent a capacity based on its strength both above and below the connection).

The beam moment at the centerline of the column from the right end of the left beam (where the shear is lower) is: $M_{b1}^* = 21{,}900$ kip-in. The beam moment at the centerline of the column from the left end of the right beam (where the shear is greater) is: $M_{b2}^* = 22{,}300$ kip-in. The total moment at the column centerline is: $M_{b1}^* + M_{b2}^* =$ 44,200 kip-in.

The column capacity is calculated considering both a reduction due to axial force and an increase in projecting the column moment corresponding to that capacity from the beam flange elevation to the beam centerline. The column shear corresponding to the probable beam strength is used to project the column flexural capacity from the point of maximum moment (at the beam flange level) to the beam centerline for purposes of comparison to the projected beam moment. Figure 8.59 shows this projection.

$$\sum M_c^* = 2\left[\left(F_y - \frac{P_u}{A}\right)Z + V_c \frac{1}{2} d_b\right]$$

$$\sum M_c^* = 2\left[\left(\frac{50-291}{47.6}\right)515 + (237.6)\frac{1}{2}(24.3)\right] \tag{8.70}$$

8.8.6.3 Panel-Zone Shear

The panel-zone shear demand is computed from the moments at the column face and reduced by the estimated column shear. The moment at the column face from one of the two connecting beams (Beam 2) has already been converted into a flange force (R_{u2}) for purposes of checking the need for continuity plates. The flange force (R_{u1}) at the opposite column face is similarly calculated from the moment from the other beam (Beam 1), and the resulting column panel-zone shear is computed.

Because the distance s_h is taken to be zero for this connection and identical beam sizes are used on each side, the moments at the opposite column faces are equal. Where s_h is greater than zero the gravity shear affects the projection of the moment to the column

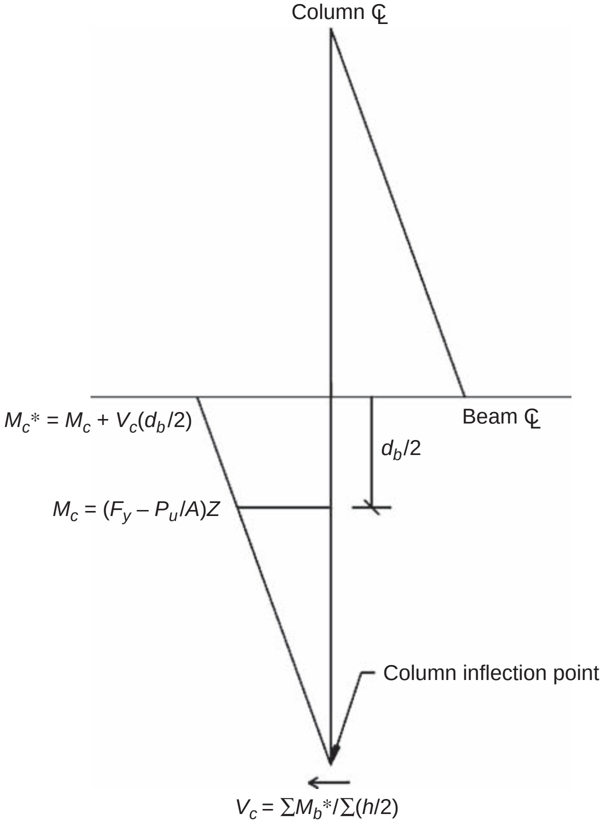

FIGURE 8.59 Projection of estimated column moment capacity to beam centerline.

face, increasing the moment on one side of the column and decreasing it on the other.

$$V_u = R_{u1} + R_{u2} - V_c \tag{8.71}$$

$$R_u = \frac{M_f}{(d_b - t_{bf})} \tag{8.72}$$

$$V_u = \frac{M_{f1}}{(d_b - t_{bf})} + \frac{M_{f2}}{(d_b - t_{bf})} - V_c$$

$$= 2\left[\frac{19{,}600}{(24.3 - 0.875)}\right] - 238$$

$$= 835 \text{ kips} + 835 \text{ kips} - 238 \text{ kips}$$
$$= 1430 \text{ kips}$$

The panel-zone shear capacity is:

$$\phi R_n = \phi\left(0.6F_yA_w + \frac{1.8b_{cf}t_{cf}^2F_y}{d_b}\right)$$

$$= 1.0\left[0.6(50)(27.6)(0.660) + \frac{1.8(14.0)(1.08)\,2(50)}{(24.3)}\right] \qquad (8.73)$$

$$= 607 \text{ kips}$$

$$\phi R_n \le R_u$$

Doubler plates are required. The deficit in web strength will be corrected by the addition of a doubler.

$$\phi R_n = \phi 0.6F_y t_{dp} d \qquad (8.74)$$

$$\phi R_n \ \ge \ R_u$$

$$t_{dp} \ge \frac{R_u}{(\phi 0.6\ F_y\ d)}$$

$$\ge \frac{1430 - 607}{(1.0)\ 0.6\ (50)(27.6)}$$

$$t_{dp} \ge 1.00 \text{ in}$$

The minimum doubler thickness (without bracing) is:

$$t_{dp} \ge \frac{d_z + w_z}{90} \qquad (8.75)$$

$$\ge \frac{d_{b-2}t_{bf} + d_{c-2}t_{cf}}{90}$$

$$\ge \frac{24.3 - 2(0875) - 27.6 - 2(1.08)}{90} = 0.53 \text{ in}$$

Both the web and the doubler satisfy the limit. If either did not a plug weld (or series of plug welds) could be added connecting the doubler to the web and thus reducing the unbraced lengths d_z and w_z.

The doubler extends above and below the connection by 6 in. The welds at the top and bottom of the doubler are the AISC minimum welds (Figures 8.60 and 8.61). These help prevent shear buckling of the doubler. However, the main force transfer into the doubler is through the grove weld to the column flange. Note that AISC 341

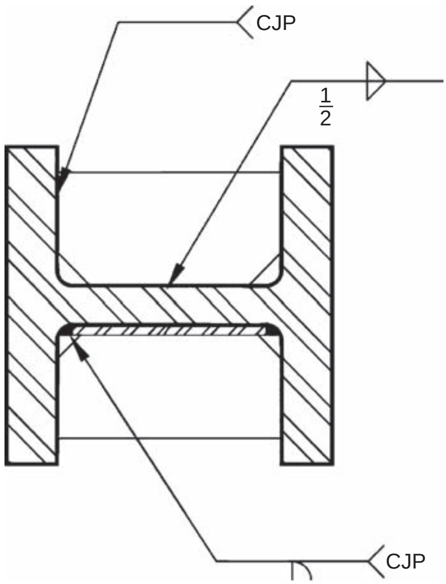

Figure 8.60 Doubler plate.

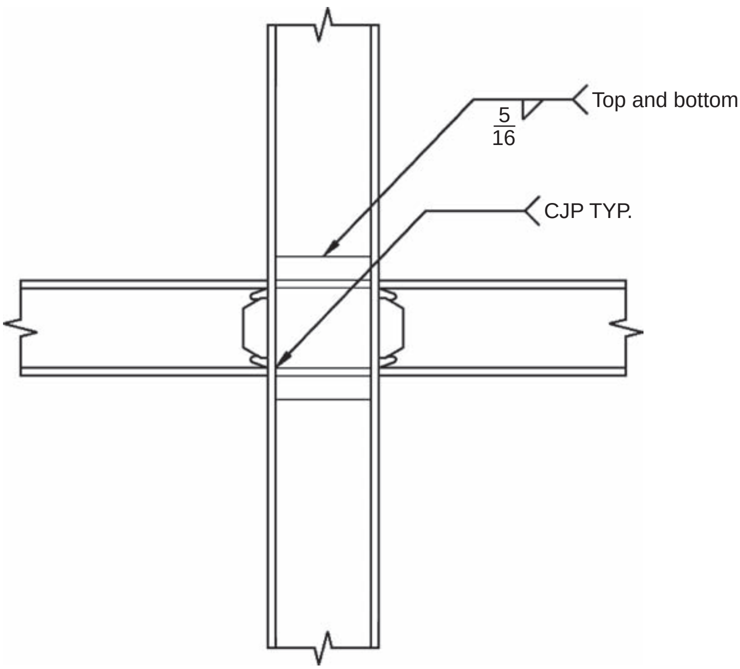

Figure 8.61 Doubler plate together with continuity plates.

indicates that these welds be designed for certain forces; in actuality the force patterns are much more complicated than the code indicates; the approach used here is supported by research (Lee et al. 2005b), although it may be at odds with AISC 341.

8.8.6.4 Continuity Plates

The need for continuity plates is checked considering the moment at the column face to be delivered as a force couple to the column flange:

$$R_u = \frac{M_f}{d_b - t_{bf}} \tag{8.76}$$

$$= \frac{19.558 \text{ kip-in}}{24.3 \text{ in} - 0.875 \text{ in}}$$

$$= 835 \text{ kips}$$

This demand need not exceed the maximum force that the flange can deliver. Based on the continuity plate criterion Eq. (8.77) this maximum is:

$$R_u \leq 1.8\, b_{bf}\, t_{bf}\, F_{yb}\, R_{yb} \tag{8.77}$$

$$= 786 \text{ kips}$$

This demand is compared to the column web local yielding and crippling limit states. Two additional checks are performed on the column flange. Should any of these limit states be exceeded, continuity plates are required. The designer may consider a larger column section, smaller beam section, use of a doubler (or thicker doubler), or other adjustments to the design as well.

8.8.6.4.1 Column Web Local Yielding For this check the reinforced web thickness including the doubler is considered. Thus the effective web thickness is:

$$t_w = t_{wc} + t_d = 0.660 + 1.00 = 1.66 \text{ in}$$

$$\phi R_n \leq \phi(5k + N)F_y t_w \tag{8.78}$$

$$\phi R_n \leq \phi(5k + t_{wf})F_y t_w$$

$$\phi R_n \leq (100)[5(1.87) + (0.875)](50)(1.66) = 848 \text{ kips}$$

$$\phi R_n \leq R_u$$

8.8.6.4.2 Column Web Crippling

$$\phi R_n = \phi 0.80 t_w^2 \left[1 + 3\left(\frac{N}{d}\right)\left(\frac{t_w}{t_f}\right)^{1.5}\right]\sqrt{\frac{EF_{yw}t_f}{t_w}} \tag{8.79}$$

$$\phi R_n = (0.75)0.80(1.66)^2$$

$$\left[1 + 3\left(\frac{0.875}{27.6}\right)\left(\frac{1.660}{1.08}\right)^{1.5}\right]\sqrt{\frac{29{,}000(50)1.08}{1.660}}$$

$$= 1900 \text{ kips}$$

$$\phi R_n \leq R_u$$

8.8.6.4.3 Column Flange Bending (Strength) This check is mandated by AISC 358. It supersedes the flange-bending check in AISC 360:

$$t_{cf} \geq 0.4\sqrt{1.8 b_{bf} t_{bf}\left(\frac{F_{yb}R_{yb}}{F_{yc}R_{yc}}\right)} \tag{8.80}$$

which can be rearranged into the format of familiar equations for flange local bending:

$$6.25\, tcf^2 F_{yc}R_{yc} \geq 1.8 b_{bf} t_{bf} F_{yb} R_{yb} \tag{8.81}$$

$$401 \text{ kips} \leq 786 \text{ kips}$$

This is no good (reinforcement required).

8.8.6.4.4 Column Flange Bending (Stiffness)

$$t_{cf} \geq \frac{b_{bf}}{6} \tag{8.82}$$

$$1.08 \text{ in} \geq 9.07 \text{ in}/6$$

$$1.08 \text{ in} \leq 1.51 \text{ in}$$

This is no good (reinforcement required).

Two of these checks indicate insufficient capacity in the column. (specifically the column flange, as the web has already been reinforced with a doubler plate), and thus continuity plates are required. The continuity plate must be designed to resist the difference between the demand and the capacity:

$$R_{uCP} = R_u - \phi R_n \tag{8.83}$$

$$= 786 \text{ kips} - 401 \text{ kips} = 385 \text{ kips}$$

In addition, its minimum thickness is governed by AISC 358, which states that the thickness must match the beam flange thickness (0.875 in for a W24 × 94) for two-sided connections.

Assuming the full beam flange width is effective, the required plate thickness is determined:

$$t_{CP} = \frac{R_u}{\phi F_y b_f} = \frac{385}{0.9(50)(9.07)} = 0.94 \text{ in} \tag{8.84}$$

One-inch continuity plates will be used.

8.8.7 Detailing

Detailing of the connection follows the requirements of AISC 358, as illustrated in Figure 8.62.

In addition, all welds of this connection are designated as "demand critical," indicating that they require high notch toughness. Also, the weld access hole requires a special geometry defined in AWS D1.8.

Finally, the region of the connection where inelastic strain is expected must be kept free of notches and defects caused by welded or shot-in attachments. The region to be kept clear, the "protected zone," extends from the column face one full beam depth in, as shown in Figure 8.63.

8.8.8 Bracing

In order for the beam to be able to undergo flexural yielding, lateral torsional buckling must be prevented, not only initially but through large inelastic rotations. This is done through lateral bracing at the beam-to-column connection, near the plastic hinge, and along the beam length.

The required bracing forces and stiffnesses are as shown below.

8.8.8.1 Bracing at the Beam-to-Column Connection

The column is braced at the top and bottom flange level. The required bracing force is:

$$P_{br} = 0.02 F_y b_f t_{bf} \tag{8.85}$$

$$P_{br} = 0.02(50)(9.07)(0.875) = 7.9 \text{ kips}$$

8.8.8.2 Bracing Near the Plastic Hinge

A brace is ostensibly required near the plastic hinge by AISC 358. However, in most building conditions this requirement is waived by

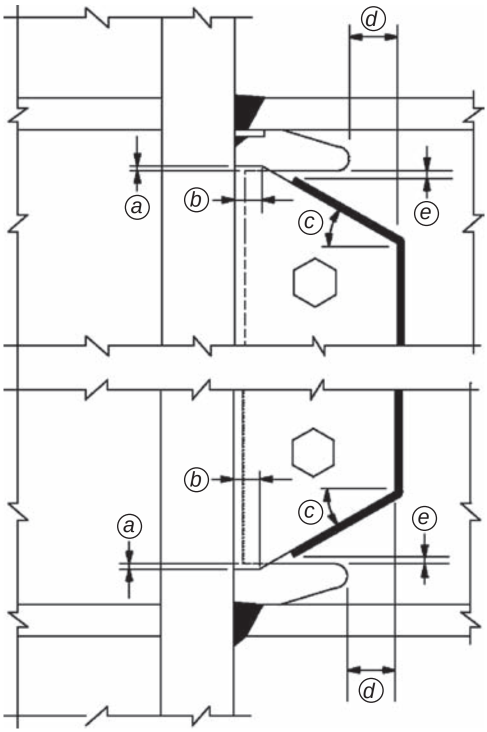

Notes:
a. 1/4 in (3 mm) minimum, 1/2 in (6 mm) maximum.
b. 1 in (25 mm) minimum.
c. 30° (±10°).
d. 2 in (50 mm) minimum.
e. 1/2-in (6 mm) minimum distance, 1-in (25 mm) maximum distance, from end of fillet weld to edge of weld access hole.

Figure 8.62 WUF-W beam-to-column connection (from AISC 358). (*Copyright © American Institute of Steel Construction. Reprinted with permission. All rights reserved.*)

an exception that allows the torsional stabilizing effect of the composite slab to substitute for this discrete brace.

$$P_u = \frac{0.06R_y Z F_y}{h_o} \tag{8.86}$$

$$\beta_{br} = \frac{1}{\phi}\left(\frac{10M_r C_d}{L_b h_o}\right) \tag{8.87}$$

where $h_o = d - t_f$ and $h_o = 24.3\text{ in} - 0.875\text{ in} = 23.4\text{ in}$

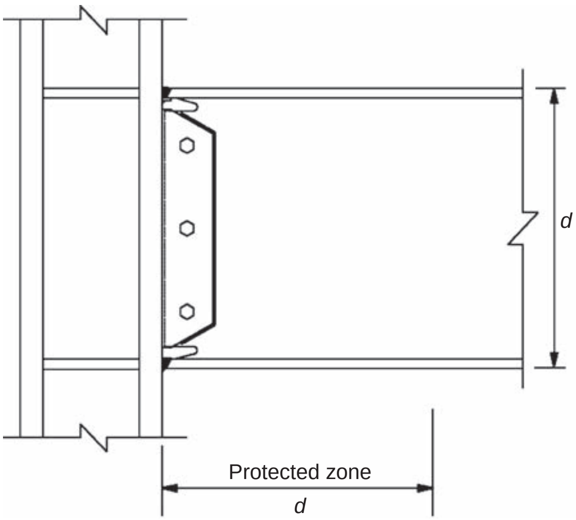

FIGURE 8.63 Protected zone (from AISC 358). (*Copyright © American Institute of Steel Construction. Reprinted with permission. All rights reserved.*)

Note that L_b should be taken to be L_q, the maximum unbraced length corresponding to the flexural demand, M_r, which is taken to be the expected flexural strength in this application. Thus the length L_q may be assumed to be equal to the limiting length L_p.

$$M_r = M_u = R_y Z F_y \tag{8.88}$$

$$M_r = 1.1(254)(50) = 14{,}000 \text{ kip-in}$$

$$C_d = 1.0$$

$$\phi = 0.75$$

$$P_{br} = \frac{0.06(1.1)(254)(50)}{(23.4)} = 35.8 \text{ kips}$$

$$P_{br} = \frac{10(14{,}000)(1.0)}{0.75(84)(23.4)} = 94.6 \text{ kips/in}$$

8.8.8.3 Bracing Along the Beam

$$P_{br} = \frac{0.02 M_r C_d}{h_o} \tag{8.89}$$

$$\beta_{br} = \frac{1}{\phi}\left(\frac{10 M_r C_d}{L_b h_o}\right) \tag{8.90}$$

$$L_b \le \frac{0.086 r_y E}{F_y} \tag{8.91}$$

$$P_{br} = \frac{0.02(14{,}000)(1.0)}{(23.4)} = 11.9 \text{ kips}$$

$$\beta_{br} = 66.3 \text{ kips/in from above}$$

$$L_b \le \frac{0.086(1.98)(29{,}000)}{(50)} = 98.8 \text{ in}$$

The beams will be braced at third points along the span.

8.8.9 Completion of Design

Several items remain to complete the design. These include:

- Column splices
- Base plates
- Foundations
- Diaphragms, chords, and collectors

Although each one of these items is necessary and important, the execution is similar to that of many other components of a building design.

8.9 Self-Study Problems

Problem 8.1 For the SMF shown, design the beam-to-column connections for the first story beam using only the following types of connections prequalified per AISC 358.

(a) WUFW connections
(b) Welded flange plate (WFP) connections
(c) Reduced beam section (RBS) connections
(d) Bolted stiffened end plate (BSEP) connections
(e) Bolted flange plate (BFP) connections
(f) Bolted bracket (BB) connections
(g) Free flange (FF) connections (using FEMA 350 connections details in this case)

Assume that, at the story under consideration, the beam is W30 × 173, and the columns are W14 × 311. All loads are shown below. Assume ASTM A992 Gr. 50 steel for beams and columns.

Check that the design satisfies the strong-column/weak-beam requirements, as well as all other applicable detailing requirements.

If one or many limits of applicability are found to be violated for a specific connection type, just highlight the violations and continue calculations as if the connection was permitted.

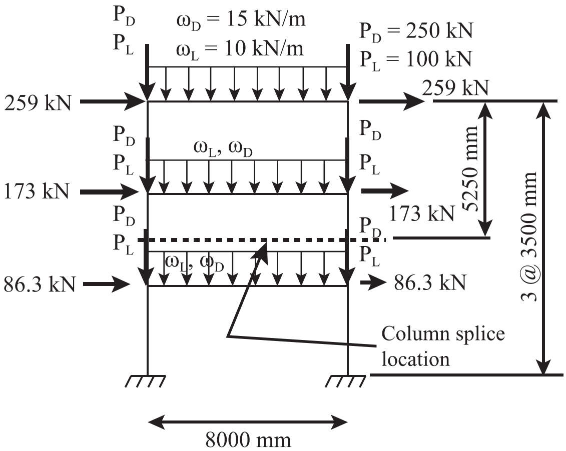

Problem 8.2 A single-story frame like the one shown consists of two exterior vertical members that serve as columns to resist the gravity loads, and a vertical member with RBS at its ends inserted at midbay of the frames to resist the lateral loads.

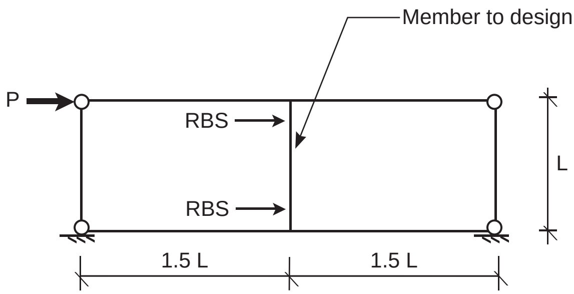

Here, for $L = 10'$ and $P = 100$ kips:

(1) Design the lightest W12 shape that can be used as the mid-bay vertical member, having a 50% reduction in flange width at the RBS locations, to resist the applied loads and to meet the AISC 358 specified limitations for the pre-qualified connection details. Clearly show the geometry/dimensions of the selected RBS.

(a) Design the vertical member assuming that the shear force in that member does not affect its flexural plastic strength.

(b) For the resulting vertical member designed in (a), calculate the flexural plastic strength of the member taking into account the presence of shear in that member. Indicate by how much (in %) the calculated strength of the structure is reduced as a result of this more refined calculation.

(c) Compare the results in (a) and (b) and comment on why the difference is significant or insignificant. If significant, explain what could be done to compensate for this.

(2) Draw the moment and axial force diagrams for the top horizontal beam of that system, indicating the magnitude of the moments and forces that would have to be considered for the design of that beam.

Additional notes:

- The beams have simple connections at their ends.
- Organize design iterations in a tabular format.

There is no gravity load applied to this frame.

Optional design aspects that could be considered in this problem include: (a) design the shear connection of the vertical member to the beams; (b) design the beams, including checking the panel zone strength; and (c) check if continuity plates in the beams are needed.

Problem 8.3 Design a prequalified RBS connection for the beam of the SMRF structure shown. More specifically:

(1) Select an appropriate geometry for the RBS and location of the RBS along the beam length.
(2) Check whether the selected beams and columns meet the specified limitations and details of the prequalified connection.
(3) Check whether moment at face of column is acceptable.
(4) Check whether column panel zone strength is acceptable.

There is no gravity load applied to this frame.

Optional design aspects that could be considered in this problem include: (a) design the shear connection of the beam to the columns; (b) check if continuity plates are needed in the columns.

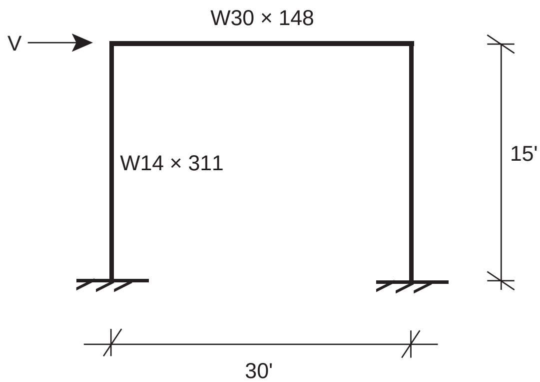

Problem 8.4 The structure shown in the figure below has RBS connections in each of its two beams. For simplicity in this problem:

- The depth of columns and beams are neglected for this problem (i.e., consider stick-members, as shown in the figure).
- The RBS are located at a distance of $L/10$ from the columns, and this eccentricity must be taken into account in calculations and in showing the resulting plastic collapse mechanism.

- M_p of the columns is assumed to be sufficiently large to ensure that plastic hinging only takes place in the two beams.
- All beams are W27 × 161.

Here:

(a) Assuming that the beam flanges have been cut to 50% of their original width, calculate the resulting M_p value at the RBS (in k-ft).
(b) Using the upper bound method, find the maximum load, V, that can be applied (in terms of L, h, M_p), and show the resulting plastic collapse mechanism.

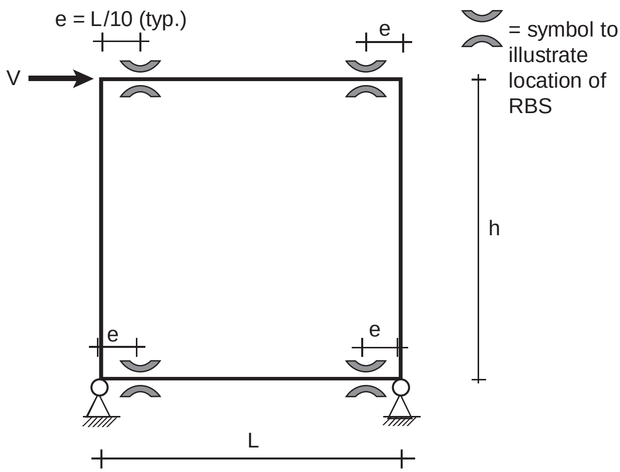

Problem 8.5 A twenty-story building was designed with special moment-resisting frames having RBS beam-to-column connections. The W33 × 354 beams have RBS connections with radius cuts per a geometry in compliance with AISC 358, and fully welded to the web of a W14 × 808 column. Both the columns and beams are of High Performance Steel (HPS) Grade 70.

(a) Identify all issues that make this design noncompliant to the AISC 358 requirements and details for prequalified RBS connections.
(b) Describe in two or three short sentences what would be required to use this proposed RBS connection design on a that specific building project. Cite the appropriate AISC 341 and 358 requirements.

Problem 8.6 What is the physical phenomenon intended to be captured by the C_{pr} factor in AISC 358?

Problem 8.7 Which of the prequalified types of welded connections can be used to connect a W36 × 256 to a W14 column?

Problem 8.8 (Project-Type Problem) Using examples, compare the designs that would result using traditional elastic versus plastic designs.

(a) For low-rise (2 to 5 stories) moment-resisting frames
(b) For mid-rise (8 to 12 stories) moment-resisting frames

Problem 8.9 (Project-Type Problem) Write a computer program to do the lower-bound systematic method of plastic analysis using the simplex algorithm.

References

AIJ. 1995. *Performance of Steel Buildings during the 1995 Hyogoken-Nanbu Earthquake.* (In Japanese with English summary). Tokyo: Architectural Institute of Japan.

AIJ. 1996. *Technical Recommendations for Steel Construction for Buildings* (Part 1 Guide to Steel-Rib Fabrication), 4th ed. Tokyo: Architectural Institute of Japan (in Japanese).

AISC. 1992. *Seismic Provisions for Structural Steel Buildings.* Chicago: American Institute of Steel Construction.

AISC. 1994. Proceedings of the AISC Special Task Committee on the Northridge Earthquake Meeting, American Institute of Steel Construction, Chicago, Illinois.

AISC. 2005. *Seismic Provisions for Structural Steel Buildings—ANSI/AISC 341-05.* Chicago: American Institute of Steel Construction.

AISC. 2010a. *Prequalified Connections for Special and Intermediate Steel Moment Frames for Seismic Applications—ANSI/AISC 358-10.* Chicago: American Institute of Steel Construction.

AISC. 2010b. *Seismic Provisions for Structural Steel Buildings—AISC 341-10.* Chicago: American Institute of Steel Construction.

AISC. 2010c. *Specification for Structural Steel Buildings—ANSI/AISC 360-10.* Chicago: American Institute of Steel Construction.

Allen, J., Partridge, J. E., Radau, S., and Richard, R. M. 1995. "Ductile Connection Designs for Welded Steel Moment Frames," *Proc. 64th Annual Convention, Structural Engineers Association of California*, p. 253–269.

ASCE. 2010. *Minimum Design Loads for Buildings and Other Structures, Standard ASCE/SEI 7-10*. Reston, VA: American Society of Civil Engineers.

Astaneh, A., Nader, M. N., and Malik, L. 1989. "Cyclic Behavior of Double Angle Connections." *Journal of Structural Engineering, ASCE,* vol. 115, no. 5, 1101–1118.

ATC. 1992. *Guidelines for Cyclic Testing of Components of Steel Structures, ATC-24.* Redwood City, CA: Applied Technology Council.

AWS. 2009. *AWS D1.8-09 Structural Welding Code—Seismic Supplement*. Miami, FL: American Welding Society.

Bartlett, F. M., Dexter, J. D., Graeser, M. D., Jelinek, J. J., Schmidt, B. J., and Galambos, T. V. 2003. "Updating Standard Shape Material Properties Database for Design and Reliability." *Engineering Journal, AISC*, vol. 40, no. 1, 2–14.

Becker, R. 1975. "Panel Zone Effect on the Strength and Stiffness of Steel Rigid Frames." *Engineering Journal, AISC*, vol. 12, no. 1, 19–29.

Bennett, D. 1995. *Skyscrapers*. New York: Simon and Schuster.

Bernal, D. 1987 "Amplification Factors for Inelastic Dynamic P-Delta Effects in Earthquake Analysis." *Earthquake Engineering and Structural Dynamics*, vol. 15, no. 5, 635–651.

Bernal, D., Nasseri, A., and Bulut, Y. 2006. Instability Inducing Potential of Near Fault Ground Motions SMIP06 Seminar on Utilization of Strong-Motion Data, p. 41–62.

Bertero, V. V., Anderson, J. C., and Krawinkler, H. 1994. "Performance of Steel Building Structures during the Northridge Earthquake," *Report No. UCB/EERC-94/09*. Berkeley: Earthquake Engineering Research Center, University of California.

Bertero, V. V., Krawinkler, H., and Popov, E. P. 1973. "Further Studies on Seismic Behavior of Steel Beam-to-Column Subassemblages," *Report No. UCB/EERC-73/27*. Berkeley: Earthquake Engineering Research Center, University of California.

Blodgett, O. 1995. "Evaluation of Beam to Column Connections." *SAC Steel Moment Frame Connections, Advisory No. 3, SAC-95-01*. Sacramento: SAC Joint Venture.

Bronson, W. 1959. *The Earth Shook, the Sky Burned—A Moving Record of American's Great Earthquake and Fire: San Francisco April 18, 1906*. San Francisco: Chronicle Books, p. 192.

Bruneau, M., and Mahin, S. A. 1991. "Full Scale Tests of Butt Welded Splices in Heavy Rolled Steel Sections Subjected to Primary Tensile Stresses." *Engineering Journal, AISC*, vol. 28, no. 1, 1–17.

Bruneau, M., Mahin, S. A., and Popov, E. P. 1987. "Ultimate Behavior of Butt Welded Splices in Heavy Rolled Steel Sections." *Report UBC/EERC-87/10*. Berkeley: Earthquake Engineering Research Center, University of California.

Charney, F. A., and Horvilleur, J. F. 1995. "A Technique for Evaluating the Effect of Beam-Column Joint Deformation on the Lateral Flexibility of Steel Frame Building Structures." *The Structural Design of Tall Buildings*, vol. 4, no. 1, 3–13.

Chen, S. J., and Yeh, C. H. 1994. "Enhancement of Ductility of Steel Beam-to-Column Connections for Seismic Resistance," *SSRC Technical Session*. Bethlehem, PA: Lehigh University.

Chen, S. J., Yeh, C. H., and Chu, J. M. 1996. "Ductile Steel Beam-to-Column Connections for Seismic Resistance." *Structural Journal, ASCE*, vol. 122, no. 11, 1292–1299.

Chen, W. F., and Liew, J. Y. R. 1992. "Seismic Resistant Design of Steel Moment-Resisting Frames Considering Panel-Zone Deformations." *Stability and Ductility of Steel Structures under Cyclic Loading*, Fukumoto, Y., and Lee, G., editors. p. 323–334.

Chen, W. F., Kishi, N., and Komuro, M. 2010. *Semi-Rigid Connections Handbook*. Fort Lauderdale, FL: J Ross Pub.

Choi, J., Stojadinovic, B., and Goel, S. C. 2003. "Design of Free Flange Moment Connection." *Engineering Journal*, *AISC*, vol. 40, no. 1, 25–41.

CSA. 2009. *Design of Steel Structures*., Mississauga, Ont, Canada: Canadian Standard Association.

Davidson, B. J., and Fenwick, R. C. 2004. "Design for P-Delta Effects as Proposed for the Australian and New Zealand Loadings Standards." SSRC/NASCC 2004 Joint Annual Stability Conference, Long Beach, California, March 2004.

EERI. 1990. "Loma Prieta Earthquake Reconnaissance Report." *Earthquake Spectra,* supplement C to vol. 6, Oakland, CA.

EERI. 1995. "Northridge Earthquake Reconnaissance Report. Vol. 1." *Earthquake Spectra,* supplement C to vol. 11, Oakland, CA.

EERI. 1996. "Northridge Earthquake Reconnaissance Report. Vol. 2." *Earthquake Spectra,* supplement C to vol. 11, Oakland, CA.

EERI. 1994. "Connections: Henry J. Degenkolb." *EERI Oral History Series*. Oakland, CA: Earthquake Engineering Research Institute, p. 226.

EERI. 1997. "Connections: George W. Housner." *EERI Oral History Series*. Oakland, CA: Earthquake Engineering Research Institute, p. 275.

Elnashai, A. S., and Elghazouli, A. Y. 1994. "Seismic Behavior of Semi-Rigid Steel Frames." *Journal of Constructional Steel Research,* vol. 29, no. 1–3, 149–174.

El-Tawil, S., Mikesell, T. D., Vidarsson, E., and Kunnath, S. K. 1999. "Inelastic Behavior and Design of Steel Panel Zones." *Journal of Structural Engineering, ASCE*, vol. 125, no. 2, 183–193.

El-Tawil, S. 2000. "Panel Zone Yielding in Steel Moment Connections." *Engineering Journal, AISC*, vol. 37, no. 3, 120–135.

Engelhardt, M. D., and Husain, A. S. 1993. Cyclic Loading Performance of Welded Flange-Bolted Web Connections. *Journal of Structural Engineering. ASCE*, vol. 119, no. 12, 3537–3550.

Engelhardt, M. D., and Sabol, T. A. 1994. "Testing of Welded Steel Moment Connections in Response to the Northridge Earthquake." *Progress Report to the AISC Advisory Committee on Special Moment-Resisting Frame Research*.

Engelhardt, M. D., and Sabol, T. A. 1995. "Lessons Learned from the Northridge Earthquake: Steel Moment Frame Performance." *Proceedings, New Directions in Seismic Design*. Tokyo. October. 1–12.

Engelhardt, M. D., and Sabol, T. A. 1996. "Reinforcing of Steel Moment Connections with Cover Plates: Benefits and Limitations." *Proceedings, U.S.-Japan Seminar on*

Innovations in Stability Concepts and Methods for Seismic Design in Structural Steel, Honolulu, Hawaii.

Engelhardt, M. D., Winneberger, T., Zekany, A. J., and Potyraj, T. J. 1996. "The Dogbone Connection: Part II." *Modern Steel Construction,* vol. 36, no. 8, 46–55.

Englekirk, R. 1994. *Steel Structures—Controlling Behavior through Design.* New York: John Wiley & Sons.

Englekirk, R. E. 1999. "Extant Panel Zone Design Procedures for Steel Frames are Questioned." *Earthquake Spectra, EERI*, vol. 15, no. 2, 361–370, Oakland, CA.

FEMA. 2000a. "Recommended Seismic Design Criteria for New Steel Moment-Frame Buildings," *Report FEMA-350*. Washington, D. C.: Federal Emergency Management Agency.

FEMA. 2000b. "Recommended Seismic Evaluation and Upgrade Criteria for Existing Welded Steel Moment-Frame Buildings." *Report FEMA-351*. Washington, D. C.: Federal Emergency Management Agency.

FEMA. 2000c. "Recommended Postearthquake Evaluation and Repair Criteria for Welded Steel Moment-Frame Buildings." *Report FEMA-352*. Washington, D. C.: Federal Emergency Management Agency.

FEMA. 2000d. "Recommended Specifications and Quality Assurance Guidelines for Steel Moment-Frame Construction for Seismic Applications." *Report FEMA-353*. Washington, D. C.: Federal Emergency Management Agency.

FEMA. 2000e. "State of the Art Report on Systems Performance of Steel Moment Frames Subject to Earthquake Ground Shaking." *Report No. FEMA-355C*. Washington, D. C.: Federal Emergency Management Agency.

FEMA. 2000f. "State-of-the-Art Report on Connection Performance." *Report No. FEMA-355D*. Washington, D. C.: Federal Emergency Management Agency.

FEMA. 2000g. "State of the Art Report on Past Performance of Steel Moment-Frame Buildings in Earthquakes." *Report No. FEMA-355E*. Washington, D. C.: Federal Emergency Management Agency.

FEMA. 2009. "Quantification of Building Seismic Performance Factors." *FEMA Report P-695*, Washington, D. C.: Federal Emergency Management Agency.

Fielding, D. J., and Chen, W. F. 1973. "Steel Frame Analysis and Connection Shear Deformation." *Journal of the Structural Division, ASCE,* vol. 99, ST1, 1–18.

Fielding, D. J., and Huang, J. S. 1971. "Shear in Steel Beam-to-Column Connections." *Welding Journal.* July.

Freeman, J. R. 1932. *Earthquake Damage and Insurance*. New York: McGraw-Hill, p. 904.

Ghobarah, A., Osman, A., and Korol, R. M. 1990. "Behaviour of Extended End-Plate Connections under Cyclic Loading." Engineering Structures, vol. 12, 15–26, ElsevierScience Publishers, London, England.

Ghobarah, A., Korol, R. M., and Osman, A. 1992. "Cyclic Behavior of Extended End-Plate Joints." ASCE *Structural Journal,* vol. 118, no. 5, 1333–1353.

Graham, J. D., Sherbourne, A. N., and Khabbaz, R. N. 1959. *Welded Interior Beam-to-Column Connections.* Chicago: American Institute of Steel Construction.

Goel, S. C., and Stojadinovic, B., and Lee, K. H. 1997. "Truss Analogy for Steel Moment Connections," *Engineering Journal*, *AISC*, vol. 33, no. 2, 2nd Quarter, 43–53.

Hajjar, J. F., Dexter, R. J., Ojard, S. D., Ye, Y., and Cotton, S. C. 2003. *Continuity Plate Detailing for Steel Moment-Resisting Connections*, vol., no. 4, 189–211.

Hamburger, R. O. 1996. "More on Welded Moment Connections." *NEWS*. April. San Francisco: Structural Engineers Association of California (also available at http://www.seaoc.org/seaoc/seaonc/nl496/ncnl496.htm).

Hamburger, R. O., Malley, J. O., and Miller, D. K. 2007. "New AWS D1.8 Seismic Welding Supplement Outlined." *Welding Journal*, p. 28–31, February 2007.

Hamburger, R. O., Krawinkler, H., Malley, J. O., and Adan, S. M. 2009. "Seismic Design of Steel Special Moment Frames: A Guide for Practicing Engineers." *NEHRP Technical Brief No. 2, Report NIST GCR 09-917-3*. Gaithersburg, MD: National Institute of Standards and Technology.

Ibarra, L. F., Medina, R. A., and Krawinkler, H. 2005. "Hysteretic models that incorporate strength and stiffness degradation." *Earthquake Engineering and Structural Dynamics,* 34, 1489–1511.

ICBO. 1988, 1997. *Uniform Building Code*. Whittier, CA: International Conference of Building Officials.

Iwankiw, R. N., and Carter, C. J. 1996. "The Dogbone: A New Idea to Chew On." *Modern Steel Construction*, vol. 36, no. 4, 18–23.

Kato, B. 1973. "Brittle Fracture of Heavy Steel Members," *Proceedings of the National Conference on Tall Buildings. Architectural Institute of Japan*, August, Tokyo, 99–100.

Kato, B., and Morita, K. 1969. "Brittle Fracture of Heavy Steel Structural Members" (in Japanese). *Transactions of the Architectural Institute of Japan*, no. 156, February, Tokyo.

Kaufmann, E. J., Xue, M., Lu, L. W., and Fisher, J. W. 1996. "Achieving Ductile Behavior of Moment Connections." *Modern Steel Construction*, vol. 36, no. 1, 30–39.

Kawashima, K., MacRae, G. A., Hoshikuma, J., and Nagaya, K. 1996. "Residual Displacement Response Spectrum And Its Application To Reinforced Concrete Bridge Piers." *Wind and Seismic Effects: Proceedings of the 28th Joint Meeting of the US-Japan*, August 1996.

Kim, T., Whittaker, A. S., Gilani, A. S. J., Bertero, V. V., and Takhirov, S. M. 2000. "Cover-plate and flange-plate reinforced steel moment-resisting connections." Report PEER 2000/07, Pacific Earthquake Engineering Research Center, University of California at Berkeley, Berkeley, California.

Krawinkler, H. 1978. "Shear in Beam-Column Joints in Seismic Design of Steel Frames." *Engineering Journal, AISC*, vol. 5, no. 3, 82–91.

Krawinkler, H., Bertero, V. V., and Popov, E. P. 1971. "Inelastic Behavior of Steel Beam-to-Column Subassemblages." *Report No. UCB/EERC-71/7*. Berkeley: Earthquake Engineering Research Center, University of California.

Krawinkler, H., Bertero, V. V., and Popov, E. P. 1975. "Shear Behavior of Steel Frame Joints." *Journal of the Structural Division, ASCE*, vol. 101, ST11, 2317–2336.

Krawinkler, H. 2006. "Importance of Good Nonlinear Analysis." *Struct. Design Tall Spec. Build*, vol. 15, 515–531.

Lavan O., Sivaselvan, M. V., Reinhorn A. M., and Dargush, G. F. 2009. "Progressive Collapse Analysis Through Strength Degradation and Fracture in the Mixed Lagrangian Framework." *International Journal of Earthquake Engineering and Structural Dynamics*, 38, no. 13, 1483–1504.

Lee, C. H., Jeon, S. W., Kim, J. H., and Uang, C. M. 2005a. "Effects of Panel Zone Strength and Beam Web Connection Method on Seismic Performance of Reduced Beam Section Steel Moment Connections." *Journal of Structural Engineering, ASCE,* vol. 131, no. 12, 1854–1865.

Lee, D., Cotton, S. C., Hajjar, J. F., Dexter, R. J., and Ye, Y. 2005b. "Cyclic Behavior of Steel Moment-Resisting Connections Reinforced by Alternative Column Stiffener Details: II. Panel Zone Behavior and Doubler Plate Detailing." *Engineering Journal, AISC*, vol. 42, no. 4, 215–238.

Leet, K., Uang, C. M., and Gilbert, A. 2011. "*Fundamentals of Structural Analysis,*" 4th ed. New York: McGraw-Hill.

Leon R, Forcier, G. P., Roeder, C. W., and Reece, F. R. 1994. "Cyclic Performance of Riveted Connections." *ASCE Struct Congr XII*, Atlanta, p. 1490–1495.

Lignos, D. G., Krawinkler, H., and Whittaker, A. S. 2008. "Shaking Table Collapse Tests of Two Scale Models of a 4-Story Moment Resisting Frame." *Paper No. 12-01-0186, Proceedings of the 14th World Conference on Earthquake Engineering*, Beijing.

Liu, J., and Astaneh, A. 2000. "Cyclic Testing of Simple Connections Including Effects of Slab." *Journal of Structural Engineering*. vol. 126, no. 1, 32–39.

Liu, J. 2003. "Examination of Expected Yield and Tensile Strength Ratios," *Draft Addendum Report*. Chicago: American Institute of Steel Construction.

MacRae, G. A., Carr, A. J., and Walpole, W. R. 1990. "The Seismic Response of Steel Frames." *Research Report 90-6*. Christchurch, NZ: Department of Civil Engineering, University of Canterbury.

MacRae, G. A., and Kawashima, K. 1993. "The Seismic Response of Bilinear Oscillators Using Japanese Earthquake Records." *Journal of Research*, vol. 30, Public Works Research Institute, Tsukuba, Japan.

MacRae GA. 1994. "P−Δ effects on single-degree-of-freedom structures in earthquakes." *Earthquake Spectra*; vol. 10, no. 3, 539–568.

MacRae, G. A., Priestley, M. J. N., and Tao, J. 1993. "*P*-Δ Effects in Seismic Design." *Report No. SSRP-93/05*. San Diego: Department of Applied Mechanics and Engineering Sciences, University of California.

MacRae, G. A., Urmson, C. R., Walpole, W. R., Moss, P., Hyde, K., and Clifton, G. C. 2009. "Axial Shortening of Steel Columns in Buildings Subjected to Earthquakes." *Bulletin of the NZ Society of Earthquake Engineering*, vol. 42, no. 4, 275–287.

MacRae, G. A., Kimura, Y., and Roeder, C. 2004. "Effect of Column Stiffness on Braced Frame Seismic Behavior." *Journal of Structural Engineering, ASCE,* vol. 127, no. 5, 490–497.

NRCC. 2010. *National Building Code of Canada*. Ottawa, Ont., Canada: National Research Council of Canada.

Mazzolani, F. M., and Piluso, V. 1996. *Theory and Design of Seismic Resistant Frames*. London: E&FN Spon.

Miller, D. K. 2006. *Design Guide 21: Welded Connections—A Primer for Engineers.* Chicago: American Institute of Steel Construction.

Miranda, E., and Akkar, S. D. 2003. "Dynamic Instability of Simple Structural Systems." *Journal of Structural Engineering, ASCE*, vol. 129, no. 1, 1722–1726.

Nakashima, M., Inoue, K., and Tada, M. 1998. "Classification of Damage to Steel Buildings Observed in the 1995 Hyogoken-Nanbu Earthquake." *Engineering Structures*, vol. 20, no. 4–6, 271–281.

Nakashima, M., and Sawaizumi, S. 2000. "Column-to-Beam Strength Ratio Required for Ensuring Beam-Collapse Mechanisms in Earthquake Response of Steel Moment Frames," *Proceedings, 12WCEE, paper #1109/6/A*, Auckland, New Zealand.

Nakashima, M., Roeder, C. W., and Maruoka, Y. 2000. "Steel Moment Frames for Earthquakes in the United States and Japan." *Journal of Structural Engineering, ASCE*, vol. 126, no. 8, 861–868.

Nakashima, M., Kato, M., and Okazaki, T. 2004. "Collaboration between Practice and Research for Development of Steel Construction in Japan." *Journal of Steel Structures, Korean Society of Steel Construction*, vol. 4, no. 4, 249–262.

Nakashima, M. 2001. "APPENDIX C. Overview of Damage to Steel Building Structures Observed in the 1995 Kobe Earthquake." *Past Performance of Steel Moment-Frame Buildings in Earthquakes, Federal Emergency Management Agency, Report FEMA-355E*, June 2001, C-1-C24.

Nelson, R. F. 1995. "Proprietary Solution." *Modern Steel Construction*, vol. 36, no. 1, 40–44.

Noel, S., and Uang, C. M. 1996. "Cyclic Testing of Steel Moment Connections for the San Francisco Civic Center Complex." *Test report to HSH Design/Build Structural Systems Research Project. Division of Structural Engineering Report No. TR-96/07,* San Diego: University of California.

Obeid, K. 1996. "Steel Moment Frame Connections: Shear in the Panel Zone." *NEWS*. April. San Francisco: Structural Engineers Association of California.

Osman, A., Korol, R. M., and Ghobarah, A. 1990. "Seismic Performance of Extended End-Plate Connections." *Proceedings of the 4th National U.S. Conference on Earthquake Engineering*. Oakland, CA: Earthquake Engineering Research Institute.

Plumier, A. 1990. "New Idea for Safe Structures in Seismic Zones." *IABSE Symposium*, Brussels, Belgium: University of Liege.

Popov, E. P. 1968. *Introduction to Mechanics of Solids*, Englewood Cliffs, NJ: Prentice Hall.

Popov, E. P. 1987. "Panel Zone Flexibility in Seismic Moment Joints." *Journal of Constructional Steel Research*, vol. 8, no. 1, 91–118.

Popov, E. P., Amin, N. R., Louie, J. J., and Stephen, R. M. 1985. "Cyclic Behavior of Large Beam-Column Assemblies." *Earthquake Spectra*, *Earthquake Engineering Research Institute,* vol. 1, no. 2, 203–238.

Popov, E. P., and Bertero, V. V. 1973. "Cyclic Loading of Steel Beams and Connections." *Journal of the Structural Division, ASCE*, vol. 99, ST6, 1189–1204.

Popov, E. P., Bertero, V. V., and Chandramouli, S. 1975. "Hysteretic Behavior of Steel Columns," *Report UCB/EERC-75-11*. Berkeley: Earthquake Engineering Research Center, University of California.
Popov, E. P., and Pinkney, R. B. 1969. "Cyclic Yield Reversals in Steel Building Connections." *Journal of the Structural Division, ASCE*, vol. 95, no. ST3, 327–353.
Popov, E. P., and Stephen, R. M. 1972. "Cyclic Loading of Full-Size Steel Connections," *Bulletin No. 21*. New York: American Iron and Steel Institute.
Popov, E. P., and Stephen, R. M. 1970. "Cyclic Loading of Full-Size Steel Connections," *Report UCB/EERC-70-3*. Berkeley: Earthquake Engineering Research Center, University of California.
Popov, E. P., and Stephen, R. M. 1977. "Tensile Capacity of Partial Penetration Welds." *ASCE Journal of the Structural Division*, vol. 103, no. ST9.
Popov, E. P., and Tsai, K. C. 1989. "Performance of Large Seismic Steel Moment Connections under Cyclic Loads." *Engineering Journal*, *AISC*, vol. 26, no. 2, 51–60.
Popov, E. P. Tsai, K. C., and Engelhardt, M. D. 1989. "On Seismic Steel Joints and Connections." *Engineering Structures*, vol. 11, no. 4, 193–209.
Radziminski, J. B., and Azizinamini, A. 1986. "Low Cyclic Fatigue of Semi-Rigid Steel Beam-to-Column Connections." *Proceedings of the 3rd U.S. National Conference on Earthquake Engineering*, vol. 2, 1285–1296. Oakland, CA: Earthquake Engineering Research Institute.
Ricles, J. M., Mao, L., Kaufmann, E. J., Lu, L., and Fisher, J. W. 2000. "Development and Evaluation of Improved Details for Ductile Welded Unreinforced Flange Connections." *Report No. SAC/BD-00/24*. Sacramento, CA: SAC Joint Venture.
Roeder, C. W. Carpenter, J. E., and Taniguchi, H. 1989. "Predicted Ductility Demands for Steel Moment-Resisting Frames." *Earthquake Spectra*, vol. 5, no. 2, 409–427.
Roeder, C. W., and Foutch, D. A. 1995. "Experimental Results for Seismic Resistant Steel Moment Frame Connections." *Journal of Structural Engineering*, *ASCE*, vol. 122, no. 6, 581–588.
Roeder, C. W., Knechtel, B, Thomas, E., Vaneaton, A, Leon, R. T., and Preece, F. R. 1996. "Seismic Behavior of Older Steel Structures." *Journal of Structural Engineering*, *ASCE*, vol. 122, no. 4, 365–373.
Rodgers, J. E., and Mahin, S. A. 2006. "Effects of Connection Fractures on Global Behavior of Steel Moment Frames Subjected to Earthquakes." *Journal of Structural Engineering, ASCE*, vol. 132, no. 1, 78–88.
Rosenbaum, D. B. 1996. "Welds in Bay Area Hit by Quake, Too." *Engineering News Record*, vol. 237, no. 11, 10.
Rutenberg, A., and DeStefano, M. 2000. "Approximate Stability Bounds on the Seismic Force Reduction Factor," *Paper no. 1635, Proceedings of the 12th World Conference on Earthquake Engineering*, Auckland, New Zealand.
SAC. 1995a. "Steel Moment Frame Connections—Advisory No. 3." *SAC-95-01*. Sacramento, CA: SAC Joint Venture.
SAC. 1995b. "Interim Guidelines: Evaluation, Repair, Modification and Design of Welded Steel Moment Frame Structures." *Program to Reduce the Earthquake Hazards of Steel Moment Frame Structures*. *Federal Emergency Management Agency, Report FEMA 267/SAC-95-02*. Sacramento, CA: SAC Joint Venture.
SAC. 1997. "Interim Guidelines Advisory No. 1: Supplement to FEMA 267." *Program to Reduce the Earthquake Hazards of Steel Moment Frame Structures. Federal Emergency Management Agency, Report FEMA 267A/SAC-96-03*. Sacramento, CA: SAC Joint Venture.
SAC. 1999. "Interim Guidelines Advisory No. 2: Supplement to FEMA 267." *Program to Reduce the Earthquake Hazards of Steel Moment Frame Structures. Federal Emergency Management Agency, Report FEMA 267B/SAC-99-01*. Sacramento, CA: SAC Joint Venture.
Sarraf, M., Bruneau, M. 1994. "Experimental Study on Cyclic Behavior of Riveted Stiffened-Seat Angle Connections." *Ottawa Carleton Earthquake Engineering Research Centre report OCEERC 94-01*, Ottawa, December 1994, p. 172.
Sarraf, M., and Bruneau, M. 1996. "Cyclic Testing of Existing and Retrofitted Riveted Stiffened-Seat Angle Connections." *ASCE Structural Journal*, vol. 122, no. 7, 762–775.

Schneider, S. P., Roeder, C. W., and Carpenter, J. E. 1992. "Seismic Behavior of Moment-Resisting Steel Frames: Experimental Study." *ASCE Structural Journal*, vol. 119, no. 6, 1885–1902.

SEAOC. 1995. *Interim Recommendations for Design of Steel Moment-Resisting Connection*. Sacramento, CA: Structural Engineers Association of California.

SEAOC. 1980, 1988, 1990. *Recommended Lateral Force Requirements and Commentary*. Sacramento, CA: Seismology Committee, Structural Engineers Association of California.

Sivaselvan, M. V., and Reinhorn, A. M. 2000. "Hysteretic models for deteriorating structures." *J. Eng. Mech., ASCE*, vol. 126, 633–640.

Sivaselvan, M. V., and Reinhorn, A. M. 2002. "Collapse Analysis: Large Inelastic Deformations Analysis of Planar Frames." *Journal of Structural Engineering, ASCE*, vol. 128, no. 12, 1575–1583.

Sivaselvan, M. V., and Reinhorn, A. M. 2006. "Lagrangian Approach to Structural Collapse Simulation." *J. Eng. Mech., ASCE*, vol. 132, 795–805.

SSPC. 1994. *Statistical Analysis of Tensile Data for Wide Flange Structural Shapes*. Structural Shape Producers Council, Washington, D.C.

Stockmann, M., and Schlafly, T. J. 2008. "Digging Through the Rubble, Part 1 and 2." *Modern Steel Construction*, October and November.

Stojadinovic, B., Goel, S. C., Lee, K. H., Margarian, A. G., and Choi, J. 2000. "Parametric Tests on Unreinforced Steel Moment Connections." *Journal of Structural Engineering, ASCE*, vol. 126, no. 1, 40–49.

Suita, K., Tamura, T., Morita, S., Nakashima, M., and Engelhardt, M. D. 1999. "Plastic Rotation Capacity of Steel Beam-to-Column Connection Using a Reduced Beam Section and No Weld Access Hole Design—Full-Scale Tests for Improved Steel Beam-to-Column Subassemblies Part 1." *Journal of Structural and Construction Engineering, AIJ*, vol. 526, 177–184.

Suita, K., Yamada, S., Tada, M., Kasai, K., Matsuoka, Y., and Sato, E. 2008. "Results of Recent E-Defense Tests on Full-Scale Steel Buildings: Part I—Collapse Experiments on 4-Story Moment Frames," *Paper no. 266, Proceedings, ASCE Structures Congress*, Vancouver, Canada.

Tremblay, R., Bruneau, M., Nakashima, M., Prion, H. G. L., Filiatrault, A., and DeVall, R. 1996. "Seismic Design of Steel Buildings: Lessons from the 1995 Hyogoken Nanbu Earthquake." *Canadian Journal of Civil Engineering*, vol. 23, no. 3, 757–770.

Tremblay, R. Timler, P., Bruneau, M., and Filiatrault, A. 1995. "Performance of Steel Structures during the January 17, 1994, Northridge Earthquake." *Canadian Journal of Civil Engineering*, vol. 22, no. 2, 338–360.

Tsai, K. C., and Popov, E. P. 1990a. "Cyclic Behavior of End-Plate Moment Connections." *ASCE Structural Journal*, vol. 116, no. 11, 2917–2930.

Tsai, K. C., and Popov, E. P. 1990b. "Seismic Panel Zone Design Effect on Elastic Story Drift in Steel Frames." *ASCE Structural Journal*, vol. 116, no. 12, 3285–3301.

Tsai, K. C., and Popov, E. P. 1988. "Steel Beam-Column Joints in Seismic Moment-Resisting Frames," *Report UCB/EERC-88/19*. Berkeley: Earthquake Engineering Research Center, University of California.

Tsai, K. C., Wu, S., and Popov, E. P. 1995. "Experimental Performance of Seismic Steel Beam-Column Moment Joints." *ASCE Structural Journal*, vol. 121, no. 6, 925–931

Uang, C. M. 1995. *Dynamic Testing of Large-Size Steel Moment Connections*. VHS-video of tests. San Diego: University of California.

Uang, C. M., and Bondad, D. M. 1996. "Dynamic Testing of Full-Scale Steel Moment Connections." *Proceedings of 11th World Conference on Earthquake Engineering, Acapulco, Paper 407*. CD-ROM. New York: Pergamon Press.

Uang, C. M., and Noel, S. 1995. "Cyclic Testing of Rib-Reinforced Steel Moment Connection with Reduced Beam Flanges." *Test report to Ove Arup & Partners. Structural systems research project. Division of Structural Engineering Report No. TR-95/04*. San Diego: University of California.

Uang, C. M., and Noel, S. 1996. "Cyclic Testing of Strong- and Weak-Axis Steel Moment Connection with Reduced Beam Flanges." *Final Report to the City of*

Hope. Division of Structural Engineering Report No. TR-96/01. San Diego: University of California.

Vian, D., and Bruneau, M. 2001. "Experimental Investigation Of P-Delta Effects To Collapse During Earthquakes," *Technical Report MCEER 01-0001*. Buffalo, NY: Multidisciplinary Center For Earthquake Engineering Research, University at Buffalo (available at http://civil.eng.buffalo.edu/users_ntwk/experimental/case_studies/vian/).

Vian, D., and Bruneau., M. 2003. "Tests to Structural Collapse of Single Degree of Freedom Frames Subjected to Earthquake Excitation." *Journal of Structural Engineering, ASCE*, vol. 129, no. 12, 1676–1685.

Villaverde, R. 2007. "Methods to Assess the Seismic Collapse Capacity of Buildings Structures: State of the Art." *Journal of Structural Engineering, ASCE*, vol. 133, no. 1, 57–66.

Wolfe, J., Nienberg, M., Manmohan, D., Halle, J., and Quintana, M. 1996. "Welding Alert, Cover Plated Moment Frame Connections." *NEWS*, April. San Francisco: Structural Engineers Association of California.

Wakabayashi, M. 1986. *Design of Earthquake-Resistant Buildings*. New York: McGraw-Hill.

Whittaker, A., Bertero., V., and Gilani, A. 1995. "Testing of Full-Scale Steel Beam-Column Assemblies." *SAC Phase I Report*. Sacramento, CA: SAC Joint Venture.

Whittaker, A., and Gilani, A. 1996. "Cyclic Testing of Steel Beam-Column Connections." *Report No. EERC-STI/96-04*. Berkeley: Earthquake Engineering Research Center, University of California.

Whittaker, A., Gilani, A., Takhirov, S. and Ostertag, C. 2002. "Forensic studies of a large cover-plate steel moment-resisting connection." The Structural Design of Tall Buildings, no. 11, 265–283.

Wong, C. H., El Nimeiri, M. M., and Tang, J. W. 1981. "Preliminary Analysis and Member Sizing of Tall Tubular Steel Buildings." *AISC Engineering Journal*, 2nd quarter.

Xue, M., Kaufmann, E. J., Lu, L. W., and Fisher, J. W. 1996. "Achieving Ductile Behavior of Moment Connections—Part II." *Modern Steel Construction*, vol. 36, no. 6, 38–42.

Youssef, N. F. G., Bonowitz, D., and Gross, J. L. 1995. "A Survey of Steel Moment-Resisting Frame Buildings Affected by the 1994 Northridge Earthquake." *Report NISTIR 5625*. Gaithersburg, MD: National Institute of Standards and Technology, Technology Administration, United States Department of Commerce.

Zareian, F., and Krawinkler, H. 2007. Assessment of probability of collapse and design for collapse safety. Earthquake Engineering and Structural Dynamics, no. 36, 1901–1914.

Ziemian, R. D. 2010. "Guide to Stability Design Criteria for Metal Structures, 6th Edition." Wiley, p. 1120.

This page intentionally left blank

CHAPTER 9

Design of Ductile Concentrically Braced Frames

9.1 Introduction

9.1.1 Historical Developments

A braced frame is essentially a planar vertically cantilevered truss. Notwithstanding cast iron trussed arches, such as those built by Tilford as early as 1796, straight metal trusses were first used in Earl Trumbull's 1840 bridge spanning the Erie canal, and frequently thereafter using Squire Whimple's more economical bowstring truss concept that relied on brittle cast iron for compression members and more forgiving wrought iron for tension members (DeLony 1992, Griggs 2009). Not surprisingly, in early steel buildings without heavy masonry cladding that could provide lateral stability, trusses were also introduced—for example, discrete bracing rods are visible in sketches of the cast iron Crystal Palace built in London in 1851 (lost to fire in 1936). Likewise, the architects of the 1853 New York Crystal Palace (lost to fire in 1858) described its roof as "braced against the action of the wind by a system of horizontal wrought-iron trusses similar to the vertical supports of the gallery floors" (Carstensen and Gildemeister 1918).

With the arrival of processes to economically make steel of reliable quality, steel bridges followed, the 6442-foot (1964-meter) James Eades trussed-arch bridge built in 1874 in St. Louis being the first major bridge to use steel, and the 2.5 km (1.5 m) 1890 Forth Bridge in Scotland being the first all-steel bridge [with a world record span of 521.3 m (1710 ft) until 1917] (Bennett 1999). Note that the 1889 Eiffel tower, which is conceptually a tall tapered three-dimensional braced frame, was made of puddled iron (a refined form of wrought iron). Because of their high strength and stiffness to resist lateral loads, steel braced frames rapidly became popular to resist wind forces when implemented in buildings and industrial structures in the nineteenth century, and particularly so as architects pushed high-rise construction to greater heights in the early twentieth century. Ketchum (1918) described how diagonal bracing, knee-bracing, portal bracing, and brackets could be used to resist wind loads, providing plans and elevations for actual buildings, and described diagonal bracing as being the most effective and desirable for this purpose (noting that architects at the time required braces to be hidden in walls). Many of these diagonal braces were slender rods, only able to resist tension forces (a.k.a. tension-only braces), and braces, like the rest of the steel frame, were often encased in concrete or masonry for fireproofing. Interestingly, formal regulations for wind design requirements only appeared in the earliest part of the twentieth century—specified earthquake design requirements following only much later—as mentioned in Chapter 8.

Design requirements for braced frames evolved continuously over time, and the engineer is cautioned that noncompliance with all of the latest specified design requirements may not necessarily lead to inadequate performance. For example, nowadays, members subjected to axial compression in nonseismic applications are required to be compact, which means that the width-to-thickness ratio of the parts that constitute the cross-section must be sufficiently large to ensure that the stress at which local buckling would develop is greater than F_y. In early steel design practice (in an allowable stress perspective), some design codes only required that this local buckling critical stress be greater than the stress at which global member buckling occurred, which for slender members in compression, can result in substantially more liberal width-to-thickness ratios and satisfactory behavior nonetheless (in a non-seismic context). Information on archaic steel design practices can be found in older steel design textbook (e.g., Ketchum 1918) and various other documents (e.g., Brockenbrough 2002, Friedman 1995).

Although architects in many applications predominantly preferred the open spaces afforded by moment-resisting frames, with the emergence of seismic regulations in the 1960s and 1970s, braced frames slowly gained popularity in regions of high seismicity because they required less steel than moment-resisting frames to resist the prescribed seismic forces, and more easily could meet the specified frame drift limits.

The initial studies on the seismic performance of braced frames were conducted in the 1970s for the oil industry to characterize the inelastic cyclic behavior of axially loaded tubular steel members used in offshore drilling platforms. Although braces having circular and rectangular hollow sections are also used as braces in buildings, the scope of subsequent research expanded to include other cross-sections typically encountered in buildings, such as I-shaped sections, double angles stitched together to form T-shaped sections, solid T-shaped sections, single angles, channels, and tension-only rods and angles. Behavior of the welded or bolted gusset plates providing brace connections to the framing system were also found to play an important role on system behavior. Much of that early research instructed many of the specified code provision, details, and limitations in effect since.

Seismic provisions for the analysis, design, and detailing of concentrically braced frames (CBFs) were gradually introduced into seismic regulations and guidelines. In the United States, this started in California in the late 1970s (SEAOC 1978) and on a nationwide basis in the early 1990s (AISC 1992). These were progressively updated in subsequent editions of various regulations and guidelines, such as the Structural Engineers Association of California (SEAOC) Recommended Lateral Force Requirements (SEAOC 1996), the Uniform Building Code (ICBO 1994), the NEHRP Recommended Provisions for the Development of Seismic Regulations for New Buildings (BSSC 1995), and the AISC LRFD Specification (AISC 1993). The consolidation of building codes that occurred in the United States in 2000 made it possible to concentrate the seismic design requirements for steel structures in the AISC Seismic Provisions (ANSI Standard AISC 341) (AISC 1997, 2002, 2005, 2010a), then referenced by the International Buildings Code or other state or city buildings codes as appropriate.

Note that in the aftermath of the Northridge earthquake, in light of the fractures discovered in moment-resisting frames, new steel buildings in California became more frequently designed with braced frames. Owners and architects who earlier wished to avoid at all cost the obstructions created by braces, suddenly were able to charge a premium for the offices having windows crossed by braces, which the public came to associate with seismic safety. Ironically, although a large number of tests were conducted to investigate and better understand how to design reliable ductile moment-resisting frames after the 1994 Northridge earthquake, relatively fewer tests investigated the cyclic behavior of concentrically braced frames (CBFs); research relying on past experimental results for individual braces typically reports less than a hundred data points (e.g., Lee and Bruneau 2002; Tremblay 2002, 2008; Uriz and Mahin 2008). This is surprising given the reliance on compression brace energy dissipation by existing codes and guidelines for many years, and the complex mechanisms leading to substantial strength degradation upon cyclic plastic hinging at midspan of braces, as explained throughout this chapter. As such, contemporary research has been most instructive and findings have been implemented in the latest editions of AISC 341 (AISC 1997, 2002, 2005, 2010a) and CSA S16 (CSA 1994, 2001, 2009).

Note that, in this chapter, given that providing an understanding of the evolution of seismic design requirements is within the scope of this book, a number of obsolete design provisions are reviewed and contrasted with current requirements. This is useful in the perspective of seismic retrofit.

Also, because differentiation is necessary for clarity, C_u and T_u are used in this chapter for the axial compression and tension strength of braces, respectively, instead of P_u, which is used interchangeably in AISC 341 and 360 (AISC 2010a and 2010b, respectively) for both values. Likewise, C_r and T_r are used instead of ϕP_u. Acronyms are also used to refer to concentrically braced frames (CBFs), special concentrically braces frames (SCBFs), and ordinary concentrically braces frames (OCBFs), the latter two being defined in Section 9.1.3.

9.1.2 General Behavior and Plastic Mechanism

As described in Chapter 7, seismic design considers forces substantially smaller than those that would have to be considered to achieve full elastic response during an earthquake. This is possible provided that designated elements of the structural system are designed to yield at these lower forces, and detailed to have a ductile response. These ductile elements then limit the forces applied to the rest of the system, per capacity design principles.

During earthquakes, CBFs are expected to yield and dissipate energy through postbuckling hysteretic behavior of their bracing members. For drift in one specific direction, this is achieved by buckling of the braces in compression, followed by yielding of the braces in tension, as schematically illustrated in Figure 9.1. Under cyclic loading, for loads acting in the reversed direction, the previously buckled brace will yield in tension, whereas the brace previously yielded in tension will buckle. Typical postearthquake evidence of brace inelastic buckling is shown in Figure 9.2. Therefore, to survive an earthquake, the braces must be able to sustain large inelastic displacement reversals without significant loss of strength and stiffness.

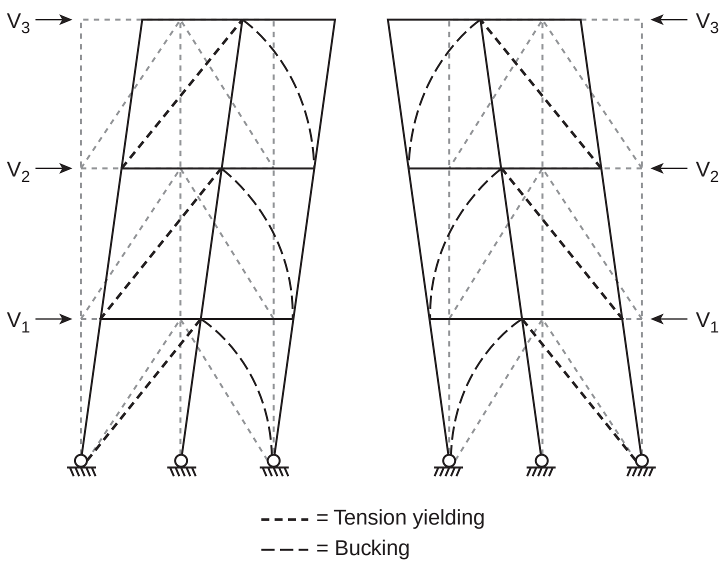

FIGURE 9.1 Schematic of CBF inelastic behavior.

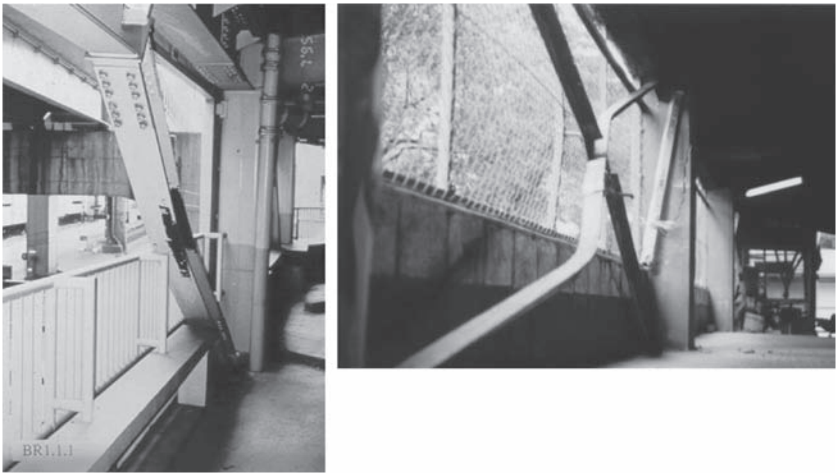

(a) (b)

FIGURE 9.2 Postearthquake residual inelastic brace buckling: (a) brace with low member slenderness; (b) brace with high member slenderness. (*Part a, courtesy of M. Nakashima, Disaster Prevention Research Institute, Kyoto University, Japan.*)

To achieve this behavior, special ductile detailing is required. Many braced frame structures designed without such ductile detailing consideration have suffered extensive damage in past earthquakes, including failure of bracing members and their connections (e.g., AIJ 1995; Tremblay et al. 1995, 1996)—examples of such failures are presented as appropriate throughout this chapter.

Given that braces are the designated energy dissipating element in CBFs, a review of their cyclic inelastic behavior is presented in Section 9.2. An understanding of the characteristics of that cyclic behavior is key to integrate capacity design principles in the design of CBFs to achieve the intended ductile performance. Hysteretic behavior and design of CBFs are both addressed in Section 9.3.

9.1.3 Design Philosophy

To provide adequate earthquake resistance, CBFs must be designed to have appropriate strength and ductile response. To achieve this, diagonal braces must be specially designed to sustain plastic deformations and dissipate hysteretic energy in a stable manner through successive cycles of buckling in compression and yielding in tension. The design strategy is to ensure that plastic deformations only occur in the braces, leaving the columns and beams undamaged, thus allowing the structure to survive strong earthquakes without losing its gravity-load resistance.

Early thinking on the design and detailing of such braces, as implemented in seismic regulations and guidelines at the time, was that bracing members with low member slenderness, KL/r (Section 9.2.2), and width-to-thickness ratio, b/t (Section 9.2.3), have superior seismic performance, on the premise that compressed braces with low KL/r can provide more significant energy dissipation. As described in more details in Section 9.2, upon buckling, flexure develops in the compression member and a plastic hinge eventually develops at the middle length of the brace, that is, at the point of maximum moment. It is through the development of this plastic hinging that a member in compression can dissipate energy during earthquakes. Low b/t limits are prescribed to prevent brittle failure due to local buckling during this plastic hinging, because the reversed cyclic loading induced by earthquakes leads to repeated buckling and straightening of the material at the local buckling location, which, combined with high strains at the tip of the local buckle, precipitate low-cycle fatigue.

The more recent thinking on these matters recognizes the importance of delaying low-cycle fatigue at the plastic hinge location, and allows the use of more slender braces that correspondingly have lower ductility demands in compression, relying proportionally more on tension yielding of the braces to dissipate seismic energy. The drawback of this approach is a greater difference between the strength of the braces in compression and tension, and thus greater demands that this imbalance can impose on the elements of the CBFs that must be protected (i.e., remain elastic) through application of capacity design principles.

Various editions of the design specifications have reflected this change in philosophy, along with other tweaks intended to make the design intent transparent. However, the most ductile CBFs have consistently been assigned structural response modification factor, R, on the order of 75% of the maximum value assigned to special moment-resisting frames (see Chapter 7). This penalty is attributed mainly as a consequence of the less ideal energy dissipation provided by the compression brace, the observed pinching of the hysteretic curves of the braced frame due to the strength degradation of the compression brace, and the absence of effective strength hardening as typically occurs in moment frames.

Note that two types of CBF systems are permitted by AISC 341, namely, *Special Concentrically Braced Frames (SCBFs)* and the *Ordinary Concentrically Braced Frames (OCBFs)*. Emphasis here is on SCBFs, which are designed for stable inelastic performance and energy dissipation capability, and correspondingly for the largest force reduction factor, R. Some of the ductile detailing requirements are relaxed for the OCBF in the perspective that these would be subjected to less inelastic demand, being designed to a smaller reduction factor. However, if demands from an earthquake were to exceed the design level, structures with SCBFs could be advantaged over OCBFs, in spite of the higher design force level considered in the latter case.

Typical CBF configurations are presented in Figure 9.3. These were originally developed to resist wind loads in the linearly elastic range, but are not necessarily adequate for seismic design. Some

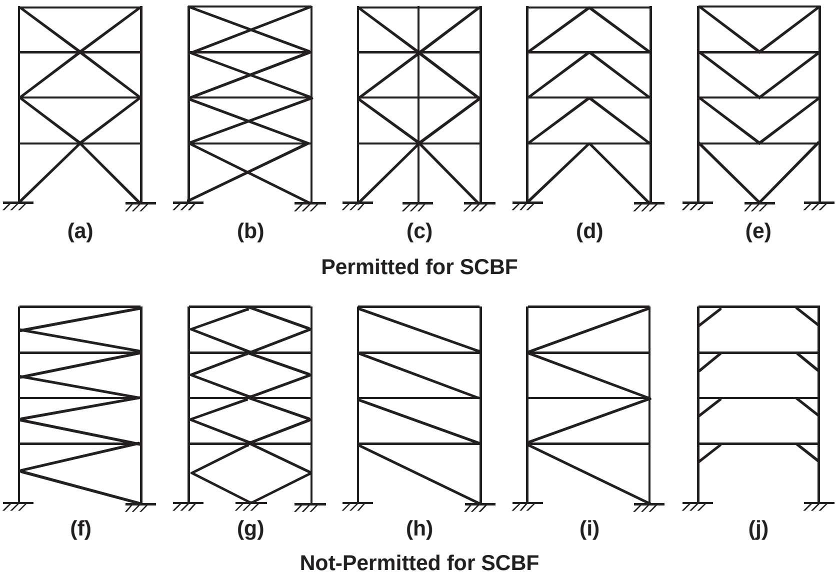

Figure 9.3 CBF configurations permitted and prohibited in seismic regions: (a to c) X-braced frames; (d to e) inverted V-braced and V-braced frames, also known as inverted chevron-braced and chevron-braced frames, respectively; (f to g) K-braced and double K-braced frames; (h to i) single diagonal braced frames; (j) knee-braced frame.

configurations are prohibited in seismic regions because they exhibit poor cyclic inelastic response or induce undesirable demands in other structural elements. For example, the K-braced frame configuration shown in Figure 9.3f is problematic. If one of the diagonal braces were to buckle, increasing force in the tension brace would be transferred as shear in the adjacent column. The resultant horizontal force from these two unequal brace forces, applied at midheight of the column, could produce a plastic hinge in the column at the brace-to-column intersection point and result in undesirable column failure. Note that the single brace configurations of Figures 9.3h and 9.3i, although prohibited, would be permitted if used together with their respective mirror image along the same line of bracing (Figure 9.3c can be seen as one such example for single-braced frames of the type shown in Figure 9.3i).

The severely pinched hysteresis curves exhibited by *tension-only* braced frames have been presented in Chapter 6. Such frames have been commonly used to resist wind forces in nonseismic regions, typically with X-braced configuration (Figure 9.3b) having angles, rods, or flat bar braces of high slenderness (often $KL/r > 300$). The cyclic inelastic behavior of a tension-only braced frame is characterized by yielding and elongation of the tension braces, and buckling of the compression braces at near-zero levels of axial load due to their high slenderness. Upon repeated cyclic loading, each brace accumulates residual axial displacements, and the X-braced frame loses its lateral stiffness in the vicinity of zero frame displacement, defeating to some degree the intent of adding the braces to the frame. AISC 341-10 does not permit the use of tension-only braces in SCBFs, but allows it for OCBFs. CSA S16-09 allows their use for low-rise buildings up to a height of 20 m (with a progressively reducing *R* factor between 16 m and 20 m in height), provided all columns in the building are continuous and of constant cross-section over the entire building height. Tremblay and Filiatrault (1996) demonstrated that, contrary to earlier expectations, impact forces on the braces and their connections due to the sudden straightening of previously taut slender tension-only braces are limited by the yield strength of the braces; they observed an increase in yield strength of up to 15% due to strain rate effects (Chapter 2), as commonly observed in other CBF studies with conventional braces. Strain-rate effects are generally not considered by seismic design codes and specifications at this time.

9.2 Hysteretic Behavior of Single Braces

9.2.1 Brace Physical Inelastic Cyclic Behavior

An understanding of the physical inelastic behavior of an individual brace member subjected to reversed cycles of axial loading is necessary to design ductile braced frames using the concepts presented in this chapter.

The behavior of axially loaded members is commonly expressed in terms of the axial load, P, axial deformation, δ, and transverse displacement at midlength, Δ. According to convention, tension forces and deformations are taken as positive, and compression forces and deformations as negative. A simplified hysteretic curve for a generic brace member is presented in Figure 9.4.

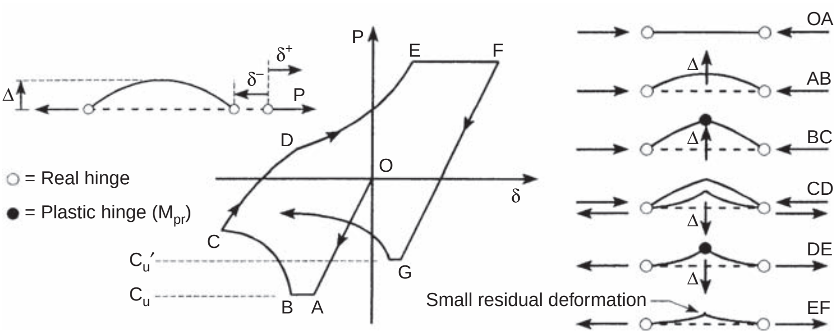

FIGURE 9.4 Sample hysteresis of a brace under cyclic axial loading.

Starting from the unloaded condition (point O in Figure 9.4), the brace is compressed in the linearly elastic range. Buckling occurs at point A, when $P = C_u$. Slender braces that buckle elastically at point A can sustain their applied axial load as the brace deflects laterally, with a corresponding axial shortening (shown as the plateau AB in Figure 9.4). At that point, if brace behavior remained elastic, unloading would occur along the line BAO if the axial compressive load was removed.

During buckling, due to its transverse deflections, the brace is subjected to flexural moments. Considering equilibrium in the deformed configuration, using a free-body diagram of a segment of the brace from its end to a distance x from it, the flexural moment at any point x is calculated as the product of the axial force and the lateral displacement at that point. As such, the shape of the moment diagram is proportional to the deflected shape, with the maximum moment occurring at the point of maximum transverse displacement (i.e., at midspan for the pin-pin brace shown in Figure 9.4). Assuming bilinear elasto-plastic flexural behavior, as transverse displacement of the brace further increases under the constant axial force, the plastic moment of the brace is eventually reached and a plastic hinge forms (point B in Figure 9.4). The value of the transverse displacement, Δ, when this happens can be obtained accounting for flexure-axial load interaction in the brace (Chapter 3)—recognizing, however, that for actual material behavior and residual stresses, the development of plastic hinging would be gradual.

Further increases in axial displacements produce corresponding increases in Δ and in plastic hinge rotations (segment BC), resulting in a deflected shape having a plastic kink, as schematically shown in Figure 9.4. The axial resistance of the brace drops along segment BC: because the moment at midlength ($M = P\Delta$) cannot increase beyond the plastic moment, an increase in Δ must be accompanied by a decrease in P. However, the path from point B to point C is nonlinear due to flexure-axial load interaction at the plastic hinge, recognizing that a decrease in axial load produces an increase in moment capacity.

Upon unloading (from point C in Figure 9.4) to $P = 0$, the brace retains a residual axial deflection, δ, and a residual transverse deflection, Δ, including a kink in the brace due to residual plastic rotations.

When the brace is loaded in tension from $P = 0$ to point D, the behavior is elastic. At point D, the product of the axial load and the transverse displacement equals the plastic moment of the brace (similar to the equilibrium described at point B earlier), and a plastic hinge forms at midlength of the brace. However, along segment DE, the plastic hinge rotations act in the reverse direction of that along segment BC and effectively reduce the magnitude of the transverse deflection, Δ. As a result, axial forces larger than that at point D can be applied.

It is not possible to completely remove the transverse displacement and return the brace to a perfectly straight condition. The theoretical axial force required to produce additional plastic hinge rotations tends to infinity as the transverse displacement approaches zero, but the axial force in the brace cannot exceed its tensile yielding resistance (= AF_y), and residual transverse deflections cannot be avoided. Tension yielding is shown as segment EF in Figure 9.4.

Upon reloading in compression, the brace therefore behaves as a member having an initial deformation, and its buckling capacity upon reloading (C_u' at point G) is typically lower than its buckling capacity upon first loading (C_u at point A). The ratio C_u'/C_u depends primarily on the slenderness ratio (KL/r), and expressions used in the past to capture this relationship are presented in Section 9.2.3. The length of the elastic buckling plateau (segment AB) also reduces upon each subsequent inelastic cycle as a result of the residual initial deflection. Beyond these two differences, the shape of the hysteresis curves (OABCDEF) in subsequent inelastic cycles remains basically unchanged. Analytical models to capture all phases of this hysteretic behavior are briefly discussed in a later section.

Quantitative assessments of the hysteretic behavior and energy dissipation capacity of braces have typically been obtained from tests of members subjected to repeated cyclic inelastic axial displacements. Results have included either complete hysteresis curves for a given experiment's loading history or simply the envelope of all hysteresis curves (Black et al. 1980). Both approaches are used in the following sections. Slenderness ratio has a dominant impact on the shape of the hysteresis curves. For a slender brace (large KL/r), segment OA will be rather small, whereas the plateau segment AB could be rather long, resulting in relatively small hysteretic energy dissipation capacity in compression. For stocky braces (small KL/r), the reverse is true, and segment AB may not exist. The effect of slenderness is further investigated in the next section.

9.2.2 Brace Slenderness

The cyclic behavior of a brace largely depends on its slenderness, KL/r, where K is an effective length factor, L is the brace clear span, and r is the radius of gyration of the member about the buckling axis under consideration. The radius of gyration, r_i, about axis i, is equal to $\sqrt{I_i/A}$, where I_i is the second moment of area of the component about axis i, and A is the cross-sectional area of the member. Note that some design standards or research documents alternatively refer to the non-dimensional slenderness ratio, λ, defined as $(KL/r)(\sqrt{F_y/\pi^2 E})$.

Data for A, I_i, and r_i for standard structural shapes is typically tabulated in design manuals and handbooks (AISC 2011 and CISC 2010). The largest slenderness ratio obtained, considering the possible buckling axes for a given member, governs behavior and is used for design.

Representative hysteresis curves for braces having slenderness ratios of 120, 80, and 40 are shown in Figure 9.5 in terms of axial force, P, and axial deformations, δ, along with their corresponding brace lateral displacements, Δ. In all cases, large residual lateral deformations remains upon unloading (i.e., when $P = 0$) as a consequence of inelastic buckling. Increasing magnitude of the lateral deformations is a consequence of brace "growth" due to incremental plastic elongations in subsequent cycles of tension yielding, and the relative lesser plastic axial shortening of the brace before its buckling in compression; the progressively longer brace must therefore displace laterally more to fit in its same original clear span. Note that, as this residual lateral displacement increases in subsequent cycles, the buckling capacity of the brace reduces, equivalently to that of a brace having an initial curvature or camber. The Bauschinger effect (Chapter 2) also contributes to this reduction in compressive strength in subsequent cycles.

It is also observed in Figure 9.5 that increases in slenderness correspond to reductions in hysteretic energy dissipated by the brace in compression (i.e., area under the hysteresis curves), together with reductions of the compression strength (as a percentage of the corresponding tensile strength). Similar observations are possible from Figure 9.6a, using envelopes of the hysteresis curves for different braces having slenderness ratios of 40, 80, and 120, in terms of normalized axial load versus normalized axial displacement. An example of how such an envelope is obtained is shown in Figure 9.6b.

The hysteresis curves for more compact members would approach that of the material itself, whereas those for more slender ones would approach the tension-only behavior described in Chapter 6.

Figure 9.5 also illustrates the variation of axial stiffness at various displacements, and the consequent corresponding loss of tangent stiffness of a braced frame as it is unloaded (to zero axial load) or returns to its original plumb position. For example, data in Figure 9.5a shows the axial tangent stiffness of the brace at zero axial load to be approximately 1700 kips/in (29.4 kN/mm) in the first loading cycle and approximately 20 kips/in (0.35 kN/mm) in the loading cycle to $\delta = 35$ mm (1.38 in). If two such braces formed an inverted-V CBF configuration, the lateral stiffness of the braced frame near the point of zero lateral displacement would be less than 5% of the elastic stiffness of the frame. Large drifts are required to re-engage the brace in tension to its full stiffness.

The normalized lateral deflected shape of two braces having different end-conditions and slenderness ratios are shown in Figure 9.7. For the pin–pin brace shown in Figure 9.7a, the somewhat parabolic elastic deflected shape becomes progressively more linear in segments between the midspan plastic hinge and actual hinges as inelastic behavior further develops (the non-normalized magnitude of the

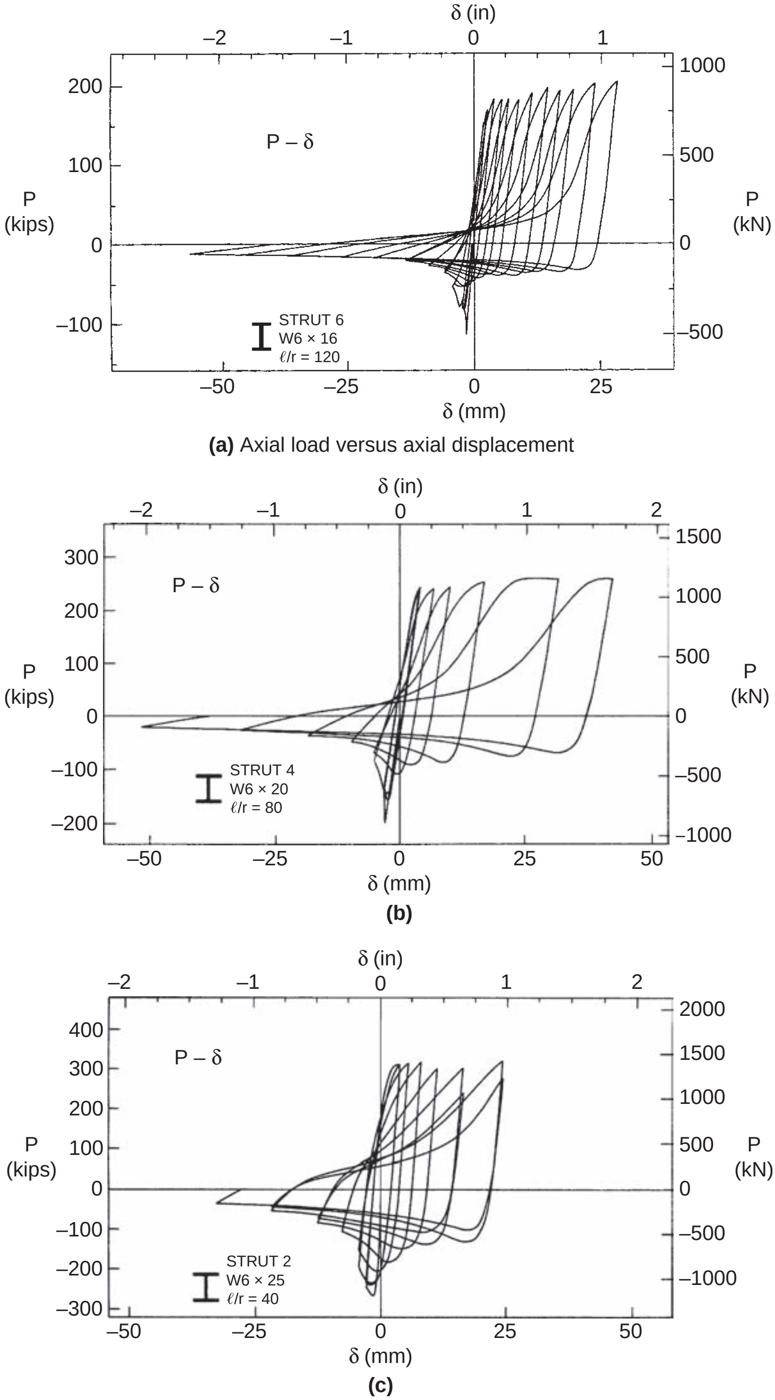

Figure 9.5 Cyclic behavior of braces having slenderness ratios of 120, 80, and 40: (a, b, c) axial force versus axial displacement hysteresis curves; (d, e, f) axial force versus brace lateral displacement. (*Black et al. 1980, with permission from EERC, University of California, Berkeley.*)

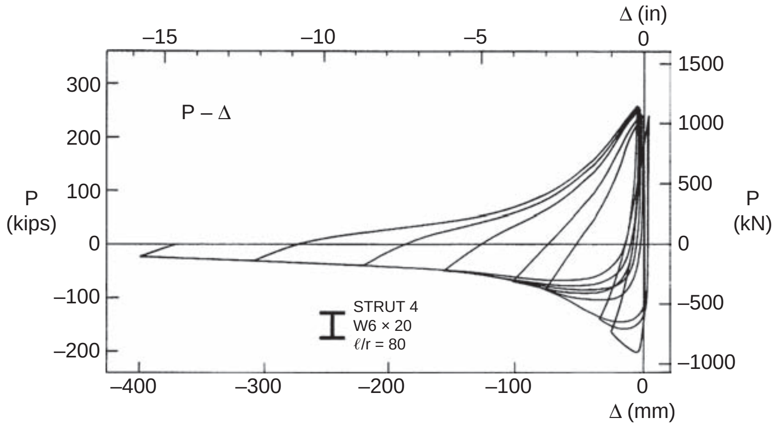

(d)

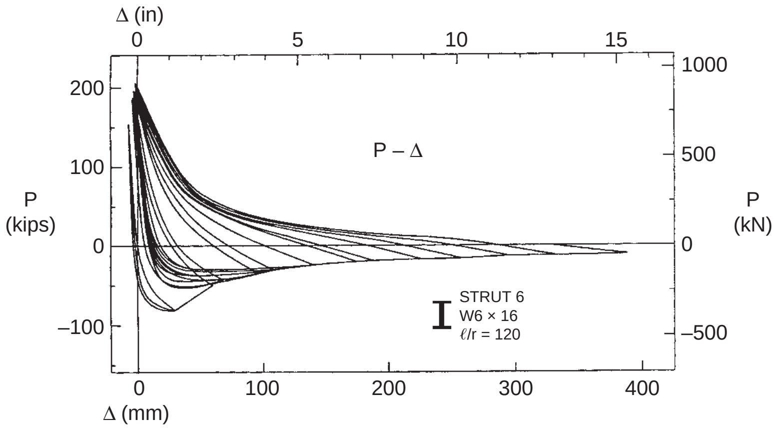

(e)

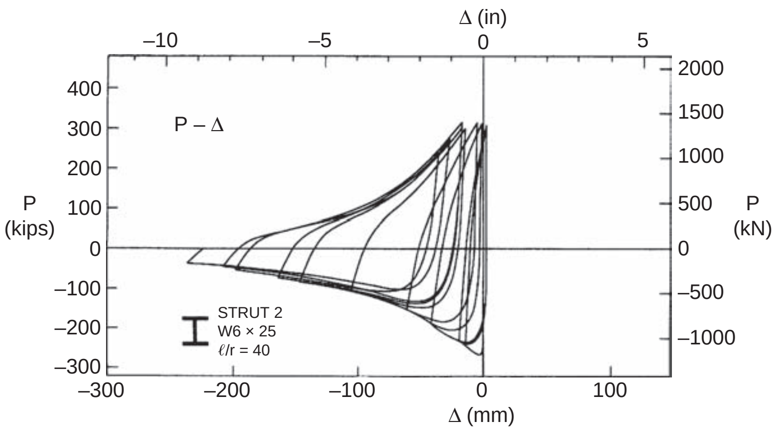

(f)

Figure 9.5 (*Continued*)

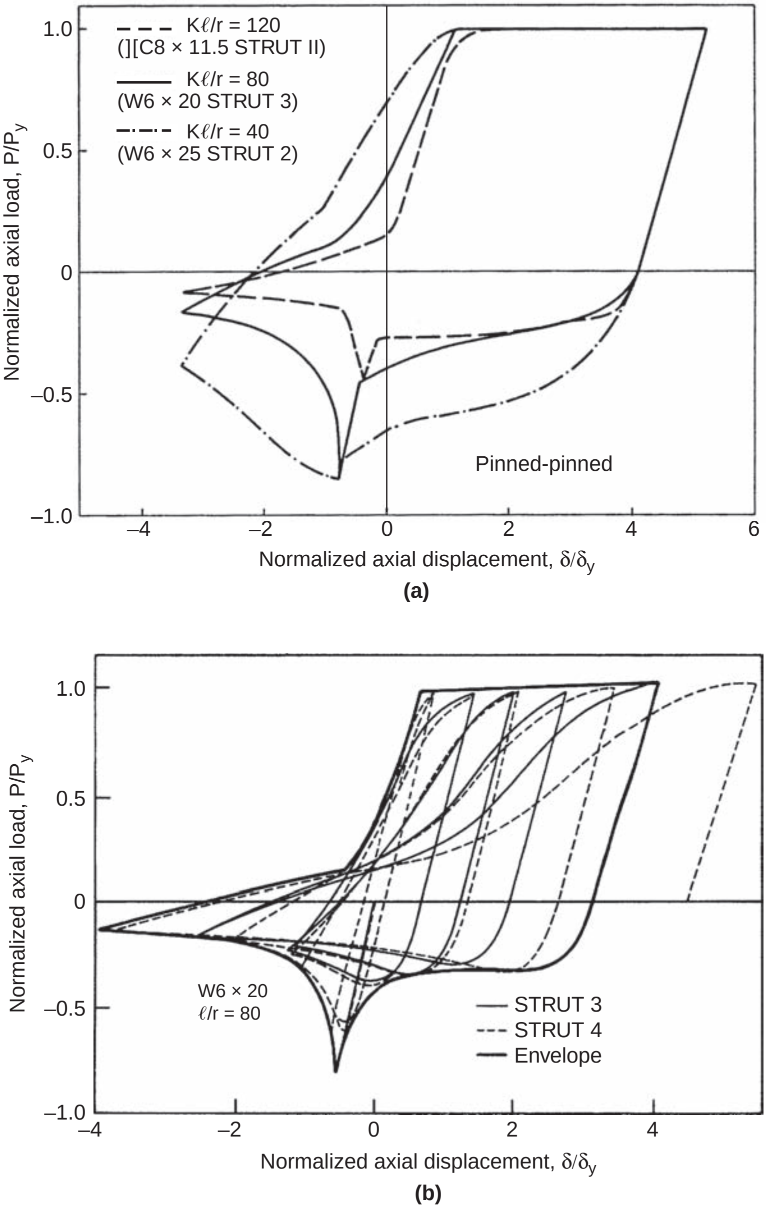

FIGURE 9.6 Normalized envelopes for braces: (a) comparison of normalized axial force versus normalized axial displacement; (b) graphical definition of envelope. (*Black et al. 1980, with permission from EERC, University of California, Berkeley.*)

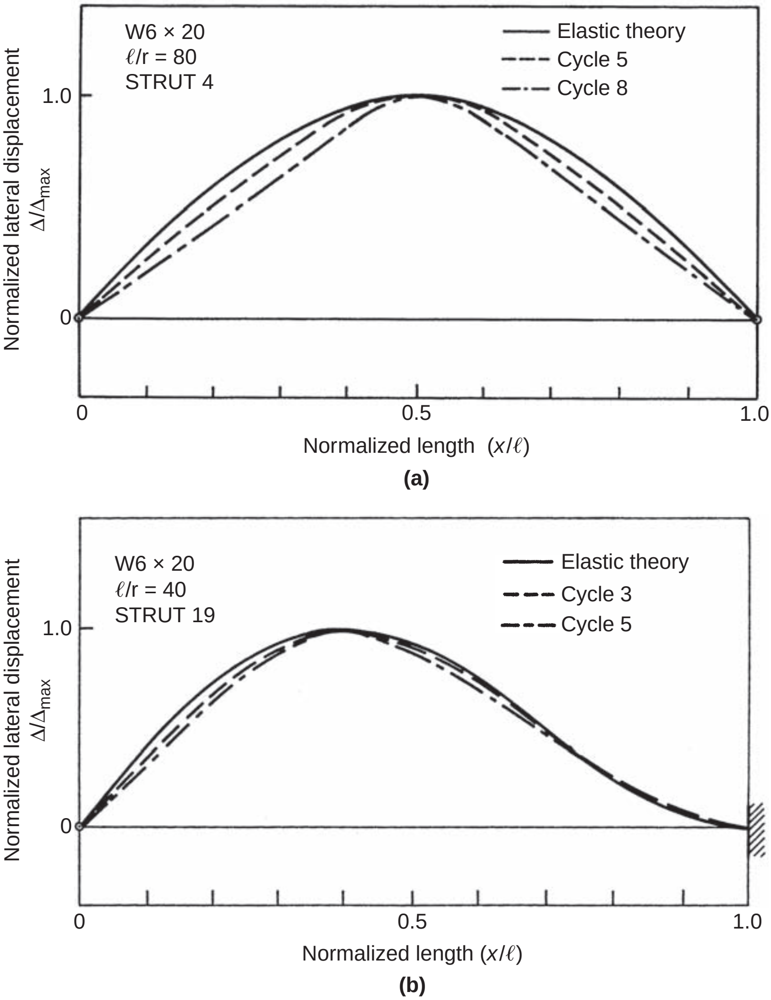

Figure 9.7 Elastic and inelastic buckled shapes for I-shaped beams: (b) pinned-fixed end conditions. (*Black et al. 1980, with permission from EERC, University of California, Berkeley.*)

lateral displacements would correspondingly increase as this happens). Likewise, for the brace pinned at one end and fixed at the other shown in Figure 9.7b, straight segments connect the plastic and actual hinges at large inelastic excursions. Nonetheless, the deflected shapes are quite similar, and use of the effective length, *KL*, based on elastic analysis, is appropriate to calculate the strength and characterize behavior of braces undergoing cyclic inelastic buckling. This conclusion is further supported by comparison of the envelopes of hysteresis curves of braces having various end-conditions, shown in Figure 9.8.

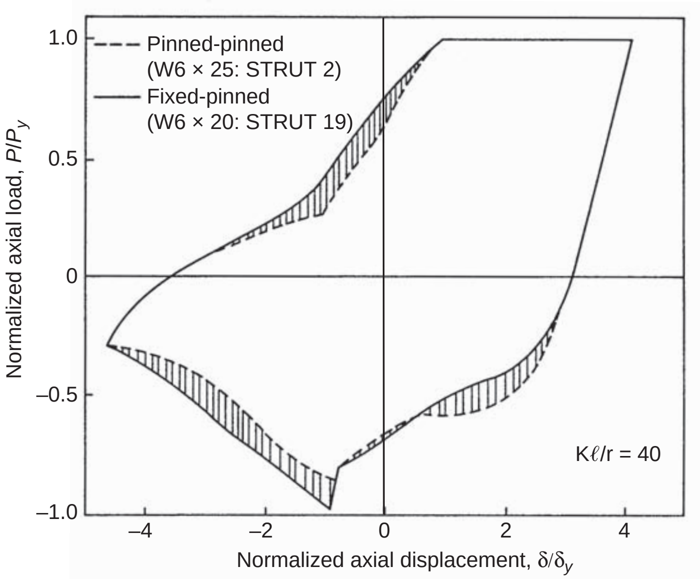

(a) I-shaped brace response

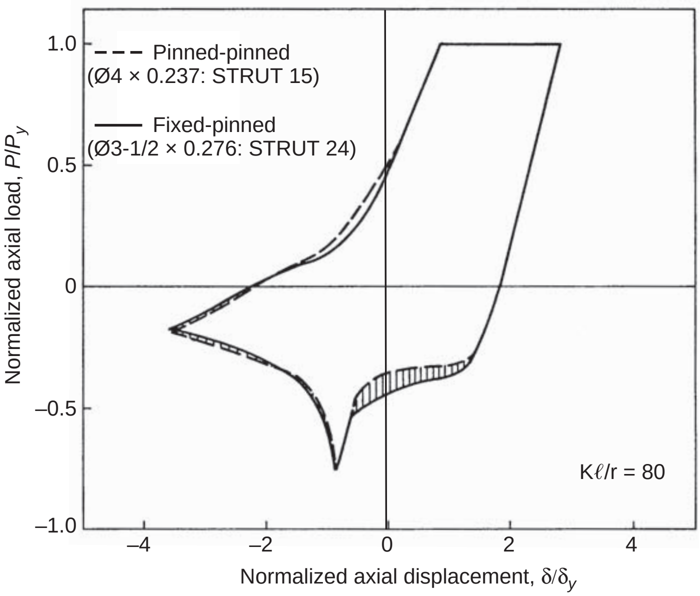

(b) Circular tube brace response

Figure 9.8 Hysteretic curves for braces with different end conditions. (*Black et al. 1980, with permission from EERC, University of California, Berkeley.*)

Marginal differences in hysteretic energy dissipation can be seen between braces having pinned–pinned and fixed-pinned end conditions, for either I-shaped (Figure 9.8a), circular tube braces (Figure 9.8b), or double-angle braces (Black et al. 1980, Popov and Black 1981).

Incidentally, cross-sectional shape also has a marginal impact on the envelope of hysteretic response for braces having the same slenderness ratio, as shown in Figure 9.9 (Black et al. 1980), although different shapes can have substantially different behavior in terms of local buckling and low-cycle fatigue life, as described later.

On the strength of the above observations, early seismic design requirements for ductile CBFs were formulated promoting the use of stockier braces that could contribute to the total hysteretic energy dissipation. Representatively, the 1992 edition of the AISC seismic provisions only permitted the use of braces having slenderness ratio less or equal to $720/\sqrt{F_y}$ (= $1900/\sqrt{F_y}$ in S.I. units), which corresponded to KL/r values of 102 and 120 for F_y of 50 ksi and 36 ksi, respectively. The 1995 edition increased this limit to $1000/\sqrt{F_y}$, corresponding to 141 and 167 for the same two steel grades respectively. The 2010 edition allows the use of KL/r values of up to 200 when capacity design principles are considered in the design of the columns. The rationale for these changes is presented later.

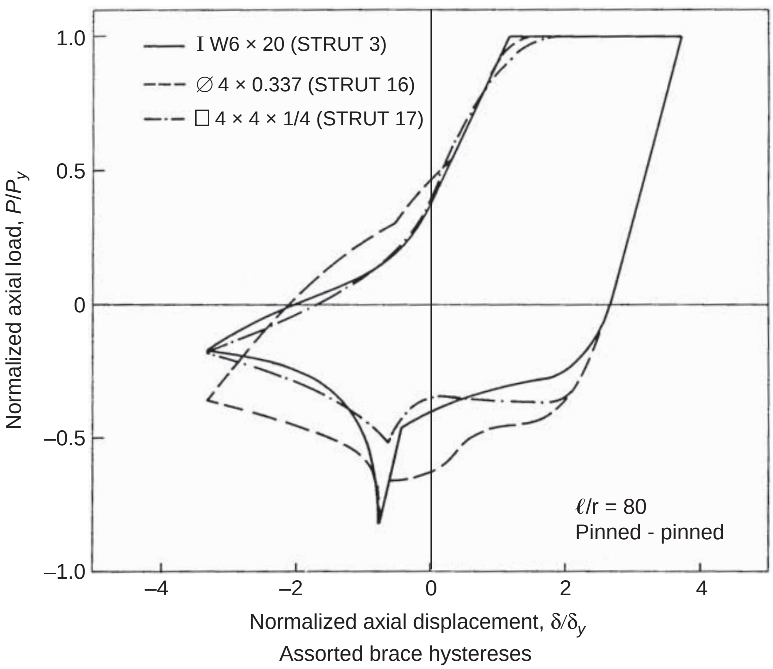

Figure 9.9 Hysteretic curves for braces with different cross-sectional shapes. (*Black et al. 1980, with permission from EERC, University of California, Berkeley.*)

Note that because minimum weight considerations often drive the design of braces, actual ductile CBFs typically have braces with slendernesses close to the specified upper limit.

9.2.3 Compression Strength Degradation of Brace Under Repeated Loading

Knowledge of the actual force resisted by a brace throughout its cyclic response is important, as variations in this value affect how forces flow throughout the structural system, and consequently how connections and other structural members must be designed to resist these demands (as is further described in later sections).

Figures 9.5 and 9.6 above also show the progressive reduction in buckling strength in subsequent inelastic loading cycles (i.e., point G in Figure 9.2). Early seismic design requirements specified that a reduced compressive strength, C_r', be considered in design instead of the value otherwise used in nonseismic applications, C_r. The ratio C_r'/C_r was understood to depend primarily on the slenderness ratio, KL/r; sample expressions that were used then to capture this relationship include:

SEAOC 1990

$$C_r' = \frac{C_r}{1+0.50\left(\dfrac{KL}{r\pi}\sqrt{\dfrac{0.5F_y}{E}}\right)} \tag{9.1a}$$

CSA 1994

$$C_r' = \frac{C_r}{1+0.35\left(\dfrac{KL}{r\pi}\sqrt{\dfrac{F_y}{E}}\right)} \tag{9.1b}$$

Using these equations, for a slenderness ratio equal to 0, $C_r' = C_r$, whereas for a Grade A36 steel brace with a slenderness ratio of 130, $C_r' = 0.67C_r$. For simplicity, the design strength of a brace per the AISC LRFD Specification (AISC 1992) was calculated as $0.8\phi_c P_n$ where ϕ_c was the resistance factor for compression components, and P_n the nominal axial strength of the brace (i.e., $C_r = \phi_c P_n$). Interestingly, $C_r' = 0.8C_r$ would be obtained from Equation 9.1a with a slenderness ratio of approximately 65, which was equivalent to the average C_r' obtained over the range of permissible KL/r values at the time. Designing braces assuming their strength to be C_r' was equivalent to neglecting the first cycle strength C_r and assuming that brace compression strength did not further degrade after the second cycle (which is incorrect). Note that both C_r' or C_r were to be considered in capacity design calculations, depending on which case would deliver the maximum load to other components or systems (as shown in later sections). Later editions of the AISC Seismic Provisions dropped the 0.8 factor, recognizing that other factors had a greater impact on achieving satisfactory CBF cyclic response.

One such factor is degradation of brace strength after repeated cycles of inelastic deformations. For capacity design purposes, the capacity of the brace in compression when the entire frame reaches its maximum sway deformation, which is defined as C_r'' here, can be substantially lower than C_r' and thus more relevant to consider in design. Indeed, as plastic hinging develops in the middle of the brace, C_r'' drops as deformation increases. This means that at maximum sway, when the tension brace has yielded, only a small fraction of the original compression buckling strength of the other brace is effective.

Lee and Bruneau (2002, 2005) quantified the strength degradation of braces upon repeated cycling by extracting compression excursion from the complete hysteretic force-displacement curve obtained from 66 tests by various researchers, and overlaying them to start from the same zero displacement, as shown in Figure 9.10 (ϕ taken as 1.0 for this purpose) in terms of δ/δ_B, where δ_B is the axial displacement at first buckling. For a typical curve, schematically idealized in that figure, the magnitude of axial deformations typically increased in subsequent cycles as a consequence of the testing protocols adopted (note that only cycles that produced displacements exceeding the

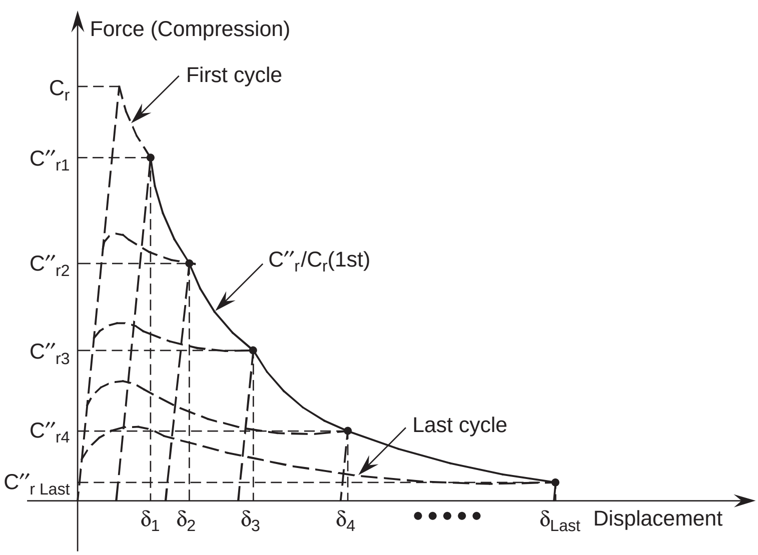

FIGURE 9.10 Definition of normalized buckling capacity, C_r''/C_r(1*st*). (*Lee and Bruneau 2002, courtesy of MCEER, University at Buffalo.*)

previously obtained values were considered). In the "*nth*" cycle, beyond first buckling (defined experimentally as C_r), compressive strength of the brace at the point of maximum displacement for that compressive excursion, δ_n, was labeled C''_{rn}, the numeral subscript indicating the cycle number. These value of C_r'' were then divided by C_r for normalization. This normalized strength is labeled $C''_r/C_r(1st)$, the qualifier "1st" implying "the strength obtained the first time this displacement is reached." Figure 9.11 shows a typical curve obtained following this procedure. That curve can be considered a normalized force-displacement envelope of the brace in compression.

Furthermore, the brace compressive strength recorded during the last cycle of testing was also of interest. It was calculated at each of the previously considered displacement points, δ_n, as shown in Figure 9.12, giving results as typically shown in Figure 9.13. This normalized strength was labeled $C_r''/C_r(last)$, the qualifier "last" implying "the strength obtained during the last cycle of testing."

Using the same displacement points to calculate both $C''_r/C_r(1st)$ and $C''_r/C_r(last)$ makes it possible to calculate the ratio of these values. A large ratio indicates a considerable drop in strength at a specific displacement, δ/δ_B, whereas a lower ratio expresses rather stable strength degradation from the first to last cycle. A typical result is shown in Figure 9.14. Lee and Bruneau (2002) present results for all braces considered, together with similar data on the normalized hysteretic energy dissipation of compression braces.

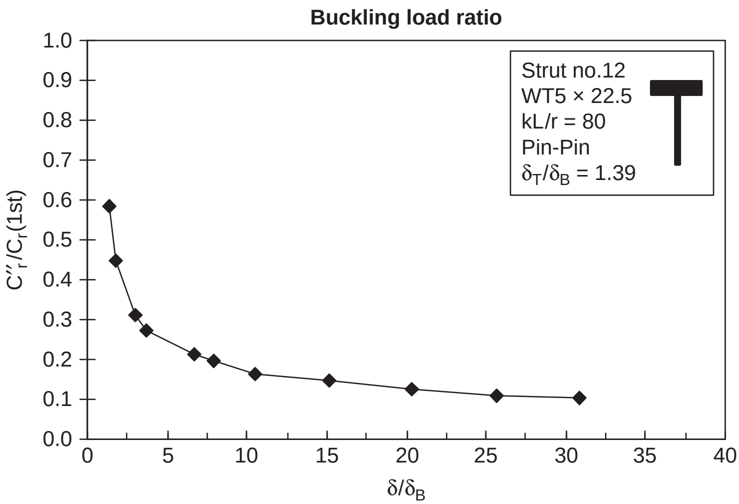

Figure 9.11 Example of normalized maximum compression strength reached upon repeated cyclic inelastic displacements, $C_r''/C_r(1st)$. (*Lee and Bruneau 2002, courtesy of MCEER, University at Buffalo.*)

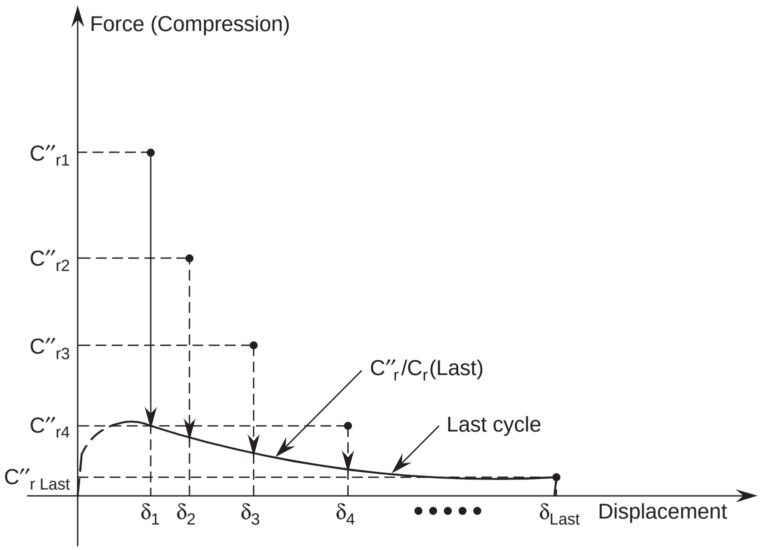

Figure 9.12 Definition of normalized buckling capacity, C_r''/C_r(*last*). (*Lee and Bruneau 2002, courtesy of MCEER, University at Buffalo.*)

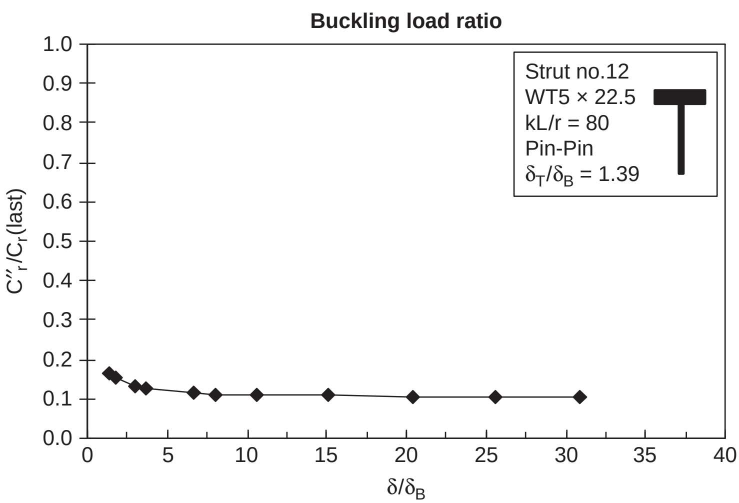

Figure 9.13 Example of normalized maximum compression strength reached upon repeated cycling data, C_r''/C_r(*last*). (*Lee and Bruneau 2002, courtesy of MCEER, University at Buffalo.*)

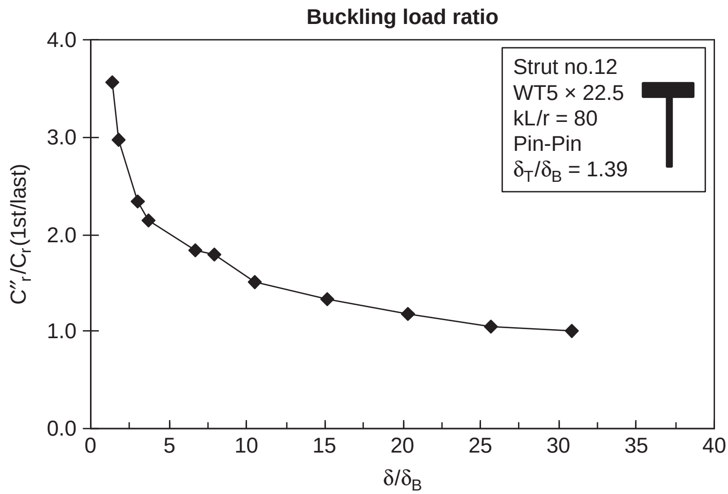

FIGURE 9.14 Example of normalized maximum compression strength reached upon repeated cyclic inelastic displacements, $C_r''/C_r(1st/last)$. (*Lee and Bruneau 2002, courtesy of MCEER, University at Buffalo.*)

Results obtained indicated that reduction in the normalized C_r''/C_r (1*st*) envelope is particularly severe for the W-shaped braces having KL/r above 80, dropping to approximately 0.2 when the normalized displacements exceed 5. Behavior is not significantly worse for KL/r in the 120 to 160 range. Tubes perform relatively better, over all slenderness range, with double-angle braces in-between these two cases. Results for C_r''/C_r(*last*) and C_r''/C_r(1*st/last*) showed that the compression capacity at low δ/δ_B values drops rapidly upon repeated cycling, and that C_r''/C_r(1*st*) is effectively equal to C_r''/C_r(*last*) at normalized displacements above 3 in most instances.

These results indicated that when a braced bent having braces with *KL/r* greater than 80 reaches its expected displacement ductility of 3 to 4, the compression strength of a brace has already dropped to approximately 20% of its original buckling strength (40% for square HSS). Similar results were obtained for normalized energy dissipation capacity in compression. Given that most braces in actual design have slenderness above 80, this confirmed that limits on *KL/r* specified by the various seismic design specifications are not correlated to brace effectiveness in compression—they can, however, relate to other factors, as shown in the next sections.

A similar study conducted in parallel by Tremblay (2002), considering 76 tests from 9 experimental programs, compared various approaches to quantify postbuckling brace compression strength (expressed as C_u' in that case, but equivalent to C_r'' with $\phi = 1$ considered above). Recognizing that the postbuckling strength depends on

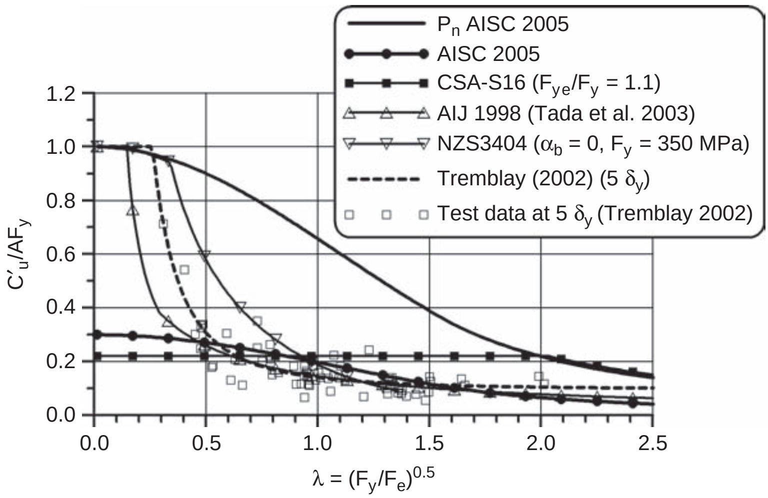

Figure 9.15 Postbuckling compression strength. (*Courtesy of Robert Tremblay, Département des génies civil, géologique et des mines, EcolePolytechnique, Montréal.*)

the magnitude of inelastic deformations, Figure 9.15 presents resulting strength degradations as a function of the normalized slenderness ratio for the case of braces axially deformed up to five times their tension yield displacement. Note that the actual effective braced length for each of the experiments considered was used in this study. The equations for minimum postbuckling strength provided by various design codes and standards are plotted in this figure for comparison against the test data and average compression strength obtained from regression analysis of the data. Results in Figure 9.15 show that the value of $0.3\phi_c Pn$ introduced for V and inverted V braces in the 1995 AISC Seismic Provisions (based on the work of Hassan and Goel, 1991) matches well the data over λ ranging from 0.5 to 1.5 (i.e., KL/r of 38 to 113 for $F_y = 50$ ksi), but becomes quite conservative for stockier braces. Results also show that using a constant value independent of slenderness provides a poor match (such as for the case of the value $0.2A_gR_yF_y$ introduced in CSA S16.1-01, and retained in CSA S16-09).

Note that both C_r'' or C_r are to be considered in capacity design calculations, depending on which case would deliver the maximum load to other components or systems (as shown in later sections), although this has not always been stated explicitly in design codes or standards.

9.2.4 Brace Compression Overstrength at First Buckling

Tremblay (2002) also quantified the brace initial compression strength compared with AISC and CSA design equations (Figure 9.16—the Class 1 designation refers to compact sections per CSA S16). This

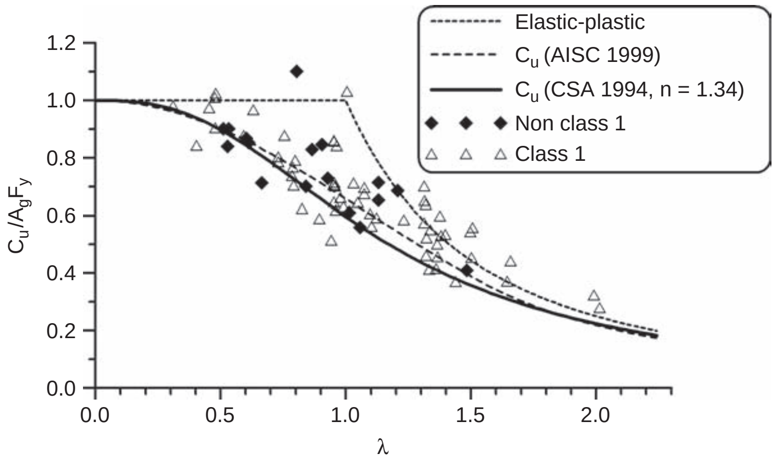

FIGURE 9.16 Experimentally obtained compression strengths at first buckling. (*Courtesy of Robert Tremblay, Département des génies civil, géologique et des mines, EcolePolytechnique, Montréal.*)

value is important to estimate the maximum forces applied by braces in compression to their connections and other structural elements.

Expected compression strength was found to be typically greater than the calculated nominal strength, particularly for more slender braces, likely as a consequence of conservative assumptions built in the design equations with respect to initial imperfections and residual stress conditions. Tremblay found the average overstrength over all slenderness ranges to be 1.09 and 1.16 compared with the AISC 341 and CSA S16 design equations, respectively, with coefficients of variation of 0.16 and 0.17.

Subsequently, the AISC 341-05 required that connections be designed for $1.1R_yP_n$, with P_n being the nominal compression strength per AISC 360, whereas AISC 341-10 further defined P_n for this particular application to be 1.1 times the lesser of $R_yF_yA_g$ and 1.14 $F_{cre}A_g$, where F_{cre} is F_{cr}, determined per AISC 360 Chapter E, substituting the expected yield stress R_yF_y in lieu of F_y in these equation. Note that 1.14 is equal to 1/0.877. Recall that the compressive flexural-buckling strength of compact members per AISC 360 is given by:

$$F_{cr} = \left[0.658^{\frac{F_y}{F_e}}\right]F_y \quad \text{when} \quad \frac{KL}{r} \leq 4.71\sqrt{\frac{E}{F_y}} \quad (\text{equivalent to } F_e \geq 0.44F_y) \tag{9.2a}$$

and

$$F_{cr} = 0.877F_e \quad \text{when} \quad \frac{KL}{r} \geq 4.71\sqrt{\frac{E}{F_y}} \tag{9.2b}$$

where

$$F_e = \frac{\pi^2 E}{\left(\dfrac{KL}{r}\right)^2} \tag{9.2c}$$

The equivalent CSA S16 clause uses $1.2R_yC_u$.

Note that these overstrength values were determined considering the actual KL/r values corresponding to the experiments reviewed. Designer are cautioned that, for the same reasons, although considering higher values of KL/r may be conservative for brace design, it would be inappropriate for assessing the demands imposed by the brace on its connections and other frame elements.

9.2.5 Evolution of Codified Strength and Slenderness Limits

Table 9.1 summarizes how the AISC Seismic Provisions, from their 1992 edition through 2010, have accounted for some of the parameters described above. This timeline perspective of codified requirements can be useful when reviewing the seismic design of existing buildings, or when studying design aids and tutorials developed referencing earlier editions of the provisions, as the frequent changes that occurred over those two decades can be perplexing.

9.2.6 Local Buckling

Local buckling is another factor that has a major impact on the behavior of braces. First, local buckling leads to rapid degradation of compressive and flexural strength of the brace. Second, and more importantly, the large local strains that develop at the buckled plate surfaces are susceptible to low-cycle fatigue upon repeated cycles of inelastic deformations, and thus cracking leading to fracture. Because braces in a concentrically braced frame provide a structure's lateral stiffness and strength and are the elements that dissipate the seismic energy, their fracture risks leading to frame collapse.

In stocky braces, it is desirable to delay local buckling as much as possible during compression yielding (beyond preventing its development before axial yielding). Instances of axial local buckling, rapidly followed by fracture of the brace, are shown in Figure 9.17 for built-up braces (Lee and Bruneau 2004). Note that, in some stocky braces, local buckling produces lateral displacements that can trigger global brace buckling. Instances of stocky braces are less common in practice, because design for minimum weight typically leads to smaller braces of slenderness close to the permitted upper limits.

In braces that buckle inelastically, compression energy dissipation develops through plastic flexural hinging at midspan of the brace. The large plastic curvatures that typically develop at that location can potentially lead to local buckling. Upon repeated cyclic loading, the local buckling and straightening of the material at that location induces cracks that may propagate and lead to fracture.

Categories	1992 Edition	1997 Edition		2002 Provisions[b]		2005 Provisions		2010 Provisions	
		OCBF	SCBF	OCBF[c]	SCBF	OCBF	SCBF	OCBF	SCBF
R	5	5	6	5	6	3.25	6	3.25	6
C_r	$0.8\phi_c P_n$	$0.8\phi_c P_n$	$\phi_c P_n$	—	$\phi_c P_n$	$0.8\phi_c P_n$	$\phi_c P_n$	$\phi_c P_n$	$\phi_c P_n$
$(KL/r)_{max.}$	$\frac{720}{\sqrt{F_y}}$	$\frac{720}{\sqrt{F_y}}$	$\frac{1000}{\sqrt{F_y}}$	—	$\frac{1000}{\sqrt{F_y}}$	$\frac{720}{\sqrt{F_y}}$	$\frac{680}{\sqrt{F_y}}$ or 200^e	$\frac{680}{\sqrt{F_y}}$ [f]	200
Tension on Connection	$A_g F_y$	$R_y A_g F_y$	$R_y A_g F_y$	—	$R_y A_g F_y$	$R_y A_g F_y$	$R_y A_g F_y$	Note[g]	$R_y A_g F_y$
Moment on Connection[d]	M_n	$1.1 R_y M_p$	$1.1 R_y M_p$	—	$1.1 R_y M_p$	—	$1.1 R_y M_p$	Note[g]	$1.1 R_y M_p$
Compression on Connection	—	GS[h]	GS[h]	—	GS[h]	—	$1.1 R_y P_n$	Note[g]	1.1 times (lesser of $R_y F_y A_g$ and $1.14 F_{cre} A_g$[i])
Expected Postbuckling Compression Strength	—	—	$0.3\phi_c P_n^f$	—	$0.3\phi_c P_n^f$	—	$0.3 P_n^f$	Note[g]	0.3 times (lesser of $R_y F_y A_g$ and $1.14 F_{cre} A_g$)[j]

[a]($\phi_c = 0.85$ for 2002 editions and earlier; $\phi_c = 0.9$ since 2005 edition)
[b]Provisions for OCBF were eliminated, except for what was previously required for low-rise buildings
[c]Low-rise and roof structures only, designed for the Amplified Seismic Loads, $\Omega_o E$, with $\Omega_o = 2$.
[d]Except when brace connection can accommodate inelastic rotation associated with brace postbuckling deformations (e.g., gusset hinging).
[e]KL/r up to 200 permitted when columns designed considering maximum load transferred to the column (considering R_y times the nominal strength of the connecting brace elements).
[f]Only required for V or Inverted V configurations
[g]Designed for Amplified Seismic Loads, unless designed as per SCBF requirements
[h]Generic statement: "The design of gusset plates shall include consideration of buckling"
[i]F_{cre} is F_{cr}, determined per AISC 360 Chapter E using expected yield stress $R_y F_y$ in lieu of F_y. Note that 1.14 is equal to 1/0.877.
[j]Commentary states that two separate analyses are required: one with all braces at their maximum forces, and one with tension braces at their maximum strength and compression braces at their low postbuckling strength

TABLE 9.1 Changes in AISC CBF Provisions from 1992 to 2010[a]

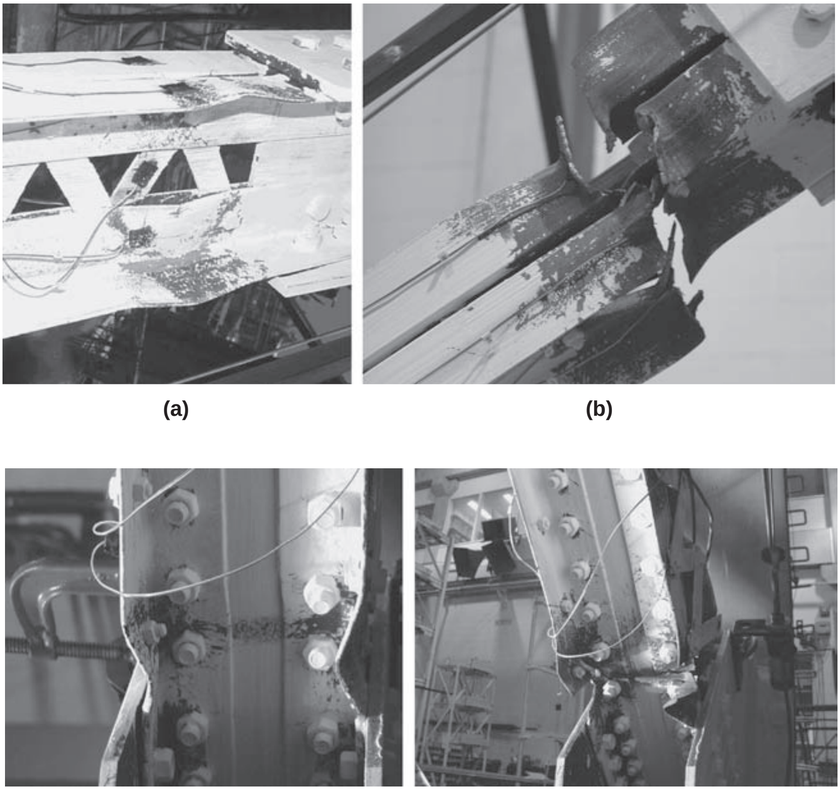

(a) (b)

(c) (d)

Figure 9.17 Axial local buckling in stocky built-up brace: (a) initiation of local buckling; (b) fracture subsequent to cycles of inelastic displacements, for brace with latticed web; (c) and (d) same for beam with solid web. (*Lee and Bruneau 2004, Courtesy of MCEER, University at Buffalo.*)

Braces of rectangular hollow structural shapes (a.k.a. tubes) are particular prone to local buckling and subsequent fractures during cyclic inelastic deformations (e.g., Bonneville and Bartoletti 1996, Gugerli and Goel 1982, Liu and Goel 1987, Shaback and Brown 2003, Tremblay 2002, Tremblay et al. 2003, Uang and Bertero 1986), with cracking often initiating at their rounded corners where high strains have been introduced during their fabrication (by bending of a flat plate into the final tubular shape). This is unfortunate because the high radius of gyration of rectangular tubes for a given cross-sectional area makes them otherwise highly desirable and commonly used as seismic braces. In some instances, fracture has been observed to develop rapidly following the onset of local buckling. This phenomenon, from local buckling to fracture, is illustrated in Figure 9.18 for a tubular brace. Example of such brace buckling and fractures observed following earthquakes are shown in Figure 9.19.

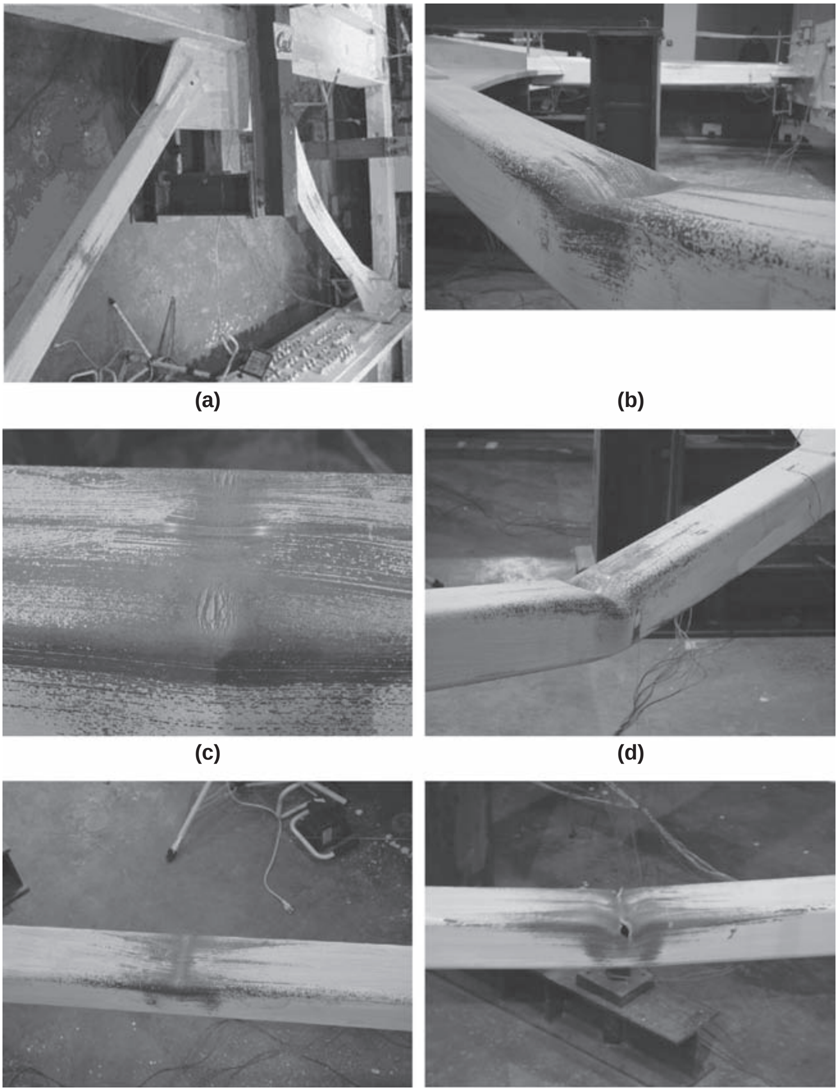

(a) (b) (c) (d) (e) (f)

Figure 9.18 Stages in fracture of cyclically loaded braces: (a) buckled and restraightened brace at 0.67% drift; (b) local buckle developed during out-of-plane buckling; (c) initial tears at corner of straightened brace at 0.67% drift; (d) out-of-plane buckling of brace; (e) corresponding point of fracture initiation in strengthened brace at 1.34% drift; (f) fractured corners; (g) fractured face; (h) complete fracture. (*Uriz and Mahin 2008, with permission from PEER, University of California, Berkeley.*)

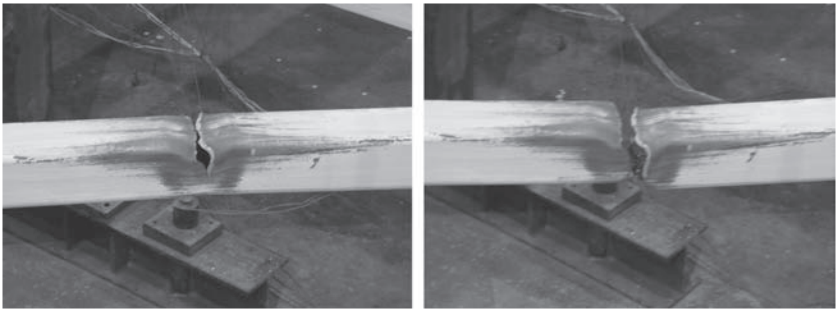

(g) (h)

Figure 9.18 (*Continued*)

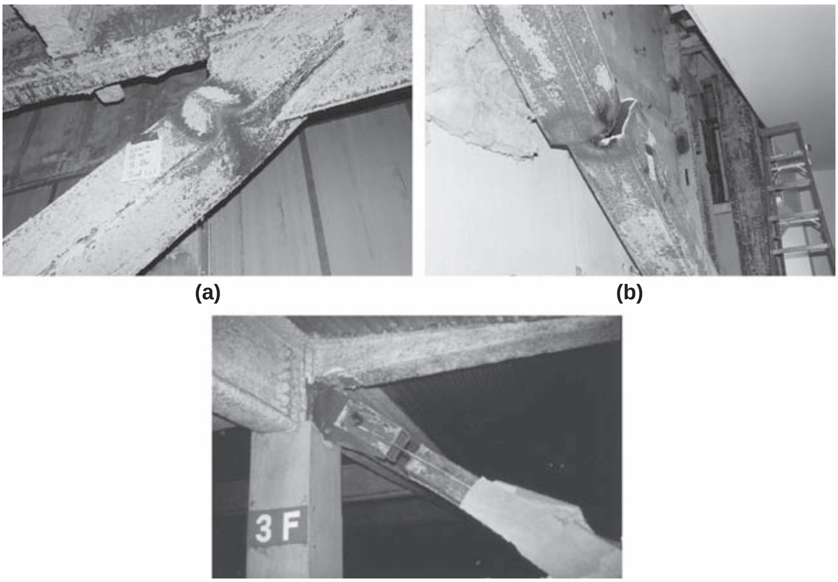

(a) (b)

(c)

Figure 9.19 Rectangular HSS braces: (a and b) buckled and fractured—Northridge earthquake. (*Courtesy of Degenkolb Engineers*); (c) fractured—Kobe earthquake. (*Courtesy of Dennis Mitchell, Department of Civil Engineering and Applied Mechanics, McGill University.*)

Preventing local buckling is paramount to precluding premature material fracture. For all structural shapes, the strategy adopted by codes and standards for delaying the onset of local buckling has been to limit the width-to-thickness ratio of braces. Given that braces develop flexural plastic hinges during their buckling, limits on width-to-thickness ratios must be at least as stringent as those for highly ductile flexural members, and more stringent in some cases given the large axial loads simultaneously resisted by braces.

Given that the limits specified for seismic design were more stringent than those defining compact members (i.e., smaller than λ_p in AISC 360), members meeting these requirements were called "seismically compact" in some past codes and specifications (e.g., AISC 341-05). This terminology has been superseded in AISC 341-10 by the designations of "moderately ductile" for members anticipated to undergo plastic rotation of up to 0.02 rad, and "highly ductile" for members anticipated to undergo plastic rotation of 0.04 rad or more.

The width-to-thickness ratio for the flanges of rolled or built-up I-shaped sections, channels, and tees, as well as legs of angles (single angles, double angle members with separators, or outstanding legs of pairs of angles in continuous contact) and stem of tees, is limited to $0.30\sqrt{E/F_y}$ for highly ductile members (which includes braces of SCBF), and $0.38\sqrt{E/F_y}$ for moderately ductile members (which includes braces of OCBF). Except for round and rectangular HSS, stems of WTs and webs in flexural compression, the width-to-thickness ratio limits for moderately ductile members correspond to λp values in AISC 360.

The rapid strength deterioration and fracture under inelastic cyclic loading of braces having hollow structural shapes has long been recognized. Based on results from their respective research, Tang and Goel (1987) and Uang and Bertero (1986) recommended that the limit on the width-to-thickness ratio (b/t) for rectangular tubes be reduced from the value then specified. Tang and Goel recommended a b/t limit of $95/\sqrt{F_y}$ ($= 250/\sqrt{F_y}$ in S.I. units) for rectangular tube sections. Uang and Bertero (1986) recommended a limit of $125/\sqrt{F_y}$ ($= 330/\sqrt{F_y}$ in S.I. units) with a slenderness ratio, KL/r, limit of 68, (their study considered braces having $48 \le KL/r \le 61$ and $12.7 \le b/t \le 20.5$, these latter values being less than the AISC b/t limit of 26 at the time). From 1992 to 2005, the AISC Seismic Provisions limit for seismically compact rectangular HSS braces was $110\sqrt{F_y}$, equivalent to $0.64\sqrt{E/F_y}$. In AISC 341-10, this limit was retained for moderately ductile braces, but reduced to $0.55\sqrt{E/F_y}$, equivalent to $94\sqrt{F_y}$, for highly ductile braces, on the basis of additional research results (Fell et al, 2006, Uriz and Mahin 2008). AISC 341-10 similarly reduced by 15% the previous seismically compact limit of $0.044E/F_y$ for the diameter-to-thickness ratio limit of round HSS in SCBF, to $0.038E/F_y$ for highly ductile braces; moderately ductile braces (in OCBF) remained at the previous limit. However, as local buckling and low-cycle fatigue life of braces also correlate to member slenderness, future research is anticipated to further affect these limits.

As an alternate approach to delay the onset of local buckling in tubular braces, Liu and Goel (1987) and Lee and Goel (1987) proposed filling them with expansive concrete. They investigated the hysteretic response of similar braces, comparing hollow steel braces b/t ratios approximately equal to 30 and 14, with a brace having the lower b/t ratio and filled with concrete. Liu and Goel reported similar overall buckling modes for the three specimens prior to plastic hinge formation and local buckling, but that following plastic hinge formation, the braces with the smaller b/t ratio and concrete fill performed substantially better because local buckling in the plastic hinge zones was delayed and the strength of the brace remained relatively constant with repeated cycling. For the two hollow tubular sections tested, the compression flange in the brace at the plastic hinge buckled inward and the brace webs bulged outward (Figure 9.20a). For the concrete-filled braces, because of concrete restraining any significant inward buckling, the flange of the tube buckled outward; the zone of local buckling lengthened to approximately the width of the tube and its severity was reduced (Figure 9.20b), reducing the magnitude of strains in the plastic hinge zone due to local buckling, delaying the onset of fracture, and lessening degradation of the brace compression strength. Other researchers reported similar benefits with concrete filled tubes (e.g., Broderick et al. 2005, Zhao et al. 2002).

9.2.7 Low-Cycle Fatigue Models

While the emphasis of early editions of seismic provisions was on limiting member slenderness, KL/r, to relatively low values, research results raised concerns that ductile braces designed in full compliance with these requirements would not necessarily have a low-cycle fatigue life sufficient to survive the large cyclic deformations imposed by severe earthquakes (Archambault et al. 1995, Fell et al. 2009, Tang and Goel 1987), as cracking and early fracture develop due to severe local buckling in the regions of plastic hinges. Global member slenderness limits for braces were relaxed in more recent editions of seismic design code and standards as a way to reduce plastic hinge rotation demands in the braces, and thus to delay or prevent low-cycle fatigue fractures. As KL/r increases, inelastic demand during brace buckling decreases, leading to lower strains at the plastic hinge location, suggesting that increased member slenderness is beneficial, and that KL/r is the most important parameter controlling global behavior and response (e.g., Fell et al. 2009, Jain et al. 1978, Lee and Bruneau 2005, Tang and Goel 1989, Tremblay 2002, Tremblay et al. 2003). Arguably, slender braces only developing elastic buckling (i.e., without plastic hinging) could have a more desirable behavior, at the cost of low compression strength and no energy dissipation in compression. In the absence of plastic hinging in the middle of the brace, provided no local buckling otherwise developed in the brace, there is no need to be concerned about low-cycle fatigue life of the brace. Future research will enlighten design decisions in this regard.

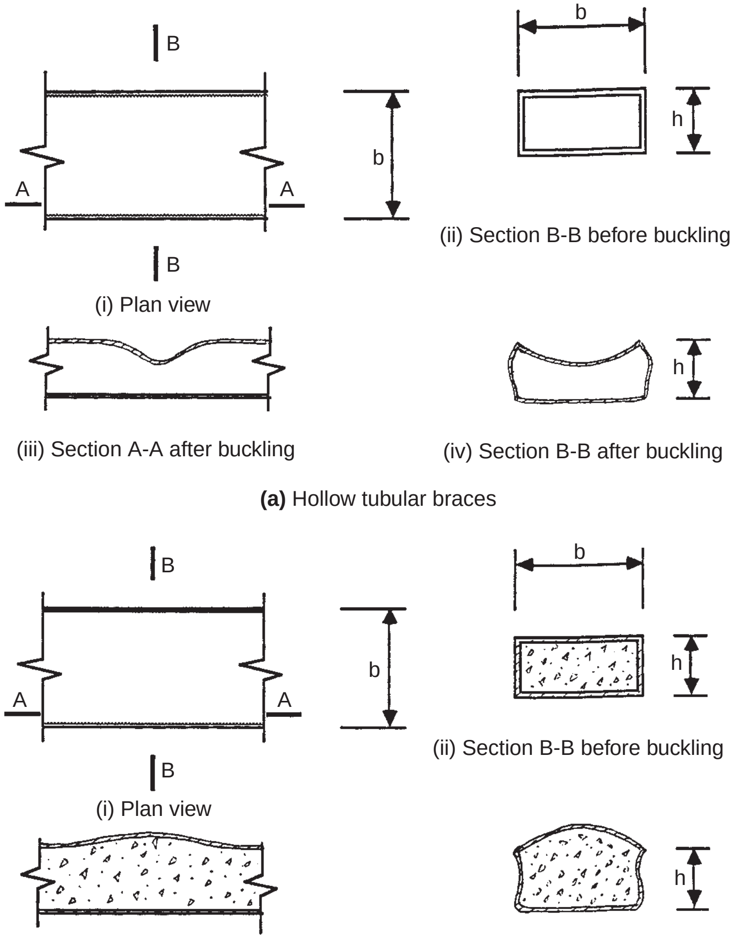

(i) Plan view

(ii) Section B-B before buckling

(iii) Section A-A after buckling

(iv) Section B-B after buckling

(a) Hollow tubular braces

(i) Plan view

(ii) Section B-B before buckling

(iii) Section A-A after buckling

(iv) Section B-B after buckling

(b) Concrete-filled tubular braces

Figure 9.20 Buckled sections in tubular steel braces at plastic hinge locations. (*Courtesy of S. Goel, Department of Civil and Environmental Engineering, University of Michigan.*)

Tools to assess the low-cycle fatigue life of braces will be required for this purpose. This section briefly reviews some of the fracture criteria that have been developed for tubular bracing members. Note that, typically, wherever Δ has been used in fracture models, it actually corresponds to the axial elongation of the brace, that is, δ per the notation used in all other sections.

9.2.7.1 Member Hysteresis Models (Phenomenological Models)

One category of low-cycle fatigue models consists of criteria related to the hysteretic behavior of brace members. Tang and Goel (1987) first proposed the following empirical equation to quantify the fracture life of rectangular tubular bracing members:

$$N_f = 262\frac{(B/D)(60)}{[(B-2t)/t]^2} \qquad \text{for} \qquad \frac{KL}{r} \leq 60 \tag{9.3a}$$

$$N_f = 262\frac{(B/D)(KL/r)}{[(B-2t)/t]^2} \qquad \text{for} \qquad \frac{KL}{r} > 60 \tag{9.3b}$$

where N_f is the fracture life expressed in terms of a number of equivalent cycles, B and D are respectively the gross width and depth of the section defined such that $B > D$, and t is the thickness of the section. To determine if fatigue life is exceeded, the calculated time history of brace deformations must be converted into equivalent cycles per a procedure outlined in Tang and Goel (1987), equivalent to a rainflow counting method (Chapter 2) in which only the half cycles from a compression peak to the point of maximum tension (or minimum compression) in a cycle are counted to contribute to fatigue life.

Lee and Goel (1987) reformulated this model by considering the effect of F_y and eliminating the dependency on KL/r. In this criterion, the nondimensional parameter Δ_f is used instead of N_f to quantify the fracture life of a tubular bracing member. This method proceeds per the following steps:

(a) The hysteresis curves (P vs. Δ) are converted to normalized hysteresis curves (P/P_y vs. Δ/Δ_y).

(b) The deformation amplitude (tension excursion in a cycle) is divided into two parts, Δ_1 and Δ_2, defined at the axial load $P_y/3$ point, as illustrated in Figure 9.21. Δ_1 is the tension deformation from the load reversal point to $P_y/3$, whereas Δ_2 is from $P_y/3$ point up to the unloading point.

(c) $\Delta_{f,exp}$ is obtained by adding 0.1 times Δ_1 to Δ_2 in each cycle and summing up for all cycles up to the failure [i.e., $\Delta_f = \Sigma(0.1\Delta_1 + \Delta_2)$]. This reflects a belief that straightening and stretching of the brace has a greater impact on fracture life than compressive deformation excursions.

(d) The theoretical fracture life, Δ_f is expressed as follows:

$$\Delta_f = C_s\frac{(46/F_y)^{1.2}}{[(B-2t)/t]^{1.6}}\left(\frac{4B/D+1}{5}\right) \tag{9.4}$$

where C_s is an empirically obtained constant calibrated from test results, and F_y is the yield strength of the brace (ksi). The numerical

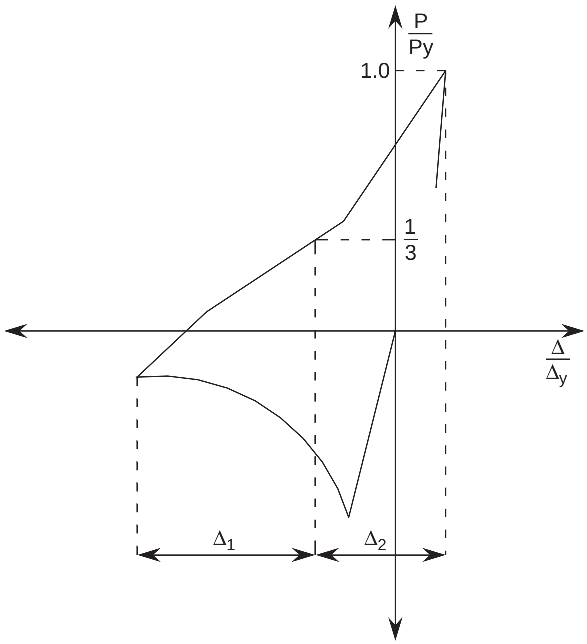

Figure 9.21 Definition of Δ_1 and Δ_2. (*Lee and Goel model.*) (*Lee and Bruneau 2002, courtesy of MCEER, University of Buffalo.*)

constant C_s, originally given as 1335 by Lee and Goel (1987), was recalibrated using the test results of Gugerli and Goel (1982) and Lee and Goel (1987), and found to be 1560 by Hassan and Goel (1991). Fracture is assumed to occur when $\Delta_{f,exp} = \Delta_f$.

Based on a review of additional and previous test results, Archambault et al. (1995) found the Lee and Goel model to underestimate the fracture life of tubular bracing members having large slenderness ratios, and modified it by reintroducing the effect of slenderness ratio, KL/r, and recalibrating against the available data. They introduced the term, Δ_f^* (to differentiate it from Δ_f used by Lee and Goel), and expressed fatigue life as:

$$\Delta_f^* = C_s \frac{(317/F_y)^{1.2}}{[(B-2t)/t]^{0.5}} \left(\frac{4B/D+1}{5}\right)^{0.8} \times (70)^2 \qquad \text{for} \qquad \frac{KL}{r} < 70 \tag{9.5a}$$

$$\Delta_f^* = C_s \frac{(317/F_y)^{1.2}}{[(B-2t)/t]^{0.5}} \left(\frac{4B/D+1}{5}\right)^{0.8} \times (KL/r)^2 \qquad \text{for} \qquad \frac{KL}{r} \geq 70 \tag{9.5b}$$

where the C_s = 0.0257 based on calibration to experimental results and F_y is in MPa. Figure 9.22 compares the trends in predicted

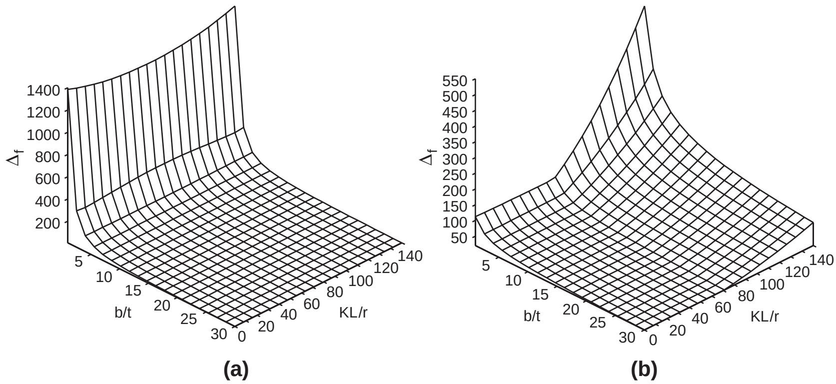

Figure 9.22 Trends in predicted fracture life, as a function of b/t and KL/r, per: (a) Tang and Goel model; (b) Archambault et al. (1995) model. (*Lee and Bruneau 2002, courtesy of MCEER, University at Buffalo.*)

fracture life, for the Lee and Goel versus the Archambault et al. (1995) models (Lee and Bruneau 2002).

Additional test results and recalibration by Shaback and Brown (2003) led to the following revisions to the model:

$$\Delta_f^* = 0.065\frac{(350/F_y)^{-3.5}}{[(B-2t)/t]^{1.2}}\left(\frac{4B/D-0.5}{5}\right)^{0.55} \times (70)^2 \quad \text{for} \quad \frac{KL}{r} < 70 \tag{9.6a}$$

$$\Delta_f^* = 0.065\frac{(350/F_y)^{-3.5}}{[(B-2t)/t]^{1.2}}\left(\frac{4B/D-0.5}{5}\right)^{0.55} \times \left(\frac{KL}{r}\right)^2 \quad \text{for} \quad \frac{KL}{r} \geq 70 \tag{9.6b}$$

Phenomenological models for assessing the low-cycle fatigue life of braces having other types of cross-sectional shapes have not been as intensely pursued, even though such fractures have been observed following local buckling at the plastic hinge locations, such as in circular hollow sections (e.g., Elchalakani et al. 2003, Tremblay et al. 2008) and W shapes (http://exp.ncree.org/cbf/index.html, Roeder et al. 2010). Lee and Bruneau (2002) adapted the above equations for built-up latticed braces made of angles, on the basis of limited experimental results, and Goel and Lee (1992) proposed a fracture criterion for concrete-filled tubular bracing members.

9.2.7.2 Continuum Mechanics Models (Physical Models)

A second approach taken to model the low-cycle fatigue of cyclically loaded brace members has been to implement fatigue models in finite element programs, either tracking plastic strain histories at all locations of interest (e.g., Yoo et al. 2008) or explicitly modeling plastic damage and fracture (e.g., Huang and Mahin 2010, Kanvinde and Deierlein 2007), and calibrating model parameters based on past experimental data for braces.

For example, Huang and Mahin (2010) developed a continuum mechanics damage plasticity model to account for low-cycle fatigue, combined with an existing erosion algorithm to simulate cracking. Recognizing that additional research is required to determine how to best calibrate the damage parameters of such models, analyses provided good correlation with experimental results in chosen illustrative examples. Sample simulation results are shown in Figure 9.23.

As an intermediate step between phenomenological models and full-blown continuum mechanics, Uriz and Mahin (2008) developed an approach for modeling low-cycle fatigue using fiber-hinge models (Uriz et al 2007), a Menegotto-Pinto material model, a modified

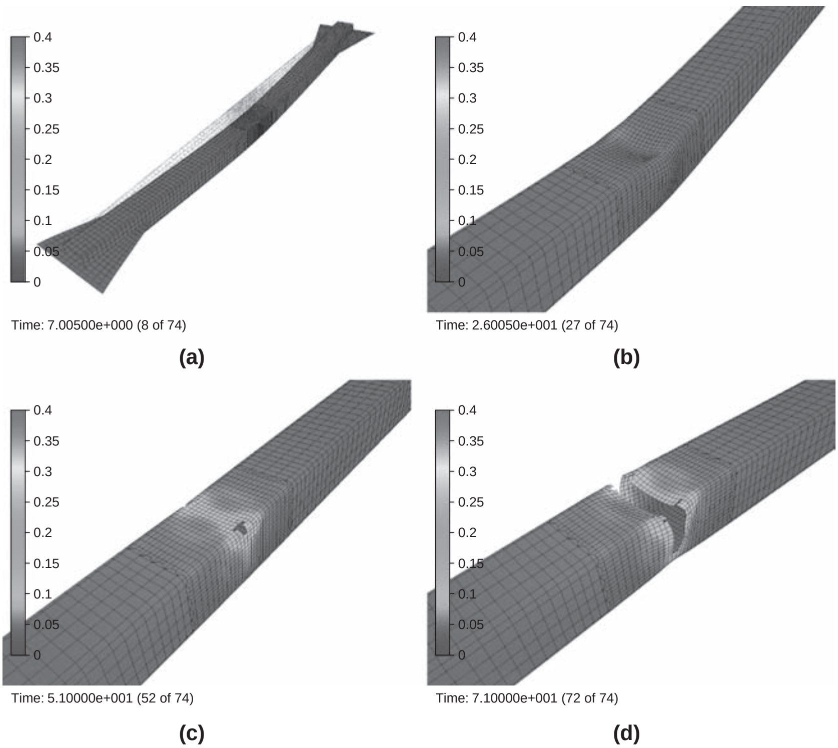

FIGURE 9.23 Finite element modeling of low-cycle fatigue of brace: (a) global buckling; (b) local buckling; (c) crack initiation; (d) fracture. (*Huang and Mahin 2010, with permission from PEER, University of California, Berkeley.*)

rainflow cycle counting procedure with the Coffin-Manson model (Chapter 2), and calibration using data for rectangular tubular braces. Although the accuracy obtained with this approach was comparable with that obtained with the phenomenological models, calibration allows further investigation of other cross-sectional types, boundary conditions, lengths, b/t ratios, and material properties; using such an approach, Uriz and Mahin verified that braces using wide-flange shapes typically have a significantly better low-cycle fatigue life than other cross-sections. However, fiber model elements are limited in that they cannot model cross-sectional changes due to local buckling, nor strain and stress concentrations due to crack opening.

9.2.8 Models of Single Brace Behavior

Computationally efficient element models of single brace for use in nonlinear inelastic analysis programs have been developed since the mid 1970s to capture the hysteretic axial force versus axial displacement behavior of braces. Use of these models is substantially less computationally intensive than finite element approaches based on computational mechanics or fiber hinges, but they cannot model local buckling. Most of these models also do not address low-cycle fatigue and fracture, although some have been linked to subroutines tracking cycles and/or yielding excursions against predicted life.

First formulated were phenomenological models constructed of empirical functions and coefficients that needed to be calibrated on experiment-specific data to replicate the various stages of behavior (e.g., Higginbotham and Hanson 1976; Ikeda et al. 1984; Jain et al. 1977, 1978; Jain and Goel 1978; Maison and Popov 1980). Later developments favored models that relied on physical theory to characterize the various branches of the hysteresis loops as well as the transitions from any branch to possible others during the loading history. Physical theory models are intended to predict the behavior of any brace from knowledge of member geometry and material properties (e.g., Dicleli and Calik 2008; Gugerli and Goel 1982; Ikeda and Mahin 1984; Jin and El-Tawil 2003; Nonaka 1987, 1989; Soroushian and Alawa 1990; Zayas et al. 1981), although some of these models neglect to account for Baushinger effects (which can significantly impact the shape of the hysteresis curves) or use complex empirical coefficients to model this effect. Although physical models generally only consist of two elastic members and a plastic hinge, they can reasonably capture brace axial hysteretic behavior (and in some cases out-of-plane deformations), as illustrated in Figure 9.24 for the Dicleli and Calik (2008) model.

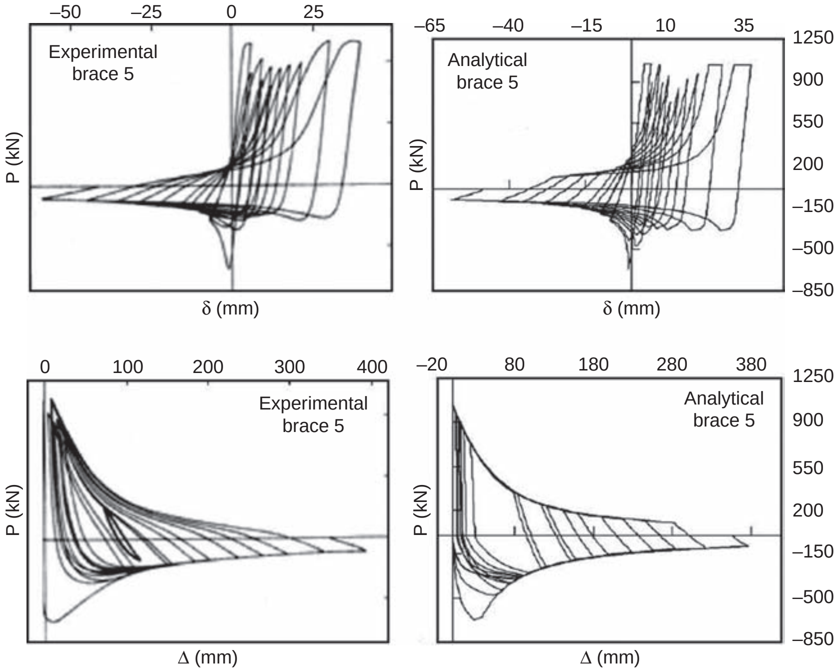

FIGURE 9.24 Sample results obtained using a Physical Theory Model. (*Courtesy of Murat Dicleli, Department of Civil Engineering, Middle East Technical University, Ankara, Turkey.*)

9.3 Hysteretic Behavior and Design of Concentrically Braced Frames

9.3.1 System Configuration and General Issues

9.3.1.1 Capacity Design and Analysis

Figure 9.2 shows frame configurations permitted or prohibited by AISC 341. Any of the permitted configurations can be designed to perform in a ductile and stable manner during earthquakes. However, a successful design, irrespective of configuration, must recognize and account for the redistribution of forces within the structural system, as braces buckle in compression, yield in tension, and lose compression strength upon larger drifts and during repeated loadings. Explicit recognition of this important redistribution is relatively recent in design codes and standards. Braced frames designed in the absence of such enforced capacity design principles may exhibit an erratic behavior during severe earthquakes due to possible beam and column buckling or connection failures.

Although most contemporary codified design requirements have embraced capacity design principles that are generally applicable for any frame configuration, many codes and standards still treat V- and inverted V-braced frames with separate requirements, in recognition of their unique characteristics as a result of the unbalanced forces applied to their beams during brace yielding and buckling (Section 9.3.3). Such a differentiation is therefore kept in the organization of this section.

Braces are the first elements designed in a concentrically braced frame. The forces to consider for their design are typically obtained from an elastic analysis, but their behavior is highly nonlinear due to brace buckling and yielding, as described in Section 9.2. Braces are the designated energy dissipating mechanisms for this type of structural system. Yielding and buckling of braces typically develop at drifts of 0.3 to 0.5%, and postbuckling axial deformations of braces can reach up to 20 times their yield deformation. Section 9.2 has outlined the desirable features of braces to ensure they can reach such deformations and survive severe earthquakes without premature brace fractures. These important requirements limiting member slenderness and width-to-thickness ratios are not repeated in this section, but are mandatory given that brace rupture can lead to excessive demands on beams and columns and possible collapse. However, issues related to determination of the effective length of brace, not previously addressed, is presented in Section 9.3.2.

Having designed the braces, their strengths dictate the demands on the remaining components of the structural systems. These demands on beams, columns, connections and other parts, are reviewed in details below, building on the information presented in the previous sections rather than repeating it. These components are designed to remain elastic, and the following discussion focuses on the determination of demands for the design of these structural elements, one exception being that, in many instances, ductile behavior of the brace gusset connectors is also essential to achieve satisfactory, as described in a later section.

Note that nonlinear inelastic analysis of braced frames assuming pin connections at the intersection of all members (as done in truss analysis) will unavoidably predict concentration of damage in a single level of the braced frame, because such an idealized model provides no means for yielding to spread to other levels, as shown by the example of Section 6.3.1. This is a consequence of the postbuckling degradation of compression strength and further aggravated by the absence of significant strain hardening in the braces. However, results from such simplified models disagree with field observations following earthquakes that demonstrate the spreading of yielding and buckling along building height. This is because the pin connections model fails to recognize the key role played by all columns (including those not part of the SCBF) to distribute forces along the height of buildings. MacRae et al. (2004, 2010) provided a "continuous column concept" and procedure to estimate the likely drift concentration in frames of different heights, which may in turn be used to estimate the column stiffness required to achieve the desired performance. Extrapolating this concept, Wada et al. (2009) proposed rocking rigid walls (pinned at their base) that were effectively implemented in a building to evenly distribute energy dissipation along building height.

Therefore, as a minimum, the continuity of the braced-frame columns must be modeled. Likewise, for tension-only structures, CSA S16 requires every column in the building to be fully continuous over the building height to prevent concentration of inelastic demand in a single story.

9.3.1.2 Brace Layouts for Balanced Lateral Strengths

Energy dissipation by tension yielding of braces is more reliable than by buckling of braces in compression, even for braces of low slenderness and compactness. Consequently, to ensure a minimum of structural redundancy and a good balance of energy dissipation between compression and tension members, structural layouts that predominantly depend on the compression resistance of braces (rather than their tension resistance) must be avoided in an earthquake-resistant design perspective. Examples of unacceptable braced-frame layouts are shown in Figure 9.25, along with recommended alternatives. Four braces in compression and only one brace in tension resist the load applied on the five-bay braced frame shown in Figure 9.25a. The four braces in the braced-core of Figure 9.25c are all in compression when resisting the torsional moment resulting from seismically induced inertial force acting at the center of mass (for simplicity, columns resisting only gravity loads are not shown in that figure). Better designs are shown in Figs. 9.25b and 9.25d for each of those cases, respectively.

Seismic design codes prevent the use of nonbalanced structural layouts by requiring that braces along a given structural line be deployed such that at least 30% but no more than 70% of the total lateral horizontal force acting along that line is resisted by tension braces (which is equivalent to making the same requirement for compression braces). Note that although the wording of such clauses would not cover the case shown in Figure 9.25c, the intent of the clauses would. Codes typically waive this requirement if nearly elastic response is expected during earthquakes (which AISC 341 approximates with a special "amplified seismic load" condition described later).

This requirement has sometimes been interpreted by considering a balance of member strengths rather than design forces. For frames having the same number of compression and tension braces, and designed for slenderness limits of $4\sqrt{E/F_y}$, this distinction was less

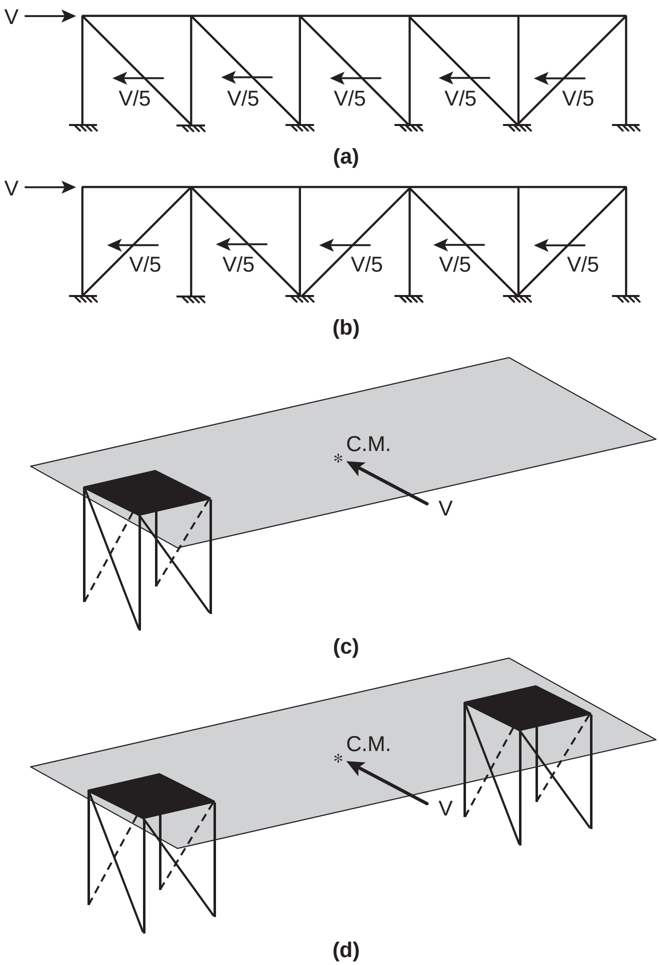

Figure 9.25 Brace layouts to ensure balanced lateral strength: (a and c) unacceptable layouts; (b and d) acceptable alternative layouts.

significant (i.e., for $F_y = 50$ ksi, the slenderness limit becomes 98, and the compression strength of a brace for that slenderness is half of the tension strength, the compression brace thus providing 33% of the braced frame strength). However, the clause refers to 30% and 70% of the lateral horizontal force based on the elastic analysis force distribution between the tension and compression members, irrespective of member strengths (i.e., for the same two-brace frame example, this force distribution is 50% and 50% as the compression brace is designed to resist half of the applied force).

Given that CSA-S16-09 allows tension-only systems in some circumstances, recognizing that no lateral force is applied to the compression braces that are neglected in the corresponding elastic analysis, the same intent is achieved by requiring instead that the "ratio of the sum of the horizontal components of the factored tensile brace resistances in opposite directions is between 0.75 and 1.33."

9.3.1.3 Impact of Design Approach on System Overstrength

The design approach adopted for braced frames can have a significant impact on their behavior. In most seismic regions, it is a standard practice to use elastic analysis to determine brace forces, which imply equal forces in the tension and compression braces when an equal number of compression and tension braces (of same area and length) resist the horizontal shear force at a given story. Brace area is determined by compression strength, and the corresponding tension strength is a consequence of this chosen area. Given that the buckling stress of a compression member decreases as a function of KL/r, the area needed to resist a given compression force increases for more slender members, and so does the corresponding brace tension yield strength.

When braces having greater KL/r values are used in concentrically braced frames, because of the resulting greater difference in tension and compression strengths, greater system overstrength is possible, as shown in Figure 9.26 (Tremblay 2003). Figure 9.26a shows brace compression strength as a function of slenderness, per CSA S16 design equations (similar curves would be obtained per other design specifications), and the corresponding degraded compression strength after displacement cycles at a specified ductility demand level. Figure 9.26b shows the corresponding tension strength, given that brace area is determined from the compression force, and therefore increases as a function of member slenderness. The sum of brace tension and degraded compression strengths, except in the approximate range of $25 < KL/r < 75$ where a slight decrease in system strength is observed, shows a net gain in overstrength for progressively more slender members (Figure 9.26c). Tremblay (2003) demonstrated that this overstrength can have a definite positive impact on achieving more stable braced frame response.

For comparison, in a tension-only design approach, braces are sized based on their tension strength alone (giving the flatline in Figure 9.26b), their compression strength being neglected. In this case, for the sum of the strengths (Figure 9.26c), the actual strength of the compression brace would provide system overstrength at low member slenderness, and progressively decreasing overstrength as slenderness increases. However, such an overstrength would be rare in practice, because the tension-only design approach typically leads to highly slender braces such as rod or flat bars.

9.3.1.4 Collector Forces versus Forces from Above

Beyond resisting gravity loads, some beams in braced frame buildings must also be designed to serve as collector elements, to transfer the

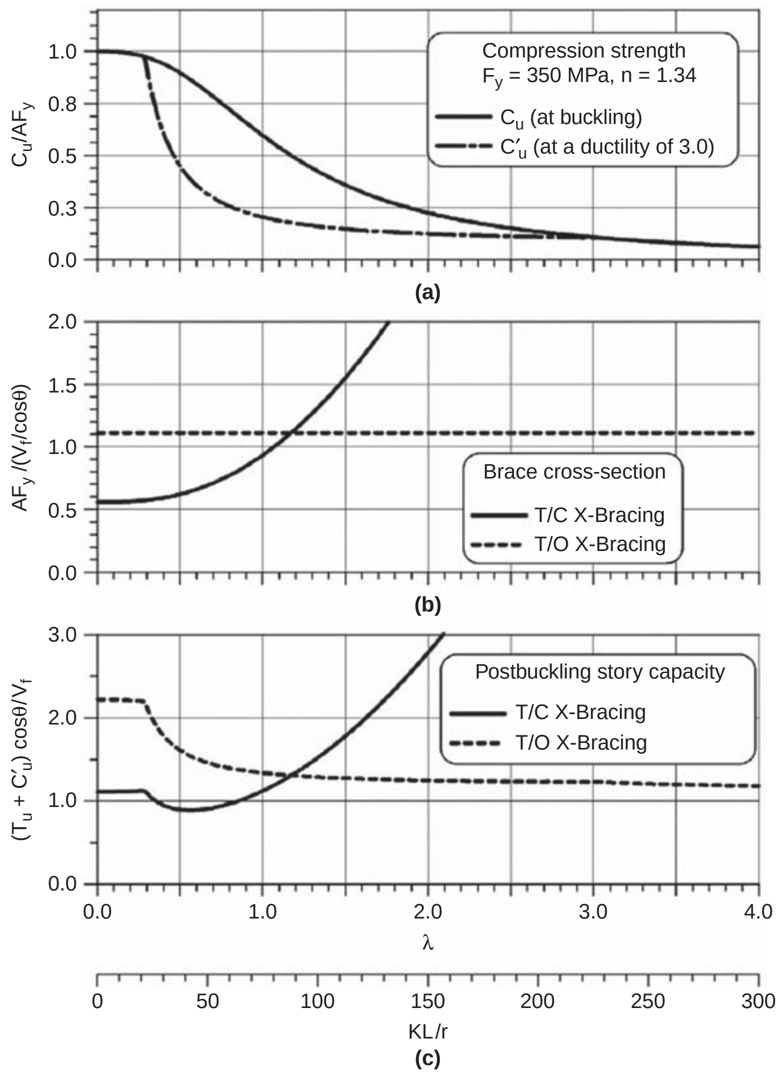

FIGURE 9.26 Comparison of strengths for design based on compression strength (T/C) versus tension-only assumption (T/O): (a) compression strength and degraded postbuckling compression strength as a function of brace area; (b) brace area as a function of lateral design force; (c) sum of brace strengths as a function of lateral design force. (*Tremblay 2003, copyright © American Institute of Steel Construction. Reprinted with permission. All rights reserved.*)

seismic inertial forces from the floor slabs into the braced bays, and in some case to facilitate load redistribution between different braced bays. Failure of these collector beams or their connections, preventing the transfer of seismic forces to the vertical lateral force-resisting system, could compromise the response of the entire building.

In the early days of seismic design, this transfer of inertial forces to the braced frames was assumed to be implicitly achieved without special detailing, whereas it is now recognized that ensuring integrity of a complete load path for the seismic inertial forces in the horizontal plane often requires that collector beams (a.k.a. drag struts or ties) be designed if to perform as intended. Per capacity design principles, the load path provided by collectors must remain elastic to ensure full development of the vertical braced frame's plastic mechanisms, which for braced frames must account for changes in load paths due to strength degradation of the compression braces (as illustrated later). Griffis and Patel (2006) and ATC (1999) provide general information and typical load paths for the design of collectors. Rogers and Tremblay (2010) provide similar information for steel roof deck diaphragms, including a ductile diaphragm alternative approach.

9.3.2 Brace Design

Typically, brace design is governed by compression strength (the limited applications of tension-only design permitted by CSA-S16 being a notable exception), which is a function of the slenderness KL/r. AISC 360 outlines standard procedures to determine the effective length factor, K, to size the braces, and higher values can be conservatively used if in the presence of uncertainties (L being typically taken as the distance from the intersecting axes of structural members in the analysis models). However, using capacity design principles to assess the demands imparted by the buckling braces on their connections and other structural elements, knowledge of the actual effective length is important, and conservatism dictates the use of lower K values.

Recommended K factors for braced frames subjected to cycles of inelastic deformations depend on brace configurations (whether braces cross or not between levels), in-plane versus out-of-plane buckling, brace connection types, and even brace cross-sectional types.

Beyond selection of appropriate K factors, seismic design issues for braces are limited to selection of structural members that meet the specified width-to-thickness ratio limits and member slenderness limits. Member properties tables only including members that meet these limits are available to expedite design (e.g., AISC 2006). Note that problems of excessive slenderness, when encountered during design, can be resolved by changing the brace configurations instead of using bigger braces (e.g., changing from X-bracing to inverted-V bracing in a particular story or bay).

9.3.2.1 Inelastic Cyclic Out-of-Plane Buckling

Early studies on the elastic behavior of X-braced frames subjected to noncyclic load showed that the tension brace can provide some resistance against *out-of-plane* buckling of the compression brace and justified the use of a value of K less than one for out-of-plane buckling. However, in the perspective of cyclic inelastic response (such as for seismic design), many engineers believed this assumption to be incorrect, given that both braces are buckled when the braced frame is returned to its original position (i.e., zero lateral frame displacement), after having successively been stretched in tension. Therefore, they recommended that a value K of 1.0 be used for out-of-plane buckling, not relying on the tension brace to provide lateral bracing in seismic applications.

Research on X-braced frames (El-Tayem and Goel 1986 for z-axis buckling of braces, Tremblay et al. 2003 for rectangular HSS) demonstrated that in spite of the above brace slackness at zero frame displacements, with out-of-plane buckling over the entire brace length, the tension brace provides resistance against out-of-plane buckling anew as it reloads at larger frame drifts. For braces connected using single gussets, El-Tayem and Goel recommended use of an effective length of 0.85 times the half diagonal length, whereas Tremblay et al. reported values ranging from 0.83 to 0.90 of L_H, where L_H is defined as the distance between the brace intersection point and the plastic hinge in the gusset (for gusset hinges meeting the $2t_g$ criterion presented in Section 9.3.5).

The above effective length values for buckling modes that include gusset hinging would expectedly vary for different gusset thicknesses, with thicker values progressively approaching full fixity conditions, although such a continuous relationship has not yet been quantified. As one data point, Nakashima and Wakabayashi (1992) reported that analyses for the out-of-plane buckling of X-braced frames with fixed-end braces using KL equal to 0.7 times the half-diagonal length provided a good match with experiment results (note that 0.7 is the theoretical effective length factor for a fix-pin brace). The above results also assume that braces are continuous through their midlength connection point, or reinforced with cover plates (Tremblay et al. 2003) or by other bridging means to provide continuous stiffness across that point when discontinuous braces are used; effective length equations derived for the case of discontinuous braces (Davaran 2001, Moon et al. 2008) are awaiting experimental verification.

Note that although elastic buckling typically develops in both segments of the compressed brace in an X-braced frame, as inelastic buckling develops, plastic hinging first develops in one of the segments; the ensuing degradation of the brace compression strength (Section 9.2.3) results in lower forces in the compression brace, preventing inelastic buckling from developing in the second brace segment. This often reported phenomenon (e.g., El-Tayem and Goel 1986, Lee and Bruneau 2004, Tremblay et al. 2003) is illustrated in Figure 9.27.

For braces spanning freely between columns and beams (e.g., configurations in Figures 9.2a, c, d, and e) and buckling out-of-plane, Astaneh-Asl et al. (1985) showed that an effective length KL of $1.0L_H$

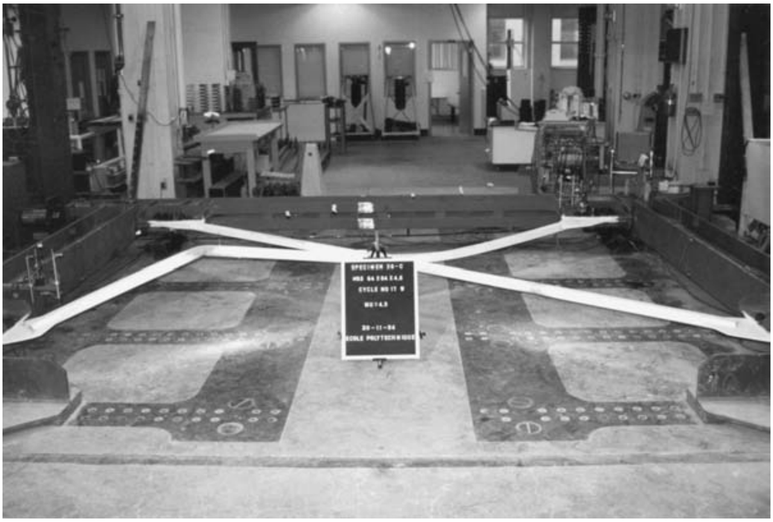

Figure 9.27 Inelastic buckling concentrated in one segment of a brace in an X-braced frame. (*Courtesy of Robert Tremblay, Département des génies civil, géologique et des mines, EcolePolytechnique, Montréal.*)

could be used (for gusset hinges meeting the $2t_g$ criterion presented in Section 9.3.5). Accounting for gusset flexural stiffness, Tremblay et al. 2003 reported values 5% to 12% lower. However, for the alternative elliptical gusset hinging (Section 9.3.5), Lehman et al. (2008) recommended using $K = 1.0$ with the actual brace length.

Finally, it must be recognized that out-of-plane brace buckling is liable to damage architectural finishes close to the braced frame (Figure 9.28). Sabelli and Hohbach (1999), Tremblay et al. (2003), and Shaback and Brown (2003) proposed equations to quantify the magnitude of this out-of-plane deformation.

9.3.2.2 Inelastic Cyclic In-Plane Buckling

For many typical brace connection details, the gussets provide more restraint against in-plane buckling of the braces than out-of-plane buckling; for equal brace slenderness, plastic moment of the gusset plate hinging out-of-plane is less than the plastic moment of the brace hinging to accommodate in-plane buckling of the brace (hinging of the gusset is unlikely in that direction). However, in many instances, in-plane buckling may occur instead of out-of-plane buckling (or be designed to occur, as in-plane buckling is more desirable to prevent damage to adjacent claddings and nonstructural elements).

For braces spanning freely between columns and beams (e.g., configurations in Figures 9.2a, c, d, and e), buckling in-plane and developing plastic hinges in the braces adjacent to the gusset,

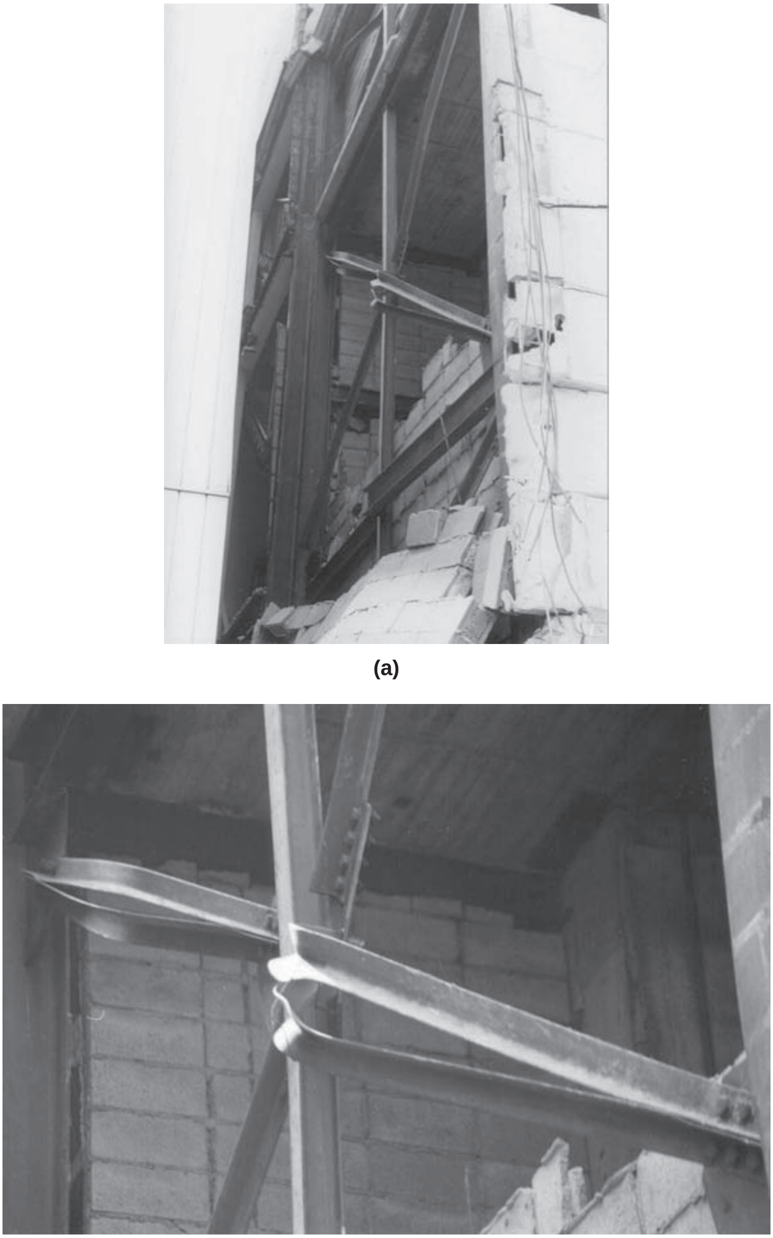

(a)

(b)

Figure 9.28 Masonry cladding damaged by out-of-plane buckling of braces: (a) global view; (b) close-up view of *z*-axis buckling of individual braces.

Astaneh-Asl and Goel (1984) recommended a value of KL of $0.5L_H$ (corresponding to fix–fix conditions). Tremblay et al. (2008) recommended a $KL = 0.9L_H$ when using a horizontal "knife-plate" gusset developed specifically to facilitate in-plane buckling (Section 9.3.5), with L_H being the distance between the plastic hinges in the gusset.

Considerably less data exists for in-plane buckling in X-braced frames. A K-value of 0.6 used with half of the full brace length has been recommended for braces developing their plastic moment capacity at their end connections (Nakashima and Wakabayashi 1992, Sabelli and Hohbach 1999).

9.3.2.3 Built-Up Braces

Double-angle braces are frequently used in braced frames, as well as other built-up shapes occasionally. For buckling modes that can impose large shear on stitches, AISC 341 requires the slenderness ratio of individual buckling elements between the stitches to be no greater than the governing slenderness of the built-up member, and that the sum of the shear strengths of the stitches exceeds the tensile strength of each element of the built-up brace. This stricter requirement than what is specified in AISC 360 was formulated based on research results that showed more severe local buckling and premature fracture in such built-up braces subjected to cyclic inelastic deformations. Furthermore, at least two stitches shall be used, with none located in the middle fourth of the brace length; bolted holes where plastic hinges are expected to form in the braces are undesirable given that the higher stresses that would be induced at the net section of such braces would lead to their premature fracture.

Built-up laced brace members of archaic construction fall beyond the scope of AISC 341. Typically, laced built-up compression members were built from angles and channels connected with bars and plates by rivets to form I-shapes and box shapes; single lacings, double lacings, battens, combined lacings and battens, and perforated cover plate configurations have all been used at times. Typical cross-sections and their original design are found in steel design textbooks published at the turn of the century (e.g., Ketchum 1920, Kunz 1915). Research on their ultimate cyclic behavior (Dietrich and Itani 1999; Itani et al. 1998; Lee and Bruneau 2004, 2008a, 2008b; Uang and Kleiser 1997) as well as observed damage following earthquakes (Tremblay et al. 1996) demonstrated the severe seismic vulnerability of laced built-up sections, largely due to their often large width-to-thickness ratios and diverse possible failure modes (which can include lacing buckling and individual component buckling, in addition to all the other issues presented in this chapter). Lee and Bruneau (2004) also proposed equations for their low-cycle fatigue life, based on limited data. The behavior of laced built-up shapes remains complex and some observed behaviors remain unexplained; for example, Lee and Bruneau (2004, 2008a) observed instances of out-of-plane buckling behavior permanently changing into in-plane buckling after a few cycles of inelastic deformation.

9.3.3 Beam Design

The effect of load redistribution due to brace buckling and yielding should be considered for the design of beams in the braced bays. To ensure ductile frame response, the resultant forces on the beams in the braced bays can be calculated using capacity design principles. Both cases of peak and degraded postbuckling compression strengths must be considered to determine the critical demands on the beams throughout the cyclic response of the frame. This section illustrates how this is accomplished for some typical braced frame configurations; in all cases here, tension and compression forces in braces are both considered positive.

9.3.3.1 V- and Inverted V-Braced Frames Configurations

The impact of unequal compression and tension brace forces on the behavior of V- and inverted V-braced frames has long been recognized (e.g., Khatib et al. 1988). If improperly accounted for, the resulting unbalanced force can negatively impact behavior of the beams, and in-turn lead to undesirable plastic collapse mechanisms. Figure 9.29 illustrates this concept for a simple frame.

In the elastic range, each brace resists half of the lateral load applied. However, once the buckling strength of the compression brace is reached, any additional increase in the lateral load, V, is entirely resisted by the brace in tension. The difference in the vertical component of the forces results in an unbalanced vertical load, P_{un}, applied to the beam at the beam-to-brace intersection point:

$$P_{un-v} = (T - C)\sin\theta \tag{9.7}$$

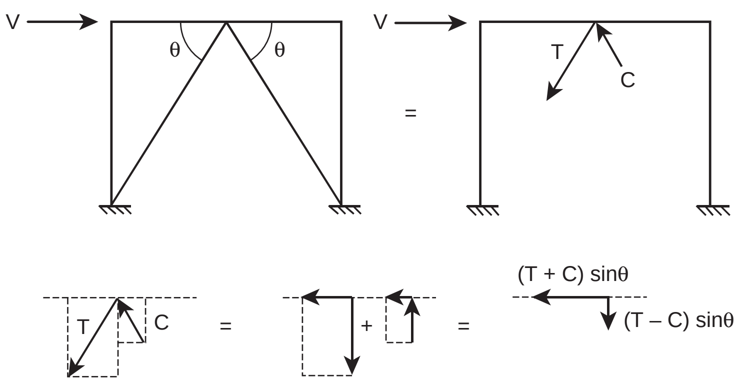

Figure 9.29 Forces acting on beam of inverted V-braced frame due to unbalanced resistance.

where the angle θ is defined in Figure 9.29. Likewise, the axial force in the beam is:

$$P_{un-h} = (T + C)\cos\theta \tag{9.8}$$

The magnitude of the unbalanced force changes as drifts increase and can be calculated taking into account the degraded strength of the brace as a function of drift (as done in Section 6.3.1 with a simplified brace hysteretic behavior).

For expediency, the horizontal unbalanced force used in design is given by Eq. (9.8) considering the tension brace expected yield strength together with the maximum expected buckling strength of the compression brace (i.e., neglecting any brace strength degradation that may have already taken place at the drift at which tension brace yielding occurs). During cyclic inelastic loading, this maximum horizontal force could be reached during the cycle when brace buckling first occurs (i.e., maximum compression strength) followed by tension yielding of the other brace. For given brace areas, the magnitude of this horizontal unbalanced force increases with decreasing brace slenderness, *KL/r*.

The largest vertical unbalanced force is reached when the tension brace has yielded and the compression braced has reached its lowest postbuckling strength. For cyclic loading, this would be the degraded compression strength described in Section 9.2.3. For given brace areas, the magnitude of this vertical unbalanced force increases with increasing brace slenderness, *KL/r*.

Note that although the braces reduce the span of the beam during elastic response, this benefit is lost during inelastic response, with the braces applying a downward pull to the beam. In fact, unless the beam is designed to consider the development of this unbalanced force, it may develop plastic hinging before yielding of the tension brace, with the undesirable resulting plastic collapse mechanism shown in Figure 9.30. Khatib et al. (1988) and others have shown that such beam flexibility and plastic mechanism can cause inelastic deformations

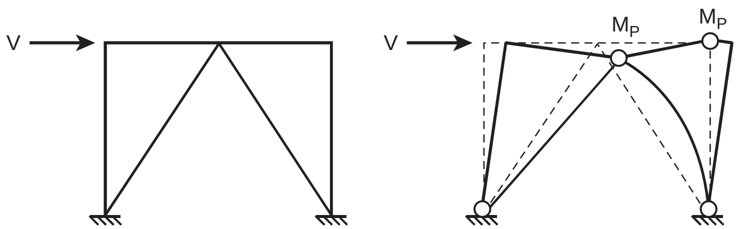

Figure 9.30 Undesirable plastic collapse mechanism of inverted V-braced frame having plastic hinge in beam.

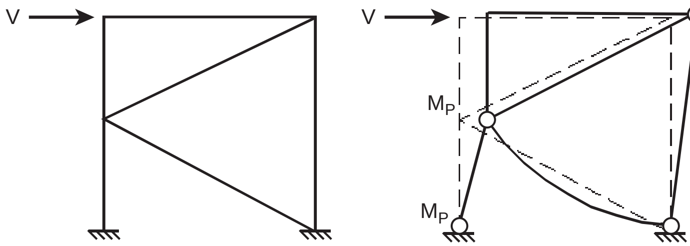

Figure 9.31 Plastic collapse mechanism of K-braced frame, with plastic hinge in column.

to concentrate in a single level of a multistory frame, with detrimental consequences.

The above concepts also explain why some braced frame configurations are undesirable in seismic regions. For example, in a K-type braced frame (Figure 9.31), the unequal buckling and tension yielding strengths of the braces would create an unbalanced horizontal load pulling at midheight of the columns, jeopardizing the ability of the structure to resist gravity loads.

The 1992 edition of the AISC Seismic Provisions indirectly attempted to account for the above behavior by requiring compression braces in V-, Inverted V-, and K-braced frames to be designed for a force 50% greater than otherwise calculated. More appropriately, the demands due to such unbalanced forces were first explicitly considered in the 1997 AISC Seismic Provisions, as a special case, for the design of V-type and inverted V-type braced frame—whereas use of K-braced frames became prohibited in SCBFs (but remained permitted in OCBFs of two stories or less, until AISC 341-05).

Consistently with the philosophy introduced in 1997, but affected by the changes outlined in Table 9.1, the AISC 341-10 requires that beams in SCBFs be designed to resist a maximum unbalanced vertical load calculated using the expected yield strength ($R_y F_y A_g$) of the braces in tension, and 30% of the brace buckling strength in compression, expressed as 0.3 times the lesser of $R_y F_y A_g$ and $1.14 F_{cre} A_g$, where F_{cre}, is F_{cr}, determined per AISC 360 Chapter E using expected yield stress $R_y F_y$ in lieu of F_y (note that 1.14 is equal to 1/0.877). As a safeguard in case of plastic hinging in the beam at the point where the braces meet, beams are required to be continuous between columns and capable of resisting their tributary gravity loads together with the above unbalanced vertical load, assuming that the braces provide no support.

Note that the demands on the beams due to the unbalanced load created by the unequal tension and compression strength scan be mitigated by alternating V- and inverted V-braced configurations from story to story to create an X-bracing patterns spanning two stories at a time, as done in Figure 9.3a. Another strategy, known as the "zipper column" is described in Section 9.4.2.

9.3.3.2 X-Braced Frame Configurations

For any other brace configuration, the same capacity design principles described above are applicable. Arguably implicit in the intent of previous editions, AISC 341-10 for the first time explicitly specified that all parts of an SCBF should be analyzed accordingly, considering a first case in which the braces in compression have reached their expected maximum buckling strength, and another in which they reach their expected postbuckling strength—together with the other braces reaching their expected strength in tension.

For X-braced and split-X-braced configurations, corresponding free-body diagrams are shown in Figure 9.32. Using the first free-body diagram for a beam supported at midlength by the intersecting braces, for a symmetrically loaded frame (i.e., $P_1 = P_2 = P$), the axial load in the beam can be calculated as:

$$\sum F_x = 0 = 2P + (T_{i+1} + C_{i+1}) \cos \theta_{i+1} - (T_i + C_i) \cos\theta_i \tag{9.9}$$

where the nominal member forces in stories i and $i + 1$ are considered. Similar equilibrium equations could be written for nonsymmetrically loaded frames (i.e., $P_1 \neq P_2$). In this case, half of the beam is in compression (P_1) and half in tension (P_2).

Recognizing that braces in adjacent stories may not reach their maximum strengths simultaneously, Redwood and Channagiri (1991)

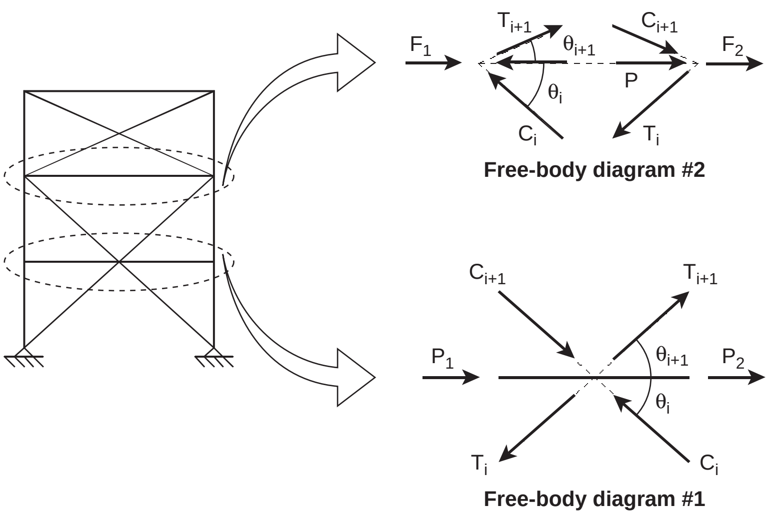

FIGURE 9.32 Free-body diagrams for calculating beam actions.

suggested that only 75% of the brace strengths in story $i + 1$ be considered for beam design:

$$P = 0.5\,(T_i + C_i)\cos\theta_i - 0.5\,(0.75)(T_{i+1} + C_{i+1})\cos\theta_{i+1} \tag{9.10}$$

Lacerte and Tremblay (2006) suggested that 50% of the brace strengths in story $i + 1$ should be used (instead of 75%) to adequately capture the variations observed in nonlinear inelastic analyses. Note that use of this 75% factor, although aligned with capacity design objectives, is not explicitly required by AISC 341-10.

In the second free-body diagram, the beam spans the full width of the braced bay, and brace buckling and yielding will produce an internal redistribution of forces. Even for the case of earthquake loads symmetrically applied to the frame, this beam acts as a load-transfer member. For a given ratio of F_1/F_2 dictated by the characteristics of the horizontal load path, the axial force in the beam, P, is obtained by solving the following two equations of equilibrium:

$$P = (T_{i+1})\cos\theta_{i+1} - (C_i)\cos\theta_i + F_1 \tag{9.11a}$$

$$P = (T_i)\cos\theta_i - (C_{i+1})\cos\theta_{i+1} - F_2 \tag{9.11b}$$

and consequently,

$$F_1 + F_2 = (T_i + C_i)\cos\theta_i - (T_{i+1} + C_{i+1})\cos\theta_{i+1} \tag{9.11c}$$

where the value of P should be taken as the maximum value calculated using either the expected buckling strength or expected post-buckling strength for the compression braces above and below the beam.

When these axial forces are combined with the moments acting on the beams due to gravity and other seismic actions, the adequacy of the beams can be checked with the standard beam-column design equations.

9.3.3.3 Transfer Beams for Irregular Layout

Although Section 9.3.3 has focused so far on the beams in the braced bays, similar capacity design principles must also be used in other situations to ensure adequate transfer of structural forces, particularly when irregular bracing layouts are encountered. For example, in addition to the forces obtained from elastic analysis, unbalanced horizontal forces due to unequal tension and compression strengths of the braces must be considered to design the transfer beams linking the two incomplete braced frames in Figure 9.33. The worst case demands shall be considered, as both elastic and inelastic behaviors develop at different stages of frame response, and continuity of the load path must be maintained throughout the entire response.

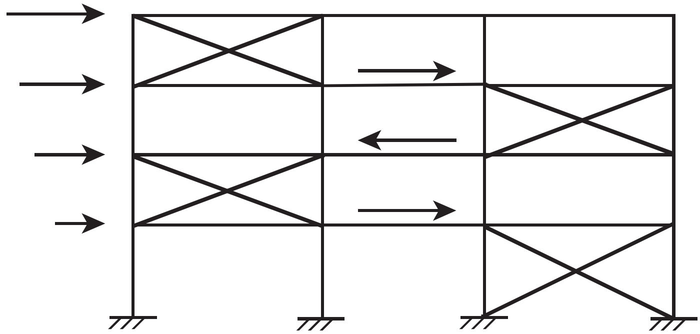

Figure 9.33 Forces in transfer beams between incompletely braced bays.

9.3.4 Column Design

The need to protect columns that resist gravity loads is obvious and recognized. Capacity design provides a reliable approach to calculate the maximum and minimum demands on columns when a complete sway mechanism develops. However, in medium and high rise structures, evidence from inelastic dynamic analyses indicates that brace yielding is not simultaneous at all the stories across the building height, and that using capacity design in those instances can be conservative (also leading to high foundation design forces).

Some of the approaches that have been proposed to estimate column forces are presented here, understanding that results from nonlinear inelastic analysis can be used to provide upper bounds to the values obtained by these methods.

9.3.4.1 Column Forces per Capacity Design

Capacity design remains a safe approach to calculate column forces for design. In spite of its conservatism for taller frames, it is appropriate for low-rise frames and the upper stories of medium- and high-rise buildings where all braces may develop their capacity simultaneously. In a study of inverted V-braced frames of up to 12 stories, Tremblay reported instances of braces simultaneously at their maximum buckling strength over the entire building height (Tremblay and Robert 2001); instances of braces yielding in tension simultaneously over four consecutive stories were commonly encountered in a later study on braced frames of split-X configuration (e.g., Figure 9.3a configuration) (Lacerte and Tremblay 2006).

Using a capacity design approach, the columns in the braced bay should be designed to remain elastic for gravity load actions acting with the forces delivered by the braces, assuming that the braces achieve their expected tensile strength together with their expected buckling or postbuckling strength (whichever gives the greater column forces, similarly to the approach described for beams).

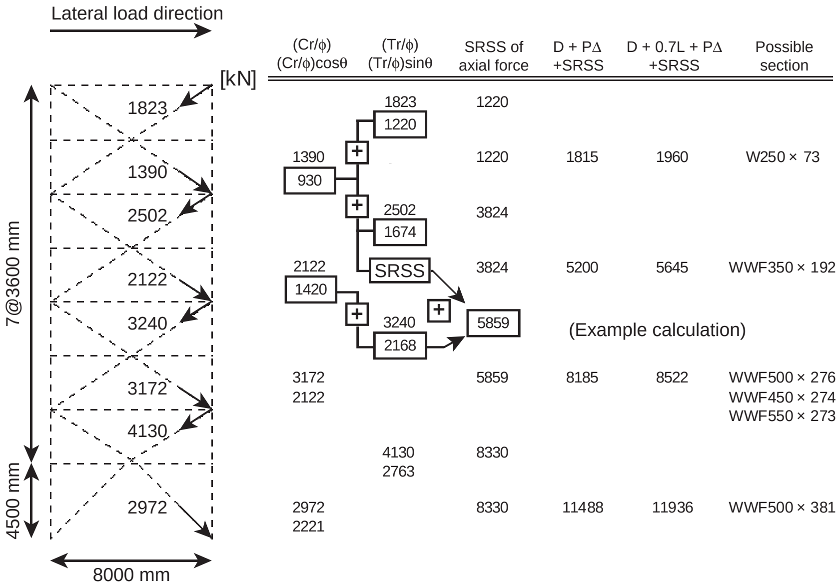

Figure 9.34 SRSS estimates of column forces in an eight-story CBF analyzed by Redwood and Channagiri (1991).

For example, for the frame in Figure 9.34 (as done in Section 6.2.2), maximum axial compression on columns would be obtained by summing the vertical components of the expected tension and compression brace strengths (e.g., that sum, not shown in Figure 9.34, would be 12,297 kN for the first-story column).

Note that in a V- or inverted V-braced frame, the shears at the ends of the beams, due to the unbalanced forces applied in their span, would also add to the demands on the columns.

9.3.4.2 Column Forces per AISC Amplified Load Combination Method

AISC 341-02 introduced an "amplified seismic load" concept to "account for overstrength of members of the Seismic Load Resisting System" to expedite design in specific instances identified by the Seismic Provisions. The approach was expedient, implementing a special load combination for which $\Omega_o E$ was used instead of the earthquake loads, E, in load combinations prescribed by the applicable building code, where Ω_o is a seismic overstrength factor (Chapter 7). Among many uses, this amplified seismic load approach was specified by AISC 341-02 and 341-05 to determine axial forces to consider for the design of columns; these axial forces were also to be considered while neglecting concurrently acting flexural forces resulting

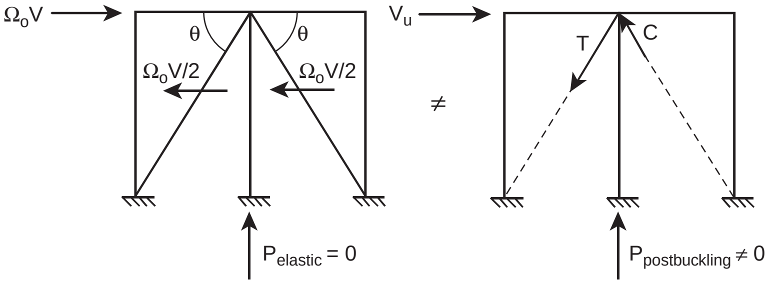

FIGURE 9.35 Comparison of design forces for a middle column from amplified elastic analysis results and from capacity design principles.

from story drifts. No references were provided to substantiate how this arbitrary procedure could approximate comparable column demands obtained from capacity design procedures or nonlinear time-history analyses.

The frame in Figure 9.35 provide one example of how the amplified seismic load method fails to predict correct appropriate column design forces: results from elastic analysis indicate that each brace resists half of the lateral load applied to the frame, and no force is applied to the middle column, whereas postbuckling analysis using capacity design principles correctly predicts that column to be subjected to compression forces due to the postbuckling behavior of the compression brace.

AISC 341-10 retained the amplified seismic load concept for a number of purposes, in which the effects of horizontal forces including overstrength are defined as E_{mh} (set as equal to $\Omega_o E$ in ASCE-7), but specified that E_{mh} be defined based on capacity design principles in a number of instances. For the design of SCBF columns, beams and connections, AISC 341-10 specifies the use of load combinations using the amplified seismic load in which E_{mh} shall be taken as the larger force determined from "(1) an analysis in which all braces are assumed to resist forces corresponding to their expected strength in compression or in tension, and (2) an analysis in which all braces in tension are assumed to resist forces corresponding to their expected strength and all braces in compression are assumed to resist their expected postbuckling strength"—effectively implementing capacity design principles.

As an upper bound, column forces obtained from that AISC 341-10 procedure need not exceed the values that would be obtained either from a nonlinear analysis, or from an elastic analysis using the amplified seismic loads applied on a model of the structure with all of its compression braces removed, that latter exception being only appropriate in those instances where the postbuckling columns compression strength case gives the more critical column demands (e.g., as in Figure 9.35). Considering that $0.3P_n$ in compression corresponds to only 4% and 15% of AF_y when $KL/r = 200$ and 100, respectively, elastic analysis of a CBF frame omitting the compression braces from the model is expedient and could give conservative column forces in those cases (provided that these analysis results also give forces in the tension braces equal to their yield strengths). For cases where the maximum compression strength of the braces gives more critical column demands (e.g., in an inverted V-braced frame), omitting the compression braces from the analysis would erroneously ignore the forces applied by the compression braces on the columns.

For design expediency, AISC 341-10 also allows columns to be designed for these axial forces while neglecting concurrently acting flexural forces resulting from story drifts (unless these moments are due to loads applied to the columns between story levels). This is not rigorously correct, because variation of up to 0.025 rad in interstory drifts at adjacent levels, which develop as a consequence of the brace inelastic behavior and subjects the columns to significant flexure (MacRae et al. 2004, Richards 2009, Sabelli 2001). Tests by Newell and Uang (2008) demonstrated the ability of heavy W14 columns of standard story-height length and having width-to-thickness ratios in compliance with AISC 341, to achieve drift capacities of 0.07 to 0.09 rad while withstanding axial force demands of up to 75% of their nominal axial yield strength, corresponding to plastic rotation capacities of approximately 15 to 25 times the member yield rotation. This suggests that heavy SCBF columns may be forgiving to the simplification permitted by AISC; future research may help determine the range over which these findings can be generalized.

9.3.4.3 Column Forces per Obsolete SRSS Method

Redwood and Channagiri (1991) proposed a square-root-sum-of-the-squares (SRSS) method to reduce demands on columns accounting for the fact that yielding does not develop at all stories simultaneously. The method sums the expected tension and compression brace forces of the first two braces above the column at the story under consideration, with an SRSS combination of the forces coming from the other braces at the stories above. The approach is illustrated for an eight-story CBF in Figure 9.34. For example, at the fourth floor, the use of the SRSS procedure results in a design axial force of 5859 kN, rather than the design axial force of 7412 kN that is obtained through capacity design procedures.

However, for a number of reasons, the method has been found to be unconservative when verified against the results from nonlinear time history analyses using some of the substantially stronger ground motion time history records that have become customarily used since 1991 (Lacerte and Tremblay 2006). Therefore, the SRSS method is presented here for completeness of historical perspective, but is not recommended for use anymore. A hybrid approach, considering the sum of forces from capacity design over a set number of stories, together with a SRSS combination of the forces from the other stories above, has not been proposed at this time.

9.3.4.4 Lateral Forces and Inelastic Rotation at Brace Point Between Floor Levels

Small accidental eccentricities in the loads applied to a beam by braces can distort it in a manner similar to what is shown in Figure 9.36. Similar torsional behavior was also experimentally observed by Schachter and Reinhorn (2007). To prevent beam instability at the braces connection point, beams in SCBFs and OCBFs must be laterally braced at their point of intersection with the braces, or alternatively be demonstrated to have sufficient out-of-plane strength and stiffness to ensure their stability. AISC 360 (Appendix A) specifies the required strength and stiffness of lateral braces.

9.3.5 Connection Design

Bolted or welded gussets are frequently used to connect braces to beams and columns in braced frames. Braces of large cross-section are sometimes directly welded to the beams and columns. Capacity design principles dictate the design of all other connections in the braced frame, considering the worst combined demands of braces tension and compression strengths, as described earlier.

Figure 9.36 Inelastic rotation at brace connection point in absence of lateral bracing.

All connections in a concentrically braced frame should be designed to be stronger than the members they connect, allowing the bracing members to yield and buckle per the intended plastic mechanism. Consequently, to accommodate the inelastic cyclic response that typically develops during a severe earthquake, connections must be designed to resist the expected tensile strength of the braces ($= R_y A F_y$), and, as a separate condition, resist the maximum compression strength of the brace acting together with the moment that develops at the flexural plastic hinge.

Note that when gussets are used, flexural hinging at the connection may develop in the gusset itself, or alternatively in the brace itself, in which case the gusset must be able to elastically resist the expected plastic moment of the brace magnified to account for some strain hardening (i.e., typically $1.1R_y M_p$ of the brace) acting simultaneously with a force equal to the maximum compressive brace strength. Net section fracture of the brace (e.g., Figures 9.37a to c), gusset buckling (e.g., Figure 9.37e), and weld failures (e.g., Figure 9.37d) are examples of undesirable failure modes; plates welded to increase brace thickness at a brace net section, and gusset stiffeners (Figure 9.38), are possible strategies to prevent such failures. Similar capacity design procedures are then used to size the design the welded or bolted parts of the connection details.

Typically, when braces buckle in the plane of their gusset, the gusset is designed to be stronger than the hinging brace. However, when braces buckle outside the plane of the gusset, plastic hinging of the gusset is preferred, because the gusset thickness required to develop hinging in the brace in that case would be substantial, and because the out-of-plane buckling behavior of braces having thicker gusset is not necessarily more ductile (Roeder et al. 2009); hinges in rectangular HSS braces have a lower low-cycle fatigue life than hinges in solid gusset plates.

To allow a plastic hinge to form in a gusset plate without excessive local straining of that plate, the commentary to AISC 341 recommends that the brace terminates at a point on the gusset such that it provides a free length between the end of the brace and the assumed line of restraint on the gusset perpendicular to the brace. Per the recommendations of Astaneh et al. (1982, 1986), the minimum recommended free length is equal to two times the gusset plate thickness (Figure 9.39), but kept short enough to preclude gusset buckling. Typical gussets sized in compliance with this recommendation are shown in Figure 9.40.

To reduce the sometimes large gusset plates that result from application of that recommendation, which can also induce local yield deformations in the beam and column, Lehman et al. (2008) proposed an alternative gusset yield pattern following an elliptical yield line path. Experimental and analytical work demonstrated that

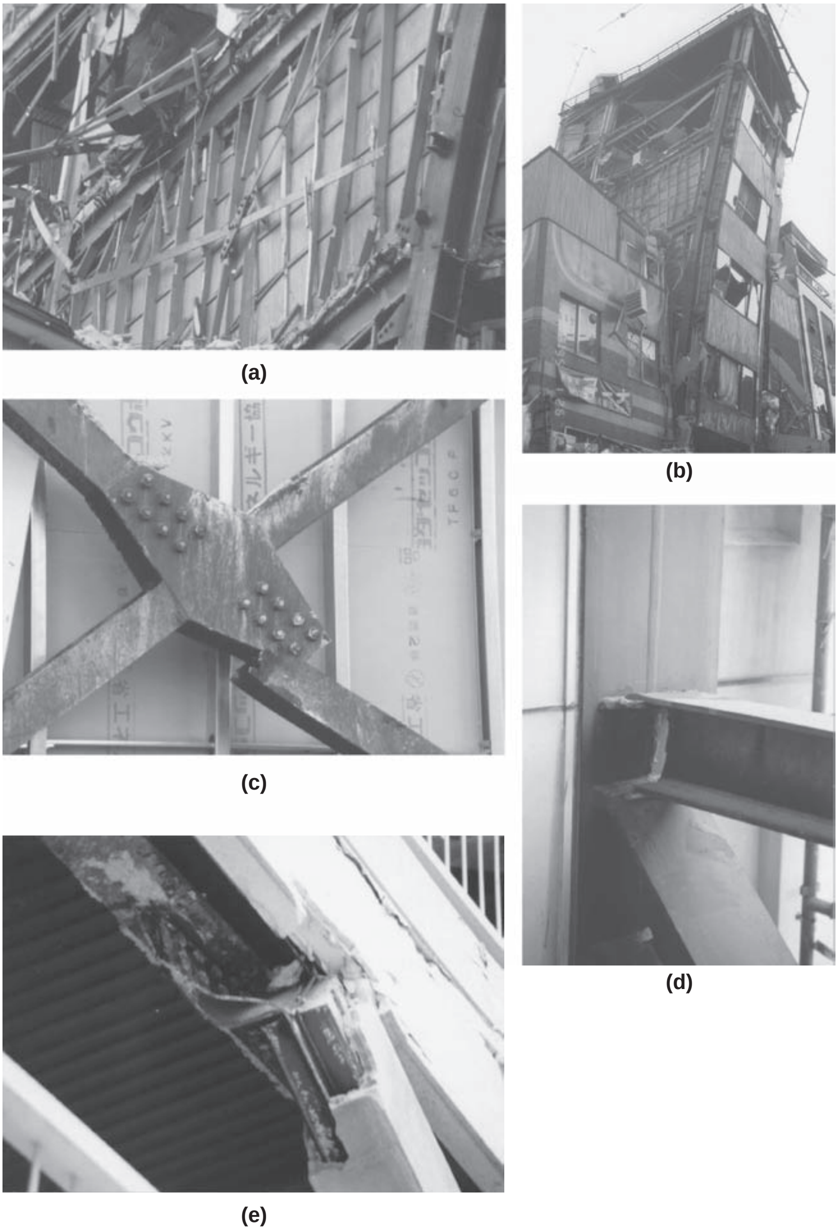

Figure 9.37 Undesirable failure modes in concentrically braces frames: (a) net section fracture of flat-bar brace; (b) global view of same building; (c) net section fracture of W-shape brace; (d) beam weld fracture; (e) gusset buckling and fracture.

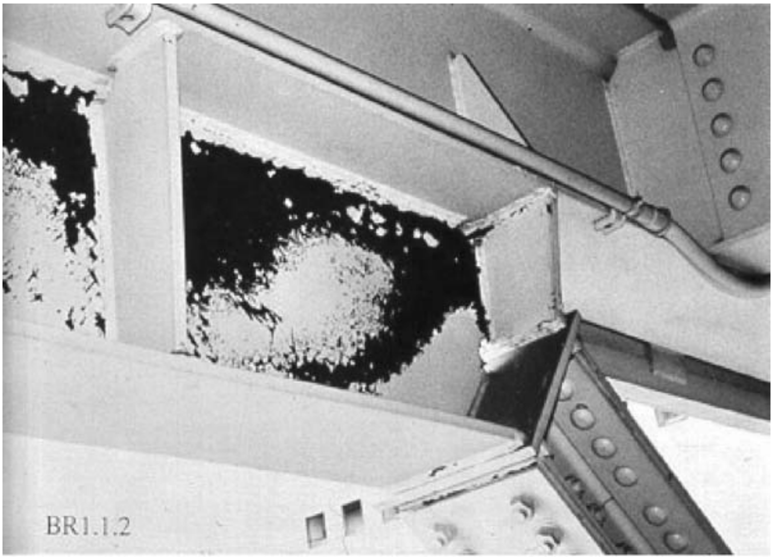

FIGURE 9.38 Stiffened gusset showing evidence of ductile yielding. (*Courtesy of M. Nakashima, Disaster Prevention Research Institute, University of Kyoto, Japan.*)

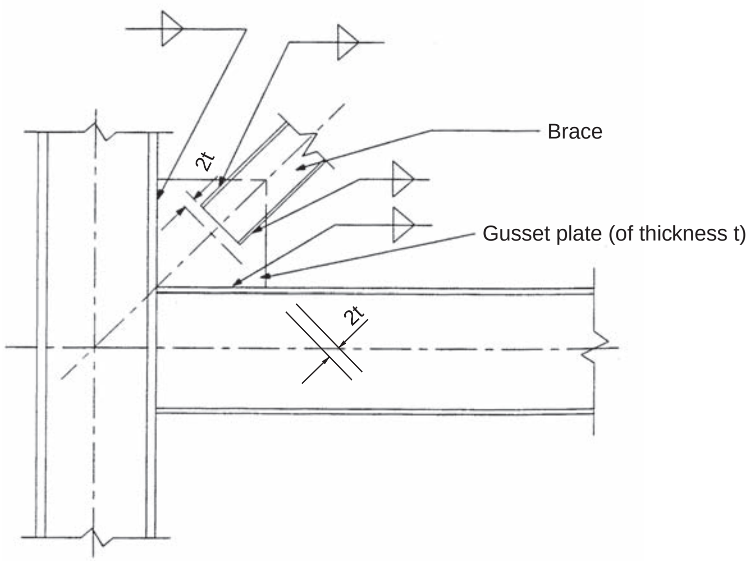

FIGURE 9.39 Brace-to-gusset plate requirements for out-of-plane buckling of braces (*AISC 1995*).

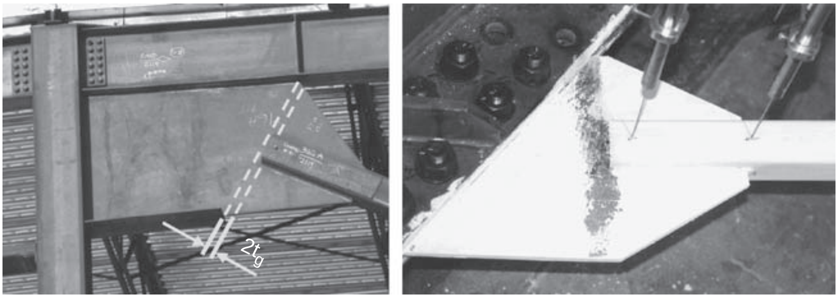

(a) (b)

Figure 9.40 Gussets with recommended free length: (a) implementation in a steel structure; (b) evidence of plastic hinging (revealed by flaked plate) during testing. (*Courtesy of Robert Tremblay, Département des génies civil, géologique et des mines, EcolePolytechnique, Montréal.*)

optimal performance was achieved with a clearance width of six to eight times the gusset thickness (Figure 9.41).

Kiland and Sabelli (2006) presented a gusset detail for which a concentric stiffener that strengthens a corner gusset against out-of-plane buckling is extended and connected to the brace. The stiffener plate is provided with a free length that permits its plastic hinging, and oriented to facilitate in-plane buckling of the brace. Experimental results (Lehman et al. 2010, Tremblay et al. 2008) demonstrated satisfactory gusset inelastic behavior (Figure 9.42). By analogy with the gusset detail shown in Figure 9.40, a minimum free length equal to twice the thickness of the knife-edge is recommended.

Beyond the above requirements, gussets are designed per the requirements of AISC 360. However, note that when excessive gussets sizes are obtained (Figure 9.43—although the design assumptions and circumstances that led to those strange and unusually large gussets are unknown), the designer should consider braces directly welded to the frame (i.e., without gussets) or steel plate shear walls (Chapter 12) as more cost-effective options.

Finally, note that proprietary braces and connections have also been developed as options to conventional brace connection details. Manufacturers of these systems should be consulted to obtain information on their cyclic inelastic performance and failure modes, as well as forces to consider for capacity design purposes.

9.3.6 Other Issues

Capacity design principles are applicable for the design of all components within the braced frame, but also to which the frame connects, particularly when the failure mode of these components is not ductile. Failure of base connections (Figure 9.44) or of structural elements where truss members connect (Figure 9.45) will negate all efforts invested to ensure ductile behavior of the structural system.

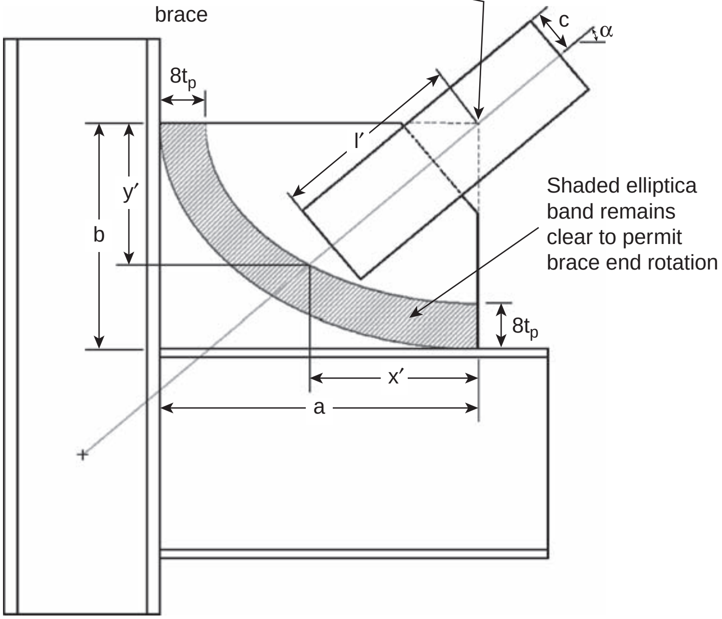

(a)

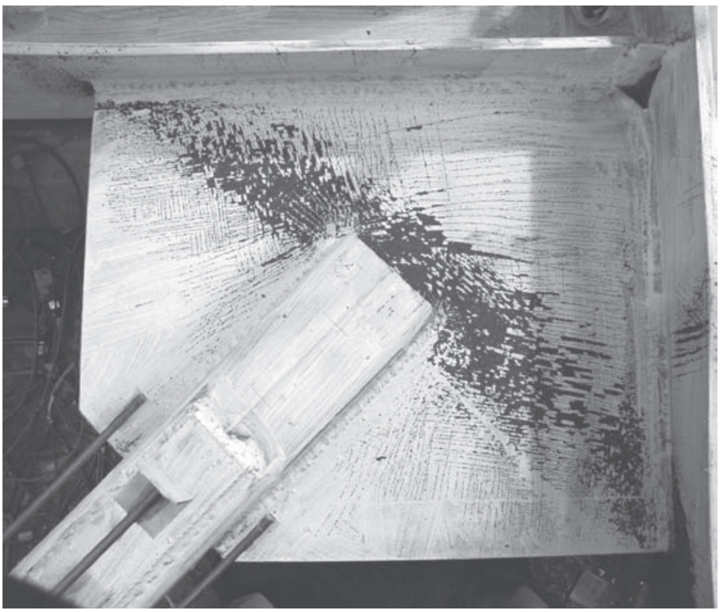

(b)

Figure 9.41 Alternative elliptical yield line concept for gusset design: (a) concept; (b) yielding pattern on correspondingly designed gusset. (*Courtesy of Charles Roeder, Department of Civil and Environmental Engineering, University of Washington.*)

Figure 9.42 Ductile gusset for in plane hinging. (*Courtesy of Charles Roeder, Department of Civil and Environmental Engineering, University of Washington*.)

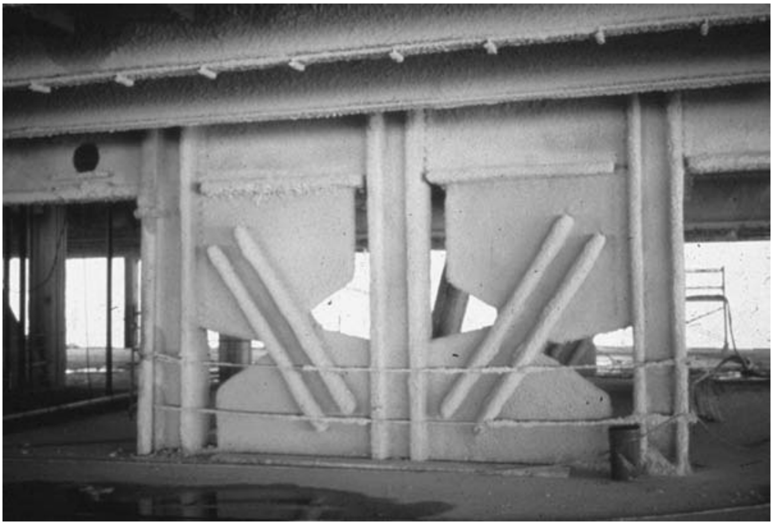

Figure 9.43 Disproportionate gusset plate sizes. (*Courtesy of J. Keith Ritchie, Canada.*)

Particular attention must be paid to column splice details. AISC only permits complete penetration groove welds in welded column splices because partial penetration groove welds perform poorly under cyclic loading (Bruneau and Mahin 1990). AISC 341 also requires that column splices be designed to develop at least 50% of the lesser

Figure 9.44 Example of failed column base connection.

Figure 9.45 Failed brace anchorage.

available flexural strength of the connected members, and a shear strength equal to $\Sigma M_{pc}/H_c$ where ΣM_{pc} is the sum of the nominal plastic flexural strengths, $F_{yc}Z_c$, of the columns above and below the splice, and H_c is the clear height of the column between beam connections. This is consistent with observations that columns can be subjected to large moments due to differences in interstory drifts during brace buckling and yielding (see Section 9.3.4).

9.4 Other Concentric Braced-Frame Systems

Although CBFs are one of the oldest structural systems, as described in Section 9.1, many innovative concepts have been proposed to enhance energy dissipation and seismic performance, building on the general principles and knowledge presented earlier. A few of these are briefly summarized in this section.

9.4.1 Special Truss Moment Frames (STMF)

Goel and Itani (1994) proposed a Special Truss Moment Frame (STMF) concept to resist earthquakes by dissipating seismic energy in specially detailed ductile truss elements. It is intended as a solution based on capacity design principles for long-span moment frames where trusses must be used instead of regular W-shape beams. STMFs have a well-defined middle special segment detailed to exhibit stable hysteretic behavior while undergoing large inelastic deformations, whereas the parts of the truss outside of that special segment are designed to remain elastic (Figure 9.46). In the X-diagonal configuration of the special segment, the braces are detailed to dissipate energy by elongation in tension (following principles similar to CBFs) in addition to plastic hinging of the top and bottom chords of the truss. In a Vierendeel configuration of the special ductile segment, the braces are removed over the segment, and the top and bottom chords of the truss provide the energy dissipation by developing plastic hinges. AISC 341 specifies minimum requirements for their design, whereas detailed design guidance and examples are presented by Goel et al. (1998), and Chao and Goel (2008a, 2008b).

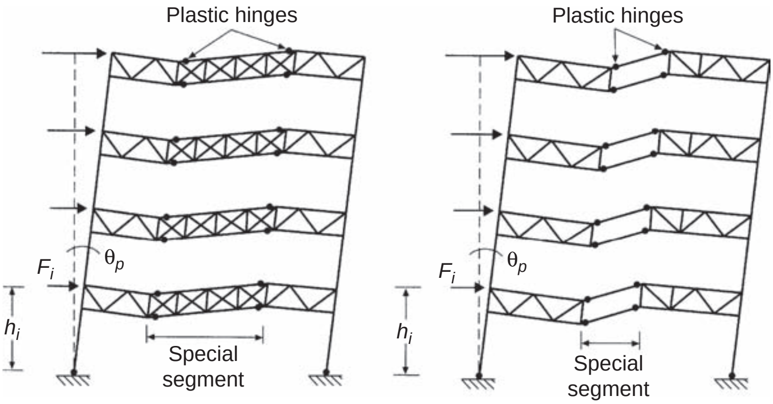

Figure 9.46 Yield mechanism in STMF. (*Courtesy of S. Goel, Department of Civil and Environmental Engineering, University of Michigan.*)

9.4.2 Zipper Frames

Khatib et al. (1988) proposed the zipper-frame concept as a way to better distribute energy dissipation across the height of CBFs and prevent concentration of energy dissipation in a single story. The concept consists of using a vertical member spanning the height of the frame, except for the first story, and linking the beams at their brace connection points. The original design intent was to spread the unbalanced vertical forces created by unequal tension and compression strengths of the braces to all of the beams, thus mitigating the loss of story strength that would otherwise develop when compression strength degradation of the braces occurs in a particular story. In the case of flexible beams developing significant vertical deformations or weak beams developing plastic hinges under the unbalanced loads, tying all the brace-to-beam intersection points together also forces the compression braces over the entire frame height to buckle simultaneously, and thereby better distribute the energy dissipation over the height of the building. Whittaker et al. (1990) reported that simultaneous brace buckling over the height of a building produces a single-degree-of-freedom mechanism, resulting in a more uniform distribution of damage over the height of the building. Nonlinear time-history analysis by Khatib et al. (1988) demonstrated this for zipper frames, with more uniform distribution of inelastic response over frame height than for other brace configurations.

Analyses by Tremblay and Tirca (2003) indicated dynamic instability of zipper frames when subjected to severe near-field and subduction earthquake ground motions, but more importantly reported that zipper struts along the frame height transferred the unbalanced vertical forces up or down in a complex manner. This makes their design per capacity design principles problematic. To provide a more systematic load path, Leon et al. (2003) proposed a "suspended zipper frame" in which the top level braces are designed to behave as an elastic "hat truss" to prevent overall collapse. Information on design recommendations and experimental validations of the concept (Figure 9.47) are presented by Yang et al. (2008a, 2008b) and Schachter and Reinhorn (2007). Note that AISC 341 provides no specific design requirements for zipper frame systems, but refers to the system in its commentary.

9.5 Design Example

The following section illustrates the design of a Special Concentrically Braced Frame (SCBF). The design applies the requirements of ASCE 7 (2010) and AISC 341 (2010). The example is not intended to be a complete illustration of the application of all design requirements. Rather, it is intended to illustrate key analysis and proportioning techniques that are intended ensure ductile response of the structure.

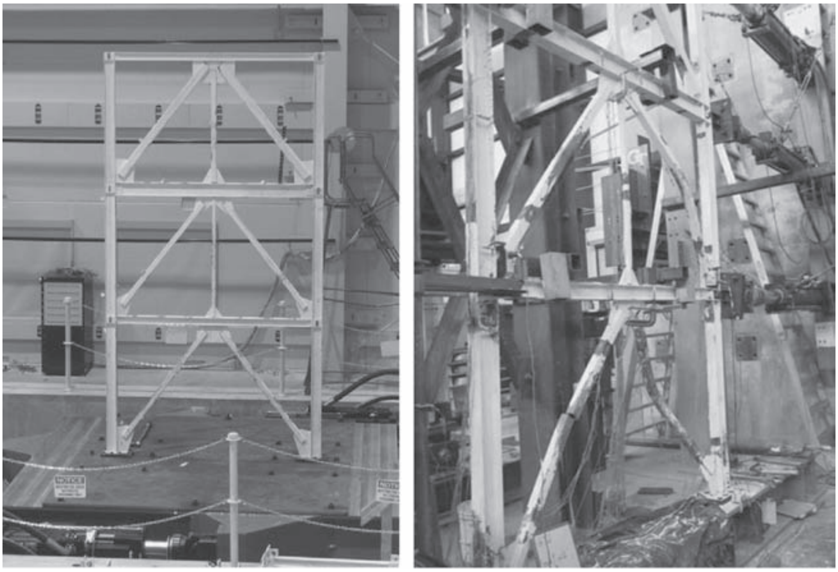

(a) (b)

Figure 9.47 Zipper frame tests: (a) shake table test specimen (*Courtesy of Andrei Reinhorn, Department of Civil, Structural, and Environmental Engineering, University at Buffalo.*); (b) static test specimen. (*Courtesy of C.S. Yang, and R.T. Leon, Department of Civil and Environmental Engineering Georgia Tech.*)

9.5.1 Building Description and Loading

The example building is identical to the one used in Chapter 8 (Special Moment Frames); more detailed seismicity and building information is included in that example. The difference in this case is that Special Concentrically Braced Frames are used. The system seismic design parameters are shown in Table 9.2.

The typical plan is shown in Figure 9.48 and the typical frame elevation is shown in Figure 9.49.

Based on the seismic-design data, a generic seismic response spectrum is constructed in accordance with ASCE 7. Because there is only

R	6
I	1.0
C_d	5
Ω_o	2

Table 9.2 Seismic Design Data

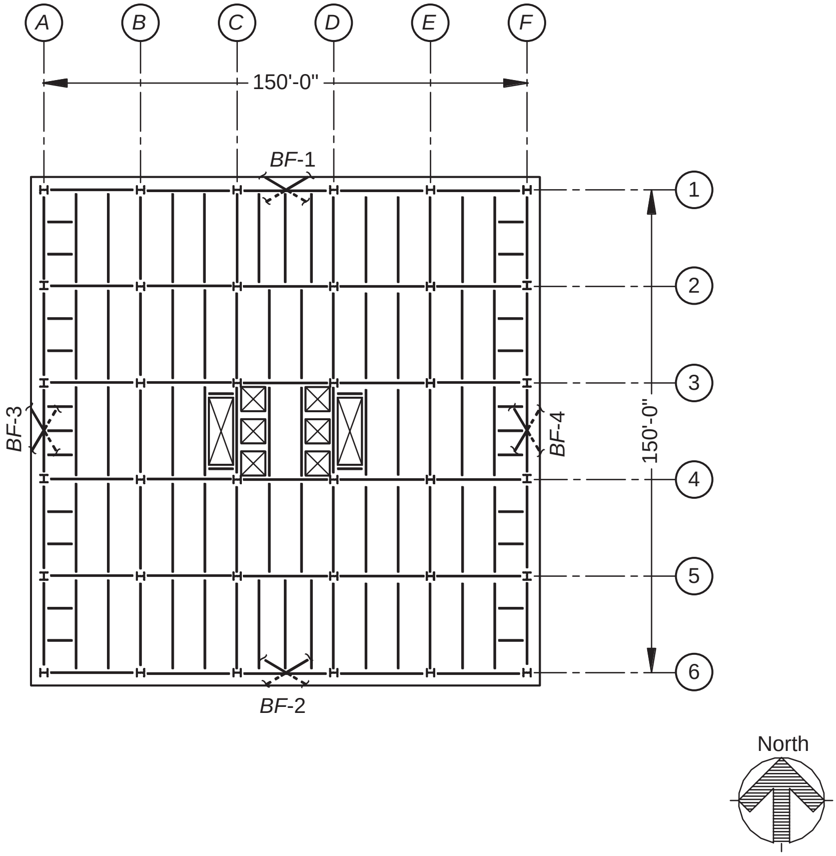

Figure 9.48 Typical floor plan.

one braced bay on each side of the structure, the design shear at every story must be multiplied by a redundancy factor ρ equal to 1.3.

9.5.2 Global Requirements

The structure must be designed to provide both adequate strength and adequate stiffness. Typically strength requirements will govern the design of lower buildings, whereas taller buildings will be controlled by drift. The threshold height is dependent on many factors, including the shape of the response spectrum, the analytical procedure used, and the braced bay configurations and proportions.

Where strength considerations govern, the design process is fairly straightforward: the braced-frame members (beams, columns, and braces) are designed to provide adequate strength, then the columns and beams in the bay are redesigned to preclude their failure when

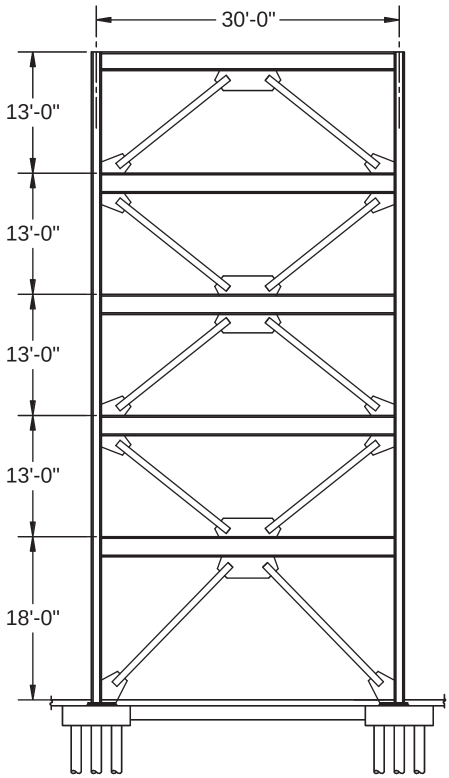

Figure 9.49 Typical frame elevation.

subjected to the forces corresponding to fully yielded and strain-hardened braces. A reanalysis may be performed to confirm that the required brace strength has not been increased because of an increase in frame stiffness (due to change of period on the response spectra when member forces are obtained from dynamic analysis).

Where drift is the governing concern, the process requires more iterations. Any increase in brace strength will in turn impose larger forces on beams and columns when the braces yield. Thus, any stiffening of the frame should be done with the required strength proportioning of the different components (brace, beam, and column) in mind.

9.5.3 Basis of Design

The design of SCBFs is based on the expectation of a global yield mechanism in which braces yield in tension and buckle in compression and plastic hinges form at the column bases. Where frame beams are connected rigidly to columns, hinging in the beam or column is

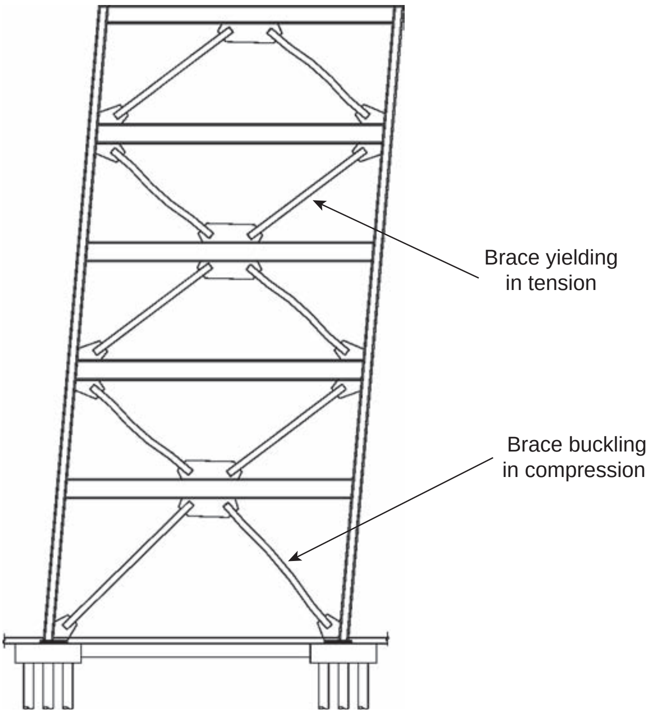

Figure 9.50 Anticipated mechanism.

also anticipated. Otherwise, large relative rotations must be accommodated in the beam-to-column connections. Figure 9.50 shows this mechanism.

Because brace buckling entails loss of strength and stiffness, SCBFs are subject to dramatic force redistributions. To determine maximum design forces, the anticipated mechanism is considered twice: once with maximum brace buckling forces, and again with braces having a reduced, postbuckling strength.

For purposes of these plastic mechanism analyses, the following brace strengths are used:
For the brace in tension:

$$T = R_y F_y A_g \tag{9.12}$$

where A_g is the gross area of the brace.

For the brace in compression (at its maximum force):

$$C_{max} = 1.14 F_{cr} A_g \tag{9.13a}$$

where F_{cr} is the critical buckling stress utilizing a yield strength of $R_y F_y$.

The value of 1.14 corrects for the factor of 0.877 used in AISC 360 equations for flexural buckling strength to account for out-of-straightness effects.

For the brace in compression (at its postbuckled, residual strength):

$$C_{min} = 0.3F_{cr}A_g \tag{9.13b}$$

An elastic analysis is used for preliminary design. Subsequently, two plastic mechanism analyses are performed, with brace forces as described above, to determine maximum forces that beams and columns within the frame must resist. The sizes of these elements are increased based on these forces. The adequacy of the revised design is reconfirmed with another elastic analysis. It is possible that more than one iteration is required to establish a design that satisfies both sets of requirements: those checked in the elastic analysis (member strength adequacy for the design base shear; drift control), and those checked in the plastic mechanism analyses (beam and column strength at the limit state).

The elastic analysis procedure used in this example is a linear Modal Response Spectrum (MRS) analysis. This is typically advantageous due to the reduction in design forces. ASCE 7 permits for this method and the reduction in overturning moment that typically results from this approach compared with the vertical force distribution prescribed by the Equivalent Lateral Force procedure of ASCE 7.

9.5.4 Preliminary Brace Sizing

Based on the results of the elastic analysis, brace sizes are obtained. Table 9.3 shows these sizes, along with their expected strengths in tension and compression as described above.

9.5.5 Plastic Mechanism Analysis

Two plastic mechanism analyses are performed on the frame. These are intended to capture both axial forces corresponding to brace inelastic action and flexural forces at the beams intersected by braces along their length. Although it is anticipated that these brace forces correspond to large drifts, and that columns may develop significant flexural forces at these drifts (due to fixity at beams or varying story drifts), these analyses are not intended to determine such flexural forces. Indeed, it is permitted to neglect them, under the assumption that limited flexural yielding in the column may be tolerated as long as overall buckling is precluded.

For purposes of member design it is sufficient to model the frame with the brace forces corresponding to each mechanism and with zero lateral drift.

Mechanism 1 combines the expected brace tension strength [Eq. (9.12)] with the maximum compression force [Eq. (9.13a)]. Braces are considered to be in compression or tension based on the

Level	Brace Size	Expected Tension Strength $R_y F_y A_g$ (kips)	Expected Compression Strength $1.14F_{cr}A_g$ (kips)	Residual Compression Strength $0.3F_{cr}A_g$ (kips)
Fifth Floor	HSS 6.625 × .312	267.50	142.09	36.43
Fourth Floor	HSS 7 × .500	441.21	246.81	62.98
Third Floor	HSS 8.625 × .500	549.78	396.16	98.79
Second Floor	HSS 9.625 × .500	619.08	489.97	121.15
First Floor	HSS 10 × .625	794.64	561.36	140.24

Table 9.3 Brace Sizes and Expected Strength

first mode displacement. That is, all of those sloping in one direction are considered to be in tension, and those sloping the opposite direction in compression. This assumption can be reversed for the analysis of asymmetric conditions. Note that these forces were derived considering simultaneous yielding of braces in adjacent stories; see Section 9.3.3.2 for a discussion of adjustments to this assumption that have been proposed.

Mechanism 2 combines the expected brace tension strength [Eq. (9.12)] with the residual compression force [Eq. (9.13b)]. The same assumptions regarding compression and tension are used.

Figure 9.51 shows the frame elevation used for both mechanism analyses. Note that the forces acting at each level to produce equilibrium with this plastic mechanism are different than those calculated from elastic analysis; in many cases, they will be much lower than the collector design forces calculated, taking into account the localized effects of higher modes. Modeling of these reactions with springs on both sides of the frame can be used to reflect the anticipated distribution of collector forces.

9.5.6 Capacity Design of Beam

As seen in Figure 9.51, the forces in the plastic mechanisms can impose both flexural and axial forces in each of the beams. The forces can be substantial, especially in the postbuckled mechanism in which the beam provides the majority of the resistance counterbalancing the forces corresponding to the capacity of the braces in tension.

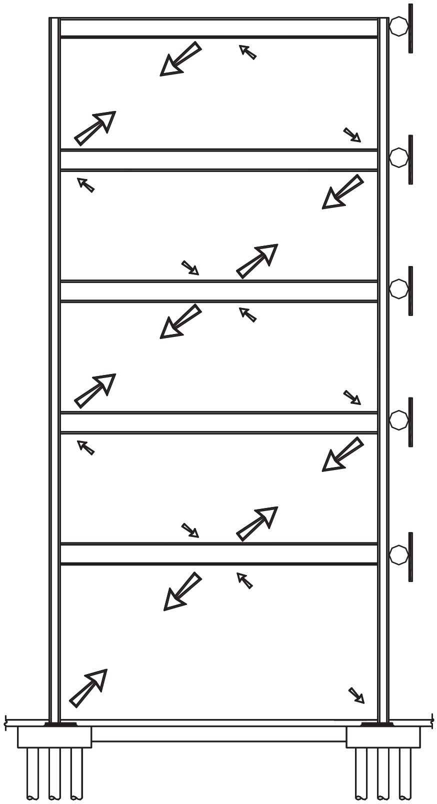

Figure 9.51 Mechanism analysis models.

The seismic axial force in the beam at the second floor is calculated based on the difference in the capacity above and below as follows:

$$F_{i+1} = V_i - V_{i+1} \tag{9.14}$$

$$V_i = (R_y F_y A_{g(i)} + 0.3F_{cr} A_{g(i)}) \cos(\theta_i) \tag{9.15}$$

$$V_2 = 565.25 \text{ kips}$$

$$V_1 = 603.27 \text{ kips}$$

$$F_2 = 38.02 \text{ kips}$$

where F_{i+1} is the total force entering into the frame (corresponding to the plastic mechanism) at level i+1 and V_i is the shear strength (corresponding to the plastic mechanism) at level i.

For simplicity the force is assumed to enter into the frame as two equal forces, one at each column. The axial force in the beam can thus be determined from static equilibrium, with the postbuckling strength case giving the larger axial (and flexural) forces in this case:

$$P_u = \frac{1}{2}(R_y F_y A_{g(1)} + 0.3F_{cr} A_{g(1)})\cos(\theta_1) - (R_y F_y A_{g(2)} + 0.3F_{cr} A_{g(2)})\cos(\theta_2) \tag{9.16}$$

$$P_u = 19.01 \text{ kips}$$

Beam flexural forces are similarly calculated based on the high tension strength and low postbuckled strength of the braces. The vertical force acting downwards on the second-floor beam is:

$$R_u = (R_y F_y A_{g(1)} - 0.3F_{cr} A_{g(1)})\sin(\theta_1) - (R_y F_y A_{g(2)} - 0.3F_{cr} A_{g(2)})\sin(\theta_2) \tag{9.17}$$

$$R_u = 175.97 \text{ kips}$$

These forces are combined with gravity shears and moments in the design of the beam. Assuming a fixed-end beam (and adequate fixity in the column and adjacent beam):

$$M_u = \frac{175.97 \text{ kips} \times 30 \text{ ft}}{8} + 0.7 \text{ kips/ft} \times \frac{(30 \text{ ft})^2}{12} = 712 \text{ kip-ft}$$

A W24 × 76 is sufficient for the combined axial and flexural forces. Note that this large size is due to the change in beam slope from the first to the second level and the change in brace size. Note also that the slab braces the section against lateral-torsional buckling. It also braces against lateral buckling, but not against torsional buckling, which will govern the axial strength.

9.5.7 Capacity Design of Column

A similar approach can be taken with the column, determining maximum forces acting on it from brace expected strengths. Thus, for the column in compression, the seismic axial force for mechanism 1 for this configuration can be calculated as:

$$P_{E_i} = \sum_{i+1}^{n}(1.14F_{cr}A_{g_x})\sin\theta_x + \sum_{i}^{n}\frac{1}{2}(R_y F_y A_{g_x} - 1.14F_{cr}A_{g_x})\sin\theta_x \tag{9.18}$$

The subtractive part of the second term, which represents the beam shear reaction due to the slightly unbalanced vertical force, is minor and is often neglected in the two-story X configuration. Note that the braces do not impart their loads to the column at the same level in all configurations. Care should be taken to ensure that the loads are determined consistently with the configuration used. Free-body diagrams, such as shown in Figure 9.52, are helpful; these should include the beam (and the shear imposed on it by the braces).

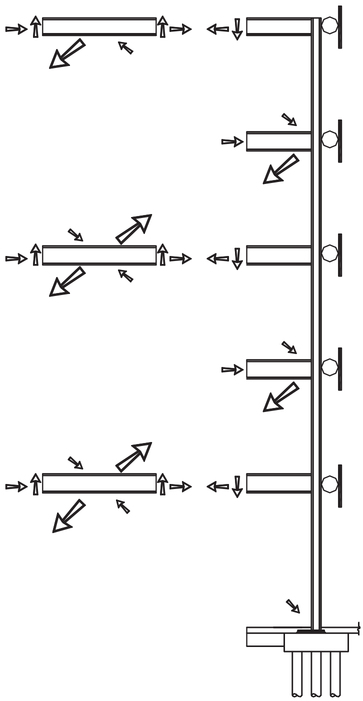

FIGURE 9.52 Free-body diagrams illustrating forces acting on column.

Note that in this configuration, the brace in compression at the first floor does not contribute to the column compression, as it connects at the base. Also, note that in mechanism 2 column axial forces will be significantly less than those from mechanism 1 for this bracing configuration.

Equation (9.18) can be conservatively simplified to:

$$P_{E_i} = \sum_i^n \frac{1}{2}(R_y F_y A_{g_x} + 1.14 F_{cr} A_{g_x}) \sin(\theta_x) \tag{9.19}$$

Thus the seismic axial force in the first-floor column can be calculated as:

$$P_E = 1553.22 \text{ kips}$$

If braces of moderate slenderness are used $(KL/r \leq \sqrt[4]{E/F_y})$ the column design can be simplified. The seismic component of the axial force need not exceed:

$$P_E \, \Omega_o E \tag{9.20}$$

where E is determined from an elastic analysis.

This seismic force is combined with gravity forces for a total load of 1850 kips. The column is designed for an effective length of $KL = 1 \times 18$ ft = 18 ft. A W14 × 176 section may be used.

Although it is in violation of values obtained from free-body diagrams, when designing in compliance to AISC-341-10, for reasons described earlier in this chapter, column flexural forces due to drift are not combined with these mechanism-based axial forces for design of the column. This would not necessarily be the case for design accomplished per other codes or standards.

9.5.8 Iterative Analysis and Proportioning

The capacity design of columns and beams inevitably leads to stiffening of the structure, altering its dynamic properties and possibly increasing the required design base shear. At least one more iteration of analysis is required to ensure compliance with the required base-shear strength. If brace sizes are increased, the beams and columns must be reassessed and another iteration becomes necessary. Otherwise, the capacity design of the beam and columns ensures that they are adequate to resist forces generated by brace yielding.

9.5.9 Connection Design

As discussed earlier, the design of an SCBF anticipates brace behavior that includes

- Tensile yielding
- The development of high compression forces
- Buckling

The first two behaviors are straight forward force requirements. Brace connections are designed for these maximum forces (which are presented in Table 9.3). Design for the higher tension governs most of the connection limit states. The limit states of web crippling (e.g., of a beam web adjacent to a connection gusset plate) and of gusset-plate buckling need only be evaluated for the expected compression strength of the brace, typically somewhat lower than the expected tension strength.

The third behavior requires a connection configured to maintain its integrity even as the brace buckles and undergoes inelastic rotation, typically out-of-the plane of the frame. No calculations are involved in evaluating this requirement. The designer simply selects a brace connection type that has demonstrated this capacity. See Figures 9.39, 9.40, and 9.41 for examples.

9.5.10 Completion of Design

Several items remain to complete the design. These include

- Brace connections
- Column splices
- Base plates
- Foundations
- Diaphragms, chords, and collectors

Although each one of these items is necessary and important, the execution is similar to that of many other components of a building design.

9.5.11 Additional Consideration: Gravity Bias in Seismic Systems

Earthquakes generally impose cyclic accelerations on structures. As these accelerations are not sustained in any single direction, moderate ductility demands in these structures do not generally result in uncontrolled displacements; buildings subject to large inelastic demands undergo inelastic drift in opposite directions at different times during the earthquake, and may be left with a residual drift after the earthquake. Typically, these residual drifts tend to be significantly lower than maximum drifts, but can be substantial at times, particularly for earthquakes excitations having large energy pulses (as observed in some accelerograms recorded near fault ruptures).

As demonstrated throughout this book, because seismic accelerations may act on a seismic system in either direction, seismic systems are conceived, tested, and designed with the expectation of cyclic demands. In real conditions, members of the seismic load-resisting systems tend to have some gravity forces present before any seismic loads are applied. However, such gravity forces tend to have a negligible effect on the yield strength of the system; they act similarly to residual stresses, causing slightly earlier yielding and rounding the transition from elastic to inelastic behavior. If the gravity forces are shared between yielding members ("fuses") and nonyielding members, the gravity forces are shed from the fuses as they yield and are transferred to the other members.

For all seismic systems, it is anticipated that nonfuse members will be designed to support the entire gravity force without reliance on the yielding fuse. For example, a moment-frame beam acting as a transfer girder should be designed to support the gravity forces as a simple-span member. Under cyclic yielding the initial fixed-end moments will "shake down" (see Section 4.5). The fuse (the plastic hinge zone of the beam) will ultimately resist only seismic moments, whereas the nonfuse portion (the rest of the beam span) will resist the entire gravity moment.

Another example of this is the V-braced (or inverted V-braced) frame, discussed in Section 9.3.3.1, in which the beam is designed for the full gravity load (in conjunction with forces imposed by the braces), regardless of the fact that an elastic analysis of the structure shows little of the force resisted in beam flexure. If the gravity forces are accounted for in the design of braces under compression in an SCBF, buckling will occur at the same lateral drift as for a similar system without gravity forces in the braces. The larger braces constitute a source of overstrength for the fully yielded structure. The degree of overstrength is a function of the ratio of gravity force to seismic force in the member.

Special consideration is required when gravity forces cannot be shed and the members of the seismic load resisting system must continue to resist them during (and after) an earthquake. Under such conditions much less structural ductility can be tolerated and both inelastic drift and inelastic member deformation may accumulate much more than in a conventional system.

Consider the structure shown in Figure 9.53. The gravity loads are resisted by a cantilever system whose back span is the braced frame at the top level. This cantilever imposes a lateral force couple on the structure, pulling to the left at the top and pushing to the right at the next level down. The brace at that level is under compression due to the gravity load. At some level of lateral force to the left, the brace will reach its elastic limit and inelastic deformation will occur. Lateral forces to the right, however, must be far greater to cause inelastic deformation; they must first overcome the gravity force and then reach the strength of the brace. Thus, there is effectively a high overstrength in one direction.

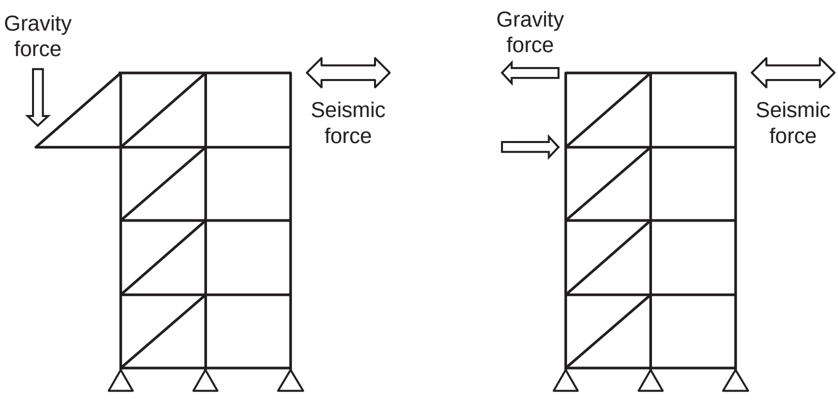

Figure 9.53 Structure with gravity bias.

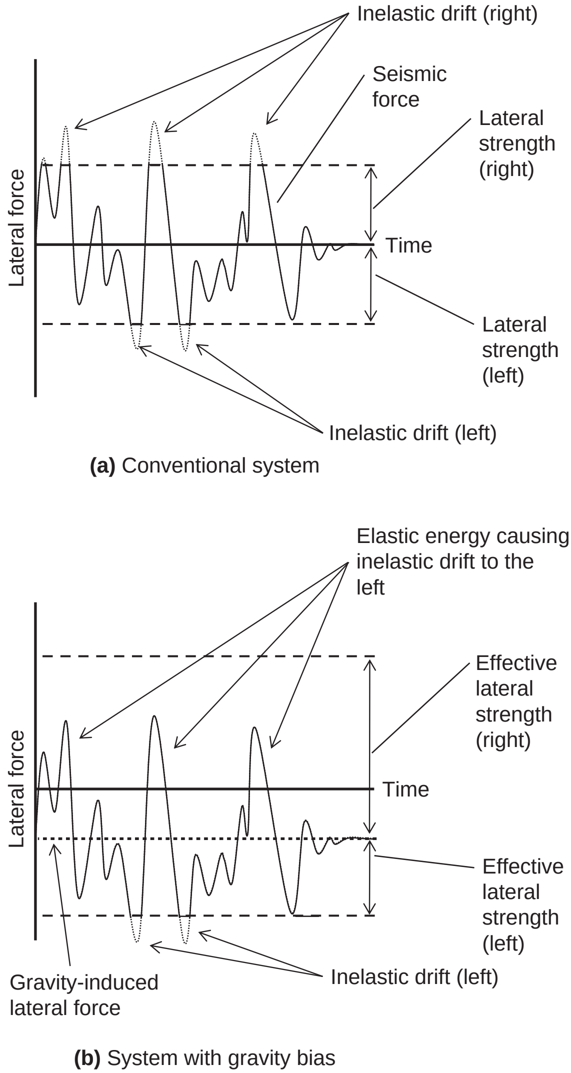

Figure 9.54 Effect of gravity bias on effective lateral strength and ductility demands.

Figure 9.54 conceptually shows the consequences of this bias. The time history response shown in Figure 9.54a is for a conventional structural system having no gravity bias; Figure 9.54b is for a similar system with gravity bias.

In the conventional system, the available strength is measured from zero lateral force. In this system, there are inelastic deformations both to the left and to the right; although these do not return the structure to zero displacement, there is significant cancellation of opposing inelastic drifts.

With gravity bias, the total system strength is effectively increased due to the design for the combined effects of gravity-induced and seismic lateral forces. The effective lateral strength can be defined as the difference between the gravity-induced lateral force and the total lateral strength; this quantity is presumably adequate in the critical direction (to the left in Figure 9.53) and much larger than necessary in the opposite direction (to the right). There are two consequences to this difference in effective strength. First, the additional overstrength in the strong direction, if sufficiently high, can prevent or dramatically reduce inelastic drift in that direction. This precludes any beneficial cancellation of inelastic drifts in opposite directions. Second, the peaks of seismic force pushing the structure to the right are stored as elastic energy, which, when released, result in additional inelastic deformations to the left. In conjunction these two effects cause a rapid accumulation of inelastic drift in the weaker direction. The structure is said to "walk" in that direction under strong cyclic motion. This effect is similar to what would happen in a braced frame having single diagonal braces, which have very different tension and compression behavior, as is discussed in Section 9.3.1.2.

9.6 Self-Study Problems

Problem 9.1 Design the members of the single-story concentrically braced frame shown below for the given loads:

(a) Perform a nonseismic design, that is, select the lightest members that satisfy the AISC 360 requirements for the factored loads.
(b) Perform a seismic design, that is, select the lightest members that satisfy the AISC 341 requirements for Special Concentrically Braced Frames.
(c) Comment on the differences between the designs and explain their causes.

For both designs

- Use square HSS Sections with A500 Gr. B (F_y = 46 ksi) for the braces.
- Use W-shapes with A992 Gr. 50 (F_y = 50 ksi) for the beam and columns.
- Assume pin-ended braces and beam and that the beam is continuous between the columns.
- Consider the beam unbraced laterally over its entire length.
- The columns are laterally braced at their tops.
- When using available design aids, to reference the sections, page numbers, and edition of the design aids used.
- Loads shown are unfactored and the lateral loads shown are seismic loads already reduced for the appropriate R value. Only consider the $1.2D + 0.5L + 1.0E$ load combination.

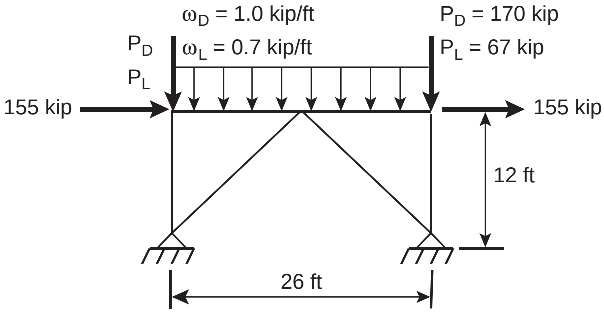

Problem 9.2 For the braced-frame structure shown here, only answer the following specific targeted questions:

(1) For each of the three cases below, calculate the axial force that will be used to design member A-B, and indicate if it is a tension or compression force.

(a) When that force is obtained using the AISC 341 Amplified Seismic Load approach, assuming that the *overstrength factor*, Ω_o, prescribed in the applicable building code is 2.0 in this case

(b) When that force is obtained by a *true capacity design approach* consistent with the AISC 341 requirements when the diagonal braces are A500 Grade B HSS 6.000 × 0.312 members

(c) When that force is obtained by a true capacity design approach consistent with the AISC 341 requirements when the diagonal braces are Buckling Restrained Braces (BRBs) (see Chapter 11). For this problem, consider the core of the BRBs' diagonal braces to be A36 steel plates of area equal to 2 in^2. For this purpose, also use a strain-hardening adjustment factor, ω, equal to 1.4, and a compression strength adjustment factor, β, equal to 1.1. Note: Knowledge presented in Chapter 11 is pre-requisite to completing this part (c).

(2) For the SCBF problem in (1.b) above, calculate the member slenderness and compactness of the HSS 6.000 × 0.312. Calculate these values explicitly, rather than using use precalculated or tabulated values of slenderness and compactness. Then, indicate if the HSS 6.000 × 0.312 is admissible to be used as a brace in an SCBF, in accordance with AISC 341.

Also note that all members are pin–pin in this frame.

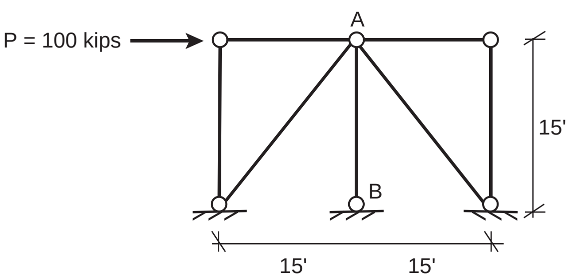

Problem 9.3 The SCBF shown is subjected to a vertical seismic excitation. Braces are HSS 9.625 × 0.50 members of ASTM A500 Grade 42 steel.

(a) Indicate if the HSS braces are acceptable for this SCBF application, and explain why.
(b) Assuming that the HSS braces are acceptable for this SCBF application, calculate what would be the maximum pull-out force to consider for the anchorage at Point A per capacity design approach using the strengths specified by AISC 341.

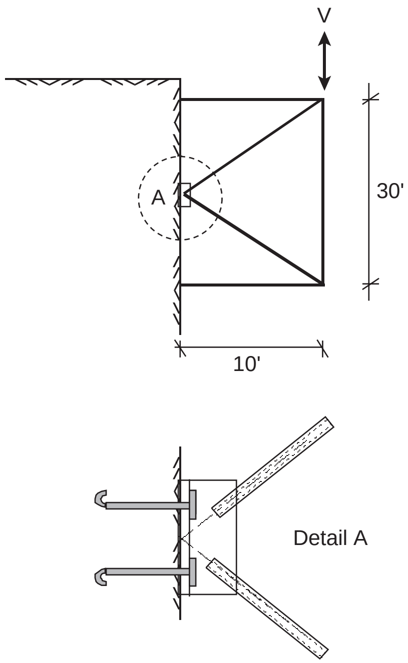

Problem 9.4 For the Special Concentrically Braced Frame (SCBF) shown:

(a) Design the lightest Round HSS (ASTM A500) that can resist the applied factored load shown and that comply with AISC 341.
(b) Design the beam in compliance with AISC 341.

There are no gravity loads acting on the beam. Optionally, the connections and columns could also be designed.

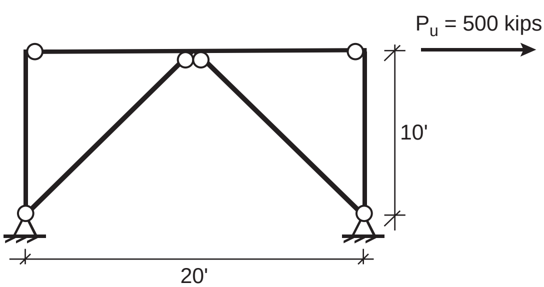

Problem 9.5 For the two-story SCBF located on design lines ② or ③ only, and shown in the figures, for the governing load combination:

(a) Design the braces below the 2nd level (i.e., the braces at the first floor).
(b) Design the girder at the 2nd level (i.e., the lower beam, not the roof beam) assuming $L_b = 15$ ft.
(c) Design the column below the 2nd level (i.e., columns at the first floor).
(d) Check the drifts at the 2nd level considering both shear and flexural drift components.
(e) Indicate what are the values of R, C_d, and Ω_o to consider for the design of this SCBF.

The specified (unfactored) gravity loads are

Roof:	DL = 60 psf	LL = 40 psf
2nd Floor:	DL = 60 psf	LL = 70 psf

Unfactored lateral loads acting on the frames have been obtained from seismic analysis of this building.

Life load reduction factors and wind loads are neglected. All members are assumed pin-ended (K = 1.0). Use W-shape columns and beams (Grade 50), and HSS shapes for braces (Grade 46).

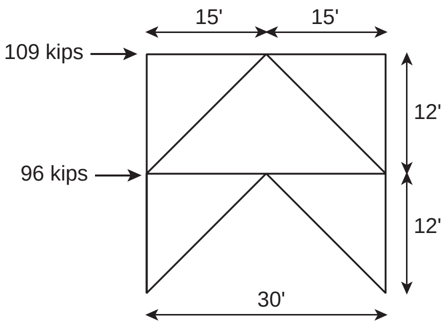

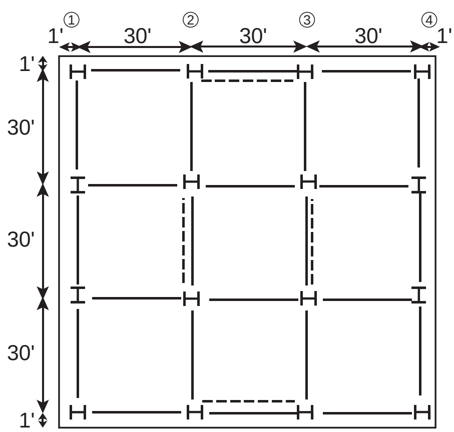

Problem 9.6 The single-story SCBF shown is subjected to an externally applied 100 kips seismic ultimate lateral load F_u (divided into two equal 50 kips load as shown in the figure). Gravity loads are neglected in this problem. For that frame:

(a) Determine if the W10 × 45 diagonal braces have adequate strength and meet the requirements of AISC 341.
(b) Using the W10 × 45 braces [assuming they are acceptable, irrespectively of the answer in part (a) above], check whether a W36 × 260 continuous girder can satisfy the capacity design requirements of AISC 341. Assume $L_b = 7.5'$ and $C_b = 1.0$ here.
(c) Using the capacity design requirements of AISC 341, size the lightest W10 column section meeting all specified requirements. Use brace and girder sizes from (a) and (b) above.
(d) Assuming W10 × 45 braces, design the discontinuous horizontal struts and zipper column in the second figure using the most economical W10 sections for each, on the basis of meeting the requirements of capacity design.

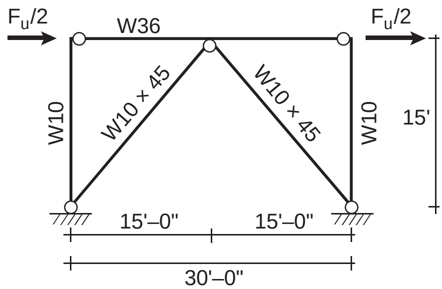

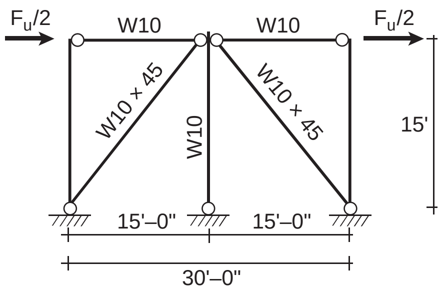

Problem 9.7 Find the maximum lateral load, V, which can be applied on the single-story STMF shown below. Provide a solution, first for the case when the X-diagonals are not present (Vierendeel), second for the case when ½-inch × 3/8-inch flat bar braces are used. It is not required in this problem to verify that the rest of the frame remains elastic. Also calculate M_p of the top and bottom chords of this STMF in the special segment (SS) region.

For this frame, all members are Grade 50 steel and

- Exterior columns are W18 × 86.
- Vertical truss members outside of the S.S. are 2L 2½ × 2½ × 3/16.
- Diagonal truss members outside of the S.S. are2L 3 × 3 × 5/16.
- Each of the top and bottom chords outside of the S.S. consists of 2L 3 × 3 × 5/16.
- Each of the top and bottom chords outside of the S.S. consists of 2L 2½ × 2½ × 3/8.

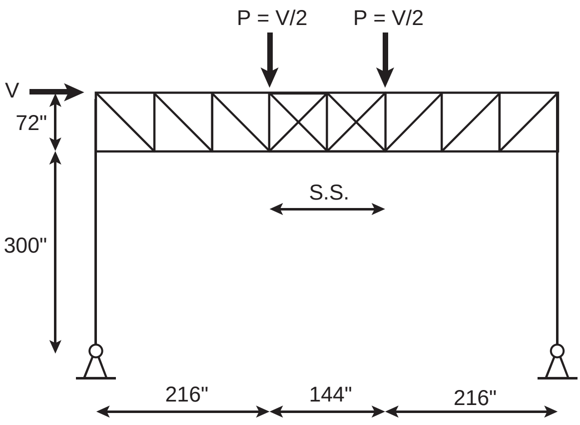

Problem 9.8 (Project-Type Problems)

(1) Write a computer program to develop the axial force versus moment (P-M) interaction diagram of any doubly symmetric beam-column, taking into account buckling of the member with formation of a plastic hinge at its midlength. Compare results from this program with codified design equations and explain the reasons for the observed differences.

(2) Review the exact analytical equations that describe the inelastic cyclic behavior of axially loaded members and provide some numerical examples for slender, intermediate, and stocky members. Examples should be by hand calculations (as much as reasonably possible).

References

AIJ. 1995. *Reconnaissance report on damage to steel building structures observed from the 1995 Hyogoken-Nanbu Earthquake*, Nakashima, M., and Bruneau, M., editors for English Edition. Osaka: Architectural Institute of Japan.

AISC. 1992. *Seismic Provisions for Structural Steel Buildings*. Chicago: American Institute of Steel Construction.

AISC. 1993. *Load and Resistance Factor Design Specification for Structural Steel Buildings.* Chicago: American Institute of Steel Construction.

AISC. 1997. *Seismic Provisions for Structural Steel Buildings*. Chicago: American Institute of Steel Construction.

AISC. 2002. S*eismic Provisions for Structural Steel Buildings ANSI/AISC 341-02.* Chicago: American Institute of Steel Construction.

AISC. 2005. *Seismic Provisions for Structural Steel Buildings ANSI/AISC 341-05.* Chicago: American Institute of Steel Construction.

AISC. 2006. *Seismic Design Manual*. Chicago: American Institute of Steel Construction.

AISC. 2010a. *Seismic Provisions for Structural Steel Buildings ANSI/AISC 341-10.* Chicago: American Institute of Steel Construction.

AISC. 2010b. *Specification for Structural Steel Buildings ANSI/AISC 360-10.* Chicago: American Institute of Steel Construction.

AISC. 2011. *Manual of Steel Construction*, 14th ed. Chicago: American Institute of Steel Construction.

Archambault, M.-H., Tremblay, R., and Filiatrault, A. 1995. "Étude du Comportement Séismiquedes Contreventements Ductilesen X avec Profilés Tubulairesen Acier." *Rapport Technique EPM GCS; 95-09,* Department of Civil Engineering, ÉcolePolytechnique, Montréal. p. 346.

Astaneh-Asl, A., Goel, S. C., and Hanson, R. D. 1982. "Cyclic Behavior of Double Angle Bracing Members with End Gusset Plates," *Report No. UMEE 82R7. A*ugust. Ann Arbor, MI: Department of Civil Engineering, University of Michigan.

Astaneh-Asl, A., and Goel, S. C. 1984. "Cyclic In-Plane Buckling of Double-Angle Bracing." *Journal of Structural Engineering, ASCE,* vol. 110, no. 9, 2036–2055.

Astaneh-Asl, A., Goel, S. C., and Hanson, R. D. 1985. "Cyclic Out-of-Plane Buckling of Double-Angle Bracing." *Journal of Structural Engineering, ASCE,* vol. 111, no. 5, 1135–1153.

Astaneh-Asl, A., Goel, S. C., and Hanson, R. D. 1986. "Earthquake-resistant Design of Double Angle Bracing." *Engineering Journal, AISC,* vol. 23, no. 4, pp. 133–147.

ATC. 1999. *ATC-48 Built to Resist Earthquakes, The Path to Quality Seismic Design and Construction: Building Safety and Earthquakes, Part D: The Seismic Load Path.* Redwood City, CA: Applied Technology Council, p. 4.

Bennett, D. 2009. *The Creation of Bridges*. Secaucus, NJ: Chartwell Books, p. 232.

Black, R. G., Wenger, W. A., and Popov, E. P. 1980. "Inelastic Buckling of Steel Struts Under Cyclic Load Reversal," *Report No. UCB/EERC-80/40.* Berkeley: Earthquake Engineering Research Center, University of California.

Bonneville, D., and Bartoletti, S. 1996. "Case Study 2.3: Concentric Braced Frame, Lankershim Boulevard, North Hollywood." *1994 Northridge Earthquake; Building Case Studies Project; Proposition 122: Product 3.2, SSC 94-06,* Seismic Safety Commission State of California, pp. 305–324.

Brockenbrough, R. L. 2002. "AISC Rehabilitation and Retrofit Guide—A Reference for Historic Shapes and Specifications." *Design Guide 15*. Chicago: American Institute of Construction.

Broderick, B. M., Goggins, J., and Elghazouli, A. Y. 2005. "Cyclic Performance of Steel and Composite Bracing Members." *Journal of Constructional Steel Research,* vol. 61, no. 4, 493–514.

Bruneau, M., and Mahin, S. A. 1990. "Ultimate Behavior of Heavy Steel Section Welded Splices and Design Implications." *Journal of Structural Engineering, ASCE,* vol. 116, no. 18, 2214–2235.

BSSC. 1995. "NEHRP (National Earthquake Hazards Reduction Program) Recommended Provisions for the Development of Seismic Regulations for New Buildings," *Report FEMA 222A.* Washington, D. C.: Building Seismic Safety Council, Federal Emergency Management Agency.

Carstensen, G., and Gildemeister C. 1918. *New York Crystal Palace–Illustrated Description of the Buildings*. New York: Riker, Thorne and Co. Publishers, p. 106.

Chao, S. H., and Goel, S. C. 2008a. "Performance-Based Plastic Design of Special Truss Moment Frames." *AISC Engineering Journal,* vol. 45, no. 2, 127–150.

Chao, S. H., and Goel, S. C. 2008b. *Performance-Based Plastic Design: Earthquake-Resistant Steel Structures*. Country Club Hills, IL: International Code Council Publications, p. 261.

CISC. 2010. *Handbook of Steel Construction*, 10th ed. Willowdale, Ont: Canadian Institute of Steel Construction.

CSA. 1994. "Limit States Design of Steel Structures." *CAN/CSA-S16.1.* Rexdale, Ont: Canadian Standard Association.

CSA. 2001. "Limit States Design of Steel Structures." *CAN/CSA-S16-01.* Rexdale, Ont: Canadian Standard Association.

CSA. 2009. "Limit States Design of Steel Structures."*CAN/CSA-S16-09.* Mississauga, Ont: Canadian Standard Association.

Davaran, A. 2001. "Effective Length Factor for Discontinuous X-Bracing Systems." *Journal of Structural Engineering, ASCE,* vol. 127, no. 2, 106–112.

DeLony, E. 1992. *Landmark American Bridges.* New York: American Society of Civil Engineers, p. 152.

Dicleli, M., and Calik, E. E. 2008. "Physical Theory Hysteretic Model for Steel Braces." *Journal of Structural Engineering, ASCE,* vol. 134, no. 7, 1215–1228.

Dietrich, A. M., and Itani, A. M. 1999. "Cyclic Behavior of Built-up and Perforated Steel Members on the San Francisco–Oakland Bay Bridge." *Report No. CCEER 99-9,* June. Reno: Center for Civil Engineering Earthquake Research, University of Nevada.

Elchalakani, M., Zhao, Z. L., and Grzebieta, R. 2003. "Tests on Cold-Formed Circular Tubular Braces under Cyclic Axial Loading." *Journal of Structural Engineering, ASCE,* vol. 129, no. 4, 507–514.

El-Tayem, A. A., and Goel, S. C. 1986. "Effective Length Factor for the Design of X-bracing Systems." *AISC Engineering Journal,* vol. 23, no. 1, 41–45.

Fell, B. V., Kanvinde, A. M., Deierlein, G. G., Myers, A. M., and Fu, X. 2006. "Buckling and fracture of concentric braces under inelastic cyclic loading." *SteelTIPS*. Moraga, CA: Structural Steel Educational Council.

Fell, B. V., Kanvinde, A. M., Deierlein, G. G., and Myers, A. T. 2009. "Experimental Investigation of Inelastic Cyclic Buckling and Fracture of Steel Braces." *Journal of Structural Engineering, ASCE,* vol. 135, no. 1, 19–32.

Friedman, D. 1995. *Historical Building Construction: Design, Materials, and Technology.* New York: W. W. Norton & Company, p. 450.

Goel, S. C., and Itani, A. M. 1994. "Seismic-Resistant Special Truss-Moment Frames." *Journal of Structural Engineering*, ASCE, vol. 120, no. 6, 1781–1797.

Goel, S. C., and Lee, S. 1992. "A Fracture Criterion for Concrete-Filled Tubular Bracing Members Under Cyclic Loading." *Proceedings of the 1992 ASCE Structures Congress*, pp. 922–925. Reston, VA: ASCE.

Griffis, L. G., and Patel, V. B. 2006. AISC Steel Design after College, http://www.aisc.org/assets/0/424/426/430/d73a3653-5bfb-4af0-aab9-8fe6f06dfacf.pdf

Griggs, Jr, F. E. 2009. "Preservation and Restoration of 19th Century Cast and Wrought Iron Bridges." *ASCE Practice Periodical on Structural Design and Construction,* vol. 14, no. 4, 159–175.

Gugerli, H., and Goel, S. C. 1982. "Inelastic Cyclic Behavior of Steel Bracing Members." *Report No. UMEE 82R1*. Ann Arbor, MI: Department of Civil Engineering, University of Michigan.

Hassan, O. F., and Goel, S. C. 1991. "Modeling of Bracing Members and Seismic Behavior of Concentrically Braced Steel Structures." *Report No. UMCE 91-1*, January. Ann Arbor, MI: Department of Civil Engineering, University of Michigan.

Higginbotham, A. B., and Hanson, R. 1976. "Axial hysteretic behavior of steel members." *Journal of the Structural Division*, vol. 102, no. 7, 1365–1381.

Huang, Y., and Mahin S. A. 2010. "Simulating the Inelastic Seismic Behavior of Steel Braced Frames Including the Effects of Low-Cycle Fatigue." *Pacific Earthquake Engineering Research Center Report No. PEER 2010/104,* Berkeley: University of California. p. 186.

ICBO. 1994. *Uniform Building Code*. Whittier, CA: International Conference of Building Officials.

Ikeda, K., and Mahin, S. A. 1984. "A Refined Physical Theory Model for Predicting the Seismic Behavior of Braced Frames." *Report No. UCB/EERC-84/12.* Berkeley: Earthquake Engineering Research Center, University of California.

Ikeda, K., Mahin, S. A., and Dermitzakis, S. N. 1984. "Phenomenological Modeling of Steel Braces under Cyclic Loading." *Report No. UCB/EERC-84/09*. Berkeley: Earthquake Engineering Research Center, University of California.

Itani, A. M., Vesco, T. D., and Dietrich, A. M. 1998. "Cyclic Behavior of As-Built Laced Members with End Gusset Plates on the San Francisco–Oakland Bay Bridge." *Report No. CCEER 98-01*, March. Reno:Center for Civil Engineering Earthquake Research, University of Nevada.

Jain, A. K., and Goel, S. C. 1978. "Hysteresis Models for Steel Members Subjected to Cyclic Buckling or Cyclic End Moments and Buckling." *UMEE Rep. No. 78R6*, Ann Arbor, MI: University of Michigan.

Jain, A. K., Goel, S. C., and Hanson, R. D. 1977. "Static and Dynamic Hysteresis Behavior of Steel Tubular Members with Welded Gusset Plates." *Report No. UMEE 77R3*, June. Ann Arbor, MI: Department of Civil Engineering, University of Michigan.

Jain, A. K., Goel, S. C., and Hanson, R. D. 1978. "Hysteresis Behavior of Bracing Members and Seismic Response of Braced Frames with Different Proportions." *Report No. UMEE 78R3*, July. Ann Arbor: Department of Civil Engineering, University of Michigan.

Jin, J., and El-Tawil, S. 2003. "Inelastic cyclic model for steel braces." *Journal of Engineering Mechanics, ASCE*, vol. 129, no. 5, 548–557.

Kanvinde, A. M., and Deierlein, G. G. 2007. "A Cyclic Void Growth Model to Assess Ductile Fracute in Structural Steels due to Ultra Low Cycle Fatigue." *Journal of Engineering Mechanics, ASCE*,vol. 133, no. 6, 701–712.

Ketchum, M. S. 1918. *Structural Engineers' Handbook,* 2nd ed. New York: McGraw-Hill Co.

Ketchum, M. S. 1920. *The Design of Highway Bridges of Steel, Timber and Concrete*. New York: McGraw-Hill Co.

Khatib, I. F., Mahin, S. A., and Pister, K. S. 1988. "Seismic Behavior of Concentrically Braced Steel Frames." *Report No. UCB/EERC-88/01.* Berkeley: Earthquake Engineering Research Center, University of California.

Kiland, J. P., and Sabelli, R. 2006. *IBC Structural/Seismic Design Manual Volume 3: Building Design Examples for Steel and Concrete.* Washington, D.C.: International Code Council.

Kunz, F. C. 1915. *Design of Steel Bridges; Theory and Practice for use of Civil Engineers and Students.* New York: McGraw-Hill Co.

Lacerte, M., and Tremblay, R. 2006. "Making use of brace overstrength to improve the seismic response of multistory split-X concentrically braced steel frames." *Canadian Journal of Civil Engineering,* vol. 33, no. 8, 1005–1021.

Lee, K., and Bruneau, M. 2002. "Review of Energy Dissipation of Compression Members in Concentrically Braced Frames." *Technical Report MCEER-02-0005,* 216 pp. Buffalo, NY:Multidisciplinary Center for Earthquake Engineering Research, State University of New York at Buffalo.

Lee, K., and Bruneau, M. 2004. "Seismic Vulnerability Evaluation of Axially Loaded Steel Built-up Laced Members." *Technical Report MCEER-04-0007,* 279 pp. Buffalo, NY: Multidisciplinary Center for Earthquake Engineering Research, State University of New York at Buffalo.

Lee, K., and Bruneau, M. 2005. "Energy Dissipation of Compression Members in Concentrically Braced Frames:Review of Experimental Data." *Journal of Structural Engineering, ASCE,* vol. 131, no. 4, 552–559.

Lee, K., and Bruneau, M. 2008a. "Seismic Vulnerability Evaluation of Axially Loaded Steel Built-up Laced Members - I: Experimental Results." *Earthquake Engineering and Engineering Vibrations Journal*, vol. 7, no. 2, 113–124.

Lee, K., and Bruneau, M. 2008b. "Seismic Vulnerability Evaluation of Axially Loaded Steel Built-Up Laced Members - II: Evaluations." *Earthquake Engineering and Engineering Vibrations Journal,* vol. 7, no. 2, 125–136.

Lee, S., and Goel, S. C. 1987. "Seismic Behavior of Hollow and Concrete-Filled Square Tubular Bracing Members," *Report No. UMEE 87-11*, December. Ann Arbor, MI: Department of Civil Engineering, University of Michigan.

Lehman, D., Lumpkin, E., Hsiao, P. C., Roeder, C., Tsai, K. C., Wu, A. C., Wei, C. Y., and Tsai, C. 2010. "Cyclic Response of Three-Story Full-Scale Concentrically Braced Frame System." *Proceedings of 9th U.S. National and 10th Canadian Conference on Earthquake Engineering,* Toronto.

Lehman, D. E., Roeder, C. W., Herman, D., Johnson, S., and Kotulka, B. 2008. "Improved seismic performance of gusset plate connections." *Journal of Structural Engineering, ASCE,* vol. 134, no. 6, 890–901.

Leon, R. T., and Yang, C. S. 2003. "Special inverted-V-Braced frames with Suspended Zipper Struts." *Proceedings of International Workshop on Steel and Concrete Composite Construction, National Center for Research on Earthquake Engineering,* Taipei.

Liu, Z., and Goel, S. C. 1987. "Investigation of Concrete-Filled Steel Tubes under Cyclic Bending and Buckling." *Report No. UMCE 87-3.* Ann Arbor: Department of Civil Engineering, University of Michigan.

Liu, Z., and Goel, S. C. 1988."Cyclic Load Behavior of Concrete-Filled Tubular Braces." *Journal of the Structural Division*, *ASCE*,vol. 114, no. 7,1488–1506.

MacRae, G. 2010. "The Development and Use of the Continuous Column Concept."*Joint Proceedings of the 7th International Conference on Urban Earthquake Engineering (7CUEE) & 5th International Conference on Earthquake Engineering (5ICEE),* Tokyo.

MacRae, G. A., Kimura, Y, and Roeder, C. 2004. "Effect of Column Stiffness on Braced Frame Seismic Behavior." *Journal of the Structural Division*, *ASCE*, vol. 130, no. 3, 381–391.Maison, B., and Popov, E. P. 1980."Cyclic Response Prediction for Braced Steel Frames." *Journal of the Structural Division*, *ASCE*, vol. 106, no. 7, 1401–1416.

Moon, J., Yoon, K. Y., Han, T. S., and Lee, H. E. 2008. "Out-of-Plane Buckling and Design of X-Bracing Systems with Discontinuous Diagonals," *Journal of Constructional Steel Research,* vol. 64, no. 3, 285–294.

Nakashima, M., and Wakabayashi, M. 1992. "Analysis and Design of Steel Braces and Braced Frames in Building Structures." *Stability and Ductility of Steel Structures under Cyclic Loading.* Fukumoto, Y. and Lee, G. C., editors. Boca Raton: CRC Press, pp. 309–321.

Newell, J. D., and Uang, C. M. 2008. "Cyclic Behavior of Steel Wide-Flange Columns Subjected to Large Drift."*Journal of Structural Engineering, ASCE,* vol. 134, no. 8, 1334–1342.

Nonaka, T. 1987. "Formulation of Inelastic Bar under Repeated Axial and Thermal Loadings." *Journal of Engineering Mechanics*, *ASCE*, vol. 113, no. 11, 1647–1664.

Nonaka, T. 1989. "Elastic-Plastic Bar under Changes in Temperature and Axial Load." *Journal of Structural Engineering*, *ASCE*, vol. 115, no. 12, 3059–3075.

Popov, E. P., and Black, R. G. 1981. "Steel Struts under Severe Cyclic Loadings." *Journal of the Structural Division*, *ASCE*. vol. 107, no. ST9, 1857–1881.

Redwood, R. G., and Channagiri, V. S. 1991. "Earthquake-Resistant Design of Concentrically Braced Steel Frames." *Canadian Journal of Civil Engineering*, vol. 18, no. 5, 839–850.

Richards, P. W. 2009. "Seismic Column Demands in Ductile Braced Frames," *Journal of Structural Engineering, ASCE,* vol. 135, no. 1, 33–41.

Roeder, C. W., Lehman, D. E., Clark, K., Powell, J., Yoo, J. -H., Tsai, K. -C., Lin, C. -H., and Wei, C. -Y. 2010. "Influence of gusset plate connections and braces on the seismic performance of X-braced frames." *Earthquake Engineering & Structural Dynamics,* n/a. doi: 10.1002/eqe.1024.

Roeder, C. W., Lehman, D. E., Lumpkin, E., and Hsiao, P. C. 2009. "Seismic Evaluation and Rehabilitation of Concentrically Braced Frames," *ATC/SEI Conference on Improving the Seismic Performance of Existing Buildings and Other Structures,* pp. 777–788.

Rogers, C., and Tremblay, R. 2010. "Impact of Diaphragm Behavior on the Seismic Design of Low-Rise Steel Buildings," *AISC Engineering Journal,* vol. 47, no. 1, 21–36.

Sabelli, R. 2001. "Research on improving the Design and Analysis of Earthquake Resistant Braces Frames," *2000 NEHRP Fellowship in Earthquake Hazard Reduction,* *Final Report to FEMA and EERI.* Oakland, CA: Earthquake Engineering Research Institute.

Sabelli, R., and Hohbach, D. 1999. "Design of Cross-Braced Frames for Predictable Buckling Behavior." *Journal of Structural Engineering, ASCE,* vol. 125, no. 2, 163–168.

Schachter, M., and Reinhorn, A. M. 2007. "Three-Dimensional Modeling of Inelastic Buckling in Frame Structures." *Report MCEER-07-0016*. Buffalo, NY: Multidisciplinary Center for Earthquake Engineering Research, State University of New York at Buffalo.

SEAOC. 1978, 1990, 1996. *Tentative Lateral Force Requirements*. Seismology Committee, Structural Engineers Association of California. Sacramento/San Francisco/Los Angeles: CA.

Shaback, B., and Brown, T. 2003. "Behavior of square hollow structural steel braces with end connections under reversed cyclic axial loading." *Canadian Journal of Civil Engineering,* vol. 30, 745–753.

Soroushian, P., and Alawa, M. S. 1990. "Hysteretic modeling of steel struts: Refined physical theory approach." *Journal of Structural Engineering, ASCE,* vol. 116, no. 10, 2903–2916.

Tang, X., and Goel, S. C. 1987. "Seismic Analysis and Design Considerations of Braced Steel Structures." *Report No. UMCE 87-4.* June. Ann Arbor, MI: Department of Civil Engineering, University of Michigan.

Tang, X., and Goel, S. C. 1989. "Brace Fractures and Analysis of Phase I Structures," *Journal of Structural Engineering, ASCE*, vol. 102, no. 8, 1960–1976.

Tremblay, R. 2002. "Inelastic Seismic Response of Bracing Members." *Journal of Constructional of Steel Research,* vol. 58, 665–701.

Tremblay, R. 2003. "Achieving a Stable Inelastic Seismic Response for Multi-Story Concentrically Braced Steel Frames." *Engineering Journal,* vol. 40, no. 2, 111–129.

Tremblay, R. 2008. "Influence of brace slenderness on the fracture life of rectangular tubular steel bracing members subjected to seismic inelastic loading." *Proceedings of ASCE/SEI Structures Congress,* Vancouver.

Tremblay, R., Archambault, M. H., and Filiatrault, A. 2003. "Seismic Performance of Concentrically Braced Steel Frames made with Rectangular Hollow Bracing Members." *Journal of Structural Engineering, ASCE,* vol. 129, no. 12, 1626–1636.

Tremblay, R., Bruneau, M., Nakashima, M., Prion, H. G. L., Filiatrault, M., and DeVall, R. 1996. "Seismic Design of Steel Buildings: Lessons from the 1995 Hyogo-ken Nanbu Earthquake." *Canadian Journal of Civil Engineering,* vol. 23, no. 3, 757–770.

Tremblay, R., and Filiatrault, A. 1996. "Seismic Impact Loading in Inelastic Tension-Only Concentrically Braced Steel Frames: Myth or Reality?" *Earthquake Engineering and Structural Dynamics,* vol. 25, no. 12, 1373–1389.

Tremblay, R., Haddad, M., Martinez, G., Richard, J., and Moffatt, K. 2008. "Inelastic Cyclic Testing of Large Size Steel Bracing Members." *Paper No.05-05-0071, Proceedings 14th Word Conference on Earthquake Engineering,* Beijing.

Tremblay, R., and Robert, N. 2001. "Seismic Performance of Low- and Medium-Rise Chevron Braced Steel Frames," *Canadian Journal of Civil Engineering,* vol. 28, no. 4, 699–714.

Tremblay, R., Timler, P., Bruneau, M., and Filiatrault, A. 1995. "Performance of Steel Structures during the January 17, 1994, Northridge Earthquake." *Canadian Journal of Civil Engineering,* vol. 22, no. 2, 338–360.

Tremblay, R., and Tirca, L. 2003. "Behavior and Design of Multistory Zipper Concentrically Braced Steel Frames for the Mitigation of Soft Story Response." *Proceedings of 4th International Conference on Behavior of Steel Structures in Seismic Areas (STESSA).* Naples, Italy. pp. 471–477.

Uang, C. M., and Bertero, V. V. 1986. "Earthquake Simulation Tests and Associated Studies of a 0.3-Scale Model of a Six-Story Concentrically Braced Steel Structure." *Report No. UCB/EERC-86/10.* Berkeley: Earthquake Engineering Research Center, University of California.

Uang, C. M., and Kleiser, M. 1997. "Cyclic Performance of As-Built Latticed Members for the San Francisco-Oakland Bay Bridge," *Report No. SSRP-97/01,* June. La Jolla, California: Division of Structural Engineering, University of California, San Diego.

Uriz, P., Filippou, F. C., and Mahin, S. A. 2007. "Model for cycle inelastic buckling of steel braces." *Journal of Structural Engineering, ASCE*, vol. 134, no. 4, 619–628.

Uriz, P., and Mahin, S. A. 2008. "Toward earthquake-resistant design of concentrically braced steel-frame structures." *Pacific Earthquake Engineering Research Center Report No. PEER 2008/08*, Berkeley: University of California. p. 401.

Wada, A., Qu, Z., Ito, H., Motoyui, S., Sakata, H., and Kasai, K. 2009. "Seismic Retrofit Using Rocking Walls and Steel Dampers." *ATC/SEI Conference on Improving the Seismic Performance of Existing Buildings and Other Structures,* San Francisco.

Whittaker, A. S., Uang, C. M., and Bertero, V. V. 1990. "An Experimental Study of the Behavior of Dual Steel Systems." *Report No. UCB/EERC-88/14.* Berkeley: Earthquake Engineering Research Center, University of California.

Yang, C. S., Leon, R. T., and DesRoches, R. 2008a. "Design and Behavior of Zipper-Braced Frames." *Engineering Structures,* vol. 30, no. 4, 1092–1100.

Yang, C. S., Leon, R. T., and DesRoches, R. 2008b. "Cyclic Behavior of Zipper-Braced Frames." *Earthquake Spectra,* vol. 26, no. 2, 561–582

Yoo, J. H., Roeder, C. W., and Lehman, D. E. 2008. "Analytical Performance Simulation of Special Concentrically Braced Frames," *Journal of Structural Engineering, ASCE,* vol. 134, no. 6, 881–889.

Zayas, A. Z., Shing, P. B., Mahin, S. A., and Popov, E. P. 1981. "Inelastic Structural Modeling of Braced Offshore Platforms for Seismic Loading." *Report No. UCB/EERC-81/04.* Berkeley: Earthquake Engineering Research Center, University of California.

Zhao, X. L., Grzebieta, R., and Lee, C. 2002. "Void-filled Cold-formed Rectangular Hollow Section Braces Subjected to Large Deformation Cyclic Axial Loading." *Journal of Structural Engineering, ASCE,* vol. 128, no. 6, 746–753.

CHAPTER 10

Design of Ductile Eccentrically Braced Frames

10.1 Introduction

10.1.1 Historical Development

Although a properly designed and constructed steel moment frame can behave in a ductile manner, it was shown in Chapter 8 that the substantial lateral flexibility of moment frames is such that their design is often governed by code-required story drift limits. Special concentrically braced frames, on the other hand, have a large lateral stiffness, but their energy dissipation capacity is hindered by brace buckling. In the early 1970s, a new steel system called the eccentrically braced frame (EBF) was proposed in Japan (Fujimoto et al. 1972, Tanabashi et al. 1974). The EBF combines the advantages of both high elastic stiffness and high ductility at large story drifts. This type of framing system dissipates seismic energy by controlled shear or flexural yielding in a small segment of the beams called links.

In the United Sates, the EBF system was first studied by Roeder and Popov (1978). In the 1980s, numerous studies on link behavior provided insight into the cyclic response of EBFs (Engelhardt and Popov 1989; Hjemstad and Popov 1983, 1984; Kasai and Popov 1986a, 1986b; Malley and Popov 1984; Manheim and Popov 1983; Ricles and Popov 1989). Experimental verifications of EBF response at the system level were also conducted in the mid- to late-1980s (Roeder et al. 1987, Whittaker et al. 1989, Yang 1985). These studies led to the development of design provisions in the 1988 Uniform Building Code and later in AISC 341 (AISC 2010).

Further studies were conducted in the past two decades, including full-scale testing of large-size links for not only building but also bridge applications (Dusicka and Itani 2002, McDaniel et al. 2003, Sarraf and Bruneau 2004, Zahrai and Bruneau 1999). Recent research on links has also extended from I-shaped rolled links to built-up sections including I-shaped sections, boxed sections (Berman and Bruneau 2008b), and double C sections (Mansour et al. 2008). With increasing emphasis on performance-based design, the concept of replaceable links has also been explored (Dusicka and Lewis 2010, Mansour et al. 2008, Ramadan and Ghobarah 1995, Stratan et al. 2003).

10.1.2 General Behavior and Plastic Mechanism

An eccentrically braced frame is a framing system in which the axial forces induced in the braces are transferred either to a column or another brace through shear and bending in a small segment of the beam. Typical EBF geometries are shown in Figure 10.1. Architecturally, EBF also provides more freedom for door opening than CBF. The critical beam segment is called a "link" and is designated by a length, *e,* in the figure. Links in EBFs act as structural fuses to dissipate the earthquake-induced energy in a building in a stable manner. In practical applications, the horizontal links have been commonly used; see

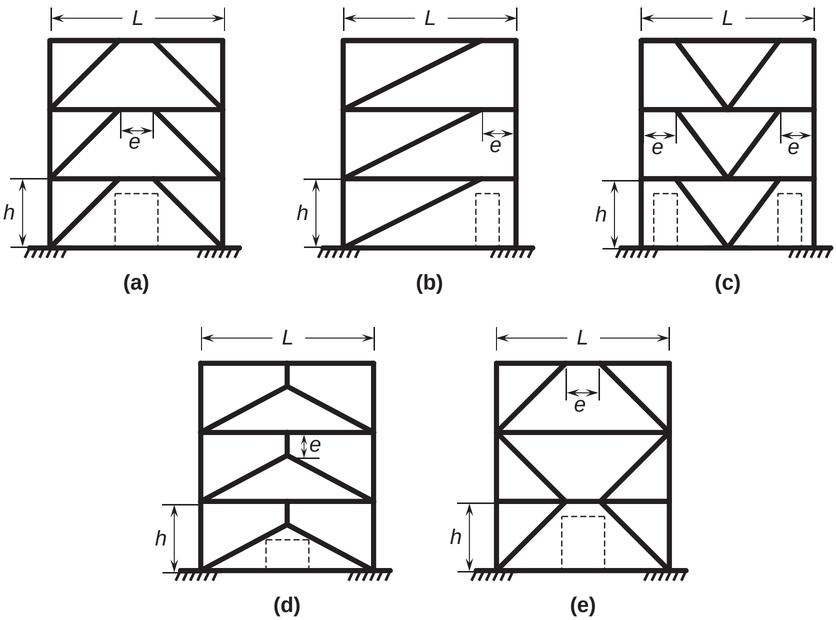

Figure 10.1 Typical EBF configurations.

(a) EBF with interior links **(b)** EBF with exterior links

Figure 10.2 Examples of EBF construction.

Figure 10.2 for two examples. Figure 10.1e shows an EBF where a link does not exist in every floor. The links in Figure 10.1d are oriented vertically; therefore, unlike all the other configurations, they are not integral with the beams.

Links in Figures 10.1b and c are connected to the columns. It has been shown in Chapter 8 that beam-to-column moment connections are vulnerable to brittle fracture. As it will be shown later, link-to-column moment connection is subjected to both high moment and high shear, making it even more vulnerable to brittle fracture. For this reason, it is highly desirable that these two configurations be avoided.

10.1.3 Design Philosophy

Figure 10.3 shows the desirable plastic mechanism of EBF. Yielding of the links, shown cross-hatched, occurs along the height of the frame. The remaining part of the structure is then designed to remain essentially elastic. A comparison of the expected plastic mechanism between SCBF and EBF is shown in Figure 10.4. In a SCBF, braces are designed and detailed as structural fuses. For an EBF, however, links need to be properly designed and detailed to have adequate strength and ductility. All the other structural components (beam segments outside of the links, braces, columns, and connections) are proportioned following the capacity design principles to remain essentially elastic during the design earthquake.

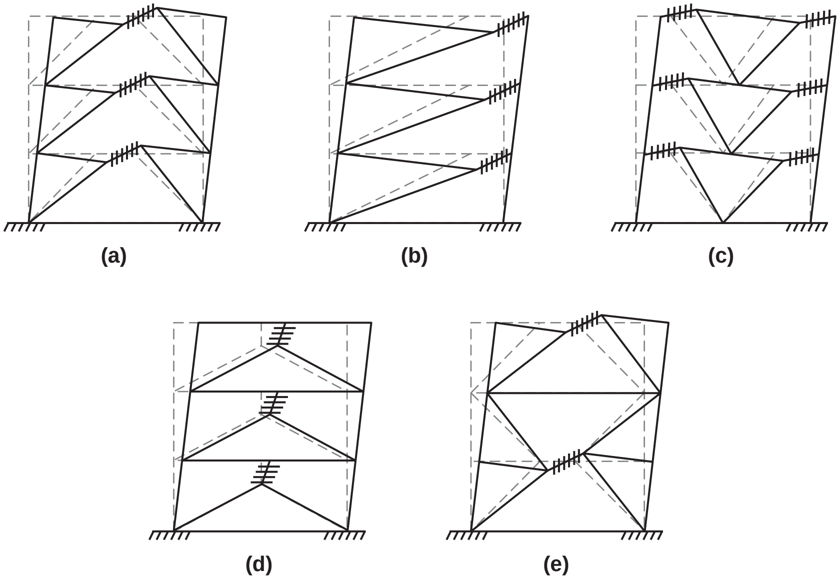

Figure 10.3 Yield mechanism of EBF.

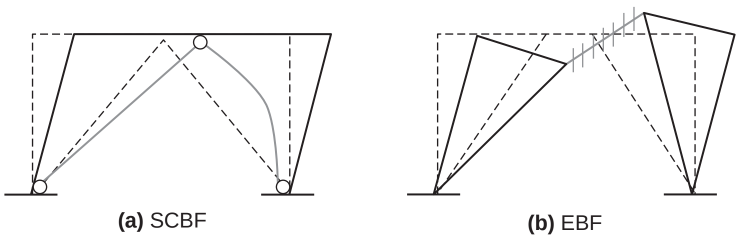

Figure 10.4 Expected deformed configuration of SCBF and EBF.

10.2 Link Behavior

10.2.1 Stiffened and Unstiffened Links

Figure 10.5 shows two I-shaped links that were tested cyclically (Malley and Popov 1983). For the specimen that did not have stiffeners, web local buckling due to shear would occur early. Such local buckling could be delayed by adding transverse stiffeners. When the stiffeners were sufficiently close, Figure 10.5b shows the formation of diagonal tension field in the subpanels. Continued large displacement cycling finally caused material tearing in the links. For the unstiffened link, tearing usually took place near the

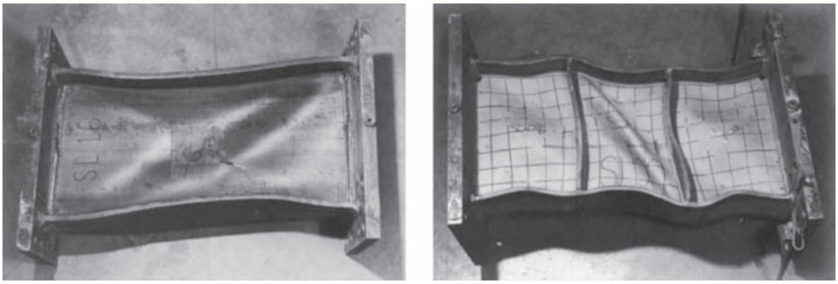

(a) Unstiffened link (W18 × 60) **(b)** Stiffened link (W18 × 40)

Figure 10.5 Unstiffened versus stiffened link. (*Malley and Popov 1983, with permission from EERC, University of California, Berkeley.)*

center of the web region due to material fatigue from severe web curvature reversals.

The effect of adding stiffeners to stiffen the link can be better demonstrated by comparing the cyclic response of two links of identical size, one without and the other with three stiffeners (Hjelmstad and Popov 1983). Figure 10.6 shows that not only the shear strength but also the energy dissipation capacity are significantly improved with the addition of web stiffeners.

10.2.2 Critical Length for Shear Yielding

Figure 10.7 shows the free-body diagram of a link. Ignoring the effects of axial force and the interaction between moment and shear in the link, flexural hinges form at two ends of the link when both M_a and M_b reach the plastic moment, M_p. A shear hinge is said to form when

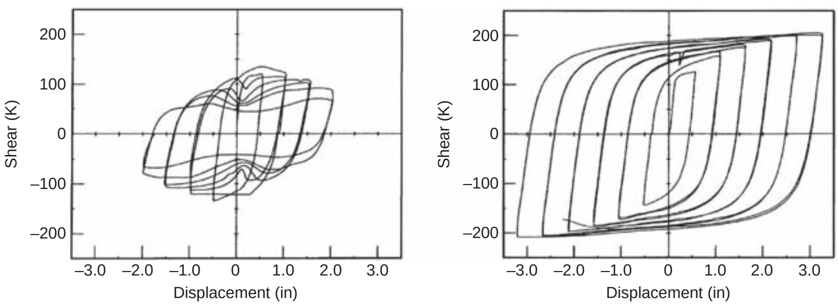

(a) Unstiffened link **(b)** Stiffened link

Figure 10.6 Cyclic response of unstiffened and stiffened W18 × 40 links, $e = 28$ in. (*Hjelmstad and Popov 1983, with permission from EERC, University of California, Berkeley*.)

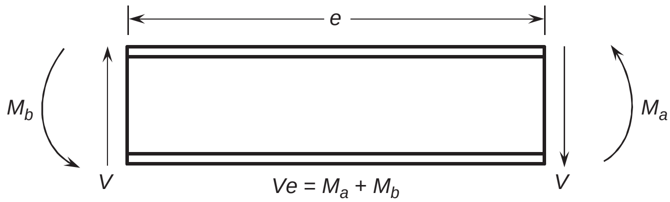

Figure 10.7 Link deformation and free-body diagram.

the shear reaches V_p. The plastic moment and shear capacities are respectively computed as follows:

$$M_p = F_y Z \tag{10.1a}$$

$$V_p = \tau_y A_{lw} \tag{10.1b}$$

where the link web area, A_{lw}, is equal to $(d - 2t_f)t_w$ and $2(d - 2t_f)t_w$ for I-shaped and built-up box sections, respectively. The yield shear stress, τ_y, is taken as $0.6F_y$ and $0.55F_y$ in AISC 341 (AISC 2010) and CSA S16 (CSA 2009), respectively. A balanced yielding condition corresponds to the simultaneous formation of flexural hinges and a shear hinge. The corresponding link length is

$$e_0 = \frac{2M_p}{V_p} \tag{10.2}$$

In a short link ($e \le e_0$), a shear hinge will form. When $e > e_0$, a flexural (or moment) hinge forms at both ends of the link, and the corresponding shear force is

$$V = \frac{2M_p}{e} \tag{10.3}$$

Based on plastic theory, Eq. (10.2) can be modified slightly to include the effect of interaction between M and V. Nevertheless, experimental results (see Figure 10.8) indicated that the interaction is weak and that such interaction can be ignored (Kasai and Popov 1986b).

Test results also showed that a properly stiffened short link can strain harden and develop a shear strength equal to $1.5V_p$. For example, Figure 10.6b shows the link shear strength reached 200 kips, but Eq. (10.1b) gives a V_p value of 126 kips based on a measured web yield stress of 39.5 ksi. The end moments of a link that has yielded in shear can continue to increase due to this strain hardening and, therefore, flexural hinges can develop. To avoid high bending strains that

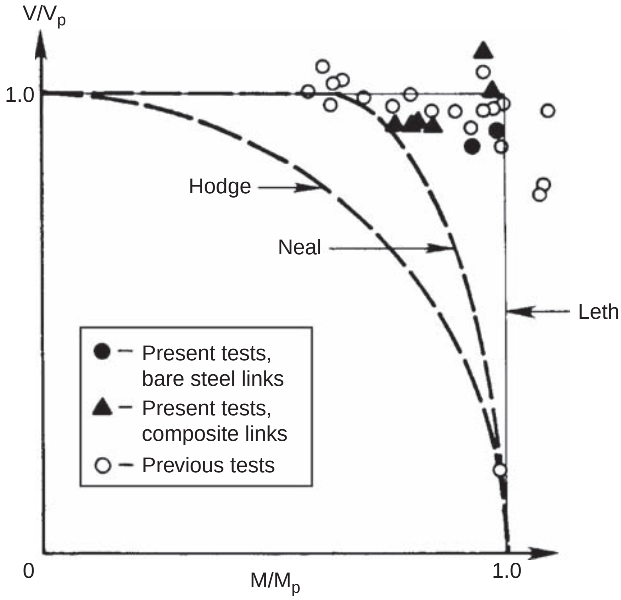

FIGURE 10.8 M-V interaction of links. (*Ricles and Popov 1987, with permission from EERC, University of California, Berkeley.*)

may lead to severe flange buckling or to failure of link flange-to-column welds, these end moments are limited to $1.2M_p$, and the maximum length, e_0, in Eq. (10.2) for a shear link is modified as follows (Kasai and Popov 1986b):

$$e_0 = \frac{2(1.2M_p)}{1.5V_p} = \frac{1.6M_p}{V_p} \tag{10.4}$$

10.2.3 Classifications of Links and Link Deformation Capacity

Experimental results have shown that the inelastic deformation capacity of an EBF can be greatly reduced when long links ($e > e_0$) are used. Following the above logic, it can be shown that flexural hinges dominate the link response when e is larger than $2.6M_p/V_p$. (If the moment at flexural hinges reaches $1.2M_p$, the corresponding shear for a link with a length of $2.6M_p/V_p$ is $0.92V_p$.) In the transition region where $1.6M_p/V_p < e < 2.6M_p/V_p$, the link undergoes simultaneous shear and flexural yielding (Engelhardt and Popov 1989). Figure 10.9 classifies links in EBFs; for design purpose a link is classified as either a short or shear link (developing only shear yielding), a long or moment link (developing only flexural yielding), or an intermediate link (developing both shear and flexural yielding).

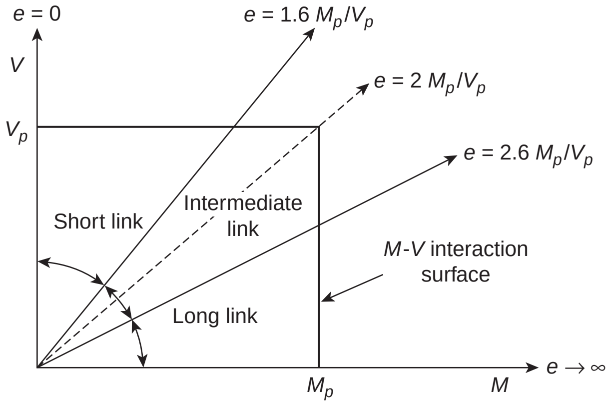

Figure 10.9 Classification of links.

The effect of link length on the failure mode and deformation capacity is demonstrated in Figure 10.10 (Okazaki et al. 2004). Figure 10.10a shows that the closely spaced stiffeners are effective in preventing shear buckling of a short link. Relatively uniform shear yielding in the web occurred along the entire link length, thus producing a large deformation capacity. On the other hand, Figure 10.10c depicts the behavior of a long link ($e \geq 2.6M_p/V_p$), where flexural buckling occurred primarily in the form of flange local buckling. The deformation capacity is very limited as the link web did not yield along its length and contribute any plastic deformation. Figure 10.10b demonstrates the behavior of an intermediate link ($1.6M_p/V_p < e < 2.6M_p/V_p$). Both shear and flexure are dominating in this case, where the plastic deformation was contributed by flexure buckling in the flanges and web shear buckling in the end panels.

The plastic mechanism in Figure 10.3 shows that the links are subjected to an inelastic rotation angle, γ_p, at the ends of the links. This link rotation angle is the plastic rotation angle between the link and the portion of the beam outside of the link. The links need to have a sufficient deformation capacity to accommodate this deformation demand. Testing shows that a link's inelastic rotation capacity is dependent on the link's length—the shorter the length, the larger the rotation capacity (Kasai and Popov 1986a). To develop a large rotation capacity, closely spaced intermediate stiffeners are needed. The allowable link deformation capacity, γ_a, as given by AISC 341 is shown in Figure 10.11.

10.2.4 Link Transverse Stiffener

Once shear buckling occurs in a stiffened link, tearing along the perimeter of the link panes due to stress concentration created by the buckled web may cause significant strength degradation. For

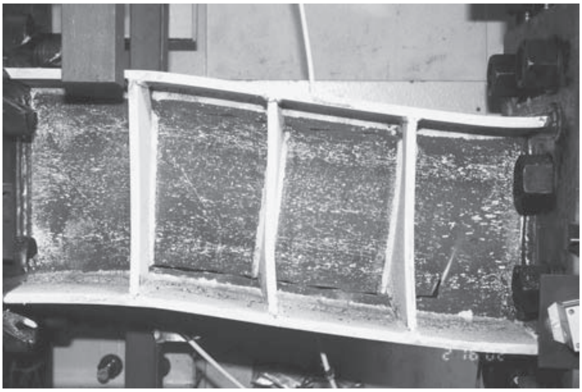

(a) Short link

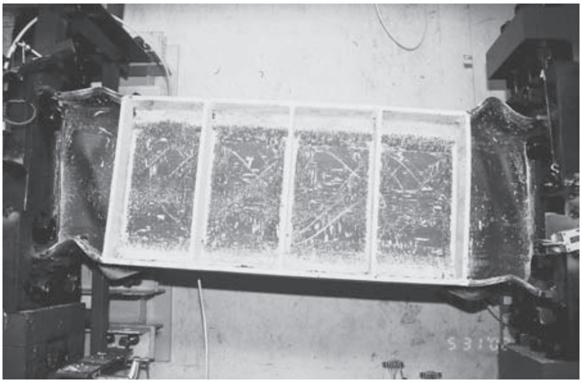

(b) Intermediate link

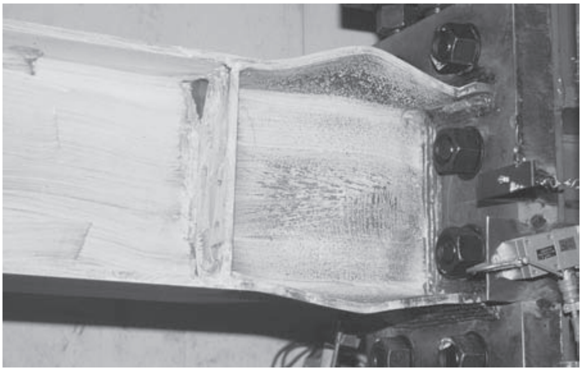

(c) Long link

Figure 10.10 Link failure modes. (*Courtesy of M.D. Engelhardt, Dept. of Civil Engineering, University of Texas, Austin.*)

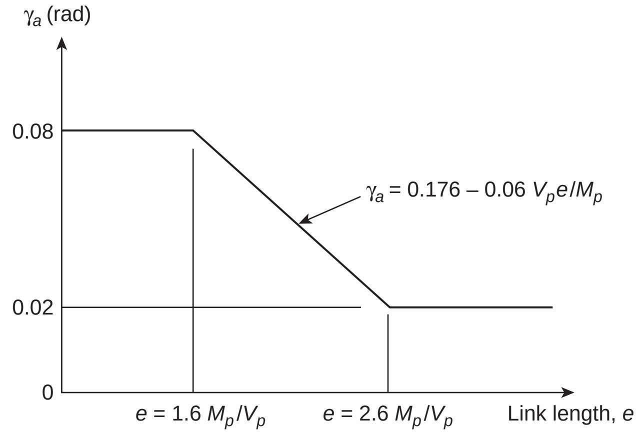

FIGURE 10.11 Allowable link rotation angles.

practical applications, allowing the link to behave in the postbuckling region can also result in hazardous lateral-torsional buckling problem. Therefore, it is appropriate to consider web buckling as the shear link design ultimate limit state (Kasai and Popov 1986a).

Figure 10.12 shows the typical hysteretic loop envelopes of a short link under cyclic loading. Depending on the loading history used for testing, the link deformation capacity, γ_u, at shear buckling can be very different. For example, the value of γ_u for a link under monotonic loading can be about twice that of the same link under symmetrically cyclic loading. Based on test data, Kasai and Popov (1986a)

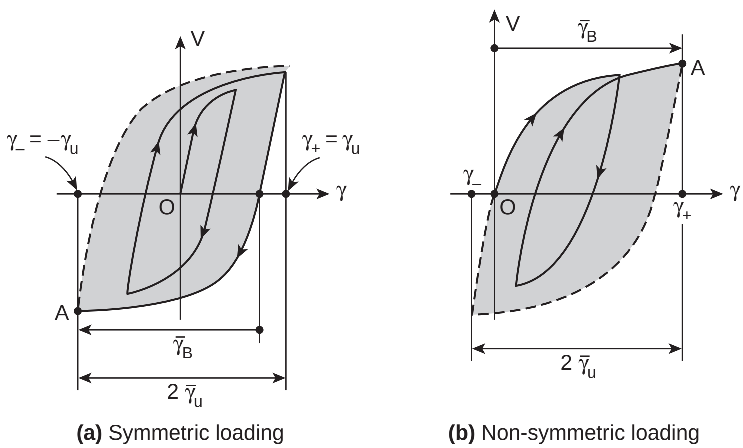

FIGURE 10.12 Buckling hysteretic loop envelopes for shear link. (*Kasai and Popov 1986a, with permission from EERC, University of California, Berkeley.*)

observed that the link buckling deformation capacity, $\bar{\gamma}_B$, shown in Figure 10.12 is a more reliable parameter for predicting the cyclic web buckling under different loading histories. $\bar{\gamma}_B$ is defined as the link deformation measured from the farthest point of zero shear when shear buckling occurs (labeled as point "A" in Figure 10.12). Based on a cyclic plastic theory, the following simple expression was derived and correlated well with the test data of A36 steel links:

$$\bar{\gamma}_B = 8.7K_s\left(\frac{t_w}{b}\right)^2 \tag{10.5}$$

where b is the web panel height, and K_s, which is a function of the panel aspect ratio, is an elastic plate buckling coefficient. For design purposes, a conservative approximation of the above equation for the range of γ_u from 0.03 to 0.09 rad can be established:

$$\frac{a}{t_w} + \frac{1}{5}\frac{d}{t_w} = C_B \tag{10.6}$$

where a = stiffener spacing; d = link depth; and C_B = 56, 38, and 29, respectively, for $\gamma_u = 0.03$, 0.06, and 0.09 rad. For other values of γ_u, C_B can be linearly interpolated. In deriving the above equation, it was assumed that the stiffener spacing is no larger than the link depth.

10.2.5 Effect of Axial Force

The presence of an axial force in a link reduces not only its flexural and shear capacities but also its inelastic deformation capacity (Kasai and Popov 1986b, Ghobarah and Ramadan 1990). When the axial force, P_u, exceeds 15% of the yield force, $P_y(= A_gF_y)$, the P-M interaction equation in Eq. (3.25) can be used to compute the reduced plastic moment, M_{pa}:

$$M_{pa} = 1.18M_p\left(1-\frac{P_u}{P_y}\right) = \frac{M_p}{0.85}\left(1-\frac{P_u}{P_y}\right) \tag{10.7}$$

Based on the von Mises yield criterion in Eq. (3.29), the reduced shear capacity is

$$V_{pa} = V_p\sqrt{1-\left(\frac{P_u}{P_y}\right)^2} \tag{10.8}$$

Defining the normalized axial force ratio ρ' as

$$\rho' = \frac{P_u/P_y}{V_u/V_y} = \left(\frac{P_u}{V_u}\right)\left(\frac{A_g}{0.6A_{lw}}\right) \tag{10.9}$$

and replacing M_p and V_p in Eq. (10.2) by M_{pa} and V_{pa}, the reduced value of e_0 when $\rho' \geq 0.5$ can be approximated as follows (Kasai and Popov 1986b):

$$e_0 = \frac{1.6M_p}{V_p}(1.15 - 0.3\rho') \tag{10.10}$$

The correction is unnecessary if $\rho' \leq 0.5$, in which case AISC 341 requires that the link length shall not exceed that given by Eq. (10.4).

10.2.6 Effect of Concrete Slab

Research conducted on composite links showed that composite action can significantly increase the link shear capacity during the first cycles of large inelastic deformations (Ricles and Popov 1989). However, composite action deteriorates rapidly in subsequent cycles due to local concrete floor damage at both ends of the link. The research also showed that the composite slab cannot be used as lateral bracing for the links. Because links are also a protected zone where shear stud connectors cannot be used, AISC 341 ignores the effect of composite action in link design.

10.2.7 Link Overstrength

The overstrength of a link is defined as the ratio between the maximum shear developed in the link and the V_{na} value, where V_{na}, the link shear strength, is the smaller of V_p or $2M_p/e$ calculated based on the actual yield stress. In deriving Eq. (10.4), it was assumed that the link will strain harden and develop a shear strength of $1.5V_p$. Recent testing conducted by Okazaki et al. (2005) confirmed this assumption, wherein the average I-shaped link overstrength was 1.41 for short links (see Figure 10.13). The overstrength tended to be lower for longer links.

Note from Figure 10.13 that a few data points from Dusicka and Itani (2002) and McDaniel et al. (2003) show very high overstrength values. These data were based on cyclic testing of large-size, I-shaped built-up shear links for bridge applications. Unlike typical rolled sections, these built-up sections have large flange area-to-web area ratios. Such high overstrength, which is not reflected in AISC 341, can be detrimental from the capacity design point of view because it may overload the other part of the structure if not properly considered in design. The higher shear overstrength of these links is mainly due to the participation of flanges in resisting shear. Manheim and Popov (1983) and Richards (2004) have recommended procedures to account for this additional strength. The concept behind these procedures is to treat each flange as a fix-ended beam. The shear resisted by each flange

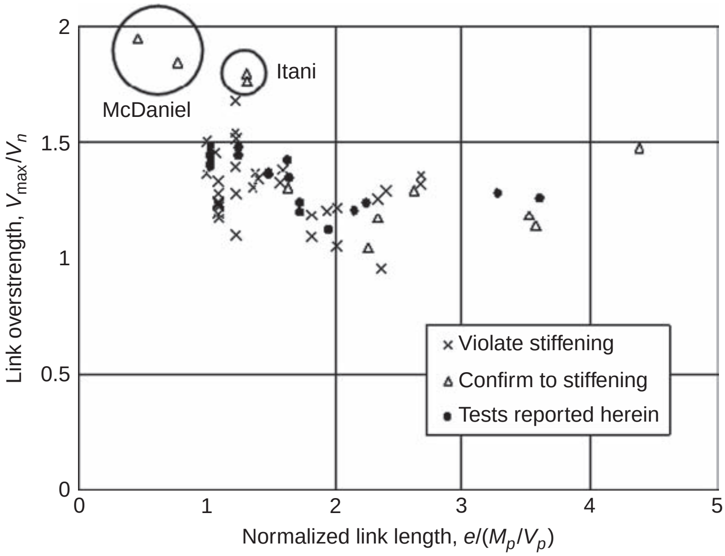

Figure 10.13 Link overstrength. (*Courtesy of M.D. Engelhardt, Dept. of Civil Engineering, University of Texas, Austin.*)

corresponds to that when the plastic moment of the flange, reduced to account for the axial force effect in the flange, is developed.

10.2.8 Qualification Test and Loading Protocol Effect

When an EBF configuration requires one end of the link to be connected to the column, AISC 341 requires that the link-to-column connection be tested by a specified cyclic loading sequence such that the connection can sustain the maximum link rotation based on the length of the link (Figure 10.11). In a testing program to evaluate some types of link-to-column connections, Okazaki et al. (2004, 2005) originally based it on the loading sequence specified in the 2002 edition of AISC 341 (AISC 2002). Test results revealed that some properly designed link specimens did not meet the code-specified rotation capacity. Furthermore, unexpected fracture pattern in the web was also observed (Figure 10.14). A subsequent analytical study concluded by Richards and Uang (2006) showed that the loading protocol used was too severe when compared with those used by researchers in the 1980s. A new loading protocol that simulated a more realistic deformation demand of the links during earthquake excitations expected in North America was then developed and adopted in the subsequent editions of AISC 341 (AISC 2005). Figure 10.15 compares both cyclic loading sequences. Testing with the revised loading sequence showed that the link specimens

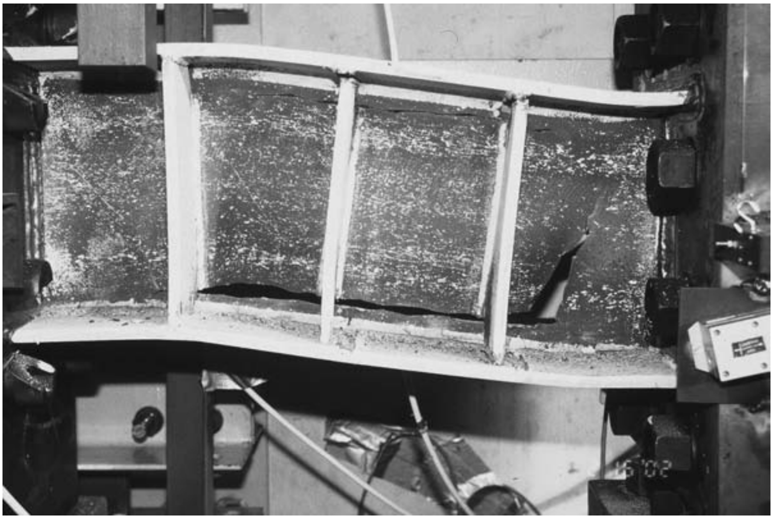

Figure 10.14 Link fracture in the web. (*Courtesy of M.D. Engelhardt, Dept. of Civil Engineering, University of Texas, Austin.*)

earlier considered by Okazaki et al. (2005) were able to deliver the code-specified rotation capacity.

10.3 EBF Lateral Stiffness and Strength

10.3.1 Elastic Stiffness

The variations of the lateral stiffness of a simple EBF with respect to the link length is shown in Figure 10.16 (Hjelmstad and Popov 1984). Note that e/L ratios of 0.0 and 1.0 correspond to a concentrically braced frame and a moment frame, respectively. The figure shows the advantage of using a short link for drift control.

10.3.2 Link Required Rotation

Consider the plastic mechanism of an interior link configuration shown in Figure 10.17a. Applying simple plastic theory, the kinematics of the plastic mechanism requires that

$$\gamma_p = \frac{L}{e}\theta_p \tag{10.11}$$

where θ_p is the plastic story drift angle (or plastic story drift ratio), and γ_p is the plastic deformation demand of the link. The expression shows that γ_p increases rapidly as the link length is reduced. Because

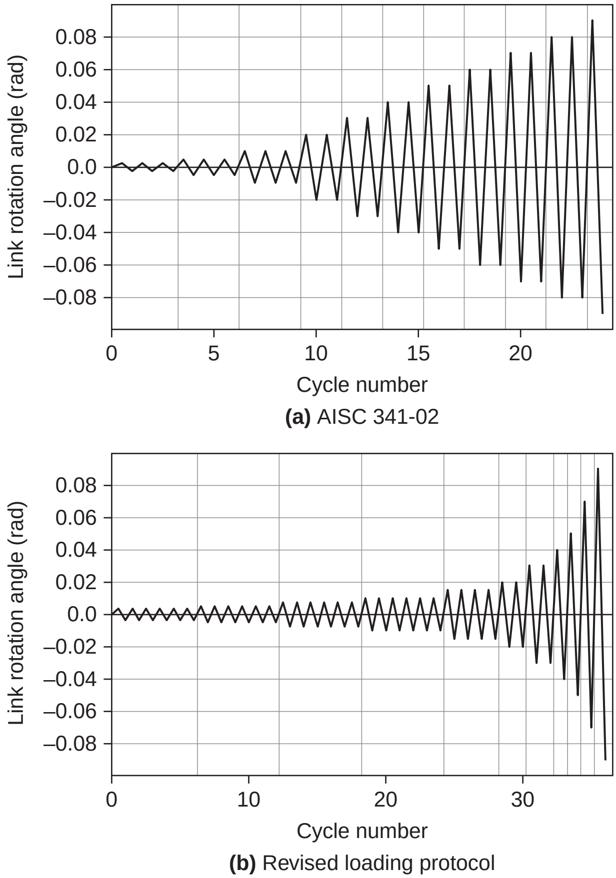

Figure 10.15 AISC link test loading sequence. (*Richards and Uang 2006.*)

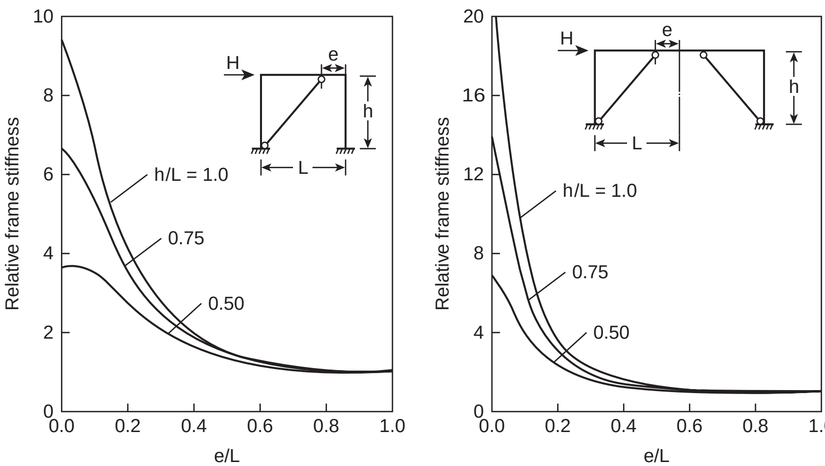

Figure 10.16 Variations of lateral stiffness with respect to e/L for two simple EBFs. (*Hjelmstad and Popov 1994, with permission from EERC, University of California, Berkeley.*)

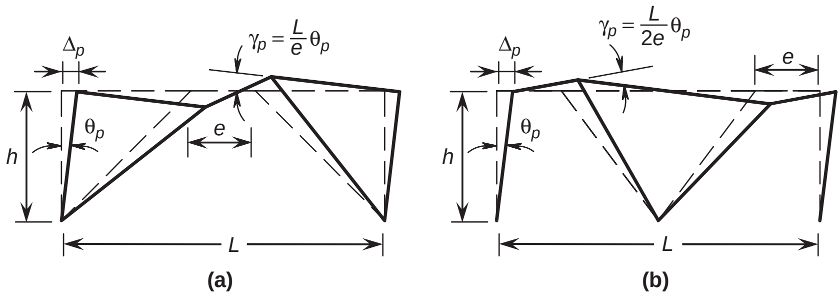

Figure 10.17 Link rotation demand.

the elastic component of the total drift angle is generally small, the plastic story drift angle, θ_p, can be conservatively estimated as the total story drift divided by the story height, h:

$$\theta_p \approx \frac{\Delta_s}{h} = \frac{C_d \Delta_e}{h} \tag{10.12}$$

where Δ_e is the story drift produced by the prescribed design earthquake force, and C_d (= 4) is the deflection amplification factor. To ensure that the deformation capacity of the link given in Figure 10.11 is not exceeded, Eq. (10.11) leads to a lower limit on the link length. Note that the kink that forms between the link and the beam outside the link also implies damage of the concrete slab at the ends of the link.

10.3.3 Plastic Analysis and Ultimate Frame Strength

Unless architectural considerations dictate otherwise, a short link is usually used so that the link will yield primarily in shear and forms a shear plastic hinge. The lateral strength of the EBF then can be calculated conveniently using simple plastic theory. Assuming that the link behaves in an elastic-perfectly plastic manner, the lateral strength, P_u, of the simple one-story split V-shaped EBF frame can be computed by equating the external work to the internal work:

$$W_E = P_u(h\theta_p) \tag{10.13a}$$

$$W_I = \int_0^e V_p \gamma_p dx = eV_p\gamma_p \tag{10.13b}$$

where V_p is the shear strength of the link. Substituting Eq. (10.11) into Eq. (10.13b), the resulting ultimate strength of the EBF frame is

$$P_u = \frac{V_p L}{h} \tag{10.14}$$

As long as the link yields in shear, the above equation shows that the ultimate strength is independent of the link length.

The simple plastic theory can also be applied to multistory frames (Kasai and Popov 1985). For example, consider the three-story EBF shown in Figure 10.3b. Assume a lateral load pattern with the applied load at the i-th floor designed as P_i. The span of the frame is L, and the height from the base to each floor is h_i. With the assumed yield mechanism, the scale load factor, α, producing the yield mechanism can be computed by equating the external and interior works.

$$W_E = \sum_{i=1}^{3} \alpha P_i h_i \theta_p \tag{10.15a}$$

$$W_I = \sum_{i=1}^{3} \int_0^e V_{pi} \gamma_p dx = e\gamma_p \sum_{i=1}^{3} V_{pi} \tag{10.15b}$$

$$\alpha = \frac{e\gamma_p \sum_{i=1}^{3} V_{pi}}{\sum_{i=1}^{3} P_i h_i} \tag{10.16}$$

where V_{pi} is the plastic shear strength of the link at the ith floor. The above calculation ignores the gravity load. If a uniformly distributed gravity load is applied to each floor, an additional external work corresponding to the assumed yield mechanism needs to be added to W_E. For the yield mechanism in Figure 10.3a, however, the external work produced by the uniform gravity load is zero due to the symmetry of the frame.

The above examples assume a short link such that a shear plastic hinge in the form of uniform yielding along the length of the link forms. For intermediate and long links, flexure and shear dominate the link strength. The ultimate strength of the frame then decreases with an increase in link length. Figure 10.18 illustrates the strength variations (Kasai and Popov 1985). This figure also indicates that the ultimate strength of an EBF with short links is significantly larger than that of a moment frame (i.e., $e/L = 1.0$).

Note from the yield mechanisms shown in Figure 10.3 that only one end of each diagonal brace is connected eccentrically to the beam to create a yielding link (the so-called active link), whereas the other end of the brace is concentrically, or in practice sometimes nearly concentrically, connected to the beam and column centerlines. Next consider two EBF configurations in Figure 10.19. Case (a) contains three active links. In Case (b), however, the braces are connected to the beams eccentrically at both the top and bottom ends. It appears at first glance that the latter case is desirable as it contains more links. But it has been shown that not all the links are fully effective (Kasai

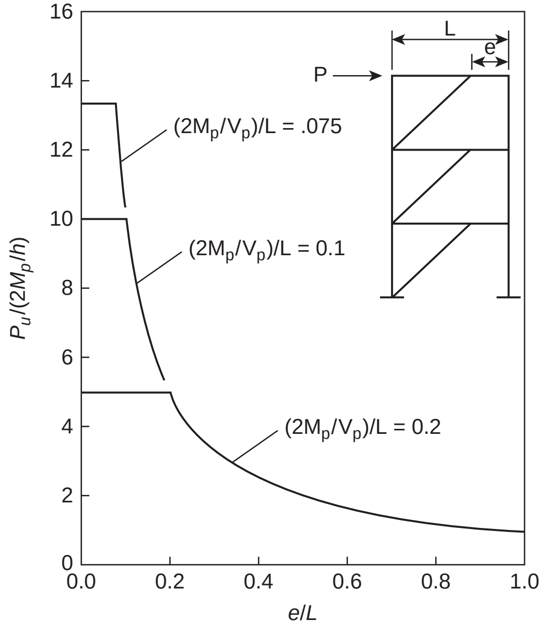

FIGURE 10.18 Variations of EBF ultimate strength with e/L. (*Kasai and Popov 1985, with permission from EERC, University of California, Berkeley.*)

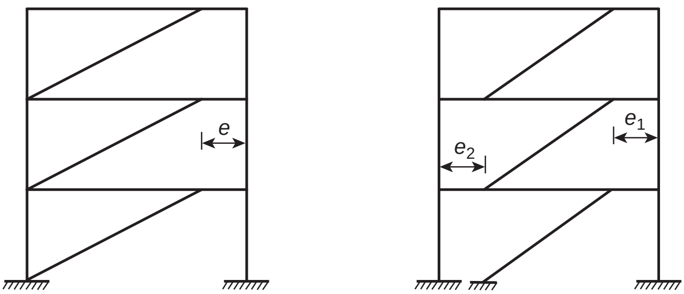

(a) EBF with active links **(b)** EBF with active and inactive links

FIGURE 10.19 EBF configurations with active and inactive links.

and Popov 1985). If the upper link has design shear strength significantly lower than that of the link in the story below, the upper link will deform inelastically and limit the force that can be developed in the brace and to the lower link. Under such circumstances, the upper link is called an active link and the bottom link is called an inactive link. Because it is difficult to design all links to be active and all the links need to be detailed and fabricated as if they are active anyway, EBF configurations that contain inactive links are not economical and are not recommended.

10.4 Ductility Design

10.4.1 Sizing of Links

Links in an EBF are designated as structural fuses and are sized for code-specified design seismic forces. So the member sizes are to be selected based on the basic seismic load combinations. It is highly desirable that the actual web area is equal to the required web area, or, if not possible, only slightly larger. In AISC 341-02, the I-shaped link sections need to be seismically compact, i.e., the width-thicknesses for both flange and web local buckling limit states need to satisfy the requirement of highly ductile members. But the stringent flange local buckling requirement ($b_f/2t_f \leq 0.30\sqrt{E/F_y}$) often requires a heavier section with a larger web area. Overdesigning links is not desirable from the capacity design point of view because it has a direct impact on the design of braces, columns, and beams outside the links. Because the moments at the ends of a shear link are not expected to be high, based on both analytical study (Richards and Uang 2005) and experimental verification (Okazaki et al. 2005), the limit of $b_f/2t_f$ has been relaxed from $0.30\sqrt{E/F_y}$ to $0.38\sqrt{E/F_y}$.

The required link rotation as computed from Eq. (10.11) also cannot be larger than the allowable rotation capacity (see Figure 10.11).

10.4.2 Link Detailing

10.4.2.1 I-Shaped Links

Full-depth web stiffeners must be placed symmetrically on both sides of the link web at the diagonal brace ends of the link. These end stiffeners are required to have a combined width not less than ($b_f - 2t_w$) and a thickness not less than $0.75t_w$ or 3/8 in, whichever is larger. The origin of this thickness requirement is described in Section 10.4.2.3.

The link needs to be stiffened in order to delay the onset of web buckling and to prevent flange local buckling. The stiffening requirement is dependent on the length of link. For a shear link with $e \leq 1.6M_p/V_p$, a relationship among the link web deformation angle, γ_p, the web panel aspect ratio as well as the beam web slenderness ratio was developed (Kasai and Popov 1986a). Based on Eq. (10.6), the link stiffener spacing can be rewritten as follows:

$$a = C_B t_w - \frac{d}{5} \tag{10.17}$$

These C_B values were slightly modified and adopted in AISC 341 as follows:

(1) When $e \leq 1.6M_p/V_p$, intermediate stiffeners are needed per Eq. (10.17), but the coefficient C_B is a function of the

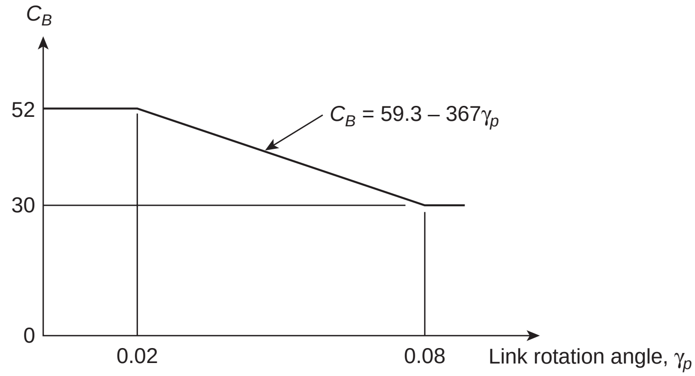

FIGURE 10.20 Variation of C_B.

deformation demand; the relationship between C_B and γ_p implied by AISC 341 is shown in Figure 10.20.

(2) When $2.6M_p/V_p \le e \le 5M_p/V_p$, intermediate stiffeners shall be provided at a distance $1.5b_f$ from each end of the link to control flange local buckling.

(3) When $1.6M_p/V_p \le e \le 2.6M_p/V_p$, intermediate stiffeners satisfying the requirements of both Cases 1 and 2 are needed.

(4) When $e > 5M_p/V_p$, intermediate stiffeners are not required.

Intermediate link web stiffeners must be of full depth. Although two-sided stiffeners are required at the end of the link where the diagonal brace intersects the link, intermediate stiffeners placed on one side of the link web are sufficient for links of depth less than 25 in. In links of depth less than 25 in the thickness of one-sided stiffeners is specified to be no less than t_w or 3/8 in (10 mm), whichever is larger. Fillet welds connecting a link stiffener to the link web shall have design strength to resist a force of $A_{st}F_y$, where A_{st} is the stiffener area. The design strength of fillet welds fastening the stiffener to the flanges shall be adequate to resist a force of $A_{st}F_y/4$.

In the testing of large-size built-up shear links, brittle fracture in the web was observed (McDaniel et al. 2003). The fracture initiated from a flange-web-intermediate stiffener junction where the region was highly restrained due to welding. An analysis of the failure showed that the cause was a stress concentration at the end of the stiffener vertical welds because the stiffener was terminated too close to the flange-to-web groove weld. It was recommended that the stiffener vertical welds be terminated from the flange-to-web weld by a minimum distance of $3t_w$. In another testing program, fracture in the web initiating from the ends of stiffener vertical welds was also observed (Figure 10.14). To delay the onset of link web fracture, Okazaki et al. (2005) suggested that the stiffener welds be terminated a distance of $5t_w$ from the k-line in the rolled section.

10.4.2.2 Built-Up Box Links

When eccentrically braced frames are desirable in locations where lateral bracing of the link cannot be achieved (such as between two elevator cores, or along the facade of building atriums), links with built-up box sections could be used, as such built-up box cross-sections are not susceptible to lateral-torsional buckling. Eccentrically braced frames having such links and without lateral bracing of the link beam performed in a ductile manner during experiments, provided the specified section compactness requirements were met (Berman and Bruneau 2007, 2008a, 2008b). Note that HSS sections cannot be used for such links, due to concerns about their low cycle fatigue life under large inelastic deformations (see Chapter 9).

However, recognizing that extremely tall and narrow boxes can experience lateral-torsional buckling (i.e., buckle about their weak axis), design provisions require that the links of built-up box sections be sized such that $I_y > 0.67I_x$, where I_y is the link's moment of inertia about an axis in the plane of the EBF, and I_x is the moment of inertia about an axis perpendicular to that plane. Furthermore, simultaneously with the other forces acting on the link beams, a lateral load acting at the brace-to-beam points and perpendicularly to the frame plane must be considered conservatively, together with a corresponding out-of-plane stiffness requirement, to further prevent weak or laterally flexible link as well as to ensure adequate lateral restraint to the brace.

Berman and Bruneau (2005) derived relationships setting the maximum spacing of stiffeners for shear yielding links (i.e., $e \leq 1.6M_p/V_p$) of built-up box sections as $20t_w - (d - 2t_f)/8$ to develop a link rotation angle of 0.08 rad, and $37t_w - (d - 2t_f)/8$ for a corresponding 0.02 rad limit. However, as experimental and finite element simulations only validated the closer stiffener spacing required for the 0.08 rad link rotation angle; that value is required for all links until further data becomes available.

Berman and Bruneau (2006, 2007, 2008a) showed the importance of providing intermediate web stiffeners for shear yielding built-up box section links with h/t_w greater than $0.64\sqrt{E/F_y}$ and less than or equal to $1.67\sqrt{E/F_y}$. For shear links with h/t_w less than or equal to $0.64\sqrt{E/F_y}$, intermediate web stiffeners are not required because they have no effect on flange buckling (which is the controlling limit state in that case). Nor are they required for links of lengths exceeding $1.6M_p/V_p$, because local buckling of both webs and flanges in flexure dominates link strength degradation in that instance; for that reason, the width-to-thickness of web and flanges in those long links is limited to $0.64\sqrt{E/F_y}$.

External intermediate stiffeners, as in Figure 10.21, were considered in the experimental and analytical work of Berman and Bruneau (2006, 2008a, 2008b); these were welded to both the webs and the flanges. However, because such stiffeners have no benefit on flange buckling, AISC 341 and CSA S16 do not require them to be connected to the flange. This suggests that intermediate stiffeners could be fabricated inside the built-up box section (which may be desirable for

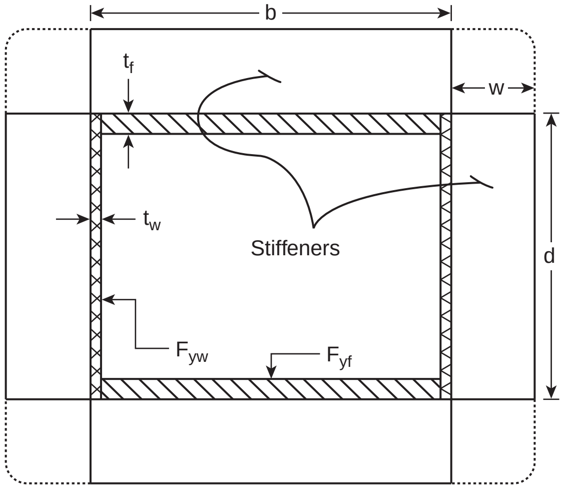

(a)

(b)

FIGURE 10.21 (a) Generic built-up box cross-section with exterior stiffeners; (b) deformed Link at 0.123 rads rotation. (*Berman and Bruneau 2005; Courtesy of MCEER, University at Buffalo.*)

architectural appeal or other reasons). Note that equations prescribing the minimum required areas and inertia for intermediate stiffeners for I-shaped sections have been derived without considering connection to the flanges (Bleich 1952, Malley and Popov 1984, Salmon et al. 2009), but web stiffeners were found to provide stability to the flanges in I-shaped links (Malley and Popov 1984); this is not the case in built-up box cross-sections.

Finally, for capacity design purposes, note that tested built-up box cross-section links (Berman and Bruneau 2005) have strain hardened 11% more in strength than wide flange links (Richards 2004); correspondingly, braces, beams (outside the link), and columns must be designed for such proportionally larger forces.

10.4.2.3 Origin of Code Specified Stiffener Thickness Requirements

The axial force in intermediate stiffeners was obtained by Malley and Popov (1984) from a free-body diagram considering a diagonal tension field developing in the beam's web. Setting this force to $A_{st}F_{yst}$, and solving for A_{st}, conservatively assuming that a one-sided intermediate web stiffener carries that entire force alone, gives

$$A_{st} = \frac{F_{uw} t_w a}{0.828 F_{yst}} \left[1 - \frac{a/h}{\sqrt{1+(a/h)^2}} \right] \tag{10.18}$$

where A_{st} = minimum cross-sectional area of one stiffener, F_{uw} = specified minimum tensile strength of link web, t_w = thickness of one link web, h = clear height of link web, a = spacing of intermediate web stiffeners, and F_{yst} = specified minimum yield strength of stiffener. A slightly more liberal value is obtained if accounting for part of the beam web to work together with the stiffener to resist the axial force. Malley and Popov suggested a contributing beam web area of $t_w b_f/2$. For comparison, ANSI/AISC 360-05 assumed $18t_w^2$ for stiffeners; note that requirements for A_{st} were eliminated in AISC 360-10.

Malley and Popov (1984) also suggested a required minimum inertia of intermediate stiffeners. Starting from the equation derived by Bleich (1952) for plates with simply supported edges free to rotate (adopted in AISC 360), the required stiffness for intermediate stiffeners is

$$I_{st} \geq j a t_w^3 \tag{10.19}$$

where

$$j \geq \frac{2.5}{(a/h)^2} - 2.0 > 0.5 \tag{10.20}$$

Malley and Popov suggested using an alternative equation for plates with edges fixed against rotation, and conservatively magnifying the requirements from this equation by 4 to arbitrarily keeping the stiffeners straight in the postbuckling inelastic range.

$$j \geq \frac{5.9}{(a/h)^2} - 2.9 \tag{10.21}$$

An example in Malley and Popov (1984) showed that, for a ratio (h/a) of 1.9, a 0.412-inch-thick intermediate stiffener would have been required for a W18 × 50 shear link (which was then rounded up to ½-inch accounting for available plate thicknesses). For the same W18 × 50 shear link, for a ratio (h/a) of 3 (i.e., approximately 50% more closely spaced stiffeners), a 0.72-inch-thick stiffener would be required per Malley and Popov's equation. The corresponding stiffener thicknesses for this same W18 × 50 example, but calculated instead per the AISC 360-05 equation, would be 0.16 in and 0.3 in, respectively, for the two different stiffener spacing considered above. Note that the requirement for thicker stiffeners at closer spacing is a consequence of the assumptions used in the derivation of this equation, namely, that transverse stiffeners be rigid enough to cause a buckling node to form along the line of the stiffener, irrespective of whether or not a tension field action is expected.

Implementation in AISC 341-10 led to the simplified requirements outlined in Section 10.4.2.1, combined with the AISC 360 requirements for standard design. Application of these AISC requirements would result in the use of a 0.375 in stiffener for the above W18 × 50 shear link example, which is significantly less than required by the Malley and Popov equation, irrespectively of stiffener spacing. Nonetheless, EBFs detailed per the AISC 341 (with 3/8-inch-thick stiffeners) have performed well in the past, suggesting that the Malley and Popov equations for sizing intermediate stiffener are too conservative.

10.4.3 Lateral Bracing of Link

To ensure stable hysteresis, an I-shaped link must be laterally braced at each end to avoid out-of-plane twisting (Hjelmstad and Lee 1989, Engelhardt and Popov 1992). Lateral bracing also stabilizes the eccentric bracing and the beam segment outside the link. The concrete slab alone cannot be relied upon to provide lateral bracing (Ricles and Popov 1989). Therefore, AISC 341 requires that both top and bottom flanges of the I-shaped link beam be braced at link ends. Bracing should have an available strength and stiffness as required for expected plastic hinge locations for highly ductile members. Lateral bracing at link ends is not required for box link due to its inherent torsional rigidity. But the moment of inertia, I_y, about an axis in the plane of the EBF shall be larger than $0.67I_x$.

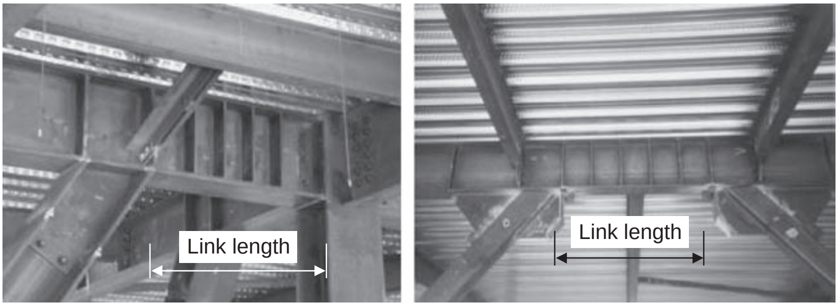

(a) Exterior link **(b)** Interior link

Figure 10.22 Lateral bracing of links.

Figure 10.22 shows two examples of the link lateral bracing; the link length, e, is also shown. Because AISC 341 specifies that lateral bracing be placed at the ends of the link, to be effective the two lateral bracings in Figure 10.22b should be placed further inward.

10.5 Capacity Design of Other Structural Components

10.5.1 General

Figure 10.23 shows the typical internal force distribution of the link, brace, and beam outside the link of two popular EBF configurations. The nominal shear strength of the link, V_n, is determined as follows:

$$V_n = \min\left\{V_p, \frac{2M_p}{e}\right\} \tag{10.22}$$

All other elements (beam segments outside the link, braces, columns, and connections) are then designed for the forces generated by the actual (i.e., expected) capacity of the links rather than the code-specified design seismic forces. That is, these elements are to be designed to resist the loads developed by the fully yielded and strain-hardened links. The capacity design concept requires that the computation of the link strength not only be based on the expected yield stress of the steel but also includes the consideration of strain hardening. The link shear strength is adjusted upward first by the material overstrength factor, R_y, and then by a cyclic hardening factor, ω:

$$V_l = \omega(R_y V_n) \tag{10.23}$$

The value of ω, to be explained below, varies with the member type.

10.5.2 Internal Force Distribution

When a yield mechanism is formed, the EBF no longer responds in the elastic range and the internal force distribution like that shown in Figure 10.23 cannot be obtained from an elastic analysis. With the adjusted link shear strength, V_l, known, however, it is possible to establish the internal seismic forces by hand calculations. A procedure to calculate the internal forces for the EBF frame in Figure 10.23a is summarized below.

(1) Drawn the free-body diagrams (see Figure 10.24).

(2) The link bends in reverse curvature. Assuming the inflection point is at midspan, the link end moment is

$$M_l = \left(\frac{e}{2}\right)V_l \tag{10.24}$$

where V_l is the adjusted link shear strength.

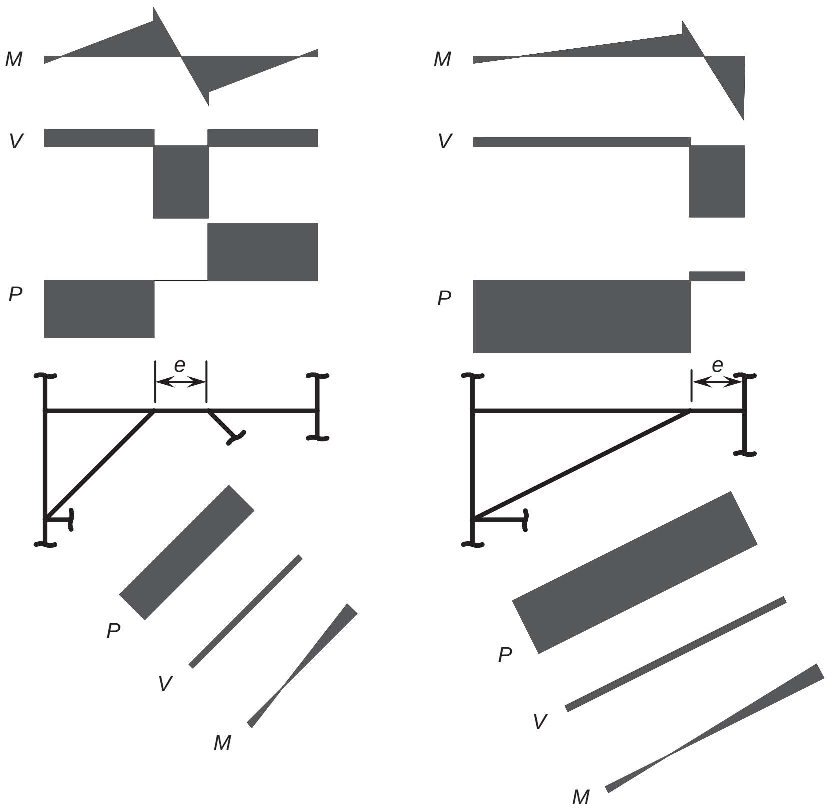

Figure 10.23 Typical internal force distributions.

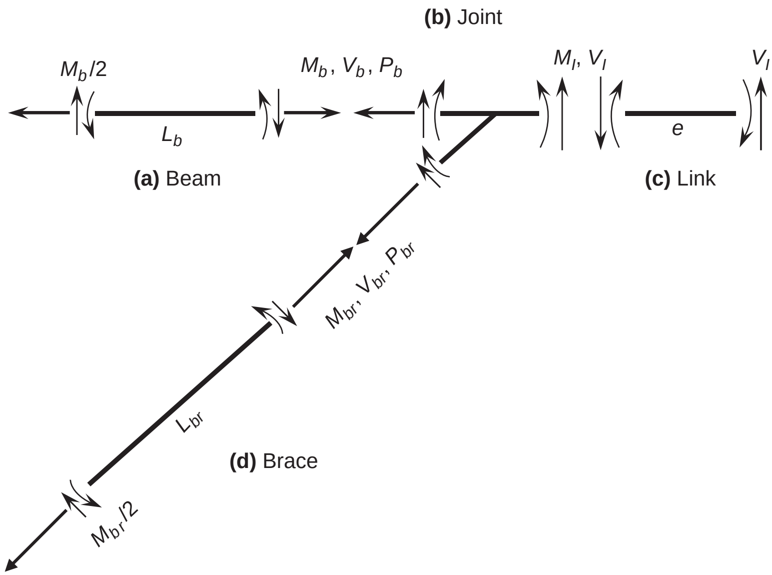

FIGURE 10.24 Free-body diagrams of link, beam, joint, and brace.

(3) Referring to the joint free-body diagram in Figure 10.24b, the link end moment is resisted by the beam and the brace. The distribution to each member is based on the relative flexural stiffness. When the far-end connections of both the beam and brace are fully restrained, the end moments in the beam and brace are

$$M_b = \left(\frac{I_b/L_b}{I_b/L_b + I_{br}/L_{br}} \right) M_l \tag{10.25a}$$

$$M_{br} = \left(\frac{I_{br}/L_{br}}{I_b/L_b + I_{br}/L_{br}} \right) M_l \tag{10.25b}$$

Half of the beam end moment is carried over to the other end. The beam shear, V_b, then can be calculated by statics:

$$V_b = \frac{1.5 M_b}{L} \tag{10.26}$$

(4) Consider the vertical equilibrium of the joint free-body. The link and the beam shear acting on the free-body is mainly balanced by the vertical component of the brace axial force. (The contribution from the brace shear force is usually small and

can be ignored in preliminary design.) Therefore, the brace axial force is

$$P_{br} = \frac{V_l + V_b}{\sin\theta} \tag{10.27}$$

where θ is the inclination angle of the brace. The above equation shows that the ratio of the brace axial force to the link shear force is controlled primarily by the geometry of the EBF and is not affected by link yielding.

(5) Consider the horizontal equilibrium of the joint free-body. The horizontal component of the brace axial force needs to be balanced by the axial force in the beam.

$$P_b = P_{br}\cos\theta = \frac{V_l + V_b}{\tan\theta} \tag{10.28}$$

Thus, the required deign forces in the beam and brace are determined.

10.5.3 Diagonal Braces

Diagonal brace is often connected to the link beam by fully restrained moment connection such that it can participate in resisting a portion of the link moment, thus reducing the moment in the beam outside of the link. In such case, the brace needs to be designed as a beam-column. Equation (10.27) also shows that the brace axial force increases as the inclination angle of the brace is reduced. So it is desirable that the angle be kept above, say, 40°.

For brace design, AISC 341 requires that the cyclic strain-hardening factor, ω, in Eq. (10.23) be taken as 1.25 for I-shaped links and 1.4 for boxed links. Note from Section 10.2.2 that cyclic testing of I-shaped links showed that the cyclic strain-hardening factor can reach 1.4 to 1.5. For economic reasons, however, a lower value of 1.25 was chosen by AISC. The justification follows. First, the material overstrength factor, R_y, for the link is already used in Eq. (10.23) to compute the required seismic force in the brace, yet the material overstrength of the brace is not considered for the calculation of its design strength. In fact, a resistance factor, ϕ, is used to compute the brace deign strength. When the effect of both material overstrength (conservatively taken as 1.1) and resistance factor (= 0.9) are considered, the effective cyclic strain-hardening factor would have been 1.53 (= 1.1/0.8 × 1.25), which matches well with the AISC implicitly assumed ω value of 1.5. In situations where a much significant strain hardening would occur (e.g., when built-up I-shaped links with thick flanges are used), it is prudent to use a larger ω value.

Because diagonal braces in an EBF are designed to remain elastic while allowing the links to deform inelastically, many of the ductility-related design provisions for braces in the SCBF system intended to permit stable cyclic buckling of braces are not needed in EBF. But AISC 341 still requires the braces to be treated as moderately ductile members for the section compactness requirement.

10.5.4 Beams Outside of Link

For all except Case (d) in Figure 10.1, the beam segment and the link are a single continuous wide flange or built-up box member. For Cases (a) and (b), the beam(s) outside the link is subjected to both high moment and high axial force (see Figure 10.23). Therefore, these beams need to be designed as a beam-column. Designing these beams is challenging in EBF design, so it is desirable to reduce both moment and axial force demand in the beam. To reduce the beam end moment, a short link can be used to reduce e in Eq. (10.24). Connecting the brace to the link beam by fully restrained moment connection also helps [Eq. (10.25a)]. To limit the beam axial force to a manageable level, the inclination angle of the brace should not be too small [Eq. (10.28)].

Because experience shows that design of the beam segment outside of the link can be problematic, to facilitate EBF design AISC 341 specifies an even lower ω value (= 1.1) for beam design; this value is 88% of the value (= 1.25) used for brace design. This relaxation is justified because, first of all, testing showed that limited yielding in the beam will not be detrimental to EBF performance, as long as stability of the beam is assured (Engelhardt and Popov 1989). Furthermore, it is assumed that the composite floor slab, which is generally ignored in computing the beam strength, will also participate in resisting the bending moment and axial force. With this background information in mind, the designer is cautioned to use a larger ω value in situations such as when the floor slab is not present or when built-up I-shaped links are used. Because AISC 341 implicitly assumes that the beam may experience limited yielding, beams should satisfy the width-thickness limitations for moderately ductile members.

To further facilitate the design of beams outside of the link when, as shown in Figure 10.1 with the exception of Case (d), a single continuous member is used for both the link and the beam at each floor level. AISC 341 allows the engineer to use the expected yield stress, R_yF_y, to compute the beam design strength. This is because any increase in yield strength in the link is also present in the beam segment.

Based on the discussion presented so far, it is obvious that the beam required design force and the link design strength are highly coupled when the same member is used for both the link and the beam segment, Figure 10.1d shows one exception when the links are oriented vertically. In this case the beam strength has to be based on F_y, not R_yF_y. This configuration is attractive when it is desirable that the gravity load-carrying capacity of the entire beam is not impaired by the yielding or buckling of the link (Fehling et al. 1992). This type of EBF configuration has also been shown to be effective for the seismic rehabilitation of not only steel but also reinforced concrete frames (Perera et al. 2004).

Because high axial force in the beam tends to cause difficulty in beam design, one way to bypass this problem is to use an EBF configuration like that shown in Figure 10.1e. In this case, the lateral loads are mainly transmitted downward to the base through the diagonal braces (Engelhardt and Popov 1989). But because the links do not exist in every floor, larger link sections are needed, and the redundancy for seismic resistance is also reduced.

10.5.5 Columns

Using a capacity design approach, columns in braced bays must have a sufficient strength to resist the sum of gravity-load actions and the moments and axial forces generated by the adjusted shear strength of the link. This procedure assumes that all links will yield and reach their maximum strengths simultaneously. Nevertheless, available multistory EBF test results showed that this preferred yielding mechanism is difficult to develop. For example, shaking table testing of a reduced-scale, six-story EBF building showed that links in the bottom two stories dissipated most of the energy (Whittaker et al. 1989). Therefore, this design procedure may be appropriate for low-rise buildings and the upper stories of medium- and high-rise buildings but may be too conservative in other instances. For this reason, AISC 341 allows the columns to be designed for a seismic effect corresponding to that when all the links reach the adjusted link strength [Eq. (10.23)] with ω equal to 1.1 (= 0.88×1.25). But an ω value of 1.25 still needs to be used when the number of stories is less than 3. Column members should also satisfy the width-thickness limitations for highly ductile members.

10.5.6 Connections

10.5.6.1 Diagonal Brace Connections

It was shown in Chapter 9 that diagonal brace connections in an SCBF need to be designed for the expected tensile and compressive strengths of the brace because the brace serves as the structural fuse. The gusset plate is also detailed to accommodate inelastic rotation due to brace buckling. Nevertheless, these stringent requirements are not needed for brace connections in an EBF because links, not braces, are structural fuses. The brace connection only needs to be designed for the same forces as the brace.

Figure 10.25a shows the detail of a diagonal brace-to-beam connection used in a full-scale, six-story EBF building tested at BRI, Japan

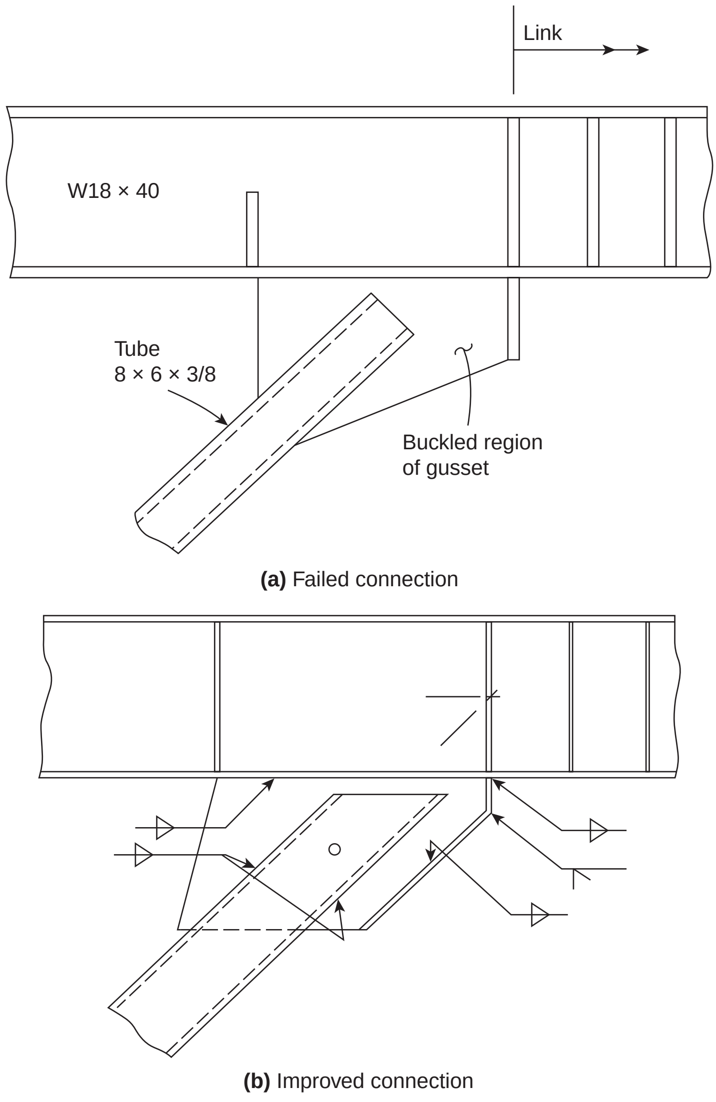

FIGURE 10.25 Brace-to-beam gusset connection. (*Courtesy of M.D. Engelhardt, Dept. of Civil Engineering, University of Texas, Austin.*)

(Roeder et al. 1987). The gusset plate buckled when the link end was subjected to a large negative bending moment. An improved detail in Figure 10.25b shows that not only the free edge of the gusset is stiffened but also the brace end is extended further toward the beam (Engelhardt and Popov 1989). See Figure 10.22b for one example in real application.

Fully restrained moment connection is needed if the diagonal brace is designed to carry a portion of the link end moment. Complete-joint-penetration groove welds, especially in the brace flanges, are generally used. Figure 10.22a shows one such example; note the designer opted to shop weld the brace-to-beam connection to avoid overhead welding in the field, and the brace was field spliced.

The design of beam-to-column connection for the end of the brace opposite the link is the same as that of SCBF.

10.5.6.2 Link-to-Column Connections

When an EBF configuration with exterior links is used, fully restrained moment connections are needed to connect the link to the column. Based on cyclic testing of pre-Northridge style I-shaped link-to-column moment connections conducted before 1994 (Malley and Popov 1984, Engelhardt and Popov 1989), it was observed that a fully welded moment-resisting connection with complete-joint-penetration groove welds in the flanges and a web connection capable of developing a shear capacity of the link performed better than a similar connection but with a bolted web connection where bolt slippage could occur. As shown in the next paragraph, however, the former connection detail is still not reliable based on testing conducted after 1994. The performance was even inferior when the link was connected to the weak-axis of the W-shaped column. A similar problem also exists when the I-shaped link is connected to a built-up box column (Tsai and Young 1991).

Okazaki et al. (2006) explored the potential of using four types of link-to-column connections with improved welds and details originally developed for post-Northridge SMF moment connections. Cyclic testing showed that the majority of test specimens, including those with welded flange-weld web connections, failed by fracture of the link flanges near the groove welds. The performance depended strongly on the link length, with the inelastic link rotation capacity decreasing significantly with an increase in the link length. Because the test results suggested that premature failure of the link flange is a concern for both short and longer links, one option that is permitted by AISC 341 is to reinforce the link near the column end. See Figure 10.26 for one example that utilizes a welded haunch; the corresponding length of the link is also shown.

Although AISC does not provide any prequalified link-to-column moment connections to date, further study by Okazaki et al. (2009) showed two promising connection details. The first one, which is suitable for shop welding and column-tree type of erection procedure, involves the use of all-around fillet welds to connect the link flanges and web to the column. See Figure 10.27 for the detail. It is suggested that the size of the fillet weld be equal to 1.5 times the thickness of the link flange or web. To avoid introducing undercuts or weld defects at the link-flange edges, which are a common location

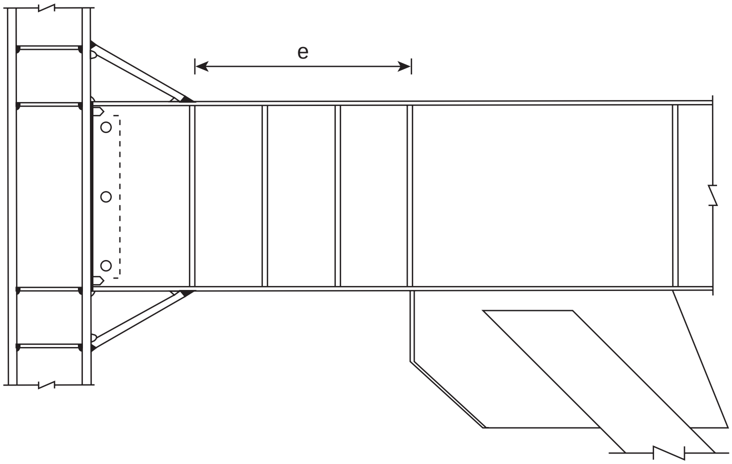

Figure 10.26 Example of reinforced link-to-column connection. (*Copyright © American Institute of Steel Construction. Reprinted with permission. All rights reserved.*)

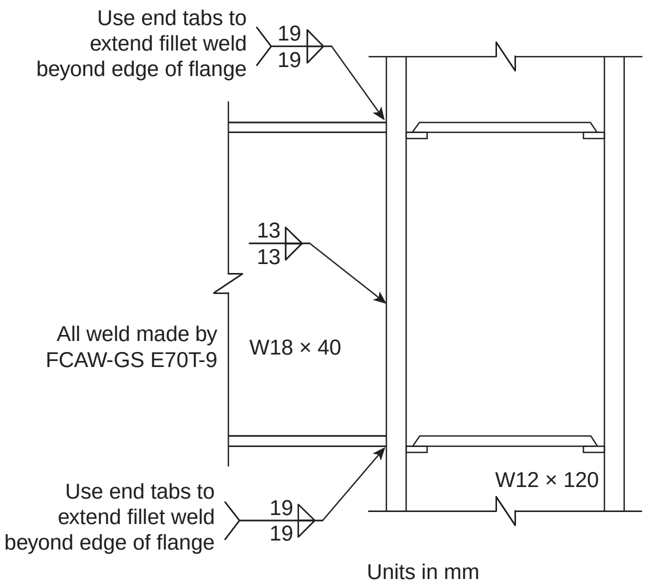

Figure 10.27 All-around fillet welded link-to-column connection. (*Courtesy of M.D. Engelhardt, Dept. of Civil Engineering, University of Texas, Austin.*)

for fracture initiation, it is important to use weld tabs to run-off the fillet welds beyond the edge of the link flange.

The second promising connection type is suitable for field welding and erection procedure, and the detail is shown in Figure 10.28a.

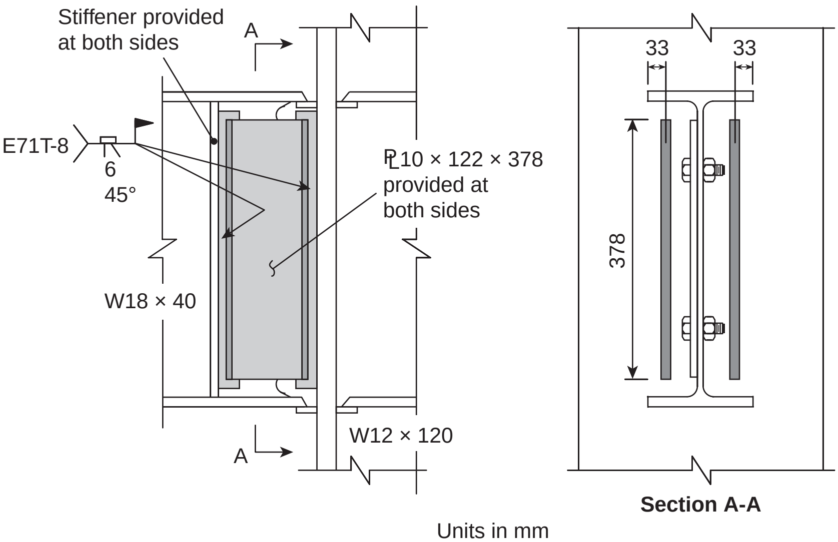

(a)

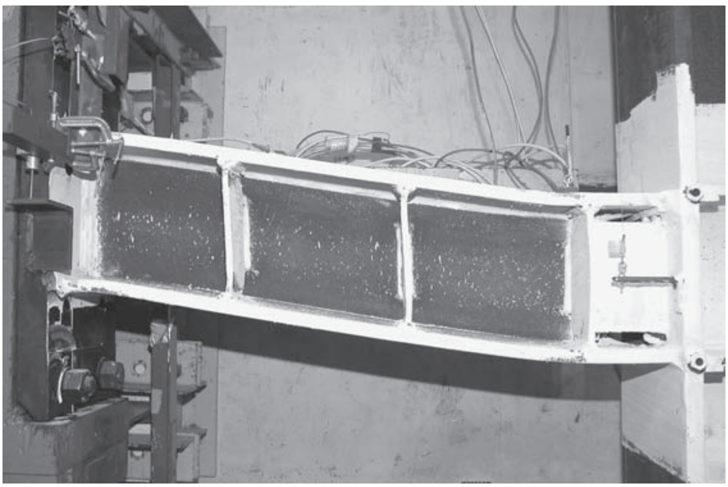

(b)

Figure 10.28 Link-to-column connection reinforced with supplemental web stiffeners. (*Courtesy of M.D. Engelhardt, Dept. of Civil Engineering, University of Texas, Austin.*)

It requires a pair of supplemental stiffeners to reinforce the first link web panel next to the column, with these stiffeners oriented parallel to the link web but offset from the link web but a short distance. To avoid welding to the link flanges, these stiffeners are of partial height. Each stiffener is welded to the column flange and the first link web stiffener by either groove or fillet weld. Figure 10.28b shows that the reinforcement is effective in preventing fracture at the link-to-column connection. The thickness of the supplemental stiffeners is selected such that the nominal plastic moment of the reinforced segment is larger than the expected link end moment.

When an exterior link is used, an elastic analysis would show that the moment at the column end is generally larger than that at the brace end, i.e., the inflection point is not at the midspan of the link. When the link is not too short, however, end moment equalization would occur due to redistribution of the moments at higher deformation levels, and Eq. (10.24) is still valid (Kasai and Popov 1986b). For link shorter than $1.6M_p/V_p$, the link shear will reach $\omega R_y V_p$, and the following end moments should be assumed in design (AISC 341-10):

$$M_{\text{column end}} = R_y M_p \tag{10.29a}$$

$$M_{\text{brace end}} = e(\omega R_y V_p - R_y M_p) \geq 0.75 R_y M_p \tag{10.29b}$$

where $\omega = 1.25$.

10.6 Design Example

The following section illustrates the design of an eccentrically braced frame. The design applies the requirements of ASCE 7 (2010) and AISC 341 (2010). The example is not intended to be a complete illustration of the application of all design requirements. Rather, it is intended to illustrate key analysis and proportioning techniques that are intended ensure ductile response of the structure.

10.6.1 Building Description and Loading

The example building is nearly identical to the one used in Chapter 8 (Special Moment Frames); more detailed seismicity and building information is included in that example. The difference in this case is that eccentrically braced frames are used and only one bay of braced frames is provided at the perimeter framing lines in each orthogonal direction. The seismic design parameters are shown in Table 10.1.

The typical plan is shown in Figure 10.29 and the typical frame elevation is shown in Figure 10.30.

R	8
I	1.0
C_d	4
Ω_o	2

Table 10.1 Seismic Design Parameters

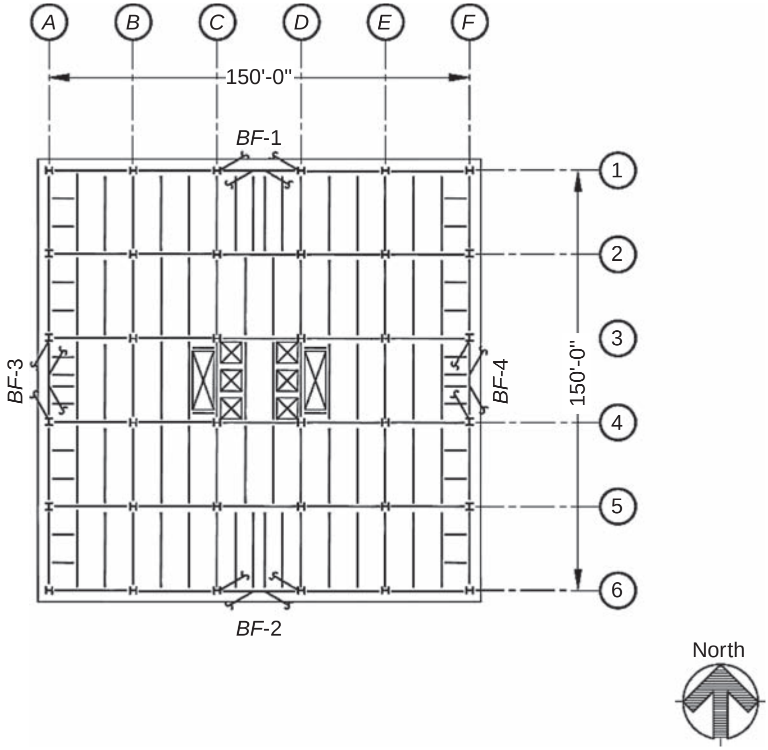

Figure 10.29 Typical floor plan.

Based on the seismic design data a generic seismic response spectrum is constructed in accordance with ASCE 7. Because there is only one braced bay on each side of the structure, the design shear at every story must be multiplied by a redundancy factor ρ equal to 1.3.

10.6.2 Global Requirements

The structure must be designed to provide both adequate strength and adequate stiffness. Typically strength requirements will govern the design of lower buildings, whereas taller buildings will be controlled by drift. The threshold height is dependent on many factors, including the shape of the response spectrum, the analytical procedure used, and the braced bay configurations and proportions.

Where strength considerations govern the design process is fairly straightforward: the braced frames are designed to provide adequate strength, then the columns, braces, and beams outside the link are redesigned to preclude their failure when subjected to the forces corresponding to fully yielded and strain-hardened links. A reanalysis may be performed to confirm that the required brace strength has not

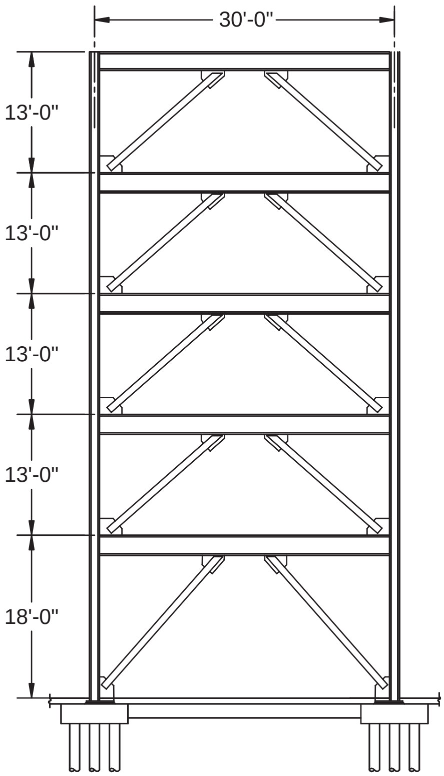

Figure 10.30 Typical frame elevation.

been increased due to an increase in frame stiffness (due to change of period on the response spectra when member forces are obtained from dynamic analysis).

Where drift is the governing concern the process requires more iteration. Any increase in link strength will impose larger forces on beams and columns when the link yields. Thus, any stiffening of the frame should be done with the required strength proportioning in mind.

Link rotation demands are also checked using the design story drift and compared with permissible maxima derived from link testing.

10.6.3 Basis of Design

The design of EBF is based on the expectation of a global yield mechanism in which links yield in shear, flexure, or a combination of the two, and plastic hinges form at the column bases. Where frame beams are connected rigidly to columns, hinging in the beam or column is also anticipated. Otherwise, large rotations must be accommodated in the beam-to-column connections. In this case, pinned beam-to-column connections are used. Figure 10.31 shows this mechanism.

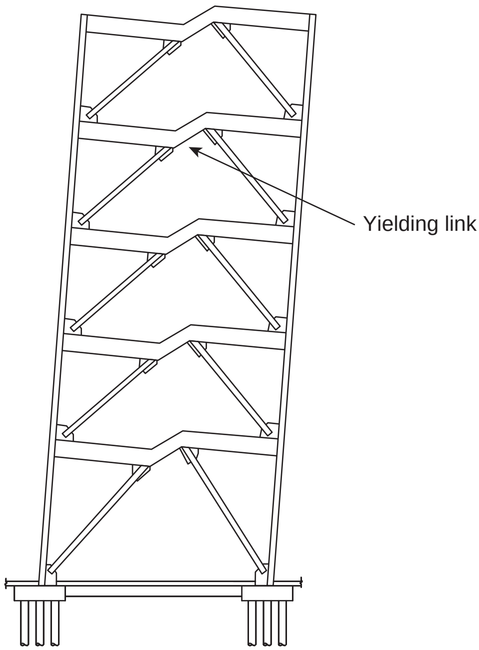

Figure 10.31 Anticipated mechanism.

The value of the link beam shear in this mechanism is adjusted for both material overstrength and strain hardening. For shear-governed, I-shaped links, this quantity is taken as

$$V_{link} = 1.25 R_y F_y \, (0.6 A_{lw}) \tag{10.30}$$

where A_{lw} is the area of the web excluding the flanges and V_{link} is the adjusted shear strength of the link, including material overstrength and strain hardening.

10.6.4 Sizing of Links

To start the preliminary design, the following steps are taken:

- Determination of base shear
- Vertical distribution of forces
- Horizontal distribution of forces to frames

These steps are not illustrated in this example.

For preliminary design purposes the frame shear can be assumed to be resisted entirely by the link and braces. Figure 10.32 shows a free-body diagram of half the frame.

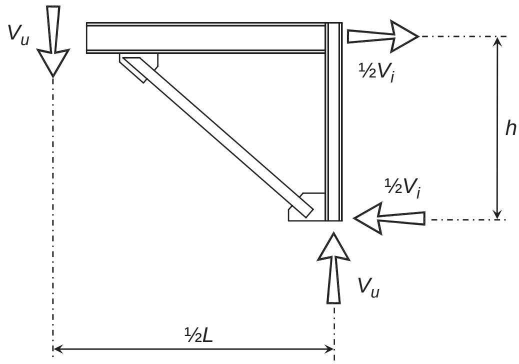

FIGURE 10.32 Free-body diagram showing link shear and frame shear.

Thus, the link shear in this configuration can be assumed to be

$$V_u = \frac{V_i h}{L} \tag{10.31}$$

where h is the story-to-story height, L is the bay width, and V_i is the shear resisted in the frame at level "i." Required link strengths thus obtained are shown in Table 10.2.

Links may be governed by shear or by flexure. Generally, shear-governed links are more ductile, and the engineer may elect to provide such links. To ensure shear-governed links, link beam sizes are selected based on their plastic shear capacity, and the link length is limited in order to limit the moment that can develop. Thus the link beams will be selected based on their shear strength:

$$\phi(0.6A_{lw}F_y) \geq V_u \tag{10.32}$$

where ϕ is 0.90, A_{lw} is the area of the web excluding flanges, and V_u is the required shear strength of the link. Preliminary link beam sizes are presented in Table 10.3.

Level	Frame Shear (kips)	Required Link Strength (kips)
Roof	201.0	87.1
Fifth Floor	361.4	156.6
Fourth Floor	477.0	206.7
Third Floor	551.5	239.0
Second Floor	589.7	353.8

TABLE 10.2 Preliminary Required Link Strengths

Level	Beam Size
Roof	W14 × 26
Fifth Floor	W18 × 46
Fourth Floor	W21 × 57
Third Floor	W21 × 73
Second Floor	W27 × 114

Table 10.3 Preliminary Link Beam Sizes

Next, to ensure shear-governed links, the link length is limited based on the ratio of its shear to flexural strength. The theoretical dividing line between shear-governed and flexure-governed links is a length of:

$$e = \frac{2M_p}{V_p} \tag{10.33}$$

where e is the clear link length from edge of connection to edge of connection; M_p is the link flexural strength, ZF_y; and V_p is the link shear strength, $0.6F_y A_w$.

Link lengths in this example are set at three quarters of this limiting value (i.e., $1.5M_p/V_p$). This is a design decision intended to guarantee shear-governed links; other approaches are acceptable. Note that the horizontal distance between the intersections of the brace centerlines (henceforth designated as x) with the beam centerline is not necessarily equal to the eccentricity, e. For preliminary design, it will be taken as equal, and the actual dimension will be substituted after members are selected and the brace-to-beam connection is configured. These link lengths, initially equal to the workpoint-to-workpoint eccentricities, x, are shown in Table 10.4.

Again, selection of such short link lengths ensures a shear-governed link. Thus, link flexure need not be checked. If link axial

Level	Workpoint Eccentricity, x (in)
Roof	30.2
Fifth Floor	37.3
Fourth Floor	40.2
Third Floor	47.9
Second Floor	59.1

Table 10.4 Workpoint Eccentricities

forces exceed 15% of AF_y, both the shear and flexural strengths are reduced and must be compared with the required strengths. In this example link axial forces are low, to the extent that such capacity reductions are not applicable.

Preliminary column and beam sizes can be determined based on the link beam sizes selected. Forces corresponding to the expected strain-hardened link strength are used to calculate maximum axial forces in both the beams and columns. Drift-induced flexural forces in the columns are neglected, as allowed by Section F3.3 of AISC 341. (This would not necessarily be the case for design accomplished per other codes or standards.) This permits a straightforward procedure for deriving design forces. The practical result of neglecting these flexural forces is that some flexural yielding is likely to occur at the design story drift. For this reason, highly ductile members are required for columns and moderately ductile members are required for beams within the eccentrically braced frames.

To derive the column and beam forces the expected strain-hardened link strengths are calculated using Eq. (10.30). The resulting values are presented in Table 10.5.

The mechanism shown in Figure 10.33 results in these forces being generated in the link. An analysis model may be constructed to calculate the corresponding forces in columns, braces, and beams, or free-body diagrams may be used. This example uses the latter approach. This latter approach is reasonable when pin-ended members are used; otherwise, it is somewhat cumbersome and possibly inaccurate to trace the expected strain-hardened link forces through each frame using free-body diagrams alone.

Figure 10.33 shows the model of the anticipated mechanism for the alternate computer analysis model approach.

The free-body diagram method employed in this example is to cut each link at the center, where the moment is taken to be zero, and impose a force there equal to the adjusted link shear strength. Corresponding column, brace, and beam forces are obtained. Figure 10.34 shows a free-body diagram of half the frame at the second floor, and Figure 10.35 shows a free-body diagram of half the beam within that frame along with associated axial shear and moment diagrams.

Level	V_{link} (kips)
Roof	137.4
Fifth Floor	250.8
Fourth Floor	330.8
Third Floor	370.1
Second Floor	598.2

Table 10.5 Adjusted Link Strengths

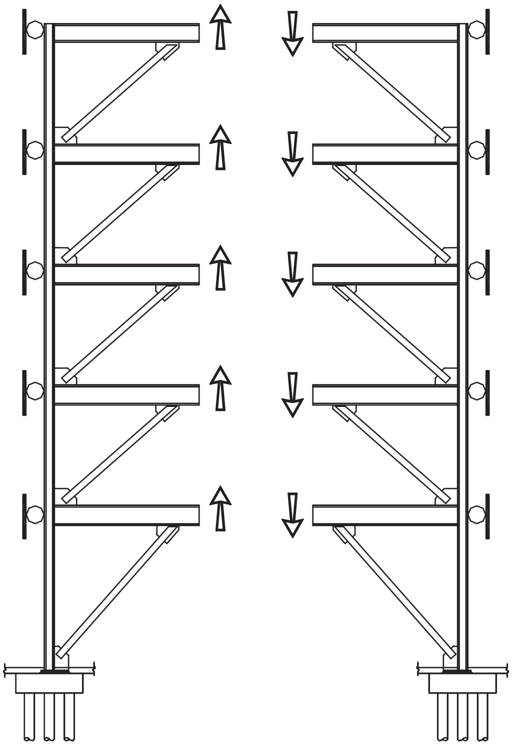

Figure 10.33 Mechanism analysis model.

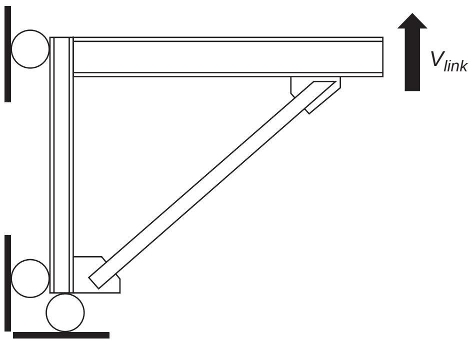

Figure 10.34 Half-frame free-body diagram.

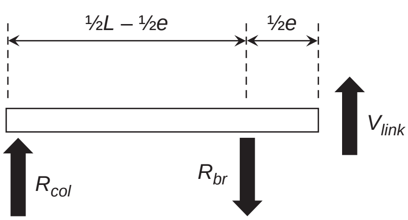

Figure 10.35 Beam free-body diagram.

The vertical seismic force in the brace at each level can be determined from the beam shear diagram, and the brace axial force can then be calculated using simple trigonometry.

$$R_{br} = V_{link}\left(\frac{L}{L-x}\right) = V_{link}\left(1+\frac{x}{2a}\right) \tag{10.34}$$

$$E_{br} = \frac{R_{br}}{\sin\theta} \tag{10.35}$$

where a is the distance from the brace/beam intersection to the column centerline, R_{br} is the vertical force in the brace corresponding to the adjusted link shear strength, E_{br} is the axial design force in the brace due to earthquake load effects, L is length of the braced bay, x is distance between brace centerline intersections with beam centerline (preliminarily taken equal to link length e), and θ is the brace angle from the horizontal.

At the second floor beam the reaction at the first floor braces is:

$$R_{br} = 598.2\left(\frac{360}{360-59.1}\right) = 715.7 \text{ kips}$$

The first floor braces seismic force is:

$$E_{br} = \frac{715.7 \text{ kips}}{\sin(55.1°)} = 872.2 \text{ kips}$$

The brace and its connections are designed to resist these forces in combination with gravity forces prescribed by ASCE 7. Preliminary brace sizes are shown in Table 10.6.

The column force from the link is determined similarly:

$$R_{col} = V_{link}\left(\frac{x}{2a}\right) = V_{link}\left(\frac{x}{L-x}\right) \tag{10.36}$$

Level	Brace Size
Fifth Floor	W14 × 43
Fourth Floor	W14 × 61
Third Floor	W14 × 68
Second Floor	W14 × 74
First Floor	W14 × 109

Table 10.6 Preliminary Brace Sizes

where R_{col} is the beam vertical reaction at the column corresponding to the adjusted link shear strength. Note that this force is directed upward, whereas the reaction at the brace acts downwards.

The first-floor upward force on the column from the second-floor link is:

$$R_{col} = 5.98.2\left(\frac{59.1}{360-59.1}\right) = 117.6 \text{ kips}$$

Simultaneously, the downward column force resulting from the overturning of the levels above is determined from the adjusted link strengths at those levels:

$$P_i = V_{link(i)}$$

Thus, the total first-floor column seismic axial force is:

$$E_1 = \sum_3^{roof} V_{link(i)} - V_{link(2)} \frac{x}{L-x} \tag{10.37}$$

$$E_1 = 137.4 + 250.8 + 330.8 + 370.1 - 117.6 = 971.5 \text{ kips}$$

Note that because this column receives force from at least three links, Section F3.3 of AISC 341 permits the seismic force to be reduced using a factor of 0.88 to represent the diminished likelihood of simultaneous strain hardening in the links to the degree assumed by the 1.25 factor. Thus,

$$E_1' = 0.88(971.5) = 854.9 \text{ kips}$$

These earthquake forces are combined with a proportion of the gravity forces using the following load combinations:

$$R_u = (1.2 + 0.2S_{DS})D + 0.5L + E \tag{10.38}$$

$$R_u = (0.9 - 0.2S_{DS})D - E \tag{10.39}$$

In this example the columns are only spliced once, four feet above the third floor. Preliminary column sizes are shown in Table 10.7. These are designed considering only the axial force and using the full story height with $K = 1.0$.

	Size
Upper Column	W14 × 68
Lower Column	W14 × 132

Table 10.7 Preliminary Column Sizes

The beams are in turn checked for the combined axial and flexural forces coming from the link. It is generally advantageous to utilize the brace to resist a portion of the link end moment and thus reduce flexural demands on the beam outside the link. The portion resisted by the brace can be determined based on the relative flexural stiffness of the beam outside the link and the brace (which depends on the moment of inertia, true length, and degree of fixity at the far end of each member), using either hand or computer methods. However, the simplified analysis used in this example does not account for such relief of flexural demands on the beam outside the link by any fixity provided at the brace-to-beam connection.

Figure 10.23 shows the moment and axial force diagrams of the beam. The moment from the link can be calculated as

$$M = V_{link}\frac{x}{2} \tag{10.40}$$

The beam axial force in this configuration is one half of the frame shear V_i at this level. This value can be calculated by rearranging Eq. (10.31) as follows:

$$P = \frac{1}{2}V_i = \frac{1}{2}V_{link}\left(\frac{L}{h}\right) \tag{10.41}$$

Note that AISC 341 permits a reduction from link capacity-based forces by applying a factor of 0.88 to the design forces for the beam outside the link. This factor has a different purpose from that in column design. In beam design, it represents tolerance of some yielding in the beam outside the link, consistent with successful test specimens in both design and observations of behavior.

$$M' = 0.88M = 0.88V_{link}\left(\frac{x}{2}\right) \tag{10.42}$$

$$M' = (0.88)598.2\left(\frac{591}{2}\right) = 15{,}564 \text{ kip-in}$$

$$P' = 0.88P = (088)\frac{1}{2}V_{link}\left(\frac{L}{h}\right) \tag{10.43}$$

$$P' = (0.88)\frac{1}{2}598.2\left(\frac{360}{216}\right) = 438.65 \text{ kips}$$

These forces are added to the flexural forces due to gravity and the vertical component of seismic load. The beam is checked for the combined effects of axial and flexural forces, with its axial capacity typically governed by torsional buckling between the orthogonal framing (assuming buckling about the weak axis is precluded by restraint provided by the deck). The second-order P-δ effect of the axial load on the flexural demand on the beam is typically minor (or nil) because of the shape of the moment diagram.

Note that if the beam is inadequate, increasing its size also increases the link strength and thus the demands on the rest of the frame (including the beam outside the link). Alternate strategies to address inadequacy of the beam include

- Local strengthening of the beam outside the link with reinforcing cover plates. Detailing of the force transfer in and out of these plates requires careful attention.
- Reduction of the eccentricity between brace centerline intersections with the beam centerline (this also reduces the link length).
- Using a rigid brace-to-beam connection to draw some of the moment into the brace (see equations in Section 10.5.2).
- Reducing or eliminating the beam axial-force demands through an alternative frame configuration, as done for example with the frame shown in Figure 10.36 (after

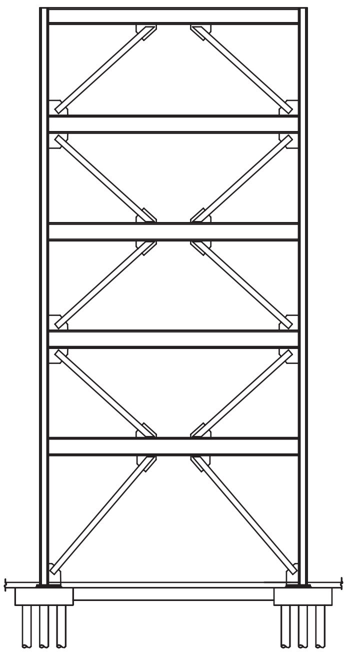

Figure 10.36 Alternate frame configuration.

Engelhardt and Popov 1989). This particular configuration would cause a large increase in link shear at the second and fourth floors, while eliminating links at the third and fifth floor. The axial force demands on the beams outside the links would be reduced dramatically at the second and fourth floors, as all of the frame shear is transferred between braces at different levels entirely within the beam-to-column connections.

Note that in the beam under consideration (for the original frame configuration assumed in this example), the combined effects calculated above using standard *P-M* interaction equations result in an excessive demand on the beam outside the link. Nevertheless, the beam size is not be revised on the basis on the above simple analysis. Instead, to reduce the flexural demand on the beams outside the link, rigidity of the brace-to-beam connections will be taken into account. In other words, a more rigorous analysis will be employed to determine the distribution of link end moment between the beam and the brace. Should the resulting combined flexural and axial demands in the beam outside the link still exceed the member's strength, use of a built-up member with a similar web but heavier flanges would then be the solution.

Using the preliminary member sizes above, a three-dimensional computer model is constructed. A modal response spectrum analysis is performed on this model using the design response spectrum. Interstory drifts are compared with the allowable drift, and the adequacy of the link member sizes is verified.

Optimization is possible at this stage because an analysis may show that some of the frame shear can be carried in the columns, allowing smaller link sizes (relative to those selected on the basis of the preliminary analysis) to be used at some levels. This reduces the resulting mechanism-based forces in beams and columns, and thus the required sizes of those members. Such downsizing is relatively straightforward for the braces and columns, but necessitates much greater attention for the beam when it is the same member as the link (which is typically the case). Reducing the demand on the beam outside the link by changing beam sizes will also reduce its capacity.

Additionally, in this case, the brace-to-beam connection is fixed in order to draw more of the moment from the strain-hardened link into the brace rather than into the beam outside the link. The division of this total moment between the brace and the beam outside the link is determined based on their relative flexural stiffness, and so it is necessary to examine the effect of reducing the brace size on the beam outside the link. Final member sizes selected, after due consideration of all the above matters, are shown in Table 10.8.

Level	Brace	Level	Beam	Link Length, *e* (in)		Column
Fifth Floor	W18 × 55	Roof	W12 × 35	24.1	Upper Column	W14 × 68
Fourth Floor	W21 × 68	Fifth Floor	W16 × 45	26.1		
Third Floor	W21 × 93	Fourth Floor	W18 × 60	31.7		
Second Floor	W21 × 101	Third Floor	W18 × 71	31.9	Lower Column	W14 × 132
First Floor	W21 × 111	Second Floor	W21 × 122	53.4		

Table 10.8 Final Member Sizes

10.6.5 Final Link Design Check

At this point member sizes have been selected and are considered final. As mentioned earlier, a reanalysis to check drift and confirm the design forces is performed after any change in member size.

With final member sizes determined, the true link dimension, *e*, may be distinguished from the frame centerline offset dimension *x*. Here, the design uses a brace-to-beam connection with direct flange-to-flange welds (connections with gussets make it possible for *e* to equal *x*). The dimension *x* represents the distance between the intersection points of the brace centerlines with beam centerline. The dimension *e* represents the distance between the brace connections. Figure 10.37 shows both dimensions.

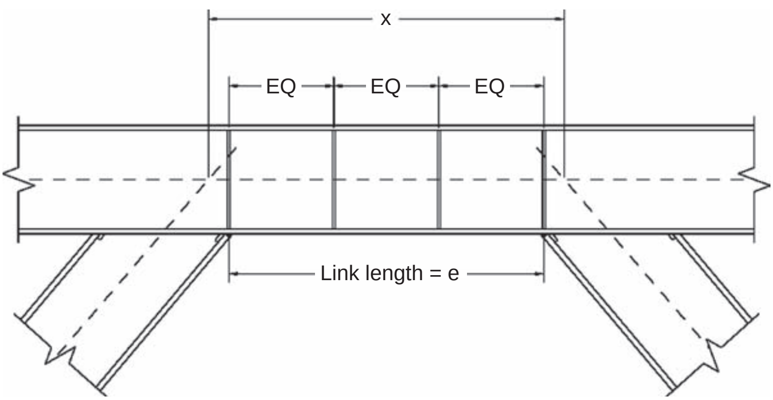

Figure 10.37 Link dimensions.

The link length e can be calculated as follows:

$$e = x + \frac{d_{beam}}{\tan\theta} - \frac{d_{brace}}{\sin\theta} \tag{10.44}$$

where d_{beam} is the beam member depth and d_{brace} is the brace member depth.

Link dimensions are given in Table 10.9. The link length, e, is compared with the ratio of moment capacity, M_p, to shear capacity, V_p. A ratio of 1.6 or lower indicates a shear-governed link; a ratio above indicates a flexure-governed link. The comparison is also used for certain detailing requirements, as illustrated in Section 10.6.7.

If the link is shear-governed, the required link shear strength from the analysis is appropriate for design of the link. If the link is governed by flexure, the required flexural strength from the analysis may not be appropriate if x is significantly different from e (this is why the design procedure for EBF in Section F3 of AISC 341 has flexural strength converted to equivalent shear strength.) The true required flexural strength should be calculated at the end of the link rather than at the centerline intersection. It may be determined from the required shear strength:

$$M_u = \frac{V_u e}{2} \tag{10.45}$$

Level	Brace	Level	Beam	x (in)	Link length e (in)	$\frac{e}{M_p/V_P}$
Fifth Floor	W18 × 55	Roof	W12 × 35	37.23	24.12	0.97
Fourth Floor	W21 × 68	Fifth Floor	W16 × 45	39.84	26.13	0.98
Third Floor	W21 × 93	Fourth Floor	W18 × 60	44.08	31.77	1.08
Second Floor	W21 × 101	Third Floor	W18 × 71	43.68	31.96	1.10
First Floor	W21 × 111	Second Floor	W21 × 122	64.67	53.46	1.24

Note that because deep braces are used, the link length e is shorter than the eccentricity x.

Table 10.9 Final Link Design

Use of this required flexural strength is equivalent to the AISC 341 formulation of the shear strength of a flexure-governed link (ASIC 341 Equation F3-7):

$$V_n = \frac{2M_p}{e} \tag{10.46}$$

In this case all links are shear governed and the results of the analysis may be used to design the link beams without adjustment for the true eccentricity, e.

For both shear-governed and flexure-governed links, the analysis gives the appropriate moments in the beam outside the link (at the force level under consideration). That is, the flexural forces in the beam outside the link relate to the centerline dimension, x, whereas the flexural forces in the link relate to the link length, e. Determination of the flexural forces corresponding to the strain-hardened link shear [Eq. (10.30)] requires special treatment as illustrated in Figure 10.35.

10.6.6 Link Rotation

The system parameters for EBF are based on tests that have shown stable, ductile behavior within certain ranges of link rotation. The seismic design provisions for EBF accordingly limit the expected link rotations to values based on these ranges. For shear-governed links with $e \le 1.6M_p/V_p$, the permissible inelastic rotation angle is 0.08 rad. The link inelastic rotation is estimated using the design story drift. The design story drift calculated by amplifying the results of an elastic analysis is a very rough estimate of actual expected drifts. The inelastic drift can be calculated as

$$\Delta_{in} = \Delta - \Delta_e \tag{10.47}$$

$$\Delta = C_d\, \Delta_e \tag{10.48}$$

$$\Delta_{in} = (C_d - 1)\Delta_e \tag{10.49}$$

where C_d is the deflection amplification factor, which is equal to 4 for eccentrically braced frames; Δ is the design story drift; Δ_e is the drift from an elastic analysis using the prescribed base shear; and Δ_{in} is the inelastic drift.

At the second floor:

$$\Delta_{in} = (4 - 1)0.326 = 0.979 \text{ in}$$

The inelastic portion of the drift is assumed to be entirely due to link rotation. This rotation is calculated based on kinematics as shown in Figure 10.17.

$$\gamma_p = \frac{\Delta_{in}}{h}\left(\frac{L}{e}\right) \tag{10.50}$$

For the current example:

$$\gamma_p = \frac{0.979}{216}\left(\frac{360}{53.46}\right) = 0.03 \text{ rad}$$

indicating that the link rotation is well below the permissible limit. At the upper stories the link inelastic rotation angle reaches as high as 0.07 rad, i.e., still below the 0.08 rad limit for shear-governed links.

When the link rotation is excessive, the building may be stiffened to reduce the drift. This can be done by increasing the column and brace size, increasing the link beam size, or decreasing the link length.

Increasing the column and brace size is straightforward, although generally these elements are not a major source of flexibility. (For taller frames, columns do contribute significant flexibility. Although it is possible to reduce the calculated link rotations by increasing the column size, it is unclear whether such a change would have an effect on the actual link rotations.) Increasing the link beam size will impose larger forces on the braces and columns. Reducing the link length will reduce drift, but also the amplification of drift into link rotation; nevertheless it is often a viable approach.

10.6.7 Link Detailing

The link requires special detailing to withstand the expected link rotations and shear deformations without flange or web buckling. Full-depth stiffeners are required on both sides of the web at each end of the link. AISC 341 has prescriptive thickness and welding requirements for these stiffeners. In addition they may be designed to transfer brace forces into the beam web. This connection design is not illustrated in this example.

These link-end stiffeners are also the location of required lateral bracing. In accordance with AISC-360-10, these braces should be designed such that

$$P_u = \frac{0.06\, R_y Z F_y}{h_o} \tag{10.51}$$

$$\beta_{br} = \frac{1}{\phi}\left(\frac{10\, M_r C_d}{L_b h_o}\right) \tag{10.52}$$

where P_u is the required strength of the lateral bracing; β_{br} is the required stiffness of the lateral bracing; and where, for the link at the second floor

$$h_o = d - t_f$$

$$h_o = 21.7 - 0.96 = 20.7 \text{ in}$$

Note that L_b should be taken to be L_q, the maximum unbraced length corresponding to the flexural demand, M_r, which is taken to be the expected flexural strength in this application. Thus, the length L_q may be assumed to be equal to the limiting length L_p.

$$M_r = M_u = R_y Z F_y \tag{10.53}$$

$$M_r = 1.1(307)(50) = 16{,}885 \text{ kip-in}$$

$$C_d = 1.0$$

$$\phi = 0.75$$

$$P_{br} = \frac{[0.06(1.1)(307 \text{ in}^3)(50)]}{(20.7 \text{ in})} = 48.8 \text{ kips}$$

$$\beta_{br} = \frac{[10(16{,}885)(1.0)]}{[0.75(123.6)(20.7)]} = 87.8 \text{ kips/in}$$

For short links with $e \leq 1.6M_p/V_p$, intermediate stiffeners are required. The spacing is a function of the predicted link rotation angle:

$$s \leq \left[59.3 - 22\left(\frac{\gamma_p}{0.06}\right)\right]t_w - \frac{d}{5} \tag{10.54}$$

where d is the link depth; t_w is the link web thickness; s is the stiffener spacing; and γ_p is the plastic link rotation angle, not to be taken less than 0.02.

$$s \leq \left[59.3 - 22\left(\frac{0.03}{0.06}\right)\right]0.06 - \frac{21.7}{5} = 24.5 \text{ in}$$

These stiffeners may be on one side of the web for beams less than 25-inch deep, as all the beams in this example are. AISC 341 has prescriptive thickness requirements for these stiffeners. It also has prescriptive welding requirements for connecting the stiffeners to the beam. Figure 10.38 shows the second-floor link beam, as a typical result for this example.

10.6.8 Completion of Design

Several items remain to complete the design. These include

- Brace connections. These would be designed to resist the same forces as the braces themselves. See Eq. (10.34) for the derivation of the brace seismic force.
- Column splices
- Base plates

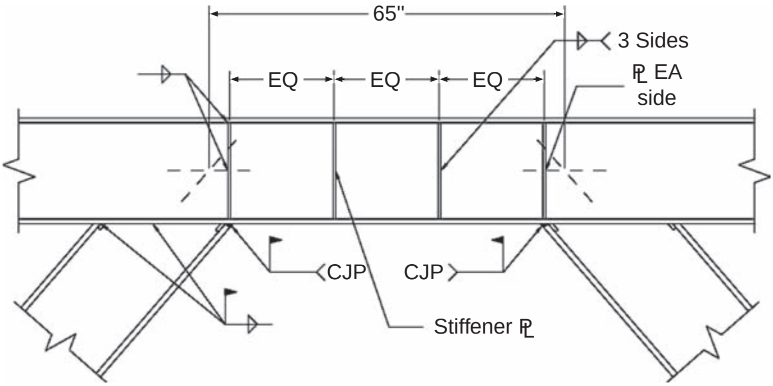

FIGURE 10.38 Second-floor link beam.

- Foundations
- Diaphragms, chords, and collectors

Although each one of these items is necessary and important, their execution is similar to that of many other components of a building design.

10.7 Self-Study Problems

Problem 10.1 Design the members of the single-story eccentrically braced frame shown below such that it satisfies AISC 341. Loads shown are unfactored and seismic loads are already reduced by the appropriate R value. Only consider the $1.2D + 0.5L + 1.0E$ load combination.

(a) Perform a nonseismic design, i.e., select the lightest members that satisfy the AISC 360 requirements for the factored loads.
(b) Perform a seismic design, i.e., select the lightest members that satisfy the AISC 341 requirements for EBFs. Include a check of the maximum link rotation angle from analysis, amplified per ASCE 7 with $I = 1.0$, versus the maximum rotation allowed by AISC 341. Also include the design of the link stiffeners per AISC 341 and the required design forces for link lateral bracing.
(c) Comment on the differences between the designs and explain their causes.

For both designs:

- Use square HSS sections with A500 Gr. B ($F_y = 46$ ksi) for the braces.
- Use W-shapes with A992 ($F_y = 50$ ksi) for the beam and columns.
- A structural analysis computer programs may be used, provided all force diagrams necessary for design are provided. In this case, to get forces on members outside of the link, an additional load case would

be necessary, with seismic loads amplified to account for the expected strength of the link and its strain hardening, per AISC 341. Hand methods of structural analysis are also acceptable (i.e., using relative stiffnesses to determine the moment into the brace and beam-outside-the-link).

- Assume the braces and beams are pin-connected to the column.
- Assume the braces are rigidly connected to the beam.
- The columns are laterally braced at their tops.
- The beam is laterally braced at the ends of the link and at the intersection with the columns.
- If using available design aids, reference all appropriate sections, page numbers, and edition of the design aids used.

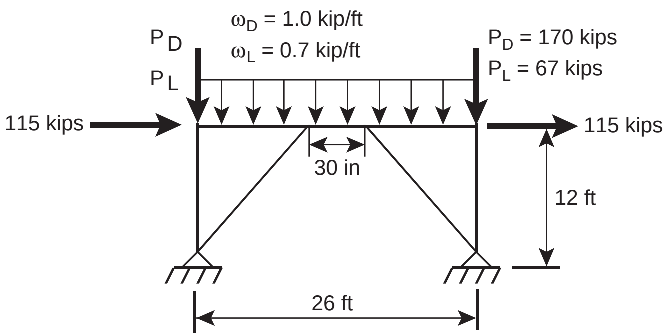

Problem 10.2 For the eccentrically braced frame structure shown here, only answer the following specific targeted questions:

(1) Determine if the link has adequate shear and flexural strengths to resist the applied loads. Check both values, even if one of the two strengths is found to be insufficient.

(2) Determine the exact value of the maximum link rotation angle (at the design story drift) that is permitted by the AISC 341 for a link of that specific length.

Consider that the W18 × 71 beam is continuous between the columns, but pinned at the column faces. The braces are pin-pin and the columns are simply supported at their bases.

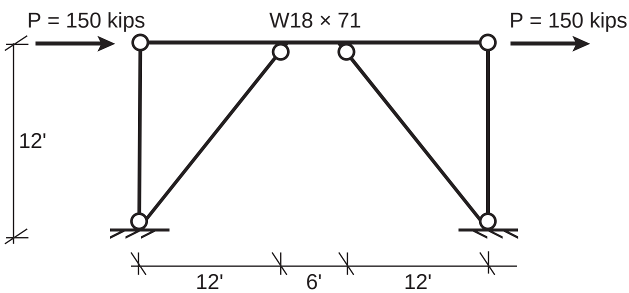

Problem 10.3 For the single-story EBF shown in the figure to this problem:

(a) Determine if a W14 × 48 link beam has adequate strength to resist the externally applied 100 kips seismic ultimate lateral load F_u (divided into two equal 50 kips load as shown in the figure following).

(b) Indicate whether the same W14 × 48 link beam meets the appropriate compactness requirements for the intended purpose.

(c) Assuming that an elastic computer analysis of this frame gives a drift $\delta_e = 0.129$ in, determine the expected corresponding plastic link rotation angle. Assume $C_d = 4.0$ and $I = 1.0$.

(d) Using capacity design, determine if the W14 × 48 beam outside of the link has adequate strength for the expected combination of axial and bending forces in that member. Assume an unbraced length of beam outside the link of 6ft 0 in.

(e) Indicate whether the W14 × 48 beam outside of the link meets the appropriate compactness requirements for the intended purpose.

(f) Using capacity design, size the diagonal braces using the most economical W10 shape.

(g) Indicate whether the braces sized in part (f) above meets the appropriate compactness requirements for the intended purpose.

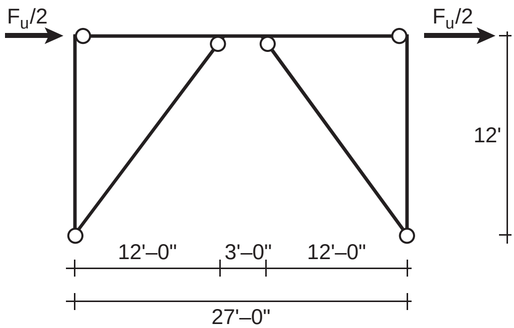

Problem 10.4 An explosion destroyed the middle column of a two-story two-bay steel frame. The dotted line in the figure below shows where that column used to be before the explosion. The rest of the frame, minus its central column, remained intact after the explosion. At the time of the explosion, that frame was only subjected to three point loads, each of magnitude P (no other gravity loads or lateral loads were applied at that time). In particular, there are no uniformly distributed loads applied to this frame.

This two-bay two-story steel frame was designed with an eccentrically braced frame on the second story, and special moment resisting frame on the first story.

Part I Calculate the maximum load, P, that can be resisted by this frame after the explosion. For simplicity, assume that the braces of the EBF and columns of the frame are infinitely strong and rigid. Also assume in this Part I that the W24 × 76 beam is of constant cross-section and able to develop its plastic moment at the face of the columns (i.e., no need to consider special SMRF connections in this *Part I*).

Part II

(a) Design a beam with an RBS detail in compliance with the AISC 341 that would allow the frame to resist the same load, *P*, as in *Part I* after the explosion. In this problem:
- Select an appropriate geometry for the RBS and location of the RBS along the beam length.
- Provide the maximum reduction in flange width permitted by AISC 341.
- Only consider possible W24 beams.
- Clearly show all appropriate free-body diagrams relevant to the calculations.
- Use a table to summarize the important values needed in this design, showing a logical process to search for the lightest possible W24 beam that would satisfy the problem statement.

(b) For the solution in Part (a), check whether the moment at face of column is acceptable.

(c) Check whether the beam selected in Part (a) meets the specified limits for this prequalified connection.

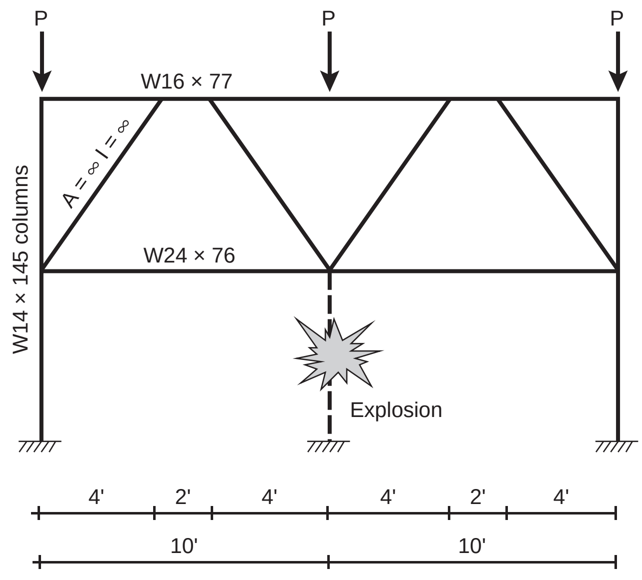

References

AISC. 2002, 2005, 2010. *Seismic Provisions for Structural Steel Buildings, ANSI/AISC 341.* Chicago: American Institute of Steel Construction.

AISC. 2010. *Specification for Structural Steel Buildings, ANSI/AISC 360-10.* Chicago: American Institute of Steel Construction.

Berman, J., and Bruneau, M. 2005. "Approaches for the Seismic Retrofit of Braced Steel Bridge Piers and Proof-of-Concept Testing of an Eccentrically Braced Frame with Tubular Link." *Technical Report MCEER-05-0004.* Buffalo, NY: Multidisciplinary Center for Earthquake Engineering Research., State University of New York at Buffalo.

Berman, J., and Bruneau, M. 2006. "Further Development of Tubular Eccentrically Braced Frame Links for the Seismic Retrofit of Braced Steel Truss Bridge Piers." *Technical Report MCEER-06-0006*. Buffalo, NY: Multidisciplinary Center for Earthquake Engineering Research, State University of New York at Buffalo.

Berman, J., and Bruneau, M. 2007. "Experimental and Analytical Investigation of Tubular Links for Eccentrically Braced Frames." *Engineering Structures,* vol. 29, no. 8, 1929–1938.

Berman, J., and Bruneau, M. 2008a. "Tubular Links for Eccentrically Braced Frames, I: Finite Element Parametric Study." *Journal of Structural Engineering, ASCE,* vol. 134, no. 5, 692–701.

Berman, J., and Bruneau, M. 2008b. "Tubular Links for Eccentrically Braced Frames, II: Experimental Verification." *Journal of Structural Engineering, ASCE,* vol. 134, no. 5, 702–712.

Bleich, F. 1952. "Buckling Strength of Metal Structures," *Engineering Societies Monographs.* New York: McGraw Hill.

CSA. 2009. "Limit States Design of Steel Structures," *CAN/CSA-S16*-09. Mississauga, Ont: Canadian Standard Association.

Dusicka, P., and Itani, A. M. 2002. "Behavior of Built-up Shear Links under Large Cyclic Deformations," *Proc., Annual Meeting, Structural Stability Research Council*.

Dusicka, P., and Lewis, G. R. 2010. "Investigation Of Replaceable Sacrificial Steel Links," *Proc., 9th U.S. National and 10th Canadian Conference on Earthquake Engineering.,* Paper No. 1659.

Engelhardt, M. D., and Popov, E. P. 1989. "On Design of Eccentrically Braced Frames." *Earthquake Spectra, EERI,* vol. 5, no. 3, 495–511.

Engelhardt, M. D., and Popov, E. P. 1992. "Experimental Performance of Long Links in Eccentrically Braced Frames." *Journal of Structural Engineering, ASCE,* vol. 118, no. 11, 3067–3088.

Fehling, E., Pauli, W., and Bouwkamp, J. G. 1992. "Use of Vertical Shear-Links in Eccentrically Braced Frames," *Proc., 10th World Conference on Earthquake Engineering* ,Madrid, vol. 8, 4475–4479, IAEE.

Fujimoto, M., Aoyagi, T., Ukai, K., Wada, A., and Saito, K. 1972. "Structural Characteristics of Eccentric K-Braced Frames." *Trans.AIJ*, no. 195, 39–49, May.

Ghobarah A., and Ramadan, T. 1990. "Effect of axial forces on the performance of links in eccentrically braced frames." *Engineering Structures,* vol. 12, no. 2, 106–113.

Hjelmstad, K. D., and Lee, S. G. 1989. "Lateral Buckling of Beams in Eccentrically Braced Frames." *Journal of Constructional Steel Research, ASCE,* vol. 14, no. 4, 251–272.

Hjelmstad, K. D., and Popov, E. P. 1983. "Cyclic Behavior and Design of Link Beams." *Journal of Structural Engineering, ASCE,* vol. 109, no. 10, 2387–2403.

Hjelmstad, K. D., and Popov, E. P. 1984. "Characteristics of Eccentrically Braced Frames." *Journal of Structural Engineering, ASCE,* vol. 110, no. 2, 340–353.

Kasai, K., and Popov, E. P. 1985. "On Seismic Design of Eccentrically Braced Frames," *Proceedings of the 8th World Conference on Earthquake Engineering,* vol. 5, 387–394, IAEE.

Kasai, K., and Popov, E. P. 1986a. "Cyclic Web Buckling Control for Shear Link Beams." *Journal of Structural Engineering, ASCE,* vol. 112, no. 3, 505–523.

Kasai, K., and Popov, E. P. 1986b. "General Behavior of WF Steel Shear Link Beams." *Journal of Structural Engineering, ASCE,* vol. 112, no. 2, 362–382.

Malley, J. O., and Popov, E. P. 1983. "Design Considerations for Shear Links in Eccentrically Braced Frames." *Report EERC-83/24.* Berkeley: Earthquake Engineering Research Center, University of California.

Malley, J. O., and Popov, E. P. 1984. "Shear Links in Eccentrically Braced Frames." *Journal of Structural Engineering, ASCE,* vol. 110, no. 9, 2275–2295,

Manheim, D. N., and Popov, E. P. 1983. "Plastic Shear Hinges in Steel Frames." *Journal of Structural Engineering, ASCE,* vol. 109, no. 10, 2404–2419.

Mansour, N., Shen, Y., Christopoulos, C., and Tremblay, R. 2008. "Experimental Evaluation of Nonlinear Replaceable Links in Eccentrically Braced Frames and Moment Resisting Frames." *Proceedings of the 14th World Conference on Earthquake Engineering*, IAEE.

McDaniel, C. C. Uang, C. M., and Seible, F. 2003. "Cyclic Testing of Built-up Steel Shear Links for the New Bay Bridge." *Journal of Structural Engineering, ASCE,* vol. 129, no. 6, 801–809.

Okazaki, T., Arce, G., Ryu, H.-C., and Engelhardt, M. D. 2004. "Recent Research on Link Performance in Steel Eccentrically Braced Frames." *Proceedings of the 13th World Conference on Earthquake Engineering,* IAEE.

Okazaki, T., Arce, G., Ryu, H.-C., and Engelhardt, M. D. 2005. "Experimental Study of Local Buckling, Overstrength, and Fracture of Links in Eccentrically Braced Frames." *Journal of Structural Engineering, ASCE,* vol. 131, no. 10, 1526–1535.

Okazaki, T., Engelhardt, M. D., Drolias, A., Schell, E., and Uang, C. M. 2009. "Experimental Investigation of Link-to-Column Connections in Eccentrically Braced Frames." *Journal of Constructional Steel Research, ASCE,* vol. 65, no. 7, 1401–1412.

Okazaki, T., Engelhardt, M. D., Nakashima, M., and Suita, S. 2006. "Experimental Performance of Link-to-Column Connections in Eccentrically Braced Frames." *Journal of Structural Engineering, ASCE,* vol. 132, no. 8, 1201–1211.

Perera, R., Gomez, S., and Alarcon, E. 2004. "Experimental and Analytical Study of Masonry Infill Reinforced Concrete Frames Retrofitted with Steel Braces." *Journal of Structural Engineering, ASCE,* vol. 130, no. 12, 2032–2039.

Ramadan, T., and Ghobarah, A. 1995. "Behaviour of Bolted Link-Column Joints in Eccentrically Braced Frames." *Canadian Journal of Civil Engineering,* vol. 22, no. 4, 745–754.

Richards, P. 2004. "Cyclic Stability and Capacity Design of Steel Eccentrically Braced Frames." Ph.D. Dissertation, University of California, San Diego.

Richards, P. W., and Uang, C. M. 2005. "Effect of Flange Width-Thickness Ratio on Eccentrically Braced Frames Link Cyclic Rotation Capacity." *Journal of Structural Engineering, ASCE,* vol. 131, no. 10, 1546–1552.

Richards, P. W., and Uang, C. M. 2006. "Testing Protocol for Short Links in Eccentrically Braced Frames." *Journal of Structural Engineering, ASCE,* vol. 132, no. 8, 1183–1191.

Ricles, J. M., and Popov, E. P. 1989. "Composite Action in Eccentrically Braced Frames." *Journal of Structural Engineering, ASCE,* vol. 115, no. 8, 2046–2065.

Roeder, C. W., and Popov, E. P. 1978. "Eccentrically Braced Steel Frames for Earthquakes." *Journal of the Structural Division, ASCE,* vol. 104, no. ST3, 391–411.

Roeder, C. W., Foutch, D. A., and Goel, S. C. 1987."Seismic Testing of Full-Scale Steel Building–Part II." *Journal of Structural Engineering, ASCE,* vol. 113, no. 11, 2130–2145.

Salmon, C. G., Johnson, J. E., and Malhas, F. A. 2009. *Steel Structures: Design and Behavior,* 5th edition. New York: Prentice Hall.

Sarraf, M., and Bruneau, M. 2004. "Performance Tests Of Innovative Ductile Steel Retrofitted Deck-Truss Bridges." *Proceedings of the 13th World Conference on Earthquake Engineering*, IAEE.

Stratan, A., Dubina, D., and Dinu, F. 2003. "Control of Global Performance of Seismic Resistant EBF with Removable Link," *Proceedings of 4th International Conference on Behavior of Steel Structures in Seismic Areas (STESSA).* Naples, Italy. pp. 455–461.

Tanabashi, R., Naneta, K., and Ishida, T. 1974. "On the Rigidity and Ductility of Steel Bracing Assemblage," *Proceedings of the 5th World Conference on Earthquake Engineering,* Rome, IAEE. vol. 1, 834–840.

Tsai, K. C., and Young, Y. F. 1991. "A study of large EBF subassemblages with link-to-box column connection," *Proceedings of the Pacific Conference on Earthquake Engineering,* pp. 69–80.

Whittaker, A. S., Uang, C.-M., and Bertero, V. V. 1989. "Seismic Testing of Eccentrically Braced Dual Steel Frames." *Earthquake Spectra, EERI,* vol. 5, no. 2, 429–449.

Yang, M.-S. 1985. "Shaking Table Studies of an Eccentrically Braced Steel Structure," *Proceedings of the 8th World Conference on Earthquake Engineering,* San Francisco, IAEE, vol. 4, 257–264.

Zahrai, S. M., and Bruneau, M. 1999. "Cyclic testing of ductile end diaphragms for slab-on-girder steel bridges." *Journal of Structural Engineering, ASCE,* vol. 125, no. 9, 987–996.

CHAPTER 11

Design of Ductile Buckling-Restrained Braced Frames

11.1 Introduction

Compared with moment-resisting frames as well as concentrically or eccentrically braced frames, buckling-restrained braced frames is a relatively new system for seismic applications. First developed in Japan in the 1970s, through further research this system gained rapid acceptance after the 1994 Northridge Earthquake and became codified in the United States in a relatively short time. This chapter first introduces the motivation and the basic idea behind the concept of buckling-restrained brace. Basic components comprising a buckling-restrained brace are then presented in Section 11.3. Section 11.4 highlights international development showing different variations of the buckling-restrained braces and typical cyclic response. Section 11.5 identifies nonductile failure modes that should be avoided, and Section 11.6 discusses different frame configurations. Section 11.7 presents the design considerations of buckling-restrained braces, which is then followed by a discussion of capacity design of other elements and testing requirements in Section 11.8. The chapter concludes with design examples.

11.2 Buckling-Restrained Braced Frames versus Conventional Frames

As described in Chapter 9, specially designed and detailed concentrically braced frames can provide high elastic stiffness to limit story drift, relying on diagonal braces to buckle and yield to dissipate energy. Although design specifications, such as AISC 341 (AISC 2010) and the CSA S16 (CSA 2009) provide requirements to limit the

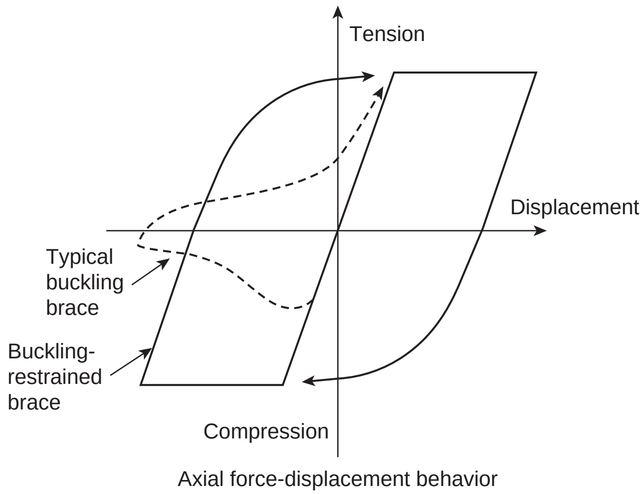

Figure 11.1 Behavior of conventional brace versus BRB. (*Courtesy of Seismic Isolation Engineering, Inc., Berkeley, CA.*)

slenderness ratio and width-thickness ratio of the brace to ensure sufficient ductility, brace buckling is inevitable. Therefore, brace buckling leads to both strength and stiffness degradation, which can in some instances cause concentration of damage to a limited number of stories and, hence, increases the potential for building collapse. The large unbalance between compression and tension brace strengths also lead to large force demands when following capacity design principles.

The disadvantages of the CBF system can be overcome if the brace can yield in both tension and compression without buckling (see Figure 11.1). A braced frame that incorporates this type of brace, i.e., buckling-restrained brace (BRB), is called a buckling-restrained braced frame (BRBF).

BRBFs have been used extensively for seismic applications in Japan after the 1995 Kobe earthquake (Reina and Normile 1997). This type of framing system also gained its acceptance in the United States a few years after the 1994 Northridge earthquake (Clark et al. 1999). Figure 11.2 shows example applications of BRBFs for new construction. BRBFs have also been applied to seismic rehabilitation of reinforced concrete buildings (Brown et al. 2001, Tremblay et al. 1999).

Compared with either moment frames or braced frames, BRBFs offer the following advantages (Shuhaibar et al. 2002):

(1) Compared with moment frames, BRBFs exhibit high elastic lateral stiffness at low-level seismic input motions, making it easy to satisfy code drift requirements.

(a) BRBF with bolted connections

(b) BRBF with pin-ended connections

Figure 11.2 Examples of BRBF: (a) with bolted connections; (b) with pin-ended connections. (*Part a courtesy of Seismic Isolation Engineering, Inc., Berkeley, CA. Part b courtesy of Star Seismic LLC, Park City, UT.*)

(2) BRBFs eliminate the undesirable buckling of conventional CBFs by yielding in both tension and compression, thereby providing larger and stable energy dissipation at high level seismic input motions.

(3) BRBFs provide economical installation through a bolted or pinned connection to gusset plates, which eliminates costly field welding and inspection.

(4) Braces act as a replaceable structural fuse, which minimizes damage to other elements and it is possible to replace damaged braces after major seismic events.

(5) BRBFs offer design flexibility because both the strength and stiffness of the braces can be easily tuned. Furthermore, it is easy to model the cyclic behavior of BRBs for inelastic analysis.

(6) For seismic rehabilitation, BRBFs can be more advantageous than the conventional bracing system because capacity design provisions for the latter system may require expensive foundation and floor diaphragm strengthening.

BRBFs may have some disadvantages:

(1) Most BRBs are proprietary.

(2) If not properly controlled, steels commonly used to fabricate restrained yielding segment may have a wide range of yield strength.

(3) Field erection tolerances are generally lower than those of conventional braced frames.

(4) Large permanent deformation may occur under high levels of seismic input because this kind of system, like many others, does not have a recentering mechanism.

(5) Criteria for detecting and replacing damaged braces need to be established.

11.3 Concept and Components of Buckling-Restrained Brace

Figure 11.3 shows the components of a typical buckling-restrained brace. The brace is composed of a ductile steel core, which is designed to yield in both tension and compression. To preclude global buckling in compression, the steel core is first placed inside a steel casing (e.g., a hollow structural section, HSS) before the casing is filled with mortar or concrete. Before casting mortar, an unbonding material or a very small air gap between the steel core and mortar is provided to minimize, or eliminate if possible, the transfer of axial force from steel core to mortar and the HSS. Because the Poisson effect also causes the steel core to expand under compression, this small gap between the steel core and mortar is needed to allow for expansion of the steel core.

Figure 11.4 shows an example of a buckling-restrained brace, which is composed of five components.

(1) Restrained yielding segment—This steel segment can be rectangular or cruciform in cross section. Although it is common that a steel plate be surrounded in a casing, more than one plate can be used, if desired. Because this segment is designed

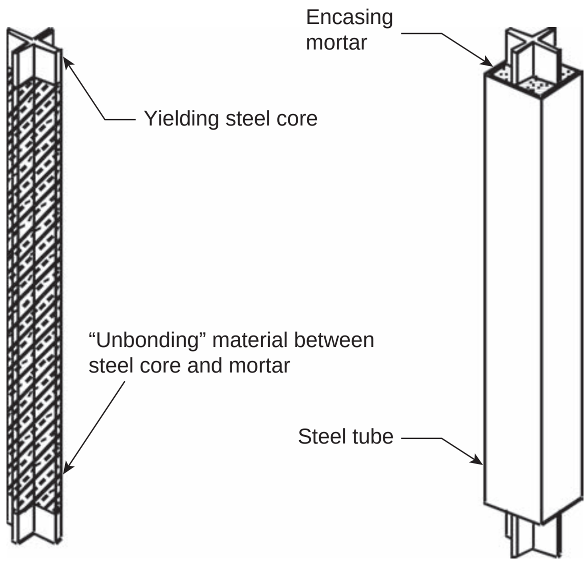

Figure 11.3 Concept of a type of buckling-restrained brace. (*Courtesy of Seismic Isolation Engineering, Inc., Berkeley, CA.*)

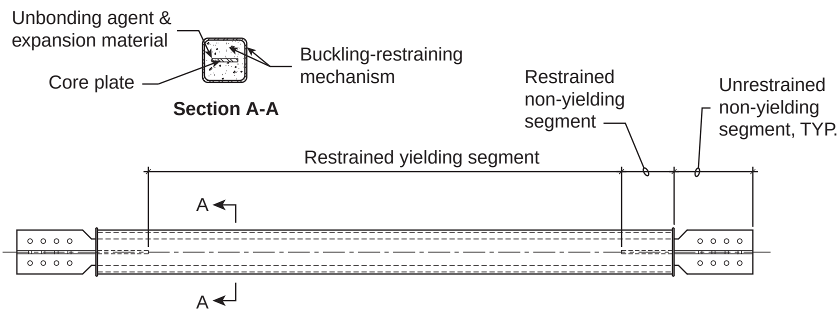

Figure 11.4 Components of BRB. (*Adapted from Wada et al. 1998 by W. López, Rutherford and Chekene, San Francisco, CA.*)

to yield under cyclic loading, mild steel that exhibits high ductility is desirable.

(2) Restrained nonyielding segment—This segment, which is surrounded by the casing and mortar, is usually an extension of the restrained yielding segment but with an enlarged area to ensure elastic response. This can be achieved by widening the restrained yielding segment or welding stiffeners to increase the area in this region.

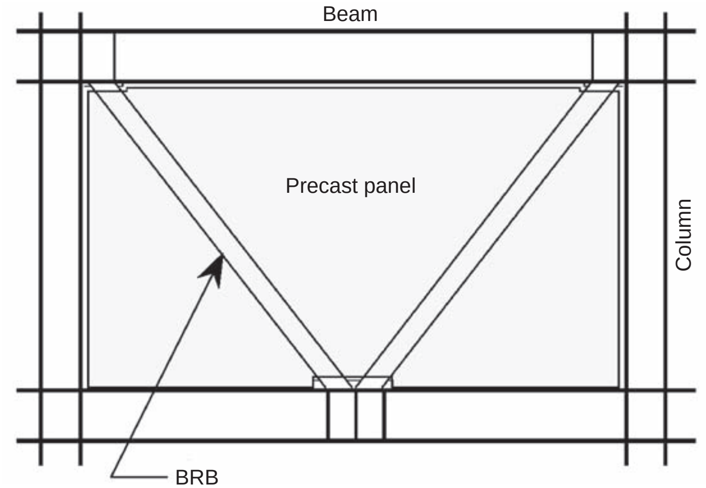

Figure 11.5 Buckling-restrained braces sandwiched between precast concrete panels. (*Courtesy of M. Nakashima, Disaster Prevention Research Institute, Kyoto University, Japan.*)

(3) Unrestrained nonyielding segment—This segment is usually an extension of the restrained nonyielding segment, except that it projects from the casing and mortar for connection to the frame. This segment can be designed as a bolted, welded, or even pin connection for field erection. Design considerations of this segment include (a) construction tolerance for ease of field erection and to facilitate the removal, and (b) local buckling prevention.

(4) Unbonding agent and expansion material—Inert material like rubber, polyethylene, silicon grease, or mastic tape that can effectively minimize or eliminate the transfer of shear force between the restrained steel segment and mortar can be used.

(5) Buckling-restraining mechanism—This mechanism is typically composed of mortar and steel casing (e.g., hollow structural shape). But steel-only BRBs that do not use mortar or concrete have also been proposed; Figures 11.5e to h and Figures 11.6b to d show some examples.

11.4 Development of BRBs

A variety of BRBs with various materials and geometries have been proposed and studied in Japan for more than 30 years. Variations of BRBs were subsequently developed in several other countries. A brief review of selected studies is presented below.

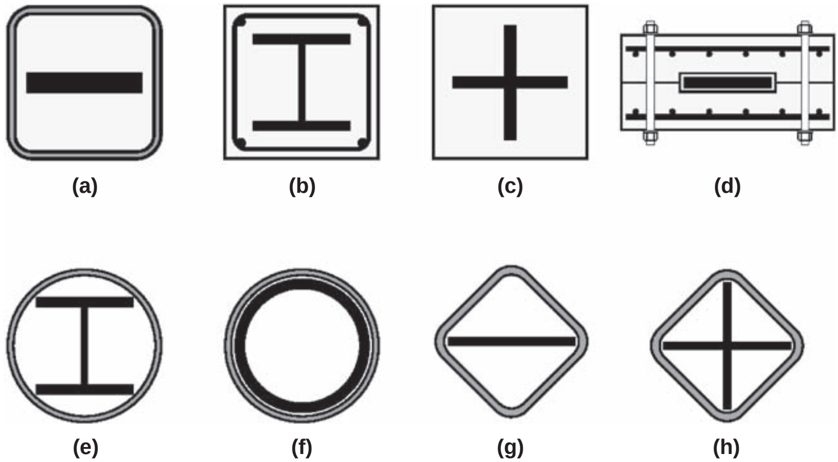

FIGURE 11.6 Cross sections of various BRBs developed in Japan. (*Courtesy of M. Nakashima, Disaster Prevention Research Institute, Kyoto University, Japan.*)

The concept of buckling-restrained braces was first developed in two forms in Japan. To avoid buckling, the yielding steel element can be either sandwiched between precast concrete panels or encased in concrete-filled steel sections. The pioneering work on buckling-restrained braces was conducted by Wakabayashi et al. (1973), who developed a system in which braces made of steel flat plates were sandwiched between a pair of precast reinforced concrete panels (see Figure 11.5). Based on both analytical and experimental studies that measured directly the interaction forces between the brace and the panels, the researchers developed both stiffness and strength requirements for the design of precast concrete panels (Inoue et al. 2001).

Extending from the concept of Wakabayashi et al. (1973), various developments on BRBs with a steel core confined by a steel casing were made in Japan in the 1980s to 1990s. Figure 11.6 shows some BRB cross sections that have been investigated. Figures 11.6a to c shows steel core plate or shape restrained by mortar- or concrete-encased HSS section, whereas the steel core plate is sandwiched by two precast concrete panels bolted together in Figure 11.6d. The steel cores used in Figures 11.6e to h were confined by an HSS casing only.

Iwata et al. (2000) reviewed the cyclic performance of four commercially available BRBs in Japan. Figure 11.7 shows the cross section of these four products. Note that an unbonding material was not used in either Type 2 or 4 specimen. The buckling-restraining mechanism of Type 3 specimen was composed of two channels and two plates connected with high-strength bolts. Soft rubber sheets (1-mm thick) were provided between the core plate and the buckling-restraining mechanism for Types 1 and 3 specimens.

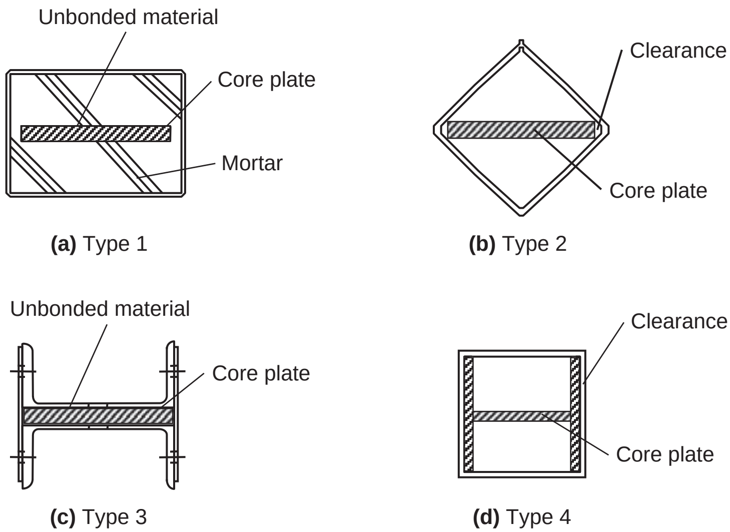

Figure 11.7 Section of four test specimens. (*Courtesy of M. Iwata, Dept. of Architecture, Kanagawa University, Japan.*)

Figure 11.8 shows the cyclic responses of all test specimens. Note that Types 2 and 4 specimens did not perform well, probably because no mortar was used to limit local buckling. The restraining effect of the Type 3 specimen was not as effective as that provided by the mortar and steel tube in the Type 1 specimen. Type 1 specimen, which sustained 14 cycles at 3% strain, outperformed the other three braces.

A BRB can also be viewed as a core-loaded casing strut (Sridhara 1990). As shown in Figure 11.9, the core in a sleeved column is loosely placed inside a sleeve and the load is applied to the core only. The idea is to decouple the compression load resistance of the core from the flexural buckling resistance of the sleeve. The compressive strength of the steel core in a sleeve depends on the relative stiffnesses of the core and the sleeve. The core, under the action of the applied load, first buckles into the first mode and presses against the inside surface of the sleeve, thus causing primarily bending stress in the sleeve. If the maximum bending stress in the sleeve is controlled, it is possible to apply additional load, causing the core to snap into higher buckling modes. The compression load capacity increased as the gap between the core and the sleeve was reduced. Nevertheless, a zero gap would result in a lower capacity because the core could not buckle into higher modes. The sleeved column concept has been verified experimentally (Kalyanaraman et al. 1994, 1998; Prasad 1992).

In North America, initially, project-specified testing was conducted to verify the cyclic performance of BRBs (Black et al. 2002,

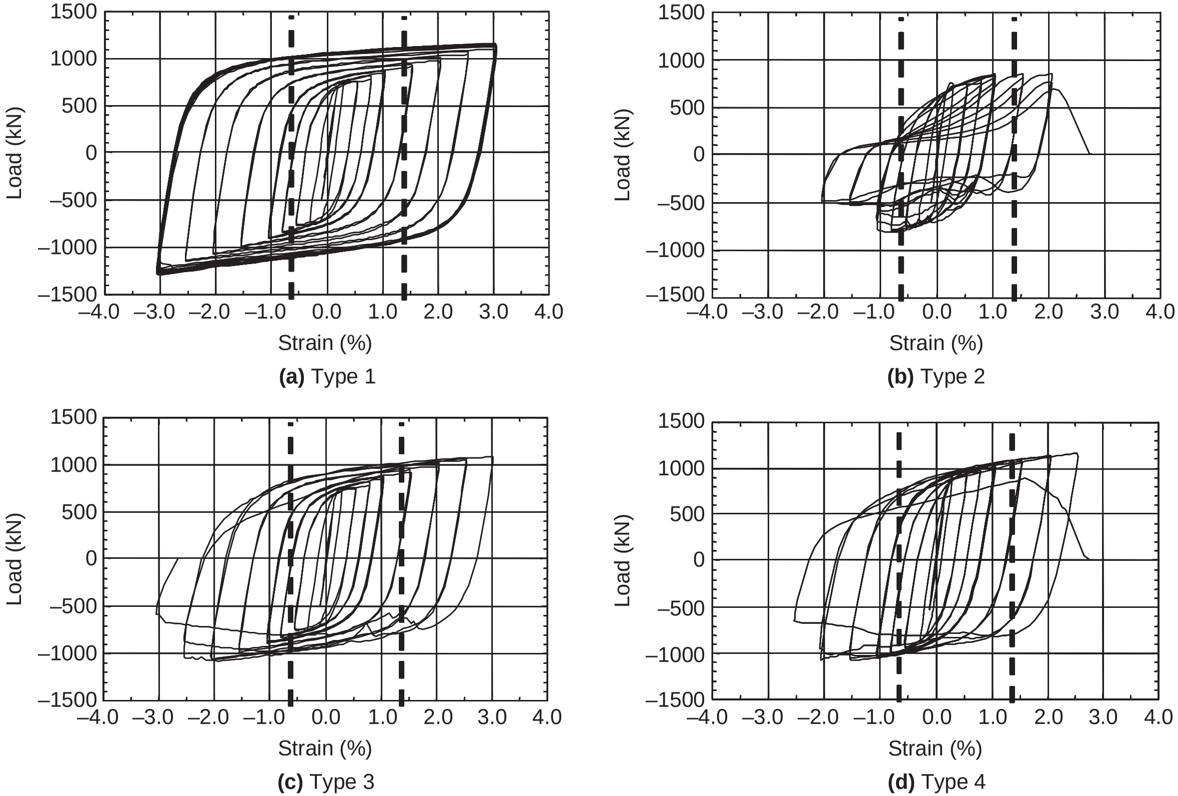

FIGURE 11.8 Cyclic response of four test specimens. (*Courtesy of M. Iwata, Dept. of Architecture, Kanagawa University, Japan.*)

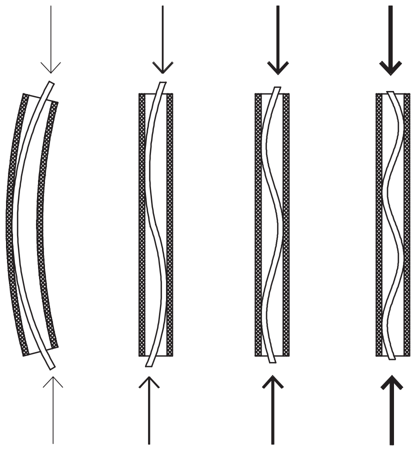

Figure 11.9 Concept of sleeved column. (*Courtesy of B.N. Sridhara, India.*)

Clark et al. 1999, Higgins and Newell 2004, López et al. 2002,Tremblay et al. 1999). Some proprietary BRBs were also developed in the United States. As BRBFs were becoming increasingly popular, there was a need to codify this system. A joint SEAOC-AISC task group developed recommended provisions for BRBF design and construction (Sabelli 2004), which were later adopted in the AISC 341 (AISC 2005). Included in these provisions is a loading protocol for testing BRBs, which was developed primarily based on the work of Sabelli (2001) and Sabelli et al. (2003), who performed a series of nonlinear dynamic analyses on model buildings to characterize the seismic demand of BRBFs. Subsequently, subassembly level testing (López et al. 2002, Tremblay et al. 2006, Tsai et al. 2002) and system level testing (Fahnestock et al. 2007, Tsai et al. 2008, Tsai and Hsiao2008b, Vargas and Bruneau 2009) of BRBFs were also conducted in the United States and elsewhere.

Typical response of the BRB is shown in Figure 11.10. The hysteresis response is very stable with a large energy dissipation capacity. The ideal hysteresis response of a BRB suggests that the strength under both tension and compression would be equal. For a given axial deformation, however, test results usually show that the compression strength is higher than the tension force. This is a small unbalance, but nonetheless it must be taken into account from a capacity design point of view. When the core steel is in compression, it will expand due to the Poisson effect and may contact the mortar. Furthermore, once higher-mode local buckling occurs in the steel core, the buckled steel core will bear against the mortar and casing, which causes the mortar-casing component to participate in load

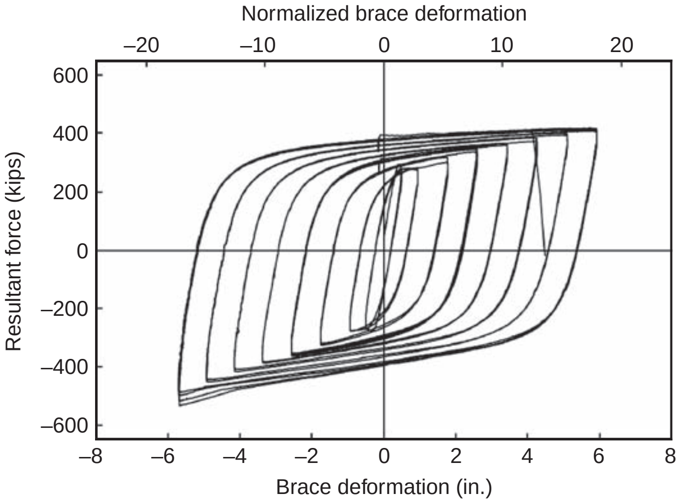

Figure 11.10 Typical hysteresis response of BRB.

sharing. Both factors contribute to a higher compressive strength. Therefore, one important goal for the development of a BRB is to minimize the compression overstrength.

11.5 Nonductile Failure Modes

To ensure that the expected yield mechanism will be developed in a BRBF, nonductile failure modes should be identified. Capacity design principles are then applied to avoid these failure modes.

11.5.1 Steel Casing

When properly designed and detailed, steel casing should not resist any significant axial load. To avoid global buckling of the BRB, steel casing should have sufficient flexural stiffness. Ignoring the contribution from mortar or concrete infill, Watanabe et al. (1988) suggested that the steel casing be designed for a flexural stiffness such that

$$\frac{P_e}{P_y} \geq 1.0 \tag{11.1}$$

where P_y is the yield strength of the restrained yielding segment, and P_e is the elastic buckling strength of the steel casing:

$$P_e = \frac{\pi^2 EI_{sc}}{L_{sc}^2} \tag{11.2}$$

In Eq. (11.2), E = Young's modulus, I_{sc} = moment of inertia of steel casing, and L_{sc} = work point-to-work point brace length.

If it is assumed that cyclic strain-hardening would increase the compressive strength of the brace by 30%, and a resistance factor, ϕ, of 0.85 is included in the numerator, then

$$\frac{\phi P_e}{1.3 P_y} \geq 1.0 \tag{11.3}$$

or

$$\frac{P_e}{P_y} \geq 1.5 \tag{11.4}$$

The above expression coincides with that proposed by Watanabe et al. (1988). Experimental testing was also conducted to confirm the above requirement.

Two other issues also need to be considered. The mortar or concrete should have sufficient stiffness and strength to accommodate the higher-mode buckling of the steel core as the plate, buckled about its weak axis, would push against the surrounding mortar or concrete. If not, localized failure like that shown in Figure 11.11 due to crushing of the concrete would result. The yielded steel core may also buckle about its strong axis if the casing wall thickness is small and the concrete cover between the edge of the steel core and casing is small (Matsui et al. 2008).

11.5.2 Brace Connection

It is common that the brace end be designed as a bolted connection for field erection, but other connection designs such as a pin connection or a welded connection are also possible. The bolted connections in Figure 11.2a require two sets of bolts and eight splice plates

Figure 11.11 Localized failure due toinsufficient concrete strength. (*Courtesy of Star Seismic LLC, Park City, UT.*)

Figure 11.12 Higher-mode buckling of steel core. (*Courtesy of CoreBrace, LLC, West Jordan, UT.*)

at each brace-to-gusset connection. Figure 11.2b shows an example where pin connections are used. For a BRB to serve its intended function, it is essential that no localized buckling in the end connection should occur.

Tsai et al. (2002) conducted cyclic testing of a half-scale subassembly. Figures 11.13a and b shows the geometry of a half-scale subassembly and the typical brace-to-beam connection details. During testing, localized buckling at the brace-to-beam connection as shown in Figure 11.13c was observed.

To prevent gusset buckling, Nakamura et al. (2000) suggested that the following criterion be satisfied for out-of-plane buckling:

$$P_{e\_trans} = \frac{\pi^2 EI_{trans}}{(KL_b)^2} \geq C_{max} \tag{11.5}$$

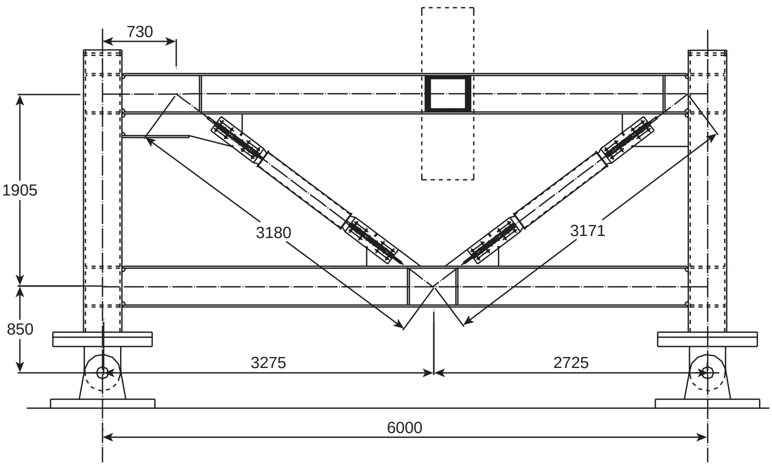

(a) Geometry (units in mm)

Figure 11.13 Geometry of subassembly test: (a) geometry (units in mm); (b) brace connection details; (c) buckling at brace end. (*Courtesy of K.C. Tsai, Dept. of Civil Engineering, National Taiwan University, Taiwan.*)

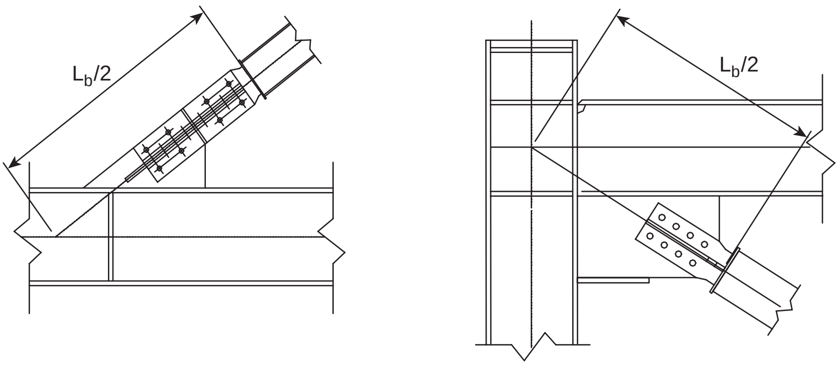

(b) Brace connection details

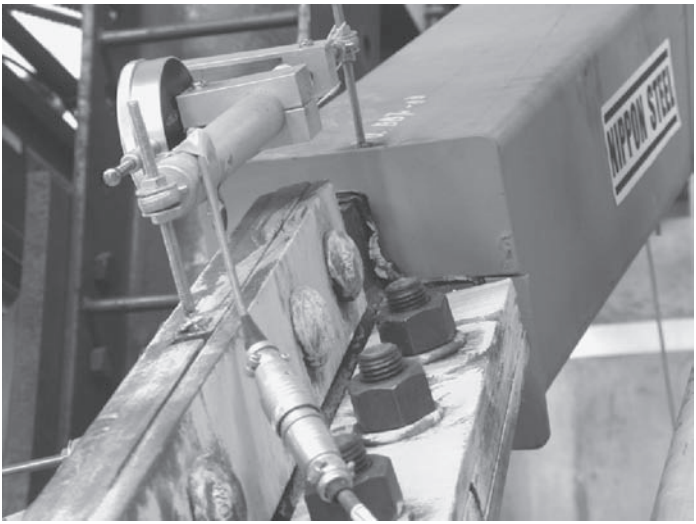

(c) Buckling at brace end

Figure 11.13 (*Continued*)

where C_{max} is the maximum compression force of the brace, I_{trans} is the out-of-plane buckling moment of inertia of the unrestrained non-yielding segment of the brace; K, the effective length factor, can be conservatively taken as 1.0; and L_b is the unbraced connection length defined in Figure 11.13b. Note that the denominator on the right-hand side of Eq. (11.5) is equivalent to using the gusset connection length as L_b and an effective length factor of 2.

Tsai and Hsiao (2008) also conducted a full-scale three-story BRBF. Buckling of the gusset connection was again observed (see Figure 11.14a). The study showed that the design procedure in the

AISC Manual for computing the compressive strength of a gusset plate with an effective length factor, K, equal to 0.65 is nonconservative. Because the brace-gusset junction is allowed to move out of plane, it is suggested that a value of K equal to 2.0 be used if the gusset plate is not stiffened (Tsai and Hsiao 2008). However, one effective way to enhance the compressive strength of a gusset plate is to provide edge stiffeners like that shown in Figure 11.14b. Also note in that latter figure the lateral bracing at the midspan of the beam. To prevent out-of-plane buckling, Koetaka et al. (2008) has shown that it is important that either lateral bracing or sufficient torsional stiffness of the beam be provided.

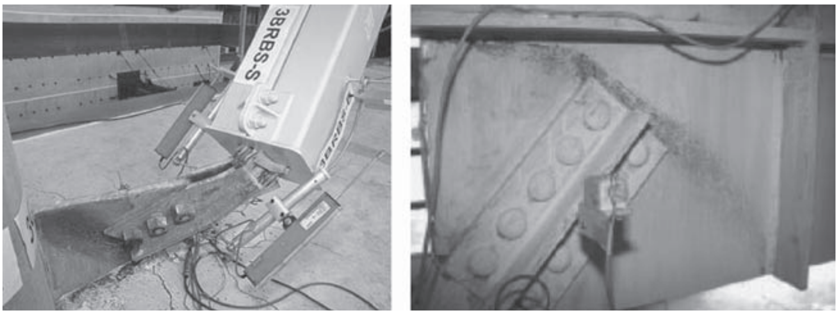

(a) Unstiffened gusset connection

(b) Edge-stiffened gusset connection

Figure 11.14 BRB gusset buckling and one stiffening scheme: (a) unstiffened gusset connection; (b) edge-stiffened gusset connection. (*Courtesy of K.C. Tsai, Dept. of Civil Engineering, National Taiwan University,Taiwan.*)

11.5.3 Frame Distortion Effect on Gusset Connection

To investigate the influence of frame distortion, which induces both axial and flexural deformations to the braces, cyclic testing of a full-story subassembly of beams, columns, and braces was conducted (Aiken et al. 2002, López et al. 2002). The test results showed that BRBs performed well and were able to withstand the rotational deformations without negative effects to their axial capacities. However, the free edge of a beam-column-brace gusset plate buckled when the brace was in tension instead of compression. Because the presence of a gusset plate stiffens the beam-column joint, the gusset plate to which the tensile brace is connected is "pinched" by the beam and column due to frame distortion (i.e., relative closing of the angle between the beam and column at that location), which caused the gusset plate to buckle.

To eliminate gusset buckling, Fahnestock et al. (2007) incorporated an improved connection detail in a 0.6-scale, four-story BRBF test frame to allow rotation while limiting flexural demands on the connection regions (see Figure 11.15). The BRBs used have true pin

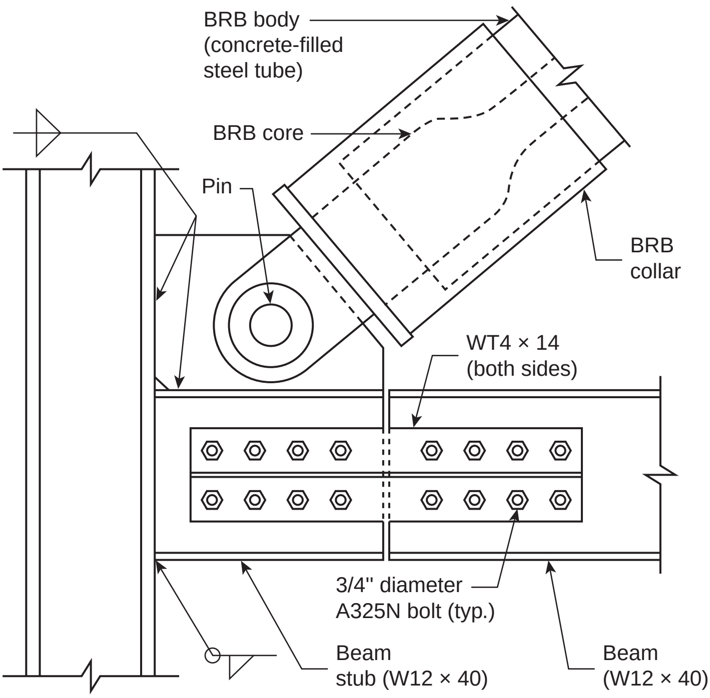

Figure 11.15 Improved beam-column-brace connection detail. (*Courtesy of L. A. Fahnestock, Dept. of Civil Engineering, University of Illinois at Urbana-Champaign, IL.*)

connections at the ends, similar to that shown in Figure 11.2b. Therefore, the pin limits the moment developed in the BRB. A bolted beam splice using double structural tees was introduced between the beam and the beam stub to transfer axial force but provide minimum flexural resistance. Test results showed that this connection detail was able to accommodate a very large story drift in the frame without causing any buckling in the gusset connection. Collars that existed at the ends of the pin-connected BRBs were also beneficial in preventing out-of-plane buckling of the gusset. Testing also revealed that large residual drifts can be one potential drawback of that particular kind of BRBFs, but this problem can be minimized if a BRBF dual system with a special moment frame as the backup system is used (Kiggins and Uang 2006).

11.6 BRBF Configuration

Buckling-restrained braced frames can be configured in numerous ways with minor differences in behavior. Figure 11.16 shows the following frame configurations: inverted V-braced, V-braced, two-story-X, and single diagonal. Note that single-story X bracing is not feasible with buckling-restrained braces. Single diagonals are often useful for low-rise construction as buckling-restrained braces can be designed for very high axial force with a moderate cost premium. Conversely, buckling-restrained braces with low axial strength do not offer much cost savings as the work of assembling the components is substantially the same.

Naturally the angle of brace inclination (and the number of braces sharing the story shear) will have an effect on axial force that an individual brace will be required to resist. Additionally, this angle of inclination has a degree of influence on the elastic stiffness of the structure. Nevertheless, none of the configurations is subject to large redistributions of forces as braces yield and the structure

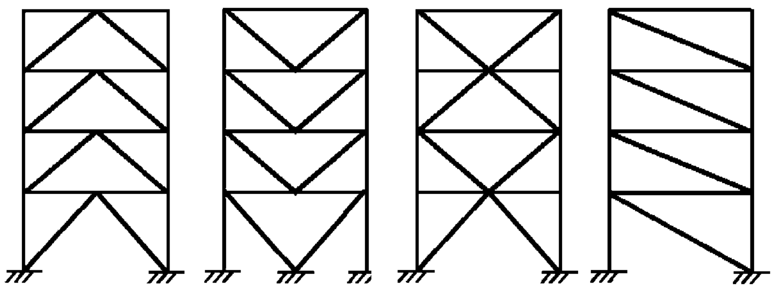

Figure 11.16 Typical BRBF configurations.

goes beyond the elastic range. However, the choice of configuration has an indirect effect on system behavior because the length of the brace available for the yielding segment will be different for each configuration. For a given bay size, the brace yielding length possible with the V-bracing configuration, for example, will be significantly less than that available with the single diagonal. Thus, braces in the V-bracing configuration will have higher strains in the yielding region and greater strain-hardening; this will affect the forces in the frame members. Such braces will also be stiffer.

A buckling-restrained braced frame need not be thought of as a frame in which all the braces are buckling-restrained members. Rather, it can be thought of as a braced frame in which the inelastic drift capacity is the product of axial ductility capacity of buckling-restrained members. Considered this way, frames can be designed using configurations that offer significant performance and cost advantages. Figure 11.17 shows a hybrid bracing configuration in which the inelastic drift capacity is the product of the ductility capacity of a pair of vertical buckling-restrained struts. The story shear is carried by conventional braces, and the overturning at the base is resisted by the buckling-restrained struts. The conventional members in effect form a vertical truss that must be stabilized by the struts. This system depends on the elastic performance of the conventional truss, which must be designed for the forces corresponding to the capacity of the ductile struts. Shears caused by higher-mode dynamic response can have a significant effect on this vertical truss; this effect is more pronounced for taller systems. For more information see Tremblay et al. (2004).

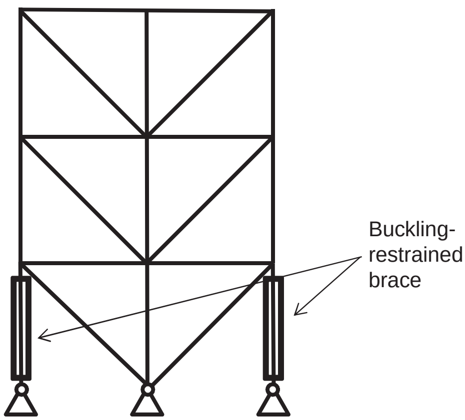

Figure 11.17 Hybrid bracing configuration.

11.7 Design of Buckling-Restrained Braces

The design of buckling-restrained braced frames is in many respects simpler than the design of special concentrically braced frames (SCBF) or other braced frames designed for ductile seismic response. Many of the restrictions and procedures considered necessary for SCBF due to the differing tension and compression behavior of buckling braces are unnecessary when the more ductile buckling-restrained braces are used. The design of braces is presented in this section, followed by capacity design of other elements in Section 11.8.

11.7.1 Brace Design

The design of a typical buckling-restrained braced frame involves sizing the brace steel cores to provide sufficient axial strength. This is a straightforward design based on the material strength. The brace axial design strength is determined by the following:

$$\phi P_{ysc} = \phi F_{ysc} A_{sc} \tag{11.6}$$

where F_{ysc} = specified minimum yield stress of the steel core, A_{sc} = cross-sectional area of the yielding segment of steel core, and $\phi = 0.90$ for the limit state of yielding. This strength applies to both tension and compression, as buckling of the core is completely restrained by the casing. This strength is compared with the required strength of the braces corresponding to the design base shear.

11.7.2 Elastic Modeling

In typical practice an elastic model is used to determine the brace required strengths. Elastic modeling is used to determine the required brace strengths and to determine the elastic dynamic characteristics of the structure. In constructing an elastic model with buckling-restrained braces, some adjustments need to be made to properly capture the elastic stiffness of this element.

Brace axial stresses are largely confined to the steel core, and the axial compression and extension of this member must be reasonably represented in the model. The model must address the nonprismatic configuration of this core (see Figure 11.4), either directly or indirectly. Some estimate must be made of the brace area outside of the yielding zone, as well as the length of the yielding and nonyielding segments. For manufactured braces the manufacturer can provide estimates based on the anticipated connection size, overall brace length, and other factors. For fabricated braces designed by the engineer, the following equation can be used to establish the effective axial stiffness of the brace (Tsai et al. 2002):

$$K_{eff} = \frac{E}{\left(\dfrac{L_{ysc}}{A_{ysc}} + \dfrac{L_{nysc}}{A_{nysc}} + \dfrac{L_{conn}}{A_{conn}}\right)} \tag{11.7}$$

where E is Young's modulus, A_{ysc} is the yielding steel core area, A_{nysc} is the area of the steel core outside of the yielding region, A_{conn} is the area of the connection (typically approximate), L_{ysc} is the length of the yielding region of the steel core, L_{nysc} is the length of the nonyielding region of the steel core, and L_{conn} is the length of the connection.

This effective stiffness is typically in the range of 1.3 and 1.8 times the stiffness of a prismatic core extending from work point to work point. Shorter braces tend to have a greater portion of their length given over to nonyielding and connection regions; the same is true of braces with high axial force.

11.7.3 Gravity Loads

Unlike most other systems, the design of buckling-restrained braces does not utilize the gravity-force distribution from the analysis. Take an inverted V-braced frame with braces of equal tension and compression strength ($\beta = 1.0$, where β is the compression strength adjustment factor to be discussed in Eq. 11.9) as an example. The effect of gravity forces in the frame will be to precompress the braces such that the vertical component of each brace force is 50% of the gravity load (Figure 11.18a). This precompression, when combined with brace axial forces due to lateral displacement, causes the brace resisting seismic loads by compression to yield somewhat earlier (i.e., at lower drift and a lower seismic force), and the opposite brace to yield somewhat later. After the brace in compression yields, the brace in tension pulls down on the beam until that brace also yields. When both braces are yielding together they exert no net vertical force on the beam, and the gravity load is resisted by beam flexure (see Figure 11.18b). As the braces unload from their yielded state both the upward thrust from the brace in compression and the downward pull from the brace in tension reduce in unison, and no change in the vertical force on the beam results; the gravity load continues to be resisted by the beam (see Figure 11.18c).

For the more typical case of braces with compression strength greater than tension strength ($\beta > 1.0$) the behavior is similar. Gravity causes initial precompression in the braces (Figure 11.19a). If this precompression is less than the difference in strength between compression and tension, the brace that develops tension under lateral

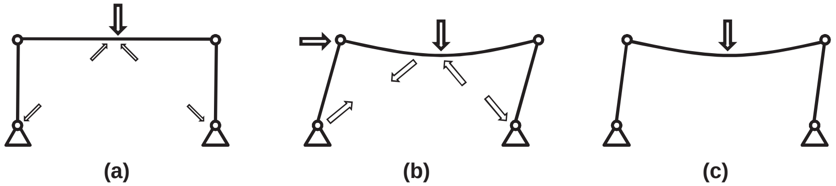

FIGURE 11.18 Effect of gravity force on frame ($\beta = 1.0$).

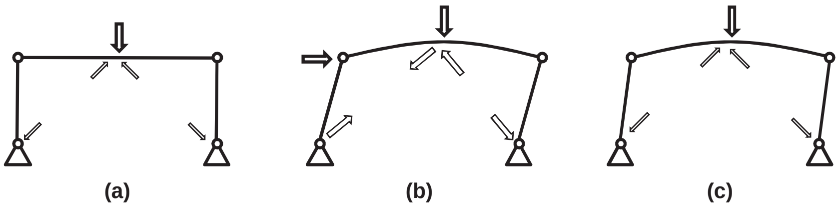

Figure 11.19 Effect of gravity force on frame (β > 1.0).

displacement yields first. The brace in compression then pushes up on the beam until that brace also yields (Figure 11.19b). At the fully yielded condition the beam is pushed up by the difference in the vertical components of brace strength and being pushed down by gravity load. (These two act in the same direction in V-braced frames.) When the braces unload, the gravity load, in conjunction with flexural forces in the beam, acts to precompress the braces for subsequent cycles (Figure 11.19c). This precompression effectively strengthens the braces for tension and weakens them for compression. The magnitude of this precompression causes the braces to yield at about the same lateral displacement, effectively negating the difference in tension and compression strengths.

In either case (β = 1.0 or β > 1.0), for all but the first cycle of loading gravity has little effect on the behavior of braces. Therefore, the degree to which they have been sized to resist gravity in addition to seismic load represents an overstrength. This overstrength will be unequal along the building height. At the top of the frame, where story shears are lowest, the brace forces due to gravity may be significant compared with those due to seismic loading. At the bottom of the frame, the seismic forces are much greater, and thus the gravity forces will be less significant in comparison.

A frame with high overstrength at the top and low overstrength at the bottom is likely to see a concentration of ductility demand at the lower levels. It is, therefore, preferable to design for the inelastic condition and not assign any gravity force to the braces. It is necessary to ensure that frame members have sufficient strength to resist the gravity forces without support from the braces. Although this is only explicitly required in AISC 341 for the load combinations that include seismic loading, it is prudent to consider utilizing this methodology for the gravity-only load combinations as well.

11.8 Capacity Design of BRBF

The design of the remainder of the brace (i.e., buckling-restraining mechanism including casing), brace connections, beams, and columns is performed using a capacity-design approach. The maximum force in the brace is evaluated based on the steel core strength (including material overstrength), the expected strain-hardening under cyclic loading, the expected compression overstrength discussed earlier, and a safety factor essentially based on judgment. AISC 341 requires that these factors be established by cyclic testing.

11.8.1 AISC Testing Requirements

Buckling-restrained braces may be of substantially different configurations, and each configuration must function properly as a mechanism. Testing is required to ensure reliable performance of the brace design. Several considerations are necessary in creating a testing program. The same considerations are necessary in evaluating the applicability of a manufacturer's testing program to a specific project. All of these considerations, along with specific similitude requirements, testing protocols, reporting requirements, and acceptance criteria are presented in Section K3 of AISC 341.

The first consideration is strength. The brace testing program must include tests that are reasonably close in strength to the proposed braces. The second consideration is the deformations imposed on the braces. These include the axial deformations and the end rotations. The deformations imposed on the tested braces should correspond to those anticipated in the structure. AISC 341 requires that braces be tested to the greater of 2% story drift or twice the design story drift; this target brace axial deformation is designated as Δ_{bm}. The empirical nature of the building code methods for estimating drift is known to give lower results than do nonlinear response history analyses. However, excessive brace deformation should not be equated to building collapse, and the adequate performance under twice building-code calculated deformations is expected to provide reasonable margin against collapse for the actual displacements during an earthquake.

Both the strain-hardening adjustment and the compression overstrength adjustment are determined via testing of braces similar to the one being designed. As strain-hardening is a function both of the maximum inelastic strain and of the accumulated inelastic strain, certain assumptions are required to establish these values for a given design. In an elastic design, the frame expected deformation is obtained by multiplying the elastic drift by a factor C_d to obtain an expected inelastic drift corresponding to the seismic hazard. As discussed in Chapter 7, story drifts obtained by this method are rough approximations. It is typical to assume that the plastic portion of the story drift is due entirely to brace axial ductility. This plastic story drift is taken to be the expected drift minus the elastic drift; the elastic drift may be calculated based on the forces necessary to cause the braces to yield and strain harden.

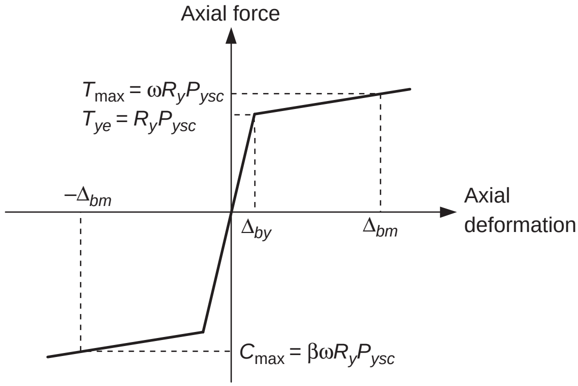

FIGURE 11.20 Definition of ω and β factors of a BRB.

For capacity design, AISC 341 requires the designer to consider the following adjusted brace tensile strength (see Figure 11.20):

$$T_{max} = \omega R_y P_{ysc} \tag{11.8}$$

where P_{ysc} $(= F_{ysc} A_{sc})$ is the axial yield strength of the steel core calculated based on the minimum specified yield stress. The factor ω is the strain-hardening adjustment factor. The above tensile strength is further increased by a compression strength adjustment factor, β, to compute the adjusted brace compressive strength:

$$C_{max} = \beta T_{max} = \beta\omega R_y P_{ysc} \tag{11.9}$$

It is worthwhile to emphasize again that the compressive strength of a BRB is larger than the tensile strength. The opposite is true for the conventional brace in an SCBF.

11.8.2 Brace Casing

Typically the casing is considered to have very low axial stress and is checked for Euler buckling, P_e, regardless of its slenderness. Safety factors are imposed because of the undesirability of this yield mode. Equation (11.4) can be used for casing design.

11.8.3 Brace Connections

Connections are required to be designed for 1.1 times C_{max} in Eq. (11.9); a safety factor of 1.1 is used to account partly the uncertainty related to the level of strain-hardening to be expected (AISC 2010). This force should be used for the design of gusset plate to avoid buckling (see Section 11.5.2). It is possible that in some buckling-restrained brace designs the brace member offers less out-of-plane rotational restraint than is commonly assumed in the design gusset plates. For this reason designers should use care in extrapolating from the design methodology employed in the tested braces.

11.8.4 Beams and Columns

The maximum brace forces, T_{max} and C_{max}, are employed in the design of beams and columns as well. AISC 341 requires that beams and columns be designed to remain "nominally elastic" at force levels corresponding to the fully yielded and strain-hardened braces. Typically a plastic mechanism analysis is performed assuming a first-mode deformation. (This method is illustrated in the design example.) In such a mechanism, the braces are assumed to resist no gravity forces; in fact they are removed from the model and instead forces are applied corresponding to the magnitude and direction of the strain-hardened brace capacities.

This capacity-design procedure for determining required strengths of frame members is intended to prevent beam and column buckling. It is not intended to prevent limited yielding in the frame members. Accordingly, moments in these members are not considered in conjunction with these large axial forces. Rather, sufficient rotational capacity is ensured through the use of highly compact sections and the use of either fully restrained beam to column connections capable of resisting moments corresponding to the flexural strength of the beam (or column) or the use of "simple" connections capable of accommodating a rotation of 0.025 radians.

11.9 Nonlinear Modeling

The use of the capacity-design procedures presented above can result in very large columns for taller buildings. For such structures the assumption of full yielding in the first mode response is unrealistic. Nonlinear models would show significantly lower column axial forces for taller buildings, a phenomenon similar to that discussed in Section 9.3.4 for SCBF. Such nonlinear models, therefore, offer significant advantages in design, provided that modeling is done correctly, the ground motions considered are appropriate and sufficient, and the results are properly interpreted to provide sufficient reliability, particularly when column buckling is the limit state under consideration.

Nonlinear brace element models should capture the elastic brace stiffness and the expected strain hardening. Bilinear models are typically used, although trilinear models create a somewhat closer match to tested brace behavior. Cyclic models can explicitly include both kinematic and isotropic strain hardening. Such modeling information is presented in Section 2.7.4.

Typically braces are kept within their ductile deformation range for design. Braces are not designed to allow their deformation capacity to be exceeded (which would allow significant compression to develop in the casing, and, at sufficiently large deformations, overall buckling of the brace). There is very little data on brace behavior beyond this range and thus capturing such behavior in a nonlinear model is problematic.

11.10 Design Example

The following section illustrates the design of a buckling-restrained braced frame. The design applies the requirements of ASCE 7 (2010) and AISC 341 (2010). The example is not intended to be a complete illustration of the application of all design requirements. Rather, it is intended to illustrate key analysis and proportioning techniques that are intended ensure ductile response of the structure.

11.10.1 Building Description and Loading

The example building is identical to the one used in Chapter 8 (Special Moment Frames), including the site seismicity; more detailed seismicity and building information is included in that example. The difference in this case is that buckling-restrained braced frames are used. The system seismic design parameters are shown in Table 11.1.

The typical plan is shown in Figure 11.21 and the typical frame elevation is shown in Figure 11.22. Based on the seismic-design data a generic seismic response spectrum is constructed in accordance with ASCE 7.

11.10.2 Global Requirements

All the aspects outlines in the corresponding discussion for the Special Concentrically Braced Frame example in Chapter 9 would be equally applicable in this case.

11.10.3 Basis of Design

The design of BRBF is based on the expectation of a global yield mechanism in which braces yield in tension and compression and plastic hinges form at the column bases. Where frame beams are connected rigidly to columns, hinging in the beam or column is also

R	8
I	1.0
C_d	5
Ω_o	2.5

Table 11.1 Seismic Design Data

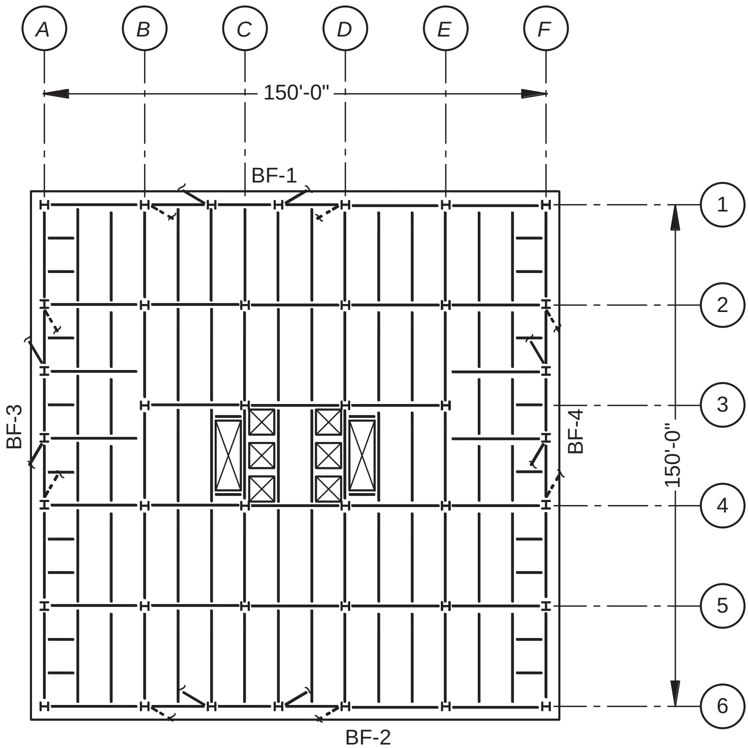

Figure 11.21 Typical floor plan.

anticipated. Otherwise, large rotations must be accommodated in the beam-to-column connections. Figure 11.23 shows this mechanism.

The analysis procedure typically used is a linear Modal Response Spectrum (MRS) analysis. This is typically advantageous due to the reduction in design forces ASCE 7 permits for this method and the reduction in overturning moment that typically results from this approach compared with the vertical force distribution prescribed by the equivalent lateral force (ELF) procedure of ASCE 7. However, for the preliminary design presented in this example, the ELF procedure will be used (see Section 11.10.4).

As required by AISC 341, the design utilizes a brace type that has been qualified by testing. Several capacity design strength requirements for the other components of the braced frames are derived from the fully strain-hardened capacity of the braces. These values are obtained as follows:

$$T_{max} = \omega R_y P_{ysc} \tag{11.10}$$

$$C_{max} = \beta\omega R_y P_{ysc} \tag{11.11}$$

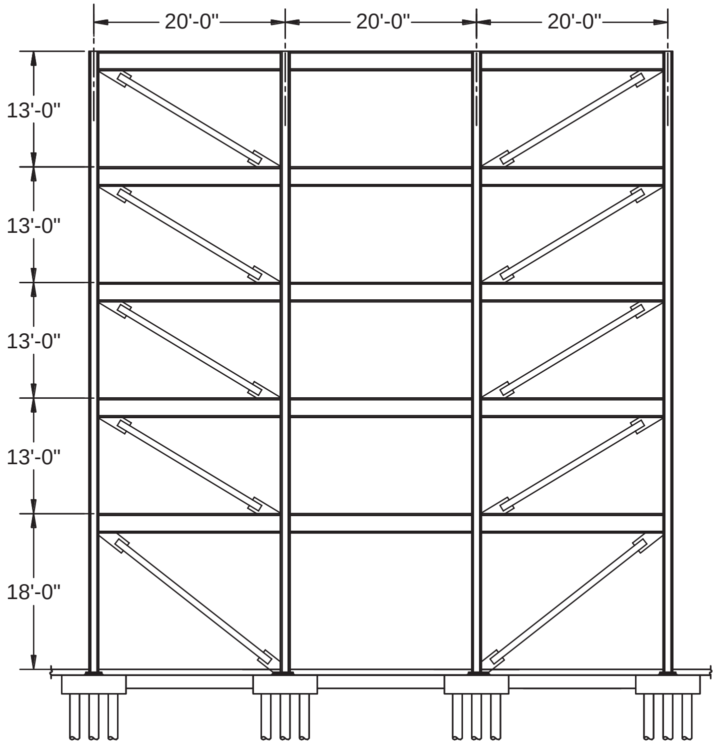

FIGURE 11.22 Typical frame elevation.

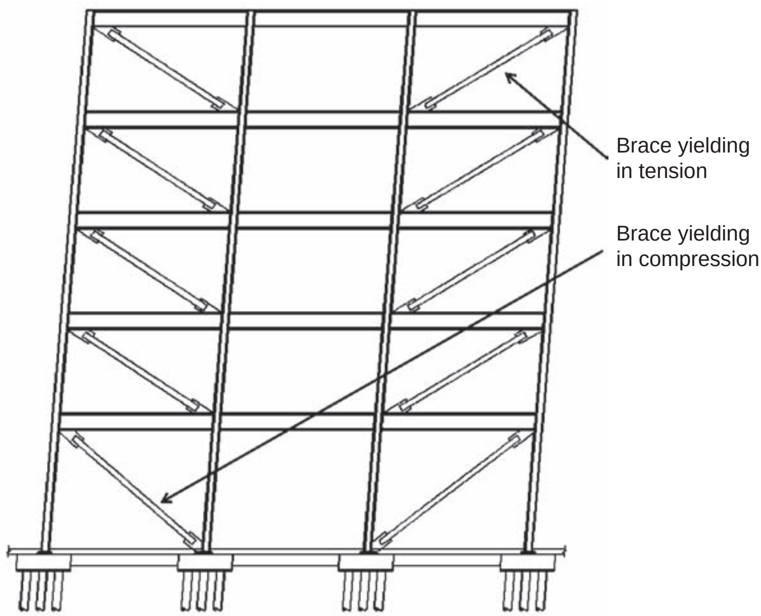

FIGURE 11.23 Anticipated mechanism.

where C_{max} is the adjusted brace strength in compression, T_{max} is the adjusted brace strength in tension, β is compression strength adjustment factor, ω is the strain-hardening adjustment factor, P_{ysc} is axial yield strength of the steel core ($F_{ysc}A_{sc}$), F_{ysc} is minimum specified yield stress of the steel core, and A_{sc} is cross-sectional area of the steel core.

Values for ω and β are obtained directly or indirectly from testing. In the case of manufactured braces, the manufacturer will typically provide these values from the body of tests pertaining to the brace type. For fabricated braces (for which testing will be performed subsequent to design) reasonable assumptions must be made with sufficiently high assumed values of β and ω so that test-obtained values do not require redesign of any members or connections.

For this design example it is assumed that a manufactured brace will be used. Therefore, a number of the BRB properties must be assumed during the design stage (as the final BRB supplier is typically unknown at that time), and this design example follows that approach. First, it is assumed that the brace type has been tested exhaustively for deformations corresponding to 2% plastic story drift will be specified. For that level of deformation the following values will be assumed: $\beta = 1.20$ and $\omega = 1.60$.

As discussed earlier, the fabrication process of buckling-restrained braces permits relatively precise proportioning (compared with other systems) to the point where material variability can be relatively significant. In this example, it is assumed that the brace core material (unknown until the BRB manufacturer is chosen) is specified with a yield stress, F_{ysc}, between 38 ksi and 46 ksi. Braces are sized assuming the lower bound of this range, and (in the absence of any statistical data establishing the variability) the material overstrength factor used for capacity design is $R_y = 46/38 = 1.21$.

11.10.4 Iterative Analysis and Proportioning

For preliminary design, the member forces can be obtained using the equivalent lateral force procedure. Initially the building period is assumed to equal the ASCE 7 upper limit for static analyses, C_uT_a. To start the preliminary design, the following steps are taken:

- Determination of base shear
- Vertical distribution of forces
- Horizontal distribution of forces to frames
- Sizing of braces

For preliminary design purposes the shear in the frame can be assumed to be entirely resisted by the braces. Accidental eccentricity effects are neglected during the initial member sizing process, knowing that the design base shear for the subsequent Modal Response Spectrum analysis will likely be less than that for the preliminary equivalent lateral force procedure analysis. Thus for this configuration the brace axial force at any level is

$$P_u = \frac{V_i}{\cos\,\theta} \tag{11.12}$$

where P_u is the brace axial force, V_i is the frame shear at level I, and θ is the brace angle from horizontal.

In buckling-restrained braced frames, it is typical to neglect gravity forces in the design of braces. This is due to the possible adverse effects that might result from the overstrength due to design for gravity forces. Assuming similar gravity forces at all levels, at upper levels, where design seismic forces are lowest, the degree of overstrength would be high. At lower levels the design seismic forces would likely be substantially higher and the overstrength much lower. Such a distribution of overstrength would be unfavorable for distributed yielding. This is in contrast to braces in special concentrically braced frames, in which gravity loads must be included in the design of braces to prevent buckling at low levels of seismic force. (For more detail see the discussion at the end of the design example in Chapter 9.)

Required brace strengths are shown in Table 11.2. Brace core areas are sized by setting the design strength equal to the required strength.

$$\phi P_{ysc} = P_u \tag{11.13}$$

$$\phi P_{ysc} = \phi F_{ysc} A_{sc} \tag{11.14}$$

$$A_{sc} = \frac{P_u}{\phi F_{ysc}} \tag{11.15}$$

where ϕ = 0.90 for the limit state of yielding. Preliminary brace core area sizes are presented in Table 11.3.

Level	Required Brace Strength (kips)
Fifth Floor	92
Fourth Floor	166
Third Floor	219
Second Floor	253
First Floor	305

Table 11.2 Preliminary Required Brace Strengths

Level	Required Brace Core Area (in^2)	Provided Brace Core Area (in^2)
Fifth Floor	2.70	3.0
Fourth Floor	4.85	5.0
Third Floor	6.40	6.5
Second Floor	7.40	7.5
First Floor	8.92	9.0

Table 11.3 Preliminary Brace Core Area Sizes

Preliminary column and beam sizes can be determined based on the brace sizes selected. Forces corresponding to the adjusted brace strengths in compression and tension are used to calculate maximum axial forces in the beams and columns. Drift-induced flexural forces are neglected, as is permitted by Section F4.3 of AISC 341. This permits a straightforward procedure for deriving design forces for the structural elements surrounding the braces. The practical result of neglecting these flexural forces is that some flexural yielding is likely to occur at the design story drift. For this reason highly ductile members are required for beams and columns.

To derive the column and beam forces, the adjusted brace strengths in compression and tension are calculated using Eqs. (11.10) and (11.11). The resulting values are presented in Table 11.4.

The mechanism shown in Figure 11.23 results in these forces being imposed on the frame, as is shown in Figure 11.24.

An analysis model similar to this figure may be constructed, or simple trigonometry may be used to obtain beam and column forces. This example uses the latter approach.

The column seismic axial force on the column in compression is

$$E_h = \sum_1^n C_{max_i} \sin\theta_i \tag{11.16}$$

Level	C_{max} (kips)	T_{max} (kips)
Fifth Floor	265	221
Fourth Floor	442	368
Third Floor	574	478
Second Floor	662	552
First Floor	795	662

Table 11.4 Adjusted Brace Strengths

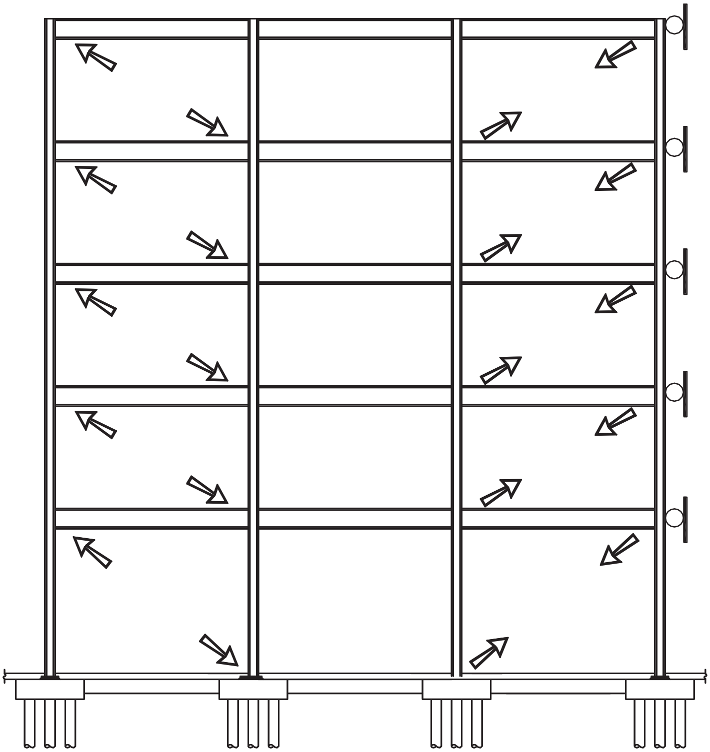

Figure 11.24 Mechanism forces applied to frame.

These forces are combined with gravity forces using the following combination:

$$R_u = (1.2 + 0.2S_{DS})D + 0.5L + E \qquad (11.17)$$

The column seismic axial force on the column in tension is

$$E_h = \sum_1^n T_{max_i} \sin\theta_i \qquad (11.18)$$

These forces are combined with gravity forces using the following combination:

$$R_u = (0.9 - 0.2S_{DS})D - E \qquad (11.19)$$

In this example columns are only spliced once: four feet above the third floor. Preliminary column sizes are shown in Table 11.5. In this configuration the exterior columns (closest to the building perimeter) receive seismic forces from all braces, whereas the interior columns only receive seismic forces from the upper four braces.

	Exterior Column	Interior Column
Upper Column	W14 × 82	W14 × 68
Lower Column	W14 × 159	W14 × 132

TABLE 11.5 Preliminary Column Sizes

The beams are similarly designed based on the brace capacity with the anticipated mechanism in mind. At each level the frame shear capacity can be attributed to the braces:

$$V_{mech(i)} = C_{max(i)} \cos \theta_i \tag{11.20}$$

where $V_{mech(i)}$ is the frame shear corresponding to the anticipated mechanism.

The axial force in the beam above is approximated as

$$P_{u(i)} = V_{mech(i)} \tag{11.21}$$

This overestimates the beam axial force somewhat as it assumes the entire force flows through the frame either from the brace above or from the collector opposite the top connection of the brace below. In the plan layout of this particular building a small portion of the force is likely to enter from the collector nearest the brace connection. In some configurations a large portion of the force must be dragged through the frame due to braces located near the end(s) of a collector line. In such cases, the brace beam axial force may exceed the value calculated in this fashion.

Beam axial forces are presented in Table 11.6. These forces are combined with moments using AISC 360 Equations H1-1a.

Note that if V-type and inverted V-type bracing had been used, the flexural demand of the unbalanced vertical load resulting from the difference in the brace maximum expected compression and tension strengths would have had to be added or subtracted, respectively to

Level	Beam Axial Force (kips)
Roof	222
Fifth Floor	370
Fourth Floor	481
Third Floor	555
Second Floor	591

TABLE 11.6 Preliminary Beam Axial Forces

Level	Beam Size
Roof	W18 × 50
Fifth Floor	W21 × 62
Fourth Floor	W21 × 73
Third Floor	W21 × 83
Second Floor	W21 × 83

Table 11.7 Preliminary Beam Sizes

the gravity moment in the brace beam (computed neglecting the support at midspan provided by the braces).

Both of the following load combinations are considered:

$$R_u = (1.2 + 0.2S_{DS})D + 0.5L + E \tag{11.22}$$

$$R_u = (0.9 - 0.2S_{DS})D - E \tag{11.23}$$

Preliminary beam sizes are presented in Table 11.7.

Using these preliminary sizes a three-dimensional computer model is constructed. As discussed in Section 11.4, the nonprismatic configuration of the brace must be addressed in the model. The effective brace stiffness is typically accounted for by modifying the Young's modulus of a brace element modeled as the yielding steel core area extending from work-point to work-point.

The modified value is

$$E' = \frac{K_{ef}L}{A_{ysc}} \tag{11.24}$$

where E' is Young's modulus adjusted to account for the nonprismatic member, K_{ef} is the brace stiffness, and L is the full length of the brace in the model.

For configurations with braces of the same length and of the same type the value of the adjusted Young's modulus is often taken as uniform for all braces. A factor of $C = E'/E$ between 1.3 and 1.8 is commonly used. In this example the Young's modulus is multiplied by a factor of 1.5 to approximate the correct stiffness of the brace.

A modal response spectrum analysis is performed on this model using the design response spectrum. Interstory drifts are compared with the allowable drift, and the brace member sizes are checked.

Because the modal response spectrum analysis is scaled to 85% of the static the base shear the preliminary sizes are found to be adequate. Optimization is possible at this stage. Braces sizes can be reduced,

<table>
<tr><th>Level</th><th>Brace Area (in²)</th><th>Level</th><th>Beam</th><th></th><th>Exterior Column</th><th>Interior Column</th></tr>
<tr><td>Fifth Floor</td><td>3.0</td><td>Roof</td><td>W18 × 50</td><td rowspan="3">Upper Column</td><td rowspan="3">W14 × 74</td><td rowspan="3">W14 × 68</td></tr>
<tr><td>Fourth Floor</td><td>4.5</td><td>Fifth Floor</td><td>W18 × 60</td></tr>
<tr><td>Third Floor</td><td>6.0</td><td>Fourth Floor</td><td>W21 × 73</td></tr>
<tr><td>Second Floor</td><td>7.0</td><td>Third Floor</td><td>W21 × 73</td><td rowspan="2">Lower Column</td><td rowspan="2">W14 × 145</td><td rowspan="2">W14 × 132</td></tr>
<tr><td>First Floor</td><td>8.0</td><td>Second Floor</td><td>W21 × 83</td></tr>
</table>

Table 11.8 Final Member Sizes

reducing the resulting mechanism-based axial forces in beams and columns and, consequently, the sizes of those members. One or two iterations typically suffice, and subsequent iterations may result in little or no change. Final member sizes are shown in Table 11.8.

11.10.5 Brace Validation and Testing

Once the BRB manufacturer has been selected, design is typically reviewed to ensure validity of the original assumptions, and/or to produce a final design. Here, it is assumed that, in consultation with the brace manufacturer, the brace designs in Table 11.9 are obtained.

In particular, with BRB properties known, it is important to verify that the strain-hardening factor, ω, and the compression overstrength factor, β, assumed in the design are consistent with those obtained from the BRB manufacturer's testing. For this purpose,

Level	Brace Area (in²)	Brace Length (in)	Yielding Length (in)
Fifth Floor	3.0	248	166
Fourth Floor	4.5	242	160
Third Floor	6.0	236	152
Second Floor	7.0	230	146
First Floor	8.0	260	175

Table 11.9 Brace Designs

brace strains are computed at the twice the design story drift at each level (Δ_i). For purposes of establishing brace strains, this drift must not be taken to be less than 1%. The design story drift is determined as follows:

$$\Delta_i = C_d \Delta_{e_i} \tag{11.25}$$

where Δ_{e_i} is the elastic story drift, and C_d is the deflection amplification factor.

The brace inelastic axial deformations are determined from the design story drift based on the frame geometry:

$$\Delta_{br_i} = \Delta_i \cos \theta_i \tag{11.26}$$

where Δ_{br_i} is the brace deformation at the design story drift.

In conjunction with the yield lengths shown in Table 11.9, these deformations can be converted to strain for use in verifying strain-hardening factors. (Note that conversion to strain requires knowledge of the yield length and is thus specific to brace type and configuration; it cannot be done generically.) Table 11.10 shows the brace strains for the braces oriented in the north-south direction.

This strain is used to extract values of the strain-hardening factor, ω, and the compression overstrength factor β from the manufacturer's testing. If these values are less than those assumed in the earlier stages of design no redesign is necessary.

Level	Elastic Story Drift, Δ_{e_i} (in)	Design Story Drift, Δ_i (in)	1% Story Drift (in)	Brace Deformation (at twice the design story drift), $2\Delta_{bri}$ (in)	Brace Core Strain (at twice the design story drift), ε_{br_i}
Fifth Floor	0.18	0.91	1.56	2.62	0.158
Fourth Floor	0.27	1.34	1.56	2.62	0.163
Third Floor	0.28	1.41	1.56	2.62	0.172
Second Floor	0.28	1.42	1.56	2.62	0.179
First Floor	0.32	1.60	2.16	3.22	0.183

Table 11.10 Brace Deformation and Strain

11.10.6 Completion of Design

Several items remain to complete the design. These include

- Brace connections
- Column splices
- Base plates
- Foundations
- Diaphragms, chords, and collectors

Although each one of these items is necessary and important, the execution is similar to that of many other components of a building design.

Self-Study Problem

Problem 11.1 Design the braces, beams, and columns, for the BRBF shown below per AISC 341. Comment on the differences between this design and the SCBF design from Problem 9.1. In that process:

- Assume that the frame is laterally braced in the out-of-plane direction at beam-to-column connections and that the beam is unbraced against compression and lateral-torsional buckling over its entire length. Use simple framing for the beam-to-column connections.
- A seismic lateral load, P_s, of 593 kN is applied at each ends of the frame. That value has already been reduced by the appropriate R value. All loads shown are unfactored.
- Only consider the loading combination of $1.2D + 0.5L + 1.0E$ and neglect the contribution of vertical ground motion.
- Use a compression strength adjustment factor, β, of 1.2 and a strain-hardening adjustment factor, ω, of 1.2.
- Use A992 steel for beam and columns, and A572 Gr. 50 steel for the BRBs.
- Use a rectangular cross-section for the BRBs and W-shapes for the beam and columns.
- When using available design aids, reference the section numbers and edition of the design aids used.

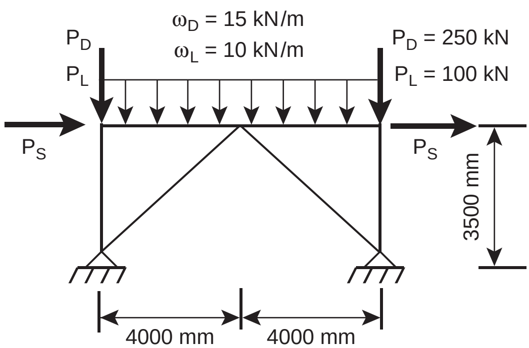

References

Aiken, I. D., Mahin, S. A., and Uriz, P. 2002. "Large-Scale Testing of Buckling-Restrained Braced Frames." *Proceedings of Japan Passive Control Symposium*, 35–44, Tokyo Institute of Technology, Japan.

AISC. 2005, 2010. *SeismicProvisions for Structural Steel Buildings, ANSI/AISC 341.* Chicago: American Institute of Steel Construction.

ASCE. 2010. *Minimum Design Loads for Buildings and Other Structures, ASCE/SEI 7-10.* Reston, VA: American Society of Civil Engineering.

Black, C., Makris, N., and Aiken, I. 2002. "Component Testing, Stability Analysis and Characterization of Buckling-Restrained Braces." *Report No. PEER-2002/08*. Berkeley: Pacific Earthquake Engineering Research Center, University of California.

Brown, A. P., Aiken, I. D., and Jafarazadeh, F. J. 2001. "Buckling-Restrained Braces Provide the Key to The Seismic Retrofit of the Wallace F. Bennett Federal Building." *Modern Steel Construction*, August, 29–37.

Clark, P., Aiken, I., Kasai, K., Ko, E., and Kimura, I. 1999. "Design Procedures for Buildings Incorporating Hysteretic Damping Devices." *Proceedings of the 69th Annual Convention*, SEAOC, Sacramento, CA.

CSA. 2009. "Limit States Design of Steel Structures." *CAN/CSA-S16-09*. Mississauga, Ont: Canadian Standard Association.

Fahnestock, L. A., Ricles, J. M. P., and Sause, R. P. 2007. "Experimental Evaluation of a Large-Scale Buckling-Restrained Braced Frame."*Journal of Structural Engineering*, 133, no. 9, 1205–1214.

Higgins, C., and Newell, J. 2004. "Confined Steel Brace for Earthquake Resistant Design." *Engineering Journal, AISC*, 4th Quarter, 187–202.

Inoue, K., Sawaisumi S., and Higashibata, Y. 2001. "Stiffening Requirements for Unbonded Braces Encased in Concrete Panels." *Journal of Structural Engineering, ASCE*, vol. 127, no. 6, 712–719.

Iwata, M., Kato, T., and Wada, A. 2000. "Buckling-Restrained Braces as Hysteretic Dampers," *Proceedings of 3rd International Conference on Behavior of Steel Structures in Seismic Areas (STESSA)*, Montreal, pp. 33–38.

Kalyanaraman, V., Sridhara, B. N., and Mahadevan, K. 1994. "Sleeved Column System." *Proceedings*, *SSRC Task Group Meetings and Task Force Sessions*, Lehigh University, Bethlehem, PA.

Kalyanaraman, V., Mahadevan, K., and Thairani, V. 1998. "Core Loaded Earthquake Resistant Bracing System." *Journal of Constructional Steel Research*, vol. 46, no. 1–3, 437–439.

Kiggins, S., and Uang, C. M. 2006. "Reducing Residual Drift of Buckling-Restrained Braced Frames as a Dual System." *Engineering Structures*, vol. 28, no. 11, 1525–1532.

Koetaka, Y., Kinoshita, T., Inoue, K., and Htani, K. 2008. "Criteria of Buckling-Restrained Braces to Prevent Out-of-Plane Buckling," *Proceedings*, *14th World Conference on Earthquake Engineering*, Beijing.

López, W. A., Gwie, D. S., Saunders, M., and Lauck, T. W. 2002. "Lessons Learned from Large-Scale Tests of Unbonded Braced Frame Subassemblage." *Proceedings of the 71st Annual Convention*, SEAOC, Sacramento, CA, pp. 171–183.

Matsui, R., Takeuchi, T., Hajjar, J. F., Nishimoto, K., and Aiken, I. 2008. "Local Buckling-restraint Condition for Core Plates in Buckling-Restrained Braces," *Proceedings of the 14th World Conference on Earthquake Engineering*, Beijing.

Nakamura, H., Maeda, Y., Sasaki, T., Wada, A., Takeuchi, T., Nakata, Y., and Iwata, M. 2000. "Fatigue properties of practical-scale unbonded braces." *Nippon Steel Technical Report*, 82, July, 51–57.

Prasad, B. 1992. "Experimental Investigation of Sleeved Column." *Proceedings*, *33rd Structural Dynamics and Materials Conference*, American Institute of Aeronautics and Astronautics, Dallas, TX.

Reina, P., and Normile, D. 1997. "Fully Braced for Seismic Survival." *Engineering News Record*, July 21, 34–36.

Sabelli, R. 2001. "Research on Improving the Design and Analysis of Earthquake-Resistant Steel-Braced Frames." *The 2000 NEHRP Professional Fellowship Report.* Oakland, CA: EERI.

Sabelli, R. 2004. "Recommended Provisions for Buckling-Restrained Braced Frames." *Engineering Journal*, AISC, vol. 41, no. 4, pp. 155–175.

Sabelli, R., Mahin, S. A., and Chang, C. 2003. "Seismic Demands on Steel Braced-Frame Buildings with Buckling-Restrained Braces." *Engineering Structures*, vol. 25, 655–666.

Shuhaibar, C., López, W. A., and Sabelli, R. 2002. "Buckling-Restrained Braced Frames," *Proceedings, ATC-17-2, Seminar on Response Modification Technologies for Performance-Based Seismic Design*, ATC and MCEER, pp. 321–328.

Sridhara, B. N. 1990. "Sleeved Column as a Basic Compression Member." *Proceedings, 4th International Conference on Steel Structures & Space Frames*, Singapore, pp. 181–188.

Tremblay, R., Ftima, M. B., and Sabelli, R. 2004. "An Innovative Bracing Configuration for Improved Seismic Response." *Proceedings of Recent Advances and New Trends in Structural Design International Colloquium*, Timisoara, Romania, pp. 419–430.

Tremblay, R., Bolduc, P., Neville, R., and Devall, R. 2006. "Seismic Testing and Performance of Buckling-Restrained Bracing Systems." *Canadian Journal of Civil Engineering*, vol. 33, no. 2, 183–198.

Tremblay, R., Degrange, G., and Blouin, J. 1999. "Seismic Rehabilitation of a Four-Story Building with a Stiffened Bracing System." *Proceedings of the 8th Canadian Conference on Earthquake Engineering*, Vancouver, pp. 549–554.

Tsai, K. C, Hsiao, P. C., Wang, K. J., Weng, Y. T., Lin, M. L., Lin, K. C., Chen, C. H., Lai, J. W., and Lin, S. L. 2008. "Pseudo-Dynamic Tests of a Full-Scale CFT/BRB Frame-Part I: Specimen Design, Experiment and Analysis."*Earthquake Engineering & Structural Dynamics*, vol. 37, no. 7, 1081–1098.

Tsai, K. C., and Hsiao P. C. 2008. "Pseudo-Dynamic Test of a Full-Scale CFT/BRB Frame-Part II: Seismic Performance of Buckling Restrained Braces and Connections." *Earthquake Engineering & Structural Dynamics*, vol. 37, no. 7, 1099–1115.

Tsai, K. C., Hwang, Y. C., Weng, C. S., Shirai, T., and Nakamura, H. 2002. "Experimental Tests of Large Scale Buckling Restrained Braces and Frames." *Proceedings, Passive Control Symposium*, December, Tokyo Institute of Technology, Tokyo.

Vargas, R., and Bruneau, M. 2009. "Experimental Response of Buildings Designed with Metallic Structural Fuses. II." *Journal of Structural Engineering, ASCE*, vol. 135, no. 4, 394–403.

Wada, A., Saeki, E., Takeuchi, T., and Watanabe, A. 1998. *Development of Unbonded Brace*. Tokyo: Nippon Steel Corporation Building Construction and Urban Development Division.

Wakabayashi, M., Nakamura, T., Kashibara, A., Morizono, T., and Yokoyama, H. 1973. "Experimental Study of Elasto-Plastic Properties of Precast Concrete Wall Panels with Built-In Insulating Braces." *Summaries of Technical Papers of Annual Meeting*, Architectural Institute of Japan, pp. 1041–1044 (in Japanese).

Watanabe, A., Hitomi, Y., Yaeki, E., Wada, A., and Fujimoto, M. 1988. "Properties of Brace Encased in Buckling-Restraining Concrete and Steel Tube." *Proceedings of the 9th World Conference on Earthquake Engineering*, Tokyo-Kyoto, IV, pp. 719–724.

CHAPTER 12

Design of Ductile Steel Plate Shear Walls

12.1 Introduction

12.1.1 General Concepts

A steel plate shear wall (SPSW) [a.k.a. special plate shear wall (SPSW) in AISC 341, steel plate wall (SPW) in CSA S16, and special steel plate wall (SSPW) in FEMA 2004] is a lateral load resisting system consisting of vertical steel plates (a.k.a. webs or infills) connected to their surrounding beams and columns and installed in one or more bays along the full height of a structure to form a cantilever wall (Figure 12.1)—note that beams and columns in SPSWs are typically called horizontal boundary elements (HBEs) and vertical boundary elements (VBEs) in AISC 341. SPSWs subjected to cyclic inelastic deformations exhibit high initial stiffness, behave in a ductile manner, and dissipate significant amounts of energy. These characteristics make them suitable to resist seismic loading. SPSWs can be used not only for the design of new buildings but also for the retrofit of existing construction. Beam-to-column connections in SPSWs may in principle be either simple shear connections or moment-resisting connections, although only the latter are allowed by AISC 341 for seismic applications.

Before key research performed in the 1980s, the design limit state for SPSWs was considered to be out-of-plane buckling of the infill panel. To prevent buckling, engineers designed SPSWs with heavily stiffened infill plates (Section 12.1.1). However, several experimental and analytical studies using both quasi-static and dynamic loading showed that the postbuckling strength and ductility of slender-web SPSWs can be substantial (Berman and Bruneau 2003a, 2004, 2005; Bhowmick et al. 2009; Caccese et al. 1993; Choi and Park 2009; Dastfan and Driver 2008; Deng et al. 2008; Driver et al. 1997a, 1998a, 2001; Elgaaly 1998; Elgaaly et al. 1993; Elgaaly and Liu 1997; Grondin and Behbahannidard 2001; Lee and

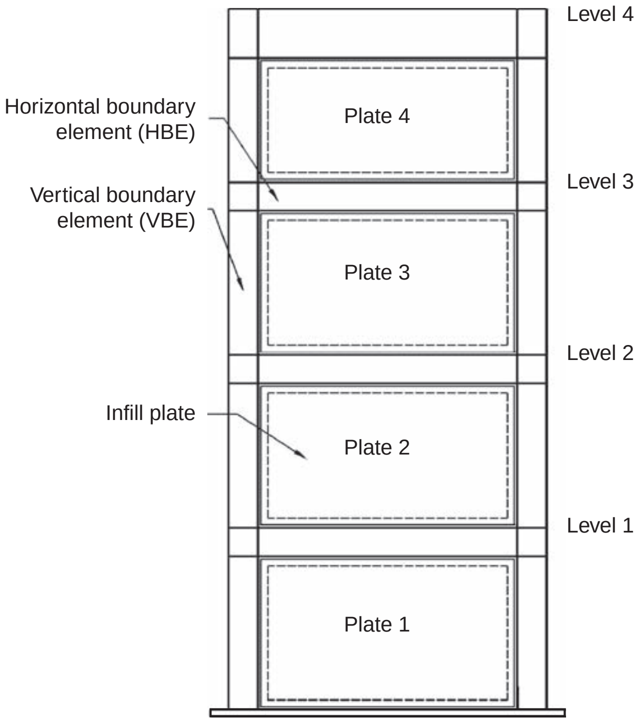

Figure 12.1 Typical steel plate shear wall. (*Berman and Bruneau 2008, reprinted with permission of the American Institute of Steel Construction.*)

Tsai 2008; Lin et al. 2010, Lubell et al. 2000; Purba and Bruneau 2009; Qu et al. 2008; Qu and Bruneau 2009, 2010a, 2010b, 2011; Rezai 1999; Roberts and Sabouri-Ghomi 1991,1992; Sabouri-Ghomi and Roberts 1992; Sabouri-Ghomi et al. 2005; Shishkin et al. 2009; Thorburn et al. 1983; Timler and Kulak 1983; Tromposch and Kulak 1987; Vian et al. 2009a, 2009b; Vian and Bruneau, 2004, 2005; Zhao and Astaneh 2004). Based on the research in the earlier references, the CAN/CSA S16-94 and CAN/CSA S16-01 provided design clauses for SPWs allowing the steel plates to buckle in shear and develop tension field action (CSA 1994, 2001, 2009). Similar clauses were then adopted by the 2003 NEHRP *Recommended Provisions for Seismic Regulations for New Buildings and Other Structures* (FEMA 2004) and in AISC 341 since 2005 (AISC 2005, 2010).

The postbuckling strength and tension field action mechanism of unstiffened steel plates can be conceptually described considering a panel bounded by rigid beams and columns, and subjected to pure shear. When a lateral load is applied horizontally to the top beam, the plate in such a panel is subject to pure shear, with compression and tension principal stresses oriented at a 45° angle to the direction of load. The buckling strength of the plate in compression depends on its depth-to-thickness and width-to-thickness slenderness ratios. These ratios are relatively high for typical building geometries and wall thicknesses, and buckling strength is correspondingly low (close to zero for thin plates)—even more so considering that plates are not initially straight or flat due to fabrication and erection tolerances. The plate therefore buckles under the diagonal compressive stresses, with fold lines perpendicular to these compressive stresses (and parallel to the principal tensile stresses). At that point, lateral loads are transferred through the plate by the principal tension stresses. This postbuckling and tension field action behavior is schematically shown in Figure 12.2a, and visible in an actual SPSW in Figure 12.2b.

This tension field mechanism has been recognized as early as the 1930s in aerospace engineering (Wagner 1931) and as early as the 1960s in steel building construction, when it was incorporated into the design process of plate girders (Basler 1961). However, note that plate girder design equations should not be used to design SPSWs because they can be misleading and give strengths inappropriate for capacity design purposes (as demonstrated in Berman and Bruneau 2004). One important reason for this is that HBEs and VBEs in SPSW are designed with sufficient strength and stiffness to allow the web plates to yield over their height and width, which is not possible for the flanges of plate girders.

Following the review of representative SPSW implementations summarized in Section 12.1.2, the fundamental behavior of SPSWs is presented in Section 12.2, while procedures for the analysis and design of SPSWs are in Sections 12.3 and 12.4, respectively. Design is covered in Section 12.5, followed by a design example in Section 12.6. Note that this chapter focuses on the behavior and design of unstiffened SPSW.

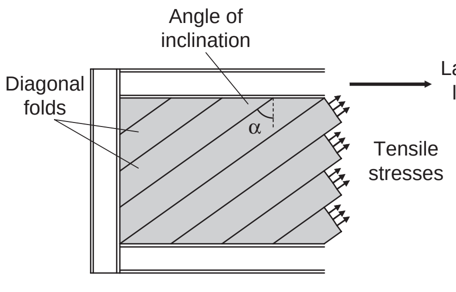

Figure 12.2 Tension field action in typical SPSW: (a) schematic idealization (*Courtesy of Diego López-García, Pontificia Universidad Católica de Chile, Chile.*); (b) web plate of SPSW specimen (at 1.8% drift). (*Berman and Bruneau 2003b, courtesy of MCEER, University at Buffalo.*)

12.1.2 Historical Developments

SPSWs have been constructed before codified requirements for their design existed. Designed and detailed based on engineering principles, their characteristics have evolved over time, reflecting improvements in knowledge on this topic as instructed by research. A comprehensive survey of buildings having SPSWs for their lateral load resisting structural system, and of determinant research on that topic at the time, has been presented by Sabelli and Bruneau (2007). The number of buildings having SPSWs and of research projects studying that structural system has increased substantially since it has been introduced in design specifications (AISC 2005, 2010; CSA 1994, 2001, 2009). Here, a few selected projects are summarized to illustrate the evolution in approaches and applications for SPSWs. Specifics on geometry, plate thicknesses, member sizes, and material properties are provided in Sabelli and Bruneau for some of these projects.

Early documented implementations of SPSWs in North America date to the 1970s. Notable examples include a 16-story expansion to an existing hospital in San Francisco, California (Dean et. al 1977; Wosser and Poland 2003), a 29-story hotel in Dallas, Texas (Architectural Record 1978a, ENR 1977), a six-story medical center in Sylmar, California (Architectural Record 1978b, ENR 1978a), a hospital retrofit in Charleston, South Carolina (Baldelli 1983), and a library retrofit in Oregon (Robinson and Ames 2000).

For the San Francisco hospital expansion, SPSW was determined to be the only practical structural system able to accommodate the high design seismic forces and sufficiently stiff to meet the tight drift limits specified for the project (intended to protect essential hospital systems from damage so they could remain in service after a severe earthquake), while limiting story heights to match the floor levels of the adjacent existing building (to accommodate the many ducts, pipes, and other mechanical and electrical items in the ceiling space). Wosser and Poland (2003) report that equivalent reinforced concrete shear walls would have been over 4-feet thick, which was architecturally unacceptable. Finite element analysis was used to model the shear walls, which were irregular in shape and had many openings. In the implemented concept, the steel plates were sized to resist the total design shear forces in the wall. The concrete cover stiffness was taken into account, but its main purpose was to prevent buckling of the steel plates. Ties on each side of the steel plate were used to attach it to the concrete layers. Typical wall details are shown in Figure 12.3.

When not cast in concrete, SPSWs designed in the 1970s were stiffened to prevent buckling of their plate, such as for the wind-resistant design of the Hyatt Regency Hotel towers in Dallas (Architectural Record 1978a; ENR 1977), where steel plate walls were chosen because conventional bracing would have encroached on interior space, and concrete shear walls would have slowed construction.

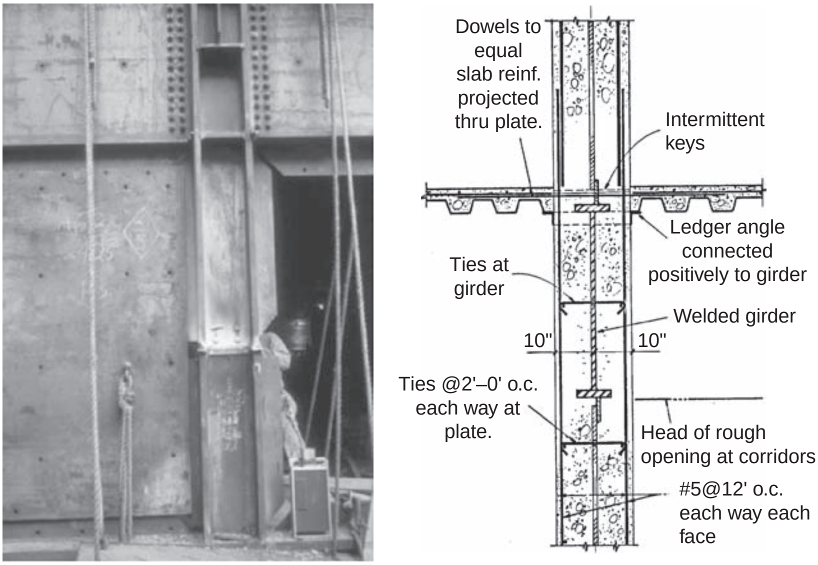

Figure 12.3 Moffit Hospital addition, typical steel shear wall, and example cross-section. (*Courtesy of Degenkolb Engineers.*)

SPSWs were also used for the Olive View Medical Center, built to replace the reinforced concrete hospital extensively damaged by the 1971 San Fernando Valley earthquake in California (Architectural Record 1978b; ENR 1978a). Perimeter and interior shear walls were used, with reinforced concrete walls in the lower two stories and SPSWs in the upper four stories as a measure to reduce the weight of the structure. The wall design was considered less costly than moment-resisting frames, and steel wall modules (Figure 12.4) were assembled using bolted splices. The peak acceleration value of 2.31g (Celebi 1997) recorded at roof level during the 1994 Northridge earthquake, for a corresponding recorded peak ground acceleration of 0.91g at the site, is often cited to emphasize the need to provide adequate bracing and protection of nonstructural elements in such stiff structures. In that case, while no structural damage was reported due to the 1994 earthquake, various nonstructural damage occurred (Naeim and Lobo 1997), including substantial water damage from various sprinkler and pipe failures which forced evacuation (OSHPD 1995).

Stiffened SPWs also provided advantages for the seismic retrofit of concrete moment-resisting frames. In one case, using steel walls instead of concrete ones minimized disruption of service in a hospital (which remained in operation during the retrofit) and allowed for future expansion (Baldelli 1983). The steel plates were connected to perimeter plates, themselves connected to the existing concrete floors

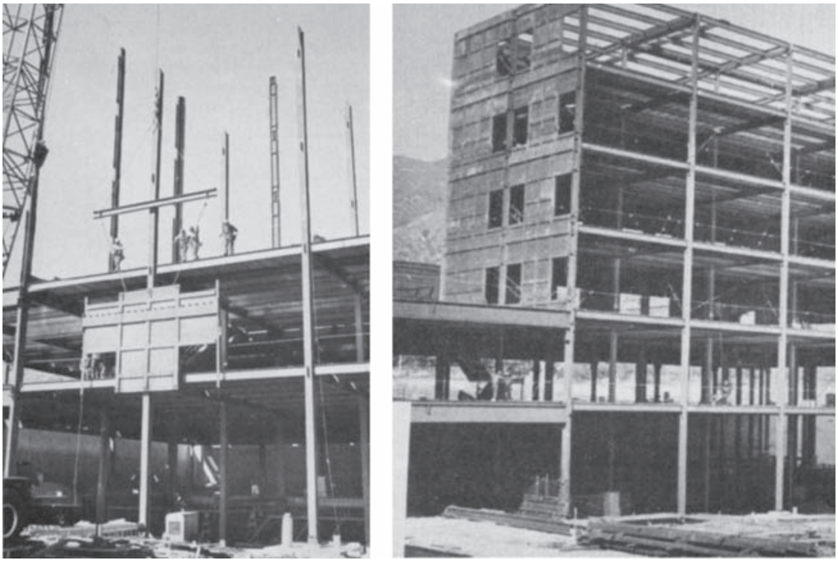

(a) (b)

Figure 12.4 Olive View Hospital steel plate assembly. (*Photos:author unknown.*)

using drilled-in and epoxied anchors. In another case, for a library, in addition to keeping the facility open during construction and preserving historical finishes, SPSW were advantageous because the moisture generated by pouring concrete would have required relocating the historical book collection to protect it against possible damage. Steel plates were designed in small panels that could be installed by hand to avoid using heavy machinery, and bolted splices were used as much possible to minimize the risk of fire from welding (Robinson and Ames 2000).

Typically in the sample implementations mentioned, although stiffened SPSWs were more expensive than alternative systems, they were advantaged by other project-specific requirements. In the early 1980s, unstiffened SPSWs started to be built in North America, starting in Canada because these were the types of SPSWs on which Canadian research focused. An eight-story building was constructed in Vancouver, British Columbia, to provide adequate seismic performance in the narrow building direction where the only locations available for lateral load resisting structural elements were adjacent to elevator shafts and staircases; eccentrically braced frames were used in the other direction (Glotman 2005).

With the publication of SPSW seismic design requirements in CAN/CSA S16 (first as an Appendix of the 1994 Edition, then in the main provisions of the 2001 Edition), implementation accelerated significantly. A series of SPSWs located around elevator shafts was found to be the best solution to resist lateral load for a 6-story building with irregular floor plan in Québec (Driver and Grondin 2001). Simplicity in construction details contributed to the cost effectiveness of the SPSW system. Two-story tiers were shop-fabricated and assembled in the field with slip-critical bolted splices.

Multiple other similar buildings have been built since. For example, a SPSW system was selected for a seven-story building in Québec, on the basis of faster construction time and gain of usable floor space, compared with other structural systems considered (including reinforced concrete walls and steel braced frames among many). The design concept relied on a core of walls located in the middle of the building (Figure 12.5a). Full height walls were prefabricated in the shop, some fabricated in half width segments and joined together on site with a vertical welded seam spanning from top to bottom (Figure 12.5b). The base of those walls was continuously anchored to the foundation.

Similar implementations followed soon after in the United States, with SPSWs around elevator shafts or other interior and exterior locations where solid walls without door and window perforations were acceptable, as typically shown in Figure 12.6 (Monnier and Harasimowicz 2007). SPSWs were also used to strengthen a building having steel moment-resisting frames that experienced damage to multiple moment connections during the 1994 Northridge Earthquake (Love et al. 2008). In that case, the existing steel moment-frame columns and girders were able to serve as VBEs and HBEs for the SPSW panels. The nonlinear pushover analyses used to validate the design used

(a) (b)

Figure 12.5 Core wall at middle of building in Montreal. (*Courtesy of Louis Crepeau, Teknika-HBA.*): (a) global view; (b) close-up view at midspan splice location.

Figure 12.6 SPSW in Portland Oregon. (*Courtesy of KPFF Consulting Engineers.*)

equivalent diagonal "strips" to model the tensile field behavior of shear panels and the force transfers in the boundary elements, and nonlinear time history analyses used tension-only diagonal strips in two directions (as described in Section 12.3).

A notable implementation in the United States (predating the SPSW design requirements of AISC 341) used a core wall system having unstiffened SPSWs in the narrow North-South direction of a 23-story building in Seattle (Figure 12.7); braced frames were used in the East-West direction. Large concrete-filled steel pipe columns were used as boundary elements to provide stiffness and resistance to overturning. SPSWs provided many competitive advantages. First, the SPW system required walls thinner than those needed for an equivalent concrete shear wall (18 in including the furring versus 28 in), resulting in savings of approximately 2% in gross square footage. Second, the system was approximately 18% lighter than an equivalent concrete core system, with a corresponding reduction in foundation loads due to gravity and overall building seismic loads. Third, construction time was reduced because the wall was fast to erect, did not require a curing period, and was easier to assemble than equivalent special concentrically braced frames. Fourth, the system was also recognized to have excellent postbuckling strength

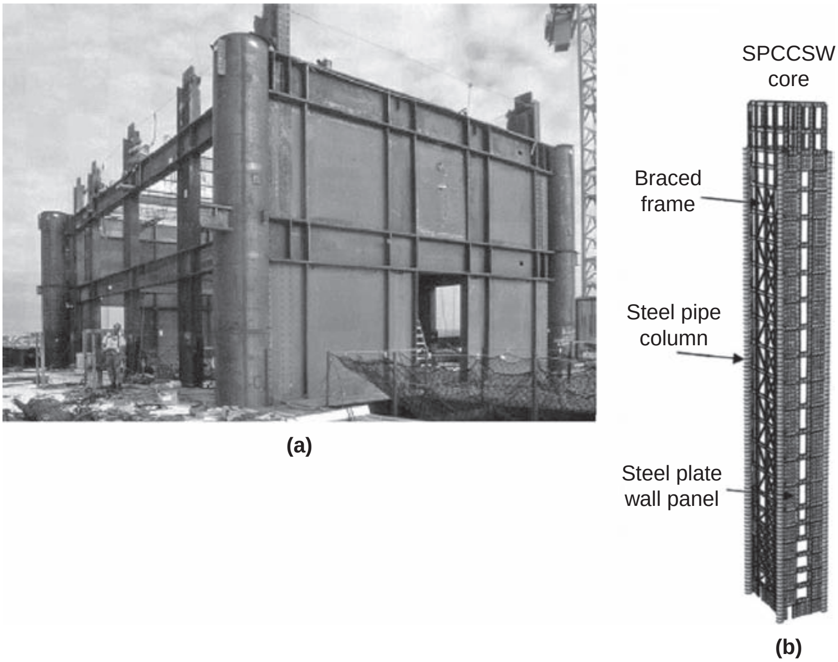

Figure 12.7 Structural system for U.S. Federal Courthouse, Seattle. (*Courtesy of Magnusson Klemencic Associates.*)

and ductility (experiments were conducted to validate the SPSW details used for this particular project).

Use of SPSWs in a 54-story hotel and condo tower completed in 2010 in Los Angeles was reported to provide all the same advantages, reducing building weight by 30% and construction time by nearly 4 months. Furthermore, use of 1-inch thick steel plates instead of 36-inch thick concrete walls provided over 20,000 extra sellable condominium square footage, for an extra $20 million in income to the developer on that prime location (Blogdowntown.com 2008, Kristeva 2010). Preassembled wall modules were also used to accelerate erection (Figure 12.8).

SPSWs also found applications in engineered low-rise buildings and large residences having sizeable open floor plans (Eatherton 2005, Eatherton and Johnson 2004, Sabelli and Bruneau 2007). In some of these cases, light-gauge steel plates were used for the SPSW webs. In other instances, the SPSWs were designed to remain elastic and capable of resisting several times the code-specified level of base shear (Figure 12.9).

In most applications, the web plates of unstiffened SPSWs have been welded to their surrounding frames (in conjunction to either welded or bolted splices), but bolted alternatives are possible.

Figure 12.8 SPSW module lifted in place to accelerate construction. (*Courtesy of Lee Decker, Herrick Corporation.*)

Figure 12.9 Residential building with SPW in San Mateo County, California, CA. (*Courtesy of GFDS Engineers and of Matthew Eatherton, Department of Civil and Environmental Engineering, Virginia Tech.*)

Figure 12.10 Example of SPSW with bolted webs. (*Courtesy of Peter Timler, Supreme Group, Edmonton, AB, Canada*.)

For example, as part of a new combined air traffic control tower built integral with office facilities, as an extension to an existing airport, bolted webs were used because they provided more construction flexibility when operating in a highly restricted and controlled environment, particularly for the structure being within airside operations (Figure 12.10).

12.1.3 International Implementations

12.1.3.1 Unstiffened SPSW

Unstiffened SPSWs have also been implemented in other countries, with sensibly the same detailing and following identical analysis and design approaches. For example (Figure 12.11), a 22-story condominium building in Mexico was constructed with SPSWs after calculations demonstrated this alternative to be of lower cost and faster to

(a) (b)

Figure 12.11 SPSWs around an elevator core in a Mexico building: (a) outside view; (b) inside view. (*Courtesy of Enrique Martinez-Romero, Mexico.*)

Figure 12.12 SPSW with bolted web. (*Courtesy of Kevin Spring, Silvester/Clark Consulting Engineers, New Zealand.*)

build than a hybrid structure of steel frames combined with concrete walls that had been used earlier in a similar building (itself more economical than an all concrete option) (Romero 2003).

In New Zealand (Figure 12.13), SPSWs were used in 2003 to strengthen the lower stories of an existing three-story reinforced concrete building and then extended to provide four additional stories of steel framing on top of the existing building (Figure 12.12). The existing concrete columns were wrapped in steel plates to provide them with some ductility before connecting the SPSW's steel plate.

In the absence of local code specifications for unstiffened SPSWs (although the system is being considered for adoption in future editions of many such specifications), international projects have typically been designed referencing CAN/CSA S16 or AISC 341.

12.1.3.2 Stiffened SPSW

Stiffened SPSWs have been preferred in Japan where elastic buckling of structural elements providing lateral load resistance is not permitted (Figure 12.13). Given the requirement that steel plates must achieve their full plastic shear strength, other types of structural configurations have emerged in which shear yielding elements are introduced, without being SPSWs in the sense considered in here. Such concepts include small shear-yielding panels connected to beams at

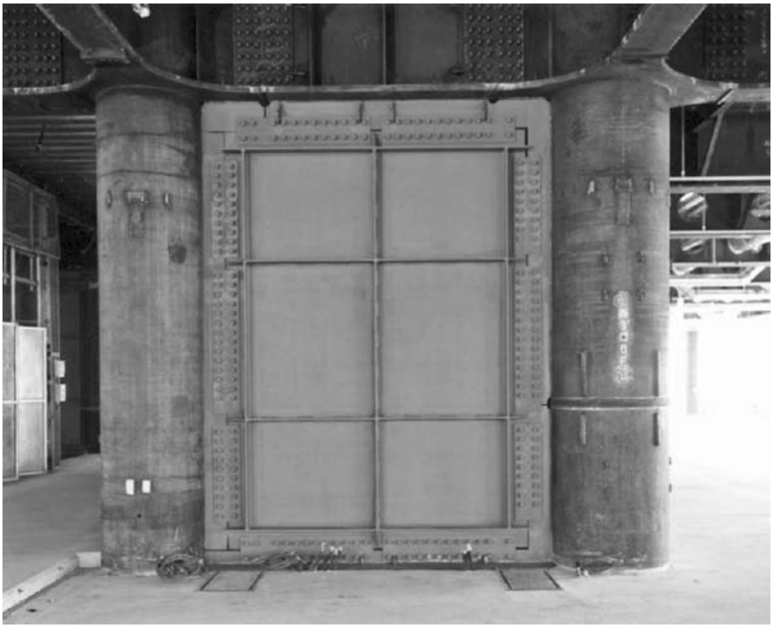

Figure 12.13 SPSW panel in Japan, with horizontal and vertical stiffeners. (*Courtesy of Nippon Steel Engineering*.)

midspan or inserted at midheight of special intermediate columns, and designed as hysteretic dampers (which are beyond the scope of this chapter).

Examples of early SPSW buildings in Japan include the Nippon Steel building and the Shinjuku Nomura building, both in Tokyo and built in the 1970s. For the former, SPSWs were used from the fourth story and above, while SPSWs embedded in concrete were used for the lower stories (Yokoyama et al. 1978). For the latter, Tokyo's third tallest building at the time (51 stories), the 10 ft × 16.5 ft steel panels were reinforced with vertical stiffeners on one side and horizontal stiffeners on the other, and each panel was reportedly connected to its surrounding steel frame with 200 to 500 bolts (ENR 1978b). The precision required for such bolting operations proved challenging and the project manager for the contractor expressed a strong determination to weld the plates in future such projects, as apparently done in another Tokyo high-rise at the time. Other Japanese buildings at the time were designed with patented precast concrete seismic wall cores and the motivation to use SPSWs stemmed from the desire to use an innovative and non-patented construction system.

The 35-story Kobe City Hall tower (Figure 12.14), subjected to the 1995 Kobe earthquake, had stiffened SPSWs from the third floor and

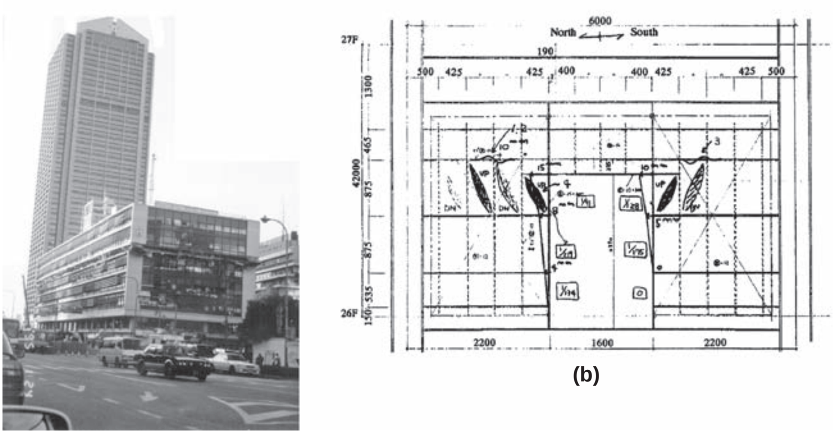

(b)

(a)

Figure 12.14 Kobe City Hall: (a) global view; (b) sketch of SPSW plate buckling on 26th story. (*Fujitani et al. 1996, Courtesy of Council on Tall Buildings and Urban Habitat.*)

above (reinforced concrete walls were used in the basement levels, and composite walls over two stories were used as a transition between the steel and reinforced concrete walls). Fujitani et al. (1996) reported minor local buckling of the stiffened steel plate shear walls on the 26th story (Figure 12.14b) and residual roof drifts of 225 mm (8.9 in) and 35 mm (1.4 in) from plumb in the north and west directions, respectively. Note that an upper story of the lower rise building of that complex (foreground of Figure 12.14a) collapsed in a soft-story mechanism at the level where a moment-resisting frame system having steel sections embedded in reinforced concrete transitioned into a regular moment-resisting reinforced concrete frame (Nakashima et al. 1995); however, this building had a significantly lower period than the adjacent tower, which attracted greater seismic forces, precluding comparison of the seismic performance between the two structures.

Following the development of special low yield steels (LYS) in Japan (Chapter 2), some tall buildings there have included SPSWs with LYS plates to dissipate energy (Yamaguchi et al. 1998). Because of their lower strength, LYS plates required to resist a given lateral load are thicker than conventional steel, resulting in fewer stiffeners required to prevent buckling. In two such 31- and 26-story buildings, walls were positioned around the stairwells in somewhat of a checkerboard pattern to minimize their overturning moments.

Finally, note that traditional structural engineering practice in Japan calls for all the beam-to-column connections in a building to be full moment-resisting connections, which provides significant redundancy compared with North American practice.

12.2 Behavior of Steel Plate Shear Walls

12.2.1 General Behavior

Lateral loads applied to a typical SPSW panel are resisted by its web plate, together with moment-frame action if moment connections are provided. A stocky or appropriately stiffened plate could provide enough compression strength to allow the plate to yield in shear. However, given that plates in SPSWs are generally slender, they buckle in compression and develop a diagonal tension field (as described in Section 12.1.1). The beams (HBEs) and columns (VBEs) to which they are connected must be able to resist these tension forces. The resulting demands on the web's boundary frame, combined to forces and deformations due to sway action, are illustrated in Figure 12.15. Note that thin web plates can provide the strength and stiffness of CBFs having large braces, without the complex brace gusset designs required in CBFs.

The angle from the vertical at which the diagonal tension field develops in unstiffened SPSWs was derived from elastic strain energy principles by Timler and Kulak (1983) as:

$$\tan^4 \alpha = \frac{1 + \dfrac{t_w L}{2A_c}}{1 + t_w h\left(\dfrac{1}{A_b} + \dfrac{h^3}{360 I_c L}\right)} \tag{12.1}$$

where t_w is the thickness of the infill plate, h is the story height, L is the bay width, I_c is the moment of inertia of the VBE, A_c is the cross-sectional area of the VBE, and A_b is the cross-sectional area of the HBE. This equation was first verified by Timler and Kulak (1983) and

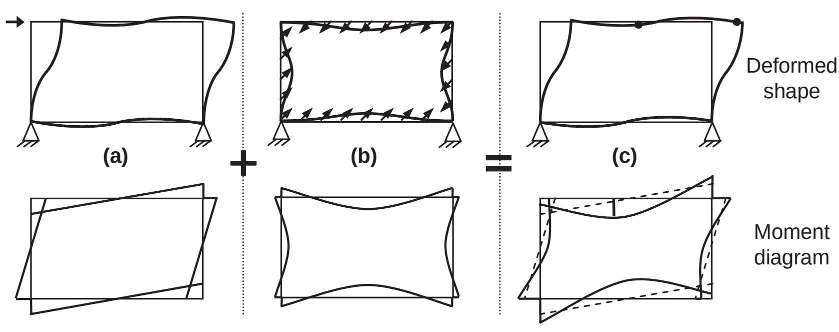

Figure 12.15 Schematic deformed shape, frame forces, and moment diagrams for: (a) frame without web plate; (b) SPSW web plate forces; (c) combined system. (*Vian and Bruneau 2005; Courtesy of MCEER, University at Buffalo.*)

Tromposch and Kulak (1987) with large-scale single-panel test specimens, and later by others. Values of this angle typically fall between 38° and 45° for well designed SPSWs.

Thorburn et al. (1983) and Timler and Kulak (1983) proposed replacing the solid web by a series of pin-ended diagonal braces for convenience in analysis, recommending a minimum of 10 strips per panel to appropriately capture the SPSW behavior; engineering judgment may dictate more for large panel aspect ratios, as the model must have enough discrete strips pulling on the HBEs and VBEs to ensure that their moment diagrams closely match the actual ones due to the tension applied by the continuous plates. This approach will be further described in Section 12.3.

Knowing the angle at which tension stresses are acting, corresponding demands on the boundary elements can be calculated. For example, for the bottom beam segment shown in Figure 12.16, and unit panel width, *ds*, oriented at angle, α, the axial force in that web strip is given by:

$$P = \sigma \cdot t \cdot ds \tag{12.2}$$

where t is the web panel thickness, and σ is the strip axial stress. The unit length along the beam, dx, is calculated from the projection of ds. The horizontal and vertical components of P, H, and V respectively, are resolved from geometry and used to calculate the

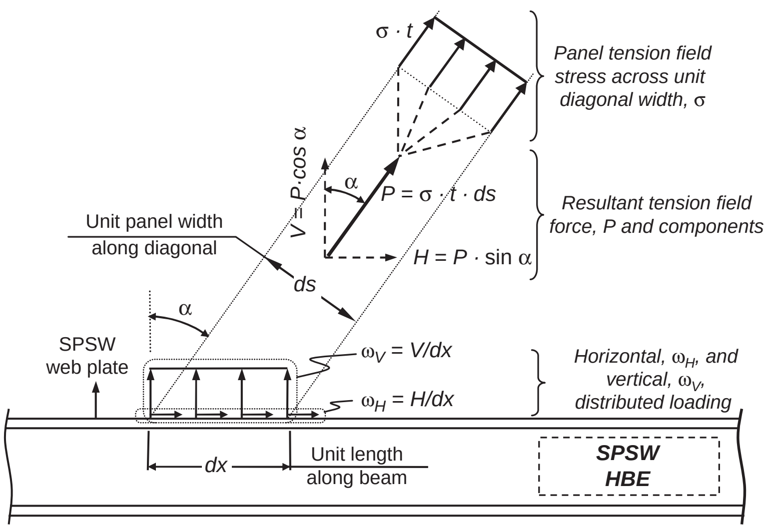

Figure 12.16 Horizontal, ω_H, and vertical, ω_V, distributed loading components of panel diagonal tension field force, P, per unit width, ds. (*Adapted from Vian and Bruneau 2005, Courtesy of MCEER, University at Buffalo.*)

distributed loads on the beam, ω_H and ω_V, respectively (note that other context-dependent notations are used for those terms throughout the chapter). By distributing those values across the projected unit length, dx:

$$\omega_H = \frac{H}{dx} = \frac{P \cdot \sin\alpha}{dx} = \frac{1}{2}\sigma \cdot t \cdot \sin 2\alpha \tag{12.3a}$$

$$\omega_V = \frac{V}{dx} = \frac{P \cdot \cos\alpha}{dx} = \sigma \cdot t \cdot \cos^2 \alpha \tag{12.3b}$$

A fully yielding web plate would apply a total horizontal force along the length of an HBE equal to:

$$F_H = \omega_H L = \frac{1}{2}\sigma_y \, t \, L \sin 2\alpha \tag{12.4}$$

If the tension field is oriented at an angle of $\alpha = 45°$, then:

$$\omega = \omega_H = \omega_V = \frac{\sigma \cdot t}{2} \tag{12.5}$$

The force applied by a web plate to its boundary VBEs can be similarly calculated. Using a similar approach, parallel and perpendicular unit stresses per unit along a VBE are respectively ½ $\sigma \sin(2\alpha)$ and $\sigma \sin^2(\alpha)$.

Using similar geometric relationships, the drift at which the web plate of a SPSW would start to yield can be estimated assuming rigid pin-ended HBEs and VBEs. The corresponding rigid "racking" behavior would impose a uniform axial strain on all of the diagonal tension field strips, ε, which can be related to drift angle, γ, as:

$$\varepsilon = \frac{\gamma \cdot \sin 2\alpha}{2} \qquad \therefore \qquad \gamma_y = \frac{2\varepsilon_y}{\sin 2\alpha} \tag{12.6}$$

which, for steel having a yield stress of 50 ksi, assuming a diagonal tension field angle of 45°, indicates that plate yielding would start at a drift of 0.34%.

The tension forces applied to the boundary frame by the yielding web plate can result in significant "pull-in" of the HBEs and VBEs. If these members are not designed in accordance with capacity design principles (Sections 12.2.2, 12.3, and 12.4), the SPSW may end up having a substantial "hour-glass" shape after cycles of inelastic behavior, as shown in Figure 12.17.

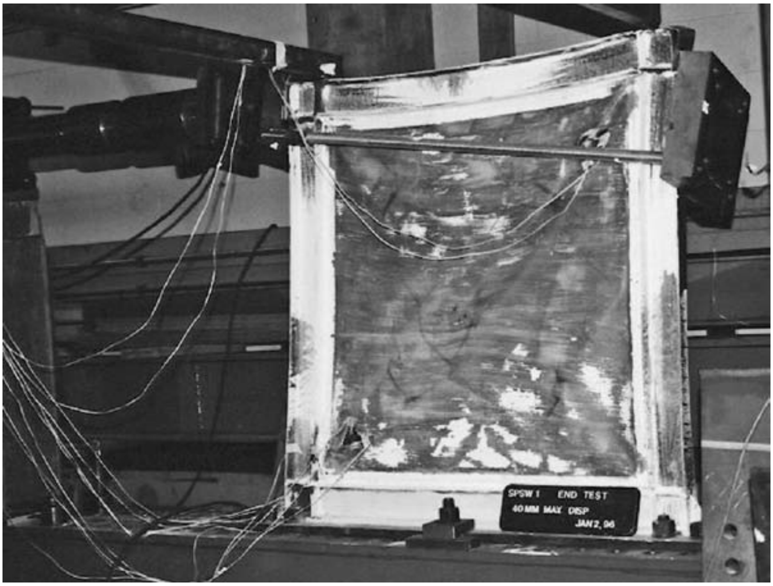

Figure 12.17 Hour-glass shape of specimen due to "pull-in" of HBEs and VBEs. (*Courtesy of Carlos Ventura, Department of Civil Engineering, University of British Columbia, Canada.*)

12.2.2 Plastic Mechanism

12.2.2.1 Kinematic Method—Simple Beam-to-Column Connection

The plastic strength of a SPSW can be obtained using the kinematic method of plastic analysis (Berman and Bruneau 2003a, 2003b). Consider the frame of width L, having inclined strips of thickness t, at a spacing s in the direction perpendicular to the strips, with the first and last (upper left and lower right) strips located at $s/2$ from the closest beam-to-column connections. When the shear force, V, displaces the top beam by a value, Δ, sufficient to yield all the strips, the external work done is equal to $V\Delta$. If the beams and columns are assumed to remain elastic, their contribution to the internal work may be neglected when compared with the internal work done by the braces, hence, the internal work is $(n_b A_{st} F_y \sin\alpha)\Delta$, where n_b is the number of strips anchored to the top beam, A_{st} is the area of one strip, F_y is the strip yield strength, and α is the angle from the strip to the vertical (complementary to the angle ϕ shown in Figure 12.18). This result can be obtained by the product of the yield force times the yield displacement of the strips, but for simplicity it can also be found using the horizontal and vertical components of these values. Note that the horizontal components of the yield forces of the strips on the columns cancel (the forces on the left column do negative internal

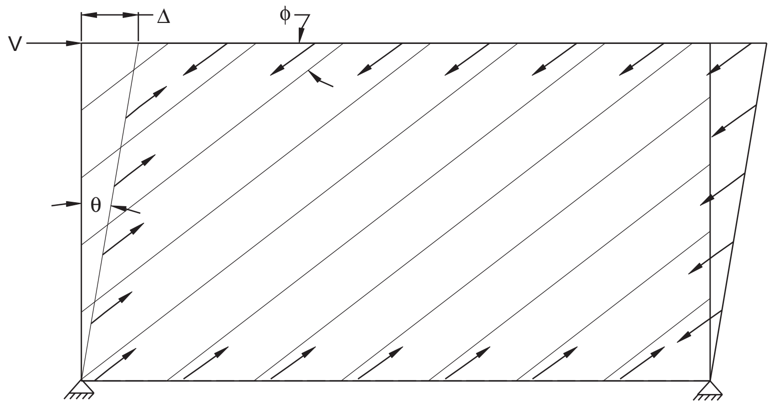

Figure 12.18 Single-story SPSW plastic mechanism. (*Adapted from Berman and Bruneau 2003b, Courtesy of MCEER, University at Buffalo.*)

work and the forces on the right column do positive internal work) and the vertical components of all the yield forces do no internal work because there is no vertical deflection. Therefore, the only internal work done is by the horizontal components of the strip yield forces anchored to the top beam. Equating the external and internal work gives:

$$V = n_b F_{st} \sin \alpha \tag{12.7}$$

Given $n_b = (L \cos \alpha)/s$ from geometry, and the strip force $F_{st} = F_y A_{st} = F_y t\, s$, substituted into Eq. (12.7), and knowing (½) sin 2α = (cos α)(sin α), the resulting base shear relationship is:

$$V = \frac{1}{2} F_y t L \sin 2\alpha \tag{12.8}$$

The same results can also be obtained using the statical method (Berman and Bruneau 2003a).

12.2.2.2 Kinematic Method—Rigid Beam-to-Column Connection

In single-story SPSWs having rigid beam-to-column connections (as opposed to simple connections), plastic hinges also need to form in the boundary frame to produce a plastic mechanism. The corresponding additional internal work is $4M_p\theta$, where $\theta = \Delta/h_S$, is the story displacement, Δ, over the story height, h_s, and M_p is the smaller of the plastic moment capacity of the beams M_{pb}, or columns M_{pc}—if strong-column/weak-beam philosophy is enforced, plastic hinges will develop in the beams; otherwise, for single-story frames that are wider than tall, if the beams (HBEs) have sufficient strength and stiffness to anchor the tension field, plastic hinges are likely to form at the top and bottom of the columns (VBEs) and not in the beams.

The resulting ultimate strength for a moment frame with plastic hinges in the columns becomes:

$$V = \frac{1}{2} F_y \, t L \sin \alpha + \frac{4M_{pc}}{h_s} \tag{12.9}$$

In design, neglecting the strength of the HBEs or VBEs results in a larger plate thickness. This translates into lower ductility demands in the walls and frame members and is conservative. Note that CSA S16-09 explicitly requires that plates be designed to resist 100% of the seismic lateral forces, but not AISC 341-10; although this was implicitly intended in the original formulation of the design requirements, it can be interpreted otherwise. A limited study of the lateral load resistance of SPSWs designed with and without consideration of the boundary frame moment-resisting action [e.g., Eq. (12.9) versus Eq. (12.8)] is summarized in Section 12.4.4.

12.2.2.3 Plastic Analysis of SPSW—Multistory Frames

For multistory SPSWs with pin-ended beams, plastic analysis can also be used to predict the ultimate capacity. Some of the key plastic mechanisms that should be considered in estimating the ultimate capacity of a steel plate shear wall are presented here. These could be used to define a desirable failure mode in a capacity design perspective, or to prevent an undesirable failure mode, as well as complement traditional design approaches.

For the soft-story plastic mechanisms at level i shown in Figure 12.19a, with plastic hinges in the HBEs, equating the internal and external work gives:

$$\sum_{j}^{n_s} V_j = \frac{1}{2} F_y \, t_i L \sin 2\alpha + \frac{4M_{pci}}{h_{si}} \tag{12.10}$$

where V_j are the applied lateral forces above the soft-story i, t_i is the plate thickness at the soft-story, M_{pci} is the plastic moment capacity of the columns at the soft-story, h_{si} is the height of the soft-story, and n_s is the total number of stories. Note that only the applied lateral forces above the soft-story do external work and they all move the same distance (Δ). The internal work is done only by the strips on the soft-story itself and by column hinges forming at the top and bottom of that soft-story. Note that the possibility of a soft-story mechanism should be checked at every story in which there is a significant change in plate thickness or column size. Additionally, the soft-story mechanism is independent of the beam connection type (simple or rigid) because plastic hinges form in the columns, not the beams.

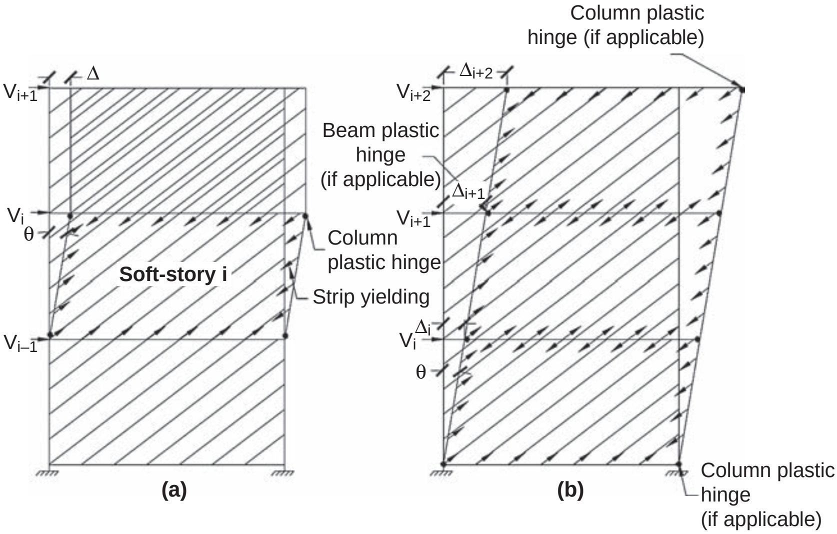

FIGURE 12.19 SPSW plastic mechanisms: (a) soft-story mechanism; (b) uniform yielding mechanism. (*Berman and Bruneau 2003b, courtesy of MCEER, University at Buffalo.*)

The desirable plastic mechanism involves uniform yielding of the plates over every story (Figure 12.19b). For this mechanism, each applied lateral force, V_i, moves a distance $\Delta_i = \theta h_i$, and does external work equal to $V_i\theta h_i$, where h_i is the elevation of the ith story. The internal work is done by the strips of each story yielding. Note that the strip forces acting on the bottom of a story beam do positive internal work and the strip forces acting on top of the same beam do negative internal work. Therefore, the internal work at any story, *I*, is equal to the work done by strip yield forces along the bottom of the story beam minus the work done by strip yield forces on the top of the same beam. This indicates that in order for every plate at every story to contribute to the internal work, the plate thicknesses would have to vary at each story in direct proportion to the demands from the applied lateral forces. Even with this in mind, this mechanism provides insight into the capacity and failure mechanism of the wall.

For this uniform plastic mechanism, the ultimate strength of a multistory SPSW having simple beam-to-column connections (obtained by equating internal and external works) is:

$$\sum_{i}^{n_s} V_i h_i = \sum_{i}^{n_s} \left(\frac{1}{2} F_y (t_i - t_{i+1}) L h_i \sin 2\alpha \right) \tag{12.11}$$

where h_i is the ith story elevation, n_s is the total number of stories, and t_i is the thickness of the plate on the ith story.

The ultimate strength of SPSW having rigid beam-to-column connections capable of developing the beam's plastic moment can also be calculated following the same kinematic approach. The resulting general equation for the uniform yielding mechanism is:

$$\sum_{i}^{n_s} V_i h_i = \sum_{i}^{n_s} \frac{1}{2} F_y (t_i - t_{i+1}) L h_i \sin 2\alpha + \sum_{i}^{n_s} 2M_{pbi} \tag{12.12}$$

where M_{pbi} is the plastic moment of the ith story beam, and the rest of the terms were previously defined (identical plastic hinge strengths are assumed at both HBE ends here—the equation can be modified if not the case). If column hinges form instead of beam hinges at the roof and base levels, values for M_{pc1} as the first story column plastic moment, and M_{pcn} as the top story column plastic moment would be substituted at those stories; this would happen if strong-column/weak-beam philosophy was not enforced at these two locations. Judgment must be used to determine when M_{pc1} and M_{pcn} may be used instead of M_{pb1} and M_{pbn}, where M_{pb1} and M_{pbn} are the plastic moment capacities of the base and roof beams, respectively.

Results from several different pushover analyses for multistory SPSW have shown that the actual failure mechanism is typically somewhere between a soft-story mechanism and uniform yielding of the plates on all stories. Finding the actual failure mechanism is tedious by hand; computerized pushover analysis is preferable. However, the mechanisms described above will provide a good estimate of ultimate strength and insights as to whether a soft-story is likely.

12.2.3 Design Philosophy and Hysteretic Energy Dissipation

The designated energy dissipating elements of a SPSW are its web plates at every story. Given the webs' negligible compression strength, these plates only yield in tension and the hysteretic behavior of a typical web plate is approximately equivalent to that resulting from a series of tension-only braces adjacent to each other. This is illustrated in Figure 12.20 for a SPSW specimen having HBEs connected to VBEs using only double-angle shear connections (Berman and Bruneau 2003b). Although these shear connectors are in principle not moment-resisting connections, the angles required to transfer the large axial forces in the HBEs (Section 12.3.3) were large enough to develop a non-negligible flexural strength during testing of the bare frame. Subtracting that bare frame contribution from the total hysteresis curve leaves the contribution of the web plates to lateral load resistance shown in Figure 12.20.

Similarly to what was observed for CBFs having tension-only braces (Section 6.3.2), note that previously yielded parts of a web plate in a SPSW panel provides little lateral load resistance in subsequent cycles unless the maximum panel drift previously reached is exceeded, because the web plate can be plastically elongated in tension, but

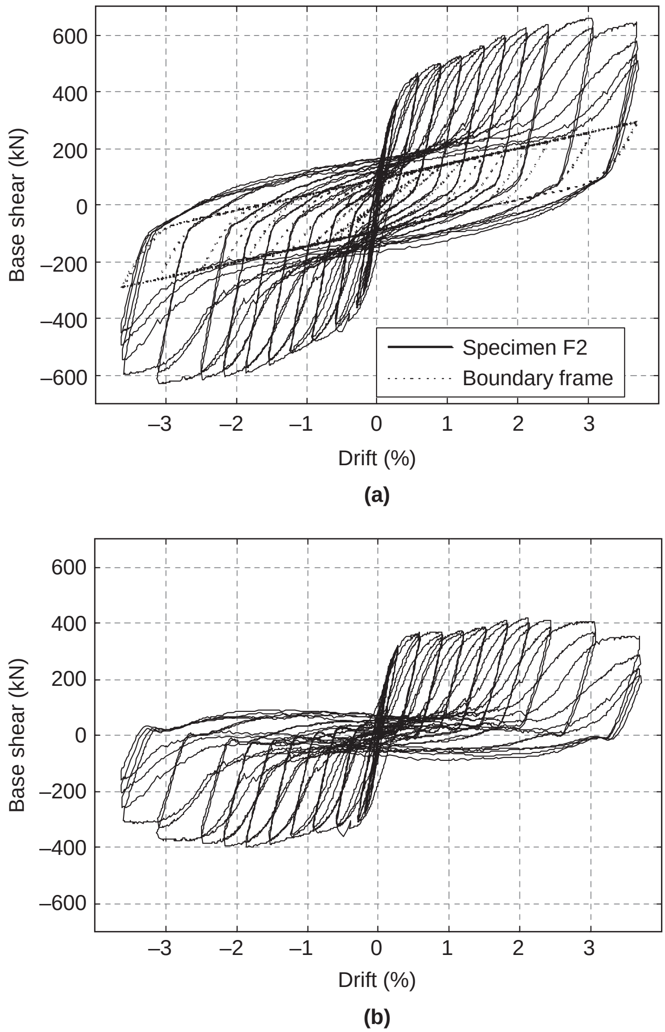

Figure 12.20 Hysteretic behavior of SPSW with simple beam-to-column connections: (a) complete SPSW and of boundary frame alone; (b) web plate only. (*Berman and Bruneau 2003b, courtesy of MCEER, University at Buffalo.*)

never shortened in compression. For the same reason, the web plate is typically observed to be loosely buckled/folded in a random pattern when the frame is returned to its original plumb position after large inelastic excursions. This behavior emphasizes the important contribution of the SPSW boundary frame (HBEs and VBEs) to limit drifts and provide complementary energy dissipation, per the plastic mechanism described in Section 12.2.1.

Capacity design principles must be used to design HBEs and VBEs, because yielding of the boundary frame could prevent full

Figure 12.21 Near and far view of local instability of columns at first story of SPSW. (*Courtesy of Carlos Ventura, Department of Civil Engineering, University of British Columbia, Canada.*)

yielding of the webs. For example, failure from global instability due to inelastic buckling of a column at the first story of a four-story SPSW tested by Lubell et al. (2000) provides an example of such undesirable behavior (Figure 12.21). Similar capacity design principles must extend to connections, panel zones, splices, and all other structural elements along the load path that must have sufficient strength to develop the desired plastic mechanism.

12.3 Analysis and Modeling

12.3.1 Strip Models

The strip model, briefly mentioned in Section 12.2.1, provides a simple and practical analytical way to capture the fundamental behavior of SPSWs. As schematically illustrated in Figure 12.22, the model proposed by Thorburn et al. (1983) consists of converting the solid steel panel into parallel pin-ended strips only able to resist tension. Under static lateral loads, simple brace elements can be used, provided none is in compression. When deep HBEs and VBEs are used, accuracy of results is enhanced by connecting the strips to these elements' flanges, using rigid offsets to link the strips to the HBEs and VBEs centerlines.

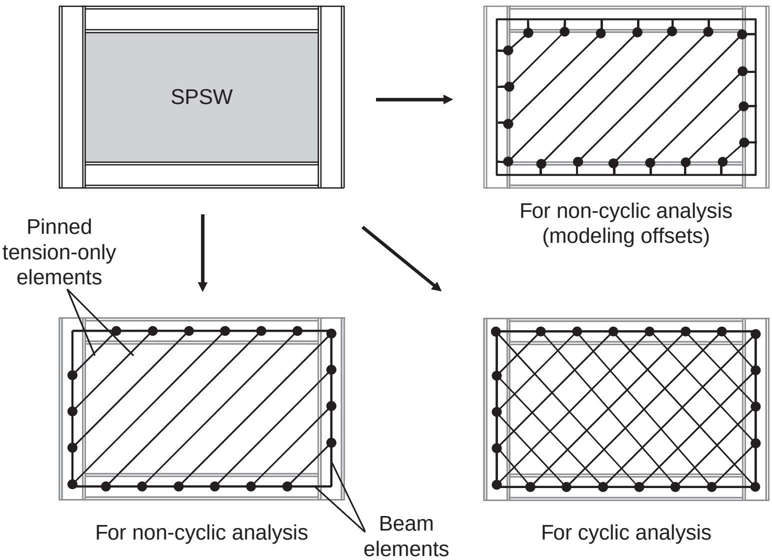

Figure 12.22 Strip model for static (linear and nonlinear) analysis of SPW and strip model for cyclic static and dynamic nonlinear analysis.

Strip orientation can be as given per Eq. (12.1), or a constant angle as described later. As mentioned in Section 12.2.1, the number of strips should be large enough to give credible moment diagrams on the HBEs and VBEs, and no less than 10 in any circumstances. Each strip has an area, A_s, equal to the web plate thickness, t_w, times the perpendicular distance between strips, which, for a panel of height, h, and width, L, having n strips, corresponds to:

$$A_s = \frac{\left[L\cos(\alpha) + h\sin(\alpha)\right]t_w}{n} \tag{12.13}$$

Timler and Kulak (1983) showed that the strip model gives accurate values of initial preyielding SPSW stiffness and of forces in boundary members under service loads. Nonlinear pushover analyses using elasto-plastic strips and HBE plastic hinges have often been shown to adequately capture the full force-displacement behavior and ultimate strength of SPSWs and their individual stories (Berman and Bruneau 2004, 2005; Driver et al. 1997a, 1998b; Qu et al. 2008, among many), as shown for a typical case in Figure 12.23.

Past research has also shown that the strip model can adequately capture the hysteretic behavior of SPSWs provided that a symmetric layout of tension-only nonlinear strips is used (e.g., Elgaaly et al. 1993, Elgaaly and Liu 1997, Lubell et al. 2000, Qu et al. 2008), as shown

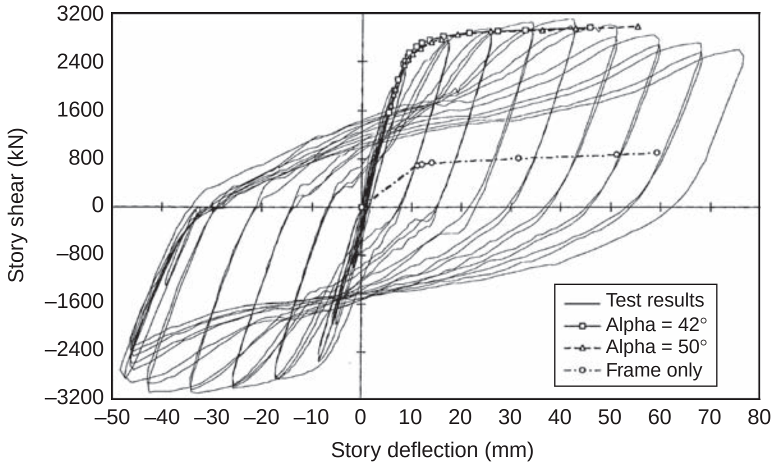

Figure 12.23 Comparison between experimental results and strip model. (*Courtesy of Robert Driver, Department of Civil and Environmental Engineering, University of Alberta*.)

in Figure 12.22. Note that the tension-only behavior considered here is similar to that presented in Chapter 6, Figure 6.12. Such models have also been successfully used in nonlinear dynamic analysis (e.g., Bruneau and Bhagwagar 2002, Qu and Bruneau 2009).

Note that in a multistory SPSW, because the value of α given by Eq. (12.1) would vary from story to story, the use of equally spaced strips would lead to a model having staggered node points at the beams (Bruneau and Bhagwagar 2002, Sabelli and Bruneau 2007, Timler et al. 1998), which is unnecessarily complicated and gives jagged moment diagrams in the HBEs. For that reason, AISC 341 and CSA S16 permit the use of a single strip inclination angle across the frame height, equal to the average of the angles calculated at each story. Timler et al. (1998) showed this simplification to be of little consequence on analytical results. AISC 341-10 and CSA-09 also permit using a constant value of 40° (based on Dastfan and Driver 2008), although CSA only allow this for web panels aspect ratios of $0.6 \le L/h \le 2.5$, when the inertia, I_b, of the top and bottom HBEs is:

$$I_b \ge \frac{t_w L^4}{CL - \left(\dfrac{t_w h^4}{I_c}\right)} \tag{12.14}$$

where I_c is the inertia of the VBE, C is equal to 650 and 267 for the top and bottom anchor HBEs, respectively, and all other terms have been defined earlier.

12.3.2 Finite Element Models

Nonlinear finite element analysis has been successfully used by researchers to replicate both the monotonic and hysteretic inelastic behavior of SPSWs, accounting for material and geometric nonlinearities (Behbahanifard et al. 2003, Driver et al. 1997b, 1998b, Elgaaly et al. 1993, Purba and Bruneau 2007, Vian and Bruneau 2005). Accurate simulations of hysteretic nonlinear inelastic response, particularly to reliably capture cyclic behavior and plate buckling, have required a large number of shell elements and substantial computational times. While suitable for research purposes, such complex analyses are unrealistic for most practical applications.

Unfortunately, simpler linear-elastic finite element models cannot reliably capture the stiffness, strength, and hysteretic characteristics of SPSWs (Elgaaly et al. 1993). Most significantly, use of elastic isotropic shell elements lead to incorrect force demands on boundary elements (for the same reasons that elastic analysis cannot capture the demands in the beams of V-braced CBFs after brace buckling, as described in Chapter 9). Furthermore, because web plates in SPSW buckle at low deformation levels, the prebuckling stiffness predicted by elastic, isotropic shell elements overestimates the actual rigidity of SPSWs. Elastic finite element analysis can also erroneously consider the wall plate as contributing to resist gravity loads and overturning moments in ways not actually possible with thin infill plates.

Use of an orthotropic membrane-element model has been proposed as a possible method to simulate the diagonal tension strip behavior (Astaneh-Asl 2001). By orienting one of the local axes of the membrane elements in a given web plate to align with the diagonal tension direction, setting material properties equal to those of steel in that direction, but to zero axial stiffness in the orthogonal direction and zero shear stiffness in any direction (or a negligible value if null values are problematic for convergence), tension field action should be simulated. Careful verification of results is warranted to ensure that data entry errors have not erroneously generated finite elements able to resist a portion of the SPSW's overturning moments. The orthotropic membrane element used as indicated above should correspond to a tension-strip model, albeit continuous. A minimum mesh size of 4×4 per panel has been recommended by Astaneh-Asl (2001). While the above approach should in principle give results similar to those obtained using the strip method, comparison for a wide range of SPSW configurations has not been reported; the orthotropic membrane-element method has also rarely been used in research.

12.3.3 Demands on HBEs

A free-body diagram to calculate the forces in an HBE due to yielding of a plate connected to it is shown in Figure 12.24. Although incomplete (for not considering other forces applied to the HBE), it is a first step to illustrate some fundamental aspects of the demands on HBEs.

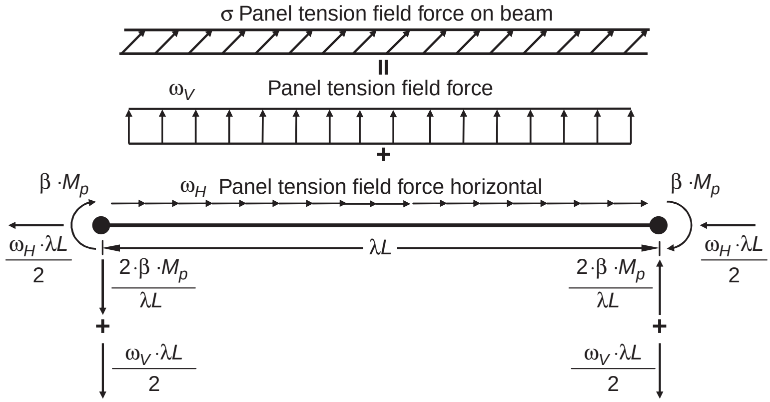

Figure 12.24 Bottom beam free-body diagram and end reactions (without the thrust forces applied by the VBEs). (*Vian and Bruneau 2005, courtesy of MCEER, University at Buffalo.*)

Web plate forces are assumed uniform, which is the case when the plate has yielded over the entire panel; in the elastic range, some variation exists depending on the flexibility of the boundary elements (note that, at a given drift, elastic stresses and strains would be uniform across the web plate for an infinitely rigid boundary frame of members having pin-ended connections, as mentioned earlier). The shape of the moment diagram created by the vertical component of the web forces depends on the relative strengths of the HBE plastic hinges and web plate, as described in Section 12. 3.3.1, which must be chosen to ensure plastic hinges at the HBE's ends, but not within its span, for reasons presented in Section 12.3.3.3. Section 12.3.3.2 proposes a possible strategy to facilitate this. Full HBE equilibrium is presented in Section 12.3.3.4.

The interaction between the shear and axial forces produced by the diagonal panel forces reduces the beam's plastic moment strength at the ends (to $\beta \cdot M_p$ in Figure 12.24, although actual values at both ends could differ), especially at the end where the shear from panel forces is additive to the shear from beam end moments (i.e., the left end in Figure 12.24). Calculation of HBE plastic hinge strength is addressed in Section 12.4.2.2. Note that except for the top and bottom HBEs that have web plates on only one side, in many equations, ω implicitly represents the resultant of tension forces from web plates above and below the HBE. Also note that when the bottom HBE is continuously anchored into the foundation, the case-specific load-paths within that HBE must be established.

12.3.3.1 HBE Moment due to Perpendicular Plate Forces

This section focuses on the HBE flexural moments due to the component of web plate yielding forces perpendicular to the HBE longitudinal axis. For HBEs having plates of different sizes above and below, the uniformly distributed load, ω, is the resultant of these opposing forces.

The equilibrium method (Chapter 4) is used to calculate the beam strength required for a specific plastic mechanism. The moment at a distance x along the statically determinate beam from the left support is obtained by superposition of the moment diagrams obtained for the end moments, M_R and M_L, and the corresponding statically determinate beam, as shown in Figure 12.25. The equation for the moment diagram, $M(x)$, for the sign convention in Figure 12.25 is:

$$M(x) = \frac{\omega \cdot x}{2} \cdot (L - x) - M_R \cdot \frac{x}{L} + M_L - M_L \cdot \frac{x}{L} \tag{12.15}$$

The location, x_{span}, of the "maximum moment within the span," M_{span}, is calculated by differentiating $M(x)$ with respect to x, setting the result equal to zero, and solving:

$$x_{span} = \frac{L}{2} - \left[\frac{M_L + M_R}{\omega \cdot L}\right] \tag{12.16}$$

Substituting Eq. (12.16) into Eq. (12.15) and simplifying:

$$M_{span} = \frac{\omega \cdot L^2}{8} + \frac{[M_L + M_R]^2}{2 \cdot \omega \cdot L^2} + \frac{M_L - M_R}{2} \tag{12.17}$$

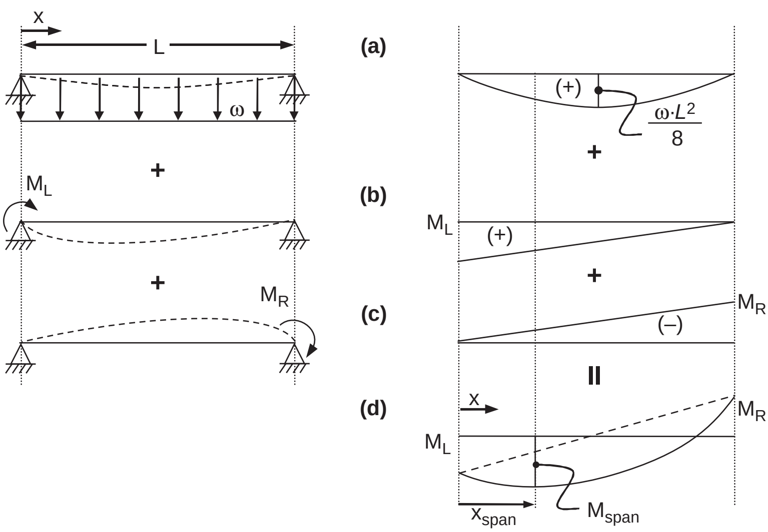

FIGURE 12.25 Deformed shape, loading, and moment diagrams for calculating beam plastic mechanisms using equilibrium method for: (a) vertical component of infill panel forces; (b) left end redundant moment; (c) right end redundant moment; (d) combined moment diagram. (*Vian and Bruneau 2005, courtesy of MCEER, University at Buffalo.*)

For illustration purposes, considering three possible cases of ultimate behavior as: (a) $M_L = M_p$ and $M_R = M_p$; (b) $M_L = 0$ and $M_R = M_p$; and (c) $M_L = -M_p$ and $M_R = M_p$; and substituting in Eq. (12.17) with $M_{span} = M_p$, the ultimate load, ω_{ult}, obtained for each case is:

$$\omega_{ult} = \begin{cases} \dfrac{4 \cdot M_p}{L^2} & \text{(a)} \\[2ex] \dfrac{2 \cdot \left(3 + \sqrt{8}\right) \cdot M_p}{L^2} = \dfrac{11.657 \cdot M_p}{L^2} & \text{(b)} \\[2ex] \dfrac{16 \cdot M_p}{L^2} & \text{(c)} \end{cases} \tag{12.18}$$

corresponding to x_{span}/L values of 0, $\left(\sqrt{2} - 1\right) \approx 0.414$, and 0.5, respectively. Similarly, for a given, ω_{max}, solving for the required M_p:

$$M_p = \begin{cases} \dfrac{\omega_{max} \cdot L^2}{4} & \text{(a)} \\[2ex] \dfrac{\left(3 - \sqrt{8}\right) \cdot \omega_{max} \cdot L^2}{2} = \dfrac{\omega_{max} \cdot L^2}{11.657} & \text{(b)} \\[2ex] \dfrac{\omega_{max} \cdot L^2}{16} & \text{(c)} \end{cases} \tag{12.19}$$

For HBEs having moment-resisting connections, setting Eq. (12.16) such that $0 \le x_{span} \le L$ gives:

$$\left| M_L + M_R \right| \le \frac{\omega \cdot L^2}{2} \tag{12.20}$$

Substituting the end-moment conditions for the three cases considered above, and solving gives:

$$\omega \ge \begin{cases} \left| \dfrac{4 \cdot M_p}{L^2} \right| & \text{(a)} \\[2ex] \left| \dfrac{2 \cdot M_p}{L^2} \right| & \text{(b)} \\[2ex] 0 & \text{(c)} \end{cases} \tag{12.21}$$

Combining these conditions with Eq. (12.18), provides a range of ω values for which M_{span} is located within the span, and an upper limit for the value of ω, when $M_{span} = M_p$ and a plastic mechanism has formed:

$$\frac{4 \cdot M_p}{L^2} \leq \omega \leq \frac{4 \cdot M_p}{L^2} \qquad \text{(a)}$$

$$\frac{2 \cdot M_p}{L^2} \leq \omega \leq \frac{2 \cdot \left(3+\sqrt{8}\right) \cdot M_p}{L^2} \qquad \text{(b)} \qquad (12.22)$$

$$0 \leq \omega \leq \frac{16 \cdot M_p}{L^2} \qquad \text{(c)}$$

Note that for case (a), both limits of the inequality are identical. Therefore, when plastic hinges form at beam-ends in the same manner presented for case (a), $x_{span} = 0$ and the third hinge required to form a beam mechanism is coincident with the left support plastic hinge (corresponding to the beam-hinge locations in a sway mechanism). Hence, case (a) is the preferred case for design to ensure no in-span hinging.

Figure 12.26 plots the normalized moments for the conditions $M_L = M_R = \kappa\ 1/8\ \omega L^2$, for various values of κ. The resulting moment diagram, $M(x)$, is normalized by the hanging moment ($\omega L^2/8$) on the vertical axis and plotted versus normalized distance from the left

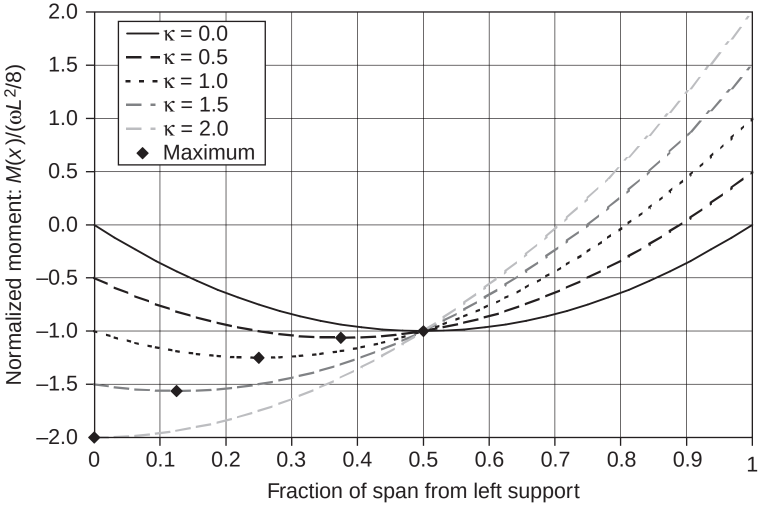

FIGURE 12.26 Normalized moment diagram for end-moment values of 0, ½, 1, 1½, and 2 times the hanging moment $\omega L^2/8$. (*Vian and Bruneau 2005, courtesy of MCEER, University at Buffalo.*)

support on the horizontal axis. As the value of the end moment increases, the maximum moment within the span shifts from midspan, reaching the left support when $M_L = M_R = ¼\ \omega L^2$. This corresponds to $\kappa = 2.0$, which is the solution for the case (a) mechanism above when $\omega = \omega_{ult}$ and $M_L = M_R = M_p$. This indicates that, for a given web plate, a fully fixed-end HBE must have twice the flexural strength of a simply supported beam to prevent plastic hinging within the span. The implications of HBE in-span plastic hinging are described in Section 12.3.3.3.

12.3.3.2 RBS to Reduce HBE Size Without In-Span Plastic Hinging

The design moment of $M_L = M_R = ¼\ \omega L^2$ determined in Section 12.3.3.1 can result in substantial HBE sizes, particularly at the top and bottom of SPSWs (a.k.a. "anchor beams, as these HBEs "anchor" the vertical component of the one-sided panel tension field forces there). To reduce HBE sizes, Vian and Bruneau (2005) proposed locally reducing their end-moment strength by using reduced beam section (RBS) connections (Chapter 8)—while the procedure was originally proposed for anchor beams, it was used in all HBEs in some instances (Qu et al. 2008, Sabelli and Bruneau 2007), as the equations are valid for any ω values.

Setting $M_{span} \leq M_p$ and $M_L = M_R = \beta \cdot M_p$ in Eq. (12.17), then:

$$M_p = \frac{\omega \cdot L^2}{8} + \frac{2}{\omega}\left(\frac{\beta \cdot M_p}{L}\right)^2 \tag{12.23}$$

which, once reorganized as a quadratic equation in terms of M_p and solved as done previously, shows that an HBE should have a plastic modulus, Z_x, satisfying the following relation:

$$M_p = Z_x \cdot F_y \geq \frac{\omega \cdot L^2}{8} \cdot \left[\frac{2}{1+\sqrt{1-\beta^2}}\right] \tag{12.24}$$

where an RBS is used at each HBE end and β is the ratio of the plastic modulus at the RBS location, Z_{RBS}, to that of the gross beam section, Z_x, and F_y and L are the yield stress and length of the anchor beam, respectively. Substituting the resultant of the vertical component of the web plate tension field forces acting on the HBE, ω as:

$$\omega = F_{yp} \cdot t \cdot \cos^2 \alpha \tag{12.25}$$

into the above equation, where t is the web plate thickness, F_{yp} is the web plate yield stress, and α is the angle of orientation, with respect to vertical, of the web plate uniform tension field stresses, the required beam plastic modulus, Z_x, becomes:

$$Z_x \geq \frac{L^2 \cdot t \cdot \cos^2 \alpha}{4} \cdot \frac{F_{yp}}{F_y} \cdot \left[\frac{1}{1+\sqrt{1-\beta^2}}\right] \tag{12.26}$$

Reduction in flange width at the RBS location can lead to substantial reduction in required HBE sizes. For example, β values of 0.9 and 0.75 reduce the required value of Z_x by 30% and 40%, respectively (Vian and Bruneau 2005).

12.3.3.3 Consequence of HBE In-Span Plastic Hinging

Designs that do not prevent in-span plastic hinges in HBEs can behave in a number of detrimental ways. Purba and Bruneau (2010) investigated this using a SPSW designed by two different approaches. A first approach did not explicitly verify that hinges could only develop at the ends of the HBEs. This can happen when using a number of common design approaches encountered in practice (even more so if using computer results indiscriminately) or when using the Indirect Capacity Design Approach described in Section 12.3.4. That latter approach was used for a first wall (SPSW-ID) in the following comparisons. The second shear wall (SPSW-CD) was designed by the Capacity Design Approach which ensures that plastic hinges can only occur at the ends of horizontal boundary elements (per Section 12.3.3.1).

Monotonic and cyclic pushover analyses as well as nonlinear time history analyses were conducted to investigate behavior. Results showed that development of plastic hinges along HBE spans (i.e., in SPSW-ID), with a plastic mechanism of the type shown in Figure 12.27, results in significant accumulation of plastic incremental deformations (see Section 4.5) and significant HBE maximum and residual vertical deformations (Figure 12.28), with incomplete yielding of the

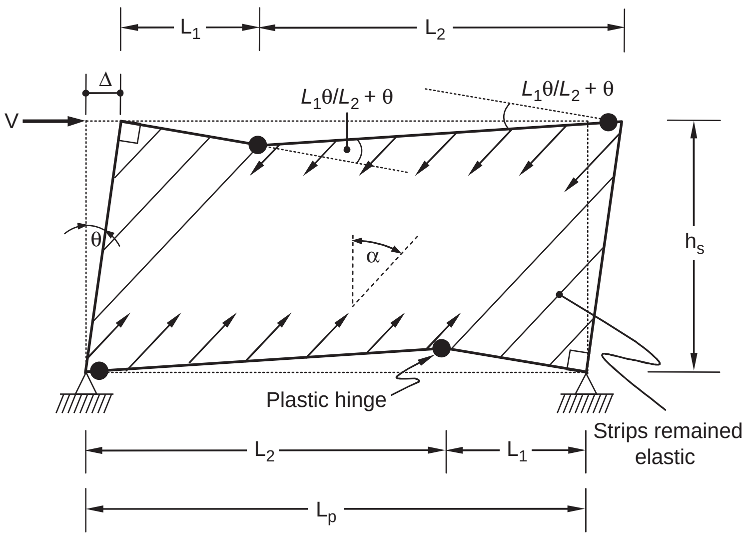

Figure 12.27 Sway and beam combined plastic mechanism for single-story SPSW. (*Purba and Bruneau 2010, Courtesy of MCEER, University at Buffalo.*)

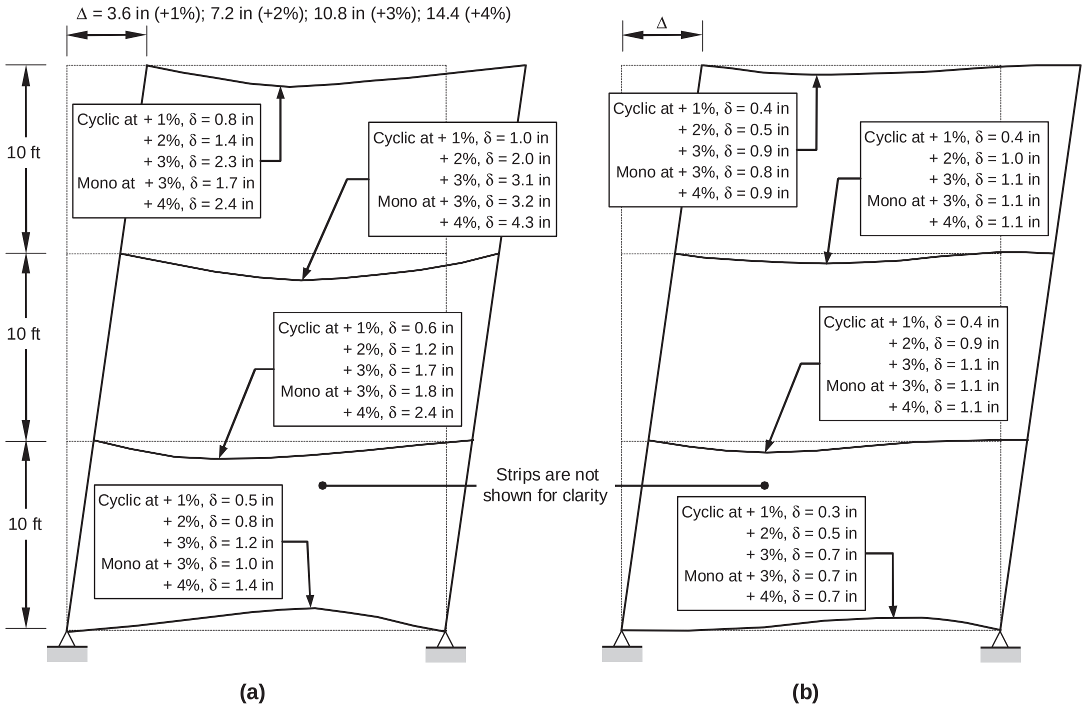

Figure 12.28 Schematic deformed shapes of: (a) SPSW-ID; (b) SPSW-CD. (*Purba and Bruneau 2010, courtesy of MCEER, University at Buffalo.*)

web plates and correspondingly lower global plastic strength compared to the values predicted by Eq. (12.8) (strength equations for the mechanism of Figure 12.27 are in Purba and Bruneau 2010). In addition, in-span hinging in SPSW-ID caused total (elastic and plastic) HBE rotations greater than 0.03 radians after the structure was pushed cyclically up to a maximum lateral drift of 3%. Nonlinear time history analysis also demonstrated that the severity of the ground excitations accentuated the accumulation of plastic incremental deformations on SPSW-ID, while this was not the case for SPSW-CD.

Figure 12.29 shows the normalized moment-rotation hysteresis of some HBEs, for the two walls considered, obtained during the cyclic pushover displacements. The normalized terms plotted are M/M_p and $\theta/\theta_{0.03}$, where M and M_p are the end moment and the corresponding HBE plastic moment capacity, respectively; θ and $\theta_{0.03}$ are the angle of rotation and the required plastic rotation capacity of a special moment-resisting frame, often specified as equal to 0.03 radians (Bertero et al. 1994, FEMA 2000). Diamond markers included on each hysteretic curve correspond to the normalized values reached at lateral drifts of positive and negative 1%, 2%, and 3%. Note that the hysteretic curves of both HBE ends are somewhat similar—except that they are the mirror image of each other—and thus only those of the HBE left end are presented.

Unlike the general hysteresis curve for special moment-resisting frames, which is typically symmetric with respect to positive and negative rotations developed under a symmetric cyclic pushover displacement history, the hysteresis curves of both SPSWs considered here are not symmetric but looping with a bias toward one direction. The tension forces from the infill plates contribute to this behavior by always pulling the HBE in the direction of the tension forces (i.e., pulling the bottom HBE up and the other HBEs down).

Interestingly, except for the bottom HBE, all the moment-resisting ends of the HBEs of SPSW-ID developed a cross-sectional rotation (i.e., cross-sectional curvature multiplied by plastic hinge length) greater than 0.03 radians after the structure was pushed cyclically up to a maximum lateral drift of 3%. In the case shown (HBE2), the total rotations even reached 0.062 radians. Such a significantly high cyclic rotation demand would be difficult to achieve using the type of moment-resisting connections used in SPSW (Section 12.4.2), or even special moment-resisting frame beam-to-column connections (Chapter 8). By comparison for SPSW-CD, all HBE total rotations obtained were less than or equal to 0.03 radians under the same cyclic pushover displacements up to 3% drift.

In an overall perspective, although failures of HBE to VBE connections have been few in SPSW tested at the time of this writing, the results in Figure 12.29 suggest that large drift may translate into large plastic rotations even for SPSW-CD. However, the plastic rotation

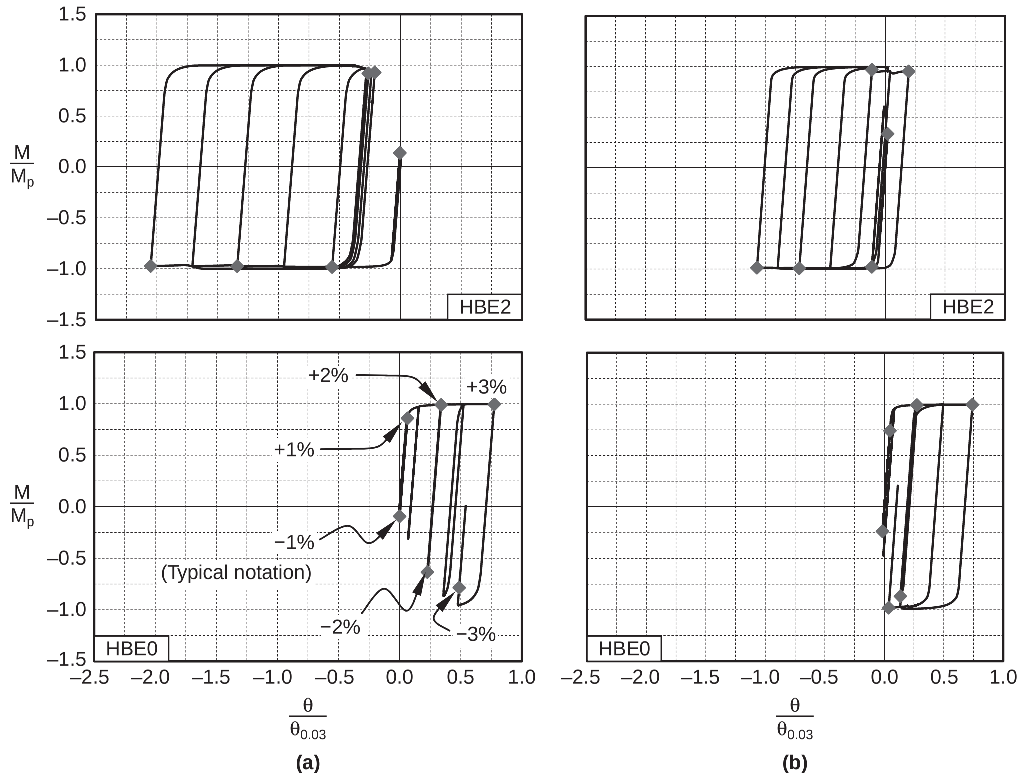

FIGURE 12.29 Normalized moment rotation hysteresis at HBE left end for: (a) SPSW-ID; (b) SPSW-CD. (*Purba and Bruneau 2010, courtesy of MCEER, University at Buffalo.*)

demands observed here were not symmetric, by contrast with moment frame behavior. In other words, a SPSW-CD HBE rotation demand of +0.0075 to –0.03 radians is less critical than a Special Moment-Resisting Frame (SMRF) beam rotation demand of +/–0.03 radians. The SPSW-ID HBE rotation demands of 0.0 to 0.06 radians, however, may approach that of the SMRF. More research is desirable in this regard.

The history of vertical deformation for a representative HBE for SPSW-ID and SPSW-CD is plotted in Figure 12.30. The accumulation of plastic incremental deformations phenomenon is still observed, with maximum and residual vertical deformations more apparent on SPSW-ID than on SPSW-CD. For example, when SPSW-CD reached a lateral drift of 1% for the first time (point A in the figure), the largest HBE vertical displacement at the same drift for SPSW-ID (point A′) was 2.25 larger (note that those two 1% drift conditions did not occur at the same time). As the ground excitation increased and caused a 2% lateral drift on both structures for the first time, the difference between the two became 4 times larger (points B and B′). Similar differences were exhibited for the maximum vertical displacement (0.9 in versus 3.2 in) as well as the residual vertical displacement at the end of the record (0.2 in versus 2.0 in). Ground motions corresponding to the more severe Maximum Considered Earthquake (MCE) level were also considered in that example. Due to the resulting higher lateral drift demands on both SPSWs, the HBE maximum

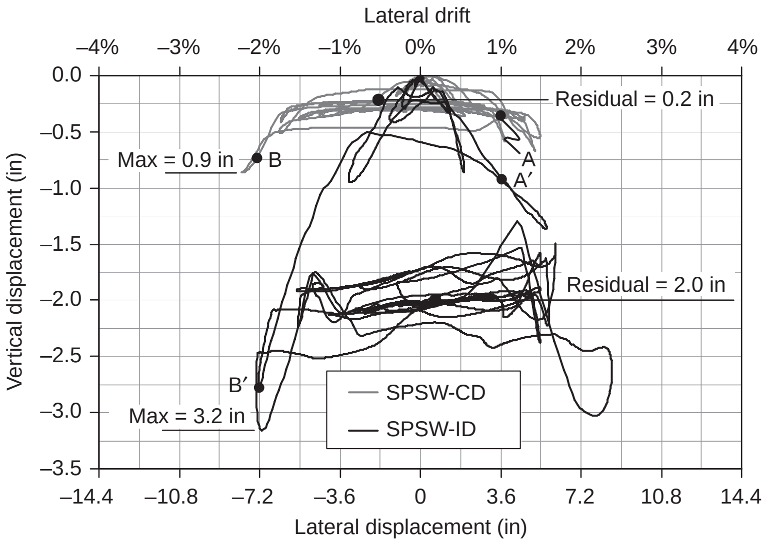

Figure 12.30 Time history of vertical displacement of HBE. (*Purba and Bruneau 2010, courtesy of MCEER, University at Buffalo.*)

vertical deformation increased to 5.1 in. in that case. By comparison for SPSW-CD, only minor changes of HBE vertical deformations occurred. Hence, when formation of in-span plastic hinges on HBEs is possible, more severe ground excitations worsen the accumulation of plastic incremental deformations phenomenon.

12.3.3.4 Complete HBE Equilibrium

In addition to the information presented in the above sections, complete equilibrium of HBEs must account for axial and shear forces acting simultaneously with flexural moments, as well as the additional shear couple considering actual beam depth. Axial forces in HBE are primarily due to the compressive forces applied by the columns that are pulled toward each other by the yielding web plate (described in Section 12.3.4), and due to the uniformly distributed longitudinal load resultant from the web plate forces applied directly to the HBEs.

Axial forces in HBE can also be introduced by restraint against shortening due to Poisson's ratio effect as the HBE web is subjected to the vertical components of infill panel yield forces; however, as reported by Qu and Bruneau (2008, 2010a), although theoretically possible, it would correspond to approximately 5% of the total axial force in an HBE. Such axial restraint may not exist in actual SPSWs. However, note that FE models of isolated HBEs having boundary conditions that restrain axial elongation would have to take this effect into account (Qu and Bruneau 2008, 2010a).

Shear forces on HBEs come from the sum of the direct web plate yield forces and of the frame sway effect. For simplicity in the following, the tension field angle, α (typically close to 45° from the vertical), is assumed to be identical above and below the HBE under consideration (as permitted in design).

To obtain the shear effect in HBE due to web plate yield forces, the tension fields acting on an HBE are decomposed into horizontal and vertical components as shown in Figure 12.31, where the subscripts $i + 1$ and i refer to the web plate above and below the HBE, respectively (depending on how beams are numbered with respect to story, a notation with i and i–1 subscripts would have been equally valid; the concepts, however, remain the same). To account for the shear effect caused by vertical components of the tension fields (i.e., ω_{ybi+1} and ω_{ybi}), the resulting vertical tension field forces [i.e., $(\omega_{ybi} - \omega_{ybi+1})$] are applied at the HBE centerline as shown in the middle part of Figure 12.31. One can obtain the corresponding shear as:

$$V_{vi}(x) = \frac{(\omega_{ybi} - \omega_{ybi+1})(L - 2x)}{2} \tag{12.27}$$

To account for the shear effects generated by the horizontal components of the top and bottom tension fields, a free-body diagram is

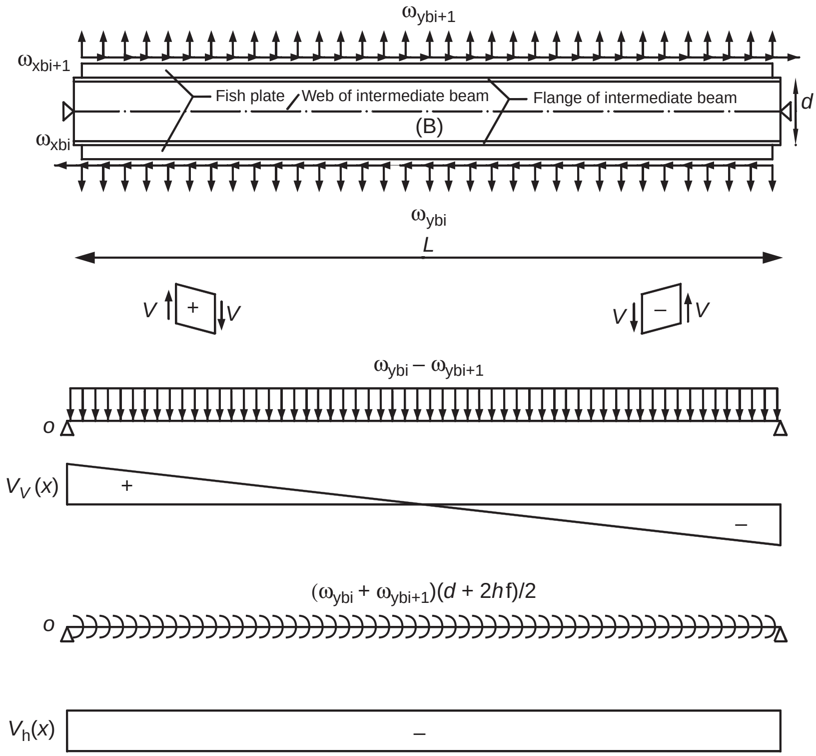

Figure 12.31 Decomposition of infill panel yield forces on the simply supported beam and the corresponding shear diagrams. (*Qu and Bruneau 2008, courtesy of MCEER, University at Buffalo.*)

shown in the bottom part of Figure 12.31, in which the horizontal components of the tension fields acting in opposite directions at the top and bottom edges of the HBE web (i.e., ω_{xbi+1} and ω_{xbi}) are equivalently replaced by uniformly distributed moments of magnitude equal to the horizontal components of the tension fields times the distance from the acting line to the beam centerline. One can obtain the corresponding shear as:

$$V_{hi}(x) = -\frac{(\omega_{xbi} + \omega_{xbi+1})d}{2} \tag{12.28}$$

Combining those effects, the resulting shear forces in an HBE due to web plate yielding is:

$$V_{bi}(x) = \frac{(\omega_{ybi} - \omega_{ybi+1})(L - 2x)}{2} - \frac{(\omega_{xbi} + \omega_{xbi+1})d}{2} \tag{12.29}$$

In many studies, the shear force in HBE due to infill panel yield forces was estimated using simple line models, in which HBE depth was usually neglected. Qu and Bruneau (2008, 2010a) found substantial differences in the moment and shears calculated by Eqs. (12.27) and (12.29), with only the latter agreeing well with finite element analysis results.

Shear forces due to frame sway action alone are obtained from the free-body diagram of an HBE having plastic hinges at both ends—generically $2M_p/(L-2e)$, where e is the distance from plastic hinge to VBE face. However, the flexural strength of HBE plastic hinges must be reduced to account for the presence of significant biaxial and shear stresses in their web (contrary to beams in moment frames, the HBEs of SPSWs can be under considerable vertical axial stresses). The uniform shear in HBE only due to moment frame sway action can be expressed as:

$$V_M = -\frac{(\beta_{RBSL} + \beta_{RBSR})R_y f_y Z_{RBS}}{L - 2e} \tag{12.30}$$

where Z_{RBS} is plastic section modulus of the assumed plastic hinge, f_y is the HBE yield strength, β_{RBSL} and β_{RBSR} are the cross-sectional plastic moment reduction factors of left and right HBE plastic hinges that can be obtained using the procedure described in Section 12.4.2, and R_y is the ratio of expected to nominal yield stress of steel. For capacity design, strain hardening due to plastic hinging should also be considered.

Note that iterations may be necessary in design since the plastic moment reduction factors, β_{RBSL} and β_{RBSR}, depend on the total shear forces acting at the plastic hinges and that these must be assumed at the beginning of the design process.

Combining all the above contributions, the resulting shear force in an HBE is:

$$V_{HBEi}(x) = \frac{(\omega_{ybi} - \omega_{ybi+1})(L-2x)}{2} - \frac{(\omega_{xbi} + \omega_{xbi+1})d}{2} - \frac{(\beta_{RBSL} + \beta_{RBSR})R_y f_y Z_{RBS}}{L-2e} \tag{12.31}$$

Note that typically, RBSs are not used in SPSWs, but the procedure here is presented for the more general case accounting for this possible option; if no RBS is present, $e = 0$, $Z_{RBS} = Z$, and other terms similarly simplify.

12.3.4 Demands on VBEs

Various methods have been described in commentary to AISC 341 and CSA S16 over time to calculate demands on VBEs, such as the "combined linear elastic computer programs and capacity design concept" (LE + CD), the "indirect capacity design approach" (ICD), the "nonlinear static analysis" (pushover analysis), and a capacity design approach (CD) called "combined plastic and linear analysis" in AISC 341-10.

The LE+CD method described in commentary to AISC 341-05 resulted in proper capacity design of boundary elements in some cases, but was shown by Berman and Bruneau (2008) to be inconsistent with respect to equilibrium and give erroneous deformed shape of the system. It has been deleted in AISC 341-10.

The ICD approach, first described in the commentary of CSA-S16-01 (CSA, 2001) and later in AISC 341-05, proposed that loads in the VBEs of a SPSW may be found from gravity loads combined with seismic loads amplified by $B = V_e/V_u$, where V_e is the expected shear strength defined as R_y times the value given by Eq. (12.8), R_y is the ratio of the expected steel yield stress to the design yield stress, and V_u is the factored lateral seismic force at the base of the wall, and where B need not be taken larger than the seismic force reduction factor, R. The design axial forces and local moments in the columns are then amplified by this factor (and so could forces in HBEs, given that the ICD approach is intended as an indirect capacity design). More specifically, the column axial forces determined from the factored design overturning moment at the base of the wall are amplified by B and kept constant for a height of either two stories or the bay width, whichever is greater. The axial forces then are assumed to linearly decrease to B times the axial forces found from the actual factored overturning moment at one story below the top of the wall.

This procedure can produce moment and axial diagrams, and SPSW deformations somewhat similar in shape to those obtained from pushover analysis. However, Berman and Bruneau (2008) demonstrated that this approach can also give incorrect results, as shown in Figures 12.32 and 12.33. Furthermore, using a single amplification factor defined at the first story can be problematic when the ratio of provided-to-needed web thicknesses varies along the height, as is the fact that the V_e factor does not include the strength of the surrounding frame (while V_u, would), which can both lead to underestimates of VBE demands.

With availability of the more accurate CD method described below, the ICD approach has been deleted in CSA S16-09.

Nonlinear static (pushover) analysis of SPSWs using strip models has been shown to give reasonable results for HBE and VBE moments and axial forces. Capacity design may be achieved by accounting for the actual thickness of the web plates and the ratio of mean to nominal web plate yield stress. However, as a design tool, nonlinear static analysis is time consuming because several iterations may be necessary to ensure capacity design of VBEs, making it tedious to use in design. Additional complexity results from having to

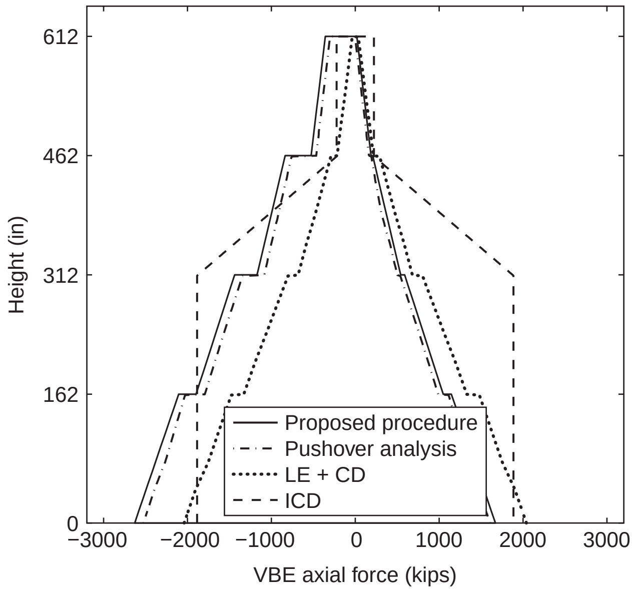

Figure 12.32 Comparison of VBE axial forces from various methods ("proposed procedure" = CD method). (*Berman and Bruneau 2008, reprinted with permission of the American Institute of Steel Construction.*)

properly account for flexural-axial plastic hinges in the HBEs. Despite these issues, nonlinear static analysis of SPSW strip models generally gives accurate results for VBE demands, and is often the method used to compare the adequacy of other proposed procedures.

The CD procedure uses a model of the VBE on elastic supports to determine the axial forces in the HBEs, together with a plastic mechanism to estimate the lateral seismic loads that cause full web-plate yielding and plastic hinging of HBEs at their ends. A simple VBE free-body diagram is then used to determine the design VBE axial forces and moments. In design, iterations may be necessary to revise some initial assumptions. This procedure has been shown to give accurate VBE results compared to pushover analysis (Berman and Bruneau 2008), as shown in Figures 12.32 and 12.33.

The uniform plastic mechanism shown in Figure 12.19 is used in the CD procedure to determine capacity design loads for the SPSW VBEs. The required capacity of VBEs is found from VBE free-body diagrams such as those shown in Figure 12.34 for a generic four-story SPSW. Those free-body diagrams include distributed loads representing the web plate yielding at story i, ω_{xci}, and ω_{yci}, moments from plastic hinging of HBEs, M_{prli} and M_{prri}, axial forces from HBEs, P_{bli} and P_{bri}, applied lateral seismic loads, found from consideration of the plastic mechanism, F_i, and base reactions for those lateral

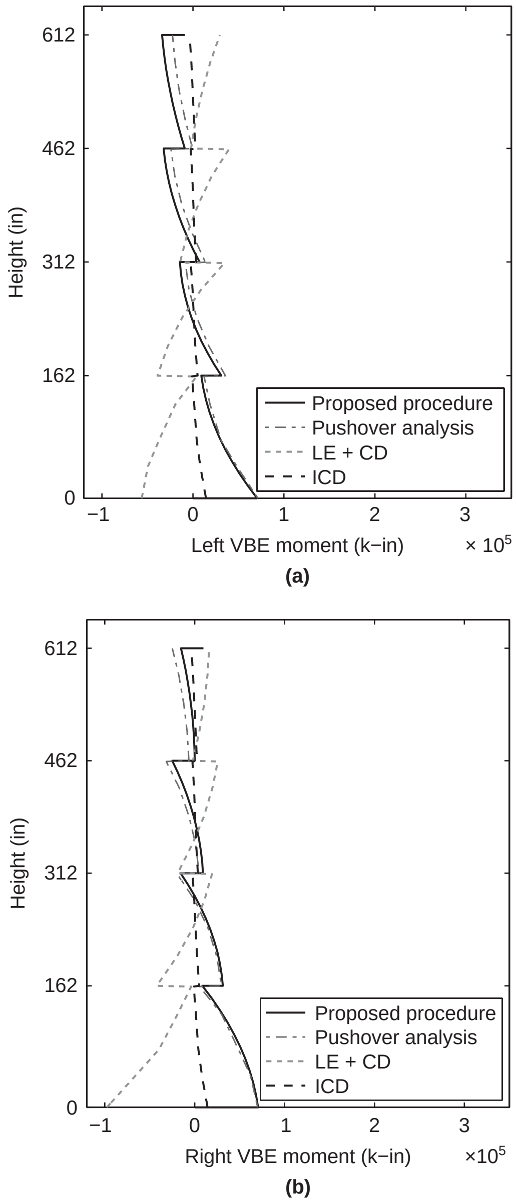

Figure 12.33 Comparison of VBE moments from various methods ("proposed procedure" = CD method). (*Berman and Bruneau 2008, reprinted with permission of the American Institute of Steel Construction.*)

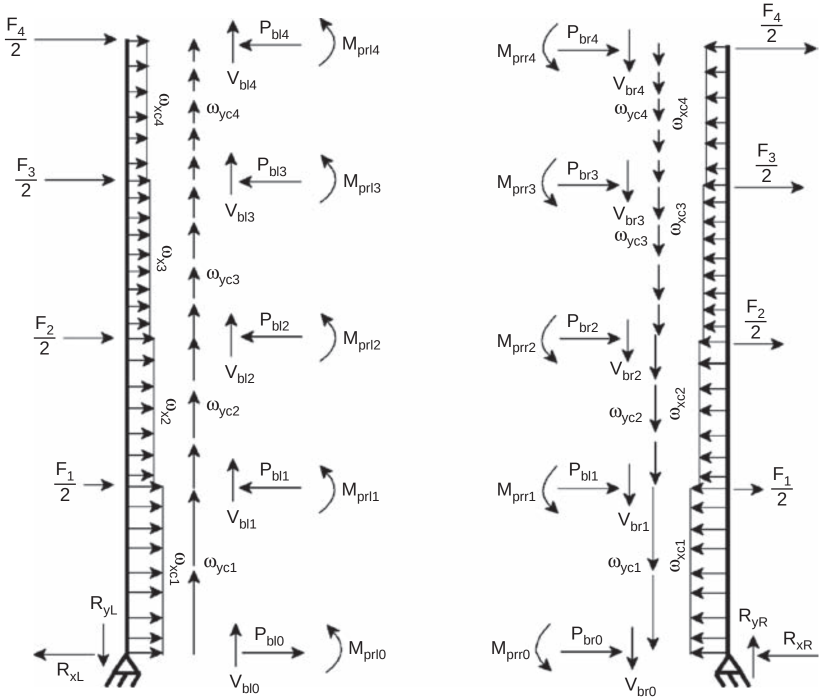

FIGURE 12.34 VBE free-body diagrams. (*Berman and Bruneau 2008, reprinted with permission of the American Institute of Steel Construction.*)

seismic loads, R_{yl}, R_{xl}, R_{yr}, and R_{xr}. The following describes how the components of the VBE free-body diagrams are determined. Here, lateral forces are assumed to be acting from left to right on the SPSW of Figure 12.34.

Using results from Section 12.2.1, the distributed loads applied to the VBEs (ω_{yci} and ω_{xci}) and HBEs (ω_{ybi} and ω_{xbi}) from web plate yielding at each story i are:

$$\omega_{yci} = \left(\frac{1}{2}\right) F_{yp} t_{wi} \sin 2\alpha \qquad \omega_{xci} = F_{yp} t_{wi} (\sin \alpha)^2 \tag{12.32}$$

$$\omega_{ybi} = F_{yp} t_{wi} (\cos \alpha)^2 \qquad \omega_{xbi} = \left(\frac{1}{2}\right) F_{yp} t_{wi} \sin 2\alpha \tag{12.33}$$

To estimate the axial load in the HBEs, an elastic model of the VBE is developed as shown in Figure 12.35. The model consists of a continuous structural member (representing the VBE) pin-supported at the base and supported by elastic springs at the HBE locations. The elastic spring stiffness at story i, k_{bi}, is equal to the HBE axial stiffness

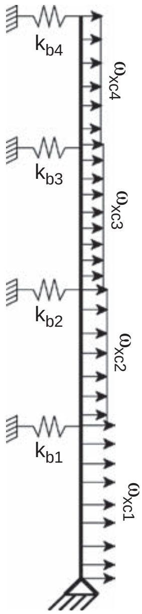

FIGURE 12.35 Elastic VBE model with HBE springs. (*Berman and Bruneau 2008, reprinted with permission of the American Institute of Steel Construction.*)

considering half the bay width (or the HBE clear length for considerably deep VBEs):

$$k_{bi} = \frac{A_{bi}E}{L/2} \tag{12.34}$$

where A_{bi} is the HBE cross-sectional area, L is the bay width, and E is the modulus of elasticity. The horizontal component of the web plates yield forces (ω_{xci}) are applied to this VBE model to get the spring forces, P_{si}, recognizing that iterations required as VBE size are revised. The rotational restraint provided by the HBEs is not modeled, because this has a negligible impact on the resulting spring forces. Note that it is also reasonable, although less accurate, to estimate the HBE axial forces from the horizontal component of web plate yielding on the VBEs, P_{si}, considering VBE lengths tributary to each HBE, i.e.,

$$P_{si} = \omega_{xci}\frac{h_i}{2} + \omega_{xci+1}\frac{h_{i+1}}{2} \tag{12.35}$$

Regardless of the method used, the spring forces are used to determine the HBE axial forces. Note that the resulting compression forces in the HBE are significant. Physically, one can envision the SPSW VBEs as being pulled toward each other by the uniformly

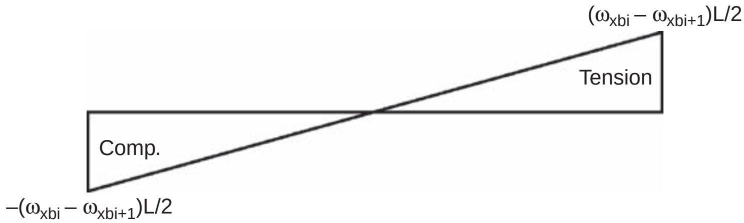

Figure 12.36 Assumed HBE axial force distribution due to horizontal component of plate yield forces on the HBE. (*Berman and Bruneau 2008, reprinted with permission of the American Institute of Steel Construction*.)

distributed forces applied by the yielding webs, and the HBEs act as "shoring" to keep the VBEs apart.

Here, the axial force component in the HBEs resulting from the horizontal component of the plate yield forces on the HBEs, ω_{xbi}, is assumed to be distributed as shown in Figure 12.36, although this may vary depending on the location of the SPSW in the floor plan. In the bottom HBE, this distribution is the reverse of that in the other HBEs. As described in Section 12.3.3.4, these axial forces are combined with the spring forces from the linear VBE model, with axial force at the left and right sides of the HBEs (P_{bli} and P_{bri}, respectively) given by:

$$P_{bli} = -(\omega_{xbi} - \omega_{xbi+1})\frac{L}{2} + P_{si} \tag{12.36}$$

$$P_{bri} = (\omega_{xbi} - \omega_{xbi+1})\frac{L}{2} + P_{si} \tag{12.37}$$

where the spring forces should be negative because they are compressing the HBEs. In the bottom HBE, because VBE bases are fixed, there is no spring force to consider as the horizontal component of force from web plate yielding is added to the VBE base reaction, and the bottom HBE axial forces on the right and left hand sides, P_{bl0} and P_{br0} are:

$$P_{bl0} = \omega_{xb1}\frac{L}{2} \quad \text{and} \quad P_{br0} = -\,\omega_{xb1}\frac{L}{2} \tag{12.38}$$

Knowledge of HBE plastic hinge strengths is also needed per the free body diagram. The substantial axial loads (and other forces, as described in Section 12.4.3) that develop in HBEs can result in significantly reduced plastic moments, M_{prl} and M_{prr}, at the left and right HBE ends, respectively. For VBE design, it is conservative to neglect this reduction. Alternatively, the procedure of Section 12.4.3 can be used.

The final forces necessary to complete the VBE free-body diagram are the applied lateral loads corresponding to the assumed plastic mechanism for the SPSW (Figure 12.19). To use Eq. (12.12), a distribution of lateral loads along the SPSW height must be assumed. The distribution specified for seismic loads by the applicable building code is an acceptable approximation observed to provide reasonable results for SPSW when solving Eq. (12.12). The base shear force, V, for the plastic collapse mechanism loading is found by summing the applied lateral loads. Horizontal reactions at the column bases, R_{xL} and R_{xR}, are determined by equally dividing that base shear and adding the pin-support reaction from the VBE model, R_{bs}, to the reaction under the left VBE and subtracting it off the reaction under the right VBE. Vertical base reactions can be estimated from overturning calculations using the applied lateral loads as:

$$R_{yl} = \frac{\sum_{i=1}^{n_s} F_i H_i}{L} \qquad \text{and} \qquad R_{yr} = -R_{yl} \tag{12.39}$$

The resulting moment, axial, and shear force diagrams obtained from the VBE free-body diagrams allow them to be designed to elastically resist web plate yielding and HBE hinging.

Figures 12.32 and 12.33 compare the axial loads and moments obtained from the LE + CD, ICD, and CD procedures for approximating VBE design loads with those from pushover analysis (Berman and Bruneau 2008). As shown, all results from the CD procedure agree well with those from pushover analysis (whereas the LE + CD and ICD methods do not). Similar results were obtained for a SPSW having constant web plate thickness over height (to simulate a case with variable overstrength along the height).

Note that from a capacity design perspective, the ratio of expected to nominal yield stress, R_y, should be incorporated into the above procedure when determining the distributed loads from plate yielding and HBE plastic moment capacity. Additionally, when deep VBEs are used, the length between VBE flanges, L_{cf}, may be substituted for the column centerline bay width, L, when applying the plate yielding loads to the HBEs. Furthermore, for simplicity Figure 12.34 uses structural members having no width; actual location of HBE hinges can be accounted for in the VBE free-body diagrams and calculating the projected column centerline moment (as done in Chapter 8 for moment frames). These refinements were not included here for simplicity and because the increase in VBE moment is generally small relative to the magnitude of the moments generated by web plate yielding and HBE hinging. Gravity loads, also not considered here, can also be added to the free-body diagram.

This procedure will provide reasonable VBE design forces for SPSWs with web plates expected to yield over their entire height, but possible overly conservative VBE axial forces for tall SPSWs where such simultaneous yielding over the entire wall height is unlikely. In those situations, nonlinear time history analysis can be used to reduce the VBE axial forces, and is currently the only reliable tool to estimate such reductions.

12.4 Design

12.4.1 Introduction

While AISC 341 only recognizes SPSWs designed with moment-resisting beam-to-column connections (i.e., HBE-to-VBE connections) and a force modification factor R of 7, the CAN/CSA-S16 standard recognizes two types of SPSWs, namely, *limited ductility* plate walls (i.e., SPW with no special requirements for beam-to-column connections and assigned a force modification factor $R = 2$) and *ductile* plate walls (i.e., SPW with moment-resisting beam-to-column connections and a force modification factor $R = 5$, which is the R value assigned to the most ductile systems in the S16 standard). Ductile walls are designed according to capacity principles, with plate yielding providing the "fuse." For "*limited ductility*" plate walls, S16 has no special seismic analysis or detailing requirements. However, little research has been conducted on limited ductility SPSWs, and this system is not considered in this chapter.

Beyond this difference, most features of CAN/CSA-S16 have been implemented in the US seismic design provisions, either in the specifications or in the commentary, and are therefore not presented in details in this section, except when notable differences exist. The following focuses primarily on the AISC 341 design procedures.

Note that a few early design requirements for SPSW have since been eliminated. For instance, FEMA 450 and AISC 341-05 restricted the aspect ratio of web plate panels to $0.80 < L/h \leq 2.5$, where L and h are panel width and height, respectively. This conservative range was primarily introduced as a cautionary measure due to the limited experience with SPSW in the USA at the time. It was deleted in AISC 341-10, after SPSWs having L/h of 0.6 (Lee and Tsai, 2008) exhibited satisfactory ductile hysteretic behavior, and recognizing that no theoretical basis exists to specify an upper limit, provided the engineer ensures that all strips yield at the target drift response (Bruneau and Bhagwagar 2002). Furthermore, as L/h increases, substantially larger HBEs are required to resist the forces described in Section 12.3, and SPSW will progressively become uneconomical.

Likewise, arbitrary web plate slenderness limits original specified by FEMA 450 (FEMA 2004) to reflect the fact that SPSW tested at that time had L/t_w ratios ranging from 300 to 800, became obsolete as tests with SPSWs having plate slenderness in excess of 3500 also behaved satisfactory (Bruneau and Berman 2005).

Finally, although not mandated, it is desirable to design SPSWs to have variable web plate thicknesses along their height, to develop uniform yielding over the wall height; use of constant plate sizes over multiple stories (due to limits in available plate stock or other reasons) may concentrate yielding in a single story, and risk the development of a soft-story mechanism.

12.4.2 Web Plate Design

In commentary to CSA S16 and AISC 341, an equivalent truss model (Thorburn et al. 1983) is recommended for preliminary design purposes. The approach consists of first designing a tension-only braced frame, using diagonal steel truss members where steel panels would otherwise be used in the SPSW. The areas of the diagonal steel truss members are designed to resist the specified lateral loads and to meet drift requirements. The truss members are then converted into steel panels. The thickness of the steel panel at story i, t_{wi}, is given by:

$$t_{wi} = \frac{2\, A_i \sin\theta_i \sin 2\theta_i}{L \sin^2 2\alpha_i} \tag{12.40}$$

where A_i and θ_i are the area and the angle of inclination (measured with respect to a vertical axis) of the equivalent truss member at story i, respectively (Figure 12.37).

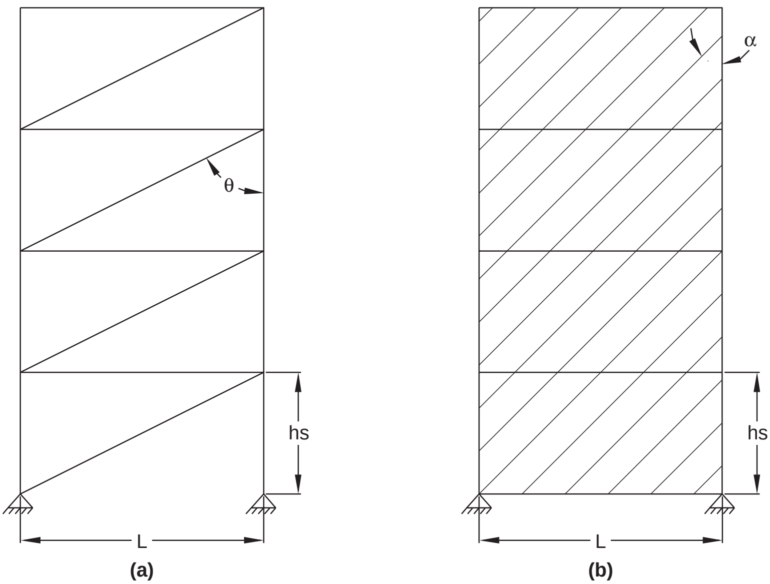

Figure 12.37 Equivalent brace analogy procedure: (a) single brace model; (b) strip model. (*Adapted from Berman and Bruneau 2003b, courtesy of MCEER, University at Buffalo.*)

While this approach is simple and useful at the preliminary design stage, the resulting strength of the steel panels is somewhat unconservative when the panel aspect ratio, L/h, is not equal to unity (Berman and Bruneau 2003a). This is illustrated in Figure 12.38 for a single-story SPSW (having simple beam-to-column connections to focus on plate behavior), where results from pushover analyses are

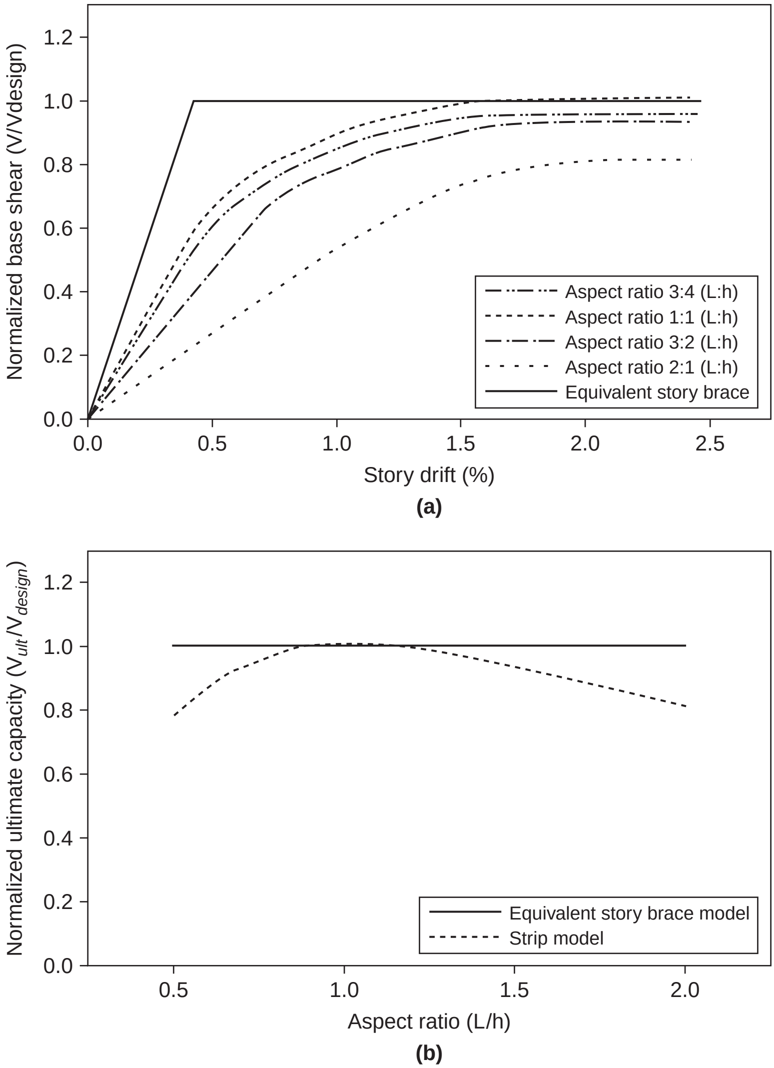

Figure 12.38 Strength of web size by equivalent brace analogy: (a) pushover results for different panel aspect ratios; (b) strengths per equivalent story brace model and corresponding strip model. (*Berman and Bruneau 2003b, courtesy of MCEER, University at Buffalo.*)

compared for SPSWs having various aspect ratios, designed for the same design base shear, having identical beam and column sizes, for plate thickness given per Eq. (12.40). Figure 12.38a shows the resulting base shear (normalized by the design base shear used to find the area of the equivalent story brace) versus story drift, and Figure. 12.38b shows how the difference between the strip model and the equivalent story brace model strengths change with aspect ratio.

The ultimate capacity of the resulting strip model is below the capacity of the equivalent story brace model for all aspect ratios, except for a ratio of 1.0, with the difference increasing as the aspect ratio further deviates from 1.0. At an aspect ratio of 2:1 (or 1:2), the strip model only resists 80% of the base shear for which it should have been designed.

It is therefore important when dividing the plate into strips (per the approach described earlier) to reanalyze/redesign the SPSW's web to fully resist the specified loads. Results in Figure 12.38 can be used to correct the thickness calculated per Eq. (12.2.1) and minimize iterations.

A simpler and more direct approach is to use the results from plastic analysis presented in Section 12.2.2 to obtain the needed web plate thicknesses. This was the approach taken in the *NEHRP Recommended Provisions for Seismic Regulations for New Buildings and Other Structures* (FEMA 2004; a.k.a. FEMA 450) which led to AISC 341-05. However, for codification purposes, Eq. (12.8) is rewritten as:

$$V_n = 0.42\, F_y\, t_w\, L_{cf}\, \sin(2\alpha) \tag{12.41}$$

where L_{cf} is the *clear* distance between VBE flanges, and α is as previously defined. Therefore,

$$t_w = \frac{V_n}{0.42\, F_y L_{cf}\, \sin(2\alpha)} \tag{12.42}$$

The *design* shear strength of a web is given by ϕV_n, where $\phi = 0.90$.

The main difference between Eqs. (12.8) and (12.41) is that the 0.50 factor is replaced by 0.42, which is 0.50 divided by an overstrength factor equal to 1.2. This is done for consistency with other lateral load resisting structural systems that are designed to resist the specified loads without considering their overstrength.

The factor of 1.2 has been estimated considering the various sources of overstrength described in the relationship (presented in Chapter 7 and repeated here for convenience):

$$R = R_\mu \Omega_o = R_\mu \Omega_D \Omega_M \Omega_S \tag{12.43}$$

that is obtained from the generic pushover curve used to define R, where R_μ is the ductility factor, Ω_o is the overstrength factor, $V_y = \Omega_o V_s$ is (for practical purposes) the fully yielded base shear, V_s is the design base shear, Ω_D is the design overstrength factor, Ω_M is the material factor, and Ω_S is the system overstrength factor. Because Eq. (12.8) was obtained from plastic analysis of the strip model, it gives the maximum strength achieved at the peak of the pushover curve, which is V_y. However, all other structural systems are typically designed for V_s. Therefore, to account for this and to use the calculated design base shear, V_s, from the equivalent lateral force procedure with Eq. (12.8) to size the infill plates of a steel plate shear wall, V_s must be amplified by the overstrength factor.

Typically, Ω_D is due to overstrength introduced when drift limits or architectural considerations controls designs, which is unlikely to be an issue for SPSWs. For the steel plate, the material factor Ω_M is also not an issue because drifts reached by SPSW do not bring the tension-only strips into the strain-hardening range (note that overstrength due to the ratio of mean to specified yield stress, R_y, is accounted for in the capacity design approach but not for sizing the plates). In the current context, the system overstrength factor Ω_S accounts for the difference between the ultimate lateral load and the load at first significant yielding. Based on pushover results, this system overstrength appears to vary between 1.1 and 1.5 depending on aspect ratio. An approximate value of 1.2 was deemed appropriate, considering that initial yielding of the plate is a localized phenomenon in the entire plate and that significant yielding must develop to be of noticeable effect, and relative to corresponding values for other structural systems.

Neglecting the contribution of plastic hinges in beams and columns in the above procedure gives a conservative design in the case of rigid beam-to-column connections. That overstrength, which can be substantial, is neglected above. This is further investigated in Section 12.4.4.

Incidentally, to modify Eq. (12.40) to similarly consider the effect of overstrength, a factor, β, should be introduced in the numerator of the expression for t. Setting Eq. (12.40) equal to Eq. (12.22), and solving for β gives $\beta = \Omega_S (\sin 2\alpha/\sin 2\theta)$ (Berman and Bruneau 2003a).

Design of the SPSW webs to resist the story shear due to the lateral loads applied along the height of the building is the first step of the design procedure. From there, a computer model must be developed, such as the strip model using the specified angle of inclination of the strips. HBEs and VBEs are then designed according to capacity design principles using the actual plate thicknesses used (which may differ from the needed sizes in some cases for practical reasons).

12.4.3 HBE Design

12.4.3.1 General Requirements

HBEs are simultaneously subjected to the flexural moments, shear and axial forces obtained per analyses such as those presented in Section 12.3. They are therefore designed using beam-column interaction equations, recognizing that they must be laterally braced such as to allow development of plastic hinges at their ends. When shear stresses and axial stresses perpendicular to the HBE's longitudinal axis are significant in the webs of HBEs, this should also be taken into account in the interaction equations. A procedure to account for these effects in calculating plastic hinge strength is presented in Section 12.4.3.2.

HBEs should also be designed such that their plastic strength is not reached at any point along their length, except at their ends. The consequences of in-span HBE plastic hinges have been presented in Section 12.3.3, where the need to design HBEs to resist $\omega L^2/4$ to achieve this intent has been demonstrated (ω being the resultant transverse component of the web plate forces pulling above and below a given HBE). In doing so, it is critical to consider both the ω resulting from elastic analysis for the specified seismic loads, as well as the ω obtained from capacity design when both plates are fully yielded. Only considering the latter case does not ensure a safe design, for example, if plates of identical sizes are used above and below an HBE, the capacity design case would give $\omega = 0$, but these plates would be subjected to different elastic forces, which an HBE would need to be able to resist (i.e., satisfactory inelastic behavior can't be achieved unless adequate elastic response is first ensured).

Beyond strength, HBE stiffness impacts the progression of yielding in web plates. Using a strip model, Bruneau and Bhagwagar (2002) showed that, at the extreme, for infinitely elastic HBEs and VBEs of low stiffness in SPSWs having large panel aspect ratios, *L/h*, some strips may even end-up in compression (e.g., strips 1 to 8 in Figure 12.39) because of HBE deflections induced by other strips in tension. Such an extreme response is unlikely in actual designs, given that HBE stiffness is related to strength. Rather, progressive yielding across the width of a given web plate is typically observed upon increasing SPSW drift, as shown in Figure 12.40c for the first-story web plate of specimens tested by Driver (1997a) and Lee and Tsai (2008) and having substantially different boundary-frame flexibility. This progression of yielding is also exhibited in the pushover curves, such as those shown in Figures 12.38 and 12.40a. HBE stiffness should be adequate to achieve development of the web plates' full yield strength at the design drift. Note that infinitely rigid pin-ended HBEs and VBEs would be required to achieve simultaneous yielding of all strips across a web plate.

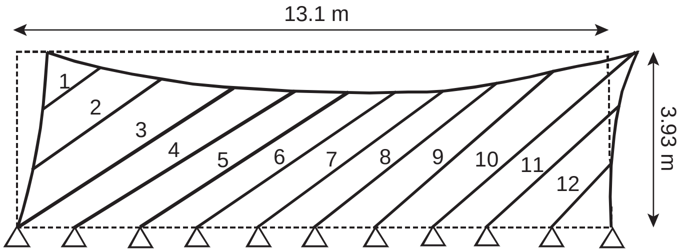

Figure 12.39 Deflection of excessively flexible elastic HBE.

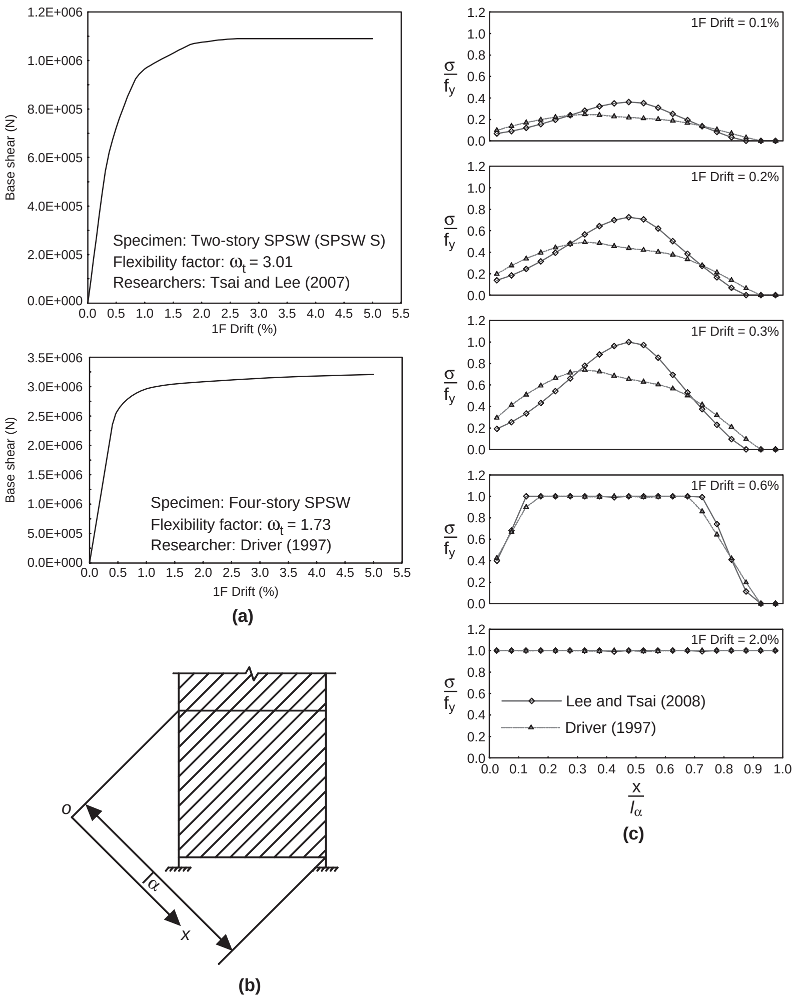

Figure 12.40 Uniformity of tension fields: (a) pushover curves; (b) schematic of tension fields; (c) uniformity of panel stresses. (*Qu and Bruneau 2008, courtesy of MCEER, University at Buffalo.*)

12.4.3.2 HBE Plastic Hinge Strength

In addition to the non-negligible impact of shear and axial stresses on the plastic hinge strength of HBEs, the tension forces applied above and below an HBE apply net vertical stresses to it. The resulting biaxial normal stresses in the HBE web may further reduce its plastic hinge strength. To illustrate by an extreme case, an HBE having a web thinner than the SPSW web plates that connect to it would yield under vertical stresses instead of the web plates, with undesirable consequences. At the other extreme, for HBE webs an order of magnitude thicker than the web plates, this effect becomes negligible.

The following procedure was developed by Qu and Bruneau (2008) to calculate HBE plastic hinge strength, expanding on principles presented in Chapter 3 to account for the effect of vertical stresses in HBE webs. The solution for an HBE subjected to equal top and bottom tension fields is presented, and used in a simplified procedure that account for the linear distribution of vertical stresses in the web of HBEs subjected to unequal top and bottom tension fields (as usually the case).

The stress diagrams for a fully plastified HBE cross-section under equal top and bottom tension fields is shown in Figure 12.41. As usual, uniform shear stress is assumed to act on the HBE web. In addition, a constant vertical tension stress is assumed in the HBE web as a result of the identical top and bottom tension fields, which is:

$$\sigma_y = \frac{\omega_{ybi}}{t_w} \tag{12.44}$$

The normalized form of the von Mises yield criterion in plane stress:

$$\left(\frac{\sigma_x}{f_y}\right)^2 - \left(\frac{\sigma_x}{f_y}\right)\left(\frac{\sigma_y}{f_y}\right) + \left(\frac{\sigma_y}{f_y}\right)^2 + 3\left(\frac{\tau_{xy}}{f_y}\right)^2 = 1 \tag{12.45}$$

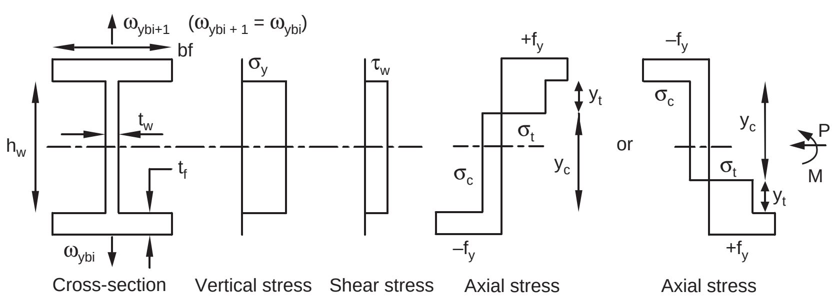

FIGURE 12.41 Stress diagrams of HBE cross-section under flexure, axial compression, shear force, and vertical stresses due to equal top and bottom tension fields. (*Qu and Bruneau 2008, Courtesy of MCEER, University at Buffalo.*)

is rearranged as a quadratic equation in terms of σ_x/f_y and solved to give the axial horizontal stress in terms of the other two terms:

$$\left(\frac{\sigma_x}{f_y}\right) = \frac{1}{2}\left(\frac{\sigma_y}{f_y}\right) \pm \frac{1}{2}\sqrt{4 - 3\left(\frac{\sigma_y}{f_y}\right)^2 - 12\left(\frac{\tau_{xy}}{f_y}\right)^2} \tag{12.46}$$

where σ_x and σ_y are the horizontal and vertical normal stresses, respectively, τ_{xy} (or τ_w) is the shear stress, and f_y is the yield stress. The reduced tension and compression axial yield strength, σ_t and σ_c are given by the "+" and "−" solutions to Eq. (12.46), respectively:

$$\left(\frac{\sigma_t}{f_y}\right) = \frac{1}{2}\left(\frac{\sigma_y}{f_y}\right) + \frac{1}{2}\sqrt{4 - 3\left(\frac{\sigma_y}{f_y}\right)^2 - 12\left(\frac{\tau_w}{f_y}\right)^2} \tag{12.47}$$

$$\left(\frac{\sigma_c}{f_y}\right) = \frac{1}{2}\left(\frac{\sigma_y}{f_y}\right) - \frac{1}{2}\sqrt{4 - 3\left(\frac{\sigma_y}{f_y}\right)^2 - 12\left(\frac{\tau_w}{f_y}\right)^2} \tag{12.48}$$

From geometry in Figure 12.41:

$$y_f = h_w - y_c \tag{12.49}$$

where y_c and y_t are the compression and tension lengths of the web, respectively.

For the common case that the neutral axis remains in the web, axial equilibrium gives:

$$\sigma_c y_c t_w + \sigma_t v_t t_w = P \tag{12.50}$$

Substituting Eq. (12.49) into Eq. (12.50) and solving for y_c gives:

$$y_c = \frac{\left(\frac{\sigma_t}{f_y}\right) + \beta_w}{\left(\frac{\sigma_t}{f_y}\right) - \left(\frac{\sigma_c}{f_y}\right)} \cdot h_w \tag{12.51}$$

where β_w is the ratio of the applied axial compression to the nominal axial strength of the web, which is given by:

$$\beta_w = \frac{-P}{f_y h_w t_w} \tag{12.52}$$

The contributions of the web and flanges to the plastic moment of the whole cross-section, M_{pr-web} and $M_{pr-flange}$, can be respectively determined as:

$$M_{pr-web} = \sigma_t t_w y_t \left(\frac{h_w}{2} - \frac{y_t}{2} \right) - \sigma_c t_w y_c \left(\frac{h_w}{2} - \frac{y_c}{2} \right) \tag{12.53}$$

$$M_{pr-flange} = f_y b_f t_f (d - t_f) \tag{12.54}$$

A cross-section plastic moment reduction factor, β, is defined to quantify the loss in plastic strength attributable to the combined effect of the axial compression, shear force, and vertical stresses acting on the HBE web. The magnitude of β can be determined as:

$$\beta = \frac{M_{pr-web} + M_{pr-flange}}{f_y Z} \tag{12.55}$$

where Z is the plastic section modulus of HBE.

For the extreme case in which the HBE web makes no contribution to the flexural resistance, the minimum value of the reduction factor, β_{min}, is obtained, and is given as:

$$\beta_{min} = \frac{M_{pr-flange}}{f_y Z} \tag{12.56}$$

Note that the above equations are valid for the cases of both positive and negative flexure.

Typical results are presented in Figure 12.42 for β in terms of other parameters defined previously (here, vertical stresses at the top and bottom edges of the intermediate HBE web are equal, i.e., $\sigma_{yi} = \sigma_{yi+1}$). As shown in that figure, the cross-section plastic moment reduction factor, β, reduces as a function of increasing axial force, shear stress, and vertical stresses. For example, for the load combination, $\beta_w = 0.40$ and $\tau_{xy}/f_y = 0.30$, β has a value of 0.91 when no vertical stress exists in the HBE web (i.e., when $\sigma_{yi}/f_y = \sigma_{yi+1}/f_y = 0$, which corresponds to a member in a conventional steel moment frame); however, β reduces to a smaller value of 0.73 when $\sigma_{yi}/f_y = \sigma_{yi+1}/f_y = 0.58$.

When an HBE is under unequal top and bottom tension field stresses, vertical stresses in the web vary linearly from the top to bottom flange. Equations (12.47) and (12.48) give different horizontal stress distributions in HBE webs under positive and negative flexure (Figure 12.43). Equations to calculate the plastic moment of HBE for those stress distributions were developed by Qu and Bruneau (2008), but the resulting closed-form solutions are substantially more complex.

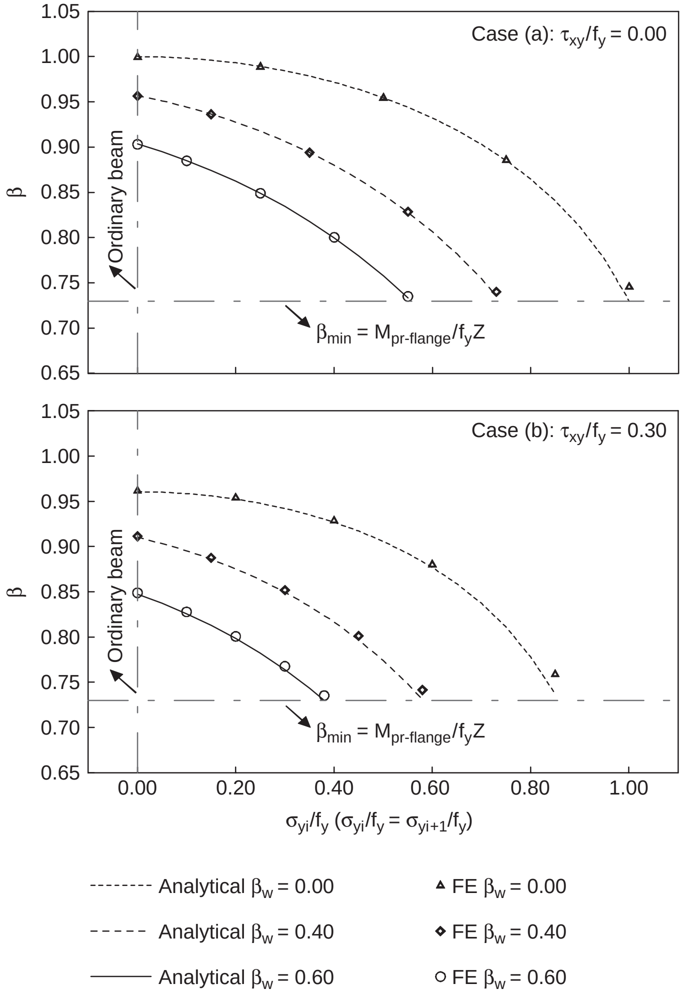

FIGURE 12.42 Plastic moment reduction factor of intermediate HBE under axial compression, shear force, and constant vertical stresses: analytical prediction versus FE results. (*Qu and Bruneau 2008, Courtesy of MCEER, University at Buffalo.*)

Note that using the average vertical stress web as an approximation would fail to capture the fact that under linear-varying vertical stresses, the positive and negative plastic moments obtained under positive and negative flexure case are different.

As a compromise between simplicity and accuracy, Qu and Bruneau proposed to use the values of the vertical stresses at the three-fourth and one-fourth points of the linearly varying stress diagram (Figure 12.44) as the magnitudes of the equivalent constant

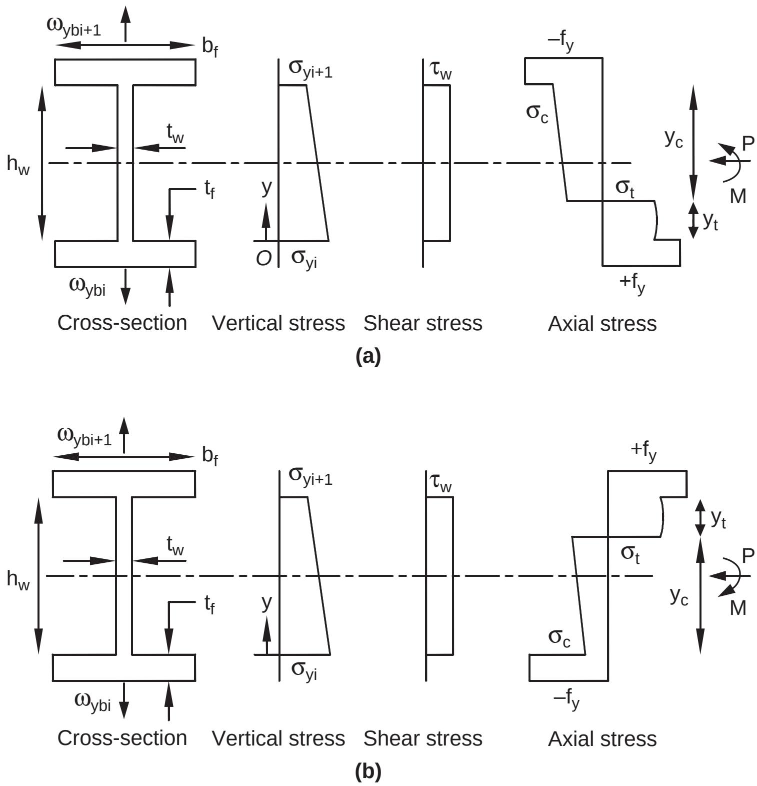

Figure 12.43 Stress diagrams of HBE cross-section under axial compression, shear force, and vertical stresses due to unequal top and bottom tension fields: (a) positive flexure; (b) negative flexure. (*Qu and Bruneau 2008, courtesy of MCEER, University at Buffalo.*)

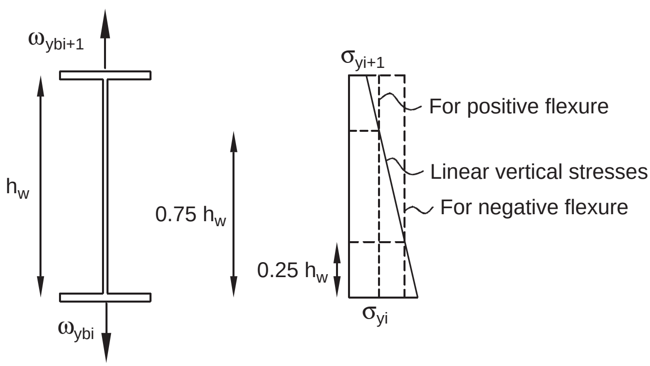

Figure 12.44 Simplification of vertical stress distribution. (*Qu and Bruneau 2008, courtesy of MCEER, University at Buffalo.*)

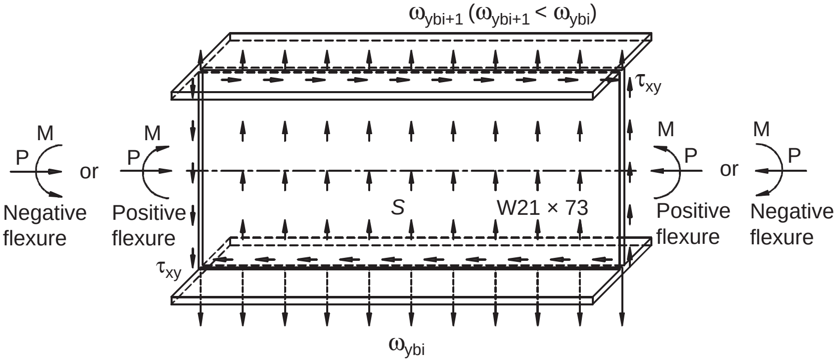

Figure 12.45 FE model of HBE under flexure, axial compression, shear force, and vertical stresses due to unequal top and bottom tension fields. (*Qu and Bruneau 2008, courtesy of MCEER, University at Buffalo.*)

vertical stresses in calculating the plastic moment for the positive and negative flexure cases, respectively. Mathematically, the magnitudes of these equivalent constant vertical stress distributions can be expressed as:

$$\sigma_{y-un} = \frac{1}{2}(\sigma_{yi} + \sigma_{yi+1}) \pm \frac{1}{4}(\sigma_{yi} - \sigma_{yi+1}) \tag{12.57}$$

where "−" and "+" are used for positive and negative flexure, respectively (defined in Figure 12.45). Then, the procedures presented above to determine the plastic moment of HBE with webs under constant vertical stress can be used. The adequacy of this approach was verified comparing results of this simplified procedure with those obtained using the more rigorous analytical procedures that were themselves in excellent agreement with finite element results (Figure 12.46). The simplified procedure is found to provide good results for both the positive and negative plastic moment-reduction factors.

Note from Figure 12.46 that when vertical tension stresses are less than 20% of f_y, their effect based on the von Mises criterion is to reduce strength by less than 4% from the case where this stress is neglected. Assuming such a discrepancy to be tolerable, or establishing another similar acceptable percentage for preliminary design, could be used to calculate a minimum required HBE web thickness.

For design purposes, a less accurate but satisfactory approach consists of neglecting the contribution of the web to flexural resistance; in that case, a constant average vertical stress acting on the web can be used when considering the combined biaxial and shear condition acting on the web. This approach is used in the example at the end of this chapter.

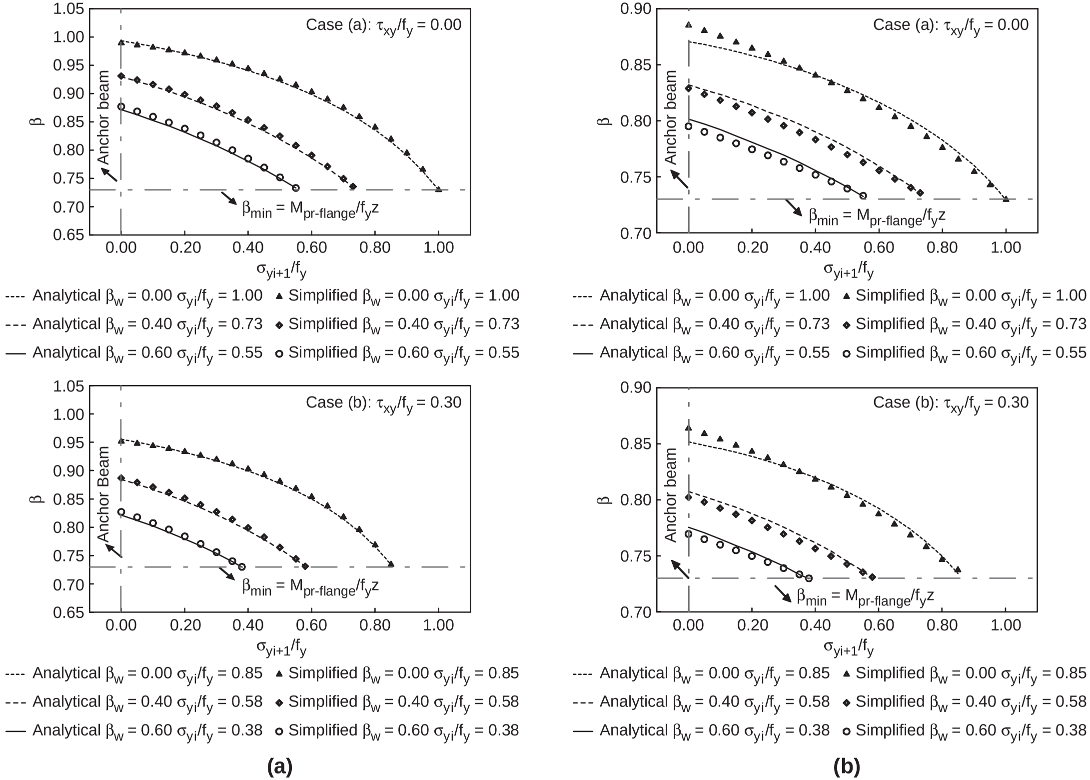

Figure 12.46 Plastic moment reduction factor of HBE axial compression, shear force, and linear varying vertical stresses: analytical prediction versus simplified approach: (a) positive flexure; (b) negative flexure. (*Qu and Bruneau 2008, courtesy of MCEER, University at Buffalo.*)

Consideration of combined biaxial and shear conditions in HBE have also explained why, when RBS were used in HBEs, plastic hinges were located closer to the VBE face rather than at the center of the RBS (Qu and Bruneau 2008, 2010a), as observed by finite element analyses and experimental results (Figure 12.47). In design, to account for the actual location of plastic hinge in RBS, the distance from the center of the RBS to the actual plastic hinge location, Δx, can be taken as:

$$\Delta x = \sqrt{2 \cdot \Delta y \cdot R - \Delta y^2} \tag{12.58}$$

$$\Delta y = \frac{(1-\eta)Z}{4t_f(d-t_f)} \tag{12.59}$$

$$R = \frac{4c^2 + b^2}{8c} \tag{12.60}$$

$$\eta = \frac{Z_{RBS}}{Z} \tag{12.61}$$

where t_f is the HBE flange thickness, d is the HBE depth, and b and c define RBS geometry (Figure 12.47). The plastic section modulus at that location can be taken as the average of the plastic section moduli of the unreduced part of the HBE, Z, and that at the RBS center Z_{RBS} (Qu and Bruneau 2008, 2011).

12.4.4 VBE Design

Per capacity design principles, VBEs must be designed to remain elastic to resist the forces calculated per Section 12.3. However, although not explicitly stated by design provisions, it is understood that for the desired SPSW plastic mechanism to develop, plastic hinging will eventually develop at the base of the columns, as it does in all sway mechanisms, and as would be demonstrated by pushover analysis.

The first S16 provisions for SPSWs only required VBEs to be designed as beam-column using conventional P-M interaction equations. However, this approach was challenged by the results of tests on quarter-scale SPSW specimens by Lubell et al. (2000), in which the VBEs designed using the strength-based approach exhibited significant "pull-in" deformation or undesirable premature out-of-plane buckling. In a subsequent discussion of the Lubell et al. SPSW specimens, Montgomery and Medhekar (2001) ascribed this poor performance to insufficient VBE stiffness, on the rationale that if VBEs deform excessively, they may be unable to anchor the infill panel

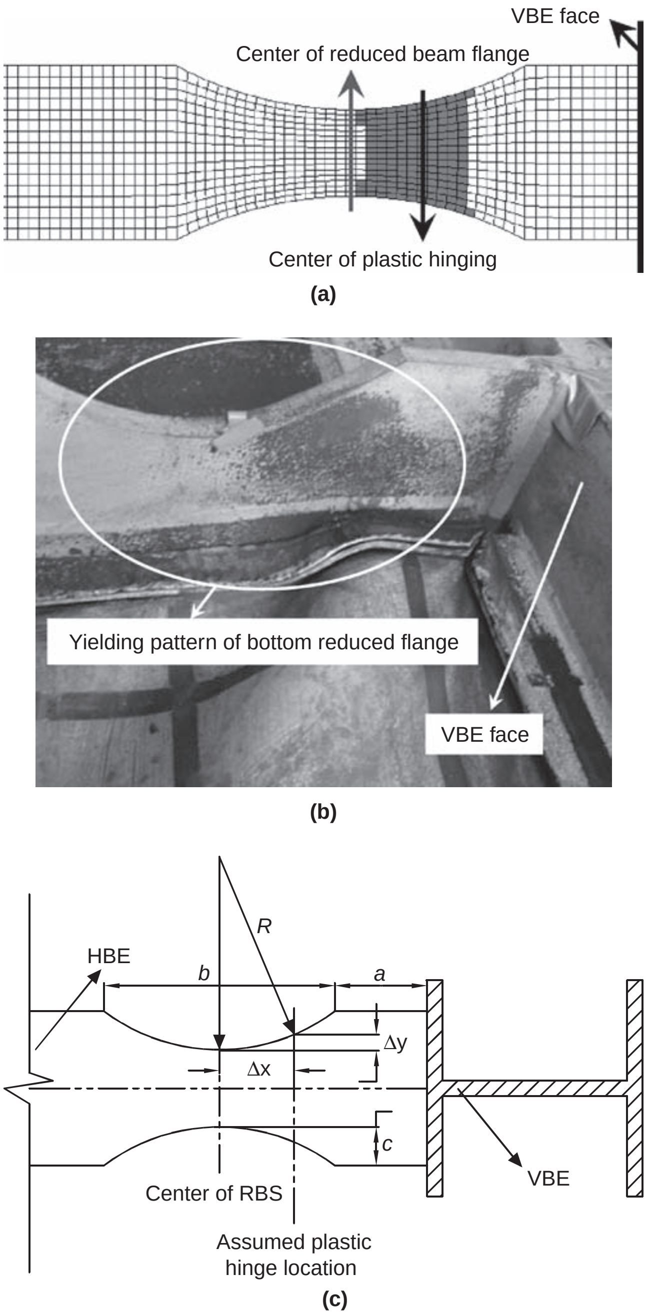

Figure 12.47 Plastic hinging in HBE RBS: (a) finite element analysis; (b) experimental observation; (c) model for design. (*Qu and Bruneau 2008, courtesy of MCEER, University at Buffalo.*)

yield forces. A nonuniform diagonal tension field may then develop and affect the VBEs inconsistently to the design assumptions.

Consequently, to ensure adequate stiffness of VBEs, CSA S16-01 introduced the flexibility factor, ω_t, proposed in the previous analytical work of plate girder theory (Kuhn et al. 1952 and Wagner 1931—summarized in Qu and Bruneau 2008, 2010b), as an index of VBE flexibility, defined as:

$$\omega_t = 0.7 h_{si} \sqrt[4]{\frac{t_{wi}}{2 I_c L}} \tag{12.62}$$

where t_{wi} is the web plate thickness, L and h_{si} are the width and height of the SPSW panel, and I_c is the inertia of a VBE adjacent to the panel (this ω_t should not be confused with other ω's in this chapter denoting distributed web plate forces). Noting that the Lubell et al. specimens had flexibility factors of 3.35, and that all other known tested SPSWs that behaved in a ductile manner had flexibility factors of 2.5 or less, CSA S16-01 empirically specified an upper bound of 2.5 on ω_t. Also intended to achieve tension fields sufficiently uniform to develop ductile behavior, limiting that flexibility factor to a value of 2.5 was intended to limit the maximum web plate stress to no more than 20% of the average stress across the entire tension field. With that upper bound of 2.5 on Eq. (12.62) and solving for I_c leads to the following requirement, first implemented in the CSA S16-01, and subsequently adopted in later FEMA 450 and AISC 341:

$$I_c \geq \frac{0.00307 t_{wi} h_{si}^4}{L} \tag{12.63}$$

However, Qu and Bruneau (2008, 2010b) showed that this existing limit is uncorrelated to satisfactory in-plane and out-of-plane VBE performance, and that the significant inward inelastic deformations of VBEs observed in past tests were not directly caused by excessive VBE flexibilities but rather by shear yielding at the ends of VBEs. Significantly, the data presented by Qu and Bruneau included a test by Lee and Tsai (2008) having $\omega_t = 3.0$, with adequate VBE shear strength and exhibiting satisfactory behavior.

As a result, both AISC 341 and CSA-S16-09 call to the designer's attention that shear yielding may be a governing limit state in VBEs. Accounting for shear, axial, and flexure interaction is recommended for VBE design to ensure their intended elastic response.

In future editions of the seismic provisions, the flexibility limit may either disappear or be kept for other reasons than the ones originally intended.

12.4.5 Distribution of Lateral Force Between Frame and Infill

Conventional design of SPSWs assumes that 100% of the story shear is resisted by the web plate, with the additional strength provided by the boundary frame moment-resisting action conservatively neglected, which has a positive impact on seismic performance of SPSWs. However, because the overstrength provided by this boundary frame can be substantial, questions arise as to whether or not the specified lateral load could be shared between the web plates and boundary frame. Qu and Bruneau (2009) investigated this considering that the percentage of the total lateral design force assigned to the infill panel is κ:

$$\kappa V_{design} = \frac{1}{2} R_{yp} f_{yp} L t_w \sin(2\alpha) \tag{12.64}$$

where V_{design} is the lateral design force applied to the SPSW; the web plate is designed by solving for t_w, and the boundary frame is designed to satisfy the capacity design principles presented earlier in this chapter. Here, the ratio of V_p to V_{design}, which is denoted as Ω_κ, is used to describe the overstrength of the SPSWs designed using different values of κ. As shown in Figure 12.48, a higher percentage of the

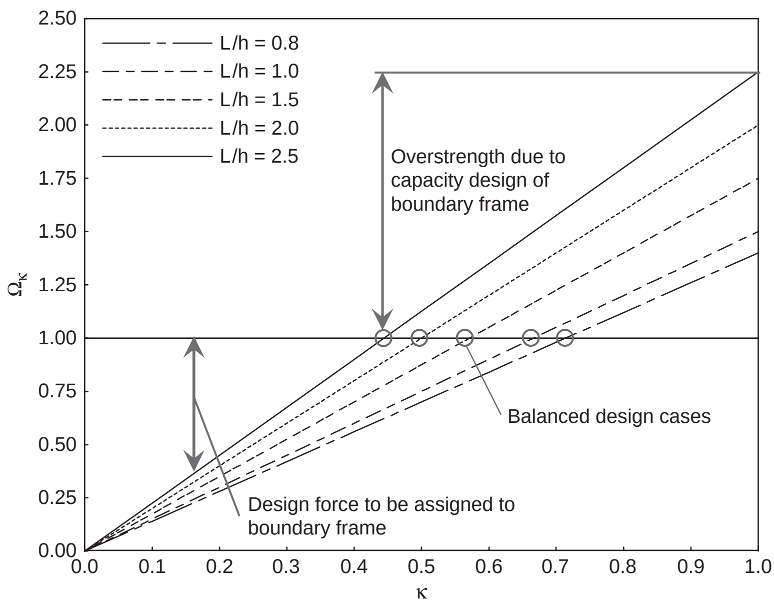

FIGURE 12.48 Relationship between Ω_κ and κ (assuming α = 45°). (*Qu and Bruneau 2008, courtesy of MCEER, University at Buffalo.*)

lateral design forces assigned to the web plate (i.e., greater value of κ) results in a greater overstrength of the wall (i.e., greater value of Ω_κ). Under the design assumption implicit to AISC 341 and CSA S16 (i.e., when $\kappa = 1.0$), SPSW overstrength varies from 1.4 to 2.25 over the range $0.8 \leq L/h \leq 2.5$ shown in Figure 12.48. Note that the example of single-story at the basis of that figure assumes VBEs pinned to the ground; greater overstrength would be obtained with VBEs fixed to the ground.

When κ is reduced to the level showed by the circles in Figure 12.48, the strength needed by the boundary frame of the SPSW to resist its share of the lateral force is exactly equal to that which will be required if that frame is designed to resist the web plate yield forces per capacity design principles. Therefore, at that particular point, defined as $\kappa_{balanced}$, the boundary frame does not provide any overstrength for the system ($\Omega_\kappa = 1.0$). Note that designs for values of κ below $\kappa_{balanced}$ have little appeal as the boundary frame has to be strengthened to fill the gap between the available strength of the wall and the expected lateral design demand (such SPSW would require greater tonnage of steel than at the balanced point and, at low κ values, would provide nothing more than an unethical way to circumvent SMRF beam-to-column design requirements).

Qu and Bruneau (2009) have provided equations to determine $\kappa_{balanced}$, and have conducted nonlinear analysis of SPSWs having various κ values. Although their limited study found that SPSWs designed using the balanced design procedure had maximum drift demands slightly greater than for SPSW designed with $\kappa = 1.0$, it also cautioned that different assumptions on the relative and respective strengths of the webs and boundary frames may lead to systems that exhibit different inelastic responses, which may consequently call for different R values to consider in their respective design, and that further research is needed to establish such a relationship. Note that systems with pinched hysteretic behaviors have been typically penalized by lower R values; this is significant here, as lessening the overstrength of the boundary frame may accentuate pinching of SPSW hysteretic curve due to the greater contribution of the web plate (which can only yield once in tension) to the total load resistance.

Awaiting future research results, it is recommended for conservatism to continue designing web plates for 100% of the story shears calculated using the current system performance factors.

12.4.6 Connection Details

For fabrication and detailing efficiency, web plates have been typically welded to their boundary frames, with connection strength to resist the expected yield strength ($\sigma = R_y F_y$) of the web plate. As for tension-only braces in CBFs, strain hardening of the web plate is not typically developed. A few different details have been used for this

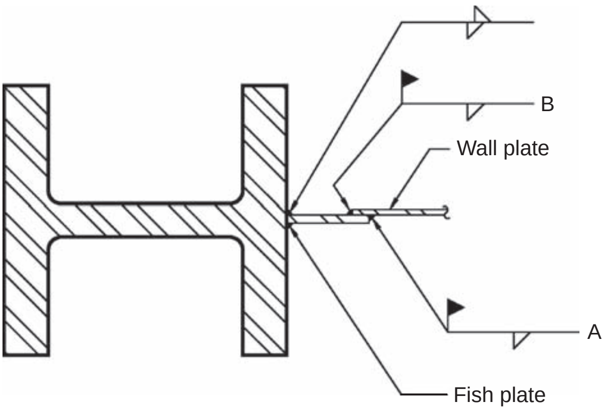

Figure 12.49 Example fish plate detail for web plate connection to HBEs and VBEs.

purpose, although the fish plate detail shown in Figure 12.49 is common due to its ease of construction (the fish plate welded in the shop facilitates web-installation in the field). Weld “B” in that figure is recommended to prevent buckling distortions from detrimentally affecting weld “A.” If thin cold-formed steel is used for the web, only weld “B” may be possible to prevent “burning-through” the web during welding.

Four details proposed by Schumacher et al. (1999) and subjected to cyclic inelastic loading performed equally well (Figure 12.50). Detail A, with web plate directly welded to the HBEs and VBEs, requires tight tolerances and is more difficult to achieve; detail B,

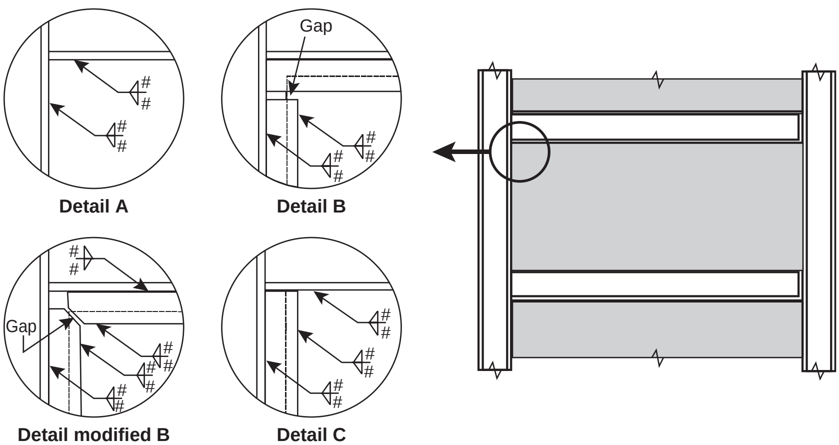

Figure 12.50 Examples of infill plate connection details.

with fish plates welded to the HBEs and VBEs, is the most common and easier to construct, allowing the web plate to be lapped and welded over the fish plates (modified B has a different corner detail); detail C has some web plate edges welded directly to the boundary members, others to a fish plate. Variations of detail B have also been used (e.g., Driver et al. 1997a and Tromposch and Kulak 1987 added a plate bridging the gap in the corners). All specimens tested by Schumacher et al. exhibited satisfactory cyclic inelastic response and energy dissipation. Small tears ultimately developed in specimens B and C, without significant impact on behavior or loss in lateral strength. Likewise, minor tears and cracks have been reported in many prior tests, generally having no significant impact on SPSW behavior (e.g., Berman and Bruneau 2003b, Vian and Bruneau 2005), but major plate connection fractures at drifts in excess of 3% have been reported (Qu et al. 2008).

As shown in Section 12.1, bolted web-plate details have also been used in the past. Tensile strength along the net section must exceed yield strength of the gross section to ensure ductile behavior of the bolted web. This may be difficult to achieve using a single line of bolts without locally increasing plate thickness with reinforcement, or even when using multiple lines of bolts for some plate materials. The same is true for bolted splices.

Two such bolted splices though the web were used in a SPSW concept for the application shown in Figure 12.7 (Hooper 2005), where the VBEs were concrete-filled tube columns. Two half-scale specimens of a three-story subset of that wall, tested by Astaneh and Zhao (2001, 2002) demonstrated satisfactory inelastic behavior up to 3.3% and 2.2% drifts, respectively. Figure 12.51 shows the deformed bolted web splice and the resulting hysteresis loops at the first story of one specimen. Challenges to ensure alignment of the bolted connections for field assembly, and construction time issues, have made welded web connections more common than bolted ones.

Finally, with a few exceptions, HBE-to-VBE connections in past experiments of SPSWs have not been SMRF of the type developed post-Northridge (Chapter 8). Rotation demands in those connections are also believed to be limited as the large stiffness of SPSWs typically would limit their drift during severe earthquakes. Therefore, the less restrictive details specified for Ordinary Moment Frames are permitted by AISC 341 (equivalently, CSA S16-09 permits connections corresponding to limited ductility moment frames).

12.4.7 Design of Openings

In some instances, openings are necessary through large SPSWs, either for access or for the passage of utilities. Single large openings can be accommodated in a given panel if fully framed by HBEs and VBEs designed per the same capacity design principles presented earlier. As such, the panel is divided in subpanels, each behaving as

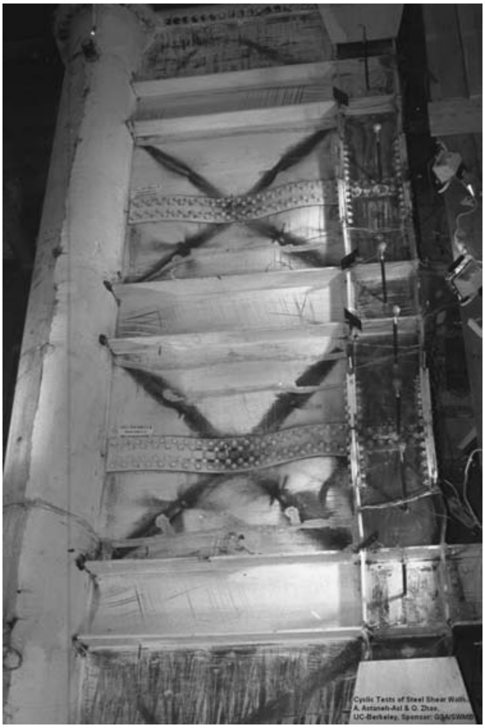

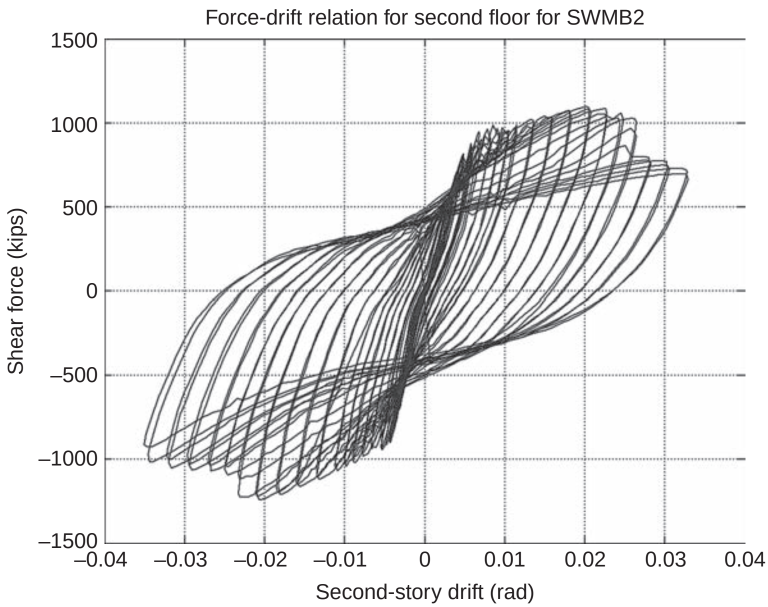

Figure 12.51 Plastic deformation of SPW and hysteretic response. (*Courtesy of Qiuhong Zhao, Department of Civil Engineering, University of Tennessee, Knoxville.*)

would be expected of individual panels, with the difference that, in some instances, a VBE could have to resist the tensions fields from web plates on two of its sides. The design of such openings is the subject of an entire chapter in Sabelli and Bruneau (2007). As a second possible solution, mostly applicable to accommodate the passage of utilities, special perforated SPSWs and walls with cut-out corners can be engineered in accordance with the principles presented in Section 12.5.

Other than those two options, the performance of SPSWs having arbitrary holes is unknown; consequently, all web plates in SPSWs (together with plastic hinge zones at the ends of HBEs) are designated as protected zones where any discontinuities, alterations, and attachments are prohibited (except that openings detailed per one the two options described above are permitted).

12.5 Perforated Steel Plate Shear Walls

12.5.1 Special Perforated Steel Plate Shear Walls

For low-rise buildings, the SPSW web thicknesses required to resist specified lateral loads are often less than the minimum panel thickness available from steel producers for hot rolled plate grades typically available in North America. In such cases, use of the minimum available thickness may result in large panel force overstrengths and, as a consequence of the capacity design principles presented earlier, substantially larger HBE and VBEs (and foundations) than would otherwise be necessary if the exact required web thickness was used. Furthermore, the use of identical plate thicknesses along the building height (having different overstrengths compared with seismic demands along that height) increases the risk of developing a soft-story mechanism.

One approach to alleviate this problem is to use light-gauge cold-formed steel plates (Berman and Bruneau 2003a, 2005), but the properties of such material can be quite variable, and axial-testing of coupons from the actual plates to be used in a given SPSW is recommended to verify if their ductility, expected yield strength, and strength at maximum expected drifts (as some light-gage steel does not exhibit a well defined yield plateau) are compatible with design assumptions. Another viable approach is to use low-yield steel (Chapter 2), provided that the strain-hardened strength of that steel at the maximum drift is taken into account (Vian and Bruneau 2005; Vian et al. 2009a, 2009b).

The approach described here, introduced in AISC 341-10 and CSA S16-09, consist of using SPSWs having a special panel perforations layout covering the entire web plate in a specified regular pattern selected to reduce the strength and stiffness of a solid panel wall to

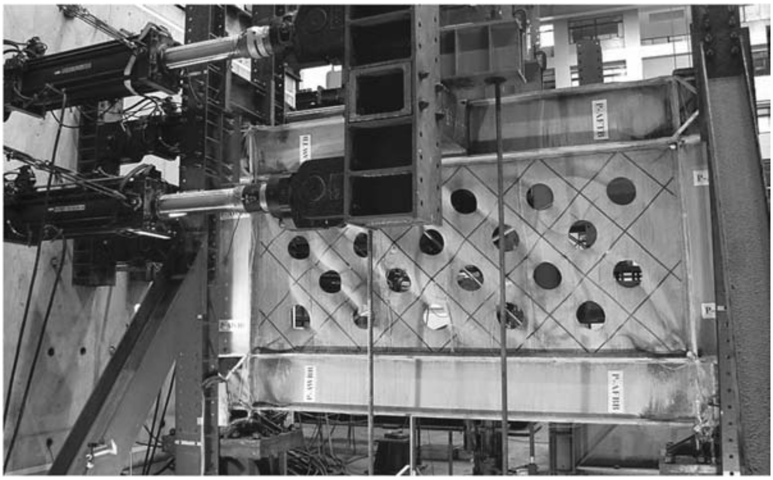

Figure 12.52 Special perforated steel plate shear walls. (*Vian and Bruneau 2005, courtesy of MCEER, University at Buffalo.*)

the levels required by design. A typical layout forcing tension strips to develop at 45° is shown in Figure 12.52. Note that the multiple holes are also convenient in allowing some utility lines and cables to pass through the web.

Five variables define the panel perforation layout geometry: the perforation diameter, D; the diagonal strip spacing, S_{diag} (measured perpendicularly to the strip); the number of horizontal rows of perforations, N_r; the panel height, H_{panel}; and the diagonal strip angle, θ. The holes regularly distributed across the web plate must be located in a grid that allows the development of continuous diagonal strips, and filling the entire plate for yielding to spread along the length of those strips (Figure 12.53). For that reason, the first holes must be located at a distance of at least D but no greater than $(D + 0.7S_{diag})$ from the web connections to the HBEs and VBEs.

Special perforated SPSW (Vian and Bruneau 2005, Vian et al. 2009a) exhibited stable force-displacement behavior and hysteretic behavior during testing, with little pinching of hysteresis loops until significant accumulation of damage (in the RBS) at large drifts (Figure 12.53).

Vian and Bruneau (2005) provided the following equation for estimating the reduction in panel stiffness due to the presence of perforations:

$$\frac{K_{perf}}{K_{panel}} = \frac{1 - \dfrac{\pi}{4} \cdot \left(\dfrac{D}{S_{diag}}\right)}{1 - \dfrac{\pi}{4} \cdot \left(\dfrac{D}{S_{diag}}\right) \cdot \left(1 - \dfrac{N_r \cdot D \cdot \sin\theta}{H_{panel}}\right)} \tag{12.65}$$

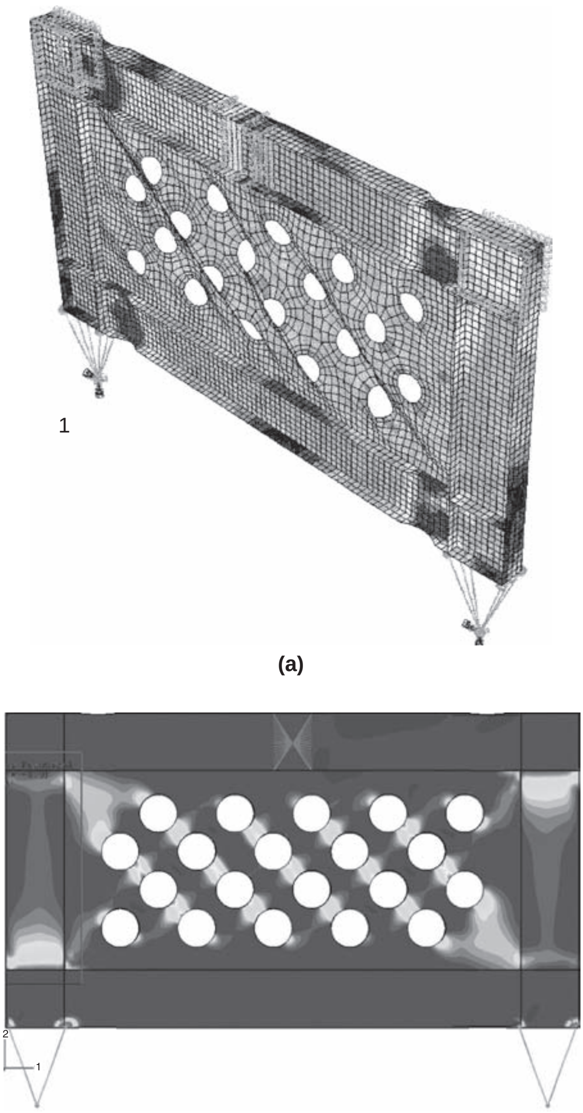

(a)

(b)

Figure 12.53 Special perforated steel plate shear walls at 3% drift. (*Vian and Bruneau 2005, courtesy of MCEER, University at Buffalo.*)

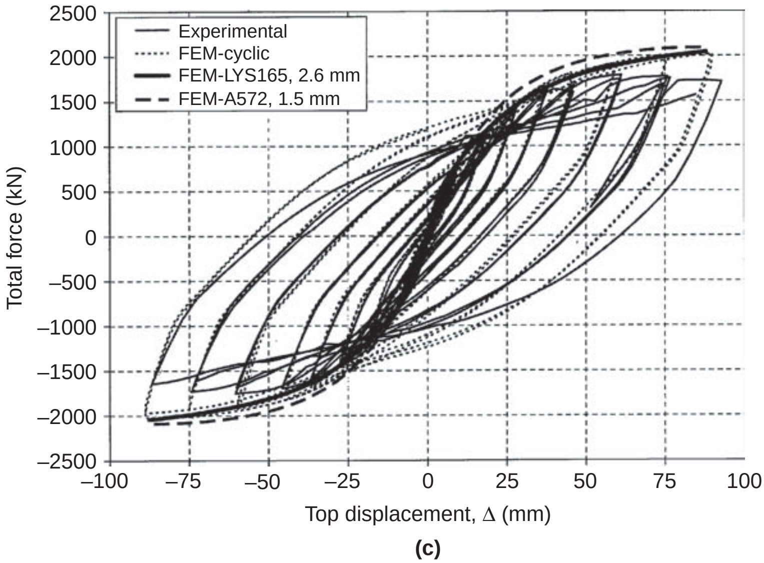

FIGURE 12.53 (*Continued*)

valid when $D/S_{diag} \leq 0.5$, and shown to give results within approximately 5% of experimental results.

Finite element models of the tested specimens provided good comparison with experimental results, and demonstrated that similar adequate ductile performance would be obtained using common North American steel grades.

Purba and Bruneau (2007, 2009) also conducted an investigation of panel strain and stress behavior for a range of hole-geometries (D/S_{diag} from 0.025 to 0.75) that led to proposed design recommendations for limiting perforation sizes to facilitate ductile response. This also included studies of individual perforated strips as a subelement of perforated SPSW. For each analysis, total uniform strip elongation was recorded when a maximum principal local strain, ε_{max}, at any point in the strip reached a value of 1%, 5%, 10%, 15%, and 20%. Results were compared with selected finite element analyses of full SPSW to verify the accuracy of the individual strip model results and to investigate the influence of the boundary element stiffness/rigidity on the stress and strain distribution in the panel.

Figure 12.54 presents total uniform strip elongation ($\varepsilon_{un} = \Delta/L$) versus perforation ratio (D/S_{diag}) for maximum principal strain (ε_{max}) values of 1, 5, 10, 15, and 20% from analyses performed using the strip and panel models. For a given D/S_{diag} and ε_{max} the total uniform strip elongation from the strip and panel models agree well. Note that no interaction was found to exist between adjacent strips that could

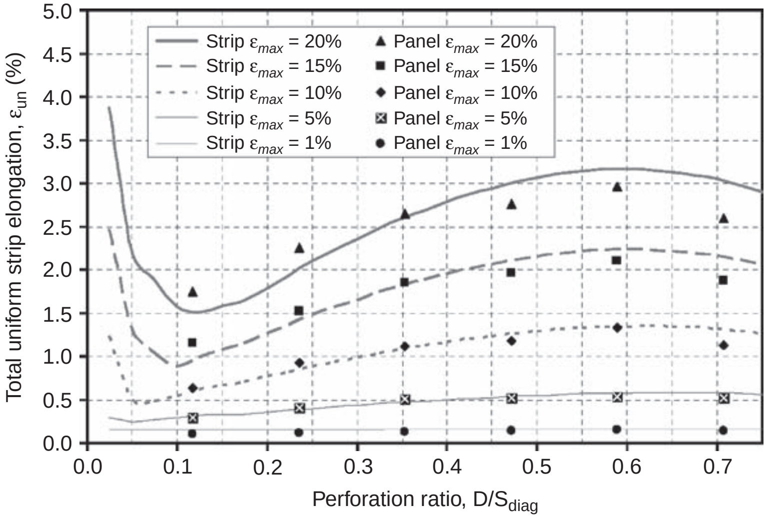

FIGURE 12.54 Uniform distributed strip axial strain ε_{un} versus perforation ratio D/S_{diag}. (*Purba and Bruneau 2007, courtesy of MCEER, University at Buffalo.*)

affect the stress distribution within an individual strip, i.e., each strip in a SPSW behaves as an independent strip. As demonstrated by the results from finite elements (Figure 12.55), this is because the boundary between each strip is free to move inward unrestrained by the adjacent strips, because the effect of Poisson's ratio in this case is simply to reduce the amplitude of the buckled wave between adjacent holes.

Figure 12.56 presents web plate strength ratios ($V_{yp.perf}/V_{yp}$) versus perforation ratios (D/S_{diag}) for frame drifts (γ) of 1%, 2%, 3%, 4%, and 5%, where $V_{yp,\text{perf}}$ and V_{yp} are the strength of the perforated and solid plates, respectively. While a polynomial regression would provide a slightly better correlation, linear regression analysis of the results led

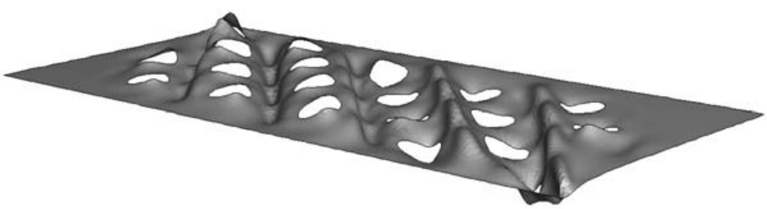

FIGURE 12.55 Magnified deformation of perforated plate. (*Purba and Bruneau 2007, courtesy of MCEER, University at Buffalo.*)

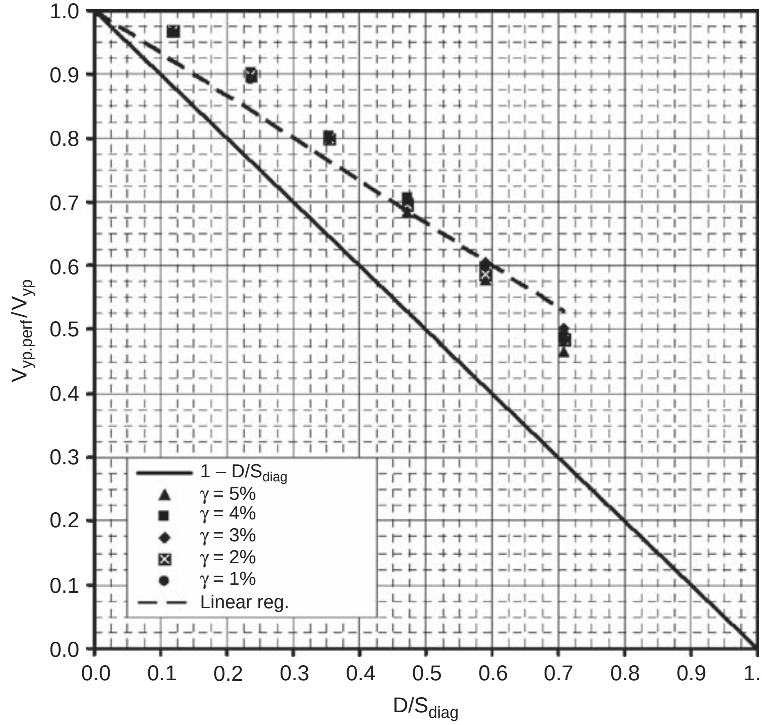

FIGURE 12.56 Web plate strength ratios ($V_{yp.perf}/V_{yp}$) versus perforation ratio (D/S_{diag}). (*Purba and Bruneau 2007, courtesy of MCEER, University at Buffalo.*)

to the following design equation for the strength of the perforated web plate, adopted by AISC 341-10 and CSA S16-09:

$$V_{yp.perf} = \left[1 - 0.7\frac{D}{S_{diag}}\right] \cdot V_{yp} \qquad (12.66)$$

for perforation ratio limited to $D/S_{diag} \leq 0.6$, this being the range addressed by past research.

Figure 12.57 illustrates how frame drift correlates to the corresponding local maximum strain in the web plate for the system considered, and vice versa, for various given perforation ratios.

12.5.2 Steel Plate Shear Walls with Reinforced Corners Cutouts

Reinforced quarter-circular cutouts at the top corners of a SPSW's web provide another option for utility passage, allowing large openings

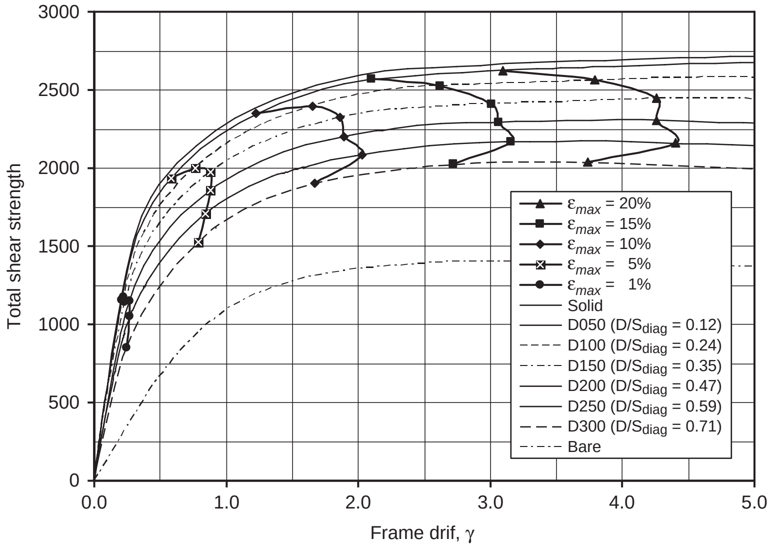

Figure 12.57 Total shear strength V_y versus frame drift, γ. (*Purba and Bruneau 2007, courtesy of MCEER, University at Buffalo.*)

where utilities are often located (Vian and Bruneau 2005). In this case, the intent is to provide strength and stiffness similar to the corresponding SPSW having a solid web. SPSWs with cutout corners exhibited satisfactory cyclic inelastic performance (Figure 12.58). Such cutouts are allowed by AISC 341 and CSA S16 provided the radius of the corner cutouts is less than one third of the infill plate clear height (which corresponds to the maximum opening size tested).

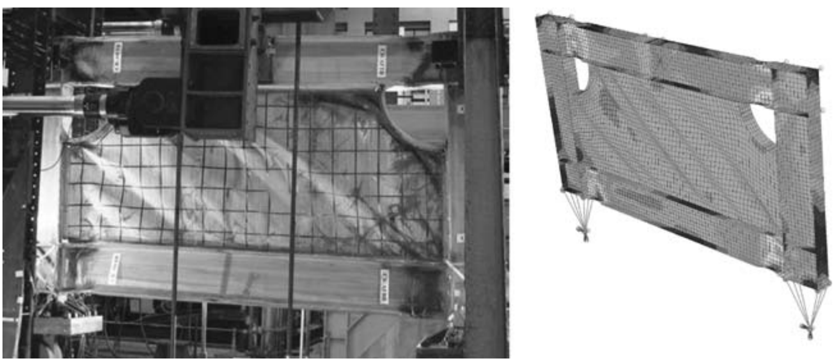

Figure 12.58 Specimen condition at 4% drift and quasi-static cyclic response of the LYS SPSW with reinforced cutout corners tested by Vian and Bruneau. (*2005, Courtesy of MCEER, University at Buffalo.*)

The plates reinforcing the corner cutouts are designed as a semi-circular arches connected to the webs, considering that:

(1) For either actual hinges or plastic moment hinges at the arch ends, the arch would resist the infill panel tension load until development of an arch plastic mechanism having a midspan plastic hinge.

(2) For arches with hinged ends, axial load and bending moment at the arch midpoint under thrusting action (Leontovich 1959) due to change of angle at the corner of the SPSW can be expressed as a function of SPSW drift by Eqs. (12.67) and (12.68) respectively, as:

$$P_{frame-pin} = \frac{15 \cdot E \cdot I}{4 \cdot \left(2-\sqrt{2}\right)^2 \cdot R^2} \cdot \gamma = \frac{15 \cdot E \cdot I}{16 \cdot e^2} \cdot \left(\frac{\Delta}{h}\right) \tag{12.67}$$

$$M_{frame.CL} = P_{frame-pin}\, e = \frac{15 \cdot E \cdot I}{8 \cdot \left(2-\sqrt{2}\right) \cdot R} \cdot \gamma = \frac{15 \cdot E \cdot I}{16 \cdot e} \cdot \left(\frac{\Delta}{h}\right) \tag{12.68}$$

$$e = \left(\frac{2-\sqrt{2}}{2}\right) R \tag{12.69}$$

where e is the arch rise perpendicular to a line through its support (Figure 12.59), and γ is the panel drift angle, equal to the drift, Δ, divided by the panel height.

(3) An expression for the maximum arch plate section thickness at midspan can be obtained by substituting Eqs. (12.67) and (12.68) into the axial-moment (P-M) interaction equation for the reinforcing plate. Note that the arch plate width is not a parameter in the interaction equation, because these forces are consequences of induced deformations.

(4) The required arch plate width is obtained by considering the strength required to resist the axial component of force in the arch due to the web plate tension at the closing corner (top right side of Figure 12.59a). For a uniformly loaded arch, with uniformly distributed load per unit length equal to the expected yield strength of the web (i.e., $\omega = t R_y F_y$), the reactions along the diagonal axis are (e.g., Young 1989; Leontovich 1959):

$$P_{panel} = \frac{R_y F_y t_w R^2}{4e} \tag{12.70}$$

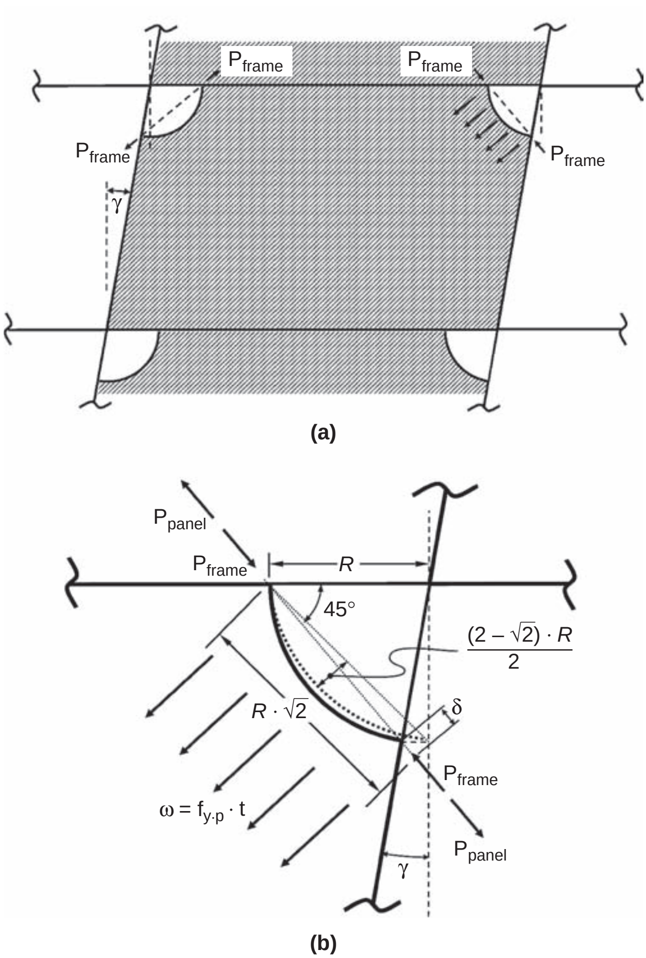

FIGURE 12.59 Forces for design of reinforced cutout corner in SPSW: (a) arch end reactions due to frame deformations, and web plate forces on arches due to tension field action on reinforced cutout corner; (b) deformed configurations and forces acting on right arch. (*Purba and Bruneau 2007, courtesy of MCEER, University at Buffalo.*)

(5) Given that the components of arch forces due to panel forces are opposing those due to frame corner opening, they can be considered as not acting simultaneously for design purposes.

(6) Note that a fish plate can be added to the arch plate to facilitate web attachment to the arch; alternatively, a T-shape bent into a quarter-circle can be used for that purpose. Either approach results in a stiffer arch section than considered by

the above equations. Purba and Bruneau (2007) showed that thickness of the flat arch-plate obtained from the above equations is adequate to withstand the loads alone, and that partial yielding of the web of the stiffer and stronger T-shaped arch is not detrimental to the system performance.

Finally, note that the HBEs and VBEs must be designed with adequate strength to resist the axial forces acting at the end of the arching reinforcement.

12.6 Design Example

The following section illustrates the design of a Special Plate Shear Wall. The design applies the requirements of ASCE 7 (2010) and AISC 341 (2010). The example is not intended to be a complete illustration of the application of all design requirements. Rather, it is intended to illustrate key analysis and proportioning techniques that are intended ensure ductile response of the structure.

12.6.1 Building Description and Loading

The example building is nearly identical to the one used in Chapter 8 (Special Moment Frames); more detailed seismicity and building information is included in that example. The difference in this case is that Steel Plate Shear Walls (SPSWs) are used and only one bay of SPSWs is provided at the perimeter framing lines in each orthogonal direction. The seismic design parameters are shown in Table 12.1.

The typical plan is shown in Figure 12.60 and the typical frame elevation is shown in Figure 12.61 (diagonal lines indicate the web plate).

Based on the seismic-design data a generic seismic response spectrum is constructed in accordance with ASCE 7. Because there is only one SPSW bay on each side of the structure, the design shear at every story must be multiplied by a redundancy factor, ρ, equal to 1.3.

12.6.2 Global Requirements

The structure must be designed to provide both adequate strength and adequate stiffness.

R	7
I	1.0
C_D	6
Ω_o	2

Table 12.1 Seismic Design Data

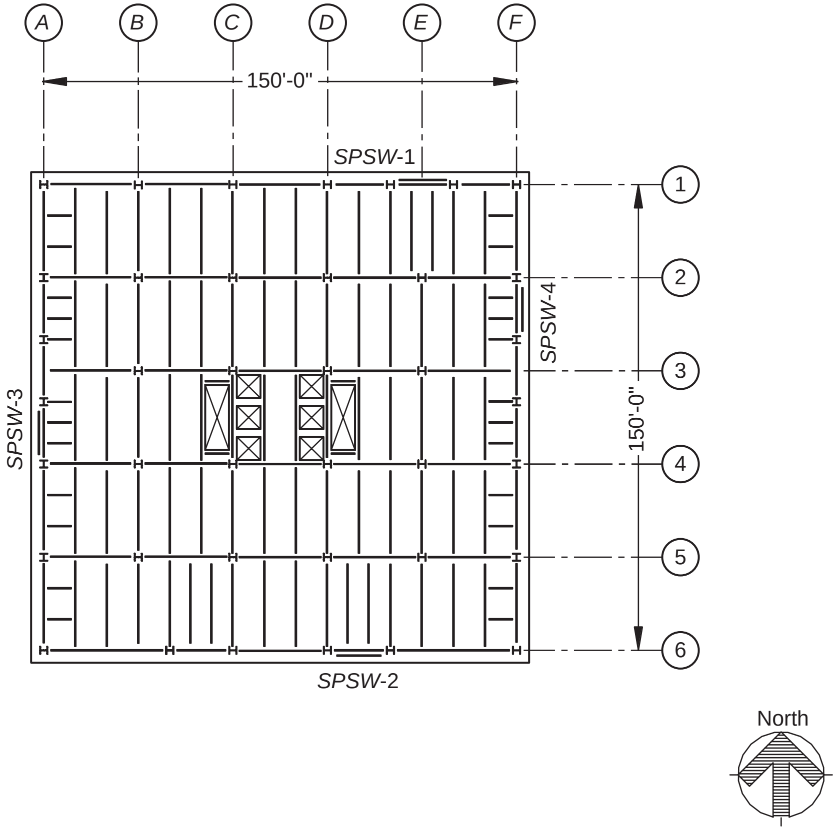

Figure 12.60 Typical floor plan.

Where strength considerations govern, the design process is fairly straightforward: the web plates are designed to provide adequate strength, then the VBEs and HBEs (i.e., columns and beams) are designed to preclude their failure when subject to the forces corresponding to fully yielded and strain-hardened webs in combination with plastic hinge formation in the beams. A reanalysis may be performed to confirm that the required strength has not been increased due to an increase in frame stiffness, and that the structure is not otherwise out of compliance with the design objectives and in need of redesign.

Where drift is the governing concern the process requires more iteration. Any increase in web strength will impose larger forces on HBEs and VBEs. Thus, any stiffening of the frame should be done with the required strength proportioning in mind.

This example assumes that strength concerns will govern (as normally the case in SPSWs) and that an equivalent lateral force

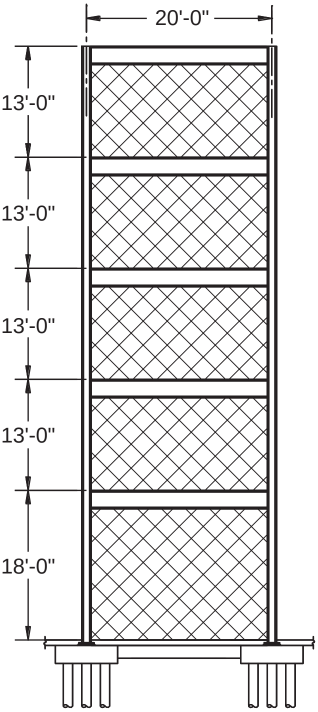

FIGURE 12.61 Typical frame elevation.

procedure is utilized. Alternatively, more elaborate analysis methods (e.g., Modal Response Spectrum Analysis) may be utilized. In either case shear demands on the web plates must be obtained. Demands on the VBEs and HBEs are governed by the plastic mechanism analysis shown in Figure 12.62. Note that in this example, "columns" and "beams" are used interchangeably with "VBEs" and "HBEs," respectively.

12.6.3 Basis of Design

The design of SPSW is based on the expectation of a global yield mechanism in which webs yield in tension, and plastic hinges form at the ends of each beam near the column face. Figure 12.62 shows this mechanism.

The value of the web strength in this mechanism is adjusted for material overstrength; significant strain hardening of the entire web is not anticipated.

Web plate nominal strength is given by Eq. (12.41). The expected web strength is given by Eq. (12.4). Both equations are functions of the angle of tension stress in the web, which is given in Eq. (12.1).

This SPSW in this example uses special perforated webs with a regular array of openings as described in Section 12.5. This permits

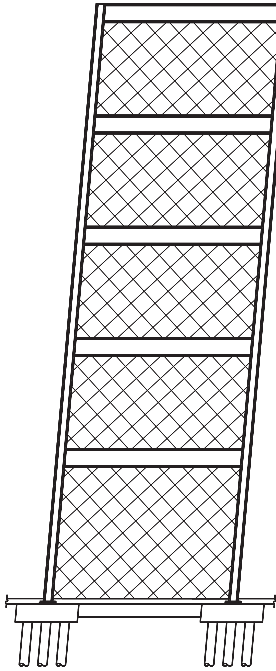

Figure 12.62 Anticipated mechanism.

use of thicker plates while limiting strength to that required. It also imposes a defined angle for the diagonal tension stress field, significantly simplifying some aspects of the design. Modified web shear strength and stiffness are given in Eqs. (12.65) and (12.66).

12.6.4 Web Design

The building can be analyzed using static methods and assuming equal stiffness in the four frames. The resulting shear demands on one frame are 50% of the total building shear. This increases to 52.5% with consideration of the "accidental eccentricity" used to test for sensitivity to torsion (this increase is a function of frame layout and stiffness.)

Web plate sizes are selected using Eq. (12.41). At this stage the entire frame shear is assumed to be in the web plate; this provides additional overstrength to the system.

Web plate designs are obtained for 1/8″, 3/16″, ¼″, and 5/16″ A36 material. It is assumed that the diameter of the opening is between 0.25 and 0.6 times the center-to-center hole spacing along the diagonal. The design strength of a web plate is obtained by combining Eqs. (12.41) and (12.66) and applying the angle of stress of 45°:

$$\phi V_{\mathrm{n}} = \phi[0.42(1 - 0.7D/S_{diag})F_y t_w L_{cf}] \tag{12.71}$$

Perforated Web Design Strength (kip/ft)				
	Plate Thickness (in)			
D/S_{diag}	0.125	0.1875	0.250	0.3125
0.25	16.8	25.3	33.7	42.1
0.30	16.1	24.2	32.3	40.3
0.35	15.4	23.1	30.8	38.5
0.40	14.7	22.0	29.4	36.7
0.45	14.0	21.0	28.0	35.0
0.50	13.3	19.9	26.5	33.2
0.55	12.6	18.8	25.1	31.4
0.60	11.8	17.8	23.7	29.6

TABLE 12.2 Design Strength of Perforated Webs

Table 12.2 gives the strength of web plates as a function of plate thickness and the ratio of hole diameter to spacing (D/S_{diag}).

The clear length between columns is assumed to be 220 in. Combining this length with Table 12.2 permits selection of web plates. These sizes are shown in Table 12.3.

Unperforated web plates of 3/16″ thickness could be considered in lieu of perforated ones at the third floor. However, as perforated web plates offer a number of practical advantages (e.g., a path of

Level	Required Strength (kips)	Web Plate Thickness (in)	D/S_{diag}	Effective Web Plate Thickness (Strength) (in) $\left(1-0.7D/S_{diag}\right)t_w$	Design Strength (kips)
Fifth Floor	219	0.125	0.60	0.073	225
Fourth Floor	400	0.188	0.40	0.135	419
Third Floor	537	0.250	0.35	0.189	586
Second Floor	630	0.250	0.25	0.206	640
First Floor	683	0.313	0.40	0.225	698

TABLE 12.3 Web-Plate Sizes

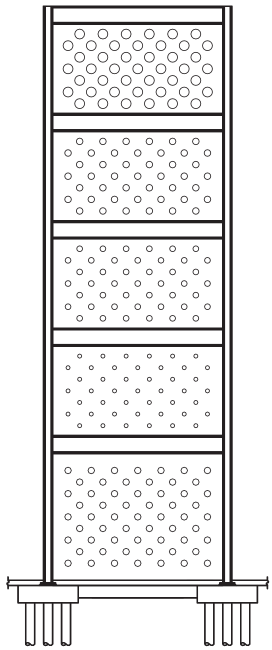

Figure 12.63 Perforated web plates.

passing conduit, thicker material that facilitates connections), perforated web plates will be used throughout. Figure 12.63 shows the perforated wall elevation.

12.6.5 HBE Design

Next, the HBEs are designed for the combined effects of gravity and the formation of the plastic mechanism, which includes both web-plate tension yielding and the formation of plastic hinges at each end. There is no defined minimum flexural strength for these plastic hinges; the beam itself is checked to make sure it does not form hinges within the span. Here, calculations are shown for a typical HBE.

First the required flexural and compression strengths are determined. As discussed in Section 12.4.3.1, the required flexural strength is computed based on the equation:

$$M_u = \frac{\omega L_{cf}^2}{4} \tag{12.72}$$

where ω is the distributed load on the beam and L_{cf} is the beam clear span between column flanges (assumed in this example to be 12 in less than the centerline distance between columns).

The web plates above and below the beam exert vertical forces on the beam as a result of the diagonal tension stress. The seismic portion of the distributed load from each plate is computed as:

$$\omega_{yb} = R_y F_y [t_{we} \cos^2(\alpha)] \tag{12.73}$$

where t_{we} is the effective web plate thickness per Eq. (12.66).

Because the angle of stress is dictated by the array of openings to be 45°, the equation can be simplified by using ½ in lieu of $\cos^2(\alpha)$. For purposes of beam design, it is assumed that both web plates may reach their full yield strength. The net downward load is:

$$\omega_{yb(i)} = \frac{1}{2} R_y F_y [t_{we(i\text{-}1)} - t_{we(i)}] \tag{12.74}$$

For the fifth floor HBE (defined as the one between the fourth and fifth floors), this vertical seismic load is:

$$\omega_{yb(5)} = \frac{1}{2}(1.3)(36)[(0.135) - (0.073)]*12 = 17.4 \text{ kips/ft}$$

As stated earlier in the chapter, this load should not be taken to be less than the load from the frame analysis. This latter load will not typically govern except in cases where the effective plate thickness above and below is identical, and thus the mechanism load would be zero.

This load is combined with the gravity load to result in a distributed load of:

$$\omega_{yb} + \omega_g = (17.4) + (3.5) = 20.9 \text{ kips/ft}$$

The design moment is therefore:

$$M_u = \frac{(20.9)(19)^2}{4} = 1715 \text{ kip-ft}$$

The axial force in the beam is due largely to the inward force of the web plates on the columns. Additionally, there is some nonuniform axial force resulting from the distributed web-plate tension. The inward force exerted by the VBE can be estimated as:

$$\begin{aligned} P_{HBE(VBE)} &= \Sigma \frac{1}{2} h_c R_y F_y t_{we} \sin^2(\alpha) \qquad (12.75) \\ &= \left(\frac{1}{2}\right)(13 * 12)(1.3)(36)[(0.073) + (0.135)]\left(\frac{1}{2}\right) \\ &= 380 \text{ kips} \end{aligned}$$

The distributed axial load is calculated similarly to the distributed vertical load:

$$\omega_{xb} = R_y F_y [t_{we} \sin^2(\alpha)] \tag{12.76}$$

As was the case for the vertical force, the defined angle of stress here (45°) permits the simplification of using ½ in lieu of $\sin^2(\alpha)$. Assuming that both web plates reach their full yield strength, the corresponding load is:

$$\omega_{xb(i)} = \frac{1}{2} R_y F_y [t_{we(i\text{-}1)} - t_{we(i)}] \tag{12.77}$$

$$= 1.45 \text{ kip/in}$$

This force is in equilibrium with collector forces at each end of the bay. The total force is:

$$P_{HBE(web)} = (L_{cf}) \frac{1}{2} R_y F_y (t_{we(i\text{-}1)} - t_{we(i)}) \tag{12.78}$$

$$= (19 * 12)\frac{1}{2}(1.3)(36)[(0.135) - (0.073)]$$

$$= 331 \text{ kips}$$

Because of the symmetrical layout of the building and the central location of the wall, equal collector forces are assumed at each end of the wall. Thus the axial forces at each end of the beam are:

$$P_{HBE} = P_{HBE(VBE)} \pm \frac{1}{2} P_{HBE(web)}$$

$$= 545 \text{ kips, } 215 \text{ kips}$$

These axial forces may be used to compute reduced flexural strength at the plastic hinge locations for purposes of computing a reduced shear demand in the beam. For simplicity, this example neglects that effect.

The shear in the beam can be estimated from the distributed load in conjunction with the shear corresponding to plastic hinge formation. The shear due to the distributed load is determined per Eq. (12.29):

$$V_{u(web)} = \frac{(\omega_y b_{i-1} - \omega_y b_i)L_{cf} \pm (\omega_x b_{i-1} + \omega_x b_i)d}{2} \tag{12.79}$$

where L_{cf} is the beam clear span between flanges.

A beam depth of 30 in is assumed.

$$V_{u(web)} = 165 \text{ kips} \pm 73 \text{ kips} = 234 \text{ kips, } 92 \text{ kips}$$

For the HBE the maximum shear is:

$$V_{u(web)} + V_g = \frac{234 + (3.5)(19)}{2} = 267 \text{ kips}$$

The component due to the plastic hinges is:

$$V_{u(HBE)} = \frac{2^*M_{pr}}{L_h} \tag{12.80}$$

where M_{pr} is the probable plastic hinge moment and L_h is the distance between expected plastic hinge locations.

Values for these can be estimated as:

$$M_{pr} = 1.1\ R_y Z F_y \tag{12.81}$$

$$L_h = L_{cf} - d_b \tag{12.82}$$

As no beam size has been selected, assumptions are required. It is assumed that a 30-in-deep beam is used, and the plastic hinge moment capacity is approximated as:

$$M_{pr} = 1.25\ M_u = 2140 \text{ kip-ft}$$

$$L_h = 19 - 2.5 = 16.5 \text{ ft}$$

$$V_{u(HBE)} = 260 \text{ kips}$$

$$V_u = V_{u(web)} + V_g + V_{u(HBE)} = 527 \text{ kips}$$

This shear occurs at the compression column. At the column in tension the shear is substantially less.

Now that HBE member forces have been obtained, the member can be designed. For simplified design it is convenient to select a flange area based on the required flexural strength and a web area based on the axial force, shear, and vertical tension. For both purposes the stress will be limited to ϕF_y.

For the flange area a distance between flange centroids of $h_o = 29$ in is assumed.

$$b_f t_f = \frac{M_u}{(h_o \phi F_y)} = 15.8 \text{ in}^2$$

A W30 × 173 has a flange area of:

$$b_f t_f = (15.0)(1.07) = 16.1 \text{ in}^2$$

This section meets the seismic compactness limits.

The web may be checked using von Mises criterion as follows:

$$\left(\frac{P_u/A_{web}}{\phi F_y}\right)^2+\left(\frac{\sigma_y}{\phi F_y}\right)^2-\left(\frac{P_u/A_{web}}{\phi F_y}\right)\left(\frac{\sigma_y}{\phi F_y}\right)+3\left(\frac{V_u/A_{web}}{\phi F_y}\right)^2\le 1 \tag{12.83}$$

In this case, as the web contribution to flexural strength is being neglected, the vertical stress is approximated as the average of the vertical forces from the web plates above and below over the HBE web thickness:

$$\sigma_{y_i}=\frac{R_yF_y\left[\dfrac{t_{wei}\sin\alpha_i^2+t_{wei-1}\sin\alpha_{i-1}^{\ 2}}{2}\right]}{t_w} \tag{12.84}$$

$$\sigma_{y(i)}=3.89\text{ ksi}$$

The web area is:

$$A_{web}=(d-2t_f)t_w=28.3\text{ in}^2$$

$$\left(\frac{P_u/A_{web}}{\phi F_y}\right)^2+\left(\frac{\sigma_y}{\phi F_y}\right)^2-\left(\frac{P_u/A_{web}}{\phi F_y}\right)\left(\frac{\sigma_y}{\phi F_y}\right)+3\left(\frac{V_u/A_{web}}{\phi F_y}\right)^2=0.54$$

Note that in this calculation the maximum axial force and shear have been used for simplicity. In the beam, the maximum axial force occurs at the VBE in tension, while the maximum shear occurs at the end next to the VBE in compression.

Thus a more refined calculation would show a lower utilization ratio.

This calculation shows that the beam has sufficient strength. It also suggests that a smaller beam could be used, taking advantage of the fact that some of the web contributes to the flexural strength.

12.6.6 VBE Design

The VBEs are designed assuming the full plastic mechanism (i.e., assuming yielding in all the web plates and HBEs above).

The maximum axial compression forces in the columns due to this loading are determined as follows:

$$E_m=\sum\frac{1}{2}R_yF_y\sin(2\alpha)\,t_{we}h+\sum V_{HBE} \tag{12.85}$$

$$V_{HBE}=V_{u(web)}+V_{u(HBE)} \tag{12.86}$$

$$V_{HBE}=\left(\frac{R_yF_y\{[t_{we}(i-1)-t_{we}(i)]\cos^2(\alpha)\}L_{cf}}{2}+\frac{2*Mpr}{L_h}\right) \tag{12.87}$$

The equations can be combined, and also simplified as the angle of stress is constrained to 45°:

$$E_{m(i)} = \frac{1}{2} R_y F_y \left[\sum t_{we} h + t_{we(i)} \frac{L_{cf}}{2} \right] + \sum \frac{2^* M_{pr}}{L_h} \qquad (12.88)$$

Column maximum axial tension forces can be determined similarly:

$$E_{m(i)} = \frac{1}{2} R_y F_y \left[\sum t_{we} h - t_{we(i)} \frac{L_{cf}}{2} \right] + \sum \frac{2^* M_{pr}}{L_h} \qquad (12.89)$$

The seismic axial force in the column on the compression side at the bottom of the fourth floor is:

$$\begin{aligned} E_m &= \frac{1}{2}(1.3)(36)(0.073 + 0.135)(13 \times 12) \\ &\quad + \frac{1}{2}(1.3)(36)(0.135)\left(\frac{19 \times 12}{2}\right) \\ &\quad + 2(1.1)(1.1)(50)(607 + 607)/(16.5 \times 12) \\ &= 759 \text{ kips} + 360 \text{ kips} + 742 \text{ kips} = 1860 \text{ kips} \end{aligned}$$

Note that the roof beam is a W30 × 173, identical to the fifth-floor beam.

On the tension side the force is:

$$E_m = 759 \text{ kips} - 360 \text{ kips} + 742 \text{ kips} = 1141 \text{ kips}$$

The axial force in the column in compression is:

$$P_u = 1.2D + 0.5L + E_m = 1900 \text{ kips}$$

The inward flexure due to web plate yielding is calculated using a model such as the one shown in Figure 12.34. The loading is:

$$\omega_{xc} = R_y F_y [t_{we} \sin^2(\alpha)] \qquad (12.90)$$

At the fourth floor the loading is:

$$\omega_{xc} = (1.3)(36)\left[0.135\left(\frac{1}{2}\right)\right](12) = 37.9 \text{ klf}$$

The preferred method of establishing column moments and shears is by means of a limited model such as is shown in Figure 12.34. Such a model is constructed for this purpose, with a preliminary column size selected based on the required axial strength and an assumed flexural demand based on:

$$M_u = \frac{\omega_{xc} h_c^2}{12} + \frac{1}{2} M_{pr} = (348 + 1530) \text{ kip-ft} = 1890 \text{ kip-ft}$$

A W14 × 398 is used in the model.

The spring stiffness used in the model for the fifth-floor beam (and the identical roof beam) is given by Eq. (12.35):

$$k_{bi} = \frac{A_{bi}E}{\frac{L}{2}} = \frac{(51)(29{,}000)}{\frac{1}{2}(19)(12)} = 12{,}970 \text{ kip/in}$$

Similar calculations are performed at every level.

The moment obtained from the model is 1895 kip-ft. The shear is 475 kips.

Using these axial and flexural forces with beam-column design equations, a W14 × 398 is verified to be adequate:

$$\phi P_n = 4780 \text{ kips } (KL = 13 \text{ ft; using design tables})$$

$$\phi M_n = \phi Z F_y = 3000 \text{ kip-ft}$$

$$P_u/\phi P_n (8/9) P_u/\phi P_n = 0.40 + (8/9)(0.63) = 0.965$$

The shear strength is also adequate.

This completes the preliminary design. As mentioned in previous examples, a preliminary design necessitates a reanalysis to determine revised building dynamic properties, and resulting changes in the base shear or modal response values.

12.6.7 Drift

In addition to providing sufficient base shear strength, the structure must also control drift to within acceptable limits. Should the drifts be determined to be excessive, redesign (and reanalysis) would be required.

A necessary component of this is establishing the effective thickness of perforated web plates for stiffness. This is a slightly different calculation than the effective thickness used in strength calculations. The effective thickness is calculated as follows:

$$t_{we} = \frac{1 - \frac{\pi}{4} \cdot \left(\frac{D}{S_{diag}} \right)}{1 - \frac{\pi}{4} \cdot \left(\frac{D}{S_{diag}} \right) \cdot \left(1 - \frac{N_r \cdot D \cdot \sin\theta}{H_{panel}} \right)} t_w \tag{12.91}$$

Level	Web Plate Thickness (in)	D/S_{diag}	Effective Web Plate Thickness (Stiffness) (in)
Fifth Floor	0.125	0.60	0.081
Fourth Floor	0.188	0.40	0.158
Third Floor	0.250	0.35	0.221
Second Floor	0.250	0.25	0.236
First Floor	0.313	0.40	0.264

Table 12.4 Web-Plate Sizes

Table 12.4 gives the effective thickness of each web plate for stiffness.

These thicknesses may be used in a model to determine drifts. It is important to note that the web plates, being only effective in tension, must be modeled in such a way as to make the compressive and shear stiffness zero (or negligible). No illustrative calculations are provided here for deflection calculation. Although drift limits must be checked, they rarely govern the design of SPSWs.

12.6.8 HBE Connection Design

The HBE and VBE form a rigid frame. They are joined with rigid connections subject to the same requirements as ordinary moment frame connections. Refer to Chapter 8 for information on how to check adequacy of column panel zones and compliance with the "Strong-Column/Weak-Beam" requirement. Additionally, the HBE end connection must be designed to resist the shear determined in Section 12.5.

12.6.9 Completion of Design

Several items remain to complete the design. These include:

- Web connection
- Layout of web-plate perforations
- Column splices
- Base plates
- Foundations
- Diaphragms, chords, and collectors

These are strength-based calculations based on conventional approaches, and therefore not presented here.

12.7 Self-Study Problems

Problem 12.1 Check the Special Plate Shear Wall shown in the following for compliance with AISC 341. All loads shown are unfactored. Only consider the load combination of 1.2D + 0.5L + 1.0E.

(a) Specifically follow the following steps:
   (1) Check the adequacy of the web plate thicknesses.
   (2) Develop a strip model using a structural analysis program and determine the VBE and HBE axial forces, moments, and shear forces for the gravity and earthquake loads shown below. Adapt the model to recognize that HBEs and VBEs must be designed per a capacity design procedure, assuming that the web plates have developed their expected tensile strength of R_yF_y. An average tension field angle can be used for the entire wall. The webplates are not allowed to carry gravity load, therefore, tension only members must be used for the web plates, or two models must be developed (one for seismic and one for gravity).
   (3) Check the VBEs and HBEs for the effects of combined axial force and moment, and for shear force.
   (4) Check adequacy of the VBEs moment of inertia.
   (5) Check the HBE-to-VBE strong-column/weak-beam requirement.

Assume that the HBEs are continuously braced against lateral torsional buckling and braced at their midpoint against compression buckling. Assume that the VBEs are laterally braced in both directions at the HBE-to-VBE connections. The web plates are A36 steel and the HBEs and VBEs are A992 Gr. 50. When using available design aids, refer the sections, page numbers, and edition of the design aids used.

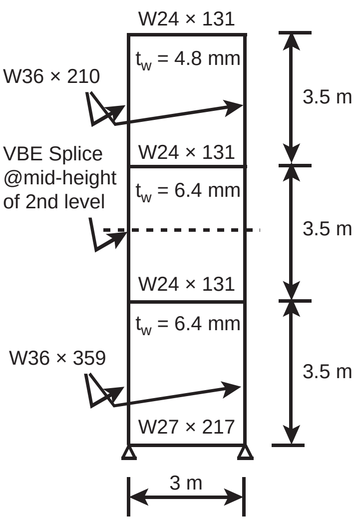

SPSW geometry and members

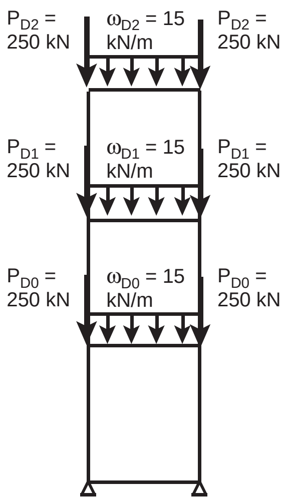

SPSW dead loads

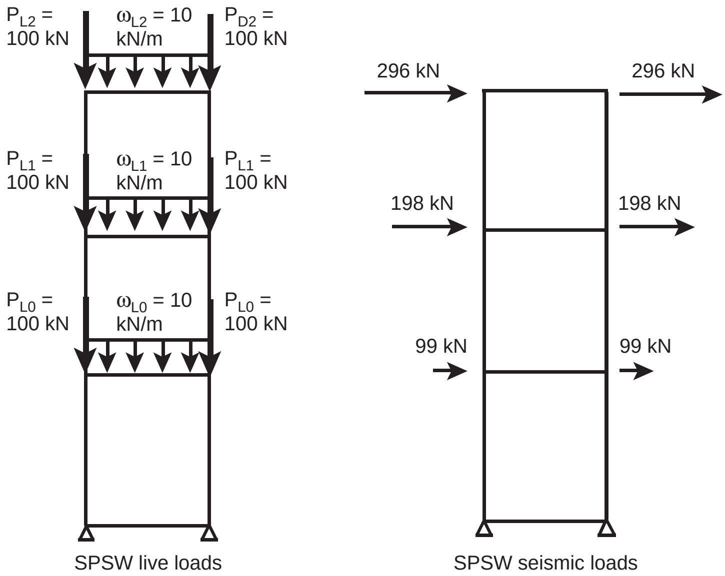

Problem 12.2 For the Steel Plate Shear Wall (SPSW) shown:

(a) Design the lightest steel plate (ASTM A529 Grade 50) that can resist the applied factored load shown and that comply with AISC 341.

(b) Compare the volume of steel for the resulting steel plate, and compare it with the total volume of the steel for the braces designed in Problem 9.4. Comment on the differences between the designs and explain their causes.

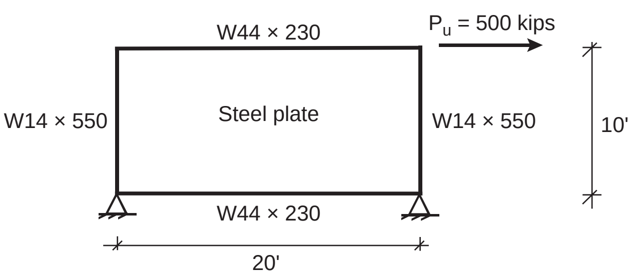

Problem 12.3 For the structure shown in Problem 8.4, if a 3/16″-thick infill steel plate is continuously welded to the beams and columns to convert that frame structure into a ductile steel plate wall, calculate the maximum load, V, (in kips) that is needed to produce the sway plastic collapse mechanism of this ductile steel plate wall structure. Here, assume that plastic hinging in beams will only develop at their ends, and that the infill plate yields at 45°. Use $L = 10$ ft and $h = 6$ ft.

References

AISC. 2005. "Seismic Provisions for Structural Steel Buildings." *ANSI/AISC 341-05*, Chicago: American Institute of Steel Construction Inc.

ASCE. 2010. *Minimum Design Loads for Buildings and Other Structures, Standard ASCE/SEI 7-10*, Reston, VA: American Society of Civil Engineers.

AISC. 2010. "Seismic Provisions for Structural Steel Buildings," *ANSI/AISC 341-10*, Chicago: American Institute of Steel Construction Inc.

Architectural Record. 1978a. "Steel-Plate Shear Walls Blunt the Wind's Force and Carry Gravity Load in a Towered Hotel." *Architectural Record*, mid-August, 116–117.

Architectural Record. 1978b. "Hospital Steel-Plate Shear Walls Were Designed for a 0.69g Earthquake." *Architectural Record*, mid-August, 118.

Astaneh-Asl, A. 2001. "Seismic Behavior and Design of Steel Shear Walls." *Steel Technical Information and Product Services Report*. Moraga, CA: Structural Steel Educational Council.

Astaneh-Asl, A., and Zhao, Q. 2001. "Cyclic Tests of Steel Shear Walls." *Report Number UCB/CE-Steel-01/01*, August. Berkeley: Department of Civil and Environmental Engineering, University of California.

Astaneh-Asl, A., and Zhao, Q. 2002. "Cyclic Behavior of Steel Shear Wall Systems." *Proceedings of the Annual Stability Conference,* Structural Stability Research Council, Seattle, WA.Baldelli, J. A. 1983. "Steel Shear Walls for Existing Buildings." *AISC Engineering Journal*, vol. 20, no. 2, 70–77.

Basler, K. 1961. "Strength of Plate Girders in Shear." *Journal of the Structural Division, ASCE*, vol. 87, no. 7, 150–180.

Behbahanifard, M., Grondin, G., and Elwi, A. 2003. "Experimental and Numerical Investigation of Steel Plate Shear Walls." *Structural Engineering Report No. 254*, Edmonton, AB, Canada: Department of Civil and Environmental Engineering, University of Alberta.

Berman, J. W., and Bruneau, M. 2003a. "Plastic Analysis and Design of Steel Plate Shear Walls." *Journal of Structural Engineering, ASCE*, vol. 129, no. 11, 1448–1456.

Berman, J. W., and Bruneau, M. 2003b. "Experimental Investigation of Light-Gauge Steel Plate Shear Walls for the Seismic Retrofit of Buildings." *Technical Report MCEER-03-0001*. Buffalo, NY: Multidisciplinary Center for Earthquake Engineering Research, State University of New York at Buffalo.

Berman, J. W., and Bruneau, M. 2004. "Steel Plate Shear Walls Are Not Plate Girders." *AISC Engineering Journal*, vol. 41, no. 3, 95–106.

Berman, J., and Bruneau, M. 2005. "Experimental Investigation of Light-Gauge Steel Plate Shear Walls." *Journal of Structural Engineering, ASCE*, vol. 131, no. 2, 259–267.

Berman, J., and Bruneau, M. 2008. "Capacity Design of Vertical Boundary Elements in Steel Plate Shear Walls." *AISC Engineering Journal*, vol. 45, no. 1, 57–71.

Bertero, V. V., Anderson, J. C., and Krawinkler, H. 1994. "Performance of Steel Building Structures during the Northridge Earthquake," *Report No. UCB/EERC-94/09*, Berkeley: Earthquake Engineering Research Center, University of California.

Blogdowntown.com. 2008. http://blogdowntown.com/2008/10/3756-la-live-tower-structure-hailed-at-steel-industry.

Bhowmick, A. K., Driver, R. G., and Grondin, G. Y. 2009. "Seismic Analysis of Steel Plate Shear Walls Considering Strain Rate and P-Delta Effects." *Journal of Constructional Steel Research*, vol. 65, 1149–1159.

Bruneau, M., and Bhagwagar, T. 2002. "Seismic Retrofit of Flexible Steel Frames Using Thin Infill Panels." *Engineering Structures*, vol. 24, no. 4, 443–453.

CSA. 1994. "Limit States Design of Steel Structures." *CAN/CSA S16-94*. Willowdale, ON, Canada: Canadian Standards Association.

CSA. 2001. "Limit States Design of Steel Structures." *CAN/CSA S16-01*. Willowdale, ON, Canada:Canadian Standards Association.

CSA. 2009. "Design of Steel Structures." *CAN/CSA S16-09*. Mississauga, ON, Canada: Canadian Standards Association.Caccese, V., Elgaaly, M., and Chen, R. 1993. "Experimental Study of Thin Steel-Plate Shear Walls Under Cyclic Load." *Journal of Structural Engineering, ASCE*, vol. 119, no. 2, 573–587.

Çelebi, M. 1997. "Response of Olive View Hospital to Northridge and Whittier Earthquakes." *Journal of Structural Engineering, ASCE*, vol. 123, no. 4, 389–396.

Choi, I. R., and Park, H. G. 2009. Steel Plate Shear Walls with Various Infill Plate Designs." *Journal of Structural Engineering, ASCE*, vol. 135, no. 7, 785–796.

Dastfan, M., and Driver, R. G. 2008. "Flexural Stiffness Limits for Frame Members of Steel Plate Shear Wall Systems." *Proceedings of the Annual Stability Conference,* Nashville, TN. Rolla, MO: Structural Stability Research Council.

Dean, R. G., Cannon, T. J., and Poland, C. D. 1977. "Unusual Structural Aspects of the H.C. Moffitt Hospitals." *Proceedings of the Structural Engineers Association of California 46th Convention*, Coronado, California, pp. 32–73.

Deng, X., Dastfan, M., and Driver, R. G. 2008. "Behaviour of Steel Plate Shear Walls with Composite Columns," Proceedings of the 2008 Structures Congress, April 24–26, Vancouver, BC, Canada: American Society of Civil Engineers.

Driver, R. G., and Grondin, G. Y. 2001. "Steel Plate Shear Walls: Now Performing on the Main Stage." *Modern Steel Construction, AISC*, September 2001.

Driver, R. G., Grondin, G. Y., Behbahanifard, M., and Hussain, M. A. 2001. "Recent Developments and Future Directions in Steel Plate Shear Wall Research." *Proceedings of the North American Steel Construction Conference*, May, Ft. Lauderdale, FL.

Driver, R. G., Kulak, G. L., Kennedy, D. J. L., and Elwi, A. E. 1997a. "Seismic Behaviour of Steel Plate Shear Walls." *Structural Engineering Report No. 215*. Edmonton, AB, Canada: Department of Civil Engineering, University of Alberta.

Driver, R. G., Kulak, G. L., Kennedy, D. J. L., and Elwi, A. E. 1997b. "Finite Element Modelling of Steel Plate Shear Walls." *Proceedings of the Structural Stability Research Council Annual Technical Session*, Toronto, 253–264.

Driver, R. G., Kulak, G. L., Elwi, A. E., and Kennedy, D. J. L. 1998a. "Cyclic Tests of Four-Story Steel Plate Shear Wall." *Journal of Structural Engineering, ASCE*, vol. 124, no. 2, 112–120.

Driver, R. G., Kulak, G. L., Elwi, A. E., and Kennedy, D. J. L. 1998b. "FE and Simplified Models of Steel Plate Shear Wall." *Journal of Structural Engineering, ASCE*, vol. 124, no. 2, 121–130.Eatherton, M., 2005. Senior Design Engineer, GFDS Engineers, San Francisco, personal communication.

Eatherton, M., and Johnson, K. 2004. "High-End Residence using Steel Plate Shear Walls in Woodside, California," *Proceedings of the SEAOC 2004 Convention: 75th Anniversary Celebration*, Monterey, California, pp. 19–29.

Elgaaly, M. 1998. "Thin Steel Plate Shear Walls Behavior and Analysis." *Thin Walled Structures*, vol. 32, no. 1–3, 151–180.

Elgaaly, M., Caccese, V., and Du, C. 1993. "Post-buckling Behavior of Steel-Plate Shear Walls Under Cyclic Loads." *Journal of Structural Engineering, ASCE*, vol. 119, no. 2, 588–605.

Elgaaly, M., and Liu, Y. 1997. "Analysis of Thin-Steel-Plate Shear Walls." *Journal of Structural Engineering, ASCE*, vol. 123, no. 11, 1487–1496.

ENR. 1977. "Shear Walls and Slipforming Speed Dallas' Reunion Project." *Engineering News Record*, July 28, 20–21.

ENR. 1978a. "Quake-Proof Hospital Has Battleship-Like Walls."*Engineering News Record*, September 21, 62–63.

ENR. 1978b. "Patent Problems, Challenge Spawn Steel Seismic Walls." *Engineering News Record*, January 26, 17.

FEMA. 2000. "Recommended Seismic Design Criteria for New Steel Moment-Frame Buildings," *Report FEMA-350*, Federal Emergency Management Agency, Washington, DC.

FEMA. 2004. "FEMA 450: NEHRP Recommended Provisions for Seismic Regulations for New Buildings and Other Structures." Building Seismic Safety Council for the Federal Emergency Management Agency, Washington, D. C.

Fujitani, H., Yamanouchi, H., Okawa, I. Sawai, N., Uchida, N., and Matsutani, T. 1996. "Damage and performance of tall buildings in the 1995 Hyogoken Nanbu earthquake,"*Proceedings of 67th Regional Conference (in conjunction with ASCE Structures Congress XIV)*, Council on Tall Building and Urban Habitat, Chicago, 103–125.

Glotman, M. 2005. Structural Engineer, Glotman Simpson, Vancouver, BC, Canada, personal communication.

Grondin, G., and Behbahanidard, M. 2001. "Cyclic Behaviour of Three-Storey Unstiffened Steel Plate Shear Wall," Canadian Society of Civil Engineers Conference.

Hooper, J. 2005. Principal and Director of Earthquake Engineering, Magnusson Klemencic Associates, Seattle, personal communication.

Kristeva, N. 2010. "Trimming the Fat." *Modern Steel Construction*, Feb. 2010.

Kuhn, P., Peterson, J. P., and Levin, L. R. 1952. "A Summary of Diagonal Tension, Part 1—Methods of Analysis." *Tech. Note 2661*. Langley Field, VA: National Advisory Committee for Aeronautics, Langley Aeronautical Laboratory.

Lee, C. S., and Tsai, K. C. 2008. "Experimental Response of Four 2-Story Narrow Steel Plate Shear Walls." *Proceeding of the 2008 Structures Congress*, Vancouver, BC, Canada.

Leontovich, V. 1959. *Frames and Arches: Condensed Solutions for Structural Analysis*. New York: McGraw-Hill, p. 472.

Lin, C. H., Tsai, K. C., Qu, B., and Bruneau, M. 2010. "Sub-structural Pseudo-dynamic Performance of Two Full-scale Two-story Steel Plate Shear Walls."*Journal of Constructional Steel Research.* vol. 66, 1467–1482.

Love, R. J., Yu, K., McNeill, S., and Zepeda, D. 2008. "Retrofit of a Critical Care Facility in Los Angeles with Steel Plate Shear Walls,"*ASCE Structures Congress*, Vancouver, B.C., pp. 1–7, (doi10.1061/41016(314)103).

Lubell, A. S., Prion, H. G. L., Ventura, C. E., and Rezai, M. 2000. "Unstiffened Steel Plate Shear Wall Performance under Cyclic Loading." *Journal of Structural Engineering,ASCE*, vol. 126, no. 4, 453–460.

Monnier, A. B., and Harasimowicz, A. P. 2007. "Shear Strength." *Modern Steel Construction*, *AISC*, January 2007.

Montgomery, C. J., and Medhekar, M. 2001. Discussion on "Unstiffened Steel Plate Shear Wall Performance Under Cyclic Load." *Journal of Structural Engineering, ASCE*, vol. 127, no. 8, 973–973.

Naeim, F., and Lobo, R. 1994. "Performance of Nonstructural Components During the January 17, 1994 Northridge Earthquake: Case Studies of Six Instrumented Multistory Buildings." *Proceedings of the ATC-29-1 ATC-29-1 Seminar on Seismic Design, Retrofit, and Performance of Nonstructural Components*. Redwood City, CA: Applied Technology Council.

Nakashima, M., Fujiwara, T., Suzuki, Y., Bruneau, M., Iwai, S., and Kitahara, A. 1995. "Damage to Engineered Buildings from the 1995 Great Hanshin Earthquake." *Journal of Natural Disaster Sciences*, vol. 16, no. 20, 71–78.

OSHPD. 1995. "Northridge Earthquake: A Report to the Hospital Building Safety Board on the Performance of Hospitals." *Office of Statewide Health Planning and Development, Facilities Development Division*, Sacramento, CA, 63 pages.

Purba, R., and Bruneau, M. 2007. "Design Recommendations for Perforated Steel Plate Shear Walls," *Technical Report MCEER-07-0011*. Buffalo, NY: MCEER, State University of New York at Buffalo, 208 pages.

Purba, R., and Bruneau, M. 2009. "Finite Element Investigation and Design Recommendations for Perforated Steel Plate Shear Walls." *Journal of Structural Engineering, ASCE*, vol. 135, no. 11, 1367–1376.

Purba, R., and Bruneau, M. 2010. "Impact of Horizontal Boundary Elements Design on Seismic Behavior of Steel Plate Shear Walls." *Technical Report MCEER-10-0007*. Buffalo, NY: MCEER, State University of New York at Buffalo.

Qu B., and Bruneau, M. 2008. "Seismic Behavior and Design of Boundary Frame Members in Steel Plate Shear Walls.." *Technical Report MCEER-08-0012*. Buffalo, NY: MCEER, State University of New York at Buffalo.

Qu, B., and Bruneau, M. 2009. "Design of Steel Plate Shear Walls Considering Boundary Frame Moment Resisting Action." *Journal of Structural Engineering, ASCE*, vol. 135, no. 12, 1511–1521.

Qu, B., and Bruneau, M. 2010a. "Capacity Design of Intermediate Horizontal Boundary Elements of Steel Plate Shear Walls." *Journal of Structural Engineering, ASCE*, vol. 136, no. 6, 665–675.

Qu, B., and Bruneau, M. 2010b. "Behavior of Vertical Boundary Elements in Steel Plate Shear Walls." *AISC Engineering Journal*, vol. 47, no. 2, pp. 109–122.

Qu, B., and Bruneau, M. 2011. "Plastic Moment of Intermediate Horizontal Boundary Elements of Steel Plate Shear Walls." *AISC Engineering Journal,* vol. 48, no. 1.

Qu, B., Bruneau, M., Lin, C. H., and Tsai, K. C. 2008. "Testing of Full-Scale Two-Story Steel Plate Shear Wall with Reduced Beam Section Connections and Composite Floors." *Journal of Structural Engineering, ASCE*, vol. 134, no. 3, 364–373.

Rezai, M. 1999. "Seismic Behaviour of Steel Plate Shear Walls by Shake Table Testing," *PhD Dissertation*, Vancouver, BC, Canada: Department of Civil Engineering, University of British Columbia.

Roberts, T. M., and Sabouri-Ghomi, S. 1991. "Hysteretic Characteristics of Unstiffened Plate Shear Panels." *Thin-Walled Structures*, vol. 12, no. 2, 145–162.

Roberts, T. M., and Sabouri-Ghomi, S. 1992. "Hysteretic Characteristics of Unstiffened Perforated Steel Plate Shear Walls." *Thin-Walled Structures*, vol. 14, no. 2, 139–151.

Robinson, K., and Ames, D. 2000. "Steel Plate Shear Walls—Library Seismic Upgrade." *Modern Steel Construction*, vol. 40, no. 1, 56–60.

Romero, E. M. 2003. "Construcción Compuesta En Edificios Altos,"*VII Simposio Internacional De Estructuras De Acero*, Veracruz, Ver. Mexico.

Sabelli, R., and Bruneau, M. 2007. *Steel Plate Shear Walls (AISC Design Guide)*. Chicago: American Institute of Steel Construction, pp. 144.

Sabouri-Ghomi, S., and Roberts, T. M. 1992. "Nonlinear Dynamic Analysis of Steel Plate Shear Walls Including Shear and Bending Deformations." *Engineering Structures*, vol. 14, no. 5, 309–317.

Sabouri-Ghomi, S., Ventura, C. E., and Kharrazi, M. H. K. 2005. "Shear Analysis and Design of Ductile Steel Plate Walls." *Journal of Structural Engineering, ASCE*, vol. 131, no. 6, 878–889.

Schumacher, A., Grondin, G. Y., and Kulak, G. L. 1999. "Connection of infill panels in steel plate shear walls." *Canadian Journal of Civil Engineering*, vol. 26, no. 5, 549–563.

Shishkin, J. J., Driver, R. G., and Grondin, G. Y. 2009. "Analysis of Steel Plate Shear Walls Using the Modified Strip Model." *Journal of Structural Engineering, ASCE*, vol. 135, no. 11, 1357–1366.

Thorburn, L. J., Kulak, G. L., and Montgomery, C. J. 1983. "Analysis of Steel Plate Shear Walls," *Structural Engineering Report No. 107*. Edmonton, AB, Canada: Department of Civil Engineering, University of Alberta.

Timler P. A., and Kulak, G. L. 1983. "Experimental Study of Steel Plate Shear Walls," *Structural Engineering Report No. 114*. Edmonton, AB, Canada: Department of Civil Engineering, University of Alberta.

Timler, P. A., Ventura, C. E., Prion, H., and Anjam, R. 1998. "Experimental and Analytical Studies of Steel Plate Shear Walls as Applied to the Design of Tall Buildings." *The Structural Design of Tall Buildings*, vol. 7, no. 3, 233–249.

Tromposch, E. W., and Kulak, G. L. 1987. "Cyclic and Static Behaviour of Thin Panel Steel Plate Shear Walls." *Structural Engineering Report No. 145*. Edmonton, AB, Canada: Department of Civil Engineering, University of Alberta.

Vian, D., and Bruneau, M. 2004. "Testing of Special LYS Steel Plate Shear Walls." *Proceedings of the 13th World Conference on Earthquake Engineering*, Paper No. 978, Vancouver, BC, Canada.

Vian, D., and Bruneau, M. 2005. "Steel Plate Walls for Seismic Design and Retrofit of Building Structures." *Technical Report MCEER-05-0010*. Buffalo, NY: Multidisciplinary Center for Earthquake Engineering Research, State University of New York at Buffalo.

Vian D., Bruneau, M., and Purba, R. 2009a. "Special Perforated Steel Plate Shear Walls with Reduced Beam Section Anchor Beams II: Analysis and Design Recommendations." *Journal of Structural Engineering, ASCE*, vol. 135, no. 3, 221–228.

Vian D., Bruneau, M., Tsai, K. C., and Lin, Y. C. 2009b. "Special Perforated Steel Plate Shear Walls with Reduced Beam Section Anchor Beams I: Experimental Investigation." *Journal of Structural Engineering, ASCE*, vol. 135, no. 3, 211–220.

Wagner, H. 1931. "Flat Sheet Metal Girders with Very Thin Metal Webs. Part I-General Theories and Assumptions, and Part III: Sheet Metal Girders with Spars Resistant to Bending—The Stress in Uprights—Diagonal Tension Fields." *Technical Memorandum Nos. 604 and 606*, National Advisory Committee for Aeronautics, Washington, D.C.

Wosser, T. D., and Poland, C. D. 2003. "Degenkolb Engineers." *Journal of Structural Design of Tall and Special Buildings*, vol. 12, 227–244.

Yamaguchi, T., et al. 1998. "Seismic Control Devices Using Low-yield-point Steel." *Nippon Steel Technical Report No. 77*, 65–72. (available at http://www.nsc.co.jp/gikai/en/contenthtml/n78/n78.html).

Yokoyama, T., Kajiyama, Y., and Komuro, H. 1978. "Structural scheme of Nippon Building B-Wing." In Japanese.

Young, W.C. 1989. *Roark's Formulas for Stress and Strain*. New York: McGraw-Hill, pp. 736.

Zhao, Q., and Astaneh-Asl, A. 2004. "Cyclic Behavior of Traditional and Innovative Composite Shear Walls." *Journal of Structural Engineering, ASCE*, vol. 130, no. 2, 271–284.

CHAPTER 13

Other Ductile Steel Energy Dissipating Systems

While the previous chapters have focused on some of the lateral load-resisting systems found in North American seismic design provisions and most commonly implemented, many other innovative steel systems have been proposed in the past to achieve the objective of ductile energy dissipation. An exhaustive presentation of all such innovations in steel design is beyond the scope of this book, but in light of the growing interest on this topic, a summary review of some of the strategies that have generally been pursued is presented in this chapter. Further information on the systems' theoretical behavior, analytical predictions of seismic response, and experimentally verified ductile performance, is available in the references cited for each respective design concept. An overview of the structural fuse concept precedes presentation of the various energy dissipation strategies to put them in design context.

13.1 Structural Fuse Concept

As indicated earlier, in seismic design, code-specified loads are reduced by a response modification factor, R, which allows the structure to undergo inelastic deformations while most of the seismic energy is dissipated through hysteretic behavior. Designs have always (implicitly or explicitly) relied on this reduction in the design forces. As emphasized throughout the previous chapters, this methodology relies on the ability of specially detailed ductile structural elements to accommodate inelastic deformations, without compromising structural stability. It is important to recognize, however, that this inelastic behavior translates into some level of damage on these elements, permanent system deformations following an earthquake, and possibly high cost for repairs (sometimes, even though the structure has not collapsed, repairs are not viable and the building must be demolished). Given that earthquakes are rare events that will not happen during the life of most structures, and given that proper ductile design will limit the extent of damage and concentrate it into special structural elements, the need for repairs following an earthquake has been seen as an acceptable tradeoff against higher seismic design loads; for steel structures, such repairs have been successfully accomplished following modern earthquakes, but they sometimes have not been trivial endeavors.

To achieve more stringent seismic performance objectives, an alternative design approach is to concentrate damage on disposable and easy to repair structural elements (i.e., "structural fuses"), while the main structure is designed to remain elastic or with minor inelastic deformations. Following a damaging earthquake, only these special elements would need to be replaced (hence the "fuse" analogy), making repair work easier and more expedient. Furthermore, in that instance, self-recentering of the structure would occur once the ductile fuse devices are removed, i.e., the elastic structure would return to its original undeformed position.

The structural fuse concept has not been consistently defined in the past. In some cases, "fuses" have been defined as elements with well-defined plastic yielding locations, but not truly replaceable as a fuse. For instance, Roeder and Popov (1977) called the segment of the beam yielding in shear in an eccentrically braced frame a "ductile fuse" because of its energy dissipation capability. Although this system has a good seismic behavior, such links are not readily disposable elements (beams would need shoring, floor slabs might require repairs, etc.), unless the links are specially detailed from the onset to be easily replaceable, as done by Mansour et al. (2006, 2009). Other researchers have used the term "structural fuse" in the same perspective for different types of structural systems (e.g., Aristizabal-Ochoa 1986, Basha and Goel 1996, Carter and Iwankiw 1998, Rezai et al. 2000, and Sugiyama 1998, to name a few). In some other cases, structural fuses were defined as elements with well-defined plastic yielding locations and used more in the context of reducing (as opposed to eliminating) inelastic deformations of existing moment-resisting frames (also termed to be a "damage control" strategy) (Connor et al. 1997; Huang et al. 2002; Wada and Huang 1999; Wada et al. 1992, 2000). In applications consistent with the definition of interest here, fuses were used to achieve elastic response of frames that would otherwise develop limited inelastic deformations for high rise buildings having large structural periods (i.e., $T > 4$s) (e.g., Shimizu et al. 1998, Wada and Huang 1995), or for systems with friction brace devices intended to act as structural fuses (e.g., Filiatrault and Cherry 1989, Fu and Cherry 2000).

Generally, because of the large number of complex parameter interdependencies that exist in systems with structural fuses, the design procedures developed for these systems have relied on nonlinear time-history analyses. A systematic and simplified design procedure to achieve and implement a structural fuse concept to limit damage to disposable structural elements for any general structure, without the need for complex analyses, has been proposed and verified experimentally by Vargas and Bruneau (2009a, 2009b) for design and retrofit purposes.

The more rigorous structural fuse definition is conceptually illustrated in Figure 13.1 using a general pushover curve and the model for a SDOF structure, in which frame and metallic fuses are represented by elasto-plastic springs acting in parallel. The total curve is trilinear with the initial stiffness, K_1, calculated by adding the stiffness of the frame and the structural fuses, K_f and K_a, respectively. Once the structural fuses reach their yield deformation, Δ_{ya}, the increment on the lateral force is resisted only by the bare frame, being the second slope of the total curve equal to the frame stiffness, K_f. V_{yf} and

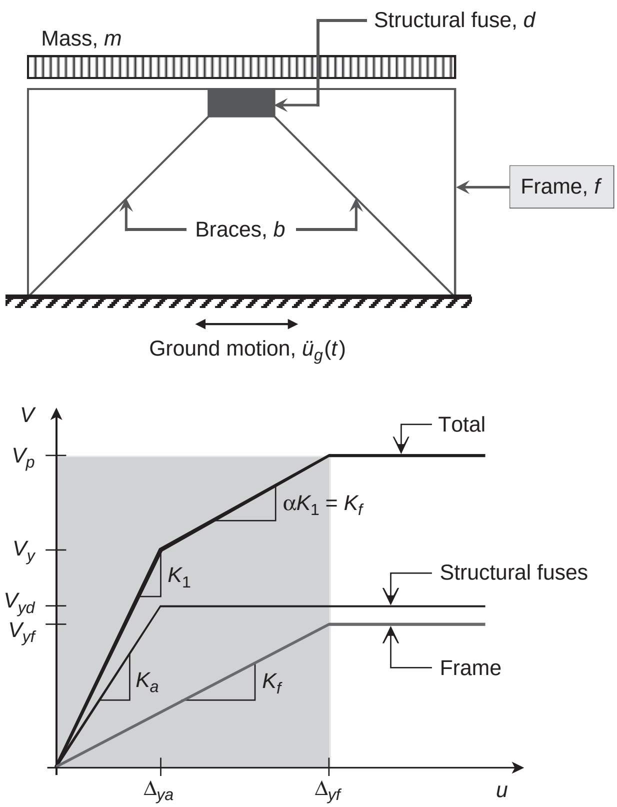

Figure 13.1 Sample model of a SDOF system with metallic fuses, and general pushover curve.

V_{yd} are the base shear capacity of the bare frame and the structural fuses, respectively, and V_y and V_p are the total system yield strength and base shear capacity, respectively. The maximum displacement ductility, μ_{max}, is the ratio of the frame yield displacement, Δ_{yf}, with respect to the yield displacement of the structural fuses, Δ_{ya}. In other words, μ_{max} is the maximum displacement ductility that the metallic fuses experience before the frame undergoes inelastic deformations. If system response is maintained to less than Δ_{yf}, replacement of the fuse can be achieved with relative ease (as experimentally demonstrated by Vargas and Bruneau 2009b). Vargas and Bruneau (2009a) reported that this performance objective is easier to attain for target designs having $K_f/(K_f + K_a) \geq 0.25$ and $\mu_{max} \geq 5$. Note that much literature also exists on the use of viscous or visco-elastic dampers and other velocity-dependant mechanical devices (instead of metallic fuses) to achieve a frame elastic-response performance objective (e.g., Constantinou et al. 1998, Soong and Constantinou 1994, Takewaki 2009), but these are beyond the current scope. Incidentally, combining viscous dampers in parallel with hysteretic energy dissipation devices (rather than for the purpose of achieving elastic response) may not be of benefit and could, in some instances, worsen seismic performance (Vargas and Bruneau 2007).

Although many of the ductile systems and approaches presented in this chapter (and the previous chapters for that matter) have not necessarily been formulated to achieve the more rigorous structural fuse design objectives, they could be adapted to serve this purpose. Finally, note that exceeding Δ_{yf} is not fatal in terms of life safety when using a relatively ductile "protected" frame; rather, it implies that self-centering upon replacement of the fuse may not occur, and the possible need for repair of the protected frame.

13.2 Energy Dissipation Through Steel Yielding

13.2.1 Early Concepts

Beyond the conventional structural framing systems described in earlier chapters to resist earthquakes, steel yielding for hysteretic energy dissipation has been implemented in devices intended to provide additional stiffness and damping to primary structural frames or to base isolation systems. Many such devices emerged in New Zealand in the early 1970s, relying on a variety of yielding mechanisms, designed to achieve long low-cycle fatigue life by using mild steels, stocky cross-sections, and to the extent possible avoiding welds in regions of plastic demands (Kelly et al. 1972; Skinner et al. 1975, 1993). Four concepts experimentally investigated at that early stage,

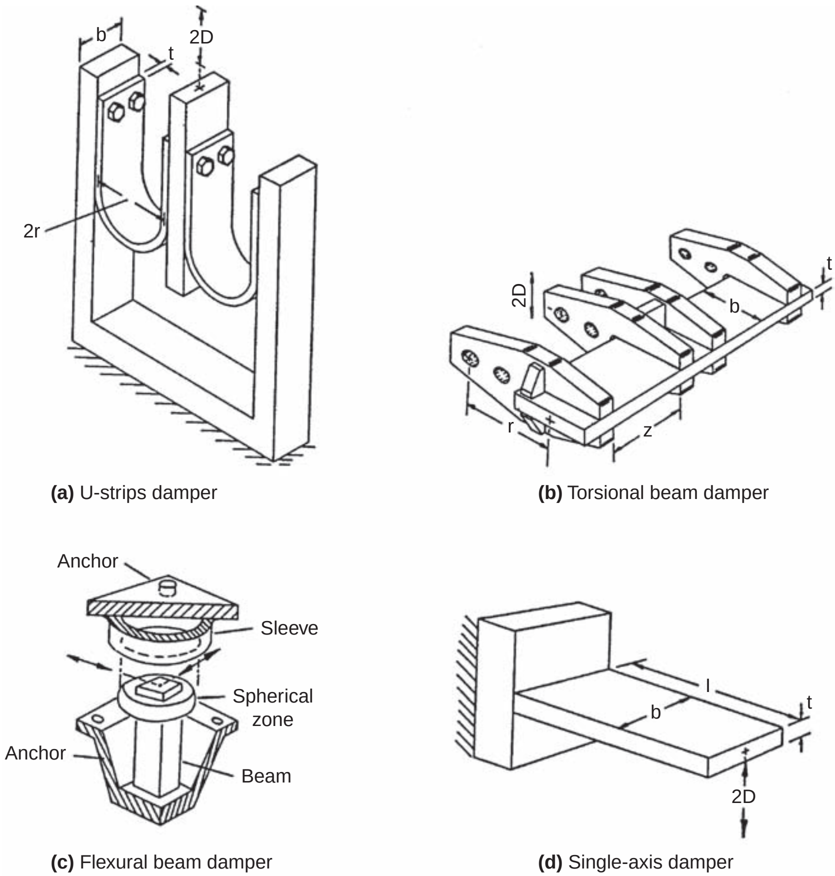

FIGURE 13.2 Steel-yielding dampers. (*Courtesy of R.I. Skinner, New Zealand.*)

schematically shown in Figure 13.2, consisted of: (a) a pair of U-shaped steel strips undergoing flexural yielding due to the up-and-down movement of the central bar to which they were tied, (b) a flat rectangular bar subjected to combined flexure and (predominantly) torsion by an eccentrically applied load at its middle, (c) a vertical cantilevering bar of square or circular cross-section yielding in flexure when subjected to bidirectional horizontal displacements at its tip, and (d) a flat rectangular cantilever plate for loading about a single axis (as part of an assembly having multiple such plates closely spaced and parallel to each other). Some of those were implemented in bridges and buildings in New Zealand (Boardman et al. 1983; Skinner et al. 1980, 1993).

13.2.2 Triangular Plates in Flexure

In the process of using flat plates in flexure for energy dissipation, it was quickly realized that triangular plates provide a superior performance, as conceptually illustrated in Figure 13.3 for single plates subjected to relative transverse end displacements and fixed at one or both ends.

Having the width of the plates match the profile of the bending diagram ensures that yielding develops simultaneously over the entire length of the plates, requiring lesser inelastic strains at large relative displacements and resulting in a more ductile device (Steimer et al. 1981, Tyler 1978). Figure 13.3 shows the moment diagram and constant curvature obtained for idealized triangular and hourglass-shaped plates. Note that practical considerations require a minimum width to transfer shear forces; furthermore, the plate length-to-thickness ratio must be large to ensure dominance of flexural over shear yielding.

Figure 13.4 shows an implementation of this concept in buildings seismically isolated using flexible piles (Boardman et al. 1983) in New Zealand, whereas Figure 13.5 shows implementation in a bridge column designed to uplift during severe earthquake excitations (Dowdell and Hamersley 2000).

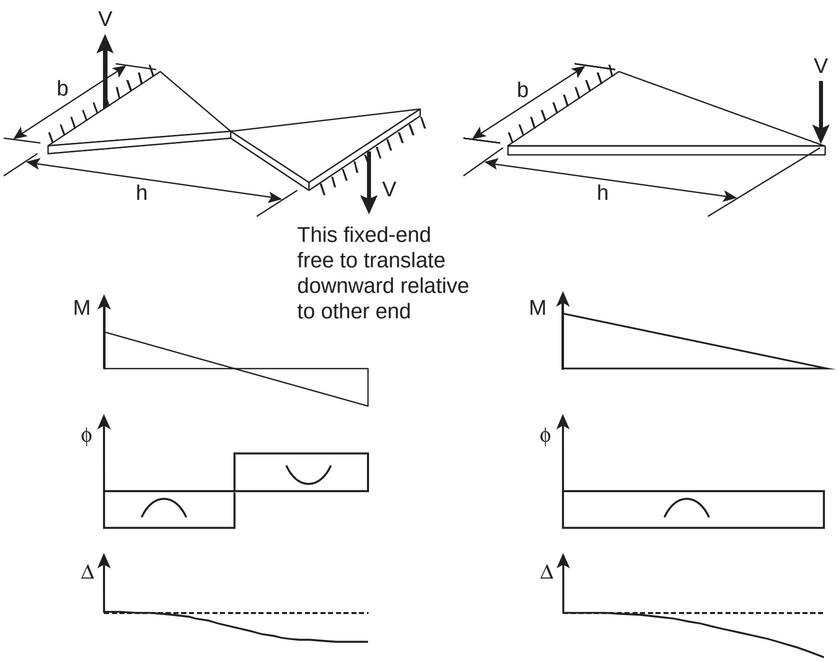

Figure 13.3 Schematic of hourglass and triangular plates subjected to relative end displacements, with moment and curvature diagrams, and deflected shapes.

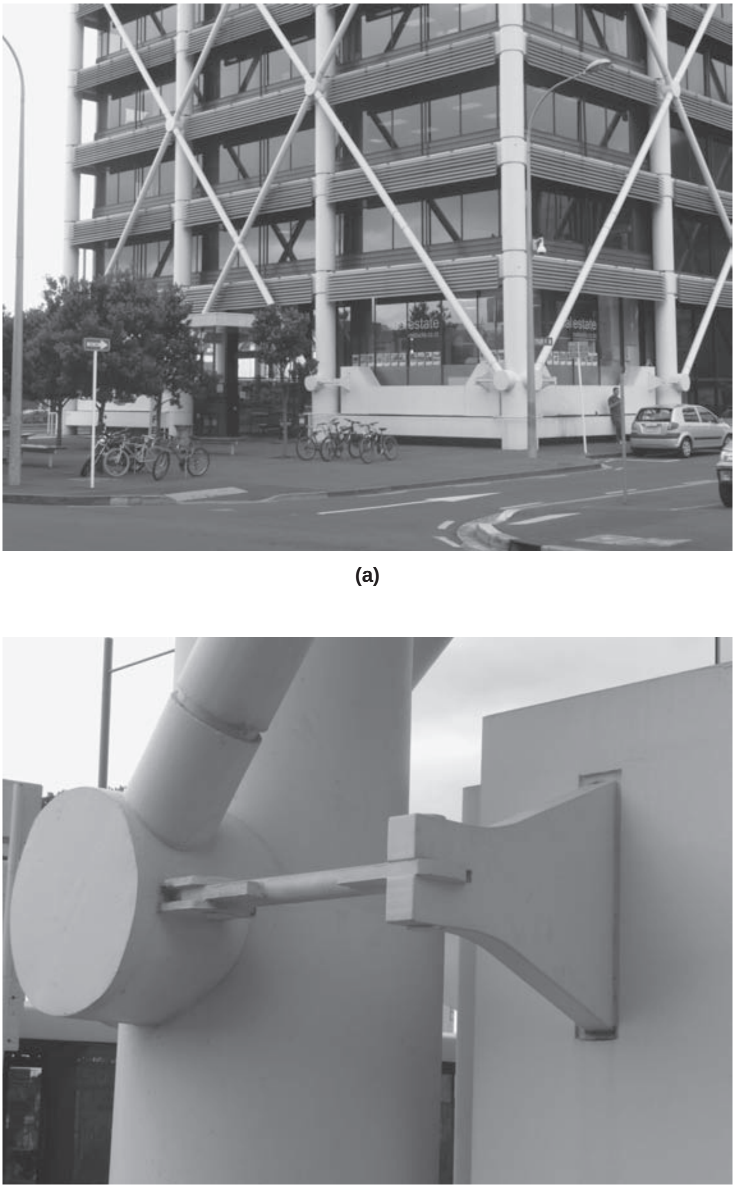

(a)

(b)

FIGURE 13.4 Triangular plate energy dissipator implemented in seismically isolated building, Auckland, New Zealand.

(a)

(b)

Figure 13.5 Triangular plate energy dissipator (fixed to the tower, pinned into a slotted vertical plate anchored into foundation) implemented in a bridge column allowed to uplift during tower rocking, Vancouver, Canada. (*Courtesy of Bruce Hamersley, Klohn Crippen Berger, Vancouver*.)

Devices made of multiple parallel single-axis, triangular- or hourglass-shaped plates have been developed and experimentally verified, such as the proprietary added damping and stiffness (ADAS) flexural-beam damper (Bergman and Goel 1987; Steimer et al. 1981; Whittaker et al. 1989, 1991) and a triangular-plate version of the ADAS damper, referred as T-ADAS (Tsai et al. 1993), shown in Figure 13.6.

ADAS devices have been used for the seismic retrofit of a number of buildings in the United States (e.g., Perry et al. 1993) and Mexico (Martinez-Romero 1993). One end of these relatively shallow devices is typically connected to a rigid beam of the existing structure, whereas the other end is tied to a rotationally stiff support (often braced for that purpose) designed to ensure double curvature of the ADAS device, as shown in Figure 13.7. The required rotational stiffness of that support is substantially less when connected to the "pin-end" of a T-ADAS device.

Rotation demands on the devices can be obtained from the corresponding plastic mechanism shown in Figure 13.8. The plastic rotational demand (γ_p) on the ADAS device is given as:

$$\gamma_p = \frac{H}{h}\theta_p \tag{13.1}$$

where H is the story height, h is the height of the ADAS device, and θ_p is the plastic story drift angle. The resulting magnification of plastic rotation demands can be substantial, given that values of H/h equal to 10 have been reported. In that case, for a 2% story drift, the corresponding plastic rotational demand in the ADAS device would be 0.20 radian. Experiments have reported stable hysteretic behavior up to 0.40 radian (Whittaker et al. 1989). Similar results have been obtained with the T-ADAS device, as shown in Figure 13.9. Note that T-ADAS devices are detailed with slotted holes to eliminate axial loads in the steel plates at large drifts.

For bridge applications, triangular plate devices have also been proposed and experimentally verified for the retrofit of certain type of steel bridges (Sarraf and Bruneau 1998a, 1998b; Zahrai and Bruneau 1999a, 1999b), and to provide energy dissipation and control the amplitude of uplifting in bridge towers allowed to rock during earthquakes (Pollino and Bruneau 2007, 2008, 2010a, 2010b). In some specific bridge superstructure applications in which relatively low inertia forces are developed under seismic excitations, such as in the diaphragms of steel slab-on-girder bridges, for example, it was found that triangular plate devices could be designed to be the primary lateral load-resisting force system, rather than primarily serving a hysteretic damping function (Zahrai and Bruneau 1999b).

The fundamental parameters defining response of a single cantilever triangular plate can be derived from basic structural

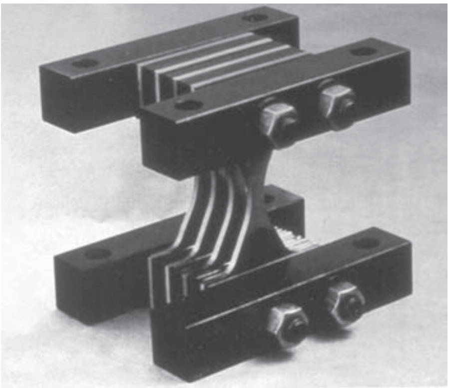

(a)

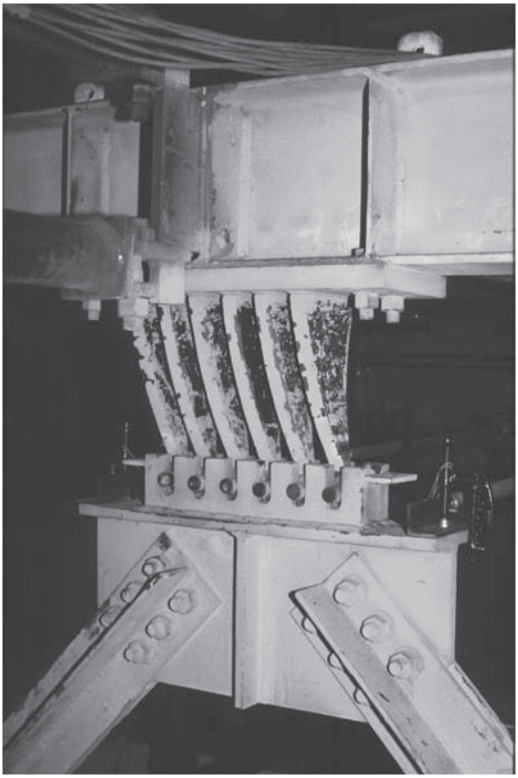

(b)

Figure 13.6 Yielding multi-plate flexural devices: (a) ADAS (*Courtesy of CounterQuake Corporation*); (b) T-ADAS, during test at large deformations. (*Courtesy of K.C. Tsai, National Taiwan University,Taipei*.)

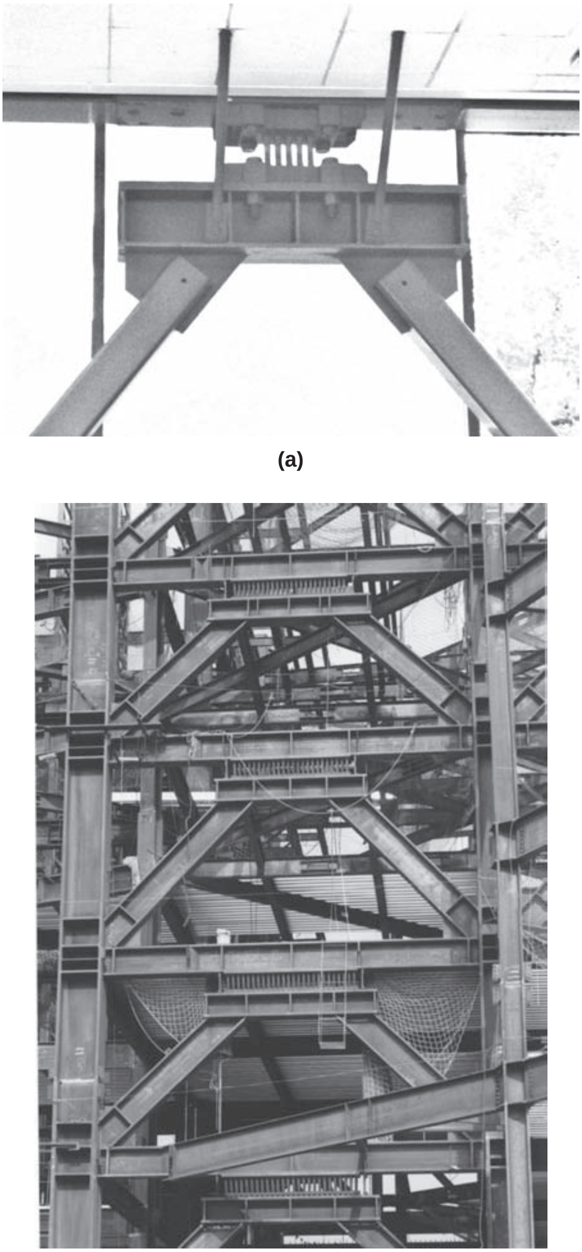

(a)

(b)

Figure 13.7 Implementation examples for: (a) ADAS, building in San Francisco; (b) T-ADAS, building in Taipei, Taiwan. (*Part b, courtesy of K.C. Tsai, National Taiwan University, Taipei.*)

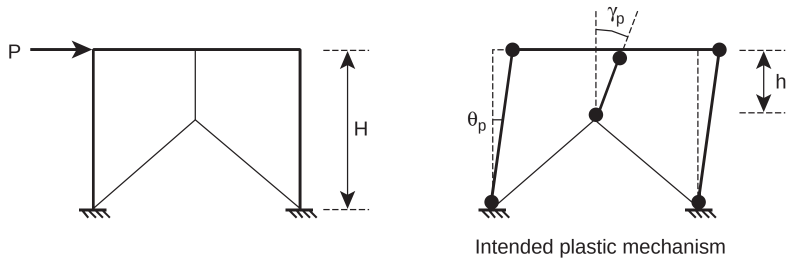

Figure 13.8 Plastic mechanism of frame having yielding device on top of a braced support system.

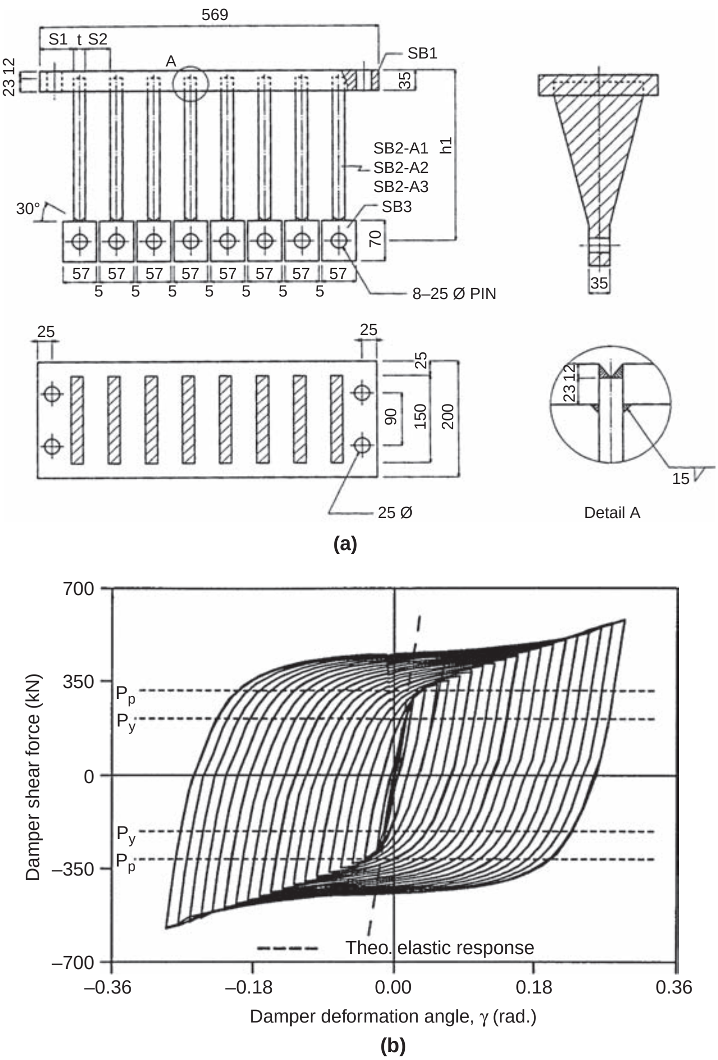

Figure 13.9 Cyclic testing of T-ADAS device: (a) details of device; (b) cyclic hysteretic behavior results. (*Courtesy of K.C. Tsai, National Taiwan University, Taipei.*)

engineering principles, neglecting shear deformations, with stiffness and strength scaled by the number of plates, N, for a device having multiple plates of identical thickness (Tsai et al. 1993). The elastic stiffness, k_e, of the T-ADAS element is given by:

$$k_e = \frac{Ebt^3N}{6h^3} = \frac{NEb}{6}\left(\frac{t}{h}\right)^3 \tag{13.2}$$

where E is Young's modulus, b is the base width of the plate, t is the thickness of the plate, and h is the height of the plate. The yield strength, V_y, of the T-ADAS element is equal to:

$$V_y = \frac{F_y bt^2N}{6h} \tag{13.3}$$

where F_y is the steel yield stress. The corresponding yield lateral displacement, Δ_y, is given by:

$$\Delta_y = \frac{F_y h^2}{Et} \tag{13.4}$$

where all terms are defined above. The yield rotational angle, γ_y, is defined as the yield lateral displacement divided by the height of the plate:

$$\gamma_y = \frac{F_y h}{Et} \tag{13.5}$$

The plastic strength, V_p, of an N-plate ADAS element is equal to:

$$V_p = \frac{F_y bt^2N}{4h} \tag{13.6}$$

Likewise, the mechanical characteristics of an X-plate ADAS device can be similarly obtained, with all parameters as defined above, noting that h here is the height of the entire X-plate, and that twice the shear force is required to yield the same cross-section in double curvature.

Correspondingly, the elastic stiffness, yield strength, yield displacement yield rotational angle, and plastic strength of an ADAS device are respectively given by:

$$k_e = \frac{2Ebt^3N}{3h^3} = \frac{2NEb}{3}\left(\frac{t}{h}\right)^3 \tag{13.7}$$

$$V_y = \frac{F_y bt^2N}{3h} \tag{13.8}$$

$$\Delta_y = \frac{F_y h^2}{2Et} \tag{13.9}$$

$$\gamma_y = \frac{F_y h}{2Et} \tag{13.10}$$

$$V_p = \frac{F_y b t^2 N}{2h} \tag{13.11}$$

Triangular plate systems can be conveniently designed to provide a wide range of combinations of strength, stiffness, and yield displacements (yield rotational angle) by judicious selection of the number of plates, as well as their length, width, and thickness. In particular, the preceding equations show that reducing the height-to-thickness ratio (h/t) rapidly increases stiffness of the device.

Similar unidirectional concepts that instead rely on yielding under deformations in the plane of the steel plate can also be found in the literature. For example, the double-curvature "honeycomb damper" shown in Figure 13.10 has been implemented in buildings in Japan (Kajima 1991). Another approach relying on combined shear and flexural yielding has been studied by El-Bahey and Bruneau (2010a, 2010b).

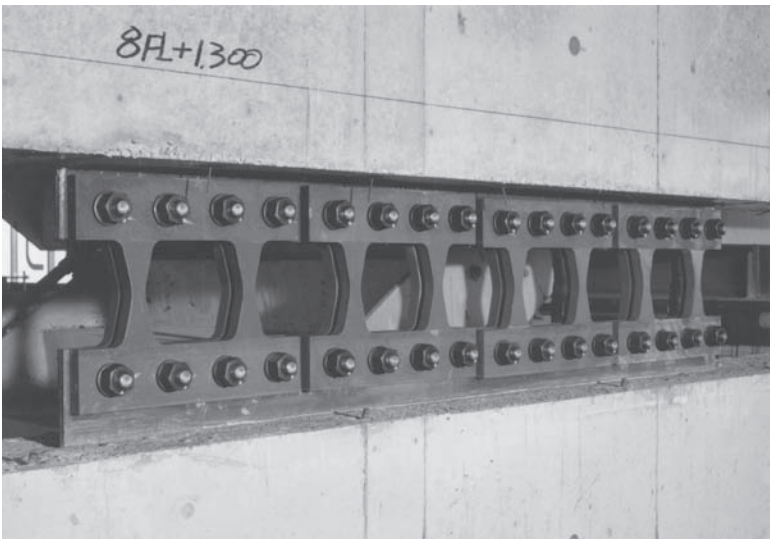

(a)

Figure 13.10 Kajima Honeycomb system: (a) implementation in Japan; (b) schematic showing loading direction; (c) typical hysteretic behavior. (*Courtesy of Kajima Corporation, Tokyo, Japan.*)

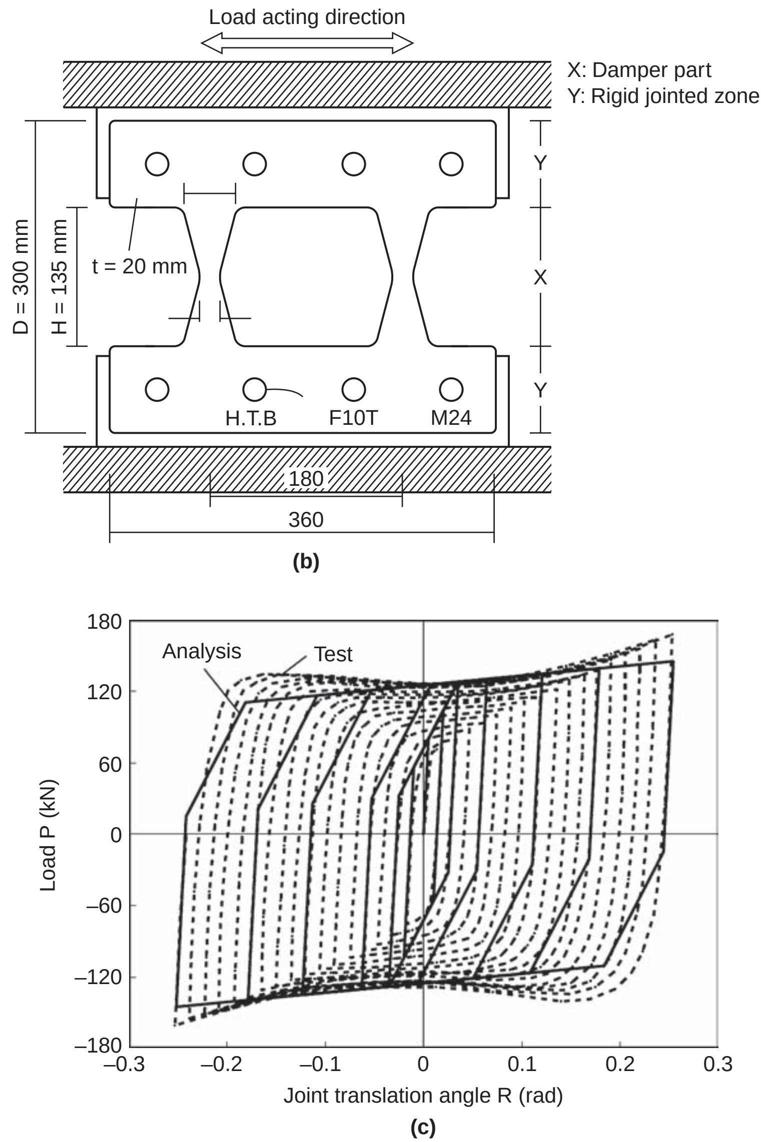

Figure 13.10 (*Continued*)

13.2.3 Tapered Shapes

Combining the idea of cross-section properties varying to follow the moment diagram, together with the concept shown in Figure 13.2c, some proprietary devices have been developed with single-taper or double-taper bars behaving, respectively, in single or double curvature when subjected to bidirectional excitations (sometimes called omnidirectional devices in the literature, but referring to arbitrary displacements within a plane). A single taper device is shown in Figure 13.11a, together with its corresponding force-displacement hysteretic curve (Figure 13.11b). Figures 13.11c and d show a ring of double-tapered bar implemented in a specific type of seismic isolation bridge bearing in conjunction with a detail that only engages the energy dissipators during earthquake excitations, to prevent their fatigue under service condition. A typical implementation is shown in Figure 13.11d. Other proprietary tapered bar systems have also been developed and implemented in Japan (Kajima 1991).

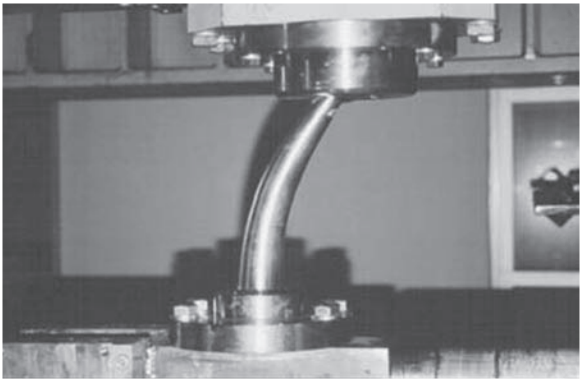

(a)

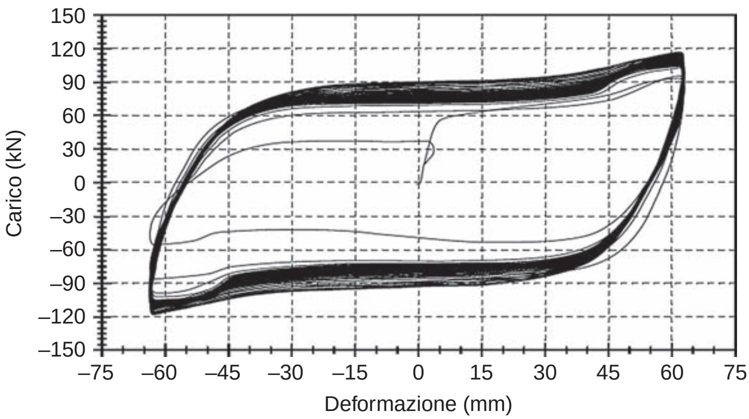

(b)

Figure 13.11 Tapered bar for energy dissipation: (a) test of a single-taper bar; (b) corresponding hysteretic behavior; (c) seismic isolation bridge bearing having an array of double-taper bars, shown during testing under differential horizontal movements; (d) implementation of isolator in a bridge in Oregon. (*Courtesy of FIP Industriale.*)

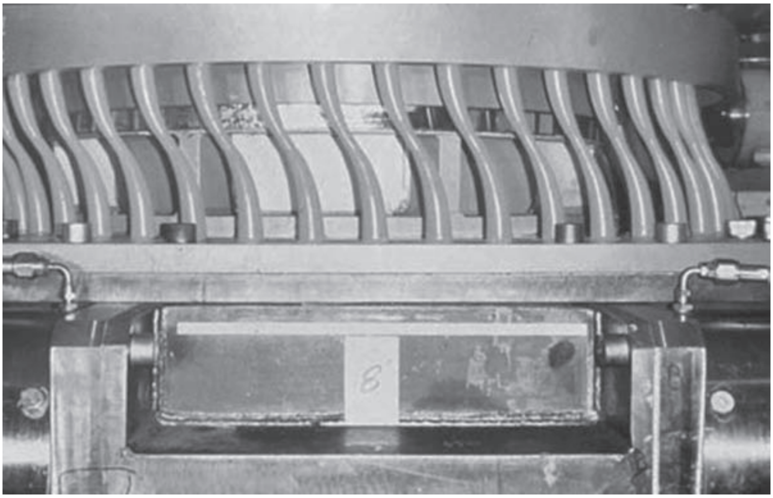

(c)

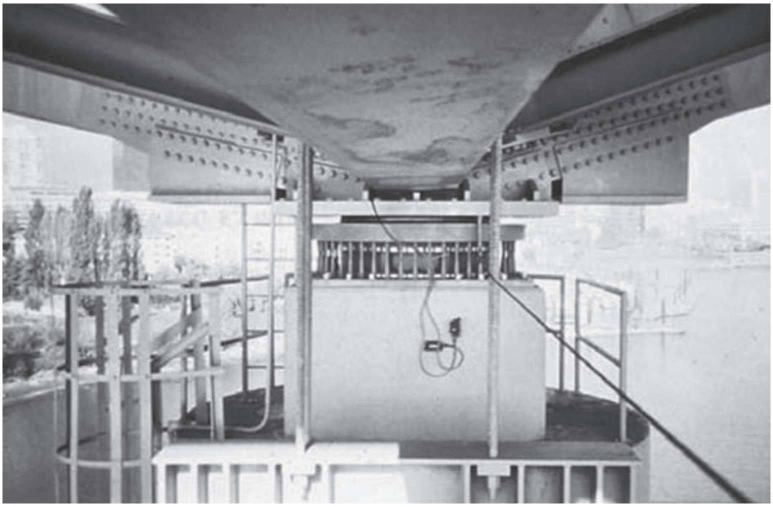

(d)

Figure 13.11 (*Continued*)

13.2.4 C-Shaped and E-Shaped Devices

Proprietary C-shaped (a.k.a. crescent-shape) hysteretic members have also been developed. Their variable cross-section and semicircular shape of constant radius, r, are designed to achieve uniform plastification over the entire member length (Castellano et al. 2009; Marioni 1997, 2000). Deformations of an individual C-shaped member, shown in Figures 13.12a and b during testing, can be substantial, with angular opening of 180° or more in extreme conditions. The corresponding hysteretic behavior is shown in Figure 13.12c. Casarotti (2004) has presented equations that describe the behavior of the elements. Note that in addition to large flexural

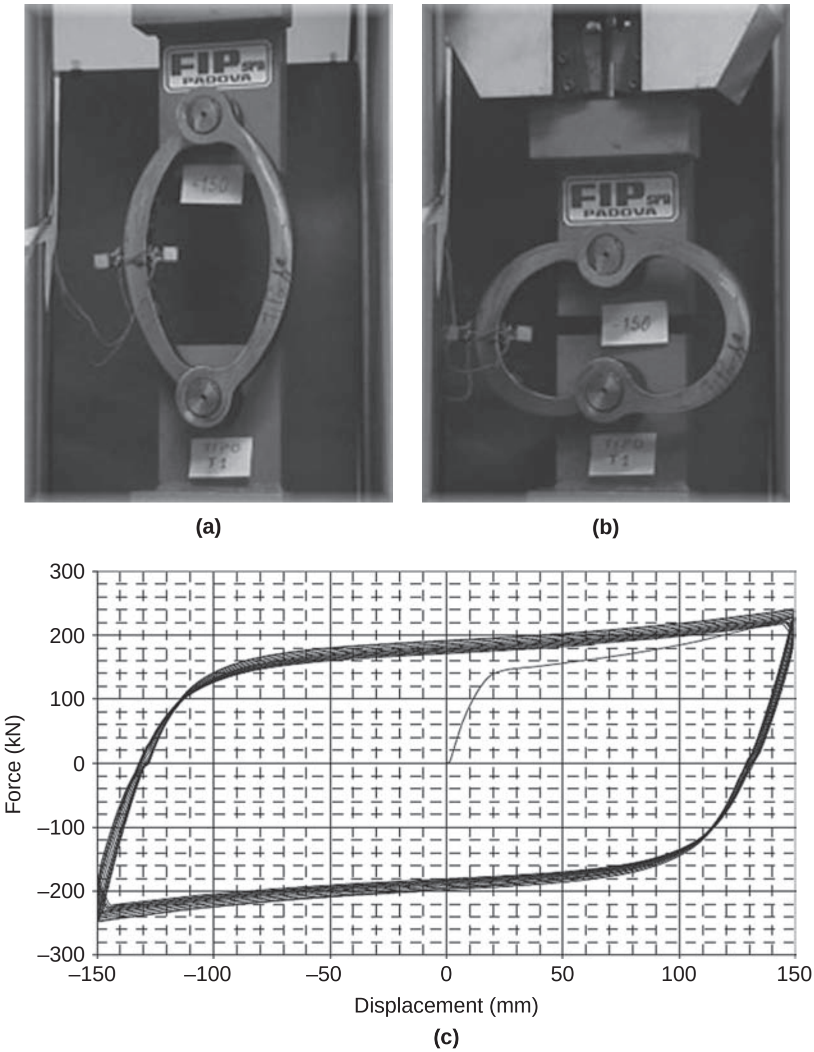

FIGURE 13.12 C-shaped energy dissipation elements: (a) tested in tension; (b) tested in compression; (c) corresponding hysteretic behavior; (d) implementation of multiple elements in a seismic base isolation device. (*Figures a, b and c, courtesy of FIP Industriale—designed, patented, manufactured and tested by FIP Industriale; Figure d, Courtesy of AIGA—designed, patented, manufactured and tested by ALGA.*)

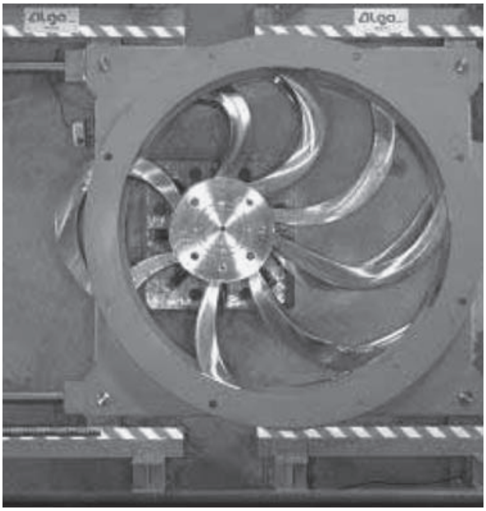

(d)

Figure 13.12 (*Continued*)

strains, these members are also subjected to substantial axial forces; for that reason, they are usually used in configurations that pair each compression element with a tension counterpart. A base-isolation device constructed with an array of such C-shaped elements is shown in Figure 13.12d in its off-center deformed configuration (Ciampi and Marioni 1991). Again, in such bridge implementations, shock transmission devices are also integrated into the system to ensure that creep, shrinkage, and displacements caused by temperature can be accommodated, but that the device is engaged during rapid movements such as during an earthquake. Ghasemi et al. (2000) and Roussis et al. (2002, 2003), investigating the failures of such bearings in a bridge during a large earthquake, demonstrated the importance of properly estimating the displacement demands on any hysteretic energy dissipation systems whose satisfactory performance is only possible up to a given displacement.

A variant of these devices, known as E-devices, also have been developed. Experimental results on the typical behavior of such devices in a bridge-bearing application are available in Ciampi and Marioni (1991) and Tsopelas and Constantinou (1997).

A number of alternative ductile hysteretic energy dissipation systems have also been proposed for implementation as primary load-resisting systems in frames, such as a disposable knee brace system yielding in either shear or flexure (e.g., Aristizabal-Ochoa 1986; Balendra et al. 1990, 1994; Sam et al. 1995) and vertical links yielding in shear (e.g., Fehling et al. 1992, Ghobarah and Elfath 2001; Nakashima 1995, Zahrai and Bruneau 1999b), to name a few. Because of space constraints, it is not possible to illustrate and provide design details on all possible systems, or even list all the concepts that have been developed over the years. However, the sample strategies described above hint at the breadth of possible design strategies and structural fuses concepts relying on hysteretic energy dissipation.

13.3 Energy Dissipation Through Friction

Although energy dissipation through friction is not per se a ductile behavior attributable to the plasticity of steel, various structural steel systems that rely on friction for hysteretic behavior have been proposed and sometimes implemented in buildings. The repeatability and smoothness of the hysteretic curves generated by friction, as well as the amount of energy dissipated for a given displacement amplitude, naturally depend, among many things, on the finishes of the materials that are sliding with respect to each other, the magnitude of the clamping pressure keeping them in contact, and the method used to apply that pressure more or less uniformly. In spite of the excellent hysteretic behavior exhibited by a few friction-based systems, applications have been limited, partly because of lingering concerns over the risk of: (1) potential fusion of the surfaces in contact over long periods without movement, either because of cold-welding (AWS 1991, Messler 1999) or, more commonly, due to corrosion; (2) degradation of the friction properties during repeated cycles as debris are ground off the surfaces in contact; and (3) possible loss of pretension when friction-induced heat expands the volume of the plates in contact and stretches the bolts that clamp them, or alternately when plate thickness is lost because of wear. More information on those topics can be found in Soong and Constantinou (1994) and Constantinou et al. (1999). Also, as a consequence of their design configuration, many friction-based systems only allow sliding up to a predetermined displacement limit, which requires conservative estimates of the maximum displacement demands to accordingly detail the friction device.

Studies for seismic-resistant implementations in steel structures have focused on macrobehavior observed experimentally rather than approaches based on tribology or nano-tribology principles. Generally, nonlubricated friction surfaces have been considered for implementation in structures. Experimental investigation of dynamic hysteretic friction for implementation in steel structures appeared in the early 1980s, considering steel-on-steel as well as other surfaces (Pall et al. 1980, Takanashi et al. 1981)—although analytical studies investigating the benefit of friction (a.k.a. "coulomb damping") to dissipate seismic energy had been published before then (e.g., Keightley 1977). Out of the various materials considered in these studies, shown in Figure 13.13, brake lining pads sandwiched between steel plates

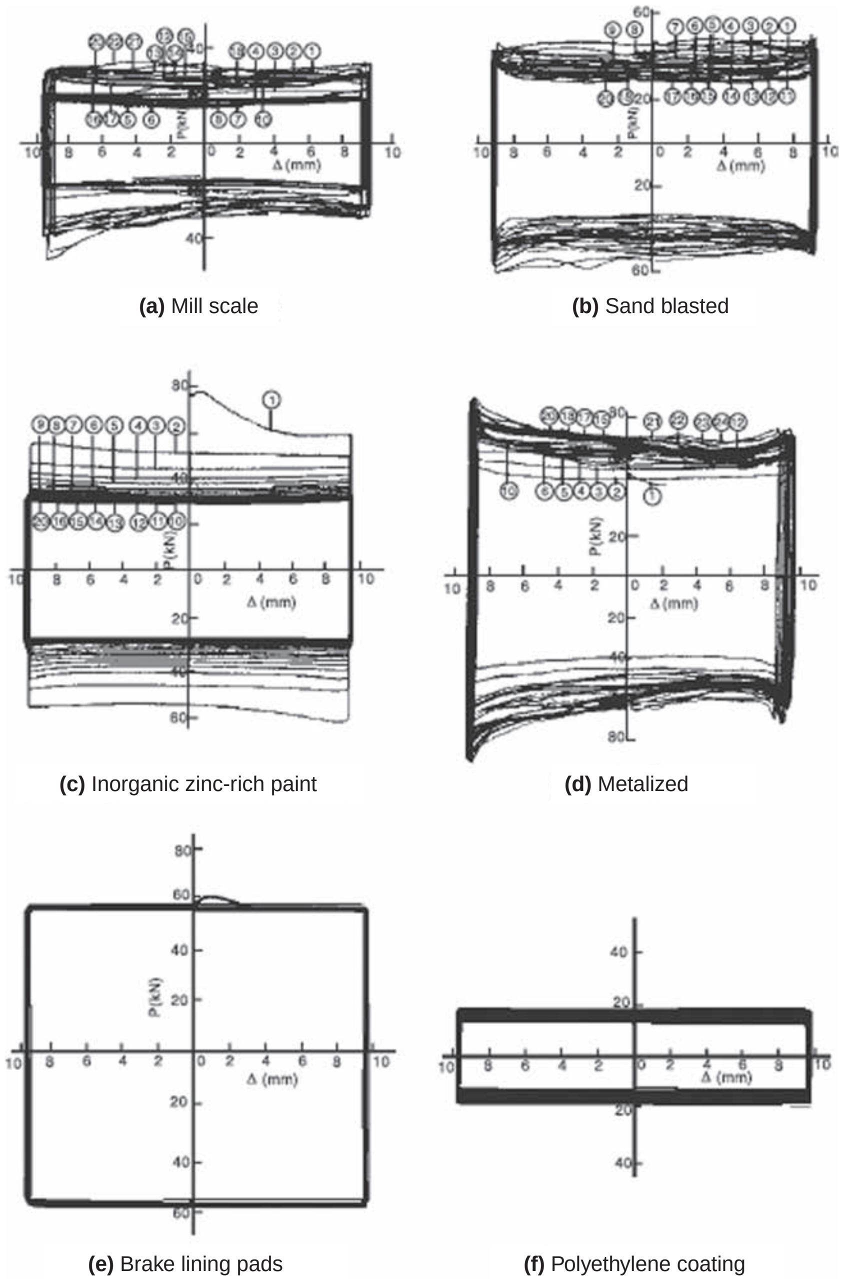

(a) Mill scale

(b) Sand blasted

(c) Inorganic zinc-rich paint

(d) Metalized

(e) Brake lining pads

(f) Polyethylene coating

Figure 13.13 Hysteretic curves for friction on various interfaces. (*Courtesy of A. Pall, Pall Dynamics Limited.*)

with mill-scale surfaces (Figure 13.13e) provided the most stable and repeatable hysteretic loops; steel-on-steel surfaces, even when sand-blasted, metalized, or painted, exhibited nonconstant strength over the sliding travel-distance, as well as a substantial loss of strength upon repeated cycles. From those observations, Pall and Marsh (1982) developed and patented a friction-braced system that demonstrated good energy dissipation characteristics when subjected to earthquake excitations (Filiatrault and Cherry 1987, 1988; Kelly et al. 1988).

The friction performance of bimetallic surfaces was subsequently investigated by other researchers. Multiple dynamic tests on slotted bolt connections by Tremblay (1993) and Tremblay and Stiemer (1993) confirmed that sliding connections fabricated using ordinary structural steels exhibited a highly variable slip strength, increasing upon successive reversals of slip, irrespective of bolt pretension level, bolt washer types, and material surface preparation, particularly at the frequency of applied loading likely to be encountered during earthquakes (dynamic tests were mostly conducted at 1 Hz in that study). The use of dissimilar steels at the faying surfaces somewhat enhanced performance when the difference in strength and chemical composition was substantial, but not enough to eliminate all undesirable characteristics. However, pairing annealed cobalt-based corrosion-wear resistant alloys plates with steel ones was observed to provide satisfactorily stable hysteretic behavior more manageable in a capacity design perspective. For comparison, Figure 13.14 illustrates hysteretic behaviors obtained for representative material pairings. At high frequencies of excitation, expansion of the plates caused by the heat generated by friction was found to induce significant plastic elongation of the bolts, and, unless bolts were retightened between tests, lower friction strength was measured (up to roughly 50% less) in subsequent excitations after cooling.

Simultaneously conducting experiments on slotted bolted connections, Grigorian and Popov 1994, observed highly variable behavior for steel-on-steel friction, but suitable stable hysteretic performance for brass on steel interface. Representative results are shown in Figure 13.15. A range of slip coefficients, μ, of 0.26 to 0.30 was reported for the steel bearing on brass condition.

Based on the previous experimental results, Tremblay (1993) proposed a friction-brace connection with cobalt-and-steel plates and experimentally verified its behavior in a single-story braced bent (Figures 13.16a and b). Loss of bolt pretension in that case was substantially less than previously observed, but still an issue; repeatable behavior in subsequent tests was achieved by retorquing the bolts prior to retesting.

In parallel, Yang and Popov (1995) proposed and cyclically tested a friction-based moment resisting connection with brass shims sandwiched between steel plates (Figures 13.16c and d), building on the results of Grigorian and Popov (1994) who conducted shake

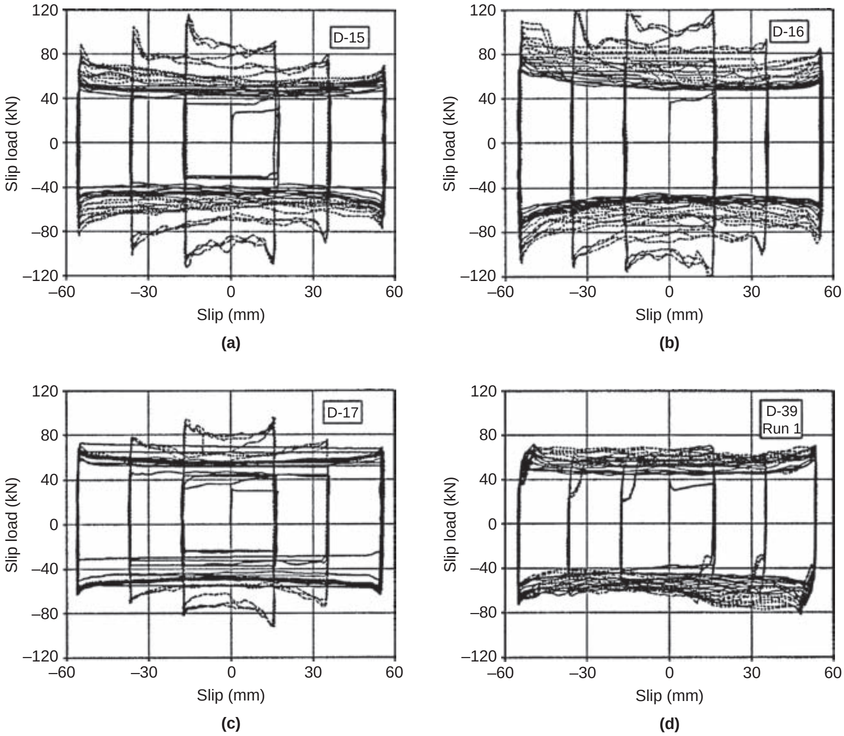

Figure 13.14 Friction hysteretic behavior of plates sliding at 1 Hz and subjected to identical bolt pretension: (a) steel plates with mill scale finish; (b) steel plates with sandblasted finish; (c) steel plates with polished finish; and (d) steel plate with mill scale finish and cobalt-chromium alloy plates. (*Courtesy of Robert Tremblay, Département des génies civil, géologique et des mines, Ecole Polytechnique, Montréal.*)

table tests of a three-story frame with braces having slotted bolt connections with brass shims. However, details to accommodate beam growth to prevent slab damage weren't investigated for that moment connection.

Solutions were not proposed either to address concerns related to bimetallic surfaces. Constantinou et al. (1999), citing experience with bridge sliding bearings, summarized a number of documented problems that have arisen for various commonly used bimetallic pairings, including: (1) increase of friction coefficient over time as the real area of contact (at the asperities) increases due to creep under load applied for a period of time before sliding (load dwell effect); (2) cold welding of steel-on-steel or bronze-on-bronze interfaces; and (3) corrosion of steel-on-steel interfaces, or of well-known galvanic couples such as steel-on-bronze (e.g., American Association of State Highway and Transportation Officials 1999, ASM 2006, British Standards Institution 1990, National Physical Laboratory 1982, Transportation Research Board 1997). As shown in Figure 13.17, although low-carbon steel can

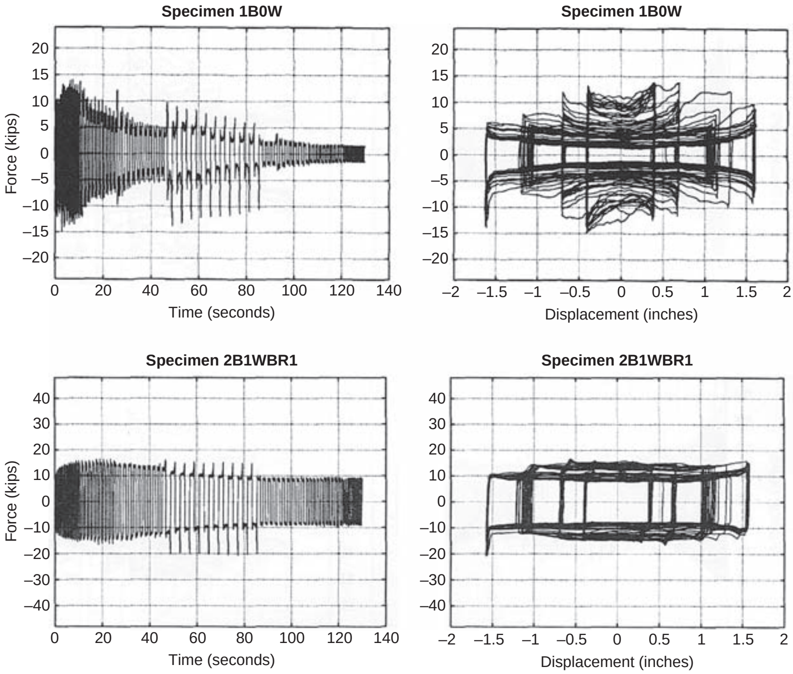

Figure 13.15 Representative results for slotted-bolted connections for steel-steel interface (top) and steel-brass interface (bottom). (*Grigorian and Popov 1994, with permission from EERC, University of California, Berkeley.*)

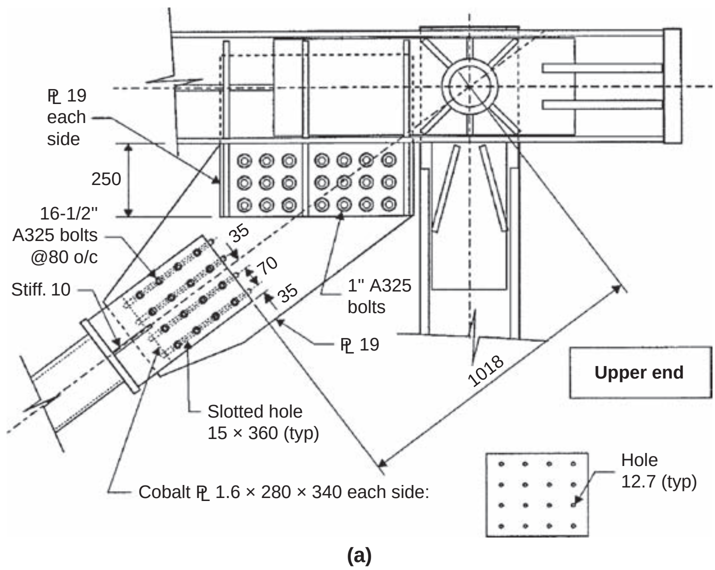

Figure 13.16 Proposed slotted bolted connections: [(a) and (b)] Tremblay (1993) axial brace connection; [(c) and (d)] Yang and Popov (1995) moment-resisting connection. (*Part a and b courtesy of Robert Tremblay, Département des génies civil, géologique et des mines, Ecole Polytechnique, Montréal; Part c and d with permission from EERC, University of California, Berkeley.*)

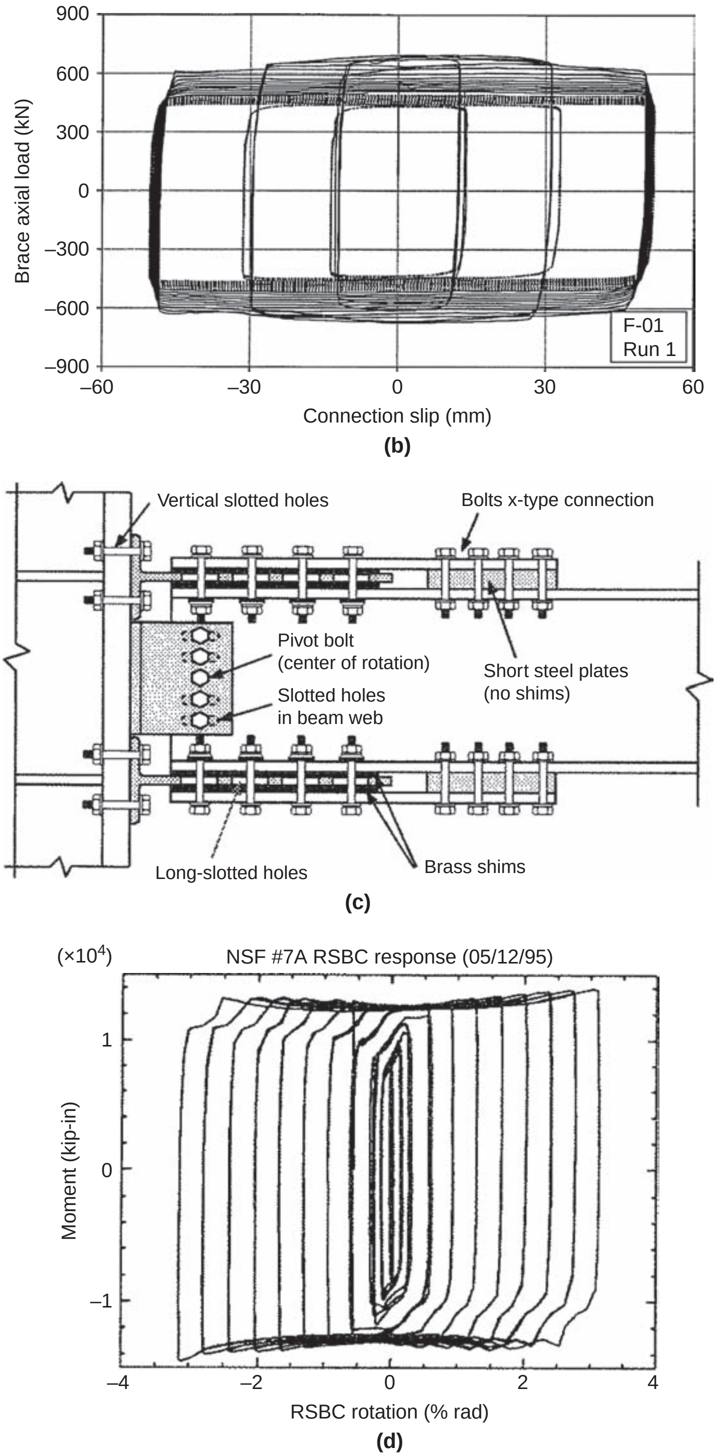

FIGURE 13.16 (*Continued*)

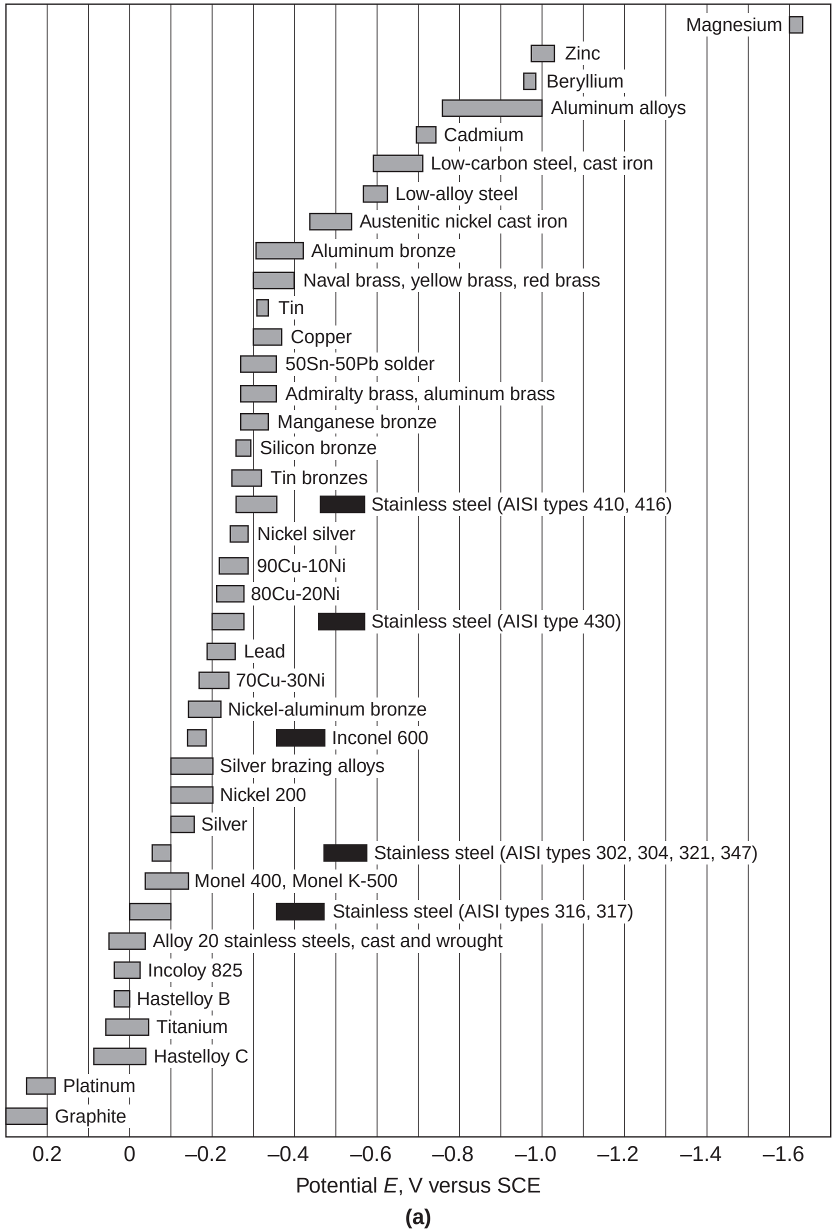

Figure 13.17 Bimetallic corrosion: (a) galvanic series for various metals in seawater—metals listed are sacrificial when paired with other metals below them; (b) schematic of sacrificial bimetallic corrosion when a coating is scratched, for selected pairings. (*Part a from R. S. Treseder, Ed., The NACE Corrosion Engineer's Reference Book, National Association of Corrosion Engineers, 1980, with permission from NACE.*)

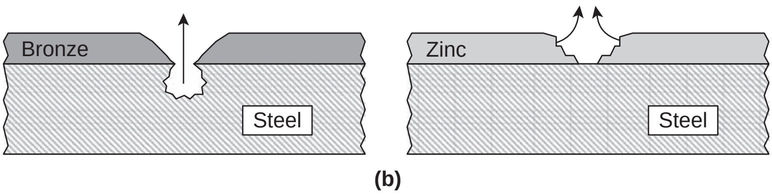

Figure 13.17 (*Continued*)

be a noble material protected by zinc as an active sacrificial material (through hot-dipped zinc galvanizing for example), constructional steel becomes the active sacrificial metal when paired with brass or bronze (ASM 2006). A legitimate question remains as to how fast some of these reported problems develop when only exposed to atmospheric humidity.

Energy dissipating systems have nonetheless received continued attention. Chi and Uang (2000) conducted dynamic and static tests on 20 slotted-brace connections using steel-steel, steel-brass, and brake liner friction surfaces, to determine usable friction coefficients and overstrength factors. In all cases, friction coefficients measured were below published values, and measured overstrength factors ranged from 1.16 for brake linings, to 1.54 for brass shims, to 2.7 or 4.0 for steel shims, for respective selected friction coefficients of 0.4, 0.3, and 0.6 or 0.4. Kim et al. (2004) reported that the asbestos heavy-duty brake lining pads of the type considered by Pall and Marsh (1982) were no longer being produced, and investigated the behavior of various nonasbestos organic composites (NAO) on mild-steel and stainless steel interfaces. NAO are composites of resin, fiber-reinforcement, friction modifiers, solid lubricant, abrasive, as well as organic and inorganic filler materials (Eggleston 2000). As partly shown in Figure 13.18, NAO with low initial friction coefficients (on the order of 0.14) were found to have superior hysteretic performance over higher friction ones (of 0.5, as measured by the brake lining quality test procedure of SAE 1997), with stable and repeatable behavior, particularly when paired with Type 304 chromium-nickel alloy stainless steel plates and specially detailed recesses to keep the lining pads in place, regardless of the number of bolts used (to apply a more uniform contact pressure) and the applied loading protocol.

Improving on the concept by Yang and Popov (1995), a sliding hinge joint (SHJ) concept developed by Clifton (1996, 2005) has been implemented in buildings in New Zealand (Gledhill et al. 2008). In this concept, a calculated clearance is left between the beam's end and the column flange to which the beam's top flange is connected by

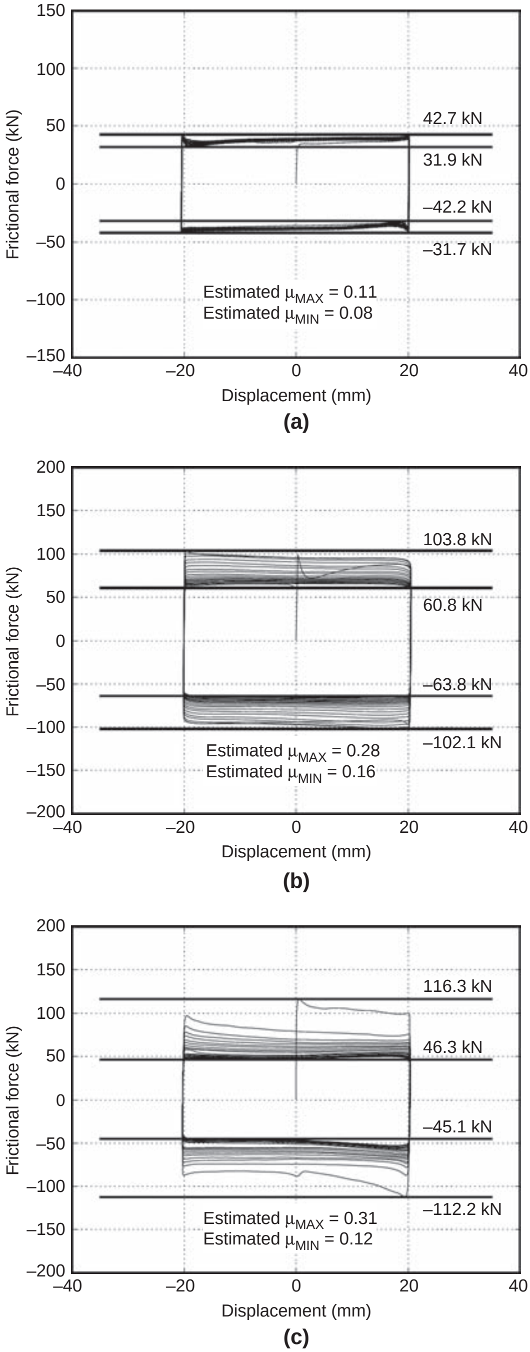

FIGURE 13.18 Friction hysteretic curves for 20 cycles at 0.17 Hz for NOA liners having low (cases a and d for grade NF-916) or high initial friction coefficient (cases b and e for grade NF-780, cases c and f for grade NF-336), with interface to sandblasted steel surfaces (cases a, b, c) or stainless steel (cases d, e, f). (*Courtesy of C. Christopoulos, Department of Civil Engineering, University of Toronto.*)

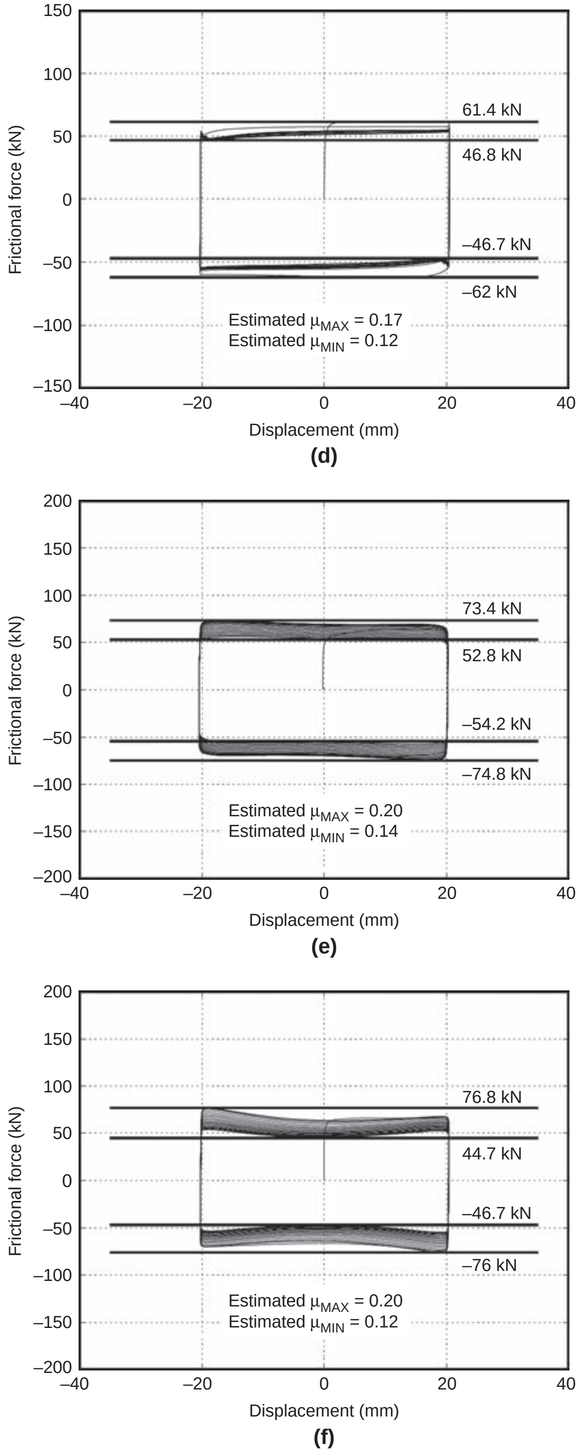

Figure 13.18 (*Continued*)

a bolted top flange plate. Hinging in that plate at the column face allows rotation of the entire beam connection about that point, minimizing the influence of the floor slab on the connection and system response. Layers of shims are inserted (as in a "double-decker sandwich") between the beam's bottom flange, a plate extending from the column flange, and a "floating plate" as shown in Figure 13.19. Slotted holes are used in the bottom flange plate which extends from the column face below the beam bottom flange. A similar sandwiching concept is used to connect the web. This configuration allows

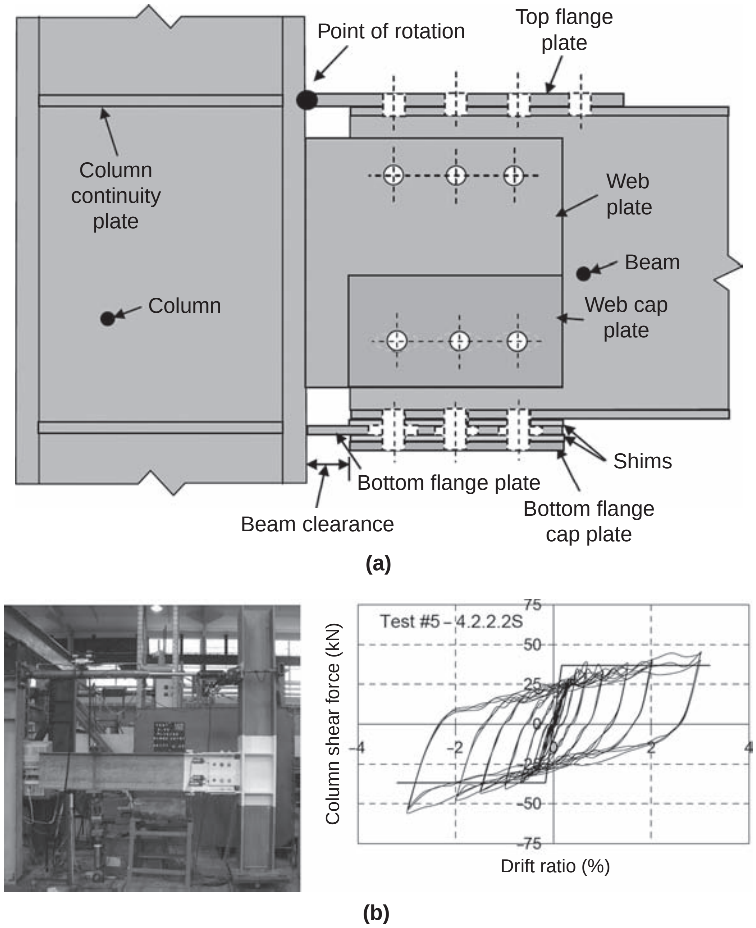

FIGURE 13.19 Sliding Hinge Joint concept: parts of the joint (a); experimental results (b); and schematics illustrating only behavior on bottom flange for simplicity (c). (*Courtesy of Professors Gregory MacRae, University of Canterbury, New Zealand, and Charles Clifton, University of Auckland, New Zealand.*)

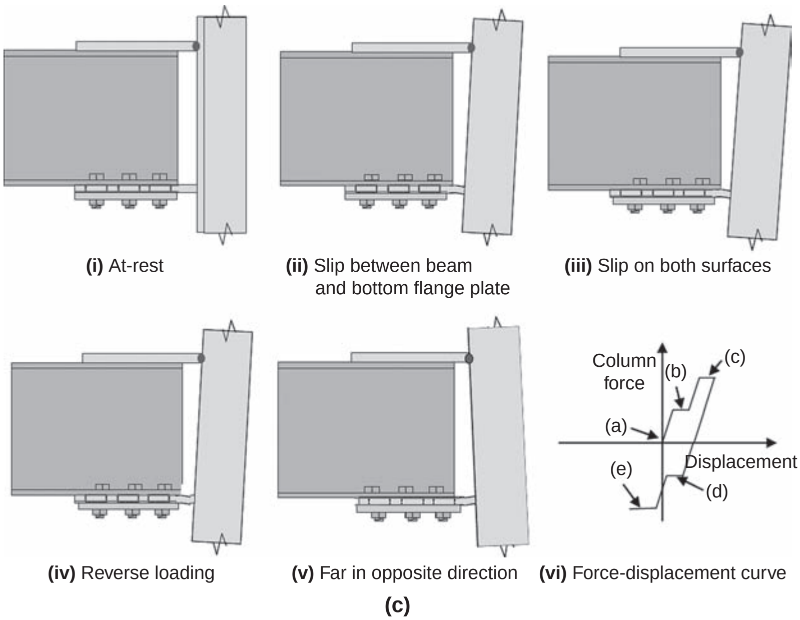

Figure 13.19 (*Continued*)

double the friction force that would be otherwise obtained. Clifton used brass shims for the original joint development, however MacRae et al. (2007) experimentally verified the connection's hysteretic behavior using steel shims as an alternative and schematically illustrated (in a decoupled way) the mechanisms that contributed to the observed response (Figure 13.19). Mechanisms of the shear-flexure interaction demands on the bolts of that connection, and their corresponding pretension loss upon repeated cycles (reducing their effectiveness in compressing the plates), as well as many other aspects that drive the fundamental behavior of this connection also have been investigated (Clifton et al. 2007). An advantage of this connection is that it is free of beam growth, and therefore does not require special details to prevent slab damage.

Recognizing the previously cited concerns, studies underway at the time of this writing are investigating the severity of corrosion, cold welding, and other issues for this type of connection in representative service conditions, as well as the influence of alternative bolts and shims on the strength and stiffness of the joint after it has undergone ultimate limit state design level rotations. This work also incorporates development of mechanisms to make the joint actively self-centering following the design level ultimate limit state event (Gregory MacRae, University of Canterbury, personal communication, March 2010; Charles Clifton, University of Auckland, personal communication, June 2010.)

13.4 Rocking Systems

Rocking in this section refers to the temporary uplifting of an element from its base (or the element below it) in an overturning motion. A considerable body of literature exists on the rocking response of various types of rigid or flexible structures and structural elements during earthquake excitations, at least going back to Housner (1963) who observed that, "the stability of a tall slender block subjected to earthquake motion is much greater than would be inferred from its stability against a constant horizontal force." Rapidly, researchers considered structural flexibility in assessing the seismic response of rocking structures (Meek 1975) and multi-degree-of-freedom uplifting structures on flexible foundations (Psycharis 1982).

Large-scale shake-table experiments of rocking structures have also been performed. Kelley and Tsztoo (1977) tested an approximately half-scale three-story steel frame that was designed with base connections to prevent horizontal movement, and mild steel torsionally yielding bars used as energy dissipating devices at the uplifting location, demonstrating superior response in terms of base shear compared with a same frame with a nonuplifting fixed base. Priestley et al. (1978) tested a simple SDOF model subjected to various dynamic excitations, to validate a proposed design equation to predict maximum rocking displacement. Toranzo et al. (2001) tested a rocking wall system for buildings that used steel flexural yielding elements placed at the uplifting locations to increase lateral strength and provide energy dissipation. Midorikawa et al. (2003) experimentally examined the response of a steel braced frame allowing uplift at column bases and yielding of specially designed base plates. Pollino and Bruneau (2007, 2010a, 2010b) formulated a rocking design procedure for bridge piers and verified its adequacy by shake table testing of tall specimens, with and without energy dissipating devices at their base, subjected to multidirectional earthquake excitations. Eatherton et al. (2008, 2009) tested pairs of braced frames linked by energy dissipating elements. In all cases, rocking about the base of the structure allowed to limit the maximum force transmitted to the structure, akin to seismic base isolation.

A few bridges currently exist in which rocking of the piers during earthquakes has been allowed, to achieve satisfactory seismic resistance. The South Rangitikei Rail Bridge, in New Zealand, was designed and constructed in the 1970s with pier legs allowed to uplift under seismic loads (Priestley et al. 1996). The North approach of the Lions' Gate Bridge, in Vancouver, British Columbia was seismically upgraded during the 1990s using a rocking approach for seismic resistance that implemented flexural yielding steel devices at the anchorage interface to control response (Dowdell and Hamersley 2000). The engineers utilized a three-dimensional nonlinear dynamic time-history model of the approach spans for prediction of maximum displacements and forces. The benefits of allowing partial uplift of the legs of bridge piers also have been recognized and adopted for the retrofit of the Carquinez Bridge (Jones et al. 1997), the Golden Gate Bridge (Ingham et al. 1997), and the San Mateo-Hayward Bridge (Prucz et al. 1997), all in California. Note that pier E17 of the San Francisco-Oakland Bay Bridge rocked during the Loma Prieta earthquake (Housner 1990). Rocking braced frames have also been implemented in buildings in New Zealand, in one case relying on Ringfeder friction springs installed at the column bases to control the amplitude of the frame leg uplifts (Gledhill et al. 2008).

Exhibiting similar behavior to rocking structures, are structures in which post-tensioned strands tying the top of the columns to their foundations provide a significant restoring force to recenter the structure, instead of gravity alone (for bridge applications, see Mander and Cheng 1997, Marriott et al. 2006, and Palermo et al. 2005, to name a few). However, such post-tensioned systems may be unnecessary in steel structures because steel columns easily resist tension forces and only need be tied at their base (as in the Gledhill et al. 2008 case, for example).

The hysteretic curves obtained from a controlled-rocking system are "flag-shaped" (Figure 13.20). Equations that describe this behavior are presented below, for the case of a two-legged bridge pier free to rock and having BRBs at the base to provide energy dissipation (Pollino and Bruneau 2007); the BRBs are considered here to behave elasto-plastically and are assumed to be implemented vertically such that they do not transfer horizontal shear at the base of the pier. Similar equations can be derived for any other chosen type of energy dissipation device.

The equations following are expressed in terms of fixed-base lateral stiffness of the existing steel truss pier (k_o); the width-over-height aspect ratio of the pier (d/h); and the cross-sectional area, effective length, and yield stress of the BRB (A_{ub}, L_{ub}, F_{yub}). The weight reacting to horizontally imposed accelerations and the vertical gravity weight carried by a pier are assumed equal and expressed as w.

The model considers motion of the pier in a direction orthogonal to the bridge deck and assumes no interaction with other piers or abutments through the bridge deck. Also, the existing anchorage connection is assumed to provide no resistance to vertical movement but is able to transfer the horizontal base shear. Note that response of an actual bridge, depending on the case at hand, may also be affected by behavior of the entire bridge system in the longitudinal and transverse directions including each pier's and abutment's properties, bridge deck properties, and the connection details between the deck and piers.

The various steps and physical behaviors that develop through a typical half-cycle are shown in Figure 13.20. By symmetry, the process repeats itself for movement in the other direction. Transition from 1st to 2nd cycle response occurs when the BRBs yield in compression and the braces carry a portion of the weight after the

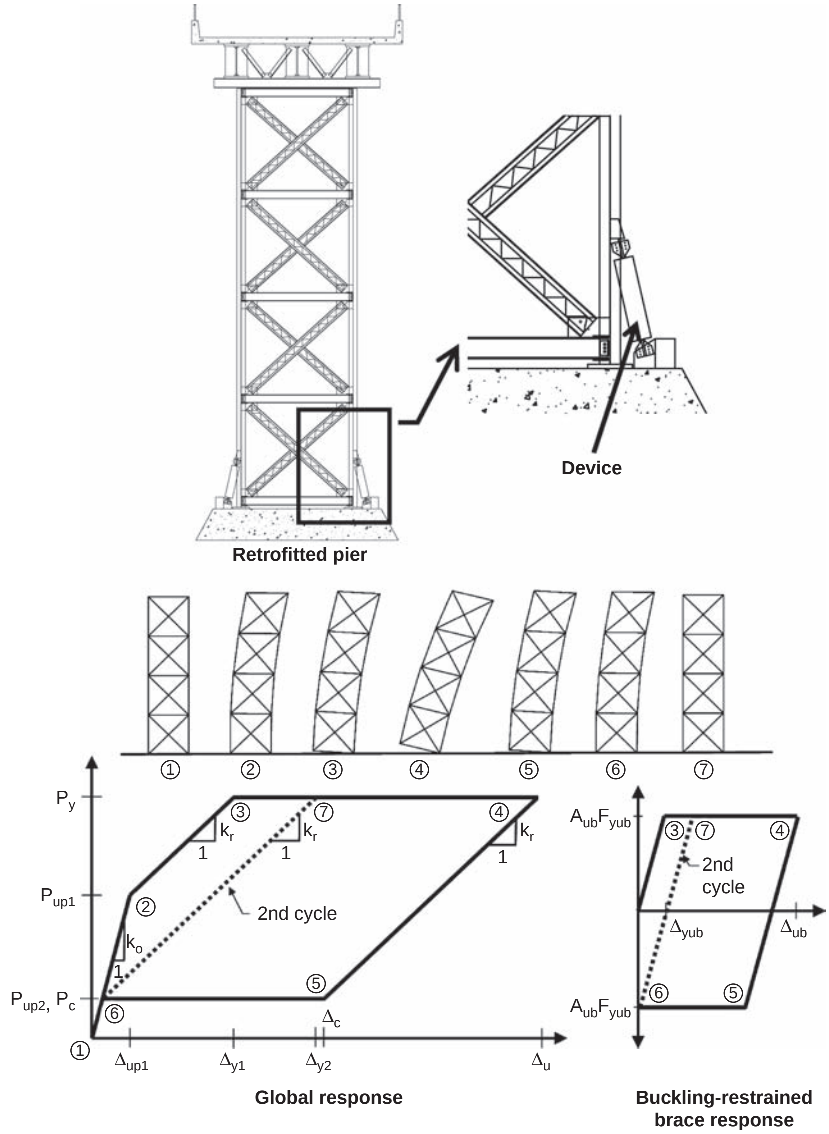

Figure 13.20 Controlled rocking of bridge tower: (a) schematic and location of energy dissipation device adjacent to columns free to uplift; (b) hysteretic behavior. (*Pollino and Bruneau 2004, Courtesy of MCEER, University at Buffalo*.)

system comes to rest upon completion of the cycle (Pollino and Bruneau 2007).

During 1st cycle response, the horizontal load applied at the top of the pier, P, as a function of the lateral displacement, Δ, before uplift begins, consists of the elastic stiffness of the pier's structural members, defined by the initial force-displacement relationship:

$$P = k_o \Delta \qquad \text{and} \qquad k_o = \frac{P}{\Delta} \tag{13.12}$$

Uplifting of a tower leg begins when the restoring moment created by the tributary vertical bridge weight is overcome by the applied moment (position 2 in Figure 13.20). The horizontal force at the point of uplift during the 1st cycle is defined by:

$$P_{up1} = \frac{w}{2}\left(\frac{d}{h}\right) \tag{13.13}$$

and the displacement at the point of uplift in the 1st cycle is defined by:

$$\Delta_{up1} = \frac{P_{up1}}{k_o} \tag{13.14}$$

After uplift, the BRB attached to the uplifting leg is activated. The global stiffness is reduced and becomes a function of the pier's lateral stiffness, k_o, and the uplifting BRB's contribution to the horizontal stiffness. The structural stiffness from uplift to the yield point (step 2 to 3 in Figure 13.20) is defined here as the elastic rocking stiffness and is expressed by:

$$k_r = \left(\frac{1}{k_o} + \frac{1}{\dfrac{EA_{ub}}{L_{ub}}\left(\dfrac{d}{h}\right)^2}\right)^{-1} \tag{13.15}$$

The horizontal force at the onset of brace yielding, P_y, and thus the structural system yield strength is defined by:

$$P_y = \left(\frac{w}{2} + A_{ub}F_{yub}\right) = \frac{w}{2}\left(\frac{d}{h}\right)(1 + \eta_L) \tag{13.16}$$

where η_L is defined here as the system's local strength ratio equal to:

$$\eta_L = \left(\frac{A_{ub}F_{yub}}{w/2}\right) \tag{13.17}$$

The corresponding system yield displacement for the first cycle, Δ_{y1}, is defined as:

$$\Delta_{y1} = \left(\frac{w}{2k_o} + \frac{A_{ub}F_{yub}}{k_r}\right)\left(\frac{d}{h}\right) = \frac{w}{2}\left(\frac{d}{h}\right)\left(\frac{1}{k_o} + \frac{\eta_L}{k_r}\right) \tag{13.18}$$

Ignoring strain hardening in the brace and any second-order effects, the system has zero postelastic stiffness and is deformed to its ultimate displacement (Δ_u). As the horizontal load is reduced, the pier first responds elastically with stiffness k_r, and the tensile force in the BRB reduces per its initial elastic properties. The applied lateral load at the top of the pier at the point of compressive yielding of the brace, (point 5 in Figure 13.20), is defined by:

$$P_c = \left(\frac{w}{2} - A_{ub}F_{yub}\right)\left(\frac{d}{h}\right) = \frac{w}{2}\left(\frac{d}{h}\right)(1-\eta_L) \tag{13.19}$$

The corresponding displacement at this point is defined as:

$$\Delta_c = \Delta_u - \left(\frac{2A_{ub}F_{yub}}{k_o}\right)\left(\frac{d}{h}\right) - \left(\frac{2L_{ub}F_{yub}}{E}\right)\left(\frac{h}{d}\right) \tag{13.20}$$

The BRB displaces plastically in compression and again is assumed to yield with no significant stiffness until the uplifted pier leg returns in contact to its support (step 5 to 6 in Figure 13.20). At this point of contact, the system stiffness is again defined by k_o.

As a BRB yields in compression and the pier settles back to its support, the BRB effectively carries a portion of the bridge weight equal to its compressive capacity (assumed to be $A_{ub}F_{yub}$). As a result of this transfer of the gravity load path (now partially through the BRBs), a smaller horizontal force is required to initiate uplift during 2nd cycle response, causing an earlier transition from stiffness, k_o, to the rocking stiffness, k_r, thus increasing the flexibility and system yield displacement from the 1st cycle response as can be seen by the 2nd cycle curve in Figure 13.20. The horizontal force at the onset of uplift can be shown equal to P_c and is defined for the 2nd and subsequent cycles as:

$$P_{up2} = P_c = \frac{w}{2}\left(\frac{d}{h}\right)(1-\eta_L) < P_{up1} \tag{13.21}$$

The yield displacement can be expressed as:

$$\Delta_{up2} = \frac{w}{2}\left(\frac{d}{h}\right)\left(\frac{1-\eta_L}{k_o} + \frac{2\eta_L}{k_r}\right) > \Delta_{up1} \tag{13.22}$$

The yield strength of the system, P_y, is unchanged. The force in the BRB changes from its compressive strength ($A_{ub}F_{yub}$) to tension yielding

($A_{ub}F_{yub}$) for the 2nd and subsequent cycles that exceed deck level displacement of Δ_{y2}. Note that the controlled rocking bridge pier system flag-shaped hysteresis curve is due to the combination of pure rocking response from the restoring moment, provided by the bridge deck weight, and energy dissipation provided by yielding of the BRBs.

For a rocking structure not having energy dissipators, the hysteretic curve would go from point 1 to 2 in Figure 13.20, then displace horizontally at constant strength up to the point of maximum displacement (assuming small displacement theory and no instability), and travel back to points 2 and 1 upon unloading. Conversely, for a rocking structure having overly strong energy dissipators, point 5 will be below the zero force axis, and the frame will not be self-centering, rather jacking itself up on the BRBs upon repeated cycles of inelastic excursion. Finally, note that for some types of rocking structures (such as braced frames), the actual hysteretic behavior will deviate from the above curve due to dynamic effects related to the vertical shear modes of excitation of the frame (Pollino and Bruneau 2008a).

Rocking behavior can also be captured in a structural model by inserting gap elements at the rocking interface (available in most structural analysis programs), in parallel with yielding elements in the case of controlled rocking. More refined analyses are also possible to consider the effects of contact surface effects (e.g., cracking, yielding, crushing, and others) using either finite elements or macro-models (Roh and Reinhorn 2009).

13.5 Self-Centering Post-Tensioned Systems

As a variant of the above rocking systems, researchers have investigated the seismic response of steel moment frames with beams post-tensioned between columns and relying on the rocking action of the beams onto the column faces. As was the case with the previously mentioned rocking systems, structural systems using post-tensioned connections have the benefit of being self-centering after an earthquake excitation

The use of dedicated tendons to join monolithic beams and columns together and exhibit nonlinear response by connection rocking rather than hysteretic energy dissipation was apparently first considered in the pre-stressed concrete industry, in parallel with work on "damage avoidance design" strategies (Ajrab et al. 2004, Bradley et al. 2008, Cheok and Lew 1991, Holden et al. 2003, Mander and Cheng 1997, Priestley and Tao 1993, Priestley et al. 1999). Implementation in steel frames followed with various tendon configuration layouts and relying on either friction, viscous, or yielding steel devices to provide energy dissipation (Christopoulos et al. 2002a, 2002b; Garlock et al. 2005, 2007; Kim and Christopoulos 2008; Pekcan et al. 2000; Ricles et al. 2001, 2002; Rojas et al. 2005). Typical connections and hysteretic behavior are shown in Figure 13.21. These systems exhibit flag-shaped hysteretic loops similar to that shown in Figure 13.20, with some

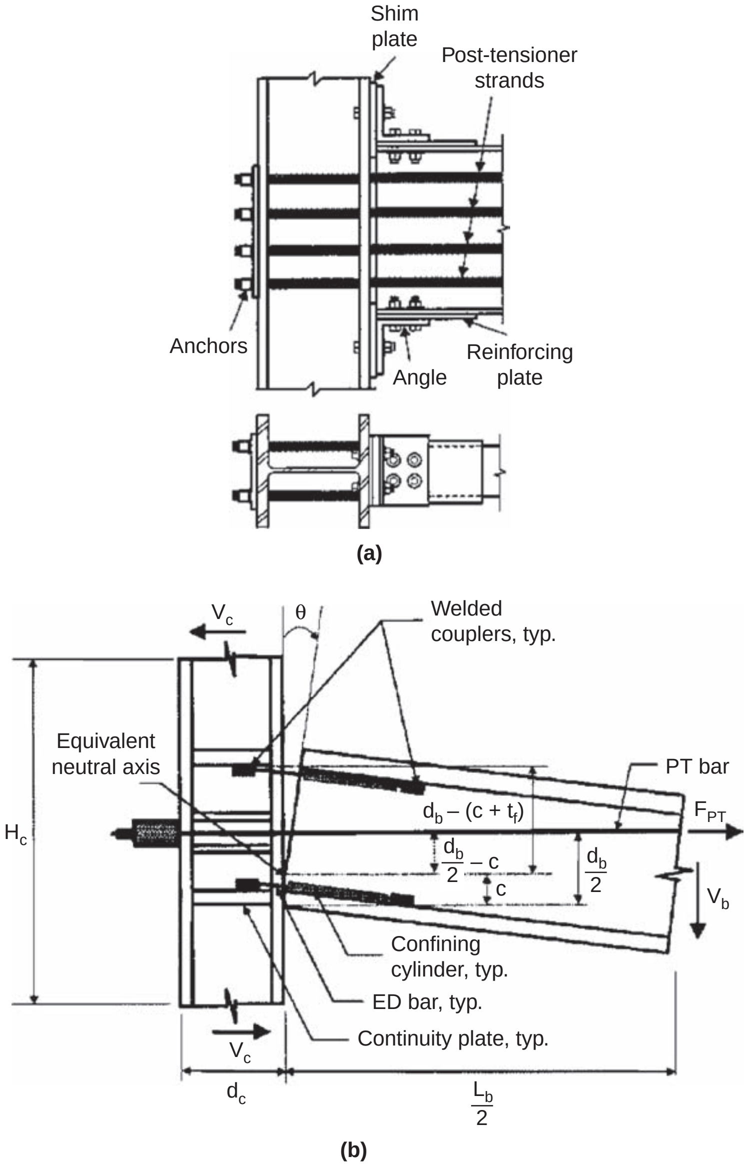

Figure 13.21 Post-tensioned rocking frame connections: (a) multistrand concept with angle yielding; (b) central-strand concept with yielding coupler bars; (c) multistrand concept with friction plates; (d) central-strand concept with friction plates. (*Figures a and c, courtesy of J.M. Ricles, Department of Civil Engineering, Lehigh University; Figures b and d, courtesy of C. Christopoulos, Department of Civil Engineering, University of Toronto.*)

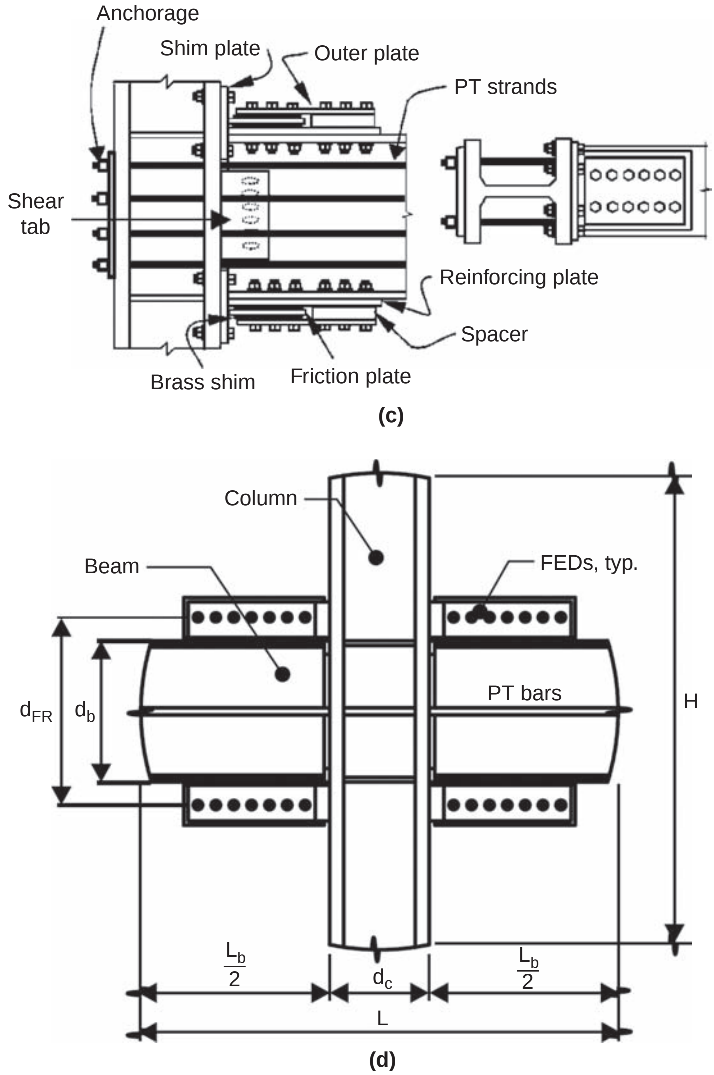

Figure 13.21 (*Continued*)

small connection-specific differences. A variant of this system is also being implemented for steel plate shear walls at the time of this writing (Berman et al. 2010). Building on this principle, but in a different configuration, a self-centering brace for use in braced frames has also been developed (Christopoulos et al. 2008, Tremblay et al. 2008).

A critical design issue that must be addressed by most of these post-tensioned frames is that the beam rocking mechanism changes the distance between columns during sway response. This would require careful special detailing of the floor system to prevent slab damage while allowing free rocking of the frames, particularly if these frames are used in both directions. Column flexibility is also required to allow rocking to develop over multiple stories, which may be difficult to achieve in tall frames having columns of substantial sizes. Alternatively, a connection detail free of beam-growth has been proposed to avoid this issue in rocking systems (Dowden and Bruneau 2011).

13.6 Alternative Metallic Materials: Lead, Shape-Memory Alloys, and Others

Dampers relying on the extrusion of lead through a constricted tube, or on the travel of a bulged shaft through a lead cylinder, have been proposed to dissipate energy during an earthquake and implemented in some structures (Cousins and Porritt 1993; Robinson and Greenbank 1975, 1976). A typical budged shaft concept is schematically shown in Figure 13.22a. Lead is typically used for this energy-dissipating purpose on account of its unique properties and low recrystallization temperature; furthermore, that material exhibits full hysteretic curves not affected by aging and with excellent low-cycle fatigue life. However, the strength developed by such devices depends on the velocity developed at the device in response to the dynamic excitations. The concept has recently received renewed attention for implementation in steel frames as part of a concept in which beams are only connected to columns by their top flanges to prevent damage to the steel frames as well as the slab (Mander et al. 2009). The concept also relies on a new generation of compact extrusion dampers having high force-to-volume ratio made possible by prestressing of the lead (Rodgers et al. 2008). The introduction of devices in connections raises many interesting new questions, including issues relating to practicing engineers' acceptance of devices to provide strength in moment frames, irrespective of velocity dependence.

As mentioned in Chapter 2, superelastic nickel-titanium (NiTi) shape-memory alloys (SMA) have also been considered by researchers for their appealing ability to recover their original shape upon unloading after plastic deformations. The applications proposed have included special passive control devices, bridge seismic restrainers, and moment-resisting connections, to name a few (e.g., Dolce et al. 2000, Desroches et al. 2004, McCormick et al. 2007, Sharabash and Andrawes 2009, Van de Lindt and Potts 2008, Wilson and Wesolowsky 2005, Youssef et al. 2008). The price premium of SMA, limited range of lengths and diameters available to meet large-scale construction needs, and questions about long-term performance, are constraints to consider in actual implementations.

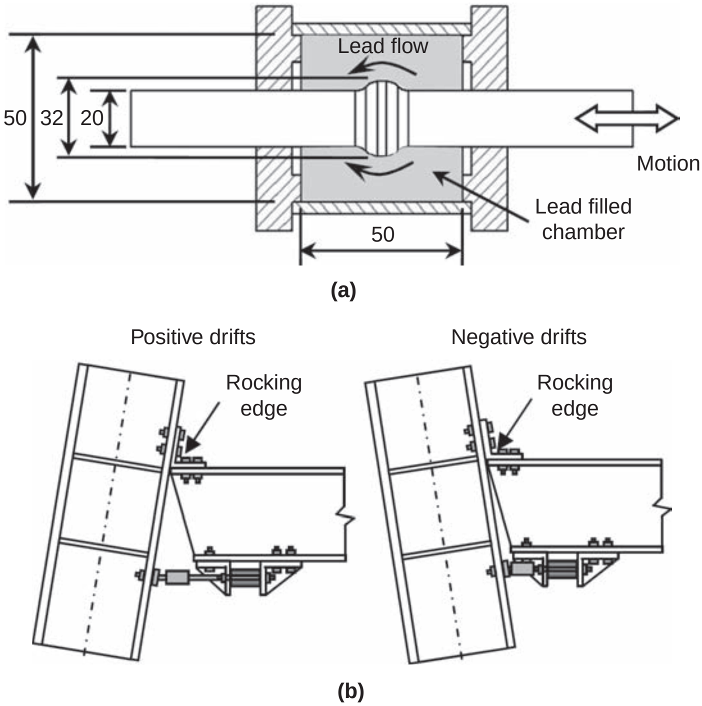

Figure 13.22 Extrusion hysteretic dampers: (a) schematic of extrusion concept; (b) proposed implementation in moment resisting frame. (*Courtesy of John B. Mander, Zachary Department of Civil Engineering, Texas A&M University*.)

Strategies relying on the use of aluminum to provide energy dissipation have also been proposed (e.g., De Matteis et al. 2007, Rai and Wallace 1998) for specialty applications. Many other metals also have desirable hysteretic behavior properties.

13.7 Validation Quantification

It is impossible to predict how emerging approaches relying on new materials or devices will evolve and which will find implementation over the next decades. Consideration of alternatives to steel will likely be driven by the constraints and economics of specific applications, as much as by expected performance objectives. However, with the increasing number of strategies proposed to achieve various objectives of seismic performance, a rigorous probabilistic-based procedure to validate the effectiveness of these solutions will be required to better inform code and standards committees, as well as building officials, and assist them in reaching final decisions.

One such procedure (FEMA 2009) has been developed to quantitatively evaluate the various seismic performance factors that are required for a new system to be considered for possible inclusion in model building codes and standards, in particular the corresponding value of the response modification coefficient (*R* factor described in Chapter 7) appropriate for such systems. Importantly, the extensive analyses required by any procedure designed for that purpose still critically depends on extensive quality experimental data to support the development of analytical models that capture the physical cyclic behavior of the structural elements considered. The reliability of results depends on the thoroughness of those models, and it is foreseen that final committee decisions, although enriched by the complementary quantitative results of systematic analyses, will continue to rely in an important way on professional judgment based on qualitative comparisons with other seismic force-resisting systems.

References

Ajrab, J. J., Pekcan, G., and Mander, J. B. 2004. "Rocking Wall-Frame Structures with Supplemental Tendon Systems." *Journal of Structural Engineering, ASCE*, vol. 130, no. 6, 895–903.

American Association of State Highway and Transportation Officials. 1999. *Guide Specifications for Seismic Isolation Design*. Washington, D. C.: AASHTO.

Aristizabal-Ochoa, J. D. 1986. "Disposable Knee Bracing: Improvement in Seismic Design of Steel Frames." *Journal of Structural Engineering, ASCE*, vol. 112, no. 17, 1544–1552.

ASM. 2006. ASM Handbook, Volume 13—Corrosion. Materials Park, OH: American Society of Metals.

AWS. 1991. "Cold welding," Welding Handbook, 8th Edition, vol. 2, *Welding Processes*. Miami, FL: American Welding Society, p. 900–908.

Balendra, T., Lim E. L., and Lee S. L. 1994. "Ductile Knee Braced Frames with Shear Yielding Knee for Seismic Resistant Structures." *Engineering Structures*, vol. 16, no. 4, 263–269.

Balendra, T., Sam, M. T., and Liaw, C. Y. 1990. "Diagonal Brace with Ductile Knee Anchor for Aseismic Steel Frame." *Earthquake Engineering Structural Dynamics*, vol. 6, no. 19, 847–858.

Basha, H. S., and Goel, S. C. 1996. "Ductile Truss Moment Frames." *Los Angeles Tall Buildings Structural Design Council, Annual Meeting*: *Modern Analysis Techniques in Practice*, Los Angeles.

Bergman, D. M., and Goel, S. C. 1987. "Evaluation of Cyclic Testing of Steel-Plate Devices for Added Damping and Stiffness." *Report UMCE 87-10*. Ann Arbor, MI: Civil Engineering Department, University of Michigan.

Berman, J, Lowes, L., Bruneau, M., Okazaki, T., and Tsai, K. C. 2010. "An Overview of NEESR-SG: Smart and Resilient Steel Walls for Reducing Earthquake Impacts." *Joint 9th US and 10th Canadian Conference on Earthquake Engineering*, Toronto, Canada, July 2010.

Boardman, P. R., Wood, B. J., and Carr, A. J. 1983. "Union House–a Cross-Braced Structure with Energy Dissipators." *Bulletin of the New Zealand National Society for Earthquake Engineering*, vol. 16, no. 2, 83–97.

Bradley, B. A., Dhakal, R. P., Mander, J. B., and Li, L. 2008. "Experimental Multi-Level Seismic Performance Assessment of 3D RC Frame Designed for Damage Avoidance." *Earthquake Engineering & Structural Dynamics*, vol. 37, no. 1, 1–20.

British Standards Institution. 1990. "Commentary on Corrosion in Bimetallic Contacts and its Alleviation," *PD 6484:1979*, BSI: London.

Carter, C. J., and Iwankiw, N. R. 1998. "Improved Ductility in Seismic Steel Moment Frames with Dogbone Connections," *Second World Conference on Steel in Construction*, Paper No. 253, Elsevier Science Ltd.

Casarotti, C. 2004. "Bridge Isolation and Dissipation Devices: State of the Art Review in Bridge Isolation, Structural Seismic Response and Modelling of Modern Seismic Isolation and Dissipation Devices." MSc Dissertation, *ROSE School*.

Castellano, M. G., Colato, G. P., and Infanti, S. 2009. "The Experience of FIP industriale in the Retrofit of Bridges through Seismic Isolation and Energy Dissipation," *Buletimul AGIR Nr*. 1-2/2009, 266–278.

Cheok, G. S., and Lew, H. S. 1991. "Performance of Precast Concrete Beam-to-Column Connections Subject to Cyclic Loading." *PCI Journal*, vol. 36, no. 3, 56–67.

Chi, B., and Uang, C. M. 2000. "Dynamic Testing of Full-Scale Slotted Bolted Connections." *Report No. TR-99/05*, La Jolla, CA: Department of Structural Engineering, University of California, San Diego.

Christopoulos, C., Filiatrault, A., and Folz, B. 2002a. "Seismic Response of Self-Centering Hysteretic SDOF Systems." *Earthquake Engineering and Structural Dyn*amics, vol. 31, no. 5, 1131–1150.

Christopoulos, C., Filiatrault, A., Uang, C.-M., and Folz, B. 2002b. "Post-Tensioned Energy Dissipating Connections for Moment-Resisting Steel Frames." *Journal of Structural Engineering, ASCE*, vol. 128, no. 9, 1111–1120.

Christopoulos, C., Tremblay, R., Kim, H.J., and Lacerte, M. 2008. "Self-Centering Energy Dissipative Bracing System for the Seismic Resistance of Structures: Development and Validation." *Journal of Structural Engineering, ASCE*, vol. 134, no. 1, 96–107.

Ciampi, V., and Marioni, A. 1991. "New types of energy dissipating devices for seismic protection of bridges," *Proc., 3rd World Congress on Joint Sealing and Bearing Systems for Concrete Structures*, Toronto, Canada. vol. 2. Buffalo, NY: National Center for Earthquake Engineering Research, p. 1225–1245.

Clifton, G. C. 1996. "Development of Perimeter Moment-Resisting Steel Frames Incorporating Semi-Rigid Elastic Joints." *New Zealand National Society for Earthquake Engineering Conference*, p. 177–184.

Clifton, G. C. 2005. *Semi-Rigid Joints for Moment Resting Steel Framed Seismic Resisting Systems.* PhD Thesis, Department of Civil and Environmental Engineering, University of Auckland.

Clifton, G. C., MacRae, G. A., Mackinven, H., Pampanin, S., and Butterworth, J. 2007. "Sliding Hinge Joints and Subassemblies for Steel Moment Frames." *Proceedings of the New Zealand Society of Earthquake Engineering Annual Conference*, Paper 19, Palmerston North, New Zealand.

Connor, J. J., Wada, A., Iwata, M., and Huang, Y. H. 1997. "Damage-Controlled Structures. I: Preliminary Design Methodology for Seismically Active Regions." *Journal of Structural Engineering, ASCE*, vol. 123, no. 4, 423–431.

Constantinou, M. C., Soong, T. T., and Dargush, G. F. 1998. "Passive Energy Dissipation Systems for Structural Design and Retrofit." *Report MCEER-98-MN01*. Buffalo, NY: Multidisciplinary Center for Earthquake Engineering Research, State University at Buffalo, 320 pages.

Constantinou, M. C., Tsopelas, P., Kasalanati, A., and Wolff, E. D. 1999. "Property Modification Factors for Seismic Isolation Bearings." *Report MCEER-99-0012*. Buffalo, NY: Multidisciplinary Center for Earthquake Engineering Research, State University at Buffalo, 180 pages.

Cousins, W. J., and Porritt, T. E. 1993. "Improvements to Lead-Extrusion Damper Technology." *Bulletin of the New Zealand National Society for Earthquake Engineering*, vol. 26, no. 3, 342–348.

De Matteis, G., Mazzolani, F. M., and Panico, S. 2007. "Pure Aluminium Shear Panels as Dissipative Devices in Moment-Resisting Steel Frames." *Earthquake Engineering and Structural Dynamics*, vol. 36, 841–859. DOI: 10.21002/eqe.

DesRoches, R., McCormick, J., and Delemont, M. A. 2004. "Cyclic Properties of Superelastic Shape Memory Alloys." *Journal of Structural Engineering, ASCE*, vol. 130, no. 1, 38–46.

Dolce, M., Donatello, C., and Marnetto, R. 2000. "Implementation and Testing of Passive Control Devices Based on Shape Memory Allows." *Journal of Earthquake Engineering and Structural Dynamics*, vol. 29, 945–968.

Dowdell, D., and Hamersley, B. 2000. "Lions' Gate Bridge North Approach: Seismic Retrofit." *Behaviour of Steel Structures in Seismic Areas: Proceedings of the Third International Conference: STESSA 2000*; Montreal, Canada, August 21-24, p. 319–326.

Dowden, D., and Bruneau, M. 2011. "NewZ-BREAKSS: Post-tension Rocking Connection Detail Free of Beam-Growth." AISC Engineering Journal, vol. 48, no. 2.

Eatherton, M., Hajjar, J. F., Deierlein, G. G., Krawinkler, H., Billington, S., and Ma, X. 2008. "Controlled Rocking of Steel-Framed Buildings with Replaceable Energy-Dissipating Fuses." *Proceedings of the 14th World Conference on Earthquake Engineering*, Beijing, China, October 12–17.

Eatherton, M., Hajjar, J. F., Deierlein, G. G., Ma, X., Billington, S., and Krawinkler, H. 2009. "Steel-Framed Rocking Structural Systems for Moderate Seismic Zones." *Proceedings of the ASCE/SEI Structures Congress 2009*, Austin, Texas, April 30–May 2. Reston, VA: ASCE.

Eggleston, D. 2000. "Automotive Friction Materials." *Technical bulletin 00010433*, Poole, UK: Precision Disc Casting LTD.

El-Bahey, S., and Bruneau, M. 2010a. "Structural Fuse Concept for Bridges." *Transportation Research Record* (a Journal of the Transportation Research Board), vol. 22, no. 1, 167–172.

El-Bahey, S., and Bruneau, M. 2010b. "Structural Fuse Concept For Bridges." *Report MCEER-10-0005*. Buffalo, NY: MCEER, State University at Buffalo, 484 p.

Fehling, E., Pauli, W., and Bouwkamp, J. G. 1992. "Use of Vertical Shear-Links in Eccentrically Braced Frames." *Proceedings of the 10th World Conference on Earthquake Engineering*, Madrid, vol. 9, 4475–4479.

FEMA. 2004. *FEMA 450 NEHRP Recommended Provisions for Seismic Regulations for New Buildings and Other Structures*. Washington, D. C.: Building Seismic Safety Council for the Federal Emergency Management Agency.

FEMA. 2009. *ATC-63 Quantification of Building Seismic Performance Factors (FEMA P-695)*, Washington, D. C.: Federal Emergency Management Agency, p. 421.

Filiatrault, A., and Cherry, S. 1987. "Performance Evaluation of Friction Damped Braced Frames Under Simulated Earthquake Loads." *Earthquake Spectra*, vol. 3, no. 1, 57–78.

Filiatrault, A., and Cherry, S. 1988. "Comparative Performance of Friction Damped Systems and Base Isolation Systems for Earthquake Retrofit and Aseismic Design." *Earthquake Engineering Structural Dynamics*, vol. 16, 389–416.

Filiatrault, A., and Cherry, S. 1989. "Parameters Influencing the Design of Friction Damped Structures." *Canadian Journal of Civil Engineering*, vol. 16, no. 5, 753–766.

Fu, Y., and Cherry, S. 2000. "Design of Friction Damped Structures Using Lateral force Procedure." *Earthquake Engineering and Structural Dynamics*, vol. 29, no. 7, 989–1010.

Garlock, M., Ricles, J. M., and Sause, R. 2005. "Experimental Studies of Full-Scale Post-Tensioned Steel Connections." *Journal of Structural Engineering, ASCE*, vol. 131, no. 3, 438–448.

Garlock, M. M., Sause, R., and Ricles, J. M. 2007. Behavior and design of post-tensioned steel frame systems. *Journal of Structural Engineering, ASCE*, vol. 133, no.3, 239–399.

Ghasemi, H., Cooper, J., Imbsen, R., Piskin, H., Inal, F., and Tiras, A. 2000. "The November 1999 Duzce Earthquake: Post-Earthquake Investigation of the Structures on the TEM." *Report No. FHWA-RD-00-146*. http://www.tfhrc.gov/structur/00-146.pdf, accessed Jul. 3, 2002.

Ghobarah, A., and Elfath, H. A. 2001. "Rehabilitation of a Reinforced Concrete Frame Using Eccentric Steel Bracing." *Engineering Structures*, vol. 23, no.7, 745–755.

Gledhill, S. M., Sidwell, G. K., and Bell, D. K. 2008. "The Damage Avoidance Design of Tall Steel Frame Buildings—Fairlie Terrace Student Accommodation Project, Victoria University of Wellington." Paper 63, *Proceeding of the 2008 Annual Conference of the New Zealand Society for Earthquake Engineering*, Wairakei New Zealand.

Grigorian, C. E., and Popov, E. P. 1994. "Energy Dissipation with Slotted Bolted Connections." *Report No, UCB/EERC-94/02.* San Francisco: Engineering Research Center.

Holden, T., Restrepo, J., and Mander, J. B. 2003. "Seismic Performance of Precast Reinforced and Prestressed Concrete Walls." *Journal of Structural Engineering, ASCE*, vol. 129, no. 3, 286–296.

Housner, G. 1963. "The Behavior of Inverted Pendulum Structures During Earthquakes." *Bulletin of the Seismological Society of America*, vol. 53, no. 2, 403–417.

Housner, G., Chairman, The Governor's Board of Inquiry on the 1989 Loma Prieta Earthquake, May 31, 1990. *Competing Against Time*. State of California, Office of Planning and Research.

Huang, Y. H., Wada, A., Iwata, M., Mahin, S. A., and Connor, J. J. 2002. "Design of Damage-Controlled Structures." *Innovative Approaches to Earthquake Engineering*, Southampton, UK: WIT Press, p. 85–118.

Ingham, T., Rodriguez, S., Nadar, M., Taucer, F., and Seim, C. 1997. "Seismic Retrofit of the Golden Gate Bridge." *Proceedings of the National Seismic Conference on Bridges and Highways: Progress in Research and Practice*, December 10–13, San Diego, CA.

Jones, M., Holloway, L., Toan, V., and Hinman, J. 1997. "Seismic Retrofit of the 1927 Carquinez Bridge by a Displacement Capacity Approach." *Proceedings of the Second National Seismic Conference on Bridges and Highways: Progress in Research and Practice*, July 8–11, Sacramento, CA.

Kajima. 1991. *Honeycomb Damper Systems*. Japan: Kajima Corporation.

Keightley, W. O. 1977. "Building Damping by Coulomb Friction," *Sixth World Conference on Earthquake Engineering*, New Delhi, p. 3043–3048.

Kelly, J. M., Aiken, I. D., and Pall, A. S. 1988. "Shake Table Tests on a Nine-Storey Friction-Damped Frame." *Proceedings of the 9th World Conference on Earthquake Engineering*, Tokyo, August, p. 156.

Kelly, J. M., Skinner, R. I., and Heine, A. J. 1972. "Mechanisms of Energy Absorption in Special Devices for Use in Earthquake-Resistant Structures." *Bulletin of the N.Z. National Society for Earthquake Engineering*, vol. 5, no. 3, 63–88.

Kelley, J., and Tsztoo, D. 1977. "Earthquake Simulation Testing of a Stepping Frame with Energy-Absorbing Devices." *Report No. EERC 77-17*. Berkeley, CA: Earthquake Engineering Research Center, College of Engineering, University of California.

Kim, M. J., and Christopoulos, C. 2008. "Friction Damped Post-Tensioned Self-Centering Steel Moment-Resisting Frames." *Journal of Structural Engineering, ASCE*, vol. 134, no. 11, 1768–1779.

Kim, H. J., Christopoulos, C., and Tremblay, R. 2004. "Experimental Characterization of Boltstressed Non-Asbestos Organic (NAO) Material-to-Steel Interfaces." *Technical Report*, Department of Civil Engineering, University of Toronto, October, 100 pages.

MacRae, G. A., MacKinven, H., Clifton, G. C., Pampanin, S., Walpole, W., and Butterworth, J. 2007. *Tests of Sliding Hinge Joints for Steel Moment Frames*. Proceedings of the 2007 NZSEE Conference: Wairakei, New Zealand, 109–114.

Mander, J., and Cheng, C. 1997. "Seismic Resistance of Bridge Piers Based on Damage Avoidance Design." *Technical Report NCEER-97-0014*. Buffalo, NY: National Center for Earthquake Engineering Research, State University of New York at Buffalo.

Mander, T. J., Rodgers, G. W., Chase, J. G., Mander, J. B., and MacRae, G. A. 2009. "Damage Avoidance Design Steel Beam-Column Moment Connection Using High-Force-to-Volume Dissipators." *Journal of Structural Engineering, ASCE*, vol. 135, no. 11, 1390–1397.

Mansour, N., Christopoulos, C., and Tremblay, R. 2006. "Design of Eccentrically Braced and Moment-Resisting Steel Frames with Replaceable Nonlinear Links." *5th International Conference on Steel Structures in Seismic Areas*, Yokohama, Japan.

Mansour, N., Christopoulos, C., and Tremblay, R. 2009. "Experimental Performance of Full-Scale Eccentrically Braced Frames with Replaceable Shear Links," *International Conference on the Seismic Behaviour of Steel Structures, STESSA 2009*, Philadelphia.

Marioni, A. 1997. "Development of a New Type of Hysteretic Damper for the Seismic Protection of Bridges." *Proceedings of the 4th World Congress on Joint Sealants and Bearing Systems for Concrete Structures*, vol. 2, American Concrete Institute, Detroit, 955–976.

Marioni, A. 2000. "Behavior of Large Base Isolated Prestressed Concrete Bridges During the Recent Exceptional Earthquakes in Turkey." http://192.107.65.2/GLIS/HTML/gn/turchi/g5turchi.htm, accessed Jul 03, 2000.

Marriott, D., Palermo, A., and Pampanin, S. 2006. "Quasi-static and Pseudo-dynamic Testing of Damage-resistant Bridge Piers with Hybrid Connections." *Proceedings of the 1st ECEES*, Sept. 3–8, Geneva.

Martinez-Romero, E. 1993. "Experiences on the Use of Supplementary Energy Dissipators on Building Structures." *Earthquake Spectra*, vol. 9, no. 3, 581–625.

McCormick, J., DesRoches, R., Fugazza, D., and Auricchio, F. 2007. "Seismic Assessment of Concentrically Braced Steel Frames with Shape Memory Alloy Braces." *Journal of Structural Engineering, ASCE*, vol. 133, no. 6, 862–870.

Meek, J. W. 1975. "Effects of Foundation Tipping on Dynamic Response." *Journal of the Structural Division, ASCE*, vol. 101, no. ST7, 1297–1311.

Messler, R. 1999. *Principles of Welding: Processes, Physics, Chemistry, and Metallurgy*. New York: Wiley-VCH, 662 pages.

Midorikawa, M., Azuhata, T., Ishihara, T., and Wada, A. 2003. "Shaking Table Tests on Rocking Structural Systems Installed Yielding Base Plates in Steel Frames." *Behaviour of Steel Structures in Seismic Areas, STESSA 2003*, p. 449–454.

National Physical Laboratory. 1982. *Bimetallic Corrosion*. Teddington, UK: National Physical Laboratory, 20 pages.

Nakashima, M. 1995. "Strain hardening behavior of shear panels made of low-yield steel. I: Test." *Journal of Structural Engineering, ASCE*, vol. 121, no. 12, 1742–1749.

Palermo, A., Pampanin, S., and Calvi, G. M. 2005. "Concept and Development of Hybrid Solutions for Seismic Resistant Bridge Systems." *Journal of Earthquake Engineering*, vol. 9, no. 6, 899–921.

Pall, A. S., and Marsh, C. 1982. "Response of Friction Damped Braced Frames." *Journal of the Structural Division, ASCE*, vol. 108, no. 6, 1313–1323.

Pall, A. S., Marsh, C., and Fazio, P. 1980. "Friction Joints for Seismic Control of Large Panel Structures." *Journal of the Prestressed Concrete Institute*, vol. 25, no. 6, 38–61.

Pekcan, G., Mander, J. B., and Chen, S. S. 2000. "Experiments on Steel MRF Building with Supplemental Tendon System." *Journal of Structural Engineering, ASCE*, vol. 126, no. 4, 437–444.

Perry, C., Fiero, E., Sedarat, H., and Scholl, R. 1993. "Seismic Retrofit in San Francisco Using Energy Dissipation Devices." *Earthquake Spectra*, vol. 9, no. 3. Oakland, CA: Earthquake Engineering Research Institute.

Pollino, M., and Bruneau, M. 2004. "Seismic Retrofit of Bridge Steel Truss Piers Using a Controlled Rocking Approach." *Technical Report MCEER-04-0011*. Buffalo, NY: Multidisciplinary Center for Earthquake Engineering Research, State University of New York at Buffalo.

Pollino, M., and Bruneau, M. 2007. "Seismic Retrofit of Bridge Steel Truss Piers Using a Controlled Rocking Approach." *ASCE Journal of Bridge Engineering*, vol. 12, no. 5, 600–610.

Pollino, M., and Bruneau, M. 2008. "Dynamic Seismic Response of Controlled Rocking Bridge Steel Truss Piers." *Engineering Structures Journal*, vol. 30, no. 6, 1667–1676.

Pollino, M., and Bruneau, M. 2010a. "Bi-Directional Behavior and Design of Controlled Rocking 4-Legged Bridge Steel Truss Piers." *Journal of Structural Engineering, ASCE*, vol. 136, no. 12, 1512–1522.

Pollino, M., and Bruneau, M. 2010b. "Seismic Testing of a Bridge Truss Pier Designed for Controlled Rocking." *Journal of Structural Engineering, ASCE*, vol. 136, no. 12, 1523–1532.

Priestley, M. J. N., Evison, R. J., and Carr, A. J. 1978. "Seismic Response of Structures Free to Rock on Their Foundations." *Bulletin of the New Zealand National Society for Earthquake Engineering*, vol. 11, no. 3, 141–150.

Priestley, M. J. N., Seible, F., and Calvi, G. M. 1996. *Seismic Design and Retrofit of Bridges*. New York: John Wiley and Sons.

Priestley, M. J. N., Sritharan, S., Conley, J. R., and Pampanin, S. 1999. "Preliminary Results and Conclusions from the PRESSS Five-Story Precast Concrete Test Building." *PCI Journal*, vol. 44, no. 6, 42–67.

Priestley, M. J. N., and Tao, J. 1993. "Seismic Response of Precast Prestressed Concrete Frames with Partially Debonded Tendons." *PCI Journal*, vol. 38, no. 1, 58–69.

Prucz, Z., Conway, W. B., Schade, J. E., and Ouyang, Y. 1997. "Seismic Retrofit Concepts and Details for Long-span Steel Bridges." *Proceedings of the 2nd National Seismic Conference on Bridges and Highways: Progress in Research and Practice*, July 8–11, Sacramento, CA.

Psycharis, I. N. 1982. "Dynamic Behavior of Rocking Structures Allowed to Uplift," Ph.D. Dissertation, California Institute of Technology, Pasadena, CA.

Rai, D. C., and Wallace, B. J. 1998. "Aluminium Shear-Links for Enhanced Seismic Performance." *Journal of Earthquake Engineering and Structural Dynamics*, vol. 27, 315–342.

Rezai, M., Prion, H. G. L., Tremblay, R., Bouatay, N., and Timler, P. 2000. "Seismic Performance of Brace Fuse Elements for Concentrically Steel Braced Frames." *Behavior of Steel Structures in Seismic Areas*, STESSA, p. 39–46.

Ricles, J. M., Sause, R., Garlock, M., and Zhao, C. 2001. "Post-Tensioned Seismic-Resistant Connections for Steel Frames." *Journal of Structural Engineering, ASCE*, vol. 127, no. 2, 113–121.

Ricles, J. M., Sause, R., Peng, S. W., and Lu., L. W. 2002. "Experimental Evaluation of Earthquake Resistant Post-Tensioned Steel Connections." *Journal of Structural Engineering, ASCE*, vol. 128, no. 7, 850–859.

Robinson, W. H., and Greenbank, L. R. 1975. "Properties of an Extrusion Energy Absorber." *Bulletin of the New Zealand Society for Earthquake Engineering*, vol. 8, no. 3, 187–191.

Robinson, W. H., and Greenbank, L. R. 1976. "Extrusion Energy Absorber Suitable for the Protection of Structures During An Earthquake." *Earthquake Engineering and Structural Dynamics*, vol. 4, no. 3, 251–259.

Rodgers, G. W., Mander, J. B., Chase, J. G., Dhakal, R. P., Leach, N. C., and Denmead, C. S. 2008. "Spectral Analysis and Design Approach for High Force-to-Volume Extrusion Damper-Based Structural Energy Dissipation." *Earthquake Engineering and Structural Dynamics*, vol. 37, no. 2, 207–223.

Roeder, C., and Popov, E. 1977. "Inelastic Behavior of Eccentrically Braced Steel Frames under Cyclic Loadings," *Report No. UCB-77/17*. Berkeley, CA: Earthquake Engineering Center, University of California.

Roh, H., and Reinhorn, A. M. 2009. "Analytical modeling of rocking elements." *Engineering Structures*, vol. 31, 1179–1189.

Rojas, P., Ricles, J. M., and Sause, R. 2005. "Seismic Performance of Post-Tensioned Steel Moment Resisting Frames with Friction Devices." *Journal of Structural Engineering, ASCE*, vol. 131, no. 4, 529–540.

Roussis, P. C., Constantinou, M. C., Erdik, M., Durukal, E., and Dicleli, M. 2002. "Assessment of Performance of Bolu Viaduct in the 1999 Duzce Earthquake in Turkey," *Technical Rep. No. MCEER-02-0001*. Buffalo, NY: Multidisciplinary Center of Earthquake Engineering Research, State University of New York at Buffalo.

Roussis, P.C., Constantinou, M.C., Erdik, M., Durukal, E., and Dicleli, M. 2003. "Assessment of Performance of Seismic Isolation System of Bolu Viaduct." *ASCE Journal of Bridge Engineering*, vol. 8, no. 4, 182–190.

Sam., M. T., Balendra, T., and Liaw, C. Y. 1995. "Earthquake-Resistant Steel Frames with Energy Dissipating Knee Elements." *Engineering Structures*, vol. 17, no. 5, 334–343.

Sarraf, M., and Bruneau, M. 1998a. "Ductile Seismic Retrofit of Steel Deck-Truss Bridges. I: Strategy and Modeling." *ASCE Journal of Structural Engineering*, vol. 124, no. 11, 1253–1262.

Sarraf, M., and Bruneau, M. 1998b. "Ductile Seismic Retrofit of Steel Deck-Truss Bridges. II: Design Applications." ASCE Journal of Structural Engineering, vol. 124, no. 11, 1263–1271.

SAE. 1997. "Surface Vehicle Recommended Practice." *SAE J661*. Warrendale, PA: Society of Automotive Engineers International.

Sharabash, A. M., and Andrawes, B. O. 2009. "Application of Shape Memory Alloy Dampers in the Seismic Control of Cable-Stayed Bridges." *Engineering Structures Journal*, vol. 31, 607–616.

Shimizu, K., Hashimoto, J., Kawai, H., and Wada, A. 1998. "Application of Damage Control Structure using Energy Absorption Panel." Paper No. T105-2, *Proceedings of the Structural Engineers World Congress 1998: Structural Engineering World Wide 1998*. San Francisco: Elsevier Science, Ltd.

Skinner, R. I., Kelly, J. M., and Heine, A. J. 1975. "Hysteretic Dampers for Earthquake-Resistant Structures." *Earthquake Engineering and Structural Dynamics*, vol. 3, 287–296.

Skinner, R. I., Tyler, R. G., Heine, A. J., and Robinson, W. H. 1980. "Hysteretic Dampers for the Protection of Structures from Earthquakes." *Bulletin of the N.Z. National Society for Earthquake Engineering*, vol. 13, no. 1. 22–36.

Skinner, R. I., Robinson, W. H., and McVerry, G. H. 1993. "An Introduction to Seismic Isolation." John Wiley and Sons, New York, p. 354 .

Soong, T. T., and Constantinou, M. C. 1994. *Passive and Active Structural Control in Civil Engineering*. Vienna: Springer-Verlag.

Steimer, S. F., Godden, W. G., and Kelly, J. M. 1981. "Experimental Behavior of a Spatial Piping System with Steel Energy Absorbers Subjected to a Simulated Differential Seismic Input." *Report No. UCB/EERC-81/09*. Berkeley, CA: Earthquake Engineering Research Center, University of California.

Sugiyama, S. 1998. "Application of Hysteresis Steel Dampers to Tall Building," Paper No. T190-5, *Proceedings of the Structural Engineers World Congress 1998*: *Structural Engineering World Wide 1998*. San Francisco: Elsevier Science, Ltd.

Takanashi, K., Tanaka, H., and Taniguchi, H. 1981. "Influence of Slipping at High Strength on Dynamic Behaviour of Frames." *Joints in Structural Steelwork: Proceedings of the International Conference on Connections*. London: Pentech Press.

Toranzo, L. A., Carr, A. J., and Restrepo, J. I. 2001. "Displacement Based Design of Rocking Walls Incorporating Hysteretic Energy Dissipators." *7th International Seminar on Seismic Isolation, Passive Energy Dissipation and Active Control of Vibrations of Structures*, Assisi, Italy, October 2–5.

Takewaki, I. 2009. *Building Control with Passive Dampers: Optimal Performance-Based Design for Earthquakes*. New York: Wiley-IEEE Press, 320 pages.

Transportation Research Board. 1977. "Bridge Bearings." *NCHRP Report 41*. Washington, D. C.: *National Cooperative Highway Research Program.*

Tremblay, R. 1993. "Seismic Behavior and Design of Friction Concentrically Braced Frames for Steel Buildings." Thesis submitted in partial fulfillment of the requirements for the degree of doctor of philosophy, University of British Columbia, Vancouver, BC: Canada. p. 496.

Tremblay, R., Lacerte, M., and Christopoulos, C. 2008. "Seismic Response of Multistory Buildings with Self-Centering Energy Dissipative Steel Braces." *Journal of Structural Engineering, ASCE*, vol. 134, no. 1, 108–120.

Tremblay, R., and Stiemer, S. F. 1993. "Energy Dissipation through Friction Bolted Connections in Concentrically Braced Steel Frames," *Report No. ATC 17-1, Seminar on Seismic Isolation, Passive Energy Dissipation, and Active Control*, vol. 2, 557–568, ATC, Redwood City, CA.

Tsai, K. C., Chen, H. W., Hong, C. P., and Su, Y. F. 1993. "Design of Steel Triangular Plate Energy Absorbers for Seismic-Resistant Construction." *Earthquake Spectra*, vol. 9, no. 3, 505–528.

Tsopelas, P., and Constantinou, M. 1997. "Study of Elastoplastic Bridge Seismic Isolation System." *Journal of Structural Engineering, ASCE*, vol. 123–124, 489–498.

Tyler, R. G. 1978. "Tapered Steel Energy Dissipators for Earthquake-Resistant Structures." *Bulletin of the N.Z. National Society for Earthquake Engineering*, vol. 11, no. 4. 282–294.

Van de Lindt, J. W., and Potts. A. 2008. "Shake Table Testing of a Superelastic Shape Memory Alloy Response Modification Device in a Wood Shearwall." *Journal of Structural Engineering*, *ASCE*, vol. 134, no. 8, 1343–1352.

Vargas, R. and Bruneau, M. 2007. "Effect of Supplemental Viscous Damping on the Seismic Response of Structural Systems with Metallic Dampers." ASCE Journal of Structural Engineering, vol. 133, no. 10, 1434–1444.

Vargas, R., and Bruneau, M. 2009a. "Analytical Response of Buildings Designed with Metallic Structural Fuses." *Journal of Structural Engineering, ASCE*, vol. 135, no. 4, 386–393.

Vargas, R., and Bruneau, M. 2009b. "Experimental Response of Buildings Designed with Metallic Structural Fuses." *Journal of Structural Engineering, ASCE*, vol. 135, no. 4, 394–403.

Wada, A., Connor, J. J., Kawai, H., Iwata, M., and Watanabe, A. 1992. "Damage Tolerant Structures," *Proceedings of 5th U.S.-Japan Workshop on the Improvement of Structural Design and Construction Practices, ATC-15-4,* Applied Technology Council, p. 27–39.

Wada, A., and Huang, Y. H. 1995. "Preliminary Seismic Design of Damage Tolerant Tall Building Structures," *Proceedings of the Symposium on a New Direction in Seismic Design,* Architectural Institute of Japan, Tokyo, p. 77–93.

Wada, A., and Huang, Y. H. 1999. "Damage-controlled structures in Japan." *U.S.–Japan Workshop on Performance-Based Earthquake Engineering Methodology for Reinforced Concrete Building Structures*, PEER Rep. 1999, vol. 10, 279–289.

Wada, A., Huang, Y. H., and Iwata, M. 2000. "Passive Damping Technology for Buildings in Japan," *Progress in Structural Engineering and Materials*, vol. 2, no. 3, 335–350.

Whittaker, A. S., Bertero, V. V., Thompson, C. L., and Alonso, L. J. 1989. "Earthquake Simulator Testing of Steel Plate Added Damping and Stiffness Elements." *Report No. UCB/EERC-89/02*. Berkeley, CA: Earthquake Engineering Research Center, University of California.

Whittaker, A. S., Bertero, V. V., Thompson, C. L., and Alonso, L. J. 1991. "Seismic Testing of Steel Plate Energy Dissipation Devices." *Earthquake Spectra*, vol. 7, no. 4, 563–604.

Wilson, J. C., and Wesolowsky, M. J. 2005. "Shape Memory Alloys for Seismic Response Modification: A State-of-the-Art Review." *Earthquake Spectra*, vol. 21, no. 2, 569–601.

Youssef, M. A., Alam., M. S., and Nehdi, M. 2008. "Experimental Investigation on the Seismic Behavior of Beam-Column Joints Reinforced with Superelastic Shape Memory Alloys." *Journal of Earthquake Engineering*, vol. 12, 1205–1222.

Yang, T. S., and Popov, E. P. 1995. "Experimental and Analytical Studies of Steel Connections and Energy Dissipaters." *Report No, UCB/EERC-95/13*. San Francisco: Earthquake Engineering Research Center.

Zahrai, S. M., and Bruneau, M. 1999a. "Cyclic Testing of Ductile End-Diaphragms for Slab-on-Girder Steel Bridges." ASCE Journal of Structural Engineering, vol. 125, no. 9, 987–996.

Zahrai, S. M., and Bruneau, M. 1999b. "Ductile End-Diaphragms for the Seismic Retrofit of Slab-on-Girder Steel Bridges." ASCE Journal of Structural Engineering, vol. 125, no. 1, 71–80.

This page intentionally left blank

CHAPTER 14

Stability and Rotation Capacity of Steel Beams

14.1 Introduction

A basic assumption made for the plastic design of framed structures is that flexural members shall have sufficient plastic deformation capacities while maintaining the plastic moment, M_p. Without sufficient plastic deformation capacity at the member level, the yield (or collapse) mechanism resulting from sequential plastification in the structure cannot be developed. The need for substantial deformation capacity is even greater for seismic design because it is expected not only that the yield mechanism will form, but also that the structure may displace beyond the point of incipient collapse (see point A in Figure 14.1) and cycle back and forth under severe earthquake shaking.

Although steel material of nominal yield strength not exceeding 65 ksi (448 MPa) usually exhibits high ductility, the plastic deformation capacity of a member is usually limited by instability. Instability in flexural members includes flange local buckling (FLB), web local buckling (WLB), and lateral-torsional buckling (LTB). For a given grade of structural steel, the vulnerability of each of the two local buckling modes can be measured in terms of the width-thickness ratio, b/t; the tendency for LTB is a function of the slenderness ratio, L_b/r_y, and the moment gradient. The AISC 360 (AISC 2010a) defines the slenderness ratio, *I*, of each buckling mode as follows:

FLB: $\lambda = b_f/2t_f$
WLB: $\lambda = h_c/t_w$
LTB: $\lambda = L_b/r_y$

where b_f is the flange width, t_f is the flange thickness, h_c is the clear depth between the flanges less twice the fillet radius, t_w is the web

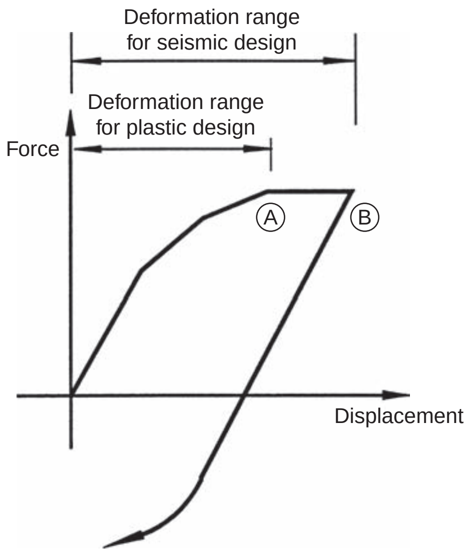

FIGURE 14.1 Schematic structureal deformation ranges.

thickness, h_b is the laterally unbraced length, and r_y is the radius of gyration about the y-y axis.

The AISC 360 presents three limiting slenderness ratios (λ_{pd}, λ_p, and λ_r) to classify each of the above three buckling limit states into four categories. Figure 14.2a shows this classification. If the slenderness ratio, λ, is larger than λ_r, the flexural member buckles in the elastic range (see curve 4 in Figure 14.2b). The flexural capacity is lower than the plastic moment, and the member does not exhibit ductile behavior. A wide-flange section having either a flange or a web width-thickness ratio larger than λ_r is called a *slender* section in the AISC 360. For values of λ between λ_r and λ_p, the member buckles in the inelastic range (see curve 3 in Figure 14.2b), and the flexural capacity exceeds the elastic moment, $M_r = (F_y - F_r)S_x$, where F_y is the yield stress, F_r is the residual stress, and S_x is the elastic section modulus. A wide flange section with

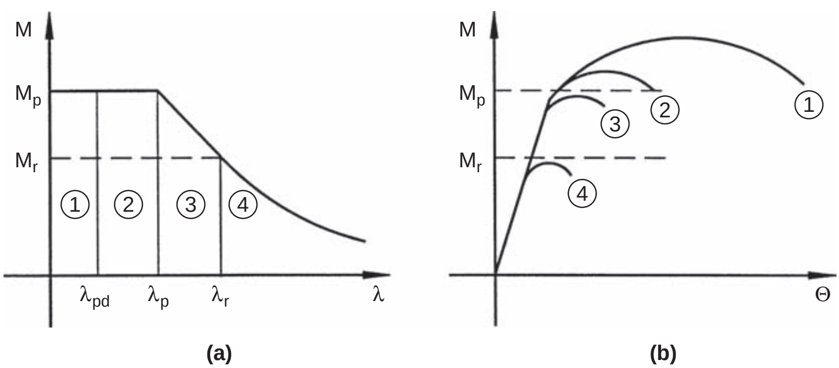

FIGURE 14.2 LRFD classification of flexural buckling limit states. (*Adapted from Yura et al. 1978.*)

flange or web width-thickness ratios falling between λ_r and λ_p is called a *noncompact* section. Flexural members with λ larger than λ_p should not be used as yielding members for either plastic or seismic design.

The plastic moment, M_p, can be reached when λ is smaller than λ_p. However, to ensure sufficient rotational capacity, λ must be further limited to λ_{pd}. The AISC 360 provides values for λ_{pd} and λ_p for the LTB limit state. If plastic design is used, the designer must limit the unbraced length (L_b) such that λ does not exceed λ_{pd}. For the FLB and WLB limit states, the AISC 360 merges λ_p and λ_{pd} into a single limiting parameter, λ_p, and λ_{pd} is not specified for these two limit states. A wide flange section whose flange and web width-thickness ratios do not exceed λ_p is called a *compact* section in the AISC 360, and such a section is expected to be able to develop a rotation capacity of at least 3 before the onset of local buckling (Yura et al. 1978), where the rotation capacity, R, is defined as follows:

$$R = \frac{\theta_h}{\theta_p} \tag{14.1}$$

See Figure 14.3 for the definitions of θ_h and θ_p.

The inelastic deformation demand for seismic applications is typically greater than that for plastic design. Therefore, the AISC Seismic Provisions (AISC 2010b) further reduces the limiting slenderness ratios, as shown in Table 14.1 such that the expected rotation capacity is about 7 to 9 (AISC 1986).

The requirement of sufficient inelastic rotation capacity is indirectly achieved when the slenderness ratio for the three instability conditions is limited. The theoretical background to these slenderness limits is presented in this chapter. It will become obvious from the following presentation that the local buckling and lateral buckling limit states are interrelated and that the treatment of this subject by code documents that assume uncoupled behavior is simplistic.

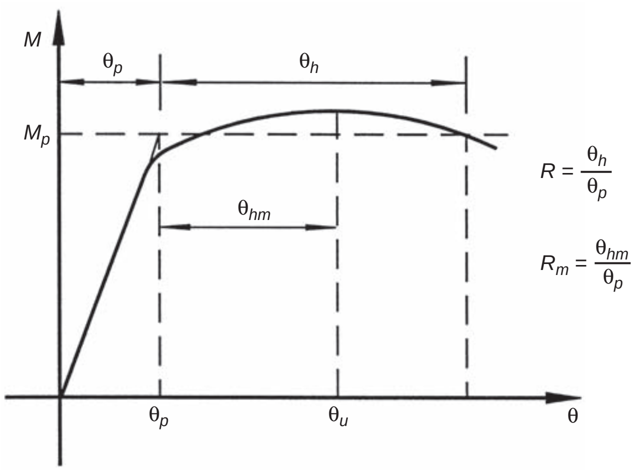

Figure 14.3 Moment-rotation relationship and definition of rotation capacity, R.

Limit States	Plastic Design	Seismic Design
FLB	$0.38\sqrt{\frac{E}{F_y}}$ $\left(\text{or } \frac{65}{\sqrt{F_y}}, F_y \text{ in ksi}\right)$	$0.30\sqrt{\frac{E}{F_y}}$ $\left(\text{or } \frac{52}{\sqrt{F_y}}, F_y \text{ in ksi}\right)$
WLB	$3.76\sqrt{\frac{E}{F_y}}$ $\left(\text{or } \frac{640}{\sqrt{F_y}}, F_y \text{ in ksi}\right)$	$2.45\sqrt{\frac{E}{F_y}}$ $\left(\text{or } \frac{520}{\sqrt{F_y}}, F_y \text{ in ksi}\right)$
LTB	$\left(0.12+0.076\frac{M_1}{M_2}\right)\frac{E}{F_y}$	$\frac{0.086E}{F_y}$

Note: M_1 and M_2 are smaller and larger moments at the unbraced beam ends, respectively; M_1/M_2 is positive when moments cause reverse curvature.

Table 14.1 AISC Slenderness Requirements

14.2 Plate Elastic and Postelastic Buckling Behavior

A wide flange section can be viewed as an assemblage of flat plates. The flange plate is an *unstiffened* element because one edge is free (i.e., not supported). The web plate is a *stiffened* element because it is connected at two ends to the flange plates. Before the inelastic buckling behavior of wide-flange beams for plastic or seismic design is described, it is worthwhile to review briefly the elastic buckling and postbuckling behaviors of plates. Note that the postbuckling behavior of a plate is very different from that of a column because a column loses strength (with increasing deformation) once the buckling load is reached, whereas a plate can develop significant postbuckling strength beyond its theoretical critical load because of stress redistribution and transverse tensile membrane action.

The mathematical solution to the elastic buckling problem for a perfect thin plate is well known (Timoshenko and Gere 1961). The small-deflection theory assumes that the deflection is less than the thickness of the plate, the middle surface of the plate does not stretch during bending (i.e., no membrane action), and plane sections remain plane. The governing differential equation for an isotropic plate (see Figure 14.4) without initial geometrical imperfections subjected to x-direction loading per unit length, N_x ($= \sigma_x t$), is as follows:

$$\frac{\partial^4\omega}{\partial x^4}+2\frac{\partial^4\omega}{\partial x^2\partial y^2}+\frac{\partial^4\omega}{\partial y^4}=\frac{1}{D}N_x\frac{\partial^2\omega}{\partial x^2} \tag{14.2a}$$

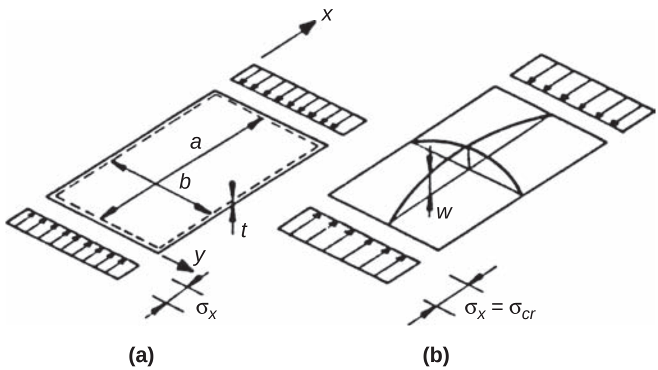

Figure 14.4 Simply supported plate. (*From Maquoi 1992, with permission.*)

where D is the flexural rigidity of the plate:

$$D = \frac{Et^3}{12(1-\nu^2)} \tag{14.2b}$$

and where E is Young's modulus, ν is Poisson's ratio (= 0.3 for steel in the elastic range), σ_x is the imposed stress, and t is the plate thickness.

The elastic critical buckling stress, obtained from solving Eq. (14.2), is as follows:

$$\sigma_{cr} = \kappa \frac{\pi^2 E}{12(1-\upsilon^2)(b/t)^2} \tag{14.3}$$

where κ is the plate buckling coefficient. For a plate simply supported on all four sides, the coefficient, κ, is given by:

$$\kappa = \left(\frac{1}{m}\frac{a}{b} + m\frac{b}{a}\right)^2 \tag{14.4}$$

where m represents the number of half-waves that occur in the loaded direction of the plate, and a/b is the plate aspect ratio. The variation of κ with respect to m and a/b is shown in Figure 14.5. For a long, narrow plate like the flange or web of a beam, the aspect ratio is large and the minimum value of κ for given boundary conditions can be used. For example, a beam flange is similar to a plate with one simply supported edge (at the web) and one free edge; the corresponding minimum value of κ from Figure 14.5 is 0.425. Likewise, the web of a beam is somewhat restrained by the two flanges, and its unloaded edges can be treated as being semirestrained; that is, restraint somewhere between simply supported and fully fixed. The value of κ can be taken as 5 in this case. This comparison of the value of κ for flange (= 0.425) and web (= 5) buckling highlights the vulnerability of flanges to local buckling.

Prior to elastic buckling, compressive stresses are uniformly distributed along the edges of a perfectly flat plate. Once the critical buckling

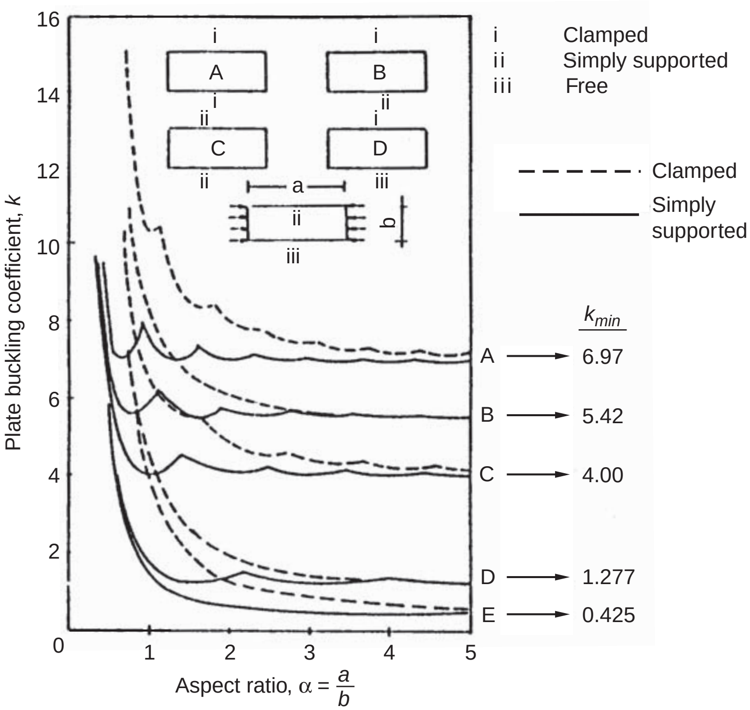

FIGURE 14.5 Plate elastic buckling coefficient, κ. (*From Gerard and Becker 1957, with permission.*)

stress is reached, the plate still exhibits significant stiffness, and the strength can be increased further. The plate postbuckling strength is due to the redistribution of axial compressive stresses and tensile membrane action that accompanies the out-of-plane bending of the plate in both the longitudinal and transverse directions. Figure 14.6 shows that the distribution of compressive stresses in the loading direction is no longer uniform after plate buckling and that the compressive stresses tend to concentrate in those portions of the plate width close to the supported edges because these portions are the stiffest in a buckled plate. Such a nonuniform distribution of the stresses can be simplified through the effective width concept proposed by Von Kármán et al. (1932).

Based on an energy method, the longitudinal stiffness of an elastic plate after buckling has been derived by several researchers; summary data is presented in Bulson (1969). Figure 14.7 shows three cases, where ε_{cr} is the longitudinal strain corresponding to a stress level σ_{cr}, and σ_{av} is the mean value of the longitudinal membrane stresses for a given longitudinal strain, ε_1, in the postbuckling range. Contrary to the case of axially loaded columns, where the postbuckling stiffness is negative, the elastic postbuckling stiffness of a plate is positive.

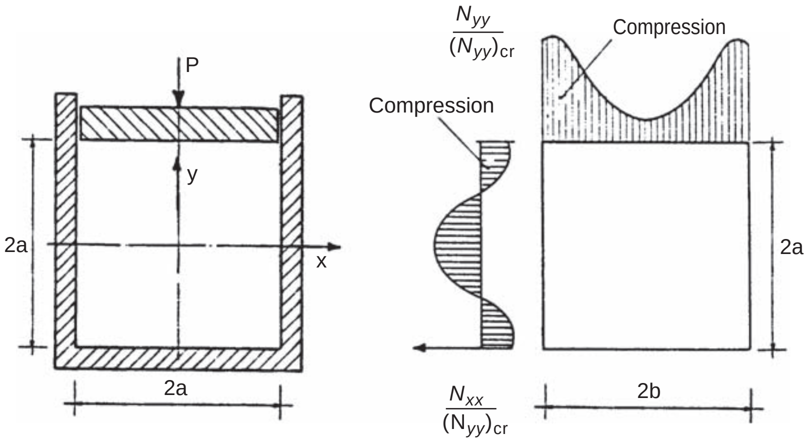

Figure 14.6 Stress redistribution of postbuckling plate. (*From Bazant and Cedolin 1991, with permission.*)

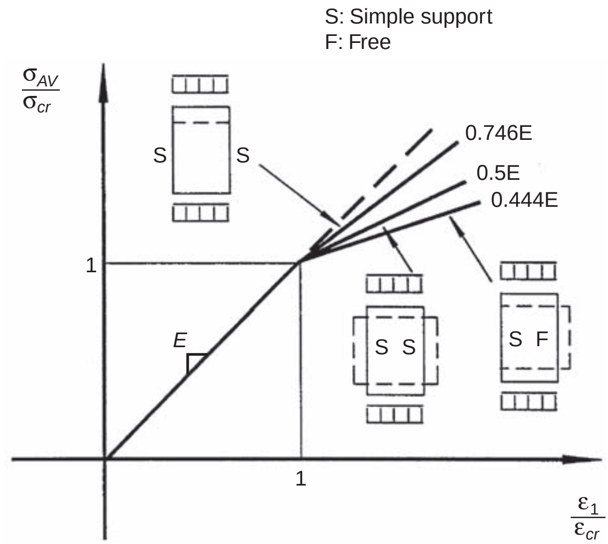

Figure 14.7 Postbuckling stiffness of loaded plate. (*Adapted from Bulson 1969.*)

Out-of-plane imperfections always exist in actual plates and assemblies of plates. Figure 14.8 compares the analytically predicted response of a perfect plate and test results, both for a plate with plan dimensions of *a* and *b*. The main effects of geometric imperfections are the elimination of a well-defined buckling load

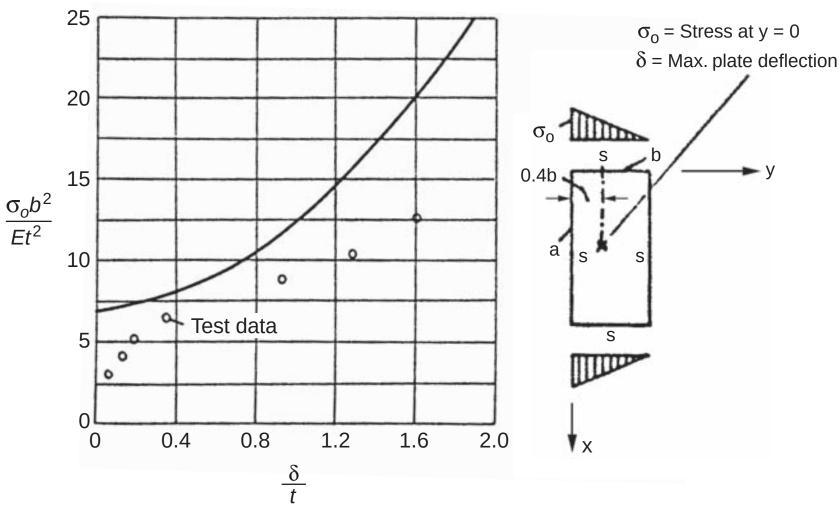

FIGURE 14.8 Test results and theoretical predictions for an axially loaded plate, $a = 2b$. (*Adapted from Bulson 1969.*)

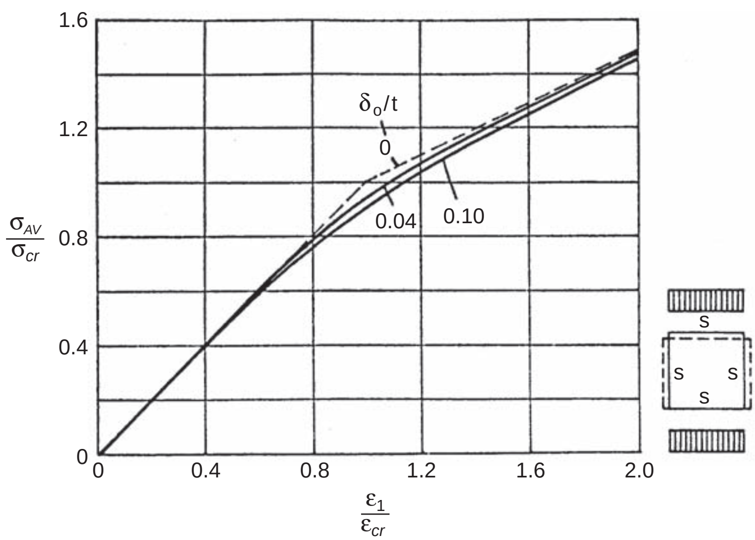

FIGURE 14.9 Effect of initial out-of-plane imperfection on plate postbuckling stiffness. (*From Bulson 1969, with permission.*)

and larger out-of-plane deflections. Nevertheless, the effect of initial geometrical imperfections on the longitudinal stiffness after plate buckling is insignificant (see Figure 14.9). Note that δ_o in Figure 14.9 is the initial deflection (i.e., imperfection) at the center of the plate.

14.3 General Description of Inelastic Beam Behavior

14.3.1 Beams with Uniform Bending Moment

Figure 14.10a shows the typical in-plane moment versus deformation relationship of a beam under uniform moment about its strong axis. The moment-end rotation curve consists of four parts:

- The elastic range (portion OA) in which the M-θ relation is linear
- The contained plastic flow region (portion AB) in which the curve becomes nonlinear because of partial yielding
- The plastic plateau (portion BC) in which the beam is fully yielded and is not capable of resisting additional moment
- The unloading region (portion CD) in which the beam becomes unstable

Nevertheless, the in-plane behavior does not completely describe the beam behavior because of simultaneous lateral deflections. As shown in Figure 14.10b, the beam starts to deflect laterally following application of load, and the deflection becomes pronounced after the compression flange begins to yield. Lateral-torsional buckling occurs just after the plastic moment is achieved. Despite significant lateral deflection perpendicular to the plane of loading, however, the beam is able to maintain its plastic moment capacity until local buckling occurs. During the entire loading process, the tension flange moves laterally by only a relatively small amount. Thus, the web is distorted because of the relative lateral displacement of compression and tension

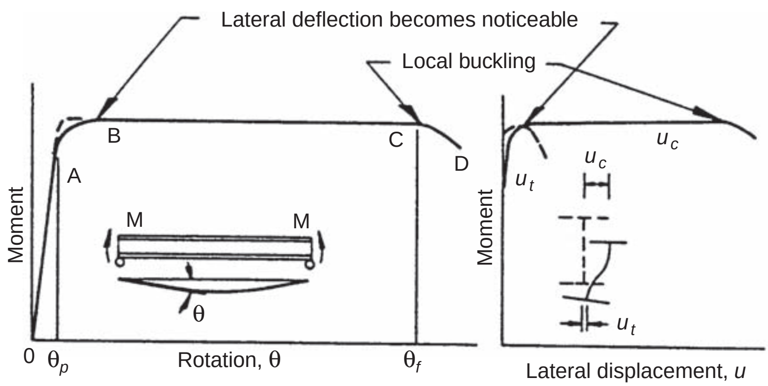

(a) Moment-rotation relation

(b) Moment-lateral displacement relation

FIGURE 14.10 Typical beam behavior under uniform moment. (*From ASCE-WRC 1971, with permission.*)

flanges. The lateral movement of the compressive flange also causes additional compressive strains to half of the beam flange as a result of flange bending about its strong axis. This movement may trigger flange local buckling and causes the beam's flexural strength to degrade.

When a member is under a uniform applied stress due to an axial compression force or uniform bending, the normal stress tends to magnify any lateral deflections. Even when lateral deflections are on the order of only 1% of the flange width, *bending yield planes* will occur at midspan, and local buckling will develop in that fully yielded region (Lay 1965b). Sufficient lateral bracing must be provided for purely axial yielding to occur without any bending yield planes.

The difference in behavior between a simply supported beam and a continuous beam is important. For a continuous beam, adjacent spans may offer significant warping restraint at the ends of the buckled span, which can lengthen the plastic plateau and result in a larger plastic rotation. Tests conducted by Lee and Galambos (1962) have shown that plastic rotation capacity increases as the length of the unbraced span decreases. All the beams tested showed considerable postbuckling strength, and in each case, a plastic hinge of sufficient rotation capacity was developed. Lee and Galambos reported that if the unbraced length of a beam is greater than $45r_y$, the beam will likely fail because of lateral-torsional buckling. Otherwise, beam failure is instigated by flange local buckling. Note that the postbuckling strength observed in these tests was mainly a result of the lateral restraint provided by the adjacent elastic spans.

14.3.2 Beams with Moment Gradient

Moments in beams in buildings generally vary along the span, that is, beams are typically subjected to a moment gradient. Figure 14.11 shows the deformation behavior of a simply supported beam with a concentrated load at the midspan (Lukey and Adams 1969). From Figure 14.11a, it can be seen that this beam behaves elastically up to load point 4. Yielding starts to occur because of the presence of residual stresses beyond that point, which causes a slight reduction in stiffness. The rotation increases rapidly once the plastic moment, M_p, is exceeded. The moment continues to increase beyond M_p, and local buckling is observed at load point 8. Local buckling does not cause degradation in strength. Instead, the moment increases with increasing rotation up to load point 10 before the strength starts to degrade. Figure 14.11b shows the corresponding lateral deflection of the compression flange. This lateral movement becomes pronounced only after load point 8 and increases rapidly after load point 14.

Under a moment gradient, yielding of the beam is confined to the region adjacent to the location of maximum moment, and it cannot spread along the length of the beam unless the moment is increased. However, as soon as M_p is reached, the steel strain hardens, and the

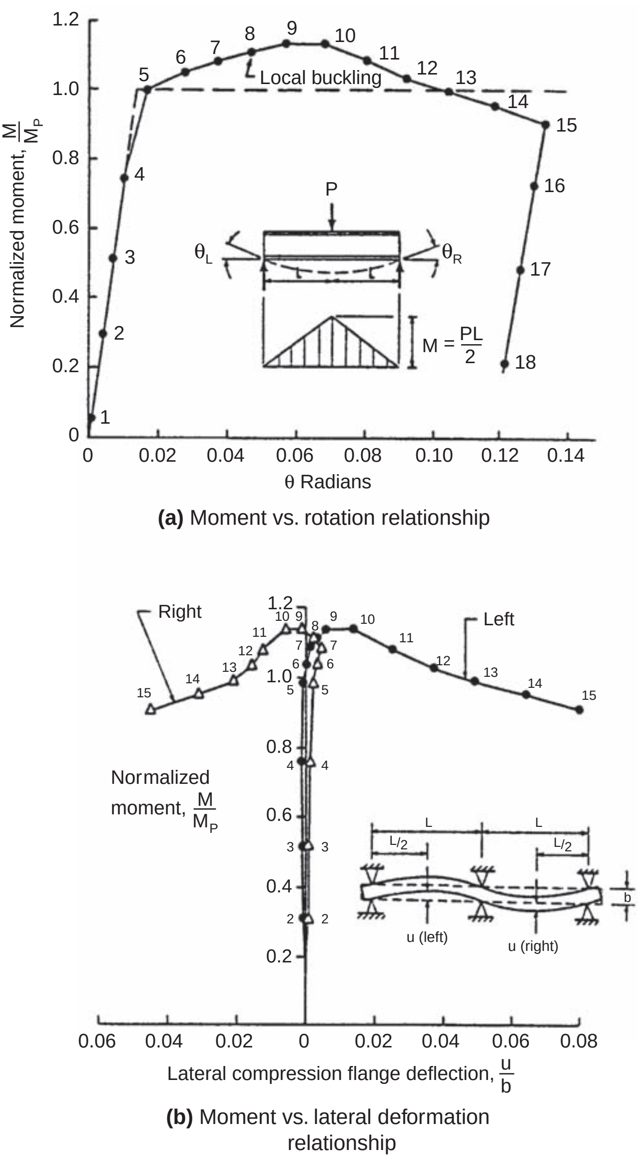

Figure 14.11 Typical beam behavior under moment gradient. (*From Lukey and Adams 1969 with permission.*)

load can be further increased. This causes the midspan moment to increase and the yielded region to spread. Local buckling will start only when the compression flange has yielded over a length sufficient to accommodate a full wavelength of the buckle shape (see Section 14.5). Note that the applied moment can still be increased after local buckling and that strength degradation will not occur until lateral-torsional buckling develops.

The lateral deflection of the compression flange typically increases rapidly after M_p is exceeded; the deflected shape of the flange also changes, and curvatures producing lateral displacements are concentrated mainly in a relatively small region at midspan where the compression flange has yielded and has reduced stiffness. Postelastic deformations will also concentrate at this location. Thus, it is not local buckling but rather lateral-torsional buckling that causes a loss in strength. After local buckling, the lateral stiffness of the compression flange is greatly reduced and lateral-torsional buckling is triggered.

The point of load application has a profound impact on the resistance to lateral-torsional buckling (Timoshenko and Gere 1961). When the load is applied close to the compression flange, the critical value of the load decreases. If it is applied to the tension flange, the critical value of the load will be much larger. For many generic solutions presented in the literature, loads are assumed to be applied at the centroid of the cross-section. The effect of the load application level on the lateral-torsional buckling resistance is shown in Figure 14.12.

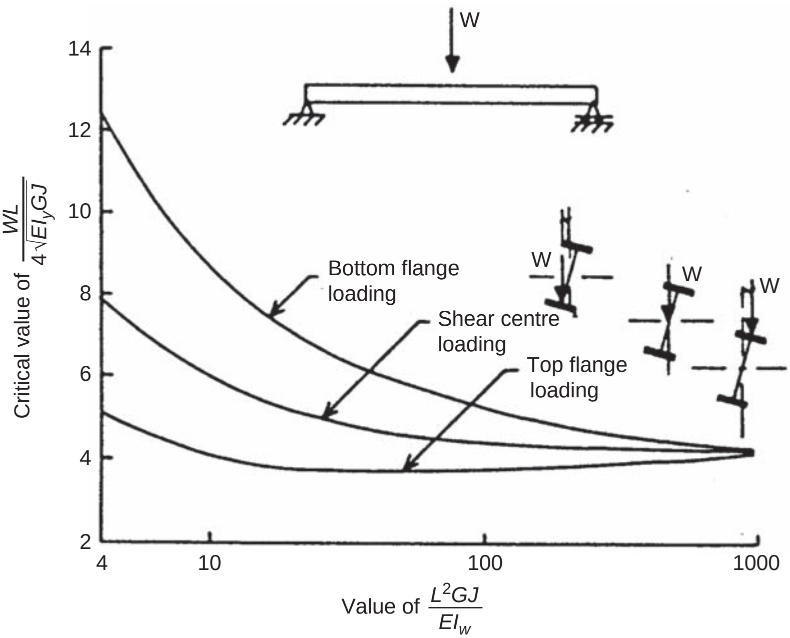

Figure 14.12 Effect of load position on lateral-torsional buckling load for parameters expressed in U.S. units only. (*From Kirby and Nethercot 1979 with permission.*)

14.3.3 Comparison of Beam Behavior Under Uniform Moment and Moment Gradient

The differences in behavior between beams with uniform bending moment and moment gradient can be summarized as follows (Galambos 1968):

- For beams subjected to uniform moment, the moment remains constant at M_p until the average strain in the compressive flange reaches the strain-hardening strain, ε_{st}, along the entire region of uniform moment. Only then can the steel strain harden and the moment exceed M_p. In contrast, yielding in a beam under moment gradient cannot spread unless the moment is increased; therefore, strain-hardening occurs as soon as M_p is reached.
- For a beam segment under uniform moment, the unbraced compressive flange deflects laterally as soon as M_p is reached, primarily as a result of the initial out-of-straightness of the beam flange. Lateral-torsional buckling usually precedes local buckling, and moment strength is not lost until local buckling develops.
- For a beam under a moment gradient, the moment at the critical section will increase because of strain-hardening and will continue to increase until the yielded length of the compressive flange is equal to a full local buckling wavelength. The beam may still resist additional load because loss of strength will not occur until lateral-torsional buckling develops. That is, flange local buckling usually precedes lateral-torsional buckling.

Inelastic buckling occurs at an average strain of an order of magnitude larger than the yield strain. The combined phenomena of yielding, strain-hardening, in-plane and out-of-plane deformations, and local distortion all occur soon after the compression flange has yielded. They interact with each other such that individual effects can be only roughly distinguished. Residual stresses and initial out-of-straightness also impact the load-displacement relation for even the simplest beam. Because it is difficult to take each of these factors into consideration, modern steel design codes usually treat local buckling and lateral-torsional buckling separately.

14.4 Inelastic Flange Local Buckling

14.4.1 Modeling Assumptions

For a beam under moment gradient, the yielded region will be subjected to moments of M_y or greater, where M_y (= $S\sigma_y$) is the yield moment, S is the elastic section modulus, and σ_y is the actual yield stress (and not the nominal yield stress, F_y). The maximum (flange) strains exceed $s\varepsilon_y$ because any moment larger than M_y requires strains above

$s\varepsilon_y$ (see Chapter 2). Therefore, any yielded portion of a beam flange under a moment gradient is in the fully yielded condition ($\varepsilon \geq s\varepsilon_y$).

For a uniform moment loading condition, if all stresses in the beam are beyond the yield stress, σ_y, the material is fully yielded. However, there exists a range of partly yielded conditions at σ_y for which, according to the slip-plane theory, parts of the member are at strain ε_y and other parts have yielded and are at strain $s\varepsilon_y$. Lay (1965) has shown that even when the lateral deflections are on the order of only one-hundredth of the flange width, bending yield planes develop at midspan. This lateral movement produces a fully yielded condition (i.e., all strains at $s\varepsilon_y$) at midspan, and local buckling may occur in that fully yielded part of the member.

A physical model for flange local buckling analysis is shown in Figure 14.13. It assumes that the flange plate is subjected to a uniform stress, F_y, over the entire flange area and that the web restrains the flange at the web-to-flange junction. The flange local buckling problem is thus reduced to a classical buckling problem. The assumed cross-sectional shape before and after buckling is shown in Figure 14.14, where only the effect of local buckling on the distorted shape is shown.

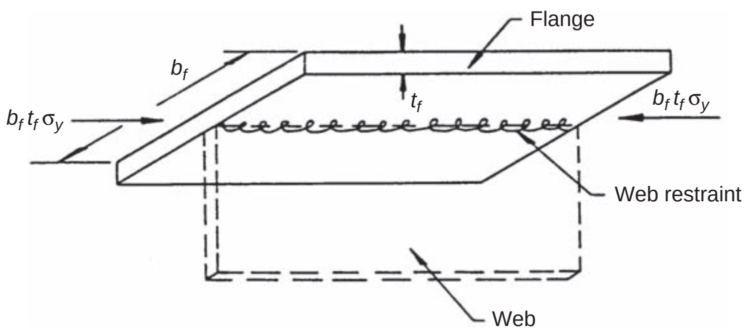

Figure 14.13 Compression flange local buckling model. (*From ASCE-WRC 1971, with permission.*)

Figure 14.14 Deformed shape of cross section after local buckling. (*From Lay 1965, with permission.*)

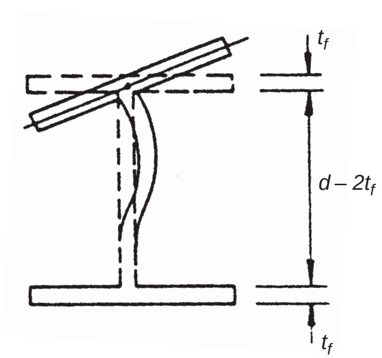

When a wide-flange steel beam is deformed well into the inelastic range, local buckling occurs and strength eventually degrades. Local buckling is either preceded or followed by lateral deflection. It is difficult to capture exactly these complex behaviors. Two approaches have been taken in the past: a solution based on buckling of an orthotropic plate and a solution based on the torsional buckling of a restrained rectangular plate. For both solutions, it is assumed that the flange is strained uniformly to its strain-hardening value, ε_{st}, and that the material has reached its strain-hardening modulus, E_{st}, that is, the plate buckles at the onset of strain-hardening. This assumption may only be reasonable for the case of uniform bending.

14.4.2 Buckling of an Orthotropic Plate

The solution based on the buckling of an orthotropic plate was presented by Haaijer and Thurlimann (1958). It assumes that the material is isotropic and homogeneous in the elastic range, that it changes during the yielding process with yielding taking place in slip bands, and that the strains in those bands jump from the value at yield, ε_y, to $s\varepsilon_y$ at the onset of strain-hardening. Because bands of elastic and yielded material coexist during yielding, the material is considered to be heterogeneous. After all the material in the yielded zone has been strained to ε_{st}, the material regains its homogeneous properties in the loading direction. However, slip produces changes in the composition of the material so that the material is no longer isotropic; that is, its properties are now direction-dependent. Therefore, to explain and predict the behavior of steel members under compression in the yielded and strain-hardening ranges, this condition of orthotropy must be recognized.

For a strain-hardened rectangular plate subjected to uniform compression (Figure 14.15), one can calculate the critical stress by solving the bifurcation equilibrium problem (i.e., solving the

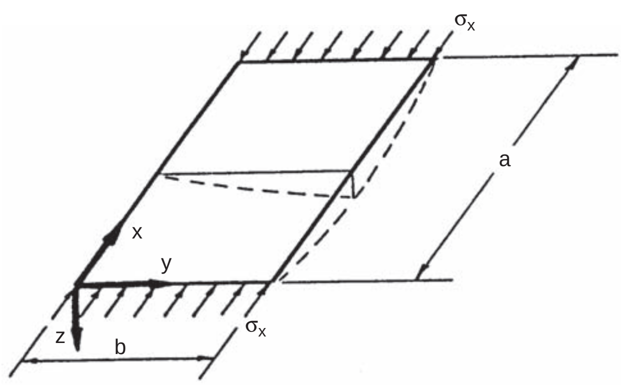

Figure 14.15 Unstiffened plate with hinged support at loaded edge. (*Haaijer and Thurlimann 1958.*)

equilibrium equations formulated in the buckled configuration). When the supported edge in the direction of loading is hinged, the critical stress is calculated and expressed by the following:

$$\sigma_{cr} = \left(\frac{t}{b}\right)^2 \left[\frac{\pi^2}{12} D_x \left(\frac{b}{a}\right)^2 + G_{st}\right] \tag{14.5}$$

where G_{st} is the strain-hardening modulus in shear, D_x is equal to $E_x/(1 - \nu_x\nu_y)$, and ν_x and ν_y are Poisson's ratios for stress increments in the x- and y-directions. For a long plate, the first term can be neglected.

When the supported edge in the loading direction in Figure 14.15 is changed to a fixed support, the buckling occurs when the aspect ratio is as follows:

$$\frac{a}{b} = 1.46 \sqrt[4]{\frac{D_x}{D_y}} \tag{14.6}$$

and the minimum buckling stress is:

$$\sigma_{cr} = \left(\frac{t}{b}\right)^2 \left[0.769\sqrt{D_x D_y} - 0.270(D_{xy} + D_{yx}) + 1.712 G_{st}\right] \tag{14.7}$$

where $D_{xy} = \nu_y D_x$ and $D_{yx} = \nu_x D_y$. Based on the tests of ASTM A7 steel, Haaijer (1957) derived the following numerical values for the five key coefficients: D_x = 3000 ksi (20,685 MPa), D_y = 32,800 ksi (226,156 MPa), $D_{xy} = D_{yx}$ = 8100 ksi (55,850 MPa), and G_{st} = 2400 ksi (16,548 MPa).

In the case of a long plate with zero rotational restraint from the web, Eq. (14.5) gives the following:

$$\sigma_{cr} = \left(\frac{2t_f}{b_f}\right)^2 G_{st} \tag{14.8}$$

When the flange plate is uniformly strained to the strain-hardening value, ε_{st}, and σ_{cr} is thus equal to σ_y, the plate width-thickness ratio at which local buckling of a perfect plate occurs is as follows:

$$\frac{b_f}{2t_f} = \sqrt{\frac{G_{st}}{\sigma_y}} \tag{14.9}$$

For A7 steel with a nominal yield stress of 33 ksi (228 MPa), the above equation gives $b_f/2t_f = \sqrt{2400/33} = 8.5$. If web rotational restraint is considered, a slightly different result will be obtained; based on experimental results, the limiting $b_f/2t_f$ ratio can be increased by about 9%, and the $b_f/2t_f$ limit becomes 9.3. Thus, Haaijer and

Thurlimann recommended flange width-to-thickness limits of $b_f/2t_f \leq 8.7$ for $\sigma_y = 33$ ksi (228 MPa) and $b_f/2t_f \leq 8.3$ for $\sigma_y = 36$ ksi (248 MPa).

Note that Haaijer and Thurlimann's solution involved the determination of five material constants and a web restraint factor that had to be calculated empirically from extensive experimental work. Because their solution was applicable to only A7 steel and did not form a sufficiently complete basis for extrapolation to other steel grades, an alternative procedure was needed. The second method, proposed by Lay (1965) and presented in the following text, requires two material constants and is applicable to different steel grades.

14.4.3 Torsional Buckling of a Restrained Rectangular Plate

It is assumed in the approach based on the torsional buckling of a restrained rectangular plate that flange local buckling occurs when the average strain in the plate reaches the strain-hardening value, ε_{st}, and that a long enough portion of the plate has yielded to permit the development of a full buckled wave. For a beam under a moment gradient, one end of the yielded region will be adjacent to a relatively stiff elastic zone, and the other end may be adjacent to a load point or connection. Both end conditions likely provide relatively stiff end restraint. In such a case, it is necessary for a longitudinal full wave length to have yielded to develop local buckling. See Figure 14.16 for the required yielded length for local buckling under uniform moment and moment gradient. Figure 14.17 shows compression flange strains measured at the onset of local buckling in tests of four beams under uniform moment. Local buckling occurs upon full yielding over half of the flange width.

The beam flange local buckling problem is solved by analogy to torsional buckling of a column. Indeed, if the flange of a wide-flange section is assumed to be unrestrained against local buckling by the web, it may be treated as a simply supported column under axial compression. Torsional buckling of such a simply supported column is described by the following equation (Bleich 1952):

$$E_{st}C_w \frac{d^4\beta}{dz^4} + (\sigma I_p - G_{st}J)\frac{d^2\beta}{dz^2} = 0 \tag{14.10}$$

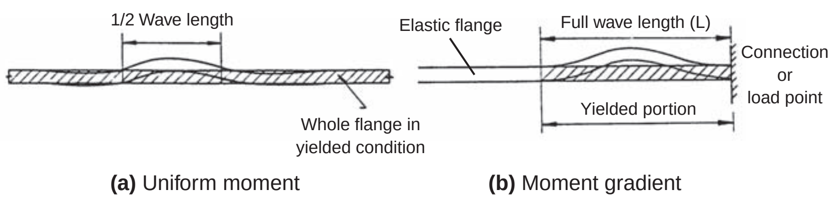

FIGURE 14.16 Required yielded length for local buckling. (*From Lay 1965, with permission.*)

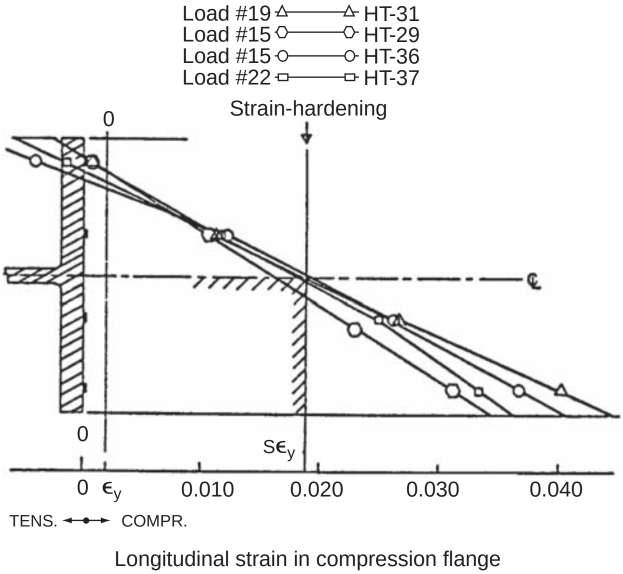

FIGURE 14.17 Strain distribution at local buckling for beams under uniform moment. (*From Lay 1965, with permission.*)

where β is the torsional angle of the member, $I_p \left(= b_f^3 t_f/12\right)$ is the polar moment of inertia of the flange, $C_w \left(= 7b_f^3 t_f^3/2304\right)$ is the warping constant of the compression flange, $J\left(= b_f t_f^3/3\right)$ is the St. Venant torsional constant for the flange, and σ is the applied compressive stress. Because warping strains occur in the loading direction, the associated strain-hardening modulus, E_{st}, must be used. Assuming $\beta = C\sin\,(n\pi z/L)$ and substituting this into the above equation, gives the nontrivial solution:

$$E_{st}C_w\left(\frac{n\pi}{L}\right)^4 + (G_{st}J - \sigma I_p)\left(\frac{n\pi}{L}\right)^2 = 0 \tag{14.11}$$

which can be rearranged to obtain the buckling stress:

$$\sigma_{cr}I_p = E_{st}C_w\left(\frac{n\pi}{L}\right)^2 + G_{st}J \tag{14.12}$$

where n is an integer and L/n is the half-wave length of a buckle. Ignoring the contribution from the warping resistance, which appears as the first term on the right-hand side of the equation, one can simplify Eq. (14.12) as follows:

$$\sigma_{cr} = \frac{G_{st}J}{I_p} = \frac{G_{st}}{\left(\frac{b_f}{2t_f}\right)^2} \tag{14.13}$$

Setting $\sigma_{cr} = \sigma_y$ because the flange is fully yielded when inelastic buckling occurs, and solving for the limiting flange width-to-thickness ratio, gives the following:

$$\frac{b_f}{2t_f} = \sqrt{\frac{G_{st}}{\sigma_y}} \tag{14.14}$$

which is identical to that derived by Haaijer [see Eq. (14.9)].

Figure 14.14 shows the assumed buckling configuration, neglecting the relative lateral displacement between two flanges. It's also assumed that the web is fully yielded under longitudinal stresses; this roughly reflects experimental observations. In reality, however, the beam web does provide some degree of rotational restraint against local buckling to the compressive flange. The web restraint can be represented by a rotational spring of constant, k, and Eq. (14.10) becomes the following:

$$E_{st}C_w \frac{d^4\beta}{dz^4} + (\sigma I_p - G_{st}J)\frac{d^2\beta}{dz^2} = k\beta \tag{14.15}$$

where k can be estimated as follows:

$$k = \left[\frac{4G_{st}}{d - 2t_f}\right]\frac{t_w^3}{12} = \frac{G_{st}t_w^3}{3(d - 2t_f)} \tag{14.16}$$

The improved solution, obtained following a procedure similar to that described earlier, is:

$$\sigma_{cr}I_p = E_{st}C_w\left(\frac{n\pi}{L}\right)^2 + G_{st}J + k\left(\frac{L}{n\pi}\right)^2 \tag{14.17}$$

The half-wave length, L/n, which produces the minimum critical stress, can be found by setting $\partial\sigma_{cr}/\partial(L/n) = 0$:

$$\frac{L}{n} = \pi\sqrt[4]{\frac{E_{st}C_w}{k}} = 0.713\frac{t_f}{t_w}\sqrt[4]{\frac{A_w}{A_f}}b \tag{14.18}$$

where A_w [$= (d - 2t_f)t_w$] and A_f ($= b_f t_f$) are web and flange areas, respectively. The half-wave length derived above is key to determining the advent of local buckling in beams.

Substituting the half-wave length into Eq. (14.17) and setting σ_{cr} to σ_y makes the limiting value of $b_f/2t_f$ the following:

$$\frac{b_f}{2t_f} = \sqrt{\frac{G_{st}}{\sigma_y} + 0.381\left(\frac{E_{st}}{\sigma_y}\right)\left(\frac{t_w}{t_f}\right)^2 \sqrt{\frac{A_f}{A_w}}} \tag{14.19}$$

Two material properties in the fully yielded state are needed: the strain-hardening moduli in compression, E_{st}, and shear, G_{st}. E_{st} can be determined from a tensile or compression test, and G_{st} must be determined indirectly. The method to determine G_{st} has been controversial. Based on the discontinuous yield process described in Chapter 2, Lay (1965) derived the following expression for the strain-hardening shear modulus:

$$G_{st} = \frac{2G}{1 + \dfrac{E}{4E_{st}(1+\nu)}\tan^2\alpha} = \frac{4E}{5.2+h} \tag{14.20}$$

where α (= 45°) is the slip angle between the yield plane and normal stress, h (= E/E_{st}) is the ratio of elastic stiffness to strain-hardening stiffness, and ν (= 0.3) is Poisson's ratio. With h equal to 33, G_{st} is 3040 ksi (20,961 MPa). The second term on the right side of Eq. (14.19) represents the beneficial contribution of web restraint against flange local buckling. For most wide-flange sections, the increase in the limiting value of $b_f/2t_f$ owing to the web restraint is between 2% and 3.2% and can be ignored. The width-thickness limiting ratio is, therefore, the same as given in Eq. (14.9).

The discussion presented so far is for beams under uniform moment. For beams subjected to a moment gradient, the maximum moment, M_o, can exceed M_p because of strain-hardening, and the stress in the flange will exceed σ_y in the yielded region. Based on limited experimental evidence, it was suggested by Lay (1965) that M_o could be taken as follows:

$$M_0 = \frac{1}{2}\left(1 + \frac{\sigma_u}{\sigma_y}\right)M_p \tag{14.21a}$$

where σ_u is the actual ultimate stress.

The corresponding average stress over the yielded region is equal to the following:

$$\sigma_y^* = \frac{1}{4}\left(3 + \frac{\sigma_u}{\sigma_y}\right)\sigma_y \tag{14.21b}$$

Replacing σ_y by σ_y^* and using an average web contribution of 2.6% in Eq. (14.19) gives the following limiting width-thickness ratio for a beam under moment gradient:

$$\left(\frac{b_f}{2t_f}\right)^2 = \sqrt{\frac{4\times 1.026G_{st}}{(3+\sigma_u/\sigma_y)\sigma_y}} = \sqrt{\left(\frac{3.16}{3+\sigma_u/\sigma_y}\right)\left(\frac{1}{\varepsilon_y}\right)\left(\frac{1}{1+h/5.2}\right)} \qquad (14.22)$$

Assuming $\sigma_u = 1.80\sigma_y$ and $h = 33$ for A36 steel, $b_f/2t_f = 8.5$. Different grades of steel will have different values of the ratio (σ_u/σ_y), yield strain (ε_y), and strain-hardening ratio (h), and therefore different limiting values of $b_f/2t_f$.

In the United States, the plastic design method was first adopted in the 1961 AISC Specification. At that time, structural steels with nominal yield strength (F_y) up to 36 ksi (248 MPa) were permitted for plastic design, and the flange $b_f/2t_f$ ratio was limited to 8.5, close to Haaijer and Thurlimann's recommendations. Research conducted thereafter made it possible to extend plastic design to higher strength steels. As a result, since 1969 the AISC Specification has permited steels with a yield stress of up to 65 ksi (448 MPa) to be used for plastic design (AISC 1989). On the basis of the work of Lay and Galambos on compact beams, $b_f/2t_f$ was limited to $52/\sqrt{F_y}$ $(137/\sqrt{F_y}$ in S.I. units). For A36 steel, $52/\sqrt{F_y}$ is 8.7, is 8.7, which is about the same value as that computed from Eq. (14.22).

It is worthwhile to mention that in 1974, the AISC Specification introduced some plastic design concepts into the allowable stress design procedures by permitting the designer to redistribute moments in a continuous compact beam. This was based on the assumption that under uniform bending, flange strains of compact beams could reach four times the yield strain, which corresponds to a rotation capacity of three. This level of plastic rotation was thought to be sufficient to justify the moment redistribution for most civil engineering structures.

The AISC limiting flange width-thickness ratios for plastic design (compact section requirements for allowable stress design) were not changed until the LRFD Specification was published in 1986 (AISC 1986). The rule for flange local buckling was based on the test results of Lukey and Adams (1969). Figure 14.18 shows the relationship between the plastic rotation capacities defined in Figure 14.3 and the normalized flange width-thickness ratio. The test results presented in Figure 14.18 indicate that beams with smaller normalized width-thickness ratios not only exhibit a larger rotation capacity but also show a slower degradation in strength after the maximum flexural capacity is reached, as is evident from the larger spread between θ_{hm} and θ_h for the more compact sections

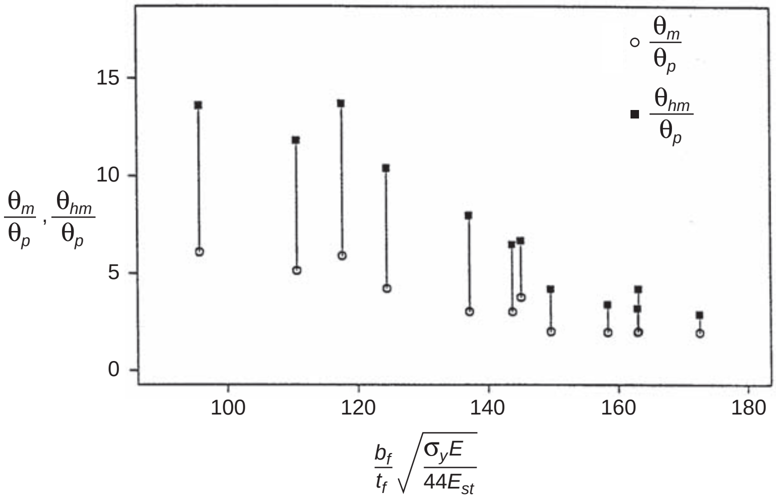

FIGURE 14.18 Peak and total rotation capacities. (*Adapted from Lukey and Adams 1969.*)

in Figure 14.18. Based on Figure 14.18, the following limiting value is required for a rotation capacity, R, of 3:

$$\frac{b_f}{2t_f}\sqrt{\frac{\sigma_y E}{44E_{st}}} \leq 78 \tag{14.23}$$

To establish a conservative width-thickness ratio limit, Yura et al. (1978) suggested that the value of E_{st} be taken as one standard deviation [150 ksi (1,034 MPa)] below the mean value [600 ksi (4137 MPa)]. Substituting $E_{st} = 450$ ksi (3,103 MPa) into Eq. (14.23) gives the following in U.S. units:

$$\frac{b_f}{2t_f} \leq \frac{65}{\sqrt{\sigma_y}} \quad \text{in U.S. units} \tag{14.24a}$$

$$\frac{b_f}{2t_f} \leq \frac{170}{\sqrt{\sigma_y}} \quad \text{in S.I. units} \tag{14.24b}$$

The AISC LRFD Specification (1986) adopted the above requirement for compact sections. Since 2005, the AISC 341 states the above expression in a nondimensional form: $b_f/2t_f \leq 0.38\sqrt{E/F_y}$. Note that the difference between the actual yield stress, σ_y, and the nominal yield stress, F_y, is ignored in the above development. The above requirement also applies to plastic design in AISC LRFD Specification and

AISC 360. This requirement is less stringent than the limit of $52/\sqrt{F_y}$ $(= 137/\sqrt{F_y}$ in SI units), which was used by the AISC Specification for plastic design prior to 1986.

14.5 Web Local Buckling

Only limited research results exist for inelastic web local buckling of wide-flange beams. Haaijer and Thurlimann (1958) studied web buckling of flexural members subjected to bending and axial load effects. Figure 14.19 shows variations in the limiting web slenderness ratio, in the form of $(d - t_f)/t_w$, with respect to the normalized axial force, $P/(\sigma_y A_w)$, and the normalized maximum compression strain in the flange, $\varepsilon_m/\varepsilon_y$. The figure shows clearly that a smaller web width-thickness ratio is required to resist higher axial loads or to achieve higher inelastic strain (or rotation capacity).

In Section 14.4, it was noted that a beam under uniform bending would be strained to $4\varepsilon_y$ for a rotation capacity, R, of 3 and that such a plastic rotation was considered in the AISC Specification to be sufficient to justify the moment redistribution for most structures. With average values of $A/A_w = 2$ and $d/(d - t_f) = 1.05$ for wide-flange shapes, the curve for $\varepsilon_m/\varepsilon_y = 4$ in Figure 14.19 is replotted as the dashed curve in Figure 14.20; this dashed curve can also be approximated by two straight lines. The results presented in Figure 14.20,

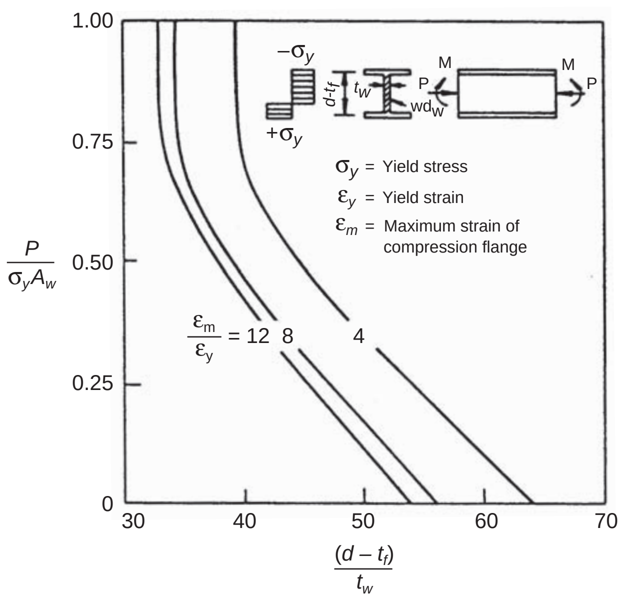

Figure 14.19 Limiting values of $(d - t_f)/t_w$ ratio of the web of a wide-flange section. (*From Haaijer and Thurlimann 1958 with permission.*)

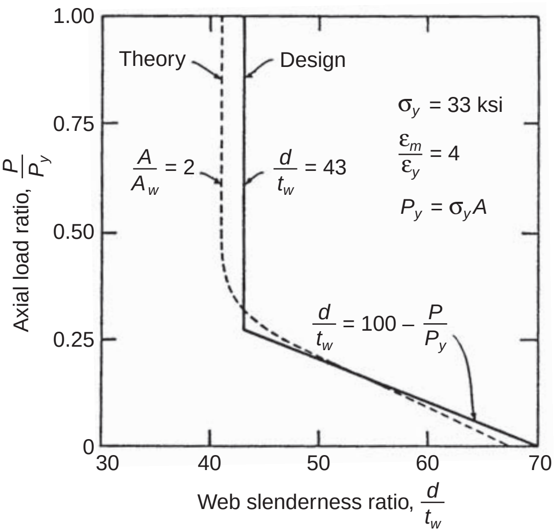

FIGURE 14.20 Maximum allowable web slenderness ratio for a beam subjected to combined moment and axial force. (*From Massonnet and Save 1965, with permission.*)

however, are applicable to only A7 or A36 steel. For higher strength steel, it was suggested that the limiting width-thickness ratio be modified by $\sqrt{36/\sigma_y}$ (Adams et al. 1965), and thus:

$$\frac{d}{t_w} = \frac{257}{\sqrt{\sigma_y}} \quad \text{for } \frac{P}{P_y} > 0.27 \quad \text{in U.S. units} \tag{14.25a}$$

$$\frac{d}{t_w} = \frac{675}{\sqrt{\sigma_y}} \quad \text{for } \frac{P}{P_y} > 0.27 \quad \text{in S.I. units} \tag{14.25b}$$

$$\frac{d}{t_w} = \frac{412}{\sqrt{\sigma_y}}\left(1 - 1.4\frac{P}{P_y}\right) \quad \text{for } \frac{P}{P_y} \le 0.27 \quad \text{in U.S. units} \tag{14.25c}$$

$$\frac{d}{t_w} = \frac{1082}{\sqrt{\sigma_y}}\left(1 - 1.4\frac{P}{P_y}\right) \quad \text{for } \frac{P}{P_y} \le 0.27 \quad \text{in S.I. units} \tag{14.25d}$$

Such a modification, which was based on satisfactory performance observed from beam and frame tests at the time, was adopted in the AISC ASD Specification for plastic design.

Based on limited test data of welded girders with unstiffened thin web, the AISC LRFD Specification specifies the following limiting value for a rotation capacity of at least 3:

$$\frac{h}{t_w} \le \frac{640}{\sqrt{F_y}} \quad \text{in U.S. units} \tag{14.26a}$$

$$\frac{h}{t_w} \le \frac{1680}{\sqrt{F_y}} \quad \text{in S.I. units} \tag{14.26b}$$

where h is defined as the clear distance between flanges less the fillet radius at each flange. Assuming an average value of $h/d = 0.9$, the above equation is equivalent to $d/t_w \le 710/\sqrt{F_y}$. Since 2005, the AISC 341 states the above expression in a nondimensional form: $h/t_w \le 3.76\sqrt{E/F_y}$. The AISC Seismic Provisions (1992) specify the following:

$$\frac{h}{t_w} \le \frac{520}{\sqrt{F_y}} \quad \text{in U.S. units} \tag{14.27a}$$

$$\frac{h}{t_w} \le \frac{1365}{\sqrt{F_y}} \quad \text{in S.I. units} \tag{14.27b}$$

Based on research conducted on cyclic stability of Reduced Beam Section for Special Moment Frame applications (Uang and Fan 2001), Eq. (14.27a) was changed to $2.45\sqrt{E/F_y}$ in the 2005 AISC Seismic Provisions. The AISC 341 beam web slenderness ratio requirements for plastic design are not as severe as those of the AISC ASD Specification for plastic design.

Dawe and Kulak (1986) used analytical techniques to study the local buckling behavior of beam-columns. The effects of flange and web interaction, inelastic behavior, and the presence of residual stresses were considered. They proposed the following limiting ratios for plastic design:

$$\frac{h}{t_w} = \frac{430}{\sqrt{\sigma_y}}\left(1 - 0.930\frac{P}{P_y}\right) \quad \text{for } 0 \le \frac{P}{P_y} \le 0.15 \quad \text{in U.S. units} \tag{14.28a}$$

$$\frac{h}{t_w} = \frac{1130}{\sqrt{\sigma_y}}\left(1 - 0.930\frac{P}{P_y}\right) \quad \text{for } 0 \le \frac{P}{P_y} \le 0.15 \quad \text{in S.I. units} \tag{14.28b}$$

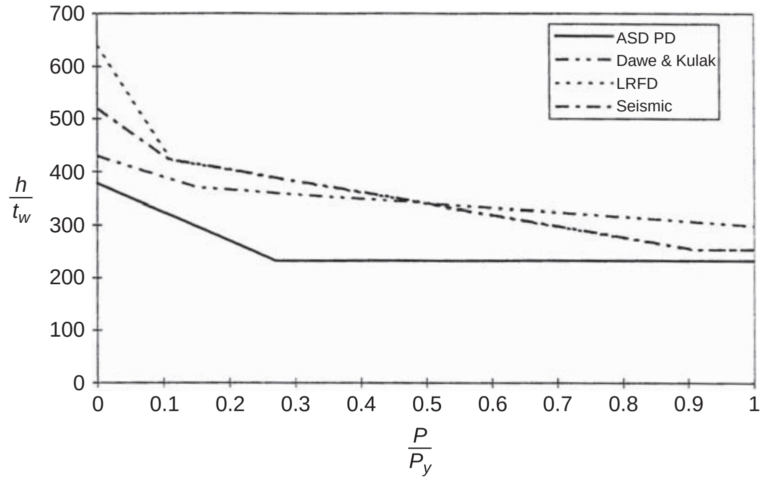

FIGURE 14.21 Comparison of rules for web local buckling.

$$\frac{h}{t_w} = \frac{382}{\sqrt{\sigma_y}}\left(1 - 0.220\frac{P}{P_y}\right) \quad \text{for } 0.15 \le \frac{P}{P_y} \le 1.0 \quad \text{in U.S. units} \tag{14.28c}$$

$$\frac{h}{t_w} = \frac{1003}{\sqrt{\sigma_y}}\left(1 - 0.220\frac{P}{P_y}\right) \quad \text{for } 0.15 \le \frac{P}{P_y} \le 1.0 \quad \text{in S.I. units} \tag{14.28d}$$

A comparison of the proposed formulae with those adopted in the AISC Specifications is presented in Figure 14.21. Based on their study, Dawe and Kulak concluded that the web slenderness ratios currently specified in North American codes are conservative.

14.6 Inelastic Lateral-Torsional Buckling

14.6.1 General

Elastic lateral-torsional buckling of wide-flange beams under uniform bending or moment gradient has been studied extensively (e.g., Bleich 1952, Timoshenko and Gere 1961). Three assumptions are common to the cited studies:

- The stiffness does not change along the length of the member.
- The shear center remains in the plane of the web.
- The cross-section of the steel member remains undistorted.

The first solution for lateral-torsional buckling of wide-flange beams in the strain-hardening range was developed by White (1956). Lee and Galambos (1962) extended White's work by considering unloading of the compression flange caused by lateral-torsional buckling. Galambos (1963) presented a solution for determining the inelastic lateral-torsional buckling strength of rolled wide-flange beam-columns. Lay and Galambos (1965) also extended White's work and related the rotation capacity of a beam under uniform bending to the lateral support spacing. Lay and Galambos (1967) used the equivalent length concept to analyze lateral-torsional buckling of beams under moment gradient. Kemp (1984) extended the Lay and Galambos solution.

14.6.2 Beam Under Uniform Moment

14.6.2.1 White's Approach

A theoretical solution for the determination of the critical unsupported length was presented by White (1956). In that solution it was assumed that lateral-torsional buckling occurs when the material has reached the onset of strain-hardening. This assumption implies that sufficient plastic rotation has developed before lateral-torsional buckling occurs (see Section 14.3), because the beam has already undergone considerable inelastic deformation before strain-hardening is reached. In White's analysis, no elastic unloading of already yielded fibers is assumed. Thus, this approach provides a lower bound solution analogous to that obtained by the tangent modulus concept of axially loaded columns (Shanley 1947). The critical spacing of lateral braces for all rolled wide-flange sections was found to be about $17r_y$ for a simply supported beam under a uniform bending moment equal to M_p. The theoretical basis follows.

Consider a beam with simple end restraints (i.e., the ends of the beam cannot translate or twist but are free to rotate laterally and the end sections are free to warp) as shown in Figure 14.22. When the beam is subjected to uniform moment, the elastic solution for lateral-torsional buckling is well established (Timoshenko and Gere 1961):

$$\frac{M}{EI_y} = \frac{\pi}{L_b}\sqrt{\frac{GJ}{EI_y} + \frac{\pi^2}{L_b^2}\frac{C_w}{I_y}} = \frac{\pi}{L_b}\sqrt{\frac{GJ}{EI_y} + \frac{\pi^2}{L_b^2}\left(\frac{d-t_f}{2}\right)^2} \qquad (14.29)$$

in which EI_y is the flexural stiffness about the section's minor principal axis, GJ is the St. Venant torsional stiffness, and L_b is the unbraced length of the member. The above equation can also be applied to yielded members if E and G are replaced by their corresponding inelastic material properties. For relatively short beams, the equation can be further simplified if one ignores the first term,

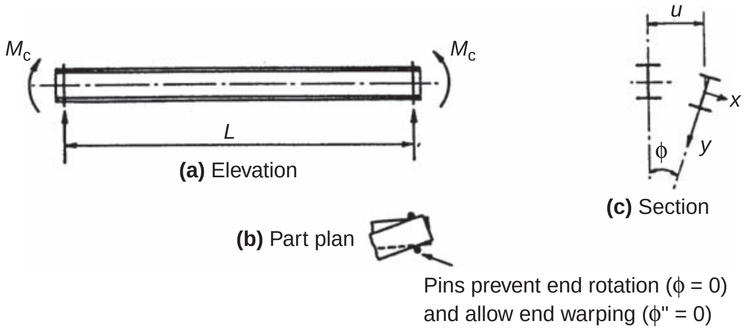

FIGURE 14.22 Simply supported beam under uniform bending. (*From Trahair 1993, with permission.*)

which represents the contribution due to St. Venant torsion. Substituting $M_p (= Z_x \sigma_y)$ for M:

$$\frac{Z_x \sigma_y}{E' I_y} = \left(\frac{\pi}{L_b}\right)^2 \left(\frac{d - t_f}{2}\right) \tag{14.30}$$

where $E'I_y$ is the effective flexural stiffness. Because White did not consider unloading of the compression flange upon buckling, $E'I_y$ can be expressed as the tangent modulus stiffness:

$$E' I_y = \frac{1}{h} E I_y \tag{14.31}$$

From Eq. (14.30), the limiting slenderness for this lower bound solution can be solved as follows:

$$\frac{L_b}{r_y} = \pi \sqrt{\frac{E'}{\sigma_y}} \sqrt{\frac{A(d - t_f)}{2Z_x}} = \pi \sqrt{\frac{1}{h \varepsilon_y}} \sqrt{\frac{A(d - t_f)}{2Z_x}} \tag{14.32}$$

If one assumes $h = 33$ for A36 steel and takes an average value of 1.2 for $A(d - t_f)/2Z_x$ for wide-flange sections, the limiting L_b/r_y ratio is about 17. This limit is optimal because closer spacing of lateral bracing would not provide greater plastic deformation capacity because of local buckling.

Lee and Galambos (1962) extended White's work by considering the unloading effect of the compression flange on lateral buckling. The method is analogous to the reduced modulus concept of axially loaded columns. Lee and Galambos showed that the critical lateral spacing, based on such an upper bound solution, is $45r_y$. If $L_b/r_y < 45$, the Lee and Galambos experiments on continuous beams showed that failure is initiated by local buckling of the compression flange and that post buckling strength reserve is quite large. The postbuckling strength provided by a continuous beam is mainly due to the lateral restraint provided by the adjacent elastic spans, which offer both in-plane and out-of-plane moment restraints as well as significant warping restraint at the ends of the buckled span.

14.6.2.2 Lay and Galambos' Approach

Lay and Galambos (1965) extended White's work to determine the suboptimum lateral support spacing. In that work, the lateral support spacing was related to the rotation capacity. For the simply supported beam under uniform bending moment shown in Figures 14.23a and b, Figure 14.23c shows the deformed configuration of the section after buckling. It is assumed that longitudinal hinges are located at the mid-height of the web and at the junction between the web and tension flange. Compared with the observed deformed shape shown in Figure 14.24b, the model simulates well with the observed web deformation pattern. The major difference between the model and actual deformed shape is that, in reality, the tension flange tends to twist rather than allowing a hinge to form at its junction with the web.

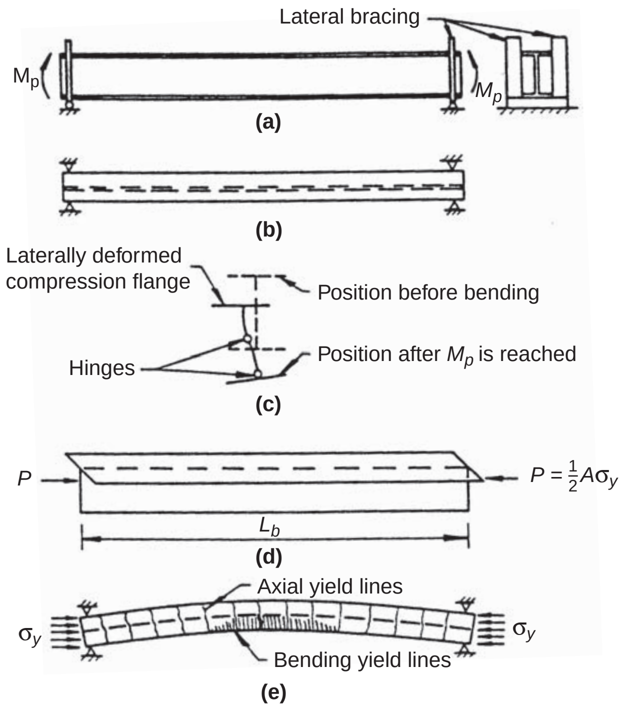

Figure 14.23 Buckling of a beam under uniform moment. (*From ASCE-WRE 1971, with permission.*)

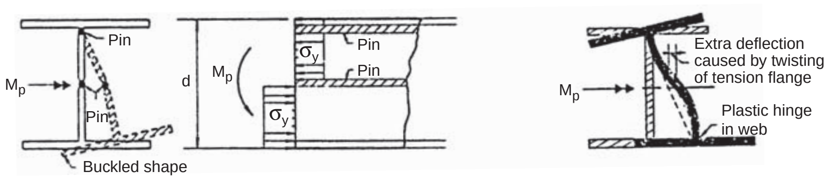

(a) Beam model **(b)** Observed deformed shapes

Figure 14.24 Lateral buckling model of cross section. (*From Lay and Galambos 1965, with permission.*)

The physical model shown in Figure 14.23d is therefore used to solve the bifurcation problem. This model is conservative for the lateral buckling calculation because it assumes that the beam web contributes to the loaded area without increasing the lateral flexural stiffness. Therefore, the compression portion of the beam is isolated from the beam under uniform moment, and the lateral-torsional buckling problem is reduced to that of a column under an axial force $P = A\sigma_y/2$, where A is the cross-sectional area of the beam. This compression T-column is also assumed to be pin-ended. The critical load of this T-shaped column is as follows:

$$P_{cr} = \frac{A\sigma_y}{2} = \frac{\pi^2 cEI}{L_b^2} \tag{14.33}$$

where cEI (= $cEI_y/2$) represents the inelastic flexural stiffness of the T-column after yielding. The limiting slenderness ratio resulting from the above equation is:

$$\frac{L_b}{r_y} = \pi\sqrt{c}\sqrt{\frac{E}{\sigma_y}} \tag{14.34a}$$

The above expression is valid only for simply supported beams. If the unbraced beam segment is continuous with adjacent spans, an effective length factor, K, may be used to account for the restraint offered by the adjacent spans:

$$\frac{KL_b}{r_y} = \pi\sqrt{c}\sqrt{\frac{E}{\sigma_y}} \tag{14.34b}$$

Based on calculation of effective length factors and experimental observation, for the usual case of elastic adjacent spans, K may be taken as 0.54; for yielded adjacent spans, K may be taken as 0.8.

Next, consider the associated rotation capacity, R. For a beam under uniform bending, the relationship between the rotation capacity and the average strain, ε_{av}, in the beam flange is as follows:

$$R = \frac{\theta}{\theta_p} - 1 \approx \frac{\varepsilon_{av}}{\varepsilon_y} - 1 \tag{14.35}$$

When an optimal lateral bracing is provided such that lateral-torsional buckling occurs when ε_{av} reaches ε_{st} (= $s\varepsilon_y$), the rotation capacity is:

$$R = \frac{\varepsilon_{av}}{\varepsilon_y} - 1 = \frac{s\varepsilon_y}{\varepsilon_y} - 1 = s - 1 \tag{14.36}$$

For a suboptimum situation in which $\varepsilon_{av} < \varepsilon_{st}\varepsilon_{av} = (1 - \phi)\varepsilon_y + \phi s\varepsilon_y$ [see Eq. (2.9)], the rotation capacity is:

$$R = (s - 1)\phi \tag{14.37}$$

It should be noted that the rotation capacity, R, in Eqs. (14.36) and (14.37) is valid for the case in which the inelastic action involves axial yield lines only. In reality, lateral bending is inevitable because of geometric imperfections, and bending yield lines will develop. The axial yield lines shown in Figure 14.23e are those due to the force, P, and spread across the whole width of the flange. The bending yield lines in the more severely compressed half of the flange are due to the lateral displacement of the compression flange upon buckling. Lay and Galambos showed that the rotation capacity considering the effects of bending and axial yield lines is as follows:

$$R = \left[\frac{2}{\pi} + \frac{1}{2}\left(1 - \frac{2}{\pi}\right)\left(1 - \frac{1}{\sqrt{h}}\right)\right](s - 1)\phi \approx 0.8(s - 1) \tag{14.38}$$

where $h = 33$ for a fully yielded member ($\phi = 1$) is used for the simplification.

Based on a discontinuous yield concept (see Chapter 2), in which the strain is equal to ε_{st} at the yield lines and ε_y elsewhere, and a compression flange model shown in Figure 14.23e, Lay and Galambos then considered the stiffness reduction owing to effects of both axial and bending yield lines to derive the coefficient c in Eq. (14.34b) as a function of R:

$$c = \frac{1}{1 + 0.7Rh\left(\dfrac{1}{s - 1}\right)} \tag{14.39}$$

In deriving this expression, it is assumed that unloading occurs once flange local buckling takes place, that is, when the average strain at the center of flange is equal to the strain-hardening strain. Substituting Eq. (14.38) into Eq. (14.39) gives the following:

$$c = \frac{1}{1+0.56h} \tag{14.40}$$

and Eq. (14.34b) becomes:

$$\frac{KL_b}{r_y}\frac{\sqrt{\varepsilon_y}}{\pi} = \frac{1}{\sqrt{1+0.56h}} \tag{14.41}$$

If h = 33 and K = 0.54, the following limiting slenderness ratio results:

$$\frac{L_b}{r_y} = \frac{225}{\sqrt{\sigma_y}} \quad \text{in U.S. units} \tag{14.42a}$$

$$\frac{L_b}{r_y} = \frac{591}{\sqrt{\sigma_y}} \quad \text{in S.I. units} \tag{14.42b}$$

The above limiting ratio is valid only for low-yield strength steels. Some limited test results with Grade 65 steel have shown that Eq. (14.42) is not conservative for high strength steel (ASCE-WRC 1971). Instead, it was found that $L_b/r_y = 1375/\sigma_y$ (= $9480/\sigma_y$ in S.I. units) not only fits the test results well for high strength steel but also approximates Eq. (14.42) for lower strength steels. The limiting L_b/r_y ratio of $1375/\sigma_y$ (= $9480/\sigma_y$ in S.I. units) was adopted in the AISC Specifications for plastic design in 1969.

14.6.3 Beam Under Moment Gradient

14.6.3.1 Equivalent Length Approach

Lay and Galambos (1967) performed inelastic lateral buckling analysis of beams under a moment gradient using the model shown in Figure 14.25. Once again, the compression half of the beam is considered to act as an isolated column, and lateral-torsional buckling is assumed to be equivalent to buckling of an isolated column under the beam bending stresses. Mathematically, the modeling is equivalent to disregarding the contribution of St. Venant torsion to the strength of the beam. Given that the St. Venant torsion contribution is actually significant for most beams under moment gradient, the proposed solution therefore provides a lower bound estimate of a beam's lateral-torsional buckling strength.

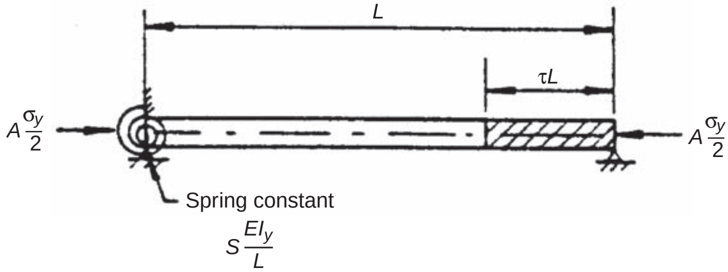

FIGURE 14.25 Lateral buckling model of beam under moment gradient. (*From Lay and Galambos 1967 with permission.*)

In this model, the yield moment, M_y, is taken as the moment at which yielding first occurs in the flange (ignoring residual stresses). Lay and Galambos assumed an average value of $M_y = 0.94M_p$. The variation of moment along the beam length causes not only a transition of material properties from elastic to yielded, but also a change in the compression stresses over the length of the beam. After M_p is reached, the lateral displacements usually increase rapidly. The deflected shape also changes, and the curvatures producing lateral displacement are concentrated in the yielded region. White's study (1956) showed that the extent of yielding has a much greater influence on lateral buckling behavior than does the variation in normal stress. Thus, it was further assumed that normal stresses on the compression tee remain at σ_y and do not reduce with decreasing bending moment. The conservatism introduced by this assumption is offset to some extent by the fact that normal stresses exceed σ_y in the yielded length (τL) as a result of strain-hardening. The buckling equation for the column may be expressed as follows:

$$\frac{\tan(\lambda_b \pi \tau/\sqrt{c})}{\tan[\lambda_b \pi(1-\tau)]} + \frac{1}{\sqrt{c}}\left[\frac{\lambda_b \pi + S\left[\frac{1}{\lambda_b \pi} - \cot(\lambda_b \pi(1-\tau))\right]}{\lambda_b \pi + S\left[\frac{1}{\lambda_b \pi} + \tan(\lambda_b \pi(1-\tau))\right]}\right] = 0 \tag{14.43}$$

where c is the ratio of the lateral bending stiffness in the yielded region to the elastic value, S represents the elastic restraint of an adjacent span ($S = 0$ for a pinned end and $S \to \infty$ for a fixed end), and the limiting slenderness ratio for lateral-torsional buckling, L_b/r_y, is expressed in the nondimensional form as λ_b:

$$\lambda_b = \frac{L_b}{r_y \pi}\sqrt{\frac{\sigma_y}{E}} \tag{14.44}$$

Lay and Galambos (1965) considered the properties of bending yield planes and derived the following formula for c:

$$c = \frac{2}{h + \sqrt{h}} \tag{14.45}$$

For a given value of S, the relationship between λ_b and τ can be constructed for a particular grade of steel (see Figure 14.26). Note that Eq. (14.43) was derived on the basis that the wide flange section was compact, that is, a section that satisfies the limiting flange width-thickness ratio of Eq. (14.22) and does not buckle locally until it is fully yielded. At this point, it is important to establish whether the yielded length associated with lateral-torsional buckling is greater or less than that required to cause local buckling. Given that, for a beam under moment gradient, yielding will be concentrated in a restricted region of length, τL_b, and the possibility of local buckling within this region must be considered. It has been shown in Section 14.4 that τL_b must be of a sufficient length for a full local buckling wave to form. The full wavelength of a local buckle has been given as $2l$, where, from Eq. (14.18), $l/b_f = 0.71(t_f/t_w)(A_w/A_f)^{1/4}$. Therefore, the local buckling criterion to be applied to a compact section under moment

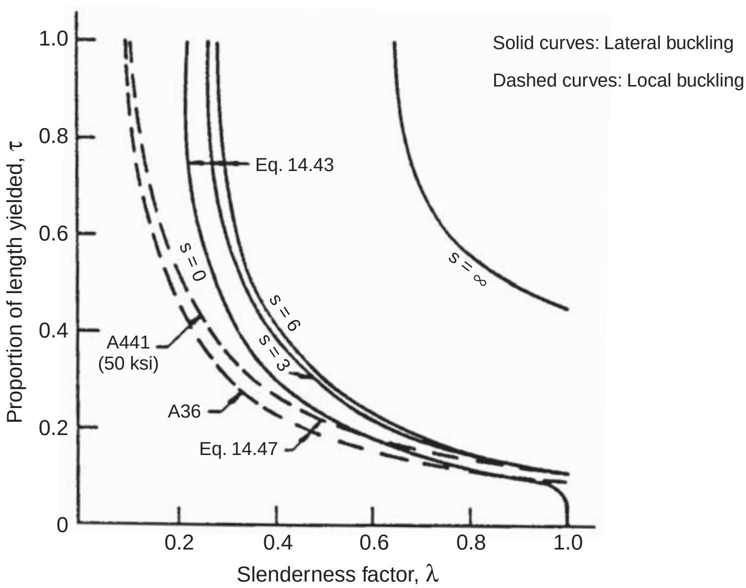

Figure 14.26 Relationship of flange local buckling and lateral-torsional buckling. (*From Lay and Galambos 1967, with permission.*)

gradient is that the yielded length, $\tau_{lb}L_b$, should be equal to the full wavelength of the local buckle:

$$\tau_{lb}L_b = 2l = 1.42\left(\frac{t_f}{t_w}\right)\sqrt[4]{\frac{A_w}{A_f}}\,b_f \tag{14.46}$$

Based on the geometric properties of available wide-flange sections, an average value of $8.33r_y$ can be obtained for the right-hand side of Eq. (14.46). Therefore, Eq. (14.46) can be expressed as the following nondimensional form [see Eq. (14.44)]:

$$\tau_{lb}\lambda_b = 2.65\sqrt{\varepsilon_y} \tag{14.47}$$

Using Eq. (14.47), the proportion (τ) of the beam length that must be yielded to trigger flange local buckling is superimposed on Figure 14.26 for a direct comparison with the required length to initiate lateral-torsional buckling. For the practical cases of inelastic beams under moment gradient, it can be seen that a smaller value of τ is required to cause flange local buckling than to cause lateral-torsional buckling. That is, failure will generally be initiated by flange local buckling rather than by lateral-torsional buckling. Because the beam behavior under moment gradient is most likely to be governed by flange local buckling, Lay and Galambos (1967) suggested that lateral bracing be provided according to the criterion of Eq. (14.41) for a beam under uniform bending moment, but with a value of R equal to 1. It was recommended that for the moment ratio $-0.5 \le q = M_1/M_2 \le 1.0$ [where M_1 is the smaller moment at the end of the unbraced length, M_2 is the larger moment at the end of the unbraced length, and (M_1/M_2) is positive when moments cause reverse curvature and negative for single curvature], the limiting L_b/r_y ratio be taken as 70, 55, and 45 for σ_y of 36, 50, and 65 ksi (248, 345, and 448 MPa), respectively. This recommendation can be approximated by the following:

$$\frac{L_b}{r_y} = \frac{1{,}375}{\sigma_y} + 25 \quad \text{when } -0.5 < \frac{M_1}{M_2} < 1.0 \quad \text{in U.S. units} \tag{14.48a}$$

$$\frac{L_b}{r_y} = \frac{9480}{\sigma_y} + 25 \quad \text{when } -0.5 < \frac{M_1}{M_2} < 1.0 \quad \text{in S.I. units} \tag{10.48b}$$

This limit on slenderness ratio has been adopted by the AISC Specifications for plastic design since 1969.

14.6.3.2 Bansal's Experimental Study

To study the lateral instability of beams, 34 continuous steel beams having specified yield strengths of 36, 50, and 65 ksi (248, 345, and 448 MPa, respectively) were tested by Bansal (1971). Bansal reported that the deformation capacity of a beam is inversely proportional to its yield strength when the behavior is controlled by lateral instability. For given lateral slenderness ratio, type of loading, and support conditions, higher strength steel beams are more prone to lateral-torsional buckling.

Figure 14.27 shows the test results of those beams that developed a plastic mechanism. The abscissa represents the normalized lateral

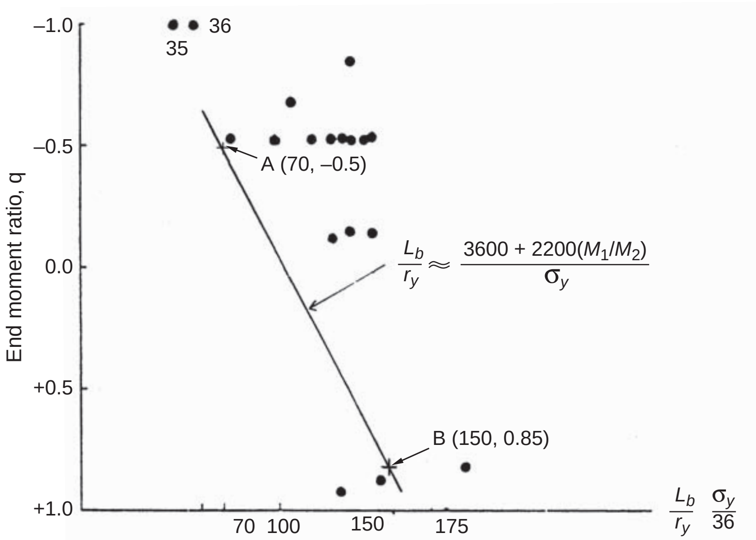

(a) End moment ratio versus normalized slenderness

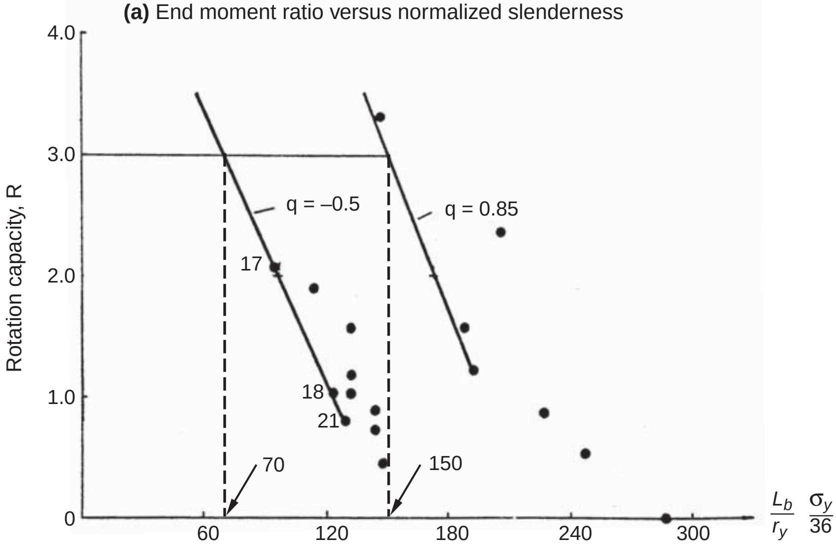

(b) Rotation capacity versus normalized slenderness

Figure 14.27 Relation of rotation capacity, moment ratio, and lateral slenderness ratio for parameters expressed in U.S. units only. (*Adapted from Bansal 1971.*)

slenderness ratio $(L_b/r_y)(\sigma_y/36)$. Figure 14.27b shows the relationship between the slenderness ratio and the rotation capacity, R. The group of points on the left is for the beams with single curvature ($q \le 0$); the group on the right is for the beams with reverse curvature ($q > 0$). Lines are drawn on Figure 14.27b linking data points for $q = -0.5$ (specimens 17, 18, 21) and $q = 0.85$. The modifed stenderness ratio $(L_b/r_y)(\sigma_y/36)$ necessary to achieve a rotation capacity of 3 for q equal to -0.5 and 0.5 are calculated from the intersection points of ($R = 3$, $q = -0.5$) and ($R = 3$, $q = -0.85$), respectively, to be 70 and 150, respectively. Using these data, points A and B in Figure 14.27a can be identified. The line passing through these points represents the limiting slenderness ratio for a rotation capacity of 3:

$$\frac{L_b}{r_y} \approx \frac{3600 + 2200(M_1/M_2)}{\sigma_y} \quad \text{in U.S. units} \tag{14.49a}$$

$$\frac{L_b}{r_y} \approx \frac{24822 + 15169(M_1/M_2)}{\sigma_y} \quad \text{in S.I. units} \tag{14.49b}$$

With the nominal yield strength, F_y, substituted for σ_y, the above limiting slenderness ratio was adopted by the AISC LRFD Specification for plastic design. The 2005 AISC 360 expresses the above equation in a nondimensional form:

$$\frac{L_{pd}}{r_y} = \left(0.12 + 0.076\left(\frac{M_1}{M_2}\right)\right)\left(\frac{E}{F_y}\right) \tag{14.49c}$$

Equation (14.49c) has been modified in the 2010 AISC 360 to account for nonlinear moment diagrams and for situations in which a plastic hinge does not develop at the brace location corresponding to the larger end moment:

$$\frac{L_{pd}}{r_y} = \left(0.12 - 0.076\left(\frac{M_1'}{M_2}\right)\right)\frac{E}{F_y} \tag{14.49d}$$

where M_{mid} = moment at middle of unbraced length and M_1' = effective moment at end of unbraced length opposite from M_2. When the magnitude of the bending moment at any location within the unbraced length exceeds M_2, $M_1'/M_2 = +1$. Otherwise, $M_1' = M_1$ when $M_{mid} \le (M_1 + M_2)/2$ and $M_1' = 2M_{mid} - M_2 < M_2$ when $M_{mid} > (M_1 + M_2)/2$.

Figure 14.28 shows a comparison of the lateral bracing requirements for two different steel strengths per the AISC LRFD Specification and AISC ASD Specification. Based on Bansal's test results, it is clear that the more relaxed lateral bracing requirements specified in the AISC LRFD Specification are justified.

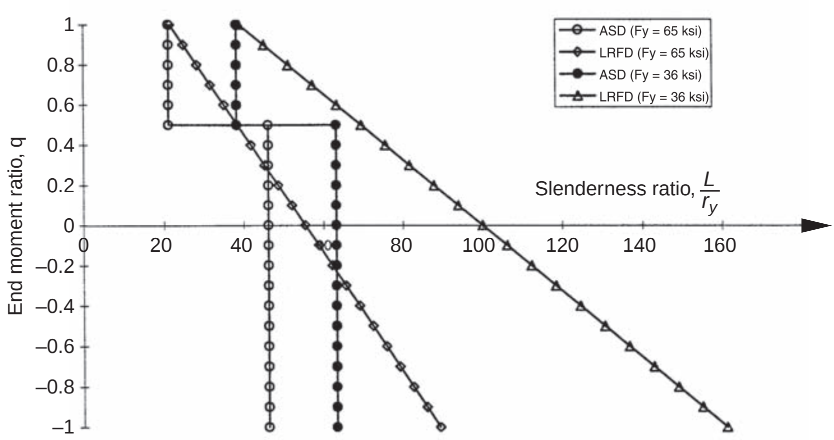

FIGURE 14.28 Comparison of rules for lateral-torsional buckling.

14.7 Code Comparison

A worldwide survey of the classifications of beam section compactness and lateral bracing requirements in major steel design codes was made by SSRC (Ziemian 2010). A similar comparison of the beam section local buckling rules adopted in North America, Australia, and Eurocode 3 was also provided by Bild and Kulak (1991). Except for the design codes in the United States, the codes studied by these researchers have adopted a four-class system. Depending on the width-to-thickness ratio, λ, with respect to three limiting values (λ_{pd}, λ_p, and λ_r), the classification is consistent with the four curves shown in Figure 14.2. Class 1 sections, also known as the plastic sections with $\lambda \leq \lambda_{pd}$, are required for plastic design. Class 2 sections, also termed compact sections with $\lambda_{pd} < \lambda \leq \lambda_p$, do not have sufficient rotation capacity for plastic design. Note that the compact section defined in that case is not the same as that defined in the AISC 360. As mentioned in Section 14.1, the AISC 360 values for λ_{pd} and λ_p for local buckling are merged; that is, compact sections are also plastic sections.

Expressing λ_{pd} for plastic sections in the following general format:

$$\lambda_{pd} = \delta/\sqrt{F_y} \quad \text{in U.S. units} \tag{14.50}$$

facilitates a comparison of the values of θ used in various countries to prevent flange local buckling. Results are presented in Figure 14.29a. Note that the AISC ASD and AISC 360 provide lower and upper bounds to values of θ. Figure 14.29b presents values of θ used for seismic design. Note that the requirements for seismic design are comparable to those of the AISC ASD Specification for plastic design (AISC 1989). A similar comparison for the web local buckling requirements is shown in Figure 14.30.

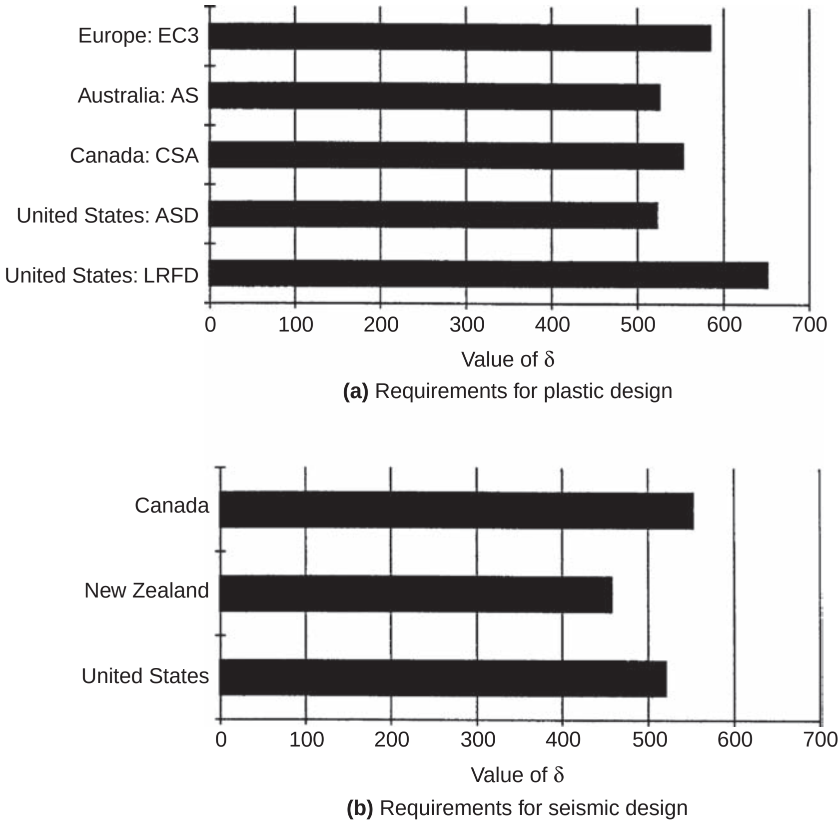

FIGURE 14.29 Comparison of flange local buckling requirements.

It is interesting to compare compactness requirements of seismic codes in the United States and Japan. The Japanese limit state design code (AIJ 1990) considers the interaction of flange and web local buckling modes. For ductility Class 1, which corresponds to a rotation capacity of 4 (Fukumoto and Itoh, 1992, Kato 1989), the following formula is specified:

$$\frac{\left(\frac{b}{t_f}\right)^2}{\left(\frac{200}{\sqrt{\sigma_{yf}}}\right)^2} + \frac{\left(\frac{d}{t_w}\right)^2}{\left(\frac{1270}{\sqrt{\sigma_{yw}}}\right)^2} \leq 1 \quad \text{in S.I. units} \tag{14.51}$$

where σ_{yf} and σ_{yw} are the actual yield stresses of the flange and web materials, respectively. A comparison of the above equation with the AISC LRFD requirements for seismic design is shown in Figure 14.31.

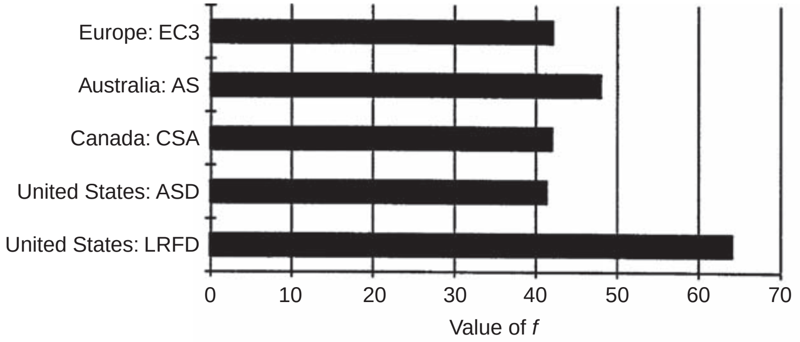

(a) Requirements for plastic design

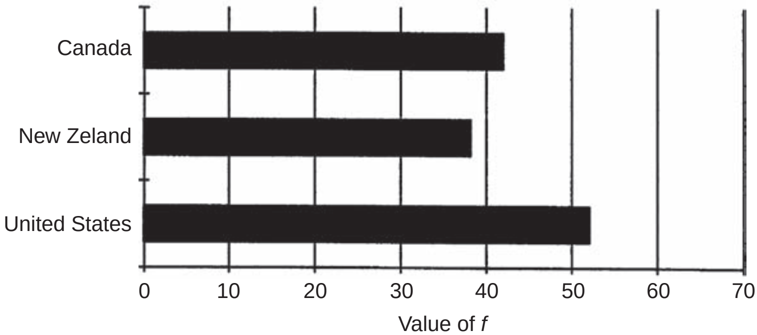

(b) Requirements for seismic design

FIGURE 14.30 Comparison of web local buckling requirements.

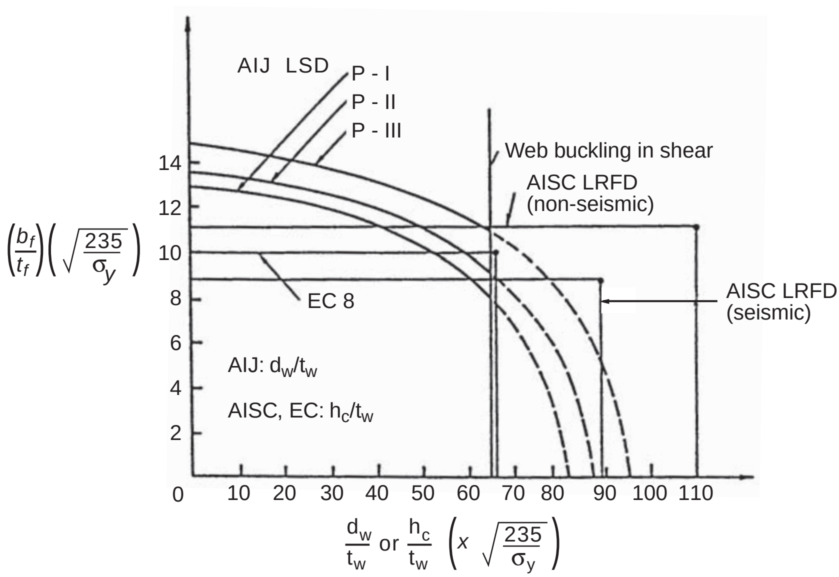

FIGURE 14.31 Comparison of local buckling requirements for Japanese and U.S. seismic provisions for σ_y, in MPa. (*Fukumoto and Itoh 1992.*)

14.8 Interaction of Beam Buckling Modes

The AISC 360 sets limits on the width-thickness ratio of beam flanges and webs to avoid premature local buckling and on the maximum laterally unsupported length (L_b) to delay lateral-torsional buckling. The AISC 360 considers each buckling mode as an independent limit state. The advantage of this design approach lies in its simplicity. However, uncertainties arise because this simple approach ignores the interaction between local buckling and lateral-torsional buckling.

Much test evidence shows that flange local buckling, web local buckling, and lateral-torsional buckling interact. The flange restrains the web and vice versa. This can be easily seen from the physical model of flange local buckling shown in Figure 14.13. In Lay's derivation of the slenderness ratio limit for flange local buckling, web restraint was treated as a spring with positive stiffness. However, if the web buckles prior to the flange, the beneficial restraint from the beam web is lost, and the buckled web may be regarded as a spring with negative stiffness. As a result, the amplitude and wavelength of flange local buckling will be affected by web local buckling.

Section 14.3 discussed the relation between local buckling and lateral-torsional buckling under different moment patterns. Recall that under uniform moment, lateral-torsional buckling triggers flange local buckling, whereas under moment gradient, if adequate lateral bracing is provided, flange buckling occurs first, provided that the yielded zone is sufficiently long to accommodate a full wavelength of the buckle. In the latter case, even though flange buckling will not cause an immediate loss of strength, it triggers lateral-torsional buckling, after which strength is lost. To evaluate the beam rotation capacity, one should consider the interactions of different modes.

To describe this interaction, consider a beam under moment gradient in which flange local buckling has occurred in the yielded compression region. The beam has not buckled laterally, so both halves of the compression flange participate in the flange local buckling. When lateral-torsional buckling occurs, the half-flange that undergoes additional compression in the process of lateral deflection will lose stiffness rapidly because of the local buckle, whereas the other half-flange will behave in a manner similar to that for an unbuckled flange. If the bending stiffness of such a flange is taken to be c_bEI_y, where c_b is a factor with a value less than 1.00, the bending stiffness of the unbuckled half-flange can be approximated as $c_bEI_y/8$. When this value is used, the solid curves shown in Figure 14.26 are obtained for lateral-torsional buckling after a local buckle has occurred. Clearly, the beam is considerably weakened as a result. It may be concluded that local buckling in a beam under moment gradient will lead to lateral buckling and that these two effects in combination are likely to cause a loss in strength.

The onset of local buckling of the compression flange is not by itself the cause of strength deterioration, and additional ductility can be realized once local buckling commences. The compatibility requirement for longitudinal strains across the compression flange in the region of local buckling induces membrane effects that resist the out-of-plane deformations of the flange. However, the onset of lateral buckling in a locally buckled beam results in immediate attainment of the maximum moment and subsequent unloading. This phenomenon is caused by two contributing factors. First, the lateral displacement permits strain compatibility to be maintained as one half of the flange continues to buckle locally in compression. Second, local buckling on the same half of the flange significantly reduces the resistance of the cross section to lateral buckling.

That phenomenon was demonstrated by Dekker (1989). In order to investigate the effect of flange local buckling alone under moment gradient, Dekker fabricated several T-shaped beams in such way that their plastic neutral axis was sufficiently close to the compression flange to eliminate web local buckling. The compression flange of each beam was provided with continuous lateral support to avoid lateral-torsional buckling. Interestingly, flange local buckling was observed to develop in a symmetrical manner about the web (i.e., both halves of the flange buckled toward the neutral axis), and the conventional anti-symmetric flange buckling mode with each half of the compression flange moving in opposite directions was not observed. Figure 14.32

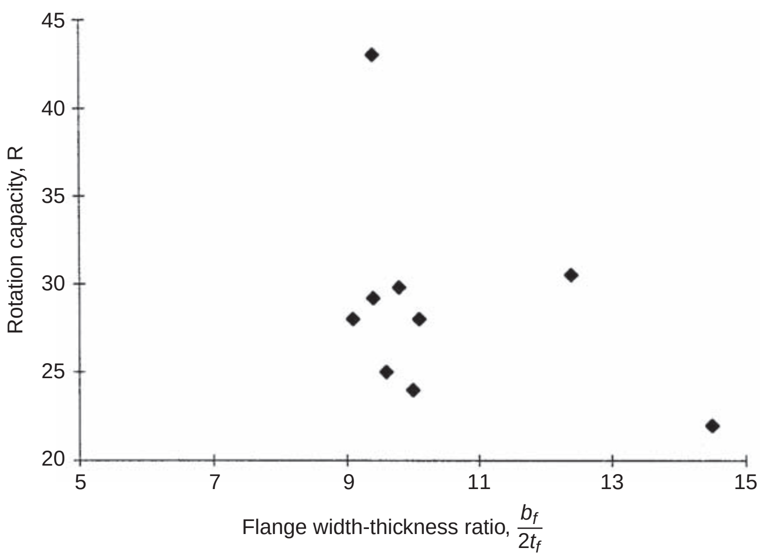

FIGURE 14.32 Flange width-thickness ratio versus rotation capacity based on Dekker's (1989) isolated flange local buckling test results.

summarizes the width-thickness ratios and the rotation capacities of all the specimens tested. Note that $b_f/2t_f$ ratios were as high as 14.5. Dekker reported that flange local buckling did not cause a loss in strength until large rotation capacities (>20) were reached. The typical failure mode involved tensile fracture of the T-beam.

Kemp (1986, 1991, 1996) proposed that beam rotation capacity be related to the slenderness ratio for each of three buckling modes. Kemp normalized the slenderness ratio by the material yield stress of each buckling mode as follows:

$$\text{FLB: } \lambda_f = \frac{b_f/2t_f}{\sqrt{\sigma_{yf}/36}} \quad \text{in U.S. units} \tag{14.52a}$$

$$\lambda_f = \frac{b_f/2t_f}{\sqrt{\sigma_{yf}/250}} \quad \text{in S.I. units} \tag{14.52b}$$

$$\text{WLB: } \lambda_w = \frac{d/t_w}{\sqrt{\sigma_{yw}/36}} \quad \text{in U.S. units} \tag{14.52c}$$

$$\lambda_w = \frac{d/t_w}{\sqrt{\sigma_{yw}/250}} \quad \text{in S.I. units} \tag{14.52d}$$

$$\text{LTB: } \lambda_L = \frac{L_i/r_{yc}}{\sqrt{\sigma_{yf}/36}} \quad \text{in U.S. units} \tag{14.52e}$$

$$\lambda_L = \frac{L_i/r_{yc}}{\sqrt{\sigma_{yf}/250}} \quad \text{in S.I. units} \tag{14.52f}$$

where σ_{yf} and σ_{yw} are the actual yield stresses of the flange and web materials, respectively; L_i is the length from the section of maximum moment to the adjacent point of inflection; and r_{yc} is the radius of gyration of the portion of the elastic section in compression. Other terms have been defined previously.

Based on 44 beam test results reported by Adams et al. (1965), Lukey and Adams (1969), Kemp (1985, 1986), and Kuhlmann (1989), Kemp showed weak relationships between the rotation capacity and the normalized slenderness ratios for each local buckling mode (see Figures 14.33a and b). Figure 14.33c shows that the correlation is improved if the rotation capacity is plotted against $(L_i/r_{yc})(\sqrt{\sigma_{yf}/250})$ for lateral-torsional buckling. To consider all three buckling modes simultaneously, Kemp defined the following parameter:

$$\lambda_e = \lambda_L\left(\frac{\lambda_f}{9}\right)\left(\frac{\lambda_w}{70}\right) \tag{14.53}$$

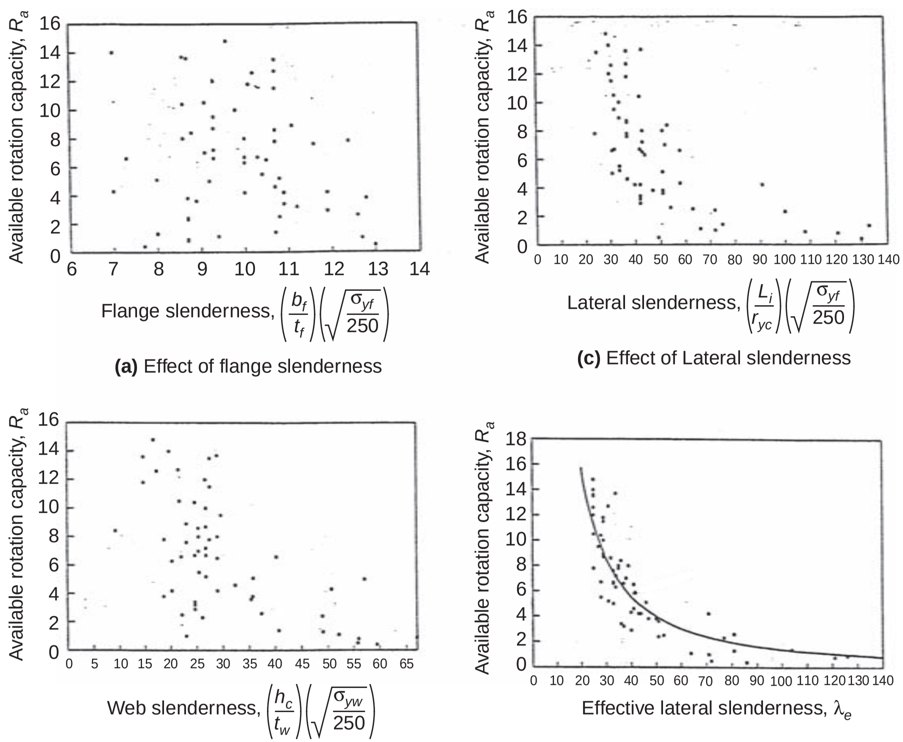

(a) Effect of flange slenderness

(c) Effect of Lateral slenderness

(b) Effect of web slenderness

(d) Effect of effective slenderness ratio

FIGURE 14.33 Relationship between rotation capacity and slenderness ratios; units of σ_y are MPa. (*From Kemp 1996 with permission.*)

Figure 14.33d demonstrates a clear relationship between the rotation capacity, R, and λ_e. An empirical fit to the data yields the following relationship:

$$R = 3.01\left(\frac{60}{\lambda_e}\right)^{1.5} \tag{14.54}$$

The database used by Kemp is based on monotonic testing of small-scale beam specimens. The results shown in Figure 14.33 imply that the buckling rules adopted in modern design codes may need to be improved.

Based on the discussion presented above, several observations can be made (Kemp 1986):

- The antisymmetric flange local buckling may be initiated under the conditions defined in Eq. (14.22). The buckling amplitude will not grow appreciably because of the membrane force associated with compatibility constraints to warping across the flange, unless these constraints are released with the onset of web local buckling or lateral-torsional buckling.
- Web local buckling may occur independently of flange buckling. However, this does not cause significant loss of strength. Web local buckling may release the compatibility constraints and hasten the development of flange buckling.
- Lateral-torsional buckling may be an independent mode of failure or may develop rapidly after flange buckling because of the reduced stiffness of the flange in the plastic region. Lateral-torsional buckling may release the constraints to flange buckling. Once lateral-torsional buckling occurs, the strength of a beam will degrade.
- The current practice of separating beam flexural buckling behavior into three independent limit states may not be appropriate. A design criterion that considers the interaction of three buckling modes is necessary to ensure adequate plastic rotation capacity.

14.9 Cyclic Beam Buckling Behavior

A moment-resisting frame is expected to form a yield mechanism and to displace laterally for a number of cycles during a design earthquake. Because the range of deformation (see Figure 14.1) exceeds the incipient collapse threshold for plastic design, beam plastic rotation demand is generally higher for seismic design.

Unfortunately, the cyclic nature of earthquake-induced excitations also reduces beam plastic rotation capacity. At the material level, the low-cyclic fatigue endurance limit is usually much higher than that required for seismic design, but the Bauschinger effect will reduce the buckling strength of steel elements. For a given displacement amplitude, a beam that would not buckle under monotonic loading may buckle under cyclic loading. Furthermore, a beam that buckles inelastically exhibits permanent deformation after the load is removed. Such residual deformations at both the section and member levels serve as geometric imperfections. Thus, the amplitude of the buckles increases as the number of cycles increases.

The effect of large alternating strains on the cyclic behavior of steel beams has been investigated by Bertero and Popov (1965). Small-scale cantilever beams, M4 × 13 (U.S. shapes) of A7 steel with a mean yield stress of 41 ksi (283 MPa) and a span of 35 in (89 cm), were loaded cyclically to failure. The value of $b_f/2t_f$ (= 5.3) of those beams was within the limit for plastic design, the web was very compact ($h/t_w = 14.4$), and L_b/r_y (=37) was small. The number of cycles required to cause complete fracture and flange local buckling versus the maximum strain at the fixed end of the beam is shown in Figure 14.34a. Of the 11 beams tested, none exhibited local buckling during the first half of the first loading cycle. This was true even in the experiment with imposed strains of 2.5%, which was greater than the strain at the onset of strain-hardening of the material, ε_{st}. Figure 14.34a shows that the number of cycles required to trigger flange local buckling is significantly reduced for cycles at larger strains. However, once flange local buckling occurs, Figure 14.34b also shows that more cycles are needed to fracture the steel beam. The large number of cycles resisted prior to fracture indicates that the low-cycle fatigue endurance of steel itself is generally not a governing factor in seismic applications.

Factors that influence inelastic beam buckling under monotonic loading also apply to cyclic loading. For example, a beam under moment gradient that satisfies the compactness requirements of modern seismic codes is less likely to show significant strength degradation under cyclic loading. Further, it is commonly observed in cyclic testing that once flange local buckling commences, it interacts with web local buckling and, more importantly, lateral-torsional buckling.

Takanashi (1973) conducted monotonic and cyclic testing of simply supported beams of two different grades of steel. The 8-in (20.3-cm) deep wide-flange steel beams tested had $b_f/2t_f = 6.3$ and $d/t_w = 36$. Lateral bracing was provided at both ends of the beam and at midspan to prevent lateral and torsional movements; the value of L_b/r_y was 65 and close to the limit presented in the 1969 AISC Specification.

Figure 14.35 shows the cyclic response of two beams with different yield stresses. For the beam with a yield stress of 41 ksi (282 MPa), Figure 14.35a shows that the beam was able to achieve a cyclic rotation ductility of 3 (or a rotation capacity of 2) after 40 cycles of increasing amplitudes. For a beam with a yield stress of 64 ksi (441 MPa),

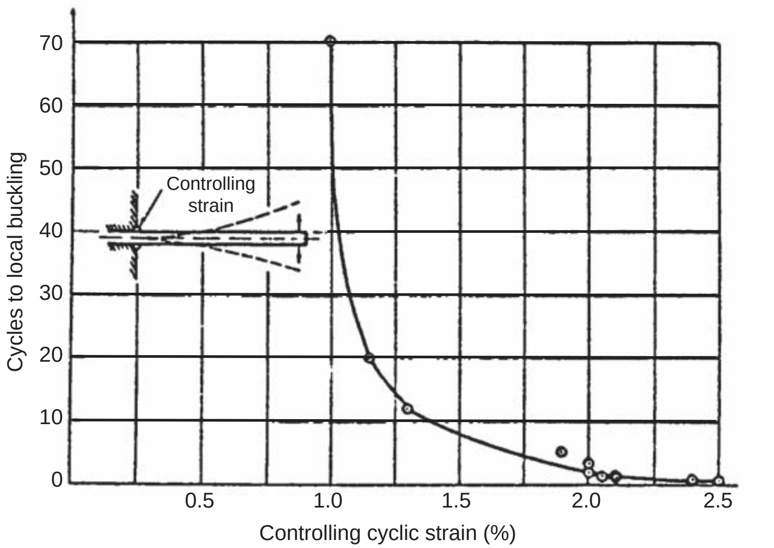

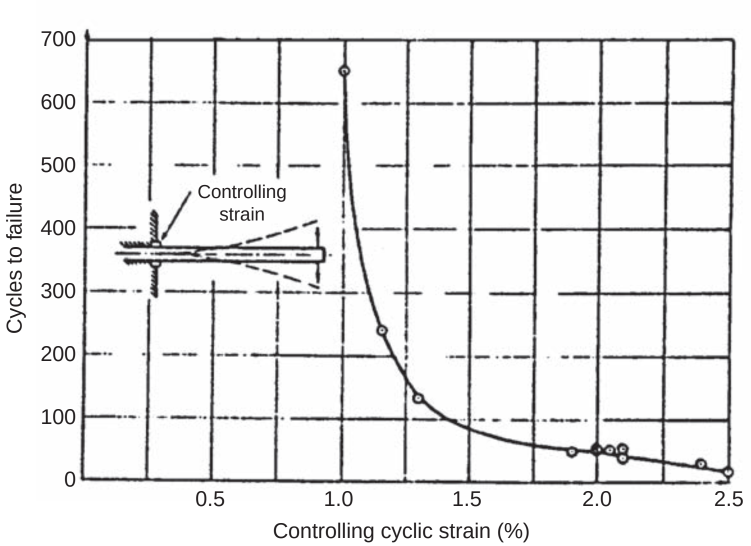

Figure 14.34 Number of cycles to cause flange local buckling and fracture. (*Bertero and Popov 1965.*)

inferior behavior was observed (Figure 14.35b). Stable hysteresis loops could be maintained only for the first 30 cycles up to a rotation ductility of 2. The beam strength degraded significantly because of lateral buckling at a rotation ductility of 2.5. Based on those results, Takanashi concluded that cyclic rotation capacity is significantly lower than monotonic rotation capacity. It should be noted, however,

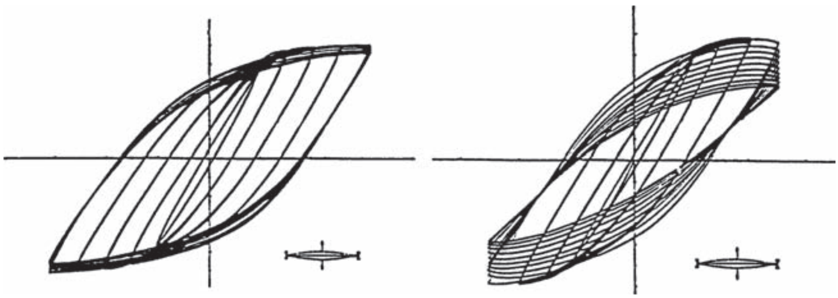

(a) Beam with σ_y = 41 ksi (282 MPa) **(b)** Beam with σ_y = 64 ksi (441 MPa)

FIGURE 14.35 Cyclic behavior of beams with different yield strengths. (*Takanashi 1973.*)

that his conclusion was based on the loading sequence shown in Figure 14.35 for a large number of inelastic cycles. Most steel beams are unlikely to experience that many inelastic cycles in a design earthquake. The cyclic rotation capacities reported by Takanashi may be conservative for seismic design.

Vann et al. (1973) also conducted cyclic and monotonic tests of beams and beam-columns of mild steel. Each specimen was clamped at one end, and a load was cyclically applied at the free end, which was braced laterally. Beam sections chosen were W8 × 13 (W200 × 19 in S.I. units) ($b_f/2t_f$ = 7.8, h/t_w = 29.9) and W6 × 16 (W150 × 24 in S.I. units) ($b_f/2t_f$ = 5.0, h/t_w = 19.1). Specimens of each cross-section were tested with unsupported lengths of $30r_y$ and $60r_y$.

Figure 14.36 shows the hysteresis behavior of a W8 × 13 beam with an unbraced length of $30r_y$. The specimen was cycled at a ductility

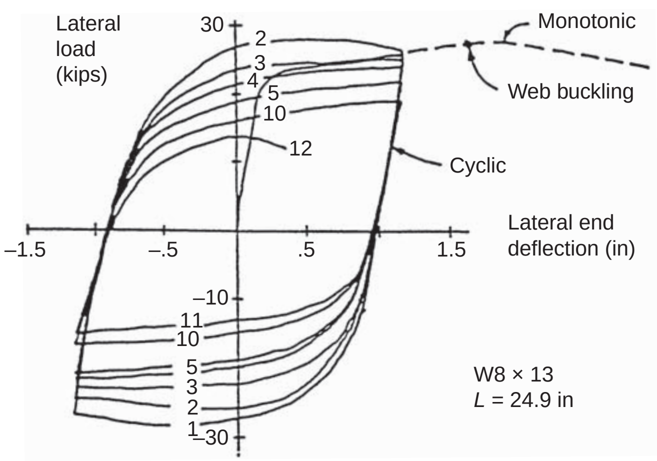

FIGURE 14.36 Beam behavior under cyclic loading. (*Vann et al. 1973.*)

ratio of 7.2. For such a properly braced beam, flange local buckling was first observed in the second half-cycle. Although flange local buckling did not cause an immediate degradation of strength, it did induce web local buckling. The loss of load capacity may be attributed primarily to web local buckling, which began in the fifth half-cycle. Figure 14.36 also demonstrates that the beam's monotonic behavior at large deflections is a reliable indicator of the cyclic behavior; that is, the drop in load following web local buckling in the monotonic test (shown in dashed line) was also observed in the corresponding cyclic test. Note that, in such cyclic tests, beam fracture usually will occur in the crest of a flange buckle and only after many cycles. Occasionally, the fracture occurs between the web and one flange, where the curvature may be high because of web local buckling.

When a beam (W6 × 16) of a more compact section but with twice the slenderness ratio, $L_b/r_y = 60$, was tested, it was observed that the specimen lost strength because of lateral-torsional buckling. Vann et al. observed that the loss of stiffness is much more significant when lateral-torsional buckling and not local buckling, is the dominant mode of failure. They also concluded that the deterioration of strength is severe only when flange local buckling is combined with either web local buckling or lateral-torsional buckling.

The effect of beam slenderness ratio on cyclic response was demonstrated by full-scale testing of an interior beam-column assembly (Noel and Uang 1996). Figure 14.37 shows the dimensions and member sizes

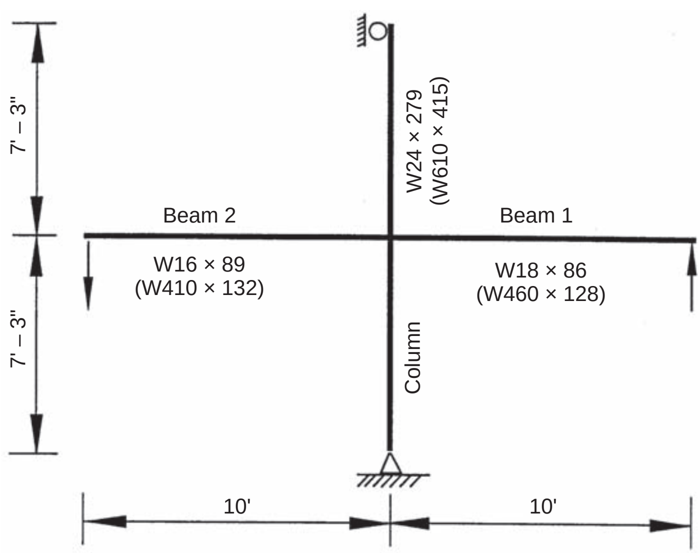

Figure 14.37 Dimensions and U.S. member shapes of test specimen (S.I. shapes in parentheses). (*Noel and Uang 1996.*)

Beam	U.S. Shapes (S.I. Shapes)	F_{yf} (ksi) (MPa)	F_{yw} (ksi) (MPa)	$b_f/2t_f$	h/t_w	L/r_y	Z_x (in^3) (mm^3)
Beam 1	W16 × 89 (W410 × 132)	47.7 (329)	47.5 (328)	5.9	27	39	175 (2,868,000)
Beam 2	W18 × 86 (W460 × 128)	50.0 (344.8)	51.5 (355)	7.2	33.4	36.5	186 (3,048,000)

TABLE 14.2 Beam Properties

of the test specimen. Table 14.2 lists the key parameters for both beams. The plastic moduli of both beams were similar, but because Beam 1 was shallower, its flanges were more compact. Equal and opposite displacements of increasing amplitude were imposed to the beam ends during testing. Each beam-column connection was strengthened with a cover plate and a haunch on the top and bottom flanges, respectively.

The load versus beam tip deflection relationships of the beams are shown in Figure 14.38. Figure 14.39 shows the buckled beams. As expected, Beam 2 experienced more severe buckling. Flange local buckling of the Beam 2 bottom flange was first observed during the first half-cycle at 3.5 in (= 8.9 cm) displacement amplitude at the cantilever tip. During the nine cycles of testing at this amplitude, both the strength and stiffness of Beam 2 degraded continuously. The corresponding hysteresis loops of Beam 1, however, were very stable and highly reproducible. Figure 14.40 demonstrates the variations of the Beam 2 strength in these nine cycles and two subsequent cycles of a displacement amplitude of 5 in. The amplitudes of local buckling and lateral-torsional buckling were measured and are included in Figure 14.40. Although flange local buckling occurred in the first

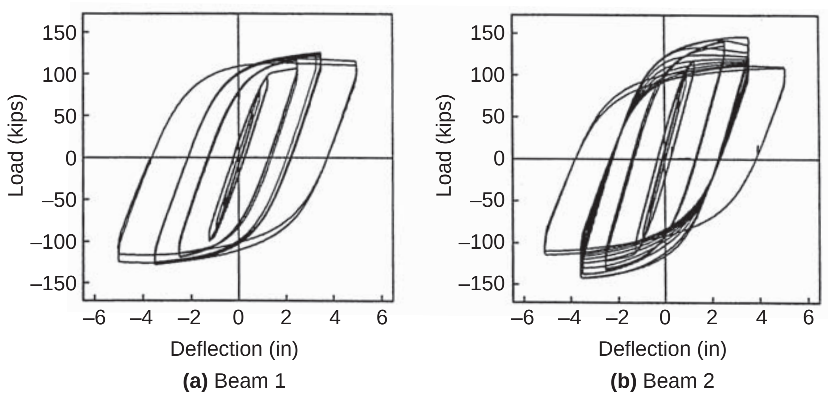

FIGURE 14.38 Load-displacement hysteresis curves. (*Noel and Uang 1996.*)

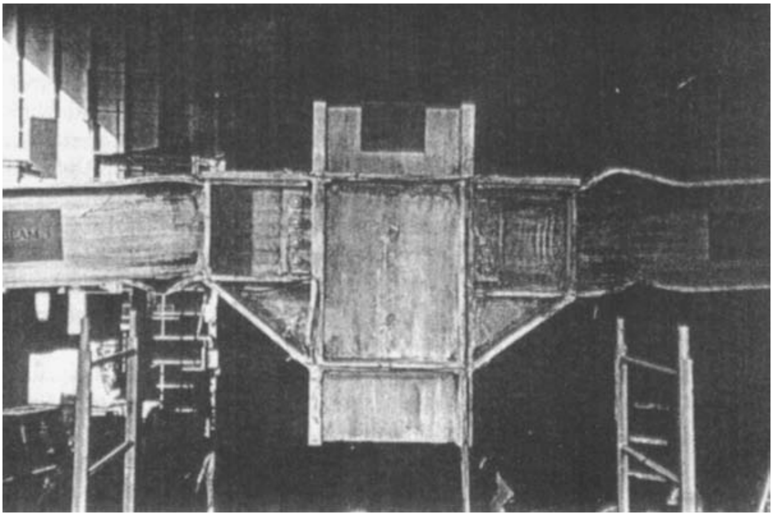

Figure 14.39 Beam-buckling patterns. (*Courtesy of Forell/Elsesser Engineers, Inc.*)

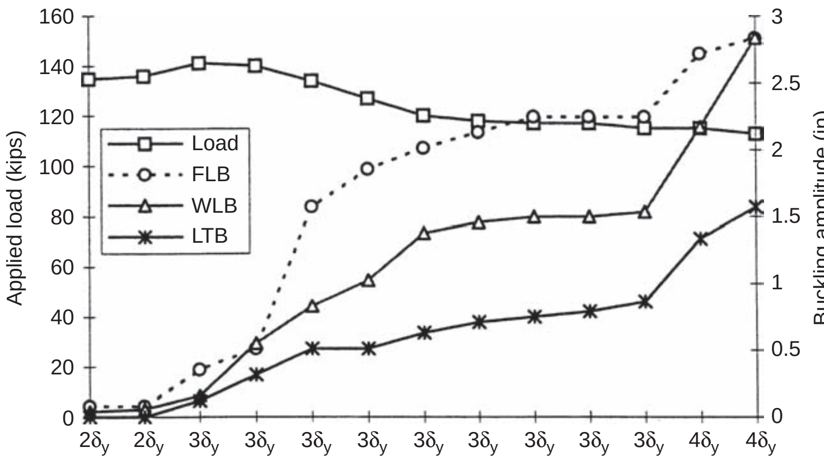

Figure 14.40 Variations of buckling amplitudes. (*Noel and Uang 1996.*)

cycle, the beam strength did not degrade until after the third cycle. From then on, web local buckling and lateral-torsional buckling accompanied flange local buckling, and the strength degraded with each cycle.

More information on the stability of beam under loading can be found in Chapter 19 of the SSRC Stability Guide (Ziemian 2010).

14.10 Self-Study Problem

Problem 14.1

(1) Which usually happens first: lateral torsional buckling, or local buckling?
(2) What is the Kemp (1996) slenderness factor? Does it appear to be an effective approach?
(3) What value has G_{st} for mild steel?

References

Adams, P. F., Lay, M. G., and Galambos, T. V. 1965. "Experiments on High Strength Steel Members." *Bulletin No. 110*, Welding Research Council, pp. 1–16.

AISC. 1986. *Load and Resistance Factor Design Specification for Structural Steel Building,* 1st ed. Chicago: American Institute of Steel Construction.

AIJ. 2002. *Standard for Limit State Design of Steel Structures*. Architectural Institute of Japan.

AISC. 1989. "Allowable Stress Design." *Manual of Steel Construction*, 9th ed. Chicago: American Institute of Steel Construction.

AISC. 1986. *Load and Resistance Factor Design Specification for Structural Steel Buildings*. Chicago, American Institute of Steel Construction.

AISC. 2010a. *Specification for Structural Steel*, ANSI/AISC 360-10, 14th ed. Chicago: American Institute of Steel Construction.

AISC. 1992, 2010b. *Seismic Provisions for Structural Steel Buildings*, ANSI/AISC 341, Chicago: American Institute of Steel Construction.

ASCE-WRC. 1971. *Plastic Design in Steel: A Guide and Commentary.* New York: American Society of Civil Engineers.

Bansal, J. P. 1971. "The Lateral Instability of Continuous Steel Beams." Thesis submitted in partial fulfillment of the requirement for the Degree of Doctor of Philosophy in Engineering. Austin: University of Texas.

Bazant, Z. P., and Cedolin, L. 1991. *Stability of Structures.* New York: Oxford University Press.

Bertero, V. V., and Popov, E. P. 1965. "Effect of Large Alternating Strains of Steel Beams." *Journal of Structural Division, ASCE*, vol. 91, no. ST1, 1–12.

Bild, S., and Kulak, G. L. 1991. "Local Buckling Rules for Structural Steel Members." *Journal of Construction Steel Research,* vol. 20, 1–52.

Bleich, F. 1952. *Buckling Strength of Metal Structures.* New York: McGraw-Hill.

Bulson, P. S. 1969. *The Stability of Flat Plates.* New York: American Elsevier.

Dawe, J. L., and Kulak, G. L. 1986. "Local Buckling Behavior of Beam-Columns." *Journal of Structural Engineering, ASCE*, vol. 112, no. 11, 2447–2461.

Dekker, N. R. 1989. "The Effect of Noninteractive Local and Torsional Buckling on the Ductility of Flanged Beams." *Civil Engineer in South Africa*, April, 121–124.

Fukumoto, Y., and Itoh, Y. 1992. "Width-to-Thickness Ratios for Plate Elements in Earthquake Engineering Design of Steel Structures," in *Stability and Ductility of Steel Structures Under Cyclic Loading* (Fukumoto, Y., and Lee, G., editors). Boca Raton, FL: CRC Press.

Galambos, T. V. 1963. "Inelastic Lateral Buckling of Beams." *Journal of the Structural Division, ASCE*, vol. 89, no. ST5, 217–241.

Galambos, T. V. 1968. "Deformation and Energy Absorption Capacity of Steel Structures in the Inelastic Range." AISI Bulletin No. 8.

Galambos, T. V., and Lay, M. G. 1965. "Studies of the Ductility of Steel Structures." *Journal of the Structural Division, ASCE*, vol. 91, no. ST4, 125–151.

Gerard, G., and Becker, H. 1957. *Handbook of Structural Stability: Part I—Buckling of Flat Planes*, Technical Note 3871 (Section 7.3). Washington, D. C.: National Advisory Committee for Aeronautics.

Haaijer, G. 1957. "Plate Buckling in the Strain-Hardening Range." *Journal of Engineering Mechanics Division, ASCE*, vol. 83, no. EM2, Paper 1212, 1–45.

Haaijer, G., and Thurlimann, B. 1958. "On Inelastic Buckling in Steel." *Journal of Engineering Mechanics Division, ASCE*, vol. 84, no. EM2, Paper 1581, 1–47.

Kato, B. 1989. "Rotation Capacity of H-Section Members as Determined by Local Buckling." *Journal of Construction Steel Research*, vol. 13, no. 2–3, 95–109.

Kemp, A. R. 1984. "Slenderness Limits Normal to the Plane of Bending for Beam-Columns in Plastic Design." *Journal of Constructional Steel Research*, vol. 4, 135–150.

Kemp, A. R. 1985. "Interaction of Plastic Local and Lateral Buckling." *Journal of Structural Engineering, ASCE*, vol. 111, no. 10, 2181–2196.

Kemp, A. R. 1986. "Factors Affecting the Rotation Capacity of Plastically Designed Members." *The Structural Engineer*, vol. 69, no. 5, 28–35.

Kemp, A. R. 1991. "Available Rotation Capacity in Steel and Composite Beam." *The Structural Engineer,* vol. 69, no. 5, 88–97.

Kemp, A. R. 1996. "Inelastic Local and Lateral Buckling in Design Codes." *Journal of Structural Engineering, ASCE,* vol. 122, no. 4, 374–382.

Kirby, P. A., and Nethercot, D. A. 1979. *Design for Structural Stability.* New York: John Wiley and Sons.

Kuhlmann, U. 1989. "Definition of Flange Slenderness Limits on the Basis of Rotation Capacity Values." *Journal of Constructional Steel Research*, vol. 14, 21–40.

Lay, M. G. 1965a. "Yielding of Uniformly Loaded Steel Members." *Journal of Structural Division, ASCE*, vol. 91, no. ST6, 49–65.

Lay, M. G. 1965b. "Flange Local Buckling in Wide-Flange Shapes." *Journal of Structural Division, ASCE*, vol. 91, no. ST6, 95–116.

Lay, M. G., and Galambos, T. V. 1965. "Inelastic Steel Beams under Uniform Moment." *Journal of Structural Division, ASCE*, vol. 91, no. ST6, 67–93.

Lay, M. G., and Galambos, T. V. 1967. "Inelastic Beams under Moment Gradient." *Journal of Structural Division, ASCE*, vol. 93, no. ST1, 381–399.

Lee, G. C., and Galambos, T. V. 1962. "Post-Buckling Strength of Wide-Flange Beams." *Journal of Engineering Mechanics Division, ASCE*, vol. 88, no. EM 1, 59–75.

Lukey, A. F., and Adams, P. F. 1969. "Rotation Capacity of Beams under Moment Gradient." *Journal of Structural Division, ASCE*, vol. 95, no. ST6, 1173–1188.

Maquoi, R. 1992. "Behavior of Plate Components," in *Stability Problems of Steel Structures* (Ivanyi, M., and M. Skaloud, M., editors). New York: Springer-Verlag.

Massonnet, C. E., and Save, M. A. 1965. *Plastic Analysis and Design, Volume 1: Beams and Frames.* New York: Blaisdell Publishing Company.

Noel, S., and Uang, C. M. 1996."Cyclic Testing of Steel Moment Connections for the San Francisco Civic Center Complex (Test Report to HSH Design/Build)." *TR-96/07*. San Diego: University of California.

Shanley, F. R. 1947. "Inelastic Column Theory." *Journal of Aeronautical Sciences*, vol. 14, no. 5, 261–264.

SSRC. 1991. *A World Review: Stability of Metal Structures* (Beedle, L. S., editor). Bethlehem, Pennsylvania: Structural Stability Research Council.

Takanashi, K. 1973. "Inelastic Lateral Buckling of Steel Beams Subjected to Repeated and Reversed Loadings," *Proceedings of the 5th World Conf. Earthquake Engineering*, vol. 1, 795–798. Rome: International Association for Earthquake Engineering.

Timoshenko, S. P., and Gere, J. M. 1961. *Theory of Elastic Stability.* New York: McGraw-Hill.

Trahair, N. S. 1993. *Flexural-Torsional Buckling of Structures.* Boca Raton, FL: CRC Press.

Uang, C. M, and Fan, C. C. 2001. "Cyclic Stability Criteria for Steel Moment Connections with Reduced Beam Section." *Journal of Structural Engineering, ASCE*, vol. 127, no. 9, 1021–1027.

Vann, W. P., Thompson, L. E., Whalley, L. E., and Ozier, L. D. 1973. "Cyclic Behavior of Rolled Steel Members." *Proceedings of the 5th World Conf. Earthquake*

Engineering, vol. 1, 1187–1193. Rome: International Association for Earthquake Engineering.

Von Kármán, T., Sechler, E. E., and Donnell, L. H. 1932. "The Strength of Thin Plates in Compression." *Transactions, ASME*, vol. 54, MP 54–55.

White, M. W. 1956. "The Lateral-Torsional Buckling of Yielded Structural Steel Members," *Fritz Engineering Lab. Rep. No. 205 E8*. Bethlehem, PA: Lehigh University.

Yura, J. A., Galambos, T. V., and Ravindra, M. K. 1978. "The Bending Resistance of Steel Beams." *Journal of Structural Engineering, ASCE*, vol. 104, no. 9, 1355–1370.

Ziemian, R. D. (editor). 2010. *Guide to Stability Design Criteria for Metal Structures*, 6th Edition. Hoboken, NJ: Wiley.

Index

M

P

S